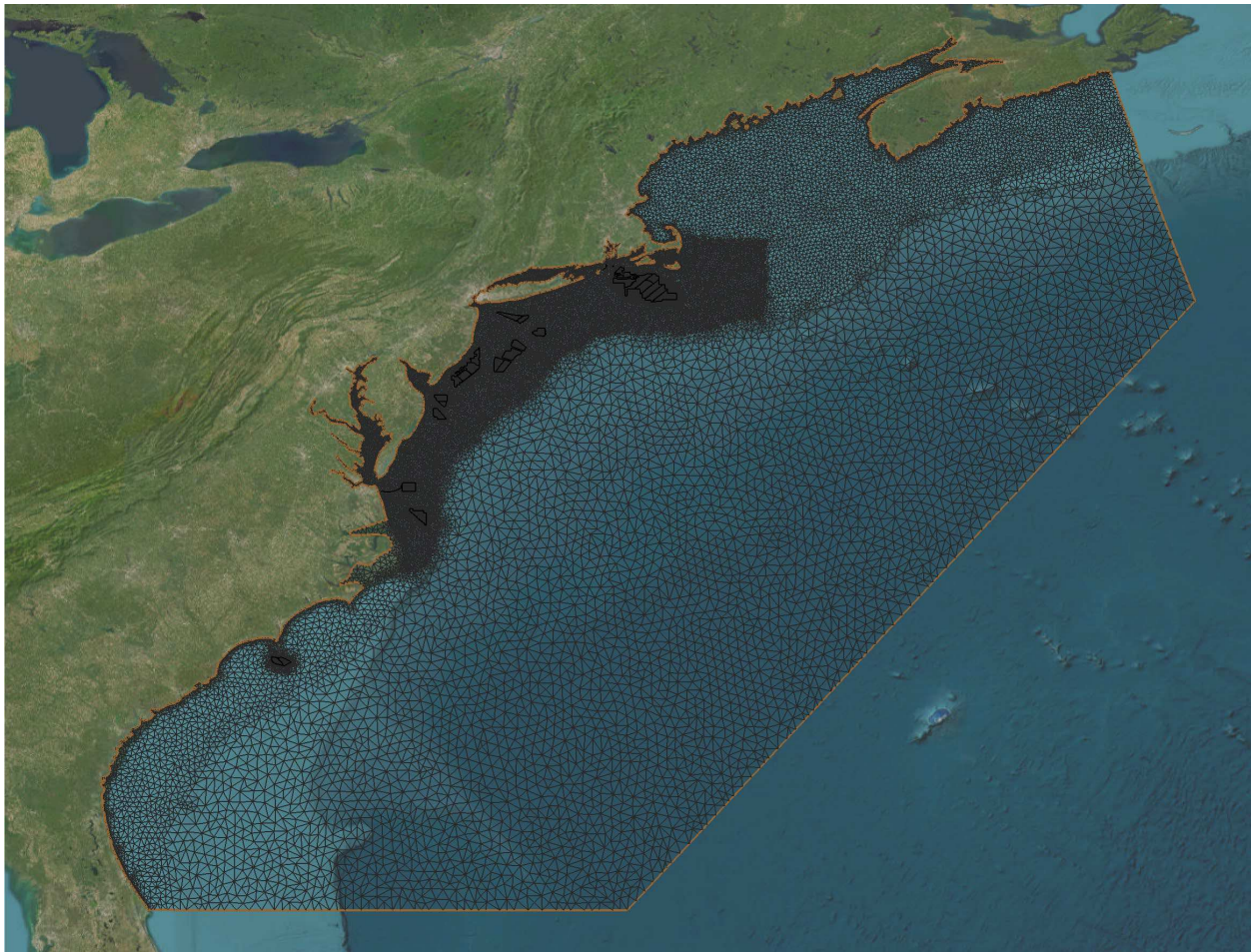


Offshore Wind Impact on Oceanographic Processes: North Carolina to New York - DHI



Offshore Wind Impact on Oceanographic Processes: North Carolina to New York - DHI

March 2025

Authors:

Thomas L. Johnson
Eleanor Simpson
Michael A. Bell
Joshua Jon van Berkel
Ole Svenstrup Petersen
Flemming Thorbjorn Hansen
Benjamin Hernandez
Yong Kai Saw
Lars O. Mortensen
David B. Snyder
Frank Thomsen

Prepared under BOEM Contract 140M0122C0010
by
DHI Water & Environment, Inc.
141 Union Boulevard, Suite 320
Lakewood, Colorado 80235
USA

DISCLAIMER

This study concept, oversight, and funding were provided by the U.S. Department of the Interior, Bureau of Ocean Energy Management (BOEM), Environmental Studies Program, Washington, DC, under Contract Number 140M0122C0010. This report has been technically reviewed by BOEM, and it has been approved for publication. The views and conclusions contained in this document are those of the authors and should not be interpreted as representing the opinions or policies of BOEM, nor does mention of trade names or commercial products constitute endorsement or recommendation for use.

REPORT AVAILABILITY

Download a PDF file of this report at https://espis.boem.gov/Final%20Reports/BOEM_2025-015.pdf.

Visit BOEM's website to [search other studies](#) funded by BOEM's Environmental Studies Program.

CITATION

Johnson TL, Simpson E, Bell MA, van Berkel JJ, Svenstrup Petersen O, Hansen FT, Hernandez B, Saw YK, Mortensen LO, Snyder DB, Thomsen F: 2024. Offshore Wind Impact on Oceanographic Processes: North Carolina to New York. Sterling (VA): U.S. Department of the Interior, Bureau of Ocean Energy Management. 336 p. Report No.: OCS Study BOEM 2025-015.

ABOUT THE COVER

Cover image (Image of model domain and mesh with Offshore Wind Farms indicated). Used with permission. All rights reserved.

ACKNOWLEDGMENTS

This project was supported by the Bureau of Safety and Environmental Enforcement (BSEE), the United States Department of the Interior (DOI); on behalf of the Bureau of Ocean Energy Management (BOEM) under contract number 140M0122C0010. We would like to thank the BOEM supervisors for this project: Ms. Jennifer Draher (Oceanographer and Contracting Officer Representative), Dr. Thomas Kilpatrick (Oceanographer), Mr. Brian Hooker (Marine Biologist), Dr. Ursula Howson (Fish Biologist) and Mr. Travis Washington (Meteorologist) all of whom provided us valuable advice and suggestions for this study.

Contents

List of Figures.....	vii
List of Tables.....	xvii
List of Abbreviations and Acronyms.....	xix
Executive Summary	1
1 Introduction.....	8
1.1 Project Background, Objectives, and General Approach	8
1.1.1 Project Background.....	8
1.1.2 Project Objectives and Sub-Objectives.....	8
1.1.3 General Approach	9
1.2 Project Scenarios and Decisions	10
1.2.1 Selection of Fisheries Species Larvae.....	10
1.2.2 Key Hydrodynamic Model Decisions.....	10
1.2.3 OSW Build-out Scenarios	10
2 Baseline Hydrodynamic Model Input Data.....	13
2.1 Overview of Geographic Coverage.....	13
2.2 Bathymetric Data.....	13
2.3 Meteorological Data	14
2.4 Oceanographic Data	14
2.5 Astronomical Tide Data.....	15
2.6 Boundary Conditions with Combined Oceanographic and Tidal Forcing	15
2.7 River Discharge.....	15
2.8 Observational Data Sources	15
2.8.1 Current Observational Data Sources	16
2.8.2 Water Level Observational Data Sources	17
2.8.3 Wave Observational Data Sources.....	18
2.8.4 Sea Temperature Observational Data Sources	19
3 Baseline Oceanography Review, Hydrodynamic Model Setup, and Baseline Results	21
3.1 Oceanographic Processes Review	21
3.2 Overview, Model Domain and Setup	23
3.2.1 Model Domain	23
3.2.2 Hydrodynamic Current Model Setup.....	24
3.2.3 Spectral Wave Model Setup.....	26
3.3 Baseline Validation.....	27
3.3.1 Baseline Wave Validation	27

3.3.2	Baseline Water Level Validation	31
3.3.3	Baseline Current Validation.....	33
3.3.4	Baseline Temperature Validation	38
3.3.5	Baseline Density Stratification Validation.....	50
3.3.6	Hydrodynamic Baseline Calibration Conclusions	52
4	Hydrodynamic Model Methodology Including Wind Turbines.....	56
4.1	Overview	56
4.1.1	Offshore Wind Farm Scenarios.....	56
4.1.2	Modeled 12 MW Wind Turbine Generator Configuration.....	63
4.1.3	Modeled 15 MW Wind Turbine Generator Configuration.....	65
4.2	Calculations of Wind Turbine Foundation Drag Coefficient.....	66
4.3	Wind Turbine Wake Loss Model	70
4.3.1	PyWake Overview	71
4.3.2	PyWake Description	71
4.3.3	PyWake Model Set-Up.....	73
4.3.4	Wind Modification	74
4.3.5	PyWake Conclusions	82
5	Hydrodynamic Model Baseline vs. Scenario Results	83
5.1	Overview	83
5.2	Changes in Current Fields	83
5.2.1	Relative Weighting of Monopile Drag vs. Wind Wake Losses	83
5.2.2	Sensitivity to PyWake.....	85
5.3	Particle Tracking	92
5.4	Effects on Waves	95
5.5	Combined Effects of Current and Waves on Bed Shear Stress and Sediment Mobility.....	99
5.6	Effects on Temperature.....	105
5.6.1	Effects on Temperature Stratification.....	105
5.6.2	Effects on Sea Surface Temperature.....	109
5.7	Other Effects on Oceanic Parameters	112
5.7.1	Sea Surface Height.....	112
5.7.2	Sea Surface Salinity.....	115
5.8	Hydrodynamic Model vs. Scenario Conclusions.....	118
5.8.1	Discussion of Specific Wind Wake Studies.....	118
5.8.2	Discussion of Chen et al. (2024) Study.....	119
6	Larval Dispersal Modeling Analyses - Methodologies	121
6.1	General Approach	121

6.1.1	Overview of Modeling Steps	121
6.1.2	Overview of Results Post-Processing.....	122
6.2	Agent-Based Model Approach	126
6.2.1	Background on ABM	126
6.2.2	Rationale for Agent-Based Modeling	128
6.2.3	Approach for Larvae Agent-Based Modeling	129
6.2.4	Ensemble Modeling Approach	133
6.3	Connectivity Analysis Approach.....	134
6.4	Agent-Based Model Set-Up and Parameterization.....	134
6.4.1	Applied Datasets	134
6.4.2	Sea Scallop	139
6.4.3	Surfclam	150
6.4.4	Summer Flounder.....	164
6.4.5	Horizontal and Vertical Dispersion Calibration.....	176
6.5	Ensemble Initialization Set-up.....	177
6.6	Connectivity Analysis Set-up.....	178
6.6.1	Connectivity Analyses	178
6.7	Agent-Based Modeling Evaluation Method.....	183
6.7.1	Pattern 1: Spatial Distribution.....	183
6.7.2	Pattern 2: Temporal Development	184
6.7.3	Pattern 3: Vertical Distribution.....	184
6.8	Results Post Processing	184
6.8.1	Baseline Post Processing	184
6.8.2	OSW Buildout Scenarios Analyses.....	185
6.9	ABM Model Performance and Calibration.....	186
7	Larval Dispersal Modeling Baseline Results and Analysis	187
7.1	Sea Scallop	189
7.1.1	Inter-Annual Variability in Sea Scallop Settlement.....	189
7.1.2	Baseline Results for 2017	190
7.1.3	Baseline Results for 2018	192
7.1.4	Baseline Results for 2020	194
7.2	Surfclam	196
7.3	Summer Flounder	200
7.4	Calibration and Evaluation of Baseline ABM Results	202
7.4.1	Sea Scallop	202
7.4.2	Surfclam	208
7.4.3	Summer Flounder.....	213

8	Larval Dispersal Modeling Scenario Results and Analysis	216
8.1	Presentation of Results	216
8.2	Interpretation of Results Plots and Charts	218
8.3	Scenario 5: 15 MW Full Build-out	221
8.3.1	Sea Scallop	221
8.3.2	Surfclam	241
8.3.3	Summer Flounder.....	247
8.4	Scenario 4: 12 MW Full Build-out	256
8.4.1	Sea Scallop	256
8.4.2	Surfclam	263
8.4.3	Summer Flounder.....	270
8.5	Sensitivity Analysis – Double the Wind-wake Effect for 15 MW Full Build-out	277
9	Larval Dispersal Modeling Conclusions	284
9.1	Baseline Larval Dispersal Evaluation.....	284
9.2	OSW Induced Changes in Settlement Dispersal	285
9.2.1	Sea Scallop and Surfclam.....	285
9.2.2	Summer Flounder.....	286
9.3	OSW Induced Changes to Connectivity.....	288
9.4	Relevance of Changes in Larval Transport and Settlement	288
10	Summary and Follow-up Research.....	292
10.1	Analysis Explanations	292
10.1.1	Hydrodynamics.....	292
10.1.2	Larval Dispersal.....	293
10.2	Follow-up Research	294
10.2.1	Localized Analyses - ABM	294
10.2.2	Observations and Modeling to Support Improvement to the Hydrodynamic Model OSW Farm Monopile and WTG Parameterization	294
11	References.....	296
11.1	References: Hydrodynamics	296
11.2	References: Wind Turbine Wake Loss Model.....	300
11.3	References: Agent-Based Models and Methods	302
11.4	References: Sea Scallop.....	307
11.5	References: Surfclam.....	309
11.6	References: Summer Flounder.....	310

Appendix A: Supplementary Hydrodynamic Modeling Results

Appendix B: Agent-Based Model Overview, Design Concepts and Details (ODD) Protocol

Appendix C: Supplementary ABM Modeling Results

Appendix D: Connectivity Mapping Overview, Design Concepts and Details (ODD) Protocol

List of Figures

Figure 1.1. Wind Energy Areas	11
Figure 2.1. Model Domain Extent from Nova Scotia to Florida	13
Figure 2.2. Acoustic Doppler Current Profiler (ADCP) Measurement Locations	16
Figure 2.3. Image Showing the High Frequency Radar Observation (HFRO) Coverage on the U.S. East Coast.....	17
Figure 2.4. Water Level Measurement Locations	18
Figure 2.5. Location of NDBC and Other Wave Buoys Used in the Wave Model Verification	19
Figure 2.6. Location of Sea Temperature Point Measurements Used in the Model Temperature Verification	20
Figure 3.1. Map of the Western North Atlantic Ocean Currents	22
Figure 3.2. Map of Mid-Atlantic Bight.....	22
Figure 3.3. Sea Surface Temperature (Winter).....	22
Figure 3.4. Sea Surface Temperature (Annual Range)	22
Figure 3.5. Density Stratification in the Mid-Atlantic Bight	23
Figure 3.6. Hydrodynamic Model Mesh for the HDM.....	24
Figure 3.7. Validation of H_{m0} Model Results Using Long Island Wave Time Series.....	28
Figure 3.8. Validation of Model Results Using Long Island Station Wave Rose Plot.....	29
Figure 3.9. Validation of Model Results by Frequency of Occurrence Using Long Island Station H_{m0} Measurements	29
Figure 3.10. Long Island Wave H_{m0} Scatter Plot of Measurement Against Model Results	30
Figure 3.11. Validation of Model Results Using Long Island Mean Wave Direction Time Series	30
Figure 3.12. Validation of Model Results by Frequency of Occurrence Measurement Using Long Island Station Mean Wave Direction Measurements	31
Figure 3.13. Validation of Model Time Series Results Using Atlantic City Water Level Measurements	31
Figure 3.14. Validation of Model Frequency of Occurrence Results Using Atlantic City Water Level Measurements	32
Figure 3.15. Model Scatter Plot Results Using Atlantic City Water Level of Measurements.....	32
Figure 3.16. Validation of Model Time Series Current Speed Results Using NYSERDA 06S ADCP Current Speed Measurements	33
Figure 3.17. Validation of Model Rose Plots Results Using NYSERDA 06S ADCP Measurements	34
Figure 3.18. Validation of Model Frequency of Occurrence Current Speed Results Using NYSERDA 06S ADCP Current Speed Measurements.....	34

Figure 3.19. Model Scatter Plot Results Using NYSERDA 06S ADCP Measurements	35
Figure 3.20. High Frequency Radar Observation (HFRO) vs. Model (SSC MIKE3) Results 1 January 2017	36
Figure 3.21. High Frequency Radar Observation (HFRO) vs. Model (SSC MIKE3) Results 1 March 2017	36
Figure 3.22. High Frequency Radar Observation (HFRO) vs. Model (SSC MIKE3) Results 1 June 2017	37
Figure 3.23. High Frequency Radar Observation (HFRO) vs. Model (SSC MIKE3) Results 1 October 2017	37
Figure 3.24. High Frequency Radar Observation (HFRO) vs. Model Surface Current Speed Bias for the Year 2017.....	38
Figure 3.25. Validation of Model Time Series Results Using Barnegat, NJ Sea Temperature Measurements	39
Figure 3.26. Validation of Model Frequency of Occurrence Results Using Barnegat, NJ Sea Temperature Measurements	39
Figure 3.27. Scatter Plot Results Using Barnegat, NJ Sea Temperature Measurements.....	40
Figure 3.28. Baseline Sea Surface Temperature: OSTIA Satellite Analysis (left), Model (center) and Difference (right)	41
Figure 3.30. Average Temperature Transects March to June (2017 & 2018 Model Results).....	43
Figure 3.31. Average Temperature Transects July to October (2017 & 2018 Model Results).....	44
Figure 3.32. Pioneer Array Station Locations – Upstream Inshore, Central Inshore, and Central Offshore	45
Figure 3.34. Average Model Temperature SW to NE Transects from March to June	48
Figure 3.35. Average Model Temperature SW to NE Transects from July to October.....	49
Figure 3.36. Density Stratification Observations (kgm^{-3}) from O'Reilly & Zetlin (1998) June-August 1977-1988 and Model Results for 2017, 2018, & 2020	51
Figure 4.1. WEAs Along the East Coast Including the Names of the WEAs.....	59
Figure 4.2. WTG Locations for MA-RI.....	60
Figure 4.3. WTG Locations for NY Bight (Northern Concessions)	60
Figure 4.4. WTG Locations for NY Bight (Mid Concessions).....	61
Figure 4.5. WTG Locations for NY Bight (Southern Concessions).....	61
Figure 4.6. WTG Locations for MD-DE	62
Figure 4.7. WTG Locations for VA-NC.....	62
Figure 4.9. Illustration of the IEA Wind 15 MW Reference Wind Turbine Generation.....	64
Figure 4.10. Thrust and Power Extraction Curve for the 12 MW WTG	65

Figure 4.11. Thrust and Power Extraction Curve for the 15 MW WTG	66
Figure 4.12. CFD Simulation of a Stratified Flow Around a Bridge Pier	67
Figure 4.13. Computational Fluid Dynamics (CFD) Processes	68
Figure 4.14. Illustration of the Velocity and Density Field	70
Figure 4.15. Conceptual Framework of the Wind Wake Loss Model.....	73
Figure 4.16. Calculated Wind Wake Velocity Deficits in an Idealized Wind Farm.....	74
Figure 4.17. Panel Illustrates the Overlaid Footprint of the Wake Deficit Area from PyWake vs. CFSR from Johnson et al. (2021)	75
Figure 4.18. PyWake Wind Field Modification Compared to 1 st Generation Wind Wake Model Used in Johnson et al. (2021) as a Function of CFSR Undisturbed Wind Speed at 10 m Height.....	76
Figure 4.19. PyWake Wind Field Difference File Modified to the HDM Grid Spacing	76
Figure 4.20. Baseline CFSR Wind Field (left) and the Modified Forcing File (right) for the 15 MW Full Build-Out (Scenario 5).....	77
Figure 4.21. PyWake Wind Speed Changes Due to the 12 MW WTG Wind Farms	78
Figure 4.22. Difference in Wind Speed at 10 m Elevation 95 th Percentile Non-Exceedance Probability, Scenario 5: 15 MW Full Build-Out - Baseline.....	79
Figure 4.23. Difference in Wind Speed at 10 m Elevation 95 th Percentile Non-Exceedance Probability, Scenario 5: 15 MW Full Build-Out - Baseline.....	80
Figure 4.24. Difference in Wind Speed at 10 m Elevation 95 th Percentile Non-Exceedance Probability, Scenario 5: 15 MW Full Build-Out - Baseline.....	81
Figure 4.25. Difference in Wind Speed at 10 m Elevation 95 th Percentile Non-Exceedance probability, Scenario 5: 15 MW Full Build-Out - Baseline.....	82
Figure 5.1. Time Series of Change in Surface Current Speed in the MA-RI WEA for 15 MW Full Build-out (Scenario 5) Due to Wind Wake Only and Monopile Foundation Drag Only.....	83
Figure 5.2. Change in Surface Currents (dCS) Due to WTG Wakes (Wind) and WTG Foundations (Tower)	84
Figure 5.3. 95 th Percentile Non-Exceedance Probability Baseline Depth Averaged Current Speed Differences in Study Area	85
Figure 5.4. 95 th Percentile Non-Exceedance Probability (Scenario 4 – Baseline) Depth Averaged Current Speed Differences in Study Area	86
Figure 5.5. 95 th Percentile Non-Exceedance Probability (Scenario 5 – Baseline) Depth Averaged Current Speed Differences in Study Area	87
Figure 5.6. 95 th Percentile Non-Exceedance Probability (Sensitivity: 15 MW Full Build-Out PyWake doubled – Baseline) Depth Averaged Current Speed Differences in Study Area.....	87
Figure 5.7. 95 th Percentile Non-Exceedance Probability Depth Averaged Current Speed Differences in MA-RI Area for Scenarios 4, 5, and the Sensitivity Analysis (FBO - Full Build-Out)	89

Figure 5.8. 95 th Percentile Non-Exceedance Probability Depth Average Current Speed Differences in the NY Bight and MD-DE Area for Scenario 4, 5, and Sensitivity Analysis (FBO - Full Build-Out).....	89
Figure 5.9. 95 th Percentile Non-Exceedance Probability Depth Averaged Current Speed Differences in the VA-NC Area for Scenario 4, 5, and the Sensitivity Analysis (FBO – Full Build-Out)	90
Figure 5.10. 95 th Percentile Non-Exceedance Probability Depth Averaged Current Speed Differences in the NC-SC Area for Scenarios 4, 5, and the Sensitivity Analysis (FBO – Full Build-Out)	90
Figure 5.11. Particle Tracking Model Particle Release Points.....	93
Figure 5.12. Scenario 1: Baseline Settled Particle Tracking Results	93
Figure 5.13. Scenario 5: 15 MW Full Build-Out Settled Particle Tracking Results	94
Figure 5.14. Difference (Scenario 5 – Baseline) Settled Particle Tracking Results.....	94
Figure 5.15. Significant Wave Height, H_{m0} 95 th Percentile Non-Exceedance Probability Plot for Scenario 1: Baseline	96
Figure 5.16. Exceedance Difference in H_{m0} for 95 th Percentile Non-Exceedance Probability – Full Model Domain	96
Figure 5.17. 95 th Percentile Non-Exceedance Probability H_{m0} Difference – MA-RI Region	97
Figure 5.18. 95 th Percentile Non-Exceedance Probability H_{m0} Difference – NY Bight and MD-DE Region.....	97
Figure 5.19. 95 th Percentile Non-Exceedance Probability H_{m0} Difference – VA-NC Region	98
Figure 5.20. 95 th Percentile Non-Exceedance Probability H_{m0} Difference – NC-SC Region	99
Figure 5.21. 95 th Percentile Non-Exceedance Probability Bed Shear Stresses in the Model Domain Scenario 1: Baseline	101
Figure 5.22. 95 th Percentile Non-Exceedance Probability Bed Shear Stresses in the Model Domain Scenario 5: 15 MW Full Build-Out.....	101
Figure 5.23. 95 th Percentile Non-Exceedance Probability RMS Bed Shear Stress Difference Under Combined Waves & Current	102
Figure 5.24. 95 th Percentile Non-Exceedance Probability RMS Bed Shear Stress Difference Under Combined Waves & Current	102
Figure 5.25. 95 th Percentile Non-Exceedance Probability RMS Bed Shear Stress Difference Under Combined Waves & Current	103
Figure 5.26. 95 th Percentile Non-Exceedance Probability RMS Bed Shear Stress Difference Under Combined Waves & Current	103
Figure 5.27. 95 th Percentile Non-Exceedance Probability RMS Bed Shear Stress Difference Under Combined Waves & Current	104
Figure 5.28. Thermal Transect Location NY Bight.....	106
Figure 5.29. Average Winter Vertical Temperature Structure of a Northeast-Southwest Transect.....	107
Figure 5.30. Average Spring Vertical Temperature Structure of a Northeast-Southwest Transect.....	107
Figure 5.31. Average Summer Vertical Temperature Structure of a Northeast-Southwest Transect	108

Figure 5.32. Average Fall Vertical Temperature Structure of a Northeast-Southwest Transect	108
Figure 5.33. Difference in Sea Surface Temperature 95 th Percentile Non-Exceedance Probability, Scenario 5: 15 MW Full Build-Out - Baseline.....	110
Figure 5.34. Difference in Sea Surface Temperature 95 th Percentile Non-Exceedance Probability, Scenario 5: 15 MW Full Build-Out - Baseline.....	111
Figure 5.35. Difference in Sea Surface Height 95 th Percentile Non-Exceedance Probability, Scenario 5: 15 MW Full Build-out - Baseline.....	113
Figure 5.36. Difference in Sea Surface Height 95 th Percentile Non-Exceedance Probability, Scenario 5: 15 MW Full Build-Out - Baseline.....	114
Figure 5.37. Difference in Sea Surface Salinity 95 th Percentile Non-Exceedance Probability, Scenario 5: 15 MW Full Build-out - Baseline.....	116
Figure 5.38. Difference in Sea Surface Salinity 95 th Percentile Non-Exceedance Probability, Scenario 5: 15 MW Full Build-Out - Baseline	117
Figure 6.1. Flow Diagram Showing Modeling Steps Involved in the ABM for the Baseline and the Build- Out Scenario	124
Figure 6.2. Flow Diagram Showing the Post Processing Workflow for the Ensemble Model Results	125
Figure 6.3. Illustration of Difference in Top-Down and Bottom-Up Population Impact Models	126
Figure 6.4. Example of Traits Possessed by Individuals in ABM.....	127
Figure 6.5. Stages of Successful Larval Dispersal	128
Figure 6.6. Example of an Agent Navigating Grid Cells	129
Figure 6.7. Implementation of the Super-Agent Concept	131
Figure 6.8. Parameterized Life Stages of a Super-Agent in the ABM Templates	132
Figure 6.9. USGS Sediment Map	137
Figure 6.10. Substrate Suitability Map for Sea Scallop	137
Figure 6.11. Sea Scallop Essential Fish Habitat Map.....	140
Figure 6.12. Sea Scallop Abundance Map and Model Spawning Areas	141
Figure 6.13. Early Life Stages of Sea Scallop as Simulated in the ABM.....	144
Figure 6.14. Parameterization of Sea Scallop Zygotes and Larval Vertical Movement Characteristics...	147
Figure 6.15. Sea Scallop Substrate Suitability Map.....	149
Figure 6.16. NEFSC Shellfish Regions, for Atlantic Surfclam, Ocean Quahog, and Atlantic Sea Scallop Surveys	151
Figure 6.17. Surfclam Essential Fish Habitat Map.....	152
Figure 6.18. Surfclam Model Spawning Areas.....	153
Figure 6.19. Early Life Stages of Surfclam as Simulated in the ABM.....	158

Figure 6.20. Parameterization of Surfclam Zygotes and Larval Vertical Movement Characteristics.....	161
Figure 6.21. Surfclam Substrate Suitability Map.....	163
Figure 6.22. Summer Flounder Essential Fish Habitat Map	165
Figure 6.23. Summer Flounder Model Spawning Areas.....	166
Figure 6.24. Early Life Stages of Summer Flounder as Simulated in the ABM.....	169
Figure 6.25. Parameterization of Summer Flounder Zygotes and Larval Vertical Movement.....	172
Figure 6.26. Parameterization of Summer Flounder Zygotes and Larval Horizontal Movement.....	173
Figure 6.27. Summer Flounder Substrate Suitability Map	175
Figure 6.28. Convergence Analysis of Sea Scallop Ensemble Model Iterations for Year 2017	177
Figure 6.29. Convergence Analysis of Surfclam Ensemble Model Iterations.....	178
Figure 6.30. Convergence Analysis of Summer Flounder Ensemble Model Iterations	178
Figure 6.31. Shellfish Specific Destinations Map – Within the Model Domain	180
Figure 6.32. Shellfish Specific Destinations Map – Colored by Region.....	181
Figure 6.33. Pertinent Fisheries Areas as Identified by CSA to be Used for Qualitative Analysis and Context.....	182
Figure 7.1. Destination Reference Map Showing Each Destination Area and Names, Colors Represent Broad Regions	188
Figure 7.2. Swarm Plot of Sea Scallop Settled Larvae Showing Total Settlement in Main Destinations for 2017, 2018, and 2020	189
Figure 7.3. Baseline Ensemble Settled Larval Sea Scallop Density 2017	190
Figure 7.4. Baseline Connectivity Matrix (left) and Connectivity Map (right) for Sea Scallop Larvae – Aggregated Ensemble Results for 2017	191
Figure 7.5. Baseline Ensemble Settled Larval Sea Scallop Density 2018	192
Figure 7.6. Baseline Connectivity Matrix (left) and Connectivity Map (right) for Sea Scallop Larvae – Aggregated Ensemble Results for 2018	193
Figure 7.7. Baseline Ensemble Settled Larval Sea Scallop Density 2020	194
Figure 7.8. Baseline Connectivity Matrix (left) and Connectivity Map (right) for Sea Scallop Larvae – Aggregated Ensemble Results for 2020	195
Figure 7.9. Baseline Ensemble Settled Larval Surfclam Density 2017	198
Figure 7.10. Baseline Connectivity Matrix (left) and Connectivity Map (right) for Surfclam Larvae – Aggregated Ensemble Results for 2017	199
Figure 7.11. Baseline Ensemble Settled Larval Summer Flounder Density 2017.....	200
Figure 7.12. Baseline Connectivity Matrix (left) and Connectivity Map (right) for Summer Flounder Larvae – Aggregated Ensemble Results for 2017	201

Figure 7.13. Settled Sea Scallop Larvae Density (2017) Compared to Observational Biomass and Essential Fish Habitat	203
Figure 7.14. Temporal Development Model Evaluation – Time Taken for Modeled Sea Scallop Eggs to Hatch.....	204
Figure 7.15. Temporal Development Model Evaluation – Time Taken for Modeled Sea Scallop Larvae to Settle	205
Figure 7.16. Vertical Movement Model Evaluation – Movement of Sea Scallop Larvae with Temperature	205
Figure 7.17. Spatial Rank Correlation Results for Sea Scallop 2017 – Correlation Line Plot	207
Figure 7.18. Spatial Rank Correlation Data for Sea Scallop.....	208
Figure 7.19. Settled Surfclam Larvae Density (2017) Compared to Observational Biomass and Essential Fish Habitat	209
Figure 7.20. Temporal Development Model Evaluation – Time Taken for Modeled Surfclam Eggs to Hatch	210
Figure 7.21. Temporal Development Model Evaluation – Time Taken for Modeled Surfclam Larvae to Settle	210
Figure 7.22. Vertical Movement Model Evaluation – Movement of Surfclam Larvae with Temperature..	211
Figure 7.23. Spatial Rank Correlation Results for Surfclam 2017 – Correlation Line Plot	212
Figure 7.24. Spatial Rank Correlation Data for Surfclam.....	213
Figure 7.25. Temporal Development Model Evaluation – Time Taken for Modeled Summer Flounder Eggs to Hatch	214
Figure 7.26. Temporal Development Model Evaluation – Time Taken for Modeled Summer Flounder Larvae to Settle	214
Figure 7.27. Vertical Movement Model Evaluation – Movement of Summer Flounder Larvae with Temperature.....	215
Figure 8.1. Swarm Plot Sea Scallop Settlement in Top 10 Destinations for 2017 – All Build Out Scenarios	217
Figure 8.2. Swarm Plot Surfclam Settlement in Top 10 Destinations for 2017 – All Build Out Scenarios	218
Figure 8.3. Destination Reference Map Showing Each Destination Area and Names, Colors Represent Broad Regions	221
Figure 8.4. Difference in Total Settled Larvae 15 MW Full Build-Out vs. Baseline 2017	224
Figure 8.5. DBSCAN (Density-Based Spatial Clustering of Applications with Noise) Difference in Total Settled Larvae 15 MW Full Build-Out vs. Baseline 2017	224
Figure 8.6. Change in Current Speed 15 MW Full Build-Out vs. Baseline 2017	224
Figure 8.7. Difference in Settled Larvae Density 15 MW Full Build-Out vs. Baseline 2017	225
Figure 8.8. DBSCAN (Density-Based Spatial Clustering of Applications with Noise) Difference in Settled Larvae Density 15 MW Full Build-Out vs. Baseline 2017	225

Figure 8.9. Change in Current Speed 15 MW Full Build-Out vs. Baseline 2017	225
Figure 8.10. Average Change in Sea Scallop Settlement in Each Destination Area 15 MW Full Build-Out vs. Baseline 2017	226
Figure 8.11. Swarm Plot Showing Sea Scallop Settlement in Top 10 Destinations for 2017	227
Figure 8.12. Sea Scallop Connectivity Difference 2017	228
Figure 8.13. Difference in Total Settled Larvae 15 MW Full Build-Out vs. Baseline 2018	231
Figure 8.14. DBSCAN (Density-Based Spatial Clustering of Applications with Noise) Difference in Total Settled Larvae 15 MW Full Build-Out vs. Baseline 2018	231
Figure 8.15. Change in Current Speed 15 MW Full Build-Out vs. Baseline 2018	231
Figure 8.16. Difference in Settled Larvae Density 15 MW Full Build-Out vs. Baseline 2018	232
Figure 8.17. DBSCAN (Density-Based Spatial Clustering of Applications with Noise) Difference in Settled Larvae Density 15 MW Full Build-Out vs. Baseline 2018	232
Figure 8.18. Change in Current Speed 15 MW Full Build-Out vs. Baseline 2018	232
Figure 8.19. Average Change in Sea Scallop Settlement in Each Destination Area 15 MW Full Build-Out vs. Baseline 2018	233
Figure 8.21. Sea Scallop Connectivity Difference 2018	235
Figure 8.22. Difference in Total Settled Larvae 15 MW Full Build-Out vs. Baseline 2020	237
Figure 8.23. DBSCAN (Density-Based Spatial Clustering of Applications with Noise) Difference in Total Settled Larvae 15 MW Full Build-Out vs. Baseline 2020	237
Figure 8.24. Change in Current Speed 15 MW Full Build-Out vs. Baseline 2020	237
Figure 8.25. Difference in Settled Larvae Density 15 MW Full Build-Out vs. Baseline 2020	238
Figure 8.26. DBSCAN (Density-Based Spatial Clustering of Applications with Noise) Difference in Settled Larvae Density 15 MW Full Build-Out vs. Baseline 2020	238
Figure 8.27. Change in Current Speed 15 MW Full Build-Out vs. Baseline 2020	238
Figure 8.28. Average Change in Sea Scallop Settlement in Each Destination Area 15 MW Full Build-Out vs. Baseline 2020	239
Figure 8.29. Swarm Plot showing Sea Scallop Settlement in Top 10 Destinations for 2020	240
Figure 8.30. Sea Scallop Connectivity Difference 2020	241
Figure 8.31. Difference in Total Settled Larvae 15 MW Full Build-Out vs. Baseline 2017	243
Figure 8.32. DBSCAN (Density-Based Spatial Clustering of Applications with Noise) Difference in Total Settled Larvae 15 MW Full Build-Out vs. Baseline 2017	243
Figure 8.33. Change in Current Speed 15 MW Full Build-Out vs. Baseline 2017	243
Figure 8.34. Difference in Settled Larvae Density 15 MW Full Build-Out vs. Baseline 2017	244

Figure 8.35. DBSCAN (Density-Based Spatial Clustering of Applications with Noise) Difference in Settled Larvae Density 15 MW Full Build-Out vs. Baseline 2017	244
Figure 8.36. Change in Current Speed 15 MW Full Build-Out vs. Baseline 2017	244
Figure 8.37. Average Change in Surfclam Settlement in Each Destination Area 15 MW Full Build-Out vs. Baseline 2017	245
Figure 8.38. Swarm Plot Showing Surfclam Settlement in Top 10 Destinations for 2017	246
Figure 8.39. Surfclam Connectivity Difference 2017.....	247
Figure 8.40. Difference in Total Settled Larvae 15 MW Full Build-Out vs. Baseline 2017	250
Figure 8.41. DBSCAN (Density-Based Spatial Clustering of Applications with Noise) Difference in Settled Larvae 15 MW Full Build-Out vs. Baseline 2017	250
Figure 8.42. Change in Current Speed 15 MW Full Build-Out vs. Baseline 2017	250
Figure 8.43. Higher Resolution Difference in Total Settled Larvae 15 MW Full Build-Out vs. Baseline 2017	251
Figure 8.44. Higher Resolution DBSCAN (Density-Based Spatial Clustering of Applications with Noise) Difference in Settled Larvae 15 MW Full Build-Out vs. Baseline 2017.....	251
Figure 8.45. Higher Resolution Change in Current Speed 15 MW Full Build-Out vs. Baseline 2017	251
Figure 8.46. Difference in Settled Larvae Density 15 MW Full Build-Out vs. Baseline 2017	252
Figure 8.47. DBSCAN (Density-Based Spatial Clustering of Applications with Noise) Difference in Settled Larvae Density 15 MW Full Build-Out vs. Baseline 2017	252
Figure 8.48. Change in Current Speed 15 MW Full Build-Out vs. Baseline 2017	252
Figure 8.49. Higher Resolution Difference in Settled Larvae Density 15 MW Full Build-Out vs. Baseline 2017	253
Figure 8.50. Higher Resolution DBSCAN (Density-Based Spatial Clustering of Applications with Noise) Difference in Settled Larvae Density 15 MW Full Build-Out vs. Baseline 2017.....	253
Figure 8.51. Higher Resolution Change in Current Speed 15 MW Full Build-Out vs. Baseline 2017	253
Figure 8.52. Change in Average Summer Flounder Settlement in Each Destination Area 15 MW Full Build-Out vs. Baseline 2017.....	254
Figure 8.53. Swarm Plot Showing Summer Flounder Settlement in Most Common Destinations for 2017	255
Figure 8.54. Summer Flounder Connectivity Difference 2017	256
Figure 8.55. Difference in Total Settled Larvae 12 MW Full Build-Out vs. Baseline 2017	259
Figure 8.56. DBSCAN (Density-Based Spatial Clustering of Applications with Noise) Difference in Total Settled Larvae 12 MW Full Build-Out vs. Baseline 2017	259
Figure 8.57. Change in Current Speed 12MW Full Build-Out vs. Baseline 2017	259
Figure 8.58. Difference in Settled Larvae Density 12 MW Full Build-Out vs. Baseline 2017	260

Figure 8.59. DBSCAN (Density-Based Spatial Clustering of Applications with Noise) Difference in Settled Larvae Density 12 MW Full Build-Out vs. Baseline 2017	260
Figure 8.60. Change in Current Speed 12 MW Full Build-Out vs. Baseline 2017	260
Figure 8.61. Average Change in Sea Scallop Settlement in Each Destination Area 12 MW Full Build-out vs. Baseline	261
Figure 8.62. Swarm Plot Showing Sea Scallop Settlement in Top 10 Destinations	262
Figure 8.63. Sea Scallop Connectivity Difference.....	263
Figure 8.64. Difference in Total Settled Larvae 12 MW Full Build-Out vs. Baseline 2017	266
Figure 8.65. DBSCAN (Density-Based Spatial Clustering of Applications with Noise) Difference in Total Settled Larvae 12 MW Full Build-Out vs. Baseline 2017	266
Figure 8.66. Change in Current Speed 12 MW Full Build-Out vs. Baseline 2017	266
Figure 8.67. Difference in Settled Larvae Density 12 MW Full Build-Out vs. Baseline 2017	267
Figure 8.68. DBSCAN (Density-Based Spatial Clustering of Applications with Noise) Difference in Surfclam Settled Larvae density 12 MW Full Build-Out vs. Baseline 2017	267
Figure 8.69. Change in Current Speed 12 MW Full Build-Out vs. Baseline 2017	267
Figure 8.70. Average Change in Surfclam Settlement in Each Destination Area 12 MW Full Build-Out vs. Baseline 2017	268
Figure 8.71. Swarm Plot Showing Surfclam Settlement in Top 10 Destinations for 2017.....	269
Figure 8.72. Surfclam Connectivity Difference 2017	270
Figure 8.73. Difference in Settled Larvae 12 MW Full Build-Out vs. Baseline 2017	272
Figure 8.74. DBSCAN (Density-Based Spatial Clustering of Applications with Noise) Difference in Settled Larvae 12 MW Full Build-Out vs. Baseline 2017	272
Figure 8.75. Change in Current Speed 12 MW Full Build-Out vs. Baseline 2017	272
Figure 8.76. Higher Resolution Difference in Total Settled Larvae 12 MW Full Build-Out vs. Baseline 2017	273
Figure 8.77. Higher Resolution DBSCAN (Density-Based Spatial Clustering of Applications with Noise) Difference in Settled Larvae 12 MW Full Build-Out vs. Baseline 2017.....	273
Figure 8.78. Higher Resolution Change in Current Speed 12 MW Full Build-Out vs. Baseline 2017	273
Figure 8.79. Difference in Settled Larvae Density 12 MW Full Build-Out vs. Baseline 2017	274
Figure 8.80. DBSCAN (Density-Based Spatial Clustering of Applications with Noise) Difference in Settled Larvae Density 12 MW Full Build-Out vs. Baseline 2017	274
Figure 8.81. Change in Current Speed 12 MW Full Build-Out vs. Baseline 2017	274
Figure 8.82. Average Change in Summer Flounder Settlement in Each Destination Area 12MW Full Build-Out vs. Baseline 2017	275
Figure 8.83. Swarm Plot Showing Summer Flounder Settlement in Top 10 Destinations for 2017	276

Figure 8.84. Summer Flounder Connectivity Difference 2017	277
Figure 8.85. Difference in Total Settled Larvae Sensitivity Test vs. Baseline 2017	279
Figure 8.86. DBSCAN (Density-Based Spatial Clustering of Applications with Noise) Difference in Total Settled Larvae Sensitivity Test vs. Baseline 2017	279
Figure 8.87. Change in Current Speed Sensitivity Test vs. Baseline 2017	279
Figure 8.88. Difference in Settled Larvae Density Sensitivity Test vs. Baseline 2017	280
Figure 8.89. DBSCAN (Density-Based Spatial Clustering of Applications with Noise) Difference in Settled Larvae Density Sensitivity Test vs. Baseline 2017	280
Figure 8.90. Change in Current Speed Sensitivity Test vs. Baseline 2017	280
Figure 8.91. Average Change in Sea Scallop Settlement in Each Destination Area Sensitivity Test vs. Baseline 2017	281
Figure 8.92. Swarm Plot Showing Sea Scallop Settlement in Top 10 Destinations for 2017.....	282
Figure 8.93. Sea Scallop Connectivity Difference 2017	283
Figure 9.1. Swarm Plot Showing Summer Flounder Settlement in Top 3 Destinations for Each Scenario	287
Figure 9.2. Delineation of Fisheries Areas in the Study Area	290

List of Tables

Table 2.1. Rivers Included as Freshwater Sources in the Hydrodynamic Model	15
Table 3.1. Main HDM Set-Up Parameters	25
Table 3.2. Wave Model Set-Up Parameters	27
Table 3.3. Wave Height (H_{m0}) Model Quality Indices.....	52
Table 3.4. Water Level Model Quality Indices	53
Table 3.5. Current Speed Model Quality Indices	53
Table 3.6. Temperature Model Quality Indices.....	55
Table 4.1. List of WEAs “with COP” and “Generic”.....	56
Table 4.2. Generic 12 MW Wind Turbine Physical Dimensions	64
Table 4.3. Generic 15 MW Wind Turbine Physical Dimensions	66
Table 5.1. Surface Current Changes Due to 15 MW Full Build-Out (Scenario 5): Wind Wakes Only and Monopile Foundation Drag Only	84
Table 5.2. Summary of Broad Maximum and Minimum Changes from Baseline of the 95th Percentile Non-Exceedance Probability Depth Averaged Current Speeds by Scenario and WEA	91

Table 5.3. Particle Model Parameters.....	92
Table 5.4. Critical Shear Stress by Particle-Size Classification for Determining Approximate Condition for Sediment Mobility at 20 Degrees Celsius	105
Table 6.1. Datasets Employed for the ABM.....	134
Table 6.2. Sea Scallop Release Period and Volume	142
Table 6.3. Sea Scallop Spawning Model Parameters	143
Table 6.4. Sea Scallop Life Cycle (Growth and Mortality) Model Parameters.....	145
Table 6.5. Sea Scallop Movement Model Parameters	148
Table 6.6. Sea Scallop Substrate Suitability and Settlement Conditions	149
Table 6.7. Number of Super-Agents Released from Each Spawning Area.....	154
Table 6.8. Surfclam Release Period and Volume	154
Table 6.9. Surfclam Spawning Model Parameters	157
Table 6.10. Surfclam Life Cycle (Growth and Mortality) Model Parameters.....	159
Table 6.11. Surfclam Movement Model Parameters	162
Table 6.12. Surfclam Substrate Suitability and Settlement Conditions	164
Table 6.13. Summer Flounder Release Period and Volume	167
Table 6.14. Summer Flounder Spawning Model Parameters.....	168
Table 6.15. Summer Flounder Life Cycle (Growth and Mortality) Model Parameters	170
Table 6.16. Summer Flounder Movement Model Parameters.....	174
Table 6.17. Summer Flounder Substrate Suitability and Settlement Conditions.....	176
Table 7.1. Explanation of Baseline Analysis Plots and Charts	187
Table 7.2. Interpretation Table for Each Correlation Coefficient Used in the Spatial POM.....	208
Table 8.1. Explanation of Scenario Analysis Plots and Charts.....	219

List of Abbreviations and Acronyms

ABM	Agent-Based Modeling
ADCP	Acoustic Doppler Current Profiler
AEP	Annual Energy Production
ASL	Atmospheric Surface Layer
BCO-DMO	Biological & Chemical Oceanography Data Management Office
BOEM	Bureau of Ocean Energy Management
BSEE	Bureau of Safety and Environmental Enforcement
CFD	Computational Fluid Dynamics
CFSR	Climate Forecast System Reanalysis
CFSv2	Climate Forecast System version 2
CODAR	Coastal Ocean Dynamics Applications Radar
CONMAP	Continental Margin Mapping Program
COP	Construction and Operation Plan
CSA	Continental Shelf Associates
DHI	DHI Water & Environment, Inc.
DBSCAN	Density-Based Spatial Clustering of Applications with Noise
DOI	U.S. Department of the Interior
DTU	Danish Technical University
EcoMon	Ecological Monitoring
EFH	Essential Fish Habitat
EIS	Environmental Impact Statement
FEHY	FEhmarbelt HYdrography
FBO	Full Build-out
FVCOM	Finite Volume Community Ocean Model
GB	Georges Bank
GEBCO	General Bathymetric Chart of the Oceans
GHR SST	Group for High Resolution Sea Surface Temperature
GIS	Geographic Information System
GODAE	Global Ocean Data Assimilation Experiment
HD	Hydrodynamic
HDM	Hydrodynamic Model
HF	High Frequency
HFRO	High Frequency Radar Observation
H_{m0}	Significant wave height
HYCOM	HYbrid Coordinate Ocean Model
IWFBL	Infinite Wind-Farm Boundary Layer
LES	Large-Eddy Simulation
LI	Long Island
MAB	Mid-Atlantic Bight
MA-RI	Massachusetts – Rhode Island
MBDB	Multibeam Bathymetry Database
MD-DE	Maryland - Delaware
MVCO	Martha's Vineyard Coastal Observatory
MW	Megawatt

MAMFC	Mid-Atlantic Fishery Management Council
MARACOOS	Mid-Atlantic Regional Association Coastal Ocean Observation System
MARMAP	Marine Resources Monitoring, Assessment and Prediction Program
MIKE	“MIKE” is a tradename for DHI software systems
MIKE ABM Lab	MIKE Agent-Based Model
MIKE ECO Lab	MIKE Ecological Model
MIKE 3 FM HD	MIKE 3 Flexible Mesh Hydrodynamic model
MIKE 21 SW	MIKE 21 Spectral Wave model
MOST	Monin-Obukhov Similarity Theory
NASEM	National Academy of Science, Engineering and Medicine
NC-SC	North Carolina – South Carolina
NCEI	National Centers for Environmental Information (NOAA)
NCEP	National Centers for Environmental Prediction (NOAA)
NDBC	National Data Buoy Center (NOAA)
NEFMC	New England Fisheries Management Council
NEFSC	Northeast Fisheries Science Center
NEPA	National Environmental Policy Act
NOAA	National Oceanic and Atmospheric Administration
NROC	Northeast Ocean Data Portal
NSF	National Science Foundation
NY	New York
OSTIA	Operational Sea Surface Temperature and Sea Ice Analysis
OSW	Offshore Wind Farms
POM	Pattern Oriented Modeling
PORTS	Physical Oceanographic Real Time Systems
Psu	Practical Salinity Unit
QQ	Quantile-Quantile
RANS	Reynolds Averaged Navier-Stokes
RMSE	Root Mean Square Error
SAR	Synthetic Aperture Radar
SEM	Standard Error of the Mean
SI	Scatter Index
SL	Standard Length
SMAST	School of Marine Science and Technology
SNE	Southern New England
SST	Sea Surface Temperature
SW	Spectral Wave
SWUS-EC	U.S. East Coast Spectral Wave Model
3D	Three dimensional
2D	Two dimensional
TL	Total Length
Ct	Thrust coefficient (turbine wind-wake parameter)
TKE	Turbulent kinetic energy
USGS	U.S. Geological Survey
VA-NC	Virginia – North Carolina
WAM	Wave Modeling Consortium
WEA	Wind Energy Area
WHOI	Woods Hole Oceanographic Institution

WRF	Weather Research and Forecasting
WTG	Wind Turbine Generator

Executive Summary

Abstract

Along the East Coast of the U.S., from Massachusetts to North Carolina, there are several planned areas for the development of offshore wind farms (OSW). OSW development has the potential to alter local and regional physical oceanic processes, via their influence on currents, mixing and waves from wind turbine generator (WTG) foundations and by extracting energy from the wind. These potential oceanic changes could alter the transport of fish and shellfish larvae and change the distribution and settlement of ecologically and commercially important species along the Atlantic Coast of the U.S. This study aims to firstly provide projections of potential changes to ocean hydrodynamics resulting from the development of the planned wind energy areas (WEAs), including current speed and direction, turbulence, waves, and bed shear stress. Secondly, agent-based modeling (ABM) is used to assess the possible resulting impacts on transport, dispersal, settlement patterns, and connectivity of Atlantic Sea Scallop, Surfclam, and Summer Flounder larvae. To achieve this, a regional integrated 3D hydrodynamic model (HDM) and ABM were developed of the Atlantic coast using MIKE Powered by DHI models.

The HDM covers an area from Nova Scotia to Florida, providing baseline oceanographic conditions for the years 2017, 2018, and 2020. Wind energy areas (WEAs) were afforded higher resolution using a flexible mesh and modeled with partial and full build-out scenarios. The scenarios for year 2017 were: baseline (no WTGs), Scenario 2: 12 MW Partial Build-out (2,083 WTGs), Scenario 3: 15 MW Partial Build-out (2,083 WTGs), Scenario 4: 12 MW Full Build-out (4,650 WTGs), Scenario 5: 15 MW Full Build-out (4,650 WTGs), and Scenario 6: 15 MW Full Build-out (4,650 WTGs) for years 2017, 2018, and 2020. The influence of monopile foundations induced drag and turbulence were assessed based on previous Computational Fluid Dynamics (CFD) model results (Johnson et al., 2021), while wind energy extraction and wake effects were estimated using the industry standard PyWake wind wake loss tool. The results of both nearfield sub-analyses were parameterized and integrated into the HDM.

*The ABM was developed using MIKE ABM Lab and used to simulate the spawning, movement, and settlement characteristics of the target larval species (Atlantic Sea Scallop (*Placopecten magellanicus*), Atlantic Surfclam (*Spisula solidissima*) and Summer Flounder (*Paralichthys dentatus*)). The baseline ABM results were evaluated by comparing the ABM results for settled larvae density against EFH demarcations (NOAA, 2018), available biomass data, and evaluated statistically using three Pattern Oriented Modeling (POM) analysis techniques.*

The HDM results showed that the introduction of the WEAs into the model domain reduced the magnitude of the currents, waves, and bed shear stresses mostly within the WEAs. Of the studied scenarios, Scenario 5: 15 MW Full Build-out produced the maximum impact on the HDM results where, in the entire domain, maximum current changes ranged from between approximately -5.0% and +1.7% in direct vicinity of each WEA.

Changes in sea scallop and surfclam settlement resulting from the introduction of the WEAs were estimated by the ABM. Settlement changes were primarily found in the New Jersey region around the confluence of OSW developments in the region, and to a lesser extent through Delmarva. Localized patches of increased settlement were found centrally and along the coast of the New Jersey region, while decreased settlement was estimated to the north of the New Jersey region for both sea scallop and surfclam and to the south of the New Jersey region for surfclam. The estimated changes in settlement are likely a result of slowed transport of larvae in both north-to-south and south-to-north directions within the New Jersey area. The estimated changes in settlement are four to five orders of magnitude lower than total settlement, and it is unlikely that there will be relevant ecological or fisheries impacts on a regional level. However, given the persistence of the changes, and the locally substantial changes identified, there

could be impacts on the localized sub-population level for these species. Changes in summer flounder settlement were also estimated along the coast, but no clear patterns or consistencies between scenarios emerged. There could be localized impacts in the New Jersey region resulting from the introduction of the OSW developments for summer flounder, as the 15 MW scenario identified change close to the OSW areas. However, it is difficult to conclude whether there will be relevant impacts for summer flounder, given their ability to move to appropriate habitat. More localized studies are likely required to provide further insight into the relevance of the local level changes identified, as well as consideration of survival and recruitment in the areas of settlement change identified in the model results.

Background

The goal of this study was to assess the potential cumulative regional impacts on oceanographic transport patterns along the East Coast of the U.S. resulting from the development of offshore wind (OSW) energy leases in the region. This modeling study assessed the potential changes in hydrodynamic conditions resulting from OSW development, and the associated impacts on the transport of fisheries pertinent larvae, namely, Atlantic sea scallop (*Placopecten magellanicus*), Atlantic surfclam (*Spisula solidissima*) and summer flounder (*Paralichthys dentatus*) larvae, from North Carolina to Massachusetts. This study built upon previous work completed on the potential impacts on larval transport, dispersal, and settlement patterns (Chen et al., 2016; Johnson et al., 2021), by extending the model domain from Johnson et al., (2021) from Nova Scotia to Florida so as to include North Carolina and northern South Carolina WEAs; as well as important oceanographic processes in the area such as the formation of the “Cold Pool”.

Objectives

The key objective of this study was to determine the regional effects of OSW developments on coastal and oceanic environmental conditions and the resulting impacts on larval dispersal and settlement, including changes in settlement patterns and connectivity. To achieve this key objective, this study aimed to develop and use fine resolution regional hydrodynamic models, with monopile drag and turbulence and wind turbine wake models to determine the changes in oceanic conditions such as current speed and direction, turbulent mixing, and bed shear stress resulting from OSW development. The second aim was to develop and integrate an agent-based model (ABM) that simulates larval dispersal, movement, and settlement for the three target species, with the hydro-dynamic model (HDM). The final aim was to analyze the potential effects of hydrodynamic changes on larval settlement and connectivity of the three target species.

Methods

The project was divided into six major tasks: 1. *Data Management*, 2. *Desktop Review and Statistical Analysis*, 3. *Model Development*, 4. *Model Calibration*, 5. *Modeling Scenarios and Analysis*, and 6. *Report and Technical Summary*. The initial stages (i.e., 1 and 2) of the project involved collecting the background studies, peer reviewed literature, oceanographic data, and ecological survey data necessary to refine the hydrodynamic, wind turbine wake, and agent-based modeling approaches. Five OSW build-out scenarios were chosen, as well as three target species.

The target species selected for analysis included:

- Atlantic Sea Scallop (*Placopecten magellanicus*),
- Atlantic Surfclam (*Spisula solidissima*), and
- Summer Flounder (*Paralichthys dentatus*).

The WEAs selected for the study were characterized as those that had a Construction and Operations Plan (COP) publicly available on BOEM’s website at the time of study initiation (i.e., labelled as “with COP”);

and those where a COP was not yet submitted but where potential leases had been identified (i.e., labelled as “Generic”). The scenarios modeled were:

- **Scenario 1: Baseline years 2017, 2018, and 2020** – modeled without any WTGs, all three species modeled for 2017. Only sea scallops modeled for 2018 and 2020.
- **Scenario 2: Partial Build-out 12 MW year 2017** - currently proposed developments with publicly available COPs, with 2,083 12 MW turbines for year 2017, all three species modeled in ABM,
- **Scenario 3: Partial Build-out 15 MW year 2017** – currently proposed developments with publicly available COPs, with 2,083 15 MW turbines for year 2017, all three species modeled in ABM
- **Scenario 4: Full build-out, 12 MW year 2017** – currently proposed developments with publicly available COPs and generic layouts for remaining lease areas, with 4,650 12 MW turbines for year 2017, all three species modeled in ABM
- **Scenario 5: Full build-out, 15 MW year 2017** – currently proposed developments with publicly available COPs and generic layouts for remaining lease areas, with 4,650 15 MW turbines for year 2017, all three species modeled in ABM
- **Scenario 6: Full build-out, 15 MW years 2017, 2018 and 2020** – currently proposed developments with publicly available COPs and generic layouts for remaining lease areas, with 4,650 15 MW turbines. Only sea scallops modeled for 2017, 2018 and 2020 in ABM.

While it was originally planned to include sequential years of analysis for Scenario 6, the year 2019 was omitted due to a late Project stage discovery of some misaligned model setup features. This led to an unacceptable level of validation for 2019 and that had consequences on ABM test results. HDM results for 2019 were therefore omitted. As the Sea scallop spawning and settlement cycle aligns with a calendar year, this decision did not affect the ability to complete an inter-annual variability analysis for this species.

Tasks 3 to 5 involved developing, calibrating, validating and then running the HDM, wind wake loss model, and ABM, which entailed the integration of selected MIKE Powered by DHI models. The HDM, developed with MIKE 3 FM HD, MIKE 21 SW and other nearfield models, was established as a 3D regional model ranging from offshore Nova Scotia to Cape Canaveral. A finer model mesh was embedded in the wind energy areas (WEAs). Localized turbulence effects of individual monopile foundations were addressed first, using a single monopile and applying a Computational Fluid Dynamics (CFD) model of water flow around turbine foundations. Based on the CFD model, a general parameterization was established for the energy conversions and thereby the impacts on current velocity, turbulence levels and mixing (thermal and salinity). Each turbine was implemented as sub-grid feature using extra source terms for: a.) the drag force from the tower as a mean momentum sink b.) a source term for turbulent kinetic energy from the extra production in the wake, and c.) increase the eddy viscosity adding mixing of momentum, temperature and salinity. The sub-grid model ensures that energy was converted accurately. This approach follows normal practice in ocean models (Rennau, 2012; Jakobsen, 2010) or wind resource modeling (Fitch, 2012). An industry standard wind wake loss model, PyWake (Pedersen et al., 2023), was implemented for this study. For each WEA region a localized wind wake model acting on the Climate Forecast System Reanalysis (CFSR) wind fields was produced by the PyWake model. These results were then transferred into the regional HDM mesh. In summary, the overall HDM implemented near and far field oceanic processes including surface wind wake losses due to the wind turbine generators (WTGs), ocean currents (both lateral and vertical) losses due to the monopile foundations, air pressure, precipitation/ evaporation, surface heat flux, water temperature and salinity.

The ABM was developed using MIKE ABM Lab templates which, via coupling with the HDM, allowed for larval dispersal modeling. ABM Lab offers an open and flexible coding environment for defining and customizing simple to advanced biological traits and processes using a series of user-defined arithmetic

expressions and state variables, which allows simulated agents (e.g., larvae) to react and interact with a dynamically changing virtual environment. ABM templates were customized for each species with their key spawning and development characteristics, movement traits, settlement requirements and habitat preferences. The ABM was subsequently tested, calibrated and evaluated. The ABM was carried out using an ensemble technique, with execution of multiple “clones” of the same model set-up. A connectivity analysis was also carried out, which tracked where larvae spawn and where they settle, in order to capture any potential changes in larval transport resulting from the introduction of the OSW developments. The ABM was evaluated by plotting the simulated settled larvae density against EFH demarcations (NOAA, 2018) and available biomass data, and statistically through the application of three Pattern Oriented Modeling (POM) analysis techniques.

Results

Hydrodynamic Results

Changes caused by the various OSW developments to current speeds, waves, bed shear stresses and thermal stratification were captured by the HDM; but were relatively modest. For example, maximum changes to 95th percentile non-exceedance probability depth averaged current speeds in all WEAs for Scenario 5 (15 MW Full Build-out), the scenario with the most pertinent change, ranged from approximately -5.0% to +1.7%. Whereas maximum changes to the 95th percentile non-exceedance probability depth averaged currents for sensitivity modeling analyses i.e., a 15 MW Full Build-out with an artificially doubled wind wake effect, resulted in changes ranging from approximately -6.1% to +2.3%. In terms of detailed wave results, the biggest reduction in 95th percentile non-exceedance probability significant wave heights (H_{m0}) were observed in the New York Bight (NY Bight) / Maryland-Delaware (MD-DE) region. Here, wave height reduction was on the order of 10 cm for waves that were on the order of 2.5 m H_{m0} or ~4% lower. Modeled changes in bed shear stress were also small, leading to the conclusion that WTGs should have no increased effect on deposition and marginal reductions in the potential of seabed sediment mobilization in the WEAs.

The effect of the WTGs on the sea surface wind stress is evident in model results of the vertical thermal stratification influenced by the slowing of the currents inside the OSW farms. The greatest effect was observed from the 15 MW full build-out scenario in the NY Bight / MD-DE WEAs. In winter, the OSW farms shifted the isotherms down slightly and expanded the bottom isotherm up ~3 m, which elongated the bottom 10 °C cold water isotherm toward the southwest by ~20 km. In spring, the isotherms shifted down by ~0.5 m in the upper 20 m of the water column, and shifted up ~0.5 m to 1.5 m at depths below 30 m. In the summer, the isotherms shifted down ~3 m in the upper 10 m of the water column, with little change between 10 m and 30 m water depths. However, in the deeper waters the isotherms moved up and expanded the size of the cooler water mass. In fall, the isotherms shifted down in the upper 20 m of the water column in the OSW farm area on the southwest side, while there was not much change noted deeper than 20 m water depths and deeper.

Sea Scallop Results

Changes in sea scallop settlement (areas of both decreased and increased settlement) were concentrated in the New Jersey and Delmarva regions and extend beyond the WEA areas (please see Figure 7.1 for WEA locations). A decrease in settlement was estimated in and around WEAs 5 and 6 to the North of the New Jersey region, and along the coast of Delaware near WEA 8 and 9. An increase in settlement was estimated along the coast of New Jersey and around WEA7, and to a lesser extent through the Delmarva region. Average changes in sea scallop settlement per destination area were four orders of magnitude lower than total settlement, and in some cases, show little to no overall change in the New Jersey region, once the smaller scale hotspots of increase and decrease were averaged over a larger area. Transport of larvae appears to be slowed within the New Jersey region, which may explain the localized hotspots of settlement change observed. The connectivity analysis showed changes in settlement were mostly from larvae originating in the Mid-Atlantic Bight (MAB). It is possible that the slowed transport of larvae from the more southern portion of the MAB spawning area results in greater settlement further south and west, with the introduction of the OSW developments, and a decrease in settlement to the north and east, suggesting overall slowing of transport south to north. There was inter-annual variability in sea scallop settlement between 2017, 2018, and 2020 years with slightly different hotspots of increase or decrease within New Jersey, but the overall patterns were the same (i.e., changes are found mainly in New Jersey, on the same order of magnitude and in the same areas).

Surfclam Results

Changes in surfclam settlement were also concentrated in the New Jersey and Delmarva regions (please see Figure 6.31) and extend beyond the WEA areas. Areas of decreased settlement were found in and around WEAs 5 and 6 to the North of the New Jersey region, as well as further south - to the east of WEAs 8 and 9. An increase in settlement was found concentrated in the middle of the New Jersey region and around WEA7, and through Delmarva. Average changes in surfclam settlement per destination area were five orders of magnitude lower than total settlement. The connectivity analysis indicated that slowed north to south transport of surfclam larvae appears to contribute to the areas of decreased settlement in the New Jersey region, while areas of increased settlement appear to a result in greater settlement of larvae originating from the south (Delmarva) as well as the New Jersey region itself.

Summer Flounder Results

Changes in summer flounder settlement are concentrated along the coast. However, the results are noisy meaning that there are no clear patterns of change in settlement between Scenarios. Additionally, with respect to the cluster analysis there were no clear consistent patterns of change between Scenarios, which were seen in the other two species. Nevertheless, there do appear to be changes in settlement occurring along the coasts of New Jersey, Long Island and around Nantucket shoals, as well as the North Carolina and South Virginia (SVA destination area) but different areas are highlighted in the different scenarios. It should be noted that the changes appear to be much smaller than the defined destination areas, which may indicate the possibility of very localized larval settlement changes resulting from the OSW developments.

Relevance of ABM Results

The relevance of scallop and surfclam ABM results are similar, whereas summer flounder results differ significantly. Hotspots of settlement change in sea scallop and surfclam larvae were identified in areas where there are harvest efforts. Over the entire modeling domain these differences are small but persistent (i.e., over the life of the projects, about 30 years). It is noted that settlement does not necessarily equal recruitment into the fishery, as individuals that settle may not reach maturity. The unknowns regarding post-settlement survival contribute to uncertainty in estimating recruitment in most marine fisheries. The relevance of the changes in settlement to recruitment of market-sized individuals into the sea scallop and

surfclam fishery will depend on growth and survival beyond settlement. It is not likely that the modeled changes in settlement will lead to measurable declines in total biomass of sea scallop and surfclam at larger regional scales (i.e., over the MAB and New Jersey region). However, spatial persistence of the change may be relevant on a local scale, where hotspots have been identified. At this local scale, changes in settlement may impact patches (subpopulations) or beds of sea scallop and surfclam and any local fisheries they may support.

The two bivalve species exhibited similar patterns in transport and settlement over the modeling domain, but summer flounder differed. No clear patterns of settlement change from baseline were observed in modeled scenarios for summer flounder, with the exception of some localized shifts in larval transport to the north or south near the WEAs. Pre-settlement summer flounder are competent swimmers which may facilitate shoreward movement towards shallow water and entrances to rivers, bays, or estuaries. Nearshore settlement is a well-established aspect of summer flounder life history, and although not specifically studied, settlement and grow-out may also occur in nearshore coastal waters. Any local scale shifts in settlement therefore may be mitigated by the ability of juvenile summer flounder to swim to appropriate habitats.

Conclusions and Suggested Further Study Areas

The main conclusion from the HDM results, is that there are likely to be perceivable changes in current speeds resulting from the development of the WEAs assessed in this study. Changes in the depth averaged current speed are both positive and negative, with decreased speeds primarily within the WEAs and increased speeds outside the WEAs. Current speed change is small in percentage, as well as in magnitude, where the maximum increase or decrease in current speed is $\sim 0.025 \text{ ms}^{-1}$. These estimated changes in current speeds result in discernable changes in settlement of sea scallop and surfclam, but less so for summer flounder.

Estimated settlement changes were primarily found in the New Jersey region for sea scallop and surfclam, with some lesser change through the Delmarva region. Average changes in settlement per destination area for sea scallop and surfclam are four and five orders of magnitude (10^4 and 10^5) lower than total baseline settlement. It is difficult to discern the population and fisheries relevance of these changes in settlement, as settlement does not necessarily equal recruitment into the fishery or to reproductive maturity. However, it appears that regional scale changes in settlement will have minimal impact on recruitment of these two species, but the persistent nature of the change in isolated hotspots, could cause localized changes (e.g., in landings) at the subpopulation scale. Summer flounder results are noisy and inconsistent, but show some change possibly related to the OSW developments. However, it is difficult to draw conclusions as to the relevance of these changes in summer flounder settlement, especially as juvenile summer flounder can move into appropriate habitat.

There are larger changes in settlement found for all species for the 15 MW scenario than the 12 MW, but changes in settlement from both scenarios are still on the same order of magnitude. For the sensitivity analysis (Scenario 5) simulation where the effects of the 15 MW wind wake model were doubled, the changes in larval settlement were approximately 1.5 to 2 times greater than Scenario 5: 15 MW full build-out, but the overall patterns remained the same. Change in sea scallop settlement was modeled for years 2017, 2018, and 2020. The results show inter-annual variability, with slightly different hotspots of increase or decrease within New Jersey, but the overall patterns of settlement change are similar for each year.

The main recommendations for potential improvement for the HDM involve improved parameterization of the monopile wake and the WTG wind wakes. There is potential for future improvement of the HDM due to some uncertainties in the hydrodynamic response resulting from ocean wakes caused by the monopiles. This uncertainty may be reduced by further study (observations and modeling) of the wake

mixing around large monopiles that may inform the parameterization within the sub-grid modeling approach. Additionally, there are uncertainties in the hydrodynamic response to the wind wakes caused by the WTG effect on air-sea interactions, that may be reduced by further study (observational and modeling) of the wake deficits, turbulence, and heat exchange around individual WTGs and large-scale OSW farms. This work on the WTG wind wakes may further inform and improve the parameterization employed in this study.

The main recommendations for potential improvement for the ABM of larval settlement and connectivity include the following collection of either dedicated separate research or relatively small modeling or analysis steps:

- Develop area and species-specific impact threshold limits for acceptability of changes in larvae settlement,
- Extend the ABM analyses for juvenile stages of target species development, especially where patterns of larval settlement change are more prominent and deemed to entail a level of impact risk. This will aid in understanding potential changes in recruitment and longer-term effects,
- Carry out localized levels of analysis through the application of dedicated local observational data / knowledge; and localized and more temporally refined ABM result post-processing for:
 - New Jersey / Delmarva areas to better understand the sea scallop / surfclam spawning variables and altered oceanic conditions causing the observed hotspots of settlement change,
 - Summer flounder – to obtain clarity around the modeling noise associated with observed settlement changes in inshore areas of Long Island/Nantucket, New Jersey / Delmarva, and North Carolina. This will allow for any localized changes in settlement and recruitment to be better understood, and
- Include the artificial reef effect (Mineur et al. 2012, Degraer et al. 2020, Glarou et al. 2020) in ABM analyses, with specific focus on the ‘Spillover Effect’ (van Berkel et al. 2020). This would allow experts to better understand the extent at which proposed OSW developments have the potential to become new habitat for fisheries relevant species and gain more insight into the relevance of oceanic response induced larval settlement changes in light of these other known OSW influences.

In summary, this study met the overall the overall objective to determine whether there are regional effects due to the OSW developments on coastal and oceanic environmental conditions that then influence the larval settlement, including changes in settlement patterns and connectivity.

1 Introduction

DHI Water & Environment, Inc. (DHI) undertook the project ‘Offshore Wind Impact on Oceanographic Processes: North Carolina to New York’. This involved the use of selected integrated MIKE Powered by DHI model components capable of assessing the influence that Offshore Wind Farms (OSW) have on the regional offshore physical environmental processes and the corresponding impacts to the distribution of the larvae of key fisheries species.

To provide further context to the study, a brief overview of relevant background information, general approach/objectives, OSW build-out analysis scenarios, and key project execution decisions are provided in the following subsections. This is followed by report sections that comprehensively describe the applied modeling methodologies and the associated results.

1.1 Project Background, Objectives, and General Approach

1.1.1 Project Background

This study was undertaken to inform the assessment of the impacts of OSW developments on the affected areas of the U.S. East Coast from the Carolinas to Massachusetts (as mandated by the National Environmental Policy Act (NEPA)). Stakeholders have indicated concerns regarding the potential impacts of OSW developments on the physical oceanographic environment, and the possibility for resulting impacts on marine ecology.

Similar previous work was completed and reported in Chen et al. (2016) and Johnson et al. (2021). These two studies were focused on potential impacts from OSW developments offshore Massachusetts and Rhode Island (MA-RI). Two model approaches were taken: Chen et al. (2016) considered the impacts of wind turbine generator (WTG) subsea foundations and employed a particle tracking model in conjunction with the Finite Volume Community Ocean Model (FVCOM) of the region. Johnson et al. (2021) considered the combined impact of subsea towers and WTG wake velocity deficits and took an agent-based modeling (ABM) approach that simulated larval dispersal of three species (Atlantic sea scallop, silver hake, and summer flounder) rather than a passive drifter particle approach.

The present study builds on the Johnson et al. (2021) study by extending the hydrodynamic model (HDM) and ABM models to include Nova Scotia to the north and Florida to the south, allowing the study of OSW developments from the Carolinas to Massachusetts. This study also includes a new refined description of the WTG wake impacts and introduced one different species of interest.

1.1.2 Project Objectives and Sub-Objectives

In order to address the above listed concerns, the present project aimed to develop a detailed HDM and ABM capable of accurately assessing potential changes in hydrodynamic flows, larval transport and larval settlement resulting from several representative OSW build-out scenarios located from the Carolinas to Massachusetts. Building on two previous studies (Chen et al., 2016 and Johnson et al., 2021) the study objectives were to investigate the oceanographic conditions existing without any OSW developments (i.e., baseline conditions) and the resulting changes from five OSW farm development scenarios. The five OSW development scenarios were studied to understand the changes to the coastal and oceanic environmental conditions including: wind (as it affected the sea surface stress), waves, currents, bottom shear stress, temperature stratification, larval transport and, ultimately, larval settlement.

To meet the primary objectives listed above, the following sub-objectives were defined:

1. Researching available datasets and information pertinent to:

- a. establishing an initial inventory of data and information for use in the model set-up, calibration, and validation of an initial long list of fisheries species larvae options,
 - b. choosing the larvae of three fisheries species based, in part, on the availability of required data and information, and
 - c. obtaining and managing the data for establishing the HDM and ABM numerical models.
2. The set-up of the baseline HDM and ABMs for the selected fisheries species that included:
 - a. MIKE 3 FM HD, MIKE 21 SW (wave), nearfield CFD and a wind wake loss models as the base for subsequent agent-based modeling, and
 - b. set-up and integration (i.e. with the hydrodynamic models) of the ABM Lab models in a manner that assured biologically realistic dispersal modeling of selected larvae species.
3. Assuring acceptable modeling via the execution of necessary calibration, validation and sensitivity of the baseline models.
4. Set-up of the HDM and ABMs to include specified OSW development scenarios to enable simulation of the dispersal effect of the OSW structures to the 3 chosen larvae.
5. Carrying out expert analysis of the modeling results.

1.1.3 General Approach

As used in Johnson et al. (2021), a finer model mesh was embedded in the WEAs to allow greater resolution of the OSW development areas and the HDM incorporated localized turbulence and wind wake effects of the WTG, both from monopile foundation drag and from WTG wakes. The model domain used in Johnson et al. (2021) was extended to encompass an area from midway along Nova Scotia southwards near to Cape Canaveral, Florida. This was deemed necessary to ensure that the oceanographic conditions throughout the model were adequately modeled. In addition, since the model covered the Massachusetts – Rhode Island region it was decided to include and re-examine this region both hydrodynamically and with the ABM.

The model was developed to simulate pertinent OSW development induced oceanographic changes and their corresponding impacts on affected environments during a multiyear period. The localized drag and turbulence effects were addressed via nearfield computational fluid dynamic (CFD) modeling of water flow near turbine foundations. The wind turbine wind wake effects were modeled using an industry standard wind wake loss model called [PyWake](#) (Pedersen et al., 2023) that was developed and is maintained by the Danish Technical University (DTU). The CFD and wind wake loss model results were integrated into the three-dimensional (3D) regional HDM. The model therefore fully implemented near and far field oceanic processes including surface wind, ocean currents (both lateral and vertical), sea-bed shear stress, air pressure, precipitation, evaporation, surface heat flux, water temperature and salinity.

While one example of particle tracking was included in the study, the primary focus on the potential impacts was based on larval transport using an ABM approach. The ABM methodology allowed for larval dispersal modeling via coupling of the ABM to the HDM. Agents were given species specific traits and reacted to generated HDM variables (e.g., water temperature) or external variables within the radius of its sensory sphere. The ABM approach was deemed to be more realistic than a pure particle model since the ABM includes the influence of pertinent larval behavior characteristics, thereby providing more refined results for assessing the effect that offshore turbines may have on larval transport.

It should be noted that no new modeling software was developed as a part of the study.

1.2 Project Scenarios and Decisions

As already indicated, there were several times during project execution where significant decisions were made with BOEM representatives that influenced the ultimate analysis, scope, and associated deliverables. In general, these included:

- The selection of which species to be modeled in the ABM,
- Defining key model parameters such as model structure and years of analysis, and
- Establishing the four OSW build-out scenarios to undergo HDM and ABM impact modeling.

1.2.1 Selection of Fisheries Species Larvae

The selection of three fisheries species larvae from a BOEM specified long-list of possible options constituted one of the initial project tasks and key analysis scope decisions. The long list was: Atlantic sea scallop (*Placopecten magellanicus*), Atlantic surfclam (*Spisula solidissima*), Summer flounder (*Paralichthys dentatus*), Black Sea Bass (*Centropristis striata*), Longfin squid (*Loligo (Doryteuthis) pealeii*), Little skate (*Leucoraja erinacea*), Spiny dogfish (*Squalus acanthias*), and *Calanus finmarchicus*.

The selection process was aided by an initial inventory of project area datasets and peer reviewed papers, established by fisheries expert colleagues from Continental Shelf Associates (CSA) with pertinent project area and subject matter knowledge. Joint deliberation on data availability for the long-list species and their representative characteristics eventually led to the selection of the following three species:

- Atlantic sea scallop (*Placopecten magellanicus*),
- Atlantic surfclam (*Spisula solidissima*), and
- Summer flounder (*Paralichthys dentatus*).

1.2.2 Key Hydrodynamic Model Decisions

The ABM study included a three-year inter-annual impact analysis for one species which required that the HDM would need to cover three years in time. The HDM was calibrated to year 2017 and validated for years 2018 and 2020. The year 2019 did not validate, so a decision was made to use the year 2020. The larval species selected for the inter-annual variability study was Atlantic sea scallop. Atlantic sea scallop spawn and settle within a calendar year so the selection of 2017, 2018 and 2020 was deemed acceptable.

Regarding the omission of the year 2019 above in Scenario 6, it was originally planned to be included in the sequence, however an erroneous setup was discovered at a very late stage. This had the consequence that the HDM results did not validate to an acceptable level. Therefore 2019 was dropped and 2020 was substituted for Scenario 6. The main issue with the year 2019 seems to be a discrepancy in the conversion of boundary data from HYCOM to MIKE along the southern boundary. A revised dataset and a change in interpolation introduced a slight shift of the Gulf Stream inflow which most notably effected the NY Bight cold pool formation. The formation of the cold pool was delayed and shortened relative to previous years. The source of that error is not fully understood at the time of writing. Therefore, as the year 2019 was an additional year, it was left out of the analyses for now. We believe that the discrepancy is only related to the year 2019 setup. This is demonstrated by the model versus observations validation analyses for the years 2017, 2018 and 2020 included in this report and appendices. Finally, sea scallops spawn and settle within a calendar year, so this decision did not affect the ability of the project to complete a three-year inter-annual variability analysis with respect the HDM or the ABM results.

1.2.3 OSW Build-out Scenarios

There are multiple WEAs for which leases have been awarded spanning from Massachusetts to North Carolina (**Figure 1.1**). The WEAs modeled were characterized as:

- 1.) Those that had a Construction and Operations Plan (COP) publicly available on BOEM’s website at the time of study initiation - these WEAs were labelled as “with COP”, and
- 2.) Those where a COP was not yet submitted, but the potential leases were identified - these WEAs were labelled as “Generic”.

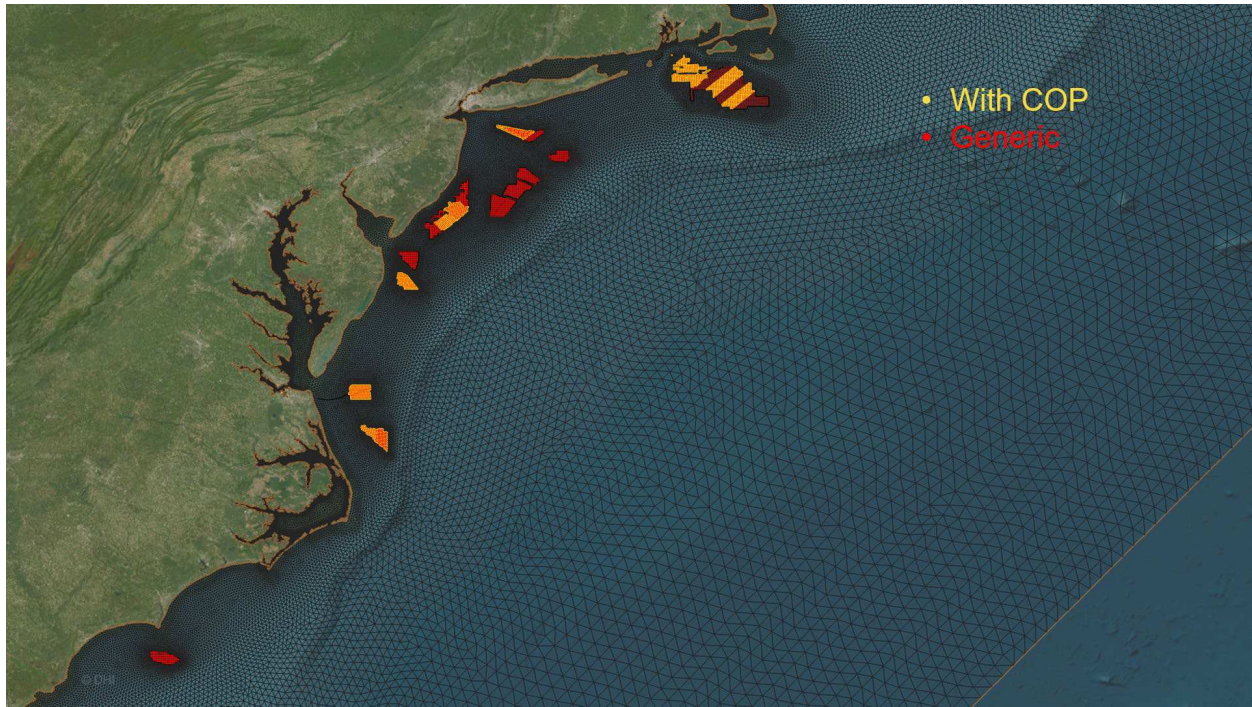


Figure 1.1. Wind Energy Areas

WEA areas that had a COP at the time of study initiation are shown in orange and those without a COP are shown in red. The model mesh detail is shown in black (Source: BOEM, 2022).

The size of the wind turbines to be deployed for many of the WEAs was not known at the time of this study. Therefore, both 12 MW and 15 MW wind turbines have been modeled. It should be noted, that since the beginning of this study, new lease and wind energy planning areas have been announced and that WEA leases announced after the commencement of this study have not been included.

Six analysis scenarios were determined, one of these is the baseline scenario, referred to as **Scenario 1**. The baseline scenario provides a reference condition, without any OSW structures, i.e., 0 tower foundations in the model and natural wind fields, but otherwise identical models, to allow for an accurate comparison to conditions with developed WEAs and an assessment of potential impacts.

The five (5) OSW build-out scenarios were:

- **Scenario 1: Baseline years 2017, 2018, and 2020** – modeled without any WTGs, all three species modeled for 2017. Only sea scallops modeled for 2018 and 2020.
- **Scenario 2: Partial Build-out 12 MW year 2017** - currently proposed developments with publicly available COPs, with 2,083 12 MW turbines for year 2017, all three species modeled in ABM,
- **Scenario 3: Partial Build-out 15 MW year 2017** – currently proposed developments with publicly available COPs, with 2,083 15 MW turbines for year 2017, all three species modeled in ABM

- **Scenario 4: Full build-out, 12 MW year 2017** – currently proposed developments with publicly available COPs and generic layouts for remaining lease areas, with 4,650 12 MW turbines for year 2017, all three species modeled in ABM
- **Scenario 5: Full build-out, 15 MW year 2017** – currently proposed developments with publicly available COPs and generic layouts for remaining lease areas, with 4,650 15 MW turbines for year 2017, all three species modeled in ABM

Additional details of these scenarios are provided in **Section 4.1.1**. The three ABM models (i.e., sea scallop, surfclam, and summer flounder) were completed for scenarios 1 through 5. In addition, the sea scallop ABM was simulated with Scenario 5 (15 MW Full Build-out) for years 2017, 2018, and 2020 to allow for inter-annual variability to be investigated. This is referred to as Scenario 6.

- **Scenario 6: Full build-out, 15 MW years 2017, 2018 and 2020** – currently proposed developments with publicly available COPs and generic layouts for remaining lease areas, with 4,650 15 MW turbines. Only sea scallops modeled for 2017, 2018 and 2020 in ABM.

2 Baseline Hydrodynamic Model Input Data

The following subsections provide a comprehensive overview of the various input data that were used to set-up the HDM.

2.1 Overview of Geographic Coverage

The geographic extent of the regional HDM was approximately from Nova Scotia to Cape Canaveral, Florida (**Figure 2.1**. Model Domain Extent from Nova Scotia to Florida in Black). The extent of the model domain is primarily driven by the requirement to have the most suitable sections for boundary conditions. The model was established in hindcast mode, using MIKE 3 FM HD. Data is included for the years 2017, 2018, and 2020, with targeted localized resolution in the project area (i.e., the WEAs where OSW leases are located from Massachusetts-Rhode Island south to South Carolina).

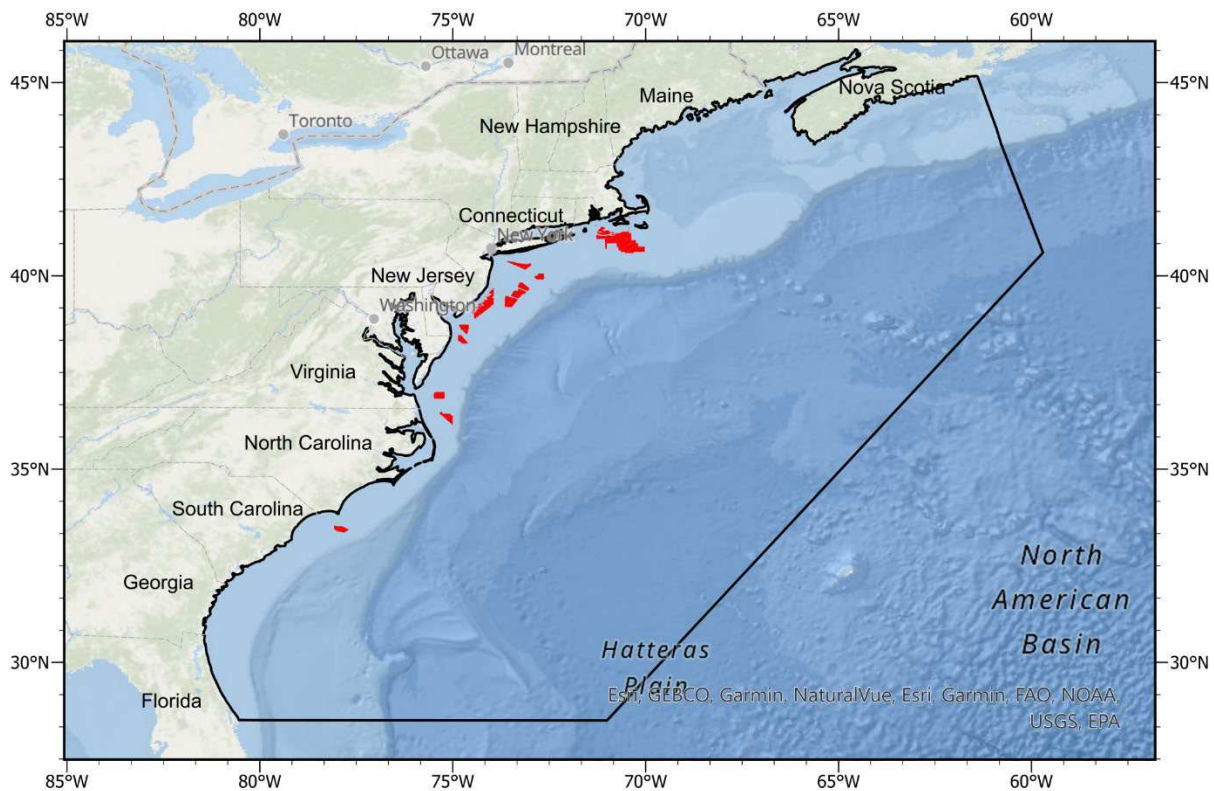


Figure 2.1. Model Domain Extent from Nova Scotia to Florida in Black

Wind Energy Areas included in Red (Credit Wind energy areas: BOEM) (Credit Bathymetry data are Esri, GEBCO, Garmin, NaturalVue, FAO, NOAA, USGS, EPA).

2.2 Bathymetric Data

The bathymetry in the HDM is based on a combination of:

1. U.S. National Oceanic and Atmospheric Administration (NOAA) survey archive at National Centers for Environmental Information (NCEI), which have high resolution gridded bathymetries for the project area,
2. MIKE C-Map digital navigational charts.

3. Data from the General Bathymetric Chart of the Oceans (GEBCO) was also used as a source for deep-water bathymetry.

Overlapping data has been prioritized in the mentioned sequence (U.S. NOAA first to GEBCO, last).

2.3 Meteorological Data

Similar to Johnson et al. (2021), the Climate Forecast System Reanalysis (CFSR) wind fields were the basis for continuous wind forcing in the 3D HDM. The CFSR wind fields cover the North Atlantic from 1979 to 2023 with two model updates. The CFSR data is comprised of surface winds, pressure and relevant air-parameters as relative humidity, cloud cover, and air temperature. The CFSR dataset was established by NOAA's National Center for Environmental Prediction (NCEP). CFSR is a coupled meteorological and oceanographic model system that uses synoptic data for initialization. The data are available on an hourly basis from January 1, 1979, through the present. The initial CFSR dataset covers the 31-year period from 1979 to 2010. More recently, the operational dataset, the Climate Forecast System version 2 (CFSv2), has been utilized in modeling and these data are available from 2010 through the present. The underlying model in CFSv2 is the same as for CFSR, however, the spatial resolution of the atmospheric model was increased from 0.3 degree to 0.2 degree, while the resolution of atmospheric pressure, relative humidity and precipitation was 0.5 degree for the entire period (interpolated to the same grid as the wind speed). In the analysis conducted for the project, the CFSv2 dataset was used.

CFSR was designed as a global, high-resolution, coupled atmosphere-ocean-land surface-sea ice system to provide the best estimate of the state of these coupled domains. The atmospheric model behind the CFSR modeling complex is NCEP's Global Forecast System. In the standard CFSR, priority is given to land properties, i.e. if an element is mixed land/water the land properties prevail. We have adjusted CFSR near-coastal mixed cells to give priority to the water properties, in order to get a better description of coastal offshore winds.

In addition to 10 m wind data, the CFSR parameters included in this project for estimating air-sea heat exchange were:

- Air temperature at 2 m,
- Air relative humidity, and
- Cloud cover.

2.4 Oceanographic Data

The 3D ocean model required salinity and temperature as well as ocean currents prescribed on the open boundaries and for initial conditions. As was done in Johnson et al. (2021), the Hybrid Coordinate Ocean Model (HYCOM) global circulation model was used with data from the HYCOM database (Helber et al., 2013). HYCOM is a layered ocean model. For the years 2017 and 2018 the spatial resolution was from 0.08-degree longitude x 0.08-degree latitude with 32 non-equidistant layers. Late in 2018, the model resolution changed to 0.08-degree longitude x 0.04-degree latitude with 41 layers, nine additional layers near the surface with the top 14 layers always sigma-z so that water shallower than 84 m are always fixed coordinates.

The HYCOM model is fully dynamic and applies a variational data assimilation technique for surface elevations and temperature. The HYCOM archive has daily 3D fields of elevation, current profiles, temperature, and salinity and covers the period of 1995 to 2023 from various model versions. This model is well established in the North Atlantic.

2.5 Astronomical Tide Data

As was done in Johnson et al. (2021), tidal boundary water levels were sourced from DHI’s global tidal model DTU10 (Andersen and Knudsen, 2009).

2.6 Boundary Conditions with Combined Oceanographic and Tidal Forcing

A combined downscaling approach was taken in order to consider ocean (baroclinic) forcing together with the tidal induced (barotropic) forcing. The current components and surface elevation from the daily ocean data (HYCOM) at the boundaries were linearly added to the hourly tidal components extracted from the DHI’s global tidal model DTU10. This procedure was applied to the years simulated (2017, 2018, and 2020).

2.7 River Discharge

Freshwater inflow from rivers is important as it affects the stratification in coastal areas and the nearshore circulation. For the present project, the major rivers of concern are shown in **Table 2.1**. There are data archives for river discharges from the U.S. Geological Survey (USGS) that cover daily data from 2010 to 2023. In total, thirty-six (36) rivers were used to model the daily freshwater inflow into the 3D model.

Table 2.1. Rivers Included as Freshwater Sources in the Hydrodynamic Model

Rivers	Rivers	Rivers
Penobscot, Maine	Mullica, NJ	Neuse, NC
Kennebec, Maine	Delaware, NJ	Cape Fear, NC
Androscoggin, Maine	Pocomoke, MD	Peedee, SC
Saco Maine	Nanticoke, DE	Santee, SC
Merrimack, MA	Susquehanna, PA	Edisto, SC
Blackstone, RI	Potomac, DC	Salkehatchie, SC
Shetucket, CT	Rappahannock, VA	Coosawhatchie, SC
Connecticut, CT	Pamunkey, VA	Savannah, GA
Quinnipiac, CT	James, VA	Ogeechee, GA
Hudson, NY	Nottoway, VA	Altamaha, GA
Hackensack, NY	Roanoke, NC	Satilla, GA
Lawrence, NJ	Tar, NC	St. Mary's, FL

2.8 Observational Data Sources

The development of numerical hydrodynamic models is dependent on the availability of observational data that can be used to calibrate and check the validity of the model results. While there are considerable observational data available for the study area, these data are held by many different entities and span many different periods, with varying quality and monitoring methodology. Data were obtained from both public and OSW developer sources to allow for calibration and validation of the HDM results.

2.8.1 Current Observational Data Sources

Subsurface currents are generally one of the most complicated parameters to measure and data are therefore scarce. A full list of the relevant Acoustic Doppler Current Profiler (ADCP) measurement data spanning 2017, 2018, and 2020 is included **Appendix A.2**.

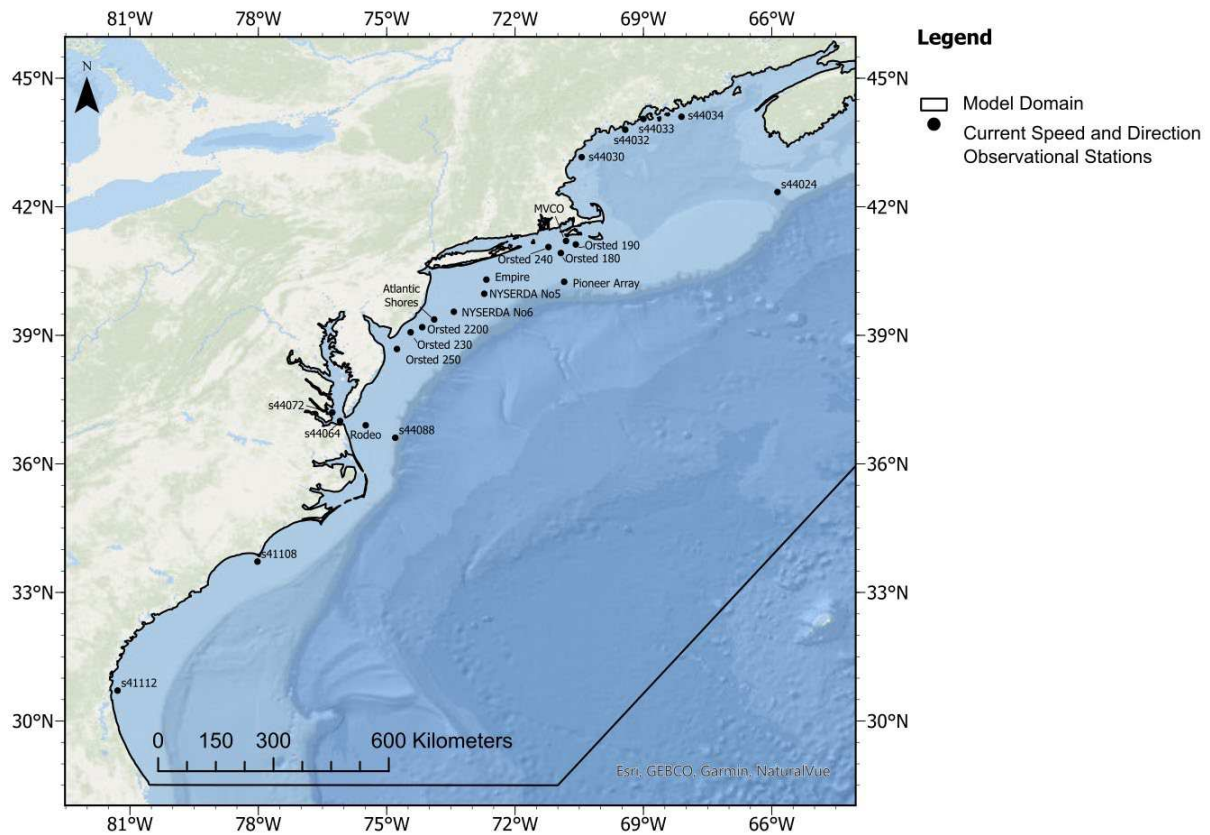


Figure 2.2. Acoustic Doppler Current Profiler (ADCP) Measurement Locations

Each ADCP station had varying temporal coverage, so the data were compared to the appropriate years that were modeled (2017, 2018, and 2020)

In addition to the ADCP measurements regional High-Frequency Radar Observations (HFRO) or CODAR surface current measurements were available for the time frame modeled. The measurements made by the HFRO are truly surface current measurements as the instrument measures the doppler shift of surface ripples on the water. It should also be understood that comparing the CODAR measurements where the instrument is sensing the top few millimeters of the water surface to an HDM where the top layer has a finite thickness that is on the order of 5 meters is in some ways qualitative. Nevertheless, the ability to review the regional current patterns using the HFRO measurements was too enticing to overlook. The HFRO data was downloaded from the MARACOOS site (Roarty, 2020). **Figure 2.3** below shows the coverage of the HFRO system.

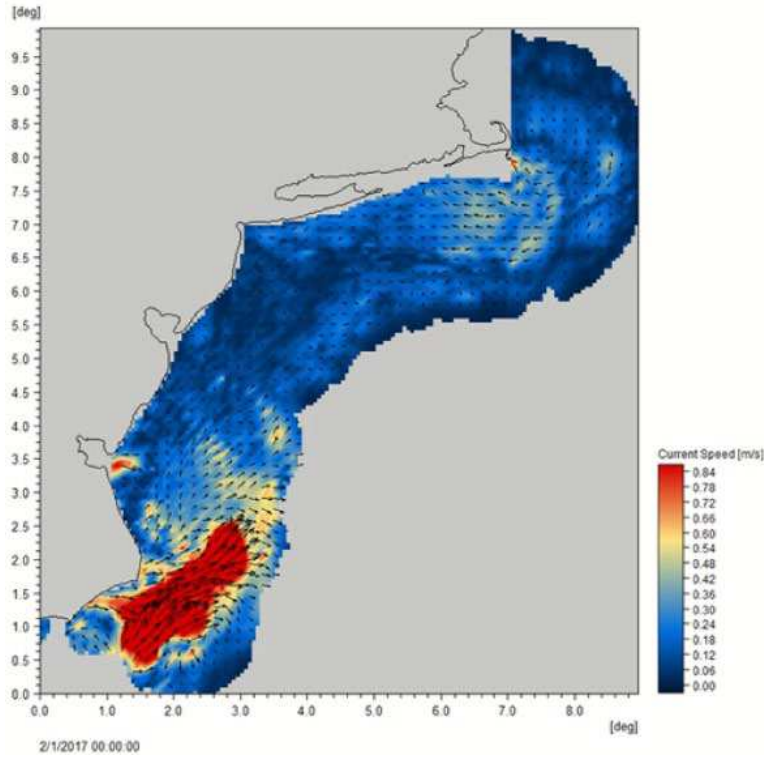


Figure 2.3. Image Showing the High Frequency Radar Observation (HFRO) Coverage on the U.S. East Coast

Snapshot of HFRO results from 1st February 2017

2.8.2 Water Level Observational Data Sources

Relevant water level measurement data collected and used from NOAA's Tides and Currents database included:

- Station ID: 8413320 - Bar Harbor, ME (44° 23.5 N, 68° 12.3 W),
- Station ID: 8418150 - Portland, ME (43° 39.5 N, 70° 14.7 W),
- Station ID: 8447435 - Chatham, MA (41° 41.3 N, 69° 57.1 W),
- Station ID: 8449130 - Nantucket Island, MA (41.285 N 70.096 W),
- Station ID: 8510560 - Montauk, NY (41° 2.9 N, 71° 57.6 W),
- Station ID: 8534720 - Atlantic City, NJ (39.357 N 74.418 W),
- Station ID: 8531680 - Sandy Hook, NJ (40° 28.0 N, 74° 0.6 W),
- Station ID: 8570283 - Ocean City Inlet, MD (38° 19.7 N, 75° 5.5 W),
- Station ID: 8651370 - Duck, NC (36° 11.0 N, 75° 44.8 W),
- Station ID: 8654467 - USGS Station Hatteras, NC (35° 12.5 N, 75° 42.3 W),
- Station ID: 8670870 - Fort Pulaski, GA (32° 2.1 N, 80° 54.2 W), and
- Station ID: 8720218 - Mayport (Bar Pilots Dock), FL -(30° 23.9 N, 81° 25.7 W).

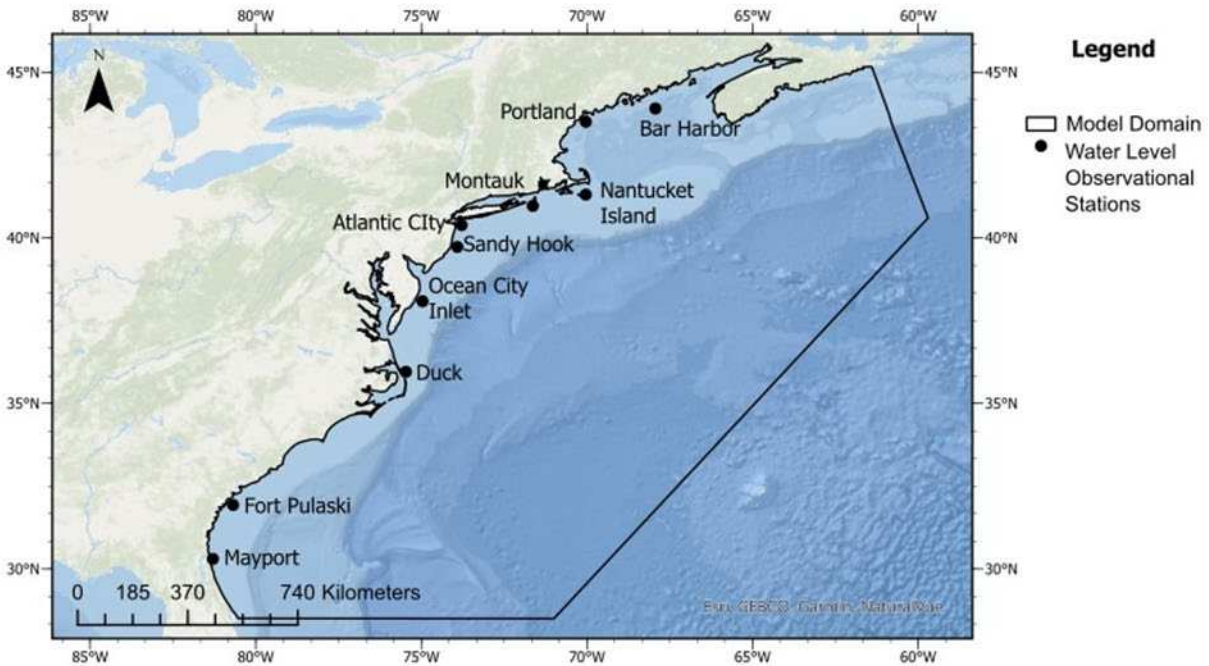


Figure 2.4. Water Level Measurement Locations

Twelve (12) NOAA stations spanning from Maine to the north to Florida in the south were used to validate the HDM with respect to water level.

2.8.3 Wave Observational Data Sources

Relevant wave measurement data were used from the NOAA National Data Buoy Center (NDBC). The NDBC and OSW farm concessionaires operate several buoys along the U.S. East Coast. Six buoys were selected to verify the wave model. They were:

- Station 44097 - Block Island, RI (40°58'2" N, 71°7'25" W), Water depth: 49 m,
- Station 44025 – Long Island, NY (40°15'30" N, 73°10'29" W). Water depth: 40.2 m,
- Station 44091 - Barnegat, NJ (39°46'5" N, 73°46'13" W). Water depth: 25.6 m,
- Station 440009 - Delaware Bay, DE (38°27'35" N, 74°41'31" W). Water depth: 24 m,
- Station 44093 - OSW Energy Area, VA (36°52'21" N, 75°29'30" W). Water depth: 26.82 m, and
- Station 41013 - Frying Pan Shoals, NC (33°26'28" N, 77°45'50" W). Water depth: 33 m.

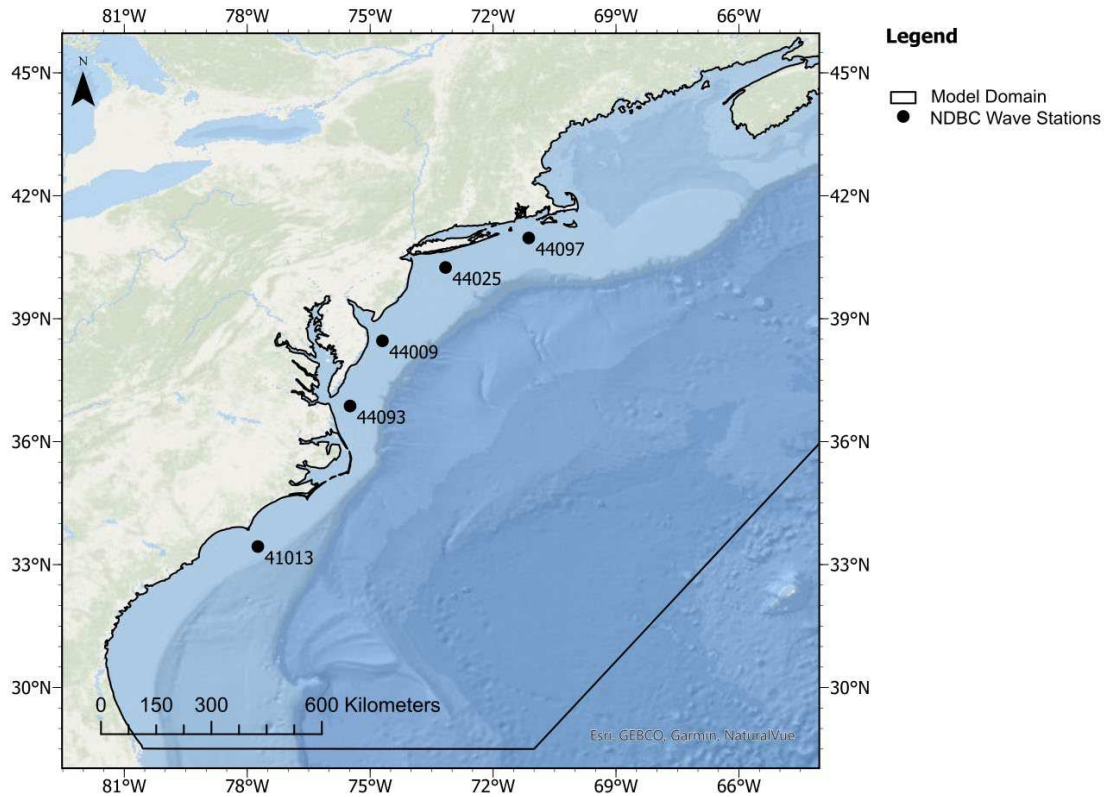


Figure 2.5. Location of NDBC and Other Wave Buoys Used in the Wave Model Verification

Six (6) NDBC wave buoys were used in model verification.

2.8.4 Sea Temperature Observational Data Sources

Observational sea surface temperature (1.5 m below water line) data was collected from NDBC buoys to compare to model results. The stations used included the following:

- Station ID: 44008 – Nantucket, MA (40.504 N, 69.248 W),
- Station ID: 44097 - Block Island, RI (40.967 N, 71.126 W),
- Station ID: 44017 - Montauk Point, NY (40.693 N, 72.049 W),
- Station ID: 44025 - Long Island, NY (40.251 N, 73.164 W),
- Station ID: 44065 - New York Harbor Entrance, NY (40.369 N, 73.703 W),
- Station ID: 44027 – Jonesport, ME (44.28 N, 67.30 W),
- Station ID: 44005 – Gulf of Maine, ME (43.20 N, 69.13 W),
- Station ID: 44098 – Jeffreys Ledge, ME (42.80 N, 70.17 W),
- Station ID: 44011 – Georges Bank (41.09 N, 66.56 W),
- Station ID: 44091 – Barnegat, NJ (39.77 N, 73.77 W),
- Station ID: 44066 – Texas Tower (39.62 N, 72.64 W),
- Station ID: 44009 – Delaware Bay, DE (38.46 N, 74.69 W),
- Station ID: 44058 – Stingray Point, VA (37.57 N, 76.26 W),
- Station ID: 44099 – Cape Henry, VA (36.91 N, 75.72 W),
- Station ID: 44014 – Virginia Beach, VA (36.60 N, 74.84 W),
- Station ID: 44095 – Oregon Inlet, NC (35.75 N, 75.33 W),
- Station ID: 41025 – Diamond Shoals, NC (35.01 N, 75.45 W),

- Station ID: 41108 – Wilmington Harbor, NC (33.72 N, 78.02 W),
- Station ID: 41013 – Fryngpan Shoals, NC (33.44 N, 33.44 W),
- Station ID: 41004 – Edisto, SC (32.50 N, 79.10 W), and
- Station ID: 41008 – Grays Reef, GA (31.40 N, 80.87 W).

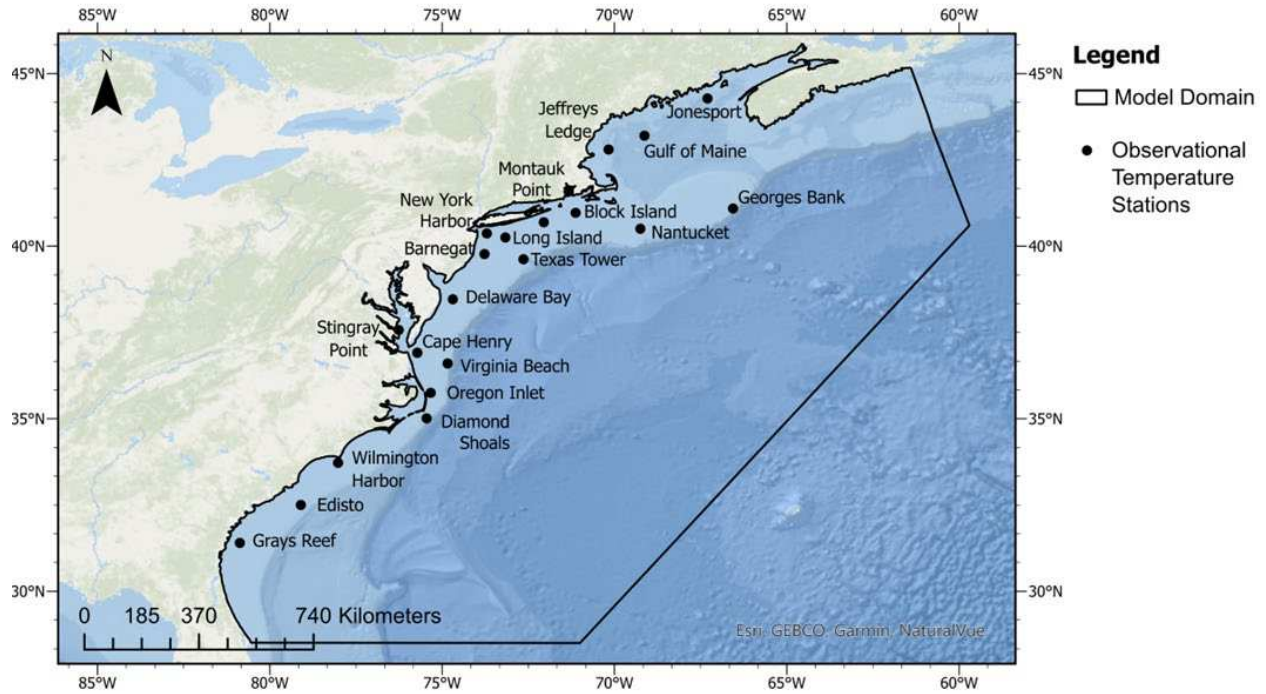


Figure 2.6. Location of Sea Temperature Point Measurements Used in the Model Temperature Verification

In addition, satellite observations were used from the UK Met Office GHR SST (Group for High Resolution Sea Surface Temperature) and provided via the Global Ocean Operational Sea Surface Temperature and Ice Analysis (OSTIA) dataset.¹ OSTIA is a Level 4 sea surface temperature analysis, which includes signals from several advanced sensors. The OSTIA analysis has a highly smoothed Sea Surface Temperature (SST) field and was specifically produced to support SST data assimilation into Numerical Weather Prediction models. See Good et. al., (2020), Donlon et. al., (2011) and Stark et. al., (2007) for further information on the OSTIA dataset.

¹ <https://podaac.jpl.nasa.gov/dataset/UKMO-L4HRfnd-GLOB-OSTIA>

3 Baseline Oceanography Review, Hydrodynamic Model Setup, and Baseline Results

3.1 Oceanographic Processes Review

The oceanographic processes of the U.S. and Canadian Atlantic Coast are well documented by numerous researchers. In general, the U.S. and Canadian Atlantic Coast is characterized by the relatively wide and shallow continental shelf (~ up to 120 m deep). The U.S. and Canadian Atlantic currents along the continental shelf and slope can be characterized by south flowing relatively cold, fresh water that originates in colder Canadian and arctic regions. These cold counter currents are commonly referred to as the Labrador Shelf and Slope Currents (Fratantoni & Pickart, 2007; Loder et al., 1998). In the southern portion of the study area the Gulf Stream starts out hugging the coast. The Gulf Stream can be characterized as warmer and denser than the south flowing cold counter currents. At Cape Hatteras the Gulf Stream separates from the coast and meanders towards the northeast. The Mid-Atlantic Bight is a mixing zone of the colder less dense water from the north with the Gulf Stream. In addition, on occasion, warm core rings are shed from the Gulf Stream and can impinge on the Southern New England Shelf and farther south. (Chen et al., 2014; Joyce et al., 1984; Zhang & Gawarkiewicz, 2015).

It is of particular note that the cold counter current flows along the Scotian Shelf through the Gulf of Maine. The Labrador current then splits and flows around Georges Banks or through the Great South Channel and along Cape Cod bringing cold bottom water to the Mid-Atlantic Bight shelf areas (**Figure 3.1 and Figure 3.2**). One significant effect of this is the formation of the “Cold Pool”. The “Cold Pool” is a relatively cool mass of near-bottom water that persists along the shelf during the spring and early summer, forming a strong vertical temperature stratification (Stevenson et al., 2004). Chen et. al. (2020) reviewed the long-term sea surface temperature variability (study period 1982-2018) of the U.S. and Canadian continental shelf and slope. Another significant force are the tidal currents, that can be relatively strong in the sounds and shallow waters along the coast where OSW development is planned.

The literature supports that there appear to be long term (decadal scale) changes to the behavior of the Gulf Stream (Chen, et al., 2014; Joyce et al., 1984; Zhang and Gawarkiewicz, 2015; Andres, 2016; Gawarkiewicz et al., 2018), warm core rings (Gangopadhyay et al., 2019) and the Cold Pool (Friedland et al., 2022). Additionally, there appear to be more occurrences of marine heatwaves (Grosselindemann et al., 2021) impinging on the mid-Atlantic bight. While these long-term climatological changes are not the topic of this study it should be noted that the models employed are used in hindcast mode and capture the oceanographic baseline processes for the years studied where the model is validated. This implies that the changes due to the OSW farms from the baseline are correct if one assumes that the hydrodynamic processes of OSW farm wind-wake and monopile drag are appropriately captured. This is the basis of the impact assessment and the use of hydrodynamic and agent-based models.

The overall wave climate for the region is dominated by persistent southeasterly swell from the North Atlantic. This southeasterly swell is supplemented by locally generated multidirectional wind driven waves. Extreme wave events in the summer and fall can result from tropical cyclones affecting the OSW development areas. In the northern portion of the study area, winter storms called Nor'easters can dominate the extreme wave conditions. The annual mean significant wave height in the offshore area is roughly 1 - 2 m while extremes may reach above 11 m.

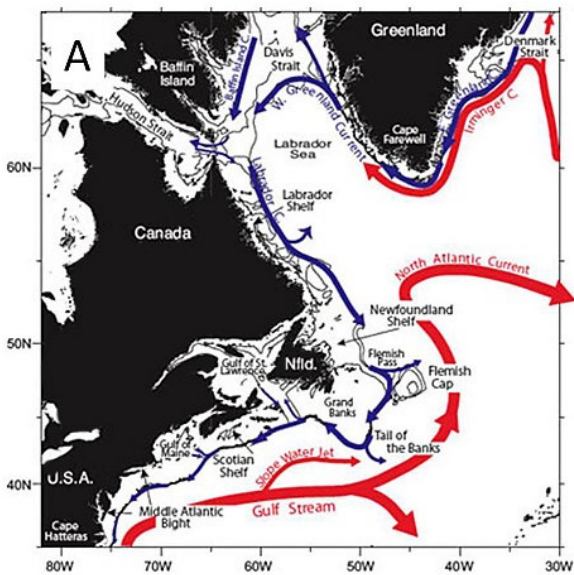


Figure 3.1. Map of the Western North Atlantic Ocean Currents

Showing two dominant current systems affecting the Mid-Atlantic region: Gulf Stream (red) and Labrador Current (blue). (Credit: Fratantoni and Pickart, 2007)

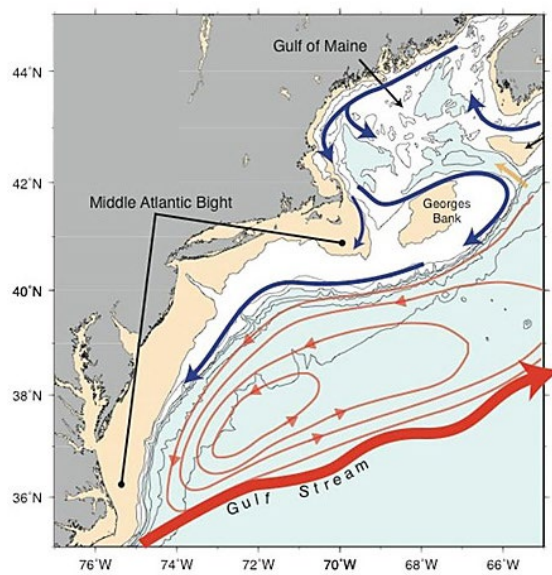


Figure 3.2. Map of Mid-Atlantic Bight

Influence on the Mid-Atlantic region of southward-flowing cool currents (blue) and warmer currents (red) associated with the Gulf Stream. (Credit: Li et al., 2015)

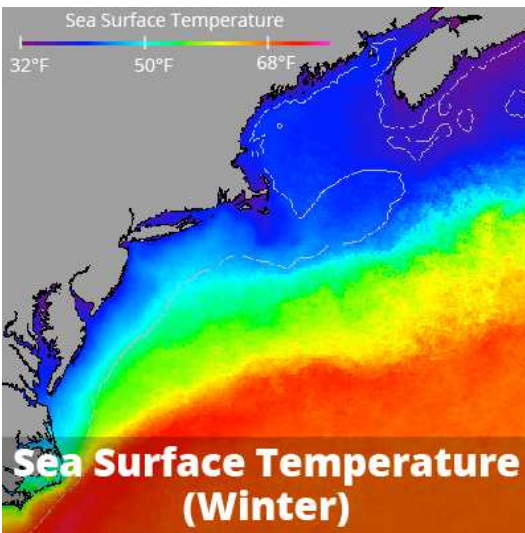


Figure 3.3. Sea Surface Temperature (Winter)

Wintertime satellite imagery reveals cold water (blue) near the Mid-Atlantic coast. Warmer water (red) lies offshore in the Gulf Stream. (Credit: National Oceanic and Atmospheric Administration (NOAA))

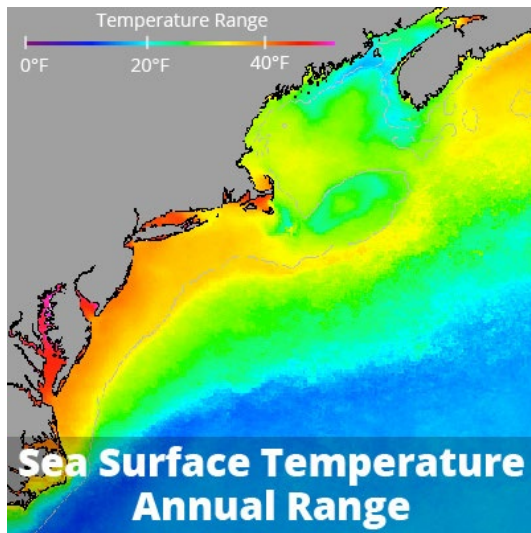


Figure 3.4. Sea Surface Temperature (Annual Range)

This map shows average annual range of sea surface temperature from 1985 to 2009 based on satellite imagery. The Mid-Atlantic coast experiences a wide range of temperatures, as indicated by red and orange. (Credit: NOAA)

With the addition of fresh water sources from the larger rivers all along the U.S. East Coast the coastal waters can become density stratified especially in the summer when the warmer fresh river waters are flowing out of the estuaries (Stevenson et al., 2004). These summer river outflows into the ocean leads to a density stratification in the near-coastal water column in the Mid-Atlantic Bight shelf region that can supplement the thermal stratification from the Gulf Stream waters which can impede the mixing between the warmer lighter upper layer and the colder denser bottom layer. With regard to stratification and referenced in **Figure 3.5** below, Sigma-t is a quantity used in oceanography to measure the density of seawater at a given temperature. σ_T is defined as $\rho(S,T)-1000 \text{ kg m}^{-3}$, where $\rho(S,T)$ is the density of a sample of seawater at temperature T and salinity S, measured in kg m^{-3} , at standard atmospheric pressure.

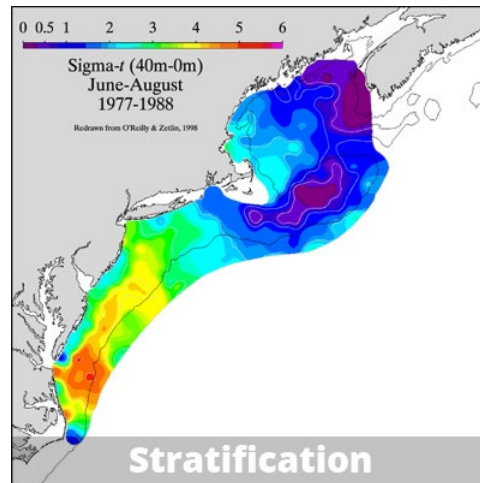


Figure 3.5. Density Stratification in the Mid-Atlantic Bight

Regional differences in summer stratification, showing strongly stratified areas (indicated by red, orange, and yellow colors) in the Gulf of Maine and the Mid-Atlantic Bight (Credit: O'Reilly and Zetlin, 1998)

It should be noted that general statements regarding the oceanography and the specifics of the model may sometimes not correlate in a one-to-one manner. However, it was a goal of the project to use field measurements (currents, water levels, temperature, wave height elevations, etc.) to verify the model results against observed conditions.

3.2 Overview, Model Domain and Setup

The details of the model setups and their calibration and validation are described in the following subsections.

3.2.1 Model Domain

The full regional model domain was found to be critical for simulation of the impacts of the development of the Mid-Atlantic renewable energy lease areas from North Carolina to Massachusetts. The influence of the Gulf stream was required and therefore the boundary of the model was extended eastward to allow the Gulf Stream to “exit” the model perpendicular to the Eastern model boundary. The model was bounded on the south near Cape Canaveral at 80.6°W 28.5°N , and extends eastwards out past the shelf to 71.0°W 28.5°N . From here, the eastern-most boundary extends to the north off the Nova Scotian shelf at 59.7°W 40.6°N . The northern boundary continues inshore to 61.4°W 45.2°N , and the remaining boundary continues along the coastline to the point near Cape Canaveral. **Figure 3.6** shows the hydrodynamic model mesh with the above referenced boundary points.

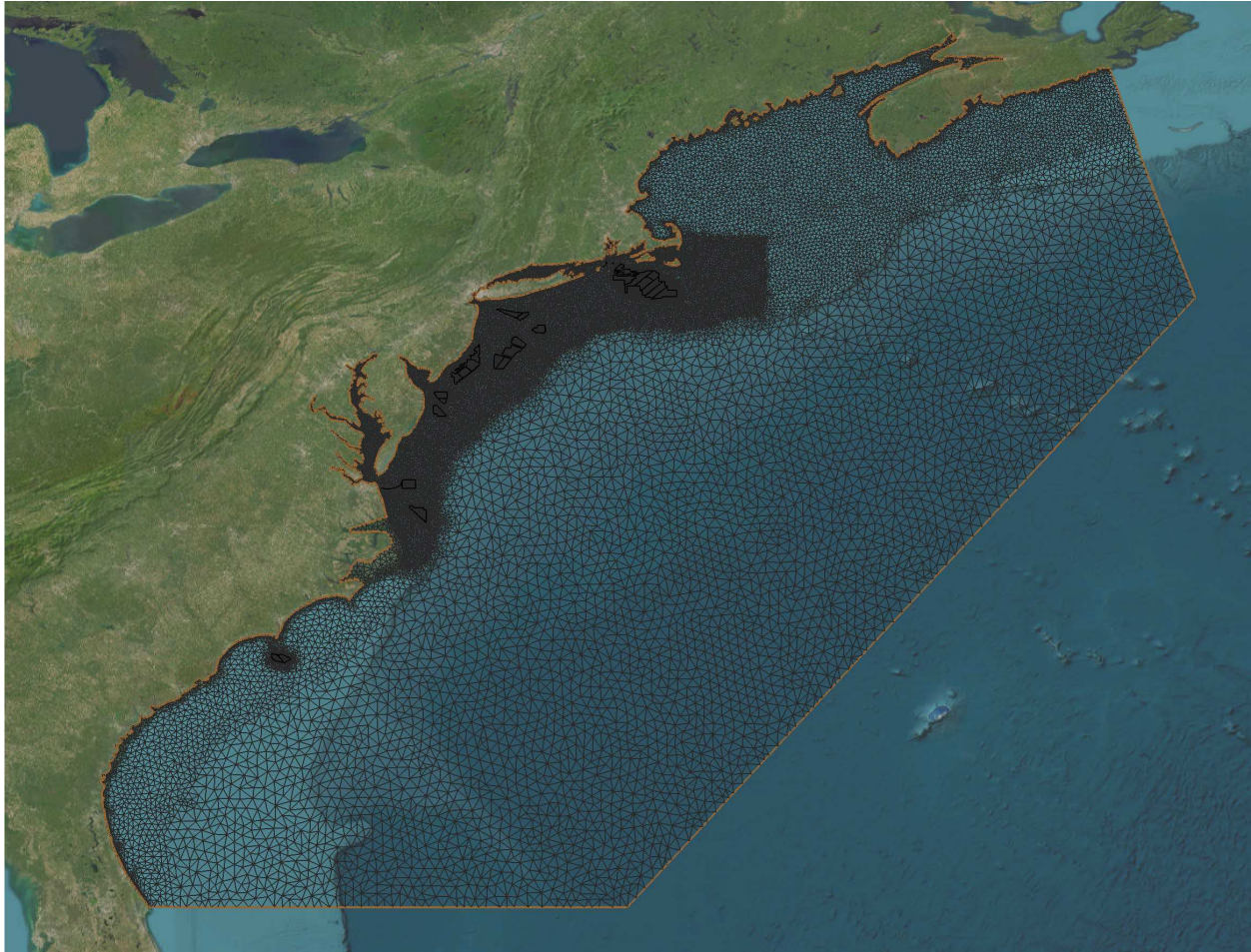


Figure 3.6. Hydrodynamic Model Mesh for the HDM
Model domain and mesh, with higher resolution segments around the WEAs.

3.2.2 Hydrodynamic Current Model Setup

In this section, some aspects of the model setup including model forcing, domain, parameterizations and their impact on model results are discussed. As mentioned in **Section 1.2.2**, the currents were modeled using DHI's general marine 3D modeling framework, MIKE 3. MIKE 3 Flexible Mesh Hydrodynamic (MIKE 3 FM HD) model is a hydrostatic full 3D ocean Reynolds Averaged Navier-Stokes (RANS) model² that uses a semi-implicit finite-volume method with high-order spatial and temporal discretization. It also uses an unstructured flexible mesh and combined sigma-z layer vertical discretization. The flexible mesh allows for efficient focusing of computer resources around the areas of interest, while avoiding unnecessary resolution and computational demands in areas where high resolution is not essential to the problem at hand. The model solves the 3D baroclinic shallow water equations, coupled via an equation of state to heat and salt transport and statistical turbulence parameters described by a k-epsilon model. The model includes all the most relevant physical processes including but not limited to tides, atmospheric forcing (winds, temperature, solar radiation, etc.), density effects, turbulent mixing, river inflows, flooding and drying, etc. **Table 3.1** below shows the reference model set-

² Full scientific documentation is available upon request or at:
https://manuals.mikepoweredbydhi.help/2017/Coast_and_Sea/MIKE_321_FM_Scientific_Doc.pdf.

up, which was used as a baseline to assess model sensitivity to variations in forcing and in some model parameters as described in the following sections. The baseline model set-up is based on DHI experience on 3D downscaling modeling.

Table 3.1. Main HDM Set-Up Parameters

Variable / Parameter	Description
Sigma Levels	20 levels on the top 100 m
Z-Levels	58 levels, 10 m to 500 m resolution below the sigma levels, reaching 5,245 m in water depth
Time/Space Discretization	First order
Horizontal Eddy Viscosity	Smagorinsky formulation, constant = 0.3
Vertical Eddy Viscosity	k- ϵ model
Bed Roughness Height	1 mm in the majority of the model. In the area of Nantucket Shoals to Georges Banks the bed roughness height is 9 cm
Wind Friction	Varying with wind speed
Initial Condition	Surface elevation from HYCOM model Salinity and temperature from HYCOM
Boundary Conditions	Salinity and temperature from HYCOM Current components and surface elevation from combining HYCOM and a tidal model
Transport Equation Solution Technique	High order discretization scheme
Number of 2D/3D Elements in Regional Model	43,512/838,957

3.2.2.1 Horizontal Viscosity

The turbulent stresses are modeled using separate approaches for horizontal and vertical directions. Horizontally a Smagorinsky coefficient for eddy viscosity was applied. The coefficient was increased from the standard value of 0.28 to 0.3. Changes in current speed showed an improvement when compared with measurements. Therefore, the 0.3 value was used for HD model simulations.

3.2.2.2 Heat Exchange

A key to the success of this project was the ability of the 3D HDM to reproduce the annual thermal fluctuations of the region. The 3D hydrodynamic model include a heat exchange module, where the heat exchange with the atmosphere is included in the 3D hydrodynamic based on four physical processes:

- Latent heat flux (or heat loss due to vaporization),
- Sensible heat flux (or the heat flux due to convection),
- Net short wave radiation, and
- Net long wave radiation.

following normal oceanographic air-sea interaction methods.³ Latent and sensible heat fluxes and long wave radiation are assumed to occur at the surface. The following paragraphs describe the methods used in 3D hydrodynamic for the four physical properties. Solar radiation is implemented using an astronomical solar height model, taking into account daylength variations.

3.2.2.2.1 Latent Heat Flux

The absorption profile for the short wave flux is approximated using Beer's law. The attenuation of the light intensity is described through the modified Beer's law. Dalton's law (Sahlberg, 1984) was used for the estimation of the evaporative heat loss (or latent flux).

3.2.2.2.2 Sensible Heat Flux

The sensible heat flux (or the heat flux due to convection) depends on the type of boundary layer between the sea surface and the atmosphere. The heat loss due to convection occurs by wind driven forced convection and free convection. The free convection was taken into account by introducing a critical wind speed at 2m/s.

3.2.2.2.3 Net Short Wave Radiation

Radiation from the sun consists of electromagnetic waves with wavelengths from 1,000 to 30,000 Angstroms. Most of this energy is absorbed in the ozone layer leaving only a fraction of the energy to reach the surface of the Earth. Furthermore, the spectrum changes when sunrays pass through the atmosphere. Most of the infrared and ultraviolet compound is absorbed such that solar radiation on Earth consists of light with wave lengths between 4,000 and 9,000 Angstroms. The intensity depends on the distance to the sun, declination angle and latitude, extra-terrestrial radiation and the cloudiness and amount of water vapor in the atmosphere (Iqbal, 1983). The radiation is calculated based on actual daylength and cloud cover.

3.2.2.2.4 Net Long Wave Radiation

A body or a surface emits electromagnetic energy at all wavelengths of the spectrum. The long wave radiation consists of waves with wavelengths between 9,000 and 25,000 Angstroms. The long wave emittance from the surface to the atmosphere minus the long wave radiation from the atmosphere to the sea surface is call the net long wave radiation and is dependent on the cloudiness, the air temperature, the vapor pressure in the air and the relative humidity. The net outgoing long wave radiation is given by Brunt's equation (Lind and Falkenmark, 1972).

3.2.3 Spectral Wave Model Setup

This section describes the wave model developed and used for the present assessment. The data was established through state-of-the-art numerical modeling using MIKE 21 SW Spectral Wave FM model developed by DHI, that simulates the growth, decay and transformation of wind-generated waves and swells in offshore and coastal areas. MIKE 21 SW Spectral Wave FM is a 3rd generation WAM model. The wave model was set up with a fully spectral, in-stationary formulation that is suitable for wave studies involving time-dependent wave events and wind conditions varying rapidly in space and in time.

The Spectral Wave model used the same mesh as the HDM so that the changes in the wave characteristics due to the change in wind forcing from the WTGs would be easily realized in the model. The impact on

³ https://manuals.mikepoweredbydhi.help/2017/Coast_and_Sea/MIKE_321_FM_Scientific_Doc.pdf

the wave height and the impact on bed shear stresses were modeled for year 2017. The spectral resolution of the wave model consisted of 25 frequencies and 16 directions. The model used atmospheric forcing from CSFR, and the offshore open boundaries were obtained from DHI global model, providing directional spectra.

Table 3.2. Wave Model Set-Up Parameters

Variable / Parameter	Description
Mesh Resolution	See Section 3.2.2
Simulation Period	Between February 1, 2017, and March 1, 2018, 1 hour interval
Basic Equations	Fully spectral, in-stationary
Discretization	25 frequencies, period ranging from 0.9 to 33s. 24 directions
Time Step (Adaptive)	0.01-3600s with a maximum time-step factor of 32
Water Level	2D HDLOC (temporally and spatially varying)
Wind Forcing	CFSR wind
Wave Breaking	Included, Specified Gamma, $\gamma = 0.8$, $\alpha = 1$
Bottom Friction	Nikuradse, equivalent roughness 0.001 m
White-Capping	$C_{dis} = 2.1$, $\Delta C_{dis} = 0.7$
Boundary Conditions	2D spectra varying in time and along line from SWUS-EC
Dimensional Growth	1.42

3.3 Baseline Validation

This section presents an overview of the final model set-up performance when compared with measurements. Model and measured data are compared in a one-to-one fashion as time series, scatter plots, current rose plots, and frequency of occurrence plots, as appropriate. The skill assessment and comparison between model and observations is made using statistical methods, that are described in detail in **Appendix A**. It should be noted that for the present purpose the normal conditions are the most important, as this will affect migration routes etc. more than the extreme events. However, extreme events were not excluded from the study.

In general validation is carried out using a relatively large number of stations and parameters, so there is a large amount of data involved. To present this in a transparent way the methods used here are standard to many offshore wind metocean projects, where focus is on quantitative comparison.

3.3.1 Baseline Wave Validation

The following wave plots (time series, wave rose, frequency of occurrence and scatter plots) are taken from the Long Island, New York station (NDBC 44025). This measurement location is just one within the OSW development areas included in this study. Five more sets of wave station validation are included in **Appendix A.2.2**.

Figure 3.7 shows synchronized timeseries of observed and modeled significant wave height and statistics (mean value, minimum, maximum, and standard deviation). This figure allows for visual inspection of the variation and the differences between the observed and modeled results. It is seen that the modeled mean H_{m0} is 10 cm higher while the maximum peak is 41 cm (7%) higher in the model. Otherwise, it appears

that the model provides a realistic representation of the observed time series and is a representation that is in line with our experience from other wave model studies.

Figure 3.8 shows a wave rose, mapping significant wave height on 16 directional 22.5° sectors. Observed (color) and modeled (grey) wave roses are overlaid. At this location it appears that the waves from SSW are over-represented in the model, while easterly directions are slightly under-represented. The wave rose is supported by two additional plots as shown in **Figure 3.11** and **Figure 3.12**. **Figure 3.11** is a timeseries of observed and modeled mean wave direction, since wave direction can often vary rapidly, the plot provides an overview of the model vs. observation variability in time. **Figure 3.12** shows the frequency of occurrence of the mean wave direction distributed on directional sectors.

Figure 3.9 shows the frequency of occurrence of the significant wave height in 0.5 m bins, both as accumulated distribution and frequency distributions. This confirms that intermediate wave heights are slightly under-represented in the model.

Figure 3.10 shows a scatter diagram of observed versus modeled significant wave height. The plot uses all available data, with a color-scale to indicate point-density, such that all data can be inspected. In addition, a quantile-quantile (QQ) line is included, matching the frequency of occurrence distribution. The mean slope QQ-line is also indicated in the box. A slope at 1.0 indicates good agreement, while a slope >1.0 indicates a positive bias of the modeled results. Statistical indicators of the goodness-of-fit are shown in the box. Details of the calculation of these statistics are shown in **Appendix A**. In general, a single parameter to quantify the validation is the unbiased Scatter Index (S.I.) which is the RMSE/mean significant wave height. Experience shows that the value will depend on the specific conditions, (i.e. which parameter, model sites, etc.), but as a rule-of-thumb values below 0.3 can be acceptable while values below 0.2 is normally a good agreement.

The specific example shows a relatively fair agreement, where the QQ slope shows about 7% over estimation in the model with a mean bias at 0.1 m. The scatter does not indicate any outliers but does show the spread. The SI index is 0.2.

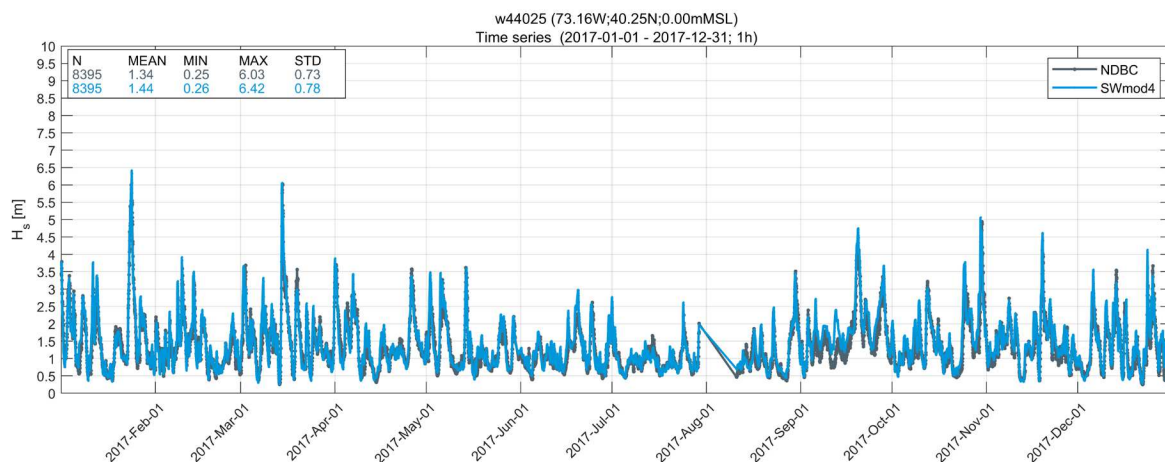


Figure 3.7. Validation of H_{m0} Model Results Using Long Island Wave Time Series

Comparison of time series measurement (gray) against model results (blue), from January 2017 to December 2017.

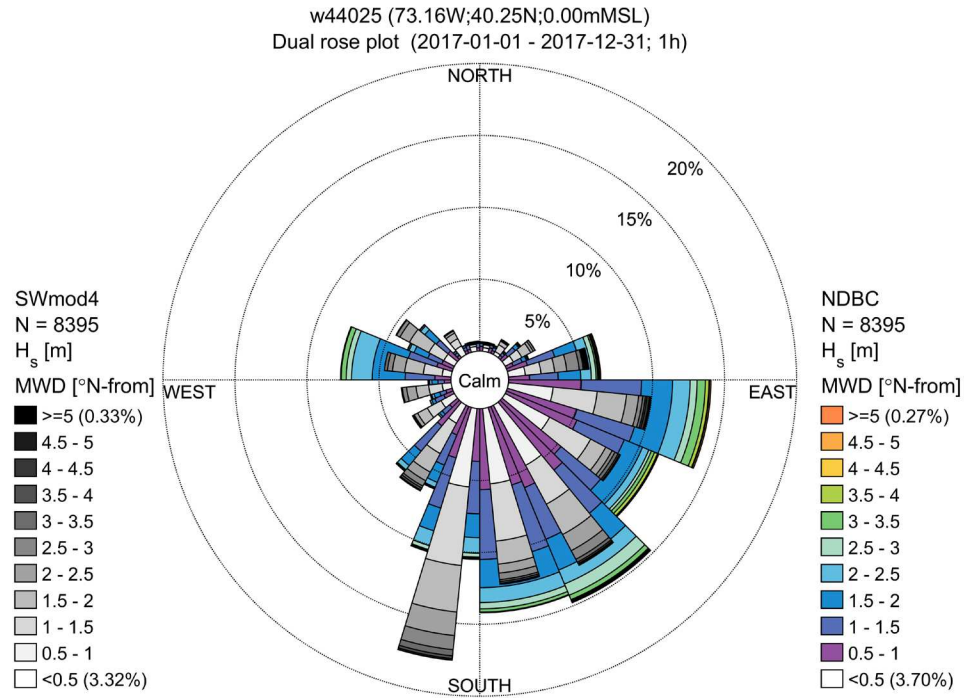


Figure 3.8. Validation of Model Results Using Long Island Station Wave Rose Plot

Comparison is performed between mean wave direction rose measurement (colored scale) and model results (gray), for data from January 2017 to December 2017.

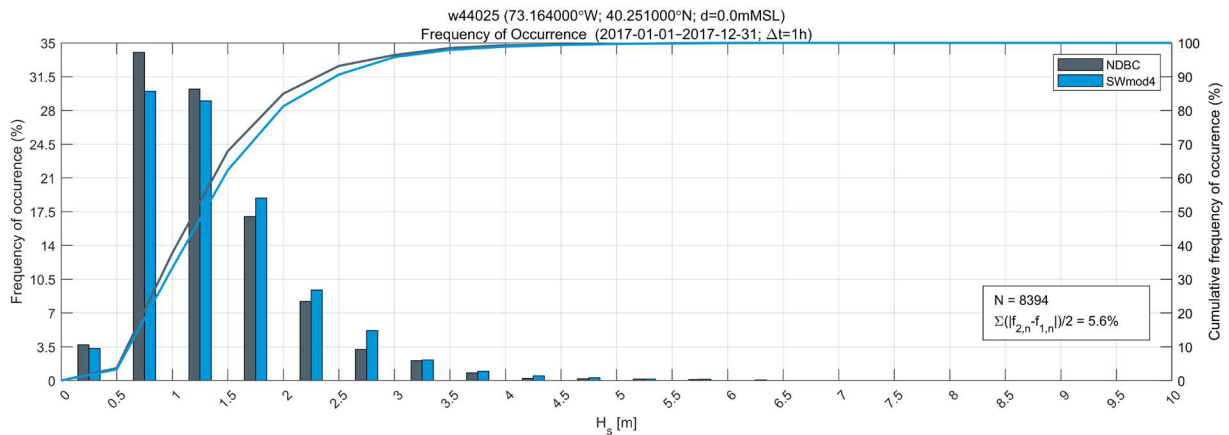


Figure 3.9. Validation of Model Results by Frequency of Occurrence Using Long Island Station H_{m0} Measurements

Wave H_{m0} frequency of occurrence measurement (gray line) is compared against that of the model results (blue line) for measurements collected between January 2017 to December 2017.

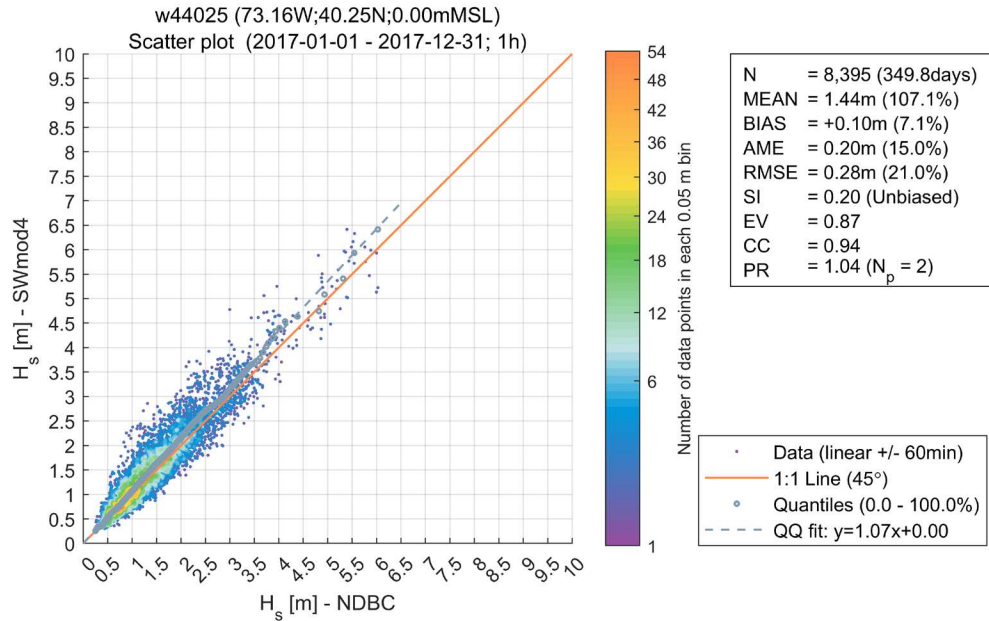


Figure 3.10. Long Island Wave H_{m0} Scatter Plot of Measurement Against Model Results

The dots indicate individual datapoints, the color indicate point-density. The gray dashed line is the quantile-quantile (QQ) line, the red line indicates perfect agreement.

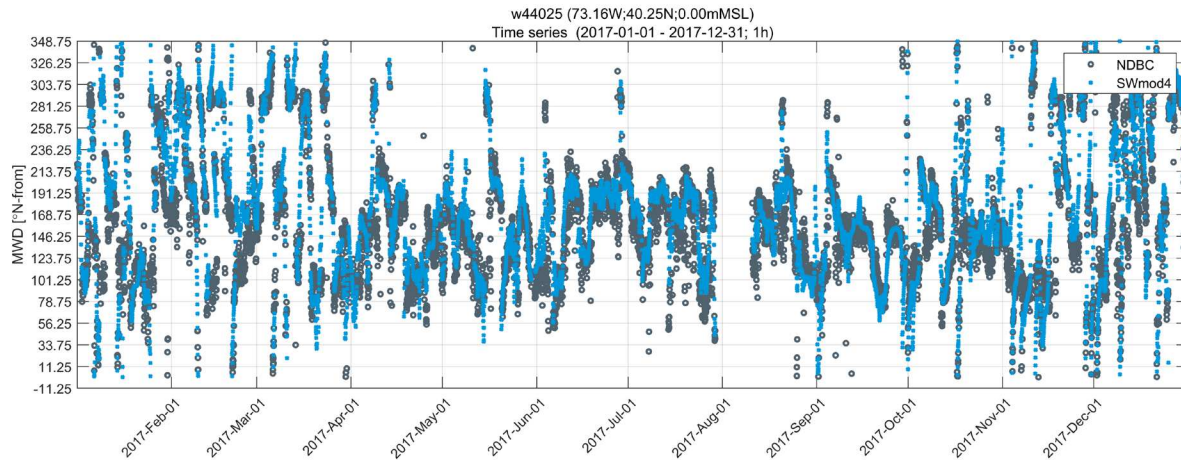


Figure 3.11. Validation of Model Results Using Long Island Mean Wave Direction Time Series

Comparison of mean wave period time series (gray) against model results (blue), from January 2017 to December 2017.

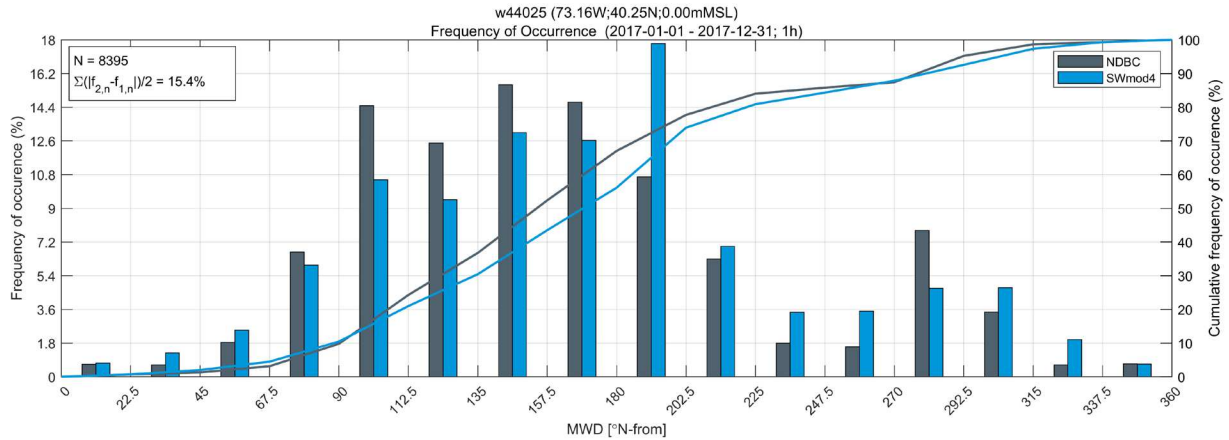


Figure 3.12. Validation of Model Results by Frequency of Occurrence Measurement Using Long Island Station Mean Wave Direction Measurements

Wave mean wave period frequency of occurrence measurement (gray line) is compared against that of the model results (blue line) for measurements collected between January 2017 to December 2017.

3.3.2 Baseline Water Level Validation

The following water level plots (**Figure 3.13**, time series, **Figure 3.14** frequency of occurrence, and **Figure 3.15** scatter plot) are taken from the Atlantic City, NJ station. The comparison between model and measurement indicate a RMSE around 0.2 m and a QQ-line slope at 1.02. This measurement location was close to the mid-point of the OSW development areas, so provides confidence in the overall model performance.

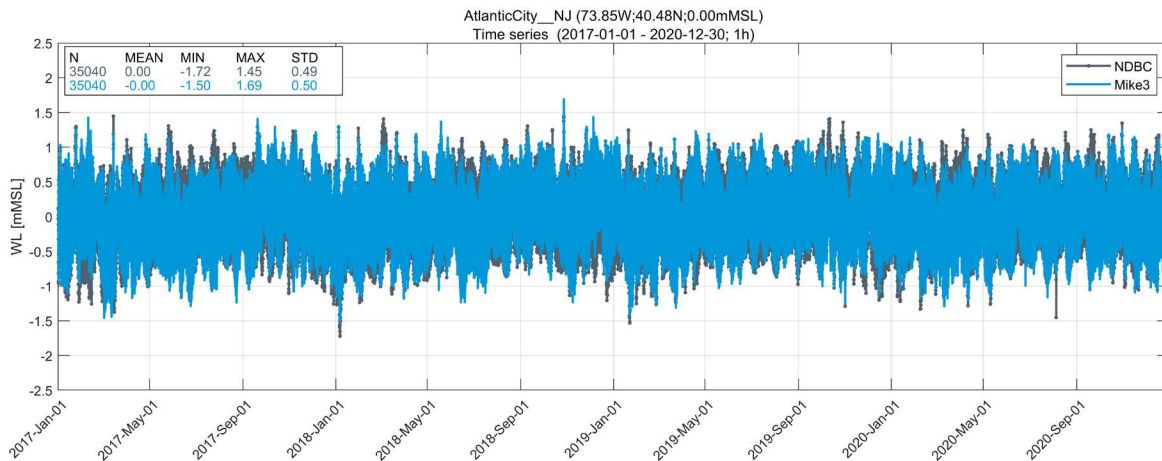


Figure 3.13. Validation of Model Time Series Results Using Atlantic City Water Level Measurements

Comparison of time series measurement (gray) against model results (blue), from January 2017 through December 2020.

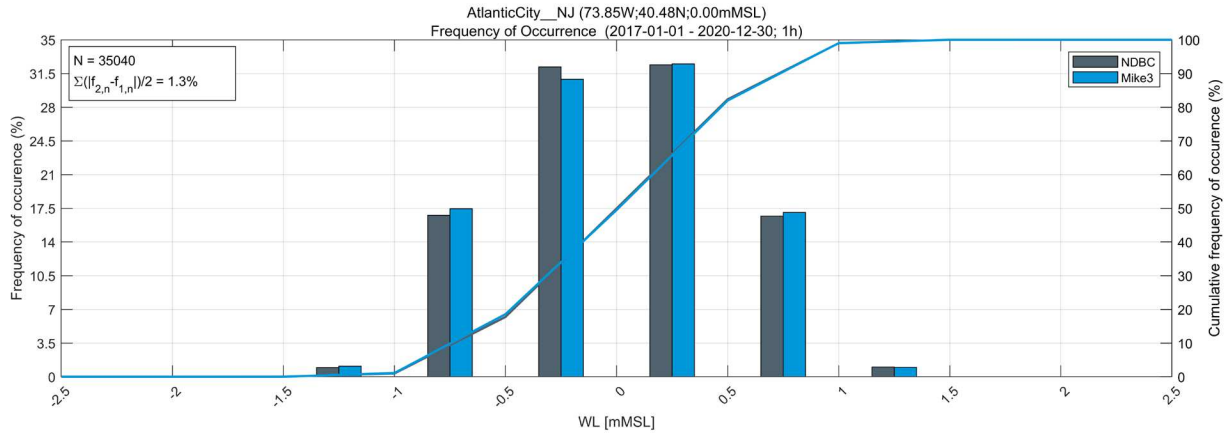


Figure 3.14. Validation of Model Frequency of Occurrence Results Using Atlantic City Water Level Measurements

Water level frequency of occurrence measurement (gray line) is compared against that of the model results (blue line) for measurements collected between January 2017 through December 2020.

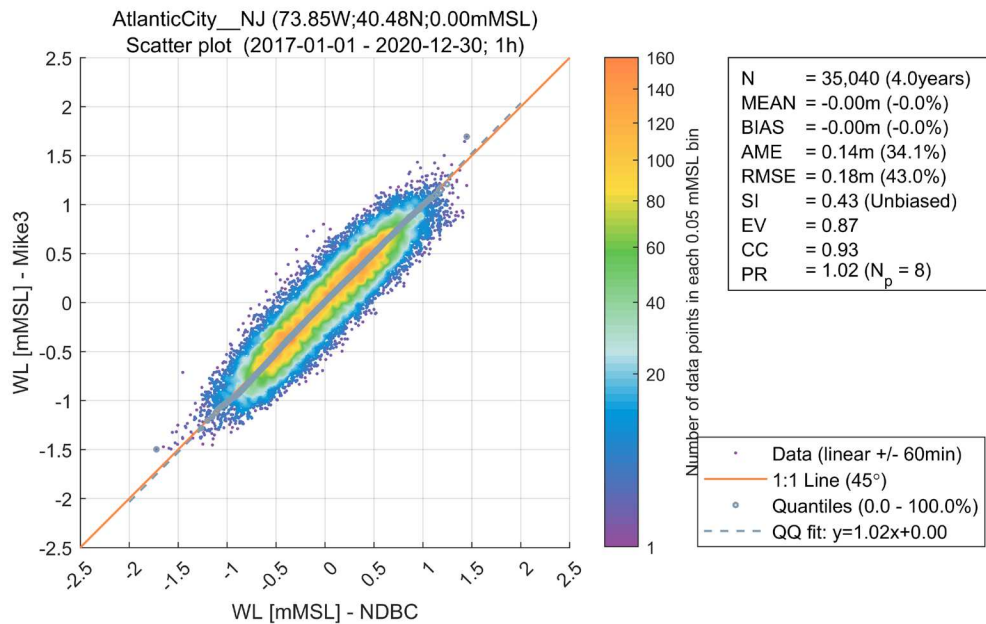


Figure 3.15. Model Scatter Plot Results Using Atlantic City Water Level of Measurements

The dots indicate individual datapoints, the color indicate point-density. The gray dashed line is the quantile-quantile (QQ) line, the red line indicates perfect agreement.

More water level validation plots of measurement vs. model results are presented in **Appendix A**.

3.3.3 Baseline Current Validation

3.3.3.1 Baseline Current Validation – Acoustic Doppler Current Profiler (ADCP) Comparisons

The following set of plots are an example of the skill of the model vs. observations. For a regional model the current validation indicate a realistic representation of the observations. Additionally, it should be noted that for the regional impact assessment, the current is essentially “integrated” by the larvae “particles” and therefore the effects of small differences in maxima are effectively evened out so that the comparisons with and without the OSW structures can be used with confidence.

The following current plots (time series, current rose, frequency of occurrence, and scatter plot) are of the NYSERDA 06S current profiler mooring. The results compared were from the near surface layer. The comparison between model current speed time series and observations showed a mean bias of the model at 4 cm s^{-1} , as indicated in the time series in **Figure 3.16**. This current measurement location is also quite close to the OSW development area, so it provides a representative picture of the overall model performance. The current rose in **Figure 3.17**, shows both measured (gray) and modeled (colored) parameters. The frequency of occurrence plot in **Figure 3.18** shows the % frequency of occurrence (vertical scale) vs. a histogram (horizontal axis) of the measured parameter. The time series and frequency of occurrence plots show both measured (gray) and modeled (blue) parameters. They also include statistics such as maximum value and standard deviation for each time series. The scatter plot in **Figure 3.19** shows the measured (horizontal axis) and modeled (vertical axis) parameter. These figures also include some statistics quantifying the accuracy of the modeled parameter such as the bias and absolute mean error.

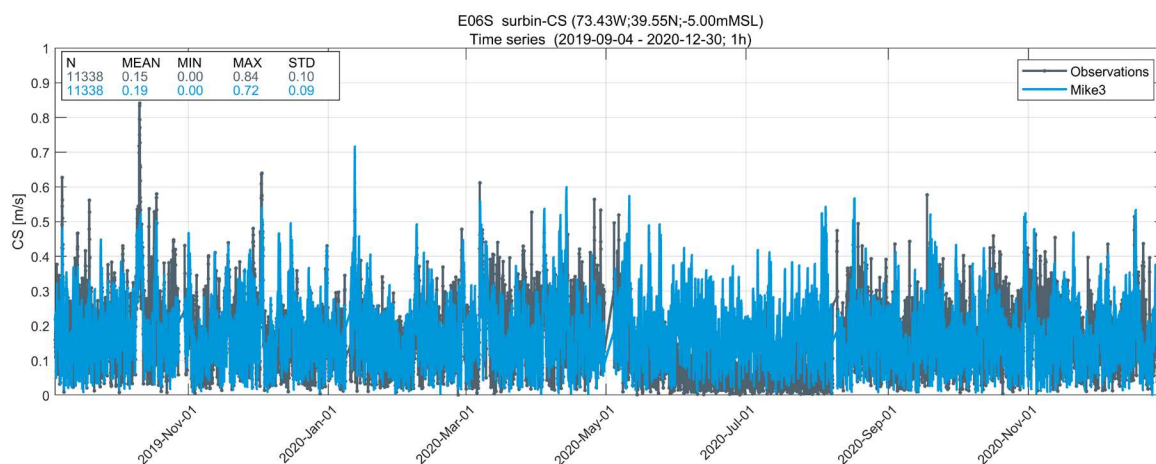


Figure 3.16. Validation of Model Time Series Current Speed Results Using NYSERDA 06S ADCP Current Speed Measurements

Comparison of time series measurement (gray) against model results (blue), from September 2019 to December 2020.

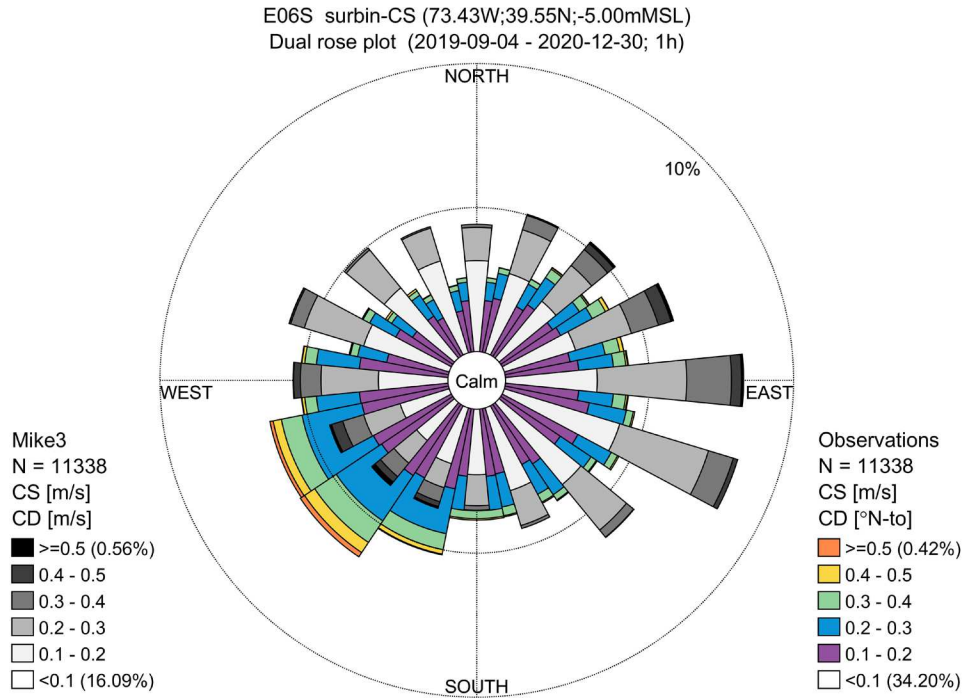


Figure 3.17. Validation of Model Rose Plots Results Using NYSERDA 06S ADCP Measurements
Comparison is performed between NYSERDA 06S ADCP current rose measurement (colored scale) and model results (gray), for data from September 2019 to December 2020.

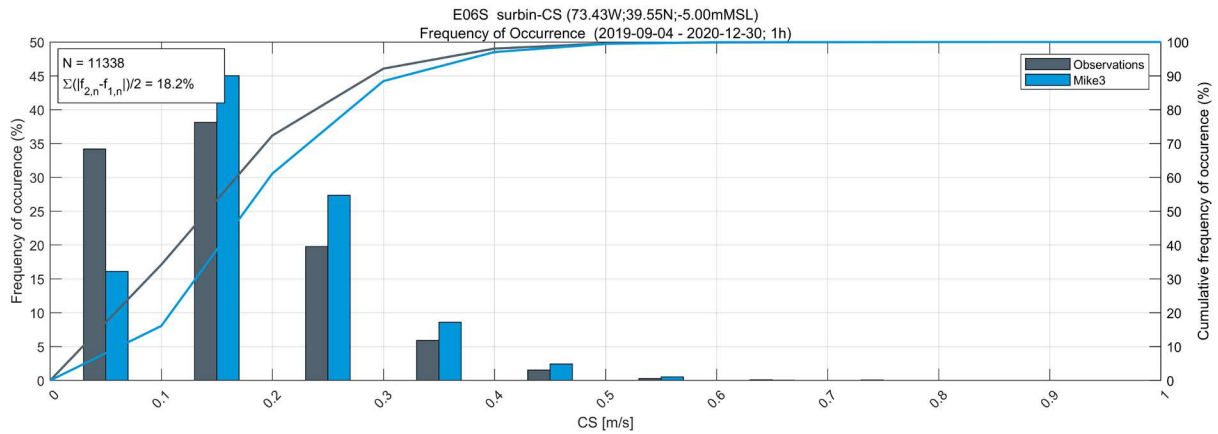


Figure 3.18. Validation of Model Frequency of Occurrence Current Speed Results Using NYSERDA 06S ADCP Current Speed Measurements

NYSERDA 06S ADCP frequency of occurrence measurement (gray line) is compared against that of the model results (blue line) for measurements collected between from September 2019 to December 2020.

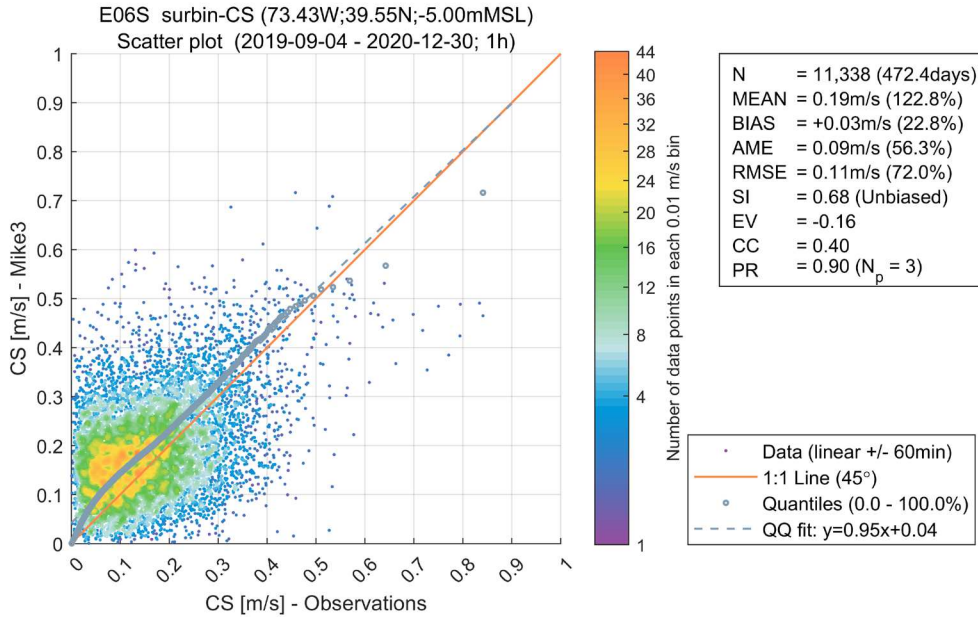


Figure 3.19. Model Scatter Plot Results Using NYSERDA 06S ADCP Measurements

The dots indicate individual datapoints, the color indicate point-density. The gray dashed line is the quantile-quantile (QQ) line, the red line indicates perfect agreement.

Similar ADCP current validation plots from other locations and depths of measurement vs. model results are presented in **Appendix A**.

3.3.3.2 Baseline Current Validation – High Frequency Radar Observation (HFRO) Comparisons

The figures below (**Figure 3.20** through **Figure 3.23**) show side by side snapshot comparisons of the HFRO Observations vs. model for the entire model domain. It should be noted that the HFRO measurements use a doppler shift measurement technique that only captures the first few millimeters of the surface, and this layer can be dominated by wind drift effects. Whereas the 3D current model by necessity integrates over a finite layer of a few meters. One should expect that there will be qualitative variances due to these different scales of the “surface layer”. However, the results do show a relatively good comparison in both magnitude and direction in areas where the current were lower and importantly in and around the WEAs. This is illustrated in **Figure 3.24** where the bias between the HFRO and model results are plotted. The bias varies in the WEAs from 0 to $+0.10 \text{ ms}^{-1}$.

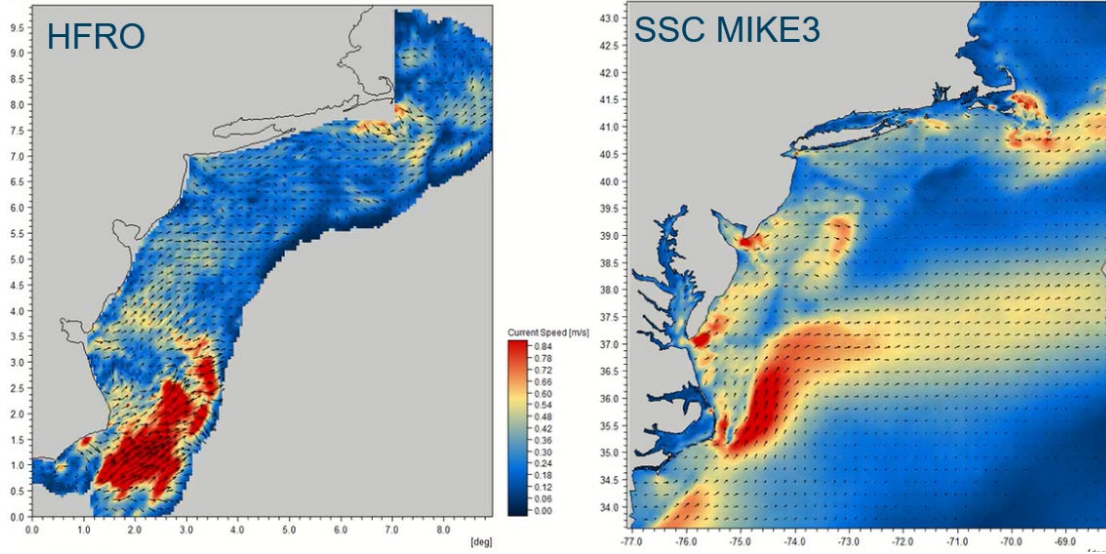


Figure 3.20. High Frequency Radar Observation (HFRO) vs. Model (SSC MIKE3) Results 1 January 2017

Observed (left) vs. model (right) for the full regional model where measurements exist.

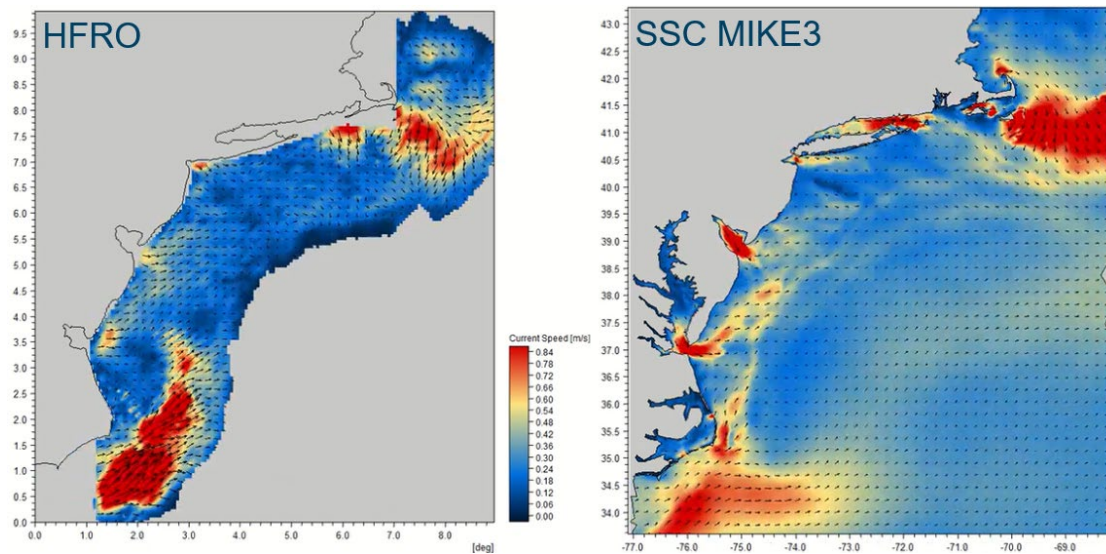


Figure 3.21. High Frequency Radar Observation (HFRO) vs. Model (SSC MIKE3) Results 1 March 2017

Observed (left) vs. model (right) for the full regional model where measurements exist.

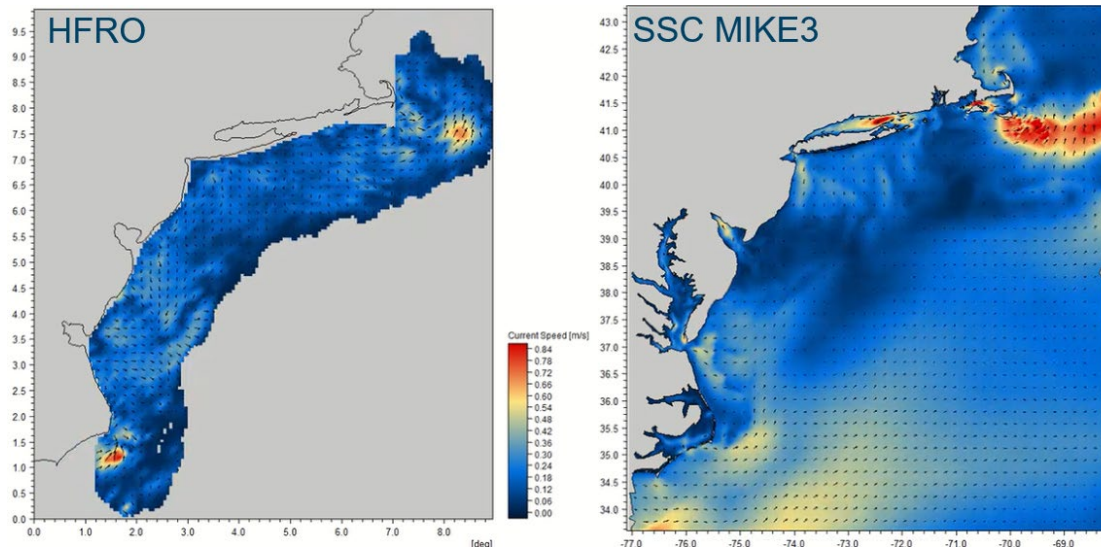


Figure 3.22. High Frequency Radar Observation (HFRO) vs. Model (SSC MIKE3) Results 1 June 2017

Observed (left) vs. model (right) for the full regional model where measurements exist.

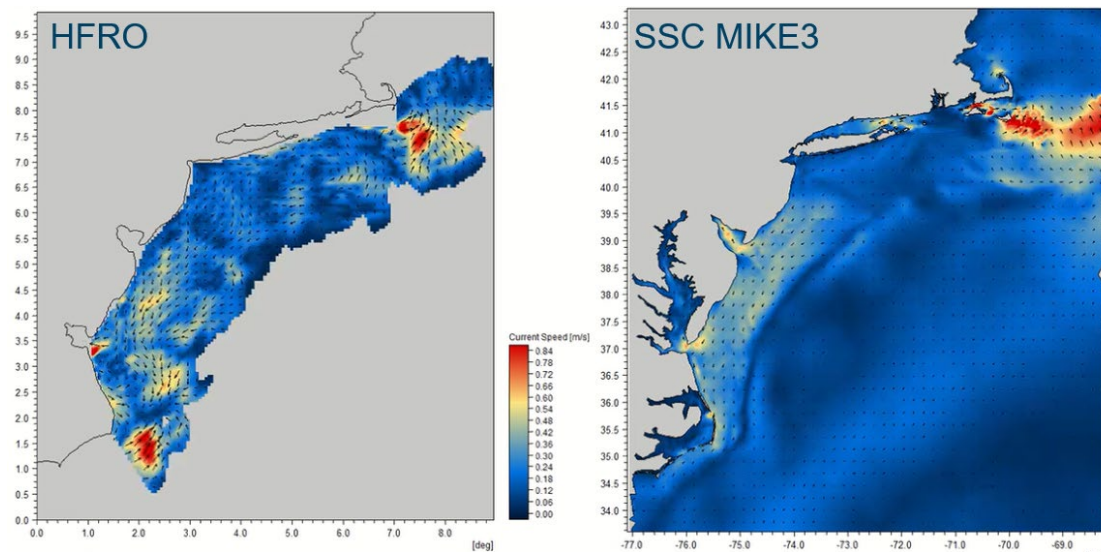


Figure 3.23. High Frequency Radar Observation (HFRO) vs. Model (SSC MIKE3) Results 1 October 2017

Observed (left) vs. model (right) for the full regional model where measurements exist.

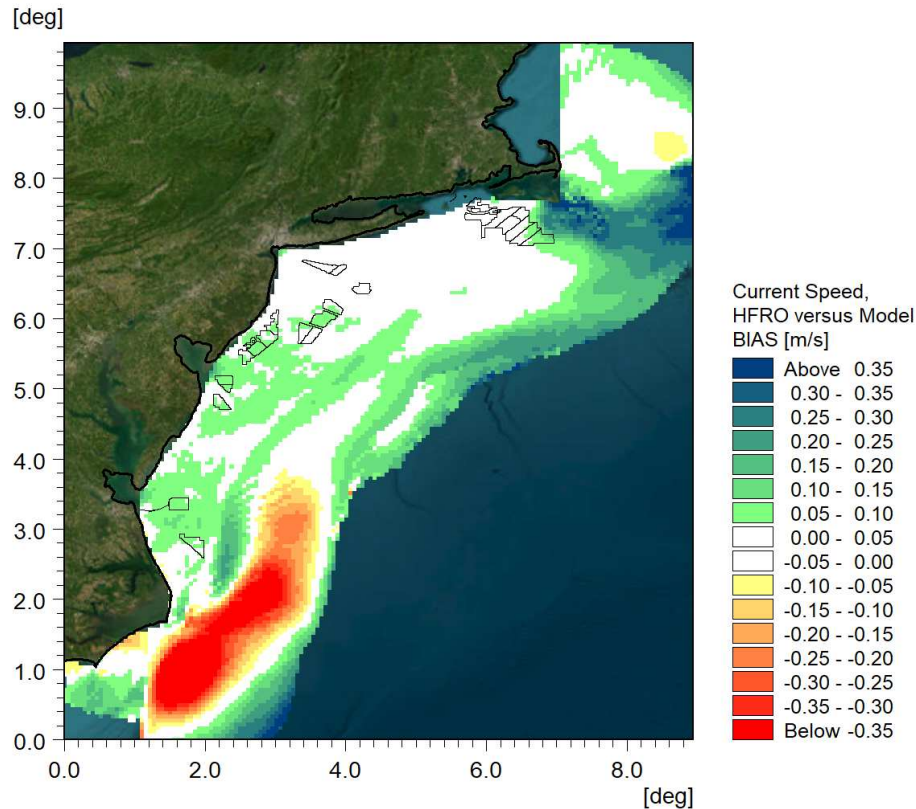


Figure 3.24. High Frequency Radar Observation (HFRO) vs. Model Surface Current Speed Bias for the Year 2017

Observed vs. model surface current speed bias for the full regional model where measurements exist. Green/blue indicates a "fast" bias in the model and red indicates a "slow" bias in the model.

3.3.4 Baseline Temperature Validation

The following sea temperature plots (**Figure 3.25**, time series, **Figure 3.26**, frequency of occurrence and **Figure 3.27**, scatter plot) are taken from the Barnegat, NJ station. The comparison between model results and measurements indicate that the model is representative of the observations at this site with a mean bias at 0.05 °C and a -1°C difference in the minimum. The scatter plot indicates that the model is underestimating temperatures by 8%. This measurement location was close to one of the OSW development areas.

More temperature validation plots from measurement stations on NDBC buoys vs. model results are presented in **Appendix A**.

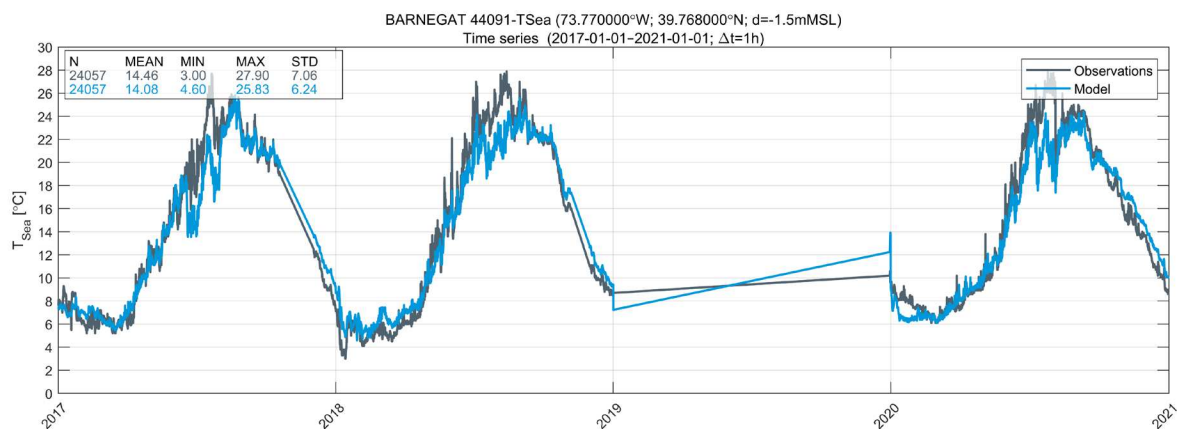


Figure 3.25. Validation of Model Time Series Results Using Barnegat, NJ Sea Temperature Measurements

Comparison of time series measurement (gray) against model results (blue), from January 2017 to December 2020.

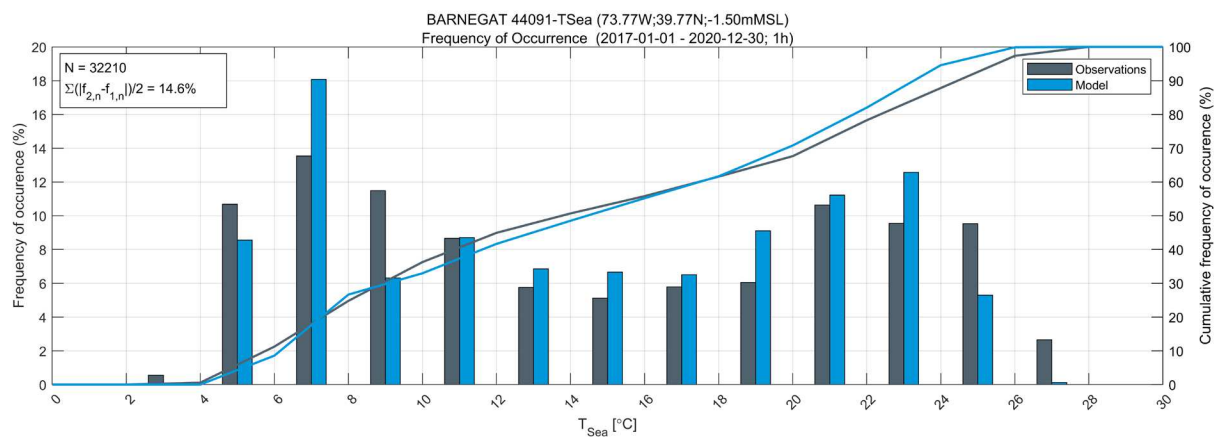


Figure 3.26. Validation of Model Frequency of Occurrence Results Using Barnegat, NJ Sea Temperature Measurements

Sea temperature frequency of occurrence measurement (gray line) is compared against that of the model results (blue line) for measurements collected between January 2017 to December 2020.

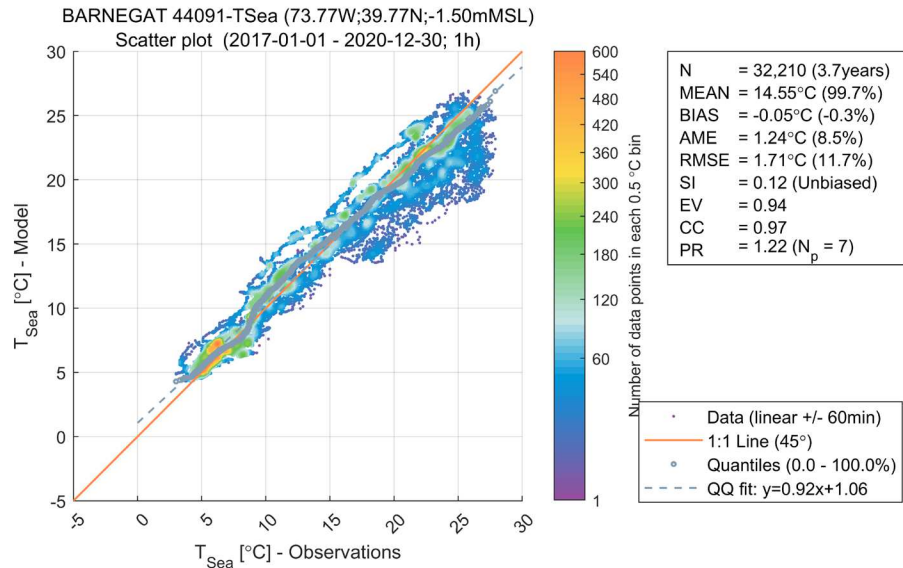


Figure 3.27. Scatter Plot Results Using Barnegat, NJ Sea Temperature Measurements

The dots indicate individual datapoints, the color indicate point-density. The gray dashed line is the quantile-quantile (QQ) line, the red line indicates perfect agreement.

In addition to point location validation, comparisons of model results to satellite imagery snapshots of the region were also completed. The satellite images were obtained from Physical Oceanography Distributed Active Archive Center website based on the Operational Sea Surface Temperature and Sea Ice Analysis (OSTIA) analysis.

Figure 3.28 below is a comparison of the sea surface temperature for the full regional model domain versus the OSTIA analysis of the satellite imagery for two seasons, spring and summer.

- Spring: The difference plot on a regional scale in the areas of OSW developments north of Cape Hatteras indicates that the modeled surface temperatures vary on the order of +2 °C off Chesapeake Bay and farther south. In the WEAs from Delaware and north the spring time sea surface temperature agreement is on the order of +/-0.5 °C.
- Summer: For the summer time, the differences in the WEAs from the Carolinas to Long Island show sea surface temperature agreement is on the order of +/-0.5 °C. The Nantucket Shoals and Grand Banks areas show differences for sea surface temperature on the order of -4 to -6 °C, but in the WEAs the differences for sea surface temperature on the order of -2 to -4 °C.

More temperature validation plots from the OSTIA satellite analysis vs model results are presented in **Appendix A**.

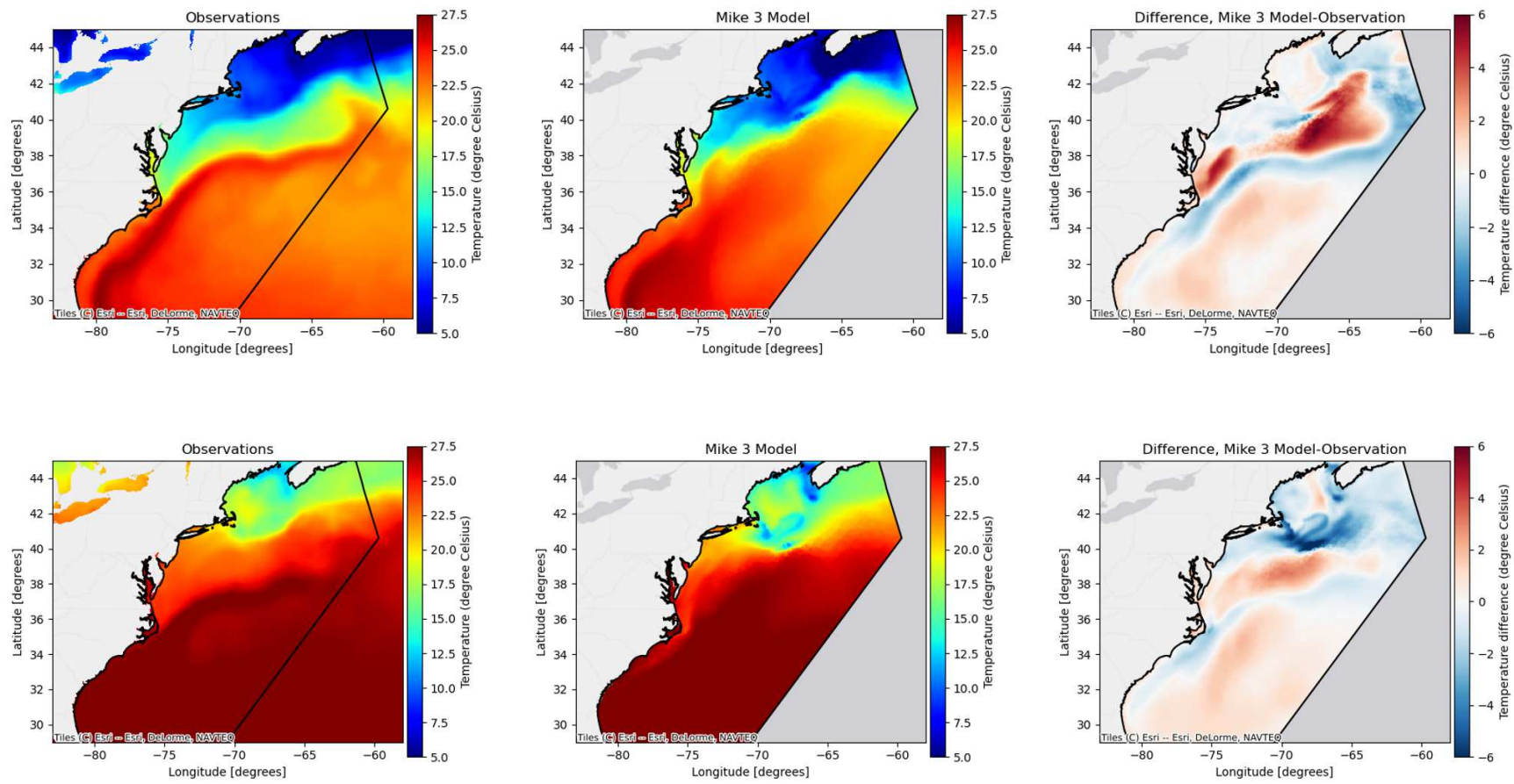


Figure 3.28. Baseline Sea Surface Temperature: OSTIA Satellite Analysis (left), Model (center) and Difference (right)
Upper is spring (April-May-June 2017) and Lower is summer (July-August-September 2017)

The general oceanography and ecology of the region is significantly influenced by the Cold Pool in the MAB (**section 3.1**). Historical climatological temperature profiles are used to characterize the average annual evolution and spatial structure of the Cold Pool. Lentz (2017) provided the authors the average temperature sections across the New England shelf for the months of March through October showing the Cold Pool bounded above by the seasonal thermocline and offshore by warmer slope water. The Lentz plots are temperature contours taken from multiple representative profiles taken between 69°W and 73°W and consolidated using a typical bathymetric transect across the New England shelf. The data for the Lentz profiles were collected between 1955 and 2014. The plots are comprised of between 8,000 and 10,000 temperature profiles per month between March and October.

A comparison was made of the model results to the average historical measurements presented in Lentz (2017). The transect in the model that correlated to the selected Lentz profiles is shown in **Figure 3.29**. The comparisons to the Lentz (2017) and the model temperature transects are **Figure 3.30** (March, April, May and June for model result years 2017 and 2018) and **Figure 3.31** (July, August, September and October for model result years 2017 and 2018). Note that the model broadly follows the monthly seasonal average measurements. However, it should be noted that the Lentz (2017) plots are composites of surveys over many years over a large geographical area between the longitudes of 69°W and 73°W.

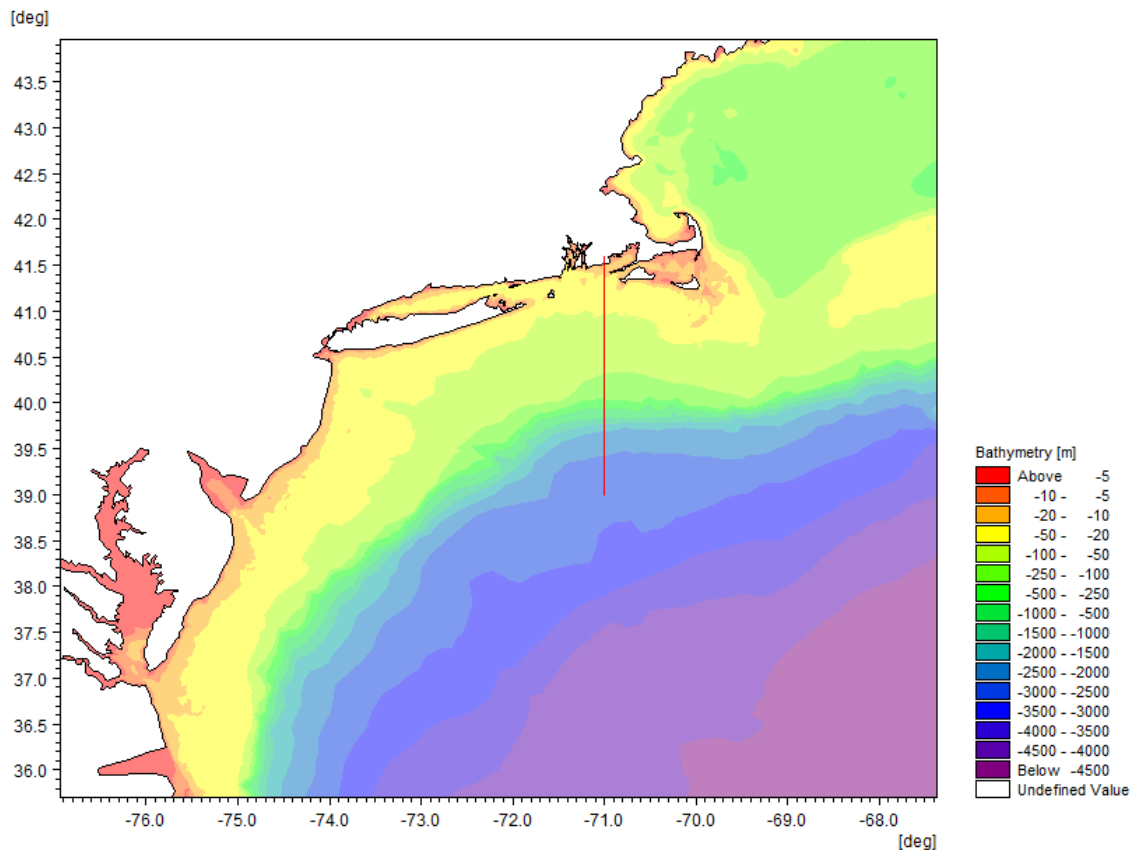


Figure 3.29. Model transect location that correlates to the Lentz (2017) profiles

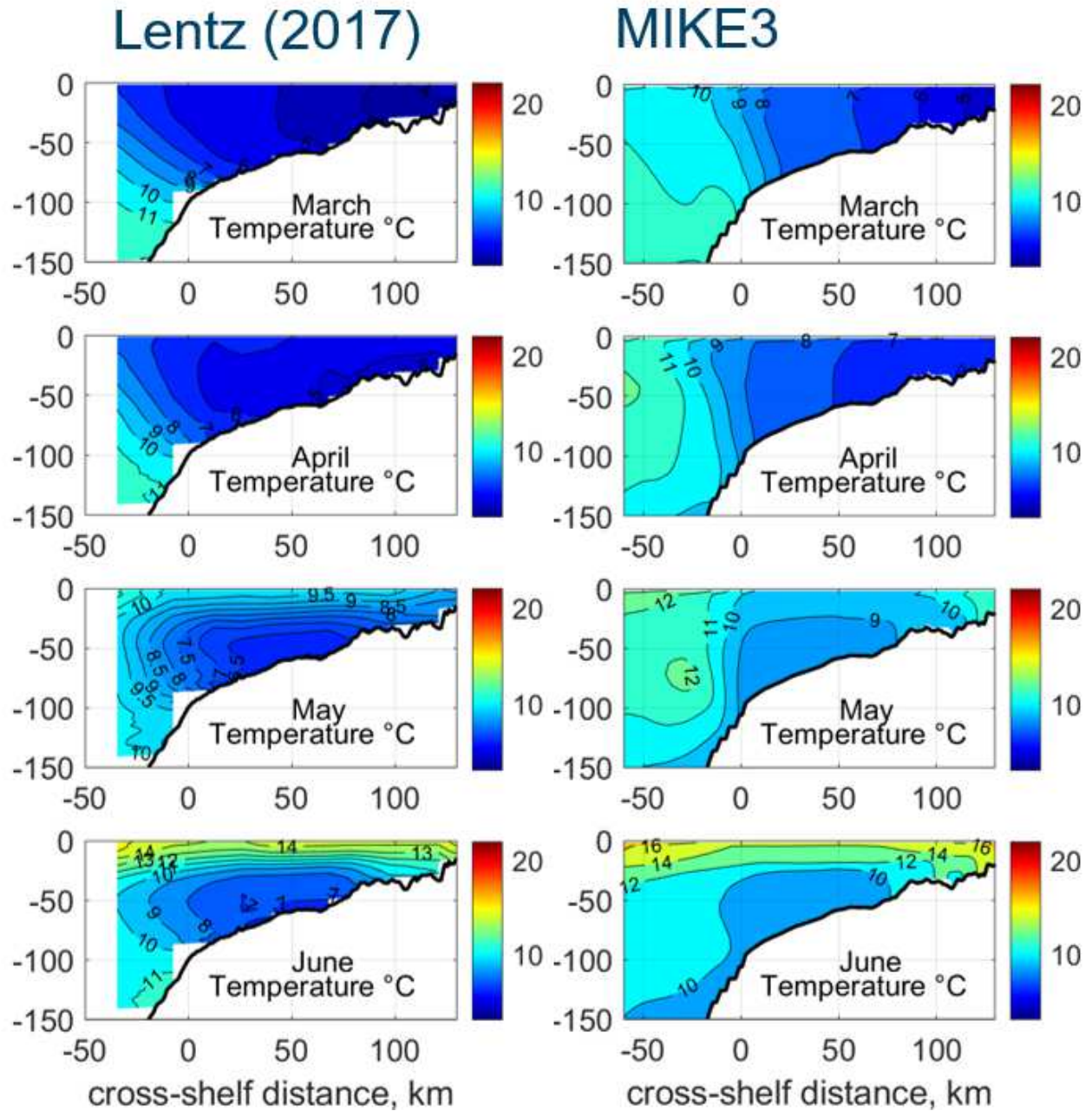


Figure 3.30. Average Temperature Transects March to June (2017 & 2018 Model Results)
 Left: Temperature climatology for months March to June from 1955-2014 (Lentz, 2017); Right: Model results for March to June from 2017 and 2018. Average temperature sections across the New England Shelf for the months of March through June showing the Cold Pool bounded above by the seasonal thermocline and offshore by warmer slope water.

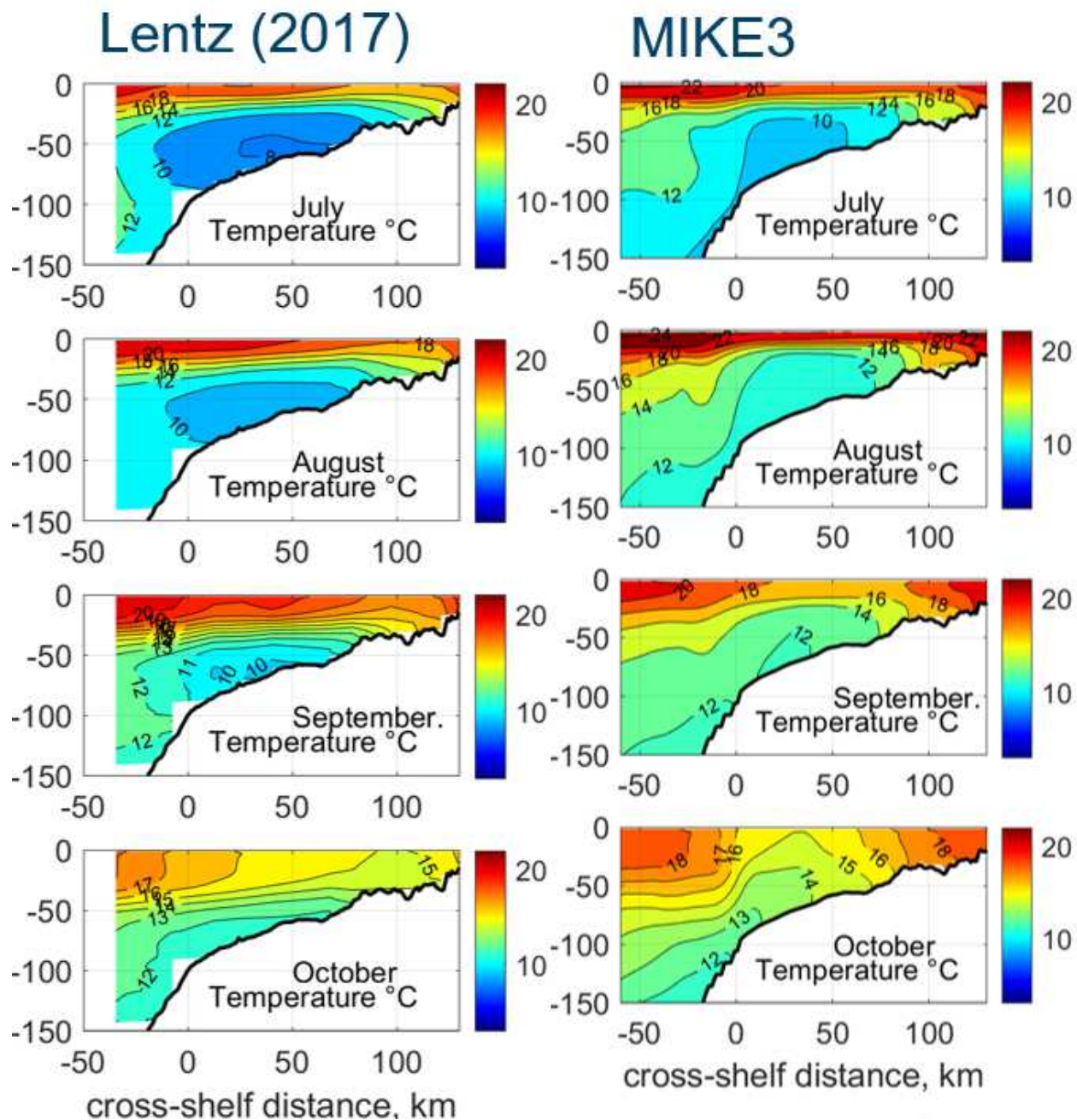


Figure 3.31. Average Temperature Transects July to October (2017 & 2018 Model Results)

Left: Temperature climatology for months July to October from 1955-2014 (Lentz, 2017); Right: Model results for July to October from 2017 and 2018. Average temperature sections across the New England Shelf for the months of July through October showing the Cold Pool bounded above by the seasonal thermocline and offshore by warmer slope water.

More comparisons of observed temperature versus model are presented as vertical profiles at Pioneer Array stations maintained by the Ocean Observing Initiative. The location of the three stations is shown in **Figure 3.32** relative to the MA-RI WEAs.

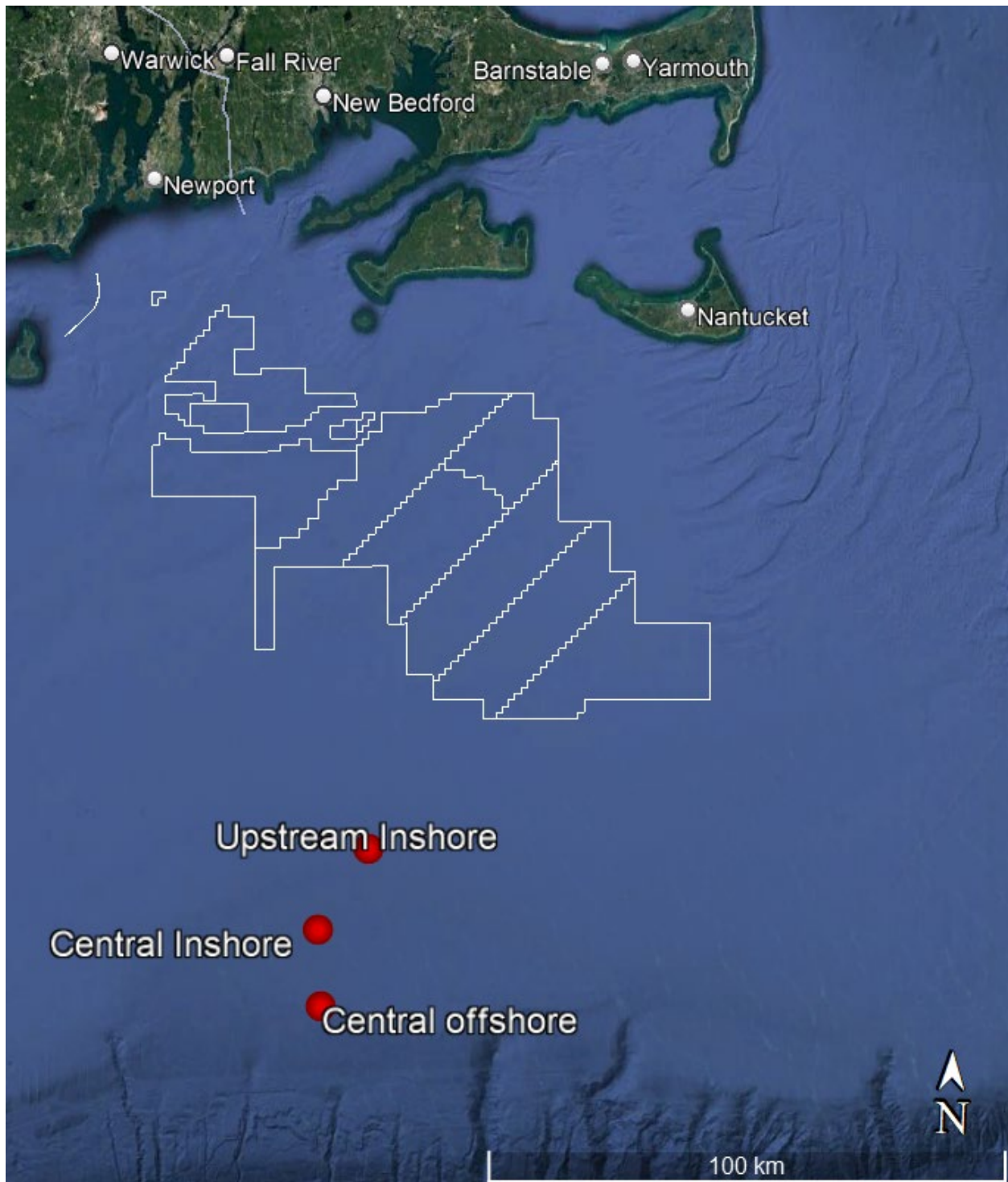


Figure 3.32. Pioneer Array Station Locations – Upstream Inshore, Central Inshore, and Central Offshore
 Stations shown relative to MA-RI WEAs to the north and the shelf break to the south

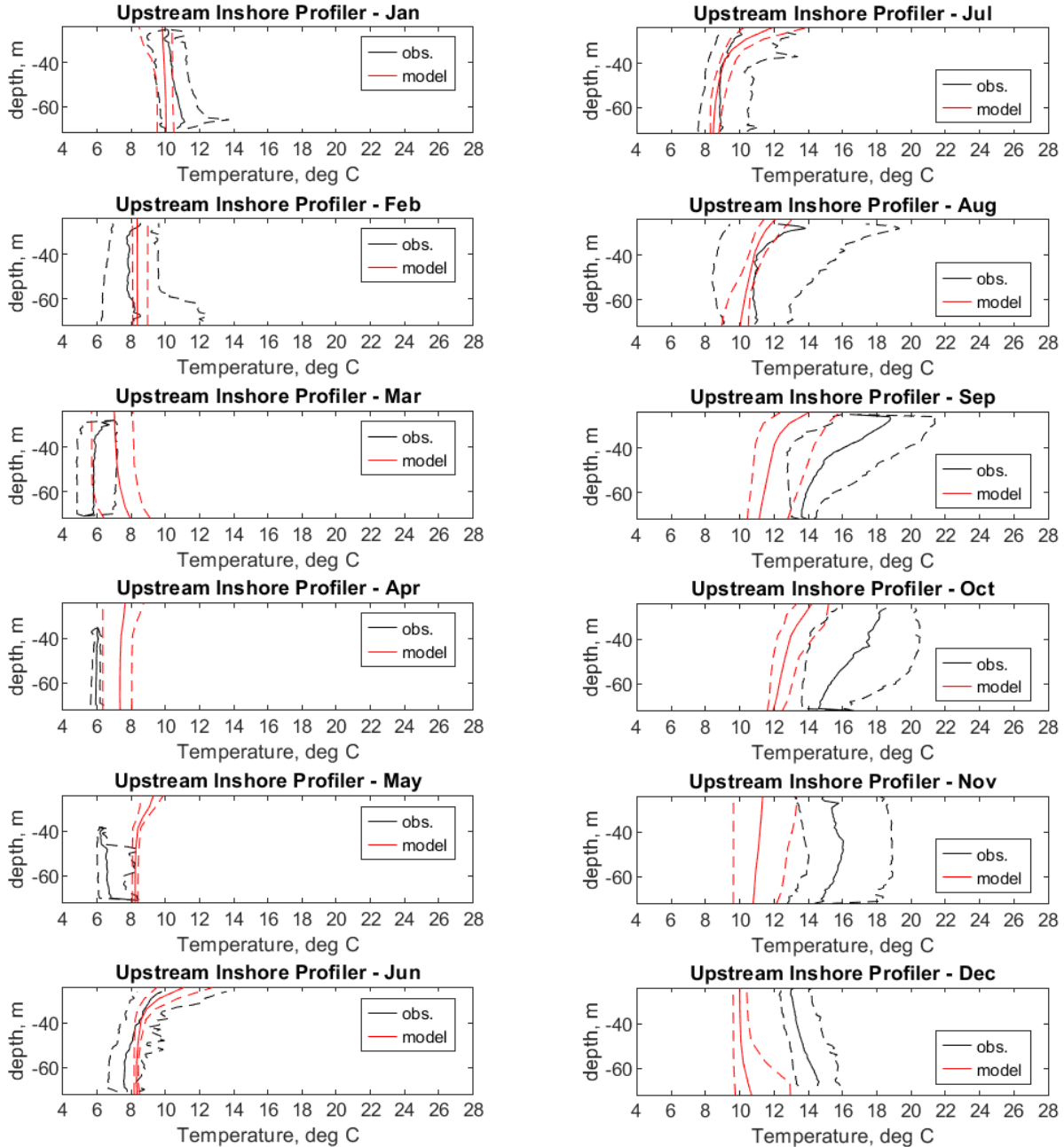


Figure 3.33. Upstream Inshore Station Vertical Temperature Profile Overlays of Monthly Observations and Model Results for 2017: January to June (left) and July to December (right)
Solid black: Mean of observations. Dashed black 5th and 95th percentile non-exceedance probability of observations.
Solid red: Mean of model results. Dashed red 5th and 95th percentile non-exceedance probability of model results

The model mean results in **Figure 3.33** are within 2°C of the observations for the months of January through September with the model predicting 3 to 4°C cooler temperatures through the water column for the months of October through December 2017. The model mean results in **Figure 3.33** are within 2°C of the observations for the months of January through September with the model predicting 3 to 4°C cooler temperatures through the water column for the months of October through December 2017. The quality of the observations in the month of May was questionable but are provided here for completeness. More

results (stations Upstream Inshore, Central Inshore and Central Offshore and years 2017, 2018 and 2020) can be found in **Appendix A**. The 5th and 95th percentile non-exceedance probability lines are provided to give an indication of the variability in temperature of both the observations and model results in the profile throughout the month.

In addition to the cross-shelf transects and the Pioneer Array temperature profiles, a series of monthly average temperatures transects for 2017 and 2018 from southwest to northeast connecting the physical NDBC measurement points from Virginia to Nantucket are presented in the following figures. While there are no observational data to compare directly against the NDBC buoy data shown in **Figure 3.25** through **Figure 3.27** and in **Appendix A**, these transects are provided to give a longitudinal transect overview of the behavior of the Cold Pool from March through October as simulated in the model.

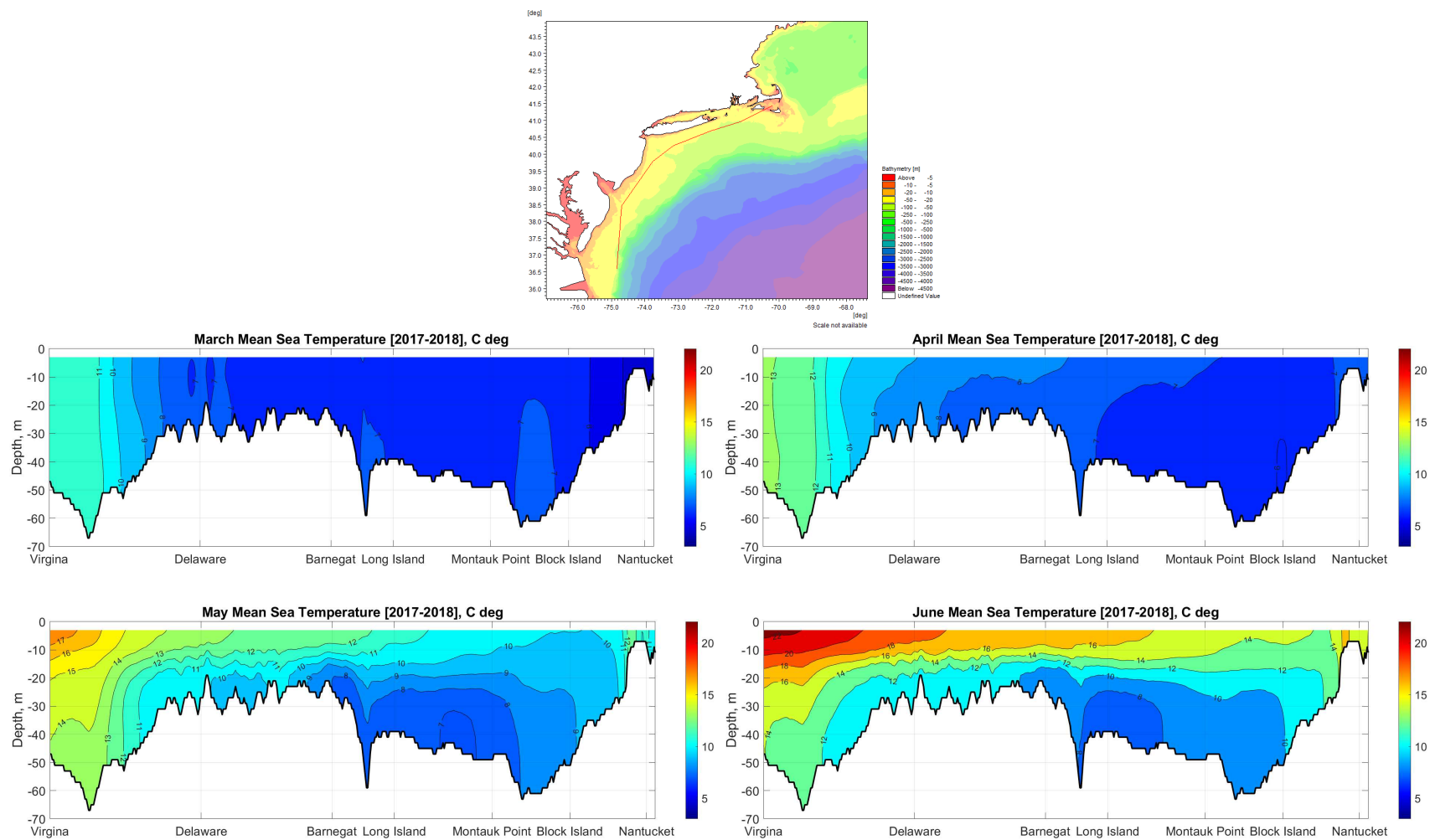


Figure 3.34. Average Model Temperature SW to NE Transects from March to June

The transect is marked by the red line in the top panel. Average temperature connecting NDBC measurement points from Virginia to Nantucket for the months of March through June showing the Cold Pool bounded above by the seasonal thermocline and offshore by warmer slope water.

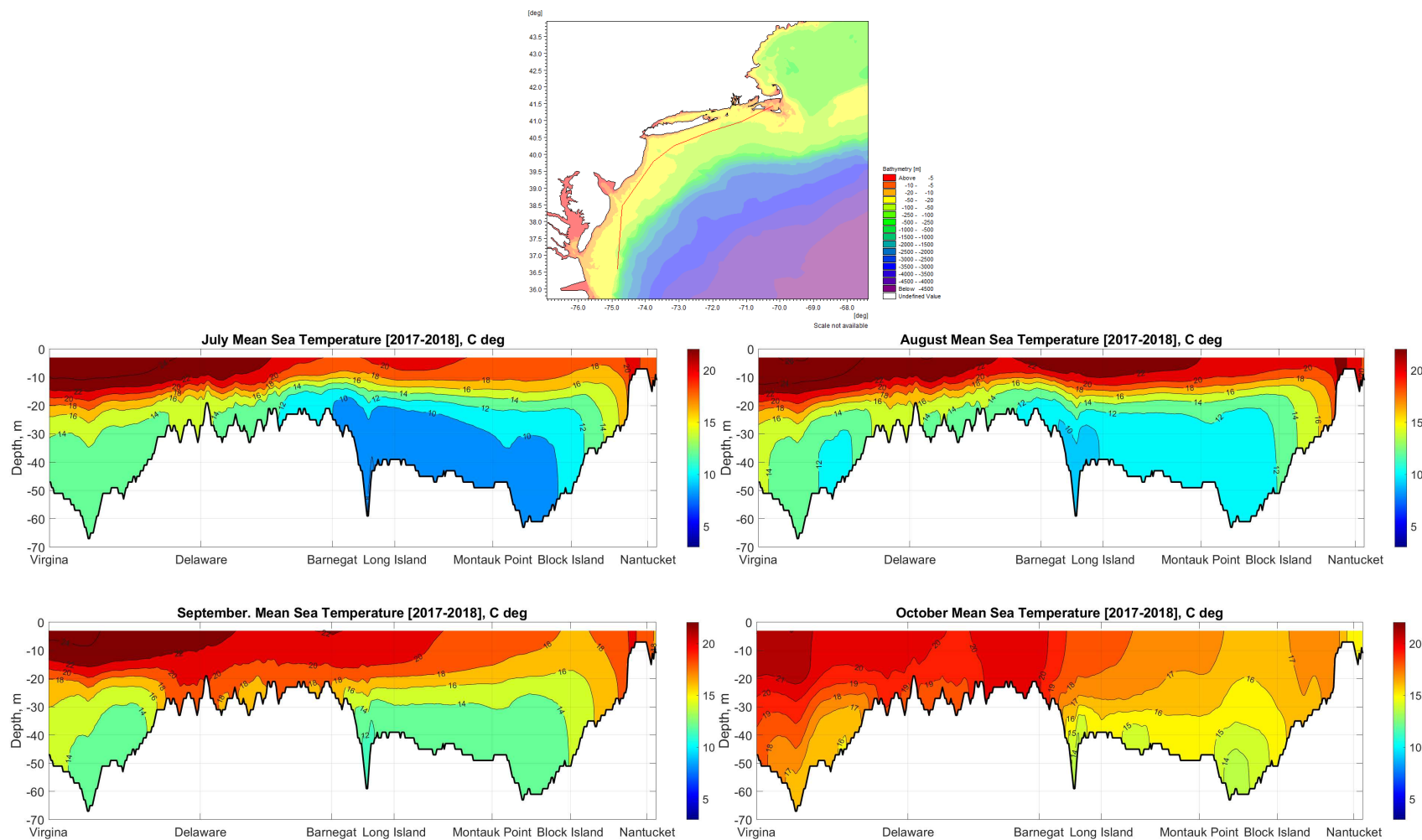


Figure 3.35. Average Model Temperature SW to NE Transects from July to October

The transect is marked by the red line in the top panel. Average temperature connecting NDBC measurement points from Virginia to Nantucket for the months of July through October showing the Cold Pool bounded above by the seasonal thermocline and offshore by warmer slope water.

3.3.5 Baseline Density Stratification Validation

One of the oceanographic characteristics of the Mid-Atlantic Bight (MAB) is the stratification that occurs in the Summer. This was discussed above in **Section 3.1**. To assess model stratification, the model was queried for salinity structure. There were no contemporaneous regional measurements of stratification to compare against for this study. However, O'Reilly and Zetlin (1998) collated data from 6,686 profiles to construct a map of the summertime (June through August) mean stability (sigma-t) density stratification measure in the MAB. The authors noted that *"Data were composited by tile before contouring."* In addition, the O'Reilly and Zetlin (1998) results were averaged over twelve years from 1977 to 1988. Whereas the model has been plotted for each of the years 2017, 2018, and 2020, which demonstrates variability year to year, but may have omitted years with strongest stratification. The variation in the model results for whole of the MAB for the years modeled was not as significant as shown in O'Reilly and Zetlin (1998), but stratification was captured by the model notably near the mouths of bays and estuaries. The area around Nantucket Shoals and Georges Banks shows to be well mixed in the model and in the results from O'Reilly and Zetlin (1998).

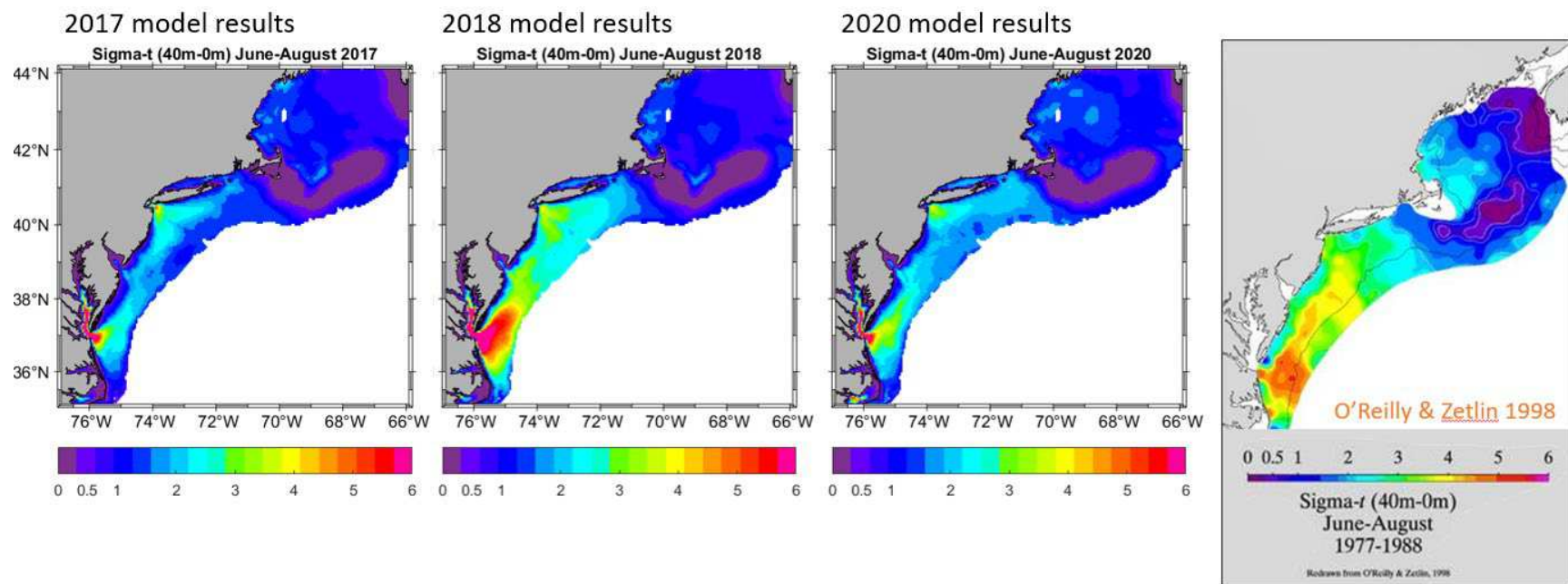


Figure 3.36. Density Stratification Observations (kgm^{-3}) from O'Reilly & Zetlin (1998) June-August 1977-1988 and Model Results for 2017, 2018, & 2020
Regional differences in summer stratification, showing strongly stratified areas (indicated by red, orange, and yellow colors) in the MAB.

3.3.6 Hydrodynamic Baseline Calibration Conclusions

As stated above, this **Section 3.3** presents an overview of the final model set-up performance when compared with measurements. Model and measured data are compared in a one-to-one fashion as time series, scatter plots, current rose plots, and frequency of occurrence plots, as appropriate. More comparisons are included in **Appendix A**. While there is no common set of statistical metrics that exists for validating ocean/coastal hydrodynamic models, there are some guidelines that are often used. For US coastal waters, the NOAA Technical report NOS CS 17 establishes a framework for calculating and evaluating operational nowcast and forecast hydrodynamic model systems (NOAA, 2003). It comprises a comprehensive development of quantified skill assessment for water levels, currents, salinity, and temperature comparisons. It has been used widely for NOAA developed nowcast and forecast models to support Physical Oceanographic Real Time Systems (PORTS) and other navigational and environmental applications in U.S. coastal waters.

The skill assessment from NOS CS 17 was adopted as one of the comparisons for the present study along with additional calculated statistics and visual comparisons. In the current speed evaluation, the calculated root mean square errors (RMSE) are compared below against the standards set by the NOS CS 17 (NOAA, 2003). These standards defined specific criteria for RMSE values, as follows:

- 0.15 m for water level.
- 3 °C for water temperature.
- 0.26 ms⁻¹ for current speed.

The above prescribed skill values were cited for the NOAA's [Gulf of Maine Operational Forecast System](#). These were used for guidance to assess the model's performance and to determine its compliance with the established standards.

Williams and Esteves (2017) provide a discussion on the Skill Index with respect to assessing wave models for shelf sea and estuaries as opposed to only using the RMSE. Skill Index is defined as the RMSE divided by the mean of the signal. A statistical metric that is similar to the Skill Index and what is provided on DHI's standard quantile-quantile plots is the scatter index (SI). SI is a non-dimensional measure of the difference calculated as the unbiased root-mean-square difference relative to the mean absolute value of the observations. Williams and Esteves (2017) only go so far as to say that a Skill Index for waves above 0.5 is not adequate. In DHI's long experience with wave modeling and numerous projects certified by Det Norske Veritas - Germanischer Lloyd (DNV-GL) and Bureau Veritas for open water, an SI below 0.2 is usually considered a small difference (i.e., excellent agreement) for significant wave heights. In confined areas or during calm conditions, where mean significant wave heights are generally lower, a slightly higher SI may be acceptable (the definition of SI implies that it is negatively biased (lower) for time series with high mean values compared to time series with lower mean values (and same scatter/spreading), although it is normalized). For a model of this size where public domain bathymetry is used, it is DHI's experience that an SI of 0.3 for H_{m0} is acceptable.

Table 3.3 through **Table 3.6** summarize the statistical measures of goodness of fit provided in the quantile-quantile plots. The accepted targets are shown at the top of each table.

Table 3.3. Wave Height (H_{m0}) Model Quality Indices

For waves there is no accepted standard however it is DHI's experience that 0.2 or below for the Scatter Index is excellent for a local model and 0.3 or below for the Scatter Index is acceptable for a regional model

Station	BIAS	RMSE	SI	CC	QQ(a)	PR
44097 - Block Island, RI	0.08	0.29	0.19	0.94	1.06	1.02

44025 - Long Island, NY	0.10	0.28	0.20	0.94	1.07	1.04
44091 - Barnegat, NJ	0.00	0.27	0.21	0.92	1.08	0.99
44009 - Delaware Bay, DE	0.18	0.35	0.26	0.91	1.22	1.19
44093 - OSW Energy Area, VA	0.04	0.25	0.21	0.92	1.13	1.25
41013 - Frying Pan Shoals, NC	0.02	0.22	0.17	0.94	1.07	1.08

Inspection of the wave height (H_{m0}) skill assessment shows for all station the SI is within limits.

Table 3.4. Water Level Model Quality Indices

For water levels the NOS CS 17 guidance is 0.15 m RMSE

Station	BIAS	RMSE	SI	CC	QQ(a)	PR
Bar Harbor Station	0.00	0.28	0.27	0.97	1.03	1.00
Portland	0.00	0.28	0.30	0.98	1.16	1.08
Nantucket Island Station	0.00	0.26	0.82	0.92	1.47	1.09
Montauk Station	-0.01	0.16	0.74	0.83	1.05	0.90
Atlantic City Station	-0.01	0.18	0.44	0.93	1.02	1.05
Sandy Hook Station	-0.01	0.19	0.40	0.94	1.01	0.99
Ocean City Inlet Station	-0.01	0.24	1.07	0.87	1.58	1.68
Duck Station	-0.01	0.17	0.50	0.92	1.04	1.05
Fort Pulaski Station	-0.02	0.20	0.29	0.97	0.94	1.00
Mayport Station	-0.02	0.21	0.44	0.95	1.16	1.17

There are a few instances of not meeting the 0.15 m RMSE target with regards to the water levels. However, this particular measure is geared toward ship underkeel clearance in the PORTS program which is more stringent than is necessary for a large regional scale shelf and open ocean model.

Table 3.5. Current Speed Model Quality Indices

For currents the NOS CS 17 guidance is 0.26 m/s RMSE for current speed

Station	Sampling location	BIAS	RMSE	SI	CC	QQ (a)	PR
Pioneer Inshore	Near Surface Layer	-0.02	0.11	0.61	0.51	0.74	0.52
Pioneer Inshore	Midwater	-0.03	0.10	0.61	0.52	0.65	0.54
Pioneer Inshore	Near Bottom	-0.02	0.09	0.62	0.47	0.68	0.58
Pioneer Upstream Inshore	Near Surface Layer	-0.02	0.11	0.60	0.46	0.79	0.57
Pioneer Upstream Inshore	Midwater	-0.02	0.09	0.59	0.45	0.75	0.66
Pioneer Upstream Inshore	Near Bottom	-0.01	0.09	0.62	0.42	0.76	0.66
Pioneer Central Surface	Near Surface Layer	-0.01	0.16	0.77	0.13	0.87	0.62
Pioneer Central Surface	Midwater	-0.04	0.11	0.69	0.19	0.79	0.69
Pioneer Central Surface	Near Bottom	-0.04	0.08	0.62	0.20	0.62	0.59
MVCO	Near Surface Layer	-0.02	0.17	0.68	0.17	0.89	0.61

Station	Sampling location	BIAS	RMSE	SI	CC	QQ (a)	PR
MVCO	Midwater	0.03	0.14	0.74	0.17	1.12	1.36
MVCO	Near Bottom	0.00	0.09	0.66	0.13	0.95	1.07
NOAA ADCP S44024	Near Surface Layer	0.08	0.23	0.47	0.52	0.82	0.82
NOAA ADCP S44024	Midwater	-0.01	0.15	0.36	0.65	0.83	0.77
NOAA ADCP S44034	Near Surface Layer	-0.02	0.13	0.71	0.35	0.57	0.44
NOAA ADCP S44034	Midwater	-0.04	0.11	0.53	0.48	0.53	0.25
NOAA ADCP S44034	Near Bottom	-0.03	0.08	0.49	0.50	0.66	0.59
NOAA ADCP S44033	Near Surface Layer	-0.02	0.15	0.65	0.50	0.75	0.61
NOAA ADCP S44033	Midwater	-0.05	0.10	0.42	0.72	0.74	0.71
NOAA ADCP S44032	Near Surface Layer	-0.03	0.14	0.86	0.27	0.49	0.25
NOAA ADCP S44030	Near Surface Layer	0.00	0.10	0.91	0.30	0.60	0.63
NOAA Station 44088	Near Surface Layer	-0.06	0.21	0.63	0.24	0.81	0.77
NOAA Station 44064	Near Surface Layer	0.16	0.22	0.54	0.75	1.38	1.12
NOAA Station 44072	Near Surface Layer	0.04	0.11	0.49	0.57	0.96	0.70
NOAA Station 41108	Near Surface Layer	0.02	0.12	0.48	0.63	1.15	1.10
NOAA Station 41112	Near Surface Layer	-0.04	0.10	0.44	0.58	0.74	0.75
Atlantic Shores	Near Surface Layer	-0.03	0.11	0.49	0.54	1.13	1.11
Atlantic Shores	Midwater	-0.06	0.11	0.42	0.60	0.86	0.87
Atlantic Shores	Near Bottom	-0.01	0.08	0.49	0.58	0.91	0.68
NYSERDA N05	Near Surface Layer	0.01	0.09	0.58	0.50	0.97	1.03
NYSERDA N05	Midwater	-0.03	0.08	0.47	0.54	0.79	0.81
NYSERDA N05	Near Bottom	0.02	0.07	0.61	0.41	0.88	0.83
NYSERDA N06	Near Surface Layer	0.04	0.11	0.74	0.33	1.00	1.11
NYSERDA N06	Midwater	-0.02	0.08	0.45	0.58	0.70	0.38
NYSERDA N06	Near Bottom	-0.01	0.06	0.44	0.57	0.78	0.54
Ørsted 180	Near Surface Layer	-0.05	0.11	0.53	0.37	0.57	0.66
Ørsted 190	Near Surface Layer	0.02	0.09	0.48	0.62	0.92	0.83
Ørsted 220	Near Surface Layer	0.02	0.12	0.70	0.39	0.78	0.62
Ørsted 230	Near Surface Layer	-0.03	0.10	0.48	0.68	0.78	0.75
Ørsted 240	Near Surface Layer	0.01	0.08	0.48	0.61	0.88	0.75
Ørsted 250	Near Surface Layer	0.01	0.17	0.63	0.34	0.65	0.28

Station	Sampling location	BIAS	RMSE	SI	CC	QQ (a)	PR
RODEO	Depth Average	0.00	0.05	0.37	0.77	1.02	0.85

Inspection of the current speed skill assessment shows that all stations and depths are within the RMSE target limits.

Table 3.6. Temperature Model Quality Indices

For temperature the NOS CS 17 guidance is 3 °C RMSE for temperature

Station	BIAS	RMSE	SI	CC	QQ(a)	PR
44008 – Nantucket, MA	-2.27	4.30	0.29	0.82	0.44	0.79
44097 - Block Island, RI	-0.07	1.49	0.12	0.95	0.84	1.07
44017 - Montauk Point, NY	-0.25	1.50	0.11	0.98	0.86	1.15
44025 - Long Island, NY	0.26	1.42	0.10	0.99	0.86	1.29
44065 - New York Harbor Entrance	0.44	1.43	0.10	0.98	0.90	1.22
44027 – Jonesport, ME	0.72	1.32	0.12	0.95	0.90	1.04
44005 – Gulf of Maine, ME	-0.13	1.61	0.15	0.97	0.76	0.92
44098 – Jeffreys Ledge, ME	-0.48	1.58	0.13	0.98	0.79	1.05
44011 – Georges Bank	1.27	4.70	0.45	0.64	0.48	0.75
44091 – Barnegat, NJ	-0.37	1.69	0.11	0.98	0.88	1.10
44066 – Texas Tower	-0.21	1.53	0.11	0.96	0.86	1.12
44009 – Delaware Bay, DE	0.12	1.28	0.08	0.98	0.91	1.09
44058 – Stingray Point, VA	0.37	0.86	0.04	1.00	1.00	1.13
44099 – Cape Henry, VA	0.96	1.74	0.09	0.98	0.95	0.83
44014 – Virginia Beach, VA	1.48	3.07	0.15	0.89	0.86	0.86
44095 – Oregon Inlet, NC	0.57	2.72	0.14	0.92	0.78	1.00
41025 – Diamond Shoals, NC	-3.08	4.30	0.12	0.71	1.30	0.85
41108 – Wilmington Harbor, NC	0.48	1.37	0.06	0.99	0.83	0.98
41013 – Fryingpan Shoals, NC	-0.83	1.65	0.06	0.93	0.93	1.01
41004 – Edisto, SC	-0.25	1.21	0.05	0.93	0.82	0.98
41008 – Grays Reef, GA	0.68	1.51	0.06	0.98	0.82	0.95

Of the twenty-one (21) temperature stations examined, there are a few outliers with regards to the temperature skill evaluation. They are stations at: Nantucket, MA, Georges Bank, Virginia Beach, VA, and Diamond Shoals, NC.

We conclude after review of the model vs. the measurements that the model performs well on a regional scale and that the hydrodynamic processes in the OSW development study areas are well represented.

4 Hydrodynamic Model Methodology Including Wind Turbines

4.1 Overview

The following section describes the methodology employed to model the WEAs in the simulations. The wind turbine locations and physical parameters for each scenario are outlined. The method of estimating the losses and mixing due to the monopile foundations is described. The wind wake loss model is also recounted and the effects on the currents and waves explained.

4.1.1 Offshore Wind Farm Scenarios

As noted in **Section 1.2.3** the scenarios studied included:

- **Scenario 1: Baseline years 2017, 2018, and 2020** – modeled without any WTGs, all three species modeled for 2017. Only sea scallops modeled for 2018 and 2020.
- **Scenario 2: Partial Build-out 12 MW year 2017** - currently proposed developments with publicly available COPs, with 2,083 12 MW turbines for year 2017, all three species modeled in ABM,
- **Scenario 3: Partial Build-out 15 MW year 2017** – currently proposed developments with publicly available COPs, with 2,083 15 MW turbines for year 2017, all three species modeled in ABM
- **Scenario 4: Full build-out, 12 MW year 2017** – currently proposed developments with publicly available COPs and generic layouts for remaining lease areas, with 4,650 12 MW turbines for year 2017, all three species modeled in ABM
- **Scenario 5: Full build-out, 15 MW year 2017** – currently proposed developments with publicly available COPs and generic layouts for remaining lease areas, with 4,650 15 MW turbines for year 2017, all three species modeled in ABM
- **Scenario 6: Full build-out, 15 MW years 2017, 2018, and 2020** – currently proposed facilities with publicly available COPs and generic layouts for remaining lease areas, with 4,650 15 MW turbines. Only sea scallops modeled for 2017, 2018 and 2020 in ABM.

Table 4.1 shows the geographic area, the lease area number and concessionaire, the designation whether it is “with COP” or “Generic”, the number of WTGs and the spacing of the WTGs at the time of study initiation. The latitude and longitude of every “with COP” and “Generic” WTGs are listed in a table in **Appendix A**.

Table 4.1. List of WEAs “with COP” and “Generic”

Geographic Area	Lease Area Number / Concessionaire	Condition	Number of Turbines	with COP only (Partial Build-Out)	COP + Generic (Full Build-Out)	Spacing (nm)
MA-RI	OCS-A 0520 - Beacon Wind LLC	generic	160	-	160	1.0
MA-RI	OCS-A 0521 - Mayflower Wind Energy LLC	with COP	151	151	151	1.0
MA-RI	OCS-A 0522 - Vineyard Northeast LLC	generic	137	-	137	1.0

Geographic Area	Lease Area Number / Concessionaire	Condition	Number of Turbines	with COP only (Partial Build-Out)	COP + Generic (Full Build-Out)	Spacing (nm)
MA-RI	OCS-A 0534 - Park City Wind LLC	with COP	114	114	114	1.0
MA-RI	OCS-A 0500 - Bay State Wind LLC	generic	177	-	177	1.0
MA-RI	OCS-A 0501 - Vineyard Wind LLC	with COP	73	73	73	1.0
MA-RI	OCS-A 0487 - Sunrise Wind LLC	with COP	127	127	127	1.0
MA-RI	OCS-A 0486 - Revolution Wind, LLC	with COP	102	102	102	1.0
MA-RI	OCS-A 0517 - South Fork Wind, LLC	with COP	18	18	18	1.0
MA-RI	OCS-A 0506 - The Narragansett Electric Co	with COP	1	1	1	1.0
MA-RI	Totals (with COP only / COP + Generic)	-	-	586	1,060	-
NY-Bight	OCS-A 0512 - Empire Offshore Wind, LLC	with COP	174	174	174	0.6
NY-Bight	OCS-A 0544 - Mid-Atlantic Offshore Wind LLC	Generic	102	-	102	0.6
NY-Bight	OCS-A 0537 - Bluepoint Wind, LLC	Generic	178	-	178	0.6
NY-Bight	OCS-A 0538 - Attentive Energy LLC	Generic	215	-	215	0.6
NY-Bight	OCS-A 0539 - Community Offshore Wind, LLC	Generic	280	-	280	0.6
NY-Bight	OCS-A 0541 - Atlantic Shores Offshore Wind Bight, LLC	Generic	194	-	194	0.6
NY-Bight	OCS-A 0542 - Invenergy Wind Offshore LLC	Generic	216	-	216	0.6
NY-Bight	OCS-A 0549 - Atlantic Shores Offshore Wind, LLC	Generic	209	-	209	0.6
NY-Bight	OCS-A 0499 - Atlantic Shores Offshore Wind 1 & 2, LLC's	with COP	198	198	198	0.6
NY-Bight	OCS-A 0498 - Ocean Wind LLC	with COP	105	105	105	0.8
NY-Bight	OCS-A 0532 - Orsted North America Inc.	Generic	207	-	207	0.6

Geographic Area	Lease Area Number / Concessionaire	Condition	Number of Turbines	with COP only (Partial Build-Out)	COP + Generic (Full Build-Out)	Spacing (nm)
NY-Bight	<i>Totals (with COP only / COP + Generic)</i>	-	-	477	2,078	-
MD-DE	OCS-A 0482 - GSOE I LLC	Generic	169	-	169	0.6
MD-DE	OCS-A 0519 - Skipjack Offshore Energy LLC	Generic	60	-	60	0.6
MD-DE	OCS-A 0490 - U.S. Wind Inc.	with COP	126	126	126	1.0
MD-DE	<i>Totals (with COP only / COP + Generic)</i>	-	-	126	355	-
VA-NC	OCS-A 0483 - Virginia Electric and Power Company	with COP	205	205	205	0.8
VA-NC	OCS-A 0508 and OCS-A 0599 - Avangrid Renewables LLC	with COP	242	242	242	0.8
VA-NC	Totals (with COP only / COP + Generic)	-	-	447	447	-
VA-NC	<i>Totals (with COP only / COP + Generic)</i>	-	-	894	894	-
NC-SC	OCS-A 0545 - TotalEnergies Renewables USA, LLC	Generic	135	-	135	0.6
NC-SC	OCS-A 0546 - Duke Energy Renewables Wind, LLC	Generic	128	-	128	0.6
NC-SC	<i>Totals (with COP only / COP + Generic)</i>	-	-	0	263	-
	<i>Overall Totals (with COP only / COP + Generic)</i>	-	-	2083	4,650	-

Additionally, **Table 4.1** shows the Wind Energy Areas with the requisite Concessionaire.

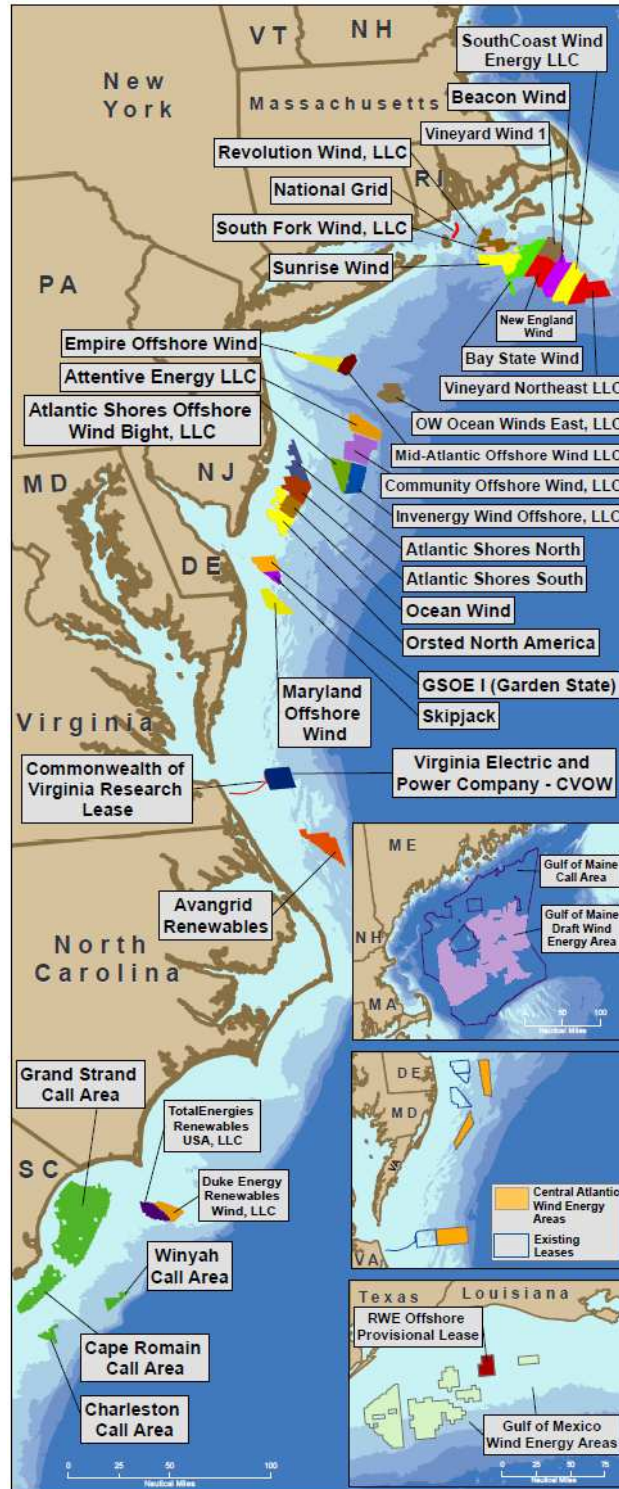


Figure 4.1. WEAs Along the East Coast Including the Names of the WEAs

As of May 2024. Credit: BOEM, <https://www.boem.gov/renewable-energy/lease-and-grant-information>

The following figures show the WTGs with the model mesh in each of the geographic locations, MA-RI, NY Bight, MD-DE, VA-NC, and NC-SC.



Figure 4.2. WTG Locations for MA-RI

Yellow circles around red dots indicate “with COP” and just red dots indicate “Generic”. The detailed model mesh is also shown.

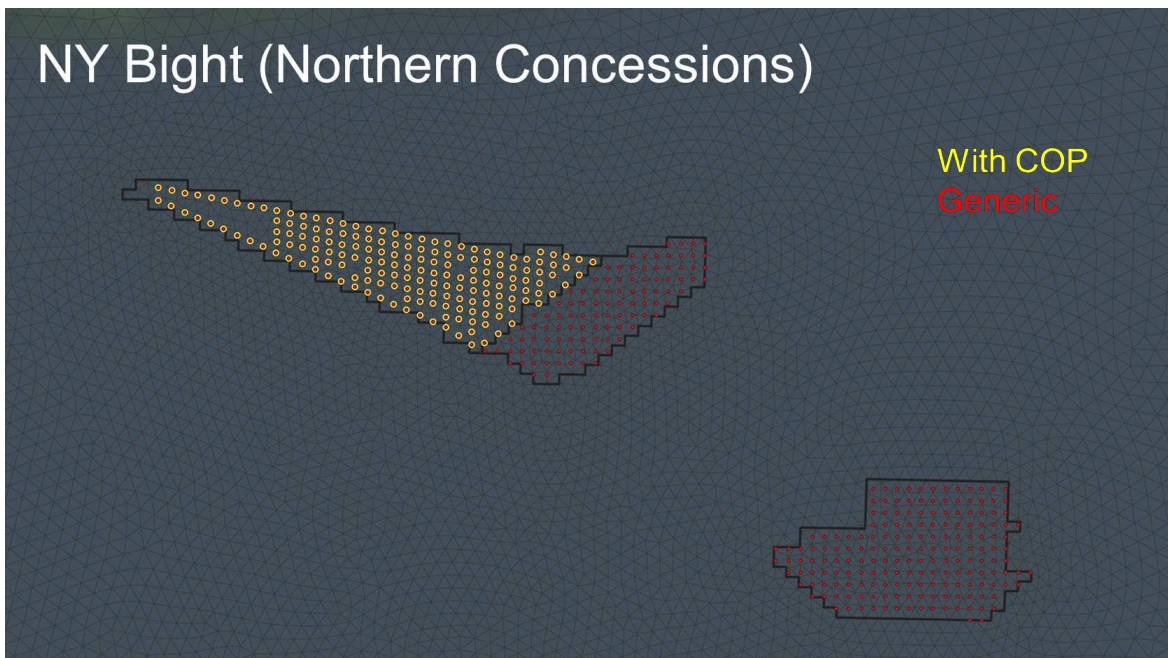


Figure 4.3. WTG Locations for NY Bight (Northern Concessions)

Yellow circles around red dots indicate “with COP” and just red dots indicate “Generic”. The detailed model mesh is also shown.

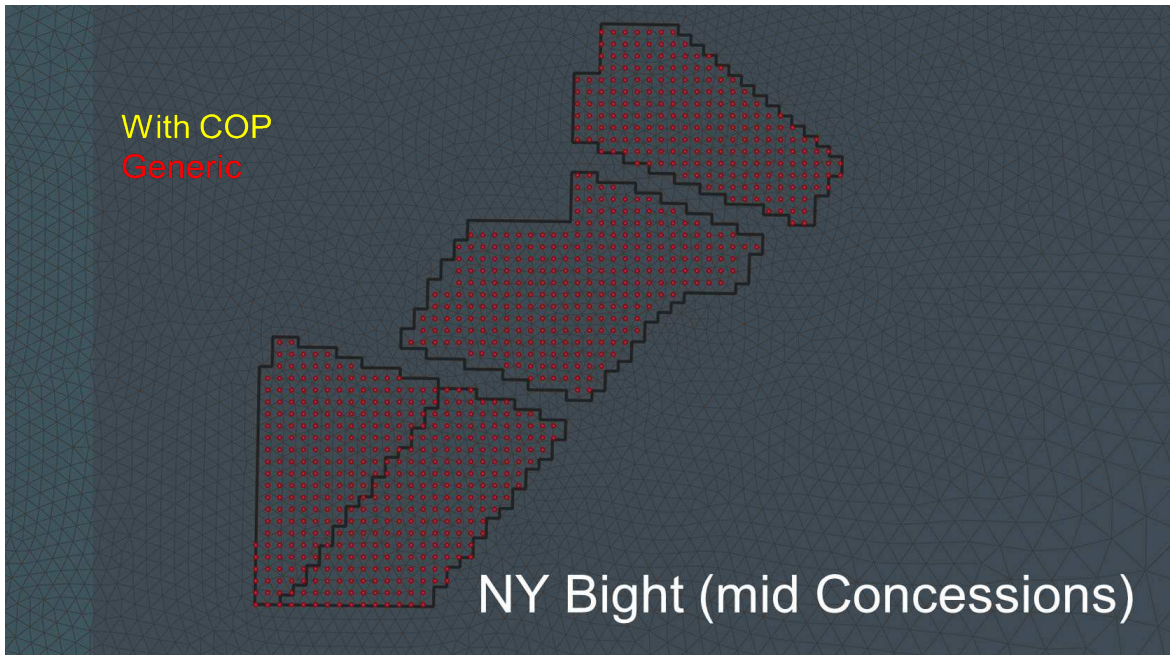


Figure 4.4. WTG Locations for NY Bight (Mid Concessions)
Red dots indicate “Generic”. The detailed model mesh is also shown.

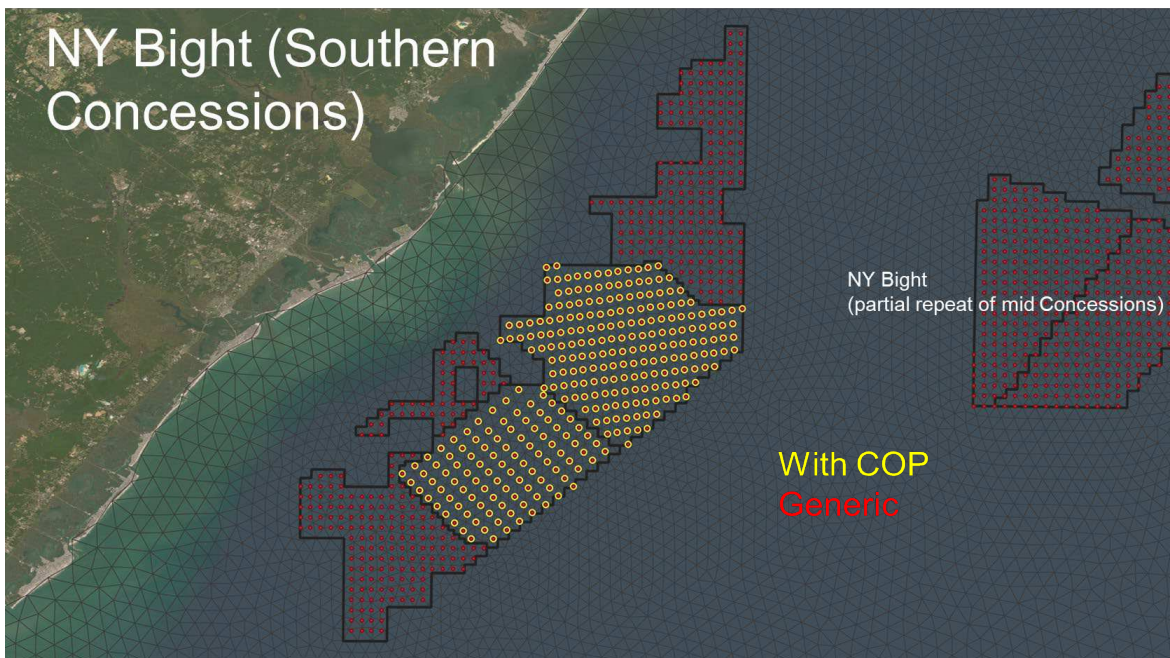


Figure 4.5. WTG Locations for NY Bight (Southern Concessions)
Yellow circles around red dots indicate “with COP” and just red dots indicate “Generic”. The detailed model mesh is also shown.

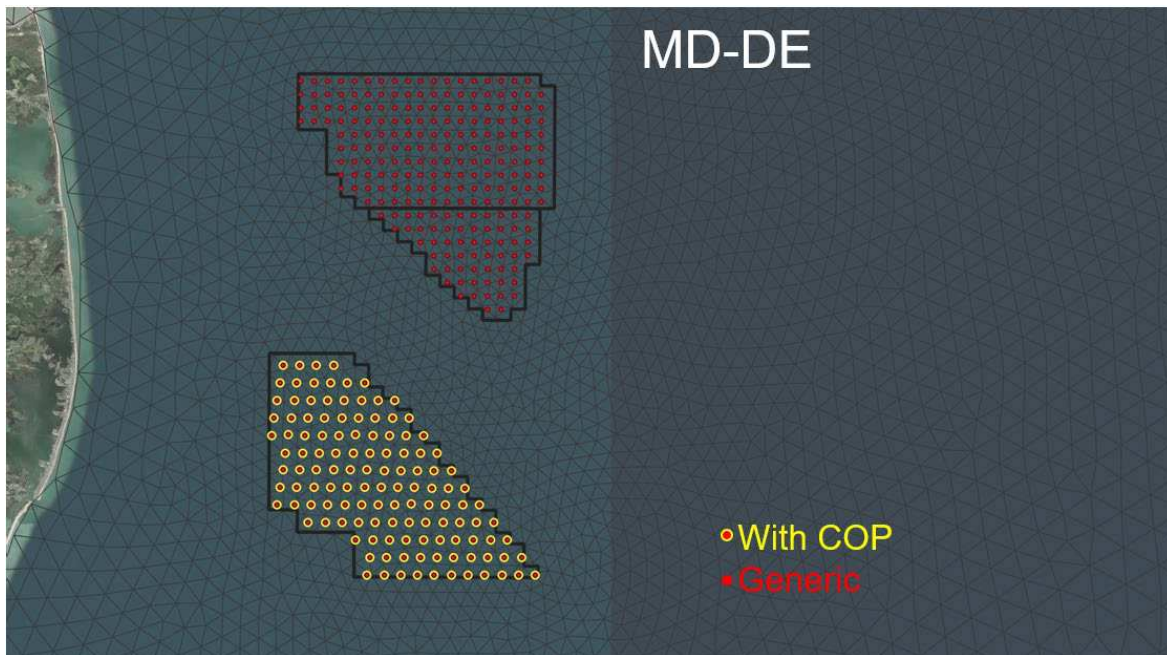


Figure 4.6. WTG Locations for MD-DE

Yellow circles around red dots indicate “with COP” and just red dots indicate “Generic”. The detailed model mesh is also shown.

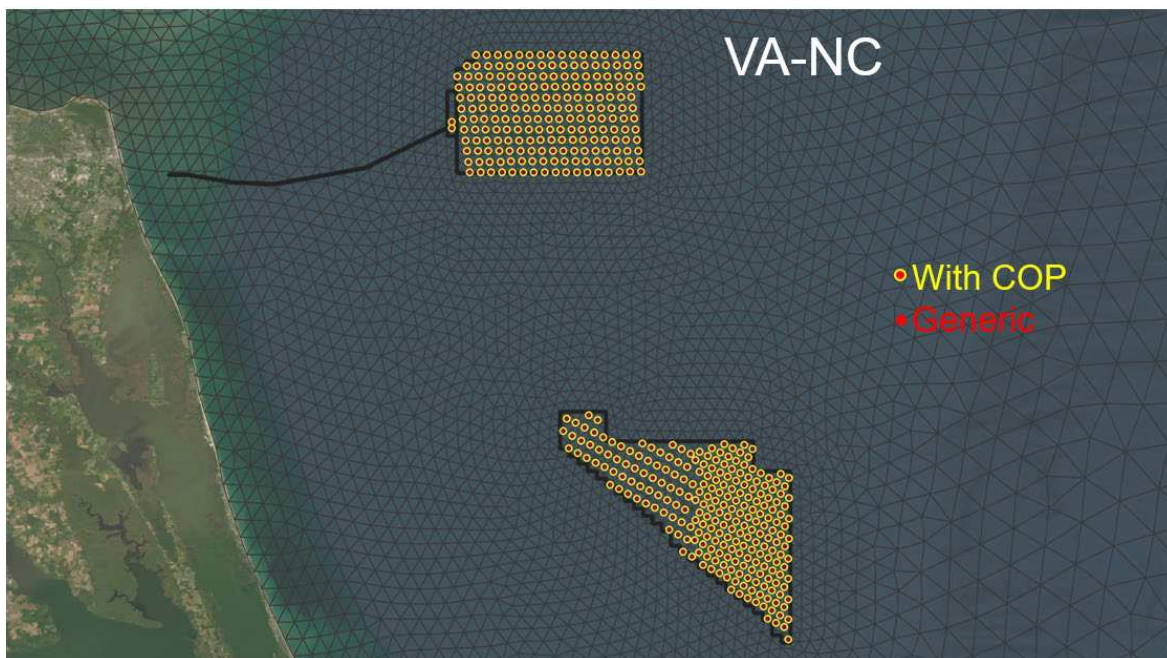


Figure 4.7. WTG Locations for VA-NC

Yellow circles around red dots indicate “with COP”. The detailed model mesh is also shown.



Figure 4.8 WTG Locations for NC-SC

Red dots indicate “Generic”. The detailed model mesh is also shown.

4.1.2 Modeled 12 MW Wind Turbine Generator Configuration

The specification of the wind turbines with respect to dimensions of the foundations and turbine characteristics are generic and guided by the U.S. [National Renewable Energy Laboratory](#) reference turbines. Commercial turbine specifications such as rated power and speed are often proprietary and difficult to acquire. We were able to obtain information for the 15 MW build out scenario but not for the 12 MW. Therefore, we used available data for a 10 MW turbine and scaled between this and 15 MW to estimate specifications for the 12 MW turbines. The physical dimensions of the modeled 12 MW wind turbine generator and monopile are listed in **Table 4.2** below. The monopile was simulated as a constant diameter cylinder with biofouling added to the outside of the structure. Biofouling was included to allow for an increase in drag on the monopile. The hub height, rotor swept diameter, thrust coefficient and cut-in wind speed are values required for the wake loss model calculations. An illustration of an OSW farm wind turbine generator is shown below in **Figure 4.9**, showing hub height, and rotor swept radius. The thrust and power extraction curve for the 12 MW WTG is shown in Error! Reference source not found..

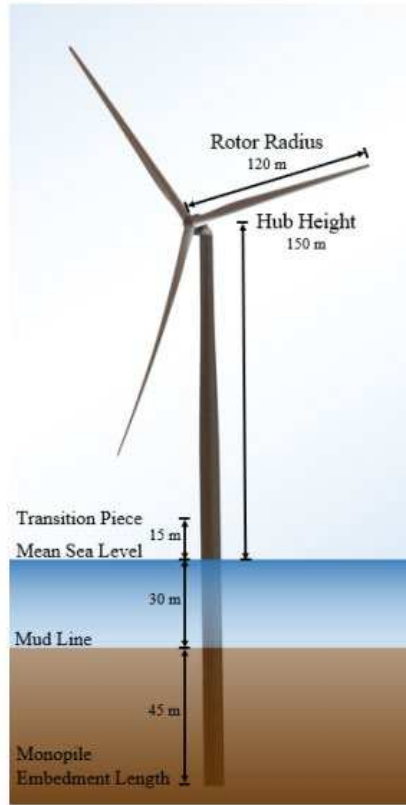


Figure 4.9. Illustration of the IEA Wind 15 MW Reference Wind Turbine Generation
Credit: IEA

Table 4.2. Generic 12 MW Wind Turbine Physical Dimensions

Item	Description	Dimension(s)
Turbine Hub Height	The average height of the wind turbine generator hub above water	125 m
Turbine Tower Diameter	The tower diameter was enhanced 10 cm with marine growth to increase the diameter and model surface roughness	9.5 m
Rotor Swept Diameter	Rotor diameter is used in the wind wake loss calculations.	215 m
Rated speed	Wind speed at which rated power is reached	10.6 m/s
Cut-in Wind Speed	Cut-in wind speed is used in the wind wake loss calculation	3 m/s
Cut-out Wind Speed	Cut-in wind speed is used in the wind wake loss calculation	25 m/s

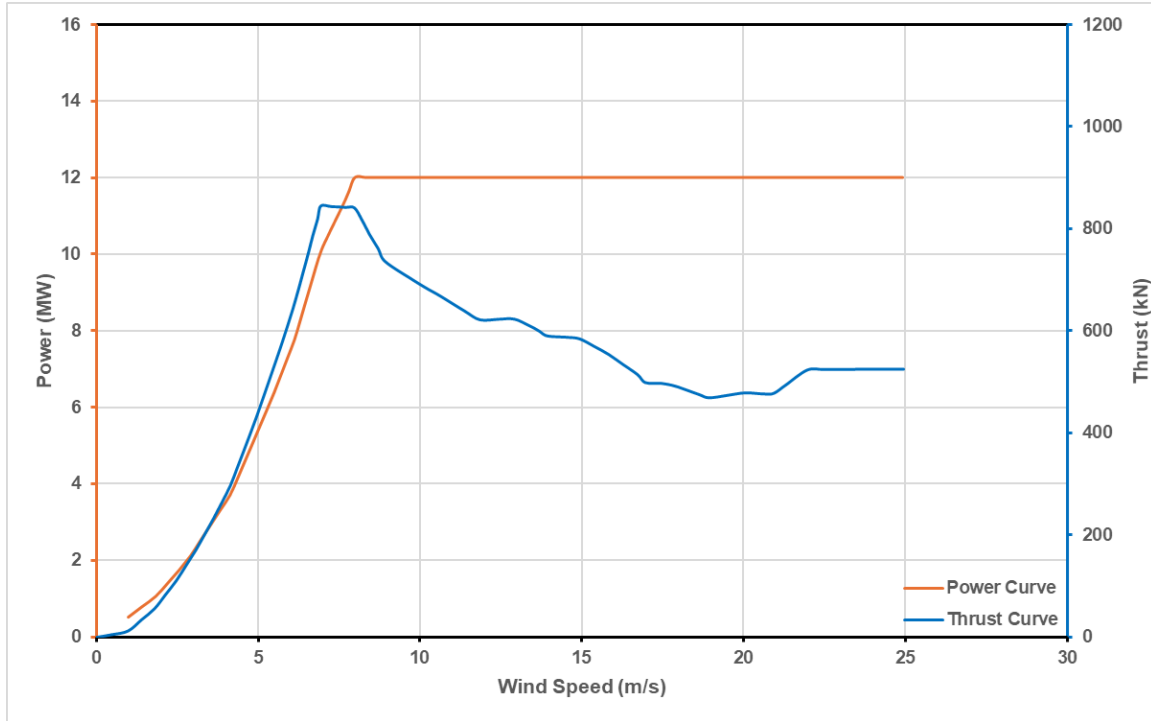


Figure 4.10. Thrust and Power Extraction Curve for the 12 MW WTG

The orange line is the power curve, and the blue line is the thrust curve

4.1.3 Modeled 15 MW Wind Turbine Generator Configuration

The specification of the wind turbines with respect to dimensions of the foundations and turbine characteristics are generic and guided by the U.S. National Renewable Energy Laboratory reference turbines. The physical dimensions of the modeled 15 MW wind turbine generator and monopile are listed in **Table 4.3**. Generic 15 MW Wind Turbine Physical Dimensions below. As with the 12 MW turbines, the monopile was simulated as a constant diameter cylinder with biofouling added to the outside of the structure. Biofouling was included to allow for an increase in drag on the monopile. The hub height, rotor swept diameter, thrust coefficient and cut-in wind speed are values required for the wake loss model calculations. The thrust and power extraction curve for the 15 MW WTG is shown in **Figure 4.11**.

Table 4.3. Generic 15 MW Wind Turbine Physical Dimensions

Item	Description	Dimension(s)
Turbine Hub Height	The average height of the wind turbine generator hub above water	150 m
Turbine Tower Diameter	The tower diameter was enhanced with 10 cm marine growth to increase the diameter and model surface roughness	10 m
Rotor Swept Diameter	Rotor diameter is used in the wind wake loss calculations.	240 m
Rated speed	Wind speed at which rated power is reached	10.6 m/s
Cut-in Wind Speed	Cut-in wind speed is used in the wind wake loss calculation	3 m/s
Cut-out Wind Speed	Cut-out wind speed is used in the wind wake loss calculation	25 m/s

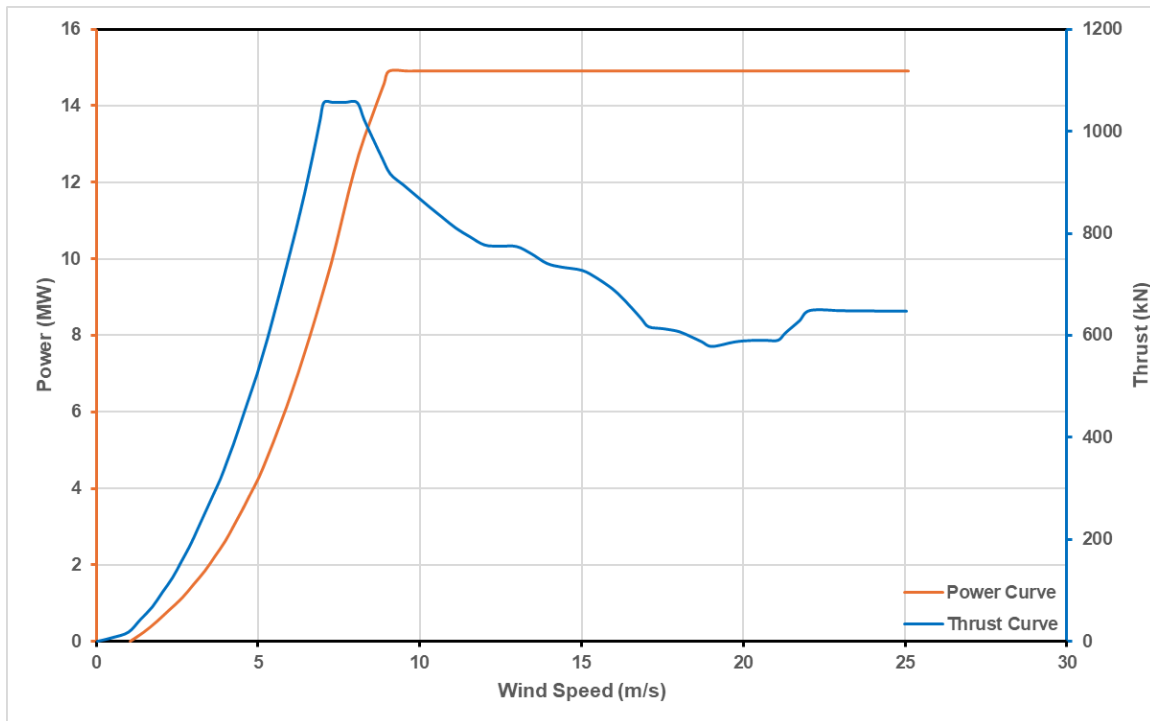


Figure 4.11. Thrust and Power Extraction Curve for the 15 MW WTG

The orange line is the power curve, and the blue line is the thrust curve

4.2 Calculations of Wind Turbine Foundation Drag Coefficient

The implementation of the turbine monopiles roughly follows Rennau et al. (2012) and Johnson et al. (2021), where the effects due to the monopile are parameterized and inserted as energy sinks/sources for each individual WTG foundation. Once the local 3D hydrodynamic model was calibrated and verified, two different wind turbine foundations were studied to gain an understanding of the localized flow around

the wind turbine foundation structures using a Computational Fluid Dynamic (CFD) model. The goal of the CFD study was to enable modeling of the WTG foundations' impact on the surrounding waters. The importance of accurately defining the drag coefficient is discussed below.

The CFD analysis was used to assess the amount of hydrodynamic resistance or blocking of the wind turbine subsea foundation, the level of boundary layer turbulence, the characteristics of the surrounding vortex structure, as well as the nature of the wake and vortex shedding. The CFD methodology was developed for earlier projects conducted by DHI that studied the effect of bridge piers on flow in a stratified sea. One of these former studies by DHI was used to determine the impact of these structures on the mixing in the highly ecologically sensitive waters of the Fehmarn Belt, that controls saline-fresh water exchange between the Baltic Sea and the Kattegat (see **Figure 4.12**). In the Fehmarnbelt study (FEHY, 2013), the level of mixing induced by a range of bridge pier shapes was calculated by CFD and validated using sophisticated physical model experiments conducted and reported by Jensen et al. (2018). The CFD model provided relationships between current velocity and mixing efficiency regarding the structure shape.

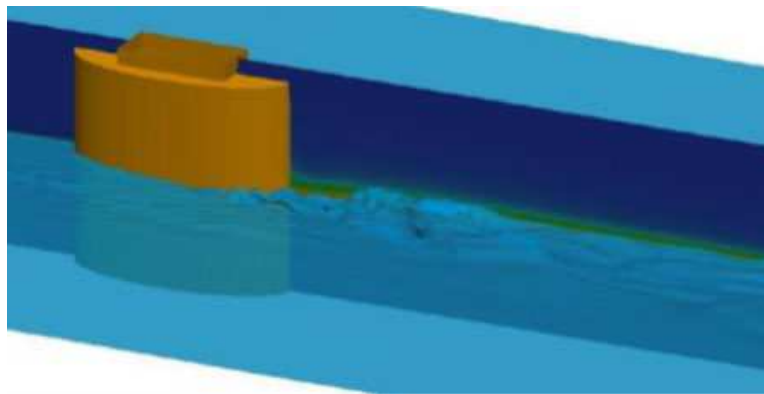


Figure 4.12. CFD Simulation of a Stratified Flow Around a Bridge Pier

The interface between the layers is shown as an iso-surface. (from: Jensen et al. 2018)

The flow around a monopile is relatively complex (see **Figure 4.13**) and has been the subject of several experimental and modeling studies. The monopile exerts a drag force on flowing water due to the blocking effect and the resistance in the boundary layer around it. Depending on the flow conditions, the monopile will initiate a downstream wake, where eddies and turbulence may impact the vertical mixing of the waters.

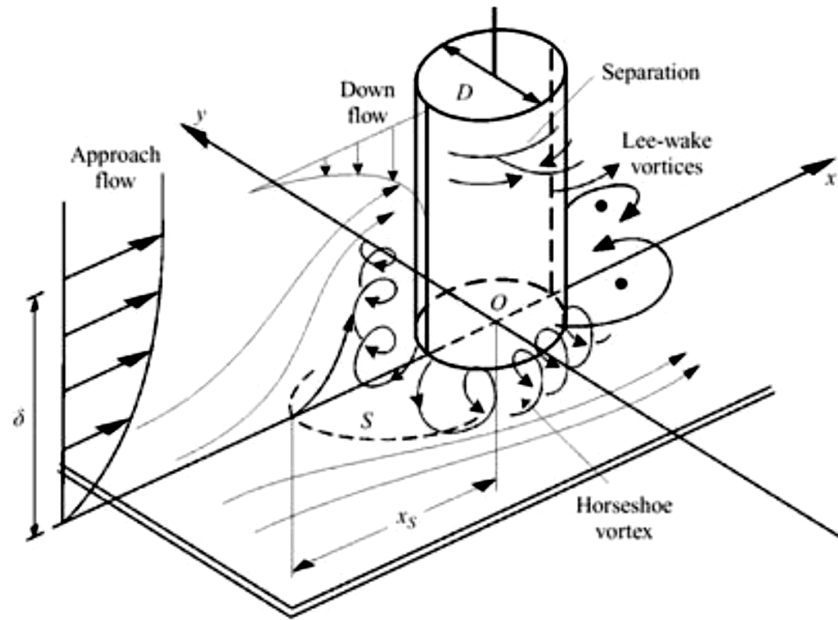


Figure 4.13. Computational Fluid Dynamics (CFD) Processes

Sketch of large turbulent flow structures generated by the presence of a vertical pylon in a flow-field.

The methodology that was employed for the study presented in this report was based on these proven techniques, which has been successfully used for the Fehmarn Belt fixed link environmental assessment and design optimization, and the Oresund Link project. These were two other major environmentally sensitive project in Europe with similar environmental concerns as Fehmarn.

While bridge piers are much more intrusive due to irregular shapes, the methodology remains reliable for (relatively) less intrusive, but more abundant, WTG monopile foundations. The CFD model work quantified the effect in terms of the enhanced mixing, following the example enumerated in Jakobsen et al. (2010) where the added resistance due to the presence of bridge piers was investigated. Also, Rennau et al. (2012) studied the regional effect of offshore wind towers in the Baltic Sea. Several detailed studies exist on the physical processes of natural mixing of stratified flows (e.g., Grubert, 1989; Fernando, 1991; Ivey and Imberger, 1991; Strang and Fernando, 2001; Peltier and Caulfield, 2003).

When a surface piercing WTG foundation is introduced into the flow, the work performed by the WTG foundation (reaction force) on the ambient water introduces turbulent kinetic energy from the generated vortex shedding and smaller scale turbulence. In a uniform non-stratified flow, the turbulent flow structures will undergo a turbulent cascade in which smaller and smaller eddies are being formed and finally dissipated into heat. In the stratified case, some of the energy will mix the two layers, either locally or propagating away as internal waves, redistributing heavy bottom water into the lighter upper layer (e.g., Rouse and Dodu, 1955; Holmboe, 1962; Smyth and Winters, 2003).

The term “mixing efficiency” is, for this study, related to the Richardson number (see Turner, 1973). The change in potential energy by mixing the vertical layers of the density profile can be related to the kinetic energy produced by the drag forces on the WTG foundation. The energy produced is the turbulent kinetic energy generated when the WTG foundation is exposed to the steady current in the numerical simulations. The turbulent kinetic energy is approximately equal to the work performed by the steady current flows around the surface piercing WTG foundation.

Work may be calculated as the integral of the force on the surface piercing WTG foundation multiplied by the speed of the current. In steady current, the inertial term of force trends to zero and the drag force remains as the key component of the work on the fluid. Therefore, the mixing efficiency is proportional to the work done on the fluid. In steady flow, this means the mixing efficiency is proportional to the drag force on the surface piercing WTG foundation. This energy conversion is the basis of the transfer of results from the CFD model to the 3D hydrodynamic model through the introduction of localized “drag” to the OSW region at each of the surface piercing WTG foundations in the model.

The 3D regional hydrodynamic solution method involves the use of a finite volume mesh with a spatially varying mesh size allowing resolution to be concentrated in key areas of interest. A typical choice of minimum mesh size of 25 m implies that foundations with a typical horizontal dimension of 12 m to 15 m are not directly resolvable in the computational mesh. Therefore, the presence of WTG foundations was parameterized. The resistance of the flow due to the WTG foundations derived from the CFD study was modeled by calculating the current induced drag force on each individual pier segment and equating this force with a shear stress contribution compatible with the 3D hydrodynamic momentum formulation. The turbulence model used to represent the disturbance due to the bottom founded structures was an enhanced κ - ϵ model that included an extra term for the drag derived from the CFD modeling and a work/turbulence production term that was used to balance out the energy dissipated. This was done to eliminate the shortcomings of the k-model. The length scale specification inherent in this model can be replaced by a transport equation for a turbulent quantity. The κ - ϵ turbulence closure formulation implemented in 3D hydrodynamic was suggested by Rodi (1980).

In this study the specific drag coefficients and mixing efficiencies were described using a CFD model. The model is a full 3D Reynolds averaged simulation based on the [OpenFOAM](#) modeling framework. The model was used to simulate the effect of one turbine to establish a general parameterization for the energy conversion and thereby the impacts on flow resistance and mixing in the 3D regional model.

The project specific CFD modeling produced the results shown below in **Figure 4.14**. The results of a simulation of a steady stratified flow past one monopile including scour protection and conditions are similar to typical conditions at the OSW sites. As expected, the results show that the monopile generates a downstream unsteady wake area. The integral drag coefficient induced by the monopile, and the scour protection is estimated to be $C_D = 1.034$ as shown in **Figure 4.14**. This coefficient applies to both 12 MW and 15 MW monopiles. The downstream mixing process, part of which can be seen as the internal waves in the density interface in **Figure 4.14**, is described using a Richardson number (or energy conversion efficiency) at 0.07 in agreement with earlier findings by Jensen et al. (2018).

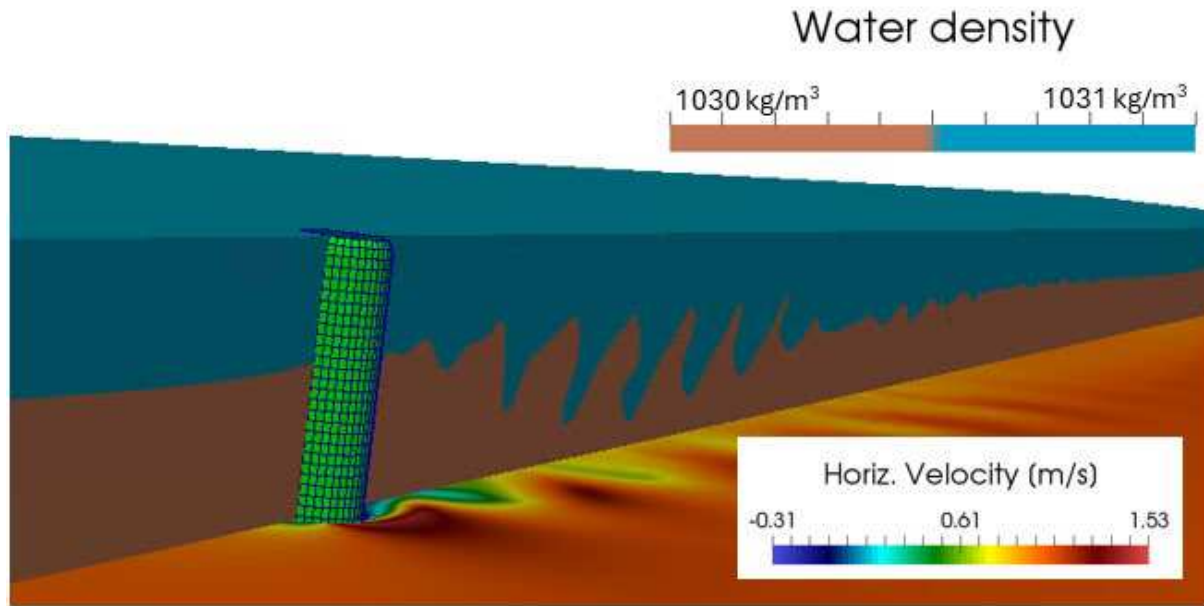


Figure 4.14. Illustration of the Velocity and Density Field

Velocity and density field in a vertical and a horizontal plane in the steady flow past a 10 m diameter monopile as modeled by the CFD model.

4.3 Wind Turbine Wake Loss Model

Wind turbine wakes have the potential to affect ocean hydrodynamics. As wind passes through a wind farm, wind turbines extract energy and create downstream wakes. These wind turbine wakes are plume-like volumes of higher turbulence and reduced wind speed (e.g., Siedersleben et al., 2019; Archer et al., 2019) and can extend from several km up to 50 km downstream a wind turbine, depending on the stability regime of the atmospheric boundary layer (ABL) (e.g., Cañadillas et al., 2020). The wake induced wind speed deficit and turbulence have the potential to interact with the sea surface. Observations of downstream impacts on the sea surface have been observed using Synthetic Aperture Radar (SAR), providing a direct measure of WEA wake velocity deficits. Christiansen and Hasager (2005) or Djath and Schulz-Stellenfleth (2019) have demonstrated up to 5% - 10% wake surface wind velocity deficits 5 km to 40 km downstream of North Sea wind farms. Impacts on the sea surface wind stress may influence wave height, stratification, current speeds, and temperature in the area (e.g., Akhtar et al., 2022; Dorrell et al., 2022; Paskyabi, 2015; Paskyabi & Fer, 2012; Zhou et al., 2012; Slawsky et al., 2015).

The downstream wake of a wind turbine is centered at the hub height (125 m to 150 m, typically depending on turbine power rating) and is therefore elevated well above the sea surface. The wakes extend downstream eventually reaching the sea surface, but the relative wind speed deficit and increased turbulence level is less than at hub height (Golbazi et al., 2022). The wakes from individual turbines inside the OSW farm interact with each other, creating complex patterns that impact power production of downstream turbines. In addition, wakes can change, sea-surface characteristics and hence currents and waves. It is important to understand the magnitude of these wake impacts, and the cumulative interaction of multiple lease areas in the region.

With the increased focus on OSW developments, several approaches to describe and quantify the impacts of wind wakes on the environment have been developed. A strong focus has been on quantification of wake interactions on the wind resource, as this has a direct impact on the financial balance of wind farms.

However, several studies have gone further, discussing the impacts on the water environment in forms of waves, currents, heat transfer, etc. Several approaches can be identified. Although the models in practice represent a broad spectrum, we can make a classification following e.g. Fischereit et al., 2022, as:

- Direct methods where each turbine and the flow around it is described in great detail. Models are 3D and typically have spatial resolution down to a few centimeters. The turbines are described with a direct implementation of the moving blades with e.g. actuator line methods or implicit sources. Turbulence is typically described with large-eddy simulation (LES) or Reynolds-averaged Navier–Stokes (RANS) models. These types of models provide close to full picture of the wakes with fluctuations and interaction but can typically only cover a few turbines to up to one wind park for short periods. These models are typically used for development or validation of simpler methods.
- Implicit methods, where the turbines are represented as so-called sub-grid features in large atmospheric models. OSW farm scale or regional scale models are based on e.g. Weather Research and Forecasting (WRF), which realistically can have nesting areas down to less than 1 km, but still cover large areas. With such a resolution, wind turbines cannot be resolved in any detail. Instead, the WRF model is equipped with suitable momentum end energy sinks and sources that can represent the action of the turbine on the mesoscale winds. A common approach is the actuator disk method developed by Fitch et al. (2012). This sort of model cannot resolve individual wakes nor the interaction but has the advantage that energy and momentum is conserved, thus respecting basic principles. This approach has been used in many wind resource studies and in a few studies where sea surface impacts are the focus.
- Analytic or Explicit methods, where an empirical model is established for each wake, describing the velocity deficit, the shape and the wake recovery. This type of model includes Jensen (1983), Frandsen (2006), Zong and Porte-Angel (2020), and many others. Explicit methods have the advantage that they are independent on any spatial resolution and are thus relatively simple.

For this study PyWake (Pedersen et al., 2023), an explicit model, was used to characterize wind turbine wakes associated with the WEAs, coupled with a MIKE 21/3 hydrodynamic (HD) flexible mesh model (DHI, 2021) to simulate the impacts of turbine wakes on sea surface wind stress affecting both the current speeds and wave heights in and around the WEAs. This is further integrated with a MIKE ECO Lab ABM to determine any resulting changes in settlement patterns of the selected species.

4.3.1 PyWake Overview

PyWake is an open-source, python-based tool developed by the Technical University of Denmark (DTU), used to simulate annual energy production (AEP) of a wind farm, turbine wake wind speed deficits, and turbulence (Al Halabi, 2023; Pedersen et al., 2023). PyWake can be used to resolve individual turbine effects to determine the effects of wind farms as a whole. PyWake also has the capability to simulate farm-to-farm effects from the interaction of wakes from multiple wind farms. Within the PyWake tool are several in-built wind farm “engineering models” that use different methods to estimate AEP, and wake associated wind speed deficits and turbulence, including the Niels-Otto Jensen Model (Jensen, 1983), Bastankhah Gaussian deficit model (BAS) (Bastankhah and Porté-Agel, 2014) and Zong Gaussian deficit model (ZON) (Zong and Porte-Angel, 2020), among others. These models can be selected by the user along with various constants and parameters.

4.3.2 PyWake Description

The ZON engineering model within PyWake, which is the newest and more sophisticated built-in engineering model offered in PyWake, was used to calculate the windspeed deficit at hub height (Zong and Porte-Angel, 2020). The ZON models wake expansion as a function of a local turbulence intensity, with wake width following Shapiro et al. (2018). ZON is capable of predicting farm-to-farm effects more

effectively than other, simpler models offered in PyWake (Fischereit et al., 2022). The Frandsen turbulence model (STF2017) (Frandsen, 2007) was implemented according to international standards (IEC61400-1:2017, International Electrotechnical Commission, 2017) that included the in-built momentum conserving superposition model in PyWake for turbine-to-turbine and farm-to-farm wake interactions.

The wind speed deficit calculated by the ZON model in PyWake is determined at the turbine hub height. In order to relate the wind speed deficit at hub height to the sea surface, we use the Monin–Obukhov similarity theory (MOST, Monin and Obukhov, 1954). MOST describes the wind speed profile of the atmospheric surface layer (ASL) as a log-linear profile based on empirical similarity scaling laws. MOST is therefore used to approximate the wind speed deficit at the reference height of 10 m from the wind speed deficit at hub height calculated by PyWake, using Eq. 1. This is a common practice in the wind industry (e.g., Paskyabi and Fer, 2012; Breedts et al., 2018; Cheng et al., 2019; Han et al., 2019; Paskyabi, 2015; van der Laan et al., 2017):

$$v_{10} = \frac{U_*^a}{k} \left[\ln \left(\frac{z}{z_0} \right) - \phi_m \left(\frac{z}{L} \right) \right] \quad \text{Eq.1}$$

Where: v_{10} is windspeed at the desired reference height of 10 m
 U_*^a is the air-side friction velocity
 k is the von Karman constant (0.41)
 z is the reference height (here 10 m)
 z_0 is the roughness length
 ϕ_m is an empirical universal stability function
 L is the Monin-Obukhov length scale (Monin and Obukhov, 1954)

MOST incorporates the ASL stability regime (i.e., stable, unstable, or neutral), which is key in determining wake extent and temperature effects induced by turbulence or changes in convection (Wu et al., 2023). Wind wake related temperature effects are also included in the MOST approach, however, here focus is on the momentum fluxes. It is likely that there is a slight over-estimation in our results of the windspeed deficit at the sea surface (i.e., our estimates are conservative) as uncertainties related to the SBL height exist.

Recent studies with detailed wake modeling indicate that wake effects (both wind speed deficit, turbulence and cooling) from large turbines (i.e., such as the large offshore wind turbines that have been considered in this study) are significantly less at the surface in comparison to conventional wind turbines (Golbazi et al., 2022). Indeed, wind speed deficit at the sea surface resulting from extreme scale turbines has been estimated as negligible (~3-4%) in stable conditions using the Fitch (2012) wind farm parameterization in the Weather Research and Forecasting model (Golbazi et al., 2022; Skamarock et al., 2021).

LES models are capable of partly resolving wind speed profiles and turbulence in the turbine wakes (e.g., Wu & Porté-Agel, 2011; Golbazi et al., 2022; Wu et al., 2023). Although more accurate, these LES models are exponentially more costly computationally (Archer et al., 2018) and were considered inappropriate for use at the scale of this study. Therefore, PyWake was selected as the best available, open source, engineering model available at the time of writing, with the MOST law to relate hub height windspeed deficit to the 10 m reference height.

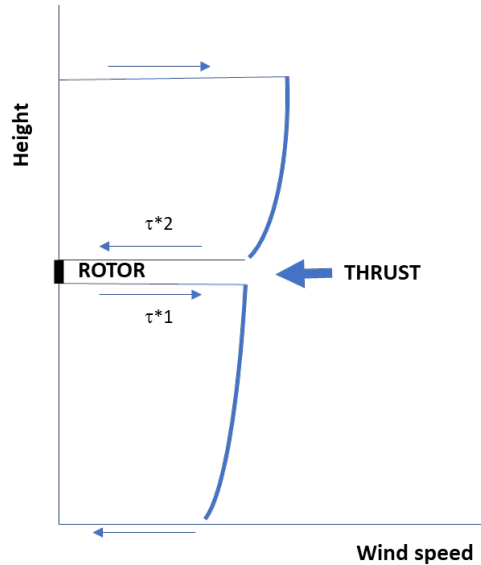


Figure 4.15. Conceptual Framework of the Wind Wake Loss Model

Thrust is the turbine thrust force, and τ^*1 and τ^*2 are the shear stress forces below and above the wind turbine rotor layer, respectively.

4.3.3 PyWake Model Set-Up

Climate Forecast System Reanalysis (CFSR) wind fields were input into the PyWake model. Not all WEAs could be incorporated into a single PyWake model run due to large computational requirements. The WEAs were therefore broken into the four areas MA-RI, NY Bight + MD-DE, VA-NC, and NC-SC. Each area encompass the WEA are with a cut-off margin at least 20 km from the turbines. For areas where there are multiple WEAs in a region, the multiple wind farms were included together to capture farm-to-farm wake effects.

The dimensions and specifications of the offshore wind turbines modeled in the WEAs scenarios and input into PyWake were based on the 12 MW and 15 MW WTGs listed in **Table 4.2** and **Table 4.3**. Generic 15 MW Wind Turbine Physical Dimensions.

The changes of the wind speed are estimated using the PyWake toolbox at hub height. The procedure is to first interpolate the CFSR wind fields from grid size 20 km x 20 km on to the higher resolution unstructured model mesh and extract a representative time series of 10 m wind from the CFSR data set for each windfarm. PyWake can only use one wind incoming time series per area, therefore a representative central point is used. This is used as the incoming 10 m wind. This is extrapolated to hub-height using the prevailing wind profile as estimated by MOST. Then the individual wakes and wake-interactions for each turbine in the area are calculated. The resulting wind-deficits are stored on an intermediate 500 m x 500 m grid and then transformed back to the surface. Subtracting the undisturbed 10 m wind then gives the change in 10 m wind speed. This change is finally applied as a correction to the CFSR 10 m wind in the area. This simple linearization enables spatial variations within the farms area to be properly accounted for. The final corrected wind fields are then compiled and applied as forcing in the wave and hydrodynamic models.

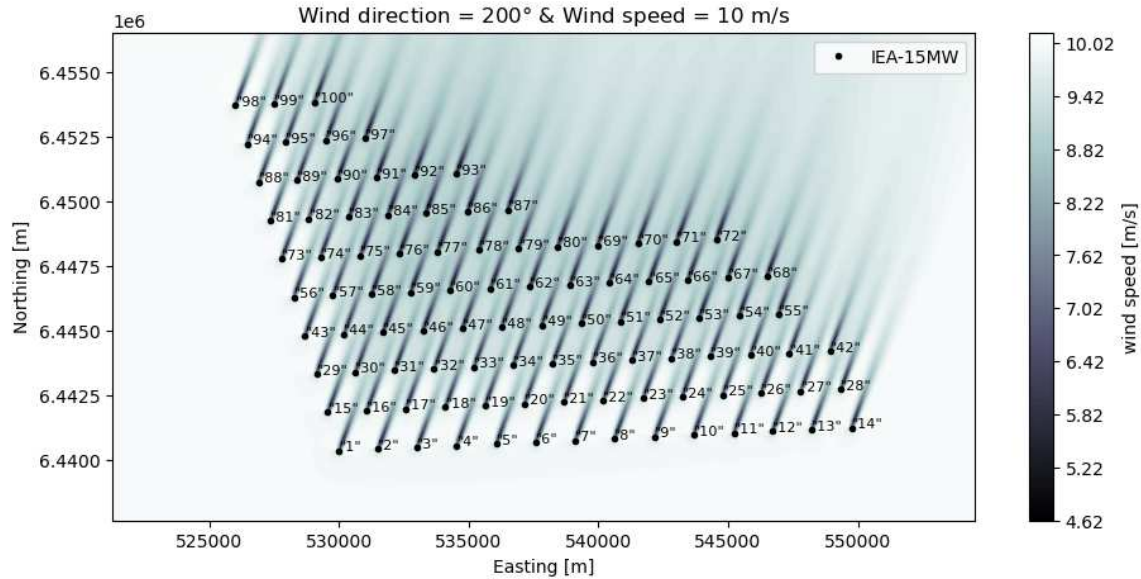


Figure 4.16. Calculated Wind Wake Velocity Deficits in an Idealized Wind Farm

The panel shows individual wakes and how they interact and extend beyond the actual farm area. Such wake-maps are subsequently merged as an adjustment to the wind map used to force the hydrodynamic models. The hydrodynamic grid has one turbine per cell.

To summarize, the PyWake individual steps in this process is as follows:

- The U.S. East Coast is divided in 4 domains, where we expect wind farm interactions. This is because the turbine-turbine interaction is a N^2 problem that grows out of hand easily. Also to be efficient, the domains are cropped 20 km – 50 km from the windfarms, as wake deficits at sea level are diminished at such distances.
- For each domain we specify the position and characteristics of each turbine and extract a representative wind speed from the CFSR wind (**Figure 4.16**. Calculated Wind Wake Velocity Deficits in an Idealized Wind Farm). With the present setup, PyWake can only handle one representative incoming wind per domain and can only handle interactions within one domain. Domain selection is therefore a balance between these two factors.
- The representative surface wind is extrapolated hourly to hub height based on the actual stability conditions, and the wind wakes are then estimated with all interactions and the actual production rate. The resulting wind field, comprising all wakes in the domain, are then mapped onto a 500 m grid and extrapolated to 10 m height using the prevailing stability conditions.
- The CFSR surface wind has been interpolated to the hydrodynamic grid where the wind in each element is corrected according to the new wake field.
- Hereafter the adjusted wind fields are applied as forcing of the hydrodynamic models.

4.3.4 Wind Modification

4.3.4.1 Comparison of PyWake to Johnson et al., 2021

In the Johnson et al. (2021) study, a first-generation wind wake model modified the CFSR 20 km by 20 km grids. The model was based on the Frandsen (1992) infinite wind farm boundary layer (IWFBFL) model with atmospheric stratification modifications per Pena & Rathmann (2014). The Frandsen model assumes horizontally homogeneous impact and the incoming wind was selected at a central point in the OSW farm. In the present study, PyWake, in contrast, is based on a 500 m by 500 m grid. The difference in the granularity of the two models for the MA-RI OSW farm region is illustrated below in **Figure 4.17**.

Panel Illustrates the Overlaid Footprint of the Wake Deficit Area from PyWake vs. CFSR from Johnson et al. (2021).

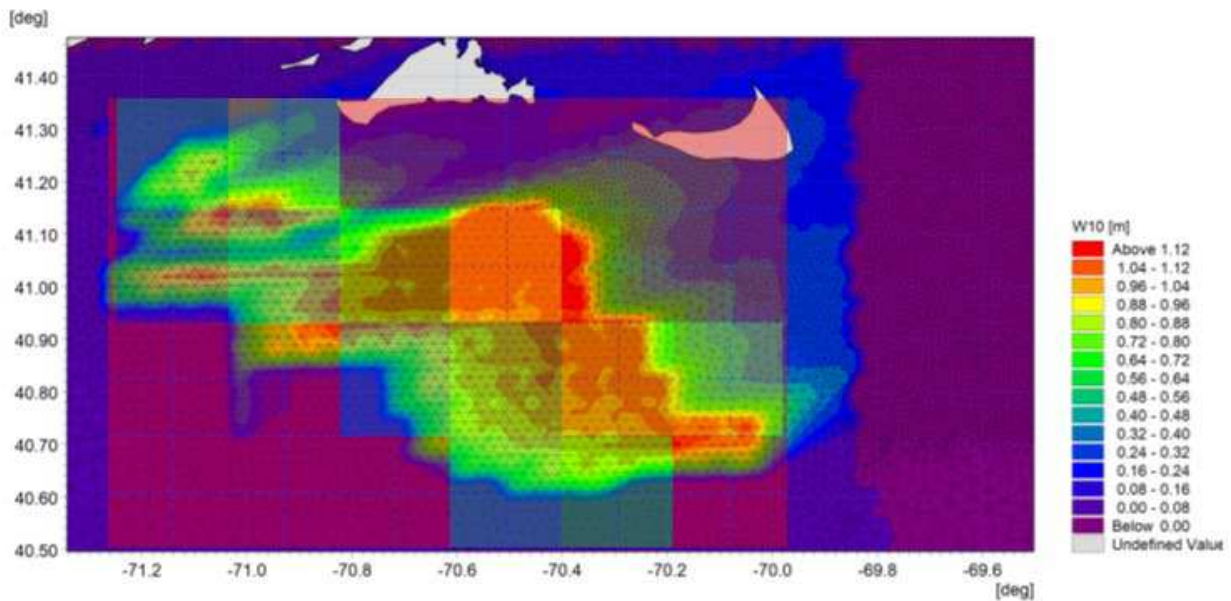


Figure 4.17. Panel Illustrates the Overlaid Footprint of the Wake Deficit Area from PyWake vs. CFSR from Johnson et al. (2021)

The contoured parameter is the 10 m wind velocity. The granular image is from the PyWake 500 m x 500 m grid and the large, shaded rectangles are from the 20 km x 20 km CFSR adjusted grid. In the adjusted CFSR grid the velocity deficit is assumed uniform within each of the large rectangles, while the larger granularity in the PyWake grid resolves each turbine and wake. The PyWake influence area can extend beyond the windfarm.

It can be seen in **Figure 4.17**. Panel Illustrates the Overlaid Footprint of the Wake Deficit Area from PyWake vs. CFSR from Johnson et al. (2021) that the former study (Johnson et al., 2021) was significantly more conservative due to the spatial description than the present study. This is further illustrated by the comparison shown in **Figure 4.18**, where the reduction of the wind speed is shown as a function of the undisturbed CFSR wind speed. The positive corrections observed in the Frandsen model were due to the interpolation in the coarse grid. This effect is not present in the Pywake methodology.

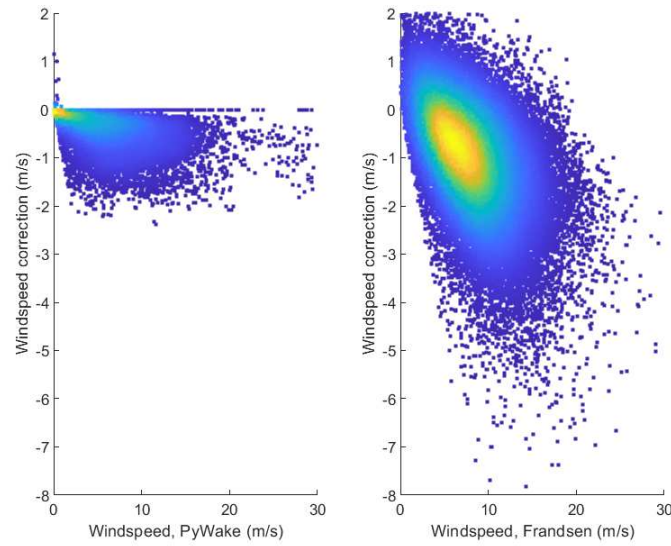


Figure 4.18. PyWake Wind Field Modification Compared to 1st Generation Wind Wake Model Used in Johnson et al. (2021) as a Function of CFSR Undisturbed Wind Speed at 10 m Height

The WEA is the MA-RI OSW farm development to allow for 1 to 1 comparison using a central point in the farm. The scale is the same for both plots. Each point is a time-step and where the color changes from purple to yellow indicates an increasingly higher density of points.

When the PyWake model is applied in the HDM the wind wake file must be aligned with the different spacing of the WTG and HDM elements as compared to the 500 m by 500 m PyWake grid spacing, as illustrated in **Figure 4.19**.

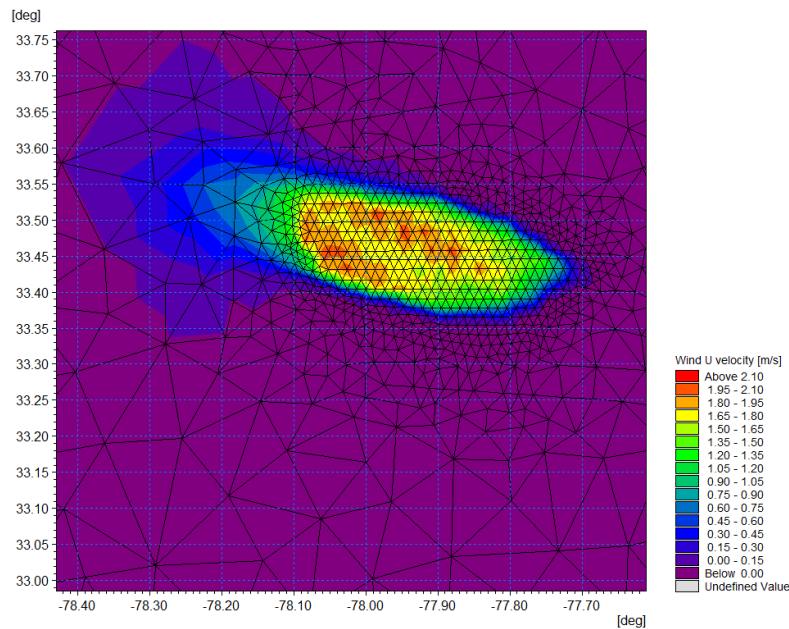


Figure 4.19. PyWake Wind Field Difference File Modified to the HDM Grid Spacing

The panel shows modification of the eastward wind velocity (U). The WEA illustrated is the NC-SC OSW farm development.

Figure 4.20 shows the baseline CFSR wind field with no wind wake and the applied forcing from the PyWake model for the 15 MW full build-out scenario (Scenario 5).

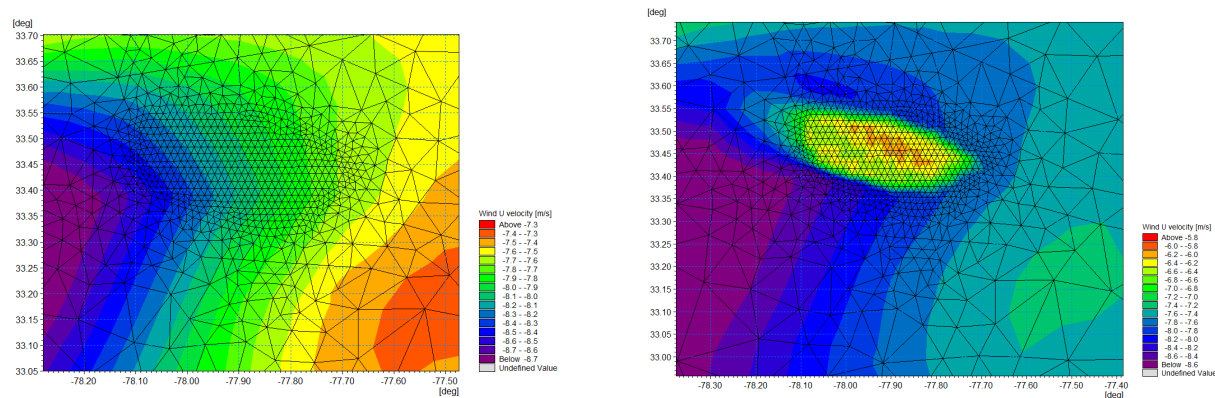


Figure 4.20. Baseline CFSR Wind Field (left) and the Modified Forcing File (right) for the 15 MW Full Build-Out (Scenario 5)

The panels show the eastward wind velocity (U) and the computational mesh applied. The WEA illustrated is the NC-SC OSW farm development.

The above figures show an improvement of the wind-wake loss modeling compared to Johnson et al., 2021.

4.3.4.2 Comparison of PyWake to Golbazi, Archer & Alessandrini, 2022

According to Golbazi et al. (2022) there have been no high-resolution modeling studies of high-capacity WTGs (with hub heights above 100 m and power extraction ratings of greater than 10 MW). To fill this gap, they produced a paper where they used a wind wake model embedded in the WRF model (Skamarock et al., 2021), to understand several aspects of the impact of the WTGs at hub height and at the sea surface. The WRF wind wake model parameterized the wind farm using an elevated sink of momentum and kinetic energy (a so-called actuator-disk approach) and an elevated source of turbulent kinetic energy (TKE) (Fitch et al., 2013 and Fitch et al., 2012). The WTG size reported detail was the DTU 10 MW power rated WTG (Bak et al., 2013) with a hub height of 119 m and a rotor diameter of 178 m. Their WRF model used an outer 4 km grid and 1.33 km nesting around the windfarms. This gives 1 WTG per grid point.

Shown in **Figure 4.21** are the average 10 m wind speed deficits in the NY Bight area over 4 summer months (May – August 2018) from the Scenario 4: 12 MW full build out simulation. In their study, Golbazi et al. (2022) estimated the 10 m wind mean speed deficit for the WEAs in the same area with a configuration resembling the configuration used in this study. As a qualitative comparison, the 0.5 ms^{-1} contour from their study is indicated. It is expected that the WRF model smooths the results more than the more granular PyWake model does. In addition, the Golbazi et al. (2022) results are for a slightly smaller WTG thus a direct comparison is not possible. However, considering that the two methods are very different and independent, we still see very similar behavior and impacts from the wakes.

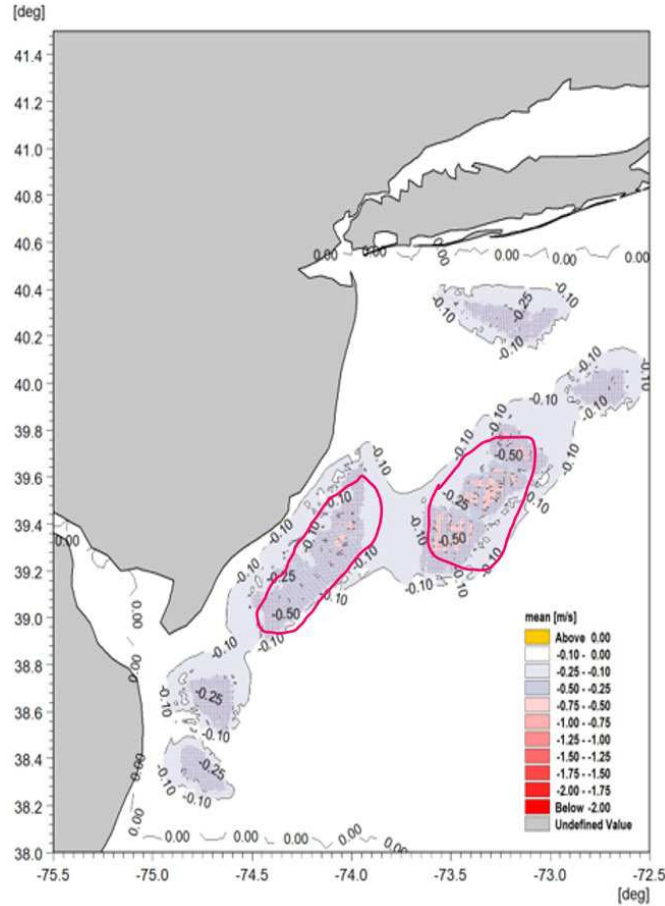


Figure 4.21. PyWake Wind Speed Changes Due to the 12 MW WTG Wind Farms

Averaged over 3 summer months (1 June-31 August 2018) at the surface. The red contours indicate the approximate locations of the Golbazi et al. (2022) 0.5 m/s contour

Finally, a seasonal analysis was performed to understand the 95th percentile non-exceedance probability of the difference between Scenario 5: 15 MW Full Build-out and Baseline. **Figure 4.22** through **Figure 4.25** show the seasonal average changes for winter (January-February-March), spring (April-May-June), summer (July-August-September) and fall (October-November-December). The largest changes can be seen in the Mid-Atlantic Bight in the fall and winter seasons. Additional plots similar to these are contained in Appendix A for Scenarios 2, 3 and 4.

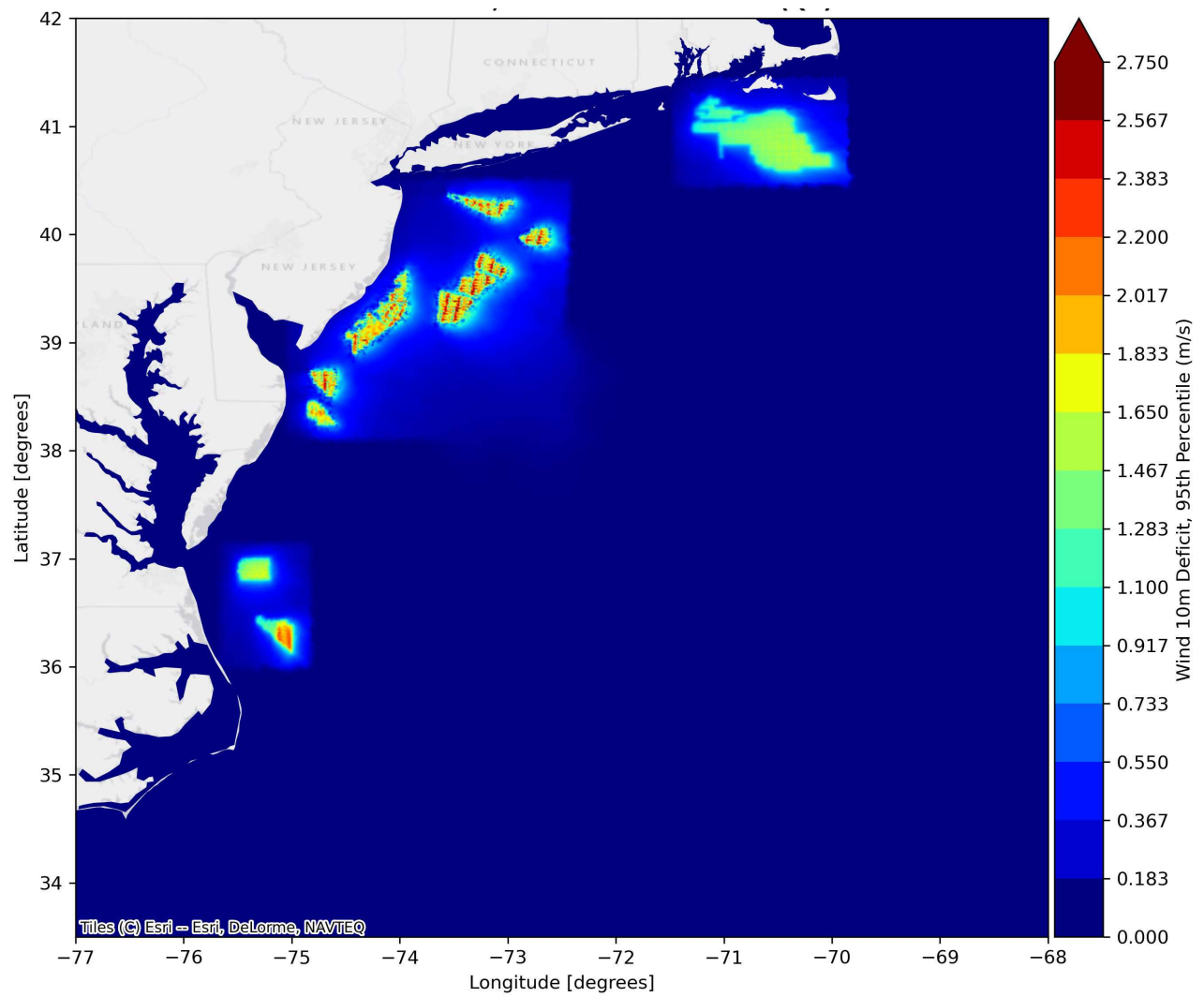


Figure 4.22. Difference in Wind Speed at 10 m Elevation 95th Percentile Non-Exceedance Probability, Scenario 5: 15 MW Full Build-Out - Baseline
 Winter, January- February-March 2017

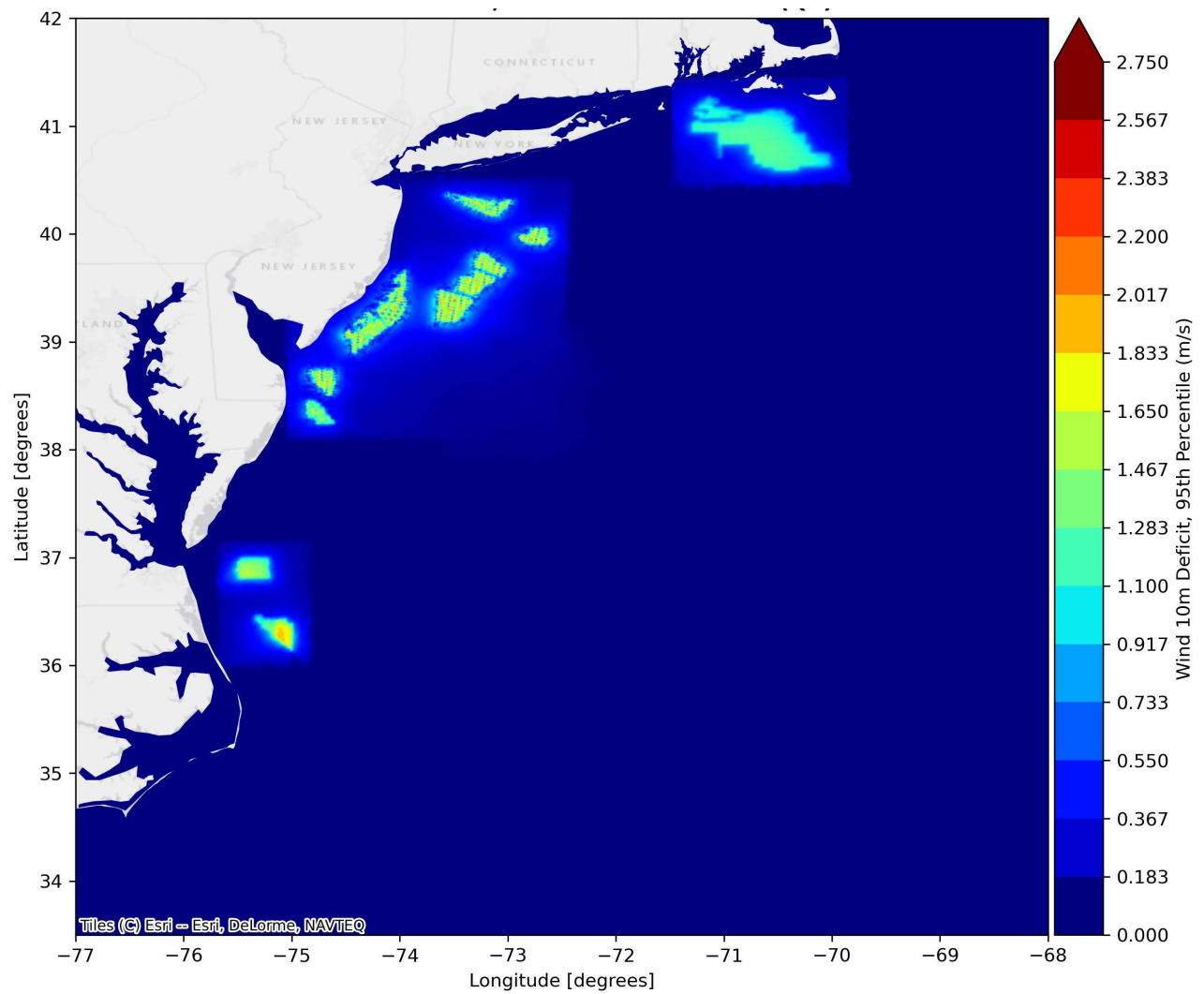


Figure 4.23. Difference in Wind Speed at 10 m Elevation 95th Percentile Non-Exceedance Probability, Scenario 5: 15 MW Full Build-Out - Baseline
 Spring, April-May-June 2017

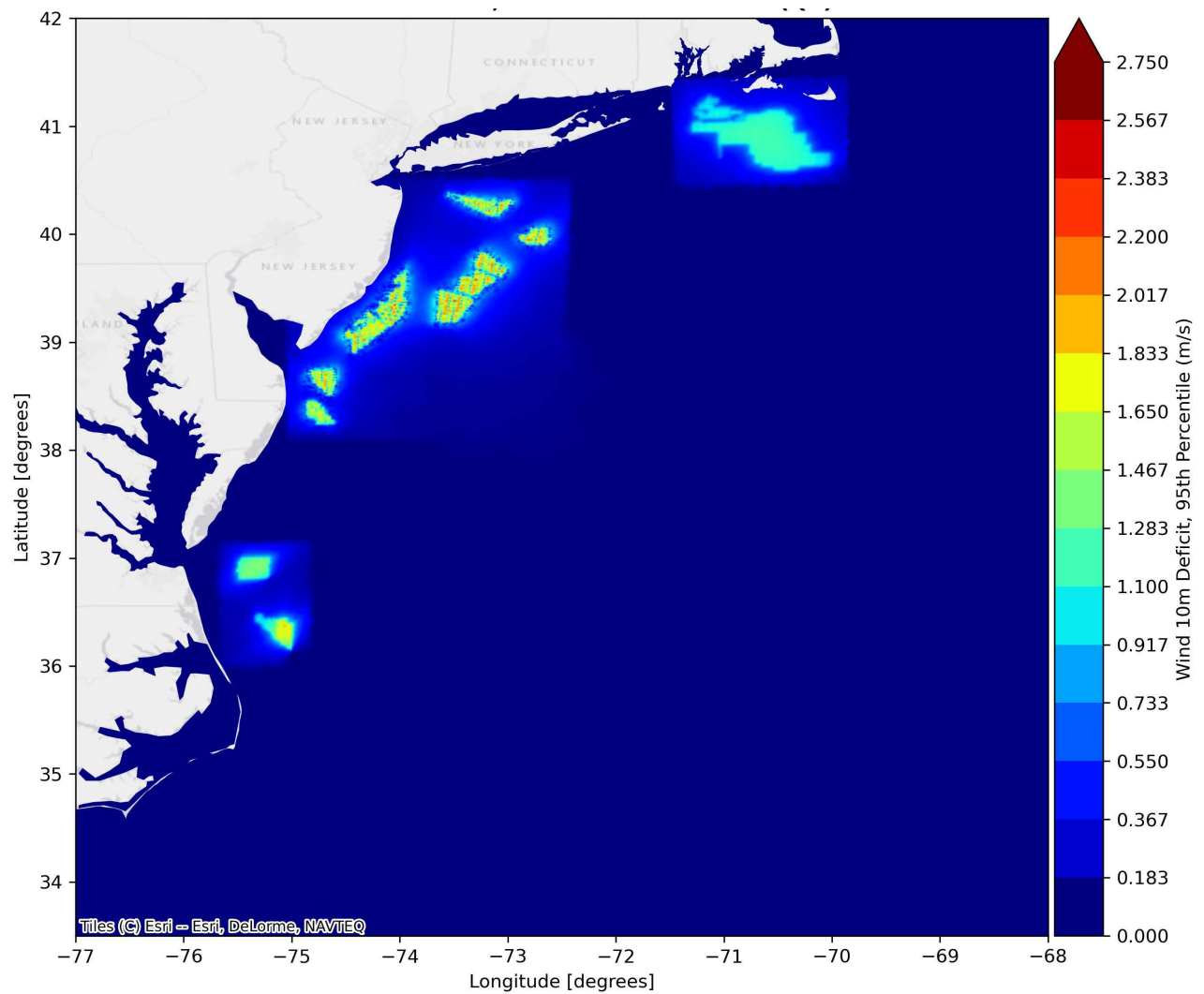


Figure 4.24. Difference in Wind Speed at 10 m Elevation 95th Percentile Non-Exceedance Probability, Scenario 5: 15 MW Full Build-Out - Baseline
 Summer, July-August-September 2017

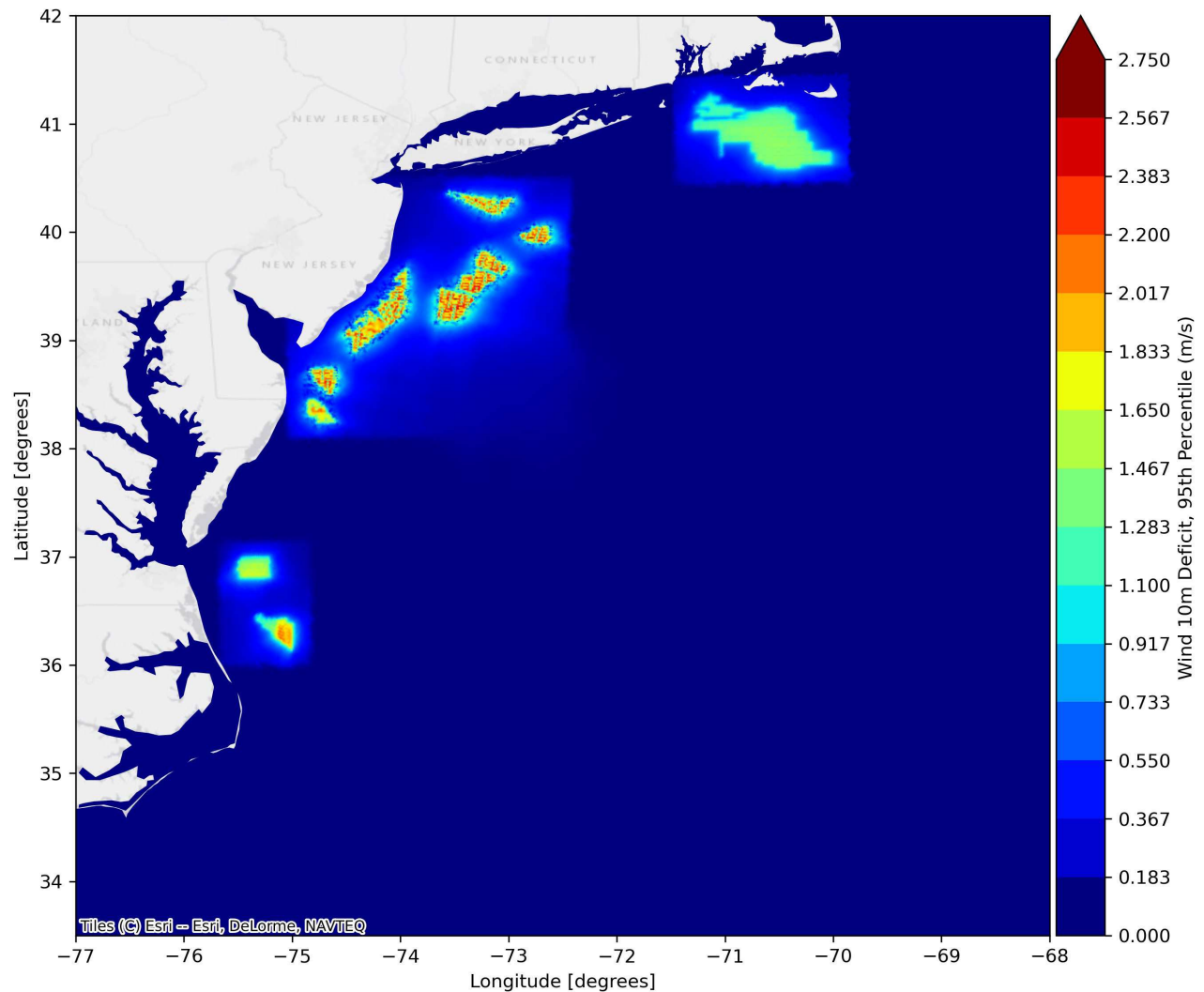


Figure 4.25. Difference in Wind Speed at 10 m Elevation 95th Percentile Non-Exceedance probability, Scenario 5: 15 MW Full Build-Out - Baseline
Fall, October-November-December 2017

4.3.5 PyWake Conclusions

The application of the PyWake model in this study was decided due to:

1. The improved formulation of the wake loss on an OSW farm scale and at a multi-OSW farm scale,
2. The improved spatial resolution afforded by the model, and
3. The acceptance of and investment in the constant improvement of the model by the wind energy industry.

When comparing to previous study by Johnson et al. (2021) and to the results presented by Golbazi et al. (2022), PyWake appears to be an improvement over the former and seemingly provides equivalent results to the latter.

5 Hydrodynamic Model Baseline vs. Scenario Results

5.1 Overview

In **Section 3.3**, the baseline hydrodynamic model output parameters were shown to compare well with empirical observations in the OSW locations. The following sections are a compilation of the effects of the OSW scenarios on the:

- Current fields;
- Particle tracking;
- Waves;
- Bed shear stress; and
- Temperature stratification.

Please note that this report highlights oceanic modeling results with respect to many of the scenarios. However, it was deemed unnecessary to present every scenario with respect to the oceanic parameters as the main focus of this report is on the effects on the distribution of larvae. Selected results for differences between baseline, Scenario 4: 12 MW full build-out, Scenario 5: 15 MW Full Build-out and, for the currents, a sensitivity simulation where the effects of PyWake were doubled for Scenario 5: 15 MW Full Build-out. Results regarding the effects of the OSW developments on waves, temperature and bed shear stress are also reported for Scenario 5: 15 MW Full Build-out.

5.2 Changes in Current Fields

5.2.1 Relative Weighting of Monopile Drag vs. Wind Wake Losses

There are two sinks for energy in the HDM, subsea drag due to the monopile foundations and the losses due to the energy extraction for the WTG at hub height and transferred down to the sea surface. Both effectively reduce the current compared to the baseline conditions without any OSW farm developments. The relative weighting of the two energy sinks is illustrated in **Figure 5.1** showing a time series of change in current speed from a central location in an OSW. It can be seen that the change is fluctuating due to the complex interaction between the drag or surface stress reductions and the surface currents. Positive changes occur, for example, when wind and currents are opposing, resulting in either a smaller reduction in current or flow re-distributions.

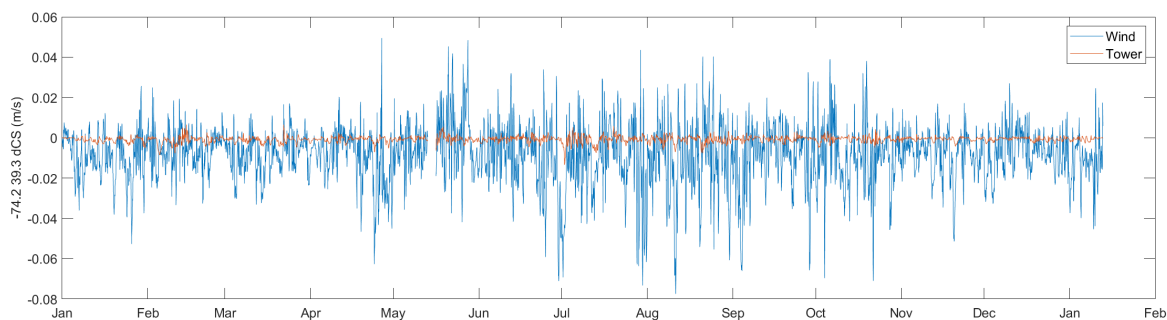


Figure 5.1. Time Series of Change in Surface Current Speed in the MA-RI WEA for 15 MW Full Build-out (Scenario 5) Due to Wind Wake Only and Monopile Foundation Drag Only
Change due to Wind Wakes only (blue) and change due to Monopile Foundations only (brown).

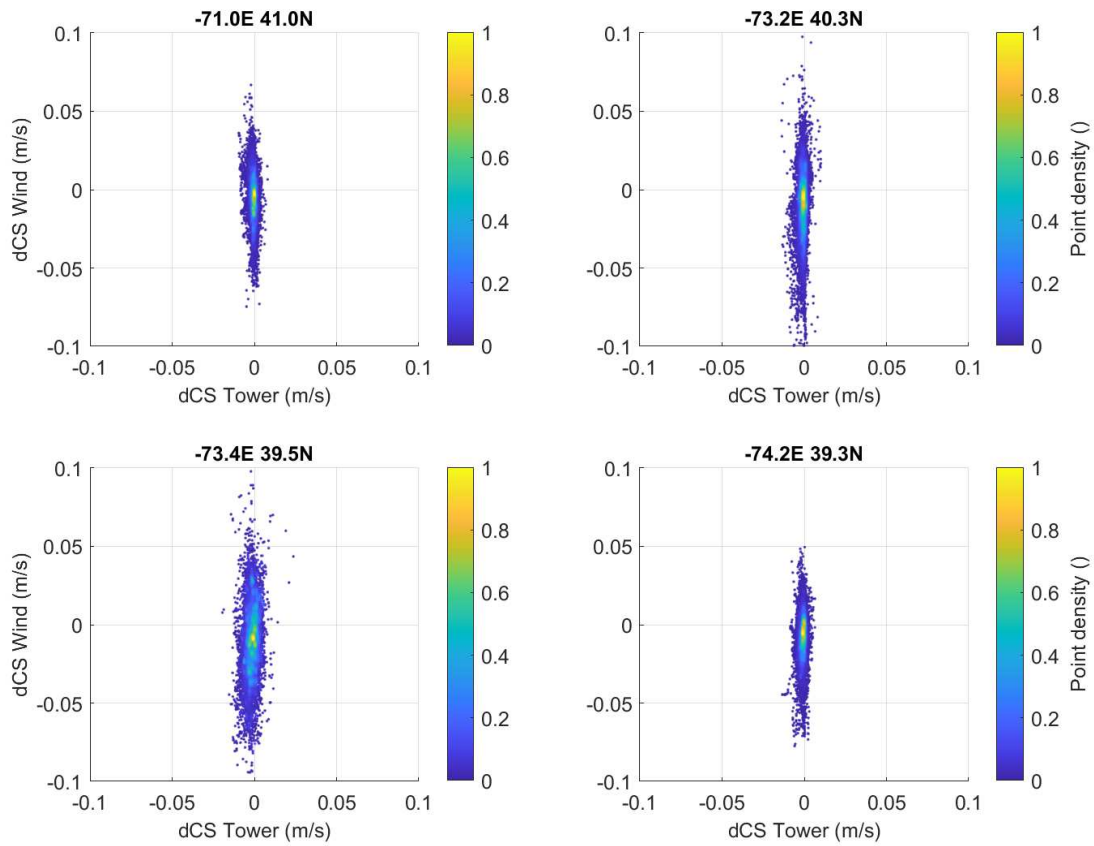


Figure 5.2. Change in Surface Currents (dCS) Due to WTG Wakes (Wind) and WTG Foundations (Tower)

At four representative locations in MA-RI, NY Bight East, NY Bight South, and NJ hourly during 2017. Contouring represents density of points

It can be seen in **Figure 5.1** that the monopile foundation drag is significantly less effective as an energy sink when compared to the wind wake loss current speed reduction for the 15 MW Full Build-out (Scenario 5) vs. baseline. In **Figure 5.2** are shown the same parameters for 4 representative locations.

Table 5.1 shows the change in surface current speed mean and standard deviation from two locations for the year 2017. We conclude that for the 15 MW Full Build-out scenario that the effect on the surface currents of wind wakes is in the order of 9 to 12 times larger than the effect of the monopile foundation drag alone.

Table 5.1. Surface Current Changes Due to 15 MW Full Build-Out (Scenario 5): Wind Wakes Only and Monopile Foundation Drag Only

Surface Current Changes (mm/s)	MA-RI	NY Bight (North)	NY Bight (South)
Mean change due to wind wakes	-4.8	-9.8	-8.8
Mean change due to Monopile Foundations	-0.5	-0.9	-1.4
Standard Deviation of change due to wind wakes	14.9	22.6	58.5

Standard Deviation of change due to Monopile Foundations	1.6	1.9	4.3
--	-----	-----	-----

5.2.2 Sensitivity to PyWake

The HDM employed was a three-dimensional model, as described in previous sections. To allow for easy comparison, the depth averaged current magnitude was calculated at each grid point and each time step in the Baseline and Scenarios 4 and 5. In addition, a sensitivity analysis was carried out to investigate the effect of doubling the wind wake effect of the 15 MW full build-out scenario in PyWake. This allows the differences in the current patterns to be easily calculated and illustrated. **Figure 5.3** illustrates the 95th percentile non-exceedance probability depth averaged current magnitude in the study area over the year 2017. Ninety five percent of the time the currents were at this level or below. The following plots (**Figure 5.4** through **Figure 5.10**) show the difference in the current speed magnitude: baseline vs. each of the scenarios. It is noted that in documenting typical effects as single values (e.g. percentage increase in current speed) spatial scales considered in the model are lost. It should be noted that by doubling the effects of PyWake the wind shear stresses at the sea surface are reduced more. While this is a rather dramatic reduction based on the sound theoretical background of PyWake and the meteorological community's understanding of the transfer function from hub height to the sea surface it was deemed a reasonable "stress test" of the model with the ultimate goal of testing the sensitivity of the PyWake wind wake loss model on the distribution of larvae.

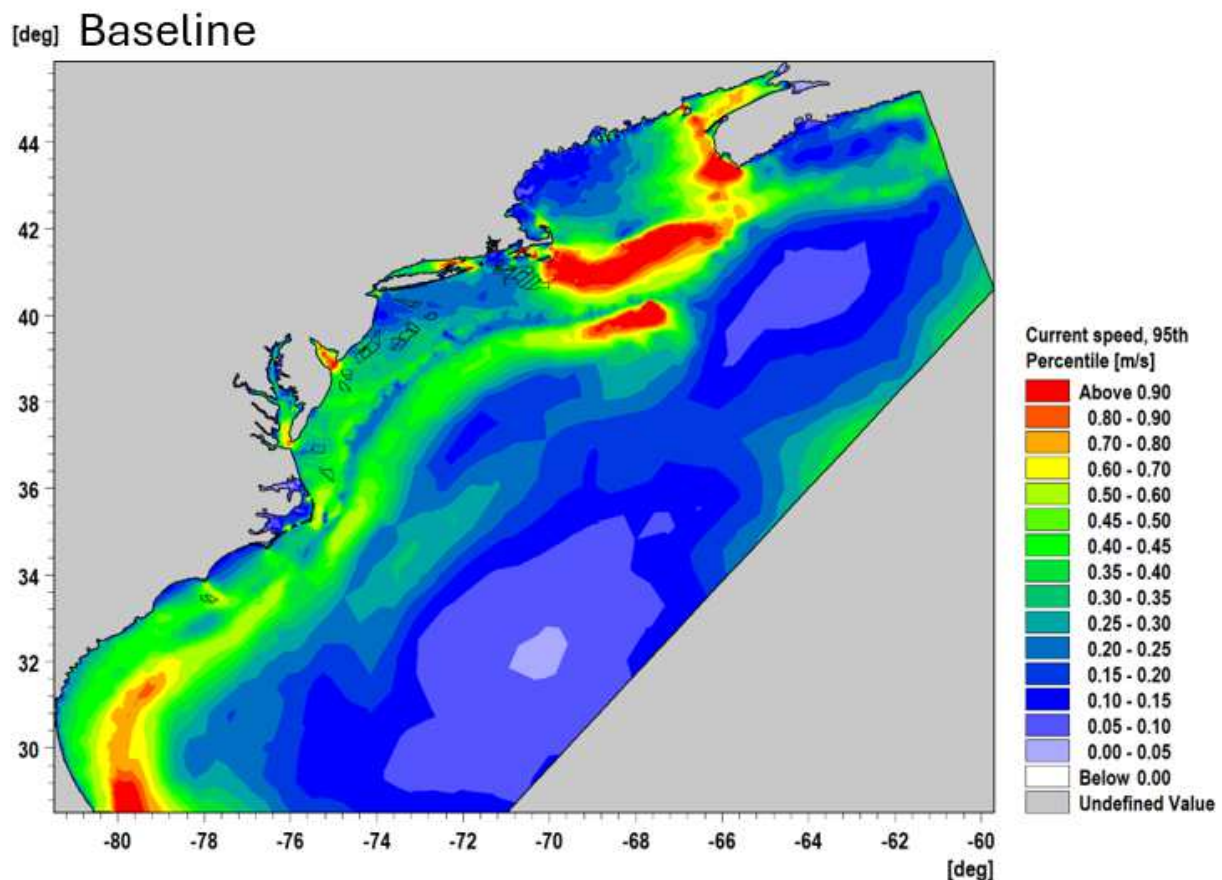


Figure 5.3. 95th Percentile Non-Exceedance Probability Baseline Depth Averaged Current Speed Differences in Study Area

From inspecting **Figure 5.3**, the 95th percentile non-exceedance probability depth averaged currents in each of the WEAs were as follows:

- MA-RI: varies from 0.60 to 0.70 m/s on the Eastern edge of the WEAs to 0.2 to 0.25 m/s on the Western edge of the WEAs
- NY Bight / MD-DE: varies from 0.35 to 0.4 m/s off the mouth of Delaware Bay to 0.1 to 0.15 m/s in a majority of the WEAs
- VA-NC: varies from 0.25 to 0.3 m/s in the North to 0.45 to 0.5 m/s in the South
- NC-SC: varies from 0.45 to 0.6 m/s

Figure 5.4 through **Figure 5.6** are the 95th percentile non-exceedance probability difference of:

- Scenario 4: 12 MW Full Build-out (2017) and Baseline depth averaged currents in the study area.
- Scenario 5: 15 MW Full Build-out (2017) and Baseline depth averaged currents in the study area.
- Scenario 6: 15 MW Full Build-out (2017) where the effects of PyWake are doubled and Baseline.

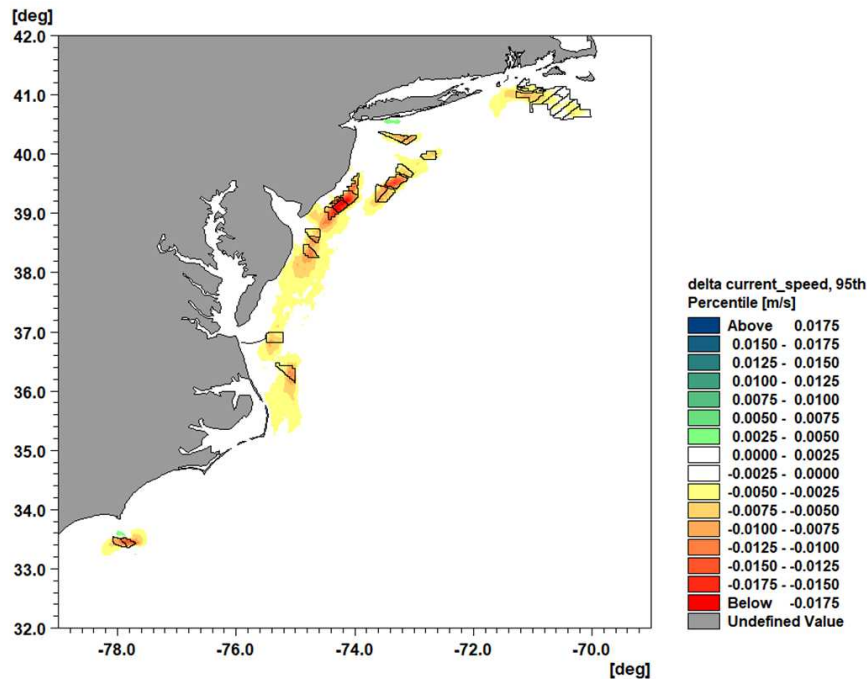


Figure 5.4. 95th Percentile Non-Exceedance Probability (Scenario 4 – Baseline) Depth Averaged Current Speed Differences in Study Area

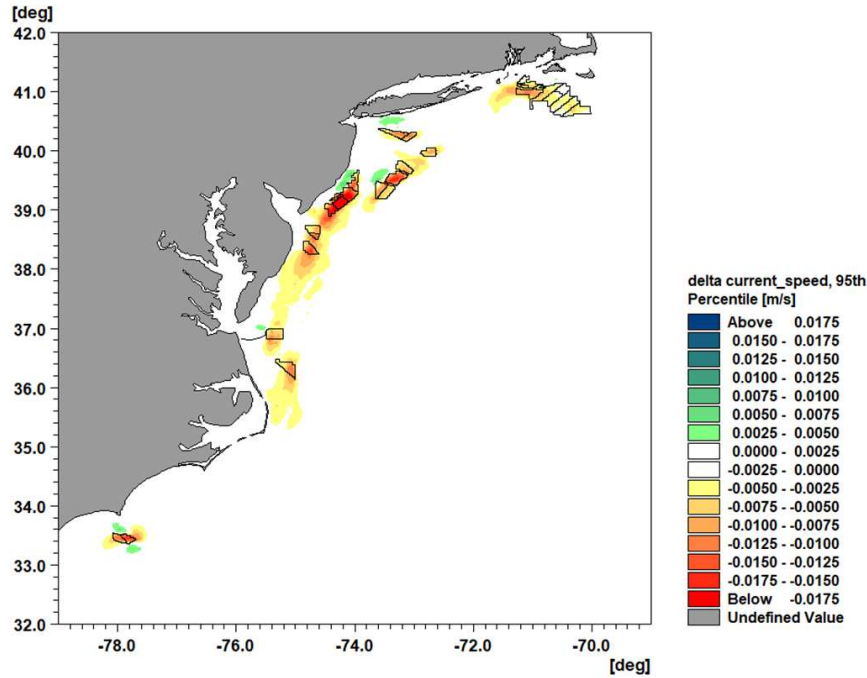


Figure 5.5. 95th Percentile Non-Exceedance Probability (Scenario 5 – Baseline) Depth Averaged Current Speed Differences in Study Area

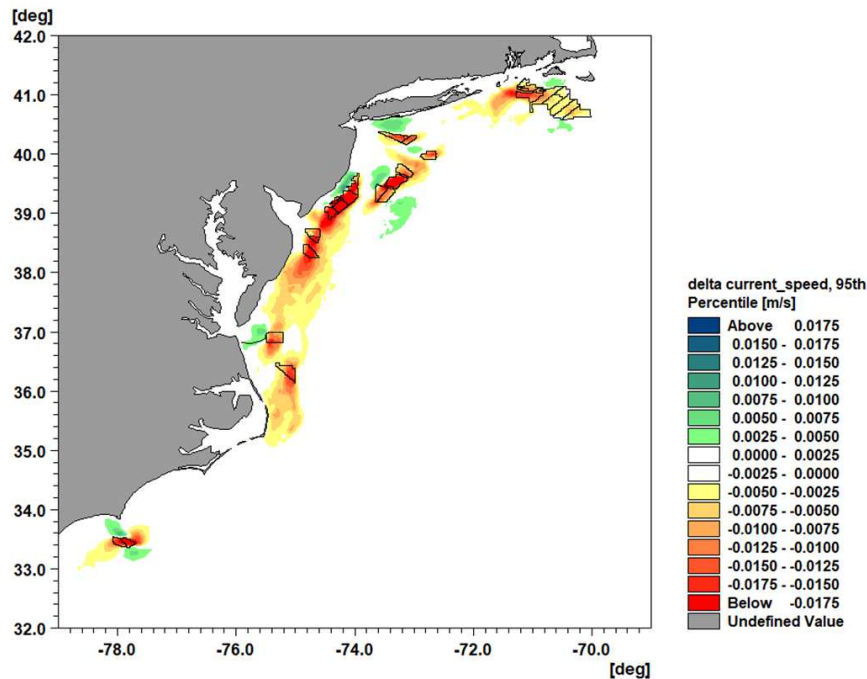


Figure 5.6. 95th Percentile Non-Exceedance Probability (Sensitivity: 15 MW Full Build-Out PyWake doubled – Baseline) Depth Averaged Current Speed Differences in Study Area

The following WEA specific zoomed-in plots are the 95th percentile non-exceedance probability difference of:

- Scenario 4: 12 MW Full Build-out (2017) and Baseline depth averaged currents in the study area.
- Scenario 5: 15 MW Full Build-out (2017) and Baseline depth averaged currents in the study area.
- Scenario 6: 15 MW Full Build-out (2017) where the effects of PyWake are doubled and Baseline.

The impact on the current speeds in the 95th percentile non-exceedance probability plots (**Figure 5.7** through **Figure 5.10**) on the observed maximum differences in current speeds were progressively larger from the 12 MW full build-out to the 15 MW full build-out to finally the largest differences in depth averaged current speeds in the 15 MW full build-out where the PyWake effect was doubled. This result is as expected since each successive scenario was essentially increasing the PyWake wind wake deficit. A broad summary is presented below in **Table 5.2** for each WEA of the maximum changes (minus and plus) due to both full build-out scenarios (4 & 5) and the sensitivity analysis (doubling the effect of PyWake in the 15 MW full build-out scenario).

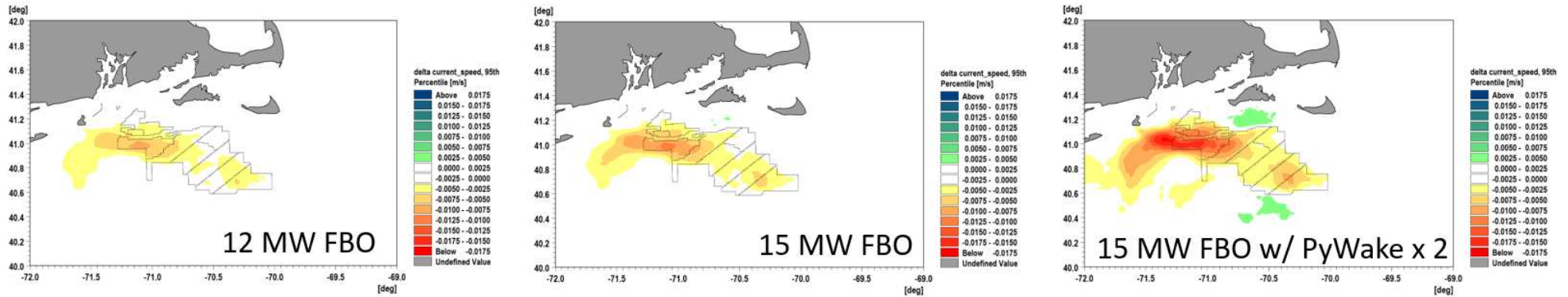


Figure 5.7. 95th Percentile Non-Exceedance Probability Depth Averaged Current Speed Differences in MA-RI Area for Scenarios 4, 5, and the Sensitivity Analysis (FBO - Full Build-Out)
Note that color scales are fixed to enable intercomparison between panels.

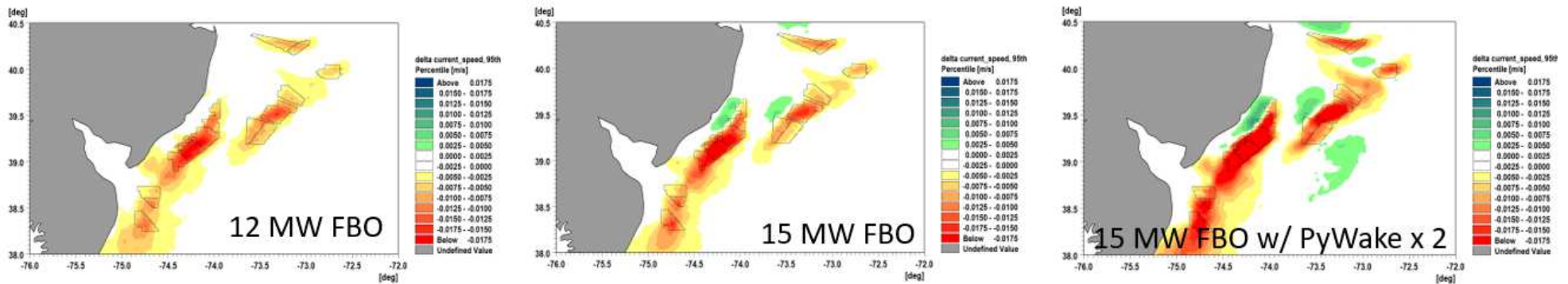


Figure 5.8. 95th Percentile Non-Exceedance Probability Depth Average Current Speed Differences in the NY Bight and MD-DE Area for Scenario 4, 5, and Sensitivity Analysis (FBO - Full Build-Out)
Note that color scales are fixed to enable intercomparison between panels.

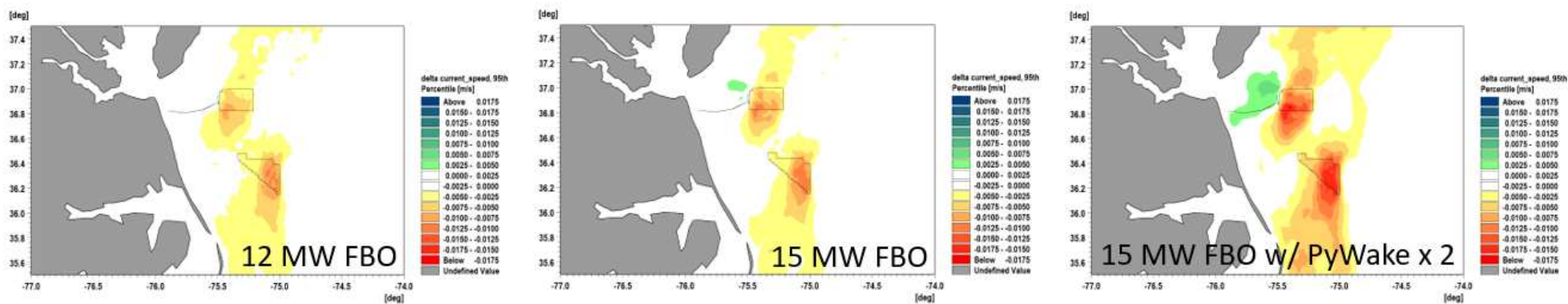


Figure 5.9. 95th Percentile Non-Exceedance Probability Depth Averaged Current Speed Differences in the VA-NC Area for Scenario 4, 5, and the Sensitivity Analysis (FBO – Full Build-Out)

Note that color scales are fixed to enable intercomparison between panels.

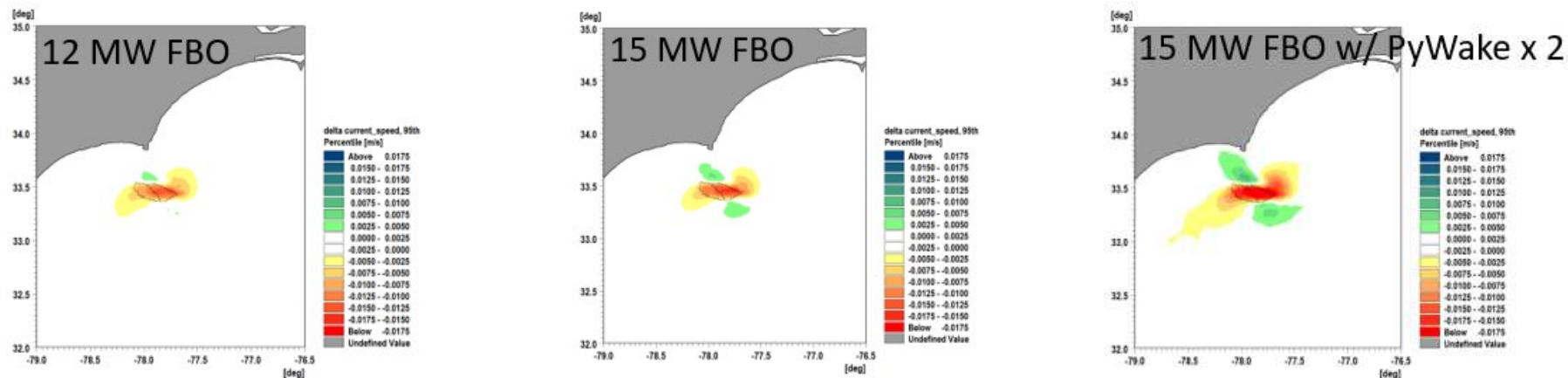


Figure 5.10. 95th Percentile Non-Exceedance Probability Depth Averaged Current Speed Differences in the NC-SC Area for Scenario 4, 5, and the Sensitivity Analysis (FBO – Full Build-Out)

Note that color scales are fixed to enable intercomparison between panels.

Table 5.2. Summary of Broad Maximum and Minimum Changes from Baseline of the 95th Percentile Non-Exceedance Probability Depth Averaged Current Speeds by Scenario and WEA

WEA	Baseline Depth Averaged Current Speed Range (m/s)	12 MW Full Build-out (Scenario 4) Maximum/ Minimum change (m/s) (%)	15 MW Full Build-out (Scenario 5) Maximum/ Minimum change (m/s) (%)	15 MW Full Build-out Effect of PyWake Doubled Maximum/ Minimum change (m/s) (%)
MA-RI	0.60 to 0.70 m/s on the Eastern edge of the WEA 0.2 to 0.25 m/s on the Western edge of the WEA	-0.0075 to -0.005 on the Western edge of the WEA ~-2.8% / + 0%	-0.0125 to -0.01 on the Western edge of the WEA Some minimal increased current speeds areas can be observed on the north outside of the WEA with a magnitude of 0.0025 to 0.005 m/s ~-5.0% / ~+1.7%	-0.0015 to -0.0125 on the Western edge of the WEA Some increased current speeds can be observed on the north and south outside of the WEA with a magnitude of 0.0025 to 0.005 m/s ~-6.1% / ~+1.7%
NY Bight / MD-DE	varies from 0.35 to 0.4 m/s off the mouth of Delaware Bay 0.1 to 0.15 m/s in a majority of the WEAs	-0.015 to -0.0125 m/s in the center of the WEAs ~-3.7% / +0%	Below -0.0175 to -0.015 m/s in the center of the WEAs Some increased current speeds can be observed on the northwest outside of the WEAs with a magnitude of 0.005 to 0.0075 m/s ~-4.3% / ~+1.7%	Below -0.0175 m/s in the center of the WEAs Some increased current speeds can be observed on the northwest and South East outside of the WEAs with a magnitude of 0.01 to 0.0125 m/s ~-4.7% / ~+1.7%
VA-NC	varies from 0.25 to 0.3 m/s in the North 0.45 to 0.5 m/s in the South	-0.0125 to -0.01 m/s in the South ~-4.1% / + 0%	-0.0125 to -0.01 m/s in all the WEAs Some increased current speeds can be observed on the west outside of the northern WEAs with a magnitude of 0.0025 to 0.005 m/s ~-4.1% / ~+1.4%	-0.0175 to -0.015 m/s in all the WEAs Some increased current speeds can be observed on the west outside of the northern WEAs with a magnitude of 0.005 to 0.0075 m/s ~-5.9% / ~+2.3%
NC-SC	varies from 0.45 to 0.6 m/s	-0.0125 to -0.01 m/s in the center of the WEAs Some increased current speeds can be observed on the north and south of the WEAs with a magnitude of 0.0025 to 0.005 m/s ~-2.1% / ~+0.7%	Below -0.0175 to -0.015 m/s in the center of the WEAs Some increased current speeds can be observed on the north and south outside of the WEAs with a maximum magnitude of 0.0025 to 0.0075 m/s ~-2.1% / ~+1.0%	Below -0.0175 m/s in the center of the WEAs Some increased current speeds can be observed on the north and south outside of the WEAs with a maximum magnitude of 0.0075 to 0.01 m/s ~-3.3% / ~+1.7%

It should be noted that for the two Scenarios 4 and 5 (12 MW and 15 MW Full Build-out) that the maximum changes to the 95th percentile non-exceedance probability current in any of the WEAs were approximately -5.0% and +1.7%. When considering Scenario 5 where the 15 MW full build-out had the PyWake effect doubled the maximum changes to the 95th percentile non-exceedance probability current in any of the WEAs were approximately -6.1% and +2.3%.

5.3 Particle Tracking

Particle tracking was an objective that was retained in the BOEM RFP. However, the emphasis of the study was rather to simulate three species of larvae as agents in Agent-Based Models (ABM). In order to provide further context to the full ABM simulations, two particle tracking simulations (Scenario 1: Baseline and Scenario 5: 15 MW Full Build-Out) were run to examine at the overall effect of the 15 MW Scenario 5, in relation to the Baseline transport of inert particles. The release locations and the release timing were selected to mimic the same locations and spawning timing of summer flounder since that species had the most extensive range in the model domain.

Table 5.3. Particle Model Parameters

Parameter	Value
Number of Particles Released	29,100
Release Timing	1 September 2017 to 1 April 2018
Release Quantities at Each of the Release Locations	S. Atlantic Bight 1400 particles Mid-Atlantic Bight 7200 particles New Jersey 6624 particles New England 6848 particles Georges Bank 7028 particles
Release Point Depth Below the Water Surface	1 m
Fall Velocity of the Particles	0.3 m/day or 3.86×10^{-6} m/s (20m in 60 days)
Mass of Each Particle	1.0 grams
Number of Particles Retained within the Regional Model Boundaries at the End of the Simulation	23,312
Percentage of particles that settled in the model before the settling period expired	14%

The following **Figure 5.11** shows the release points of the particles. **Figure 5.12** shows the baseline settled particles results. **Figure 5.13** shows the 15 MW Full Build-out scenario settled particles results.

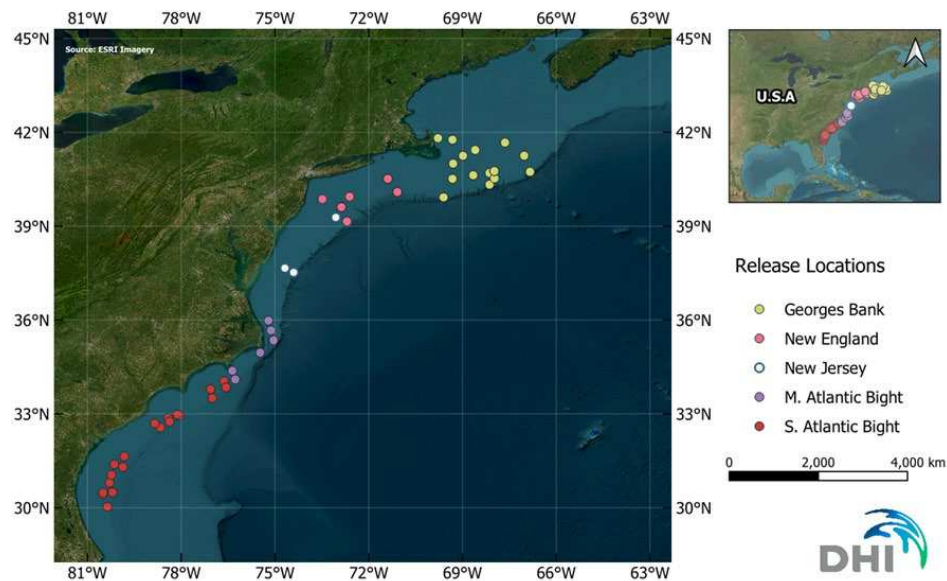


Figure 5.11. Particle Tracking Model Particle Release Points

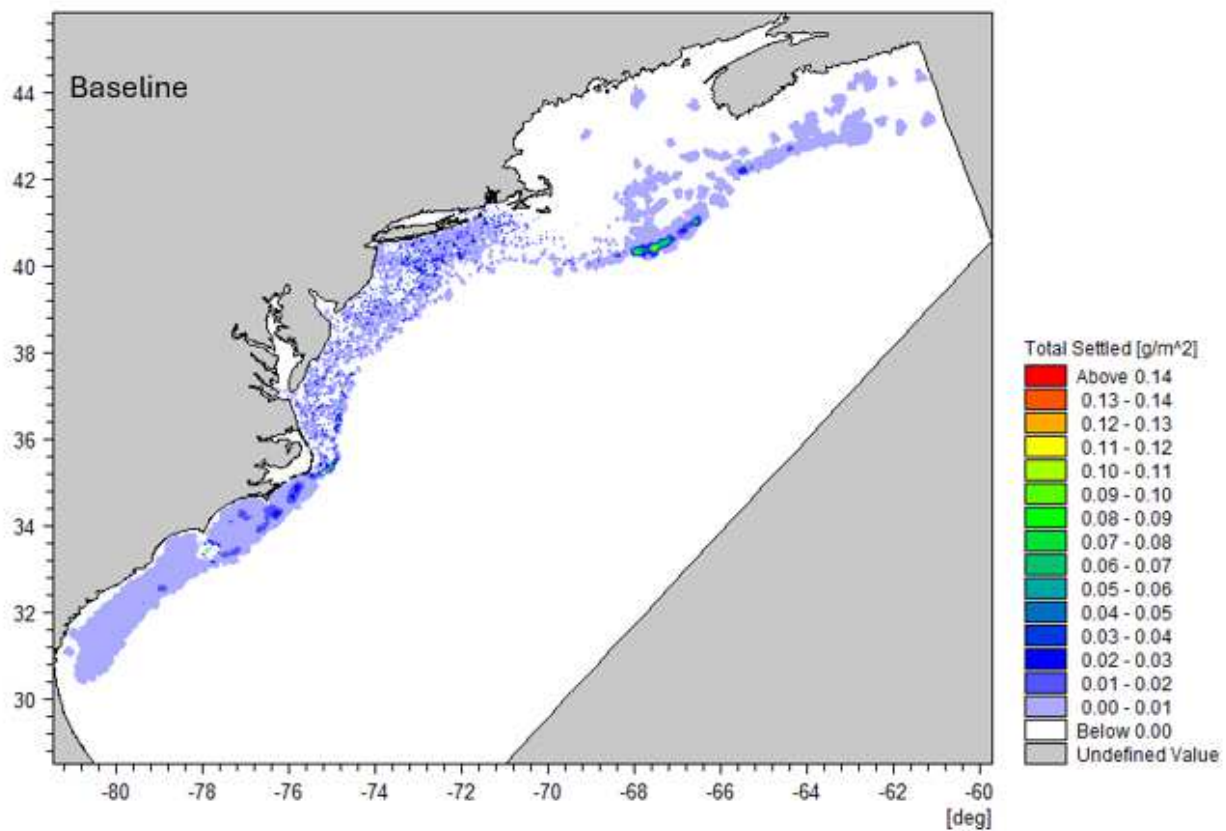


Figure 5.12. Scenario 1: Baseline Settled Particle Tracking Results

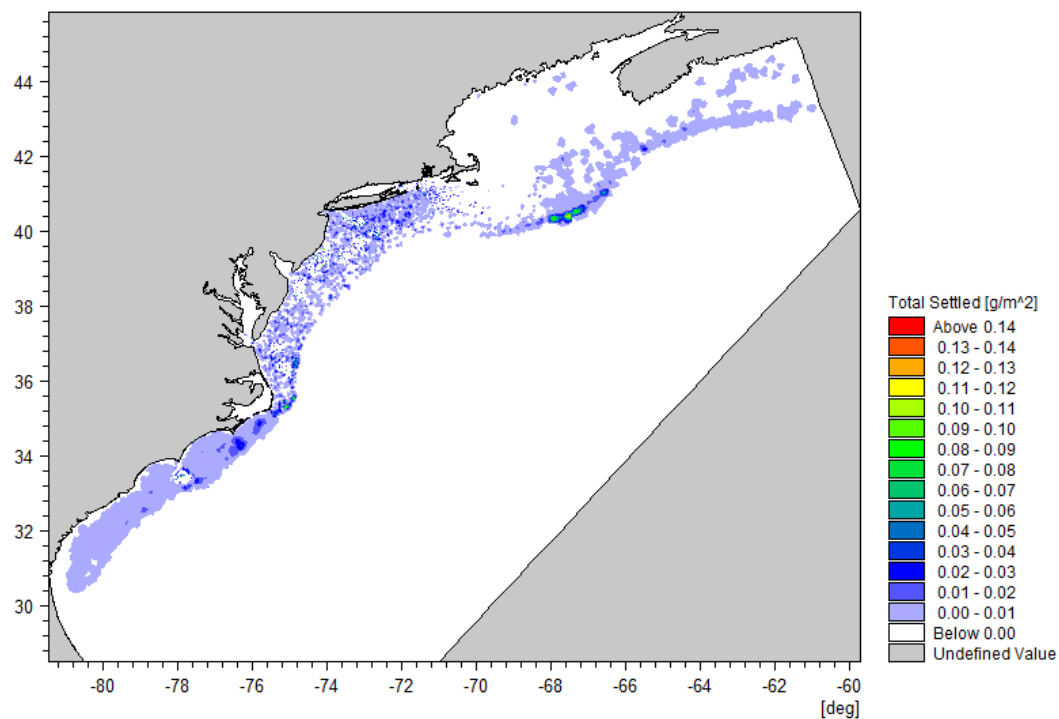


Figure 5.13. Scenario 5: 15 MW Full Build-Out Settled Particle Tracking Results

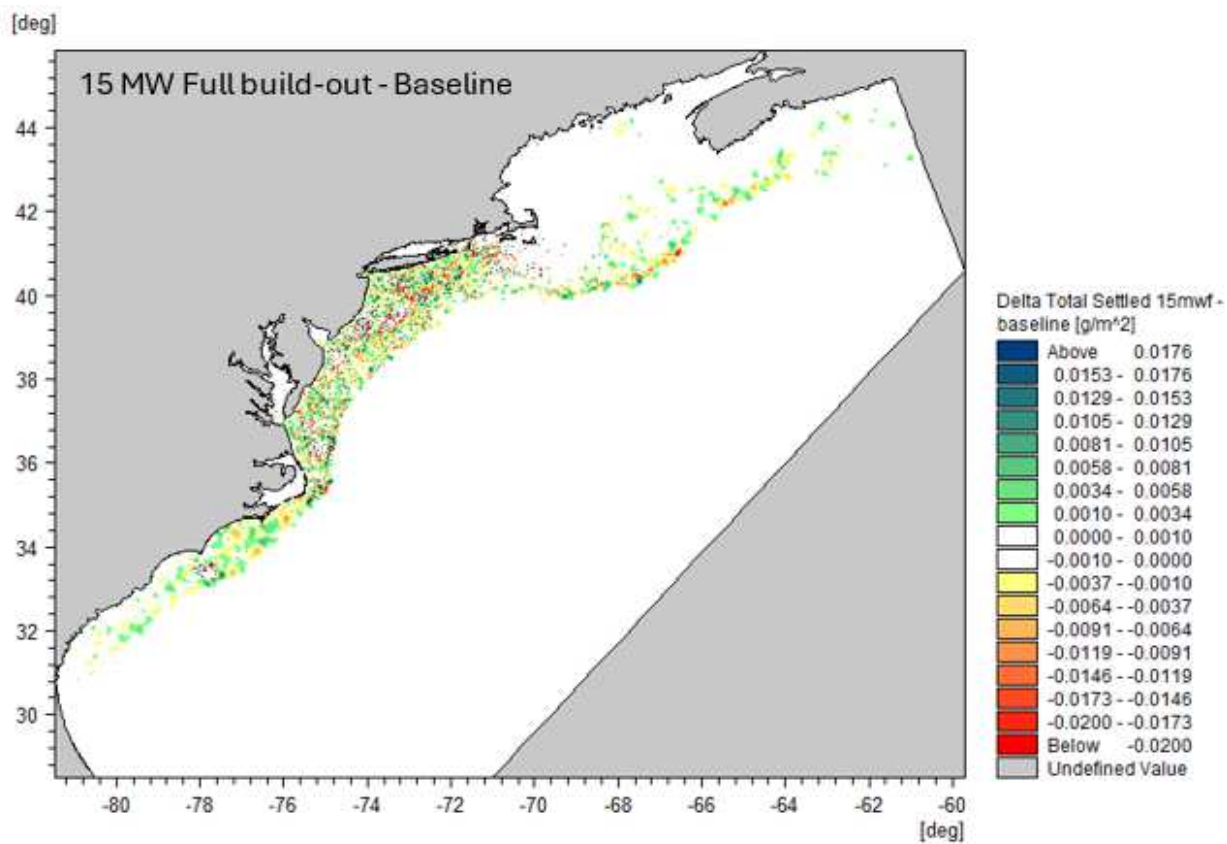


Figure 5.14. Difference (Scenario 5 – Baseline) Settled Particle Tracking Results

When the difference between the baseline and 15 MW Full Build-out results shown in

Figure 5.14 are compared to the summer flounder difference plots in **Section 8.3.3** for the same conditions the results are strikingly different. Passive drifting particles were released in the particle model at the same locations and same times as the ABM summer flounder simulation. The results demonstrate that the behavior of the larvae is important in evaluating the impacts with respect to that species and its behavior. It will be seen in **Section 6.4.4.5** that the Agent Based Model of the summer flounder larvae allows the larvae to move vertically in response to temperature cues as well as seek the coast as the species is noted to do. No further analysis was deemed necessary when these results were compared.

5.4 Effects on Waves

The spectral wave model simulates the growth, decay and transformation of wind-generated waves and swell in offshore and coastal areas. The model is developed by DHI based on the 3rd generation Wave Modeling (WAM) standard and has been applied in numerous high-profiled projects. The model includes the following physical phenomena:

- Wave growth by action of wind;
- Atlantic swell;
- Wave-induced bottom shear stresses;
- Dissipation due to bottom friction;
- Non-linear wave-wave interaction;
- Dissipation due to white-capping;
- Dissipation due to depth-induced wave breaking;
- Refraction and shoaling due to depth variations; and
- Changes in wave transmission due to turbine towers.

The discretization of the governing equation in geographical and spectral space was performed using the cell-centered finite volume method. In the geographical domain, an unstructured mesh technique was used. The time integration was performed using a fractional step approach where a multi-sequence explicit method is applied for the propagation of wave energy.

The application of the wake model modified sea surface wind shear stress thereby affecting the local wave field inside and outside the OSW. The objective of this portion of the study was to calculate the hourly sea-state in the study area for Baseline (Scenario 1) conditions and compare that to Scenario 5: 15 MW full build-out with wind-field wake loss reductions included.

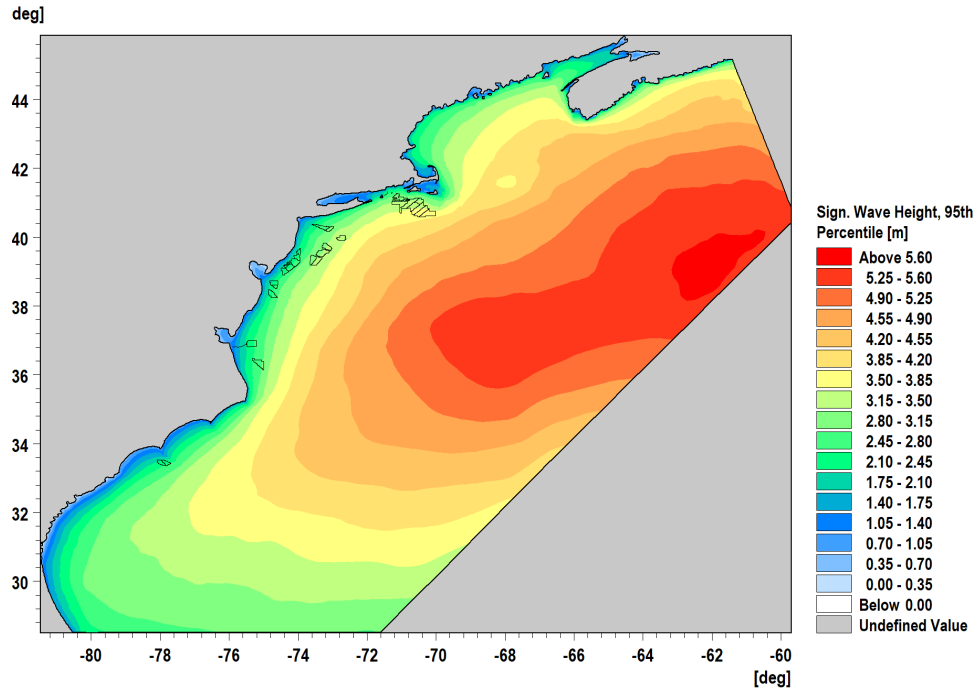


Figure 5.15. Significant Wave Height, H_{m0} 95th Percentile Non-Exceedance Probability Plot for Scenario 1: Baseline

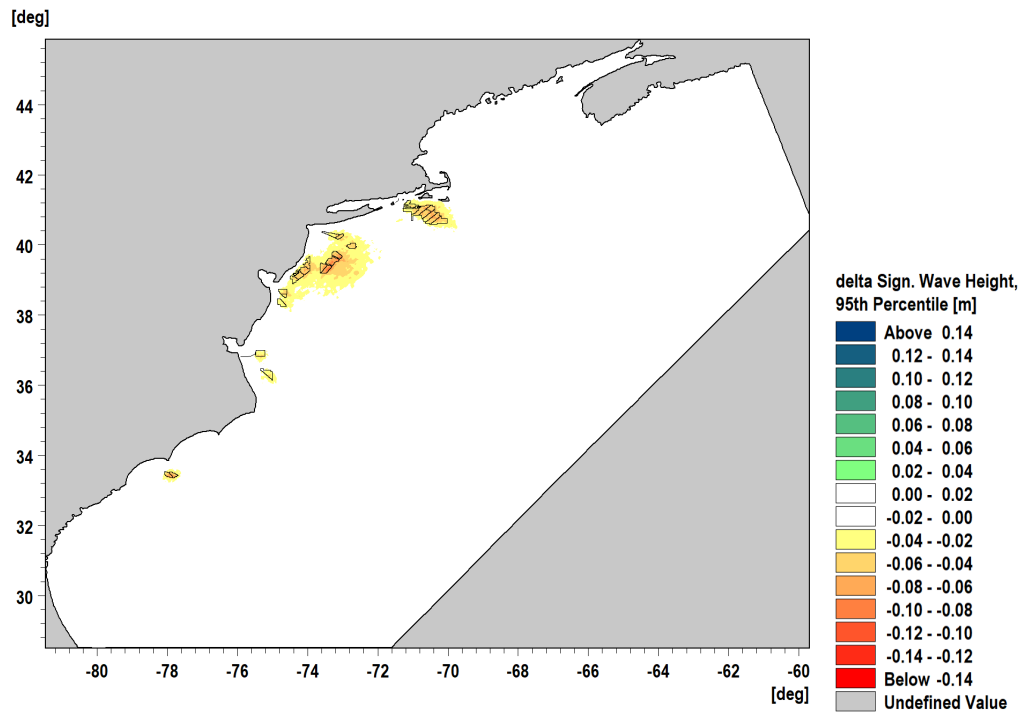


Figure 5.16. Exceedance Difference in H_{m0} for 95th Percentile Non-Exceedance Probability – Full Model Domain

Wave Height Change for Baseline minus 15 MW Full Build-out

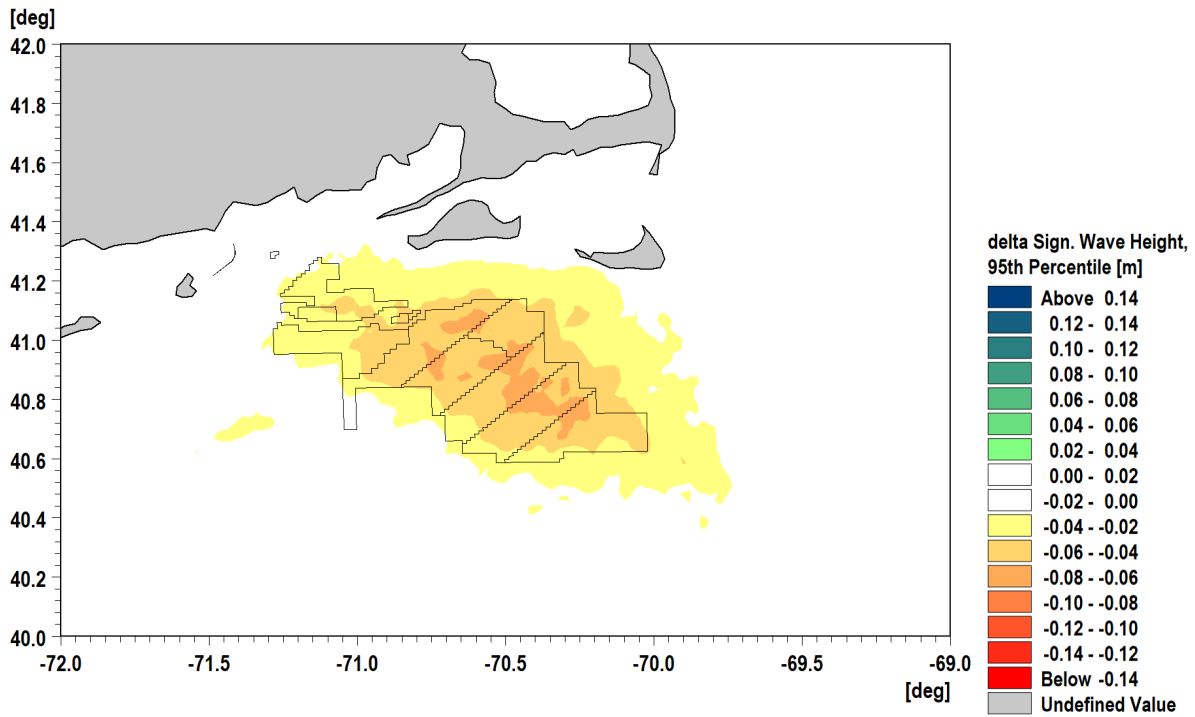


Figure 5.17. 95th Percentile Non-Exceedance Probability H_{m0} Difference – MA-RI Region
Wave Height Change for Baseline minus 15 MW Full Build-out

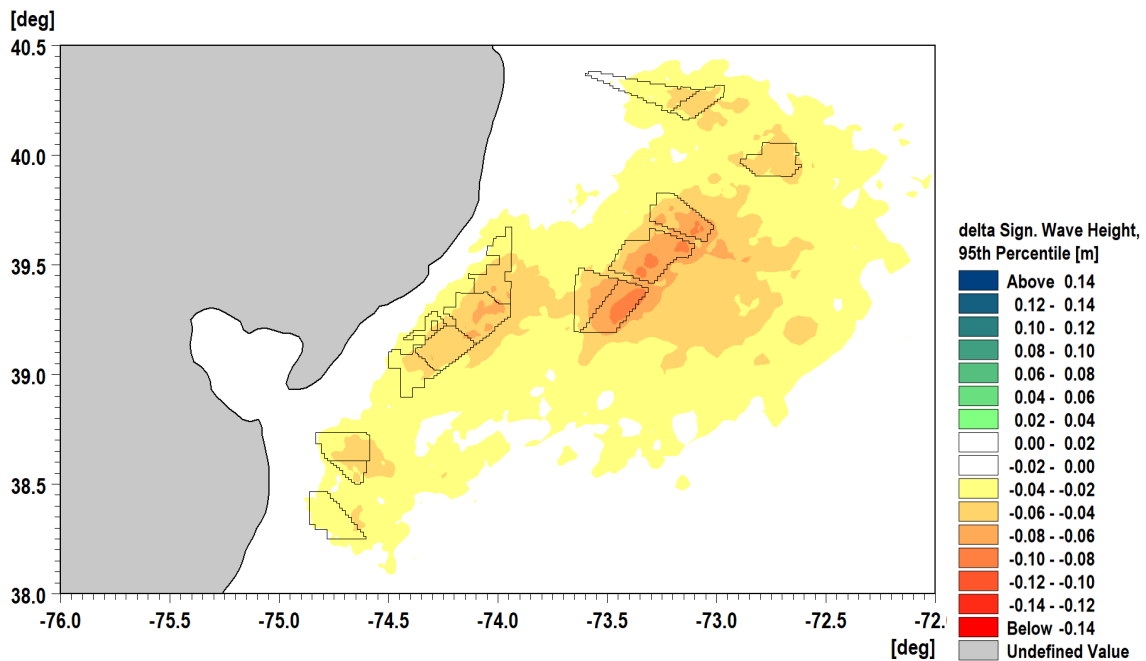


Figure 5.18. 95th Percentile Non-Exceedance Probability H_{m0} Difference – NY Bight and MD-DE Region
Wave Height Change for Baseline minus 15 MW Full Build-out

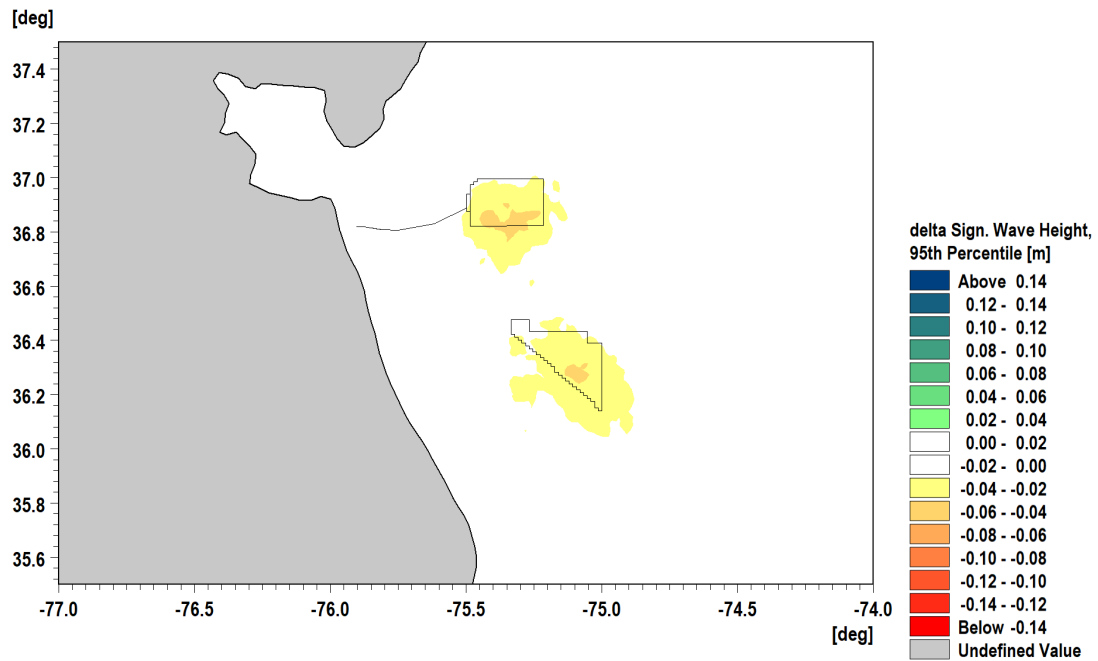


Figure 5.19. 95th Percentile Non-Exceedance Probability H_{m0} Difference – VA-NC Region
 Wave Height Change for Baseline minus 15 MW Full Build-out

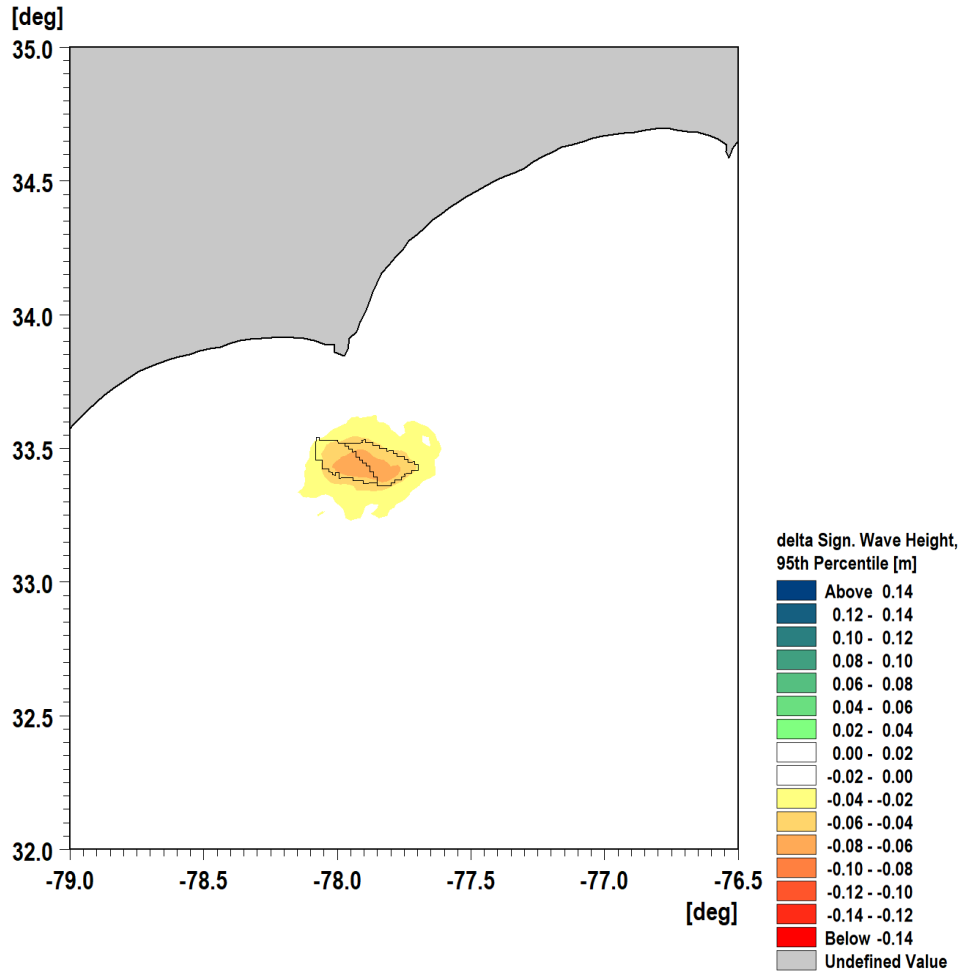


Figure 5.20. 95th Percentile Non-Exceedance Probability H_{m0} Difference – NC-SC Region
Wave Height Change for Baseline minus 15 MW Full Build-out (Scenario 5)

Inspection of the detailed wave results show that the biggest reduction in the 95th percentile non-exceedance probability H_{m0} difference was observed in the NY Bight / MD-DE region. The reduction was on the order of 10 cm for waves that were on the order of 2.5 m H_{m0} or $\sim 4\%$ lower. The wave results are used in bed shear stress analysis and exhibited little influence on sediment mobility changes (see following Section 5.5).

5.5 Combined Effects of Current and Waves on Bed Shear Stress and Sediment Mobility

Another potential impact of OSW developments on coastal and oceanic environmental conditions and habitat is on the bottom shear stress and thereby the potential for sediment transport. Bottom shear stress is driven by two physical phenomena; currents and the orbital motion induced by waves (formulated as wave radiation stress) at the seabed. Therefore, the introduction of multiple structures into the offshore area could:

1. Cause changes in the current speeds through two mechanisms:
 - a. Local acceleration of the currents around the structures

- b. Decrease in overall current due to the introduction of increased energy loss due to the drag losses
- 2. Cause changes in the wave field in and around the OSW farm thereby changing wave orbital velocities and radiation stress

These effects were studied using the HDM and the wave model separately and then combined via superposition of the effects on a time-step-by-time-step basis for the baseline and Scenario 5: 15 MW full build-out cases. Wave-current interaction was not considered in this study. The combination methodology followed Soulsby and Clarke (2005). The following plots show the 95th percentile non-exceedance probability bed shear stress results for currents and waves separately and for combined currents and waves.

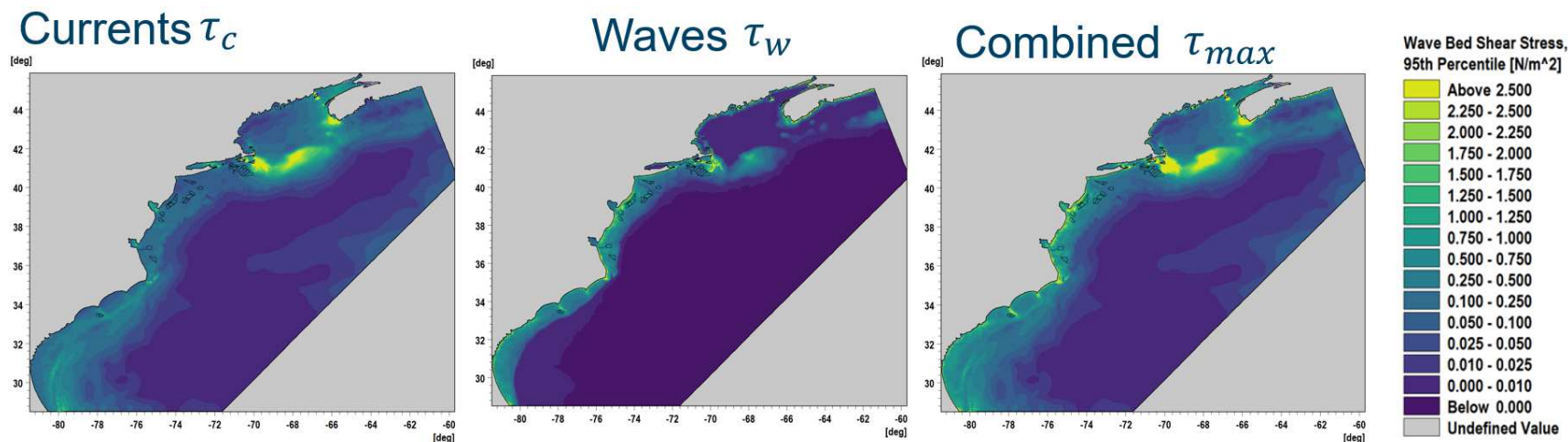


Figure 5.21. 95th Percentile Non-Exceedance Probability Bed Shear Stresses in the Model Domain Scenario 1: Baseline
 LEFT: Current only, MIDDLE: RMS Wave only, RIGHT Current + RMS Wave for time period 1 January 2017 through 31 December 2017

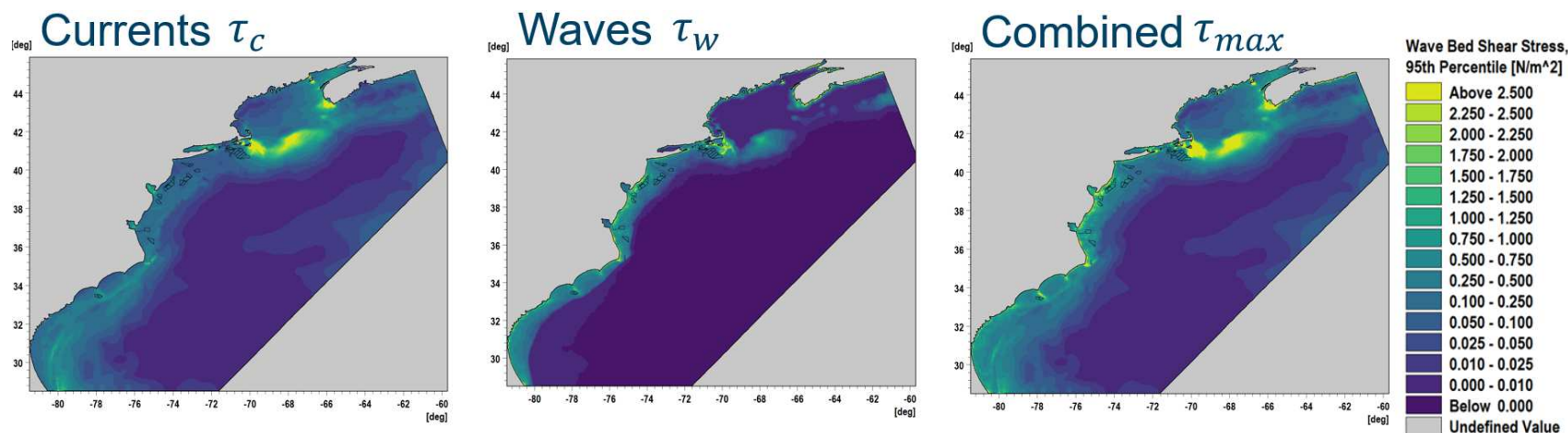


Figure 5.22. 95th Percentile Non-Exceedance Probability Bed Shear Stresses in the Model Domain Scenario 5: 15 MW Full Build-Out
 LEFT: Current only, MIDDLE: RMS Wave only, RIGHT Current + RMS Wave for time period 1 January 2017 through 31 December 2017

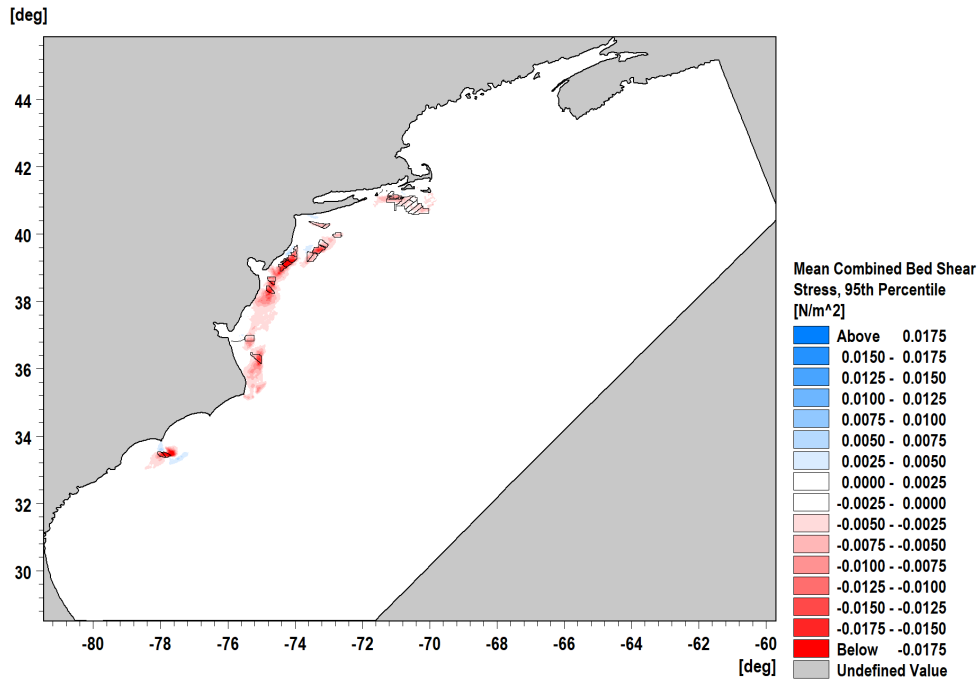


Figure 5.23. 95th Percentile Non-Exceedance Probability RMS Bed Shear Stress Difference Under Combined Waves & Current

Model domain. Scenario 5: 15 MW full build-out – Scenario 1: Baseline. For time period 1 January 2017 through 31 December 2017

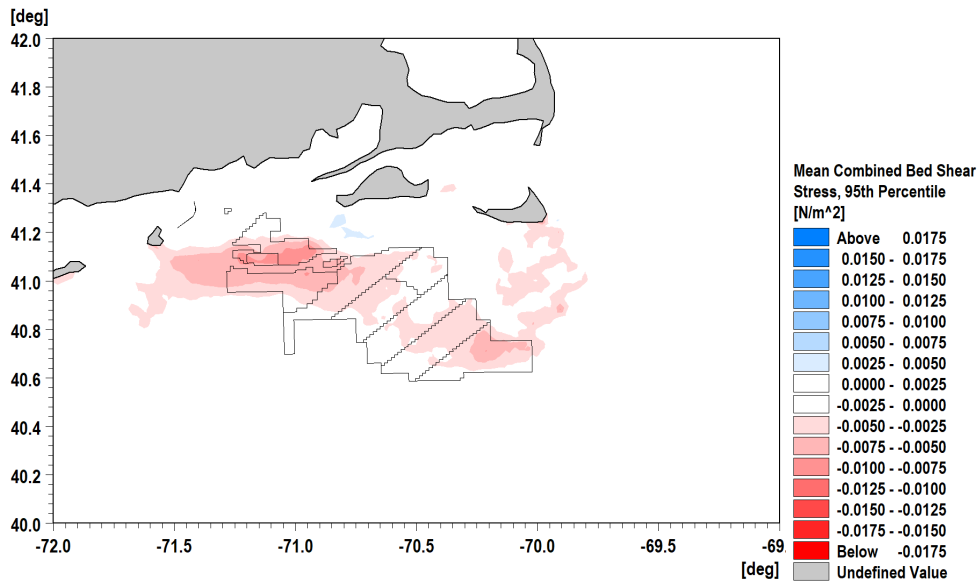


Figure 5.24. 95th Percentile Non-Exceedance Probability RMS Bed Shear Stress Difference Under Combined Waves & Current

MA-RI Region. Scenario 5: 15 MW full build-out – Scenario 1: Baseline. For time period 1 January 2017 through 31 December 2017

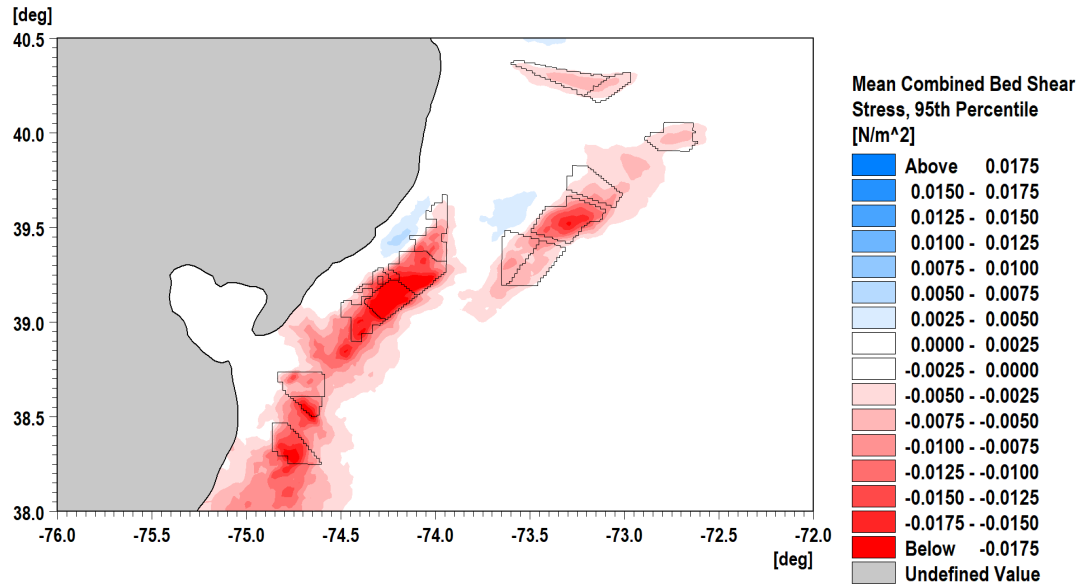


Figure 5.25. 95th Percentile Non-Exceedance Probability RMS Bed Shear Stress Difference Under Combined Waves & Current
 NY Bight and MD-DE Region. Scenario 5: 15 MW full build-out – Scenario 1: Baseline. For time period 1 January 2017 through 31 December 2017

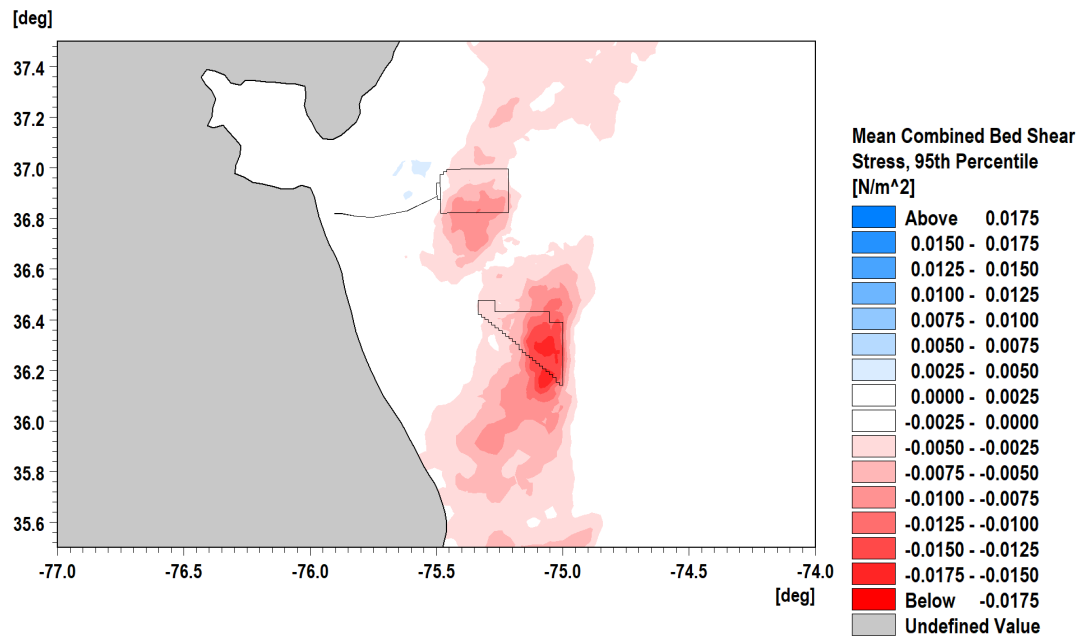


Figure 5.26. 95th Percentile Non-Exceedance Probability RMS Bed Shear Stress Difference Under Combined Waves & Current
 VA-NC Region. Scenario 5: 15 MW full build-out – Scenario 1: Baseline. For time period 1 January 2017 through 31 December 2017

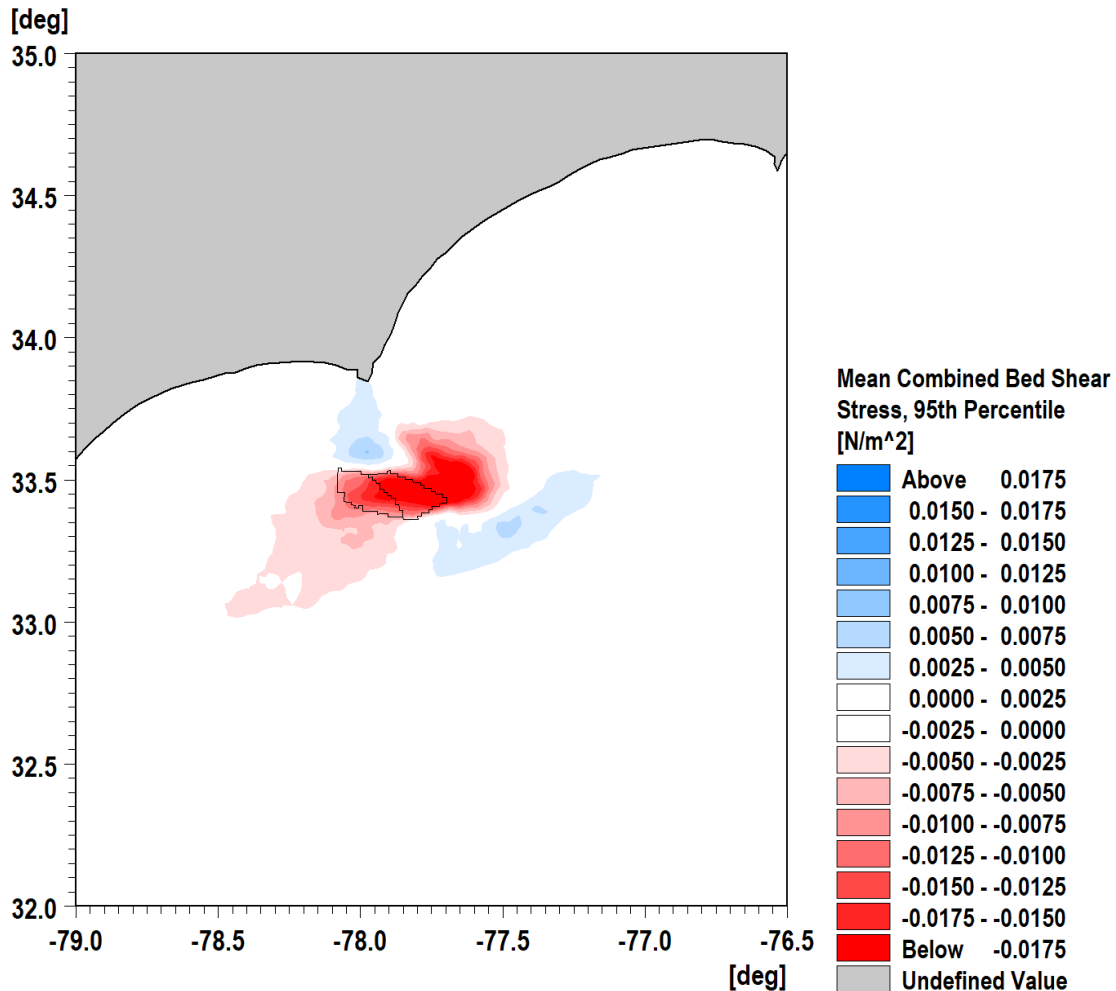


Figure 5.27. 95th Percentile Non-Exceedance Probability RMS Bed Shear Stress Difference Under Combined Waves & Current

NC-SC Region. Scenario 5: 15 MW full build-out – Scenario 1: Baseline. For time period 1 January 2017 through 31 December 2017

To put the bed shear stress results into context the red shaded areas are where the bed shear stress is reduced compared to baseline. This implies less of a tendency to mobilize sediment. The USGS classify the grain size that can be mobilized when the critical bed shear stress is exceeded, using the Shields relation for the critical bed shear stress. This is summarized in Table 5.4. By inspecting the figures one can see that the maximum 95th percentile non-exceedance probability combined bed shear stress is on the order of 0.0050 to 0.0075 N/m^2 (light blue) which is less than what is necessary to mobilize fine silt. The change in bed shear stress should have no increased effect on mobilizing the seabed in any of the OSW farm areas. On the deposition side where bed shear stresses are reduced, the maximum reduction is seen in the NC/SC WEA with a value of -0.0125 to -0.01 N/m^2 where the 95th percentile non-exceedance probability of the maximum combined is on the order of 0.25 to 0.5 N/m^2 or ~3%. These relatively small changes in bed shear stress would not have much effect on the deposition in the WEA.

Table 5.4. Critical Shear Stress by Particle-Size Classification for Determining Approximate Condition for Sediment Mobility at 20 Degrees Celsius
(Credit: USGS)

Particle Classification Name	Ranges of Particle Diameters (mm)	Critical Bed Shear Stress (τ_c) (N/m ²)
Coarse Cobble	128 – 256	112 – 223
Fine Cobble	64 – 128	53.8 – 112
Very Coarse Gravel	32 – 64	25.9 – 53.8
Coarse Gravel	16 – 32	12.2 – 25.9
Medium Gravel	8 – 16	5.7 – 12.2
Fine Gravel	4 – 8	2.7 – 5.7
Very Fine Gravel	2 – 4	1.3 – 2.7
Very Coarse Sand	1 – 2	0.47 – 1.3
Coarse Sand	0.5 – 1	0.27 – 0.47
Medium Sand	0.25 – 0.5	0.194 – 0.27
Fine Sand	0.125 – 0.25	0.145 – 0.194
Very Fine Sand	0.0625 – 0.125	0.110 – 0.145
Coarse Silt	0.0310 – 0.0625	0.0826 – 0.0110
Medium Silt	0.0156 – 0.0310	0.0630 – 0.0826
Fine Silt	0.0078 – 0.0156	0.0378 – 0.0630

Please note that this analysis does not consider details of the waves and current close to the monopile foundations where localized scour may occur.

5.6 Effects on Temperature

5.6.1 Effects on Temperature Stratification

The effect of the WTGs on the sea surface wind stress can be seen in the vertical thermal stratification due to the slowing of the currents inside the OSW farms. The greatest impact is from the 15 MW full build-out Scenario 5. The following figures show a transect of the thermal layers through the NY Bight WEAs. **Figure 5.28** is a plan view of the transect through the OSW farms. **Figure 5.29** through **Figure 5.32**. Average Fall Vertical Temperature Structure of a Northeast-Southwest Transect shows the thermal stratification for the annual mean for winter, spring, summer, and fall seasons for the combined years of 2017 and 2018. The OSW farm influence on thermal stratification changes is generally most recognizable in the results in the vicinity of the WEAs and are mainly related to:

- In the winter, the water column is generally close to well-mixed; thus, isotherms may be relatively stable, but typically the shallower isotherms shift up by 2-5 m and the deeper isotherms appear to expand to the southwest by ~20 km.
- In spring typically the isotherms shift down by ~0.5 m in the upper 20 m of water and up ~0.5 m to 1.5 m in waters deeper than 30 m.

- In summer the isotherms typically shift down by ~3 m in the upper 10 m of water. Little change is noted between 10 m and 30 m water depths and in the deeper water the isotherms move up and expand the size of the cooler water mass.
- In fall the isotherms typically shift down in the upper 20 m of water in the OSW farm area in the southwest with no change noted in water depths 20 m and deeper.

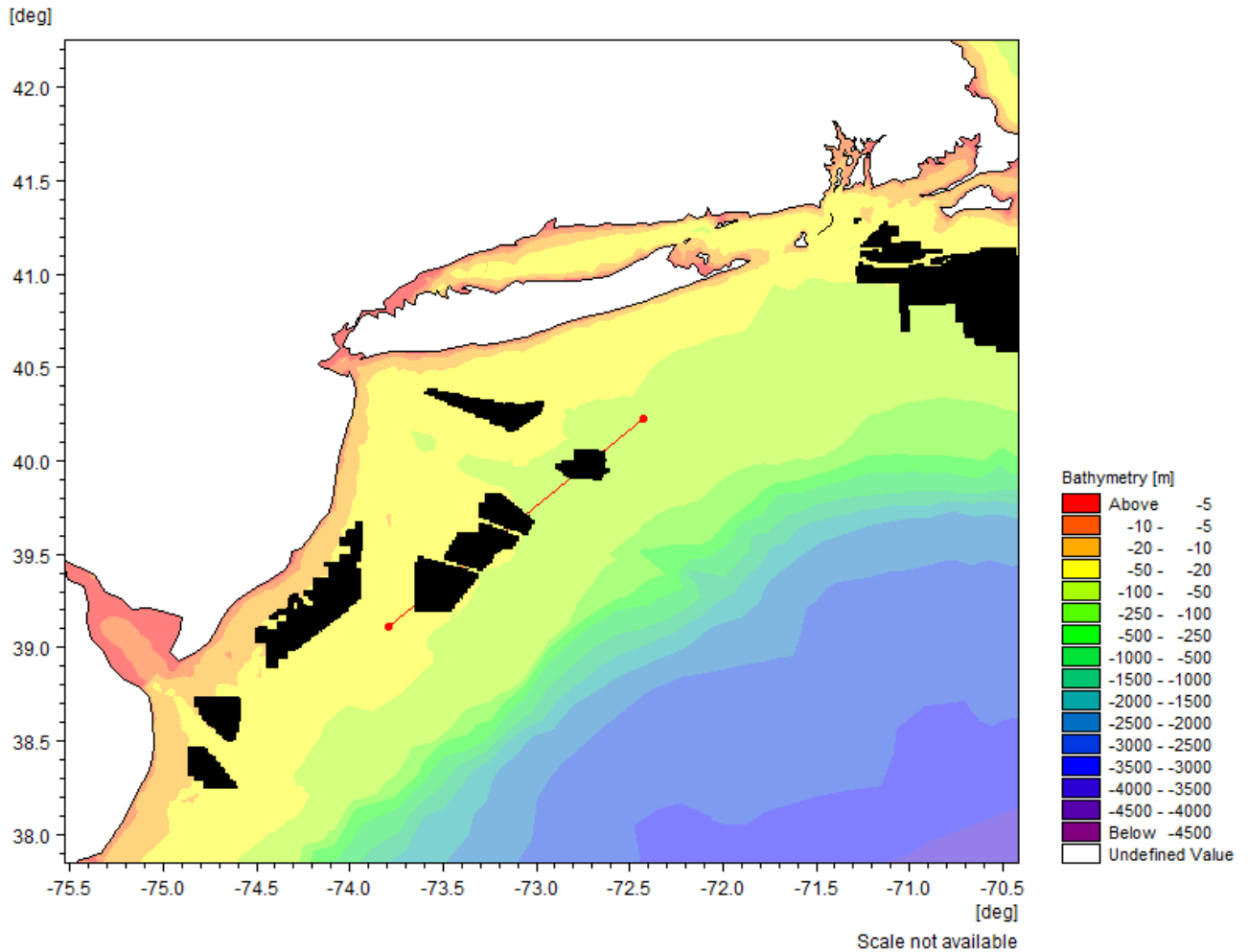


Figure 5.28. Thermal Transect Location NY Bight

The figure shows transect through the eastern NY Bight OSW farms with a line orientation from the Northeast and headed toward the Southwest.

More transects for the 15 MW full build out are included in **Appendix A**.

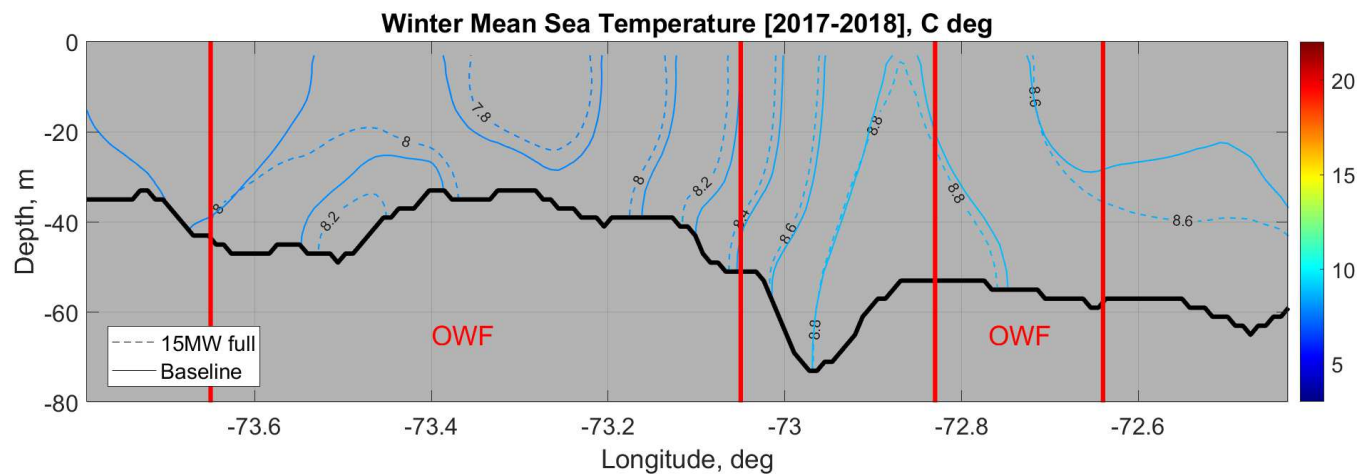


Figure 5.29. Average Winter Vertical Temperature Structure of a Northeast-Southwest Transect

The figure shows the 2017-2018 winter average temperature contours from a transect for Scenario 5: 15 MW full build-out OSW and the same transect for Scenario 1: Baseline.

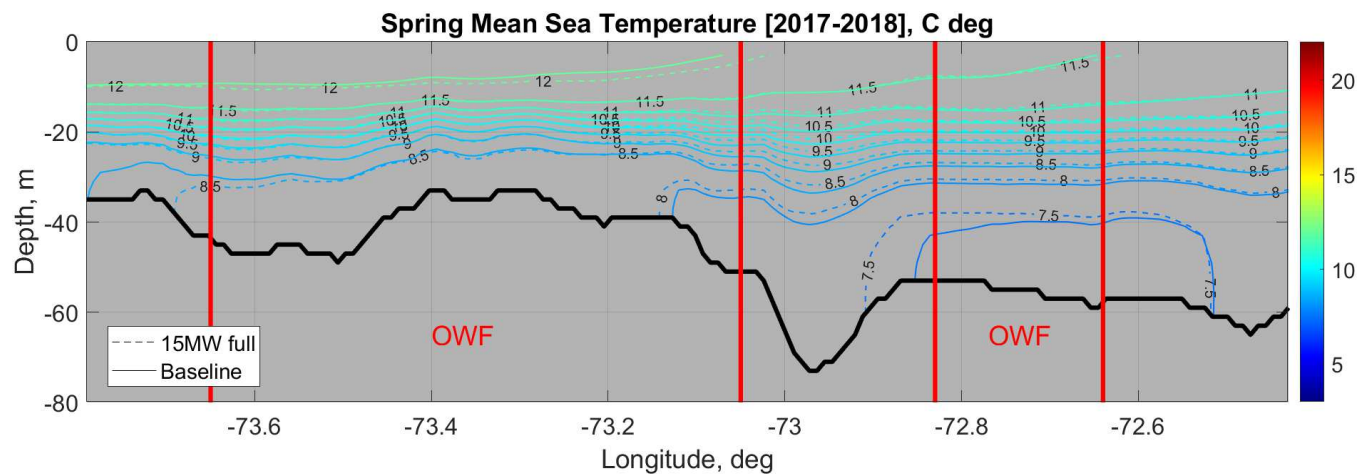


Figure 5.30. Average Spring Vertical Temperature Structure of a Northeast-Southwest Transect

The figure shows the 2017-2018 spring average temperature contours from a transect for Scenario 5: 15 MW full build-out OSW and the same transect for Scenario 1: Baseline.

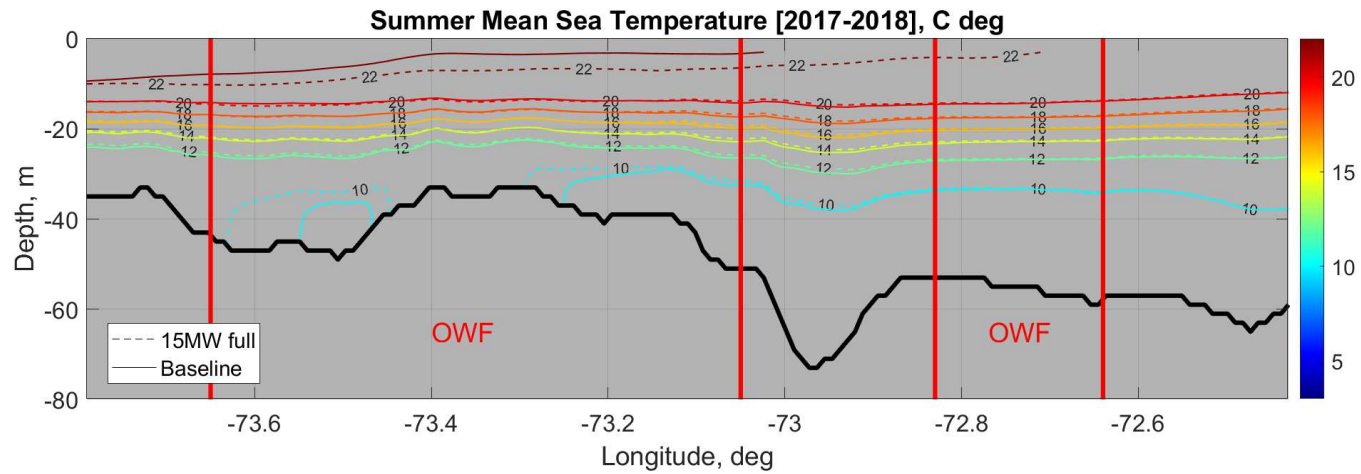


Figure 5.31. Average Summer Vertical Temperature Structure of a Northeast-Southwest Transect

The figure shows the 2017-2018 summer average temperature contours from a transect for Scenario 5: 15 MW full build-out OSW and the same transect for Scenario 1: Baseline.

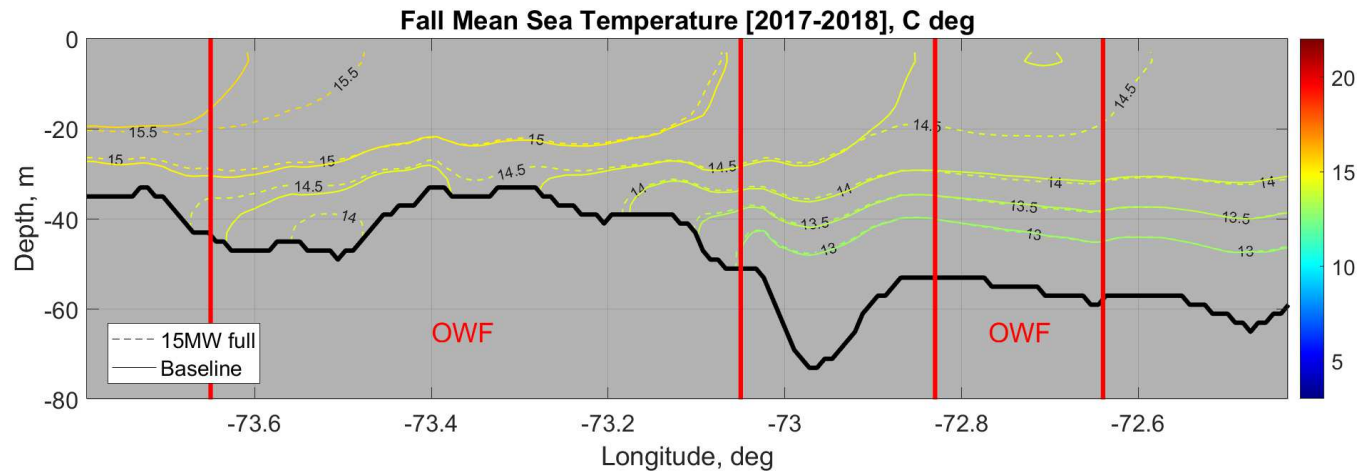


Figure 5.32. Average Fall Vertical Temperature Structure of a Northeast-Southwest Transect

The figure shows the 2017-2018 fall average temperature contours from a transect for Scenario 5: 15 MW full build-out OSW and the same transect for Scenario 1: Baseline.

5.6.2 Effects on Sea Surface Temperature

The effect of the WTGs on the sea surface temperature was analyzed seasonally for the 95th percentile non-exceedance probability of the difference between the Scenario5: 15 MW Full Build-out and Baseline for 2017. **Figure 5.33** shows the difference in Sea Surface Temperature (SST) 95th percentile non-exceedance probability for Scenario 5: 15 MW Full Build-out – Baseline for winter and spring 2017.

Figure 5.34 shows the difference in Sea Surface Temperature 95th percentile non-exceedance probability for Scenario 5: 15 MW Full Build-out – Baseline for summer and fall 2017.

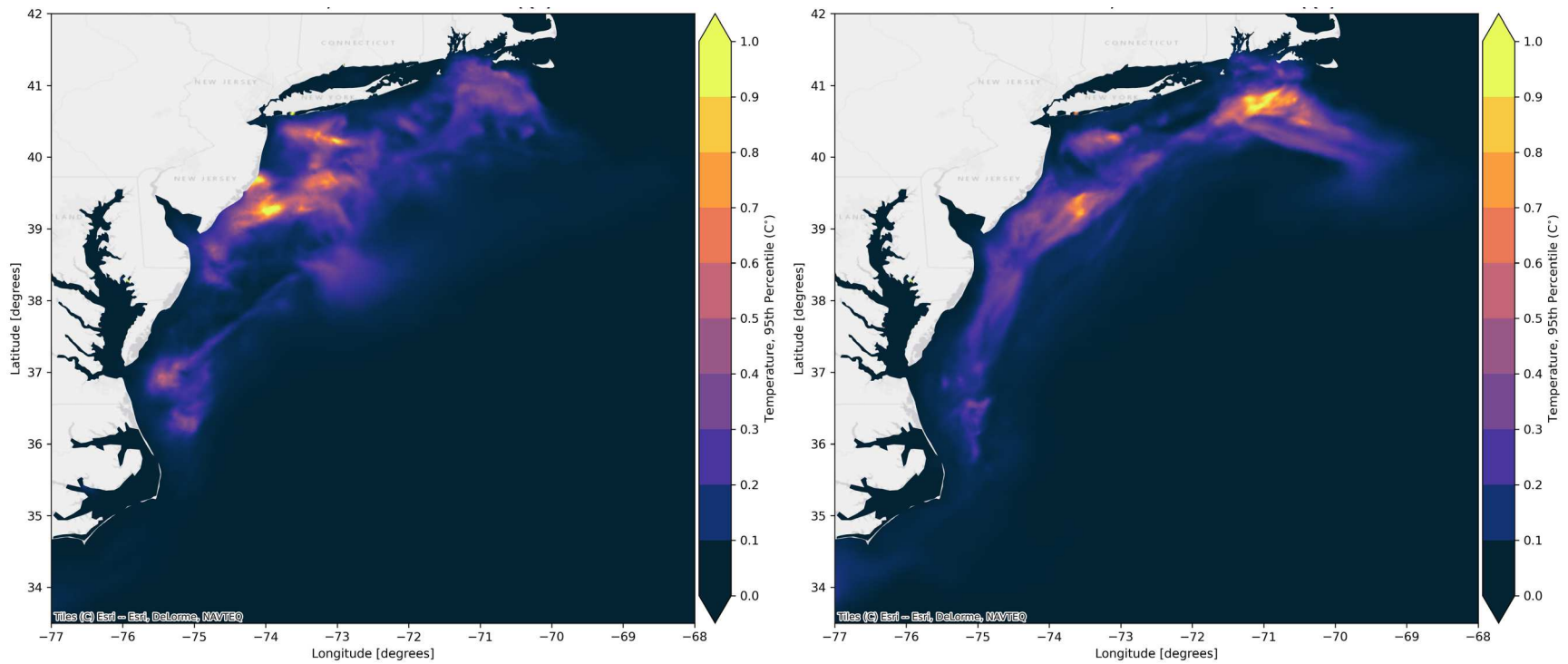


Figure 5.33. Difference in Sea Surface Temperature 95th Percentile Non-Exceedance Probability, Scenario 5: 15 MW Full Build-Out - Baseline

LEFT: Winter, January-February-March 2017; RIGHT: Spring, April-May-June 2017

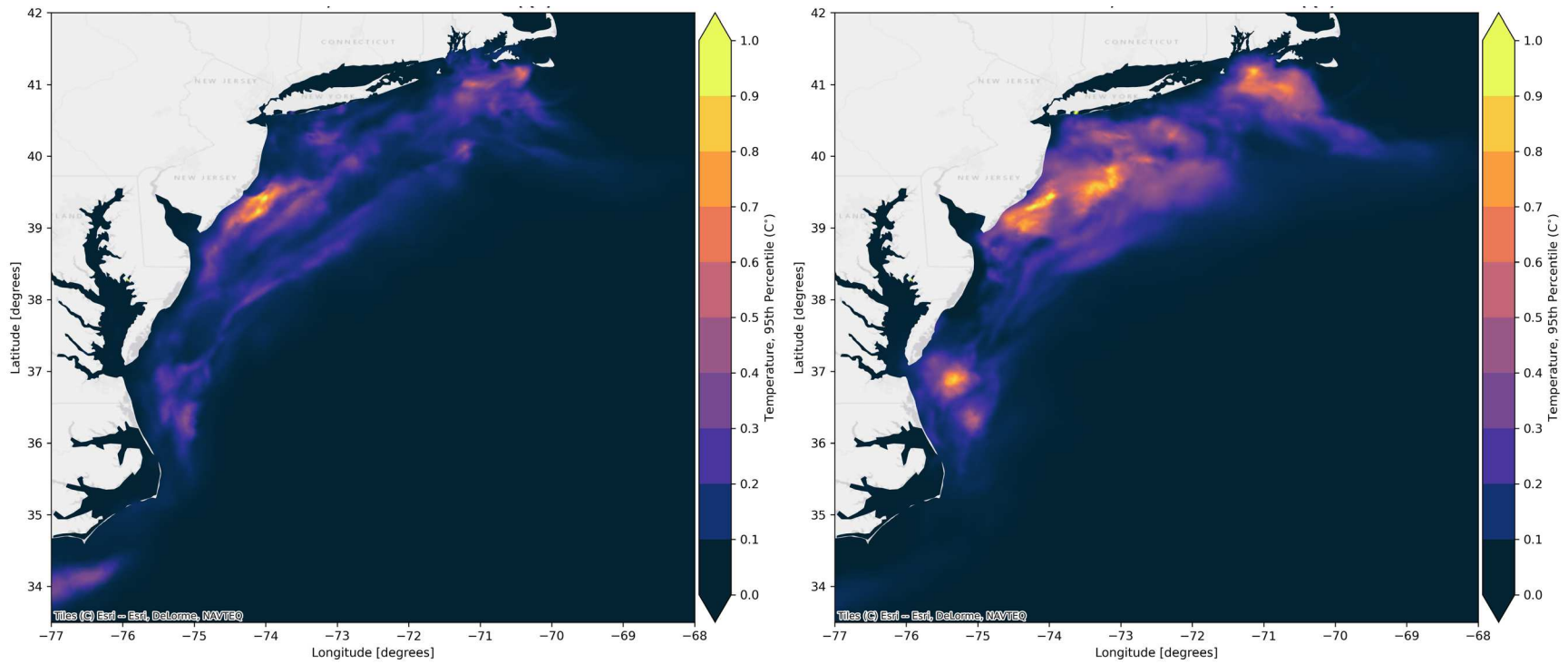


Figure 5.34. Difference in Sea Surface Temperature 95th Percentile Non-Exceedance Probability, Scenario 5: 15 MW Full Build-Out - Baseline

LEFT: Summer, July-August-September 2017; RIGHT: Fall, October-November-December 2017

5.7 Other Effects on Oceanic Parameters

5.7.1 Sea Surface Height

Figure 5.35 shows the difference in Sea Surface Height 95th percentile non-exceedance probability for Scenario 5: 15 MW Full Build-out – Baseline for winter and spring 2017. **Figure 5.36** shows the difference in Sea Surface Height 95th percentile non-exceedance probability for Scenario 5: 15 MW Full Build-out – Baseline for summer and fall 2017.

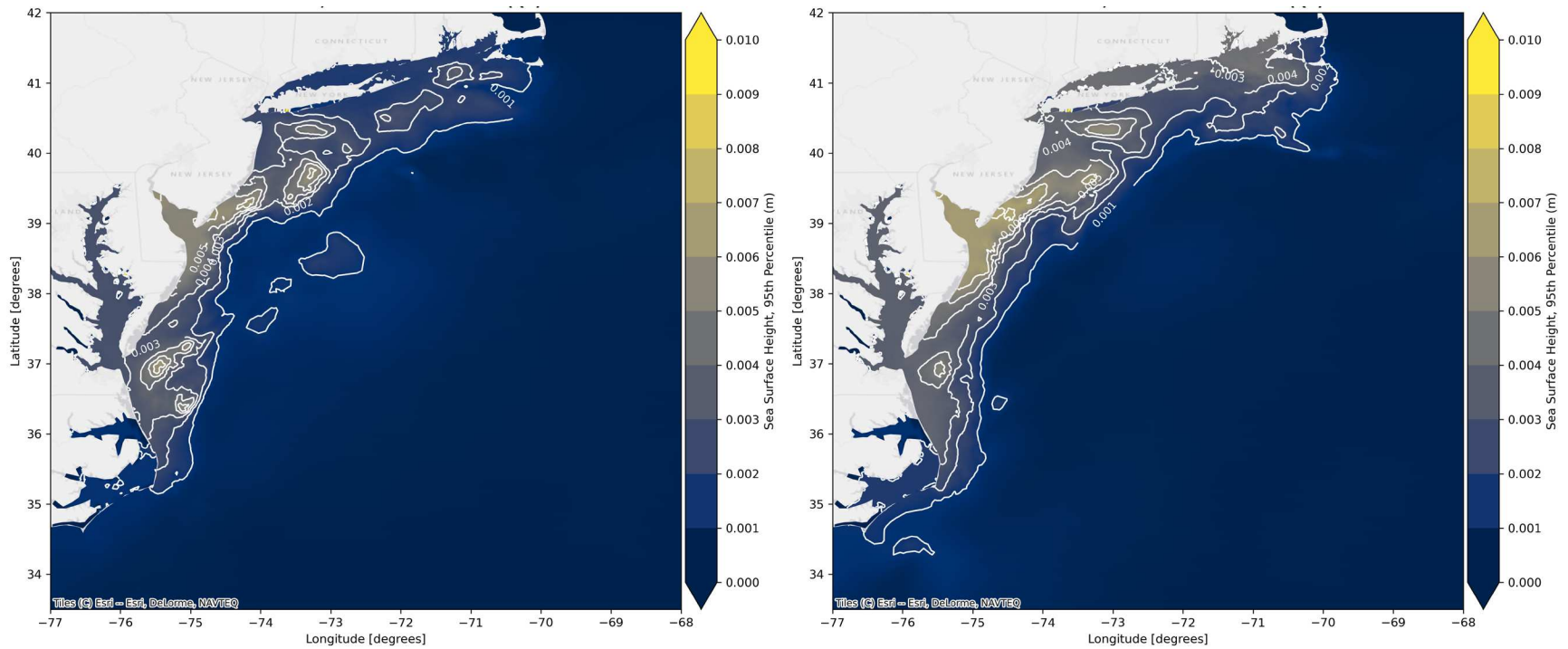


Figure 5.35. Difference in Sea Surface Height 95th Percentile Non-Exceedance Probability, Scenario 5: 15 MW Full Build-out - Baseline
 LEFT: winter, January-February-March 2017; RIGHT: spring, April-May-June 2017

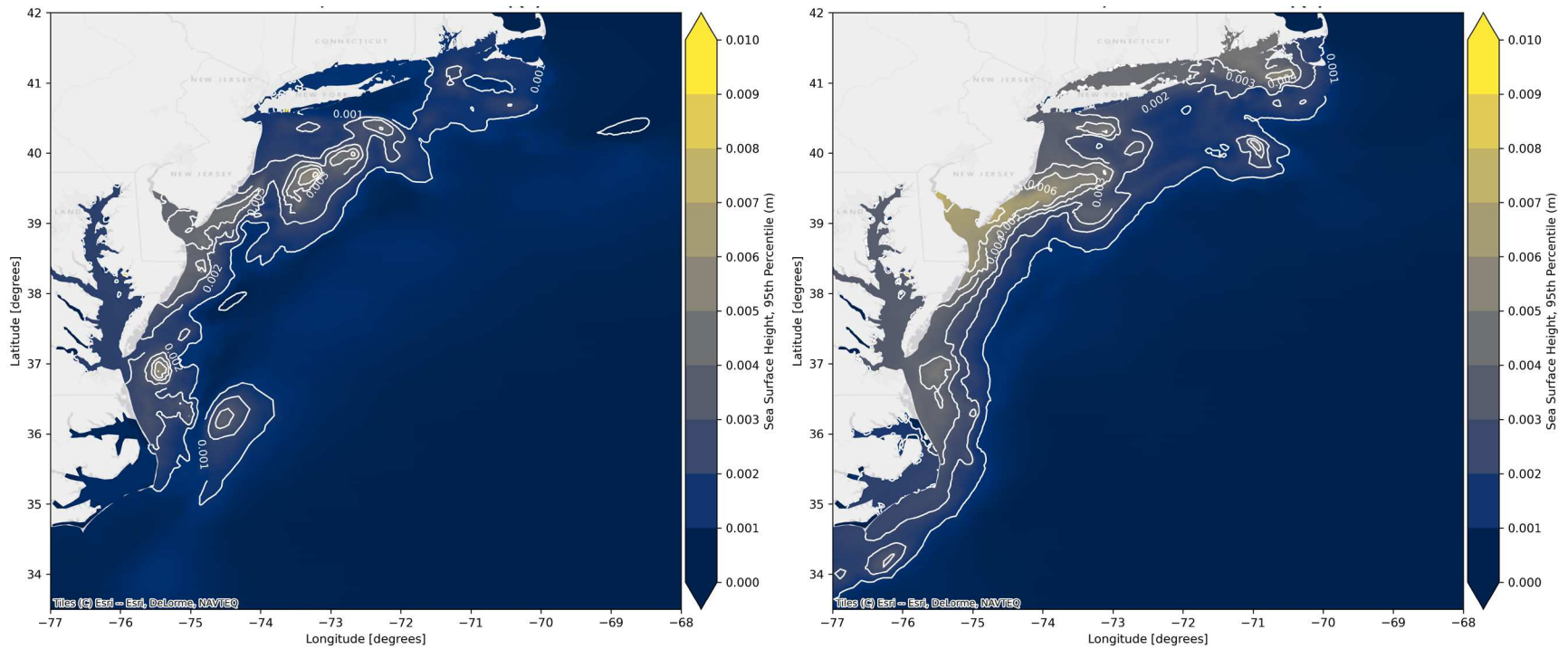


Figure 5.36. Difference in Sea Surface Height 95th Percentile Non-Exceedance Probability, Scenario 5: 15 MW Full Build-Out - Baseline
 LEFT: summer, July-August-September 2017; RIGHT: fall, October-November-December 2017

5.7.2 Sea Surface Salinity

The effect of the WTGs on the sea surface salinity was analyzed seasonally for the 95th percentile non-exceedance probability of the difference between the Scenario5: 15 MW Full Build-out and Baseline for 2017. **Figure 5.37** shows the difference in Sea Surface Salinity 95th percentile non-exceedance probability for Scenario 5: 15 MW Full Build-out – Baseline for winter and spring 2017. **Figure 5.38** shows the difference in Sea Surface Salinity 95th percentile non-exceedance probability for Scenario 5: 15 MW Full Build-out – Baseline for summer and fall 2017.

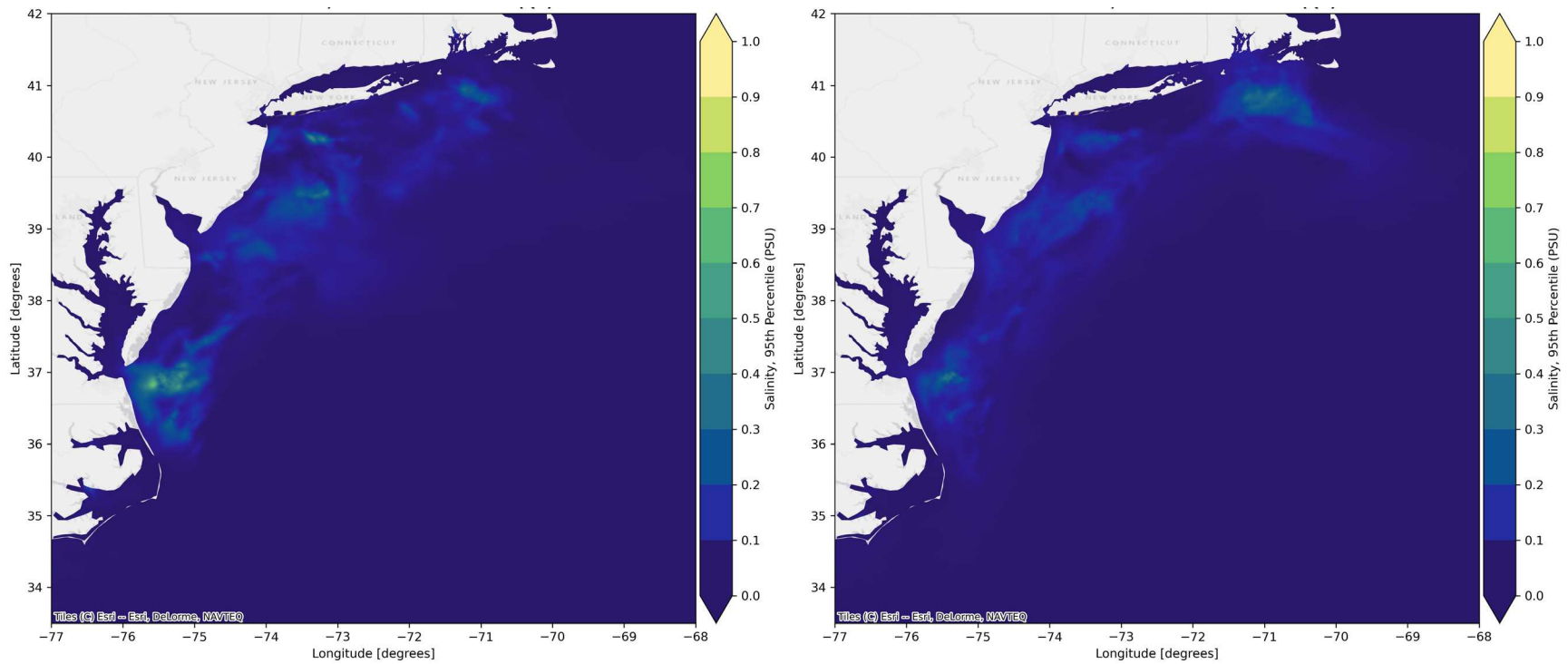


Figure 5.37. Difference in Sea Surface Salinity 95th Percentile Non-Exceedance Probability, Scenario 5: 15 MW Full Build-out - Baseline
 LEFT: winter, January-February-March 2017; RIGHT: spring, April-May-June 2017

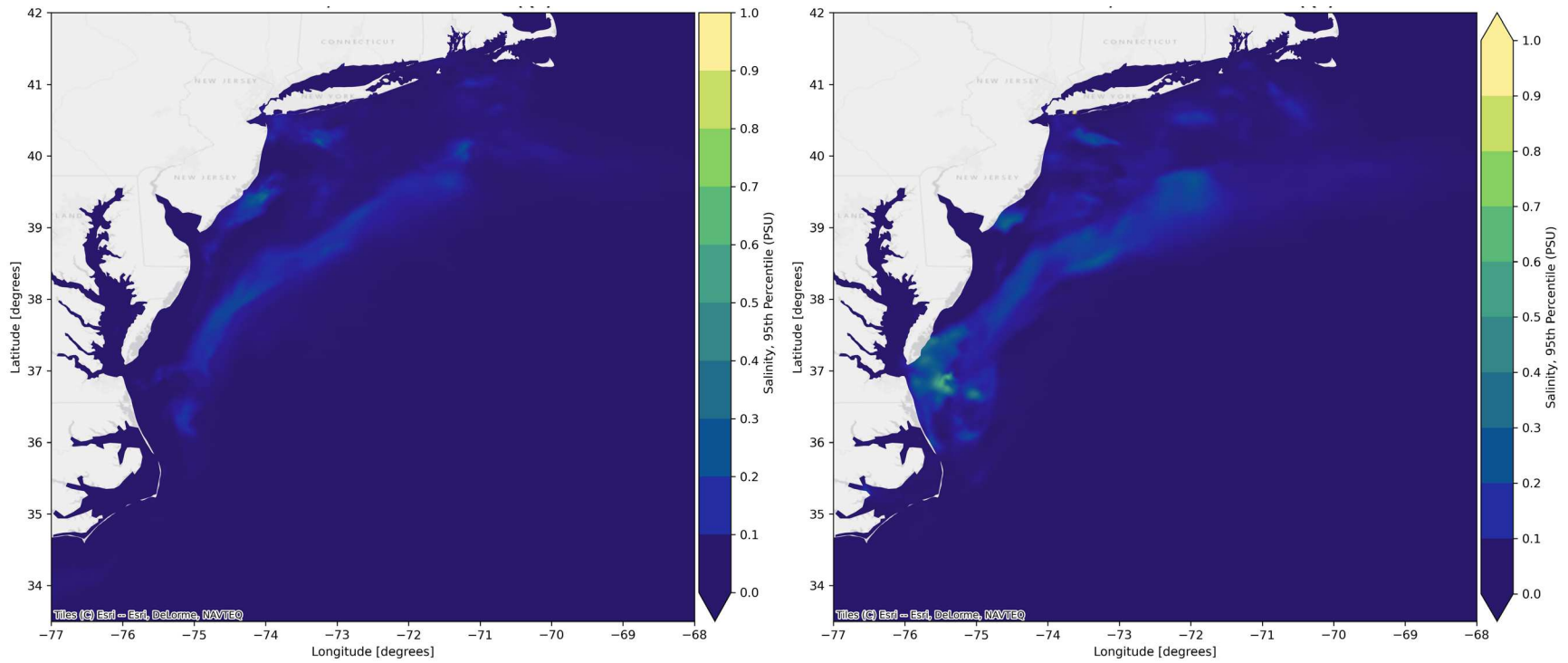


Figure 5.38. Difference in Sea Surface Salinity 95th Percentile Non-Exceedance Probability, Scenario 5: 15 MW Full Build-Out - Baseline
 LEFT: summer, July-August-September 2017; RIGHT: fall, October-November-December 2017

5.8 Hydrodynamic Model vs. Scenario Conclusions

The hydrodynamic model baseline validation was shown to be within the standards of regional modeling precision in **Section 3.3**. When comparisons are made with respect to each OSW Scenarios, the influence of the WTG foundations and the losses due to the wind energy extraction of the WTGs are taken into account through the methods described in **Section 4**.

Changes caused by the various OSW developments to current speeds, waves, bed shear stresses and thermal stratification were captured by the HDM but were relatively modest. For example, the maximum changes to the 95th percentile non-exceedance probability depth averaged current speeds (Scenario 5, 15 MW Full Build-out) in any of the WEAs were approximately -5.0% and +1.7%. The sensitivity test (15 MW Full Build-out wind wake effect doubled) the maximum changes to the 95th percentile non-exceedance probability depth averaged current speeds in any of the WEAs were approximately -6.1% and +2.3%. The detailed wave results show that the biggest reduction in the 95th percentile non-exceedance probability significant wave height (H_{m0}) was observed in the New York Bight (NTY Bight)/ Maryland-Delaware (MD-DE) region. The wave height reduction was on the order of 10 cm for waves that were on the order of 2.5 m H_{m0} or $\sim 4\%$ lower. The change in bed shear stress was also small and should have no increased effect on deposition and very little decreased effect on mobilizing the seabed in any of the WEAs. Finally, the effect of the WTGs on the sea surface wind stress can be seen in the vertical thermal stratification due to the slowing of the currents inside the OSW farms. The greatest effect was observed from the 15 MW full build-out scenario in the NY Bight MD-DE WEA. In winter, the OSW farms shift the isotherms down slightly and expands the bottom isotherm up ~ 3 m and elongates the bottom 10 degree C cold water area toward the southwest by ~ 20 km, whereas in spring the isotherms shifted down by ~ 0.5 m in the upper 20 m of the water column, and up ~ 0.5 m to 1.5 m below 30 m. In the summer, the isotherms shifted down ~ 3 m in the upper 10 m of the water column, with little change between 10 m and 30 m. However, in the deeper waters the isotherms moved up and expanded the size of the cooler water mass. In fall the isotherms shifted down in the upper 20 m of the water column in the OSW farm area on the southwest side, while there was not much change noted deeper than 20 m.

Finally, the overall conclusion of whether the changes in the hydrodynamics are relevant or not must be left to the Agent Based Modeling analysis. While the HDM can determine changes in current speed, temperature stratification, wave heights, and bed shear stress, the “integrative” process of larval dispersal under varying oceanic conditions is the outcome that is most important. The HDM is a basis upon which to assess the impacts on the selected species due to the OSW developments.

5.8.1 Discussion of Specific Wind Wake Studies

As offshore wind energy develops there has been an increasing focus on impacts on the wind resources and the potential impact on the environment in general from large offshore wind farms. The focus on cumulative impacts on the aquatic environment has initiated several related studies. One topic is the potential impact of the wind wake velocity deficit on surface interactions, and the magnitude and extent of the resulting impacts on oceanic processes.

Christiansen et al. (2020) studied the impact of offshore wind developments in the southeastern North Sea on currents and mixing. This study is focused on the impact of wind wakes on the sea surface and does not include any sub-sea effects from the WTG foundations. Wind wakes are based on a re-calibrated Frandsen-model (Frandsen, 2006) approach by fitting an exponential decay using distance from the wind farm to center line velocity deficits from SAR observations. They employ a gaussian shaped cross section. From relevant published observations, they identify 16 situations and estimate a velocity deficit at the farm at 8% and a 1/e recovery length at 32 km. The velocity deficit and wake length are therefore

independent of farm layout or production as well as atmospheric stability. Wind farm interactions are considered by a linear superposition. The wind wakes are then used to modify the 10 m wind forcing of a North Sea hydrodynamic model covering the summer 2013.

The results from Christiansen et al. (2020) indicate a surprisingly wide impact area in surface velocity in the order of -2 mms^{-1} to 4 mms^{-1} change with largest change around the farms, but also at distance in the northwest North Sea. The source of this change is not clear. The sea surface elevation change was found to be approximately -2 mm to 2 mm and surface temperature change -0.1°C to 0.1°C . They further provide estimated change of the potential energy anomaly of about -5 to 5 Jm^{-2} . In conclusion, they consider impacts on internal mixing and transport processes "far beyond the scale of the individual wind farms". Compared to the present study there are differences. WTG foundations are not considered a source of resistance or mixing, and the WTG wakes are not sensitive to stability nor actual farm operations. Furthermore, the study only covers 3 specific summer months. Therefore, the Christiansen et al. (2020) results are not directly comparable to this study.

Raghukumar et al. (2022) report on a recent site-specific study of WTG wakes on the California coast where two OSW developments are planned for Humboldt and Morro Bay, Raghukumar et al. (2022) used a high resolution WRF model to study downstream wake velocity deficits. The model was set up with a 3 km inner nesting and wind turbines implemented using the Fitch actuator disk parameterization. From thirteen years of continuous simulation, they conclude that turbine wakes can extend 200 km downstream with about 5% reduction in 10 m velocity. The wakes appear relatively extended comparing to e.g. the North Sea (Canadillas et al, 2022) or the present study. There seems also to be a distinct difference between the Humboldt (north) site, where velocity increased inside the farm and the wakes were relatively limited. At the Morro Bay (south) site there were very extended southward wakes. One explanation may be differences in the wind conditions where the North Sea is very variable while Southern California may have a more stable atmosphere, promoting longer wakes.

Compared to the present study, it is noted that the Raghukumar et al. (2022) study focuses solely on the wake effects at the water surface. They use a 3 km WRF grid, which implies about that there are ~ 4 WTG per element, thus WTG to WTG interaction may be less accurate. The relatively coarse resolution may also affect the spread of the wakes as numerical dispersion can be of relevance here. The approach is definitely interesting as it apparently can accommodate long time periods, an extended area and several windfarms, such that with a more focused validation of the wakes the methodology may be a useful supplement to future regional modeling efforts.

5.8.2 Discussion of Chen et al. (2024) Study

In a recent paper (Chen et al., 2024) they modeled potential impacts of wind energy development on the U.S. Northeast shelf with respect to oceanic changes and sea scallop larval dispersal. The paper appears to be an update of the Chen et al. (2016) study that investigated impacts from WTG foundations on hydrodynamic conditions. In the 2024 study they are using an ambitious approach combining a nested 3D ocean models (FVCOM) and a wave model (SWAN) to describe the aquatic environment. A regional WRF model is used to describe WTG wind wake impacts and an Individual Based Model is used to model larval dispersion.

Chen et al. model 100 WTGs in the Vineyard OSW farm and conclude that "*monopiles produce intricate patterns of horizontal flow shear on the lee side*" and a "*weakening of the vertical stratification mainly confined to the wind farm development area*". Also, they see "*an enhanced offshore water transport*" towards the Nantucket Lightship Closed Area. They demonstrate for some of the oceanic variables of interest a surprisingly widespread impact as, for example, the thermal diffusion coefficient appears to increase south of Georges Bank as well as near Montauk Point, while appearing relatively unchanged

inside the OSW farm. This apparently also leads to changes in surface and bottom temperatures around Cape Cod and off Montauk Point in some months.

Their study is of interest as they apply alternative methods for describing the physical impact of the WTGs. For the wind wake velocity deficit, the authors use a high resolution (1 km) WRF model where each turbine is implemented as an actuator disk (i.e., Fitch parameterization). They report seasonally averaged wind deficits on the order of $0.2\text{--}0.3\text{ ms}^{-1}$ and minor directional changes concentrated in the vicinity of the wind farm. These impacts are smaller than those found in this study (on the order of 1 ms^{-1} for winter months) and in other studies, including observational (Christiansen and Hasager, 2005), WRF models (Archer et al., 2018) and explicit models (Fischereit et al., 2022). Note that there are local differences in layout and specification of the wind farms between the Chen et al. 2024 study and this study that may affect the analyses. The discrepancy between the two studies indicate that our approach may be more conservative regarding wind wake impacts.

Chen et al., 2024 also implemented an ambitious alternative approach for WTG monopile subsea representation by modeling the towers as obstacles. They took advantage of the unstructured mesh in FVCOM and developed a mesh with 1 m spatial resolution around each obstacle with the intention of fully resolving the boundary layer around the monopile. Such an approach has been standard in CFD models (Schimmels, 2008) or idealized models (Schulze et al., 2020) but is rarely seen in regional ocean models (Schulze et al., 2020), as it can produce a very high demand on computer resources. From the paper it is not clear from the text or the figures whether this high-resolution mesh is carried into the regional model or used as a one-tower analysis tool as some figures seem to indicate. They validate the obstacle model looking at wake dynamics, i.e., the Strouhal's number and vortex shedding frequency in the wake for Reynolds numbers up to 300. However, they note that a vortex street is absent in the simulations and that the eddy shedding period is about 1 hour which implies a Strouhal number on the order of 0.005. This is somewhat smaller than 0.2 which is the normal range, which could be an indication of a too coarse spatial and temporal resolution. For both studies, the Reynolds number (Re) for a monopile will typically be on the order 10^6 , markedly larger than 300. At such high Re the boundary layer is relatively thin, on the order of centimeters. A coarser resolution may alter the boundary layer numerically and the model may produce a larger drag relative to what is expected from standard monopile drag relations (Schimmels, 2008). Although not shown, in natural flows wake turbulence typically dissipates within 10 to 20 cylinder diameters downstream. The permanent footprint will then mainly be an added resistance to the current and potentially cause extra vertical mixing that can alter the vertical structure of the water column (Rennau, 2012). This appears also to be confirmed from the paper as the thermal diffusion coefficient appears enlarged in a very narrow band (about $0.3 \cdot D$) around the monopile. In addition, it is not described how the baseline scenario is implemented as removing the monopiles may induce mesh disturbances that can promote differences in the solutions.

A direct comparison with our study is not possible as the layout of the OSW development in Chen et al. 2024 is different. However, it appears that there are differences in the distribution of the effects. These differences require a more detailed description of the Chen et al., 2024 model to allow for a more complete analysis.

6 Larval Dispersal Modeling Analyses - Methodologies

6.1 General Approach

The following section offers a description of the agent-based modeling (ABM) approach applied to this project, along with the related ensemble and connectivity modeling techniques used to complete the larval dispersal analysis. Initially, this is provided through two schematic diagrams (**Figure 6.1** and **Figure 6.2**), and corresponding explanation of the key components of the overall modeling approach. This is then followed by conceptual explanations of ABM, and the applied ensemble and connectivity techniques.

Deeper descriptions of each methodology are subsequently offered via detailed explanations of the model set-up and initialization parameters. For example:

- the ABM approach described in **section 6.2** presents:
 - a brief description of ABM
 - the rationale for agent-based modeling
 - the approach for larvae ABM including the super-agent methodology and stochasticity
 - the ensemble modeling approach
 - the connectivity analysis approach
- the connectivity analysis approach described in **section 6.3** presents:
 - a brief description of the definition of connectivity used in this study
 - the rationale and approach for the connectivity analysis
- the ABM model set-up **section 6.4** presents:
 - a summary of the primary datasets used in the parameterization and initialization of the models
 - descriptions of the key characteristics of each target species (e.g., life cycle, spawning behavior, movement features, settlement habitat) pertinent to model parameterization and initialization
 - actual applied values used in ABM set-ups
- the ensemble set-up **section 6.5** presents:
 - an explanation of the analysis undertaken, and corresponding results, to establish the number of ensemble ‘clones’ required to produce statistically defensible results
 - specifications on the approach for initializing each ensemble clones model simulation
- the connectivity set-up **section 6.6** presents:
 - a description the process for establishing origin and destination areas
 - a review of the data used to establish connectivity results
 - an explanation of data processing techniques used to establish the connectivity between origins and destinations.

In addition to the above core aspects of the modeling, the section also offers a description of the methodologies used to determine the validity of baseline larvae modeling and the techniques used to post-process the model results into illustrative plots, graphs, and matrices.

6.1.1 Overview of Modeling Steps

The ABM modeling steps, which are described in greater detail in the relevant sections of this report, are shown in **Figure 6.1**. The first step detailed in **section 6.4**, is the model set-up (shaded pink in **Figure 6.1**). Here the ABM was set-up to simulate the spawning, dispersal, growth, movement, mortality, and settlement of larvae of the three species. These ABM processes were coded into the MIKE ECO Lab model template, and parameterized based on relevant literature (e.g., the timing of spawning events is

determined based on timings found in scientific literature). The hydrodynamic model results were then coupled with the ABM and simulations were carried out. The baseline hydrodynamics (left of **Figure 6.1**) and the scenario hydrodynamics (right of **Figure 6.1**) (i.e., those with altered current speeds resulting from the OSW developments) were coupled with the ABM separately to produce baseline settlement and scenario settlement results for comparison.

ABM results were then fed into two separate steps. Agent track data, origin and destination maps (i.e., data that show where larvae spawned and where they settled) were fed into the connectivity analysis (detailed in **section 6.4.5** and shaded green in **Figure 6.1**). The connectivity analysis aims to determine the probability of settlement in different destination regions, from certain spawning locations. The connectivity results help aid the impact analysis, as the results allow for the identification of the direction of larval dispersal that may have been affected by slowed current speeds resulting in reduced settlement in certain destination areas; and for the identification of areas of increased settlement, and where the additional larvae settling in these regions came from.

ABM results were also fed into the ensemble modeling step (shaded blue **Figure 6.1**). The final timestep showing the total settlement of larvae (i.e., density of settled larvae and total settled larvae at the end of the simulation) over the model domain, and the connectivity results from the same simulation were stored together. Ensemble modeling is described in detail in **section 6.4.5**, the broad concept however, is to repeat simulations with the same input parameters and to store and average the results from these multiple model “clones”. Ensemble modeling allows for a more robust analysis of the results, given the inherent stochasticity in the ABM. Thus, the final step is the output of the ensemble connectivity and settled larvae baseline and scenario results, which are then post-processed (**Figure 6.2**).

6.1.2 Overview of Results Post-Processing

A detailed description of how the raw model results were post-processed are given in **section 6.8** and details of how results were visualized are given in **sections 7** (baseline results) and **sections 8.1** (scenario results). An overview of the post processing workflow and the different visualizations made is provided in **Figure 6.2**. Baseline (blue arrows) and scenario (orange arrows) ensemble model results were separately aggregated and averaged to give a single mean baseline and a single mean scenario result for processing. From these mean results baseline settled density and total settled larvae maps were made. In addition, the results were fed into the last step of the connectivity analysis (shaded green), where connectivity matrices and maps were then created.

Aggregated baseline and scenario ensemble results (i.e., mean settled densities and connectivity results) were then analyzed statistically and the most common settlement destinations were identified. The results from all ensembles were then visualized in a swarm plot showing the baseline settlement in the most common settlement destinations. The baseline and scenario results were also combined to show changes in settlement in the most common destination areas with the introduction of OSW developments in additional swarm plots. A description of the swarm plot as part of the Python plotting toolbox can be found here: <https://pierantraining.com/understanding-the-seaborn-swarmplot-in-python/#:~:text=A%20swarmplot%20is%20a%20type,more%20variables%20in%20a%20dataset.>

The shaded gray area indicates where baseline and scenario results were combined, compared and differenced, to aid the impact analysis (difference in baseline vs. scenario results flow are shown by purple arrows). Maps showing the difference in larval settlement were made, as well as bar charts of change, and a cluster analysis to identify hotspots of change was also carried out (see **section 6.7** for detailed methods of these analyses). Finally, the difference in connectivity with the addition of OSW farm developments was also calculated. The results and visualizations are shown and discussed in **section 7** and **section 8**.

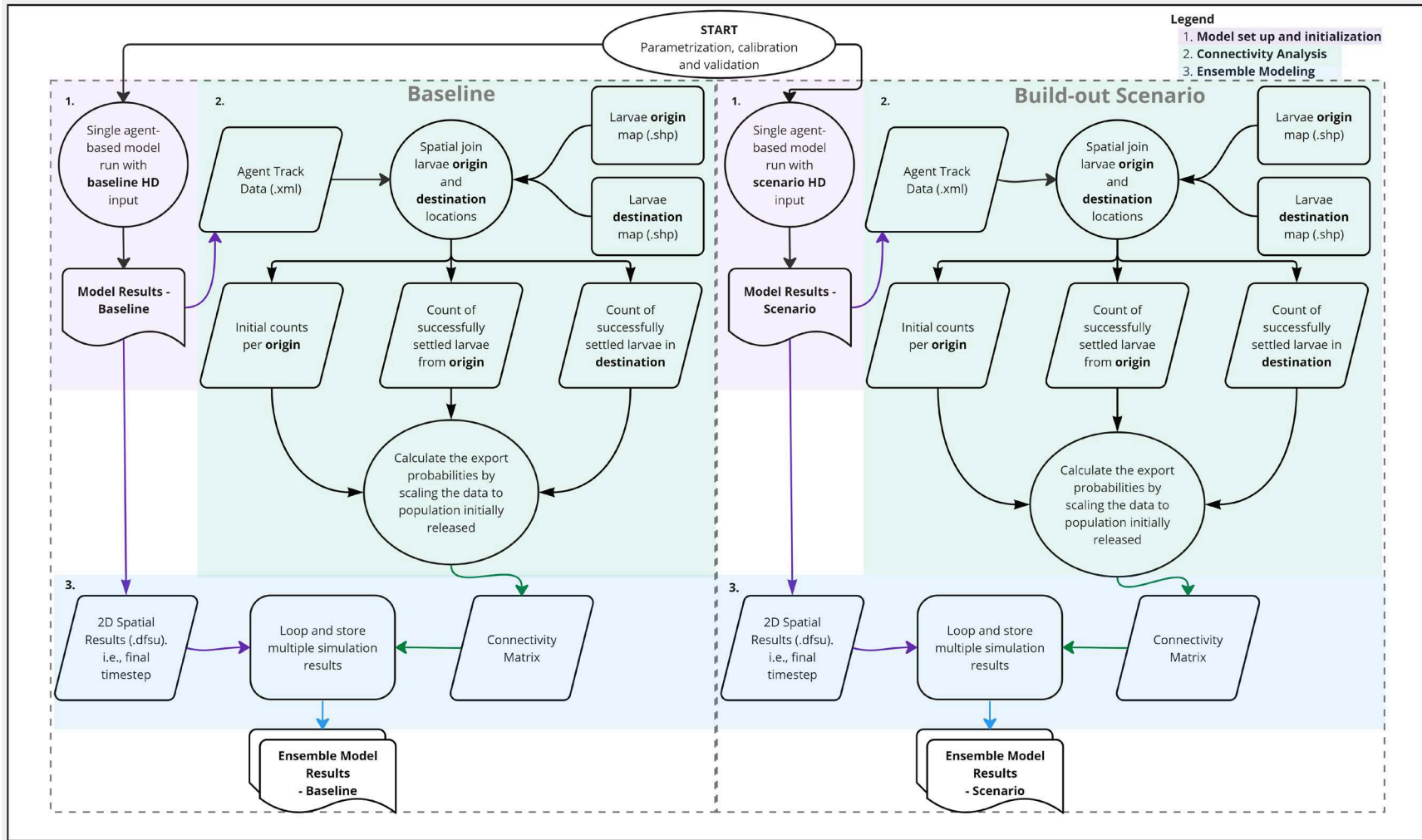


Figure 6.1. Flow Diagram Showing Modeling Steps Involved in the ABM for the Baseline and the Build-Out Scenario

Starting with model set-up and initialization (pink) where the scenario hydrodynamic model results are coupled to the ABM, to the connectivity analysis (green) and ensemble modeling (blue) where multiple model runs are completed, and results are stored. Baseline modeling is shown on the left, and scenario modeling is on the right, results from these two workflows are processed following the steps in the following figure.

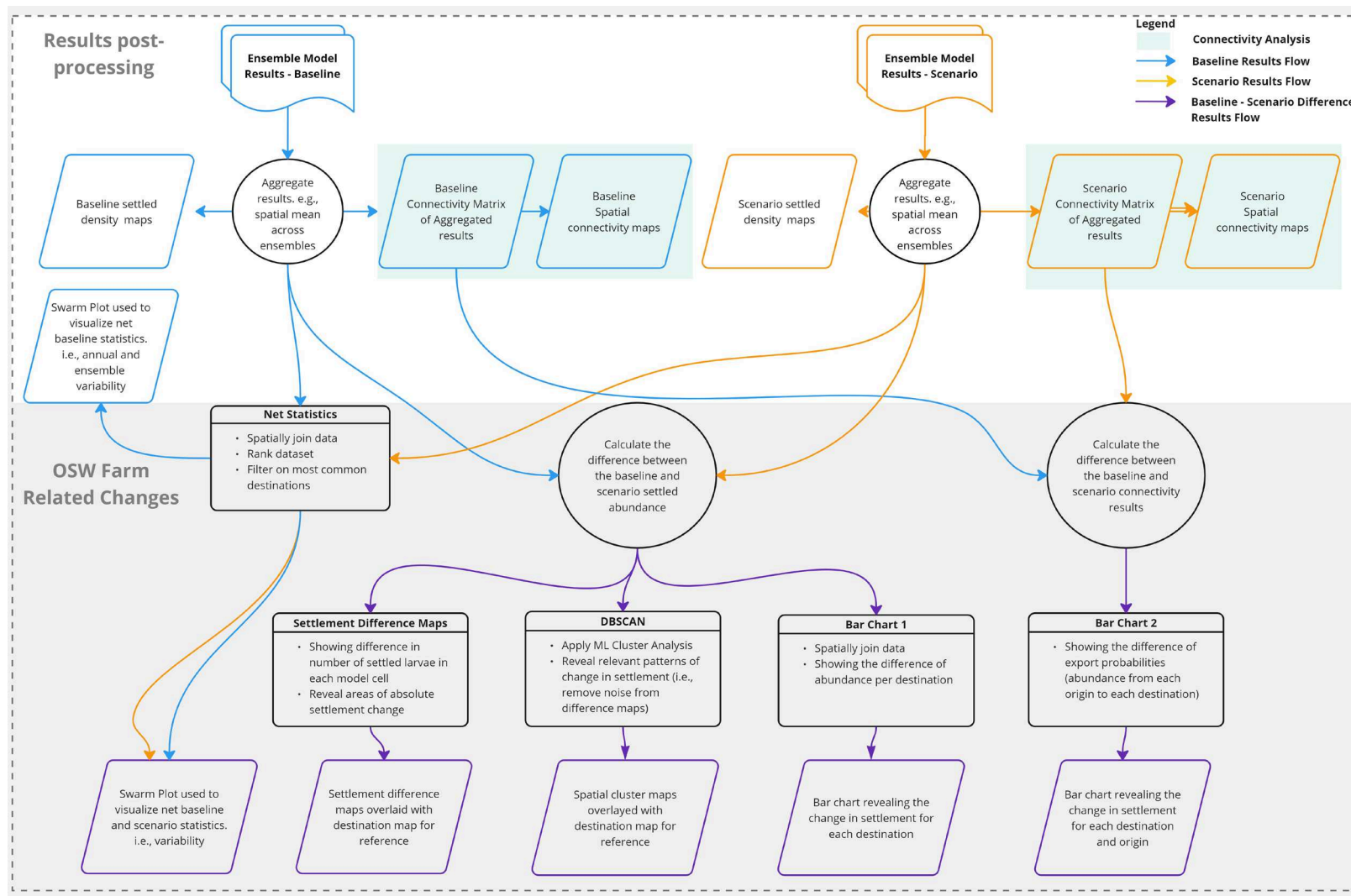


Figure 6.2. Flow Diagram Showing the Post Processing Workflow for the Ensemble Model Results

Baseline results (blue arrows) and scenario results (orange arrows) are processed to show settled density maps, connectivity results (green), and offshore wind farm related changes (gray background, purple arrows).

6.2 Agent-Based Model Approach

6.2.1 Background on ABM

ABM, also called individual-based models, simulate populations as being composed of discrete individual organisms in time and space that result due to external stimuli (Grimm, 2005). As shown in

Figure 6.3, where traditional related ecological system modeling techniques apply top-down population parameters, ABMs draw on the traits and variations between individuals to generate bottom-up models that predict behavior and movement of autonomous individuals, or agents (Johnson et al., 2021; Grimm, 2005). This is achieved by simulating the decision-making processes of an agent in relation to its interactions with other agents and the environment.

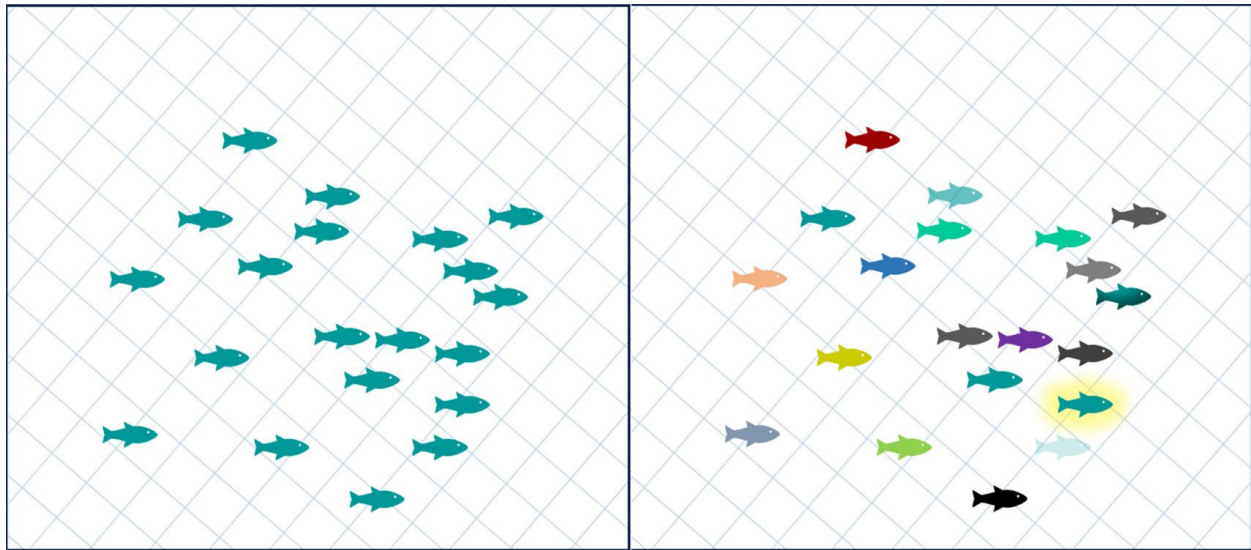


Figure 6.3. Illustration of Difference in Top-Down and Bottom-Up Population Impact Models

LEFT: Top-down population models assume all individuals in the population, or its sub-units are identical; RIGHT: Bottom-up models estimate the population effect by summing up the effect of the individuals.

ABMs adopt a pragmatic and objective approach to modeling observable actions through a detailed representation of agents that live in complex environments (An et al., 2021; Grimm and Railsback, 2005; Stillman et al., 2015). The alternative bottom-up population model focuses on the uniqueness characteristics of individuals and interactions between them and/or their environments (An et al., 2021). A core function of the model is to allow fundamental traits of the individual to be modeled stochastically, therefore making room for trait variance between individuals. The individuals or agents are released into a simulated domain, with a predetermined range of forcings, such as temperature, wind speed, water depth, noise, etc. In terms of their traits, the agents then interact with the simulated environment and other agents (Johnson et al., 2021).

The sum of the behaviors expressed by the agents is the model output which in turn, as summed by the dynamics of the individuals, provides an indication of population dynamics (Johnson et al., 2021; Thomsen et al., 2019; Mortensen et al., 2021). A general ABM consists of a series of steps, wherein each agent makes a series of “decisions”. A 2D or 3D domain is supplied, to make the ABM spatially explicit.

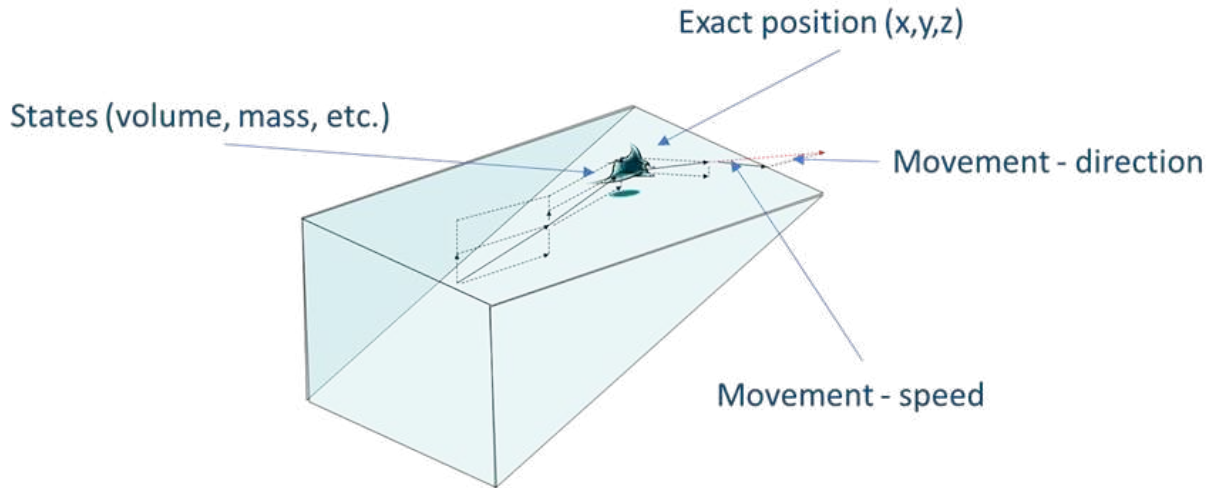


Figure 6.4. Example of Traits Possessed by Individuals in ABM

In ABM, every agent possesses individual and unique traits, simulating the variation in real world populations.

As in Johnson et al. (2021), initially, agents are released into the model domain and each agent attains the traits and states defined by the model. While the value of each trait will be different between the agents due to the stochastic selection processes defined in the ABM, they remain the same throughout the life of the agent. States, such as weight of the agent, distance traveled, etc., will change over the course of the agent's life. Ultimately, decisions made by the agents are based on their traits, combined with external forcings and internal states, which will result in a range of behaviors. This decision process of the agent takes place in form of a decision tree (**Figure 6.5**) where the yes/no answer leads to a new decision and when the end of the decision tree is reached, behaviors are executed, state variables are updated, and the process cycles to the next timestep.

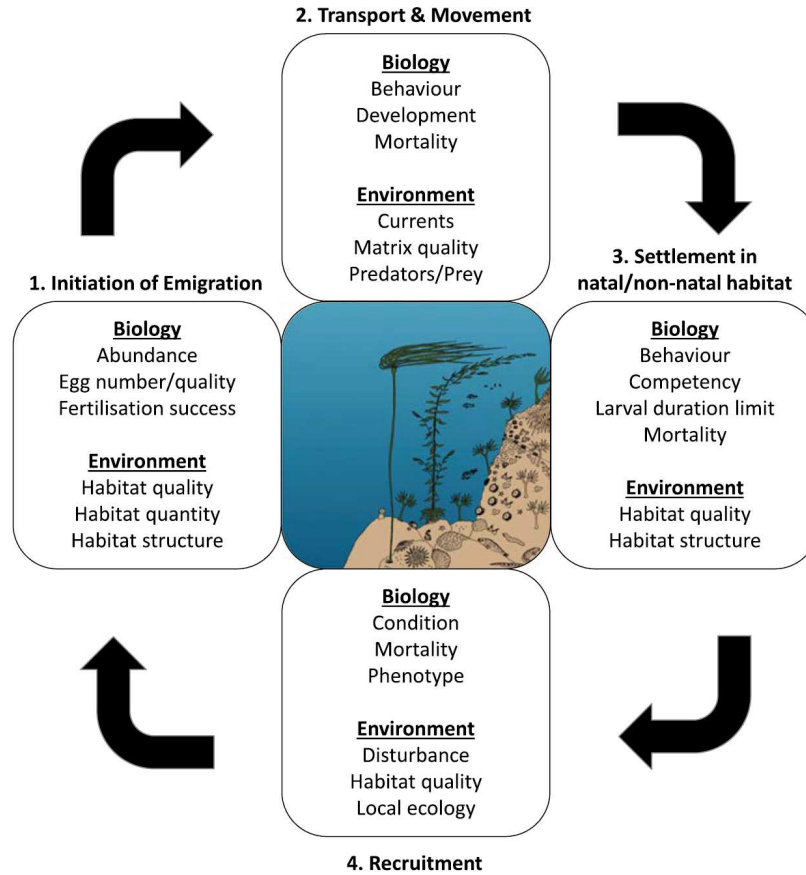


Figure 6.5. Stages of Successful Larval Dispersal

An example diagram showing the stages of larval dispersal to recruitment (From Swearer et al., 2019)

6.2.2 Rationale for Agent-Based Modeling

According to An et al. (2021), ABMs are applied under one or a combination of the following circumstances:

- agents express individual differences for some traits, and these are determinant in agent behavior
- agents interact differently locally
- agents live in time-varying and heterogeneous environment(s)
- agents adapt their behavior to the current state of themselves and/or their environment.

As the last three bullet points are applicable in different proportions to the three target species, the ABM approach was chosen due to its ability to more realistically encapsulate relevant larval transport characteristics. More specifically, it was deemed that the ABM was better able to capture:

- Settlement rate and population abundance as a function of mortality and growth parameters (Allain et al., 2007)
- Settlement probability as a function of life stage, substrate material, and environmental variables including temperature, water depth, and salinity
- Dispersal patterns, and hence recruitment rates at different sink areas, as a result of larval swimming speeds (Faillettaz et al., 2018)
- Vertical migration patterns of larvae as a function of daylight and tidal conditions (Jenkins et al., 1998; Benson et al., 2021).

Inclusion of these variables ultimately allowed for dispersal and settlement patterns to be simulated more accurately in relation to the OSW scenarios than what could have been achieved with standard passive drift particle-tracking models and/or with 2nd order advection-dispersal transport models. (Johnson et al., 2021) Another main rationale for using ABM in this study is the capability to keep track of start and end positions of all simulated organisms which in turn is the basis for connectivity analysis. In general, the term “biophysical modeling” is used to refer to the combination of HD modeling and ABM modeling.

6.2.3 Approach for Larvae Agent-Based Modeling

ABM was used to simulate the larval transport of selected species, namely the sea scallop (*Placopecten magellanicus*), surfclam (*Spisula solidissima*), and summer flounder (*Paralichthys dentatus*), and changes in these transport patterns, if any, arising from the alteration of oceanographic processes induced by the OSW build-out scenarios.

The models established for this study were developed using ABM Lab, which is part of DHI’s commercially available software suite, MIKE Powered by DHI. ABM Lab offers an open and flexible coding environment for defining and customizing simple to advanced biological traits and processes using a series of user-defined arithmetic expressions and state variables, which allows simulated agents (e.g., larvae) to react and interact dynamically changing virtual environment. This is facilitated by MIKE Zero that allows for seamless integration of agent-based models with state-of-the-art 2D and 3D hydrodynamic models using a coupled Eulerian-Lagrangian model framework.

In the integrated model, agents are not constrained by the resolution from other model output and can move independently over the grid resolution of other applied models (e.g., the HDM). The agents can gather information from the grid cells that they currently occupy as well as the surrounding cells, which drives the decision-making process of each individual agent. (Johnson et al., 2021)

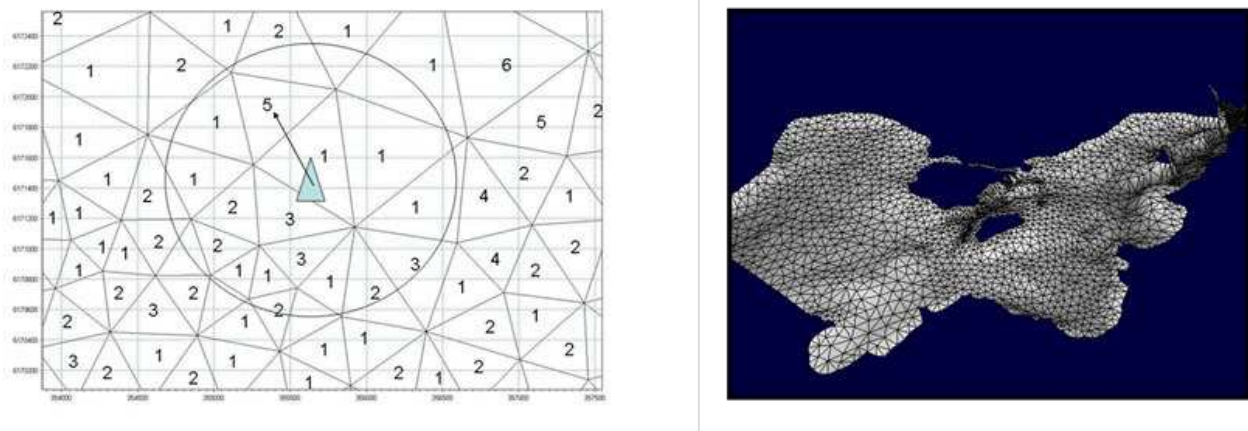


Figure 6.6. Example of an Agent Navigating Grid Cells

Left: details of the HD mesh; right: full ABM for an ocean basin. Agents in ABM lab can navigate in the same domain as the HDM, gathering information from the grid cell that the agent occupies and the surrounding cells, however the agent’s movements are not confined by the resolution of the grid cells.

Furthermore, external model time variable forcings can be introduced into the ABM as being either variable or constant across the whole spatial domain. An example of a spatio-temporally varying forcing is 2D wind fields derived from outputs of meteorological models. (Johnson et al., 2021)

The executed general Agent-Based Modeling steps included:

- Identifying relevant traits and movement behaviors (e.g., vertical movement with temperature) and associated state variables needed for each species to specify the ABM templates
- Where necessary, developing unique ABM larvae templates for each target species through customizing an existing template with algorithms and expressions that represent pertinent movement behavior variables
- Parameterizing ABMs for the covered traits variables (e.g., spawning, life cycle, mortality, movement, and settlement suitability characteristics) for each target species and coupling them with HDM output
- Executing model testing and calibration of baseline larvae dispersal by iteratively running model set-up variations until a satisfactory level of model performance was achieved
- Running production ensemble models for each target species through coupling the calibrated model to the related full HDM output files for:
 - the baseline scenarios, and subsequently
 - the build-out scenarios.

As indicated, initial modeling focus was on establishing customized baseline ABMs for each target species through template parameterization (i.e., template development and parameterization). This consisted of establishing the range of behavioral decision rules and state variables, fitted to match the selected species of larvae. This further involved adjusting the templates to fit the identified traits of target species and subsequent parameterization of these behaviors with literature-sourced values⁴. Model set-up also required initialization of the model, which generally entailed determining when, where, and how the target species larvae agents spawn and should be released into the model domain. As an ensemble modeling approach was applied, a technique where multiple model clones runs are executed (see **sections 6.2.4 and 6.4.5**), the process of determining model initialization and ensemble specifications was closely aligned.

The templates were also adjusted based on an extensive testing and calibration processes (including accuracy analysis) before the larvae build-out runs were executed (see **section 7.4**). Once this was completed, both the baseline and scenario build-out scenarios runs were executed through coupling with the applicable HDM output files. It should also be mentioned that per best practice, the ABM templates are documented in detail in **Appendix B** following the *Overview, Design concepts and Details Protocol for Describing Agent-Based and Other Simulation Models* (ODD; Grimm et al., 2020).

6.2.3.1 Super-Agent Methodology

The concept of a *super-agent* was used in the present study's models due to the high fecundity rates of mature individuals of the target fish and scallop species, each of which typically produces in the range of millions of eggs per spawning season. This allowed for the aggregation of numerous individual agents into a single entity, and is a common approach employed in ecological modeling (Scheffer et al., 1995). Aggregation of this form compacts similar pieces of information and reduces computational load for the simulation, preventing run-time from increasing beyond practical limits. Within the super-agent, the proportion and attributes of zygotes and larvae are varied and monitored over time, such that they undergo growth and mortality processes over the simulation period and are extracted and removed from the super-agent when they die or settle successfully. An illustration of this concept is shown in **Figure 6.7**. Implementation of the Super-Agent Concept.

⁴ In the cases where literature values did not exist for the species, proxy values from comparable species were applied.

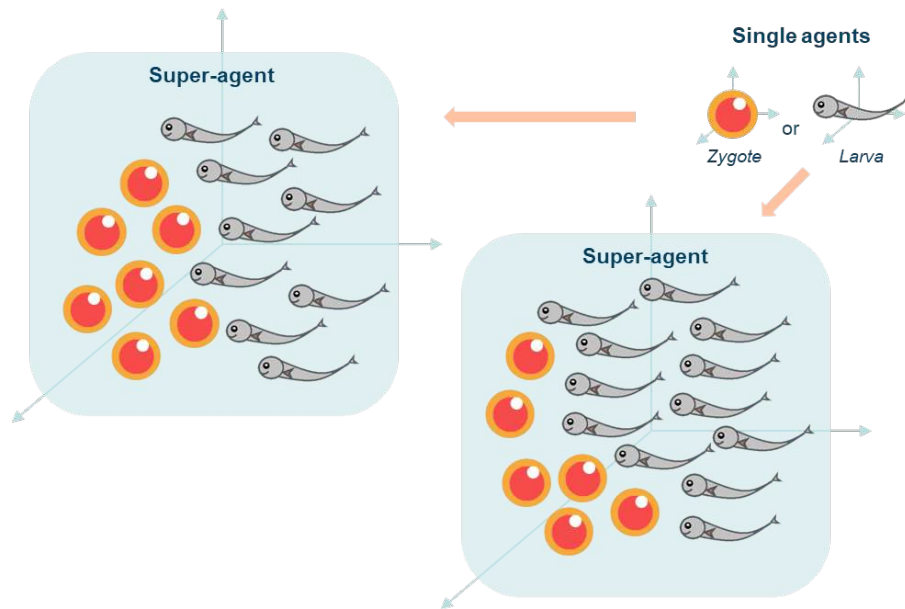


Figure 6.7. Implementation of the Super-Agent Concept

Individual zygotes and larvae are aggregated as super-agents, and progress spatially through the model domain as a single unit. Each super-agent comprises either zygotes or larvae or both zygotes and larvae, with the ratio of agent types determined by arithmetic equations governing the growth and mortality processes of the super-agent.

While relatively simple to implement, there are drawbacks to this approach, one being that it is challenging to relate super-agents to individual agents in time and space (Parry and Evans, 2008). In cases where the movement of super-agents is governed by the same set of rules as those of individuals, spatial clustering of individual agents may emerge i.e., super-agents may occupy fewer cells and show more limited dispersal patterns than individually modeled agents would. For spatially explicit ABMs it is therefore important to consider tests to compare the results of applying different super-agent scaling factors in the model (Parry and Bithell, 2012).

Additionally, **Figure 6.8** shows the parameterized life stages as modeled by a typical super-agent. Each of the arrows is a decision point in the model affected by the probability of mortality, effects of the surrounding environmental stimuli, age-dependent sigmoidal gain probability curves and in the end, the suitability of the substrate habitat in which the agent settles. The parameterized movement behavior of the super-agents differ across species and are illustrated separately in the subsequent sections in **Figure 6.14** for sea scallop, **Figure 6.20** for surfclam, and for summer flounder **Figure 6.25** (vertical movement) and **Figure 6.26** (horizontal movement).

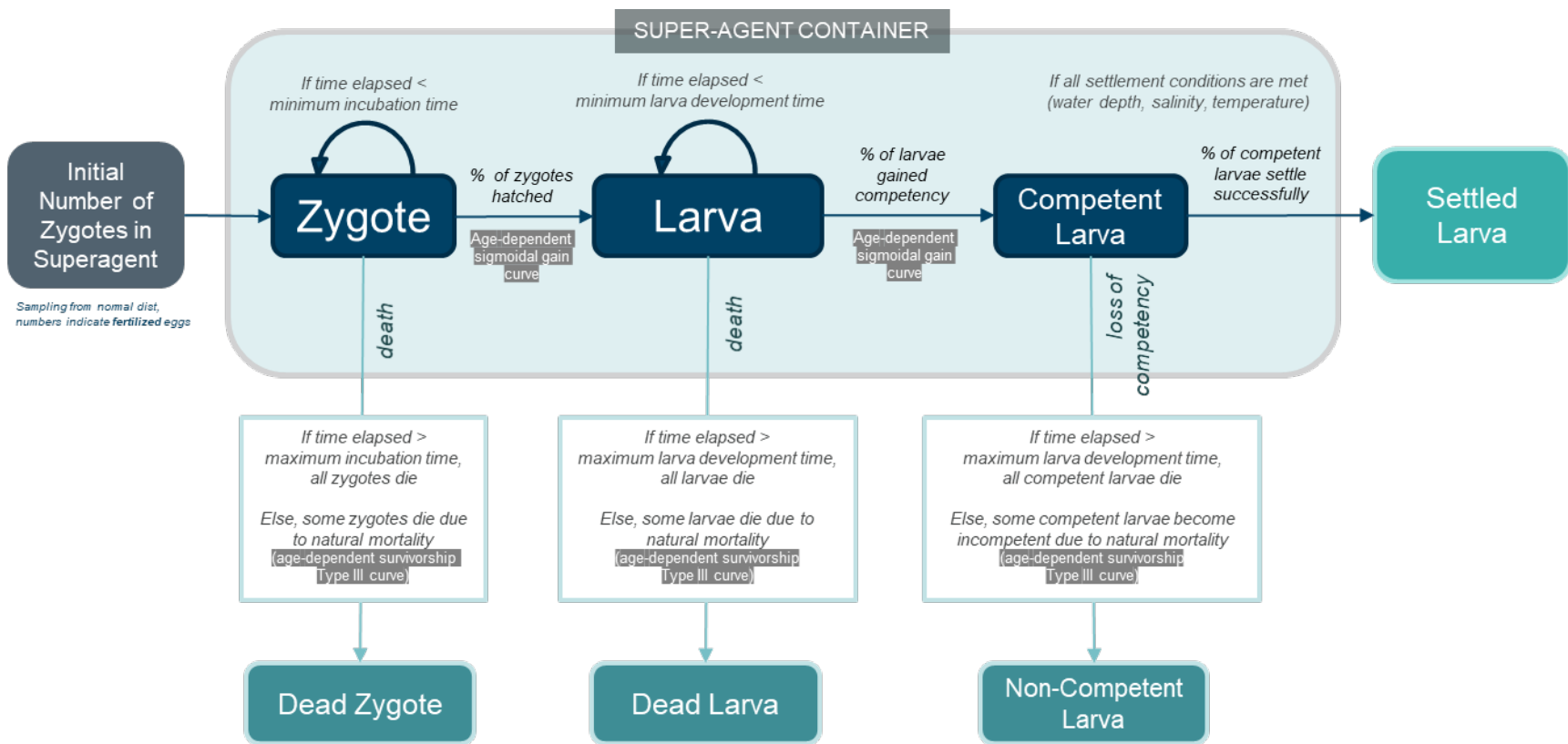


Figure 6.8. Parameterized Life Stages of a Super-Agent in the ABM Templates

A super-agent container carries zygotes and larvae, which eventually die, become incompetent, or settle successfully.

6.2.3.2 Stochasticity

It is important to emphasize that stochasticity was applied in the model to varying degrees. The following processes are either partially or fully dependent on stochastic processes:

- Upon the release of each super-agent, a random number is sampled from a normal distribution to determine the number of zygotes to be contained within the super-agent, in order to account for the varying levels of fecundity of each individual mature reproducing adult. The distributions from which random numbers are selected are based on average fecundity values and standard deviations found in the literature.
- Upon the release of each super-agent, random numbers are sampled from a normal distribution (based on values found in the literature) to determine the following growth parameters: minimum and maximum zygote incubation time and minimum and maximum larval development time, to account for varying pelagic larval duration for each individual super-agent.
- Mortality rates from time-step to time-step are controlled by an age-dependent survivorship Type III curve (Houde, 2002), with curve parameters input by the user.
- Zygote incubation and larval development rates from time-step to time-step are controlled by an age-dependent sigmoidal gain/loss curve (Tian et al., 2007), with curve parameters input by the user.
- Release points of super-agents are randomly determined by the model (within the user-determined release areas, based on potential spawning habitat) to account for the indeterministic nature of mature adult migration. (Johnson et al., 2021)

6.2.4 Ensemble Modeling Approach

Ensemble modeling is an approach used widely in climate change and agent-based modeling (Parker, 2013; An et al., 2021). An ensemble is a group of models, or model clones, that are run repeatedly (Murphy et al., 2004) where either one or a selection of variables are altered in each model run or, where stochasticity is inherent in the model, the variables are unchanged. The results are then aggregated and, due to the generation of multiple result datasets, typically analyzed statistically.

In the present study, the ABM predicts and estimates larval movement and behavior using probabilities and stochastic functions (e.g., An et al., 2021), and each model run therefore does not yield identical results. For example, agents are released from within the designated spawning areas randomly, and the incubation time for eggs to hatch, larval development time to reach competency, and mortality rates are sampled from within a normal distribution of a range of feasible values found in literature (see section 6.4.2 – 6.3.4). An ensemble modeling approach offers the ability to manage model uncertainty and increase the robustness of model results given this stochasticity. Ensemble modeling was achieved by keeping the initial conditions and inputs into the model the same, (i.e., the same hydrodynamic forcings, time period, number of larvae spawned, and larvae behavior are the same for each model simulation within the ensemble) and running the same model set-up (clone) multiple times. The results from each model run were then aggregated.

Aggregating multiple model simulation results allowed for the uncertainty in the model to be evaluated and provided more robust results than relying on one simulation result alone. See **sections 6.4.5 and 6.8** for details of ensemble modeling methods and results post-processing.

6.3 Connectivity Analysis Approach

The term marine connectivity explored in this study relates to the wider concept of Marine Functional Connectivity defined by Darnaude et al. (2022) as ‘...the dynamic spatial exchange of biomass, individuals, genes, and energy that results from the collective lifetime movements of all marine organisms, from bacteria to top-predators’. Drawing on a more specific definition of connectivity, ‘the quantification of the exchange of pelagic life stages between geographically distinct habitats or populations’ (Hansen et al., 2024). The approach of this Project was to understand how the exchange of larvae of target species between geographically distinct common larvae spawning and settlement areas could be disrupted by the oceanic changes induced by the presence of OSWs. It is emphasized that this approach was taken as connectivity is essential for maintaining ecological processes that occur at multiple scales across biological realms (Darnaude et al., 2022).

As the foundation of this analysis, Lagrangian agent-based models (Hansen et al., 2024), were already available from the ABM modeling of larvae dispersal (see **section 6.2**), the additional methodological approach for carrying out the connectivity analysis involved the following:

- establishing distinct spawning areas (i.e., which was already required for ABM initialization) and ‘destination areas’
- carrying out extensive data processing, through dedicated scripting, to ‘join’ the model results to show the spawning and destination areas for target species larvae
- Processing the connectivity results in a manner that illustrates estimated alterations in connectivity that could potentially result from the OSW farms.

Additional detail on the specifics of these methodological tasks is outlined in **section 6.6**.

6.4 Agent-Based Model Set-Up and Parameterization

6.4.1 Applied Datasets

Relevant sources of information on benthic habitat and larval life history, spawning habitats, distribution, and abundance were gathered from organizations, published literature, bibliographic and library sources, and geographic information system (GIS) datasets. **Table 6.1** below provides a list of general datasets used for the ABM.

Table 6.1. Datasets Employed for the ABM

Data Source	Description	Used for
USGS CONMAP Sediments Grainsize Distribution (USGS, 2005)	Maps of sediment classifications based on grain size distributions. GIS polygon layer.	Settlement suitability maps.
NOAA NCEI Multibeam Bathymetry Database (MBBDB) (NOAA, 2004)	Comprehensive database of multibeam bathymetric data on a global scale.	Settlement suitability depth parameter.
GEBCO Gridded Bathymetry Data (GEBCO, 2020)	Global terrain model for ocean and land at 15 arc-second intervals.	Settlement suitability depth parameter.

Data Source	Description	Used for
NOAA Essential Fish Habitat Data (EFH) Inventory (NOAA, 2018)	Geospatial habitat information of the species currently mapped in the NOAA Essential Fish Habitat Mapper	Calibration and validation of ABM settlement patterns for all species.
School for Marine Science and Technology (SMAST) Scallop Biomass Data (Stokesbury, 2016)	Scallop catches from NOAA Northeast Fisheries Science Center (NEFSC) scallop dredge surveys during the years 1966 to 2014. Accessed from Northeast Ocean Data Portal.	Calibration and validation of sea scallop ABM settlement patterns.
NEFSC Sea Scallop Potential reproductive output (Stokesbury, and Bethoney, 2020)	Spatial representation of regions of lower or higher sea scallop reproductive potential.	Identifying spawning locations for sea scallop.
Northeast Fisheries Science Center (NEFSC) Sea Scallop Survey (2022, Requested, not publicly available)	Distribution and abundance of scallops and associated fauna obtained via standardized sea scallop dredge and the stereo-optic towed camera array (HabCam).	Calibration and validation of sea scallop ABM settlement patterns.
NEFSC Scallop Biomass (Fogarty, 2019)	This dataset contains survey points for scallop catches from NOAA NEFSC scallop dredge surveys during the years 1966 to 2015. The survey collected information on total scallop biomass and meat weight biomass.	Calibration and validation of sea scallop ABM settlement patterns.
Northeast Fisheries Science Center Bottom Trawl Survey 1963 – 2023 (2023, Requested, not publicly available)	This is the Northeast Fisheries Science Center Bottom Trawl Survey database for Northwest Atlantic marine organisms, including sea scallop and surfclam. Survey cruises use a bottom trawl to sample randomly selected stations in an attempt to delineate the species.	Calibration and validation of sea scallop and surfclam ABM settlement patterns. Selection of surfclam spawning areas, based on abundance density.
NOAA Scallop Survey Station Catch (2022, Requested, not publicly available)	NOAA sea scallop survey data, with abundance data from 1982- 2022.	Calibration and validation of sea scallop ABM settlement patterns.

Data Source	Description	Used for
NOAA Clam Survey Station Catch (2022, Requested, not publicly available)	NOAA clam survey data, with abundance data for surfclam from 1982- 2022.	Calibration and validation of surfclam ABM settlement patterns. Selection of surfclam spawning areas, based on abundance density.
Northeast U.S. Ichthyoplankton Dataset – EcoMon and MARMAP (Hare, 2015)	Compilation of multi-species ichthyoplankton collection programs including the Marine Resources Monitoring, Assessment, and Prediction program (MARMAP, 1977 - 1987) and Ecosystem Monitoring (EcoMon, 1999 - present) program. Both datasets cover the Northeast U.S. Shelf from Cape Hatteras, North Carolina, to Cape Sable, Nova Scotia.	Used to determine spawning areas
NEFSC Summer Flounder Egg Data (2022, Requested, not publicly available)	Summer flounder egg data through 2021 and added length abundance (individuals per 10 m ² sea surface) for 1 mm length bins from 1 to 14 mm.	Used to determine spawning areas
NEFSC Interpolated Biomass (Shmookler, 2016)	Interpolated biomass for sea scallop and summer flounder, for spring and fall seasons.	Calibration and validation of sea scallop and summer flounder ABM settlement patterns.

6.4.1.1 United States Geological Survey Continental Margin Mapping (CONMAP)

The Continental Margin Mapping Program (CONMAP) sediments grainsize distribution for the United States East Coast Continental Margin dataset is the result of a joint program conducted by the USGS and WHOI which commenced in 1962. The sediment map, see **Figure 6.9**, is a compilation of grain-size data classified using the Wentworth (1929) grain-size scale and the Shepard (1954) scheme of sediment classification (USGS, 2005).

The sediments grainsize distribution data layer served as the basis of substrate suitability maps created for use in the ABM models. These maps were developed for sea scallop, surfclam, and summer flounder using the ABM mesh as the underlying template. Indices were thereafter derived for each substrate type based on the substrate preferences of pre-transformation larvae of each target species. For example, a grid cell located at an area of a preferred substrate type was given a higher substrate suitability index value than a grid cell located at an area of a less preferred substrate type.

The substrate suitability maps were applied as inputs in the ABM and directly influence the probability of settlement of a competent larva at any given geographical location within the model domain. An example of the sea scallop benthic suitability map is presented in **Figure 6.10**.

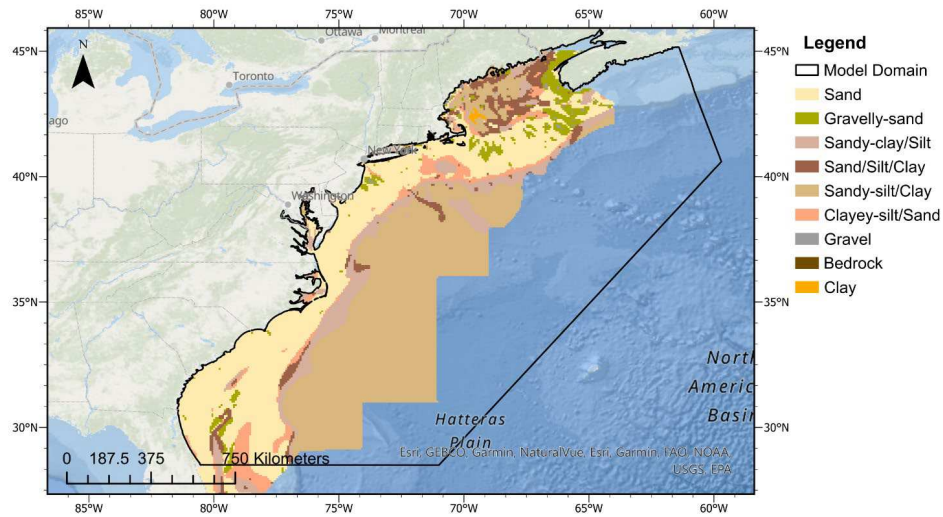


Figure 6.9. USGS Sediment Map

Atlantic benthic habitat data provided by USGS Continental Margin Maps (CONMAP) program (2005).

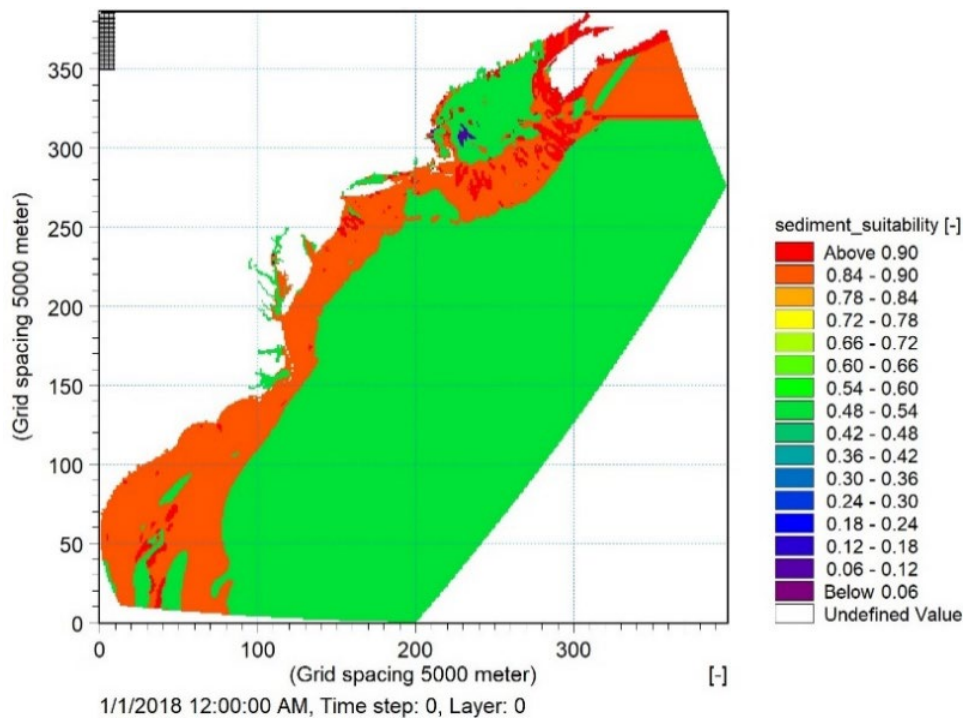


Figure 6.10. Substrate Suitability Map for Sea Scallop

substrate suitability map for sea scallop, derived from substrate preference of pre-transformation larvae and USGS sediment map.

6.4.1.2 GEBCO and NOAA NCEI: Bathymetric Data

The bathymetric data used in the HDM developed for this study is described in **Section 2.2**. For the purpose of the ABM, this bathymetric data serves as a guideline for determining the spatial extent of spawning grounds for each modeled species, based on published research data on spawning water depths.

The U.S. NOAA survey archive at NCEI provides high resolution gridded bathymetries for the project area, which is crucial for determining the settlement locations of modeled species, especially species for which settlement is only viable within set water depth thresholds (e.g., summer flounder larvae which are only observed to settle in shallow estuarine areas). Data from the GEBCO was used as a source for deep-water bathymetry.

6.4.1.3 NOAA Essential Fish Habitat (EFH) Data Inventory

Essential Fish Habitat (EFH) was officially defined by the U.S. Congress as "those waters and substrate necessary to fish for spawning, breeding, feeding or growth to maturity." in the 1996 amendments to the Magnuson-Stevens Fishery Conservation and Management Act (NOAA, 2007).

NOAA Fisheries and the regional fishery management councils provide spatial data for designated EFHs that are vital for American fisheries, covering approximately 1,000 federal managed species. Pertaining to the present study, data was accessed for the Mid-Atlantic EFH, which is designated and described by the MAFMC for 12 managed species in NOAA Fisheries' Greater Atlantic region, as well as the New England EFH, which is designated for 28 managed species by the New England Fishery Management Council (NEFMC) in NOAA Fisheries' Greater Atlantic region (NOAA, 2018).

Spatial information was accessed from the EFH data inventory for the purpose of calibration and validation of the ABM. The available data relevant for the study are as follows:

- Essential Fish Habitat for sea scallop in the Greater Atlantic region for:
 - All life stages
- Distribution and abundance of surfclam in the Greater Atlantic region for:
 - Juveniles
 - Adults
- Distribution and abundance of summer flounder in the Greater Atlantic region for:
 - Juveniles
 - Adults.

EFH areas were compared to ABM settlement results to allow for a qualitative assessment of model performance. Higher densities of larval settlement are expected to occur within the EFH boundaries, and the ABM model was calibrated accordingly to align settlement within these areas (see **section 7.4**).

6.4.1.4 SMAST and NEFSC: Sea Scallop Abundance and Biomass Data

The University of Massachusetts Dartmouth's School for Marine Science & Technology (SMAST) has performed extensive drop camera surveys aimed at providing fishery resource managers, marine scientists, and fishing communities with an independent assessment of the U.S sea scallop resource and its associated habitat (Stokesbury, 2016). This dataset contains survey points for scallop catches from NOAA Northeast Fisheries Science Center (NEFSC) over scallop dredge surveys conducted over the years of 1966 to 2014, with estimates of total scallop biomass empirically derived from the drop camera survey image data.

The NEFSC Sea Scallop Survey began in 1980 and is an annual quantitative cruise to determine the distribution and abundance of Atlantic scallops and Icelandic scallops, covering the three main areas of: MAB/Southern New England, Southern New England/Georges Bank, and Georges Bank with earlier surveys spanning as far south as Cape Hatteras (NEFSC, 2021). This dataset consists of point data of Scallop abundance and biomass.

The Pattern Oriented Modeling (POM) methods, where the temporal and spatial patterns of observed sea scallop data were compared against the ABM outputs are detailed in **section 7.4.1.1**. The NEFSC Sea Scallop Survey were used for the validation of the sea scallop model via the POM due to the greater spatial coverage of this dataset.

An additional interpolated scallop biomass raster dataset based on the NEFSC scallop survey point data (Shmookler, 2016) was also qualitatively compared to ABM settlement densities and patterns to calibrate the ABM model.

6.4.1.5 NEFSC Sea Scallop Potential Reproductive Output

Potential reproductive potential of sea scallop for the MAB, New York and Georges Bank area has been estimated by Stokesbury and Bethoney (2020). This spatial dataset displays a score of low to high reproductive potential (i.e., areas where sea scallops are most likely to spawn), based on abundance and size data collected via drop camera surveys. This dataset was used to determine spawning locations, and agent release proportions from each spawning area, for sea scallop.

6.4.1.6 NOAA Scallop and Clam Surveys

NOAA runs annual bottom trawl surveys which document abundance and length data a surfclam and sea scallop, among other species. This dataset was requested directly and is not publicly available. These point data were used to qualitatively calibrate the surfclam and sea scallop ABM, by comparing ABM settlement results to these abundance data.

6.4.1.7 NOAA Ecosystem Monitoring (EcoMon) Data and NEFSC Summer Flounder Larval Data

The EcoMon data set was provided by the Biological & Chemical Oceanography Data management Office (BCO-DMO), and it contains the abundance and proportion of ichthyoplankton of the Northeast U.S. Shelf. The ichthyoplankton data was collected from surveys including the Marine Resources Monitoring, Assessment, and Prediction (MARMAP) from 1977 to 1987 and the subsequent Ecosystem Monitoring (EcoMon) programs.

This dataset contains zooplankton biomass data sampled by bongo nets during the aforementioned surveys conducted at 120 randomly selected stations and 35 fixed stations throughout the continental shelf and slope of the northeastern U.S., from Cape Hatteras, N.C., to Cape Sable, Nova Scotia, and cover all of Georges Bank and the Gulf of Maine (NOAA, 2018).

6.4.2 Sea Scallop

6.4.2.1 General Overview

Atlantic sea scallops (*Placopecten magellanicus*), hereafter referred to as ‘sea scallops’, are a bivalve mollusk that occur in continental shelf waters of the northwest Atlantic from the Gulf of St. Lawrence to North Carolina. Sea scallops are an important commercial fishery species in the northwest Atlantic region and are managed by the NEFMC. Two major stocks are recognized relative to the project area: a Georges Bank stock and a MAB stock (Stokesbury, 2012; Stokesbury et al., 2016). In U.S. waters, the sea scallop fishery is managed by rotating fishing access among 1) areas open to sea scallop fishing, 2) areas permanently closed to all fishing to protect seafloor habitats from destruction, 3) areas temporarily closed to sea scallop fishing, and 4) areas open to limited sea scallop fishing (NEFMC, 2014). Sea scallops can live to 18 years, but most in the region are less than 9 years old.

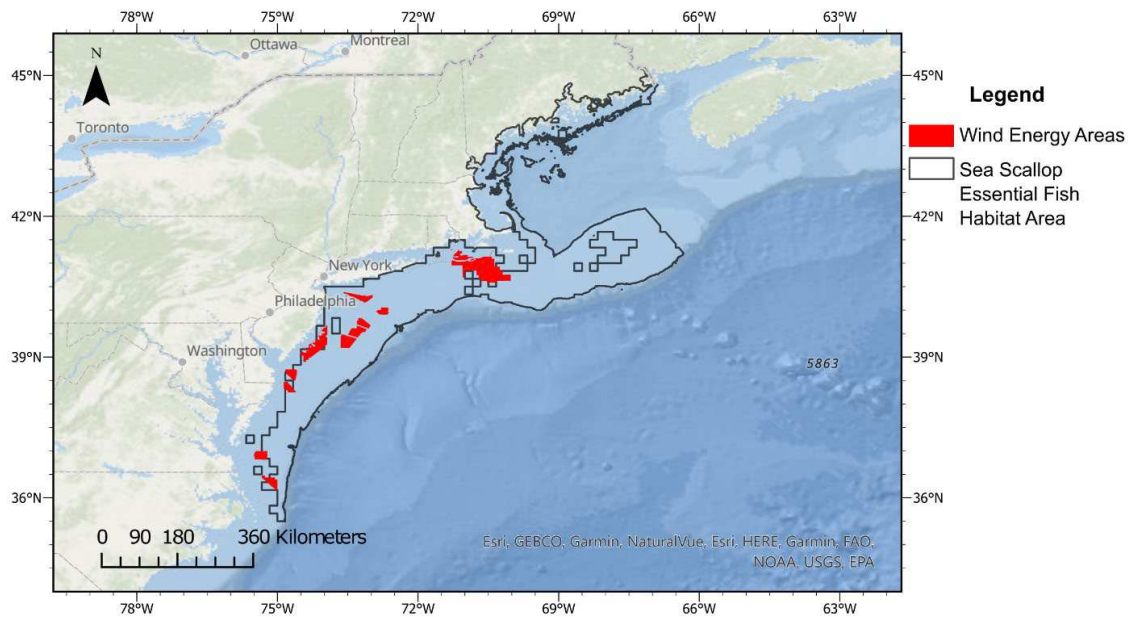


Figure 6.11. Sea Scallop Essential Fish Habitat Map

Sea scallops EFH in the Northwest Atlantic Ocean, extending from the Gulf of Maine to Cape Hatteras, North Carolina (NOAA, 2018).

Sea scallops occur within relatively narrow ranges of temperature, salinity, and water depth. They prefer water temperatures between 10°C and 15°C, with 21°C being lethal (Stewart and Arnold, 1994), and salinities greater than 26 psu (Hart and Chute, 2004). Salinities of 16.5 psu or lower can be lethal (Stewart and Arnold, 1994). Sea scallops are most commonly found in water depths ranging from 10 to 110 m but are found at depths as low as 2 m and as great as 380 m (Hart and Chute, 2004).

Sea scallops prefer areas with high current flow (Hart and Chute, 2004). Habitat-specific flow rates are difficult to measure in the field but estimated values ranging from 0.03 to 0.13 m/sec have been used in habitat suitability models (Torre et al., 2018).

6.4.2.2 Super-Agent Class Parameterization

The simulation period for the sea scallop model (May 1 to December 31) was selected to capture zygotes and larval activity during critical spawning seasons and larval migration periods. The parameterization of sea scallop spawning, life cycle, mortality, movement, and settlement suitability characteristics are detailed in the subsections below.

6.4.2.3 Spawning

Sea scallops spawn primarily during fall (August to October), to the North of Hudson Canyon, but spring events occasionally occur to the south, off Delaware and into the MAB (Hart and Chute, 2004; Stokesbury et al., 2016). Spawning occurs in waters along the continental shelf, in the MAB, Georges Bank, and the Gulf of Maine at temperatures from 6.5 to 16°C (Hart and Chute, 2004). Mature adults do not migrate during spawning seasons and sea scallop super-agent release areas (**Figure 6.12, right**) were directly derived from reproductive potential from Stokesbury and Bethoney (2020) and observed distribution and abundance data of sea scallops collected from NEFSC sea scallop surveys (NEFSC, 2021).

A total of 34,272⁵ sea scallop super-agents were released over the entire simulation period in the model domain, with each super-agent initialized to contain a number of zygotes that is sampled from a normal distribution (mean = 50,000,000, standard deviation = 200,000) in order to account for the varying levels of fecundity of each individual mature reproducing adult. The normal distribution was roughly based on the Langton et al. (1987) estimation of fecundity of sea scallops from the Gulf of Maine. Egg production by adult sea scallops was related exponentially to size (shell height). For example, an individual with a shell height of 50 mm was estimated to produce one million eggs in one season whereas a 100 mm individual produced an estimated 29 million eggs in one season (Langton et al., 1987). Fecundity estimates reported by Langton et al. (1987) ranged from 1 to 270 million eggs per individual.

An analysis of proportional biomass densities was carried out on NEFSC survey data for each spawning release area within the model to determine the relative number of agents to be released from each spawning location. This analysis revealed that of the total 34,272 agents, 17,568 (51.3%) would originate from MAB, 2,880 (9.4%) from Long Island, 11,520 (33.6%) from Georges Bank, and 2,304 (6.7%) from the Gulf of Maine. Super-agents were spawned randomly within the polygons shown in **Figure 6.12**, within set time frames presented in **Table 6.2**. In order to maintain computational efficiency, the number of super agents released was restricted to below 35,000. Sea scallop super-agents were released during the major spawning windows for their region, but were not released continuously in order to keep within this computational limit, resulting in the peaks and troughs seen in **Table 6.2**. A summary of parameters related to sea scallop spawning is presented in **Table 6.3**.

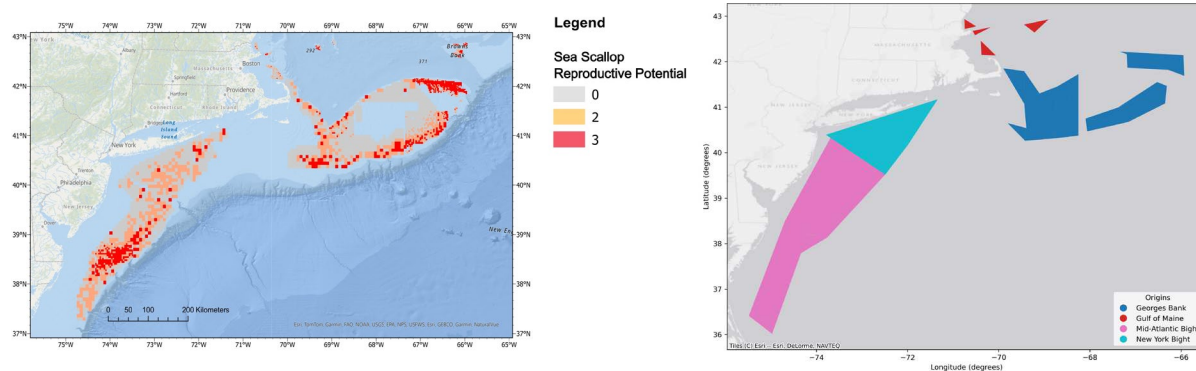


Figure 6.12. Sea Scallop Abundance Map and Model Spawning Areas

LEFT: Sea Scallop reproductive potential from Stokesbury and Bethoney 2020, RIGHT: Release areas in the sea scallop model, derived based on observed abundance data (NEFSC, 2021).

⁵ This amount of super agents was derived from various model testing aimed at optimizing computational efficiency.

Table 6.2. Sea Scallop Release Period and Volume

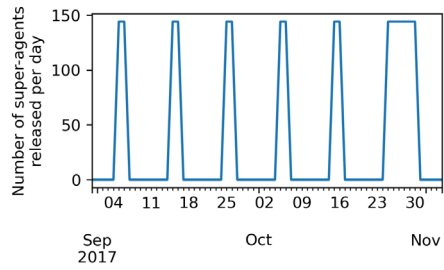
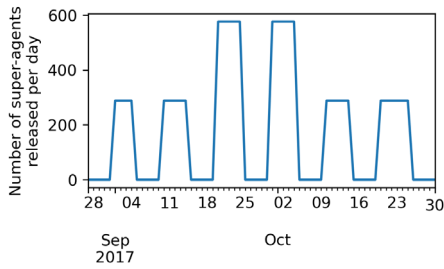
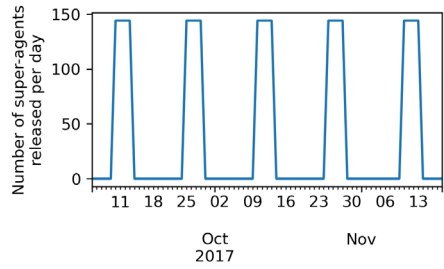
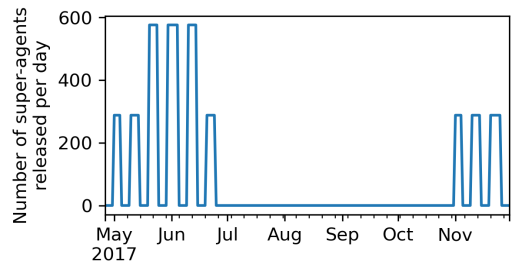
Area(s)	Release Period	Time Series
Gulf of Maine Red polygons in Figure 6.12	September 5, 2017, to October 30, 2017	
Georges Bank Blue polygons in Figure 6.12	September 1, 2017, to October 26, 2017 Peak from September 20, 2017, to October 5, 2017	
New York Bight (New Jersey to North Carolina) Pink Polygons in Figure 6.12	September 10, 2017, to November 14, 2017	
Mid-Atlantic Bight Light blue polygons in Figure 6.12	May 1, 2017, to June 25, 2017 with a peak May 20, 2017 to June 14, 2017 Another spawning event, November 1, 2017, to November 25, 2017	

Table 6.3. Sea Scallop Spawning Model Parameters

Parameter	Literature Information/Value	Parameterized Value
Timing and Duration <i>Time of year when spawning is initiated</i>	Fall (Major); Spring (Minor) North of Hudson Canyon fall only, south into Mid-Atlantic Bight Fall and late/summer spring spawning is more common. (Thompson et al., 2014; Hart and Chute 2004)	Release of super-agents in Spring and Fall occurs from May and again in September to end of November. Fall spawning occurs at all locations. Spring release of super agents occurs from May 1, 2017, to June 25, 2017, only in MAB.
Quantities <i>Particle release during spawning</i>	Overall range of <u>1-342.8 million</u> eggs per female across two studies: <ul style="list-style-type: none"> • 2.5-342.8 million (McGarvey et al., 1992) • 1-270 million (Langton et al., 1987) 	Initial number of zygotes sampled from a normal distribution: <ul style="list-style-type: none"> • Mean: 50,000,000 zygotes • Standard deviation: 200,000

6.4.2.4 Life Cycle

Sea scallop eggs hatch in approximately 2 days and transform into pelagic larvae that settle to the seafloor as juveniles after about 35-50 days in the water column, (Hart and Chute, 2004). An overview of the duration of the pelagic stages are as follows:

- Dense eggs (~0.66 mm diameter) are released near-bottom, and likely remain on the sea floor until transformation (Langton et al., 1987).
- Eggs transform into trochophore larvae after approximately two days (Culliney et al., 1974)
- Trochophore larvae transform into veliger larvae in 2 to 5 days (Tremblay et al., 1994)
- Veliger larvae persist for up to 35 days before becoming pediveligers which settle to the seafloor as juveniles in 5-15 days (Tremblay et al., 1994).

An overview of the early life stages of the sea scallop that were simulated in the model are presented in **Figure 6.13** and a summary of applied parameters related to sea scallop life cycle (growth and mortality) are presented in **Table 6.4**.

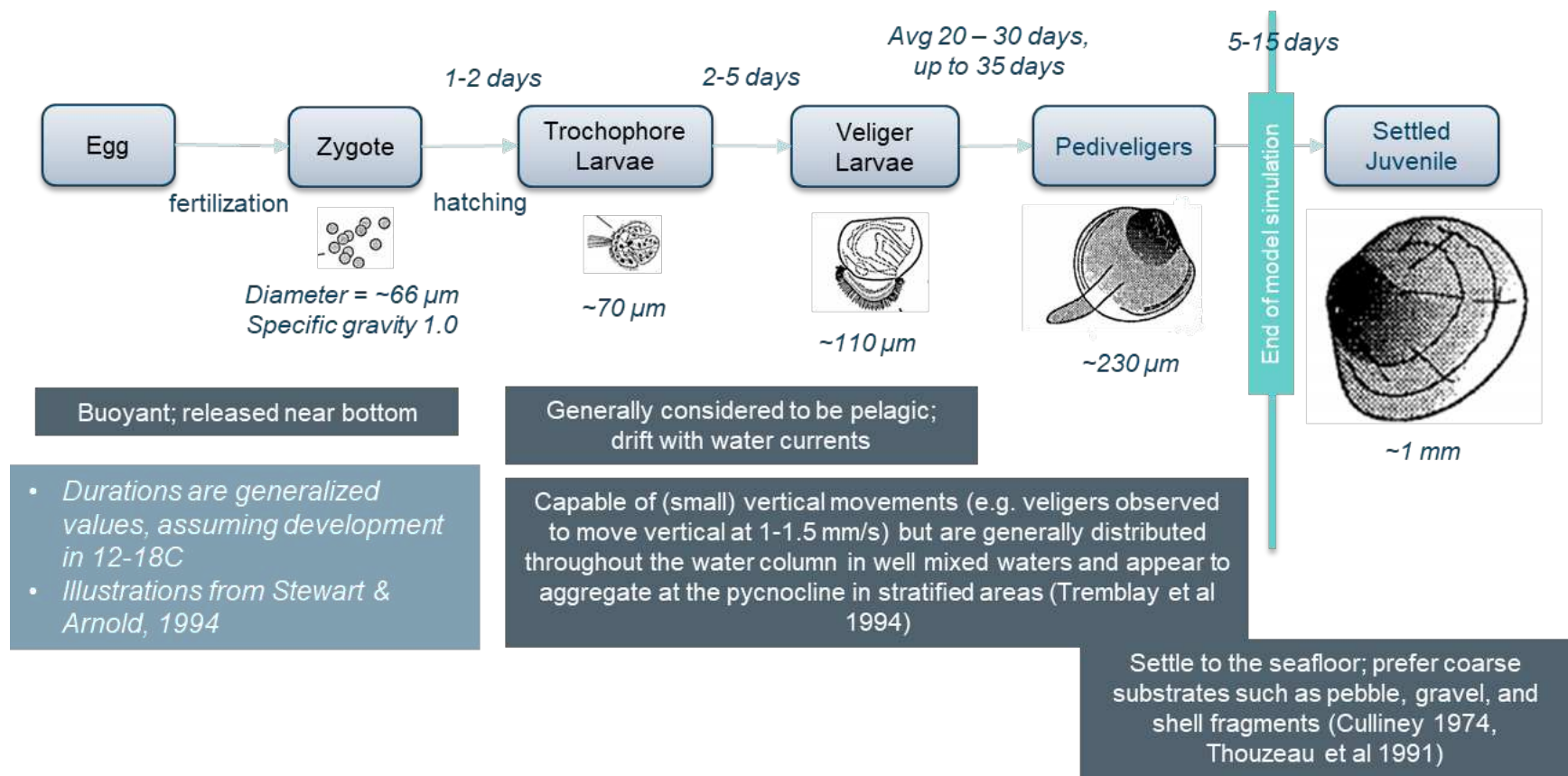


Figure 6.13. Early Life Stages of Sea Scallop as Simulated in the ABM

A sea scallop agent is simulated to undergo life stage transformation from a zygote (fertilized egg) to a pediveliger; at this point it is ready to settle to the seafloor and begin its development to become a juvenile. Life stages beyond pediveliger stage are not included in the model.

Table 6.4. Sea Scallop Life Cycle (Growth and Mortality) Model Parameters

Parameter Type	Parameter	Literature Information/Value	Parameterized Value
Life Cycle	Duration of egg stage <i>Incubation time from egg to larvae</i>	Hatch in <u>30-40 h</u> at 12°C (Culliney et al. 1974)	Minimum zygote duration sampled from normal distribution: Mean: 30 hours Variance: 2 hours Maximum zygote duration sampled from normal distribution: <ul style="list-style-type: none"> Mean: 40 hours Variance: 2 hours All durations are from the time of release of super-agent.
Life Cycle	Duration of larval stage <i>Time spent as a larva before settling/changing state</i>	Overall range of <u>28-82 days</u> across four studies: <ul style="list-style-type: none"> 40-60 days (Hart and Chute 2004) 28-50 days in total – veliger (4-23 days), trochophore (13-28 days), preveliger (28-35 days) (Culliney et al. 1974) 4-6 weeks egg to settled juvenile (McGarvey et al., 1992) 32-82 days (Pearce et al. 2004) 	Minimum larval duration sampled from normal distribution: <ul style="list-style-type: none"> Mean: 32 days Variance: 1 day All durations are from the time of release of super-agent.
Life Cycle	Number of stages between egg and adult <i>Total number of stages between egg and adult</i>	<u>4 stages</u> : egg, trochophore, veliger, preveliger (Culliney et al. 1974)	3 stages modeled: Zygotes, pre-competent larvae, and competent larvae. Trochophore and veliger larvae are broadly categorized under the 'pre-competent larvae' group and pediveliger larvae under the 'competent larvae' group.
Growth	Incubation rate of zygotes <i>Probability that a zygote will hatch and become a larva</i>	Not available	Age-dependent sigmoidal curve for incubation probability. Values are assumed and calibrated through an iterative process (see section 7.4): Maximum incubation probability: 0.7/day
Growth	Competency gain rate of larvae <i>Probability that a pre-competent larva will gain competency</i>	Not available	Age-dependent sigmoidal curve for competency gain probability. Values are assumed and calibrated through an iterative process (see section 7.4): <ul style="list-style-type: none"> Maximum competency gain probability: 0.8/day
Growth	Competency loss rate of larvae <i>Probability that competent larva will lose competency</i>	Not available	Age-dependent sigmoidal curve for competency loss probability. <ul style="list-style-type: none"> Maximum competency loss probability: 1/day

Parameter Type	Parameter	Literature Information/Value	Parameterized Value
Mortality	Mortality parameters <i>Parameters related to the selected mortality</i>	Daily constant mortality of <u>0.25/day</u> (Packer et al. 1999) (not used)	Age-dependent Type III survivorship curve for mortality rate was used in the model.: <ul style="list-style-type: none"> • Minimum daily instantaneous mortality rate: 0.01/day • Maximum daily instantaneous mortality rate: 0.3/day

6.4.2.5 Movement

Trochophores, veligers, and pediveligers are capable of some vertical movement, but are generally distributed throughout the water column in well mixed waters and appear to aggregate at the pycnocline in stratified areas (Tremblay et al., 1994). Additionally, it has been observed that sea scallop larvae can maintain position of their vertical location in the water column to stay near the thermocline. This was implemented in the model by placing a vertical control factor where the sea scallop agent would swim down if the agent's ambient temperature rises to 16.5°C and swim up if the temperature falls to 1°C (Munroe et al., 2018). Thus, at each time step, depending on the dominant life stage of the agents contained in the super-agent, the super-agent exhibits different vertical movement traits.

An overview of the sea scallop super-agent vertical movement traits as simulated in the model is presented in **Figure 6.14** and a summary of parameters related to sea scallop movement is presented in Table 6.5. The sea scallop super-agent is considered to be a passive drifter along the transverse plane, and thus its horizontal movement is purely a function of hydrodynamic forcings (i.e., horizontal current speed and direction).

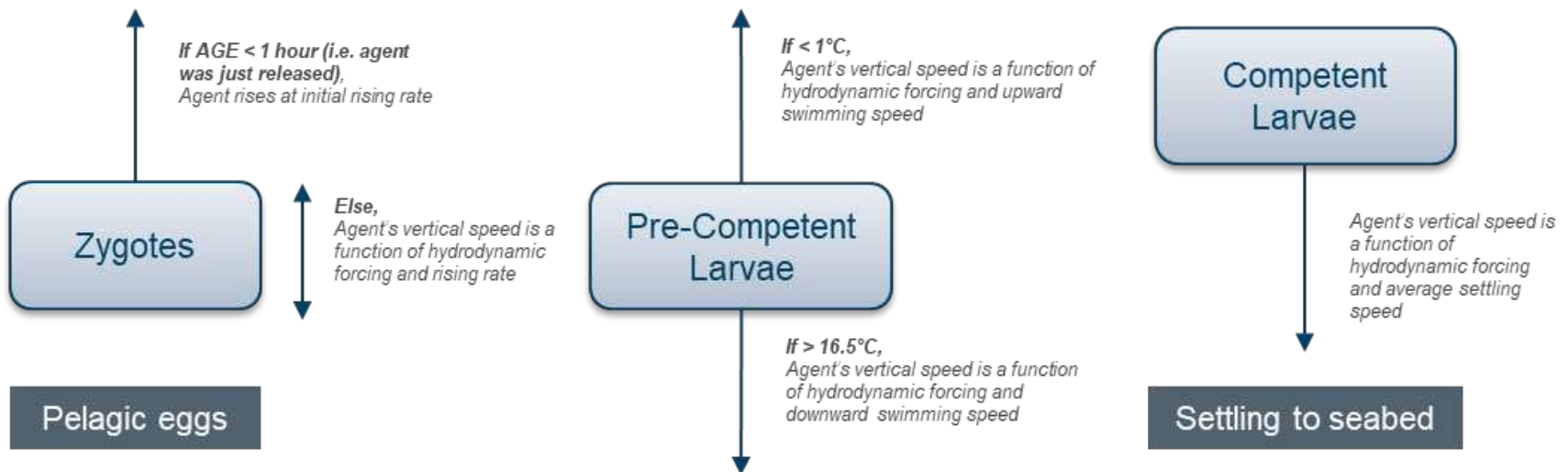


Figure 6.14. Parameterization of Sea Scallop Zygotes and Larval Vertical Movement Characteristics

Sea scallop zygotes are dense and likely stay near the seabed after fertilization. After transformation pre-competent larvae migrate vertically to stay within the thermocline (1-16.5°C) and drift passively in the horizontal. Settle-ready (competent) larvae actively sink and eventually settle on the seabed.

Table 6.5. Sea Scallop Movement Model Parameters

Parameter	Literature Information/Value	Parameterized Value
Buoyancy of egg <i>Maximum buoyancy (positive or negative) speed for fertilized zygotes</i>	<u>Negatively Buoyant</u> eggs (~0.66 mm diameter (Hart and Chute, 2004; Tremblay et al., 1994; Langton et al., 1987)	Upward speed of 0 m/s
Vertical swim speeds <i>Maximum vertical swim speed for larvae, independent of current speeds (m/s)</i>	0.003 m/s (Packer et al., 1999)	Average vertical swim speed sampled from normal distribution: Mean: 0.003 m/s Standard deviation: 0.0005 m/s
Horizontal swim speeds <i>Maximum horizontal swim speed for larvae, independent of current speeds (m/s), if present</i>	0.20 mm/s for a 250 µm veliger (Gallahger et al., 1996) (not used)	Horizontal swim speed is insignificant relative to hydrodynamic forcings – super-agent assumed to drift passively in horizontal plane.

6.4.2.6 Substrate Suitability

At settlement, pediveligers (spat) prefer coarse substrates such as pebble, gravel, and shell fragments over fine substrates like clay and fine sand (Culliney, 1974; Thouzeau et al., 1991). At broad scales (100 m to kms) settlement occurs in areas inhabited by adults (Stokesbury et al., 2016).

Substrate suitability index map for sea scallop (**Figure 6.15**) was developed based on the preferred substrate of young sea scallops, which is coarse substrate i.e. pebbles, shells, gravel, etc. Each 2D grid cell of the model mesh is assigned a settlement suitability index value between 0 to 1, with higher values indicating higher suitability.

Settling is described as a two-step process, where specific conditions must be met in order for the larvae to settle: the super-agent must contain competent larvae and be located in a grid cell where variables are within the user-determined threshold at the time step of settlement; in this case, water depths must be between 10 to 120 m and temperatures must be between 0 to 21°C for settlement to take place (**Table 6.6**).

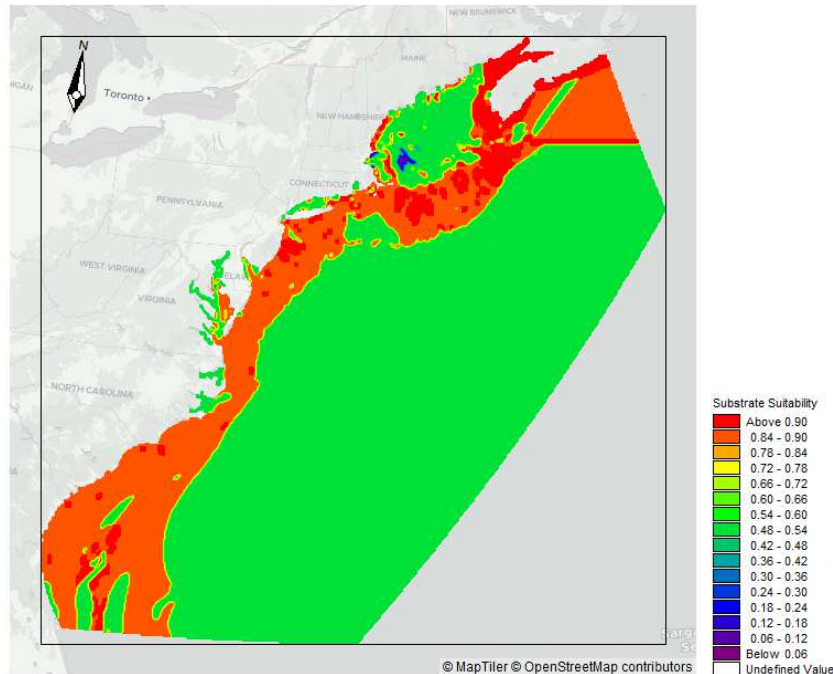


Figure 6.15. Sea Scallop Substrate Suitability Map

Substrate suitability indices were derived using benthic substrate data (USGS 2005 geographic resolution EPSG: 4269, NAD83), with higher values assigned to areas with substrate types preferred by sea scallop larvae.

Table 6.6. Sea Scallop Substrate Suitability and Settlement Conditions

Parameter	Literature Information/Value	Parameterized Value
Settling indicators <i>Conditions required for larvae to settle/incubate to juvenile</i>	Substrate type: <ul style="list-style-type: none"> • Presence of suitable substrate (gravelly sand, shell fragments) • Coarse sediment, gravel, glacial moraine • Gravel substrate (>80%); hydroids and filamentous algae (Culliney, 1974; Thouzeau et al., 1991)	The index values used for the various benthic substrate types was: <ul style="list-style-type: none"> • Sand: 0.9 • Gravelly-sand 0.95 • Clay-sand/silt: 0.5 • Clay-silt/sand: 0.5 • Sand-clay/silt: 0.5 • Sand-silt/clay: 0.5 • Sand/silt/clay: 0.5 • Gravel: 0.9 • Bedrock: 0.1 • Clay: 0.1 Water depth thresholds for settlement: <ul style="list-style-type: none"> • Minimum: 10 m • Maximum: 120 m
Temperature effects <i>Potential effects from changing temperatures</i>	Mass larval mortality at >21°C Larvae aggregate above the pycnocline (> 5°C) (Tremblay & Sinclair, 1990)	Temperature thresholds for larval survival: <ul style="list-style-type: none"> • Minimum: 0°C • Maximum: 21°C

6.4.3 Surfclam

6.4.3.1 General Overview

Atlantic surfclam (*Spisula solidissima*), hereafter referred to as ‘surfclam’, are a bivalve mollusk that occur along the continental shelf of the northwest Atlantic from the Gulf of St. Lawrence to North Carolina. Surfclam are an important commercial fishery species in the northwest Atlantic region, with 2022 landings valued at \$41.7 million (NOAA, 2022).

The Northeast Fisheries Science Center (NEFSC) conducts periodic surveys of abundance, biomass, length, and weight of various fisheries pertinent shellfish along the continental shelf region of the East Coast. NEFSC shellfish survey data for surfclam is divided by regions historically used for assessment of survey, fishery, and stock distribution patterns. These areas are Georges Bank (GB), Southern New England (SNE), Long Island (LI), New Jersey (NJ), Delmarva (DMV), and South Virginia (SVA). Surfclam are most abundant in Georges Bank, the south shore of Long Island, New Jersey, and the Delmarva Peninsula, with the two major fishing stocks found in the New Jersey and Delmarva regions (Cargnelli, 1999).

Surfclam prefer sandy habitats and prefer to settle in medium or fine sand, in areas of high-water flow (Snelgrove et al., 1998), and are most commonly found in water depths ranging from 10 to 60 m (Cargnelli, 1999). Adult surfclams can tolerate water temperatures from 1°C to 28°C (Cargnelli et al., 1999; Spruck et al., 1995) and prefer salinities greater than 28 psu (Castagna and Chanley, 1973). Larval surfclams can swim vertically and they position themselves in the water column to avoid temperatures above 20°C and less than 12°C (Shanks and Brink, 2005; Ma et al., 2006), with temperatures above 30°C being lethal (Fay et al., 1983; Wright et al., 1983).

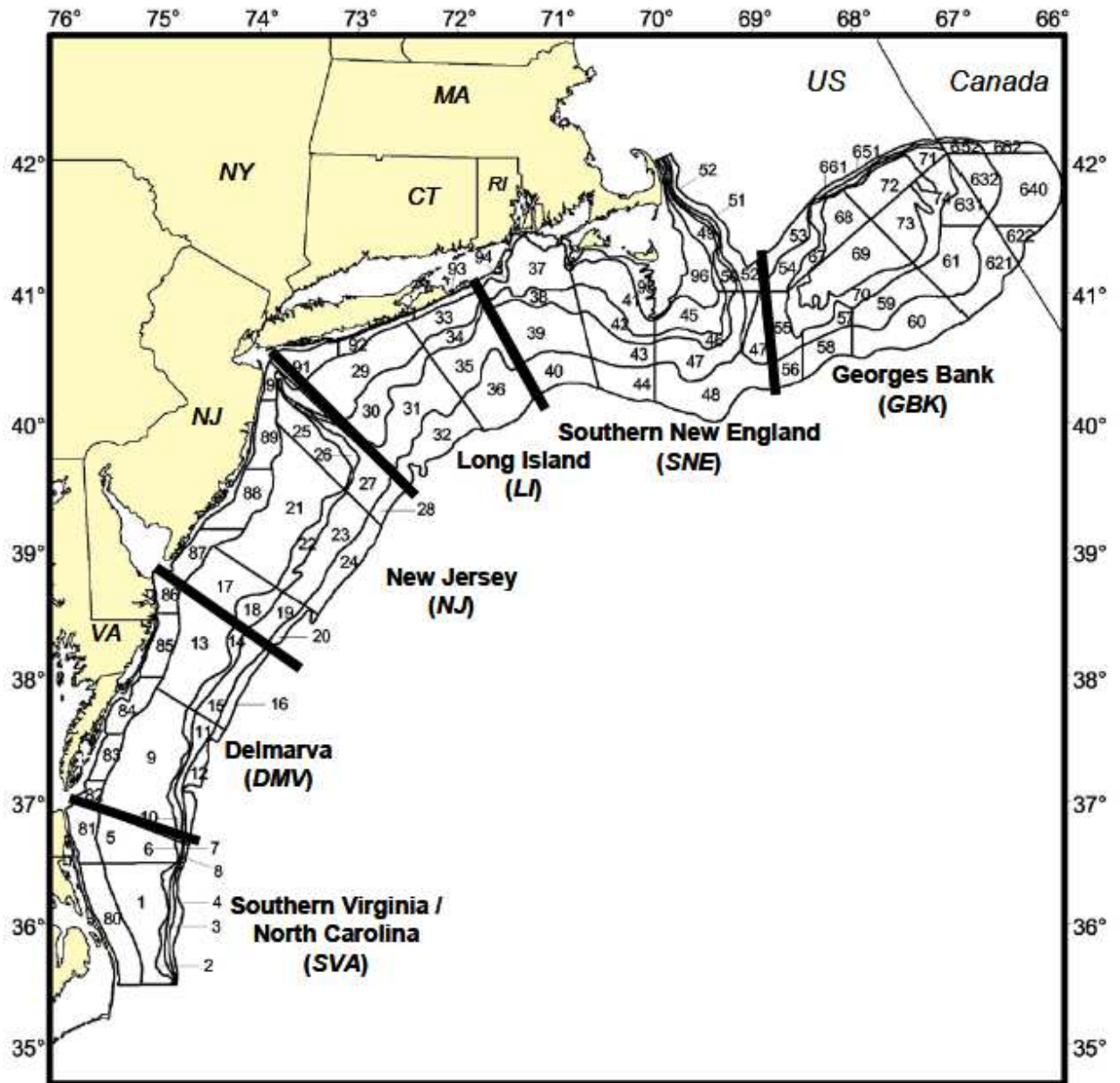


Figure 6.16. NEFSC Shellfish Regions, for Atlantic Surfclam, Ocean Quahog, and Atlantic Sea Scallop Surveys
(From Jacobson and Hennen, 2019)

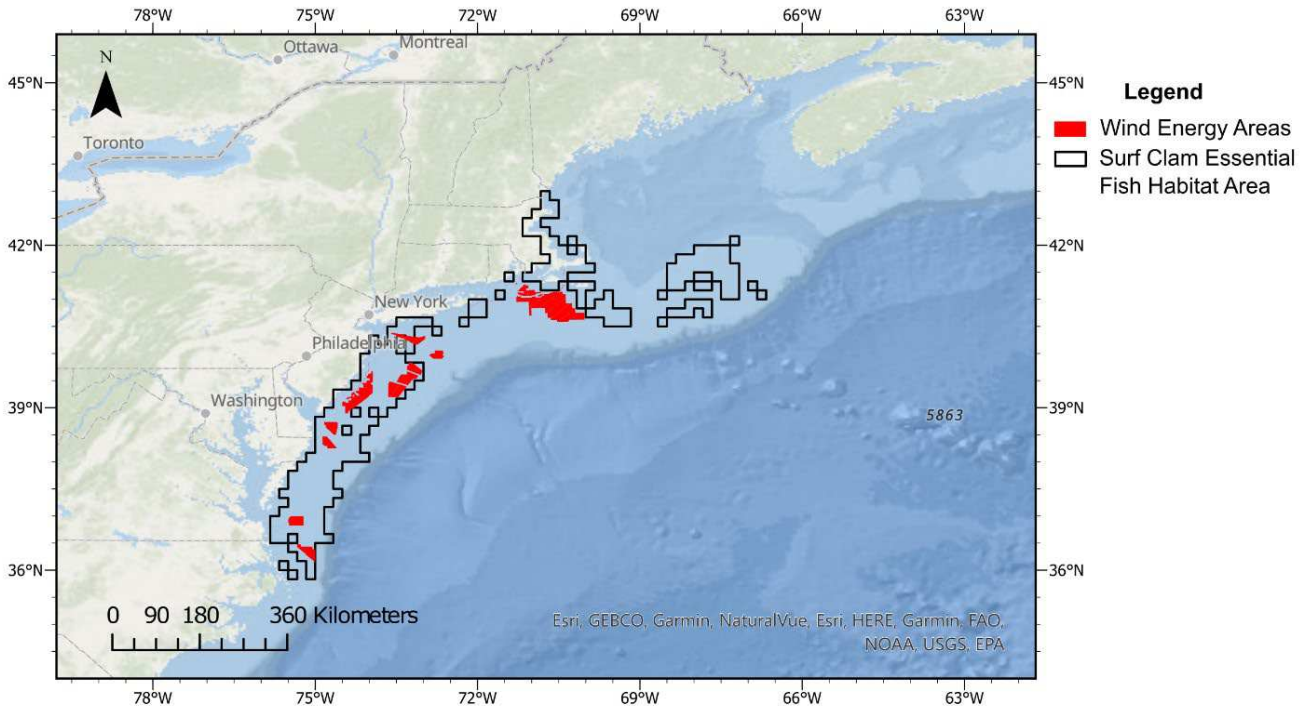


Figure 6.17. Surfclam Essential Fish Habitat Map

Surfclam Essential Fish Habitat (black) in the Northwest Atlantic Ocean, extending from Georges Bank to Cape Hatteras, North Carolina (NOAA, 2018).

6.4.3.2 Super-Agent Class Parameterization

The simulation period for the surfclam model (1st May to 31st December, for 2017 only) was selected to capture zygotes and larval activity during critical spawning seasons and larval migration periods. The parameterization of surfclam spawning, life cycle, mortality, movement, and settlement suitability characteristics are detailed in the subsections below.

6.4.3.3 Spawning

Adult surfclam do not migrate during spawning seasons and surfclam super-agent release areas (**Figure 6.18**) were directly derived from observed distribution and abundance data of surfclam collected from NEFSC clam surveys (NEFSC, 2021; NOAA Clam Survey, 2022). Spawning areas were divided by NEFSC shellfish regions (i.e., GB, SNE, LI, NJ, DMV, SVA). Surfclam are present in the Gulf of Maine and Cape Cod (Palmer, 1991; Dr. Daphne Munroe, *pers comms*), however, their management falls under state jurisdiction. Abundance and distribution data for surfclam was therefore not available for these regions. To ensure settlement of surfclam occurred the Nantucket Shoals to Long Island area an additional spawning location was included in Cape Cod, with relatively small proportional release. An analysis of proportional biomass densities was carried out on NEFSC clam survey data for each spawning release area within the model to determine the relative number of agents to be released from each spawning location. This analysis revealed that New Jersey and Delmarva areas should release the most agents. The proportions calculated and the corresponding number of super-agents released from each area are given in **Table 6.7**Figure 6.12.

A total of 30,000 surfclam super-agents were released over the entire simulation period in the model domain, with each super-agent initialized to contain a number of zygotes sampled from a normal

distribution in order to account for the varying levels of fecundity of each individual mature reproducing adult. It was not possible to find published data on surfclam fecundity. As such, values recorded for the southern subspecies *Spisula solidissima similis* were used to initialize the surfclam ABM. A mean of 3.3 million eggs per individual spawn, as determined from laboratory studies (Walker et al., 1996), was used along with a standard deviation of 1.64 million, calculated assuming a normal distribution around the mean.

Surfclam spawn primarily during summer (late June to August), with a minor fall spawning period (October) occurring in warm years where the thermocline breaks down (Ropes, 1968). Spawning occurs earlier to the south, with the South Virginia area sometimes spawning as early as May (Ropes, 1979). Spawning off New Jersey and further north occurs from June (Ropes, 1968). Spawning does not appear to be triggered by temperature (Ropes, 1968) and other environmental factors are not known to influence surfclam spawning (Cargnelli et al., 1991). Super-agents were spawned randomly within the polygons shown in **Figure 6.18**, within set time frames presented in **Table 6.8**.

Table 6.8 provides the timing and volume of super-agent release from each surfclam spawning region included in the model. The South Virginia region (Pink polygon, **Figure 6.18**) spawns earlier than the more northern regions, with a spring-summer spawning event beginning in May and continuing until mid-July. All other regions are set up to start spawning at the same time from 7th June until 25th August, and the number of agents released per day from each region were scaled proportionally to the observed biomass reported for each area in NOAA clam survey catch data set (NOAA, 2022). A minor fall spawning event in October was also included for all areas, to ensure that all possible spawning and larval transport events are simulated and evaluated. With limited data available on this spawning event, it was included as a minor release, with a uniform timing, short release period (1st to 10th October), and relatively small super-agent release, for each region.

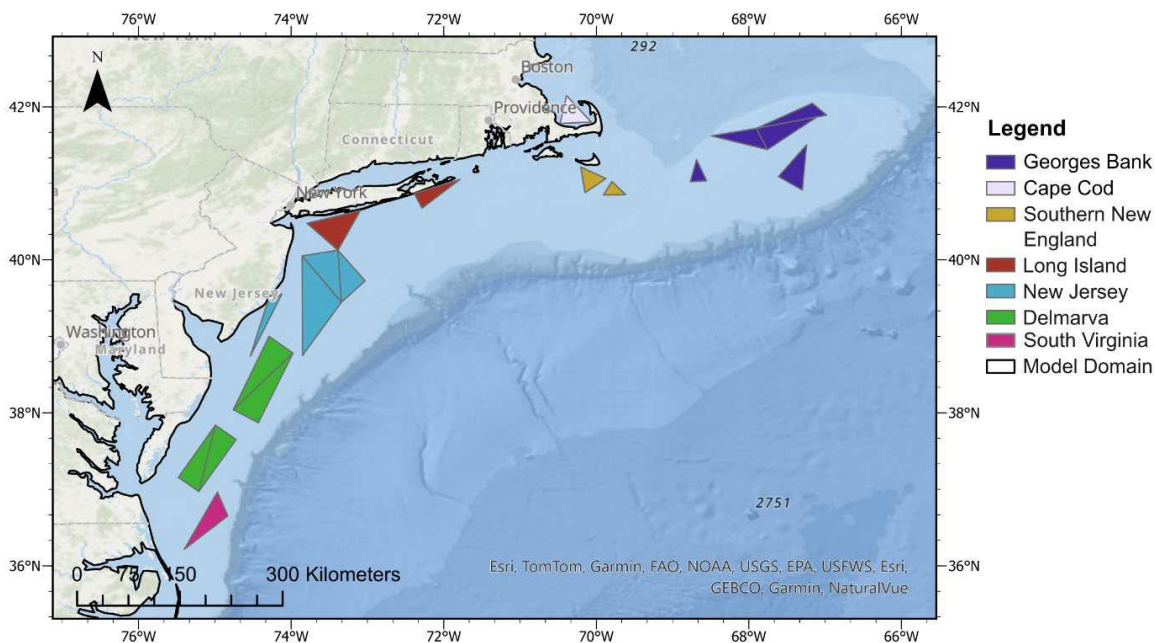


Figure 6.18. Surfclam Model Spawning Areas

Release areas in the surfclam model are derived from areas of high abundance in NOAA's clam survey dataset (NOAA, 2022).

Table 6.7. Number of Super-Agents Released from Each Spawning Area

Spawning Region	Percentage	Number of Super-Agents
Cape Cod	0.2	88
Georges Bank	13	3880
Southern New England	3	950
Long Island	9	2940
New Jersey	39	11460
Delmarva	31	9732
South Virginia	3	950

Table 6.8. Surfclam Release Period and Volume

Area(s)	Release Period	Time Series
Georges Bank (purple polygons in Figure 6.18)	7 th June – 25 th August 1 st October – 10 th October	<p>Number of super-agents released per day</p> <p>Date</p>
Cape Cod (light pink polygon in Figure 6.18)	7 th June – 25 th August 1 st October – 10 th October	<p>Number of super-agents released per day</p> <p>Date</p>

Area(s)	Release Period	Time Series																		
Southern New England (orange polygons in Figure 6.18)	7 th June – 15 th August 1 st October – 10 th October	<p>Number of super-agents released per day</p> <p>Date</p> <table><thead><tr><th>Date</th><th>Number of super-agents released per day</th></tr></thead><tbody><tr><td>5/1/2017</td><td>0</td></tr><tr><td>6/1/2017</td><td>0</td></tr><tr><td>7/1/2017</td><td>12</td></tr><tr><td>8/1/2017</td><td>12</td></tr><tr><td>9/1/2017</td><td>0</td></tr><tr><td>10/1/2017</td><td>12</td></tr><tr><td>11/1/2017</td><td>0</td></tr><tr><td>12/1/2017</td><td>0</td></tr></tbody></table>	Date	Number of super-agents released per day	5/1/2017	0	6/1/2017	0	7/1/2017	12	8/1/2017	12	9/1/2017	0	10/1/2017	12	11/1/2017	0	12/1/2017	0
Date	Number of super-agents released per day																			
5/1/2017	0																			
6/1/2017	0																			
7/1/2017	12																			
8/1/2017	12																			
9/1/2017	0																			
10/1/2017	12																			
11/1/2017	0																			
12/1/2017	0																			
Long Island (red polygons in Figure 6.18)	7 th June – 25 th August 1 st October – 10 th October	<p>Number of super-agents released per day</p> <p>Date</p> <table><thead><tr><th>Date</th><th>Number of super-agents released per day</th></tr></thead><tbody><tr><td>5/1/2017</td><td>0</td></tr><tr><td>6/1/2017</td><td>0</td></tr><tr><td>7/1/2017</td><td>37</td></tr><tr><td>8/1/2017</td><td>37</td></tr><tr><td>9/1/2017</td><td>0</td></tr><tr><td>10/1/2017</td><td>13</td></tr><tr><td>11/1/2017</td><td>0</td></tr></tbody></table>	Date	Number of super-agents released per day	5/1/2017	0	6/1/2017	0	7/1/2017	37	8/1/2017	37	9/1/2017	0	10/1/2017	13	11/1/2017	0		
Date	Number of super-agents released per day																			
5/1/2017	0																			
6/1/2017	0																			
7/1/2017	37																			
8/1/2017	37																			
9/1/2017	0																			
10/1/2017	13																			
11/1/2017	0																			
New Jersey (blue polygons in Figure 6.18)	7 th June – 25 th August 1 st October – 10 th October	<p>Number of super-agents released per day</p> <p>Date</p> <table><thead><tr><th>Date</th><th>Number of super-agents released per day</th></tr></thead><tbody><tr><td>5/1/2017</td><td>0</td></tr><tr><td>6/1/2017</td><td>0</td></tr><tr><td>7/1/2017</td><td>100</td></tr><tr><td>8/1/2017</td><td>285</td></tr><tr><td>9/1/2017</td><td>100</td></tr><tr><td>10/1/2017</td><td>0</td></tr><tr><td>11/1/2017</td><td>10</td></tr></tbody></table>	Date	Number of super-agents released per day	5/1/2017	0	6/1/2017	0	7/1/2017	100	8/1/2017	285	9/1/2017	100	10/1/2017	0	11/1/2017	10		
Date	Number of super-agents released per day																			
5/1/2017	0																			
6/1/2017	0																			
7/1/2017	100																			
8/1/2017	285																			
9/1/2017	100																			
10/1/2017	0																			
11/1/2017	10																			

Area(s)	Release Period	Time Series																
Delmarva (green polygons Figure 6.18)	7 th June – 25 th August 1 st October – 10 th October	<p>Number of super-agents released per day</p> <p>Date</p> <table><thead><tr><th>Date</th><th>Number of super-agents released per day</th></tr></thead><tbody><tr><td>5/1/2017</td><td>0</td></tr><tr><td>6/1/2017</td><td>100</td></tr><tr><td>7/1/2017</td><td>280</td></tr><tr><td>8/1/2017</td><td>100</td></tr><tr><td>9/1/2017</td><td>0</td></tr><tr><td>10/1/2017</td><td>10</td></tr><tr><td>11/1/2017</td><td>0</td></tr></tbody></table>	Date	Number of super-agents released per day	5/1/2017	0	6/1/2017	100	7/1/2017	280	8/1/2017	100	9/1/2017	0	10/1/2017	10	11/1/2017	0
Date	Number of super-agents released per day																	
5/1/2017	0																	
6/1/2017	100																	
7/1/2017	280																	
8/1/2017	100																	
9/1/2017	0																	
10/1/2017	10																	
11/1/2017	0																	
South Virginia (dark pink polygons Figure 6.18)	7 th May – 15 th July 1 st October – 10 th October	<p>Number of super-agents released per day</p> <p>Date</p> <table><thead><tr><th>Date</th><th>Number of super-agents released per day</th></tr></thead><tbody><tr><td>5/1/2017</td><td>0</td></tr><tr><td>6/1/2017</td><td>12</td></tr><tr><td>7/1/2017</td><td>12</td></tr><tr><td>8/1/2017</td><td>0</td></tr><tr><td>9/1/2017</td><td>0</td></tr><tr><td>10/1/2017</td><td>12</td></tr><tr><td>11/1/2017</td><td>0</td></tr></tbody></table>	Date	Number of super-agents released per day	5/1/2017	0	6/1/2017	12	7/1/2017	12	8/1/2017	0	9/1/2017	0	10/1/2017	12	11/1/2017	0
Date	Number of super-agents released per day																	
5/1/2017	0																	
6/1/2017	12																	
7/1/2017	12																	
8/1/2017	0																	
9/1/2017	0																	
10/1/2017	12																	
11/1/2017	0																	

Table 6.9. Surfclam Spawning Model Parameters

Parameter	Literature Information/Value	Parameterized Value
Timing and Duration <i>Time of year when spawning is initiated</i>	Spring-Summer (major) and Fall (minor). Surfclam spawn primarily during summer (June to August), with a minor fall spawning period (October) occurring in warm years where the thermocline breaks down (Ropes, 1968). Spawning occurs earlier to the south, with the South Virginia area sometimes spawning as early as May (Ropes, 1979). Spawning off New Jersey and further north occurs from June (Ropes, 1968).	Release of super-agents occurs in June in South Virginia, and later to the North, where super-agent release peaks in the first week of July. A minor fall release of super-agents occurs in the first week of October. With a small number of agents released, for 5 days.
Quantities <i>Particle release during spawning</i>	A total of 30,000 surfclam super-agents were released over the entire simulation period in the model domain. Release from each spawning areas was scaled to regional biomass proportions. Fecundity values recorded for the southern subspecies <i>Spisula solidissima similis</i> were used to parameterize the surfclam AMB (Walker et al. 1996).	A mean of 3.3 million eggs per individual Standard deviation of 1.64 million (Walker et al., 1996).

6.4.3.4 Life Cycle

Surfclam eggs are buoyant and approximately 50 to 60 μm in diameter (Walker and O'Beirn, 1996). They are released above spawning beds and hatch within 9 to 40 hours after fertilization, depending on the temperature (Loosanoff and Davis, 1963; Ropes, 1980; Walker and O'Beirn, 1996). Trochophore larvae transform to veliger and then pediveliger larvae and settle to the sea floor 18 to 35 days after fertilization (Fay et al., 1983; Walker and O'Beirn, 1996). An overview of the surfclam early life stages simulated in the model is presented in **Figure 6.19** and a summary of parameters related to the surfclam life cycle (growth and mortality) is presented in **Table 6.10**.

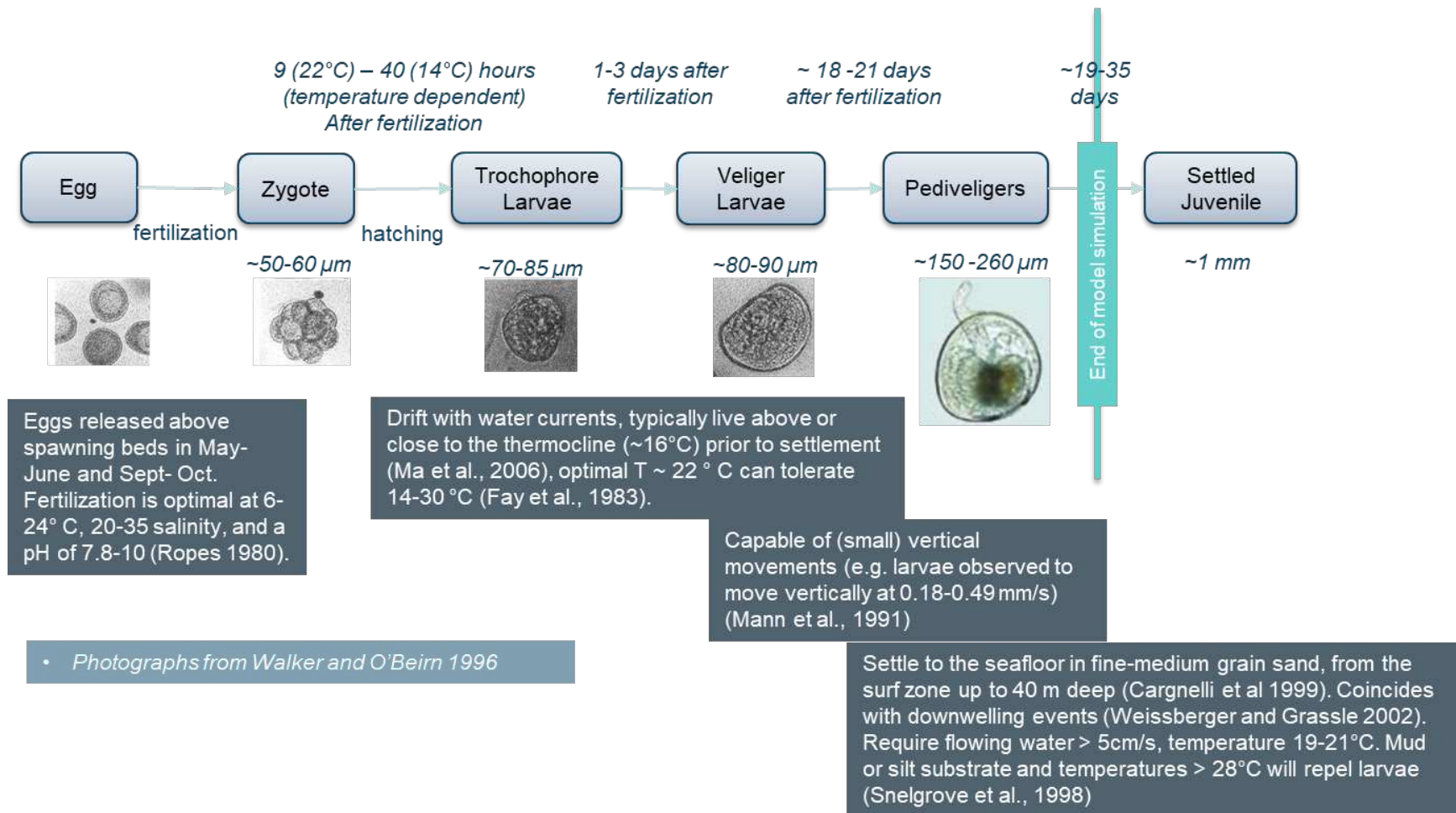


Figure 6.19. Early Life Stages of Surfclam as Simulated in the ABM

A surfclam agent is initialized as a zygote and undergoes transformation to become a pre-transformation larva. At this point, it descends to the bottom of the ocean and begins its metamorphosis process. Life stages beyond the pre-transformation larva stage are not included in the model.

Table 6.10. Surfclam Life Cycle (Growth and Mortality) Model Parameters

Parameter Type	Parameter	Literature Information/Value	Parameterized Value
Life Cycle	Duration of egg stage <i>Incubation time from egg to larvae</i>	9 to 40 hours depending on the temperature (22 °C to 14°C) (Loosanoff and Davis, 1963; Ropes, 1980; Walker and O'Beirn, 1996).	Minimum zygote duration sampled from normal distribution: Mean: 9 hours Variance: 2 hours Maximum zygote duration sampled from normal distribution: Mean: 40 hours Variance: 2 hours All durations are from the time of release of super-agent.
Life Cycle	Duration of larval stage <i>Time spent as a larva before settling/changing state</i>	19 to 35 days (Fay et al., 1983).	Minimum larval duration sampled from normal distribution: Mean: 19 days Variance: 1 day All durations are from the time of release of super-agent. Maximum larval duration sampled from normal distribution: Mean: 35 days Variance: 1 day All durations are from the time of release of super-agent.
Life Cycle	Number of stages between egg and adult <i>Total number of stages between egg and adult</i>	<u>4 stages</u> : egg, trochophore, veliger, pediveliger (Walker and O'Beirn, 1996).	3 stages modeled: Zygotes, pre-competent larvae, and competent larvae. Trochophore and veliger larvae are broadly categorized under the 'pre-competent larvae' group and pediveliger larvae under the 'competent larvae' group.
Growth	Incubation rate of zygotes <i>Probability that a zygote will hatch and become a larva</i>	Not available	Age-dependent sigmoidal curve for incubation probability. Values are assumed and calibrated through an iterative process (see section 7.4): Maximum incubation probability: 0.7/day
Growth	Competency gain rate of larvae <i>Probability that a pre-competent larva will gain competency</i>	Not available	Age-dependent sigmoidal curve for competency gain probability. Values are assumed and calibrated through an iterative process (see section 7.4): Maximum competency gain probability: 0.8/day
Growth	Competency loss rate of larvae <i>Probability that competent larva will lose competency</i>	Not available	Age-dependent sigmoidal curve for competency loss probability. Maximum competency loss probability: 1/day
Mortality	Mortality parameters <i>Parameters related to the selected mortality</i>	Not available	Age-dependent Weibull curve for competency loss probability. Minimum daily mortality rate: 0.05 Maximum daily mortality rate: 0.3 Lambda scale parameter: 0.1 Alpha shape parameter: 0.76

6.4.3.5 Movement

At each time step, depending on the dominant life stage of agents contained in the super-agent, the super-agent exhibits different vertical movement traits. Trochophores, veligers, and pediveligers are capable of some vertical movement, but are dispersed passively in the horizontal plane, as current speeds are much greater than larval swimming speeds. Horizontal movement is therefore purely a function of hydrodynamic forcings (i.e., horizontal current speed and direction). Surfclam larvae have however been observed to position themselves vertically in the water column. Larvae tend to aggregate near temperatures of 20°C, and swim away (down) from temperatures greater than 22°C and away (up) from temperatures less than 12°C (Ma et al., 2006; Shanks and Brink, 2005; Zhang et al., 2015). This was implemented in the model by placing a vertical control factor where the surfclam agent would swim down if the agent's ambient temperature rises to 21°C and swim up if the temperature falls to 12°C.

An overview of the surfclam super-agent vertical movement behavior as simulated in the model is presented in **Figure 6.20** and a summary of parameters related to surfclam movement is presented in **Table 6.11**.

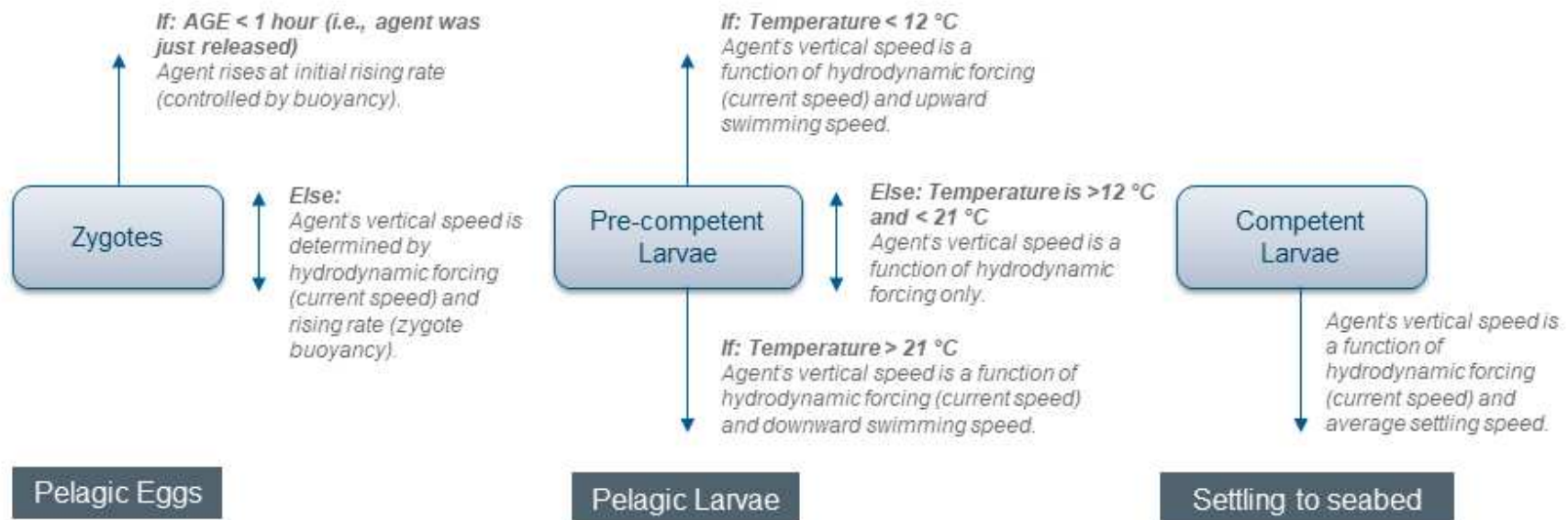


Figure 6.20. Parameterization of Surfclam Zygotes and Larval Vertical Movement Characteristics

Surfclam zygotes are pelagic and rise towards the water surface during their first hour of release from the seabed, after which the zygote drifts passively. Pre-competent larvae migrate vertically through the water column depending on temperature: larvae swim down from temperatures greater than 21°C and up from temperatures less than 12°C. Settle-ready (competent) larvae sink and eventually settle on the seabed.

Table 6.11. Surfclam Movement Model Parameters

Parameter	Literature Information/Value	Parameterized Value
Buoyancy of egg <i>Maximum buoyancy (positive or negative) speed for fertilized zygotes</i>	Not available.	Assumed to be positively buoyant with upward speed of 0.0014 m/s.
Vertical swim speeds <i>Maximum vertical swim speed for larvae, independent of current speeds (m/s)</i>	Vertical swimming speeds range between 0.18-0.49 mm/s (0.00018 – 0.00049 m/s) (Mann et al., 2019).	Average vertical swim speed sampled from normal distribution: <ul style="list-style-type: none"> • Mean: 0.00035 m/s. • Standard deviation: 0.0002 m/s.
Horizontal swim speeds <i>Maximum horizontal swim speed for larvae, independent of current speeds (m/s), if present</i>	Not available.	Horizontal swim speed is insignificant relative to hydrodynamic forcings – super-agent assumed to drift passively in horizontal plane.
Temporal changes in vertical distribution Distribution of larvae in the water column dependent on time of day	Larvae tend to aggregate near temperatures of 20°C, and swim away (down) from temperatures greater than 20°C and away (up) from temperatures less than 12°C (Ma et al. 2006; Shanks and Brink 2005; Zhang et al. 2015).	Super-agent swims up if temperature is less than 12°C and swims down if greater than 20°C. Vertical swim speed is a function of hydrodynamic forcing and vertical swimming speed, which is sampled by normal distribution: <ul style="list-style-type: none"> • Mean: 0.00035 m/s. • Standard deviation: 0.0002 m/s.

6.4.3.6 Substrate Suitability

Substrate suitability index map for surfclam (**Figure 6.21**) was developed based on the preferred substrate of young surfclam, which is sandy substrate (i.e., sand and gravelly sand) (Cargenlli et al., 1999). Each 2D grid cell of the model mesh is assigned a settlement suitability index value between 0 to 1, with higher values indicating higher suitability.

Settling is described as a two-step process, where specific conditions must be met in order for the larvae to settle: the super-agent must contain competent larvae and be located in a grid cell where variables are within the user-determined threshold at the time step of settlement; in this case, water depths must be between 10 to 60 m and temperatures must be between 0 to 21°C for settlement to take place (**Table 6.12**).

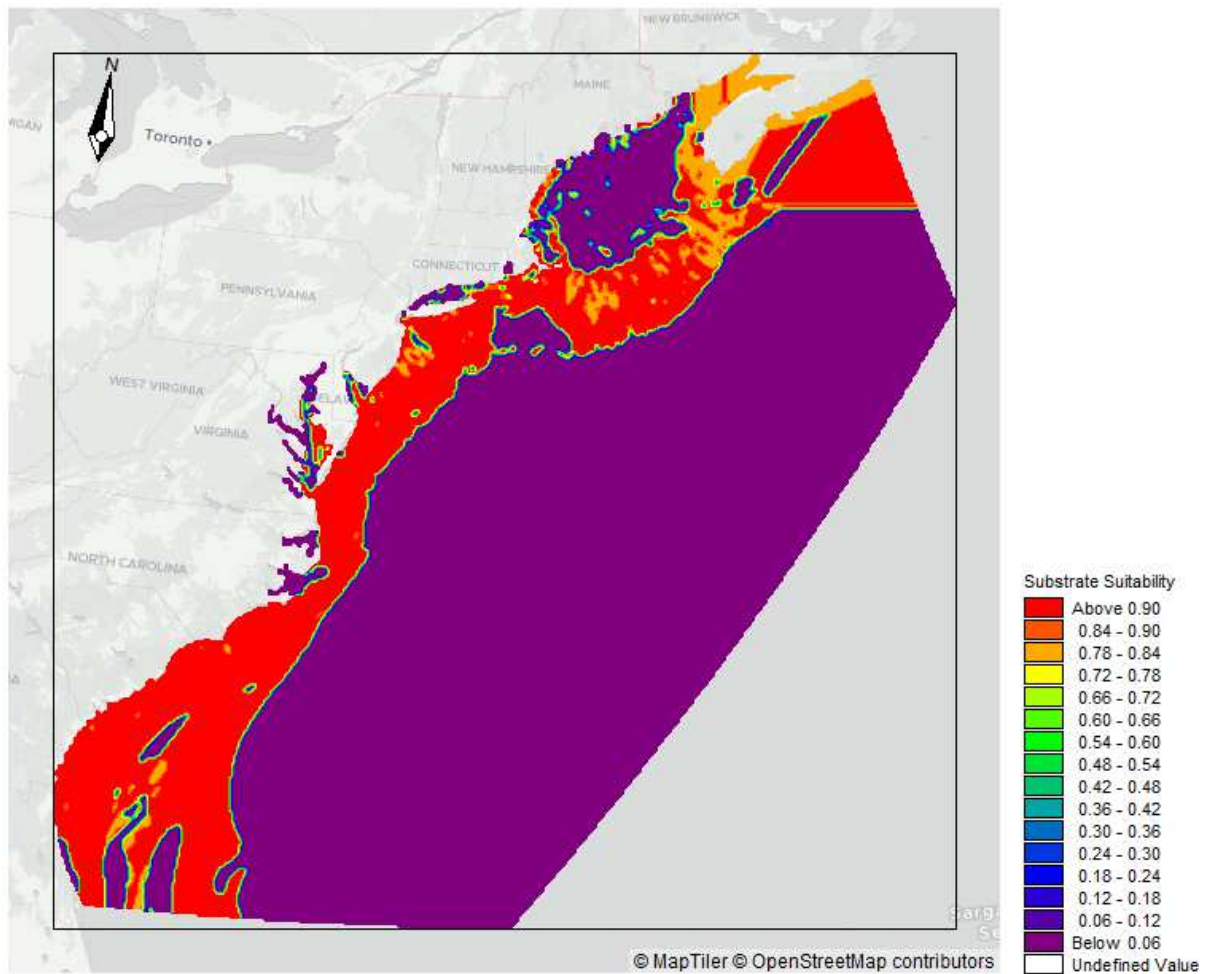


Figure 6.21. Surfclam Substrate Suitability Map

Substrate suitability indices are derived using benthic substrate data (USGS 2005 geographic resolution EPSG: 4269, NAD83), with higher values assigned to areas with substrate types preferred by surfclam larvae.

Table 6.12. Surfclam Substrate Suitability and Settlement Conditions

Parameter	Literature Information/Value	Parameterized Value
Settling indicators <i>Conditions required for larvae to settle/incubate to juvenile</i>	Substrate type: <ul style="list-style-type: none"> • Presence of suitable substrate (sand, gravelly sand) (Cargnelli et al., 1999)	The index values used for the various benthic substrate types are: <ul style="list-style-type: none"> • Sand: 0.95 • Gravelly-sand 0.85 • Clay-sand/silt: 0 • Clay-silt/sand: 0 • Sand-clay/silt: 0 • Sand-silt/clay: 0 • Sand/silt/clay: 0 • Gravel: 0 • Bedrock: 0 • Clay: 0 Water depth thresholds for settlement: <ul style="list-style-type: none"> • Minimum: 10 m • Maximum: 60 m
Temperature effects <i>Potential effects from changing temperatures</i>	Mortality of surfclam larvae occurs at 30°C (Snelgrove et al., 1998).	Temperature thresholds for larval survival: <ul style="list-style-type: none"> • Minimum: 0°C • Maximum: 30°C
Salinity effects <i>Potential effects from changing salinity</i>	Salinity tolerance of larvae between 28 and 35 (Cargnelli et al., 1999; Ropes et al., 1980).	Salinity thresholds for larval survival: <ul style="list-style-type: none"> • Minimum: 28 psu • Maximum: 35 psu

6.4.4 Summer Flounder

6.4.4.1 General Overview

Summer flounder (*Paralichthys dentatus*) is a member of the large-toothed flounder family (*Paralichthyidae*) and is distributed from central Florida to the Gulf of Maine (**Figure 6.22**). Summer flounder is economically valuable as a recreational and commercial fisheries species across its range and is managed jointly by the Atlantic States Marine Fisheries Commission and the Mid-Atlantic Fishery Management Council (Terciero, 2018). Fisheries managers historically recognized one stock for the northwest Atlantic Ocean region; however, others have presented evidence supporting the existence of two (or more) geographically segregated stocks (e.g., Kraus and Musick, 2001). Namely, a northern stock in the MAB extending from Cape Cod southward to Delaware Bay and a southern stock in the South Atlantic Bight centered off Cape Hatteras, North Carolina.

While the issue of stock definition is not fully resolved, for modeling purposes individuals that reside and spawn within the area of interest were based on the northern stock (Kraus and Musick, 2001). This application is supported by recent genetic studies that indicate a lack of distinct stocks or geographically segregated subpopulations which supports continued management of a single population (Hoey and Pinksy, 2018). In addition, genetic and otolith microchemistry signatures from archived larvae sampled over 24-year period indicated that spawning offshore Cape Hatteras contributes 7 to 50% of the summer

flounder larvae dispersing into the MAB (Hoey et al., 2020), the offshore region from Massachusetts to North Carolina (Johnson et al., 2021).

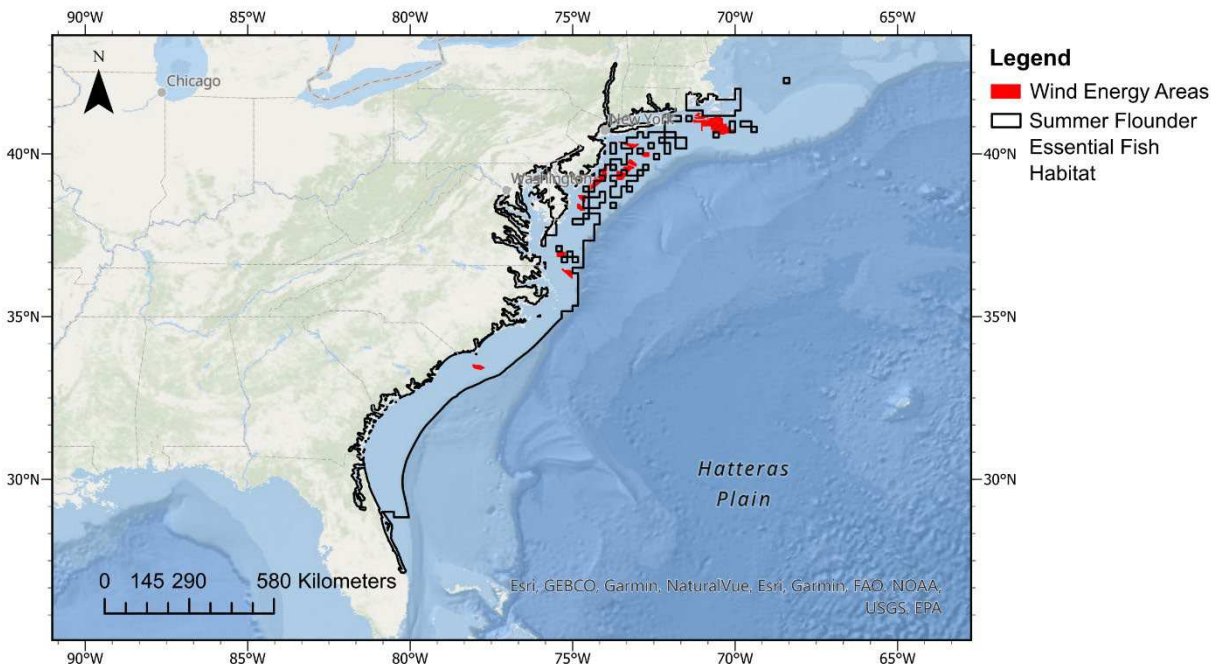


Figure 6.22. Summer Flounder Essential Fish Habitat Map

Summer flounder EFH east coast, covering the shallow estuarine waters and outer continental shelf from Florida to George's Bank (NOAA, 2018).

6.4.4.2 Super-Agent Class Parameterization Data

The simulation period for the summer flounder model (September 1, 2017, to March 31, 2018) was selected to capture zygotes and larval activity during critical spawning seasons and larval migration periods. The parameterization of summer flounder spawning, life cycle, mortality, movement, and settlement suitability characteristics are detailed in the subsections below.

6.4.4.3 Spawning

Adult summer flounders mature at about 30 cm Total Length (TL) reaching a maximum size of 83 cm TL and spend summer months in inner shelf and estuarine waters (Gilbert, 1986). During late summer and fall, in response to falling water temperatures, adults migrate offshore to spawn. Relative to the area of interest, this occurs when summer flounder migrate from the inner shelf and estuarine waters to the outer shelf. Spawning behavior is not well known but likely involves pair spawning with eggs being shed into the water column above the seafloor (< 10 m). Adults are serial spawners with female producing at least six batches of eggs per season (Morse, 1981).

For spawning in the north portion of the model domain, spatial egg distributions from plankton samples (Smith, 1973) indicates that it occurs between eastern Long Island and Nantucket shoals out to the shelf edge (e.g. Smith, 1973, Able et al., 2010). Egg densities in this area were highest during October and November but spawning can extend from September to February (Morse, 1981). The basis for determining spawning in other locations (i.e., Georges Bank, New Jersey Mid- and South – Atlantic Bight) in the study area were based on the principle that it occurs in water depths from 60 to 100 m where

temperatures range from 12 to 19°C, as derived from the research undertaken by (Able and Kaiser, 1994). The flounder super-agent release areas (**Figure 6.23**) were subsequently derived from hydrodynamic conditions and bathymetric information (Johnson et al., 2021). Super-agents were spawned randomly within the polygons shown in **Figure 6.23**, within set time frames presented in **Table 6.13**.

A total of 27,528 summer flounder super-agents were released over the entire simulation period in the model domain. In consultation with the fisheries expert from CSA it was decided that a distribution of total agents released should originate from the Georges Bank with 7,028 super-agents released (25.5%); Southern New England with 6,848 agents released (24.9%); New Jersey with 6,624 agents released (24.1%); Mid-Atlantic Bight with 5,884 agents released (21.4%), and from South-Atlantic Bight with 1,144 agents released (4%).

As with the other two modeled species, each super-agent was initialized with a random number of zygotes sampled from a normal distribution (mean = 1,700,000 zygotes, standard deviation = 200,000 zygotes). Estimated number of eggs produced per batch ranged from 27,080 to 251,280 for females measuring 37 and 68 cm TL, respectively, with fecundity positively correlated with both length and weight. This estimate was based on a mean egg production rate per female ranging from 1,077 to 1,265 eggs per gram of body weight (Morse, 1981). A summary of parameters related to summer flounder spawning is presented in **Table 6.13**.

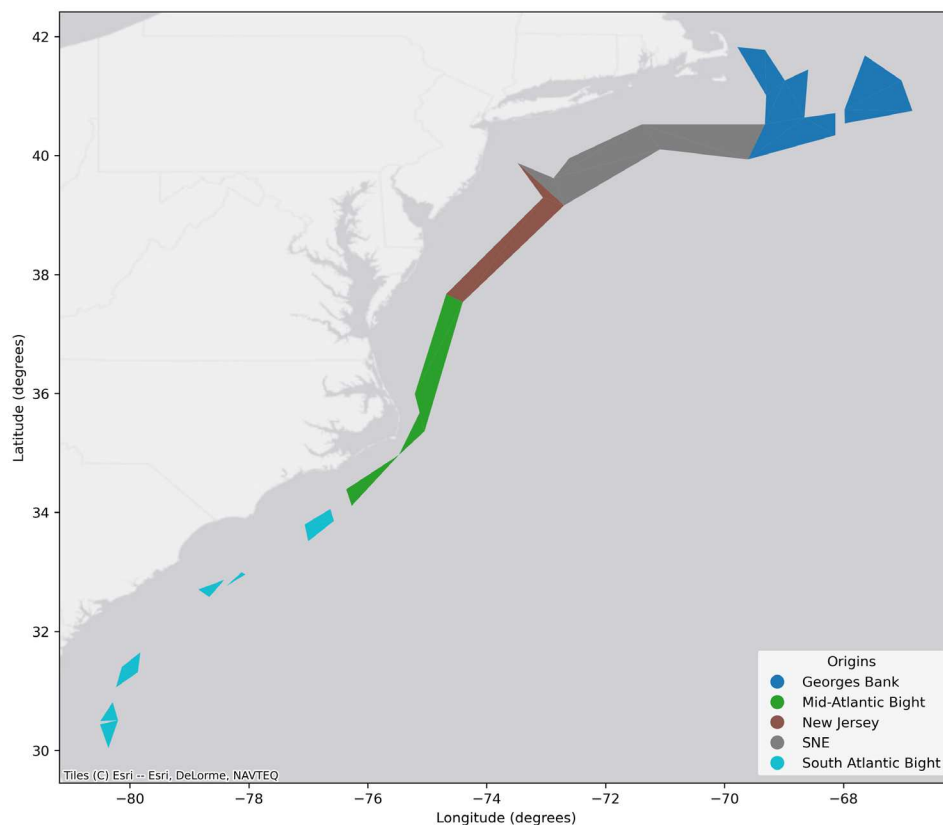


Figure 6.23. Summer Flounder Model Spawning Areas

Release areas in the summer flounder model were derived from bathymetric information and temperature conditions at which spawning activity was observed.

Table 6.13. Summer Flounder Release Period and Volume

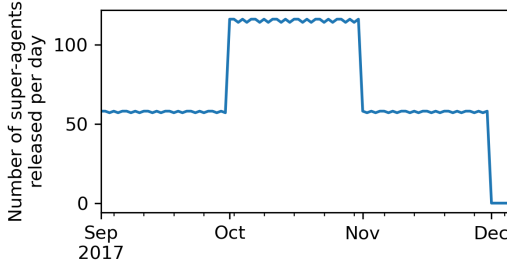
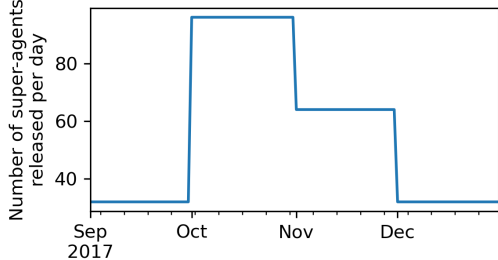
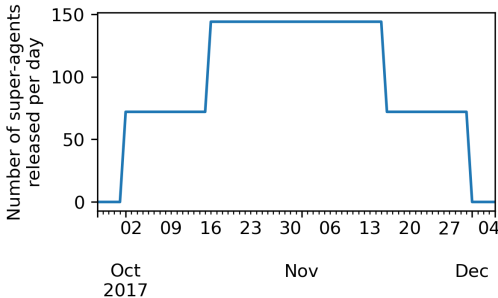
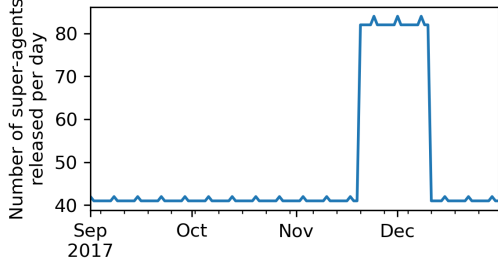
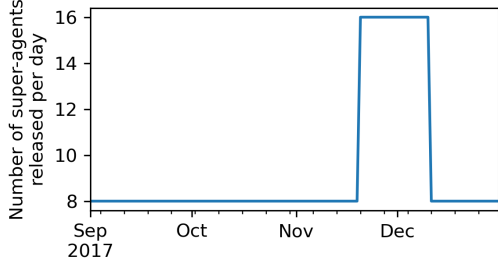
Area(s)	Release Period	Time Series
Georges Bank, Blue polygons polygons in Figure 6.23	September 1, 2017, to November 30, 2017 Peak from October 1, 2017, to October 31 2017	
Southern New England, Gray polygons in Figure 6.23	September 1, 2017, to December 31, 2017 Largest peak from October 1, 2017, to October 30 2017	
New Jersey, Brown polygons in Figure 6.23	October 1, 2017, to December 01, 2017 Largest peak from October 15, 2017, to November 15, 2017	
Mid-Atlantic Bight, Green polygons in Figure 6.23	September 1, 2017, to December 31, 2017 Largest peak from November 20, 2017, to January 10, 2017	
South-Atlantic Bight, Light Blue polygons in Figure 6.23	September 1, 2017, to December 31, 2017 Largest peak from November 20, 2017, to January 10, 2017	

Table 6.14. Summer Flounder Spawning Model Parameters

Parameter	Literature Information/Value	Parameterized Value
Timing <i>Time of year when spawning is initiated</i>	September to December, peak in October to November. One study cites July to February with peaks from September to November in water temperatures ranging 12 to 19°C (Smith 1973)	Release of super-agents occurs from September to December or September to November, depending on region.
Duration <i>Spawning period</i>	September to December (<u>120 days</u>), peak in October to November (<u>60 days</u>) (Morse 1981)	See above.
Quantities <i>Particle release during spawning</i>	Estimate of <u>0.46 to 4.18 million</u> ova per female (Morse 1981)	Initial number of zygotes sampled from a normal distribution: <ul style="list-style-type: none"> • Mean: 1,7000,000 zygotes • Standard deviation: 200,000 Peak release patterns are based on monthly abundance of eggs by region from NEFSC MARMAP offshore ichthyoplankton surveys (Hare 2015).

6.4.4.4 Life Cycle

Newly hatched larvae have eyes on either side of the body and orient their body axis perpendicular to the seafloor (Keefe and Able, 1993). These larvae have yolk sacs which may be completely absorbed in four days or less, depending on water temperature (Miller et al., 1991). Developing larvae undergo a complex metamorphosis involving multiple stages and migration of the eyes from bilaterally symmetrical positions on either side of the head to the left side of the body. The entire metamorphosis can take between 25 and 93 days to complete depending on water temperatures (Able and Kaiser, 1994). Miller et al. (1991) reported that metamorphosing larvae between 12 to 14 mm long and 30 to 70 days old enter estuaries, coastal rivers, and sounds of the MAB from October to April.

An overview of the early life stages of summer flounder that were simulated in the model is presented in **Figure 6.24** and a summary of parameters related to summer flounder life cycle (growth and mortality) is presented in **Table 6.15**.

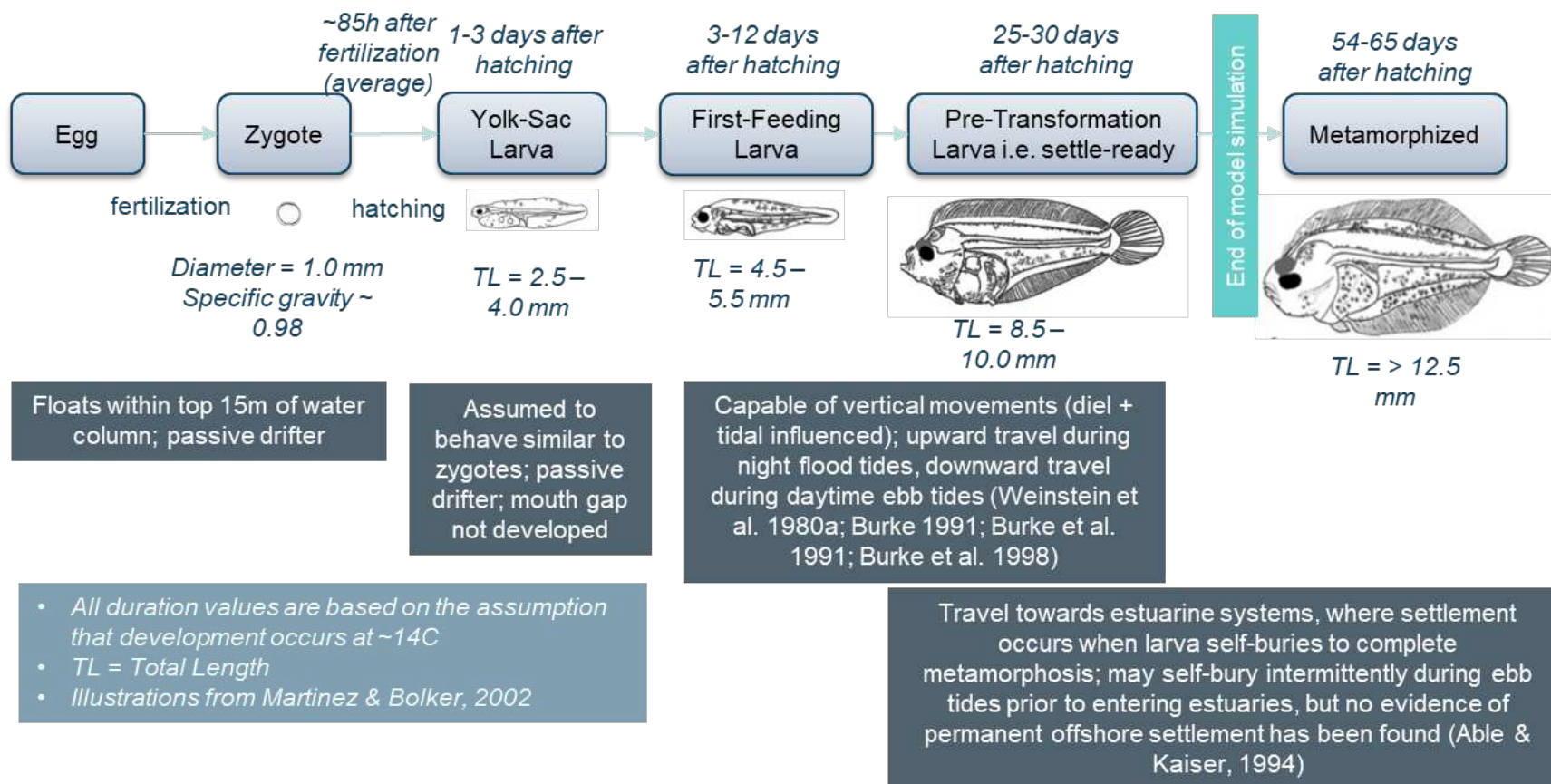


Figure 6.24. Early Life Stages of Summer Flounder as Simulated in the ABM

A summer flounder agent is initialized as a zygote and undergoes transformation to become a pre-transformation larva. At this point it is ready to settle in estuarine systems to begin its metamorphosis process.

Table 6.15. Summer Flounder Life Cycle (Growth and Mortality) Model Parameters

Parameter Type	Parameter	Literature Information/Value	Parameterized Value
Life Cycle	Duration of egg stage <i>Incubation time from egg to larvae</i>	Hatch in <u>2 to 6 days</u> , depending on ambient water temperature: <ul style="list-style-type: none"> 142 h at 9°C 85 h at 12.5°C 72 to 75 h at 18°C 60 h at 21°C 56 h at 23°C (Bisbal and Bengtson, 1995; Johns and Howell, 1980; Packer et al., 1999)	Minimum zygote duration sampled from normal distribution: <ul style="list-style-type: none"> Mean: 48 hours Variance: 2.4 hours Maximum zygote duration sampled from normal distribution: <ul style="list-style-type: none"> Mean: 96 hours Variance: 2.4 hours All durations are from the time of release of super-agent.
Life Cycle	Duration of larval stage <i>Time spent as a larva before settling/changing state</i>	Ranges from <u>20 to 99 days</u> , depending on ambient water temperature: <ul style="list-style-type: none"> 67 to 99 days at 6.6°C 31 to 62 days at 14.5°C 20 to 32 days at 16.6°C (Houde, 1989; Burke et al., 1991; Keefe and Able, 1993; van Maaren and Daniels, 2000)	Minimum larval duration sampled from normal distribution: <ul style="list-style-type: none"> Mean: 25 days Variance: 3 days All durations are from the time of release of super-agent.
Life Cycle	Number of stages between egg and adult <i>Total number of stages between egg and adult</i>	<u>8 stages</u> from hatching to metamorphosis (Martinez and Bolker, 2003)	4 stages modeled: Zygotes, yolk-sac larvae, post-feeding pre-competent larvae, and competent larvae.
Growth	Incubation rate of zygotes <i>Probability that a zygote will hatch and become a larva</i>	Not available	Age-dependent sigmoidal curve for incubation probability. Values are assumed and calibrated against observation data (see section 7.4): <ul style="list-style-type: none"> Maximum incubation probability: 0.7/day
Growth	Competency gain rate of larvae <i>Probability that a pre-competent larva will gain competency</i>	Not available	Age-dependent sigmoidal curve for competency gain probability. Values are assumed and calibrated against observation data (see section 7.1.2): <ul style="list-style-type: none"> Maximum competency gain probability: 0.5/day

Parameter Type	Parameter	Literature Information/Value	Parameterized Value
Growth	Competency loss rate of larvae <i>Probability that competent larva will lose competency</i>	Not available	Age-dependent sigmoidal curve for competency loss probability: <ul style="list-style-type: none"> Maximum competency loss probability: 0.1/day
Mortality	Mortality parameters <i>Parameters related to the selected mortality</i>	Overall range of <u>0.05 to 0.33/day</u> (Houde 1989): 0.05 to 0.33 for <i>Pseudopleuronectes americanus</i> (winter flounder) 0.05 to 0.24 for <i>Paralichthys dentatus</i> (summer flounder)	Age-dependent Type III survivorship curve for mortality rate: <ul style="list-style-type: none"> Minimum daily instantaneous mortality rate: 0.01/day Maximum daily instantaneous mortality rate: 0.3/day

6.4.4.5 Movement

Hydrated eggs average 1.0 mm in diameter and are positively buoyant (specific gravity = 1.0). These eggs float up into near-surface waters, drift passively from the spawning sites, and remain in the upper water column until yolk reserves are fully metabolized. The eggs then transform into larvae, continue to drift passively, and sink lower in the water column. During this metamorphosis, larvae move toward shore, however no clear behavioral mechanism that facilitates this continued shoreward movement is known (Able and Kaiser, 1994).

The shoreward migration behavior of summer flounder applied in the present modeling analyses was derived from a previous modeling study undertaken by Drake et al. (2017) that explored a variety of vertical swimming behaviors, including diel and ontogenetic vertical migration, with a variety of shoreward-directed swimming speeds. However, once near the mouths of estuaries or coastal rivers where tidal forces are prevalent, transforming larvae are surmised to apply selective tidal stream transport to ride the tide upstream (Miller et al., 1991; Forward et al., 1999). Here, juveniles ultimately reside within physiologically favorable segments of salinity and temperature gradients (Howson and Targett, 2020). This mechanism was also included in model development and parameterization.

An overview of the summer flounder super-agent vertical and horizontal movement behaviors simulated in the model are presented in **Figure 6.25** and **Figure 6.26**, and a summary of parameters related to summer flounder movement is presented in **Table 6.16**.

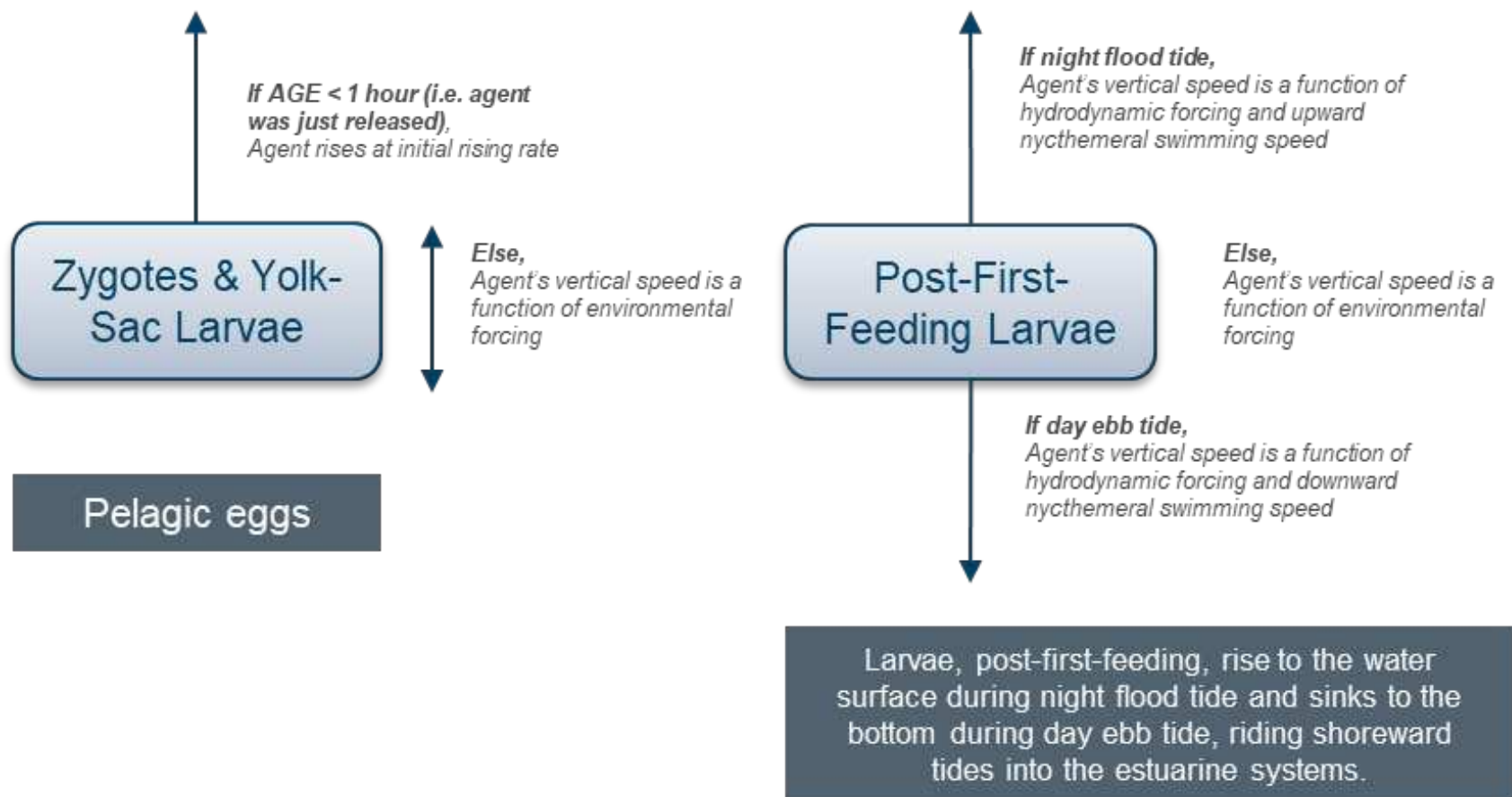


Figure 6.25. Parameterization of Summer Flounder Zygotes and Larval Vertical Movement

Summer flounder zygotes are pelagic and remain buoyant up until they become yolk-sac larvae. Once they start to feed, larvae are capable to vertical swimming, rising to the water surface during night flood tides and sinking to the bottom during day ebb tides.

Agent's horizontal speed is a function of hydrodynamic forcing

Zygotes / Yolk-Sac Larvae

Zygotes and yolk-sac larvae assumed to be passive buoyant agents; carried by currents

If outside estuaries / sounds && post-first feeding,



If inside estuaries / sounds

If flood tide,
Agent's horizontal speed is a function of hydrodynamic forcing

Else (i.e., ebb tide),
Agent's horizontal speed is a reduced function of hydrodynamic forcing

Larvae

Selective tidal stream transport; rides flood tide into estuaries, anchors to bottom during ebb tide

Larvae, post-first-feeding, gain swimming ability to move shoreward (exact behavior mechanism unknown), seeks shoreline, likely settling near estuaries and sounds throughout metamorphosis process.

Figure 6.26. Parameterization of Summer Flounder Zygotes and Larval Horizontal Movement

Agents are passive agents along the transverse plane during the early life stages (i.e., zygotes and yolk-sac larvae). Post-first-feeding, larvae gain swimming ability, migrating shoreward towards the northeastern U.S. coastline. Larvae that have entered the estuarine systems make use of selective tidal stream transport to ride flood tides upstream of the estuaries.

Table 6.16. Summer Flounder Movement Model Parameters

Parameter	Literature Information/Value	Parameterized Value
Buoyancy of egg <i>Maximum buoyancy (positive or negative) speed for fertilized zygotes</i>	Specific gravity of 1.0 – <u>buoyant</u> (Packer et al., 1999)	Maximum upward speed of 0.0012 m/s
Vertical swim speeds <i>Maximum vertical swim speed for larvae, independent of current speeds (m/s)</i>	Nychthemeral speeds (Barbut et al., 2019): <ul style="list-style-type: none"> Upward speed of <u>0.003 m/s</u> during night flood tides Downward speed of <u>0.001 m/s</u> during day ebb tides 	Vertical swim speed is function of hydrodynamic forcings and nychthemeral speeds as detailed in Barbut et al. (2019), depending on daylight and tidal conditions at given timestep.
Horizontal swim speeds <i>Maximum horizontal swim speed for larvae, independent of current speeds (m/s), if present</i>	Shoreward swimming speeds of larvae is estimated to be within the range of <u>6 cm/s</u> for species with small larvae (i.e. 9 to 11 mm) to <u>10 cm/s</u> for species with large larvae (i.e., 14 to 16 mm) (Faillettaz et al., 2018)	Shoreward swimming speed of 0.007 m/s. Shoreward direction is dynamically determined by a built-in function which calculates the direction to shore in relation to the element the agent is occupying at that time.
Temporal changes in vertical distribution <i>Distribution of larvae in the water column dependent on time of day</i>	<p>Movement of late-stage larvae into estuaries October to April. Larvae present in Narragansett Bay from Sept to December (Able and Kaiser, 1994)</p> <p>Late-stage larvae (11 to 15 mm SL) are on bottom at ebb and slack tides but move vertically into the water column on flood tide to facilitate upstream transport (Forward et al. 1999; Hare et al., 2006)</p> <p>Selective tidal stream transport into estuaries (Miller et al., 1991; Forward et al., 1999; Hare et al., 2006)</p>	<p>See above on vertical swim speeds for vertical migration to facilitate upstream transport of larvae.</p> <p>When larvae are in estuaries, selective tidal stream transport is modeled by varying the super-agent's horizontal speed based on tidal conditions; during flood tide, the horizontal speed is a function of hydrodynamic forcing, while during ebb tide, the horizontal speed is a reduced function of hydrodynamic forcing (to simulate anchoring to estuary/riverbed during ebb tide conditions).</p>

6.4.4.6 Substrate Suitability

When larvae enter the mouths and estuaries and rivers, the individuals settle to the bottom or near-bottom waters during ebb tide then migrate upward during flood tides. Individuals will ultimately settle where sediments are fine, and salinity is between 10 and 30 psu. Taylor et al. (2016) verified this for newly settled juvenile summer flounder in the estuaries of Narragansett Bay and Block Island sound. As mentioned, larvae seem to prefer (or survive best) in water temperatures ranging from 9°C to 18°C (Taylor et al., 2016).

The substrate suitability index map for summer flounder (**Figure 6.27**) is based on the preferred substrate of young summer flounder, which is typically sandy material. The summer flounder settling process is similar to that of sea scallop and surfclam except that the super-agent must be located in a grid cell of water depth, temperature, and salinity values within the user-determined thresholds at the time step of settlement. A summary of parameters related to summer flounder substrate suitability is presented in **Table 6.17**.

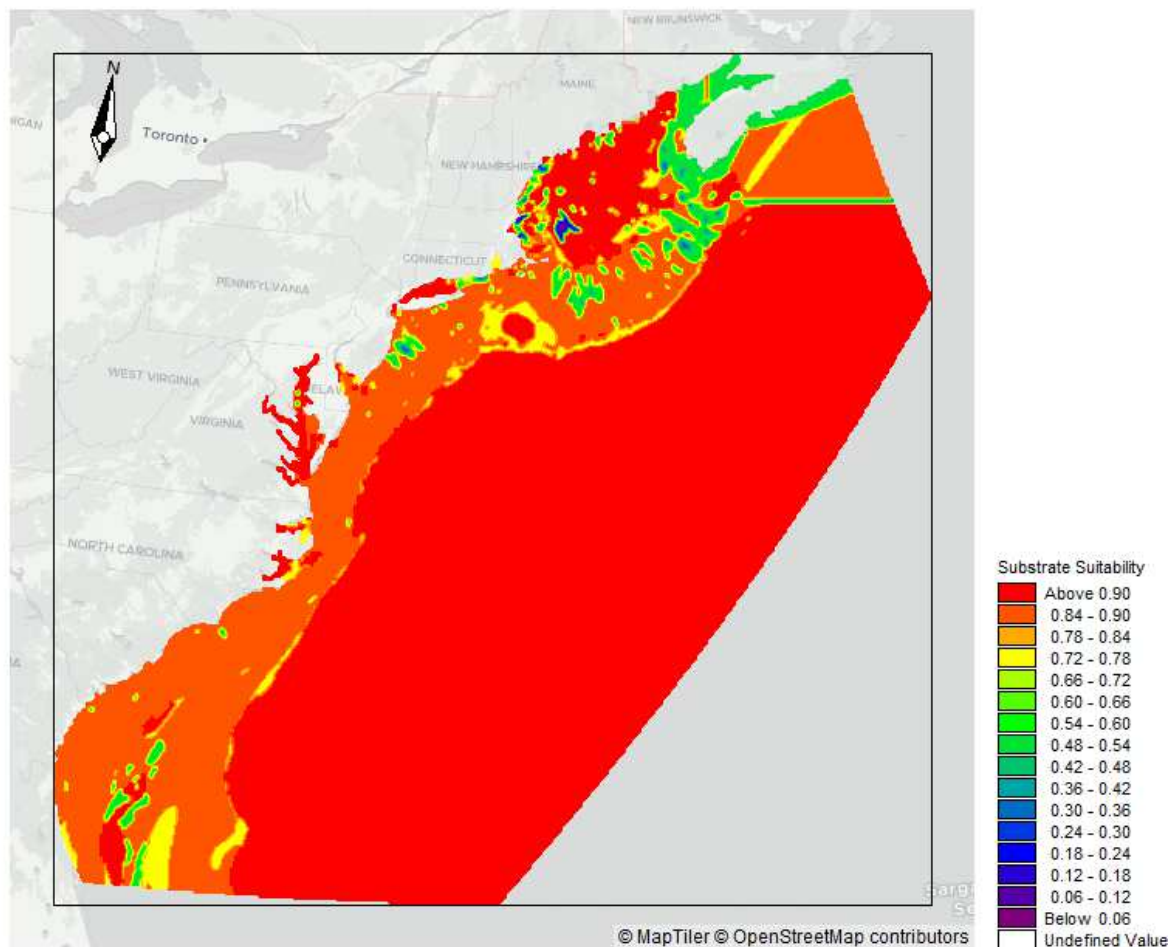


Figure 6.27. Summer Flounder Substrate Suitability Map

Substrate suitability indices are derived from the benthic substrate data (USGS 2005, geographic resolution EPSG: 4269, NAD83), with higher values assigned to areas with substrate types preferred by summer flounder larvae.

Table 6.17. Summer Flounder Substrate Suitability and Settlement Conditions

Parameter	Literature Information/Value	Parameterized Value
Settling indicators <i>Conditions required for larvae to settle/incubate to juvenile</i>	Metamorphic larvae (stages G to H-) prefer <u>sand</u> over mud substrates (Keefe and Able, 1993)	<p>The index values used for the various benthic substrate types are:</p> <ul style="list-style-type: none"> • Sand: 0.9 • Sand-clay/silt: 0.95 • Sand-silt/clay: 0.95 • Sand-clay/silt: 0.95 • Clay: 0.1 • Gravel-sand: 0.5 • Gravel: 0.3 • Bedrock: 0.1 • Outside estuaries: 0.001 x of the values above, depending on substrate type <p>Water depth thresholds for settlement:</p> <ul style="list-style-type: none"> • Minimum: 1 m • Maximum: 35 m
Temperature effects <i>Potential effects from changing temperatures</i>	High mortality in water temperatures <u>< 4.4°C</u> (Keefe and Able, 1993) Larvae survival at <u>4 to 25°C</u> (Taylor et al., 2016)	<p>Temperature thresholds for larval settlement:</p> <ul style="list-style-type: none"> • Minimum: 4°C • Maximum: 25°C
Salinity effects <i>Potential effects from changing salinity</i>	Larvae collected from <u>0 to 33</u> (Able and Kaiser 1994) Larvae found in estuarine salinities <u>0.1 to 5; 16 to 19</u> (Taylor et al., 2016)	<p>Salinity thresholds for larvae settlement:</p> <ul style="list-style-type: none"> • Minimum: 0 psu • Maximum: 35 psu

6.4.5 Horizontal and Vertical Dispersion Calibration

Horizontal and vertical dispersion of super-agents is controlled in the ABM through horizontal and vertical dispersion parameters, defined by the user. These dispersion parameters determine how freely an agent moves within the HD model domain. These parameters are included in the MIKE ECO lab ABM setup in order to account for the effects of unresolved turbulence in the hydrodynamic model and the magnitude of dispersion is scaled to the magnitude of the predicted currents. Recommended values for horizontal and vertical dispersion are available but are always a calibration factor. Values of horizontal and vertical dispersion for all species were selected from within a given range of values and the model results are analyzed. A sensitivity test was performed and the parameter with the best results against observational data (i.e., larval settlement distribution patterns in this case) was chosen. Values in the order of 1 are usually recommended for the scaling factor for horizontal dispersion and the scaling factor for the vertical dispersion is usually much smaller, e.g. ~ 0.00001 (Rodi, 1980). The values selected and used for each species ABM were $0.8\text{m}^2\text{s}^{-1}$ for horizontal dispersion and $0.0001\text{m}^2\text{s}^{-1}$.

6.5 Ensemble Initialization Set-up

For each target species, multiple test model simulations were initially carried out and the results were analyzed statistically, to find a point of “convergence”. Namely, the point at which the results of the ensemble (i.e., the collection of individual model runs) begin to stabilize and consistently produce similar outcomes, despite the inherent stochastic elements of each run. The standard error of the mean (SEM) was used for analyzing the convergence of the ensemble (e.g., Geweke, 1991). Here, the mean settled density of larvae from the last time step of the first model simulation was calculated. The mean settled density of the next model simulation was then calculated and used with the mean of the first model result to calculate the SEM. This process was repeated, so that cumulative SEM of model simulation results were calculated as further simulations were completed. The number of simulations was increased until the SEM began to stabilize.

The point at which the SEM plateaus indicate the number of simulations required in an ensemble to produce robust results. For all three species, the optimal number of simulations was identified to be ~ 25 (**Figure 6.28**, **Convergence Analysis of Sea Scallop Ensemble Model Iterations for Year 2017**, **Figure 6.29**, and **Figure 6.30**). Each full production run ensemble therefore comprises the results of 25 model simulations. This approach allowed for computational efficiency to be balanced with model robustness, as increasing the number of individual model simulations beyond 25 simulations would not improve the ensemble results (i.e., decrease the uncertainty in the results).

For each species, approximately 25,000 to 30,000 super-agents were released, which contain millions of individuals. This number of agents released was determined partly by computational efficiency, limiting the number of agents that could be included in each simulation. The number of agents released is the same for each of the 25 model clones of the ensemble, but the location of their release within the spawning area will be stochastic and the trajectory of the agents will change with each simulation. The number of agents used and the number of ensembles runs results in a stable convergence, but it is difficult to know how much of the variability between ensembles is due to stochasticity in input parameters and how much is due to the number of super agents.

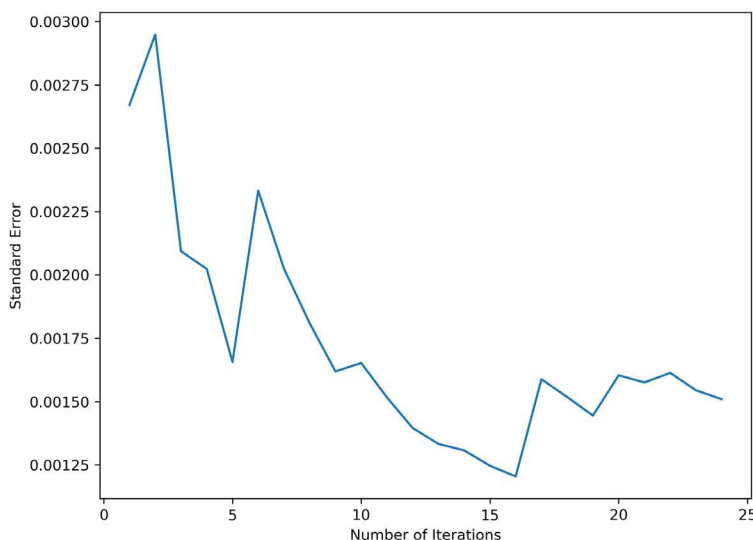


Figure 6.28. Convergence Analysis of Sea Scallop Ensemble Model Iterations for Year 2017

Shows the standard error of the ensemble results, standard error initially increases and then begins to plateau as the number of simulations is increased to 25.

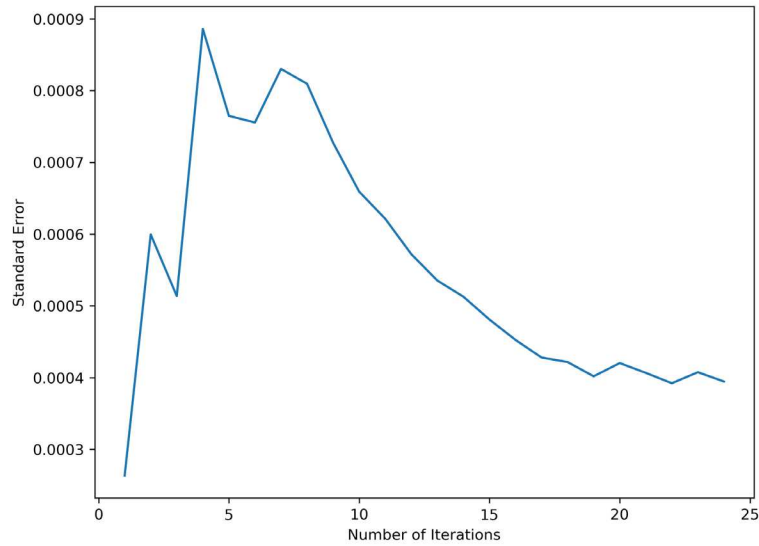


Figure 6.29. Convergence Analysis of Surfclam Ensemble Model Iterations

Shows the standard error of the ensemble results, standard error initially increases and then begins to plateau as the number of simulations is increased to 25.

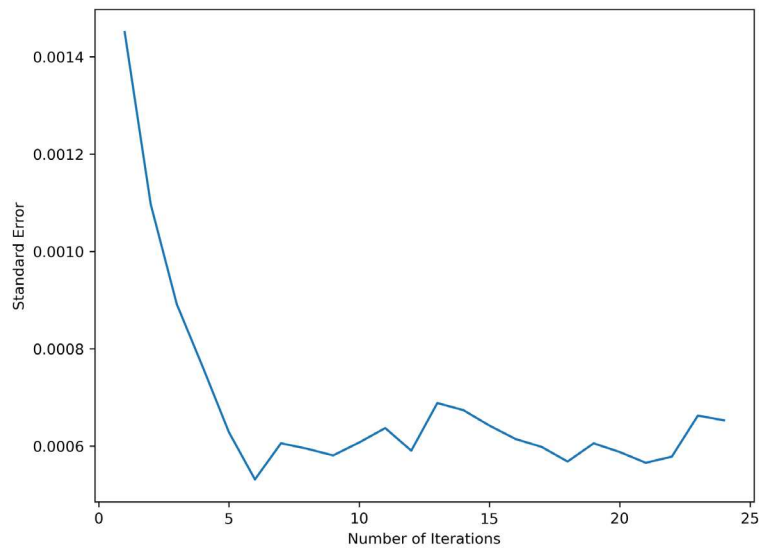


Figure 6.30. Convergence Analysis of Summer Flounder Ensemble Model Iterations

Shows the standard error of the ensemble results, standard error initially increases and then begins to plateau as the number of simulations is increased to 25.

6.6 Connectivity Analysis Set-up

6.6.1 Connectivity Analyses

The connectivity analysis was set up to track where larvae from each spawning area settle. A map of destination areas was developed ([section 6.6.1.1](#)) and the total number of larvae settling in each destination area and their origin spawning area at the end of the model simulation was recorded. In order to carry out the analysis, the following three sets of data were collected from the model results:

1. Total number of individuals released from each **spawning area**

2. Total number of individuals released from each **spawning area** that successfully settle in any of the destination areas
3. Total number of individuals that settled in each **destination area**

From these three sets of data, settlement probabilities were calculated using equation 1.

$$P_{settle(origin, destination)} = \frac{N_{origin \rightarrow destination}}{N_{origin}} \quad (\text{equation 1})$$

The settlement probability (P_{settle}) represents the proportion of larvae that disperse from a spawning area to a destination area, relative to the total number of larvae released from the spawning area (Pata, 2019). This provides a standardized way to compare movement patterns across different areas, accounting for varying numbers of larvae released from each source. $N_{origin \rightarrow destination}$ is the number of larvae from a particular spawning area that settled in a particular destination area (e.g., the number of sea scallop larvae that have spawned from the Mid-Atlantic Bight that settled in New Jersey destination area NJ5, see **(Figure 6.32. Shellfish Specific Destinations Map – Colored by Region)**, and N_{origin} is the total number of larvae that were released from a particular spawning area (in this example, the Mid-Atlantic Bight). Settlement probabilities were then normalized to the total sum of the larvae settlement probabilities (i.e., all larvae independent of spawning location).

To analyze the potential impacts of the OSW developments on larval settlement and to potentially help identify the causes of any changes in settlement densities observed in the results, the differences of baseline connectivity matrices and scenario connectivity matrices were calculated. The changes in connectivity that are displayed in the barplots in **sections 8.3 and 8.4** are therefore showing changes in connectivity that are proportional to amount of larvae released from each spawning area. As a result, smaller spawning areas can appear to contribute greatly to reduced or increased settlement in certain destination areas, where the absolute change in the number of settled individuals may be relatively small compared to other larger spawning areas. This is important to consider when evaluating impact and when comparing scenarios to the baseline. For example, a 50 % reduction in settlement from a particular spawning area with low biomass may have no measurable impact on population recruitment, while in another case with large spawning biomass, the same 50% reduction could result in population and fisheries relevant changes in recruitment.

6.6.1.1 Destination Area Mapping

The purpose of the destination map is to allow for quantification and analysis of larval distribution, connectivity and settlement along the U.S. East Coast, by providing a meaningful spatial reference for where larvae settle (**Figure 6.31 and Figure 6.32. Shellfish Specific Destinations Map – Colored by Region**). The destination map includes multiple destination units, which were grouped into broader regions, to allow for a broad regional analysis, as well as more detailed analysis of localized effects that may occur on smaller spatial scales, with special focus on and near the wind energy areas (WEAs). Destination units within the map were used to analyze potential changes in settlement patterns resulting from offshore wind development (OSW) scenarios, as well as changes in connectivity between spawning regions (i.e., comparing where larvae spawn to where they settle, in baseline and OSW development scenarios).

The destination units were grouped into six regions: Georges Bank (GB), Southern New England (SNE), Long Island (LI), New Jersey (NJ), Delmarva (DMV), and South Virginia (SVA). Regions were further tailored as needed capture the nuance in species' movement patterns and to be specifically useful for this assessment of OSW impacts.

In particular, surfclam and sea scallop inhabit similar regions of the East Coast continental shelf area, with destination maps divided by bathymetric categories to capture the high densities of larvae settlement in the nearshore and offshore regions. Full WEAs were included as individual destination units, with no further delineation by leasing state or individual. For the summer flounder destination map, the area to the south of SVA was divided by bathymetry and each estuary was resolved within the model domain as a unique destination unit. This was done as summer flounder larvae settle inshore or in estuaries, making the nearshore (shoreline to 10 m) destinations and estuaries important areas of analysis.

Additional areas, including such as important fishing grounds and habitats, were not included as specific destination units but were overlaid on top of settlement maps, to allow for qualitative analysis and to bring context to the quantitative settlement and connectivity analyses. These areas were identified by fisheries experts at CSA, and include areas of intense bottom fishing, sea scallop rotational closure areas and designated Habitat Areas of Particular Concern.

More detailed coverage of how the destination maps were developed and the rationale for choosing certain delineations are provided in **Appendix B**.

6.6.1.1.1 Shellfish Specific Destinations

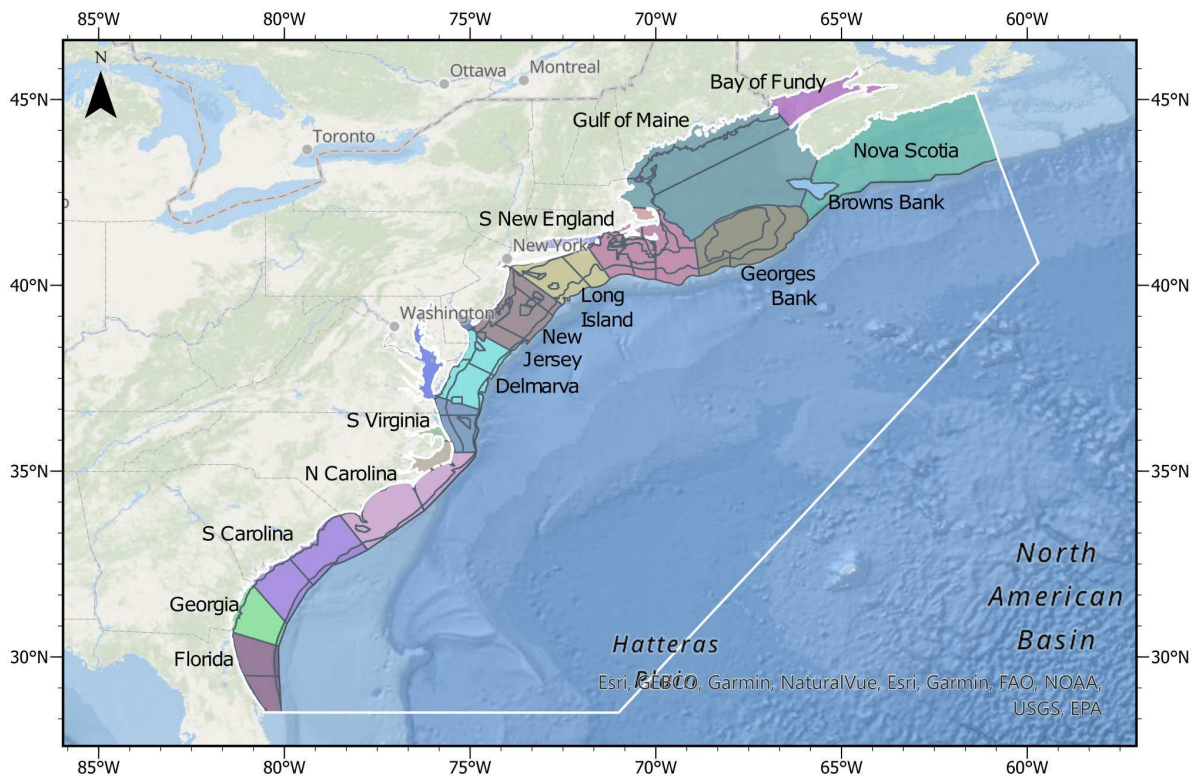


Figure 6.31. Shellfish Specific Destinations Map – Within the Model Domain
Destination Map, Colored by Region, Within the Model Domain (White Line)

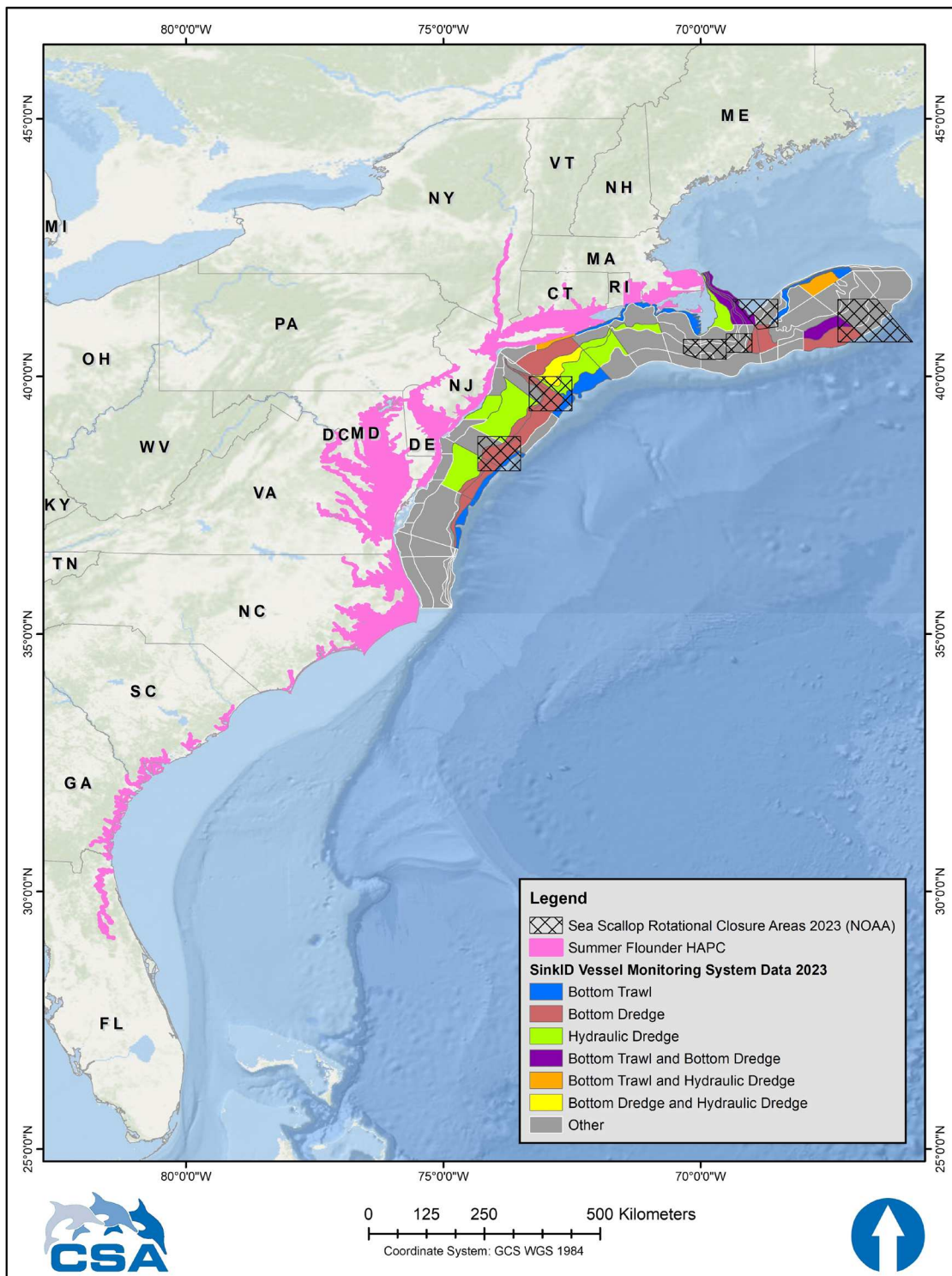


Figure 6.33. Pertinent Fisheries Areas as Identified by CSA to be Used for Qualitative Analysis and Context

6.7 Agent-Based Modeling Evaluation Method

The ABM Baseline results were evaluated using Pattern Oriented Modeling (POM), a bottom-up approach to complex systems analysis, developed to model complex ecological and agent-based systems (Grimm and Railsback, 2005). According to Grimm et al. (2005) traditional ecosystem models attempt to approximate the real system as closely as possible. Whereas POM works under the assumption that an ecosystem is so information-rich that the respective model will inevitably either leave out relevant information or become over-parameterized and lose predictive power.

As stated in Grimm et al. (1996), POM is an attempt to mimic the scientific method, as it requires the researcher to begin with a pattern found in the real system, posit hypotheses to explain the pattern, and then develop predictions that can be tested. Through this focus on the pattern, the model can be constructed to include only information relevant to the question at hand. POM also supports modeling by better enabling the identification of the appropriate temporal and spatial scale at which to study a pattern, thereby avoiding the assumption that a single process might explain a pattern at multiple temporal or spatial scales (Grimm et al., 2005). It does, however, offer the opportunity to look explicitly at how processes at multiple scales might be driving a particular pattern.

The baseline settlement patterns from all species were analyzed using POM through a comparison of model outputs with ecological patterns for the target species apparent from applied survey datasets (see **Section 6.2.3.2**) or values from peer-reviewed literature. Three overall pattern structures selected for the current analysis were spatial distribution, temporal development, and vertical distribution of agents. Each structure was analyzed using different approaches but were, to the extent possible, kept similar across species (Johnson et al., 2021).

6.7.1 Pattern 1: Spatial Distribution

The spatial distribution of modeled larvae was compared to available information on the observed spatial distribution. This was achieved by correlating the observed distributions of sea scallop and surfclam⁶ biomass data with modeled distributions of settled larvae density. This correlation analysis was conducted using three techniques:

- a Gamma Rank correlation, measures the ordinal association between two vectors (Goodman and Kruskal, 1979)
- Spearman's rho is a nonparametric measure of the monotonicity of the relationship between two datasets (Virtanen et. al., 2020)
- Kendall's tau is a measure of the correspondence between two rankings (Virtanen et. al., 2020).

While each technique applies slightly different statistical methodologies, they were selected as they compare values based on an ordinal scale rather than on absolute values.

Initially, a spatial grid with a pre-set resolution was superimposed on the model data and the associated observation data. The data within each grid cell was summarized into a grid-cell value. Subsequently, the correlation analysis was conducted pairwise between corresponding spatial-grid cells. Furthermore, to analyze the effect of resolution on the validation results, the analysis was conducted several times, using a varying grid-cell resolution between 10,000 m to 100,000 m cell size, with 10,000 m increments.

⁶ This analysis was not carried out for summer flounder because available observation data was for adults that are fully mobile with a significant range. As such, it could not be adequately used to compare summer flounder model results for larvae settlement along near shore areas.

Comparisons were also conducted visually, by plotting the model and survey distributions in the most suitable resolution, estimated from the correlation techniques.

6.7.2 Pattern 2: Temporal Development

The transformation from zygote to settled organism was scripted in the ABM as a stochastic process, with incubation times governed by probability functions. The transition between phases were adjusted through a series of probabilities that estimated the chance of an agent within the super-agent to transition into the next phase, to stay in current phase or to die. This pattern of transition into phases was used as a secondary validation pattern. As no raw data was available for direct comparison between model output and empirical survey data, referenced literature was applied as it provides indicative phase durations. These values were compared with average phase durations in the model data.

6.7.3 Pattern 3: Vertical Distribution

The vertical distribution of suspended zygotes and larvae was used as a third pattern, to ensure that the vertical position of agents coincided with observed vertical distributions of the species. While most of the vertical transport was governed by the vertical currents in the HDM, the selected species did have independent vertical movement abilities.

The initial analysis was based on the vertical depth distribution of the particles. This was analyzed by estimating the average depth of the suspended particles across the domain at every time step, along with the estimate of the standard deviation. This distribution was compared to literature information on depth distribution of the species. Additionally, for the species that could control their vertical movement the diurnal vertical movement of the particles was estimated by calculating the average vertical movement at each half hour during a diurnal cycle, including the standard deviation in vertical movement. This was also compared to literature values.

6.8 Results Post Processing

The large size of the analysis area as well as magnitude and complexity of the ABM results required careful consideration of which plots, charts or matrices would best explain estimated baseline larvae settlement patterns and the potential estimated impact of OSW induced oceanic changes on larval settlement. The subsections that follow provide an overview of the methods employed to produce the visualizations, further detail on what the plots show and how these should be interpreted is provided in **Table 7.1** and **Table 8.1**. Explanation of Scenario Analysis Plots and Charts.

6.8.1 Baseline Post Processing

Plots of mean estimated settled larval density of the baseline ensemble results were generated to illustrate the settlement distribution of each species throughout the model domain. Baseline results, however, were also shown as connectivity matrices, bar charts, and swarm plots, which are described in more detail below. All the baseline plots described below can be found in **section 7**.

6.8.1.1 Swarm Plots of Settled Larvae

A swarm plot was developed for sea scallops to demonstrate interannual variability in larvae settlement. The plot format illustrates total larval settlement in the most common destination areas, for each model clone (i.e., represented by a single scatter point) for each year modeled in the ensemble (2017, 2018, 2020). The data processing required to create these plots began by linking settled larvae data to destination areas, ranking these destinations in descending order, and saving the top 10 destinations for

settled larvae for each simulation across all scenarios. The data was further refined by isolating the most common destinations between scenarios.

6.8.1.2 Connectivity Matrices and Maps

The baseline connectivity matrix shows the percentage of the total larvae settling in each destination area, proportional to the number of larvae released from each spawning location. The matrix was generated by tabulating the percent settled larvae at a destination according to its origin.

6.8.2 OSW Buildout Scenarios Analyses

Difference plots of mean settled larval density for OSW build-out model ensemble results were generated to illustrate the change in spatial dispersal of each species. These, as well as the accompanying cluster analysis, settled larvae density difference bar chart, swarm plots of settled larvae, and the connectivity change bar charts are further explained below. All the OSW scenario results plots described here can be found in **section 8**.

6.8.2.1 Difference Plots of Mean Settled Larvae and Density and Total Settled Larvae

Difference plots were created to show the difference in settled density or total settled larvae, between the baseline and scenario model results. The baseline mean settled density (or total settled larvae) across the ensemble (i.e., for each of the 25 model simulation results that make up the ensemble) was calculated for each model element (i.e., model grid cell). Similarly, mean settled larvae density (or total settled larvae) was calculated for each OSW scenario ensemble. A spatial difference plot was then generated from the difference in the baseline and OSW scenario settled densities, showing the change in each model element from baseline to scenario.

The total settled larvae accounts for the number of larvae within an element, but smaller elements (such as those where wind farm areas are located) cannot contain the same number of larvae as larger elements (i.e., causing them to be excluded from related plot illustrations). Consequently, the results were normalized by dividing the count of larvae by the area size of each element, resulting in settled larvae density. The difference in mean settled larvae density is more effective for illustrating the impacts within the wind farms (where the elements are smaller) from each build-out scenario.

6.8.2.2 Cluster Analysis – DBSCAN Density-based Spatial Clustering of Applications with Noise

Density-Based Spatial Clustering of Applications with Noise (DBSCAN) is a clustering algorithm that is particularly noted for its effectiveness in identifying clusters of varying shapes and sizes in spatial data that includes noise and outliers and was developed by Ester et al. (1996). DBSCAN groups data points into clusters by identifying areas where there are high densities of similar data points, and separates these from points in low-density regions, which are typically considered noise.

The DBSCAN tool within the scikit-learn python package was used to identify areas (clusters) of increased or decreased settlement (both of total settled larvae and of settled density) resulting from each OSW scenario (Scikit-learn, 2024). DBSCAN requires two parameters, epsilon and minimum points. Epsilon is the search radius around each data point, to be considered for identifying similar data points, and “minimum points” is the minimum number of points required to identify high density regions that can be classed as a cluster. The choice of epsilon and minimum points was determined using a k-distance plot, which shows the distance to the nearest neighbor for each point. The point of maximum curvature on this plot, or the “elbow”, was used as an indication of the value of epsilon to be used in the cluster analysis. DBSCAN was utilized with epsilon of 0.4 and minimum points of 5 to determine clusters of change for each species and OSW scenario.

6.8.2.3 Settled Larvae Density Difference Bar Chart

The mean of absolute settled larvae in each destination area at the end of the model simulation was calculated for the baseline and scenario model results. The difference in the mean number of settled larvae between the baseline and the scenarios, were then calculated. These were plotted as absolute change in the number of larvae for each destination area.

6.8.2.4 Swarm Plots of Settled Larvae

Similar to the baseline version, swarm plots were developed for each target species for each build out scenario. Rather than examining interannual variability however, the plot format illustrates baseline and scenario total settled larvae estimated for each model clone, showing differences in settlement between the baseline and the selected scenario for each of the most common destination areas. The data processing began by linking settled larvae data to destination areas, ranking these destinations in descending order, and saving the top 10 destinations for settled larvae for each simulation across all scenarios. The data were further refined by filtering out the most common destinations between scenarios.

6.8.2.5 Connectivity Difference Bar Chart

The OSW build out scenario connectivity matrices show the change in the proportion of settled larvae in each destination area, originating each spawning region, that result from the OSW farms. First, a connectivity matrix was created for each simulation using the methods described in **section 6.5**. Then, the average of these simulations was calculated, resulting in an aggregated connectivity matrix that shows the Mean Settled Larvae, adjusted for each origin's population. The baseline matrices were compared across different scenarios by calculating the differences (i.e., subtracting one from the other).

6.9 ABM Model Performance and Calibration

Developing acceptable baseline larval settlement results that best represent observed biomass and species distribution was a key step, that allows for changes in settlement resulting in the development of OSW to be analyzed. The baseline results were calibrated (parameters adjusted until there were in best agreement with observed data or literature values) and then final “production” baseline results were evaluated via a statistical Pattern Oriented Modeling approach. The baseline results and their calibration and evaluation are detailed in the following **section 7**. To aid understanding, the results are presented and explained first, and the calibration and evaluation methods are explained thereafter.

7 Larval Dispersal Modeling Baseline Results and Analysis

This section shows the agent-based model baseline results for sea scallop, surfclam, and summer flounder through a series of plots and matrices, including settled larvae density plots, swarm plots, connectivity matrices, and connectivity maps. To aid understanding of the calibration and evaluation steps, the baseline ABM results are presented first, and details of how the baseline was calibrated and evaluated are then provided in **Section 7.4**. The following plots show baseline settled density and connectivity results for sea scallop for the years 2017, 2018, and 2020; and surfclam and summer flounder for 2017.

As a broad overview, the presented larvae density plots show the spatial distribution of settlement density, while the swarm plots show the total settled larvae in the most common destination areas for the modeled years for each model simulation completed in each ensemble. The connectivity matrix shows where larvae spawned from a specific area are most likely to settle. A more detailed description of each plot, how they were derived and how to interpret them can be found in **Table 7.1**.

Table 7.1. Explanation of Baseline Analysis Plots and Charts

Applied Plot or Chart	Explanations
Baseline Larvae Density Map	The density map shows the mean settled larvae density of the ensembled results, averaged per model grid element. The darker blue areas represent areas of elevated settled larval density, while the lighter shade represent less settled larval density.
Swarm Plot of Net Statistics of Larvae Settlement in the Most Common Settlement Destinations	<p>Swarm plots are a powerful tool for visualizing the distribution of a continuous variable across different categories, providing a representation of net statistics. Swarm plots were generated by associating settled larvae data to destination areas, ranking these destinations in descending order, and presenting the top destinations for settled larvae for each simulation across all scenarios.</p> <p>In the swarm plot, each scatter point represents the total number of settled larvae in a destination area for each model simulation. The spread of these points indicates the distribution of settled larvae across different simulations, representing net statistics of larvae settlement. A predominantly horizontal spread of points signifies less variation among simulations, while a predominantly vertical spread indicates greater variation.</p> <p>The density of points at each destination illustrates how settlement patterns change between different modeled years. For instance, if the group of scatter points in a particular destination area is generally higher or lower compared to another group, it suggests that the amount of settled larvae in that destination area has been influenced by inter-annual variability in oceanic conditions.</p>

Applied Plot or Chart	Explanations
Baseline Connectivity Matrix and Map	The baseline connectivity matrix shows the percentage of the total larvae settling in each destination area, proportional to the number of larvae released from each spawning location. The matrix was generated by tabulating the percent settled larvae at a destination according to its origin. This matrix is important in understanding larvae origins and destinations, as otherwise it would be difficult to identify settlement trends based on current direction. Each connectivity matrix was accompanied with its respective connectivity map. Each sub plot shows the settled larvae percentage in each destination area, by spawning area. Darker colors indicate higher percentages of settled larvae being received in a certain destination area.

The connectivity matrix is also visualized through the connectivity maps that link spawning areas to destination areas. These plots and subsequent analysis refer to destination areas and names as found in **Figure 7.1**.

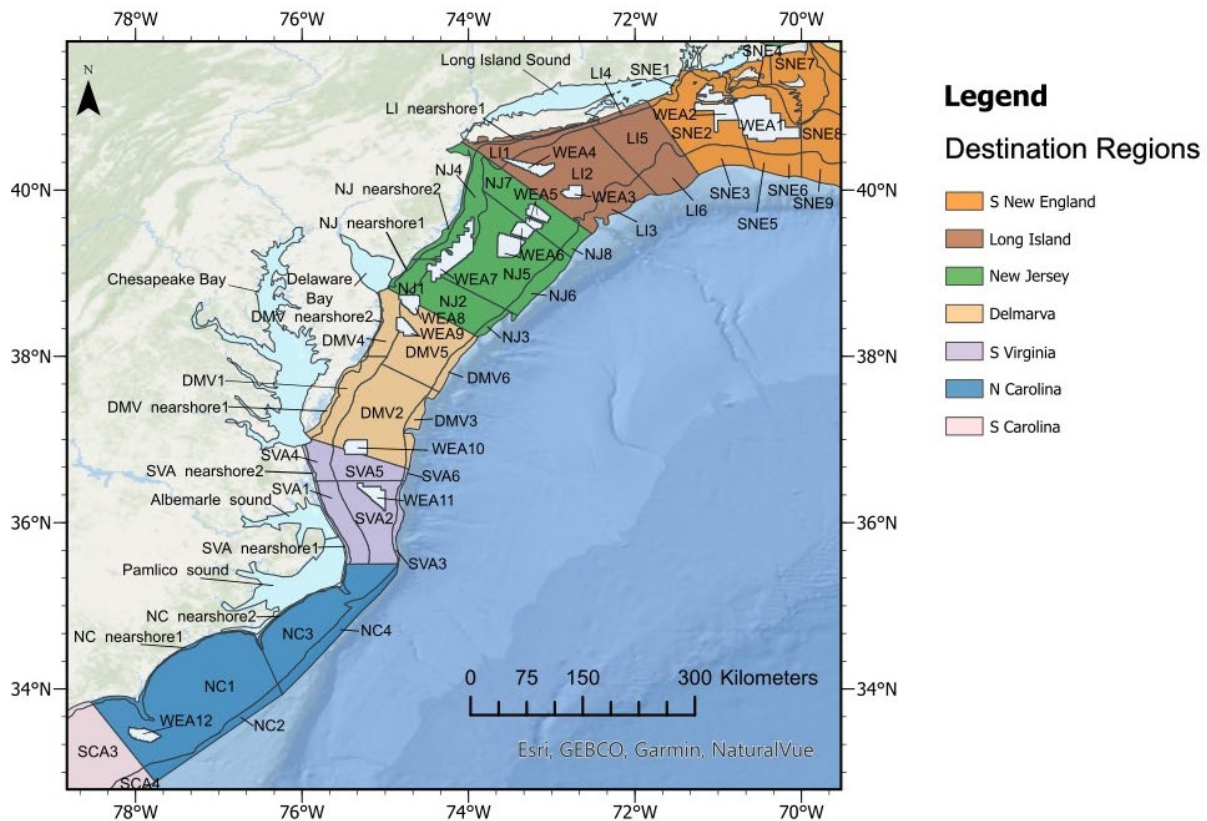


Figure 7.1. Destination Reference Map Showing Each Destination Area and Names, Colors Represent Broad Regions

7.1 Sea Scallop

7.1.1 Inter-Annual Variability in Sea Scallop Settlement

Sea scallop results were produced for 2017, 2018, and 2020. Each year is presented individually in the sections below. The swarm plot in **Figure 7.2** shows the total settled sea scallop larvae in the most common destination regions for modeled years 2017, 2018, and 2020. Each point represents the number of settled larvae estimated for the destination area from one model simulation, and each color cluster represents the results of the full ensemble of model results for a particular year.

Most sea scallop larvae tend to settle offshore New Jersey, the destination area with the greatest sea scallop settlement is NJ5. As evident from the vertical spread of color clusters, there is inter annual variability in the results. For example, settlement in 2018 is lower in NJ5 than in 2017 and 2020, which have similar absolute larvae settlement.

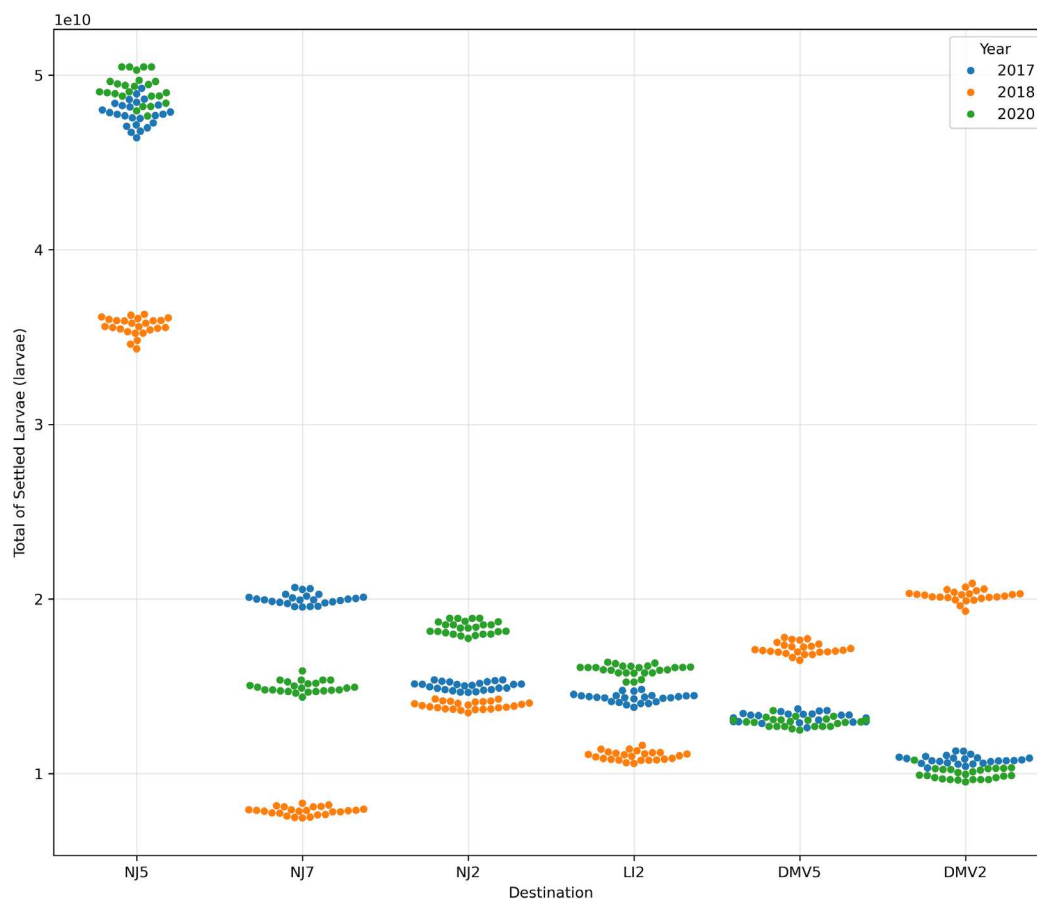


Figure 7.2. Swarm Plot of Sea Scallop Settled Larvae Showing Total Settlement in Main Destinations for 2017, 2018, and 2020

Total settled sea scallop larvae for the most settled destinations. Each point represents one model result from the total ensemble (all points of the same color). Inter-annual variability is shown as settlement differs from year to year. A greater vertical spread in the swarm shows greater variability within the ensemble (for points of the same color) and between years (for large spread between points of different colors). A greater horizontal spread shows lower variability between ensemble results and years.

7.1.2 Baseline Results for 2017

Sea scallop baseline model results for 2017 are shown in **Figure 7.3** and Error! Reference source not found.. Settled sea scallop larvae density in **Figure 7.3** is evident by darker shaded areas having the greatest settlement density. Regions where the greatest modeled sea scallop settlement occur include the Mid-Atlantic Bight offshore New Jersey, and the New York Bight along the outer coast of Long Island. Baseline settled densities are compared against observational data and essential fish habitat areas in **Section 7.4** to evaluate the model's ability to estimate larval settlement patterns and densities.

Sea scallop connectivity is described in Error! Reference source not found.. The connectivity matrix shows where the model predicts larvae spawned from specific areas (i.e., spawning areas shown in the map in the center, such as Georges Bank or Mid-Atlantic Bight) are most likely to settle (i.e., in which destination areas, see **Figure 7.1**). The matrix shows the percentage of the total larvae settling in each destination area, proportional to the number of larvae released from each spawning location (see **Section 6.3**). The Mid-Atlantic Bight appears to be the most important region for sea scallop spawning and settling, as the greatest settled larvae percentages are found in this column of the matrix. The destination areas offshore New Jersey (e.g., NJ5) and Delmarva (e.g., DMV2, DMV5) which are colored darker indicate that larvae spawned from the Mid-Atlantic Bight settle mostly in these areas. Other spawning areas also contribute to settled larvae throughout the model domain, but the percentage of settled larvae from these regions are low relative to the Mid-Atlantic Bight, due to the greater magnitude of larvae spawned from the Mid-Atlantic Bight and the proportional scaling of the results.

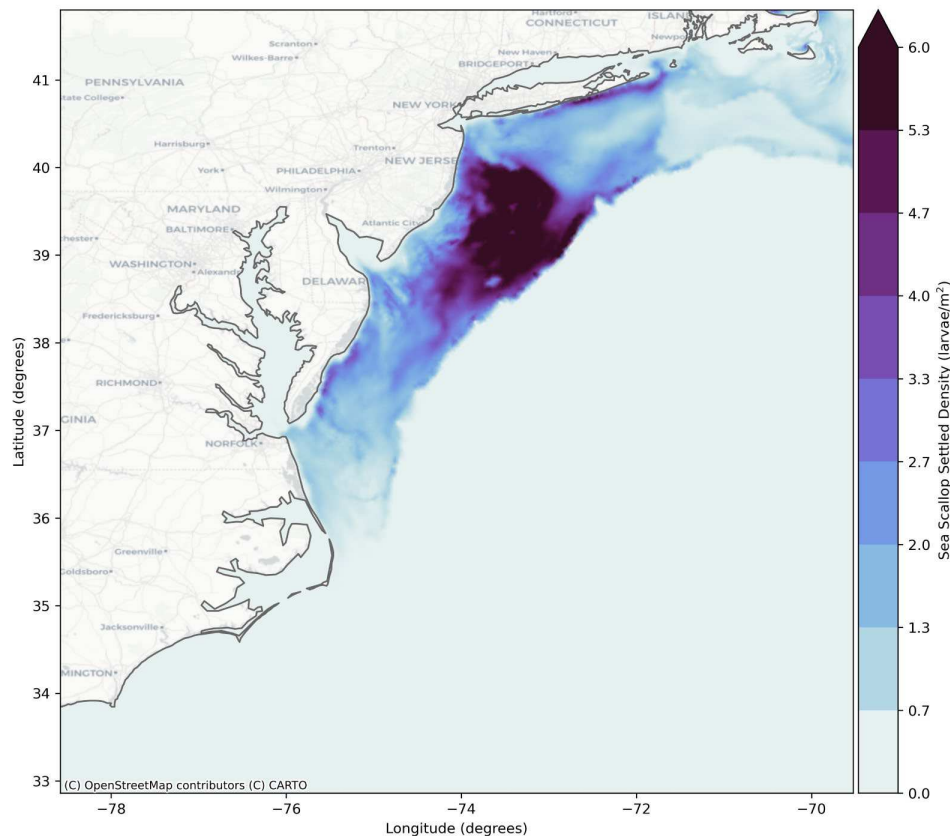


Figure 7.3. Baseline Ensemble Settled Larval Sea Scallop Density 2017

Mean settled larval sea scallop density (larvae/m²) of the ensemble results, averaged per model grid element.

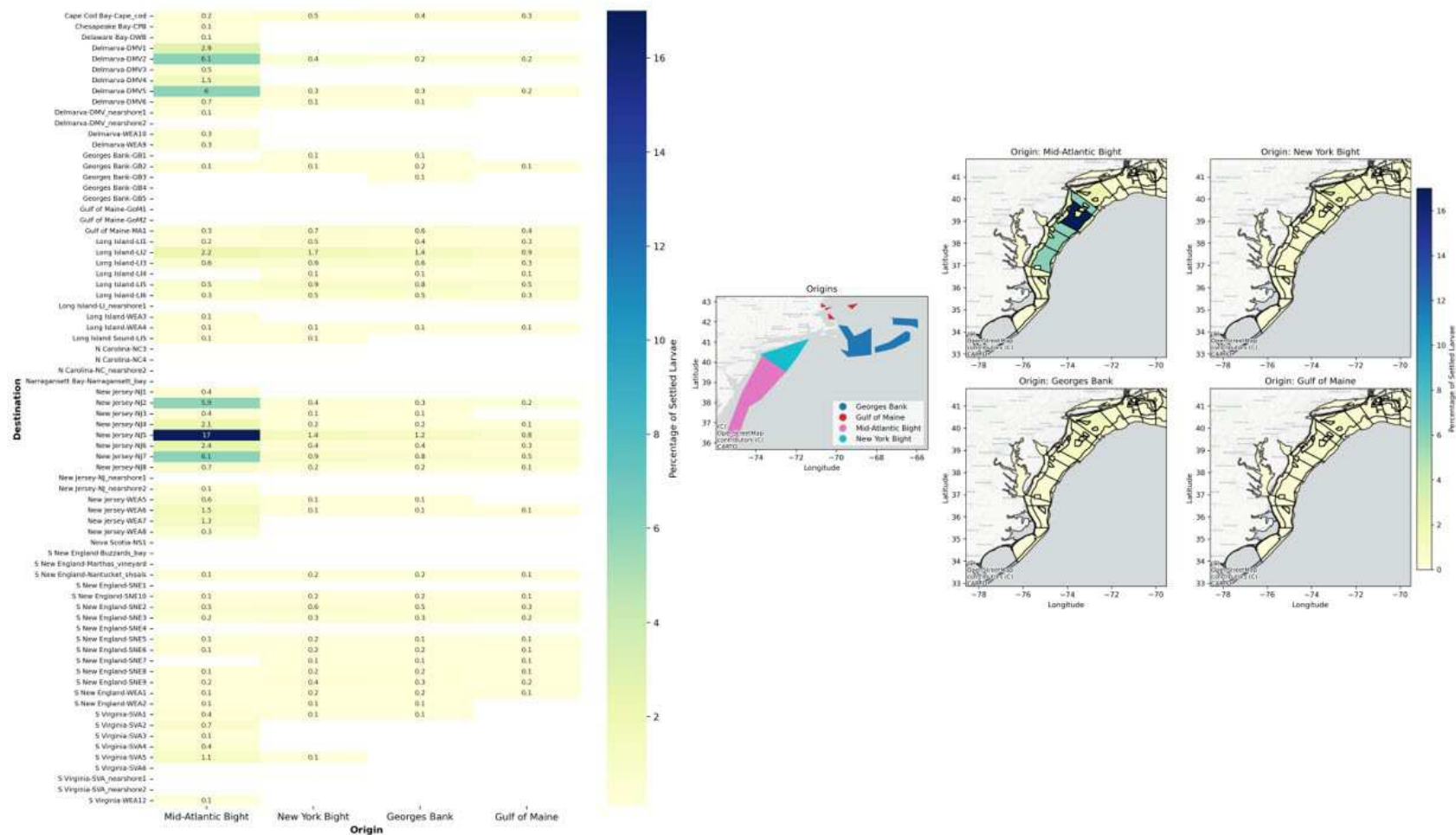


Figure 7.4. Baseline Connectivity Matrix (left) and Connectivity Map (right) for Sea Scallop Larvae – Aggregated Ensemble Results for 2017

Matrix and map show the settlement destinations by spawning origin, i.e., the number of larvae settling in a certain destination that spawned from a certain origin.

7.1.3 Baseline Results for 2018

The 2018 sea scallop baseline model results are shown in **Figure 7.5** and Error! Reference source not found.. As seen in **Figure 7.5**, the regions where the greatest sea scallop settlement occurs include the Mid-Atlantic Bight from offshore New Jersey to offshore South Virginia. The region along the outer coast of Long Island also shows higher settled density, though not as dense as that found in the Mid-Atlantic Bight.

The 2018 modeled results of sea scallop connectivity are shown in Error! Reference source not found.. Similar to 2017, the connectivity matrix indicates that the Mid-Atlantic Bight appears to be the most important region for sea scallop spawning and settlement, with the same destination areas offshore New Jersey (e.g., NJ5) and Delmarva having greatest settlement of larvae spawned from the Mid-Atlantic Bight. The 2018 connectivity matrix shows slight variations compared to 2017, as other destination areas such in Delmarva (e.g., DMV2 and DMV5) as well as South Virginia (e.g., SVA2) have relatively high settlement of larvae spawned from the Mid-Atlantic Bight.

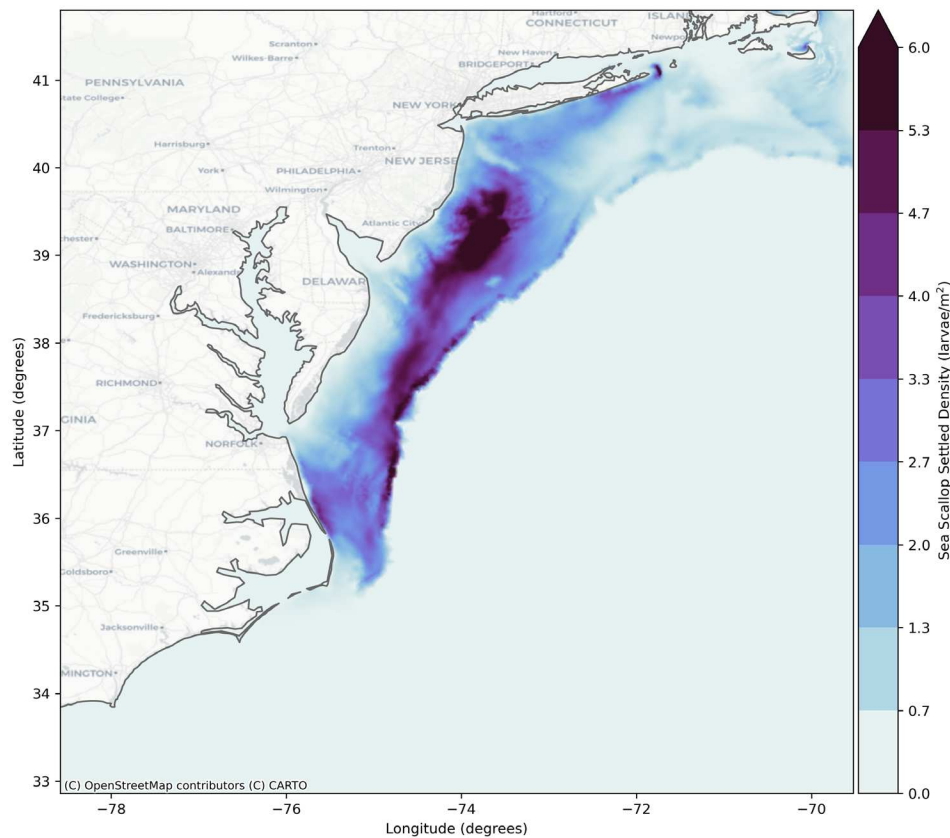


Figure 7.5. Baseline Ensemble Settled Larval Sea Scallop Density 2018

Mean settled larval sea scallop density (larvae/m²) of the ensemble results, averaged per model grid element.

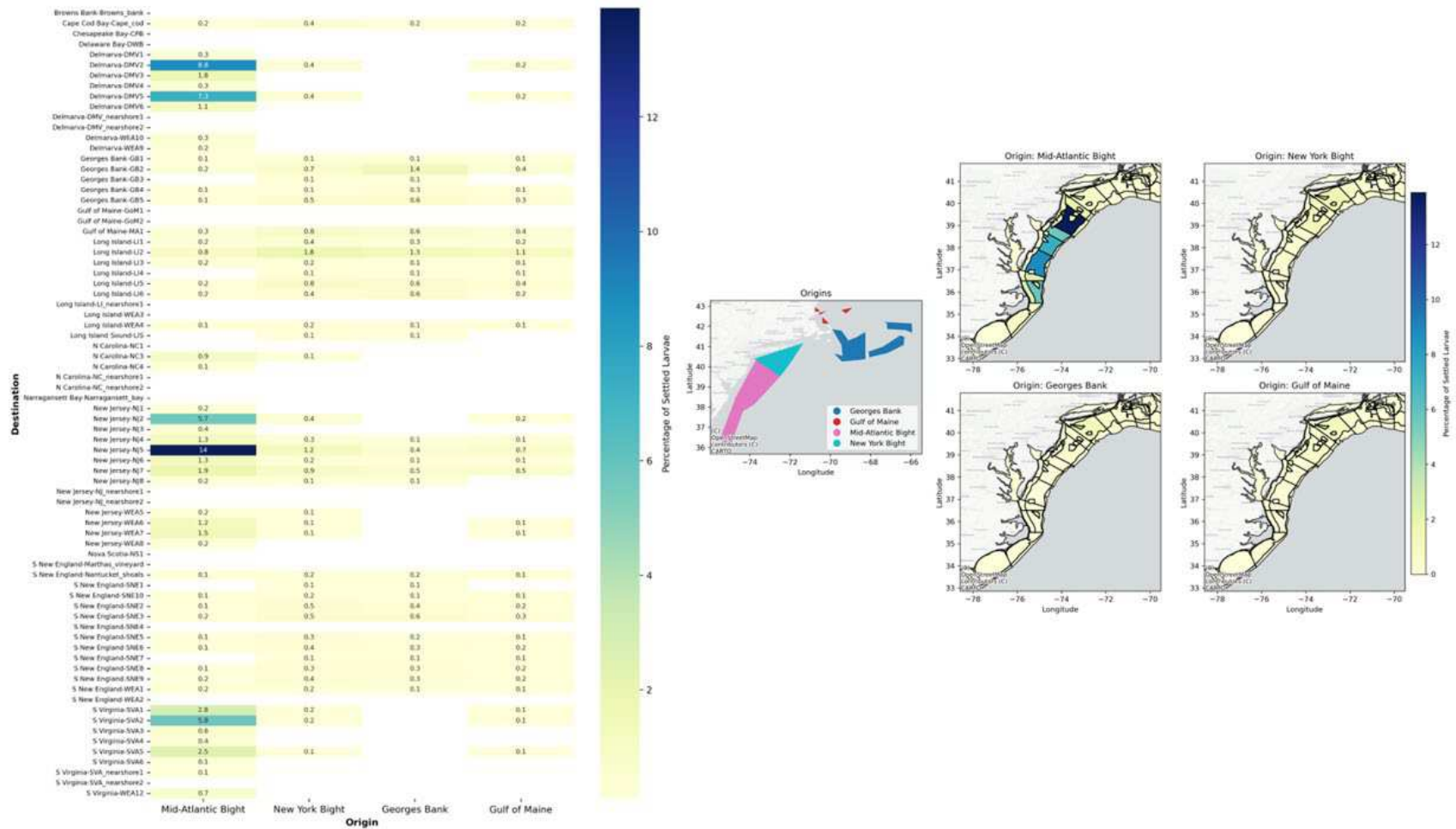


Figure 7.6. Baseline Connectivity Matrix (left) and Connectivity Map (right) for Sea Scallop Larvae – Aggregated Ensemble Results for 2018

Matrix and map show the settlement destinations by spawning origin, i.e., the number of larvae settling in a certain destination that spawned from a certain origin.

7.1.4 Baseline Results for 2020

The 2020 sea scallop baseline model results are shown in **Figure 7.** and Error! Reference source not found.. As seen in **Figure 7.**, similar to 2017 and 2018, the greatest modeled sea scallop settlement occurs predominantly in the Mid-Atlantic Bight offshore New Jersey.

The 2020 modeled results of sea scallop connectivity are shown in Error! Reference source not found. similar to 2017, the connectivity matrix indicates that the Mid-Atlantic Bight appears to be the most important region for sea scallop spawning and settlement, with the same destination areas offshore New Jersey (e.g., NJ5) and Delmarva (e.g., DMV5) having greatest settlement of larvae spawned from the Mid-Atlantic Bight.

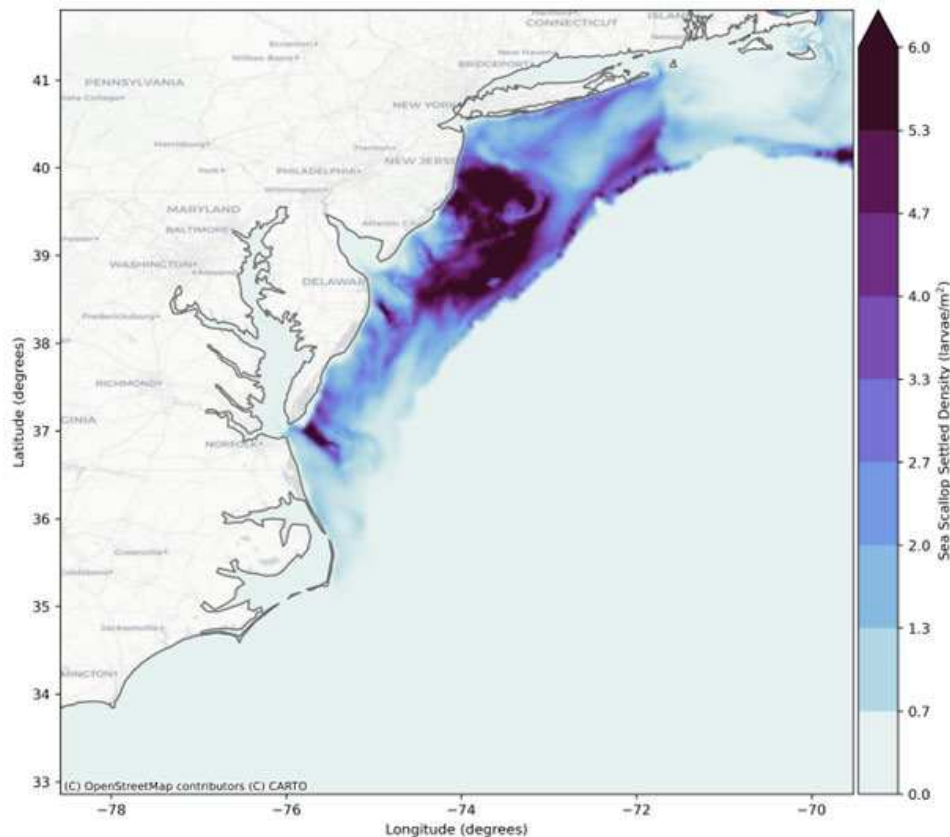


Figure 7.7. Baseline Ensemble Settled Larval Sea Scallop Density 2020

Mean settled larval sea scallop density (larvae/m²) of the ensemble results, averaged per model grid element.

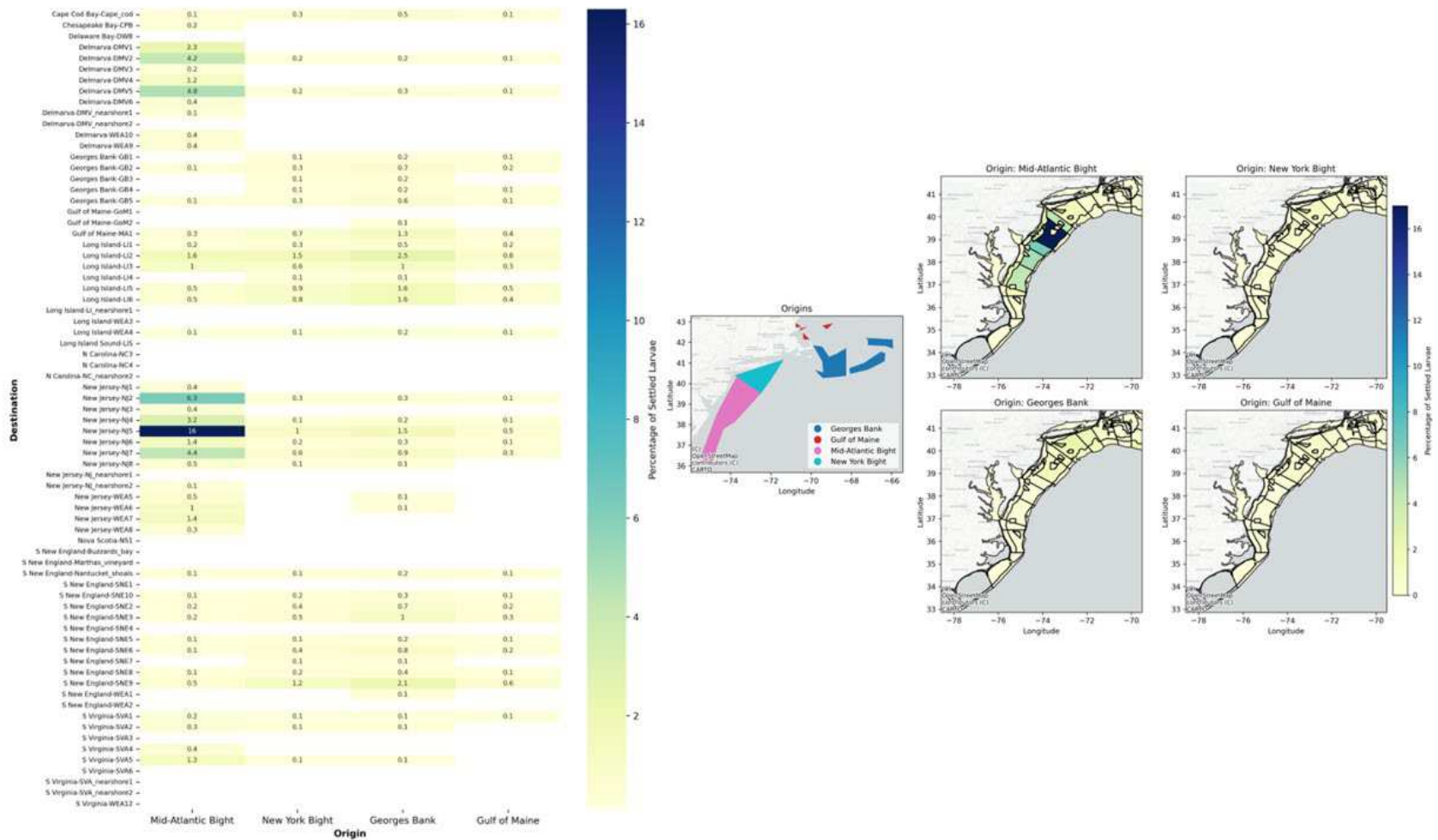


Figure 7.8. Baseline Connectivity Matrix (left) and Connectivity Map (right) for Sea Scallop Larvae – Aggregated Ensemble Results for 2020
 Matrix and map show the settlement destinations by spawning origin, i.e., the number of larvae settling in a certain destination that spawned from a certain origin.

7.2 Surfclam

The 2017 surfclam baseline model results are shown in **Figure 7.**, and

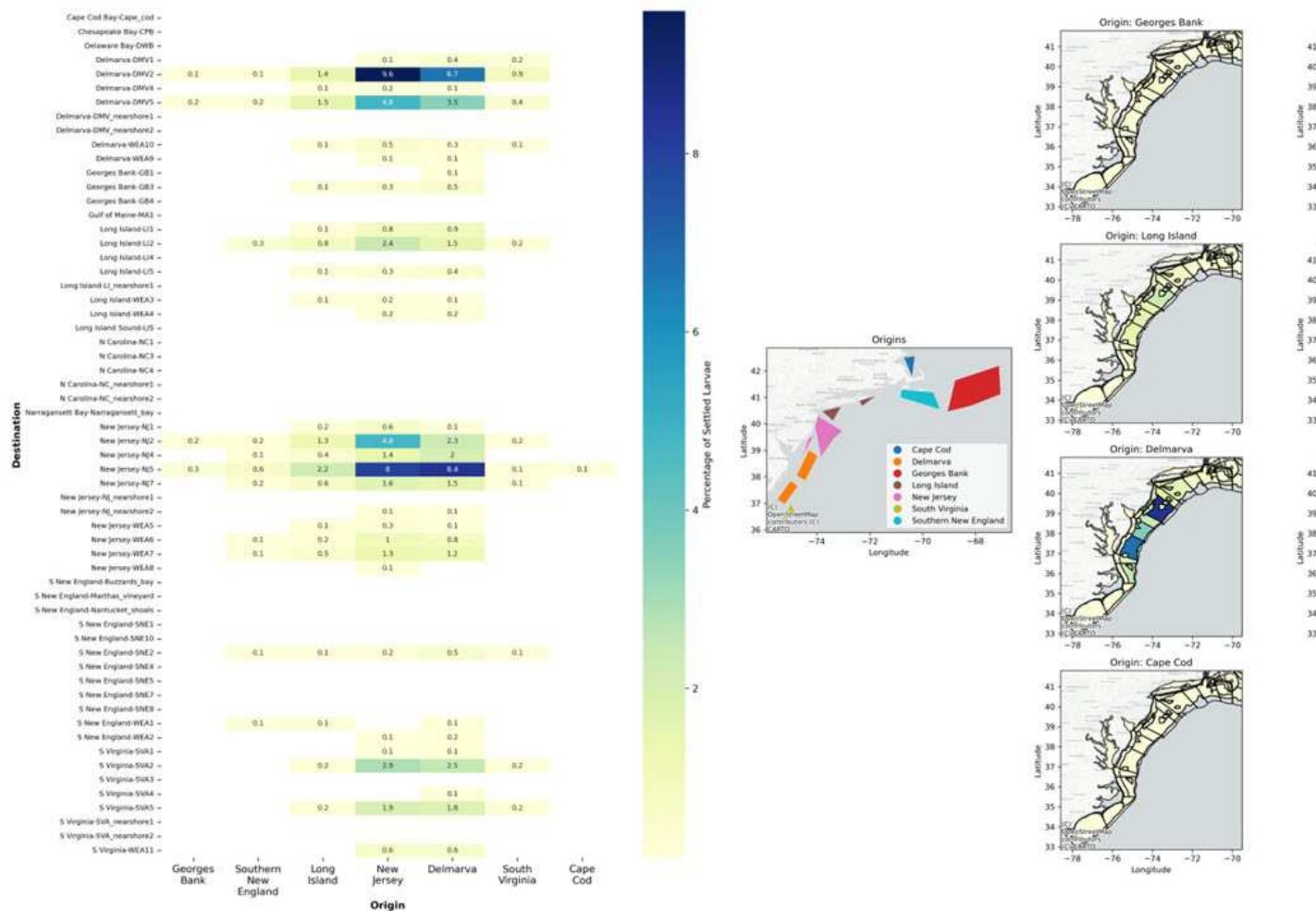


Figure 7.4. As seen in **Figure 7.**, the regions where the greatest modeled surfclam settlement occurs are predominantly offshore New Jersey southward through Delmarva to South Virginia, with some lesser settlement off the coast of Long Island and the north edge of the Hudson Canyon.

The modeled results of surfclam connectivity are shown in

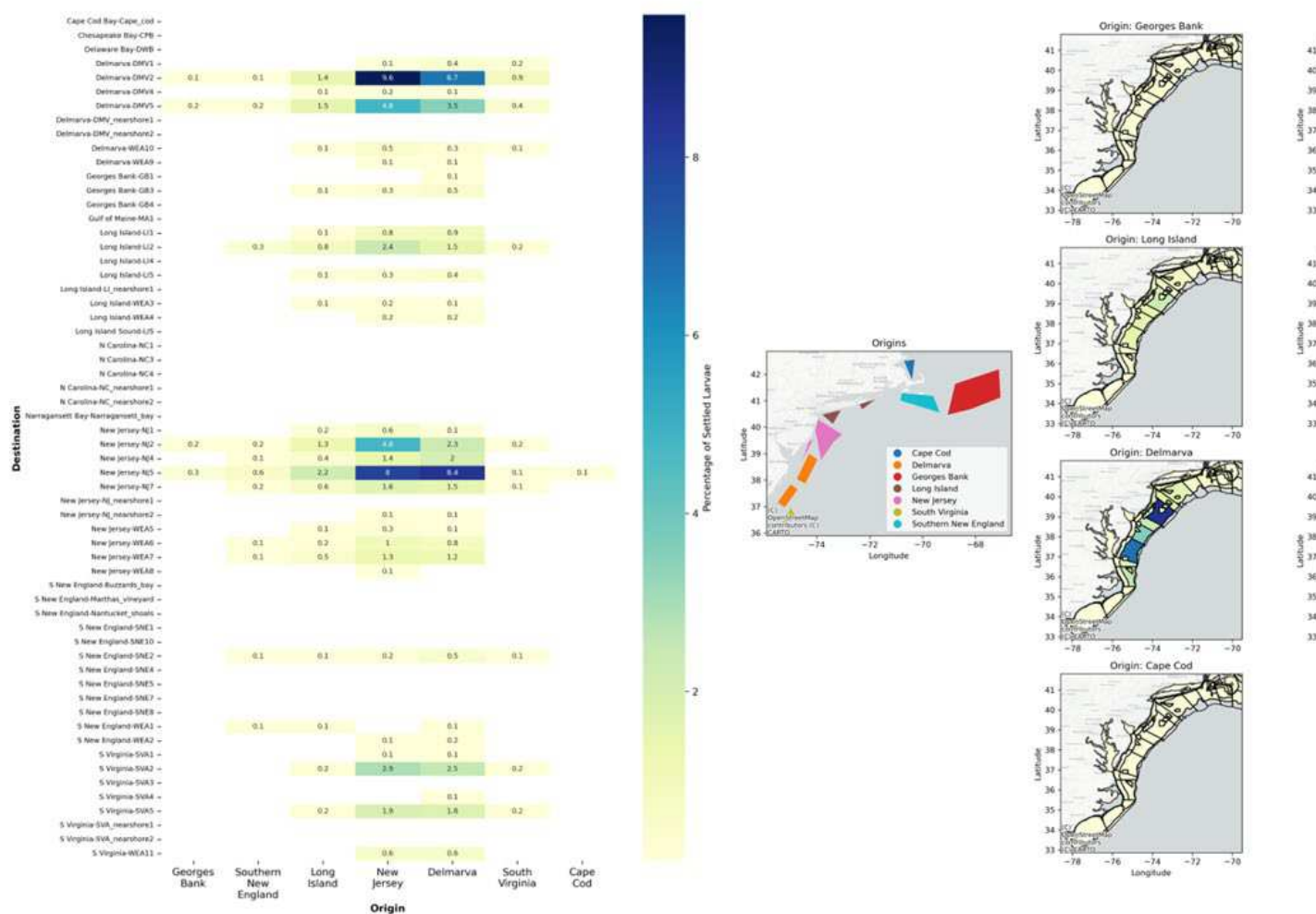


Figure 7.4. The connectivity matrix indicates that the majority of settled surfclam larvae originate from the New Jersey and Delmarva spawning areas and settle in New Jersey, Delmarva and South Virginia destination areas. Larvae spawned from New Jersey settle mostly in DMV2 followed by NJ5, while larvae spawned in Delmarva settle mostly in NJ5 followed by DMV2. A smaller proportion of larvae that settle in New Jersey and Delmarva originate from Long Island.

Larvae spawned from Georges Bank tend to remain on Georges Bank or are transported off-shelf by the gulf stream. Some seeding of New Jersey comes from South New England, but this spawning area contributes relatively small proportions of settled larvae to southern areas, due to a relatively small population and thus release of larvae in comparison to New Jersey and Delmarva.

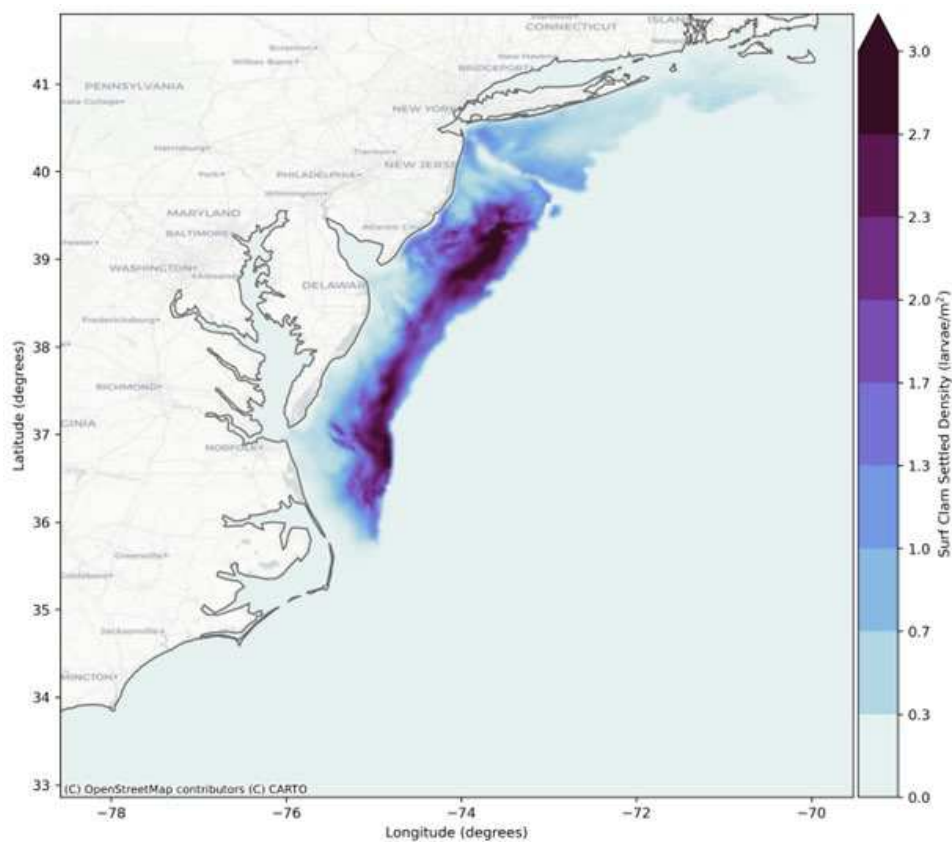


Figure 7.9. Baseline Ensemble Settled Larval Surfclam Density 2017

Mean settled larval surfclam density (larvae/m²) of the ensemble results, averaged per model grid element.

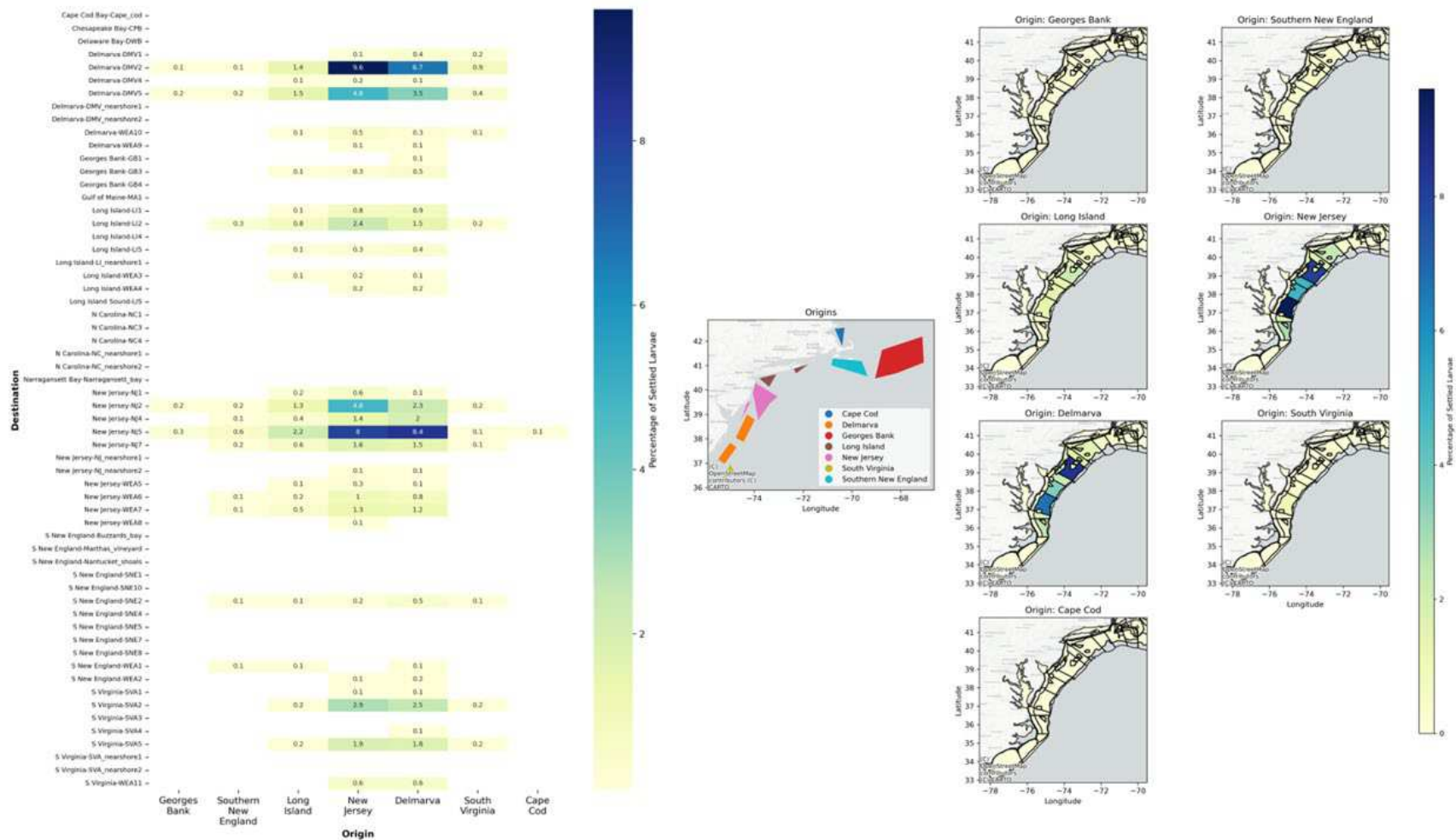


Figure 7.40. Baseline Connectivity Matrix (left) and Connectivity Map (right) for Surfclam Larvae – Aggregated Ensemble Results for 2017

Matrix and map show the settlement destinations by spawning origin, i.e., the number of larvae settling in a certain destination that spawned from a certain origin.

7.3 Summer Flounder

The 2017 summer flounder baseline model results are shown in **Figure 7.5** and Error! Reference source not found.. As seen in **Figure 7.5**, summer flounder settled densities are concentrated along the coast.

The modeled results of summer flounder connectivity are shown in Error! Reference source not found.. The connectivity matrix indicates that most spawned larvae, regardless of origin, tend to settle in Delmarva (DMV nearshore 1 and 2) and North Carolina (NC nearshore 2), followed by South Virginia (SVA nearshore 1) and New Jersey (NJ nearshore 2). There is also some settling in Long Island (LI4 and LI nearshore 1) and South New England (Marthas Vineyard).

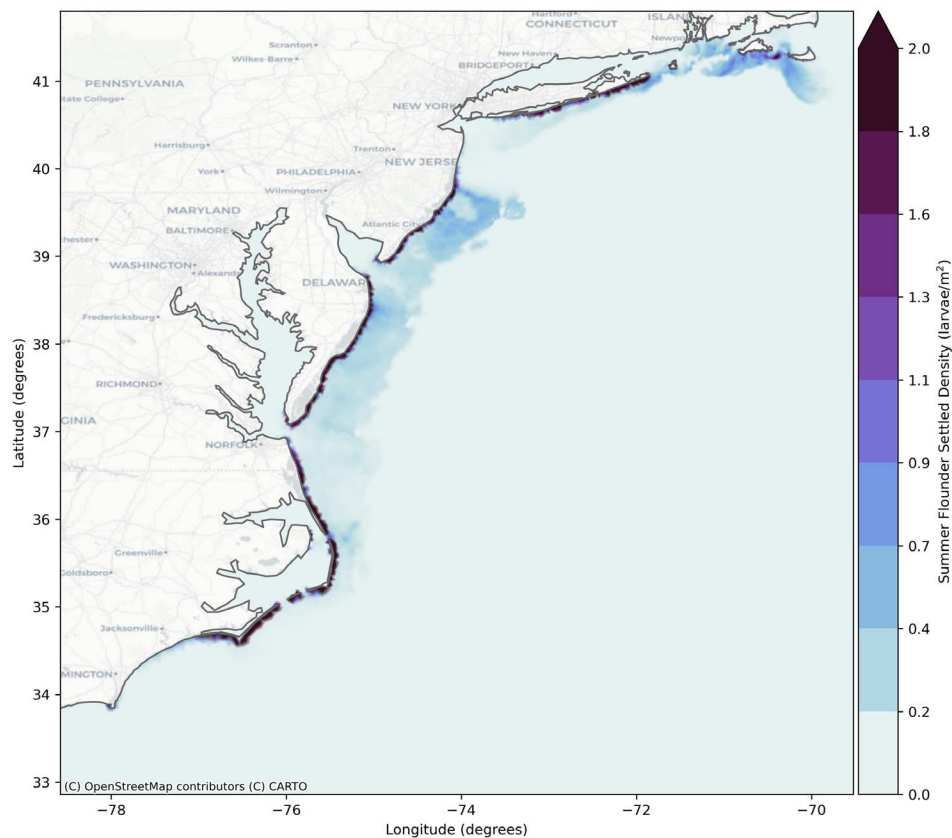


Figure 7.51. Baseline Ensemble Settled Larval Summer Flounder Density 2017

Mean settled larval surfclam density (larvae/m²) of the ensemble results, averaged per model grid element.

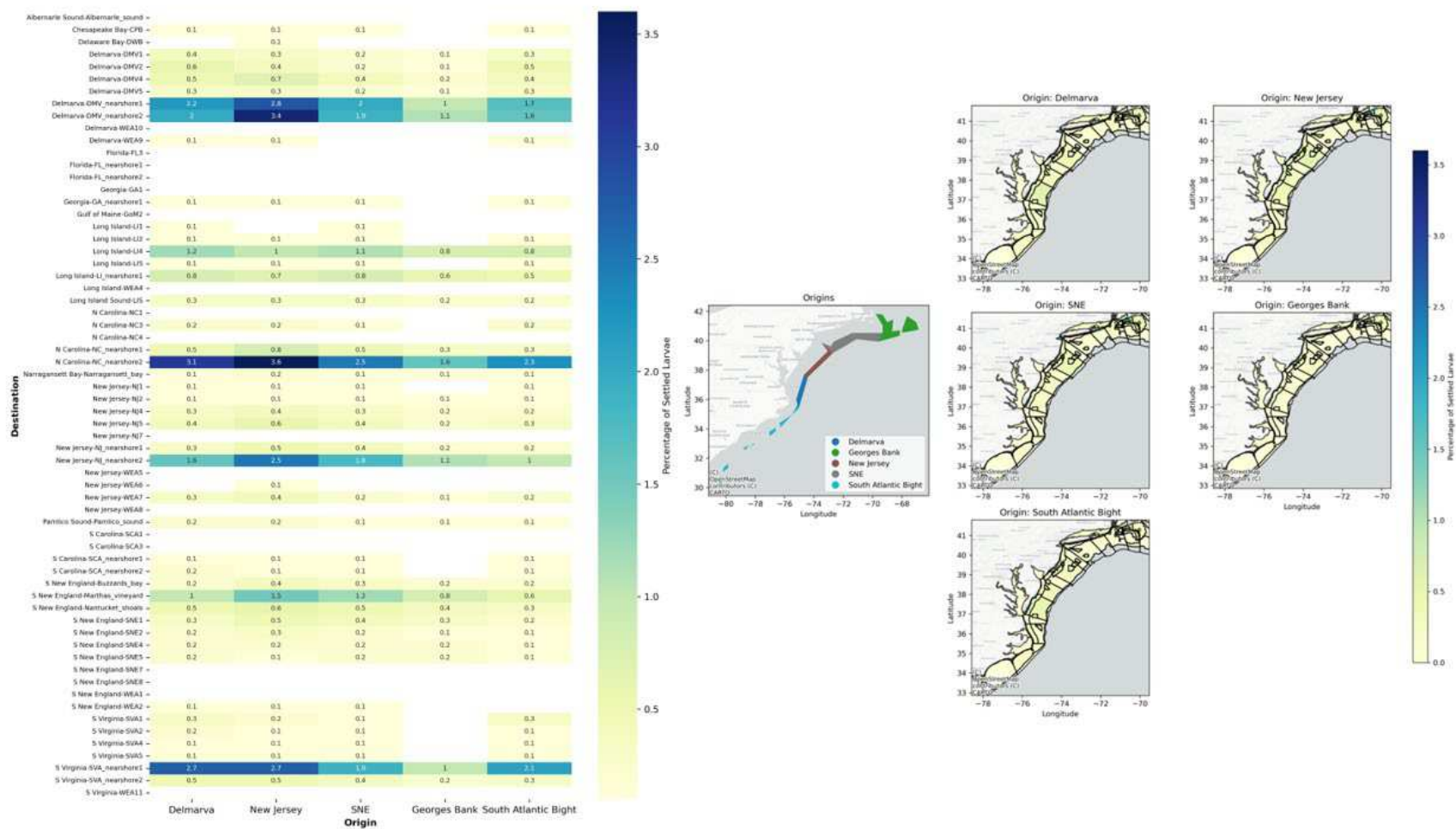


Figure 7.12. Baseline Connectivity Matrix (left) and Connectivity Map (right) for Summer Flounder Larvae – Aggregated Ensemble Results for 2017

Matrix and map show the settlement destinations by spawning origin, i.e., the number of larvae settling in a certain destination that spawned from a certain origin.

7.4 Calibration and Evaluation of Baseline ABM Results

An initial evaluation of the baseline ABM results for sea scallop and surfclam was conducted by plotting related settled larvae density results against EFH demarcations (NOAA, 2018), see **section 6.4.1.3**, and available biomass data, (**section 6.4.1**). As explained in **Section 6.7**, the evaluation of the baseline ABM results for each target species was furthered through application of three Pattern Oriented Modeling (POM) analysis techniques, namely:

- Temporal Development - via determining if the modeled transformations from zygote to settled organism occurs in accordance with observed temporal patterns
- Vertical Distribution – by determining if the modeled vertical distribution of suspended zygotes and larvae was aligned with observed vertical distributions of the species.
- Spatial Distribution - through use of Gamma Rank, Spearman's rho, and Kendall's tau correlation analyses

These methods of model evaluation were carried out multiple times and the ABM set-up was adjusted accordingly to “calibrate” the model. The results shown here are therefore the final iteration, where model output performed the best compared to observed biomass and distribution. Greater detail of the growth parameters that were calibrated are given below.

Several aspects of the spatial correlation analyses (i.e., the overlay analysis and ‘spatial distribution’ analyses), require additional explanation to ensure that the reader understands the relevance of the illustrated results. These spatial analyses were deemed acceptable for sea scallops and surfclam due to their fully sessile nature (surfclams) or their relatively limited mobility (sea scallops). The corresponding empirical biomass data and EFH maps associated with juvenile or adult life stages were therefore judged to provide an acceptable indication of where sea scallop and surfclam larvae would likely settle.

When reviewing the sea scallop and surfclam ABM baseline settlement results, it is nonetheless important to note that they are not a true ‘like for like’ comparison of high biomass areas. It is also emphasized that the observational datasets used to evaluate modeled settlement, may be more of a reflection of survey effort rather than the actual presence of settled sea scallop and surfclam larvae. Where high settled density does not match as well with observed biomass (e.g., northwest New Jersey region for sea scallop), it is noted that this could be a result of survey effort (i.e., few recent data from these areas) (*pers comms, Dr. Daphne Munroe*), as well as that settlement does not necessarily equal recruitment (e.g., Hansen et al., 2023), resulting in some areas of higher observed biomass where there is high settlement predicted by the ABM. This “mismatch” therefore does not necessarily mean that the ABM is not performing well, especially as there is a match between the model results and available data as demonstrated in the following analyses below.

Observation data for summer flounder were available only for juveniles and adults that are fully mobile and have significant ranges. Summer flounder larvae travel towards the shoreline, once they have metamorphosed to juveniles, they then move to appropriate habitats along the shore and into estuaries, however this juvenile movement is not captured by the ABM since summer flounder do not pass the larval life stage in the model. As such, the available observational data for summer flounder abundance and biomass, could not be adequately compared to model results for summer flounder larvae settlement, which is concentrated along the shoreline, and not represented in the juvenile and adult biomass data.

7.4.1 Sea Scallop

Figure 7.6 shows the settled sea scallop larvae density, displayed as the shaded areas, compared to observational biomass, displayed as proportional symbols, and EFH demarcations. Higher sea scallop

settled density occurs in the New Jersey region of the MAB, which overlaps with the areas of higher sea scallop biomass, which are concentrated toward the south of the New Jersey region of the MAB. Lower sea scallop settled density, as shown in the lighter shaded areas, extends toward Georges Bank to the north and North Carolina to the south. These areas of lower settled density match well to areas of lower proportional biomass

The good alignment and agreement between the modeled settled density and observational biomass and EFH delineations was considered sufficient to allow for the execution of all production years for sea scallop.

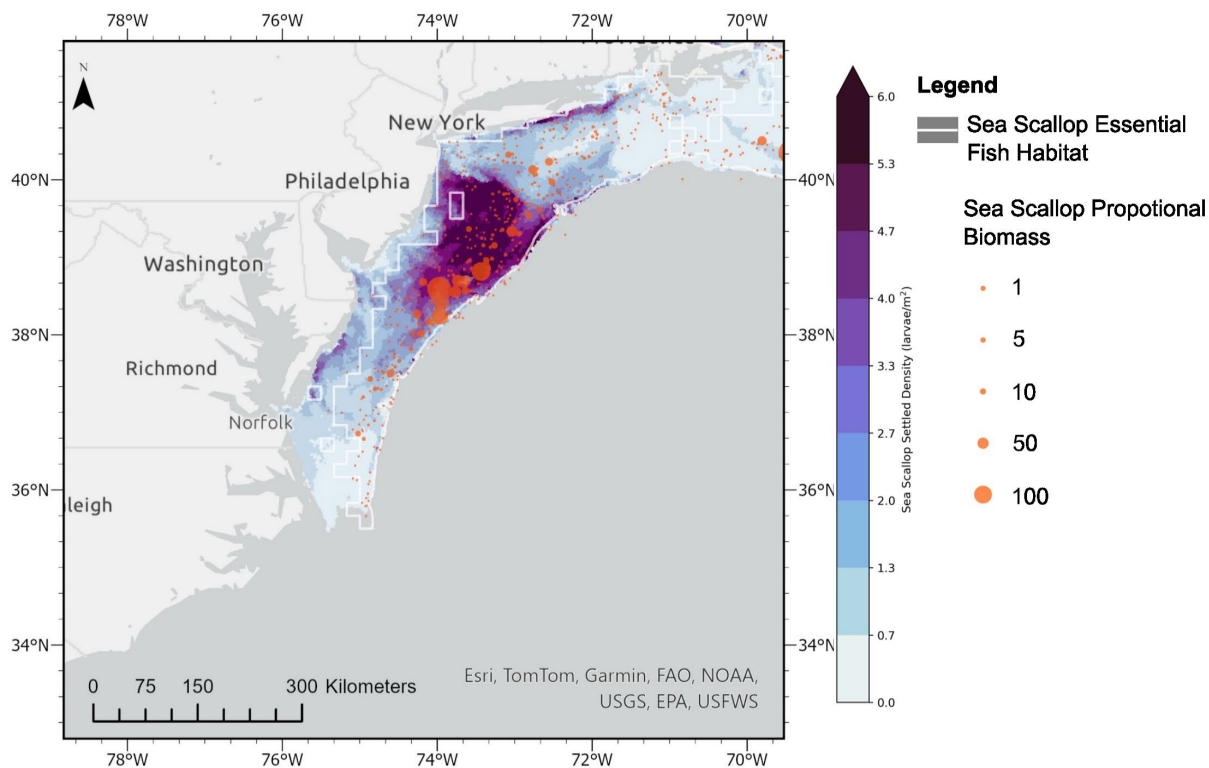


Figure 7.63. Settled Sea Scallop Larvae Density (2017) Compared to Observational Biomass and Essential Fish Habitat

Mean baseline ensemble settled density (mean of each model run for each model grid element for year 2017) with observational biomass data (NEFSC 2019) collected between 2010 and 2019 displayed as proportional symbols (orange circles) and essential fish habitat area (white line).

7.4.1.1 Pattern Oriented Modeling Results

The sigmoidal growth curves of the ABM for egg and larval development were calibrated for each species in order to achieve growth curves which matched the timescales indicated for egg and larval growth in the literature. The steepness of the curves was adjusted until the desired timeframe for egg hatching and larval development were achieved.

Figure 7.7 and **Figure 7.8** show the evaluation of the temporal development output. **Figure 7.7** shows that the time taken for modeled sea scallop eggs to hatch is between one and two days, and **Figure 7.8** shows that the time taken for all modeled sea scallop larvae to settle within one model run was below 70

days, with a peak between 40 and 60 days. This output is aligned with the findings from literature, as discussed in **Section 6.4.2**, which indicates that sea scallop eggs hatch in approximately 2 days and the larvae settle to the seafloor after approximately 28 to 82 days in the water column (Hart and Chute, 2004).

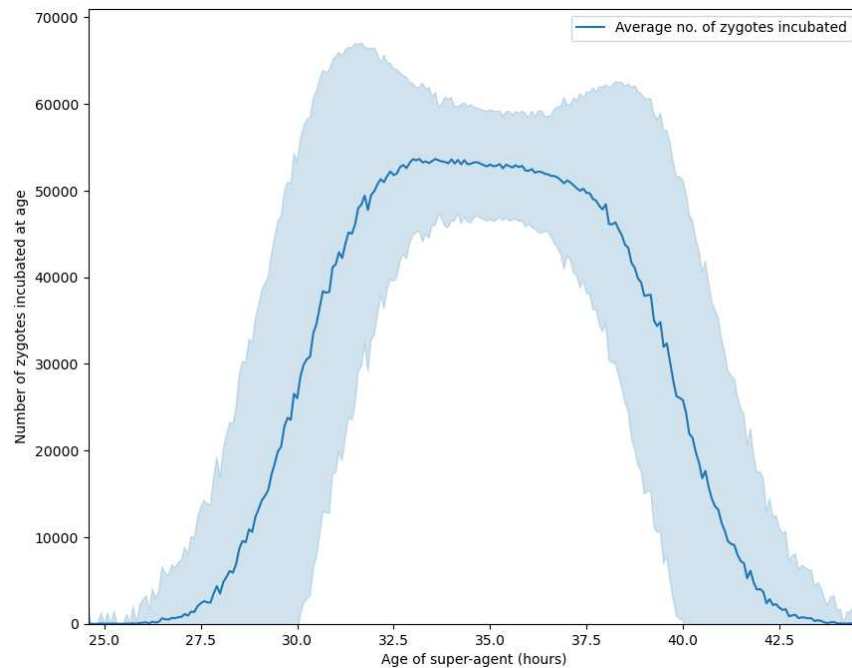


Figure 7.74. Temporal Development Model Evaluation – Time Taken for Modeled Sea Scallop Eggs to Hatch.

Time taken for all modeled sea scallop eggs to hatch within one model run for year 2017. Eggs hatch within the ranges found in the literature (see section 6.2) and the parameterized 1-2 days.

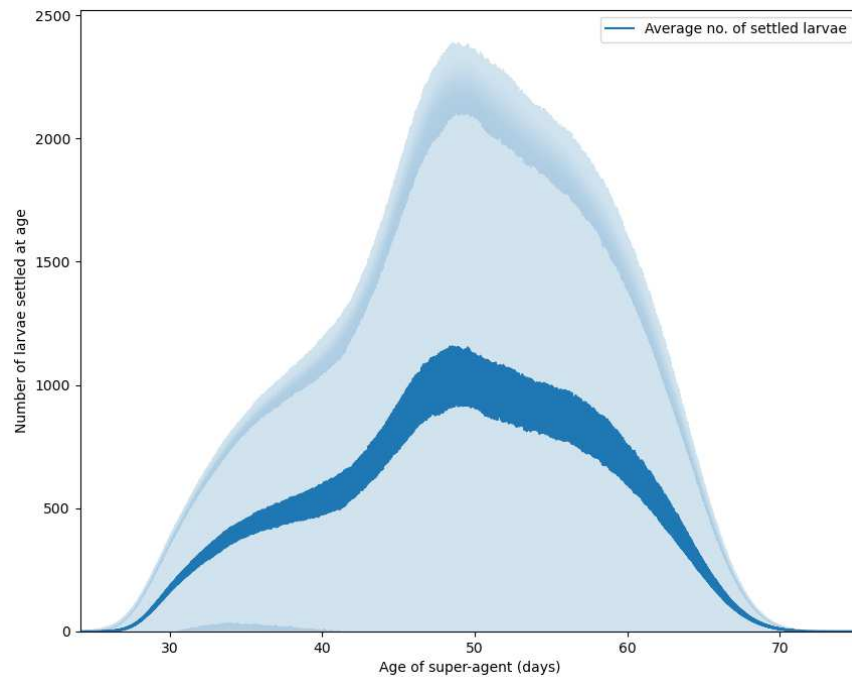


Figure 7.85. Temporal Development Model Evaluation – Time Taken for Modeled Sea Scallop Larvae to Settle

Time taken for all modeled sea scallop larvae to settle within one model run for year 2017. Larvae settle within the ranges found in the literature (see section 6.2) and the parameterized 28-82 days.

Figure 7.9 shows that vertical movement of the modeled sea scallop larvae in response to temperature, with larvae shown to move to parameterized temperature range of 6°C and 18°C. Such vertical movement is broadly aligned with findings from literature outlined in **Section 6.4.2**, that sea scallop prefer water temperatures between 10°C and 15 °C and orient themselves around the thermocline (Hart and Chute, 2004).

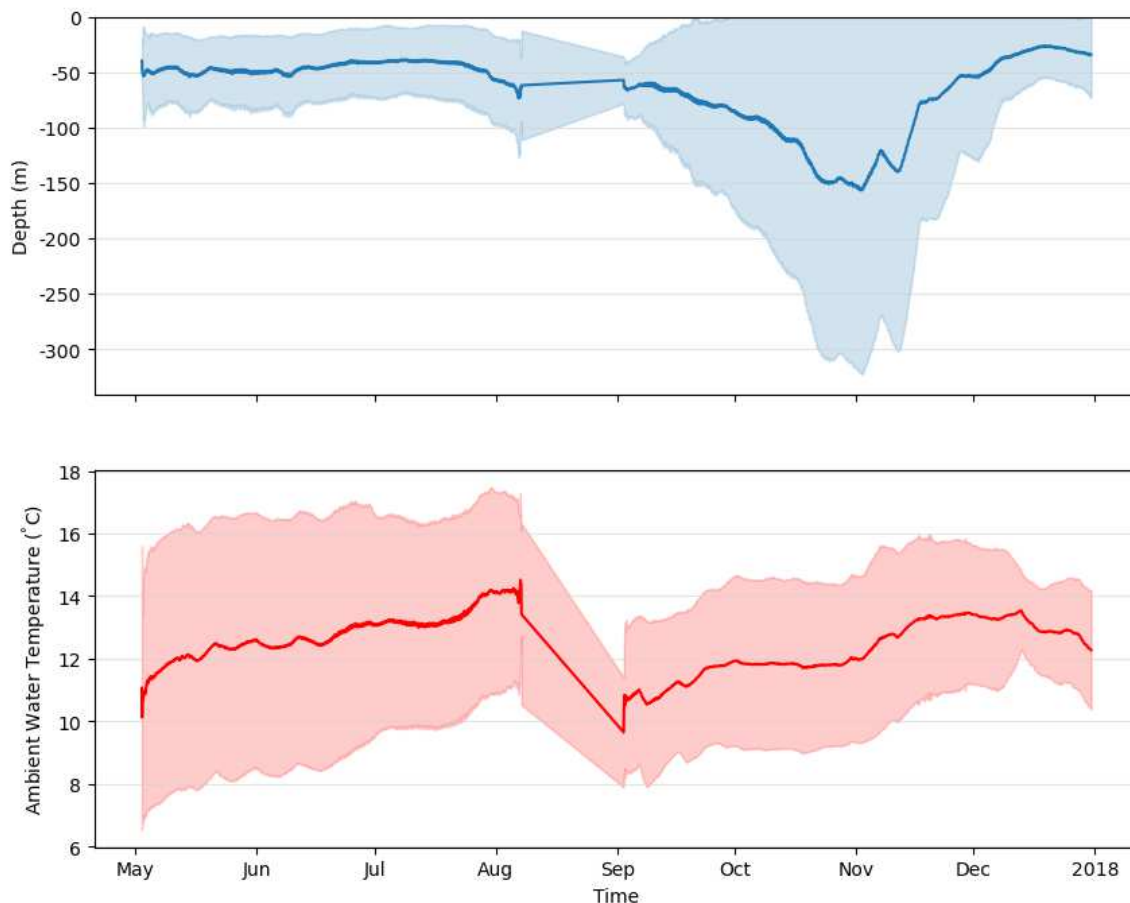


Figure 7.96. Vertical Movement Model Evaluation – Movement of Sea Scallop Larvae with Temperature

Vertical movement of all simulated agents within a single model run (i.e., not ensemble) for year 2017. Larvae move to remain within the parameterized temperature range of 6 and 18 °C. Sea scallops spawn in May in the Mid-Atlantic Bight – where temperatures are higher - the large drop in temperature occurs when additional agents are released in the North at the beginning of September.

As spatial correlation can vary with the resolution of the compared distributions, the comparisons were conducted on resolutions from 10 to 100 km² using the Kendall Tau, Spearman and Gamma Rank correlations, as seen in **Figure 7.10**. Kendall Tau, Spearman and Gamma correlations range from -1 to 1, with a value of 1 indicating a perfect positive association, a value of 0 indicating no association, and a value of -1 indicating a perfect negative association. Positive values mean that the datasets are associated in the same direction (i.e., as one variable increases, the other also increases), while negative values mean

that as one variable increases, the other decreases. Overall, the correlations increased with resolution, with an optimum around 60 to 70 km².

ABM results are difficult to validate and statistical evaluation of ABM results with POM are not often attempted (Gallagher et al., 2021). The present POM analysis therefore does not apply a specific benchmark, and there are few other similar studies to reference. In addition, the biomass data used is limited by the survey effort, with some areas of the model domain having little to no observed biomass available for comparison. With these caveats in mind, the correlation coefficients range from ~0.30 to 0.75, which can be interpreted as moderate to strong positive correlation between the model results and observed biomass (Error! Reference source not found.). These moderate-strong correlation coefficients and the generally consistent values across resolutions suggest a consistent positive association between settled larvae density and observed biomass data; and that the spatial distribution produced by the ABM represents real-world distributions well.

To illustrate correlation rankings, the modeled spatial distributions were further compared visually to the observed spatial distribution across different resolutions (**Figure 7.11**). The overall patterns of the model output to a large degree reflected the observed spatial distribution, indicating an overall good correlation between the model output and the observed spatial distribution for sea scallop.

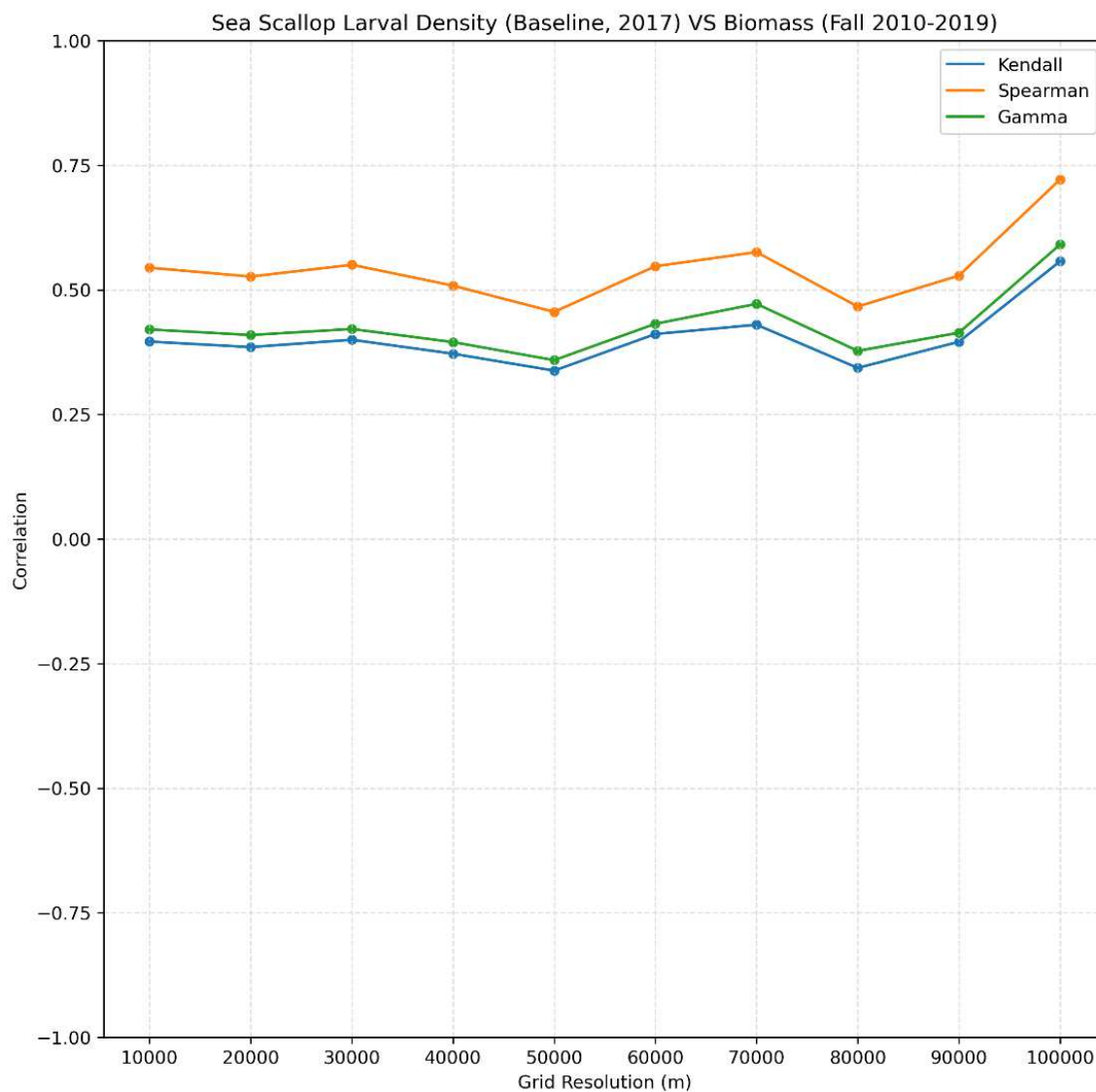


Figure 7.107. Spatial Rank Correlation Results for Sea Scallop 2017 – Correlation Line Plot
Correlation between modeled sea scallop larval settlement patterns (mean of all ensembles runs for 2017) and observed biomass (NEFSC 2010-2019). Three different correlations were calculated, the Kendall Tau, Spearman and Gamma Rank correlations. The correlation coefficients range from 0.25 to 0.75 on the y-axis. The spatial scale shown on the X-axis ranges from 10 to 100 km. The consistent positive values across different resolutions suggest a consistent positive association between settled larvae density and observed biomass data.

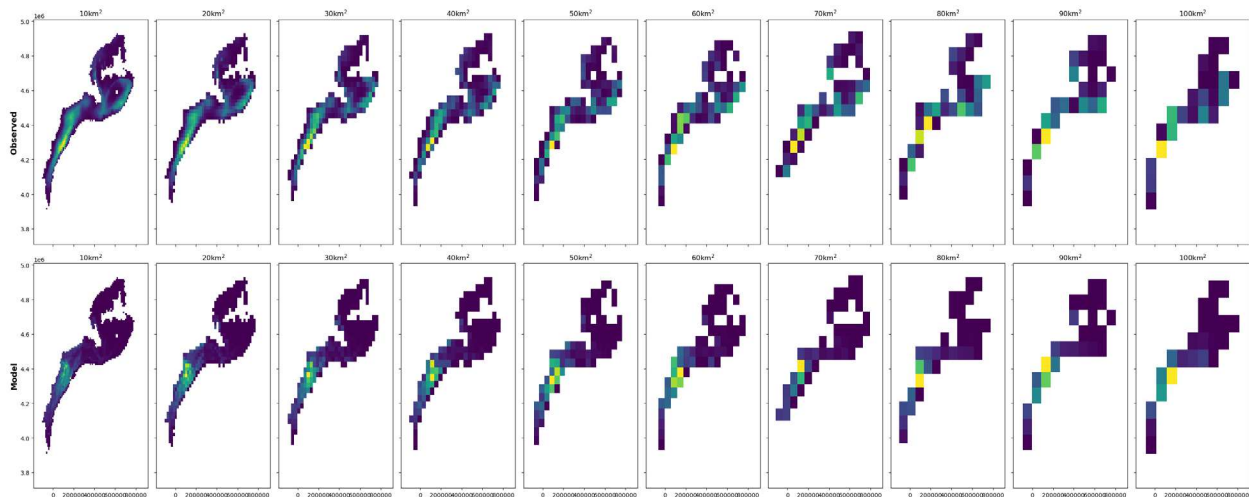


Figure 7.118. Spatial Rank Correlation Data for Sea Scallop

A visualization of the data used in the spatial correlation calculations. The top row represents the observed biomass (NEFSC 2010-2019), and the second row illustrates the modeled sea scallop larvae density at the final timestep. Each column is the same data, resampled (i.e., nearest neighbor interpolation) to a new resolution.

Table 7.2. Interpretation Table for Each Correlation Coefficient Used in the Spatial POM

Note that correlations can also be negative but are not reported here, the same ranges would apply to negative correlations. Gamma correlation interpretation from Rea and Parker (1992), Spearman and Kendall Tau interpretations from Schober et al. (2018).

Correlation Strength	Gamma	Spearman	Kendall Tau
Negligible	0–0.1	0–0.1	0–0.06
Weak	0.11–0.2	0.11–0.38	0.07–0.26
Moderate	0.21–0.4	0.39–0.68	0.27–0.49
Strong	0.41–0.79	0.69–0.89	0.5–0.71
Very Strong	>0.8	>0.9	>0.72

7.4.2 Surfclam

Figure 7.19 shows the settled surfclam larvae density, displayed as the shaded areas, compared to observational biomass, displayed as proportional symbols, and juvenile surfclam Mid-Atlantic EFH demarcations. Elevated surfclam settled density occurs in the New Jersey region southward to South Virginia through Delmarva. Lower surfclam settled density, as shown in the lighter shaded areas, extends through South New England toward Georges Bank to the north and along the shoreline to the south. These model output results align well with the EFH areas and biomass found in literature. Areas of high modeled settled density in the Delmarva region do not align with the biomass data available. However, survey effort in this area has been sparse, and recent surveys unpublished at the time of writing have confirmed surfclam abundance in this region (*pers comms.*, Daphne Munroe), and the modeled results were considered to appear reasonable by Dr. Daphne Munroe.

It should be noted surfclam biomass was not available from the NEFSC, however abundance and length data were. The biomass presented here is therefore an estimate, calculated from the weight to length ratio for surfclam (Munroe, 2022), abundance and length data from NEFSC clam surveys (NEFSC, 2022) and the average tow area reported by NEFSC (Jacobsen and Hennen, 2019).

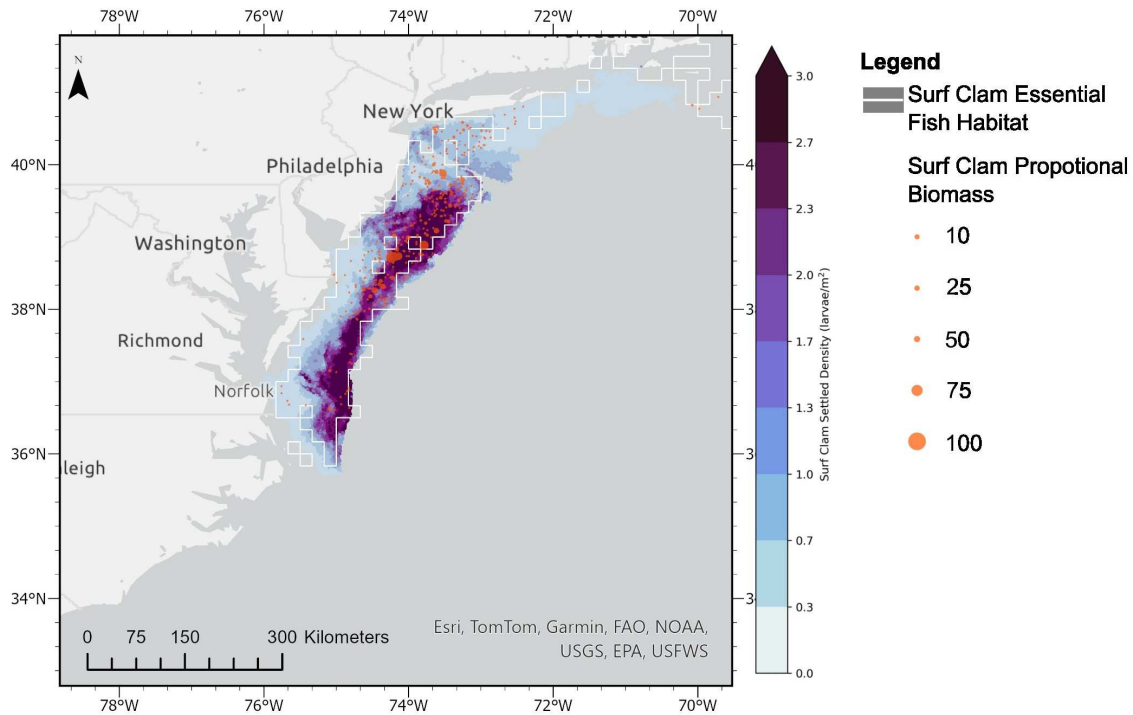


Figure 7.19. Settled Surfclam Larvae Density (2017) Compared to Observational Biomass and Essential Fish Habitat

Mean baseline ensemble settled density (mean of each model run for each model grid element for year 2017) with observational biomass data (NEFSC 2022) collected between 2018 and 2022 displayed as proportional symbols (orange circles) and essential fish habitat area (white line).

7.4.2.1 Pattern Oriented Modeling Results

Figure 7.12 and **Figure 7.13** show the temporal development output for the surfclam model. **Figure 7.12** shows that the time taken for modeled surfclam eggs to hatch is up to two days, while **Figure 7.8** shows that the time taken for all modeled surfclam larvae to settle within one model run is between 15 and 35 days, with a peak at about 25 days. These outputs are aligned with the findings from literature, as discussed in **section 6.4.3.4** where it was stated that surfclam eggs hatch within 9 to 40 hours after fertilization and that the larvae settle to the sea floor between 18 to 35 days after fertilization (Fay et al., 1983; Walker and O'Beirn, 1996).

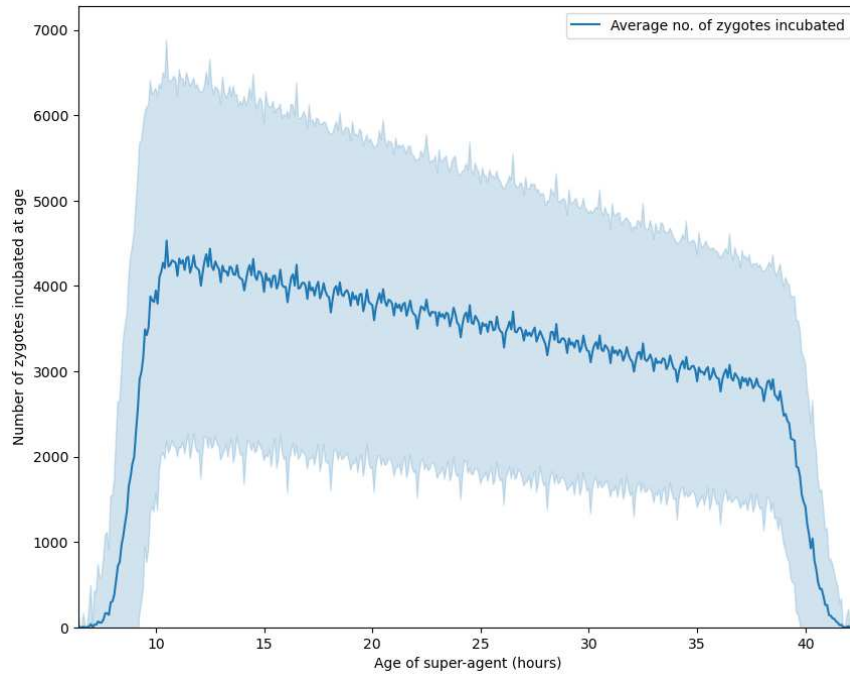


Figure 7.120. Temporal Development Model Evaluation – Time Taken for Modeled Surfclam Eggs to Hatch

Time taken for all modeled surfclam eggs to hatch within one model run for year 2017. Eggs hatch within the ranges found in the literature (see **section 6.4.3.4**) and the parameterized 9 – 40 hours.

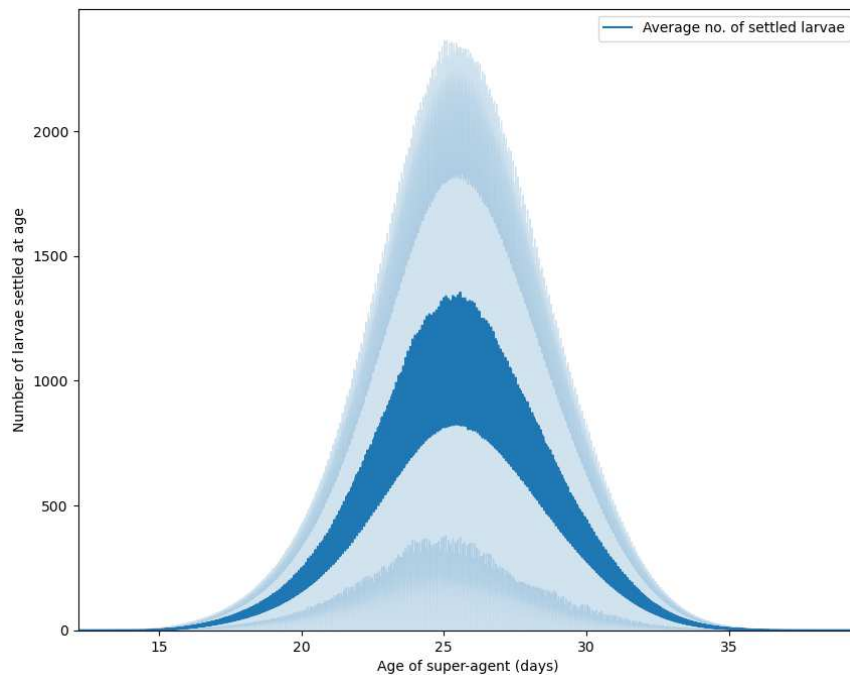


Figure 7.131. Temporal Development Model Evaluation – Time Taken for Modeled Surfclam Larvae to Settle

Time taken for all modeled surfclam larvae to settle within one model run for year 2017. Larvae settle within the ranges found in the literature (see **section 6.4.3.4**) and the parameterized 19-35 days.

Figure 7.14 shows that vertical movement of the modeled surfclam larvae in response to temperature, with larvae shown to move to parameterized temperature ranges of 12°C and 21°C. Such vertical movement is broadly aligned with findings from literature, that surfclams swim to avoid temperatures above 20°C and less than 12°C (Shanks and Brink, 2005; Ma et al., 2006), as discussed in **section 6.4.3.4**.

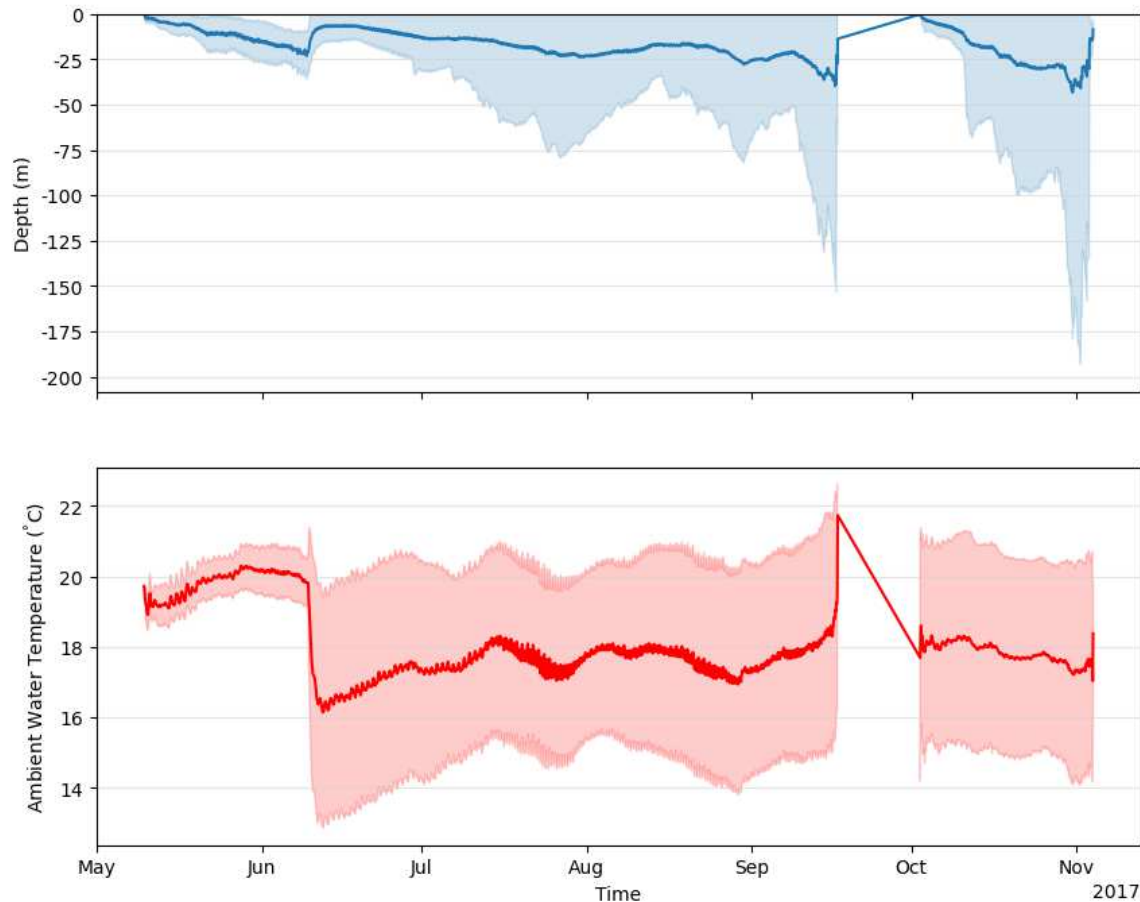


Figure 7.142. Vertical Movement Model Evaluation – Movement of Surfclam Larvae with Temperature

Vertical movement of all simulated agents within a single model run (i.e., not ensemble) for year 2017. Larvae move to remain within the parameterized temperature range of 12°C and 21°C. Surfclam spawn in May in the South only – where temperatures are higher - the large drop in temperature occurs when agents start to be released in the North in June. By the end of September surfclam larvae have either settled or died, a short gap is observed between this time and a secondary minor October spawning event.

The spatial correlation analysis using Kendall Tau, Spearman and Gamma Rank correlations is presented in **Figure 7.15**. Overall, the correlation increased with resolution, with an optimum around 60 to 70 km². The correlation coefficients range from 0.8 at lower resolutions to 0.3 and higher at higher resolutions, but are mostly > 0.5 throughout, indicating moderate-strong correlation between model results and observed biomass (Error! Reference source not found.). This and the generally consistent values across different resolutions suggest a consistency in the model and good positive correlation between settled larvae density and observed biomass data.

To further illustrate the analyzed correlation rankings, the modeled spatial distributions are further compared visually to the observed spatial distribution in their optimal resolution (**Figure 7.16**). The

overall patterns of the model output to a large degree reflected the observed spatial distribution, indicating an overall good correlation between the model output and the observed spatial distribution for surfclam.

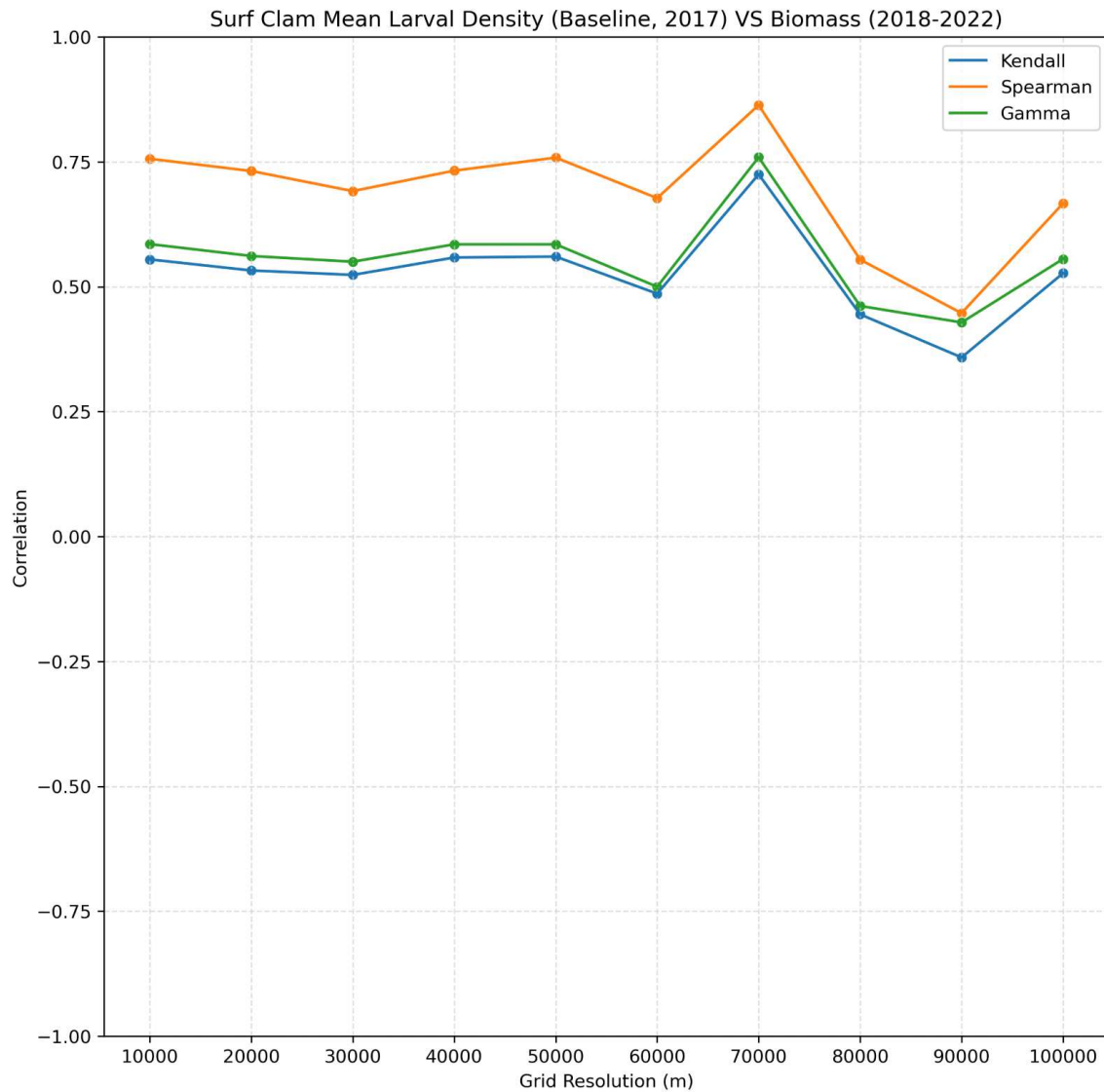


Figure 7.153. Spatial Rank Correlation Results for Surfclam 2017 – Correlation Line Plot

Correlation between modeled surfclam larval settlement patterns (mean of all ensembles runs for 2017) and observed biomass (NEFSC 2018-2022). Three different correlations were calculated, the Kendall Tau, Spearman and Gamma Rank correlations. The correlation coefficients range from 0.30 to 0.8 on the y-axis. The spatial scale shown on the X-axis ranges from 10 to 100 km. The consistent positive values across different resolutions suggest a consistent positive association between settled larvae density and observed biomass data.

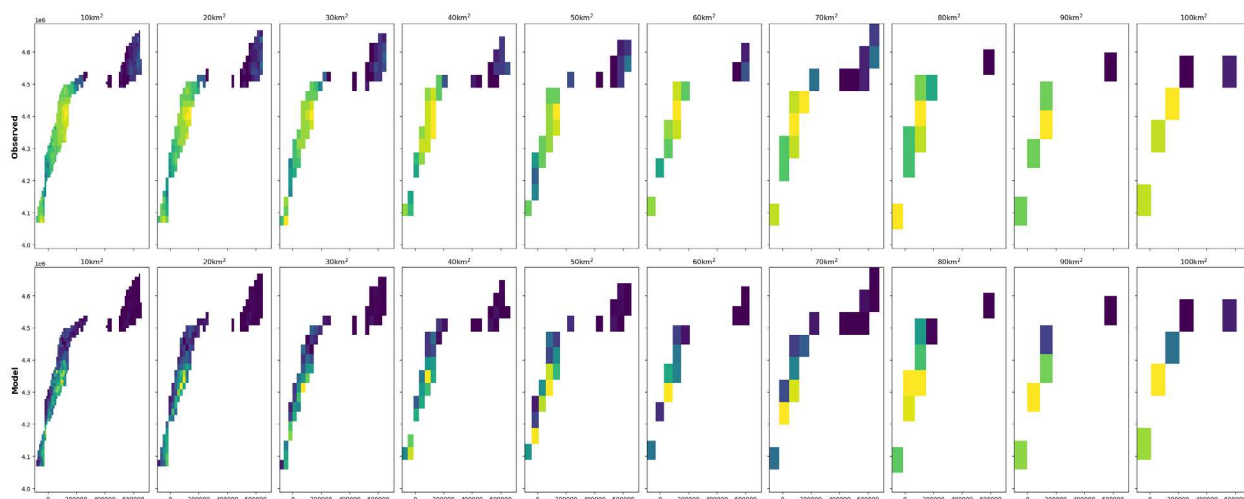


Figure 7.164. Spatial Rank Correlation Data for Surfclam

A visualization of the data used in the spatial correlation calculations. The top row represents the observed biomass (NEFSC 2010-2019), and the second row illustrates the modeled surfclam larvae density at the final timestep. Each column is the same data, resampled (i.e., nearest neighbor interpolation) to a new resolution.

7.4.3 Summer Flounder

As mentioned in **Section 7.4**, the only patterned oriented modeling accuracy evaluation carried out for summer flounder was Temporal Development and Vertical Distribution. These results are offered in **Figure 7.17** through **Figure 7.19** and the related analyses. It is noted that as there was no survey data available for comparison against real-world timings and distributions, corresponding values from literature were applied.

For temporal development, the number of days for a summer flounder egg to hatch (Bisbal and Bengtson, 1995; Johns and Howell, 1980; Packer et al., 1999) is between 2 to 6 days, whereas other sources estimate that summer flounder larvae settlement time ranges from 20 to 99 days, but that a range of 20 to 62 days is more applicable for water temperatures in the study area, (Houde, 1989; Burke et al., 1991; Keefe and Able, 1993; van Maaren and Daniels, 2000). For Vertical Distribution, the Taylor et al. (2016) study in Narragansett Bay and Block Island indicated that summer flounder larvae prefer (or survive best) in water temperatures ranging from 9°C to 18°C.

As evident in **Figure 7.17** the number of days for a summer flounder egg to hatch in the 2017 model results were on average ~3 days, which corresponds with the expected incubation time. When examining the time for larvae settlement in **Figure 7.18**, it is evident that the average larvae settlement time was approximately 42 days, with lower values at approximately 24 and upper values at 65, which falls with expected range. **Figure 7.19** illustrates the vertical distribution of summer flounder larvae in relation to water depth. As apparent, the modeled larvae maintained their position in the water column to stay within the preferred water temperatures indicated in literature.

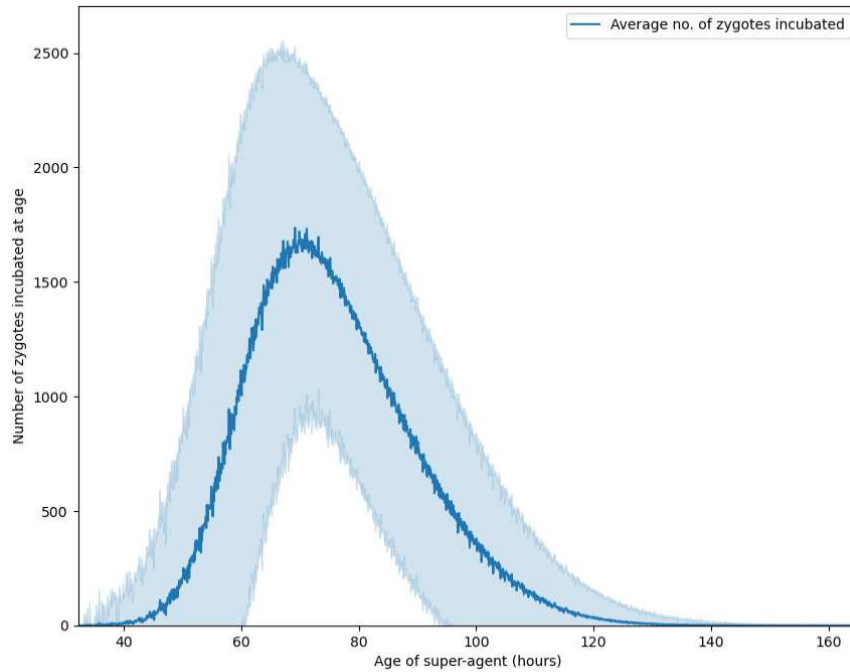


Figure 7.175. Temporal Development Model Evaluation – Time Taken for Modeled Summer Flounder Eggs to Hatch

Time taken for all modeled summer flounder eggs to hatch within one model run for year 2017. Eggs hatch within the ranges found in the literature (see **section 6.4.4.4**) and the parameterized 2 – 6 days.

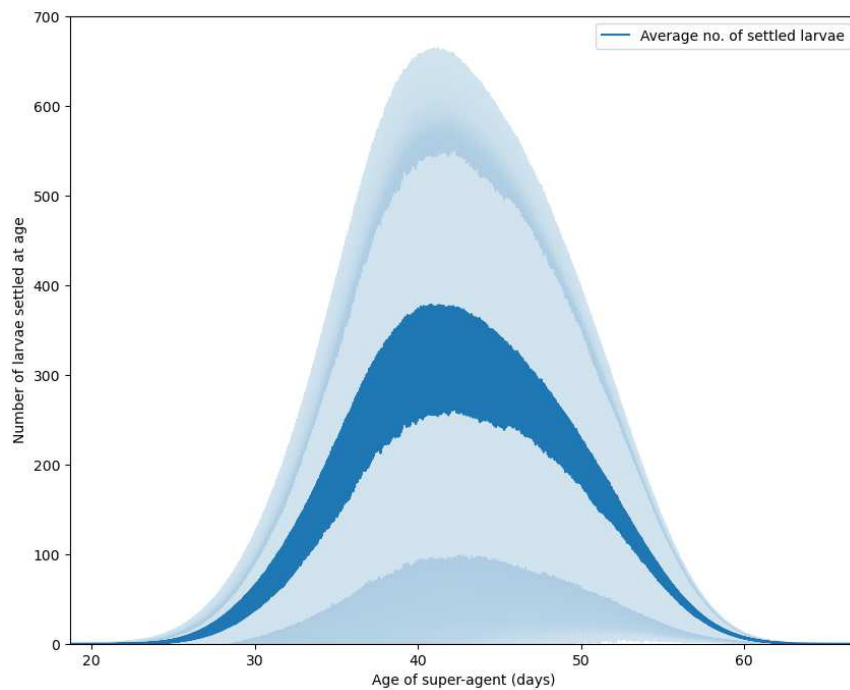


Figure 7.186. Temporal Development Model Evaluation – Time Taken for Modeled Summer Flounder Larvae to Settle

Time taken for all modeled summer flounder larvae to settle within one model run for year 2017. Larvae settle within the ranges found in the literature (see **section 6.4.4.4**) and the parameterized 20-65 days.

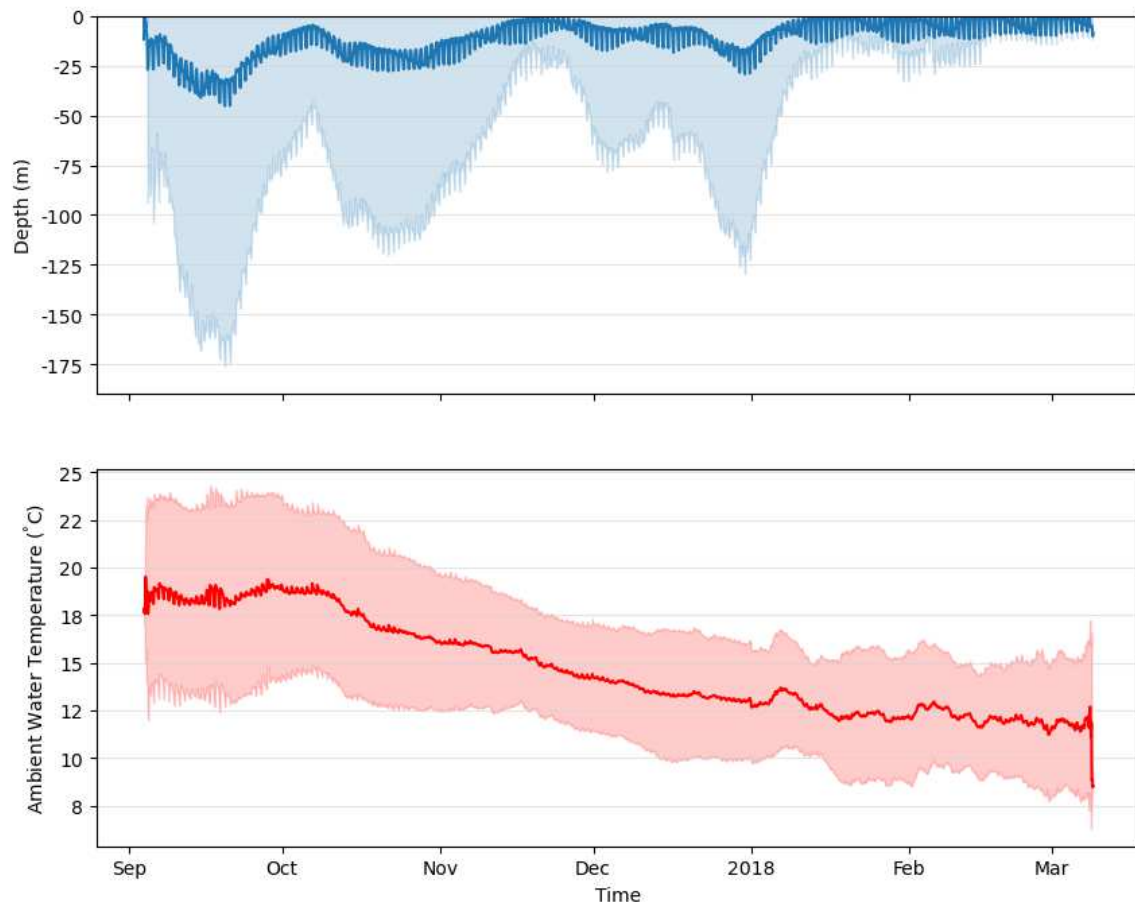


Figure 7.197. Vertical Movement Model Evaluation – Movement of Summer Flounder Larvae with Temperature
 Vertical movement of all simulated agents within a single model run (i.e., not ensemble) for year 2017. Larvae move to remain within the parameterized temperature range of 8 and 21 °C.

8 Larval Dispersal Modeling Scenario Results and Analysis

The subsequent sections provide the results of the analyses associated with the execution of the ABM of OSW build-out scenarios for sea scallop, surfclam and summer flounder. Namely, a descriptive analysis of the change of each species' larval distribution in relation to OSW build-out scenarios, and an overall concluding analysis of the effect of OSW induced changes to oceanic responses and the corresponding effect on larvae connectivity and settlement distribution. This broader closing analysis draws on the totality of results and provides a general synopsis of their relevance.

8.1 Presentation of Results

As a reminder, the modeled OSW build-out scenarios are noted below:

- **Scenario 1: Baseline** with no wind turbine generators
- **Scenario 2: Partial Build-out 12 MW 2017** - currently proposed developments “with COP”, with 12 MW turbines for year 2017
- **Scenario 3: Partial Build-out 15 MW 2017** – currently proposed developments “with COP”, with 15 MW turbines for year 2017
- **Scenario 4: Full build-out, 12 MW 2017** – currently proposed developments “with COP” and “Generic” layouts for remaining lease areas, with 12 MW turbines for year 2017
- **Scenario 5: Full build-out, 15 MW 2017** – currently proposed developments “with COP” and “Generic” layouts for remaining lease areas, with 15 MW turbines for year 2017

While this section (**Section 8**) provides an analysis of the totality of the generated ABM results, the decision was made to limit the in-depth written analyses of model result illustrations to Scenario 4, 5 and 6, as well as results for a sensitivity analysis of a doubled wind wake effect.

Scenario 2 is presented in **section 8.4**, while Scenario 4 is presented in **section 8.3**. The modeling results of the partial build-out scenarios, Scenarios 3 and 5, are presented in **Appendix C** and their relevance to overall larvae dispersal results is covered in the closing analyses in **section 9**. The wind wake sensitivity is offered in **section 8.5**. The rationale for the limiting in-depth analyses in the main body of the report was based on an effort to condense evaluations and to ensure that it was focused on the most pertinent Project results. To provide a summary over-view of the results for all scenarios, settled larvae per destination area - of all ensemble model clones and for all scenarios are presented in swarm plots (see **Table 8.1**. Explanation of Scenario Analysis Plots and Charts for a detailed explanation of how to interpret swarm plots). The aim of the swarm plots was to visualize the variability in results between all scenarios and highlight pertinent scenarios that best represent important shifts in settlement. Swarm plots generated for sea scallop and surfclam are illustrated in **Figure 8.1** and **Figure 8.2**. Here, blue points represent baseline model clone results, and the varied colored points represent OSW scenario model clone results (i.e., for the top 10 settlement destination areas). Destination areas where the total settlement points are intermingled, is an indication of little variation in results between (i.e., at the destination area level). However, where points are distinctly grouped and/or vertically spread out from the intermingled points is an indication of distinct variation in decreases (grouped below) or increase (grouped above) in settled larvae in those destination area. As apparent, for some destination areas Sensitivity, Full 15 MW and Full MW scenarios form discernable groupings above or below mixed points. Thereby making it clear that these scenarios were the appropriate bookends to explore pertinent results more thoroughly.

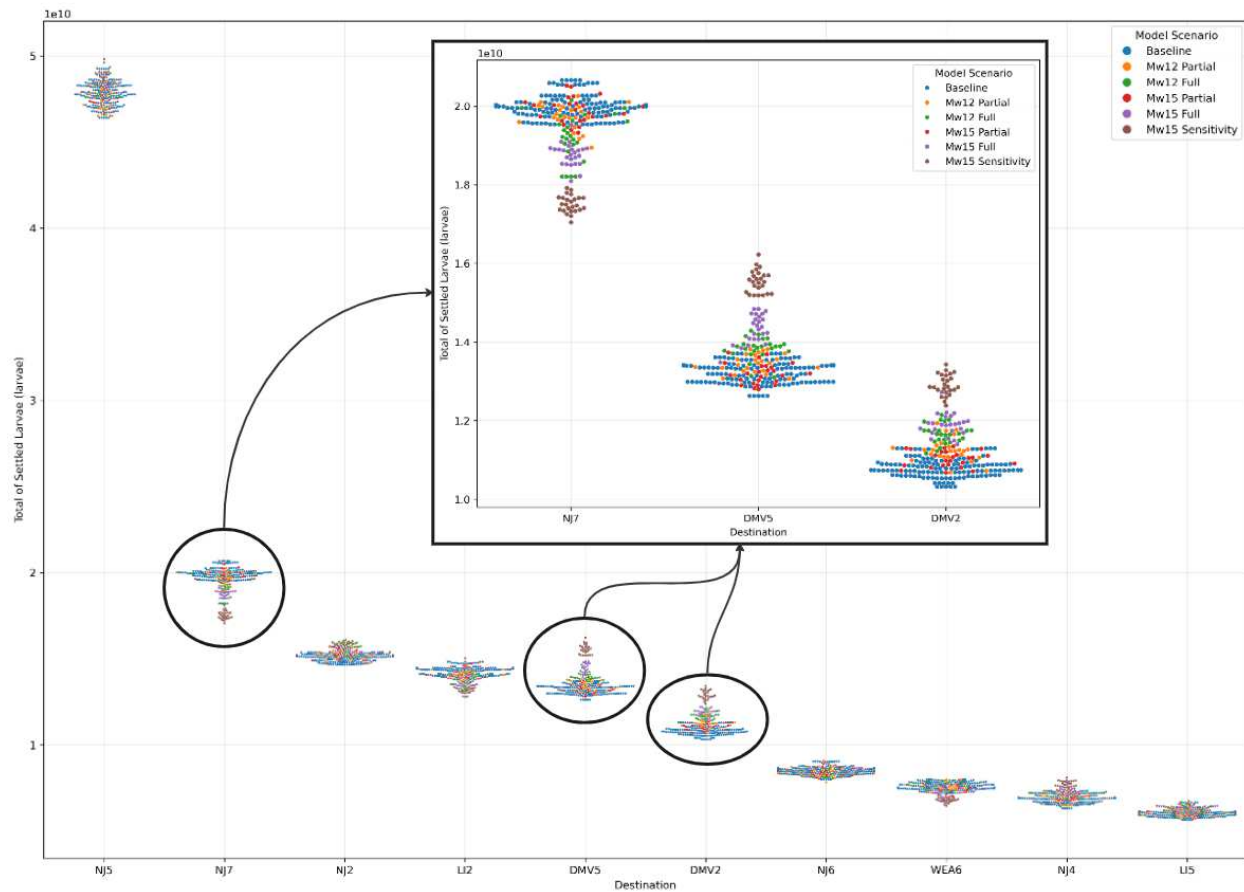


Figure 8.1. Swarm Plot Sea Scallop Settlement in Top 10 Destinations for 2017 – All Build Out Scenarios

Swarm plot shows the total settlement in each of the most common destination areas for each model run of the ensemble (i.e., each point represents a model result) for 2017. Blue points show the baseline results, orange are Scenario 2: 12 MW partial, green Scenario 4: 12MW full build-out, red Scenario 3: 15 MW partial, purple Scenario 5: 15 MW full build-out scenarios and brown is the sensitivity test.

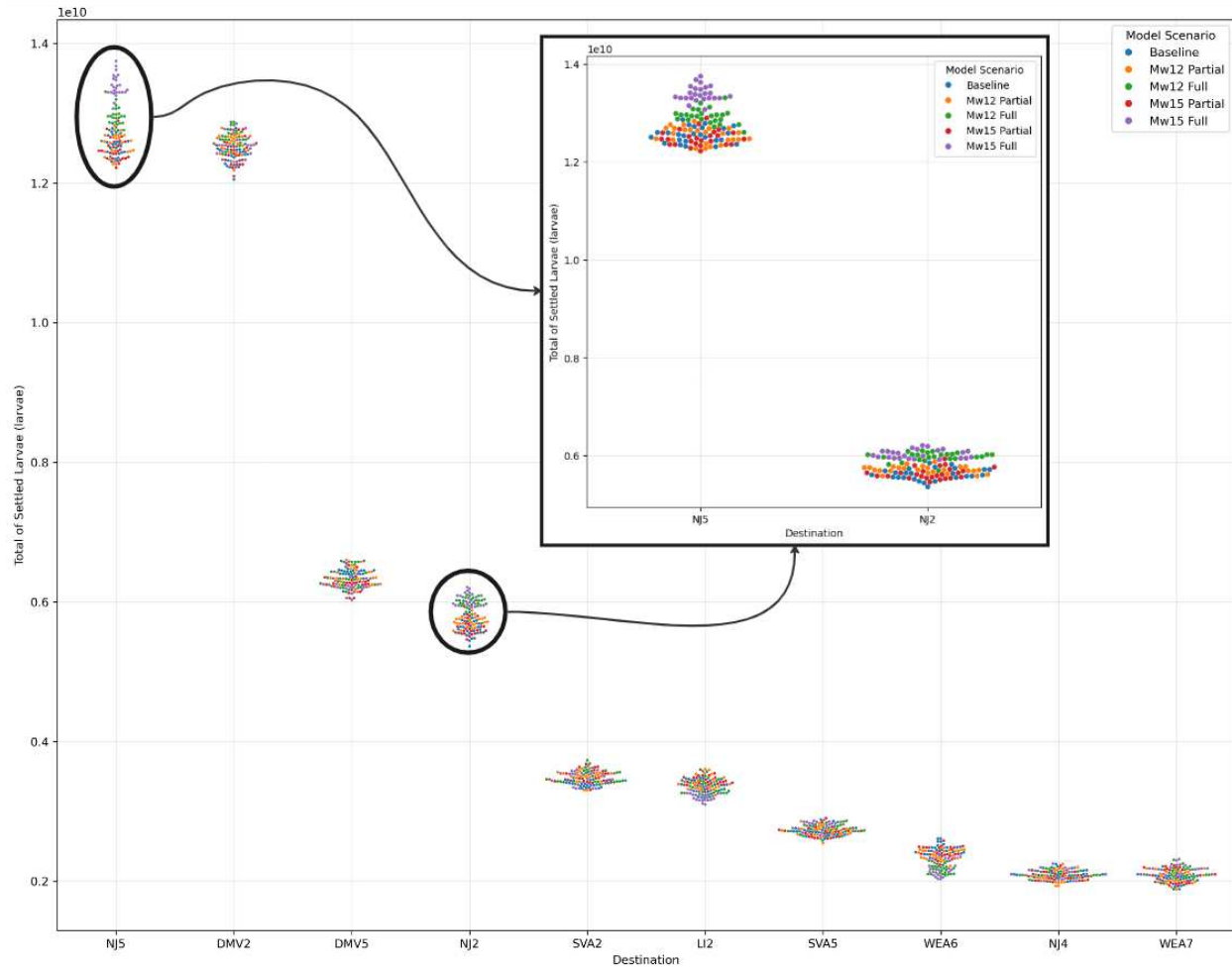


Figure 8.2. Swarm Plot Surfclam Settlement in Top 10 Destinations for 2017 – All Build Out Scenarios

Swarm plot shows the total settlement in each of the most common destination areas for each model run of the ensemble (i.e., each point represents a model result) for 2017. Blue points show the baseline results, orange are Scenario 2: 12 MW partial, green Scenario 4: 12MW full build-out, red Scenario 3: 15 MW partial, purple Scenario 5: 15 MW full build-out scenarios and brown is the sensitivity test.

8.2 Interpretation of Results Plots and Charts

As explained in **Section 6.8**, careful consideration of was given to what model result plots, charts or matrices that would best explain the OSW induced oceanic influences on larvae dispersal patterns. To aid the reader in understanding these and the corresponding analyses, this section provides an explanation of the particularities that the reader should be aware of when interpreting each type of result illustration as well as how to draw connections between them.

Table 8.1. Explanation of Scenario Analysis Plots and Charts

Applied Plot or Chart	Explanations
Difference in Mean Settled Larvae and Mean Settled Larvae Density Plots	<p>The following analyses present difference plots for both Mean Settled Larvae and Mean Settled Larvae Density. The results illustrating the difference in mean settled larvae provide an intuitive representation of absolute shifts in larvae settlement, as they offer a count of larvae. This metric accounts for the number of larvae within an element, but smaller elements (such as those where wind farm areas are located) cannot contain the same number of larvae as larger elements (i.e., causing them to be excluded from related plot illustrations). Consequently, the results were normalized by dividing the count of larvae by the area size of each element, resulting in settled larvae density. The difference in mean settled larvae density is more effective for illustrating the impacts within the wind farms (where the elements are smaller) from each build-out scenario. Since density values can be challenging to interpret, both metrics (settled larvae and settled larvae density) were included in the outputs to provide a comprehensive view of the analysis.</p>
Difference in Mean Settled Larvae DBSCAN (Cluster Analysis) Plots	<p>The DBSCAN machine learning tool is used to identify clusters within complex multi-dimensional data, specifically focusing on location (longitude and latitude) and changes in settlement patterns. DBSCAN is particularly effective at detecting clusters in noisy datasets, where data may be scattered or ambiguous. The presented cluster analyses highlight shifts in settlement patterns due to varying oceanographic conditions, by comparing a development scenario to baseline conditions. The results are visualized using a diverging color palette, with red clusters indicating increased settlement and blue clusters indicating decreased settlement. Cluster numbers are simply a classification of the cluster and do not signify a magnitude, the order in which the cluster numbers are presented is determined by the gradients of the cluster colors. The gradients of the cluster colors (e.g., darker red clusters indicate more increased settlement) indicate the magnitude of the increased or decreased settlement.</p>
Difference in Mean Settled Larvae in Each Destination Area Charts	<p>In these charts, it is emphasized that presented values do not represent real world differences in absolute numbers of larval settlement change, rather they are dependent on the number of larvae released in the ABM, which in the absence of data were estimated and constrained by computational performance.</p> <p>The 2D spatial model results, which include the number of settled larvae (larvae count), were linked to a destination map. The larvae count for each destination area were then averaged across multiple simulations (per ensemble), resulting in a dataset that shows the Mean Settled Larvae for each destination area. To understand changes in larvae settlement, the difference (delta) was calculated between various build-out scenarios and the baseline mean settled larvae. Finally, a bar chart was created to visually display these changes, using a color palette where red indicates more settlement and blue indicates less settlement, centered around zero for each destination area. The overall average decrease or increase shown in this bar plot represents the overall trends within a destination area, which is in relation to the destination area size, and thus large overall change is found in smaller areas.</p>

Applied Plot or Chart	Explanations
Swarm Plot of Net Statistics of Larvae Settlement in the Most Common Settlement Destinations	<p>Swarm plots are powerful for visualizing the distribution of a continuous variable across different categories. Swarm plots are a powerful tool for visualizing the distribution of a continuous variable across different categories, providing a representation of net statistics. The data processing began by linking settled larvae data to destination areas, ranking these destinations in descending order, and saving the top 10 destinations for settled larvae for each simulation across all scenarios. The data was further refined by filtering out the most common destinations between scenarios.</p> <p>In the swarm plot, each scatter point represents the total number of settled larvae in a destination area for each model simulation. The spread of these points indicates the distribution of settled larvae across different simulations, representing net statistics of larvae settlement. A predominantly horizontal spread of points signifies less variation among simulations, while a predominantly vertical spread indicates greater variation.</p> <p>The density of points at each destination illustrates how settlement patterns change due to different build-out scenarios. For instance, if the group of scatter points in a particular destination area is generally higher or lower compared to another group, it suggests that the amount of settled larvae in that destination area has been significantly influenced by changes in oceanic conditions. This visualization helps in understanding the net impact of various scenarios on larvae settlement patterns.</p>
Connectivity Difference Charts	<p>Connectivity difference bar charts play a crucial role in impact analysis by showing how larvae settlement is affected and in which direction. Understanding differences in settlement and current speed can be challenging because they involve different spatial areas, making it hard to know where the larvae come from and where they settle while being influenced by currents. Connectivity difference charts help clarify this by showing the origins and destinations of larvae.</p> <p>First, a connectivity matrix was created for each simulation using the methods described in Section 6.5. Then, the average of these simulations was calculated, resulting in an aggregated connectivity matrix that shows the Mean Settled Larvae, adjusted for each origin's population. These matrices were compared across different scenarios by calculating the differences (delta).</p> <p>This delta connectivity matrix is then displayed as a stacked bar chart. The stacked bars show the change in mean settled larvae, adjusted for each origin's population, and the colors within each bar indicate the origins of the larvae. The x-axis represents the destinations where the larvae settled.</p> <p>The changes in connectivity that are displayed in the barplots therefore show changes in connectivity that are proportional to amount of larvae released from each spawning area. As a result, smaller spawning areas can appear to contribute greatly to reduced or increased settlement in certain destination areas, where the absolute change in the number of settled individuals may be relatively small compared to other larger spawning areas. This is important to consider when evaluating impact and when comparing scenarios to the baseline. For example, a 50 % reduction in settlement from a particular spawning area with low biomass may have no measurable impact on population recruitment, while in another case with large spawning biomass, the same 50% reduction could result in population and fisheries relevant changes in recruitment.</p>

For geographic reference when reviewing the analyses, please refer to the repeated destination area reference map **Figure 8.3**. Destination Reference Map Showing Each Destination Area and Names, Colors Represent Broad Regions below.

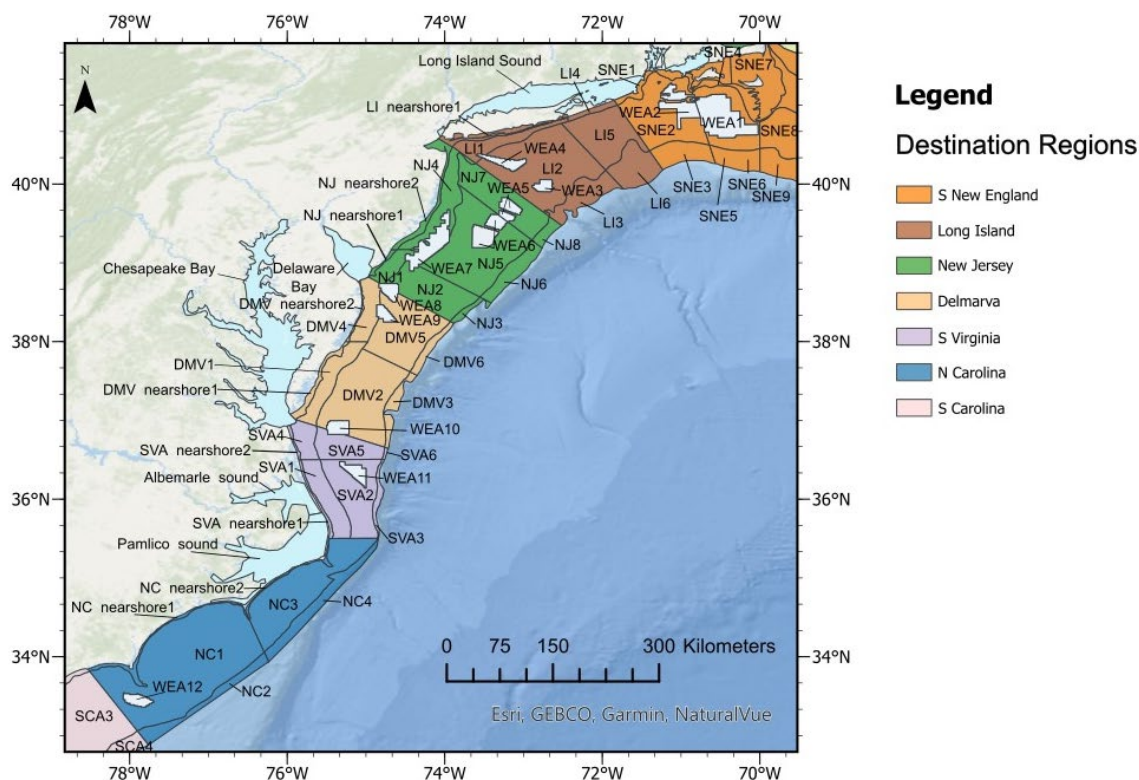


Figure 8.3. Destination Reference Map Showing Each Destination Area and Names, Colors Represent Broad Regions

8.3 Scenario 5: 15 MW Full Build-out

8.3.1 Sea Scallop

8.3.1.1 2017

Changes in total sea scallop settlement induced by the 15 MW OSW build-out areas (WEAs) against the 2017 baseline are shown in the difference plot in **Figure 8.4**, which illustrates the difference in mean total settled larvae within the study area. The cluster analysis in **Figure 8.5** is designed to remove noise from the difference plot results and identify hotspots of change. The difference plot and cluster analysis are shown alongside current speed change in **Figure 8.6**. The difference in mean settled density is shown in **Figure 8.7**, and a similar cluster analysis for settled density is included in **Figure 8.8**, and current speed change is repeated in **Figure 8.9**.

The most notable shift in sea scallop larval settlement illustrated by the two difference plots in **Figure 8.4** and **Figure 8.7**, occurs in the Mid-Atlantic Bight (MAB), south of the New York Bight (NYB), and offshore Delaware, with increase or decrease in settlement between 1 and 10 million larvae in these regions. Shown by the blue regions in **Figure 8.4** and **Figure 8.7**, there is an estimated decrease in settlement to the north of the MAB, south of the NYB and along the coast of Delaware. Estimated decrease in settlement in the New Jersey region is observed within and to the north of WEAs 5 and 6, in

the eastern portion of NJ5 and in NJ7. There is also an estimated decrease in settlement found just offshore Delaware, in DMV4 east of WEAs 8 and 9. Observed increase (red regions) in estimated sea scallop settlement is evident offshore New Jersey between WEA7 and WEA6, (in the western portions of NJ5 and NJ2), and south through Delmarva (DMV5 and DMV2) to South Virginia (SVA5).

The cluster analysis (**Figure 8.5** and **Figure 8.8**) results show similar broad patterns of change in sea scallop settlement as the difference plots discussed above, with clusters of decreased settlement off New Jersey concentrated around the WEAs 5 and 6, and Delaware, (NJ7, NJ5 and DMV4) and clusters of increased settlement in New Jersey and Delmarva (NJ5, NJ2 and DMV5).

The change in average sea scallop larval settlement per destination area (**Figure 8.10**) and the swarm plot of the most common settlement destination areas (**Figure 8.11**), both provide a broader destination area perspective of the net changes in settlement of sea scallop larvae. **Figure 8.10** illustrates the change in settlement averaged over the entire destination area, where overall patterns of settlement change reinforce the regional patterns shown in **Figure 8.4** and **Figure 8.7**. Namely, overall increased settlement in the Delmarva destination areas (with the exception of decreased settlement near Delaware Bay in DMV4) and increase in South Virginia destination areas. **Figure 8.11** shows there is a mix between increased and decreased settlement estimated within destination areas offshore New Jersey and Long Island, whereas the greatest estimated decrease in settlement occurs in NJ7, WEA 5 and DMV4. It is emphasized, however, that while the greatest average estimated increases in settlement are found in DMV6 and NJ3 in **Figure 8.10**, the absolute greatest increases in settlement volume are actually found in the significantly larger NJ2 and NJ5 destination areas.

These patterns of increased or decreased settlement in each destination area are also shown in the swarm plot in **Figure 8.11**. Here, NJ5 is the destination with the greatest settlement, where the highly mixed swarm plot indicates that there is no clear increase or decrease resulting from the OSW developments when averaged over the destination area, despite clear bands of decrease and increase being apparent in the difference plots. Destinations with similar mixed swarm results include NJ2 and NJ6. Destination areas NJ7 and LI2, however, show a clear change from the baseline, with a decrease in total settlement found in almost every 15MW scenario result. DMV5 and DMV2 and to some extent NJ2 show an estimated increase in the total settlement for most or all of the ensemble model clone results.

It should be noted when considering the relevance of these changes in settlement, that the largest change in settlement per destination area shown in the difference bar plot is four orders of magnitude lower than the total settlement in each destination area shown in the swarm plot.

A general understanding of the OSW induced oceanic influences on the observed shifts in sea scallop dispersal can be surmised through analyses of current speeds in **Figure 8.6** and **Figure 8.9** and larvae connectivity in **Figure 8.12**. Current speeds are noticeably reduced within and to the south of the 15 MW WEAs at levels that do not exceed 0.025 ms^{-1} . There are also areas of marginal elevated current speeds, i.e., $\leq 0.008 \text{ ms}^{-1}$, in the vicinity of the WEAs, noticeably along Long Island, west of WEAs 5 and 6, and along the New Jersey coast; as well as along nearshore areas near Delaware Bay and North Carolina. While there appears to be no clear direct spatial correlation with changes in larval settlement, closer analyses suggests that reductions in current speeds, especially in and around WEAs, marginally slow larvae transport in key connectivity corridors leading to reduced settlement in some areas and corresponding increases in others.

Due to the highly spatially and temporally dynamic interface between larvae transport and oceanic conditions, it was deemed excessive to illustrate this theory at a highly refined temporal and local scale. An analysis of the connectivity results in **Figure 8.12**, however, provides additional credence of how current speed changes affect the distribution and ultimately the settlement destination of larvae. Most settled sea scallop larvae in the model domain originate from the MAB. The New York Bight, Georges

Bank, and the Gulf of Maine do contribute to some larval settlement, but these spawning areas contribute relatively low proportions of settled larvae in comparison to the MAB. The changes in connectivity seen in **Figure 8.12** are proportional changes, scaled to the number of larvae released from each spawning region. Large proportional changes can therefore be seen in some destination areas of larvae originating from the Gulf of Maine and Georges Bank, however the absolute change in the number of larvae settling from these spawning regions is low relative to the MAB.

Sea scallop larvae that spawn in the MAB appear to be transported both south to north and north to south in our model results, settling in the Long Island, New Jersey and Delmarva regions. With the introduction of the 15 MW WEAs, settlement of larvae spawned from the MAB is decreased in the New Jersey regions in NJ7, NJ5, WEA5 and WEA6; and increased further south in NJ2, NJ4 and WEA7 (**Figure 8.12**). These changes in connectivity indicate that the blue areas of reduced settlement in the New Jersey destination areas seen in the difference plots could be explained by slower south to north transport from the MAB spawning area, which results in larvae settling in areas further south (i.e., not being transported as far north). Transport of larvae from the MAB to the south could also be slowed, as indicated in the Delmarva region, where larvae from the MAB that would have settled in DMV4 appear to be shifted into destination areas further north such as DMV5 and NJ2.

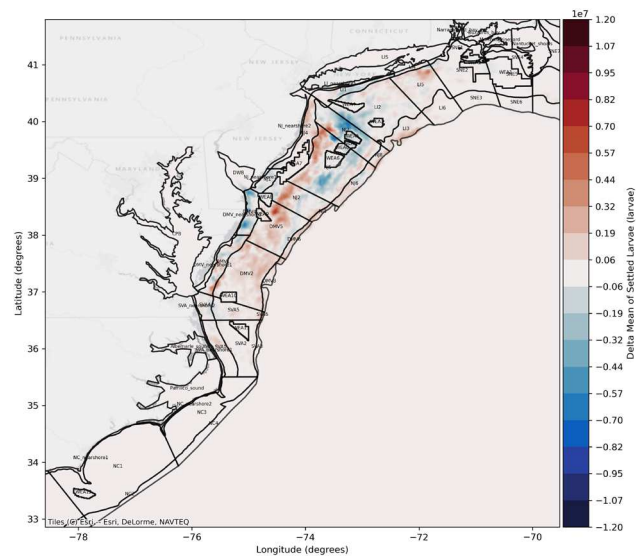


Figure 8.4. Difference in Total Settled Larvae 15 MW Full Build-Out vs. Baseline 2017

Difference in total sea scallop larvae settled larvae for model year 2017. Showing the difference in the mean of all ensemble baseline results and mean of all ensemble Scenario 5: 15 MW Full Build-out results. Settled larvae averaged for each model grid element. Red shows an increase in settlement in the 15 MW scenario compared to the baseline, blue shows a decrease in settlement compared to the baseline.

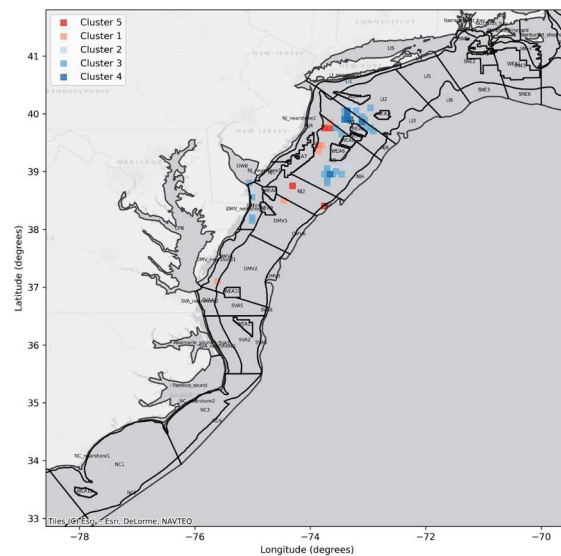


Figure 8.5. DBSCAN (Density-Based Spatial Clustering of Applications with Noise) Difference in Total Settled Larvae 15 MW Full Build-Out vs. Baseline 2017

Spatial clusters identified using DBSCAN to filter out noise from the difference plot and identify areas of greatest change. Clusters of settlement increase are identified in red and clusters with settlement decrease are shown in blue.

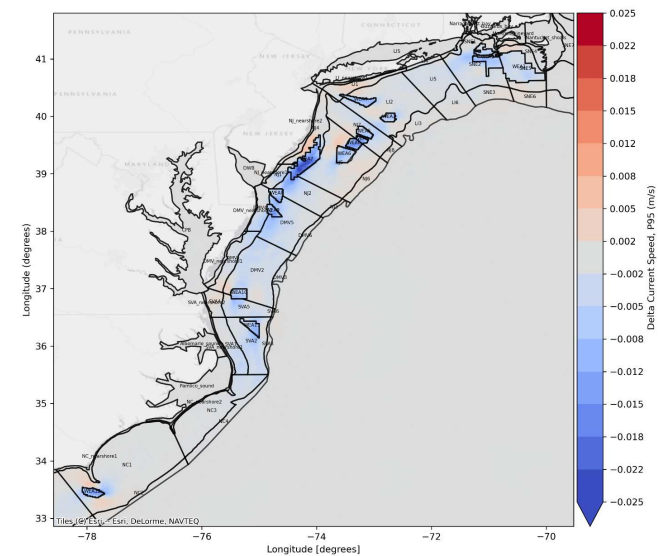


Figure 8.6. Change in Current Speed 15 MW Full Build-Out vs. Baseline 2017

Difference in the depth averaged current speed for model year 2017. Showing the difference in the 95th percentile non-exceedance probability baseline results and 95th percentile non-exceedance probability Scenario 5: 15 MW Full Build-out results.

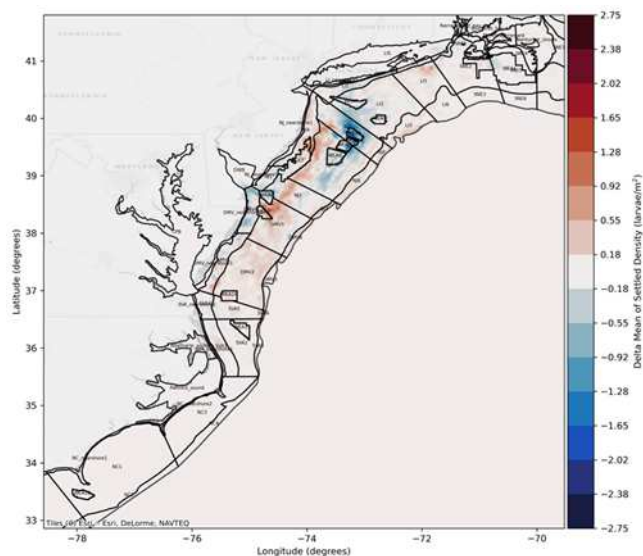


Figure 8.7. Difference in Settled Larvae Density 15 MW Full Build-Out vs. Baseline 2017

Difference in sea scallop settled larvae density for model year 2017. Showing the difference in the mean of all ensemble baseline results and mean of all ensemble Scenario 5: 15 MW Full Build-out results. Settled larvae density averaged for each model grid element. Red shows an increase in settlement in the 15 MW scenario compared to the baseline, blue shows a decrease in settlement compared to the baseline.

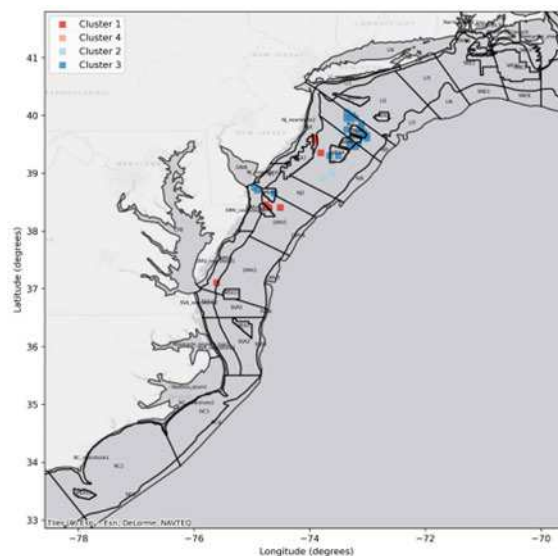


Figure 8.8. DBSCAN (Density-Based Spatial Clustering of Applications with Noise) Difference in Settled Larvae Density 15 MW Full Build-Out vs. Baseline 2017

Spatial clusters identified using DBSCAN to filter out noise from the difference plot and identify areas of greatest change. Clusters of settlement increase are identified in red and clusters with settlement decrease are shown in blue.

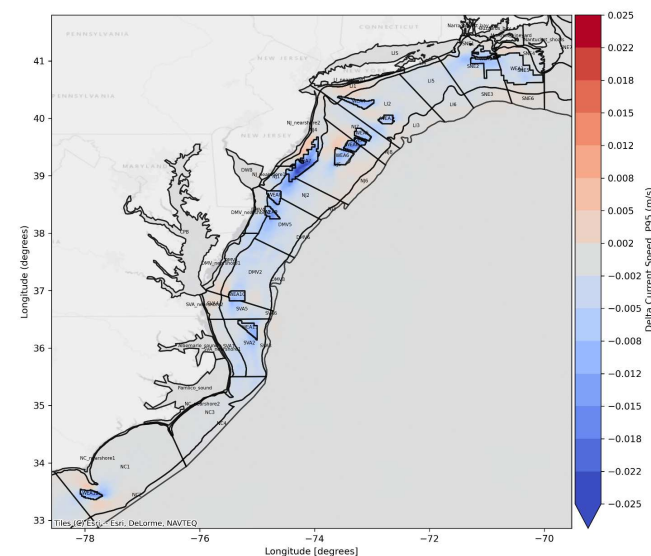


Figure 8.9. Change in Current Speed 15 MW Full Build-Out vs. Baseline 2017

Difference in the depth averaged current speed for model year 2017. Showing the difference in the mean of 95th percentile non-exceedance probability ensemble baseline results and mean of 95th percentile non-exceedance probability ensemble Scenario 5: 15 MW Full Build-out results.

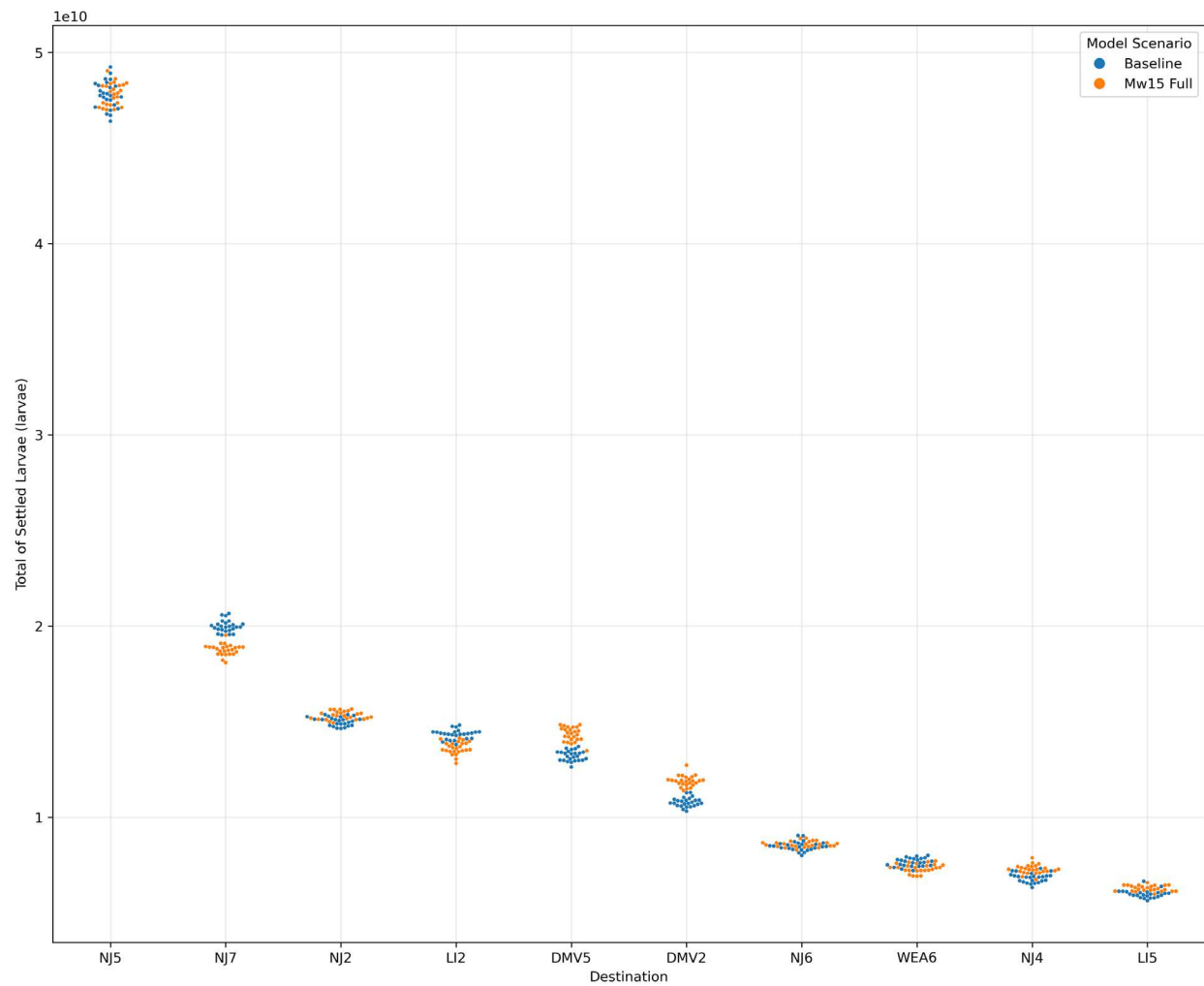


Figure 8.11. Swarm Plot Showing Sea Scallop Settlement in Top 10 Destinations for 2017

Swarm plot shows the settlement for each model run of the ensemble (i.e., each point represents a model result) for 2017. Blue points show the baseline results and orange show the Scenario 5: 15 MW Full Build-out number of settled larvae in the top 10 destinations where there is greatest larval settlement.

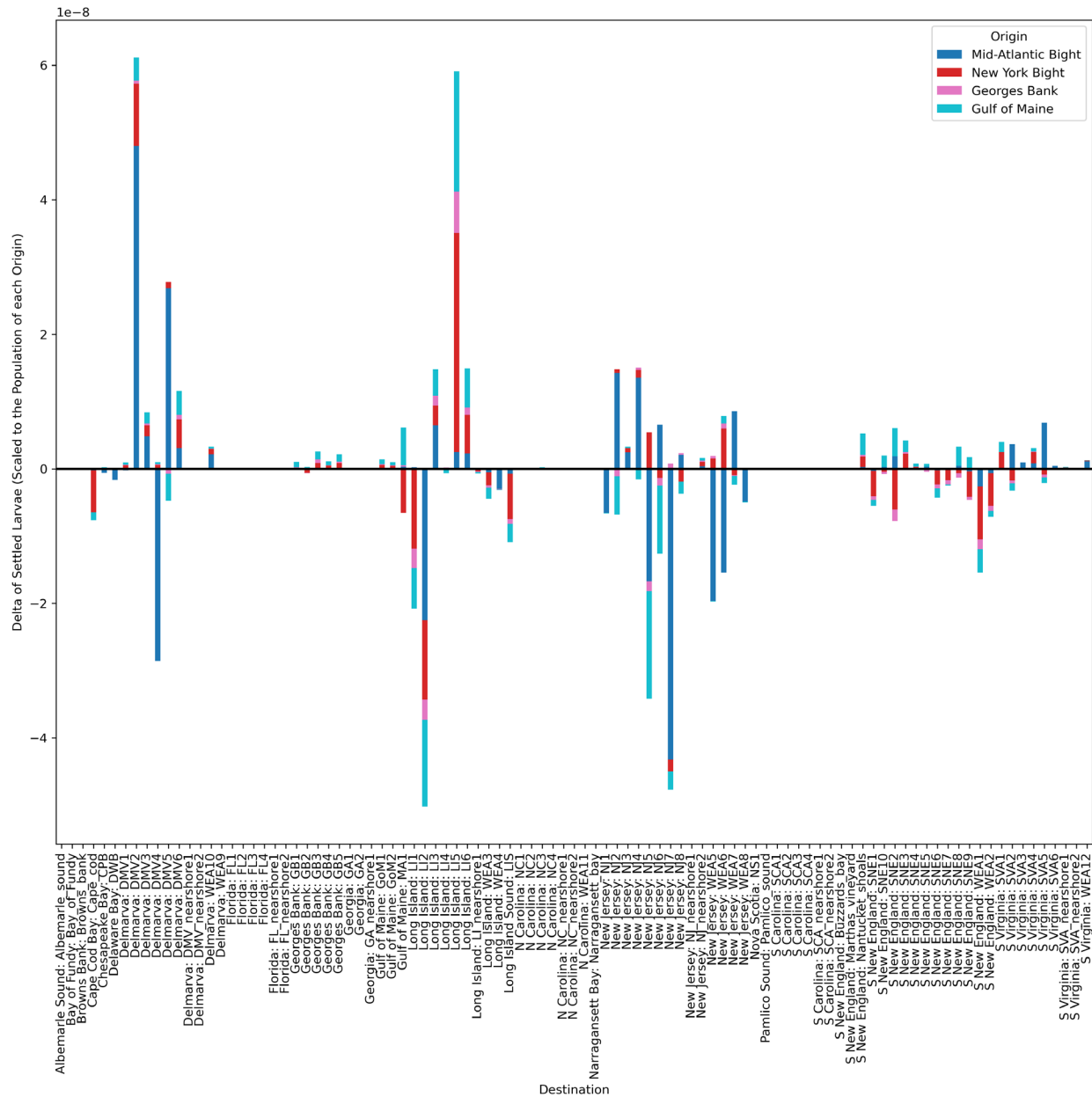


Figure 8.12. Sea Scallop Connectivity Difference 2017

Bar chart shows the difference in sea scallop larvae settlement in each destination area, by origin for model year 2017. Bars are colored by origin area and results show the difference in export probabilities, i.e., the difference in the likelihood of settlement scaled to the number of larvae released from a particular origin region between the baseline and 15MW full build-out results. Bars below the x axis, show a decrease in settlement in a particular destination area, results above the x axis show an increase in a settlement in a destination area.

8.3.1.2 2018

Similar to the 2017 results shown in the section above, changes in total sea scallop settlement induced by the 15 MW OSW build-out areas (WEAs) against the 2018 baseline are shown in the difference plot in **Figure 8.13**, which illustrates the difference in mean total settled larvae within the study area. The cluster analysis in **Figure 8.14** is designed to remove noise from the difference plot results and identify hotspots of change. The difference plot and cluster analysis are shown alongside current speed change in **Figure**

8.15. The difference in mean settled density is shown in **Figure 8.16**, and a similar cluster analysis for settled density is included in **Figure 8.17**, and current speed change is repeated in **Figure 8.18**.

The difference in mean total settled larvae within the study area is shown in , which ranges between 1 and 10 million larvae. Changes in settled density are also shown in **Figure 8.16**. The broad patterns of change in sea scallop larval settlement seen in these two difference plots are similar to those for 2017, with areas of larvae settlement decrease (shown in blue in **Figure 8.13** and **Figure 8.16**) estimated mainly offshore New Jersey south of WEAs 5 and 6 and areas of larvae settlement increase (shown in red in **Figure 8.13** and **Figure 8.16**) also estimated offshore New Jersey, west of WEA7. Settlement increase continues south through Delmarva (DMV2 and 5) into South Virginia (SVA2). There are also some areas of increased and decreased larval settlement estimated offshore Long Island (LI2 and LI5). Notable differences between the 2017 and 2018 results are an area of increased settled density in WEA6 and an area of decreased settlement just north of WEA7 in 2018.

The cluster analyses of total settled larvae and settled larvae density (**Figure 8.14** and **Figure 8.17**) show hotspots of change in sea scallop settlement, with clusters of decreased and increased settlement in agreement with the patterns seen in the difference plots. Decreased settlement clusters are found offshore New Jersey to the east side of NJ5 around WEAs 5 and 6, and closer to shore in NJ4 to a lesser extent offshore South Virginia (SVA1 and SVA5). Clusters of increased settlement are apparent offshore New Jersey in WEA7, offshore Delaware, to the east of WEAs 8 and 9, in DMV5, and in South Virginia east of WEA 11 in SVA2.

Similar patterns in settlement change identified in the cluster analysis are found in showing the average settlement change per destination area. Average increase in mean settled larvae (**Figure 8.19**) is seen in the Delmarva destination areas (DMV 5 and DMV3) and South Virginia (SVA2 and SVA6), while overall decrease in mean settled larvae occur in the settlement destination area off Long Island (LI4) and New Jersey (NJ4) and South Virginia (SVA1 and SVA5). The overall average change in NJ5 is low, and the large clusters of decreased settlement that were found in this destination area appear to be balanced by areas of increased settlement.

The swarm plot in **Figure 8.20** shows that the greatest magnitude of settlement is in New Jersey (NJ5, NJ2, NJ7), Delaware (DMV2 and DMV5), Long Island (LI2), and South Virginia (SVA2 and SVA1). Destination areas with greatest net change in total larval settlement are those where there is clear stratification between the orange (15MW scenario) and blue (baseline) points. Those with little change can be identified where there is a mix between orange and blue points. The most populated destination areas with clear increase in settlement with the introduction of OSW build out areas are DMV5 and NJ2. Which is consistent with patterns of increase identified in the difference plot and cluster analysis.

It should be noted when considering the relevance of these changes in settlement, that the largest change in settlement per destination area shown in the difference bar plot is four orders of magnitude lower than the total settlement in each destination area shown in the swarm plot.

The change in patterns of connectivity, together with settlement changes and the changes in current speeds can be investigated to help suggest the direction and areas in which larvae transport has slowed or increased resulting from the OSW. Similar to 2017, the decrease in current speed induced by the OSW areas (**Figure 8.15** and **Figure 8.18**) could be resulting in both slowed south-to-north and north-to-south transport of larvae from the MAB spawning area. With the introduction of the 15 MW WEAs, settlement of larvae spawned from the MAB is decreased in the New Jersey regions in NJ4, NJ5, WEA5, 6 and 7 (**Figure 8.21**), the same areas where clusters of settlement decrease were identified in (**Figure 8.14**). Settlement of larvae spawned from the MAB is increased further south in NJ2 (**Figure 8.21**) which was identified as an area of settlement increase in (**Figure 8.13**). These changes in connectivity indicate that the blue areas of reduced settlement in the New Jersey areas could be explained by slower south to north

transport from the MAB spawning area, which results in larvae settling further south (i.e., not being transported as far north). However, the additional presence of north-south movement of larvae makes this conclusion difficult to assert completely.

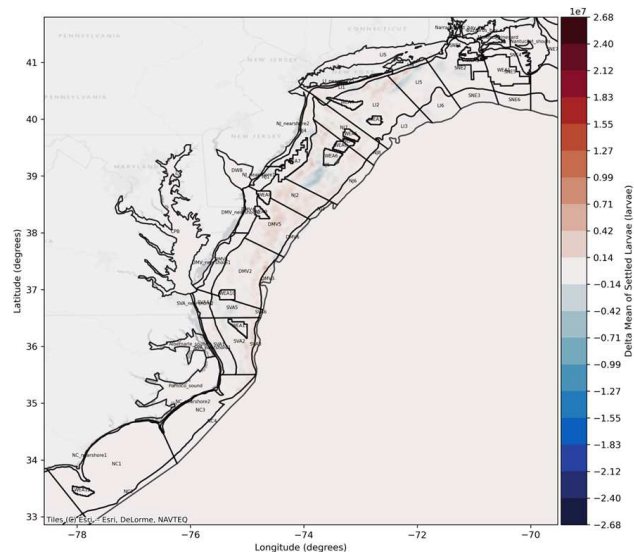


Figure 8.13. Difference in Total Settled Larvae 15 MW Full Build-Out vs. Baseline 2018

Difference in total sea scallop larvae settled larvae for model year 2018. Showing the difference in the mean of all ensemble baseline results and mean of all ensemble Scenario 5: 15 MW Full Build-out results. Settled larvae averaged for each model grid element. Red shows an increase in settlement in the 15 MW scenario compared to the baseline, blue shows a decrease in settlement compared to the baseline.

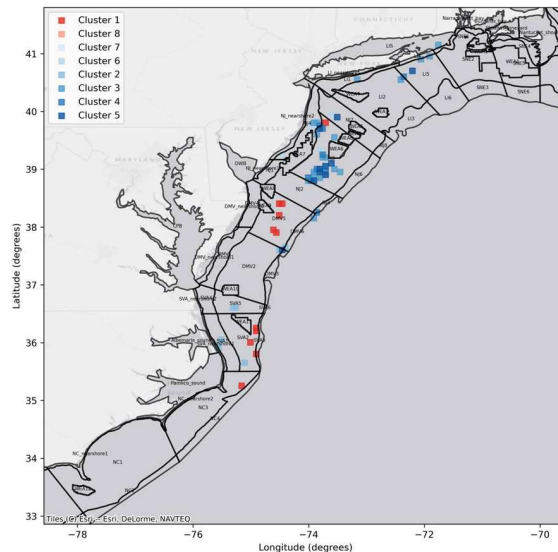


Figure 8.14. DBSCAN (Density-Based Spatial Clustering of Applications with Noise) Difference in Total Settled Larvae 15 MW Full Build-Out vs. Baseline 2018

Spatial clusters identified using DBSCAN to filter out noise from the difference plot and identify areas of greatest change. Clusters of settlement increase are identified in red and clusters with settlement decrease are shown in blue.

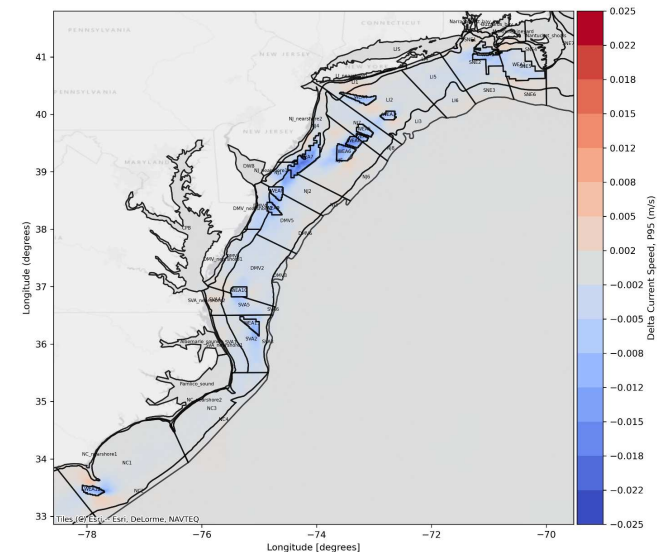


Figure 8.15. Change in Current Speed 15 MW Full Build-Out vs. Baseline 2018

Difference in the depth averaged current speed for model year 2018. Showing the difference in the 95th percentile non-exceedance probability baseline results and 95th percentile non-exceedance probability Scenario 5: 15 MW Full Build-out results

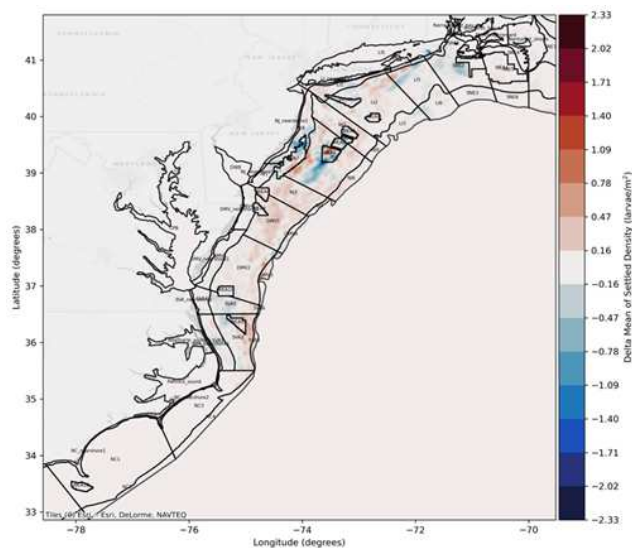


Figure 8.16. Difference in Settled Larvae Density 15 MW Full Build-Out vs. Baseline 2018

Difference in sea scallop settled larvae density for model year 2018. Showing the difference in the mean of all ensemble baseline results and mean of all ensemble Scenario 5: 15 MW Full Build-out results. Settled larvae averaged for each model grid element. Red shows an increase in settlement in the 15 MW scenario compared to the baseline, blue shows a decrease in settlement compared to the baseline.

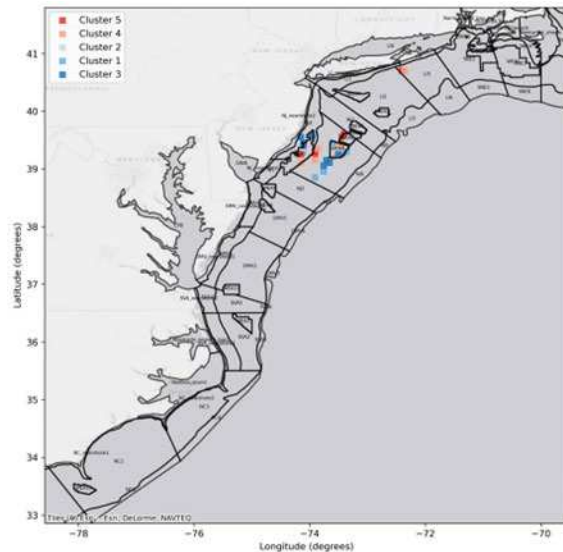


Figure 8.17. DBSCAN (Density-Based Spatial Clustering of Applications with Noise) Difference in Settled Larvae Density 15 MW Full Build-Out vs. Baseline 2018

Spatial clusters identified using DBSCAN to filter out noise from the difference plot and identify areas of greatest change. Clusters of settlement increase are identified in red and clusters with settlement decrease are shown in blue.

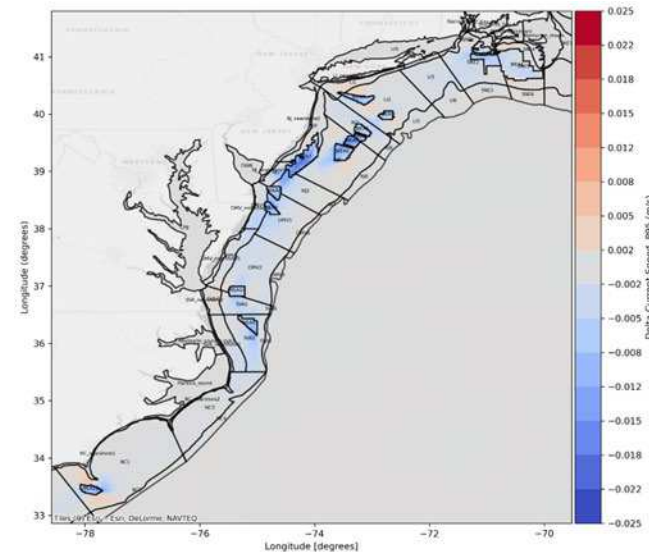


Figure 8.18. Change in Current Speed 15 MW Full Build-Out vs. Baseline 2018

Difference in the depth averaged current speed for model year 2018. Showing the difference in the mean of 95th percentile non-exceedance probability ensemble baseline results and mean of 95th percentile non-exceedance probability ensemble Scenario 5: 15 MW Full Build-out results.

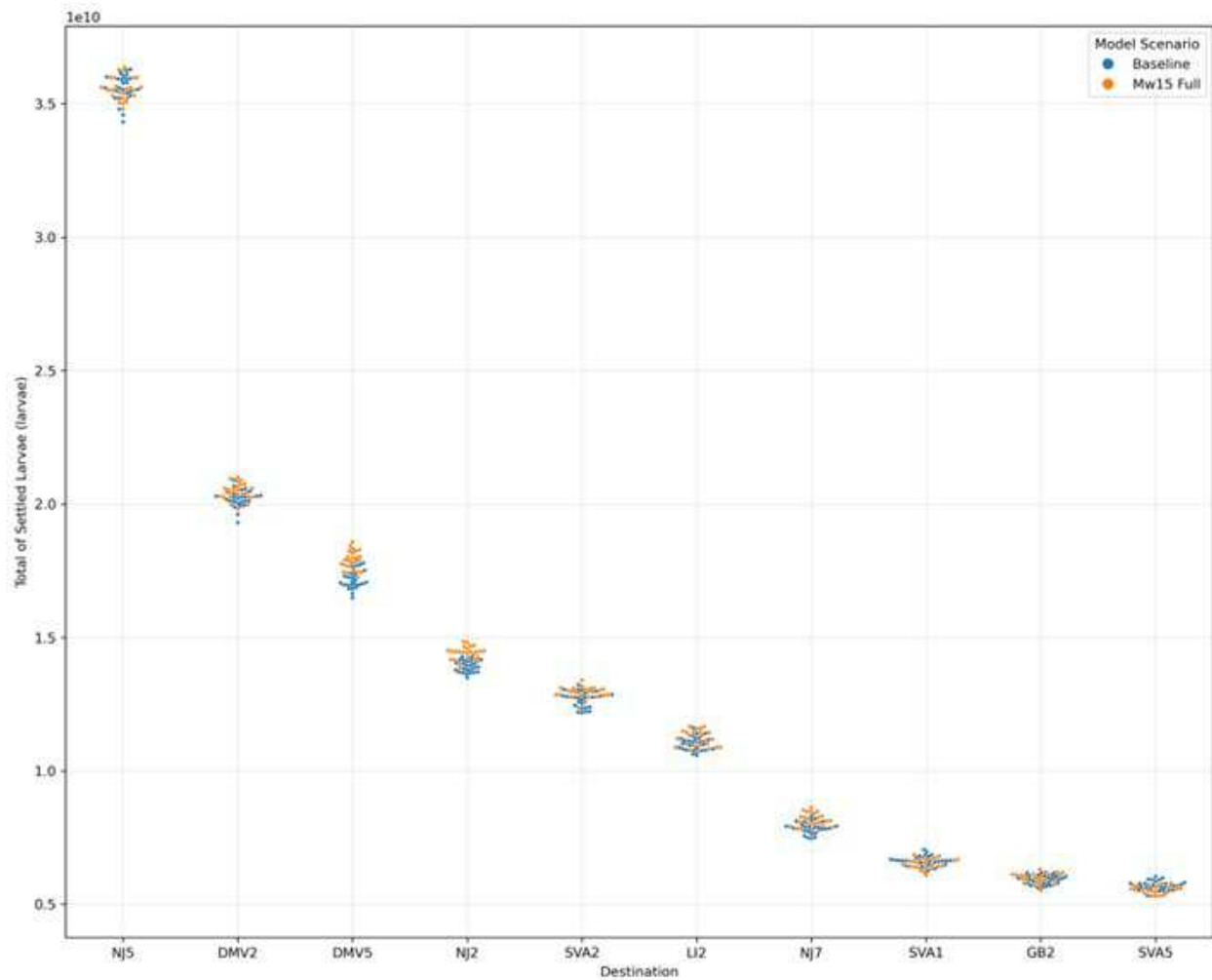


Figure 8.20. Swarm Plot Showing Sea Scallop Settlement in Top 10 Destinations for 2018
 Swarm plot shows the settlement for each model run of the ensemble (i.e., each point represents a model result) for 2018. Blue points show the baseline results and orange show the Scenario 5: 15 MW Full Build-out number of settled larvae in the top 10 destinations where there is greatest larval settlement.

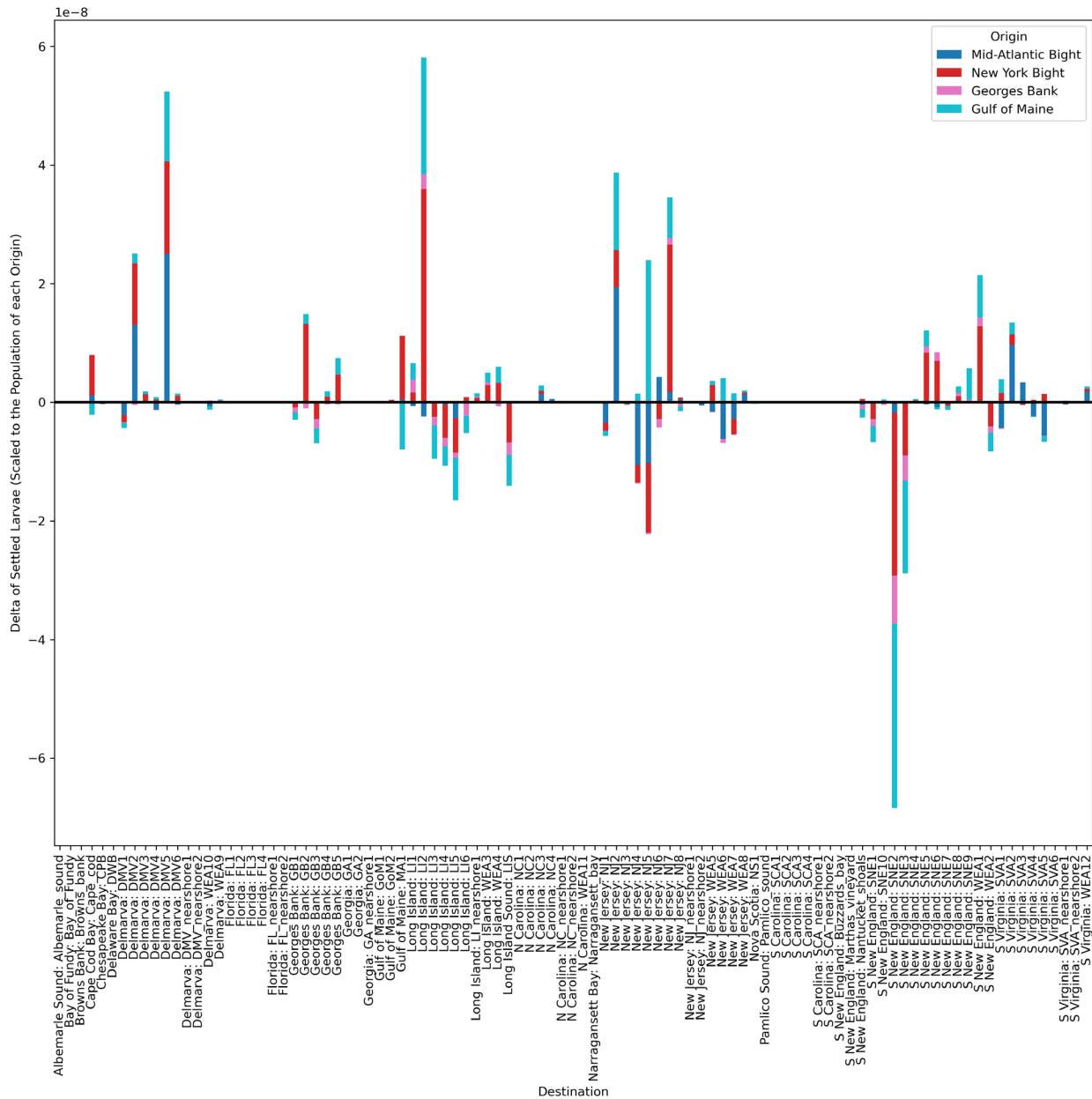


Figure 8.21. Sea Scallop Connectivity Difference 2018

Bar chart shows the difference in sea scallop larvae settlement in each destination area, by origin for model year 2018. Bars are colored by origin area and results show the difference in export probabilities, i.e., the difference in the likelihood of settlement scaled to the number of larvae released from a particular origin region between the baseline and 15MW full build-out results. Bars below the x axis, show a decrease in settlement in a particular destination area, results above the x axis show an increase in a settlement in a destination area.

8.3.1.3 2020

Similar to the 2017 and 2018 results, changes in total sea scallop settlement induced by the 15 MW OSW build-out areas (WEAs) against the 2020 baseline are shown in the difference plot in **Figure 8.22**, which illustrates the difference in mean total settled larvae within the study area. The cluster analysis in **Figure 8.23** is designed to remove noise from the difference plot results and identify hotspots of change. The difference plot and cluster analysis are shown alongside current speed change in **Figure 8.24**. The

difference in mean settled density is shown in **Figure 8.25**, and a similar cluster analysis for settled density is included in **Figure 8.26**, and current speed change is repeated in **Figure 8.27**.

The difference in mean settled larvae and settled larvae density within the study area is shown in **Figure 8.22** and **Figure 8.25** against the 2020 baseline. Broad patterns of settlement are slightly different to those seen 2017 and 2018. With decreased settlement to the south of WEAs 5 and 6 offshore of New Jersey (eastern portions of NJ2 and NJ5, closer to the shelf) and offshore Delaware to the east of WEAs 8 and 9 (DM4). Areas of larvae settlement increase (shown in red in **Figure 8.22**) are seen on the western side of NJ2 and NJ5 closer to and within WEA 7, within WEA6, southward toward Delaware (DWV5 and DWV2) and South Virginia (SVA5). The cluster analysis (**Figure 8.23** and **Figure 8.26**) shows the broad patterns of change in sea scallop settlement, reflecting the key areas discussed above, with clusters of decreased settlement offshore New Jersey (eastern portions of NJ2 and NJ5), and offshore Delaware (DWV4). Clusters of increased settlement occurred off New Jersey, closer to shore within WEA7 and within and to the south of WEA6.

Areas of increased mean settled larvae (**Figure 8.28**) occurred in the Long Island (LI3 and LI4), Delmarva (DMV5) and South Virginia (SVA5) regions, with a lesser extent in New Jersey (NJ4 and WEA6). Areas of decreased mean settled larvae occurred predominantly in Delmarva (DMV4 and WEA9), with a lesser extent in New Jersey (NJ1 and WEA5) (**Figure 8.28**). The swarm plot in

Figure 8.29 shows that the greatest magnitude of settlement is in New Jersey (NJ5, NJ2, NJ7, NJ4), Long Island (LI2) and Delaware (DMV5). Destination areas with greatest net change are those where there is clear stratification of increase and decrease in settlement, while those with little net change are where there is a mix between increase and decrease within destination areas. Clear increase in settlement from the baseline are seen in NJ5 and DMV5, whereas mixed scattered in other destination areas indicate a mix of both increase and decrease occurring at a finer scale.

It should be noted when considering the relevance of these changes in settlement, that the largest change in settlement per destination area shown in the difference bar plot is four orders of magnitude lower than the total settlement in each destination area shown in the swarm plot.

The change in patterns of connectivity, together with settlement changes and the changes in current speeds can be investigated to help suggest the direction and areas in which larvae transport has slowed or increased resulting from the OSW. The 2020 model year differs to 2017 and 2018 as the greatest decrease in connectivity is seen from larvae spawning in the NYB (red bars), **Figure 8.30**, while increased settlement is mainly originating from spawning areas in the MAB. This indicates that the areas of reduced settlement could be a result in the decrease in current speed induced by the OSW areas causing slowed north-to-south transport of larvae from the NYB.

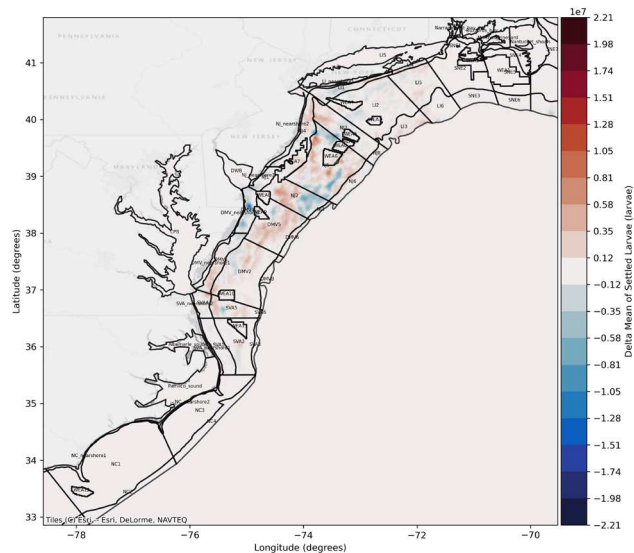


Figure 8.22. Difference in Total Settled Larvae 15 MW Full Build-Out vs. Baseline 2020

Difference in total sea scallop settled larvae for model year 2020. Showing the difference in the mean of all ensemble baseline results and mean of all ensemble Scenario 5: 15 MW Full Build-out results. Settled larvae averaged for each model grid element. Red shows an increase in settlement in the 15 MW scenario compared to the baseline, blue shows a decrease in settlement compared to the baseline.

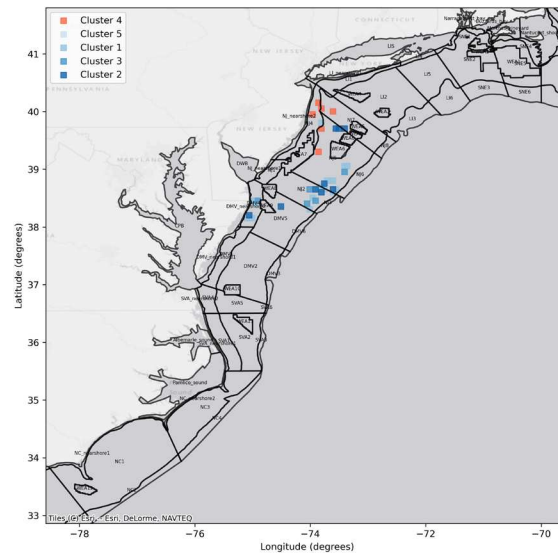


Figure 8.23. DBSCAN (Density-Based Spatial Clustering of Applications with Noise) Difference in Total Settled Larvae 15 MW Full Build-Out vs. Baseline 2020

Spatial clusters identified using DBSCAN to filter out noise from the difference plot and identify areas of greatest change. Clusters of settlement increase are identified in red and clusters with settlement decrease are shown in blue.

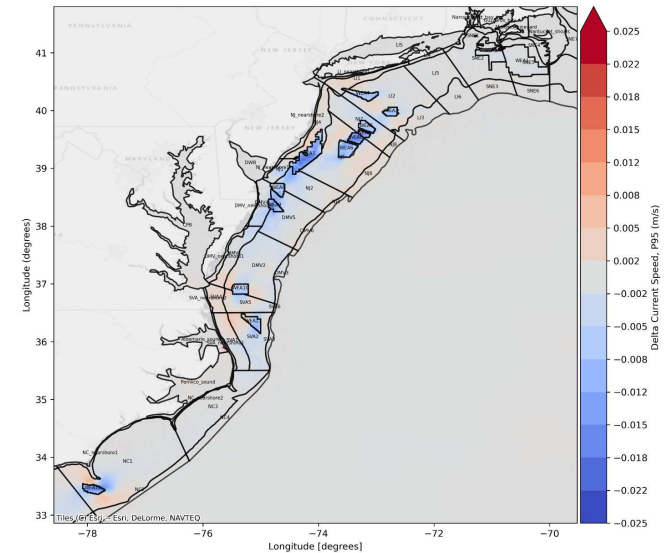


Figure 8.24. Change in Current Speed 15 MW Full Build-Out vs. Baseline 2020

Difference in the depth averaged current speed for model year 2020. Showing the difference in the 95th percentile non-exceedance probability baseline results and 95th percentile non-exceedance probability Scenario 5: 15 MW Full Build-out results

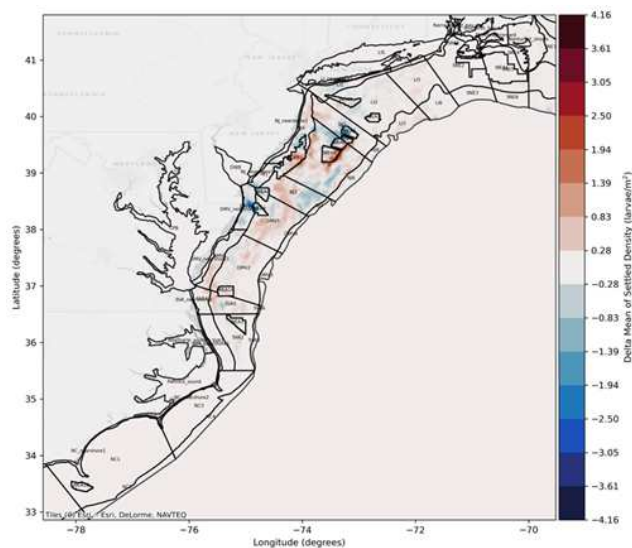


Figure 8.25. Difference in Settled Larvae Density 15 MW Full Build-Out vs. Baseline 2020

Difference in sea scallop settled larvae density for model year 2020. Showing the difference in the mean of all ensemble baseline results and mean of all ensemble Scenario 5: 15 MW Full Build-out results. Settled larvae averaged for each model grid element. Red shows an increase in settlement in the 15 MW scenario compared to the baseline, blue shows a decrease in settlement compared to the baseline.

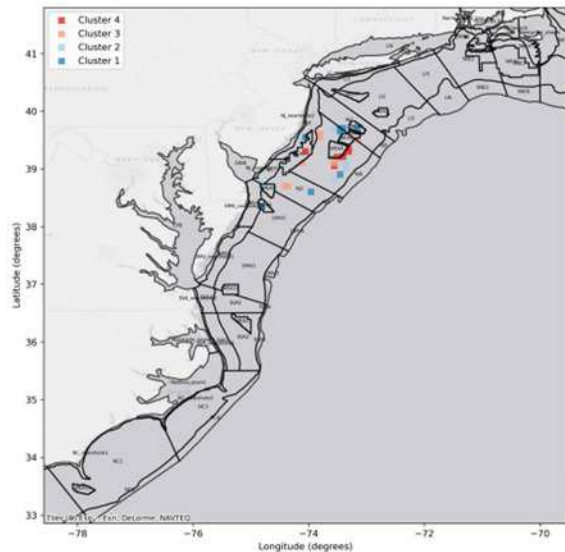


Figure 8.26. DBSCAN (Density-Based Spatial Clustering of Applications with Noise) Difference in Settled Larvae Density 15 MW Full Build-Out vs. Baseline 2020

Spatial clusters identified using DBSCAN to filter out noise from the difference plot and identify areas of greatest change. Clusters of settlement increase are identified in red and clusters with settlement decrease are shown in blue.

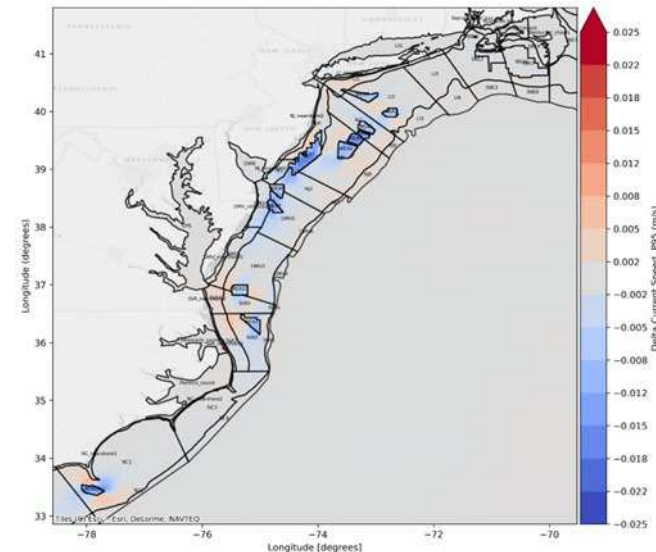


Figure 8.27. Change in Current Speed 15 MW Full Build-Out vs. Baseline 2020

Difference in the depth averaged current speed for model year 2020. Showing the difference in the mean of 95th percentile non-exceedance probability ensemble baseline results and mean of 95th percentile non-exceedance probability ensemble Scenario 5: 15 MW Full Build-out results.

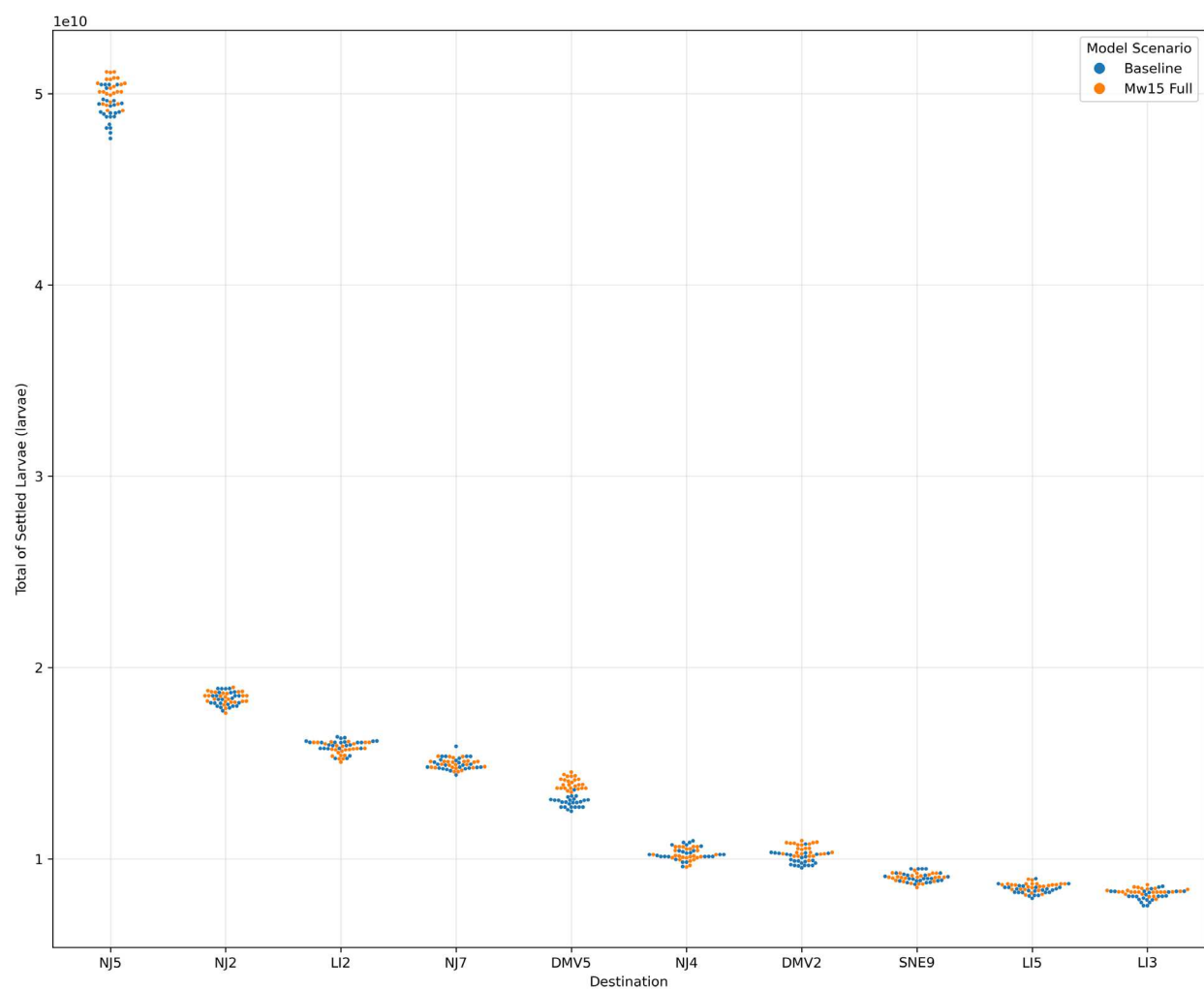


Figure 8.29. Swarm Plot showing Sea Scallop Settlement in Top 10 Destinations for 2020

Swarm plot shows the settlement for each model run of the ensemble (i.e., each point represents a model result) for 2020. Blue points show the baseline results and orange show the Scenario 5: 15 MW Full Build-out number of settled larvae in the top 10 destinations where there is greatest larval settlement.

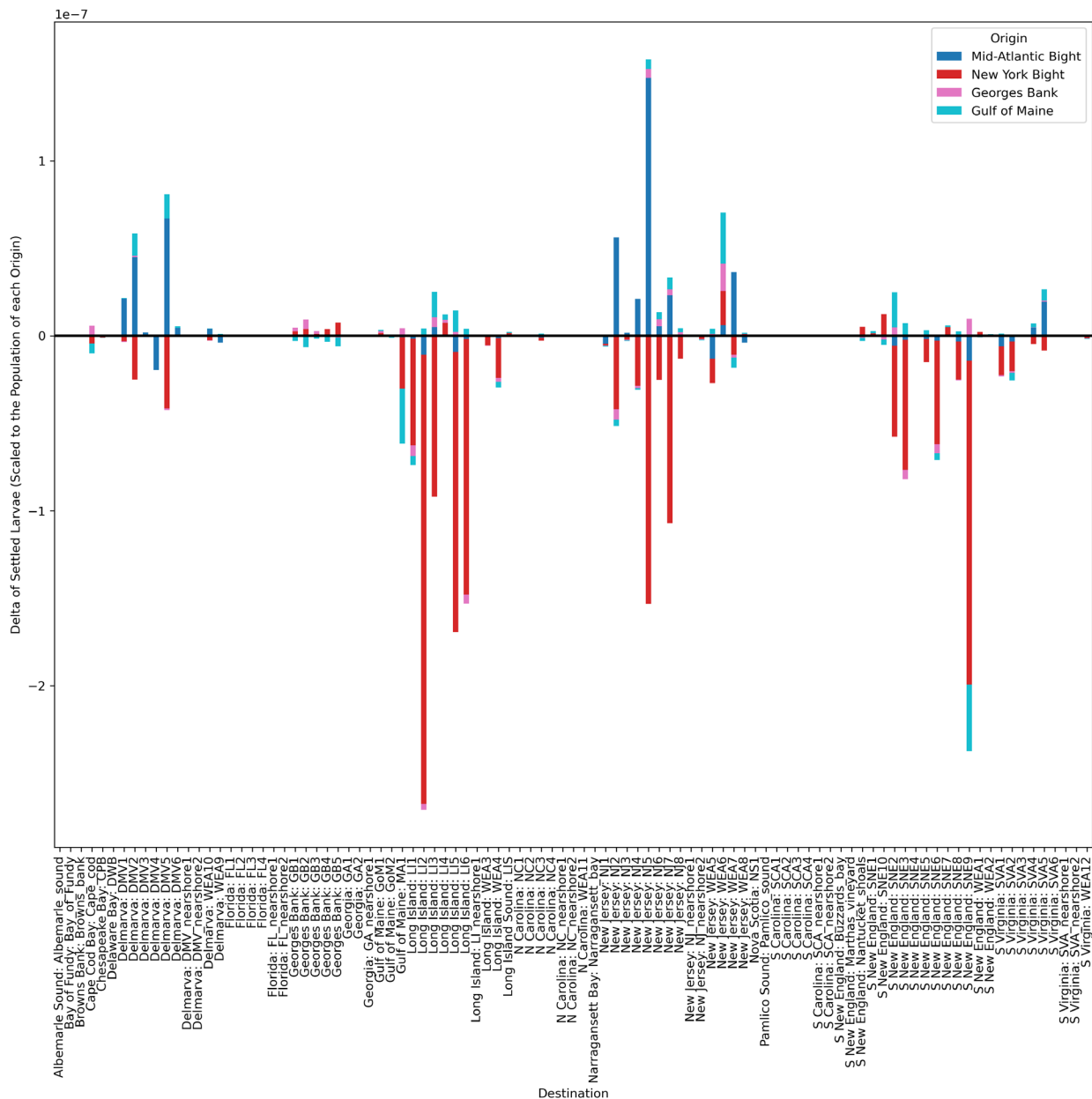


Figure 8.30. Sea Scallop Connectivity Difference 2020

Bar chart shows the difference in sea scallop larvae settlement in each destination area, by origin for model year 2020. Bars are colored by origin area and results show the difference in export probabilities, i.e., the difference in the likelihood of settlement scaled to the number of larvae released from a particular origin region between the baseline and 15MW full build-out results. Bars below the x axis, show a decrease in settlement in a particular destination area, results above the x axis show an increase in a settlement in a destination area.

8.3.2 Surfclam

Change in total surf clam settlement induced by the 15 MW OSW build-out areas (WEAs) for 2017 are shown in the difference plot in **Figure 8.31**, which illustrates the difference in mean total settled larvae within the study area. The cluster analysis in **Figure 8.32** is designed to remove noise from the difference plot results and identify hotspots of change. The difference plot and cluster analysis are shown alongside

current speed change in **Figure 8.33**. The difference in mean settled density is shown in **Figure 8.34**, and a similar cluster analysis for settled density is included in **Figure 8.35**, and current speed change is repeated in **Figure 8.36**.

The difference in mean total settled surfclam larvae and settled larvae density within the study area is shown in **Figure 8.31** and **Figure 8.34** against the 2017 baseline, illustrating the difference in mean settled larvae within the study area. The most notable shift in surfclam larval settlement occurs in New Jersey, with both areas of larvae settlement decrease (shown in blue in **Figure 8.31** and **Figure 8.34**) and increase (shown in red in **Figure 8.31** and **Figure 8.34**) seen mainly offshore of New Jersey (NJ2 and NJ5). A lesser extent of increases and decreases occur southward in the Delmarva region. Increases and decreases in settlement range between 1 and 10 million larvae.

The cluster analysis (**Figure 8.32** and **Figure 8.35**) shows the broad patterns of change in surfclam settlement, reflecting the key areas discussed above, with a cluster of increased settlement offshore New Jersey east of WEA7 and south of WEA6 (NJ5). Two clusters of decreased settlement are apparent, one offshore New Jersey in and around WEA5 and WEA6 and one further south to the east of WEA8 and WEA9. Patterns of average change in settlement over destination areas (**Figure 8.37**) are similar to those shown in the difference plots and cluster analyses, with the largest destination area settlement changes in the New Jersey region (increased settlement in NJ2 and NJ5 and decreased settlement in NJ7 and WEA6).

The swarm plot in **Figure 8.38** shows that the greatest magnitude of surfclam larval settlement is in New Jersey (NJ5, NJ2, and NJ4), Delaware (DMV2 and DMV5), South Virginia (SVA2 and SVA5), and Long Island (LI2). Destination areas with greatest net change are those where there is clear stratification of increases and decreases in settlement, shown in NJ5, NJ2, WEA 6 and to a lesser extent DMV5 and LI2. Those with little net change is where there is a mix between increases and decreases within destination areas. It should be noted when considering the relevance of these changes in settlement, that the largest change in settlement per destination area shown in the difference bar plot (**Figure 8.37**) is five orders of magnitude lower than the total settlement in each destination area shown in the swarm plot.

An analysis of the connectivity results in **Figure 8.39** suggests how current speed changes could affect the distribution and ultimately the settlement destination of larvae. The slowing of current speeds appears to be mainly affected the north to south distribution of larvae, as the greatest decreases seen in the two areas of overall decrease in a) NJ5 and NJ2 and b) DMV5 are resulting from a reduction in larvae from northern spawning areas of Cape Cod, Long Island, and South New England. The increase in larvae seen in the center of the MAB appears to be a result of an increase in larvae settling from Delmarva and New Jersey areas, also suggesting a decrease in south to north transport. The increase in settlement in the middle of the region with decreases in settlement to the north and to the south also support this hypothesis. It appears that larvae are influenced by current speed decreases throughout the New Jersey region generally.

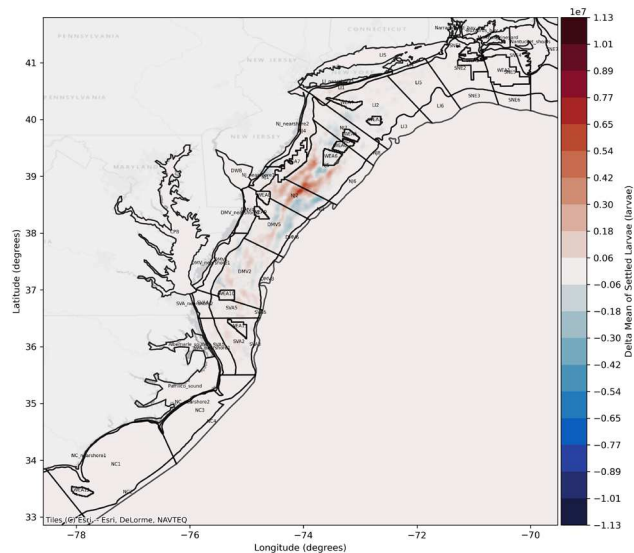


Figure 8.31. Difference in Total Settled Larvae 15 MW Full Build-Out vs. Baseline 2017

Difference in total surfclam settled larvae for model year 2017. Showing the difference in the mean of all ensemble baseline results and mean of all ensemble Scenario 5: 15 MW Full Build-out results. Settled larvae averaged for each model grid element. Red shows an increase in settlement in the 15 MW scenario compared to the baseline, blue shows a decrease in settlement compared to the baseline.

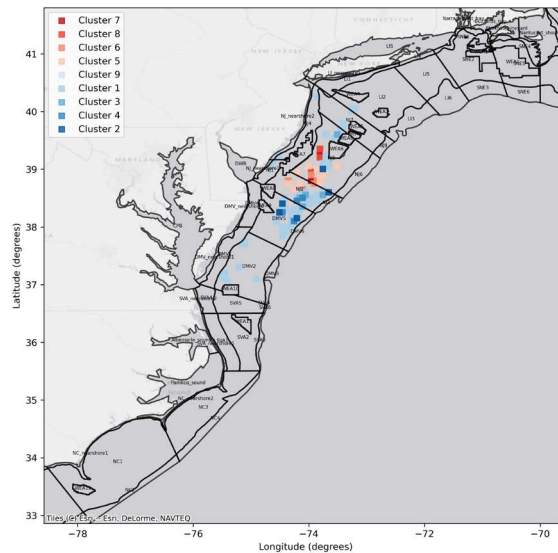


Figure 8.32. DBSCAN (Density-Based Spatial Clustering of Applications with Noise) Difference in Total Settled Larvae 15 MW Full Build-Out vs. Baseline 2017

Spatial clusters identified using DBSCAN to filter out noise from the difference plot and identify areas of greatest change. Clusters of settlement increase are identified in red and clusters with settlement decrease are shown in blue.

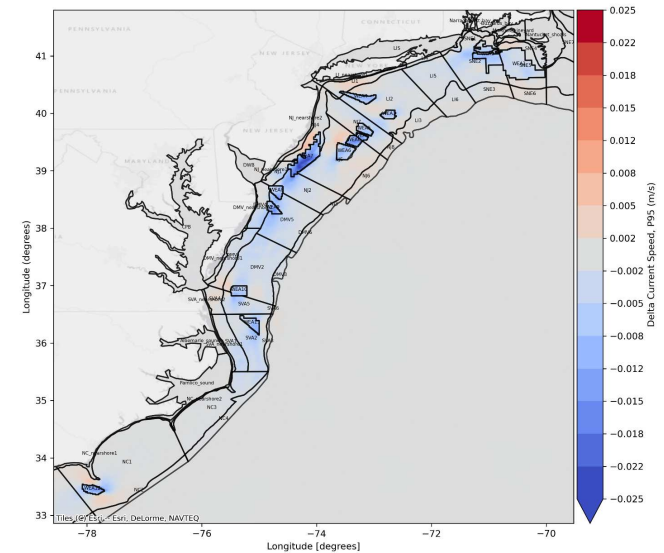


Figure 8.33. Change in Current Speed 15 MW Full Build-Out vs. Baseline 2017

Difference in the depth averaged current speed for model year 2017. Showing the difference in the 95th percentile non-exceedance probability baseline results and 95th percentile non-exceedance probability Scenario 5: 15 MW Full Build-out results

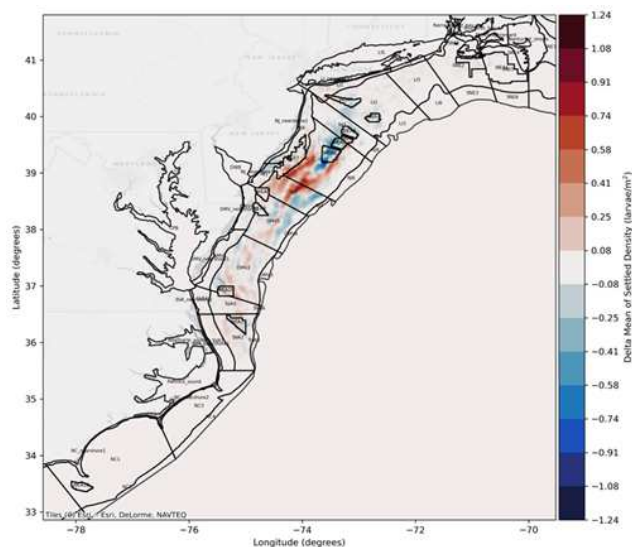


Figure 8.34. Difference in Settled Larvae Density 15 MW Full Build-Out vs. Baseline 2017

Difference in surfclam settled larvae density for model year 2017. Showing the difference in the mean of all ensemble baseline results and mean of all ensemble Scenario 5: 15 MW Full Build-out results. Settled larvae averaged for each model grid element. Red shows an increase in settlement in the 15 MW scenario compared to the baseline, blue shows a decrease in settlement compared to the baseline.

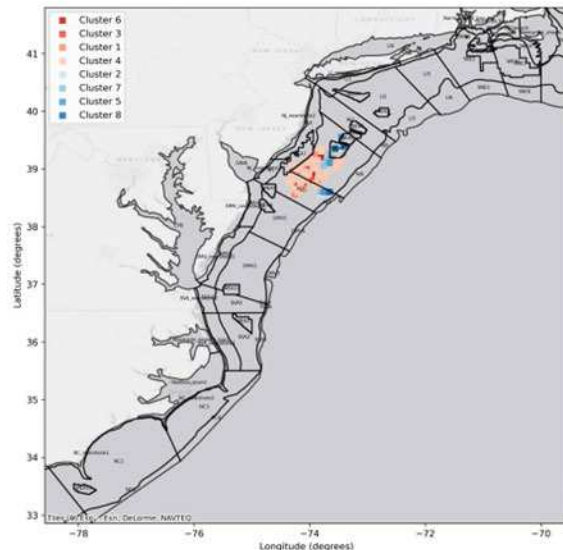


Figure 8.35. DBSCAN (Density-Based Spatial Clustering of Applications with Noise) Difference in Settled Larvae Density 15 MW Full Build-Out vs. Baseline 2017

Spatial clusters identified using DBSCAN to filter out noise from the difference plot and identify areas of greatest change. Clusters of settlement increase are identified in red and clusters with settlement decrease are shown in blue.

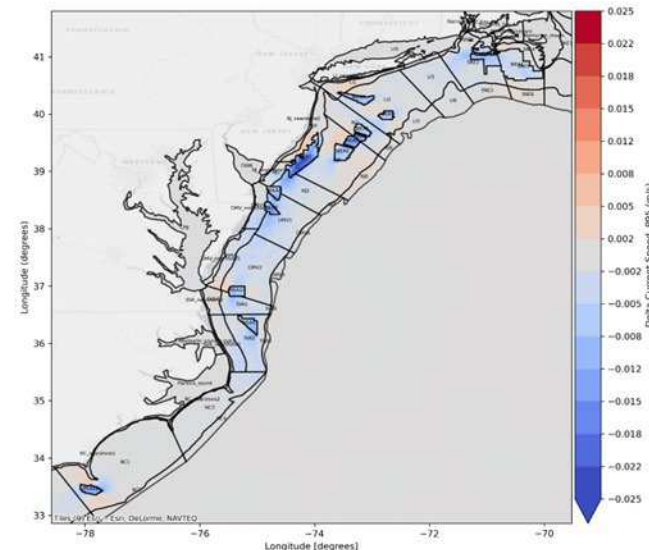


Figure 8.36. Change in Current Speed 15 MW Full Build-Out vs. Baseline 2017

Difference in the depth averaged current speed for model year 2017. Showing the difference in the mean of 95th percentile non-exceedance probability ensemble baseline results and mean of 95th percentile non-exceedance probability ensemble Scenario 5: 15 MW Full Build-out results.

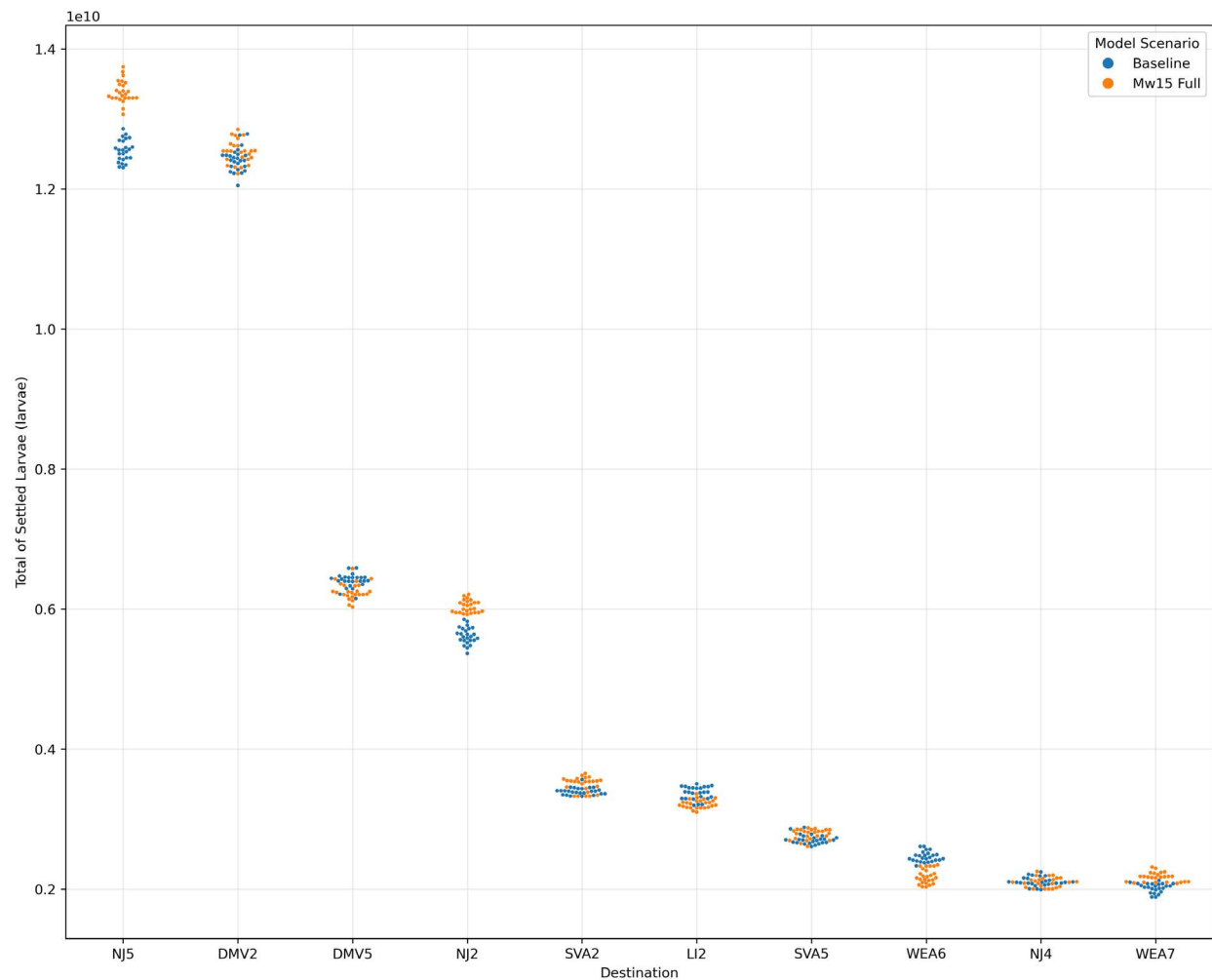


Figure 8.38. Swarm Plot Showing Surfclam Settlement in Top 10 Destinations for 2017

Swarm plot shows the settlement for each model run of the ensemble (i.e., each point represents a model result) for 2017. Blue points show the baseline results and orange show the Scenario 5: 15 MW Full Build-out number of settled larvae in the top 10 destinations where there is greatest larval settlement.

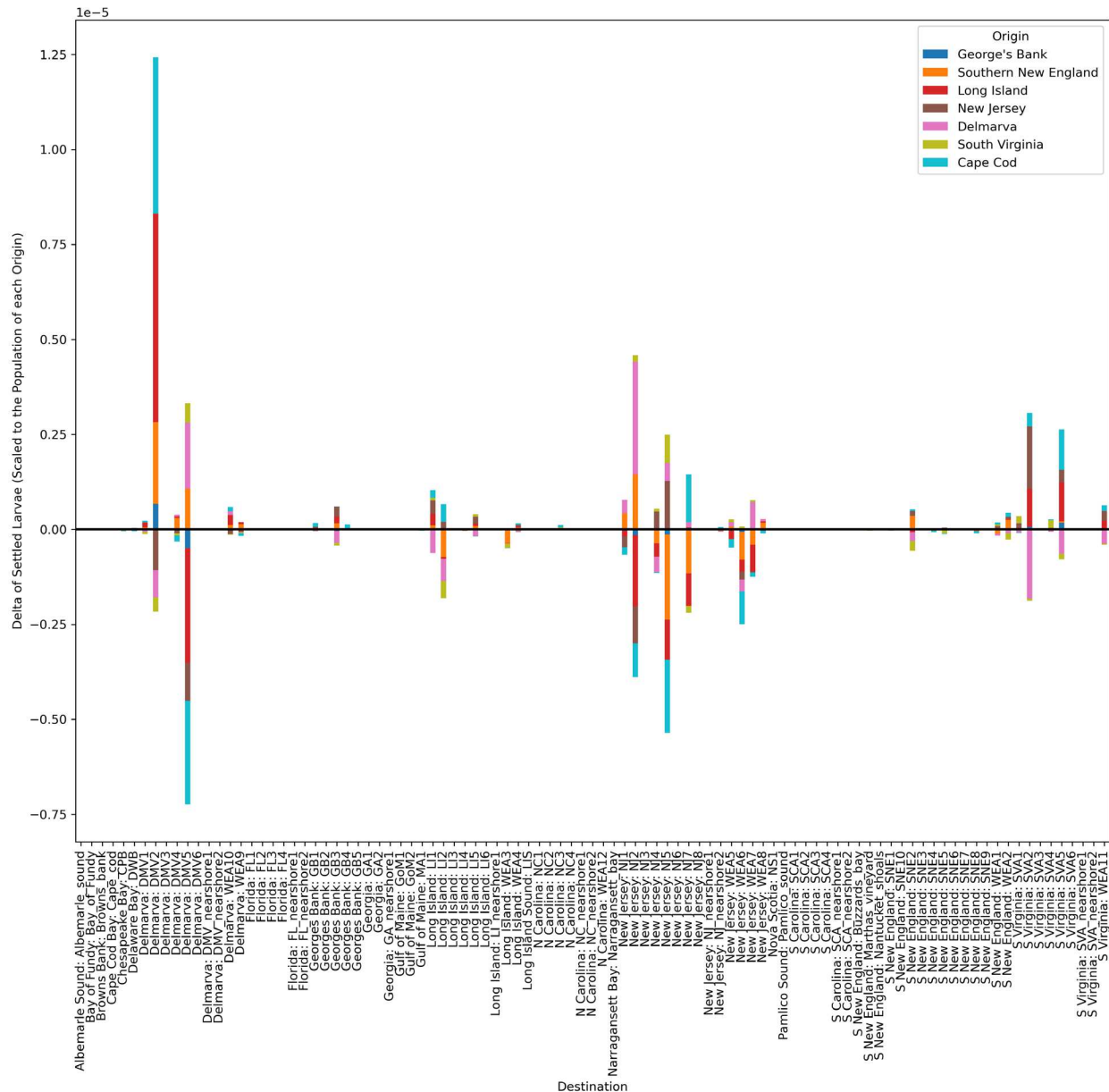


Figure 8.39. Surfclam Connectivity Difference 2017

Bar chart shows the difference in surfclam larvae settlement in each destination area, by origin for model year 2017. Bars are colored by origin area and results show the difference in export probabilities, i.e., the difference in the likelihood of settlement scaled to the number of larvae released from a particular origin region between the baseline and 15MW full build-out results. Bars below the x axis, show a decrease in settlement in a particular destination area, results above the x axis show an increase in a settlement in a destination area.

8.3.3 Summer Flounder

While the difference plots for sea scallop and surfclam reveal regional patterns of change in settlement concentrated in the New Jersey region, changes in summer flounder settlement are concentrated along the coast and are less apparent in the total settled larvae difference plot in **Figure 8.40** and cluster analysis plot **Figure 8.41**; and have little to no overlap with areas of current speed change (**Figure 8.42**).

Some changes in total summer flounder settlement are however, discernable along the coast in higher resolution plots in **Figure 8.43**, **Figure 8.44** and **Figure 8.45**. Few areas of change in settled larvae density are apparent throughout the model domain (**Figure 8.46**, **Figure 8.49**) and the cluster analysis of settled density identified no clusters of increased or decreased settlement (**Figure 8.47**, **Figure 8.50**). Again, areas of settled density change have little overlap with areas of current speed change (**Figure 8.51**).

Where change is discernable in the total settled larvae results, areas of estimated reduced settlement are apparent to the west of WEA7 in nearshore destination areas of New Jersey. An area of estimated increase in summer flounder settlement (red cluster) is also found in the New Jersey nearshore to the north of WEA7. Further clusters of increased settlement are also found around the mouth of Delaware Bay, to the west of WEAs 8 and 9 along the nearshore of Delmarva. The limited number of clusters of total settled larvae and no clusters identified for settled density identified by DBSCAN, indicates that there are few areas of settlement change estimated for summer flounder that can be distinguished from noise in the modeled results.

The change in average summer flounder larvae settlement per destination area (**Figure 8.52**) provides a broader destination area perspective of the average changes in settlement of summer flounder larvae. This bar plot show that on a destination area level, the largest decreases in average settlement are found in the nearshore destination areas of South Virginia (SVA nearshore 1 and 2) and Long Island (LI 4) despite no clusters of change being identified in these destination areas. In North Carolina there is an apparent shift in settlement south, with decreased settlement in NC nearshore 2 and increased settlement in NC nearshore 1. It should be noted when considering the relevance of these changes in settlement, that the largest change in settlement per destination area shown in the bar plot (**Figure 8.52**) is three orders of magnitude lower than the total settlement in each destination area, shown in the swarm plot. In addition, although there are some areas of total settlement change identified in the cluster analysis and average settlement bar chart, the swarm plot (**Figure 8.53**) highlights that there is high variability among ensembles and, due to the mixed nature of the blue and orange points, there is little to no clear difference between baseline and scenario results at the destination area level. There are also inconsistencies in areas of average settlement change identified for summer flounder across scenarios (please see bar plots for each scenario in Appendix C). Some areas of increased settlement shown in the 15MW scenario show decrease in other scenarios and vice versa (e.g., South Virginia Nearshore 1).

However, the bar plot shows the change in settlement averaged over destination areas, which potentially obscures the finer scale changes in settlement seen in the difference and cluster plots. This inconsistency is apparent in the average increase in settlement in NJ nearshore 1 and 2 shown in the bar plot (**Figure 8.52**), despite observable clusters of decreased settlement in New Jersey in **Figure 8.41**. The higher resolution difference plots in **Figure 8.43** and **Figure 8.46** illustrate areas of increased and decreased settlement along the coastal areas at a finer spatial scale than what is provided by destination area result illustrations.

The lack of a) identified clusters of change, b) that the mixed and noisy changes in total settlement are on a spatial scale smaller than destination areas, and c) inconsistencies between scenario results, make the interpretation of the connectivity plot (**Figure 8.54**) challenging and less meaningful than for the other species. However, some broader picture insights can be surmised. There is some overlap in the areas of greatest settlement increase and decrease and changes in connectivity. For example, in LI4 there is an average decrease in settlement in the bar plot (**Figure 8.52**) and a decrease in this destination area in the connectivity plot, from larvae originating from all regions. The average increase in settlement seen in NJ nearshore1 and 2 in **Figure 8.52**, is also shown to originate from all regions in the connectivity plot. These areas of decreased and increased larval settlement are also apparent in the 12 MW connectivity results (**section 8.4.3**), although there isn't much consistency between the two scenario results within the other destination regions.

It is possible that the diffuse shoreward transport of summer flounder larvae from east coast broad outer shelf spawning areas could be influenced by marginally reduced current speeds in and around OSW areas. This hypothesis is supported by the observation that the intensity of settlement change occurs where OWS areas are closest to shore e.g., westward of WEAs 7, 8 and 9 in Long Island and New Jersey destination areas. These results suggest that a finer scale local assessment of settlement change for Summer Flounder, concentrated around WEAs 7, 8 and 9, may allow for greater understanding of changes in larval settlement that may occur with the introduction of OSW developments.

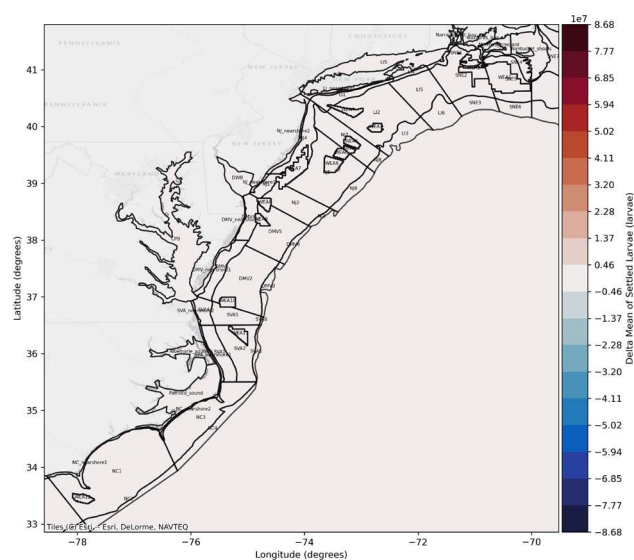


Figure 8.40. Difference in Total Settled Larvae 15 MW Full Build-Out vs. Baseline 2017

Difference in total summer flounder larvae settled larvae for model year 2017. Showing the difference in the mean of all ensemble baseline results and mean of all ensemble Scenario 5: 15 MW Full Build-out results. Settled larvae averaged for each model grid element. Red shows an increase in settlement in the 15 MW scenario compared to the baseline, blue shows a decrease in settlement compared to the baseline.

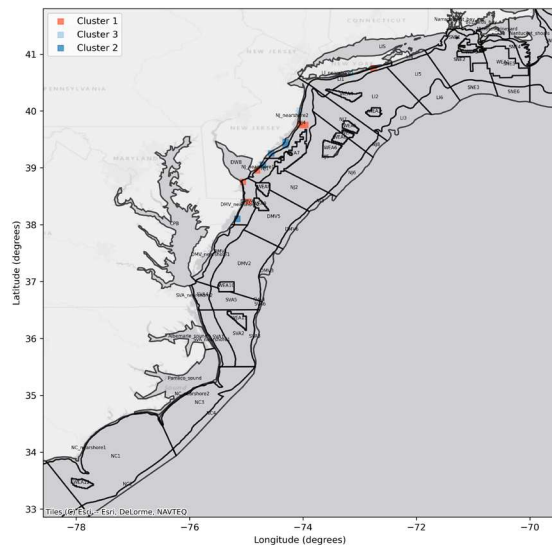


Figure 8.41. DBSCAN (Density-Based Spatial Clustering of Applications with Noise) Difference in Settled Larvae 15 MW Full Build-Out vs. Baseline 2017

Spatial clusters identified using DBSCAN to filter out noise from the difference plot and identify areas of greatest change. Clusters of settlement increase are identified in red and clusters with settlement decrease are shown in blue.

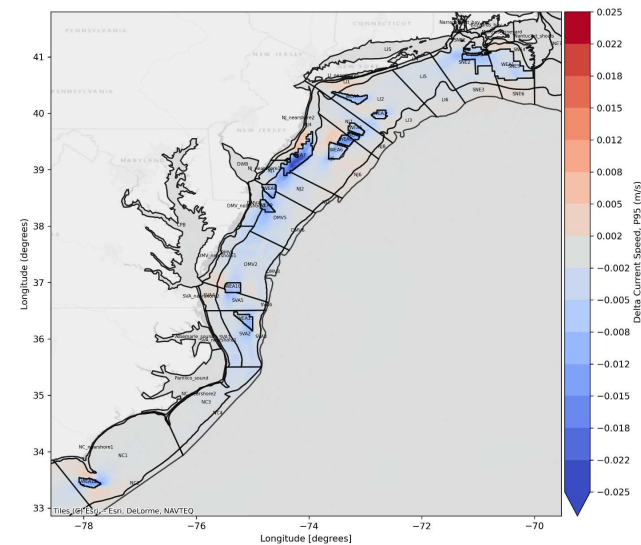


Figure 8.42. Change in Current Speed 15 MW Full Build-Out vs. Baseline 2017

Difference in the depth averaged current speed for model year 2017. Showing the difference in the 95th percentile non-exceedance probability baseline results and 95th percentile non-exceedance probability Scenario 5: 15 MW Full Build-out results.

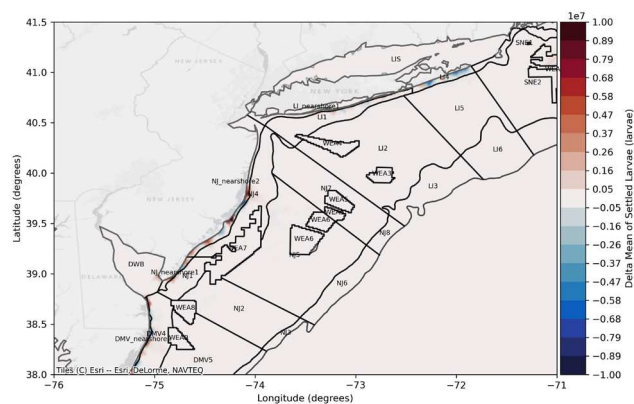


Figure 8.43. Higher Resolution Difference in Total Settled Larvae 15 MW Full Build-Out vs. Baseline 2017

Difference in total summer flounder settled larvae for model year 2017. Showing the difference in the mean of all ensemble baseline results and mean of all ensemble Scenario 5: 15 MW Full Build-out results. Settled larvae averaged for each model grid element. Red shows an increase in settlement in the 15 MW scenario compared to the baseline, blue shows a decrease in settlement compared to the baseline.

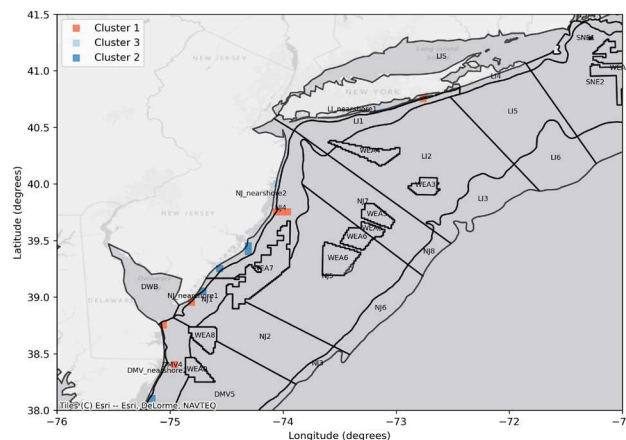


Figure 8.44. Higher Resolution DBSCAN (Density-Based Spatial Clustering of Applications with Noise) Difference in Settled Larvae 15 MW Full Build-Out vs. Baseline 2017

Spatial clusters identified using DBSCAN to filter out noise from the difference plot and identify areas of greatest change. Clusters of settlement increase are identified in red and clusters with settlement decrease are shown in blue.

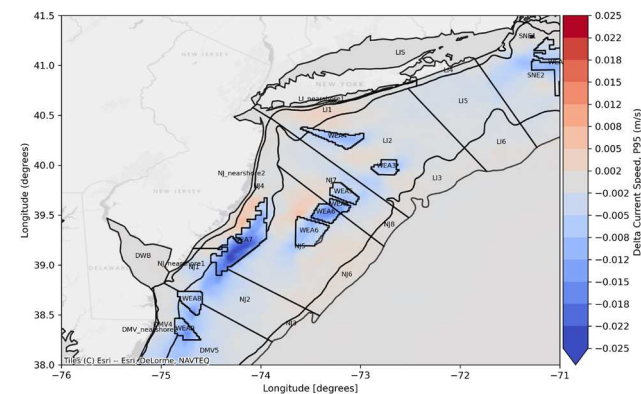


Figure 8.45. Higher Resolution Change in Current Speed 15 MW Full Build-Out vs. Baseline 2017

Difference in the depth averaged current speed for model year 2017. Showing the difference in the mean of 95th percentile non-exceedance probability ensemble baseline results and mean of 95th percentile non-exceedance probability ensemble Scenario 5: 15 MW Full Build-out results.

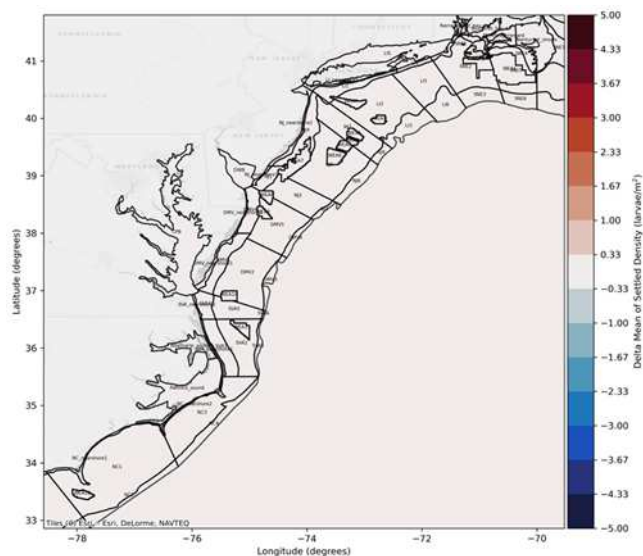


Figure 8.46. Difference in Settled Larvae Density 15 MW Full Build-Out vs. Baseline 2017

Difference in summer flounder settled larvae density for model year 2017. Showing the difference in the mean of all ensemble baseline results and mean of all ensemble Scenario 5: 15 MW Full Build-out results. Settled larvae averaged for each model grid element. Red shows an increase in settlement in the 15 MW scenario compared to the baseline, blue shows a decrease in settlement compared to the baseline.

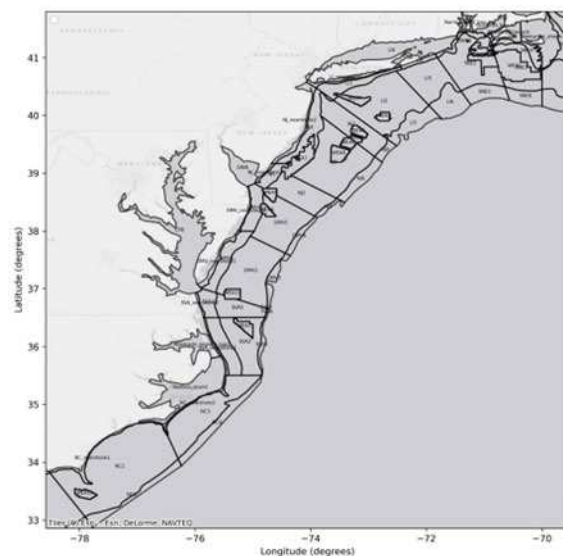


Figure 8.47. DBSCAN (Density-Based Spatial Clustering of Applications with Noise) Difference in Settled Larvae Density 15 MW Full Build-Out vs. Baseline 2017

Results of DBSCAN cluster analysis, with no discernable clusters of settled density change in summer flounder identified.

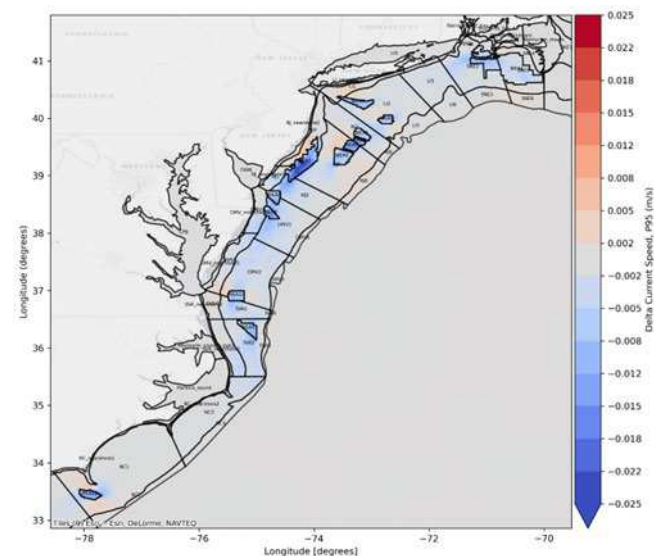


Figure 8.48. Change in Current Speed 15 MW Full Build-Out vs. Baseline 2017

Difference in the depth averaged current speed for model year 2017. Showing the difference in the mean of 95th percentile non-exceedance probability ensemble baseline results and mean of 95th percentile non-exceedance probability ensemble Scenario 5: 15 MW Full Build-out results.

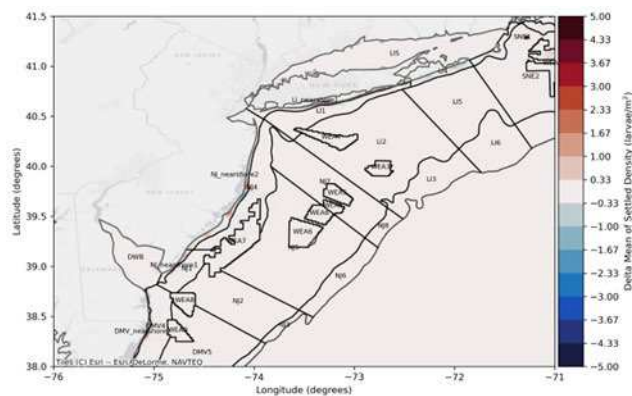


Figure 8.49. Higher Resolution Difference in Settled Larvae Density 15 MW Full Build-Out vs. Baseline 2017

Difference in summer flounder settled larvae density for model year 2017. Showing the difference in the mean of all ensemble baseline results and mean of all ensemble Scenario 5: 15 MW Full Build-out results. Settled larvae averaged for each model grid element. Red shows an increase in settlement in the 15 MW scenario compared to the baseline, blue shows a decrease in settlement compared to the baseline.

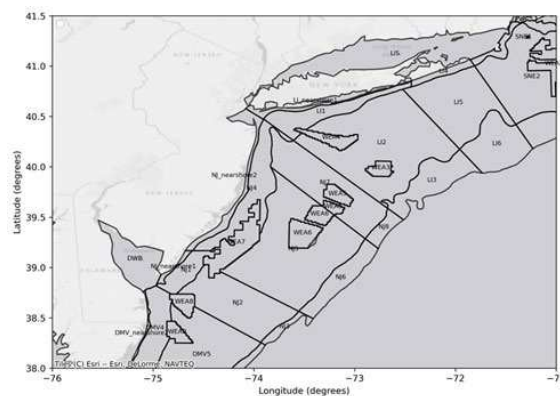


Figure 8.50. Higher Resolution DBSCAN (Density-Based Spatial Clustering of Applications with Noise) Difference in Settled Larvae Density 15 MW Full Build-Out vs. Baseline 2017

Results of DBSCAN cluster analysis, with no discernable clusters of settled density change in summer flounder identified.

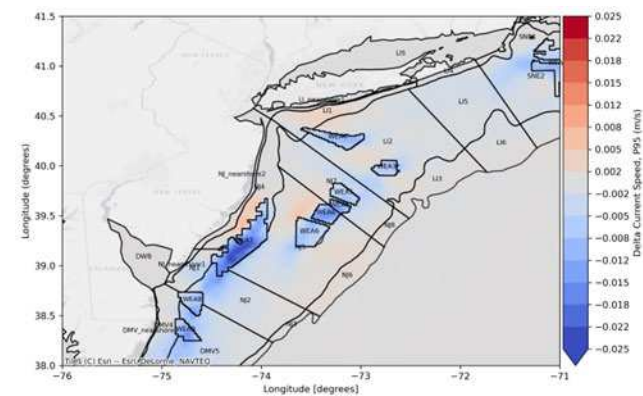
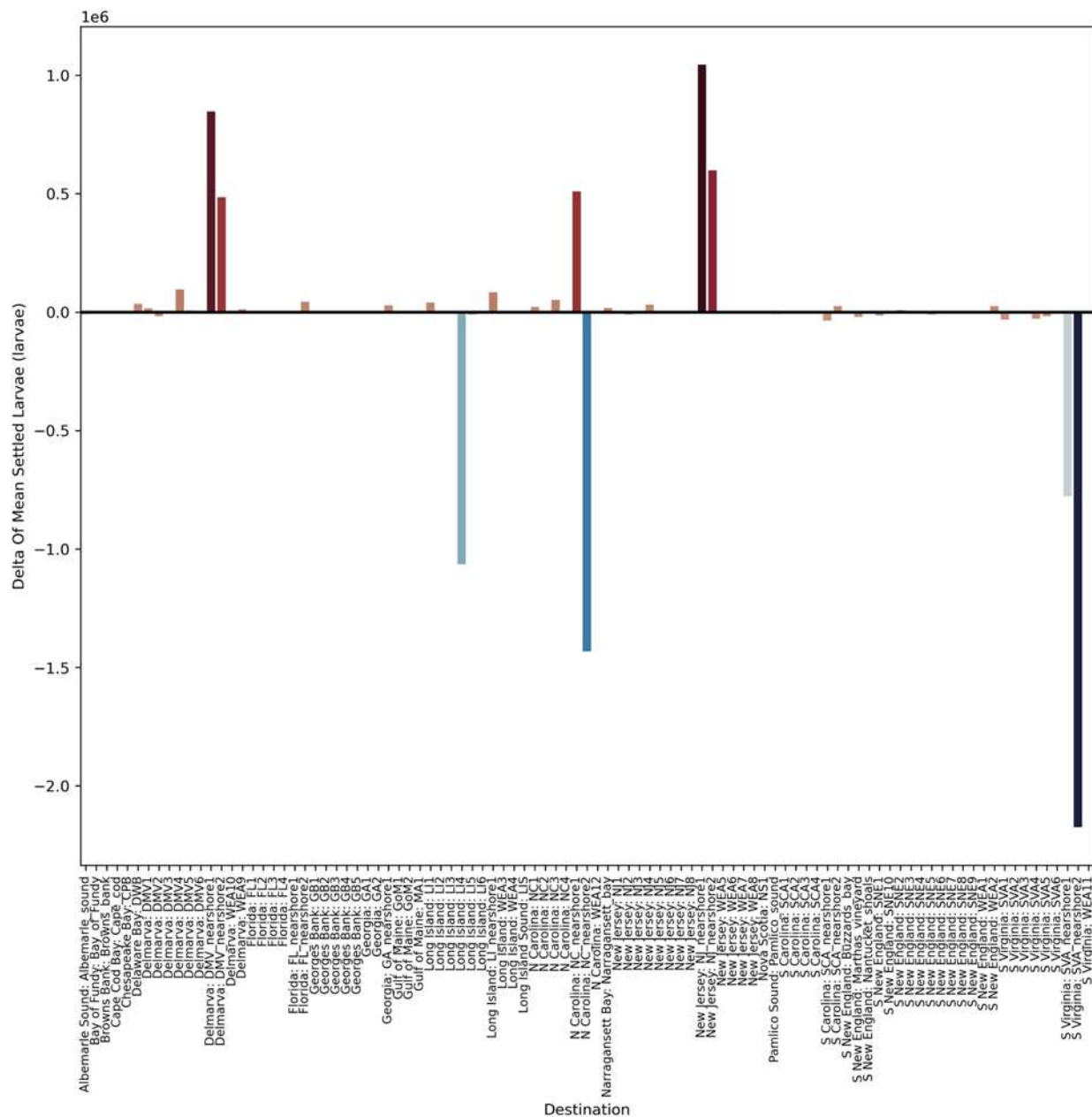


Figure 8.51. Higher Resolution Change in Current Speed 15 MW Full Build-Out vs. Baseline 2017

Difference in the depth averaged current speed for model year 2017. Showing the difference in the mean of 95th percentile non-exceedance probability ensemble baseline results and mean of 95th percentile non-exceedance probability ensemble Scenario 5: 15 MW Full Build-out results.



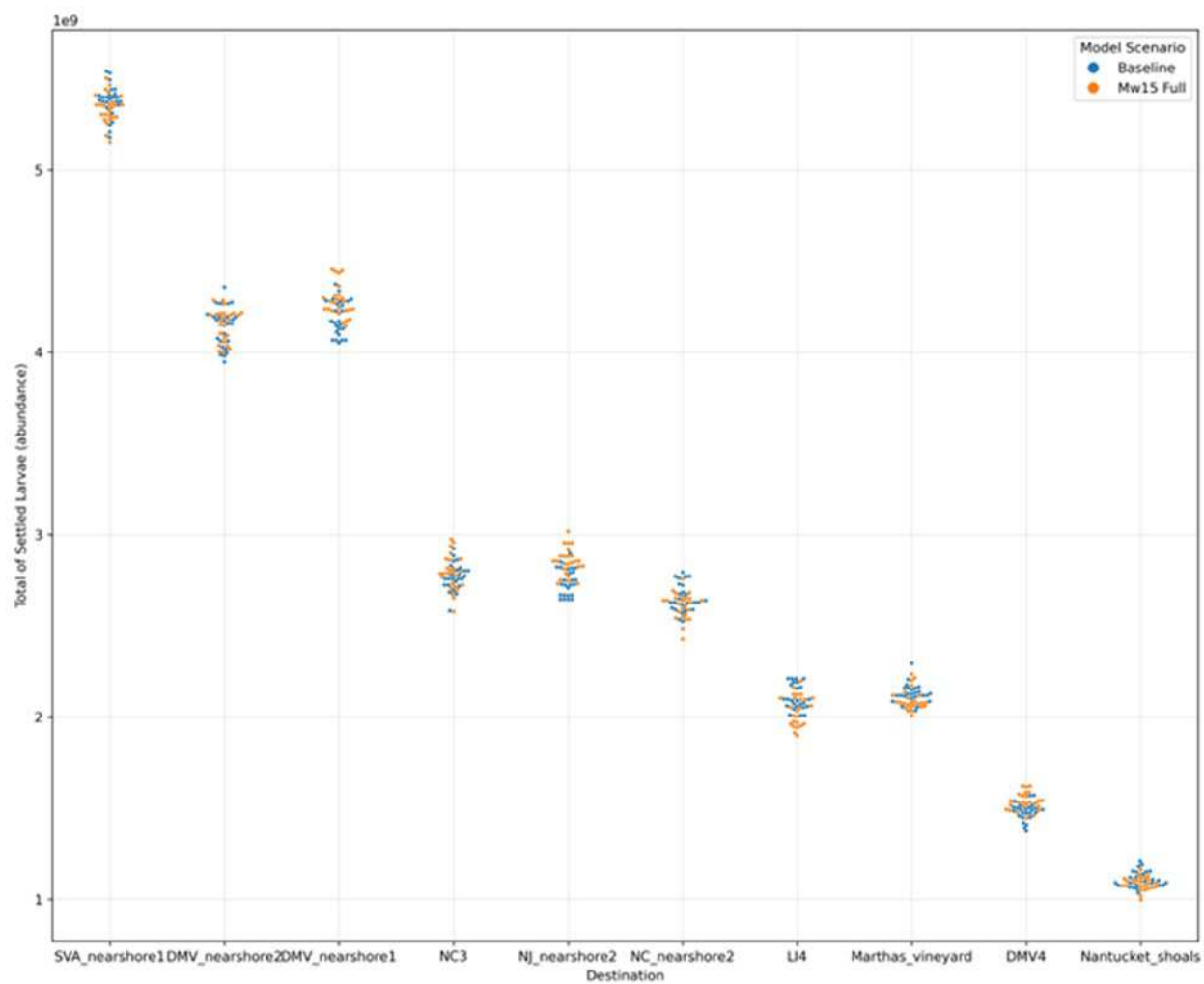


Figure 8.53. Swarm Plot Showing Summer Flounder Settlement in Most Common Destinations for 2017

Swarm plot shows the settlement for each model run of the ensemble (i.e., each point represents a model result) for 2017. Blue points show the baseline results and orange show the Scenario 5: 15 MW Full Build-out number of settled larvae in the most common destinations, where there is greatest larval settlement.

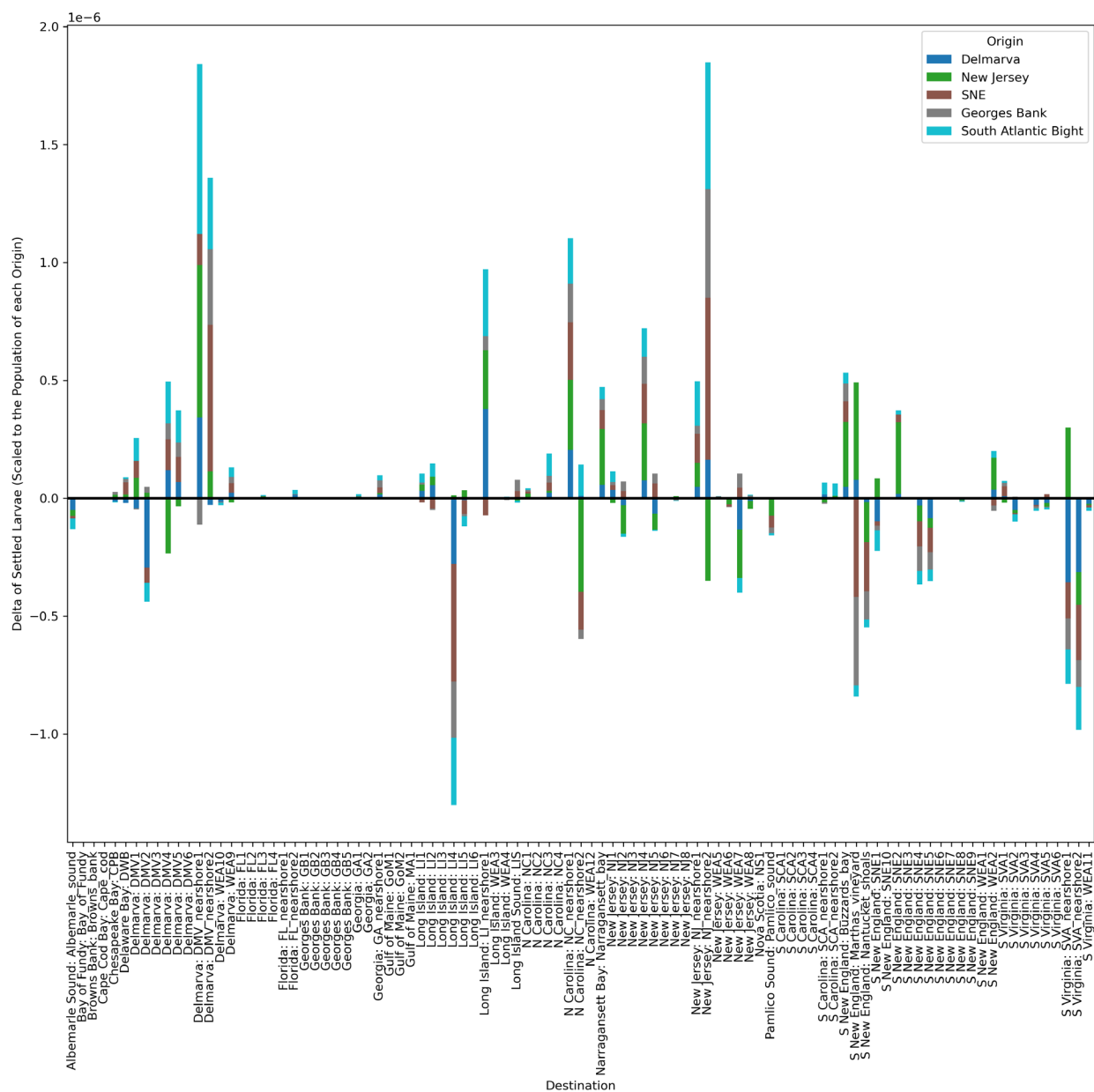


Figure 8.54. Summer Flounder Connectivity Difference 2017

Bar chart shows the difference in summer flounder larvae settlement in each destination area, by origin for model year 2017. Bars are colored by origin area and results show the difference in export probabilities, i.e., the difference in the likelihood of settlement scaled to the number of larvae released from a particular origin region between the baseline and 15MW full build-out results. Bars below the x axis, show a decrease in settlement in a particular destination area, results above the x axis show an increase in a settlement in a destination area.

8.4 Scenario 4: 12 MW Full Build-out

8.4.1 Sea Scallop

Changes in total sea scallop settlement induced by the 12 MW OSW build-out areas (WEAs) against the 2017 baseline are shown in the difference plot in **Figure 8.55**, which illustrates the difference in mean

total settled larvae within the study area. The cluster analysis in **Figure 8.56** is designed to remove noise from the difference plot results and identify hotspots of change. The difference plot and cluster analysis are shown alongside current speed change in **Figure 8.57**. The difference in mean settled density is shown in **Figure 8.58**, and a cluster analysis for settled density is included in **Figure 8.59**, and current speed change is repeated in **Figure 8.60**.

Changes in total sea scallop settled larvae (**Figure 8.55**) and settled larvae density (**Figure 8.58**) show similar patterns to the 15MW scenario results, but a slightly smaller change. The most notable shift in sea scallop larval settlement occurs in the MAB, with areas of larvae settlement decrease (shown in blue in these figures) seen mainly offshore of New Jersey concentrated around WEAs 5 and 6 (NJ5 and NJ7) and offshore Delaware in DMV4. Areas of larvae settlement increase (shown in red in these figures) are seen closer to shore along New Jersey (around WEA7) southward through Delmarva to South Virginia. There is also settlement increase to the north offshore Long Island. The change in larval settlement is less when compared to the 15MW full build-out scenario but is still on the same order of magnitude (i.e., the mean difference in total larval settlement for both scenarios is up to 10^7 larvae).

The cluster analysis (**Figure 8.56** and **Figure 8.59**) show the hotspots of change in sea scallop settlement, reflecting the same key areas as the difference plots. There are clusters of decreased settlement (blue) offshore New Jersey in WEAs 5 and 6 and adjacent New Jersey destination areas NJ5, and NJ7. Clusters of increased settlement (red) are more spread out from New Jersey through Delmarva to South Virginia, with some increased settlement off Long Island. Main clusters of increased settlement appear to be north of WEA7 and between WEA7 and WEA8 in NJ2.

The average change in sea scallop larvae settlement per destination area (**Figure 8.61**) reinforces the regional patterns shown in the difference plots and cluster analysis. Namely, overall increase in mean settled larvae occurs from Long Island (LI3, LI4, LI5) southward, including New Jersey (NJ5, NJ6, WEA7, WEA8), Delmarva (DMV1, DMV2, DMV5, DMV6) and South Virginia (SVA5). Overall decreases occur in fewer areas, with Delmarva (DMV4) and New Jersey (NJ1, NJ3 and WEA 5) as the main locations for net decrease in sea scallop larvae settlement.

The swarm plot in **Figure 8.62** shows that the greatest magnitude of settlement is in New Jersey (NJ5, NJ2, NJ7), Long Island (LI2), and Delaware (DMV2 and DMV5). Destination areas with greatest net change are those where there is clear stratification of increase and decrease in settlement, while those with little net change is where there is a mix between increase and decrease within destination areas. The swarm plots show that NJ7 and LI2 tend toward a decrease in settlement, while NJ2, DMV5 and DMV2 tend toward an increase, with NJ5 and NJ6 relatively stable in terms of net settlement.

As seen in **Figure 8.57** and **Figure 8.60**, current speeds are noticeably reduced within and to the south of the 12 MW WEAs at levels that do not exceed 0.025 ms^{-1} . There are also areas of marginally elevated current speeds, i.e., $\leq 0.008 \text{ ms}^{-1}$, in the vicinity of the WEAs, noticeably along Long Island, west of WEAs 5 and 6, and along the New Jersey coast; as well as along nearshore areas near Delaware Bay and North Carolina. While there appears to be no clear direct spatial correlation with changes in larval settlement, closer analyses suggests that reductions in current speeds, especially in and around WEAs, marginally slow larvae transport in key connectivity corridors leading to reduced settlement in some areas and corresponding increases in others. An analysis of the connectivity results in **Figure 8.63** suggests how current speed changes could affect the distribution and ultimately the settlement destination of larvae.

Sea scallop larvae that spawn in the MAB appear to be transported both south to north and north to south in our model results, settling in the Long Island, New Jersey and Delmarva regions (Error! Reference source not found.). With the introduction of the 12 MW WEAs the largest decrease in settlement is seen

in destination areas NJ2, NJ5 and DMV4. The connectivity change plot (**Figure 8.63**) shows that the reduction in settlement in NJ2 is primarily from the New York Bight, whereas the reduction in settlement in NJ5 and DMV4 is a result of fewer larvae settling from the Mid-Atlantic Bight. These changes in connectivity indicate that the blue areas of reduced settlement in the New Jersey areas can be explained by slower south to north transport from the MAB spawning area, which results in larvae settling further south (i.e., not being transported as far north), as well as slowed north to south transport, resulting in fewer larvae from the New York Bight settling in NJ2. Transport of larvae from the MAB to the south is also slowed, as indicated in the Delmarva region, where larvae from the MAB that would have settled in DMV4 appear to be shifted into destination areas further north such as DMV5 and NJ2.

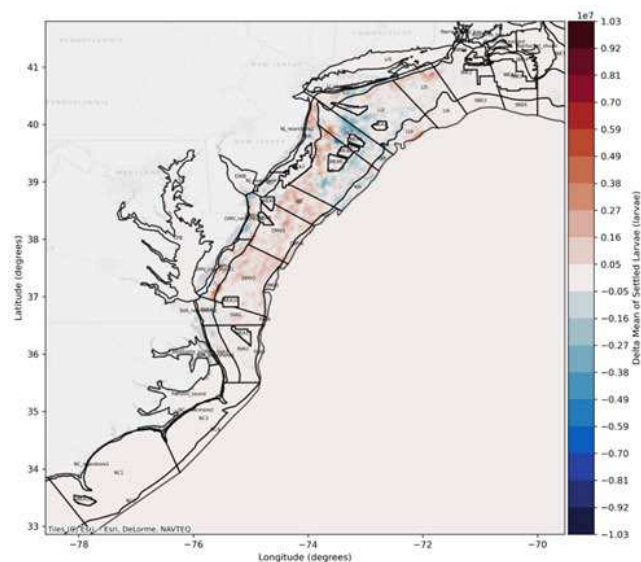


Figure 8.55. Difference in Total Settled Larvae 12 MW Full Build-Out vs. Baseline 2017

Difference in total sea scallop settled larvae for model year 2017. Showing the difference in the mean of all ensemble baseline results and mean of all ensembles 12 MW full build-out results. Settled larvae averaged for each model grid element. Red shows an increase in settlement in the 12 MW scenario compared to the baseline, blue shows a decrease in settlement compared to the baseline

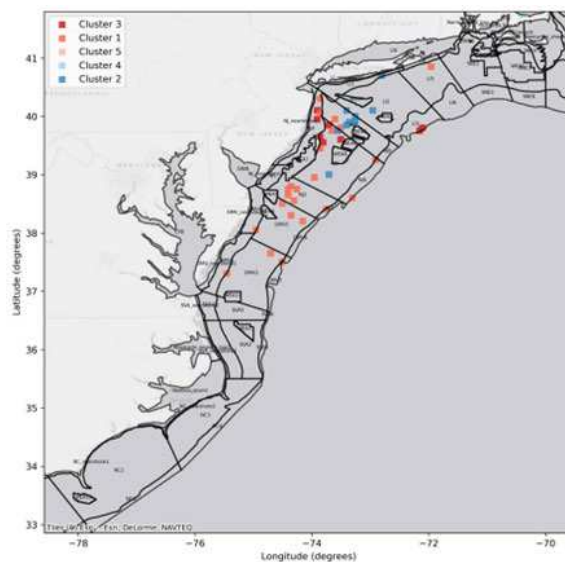


Figure 8.56. DBSCAN (Density-Based Spatial Clustering of Applications with Noise) Difference in Total Settled Larvae 12 MW Full Build-Out vs. Baseline 2017

Spatial clusters identified using DBSCAN to filter out noise from the difference plot and identify areas of greatest change. Clusters of settlement increase are identified in red and clusters with settlement decrease are shown in blue.

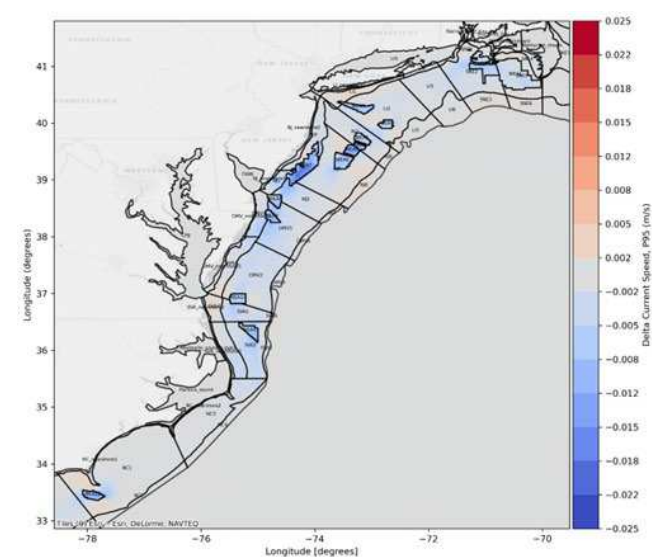


Figure 8.57. Change in Current Speed 12MW Full Build-Out vs. Baseline 2017

Difference in the depth averaged current speed for model year 2017. Showing the difference in the 95th percentile non-exceedance probability baseline results and 95th percentile non-exceedance probability 12 MW full build-out results.

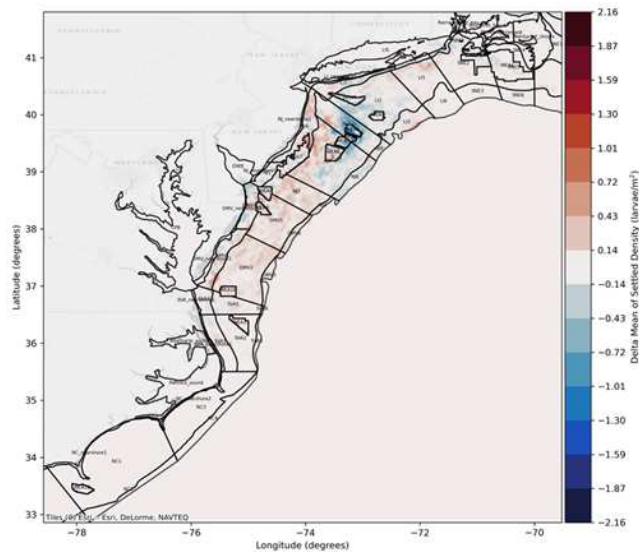


Figure 8.58. Difference in Settled Larvae Density 12 MW Full Build-Out vs. Baseline 2017

Difference in sea scallop settled larvae density for model year 2017. Showing the difference in the mean of all ensemble baseline results and mean of all ensembles 12 MW full build-out results. Settled larvae averaged for each model grid element. Red shows an increase in settlement in the 12 MW scenario compared to the baseline, blue shows a decrease in settlement compared to the baseline.

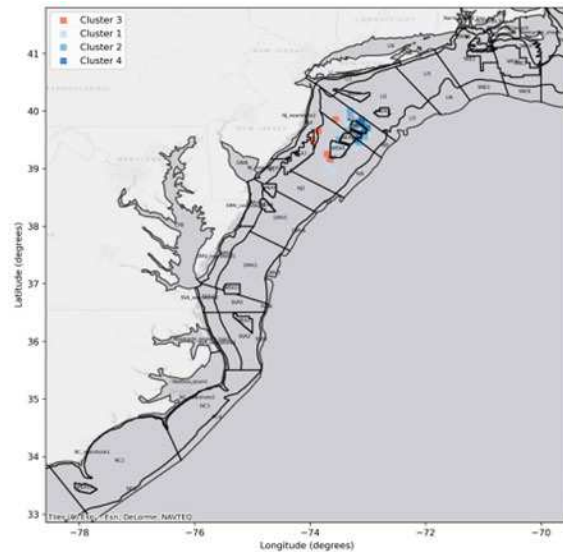


Figure 8.59. DBSCAN (Density-Based Spatial Clustering of Applications with Noise) Difference in Settled Larvae Density 12 MW Full Build-Out vs. Baseline 2017

Spatial clusters identified using DBSCAN to filter out noise from the difference plot and identify areas of greatest change. Clusters of settlement increase are identified in red and clusters with settlement decrease are shown in blue.

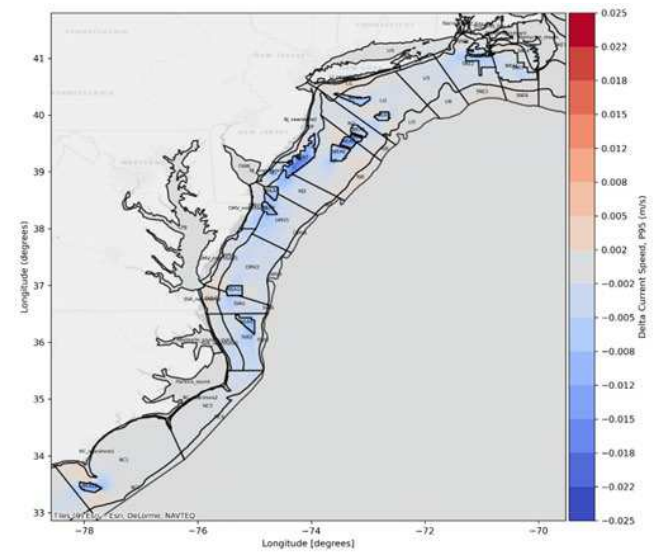
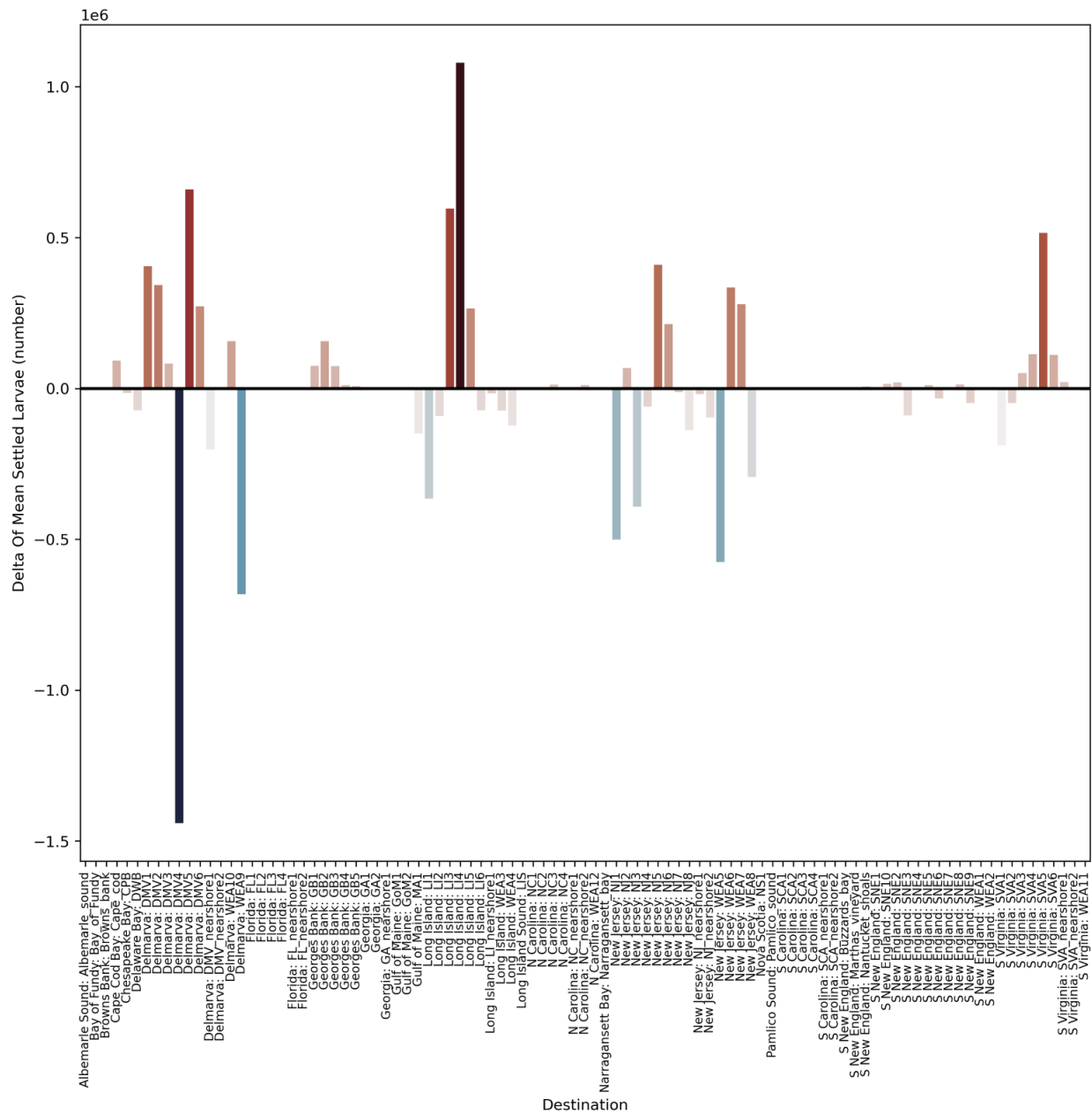


Figure 8.60. Change in Current Speed 12 MW Full Build-Out vs. Baseline 2017

Difference in the depth averaged current speed for model year 2017. Showing the difference in the 95th percentile non-exceedance probability ensemble baseline results and 95th percentile non-exceedance probability ensemble 12 MW full build-out results.



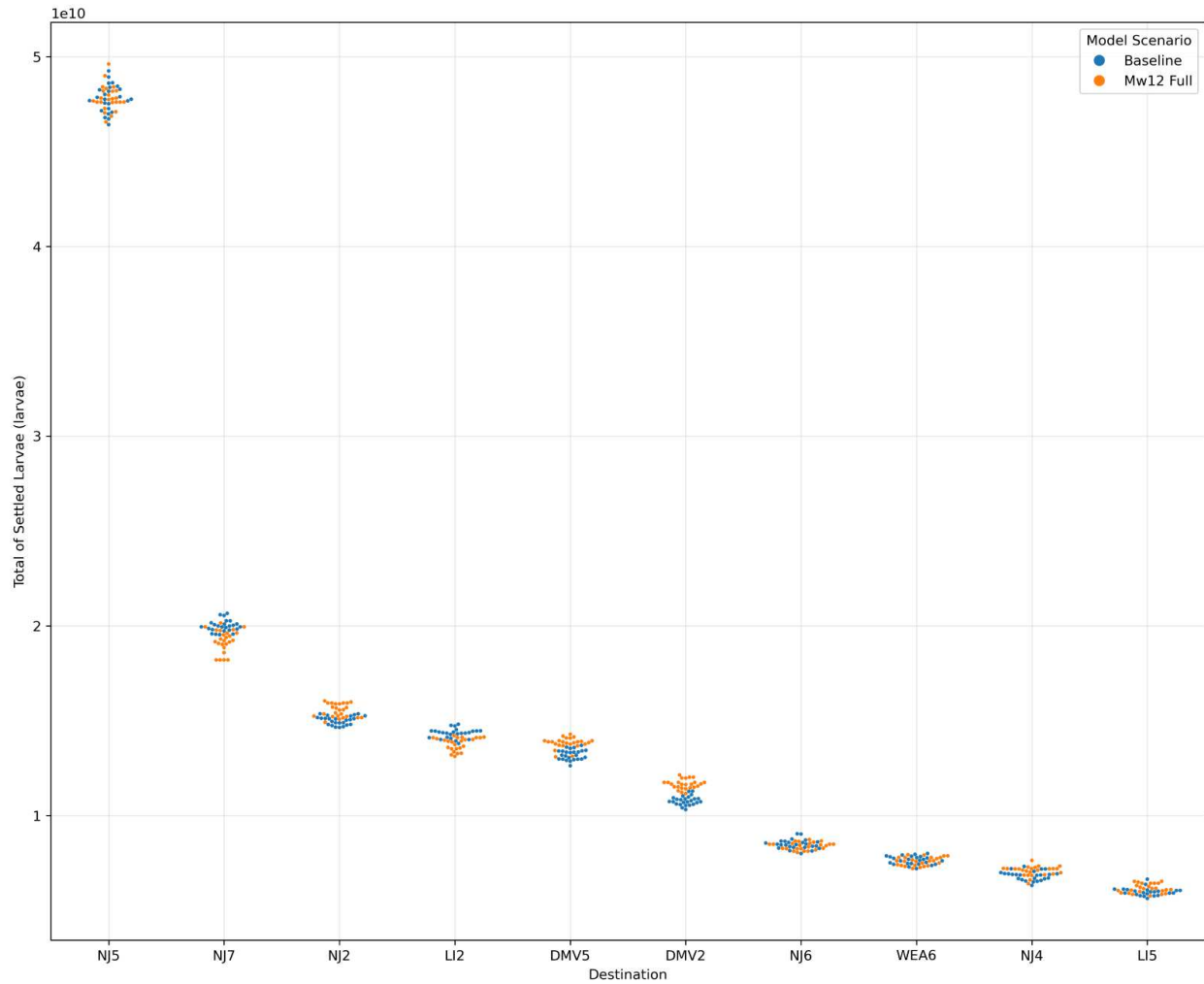


Figure 8.62. Swarm Plot Showing Sea Scallop Settlement in Top 10 Destinations

Swarm plot shows the settlement for each model run of the ensemble (i.e., each point represents a model result) for 2017. Blue points show the baseline results and orange show the 12 MW full build-out number of settled larvae in the top 10 destinations where there is greatest larval settlement.

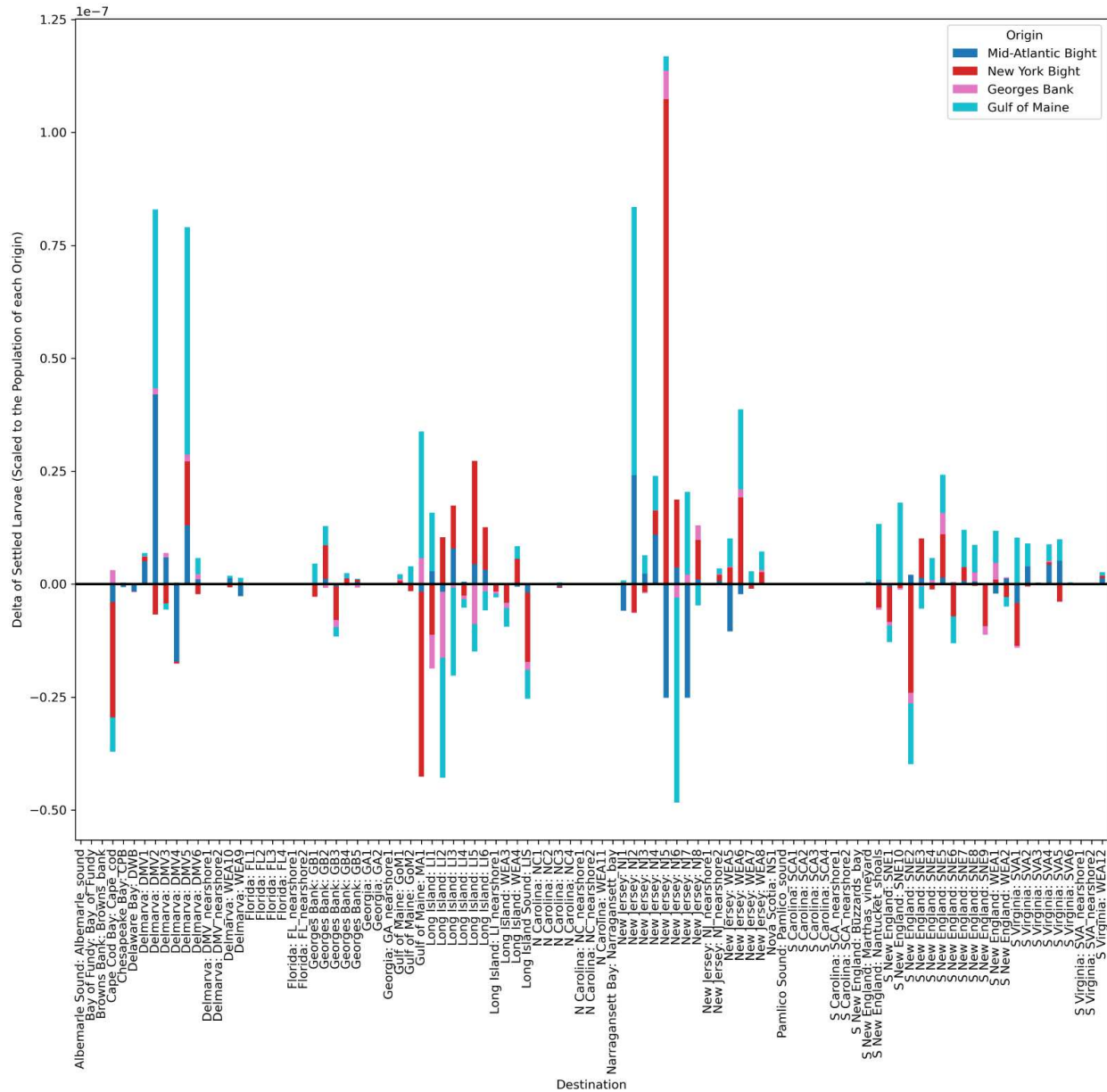


Figure 8.63. Sea Scallop Connectivity Difference

Bar chart shows the difference in sea scallop larvae settlement in each destination area, by origin for model year 2017. Bars are colored by origin area and results show the difference in export probabilities, i.e., the difference in the likelihood of settlement scaled to the number of larvae released from a particular origin region between the baseline and 12 MW full build-out results. Bars below the x axis, show a decrease in settlement in a particular destination area, results above the x axis show an increase in a settlement in a destination area.

8.4.2 Surfclam

Changes in total surfclam settlement induced by the 12 MW OSW build-out areas (WEAs) against the 2017 baseline are shown in the difference plot in **(Figure 8.64)**, which illustrates the difference in mean total settled larvae within the study area. The cluster analysis in **(Figure 8.65)** is designed to remove noise from the difference plot results and identify hotspots of change. The difference plot and cluster analysis are shown alongside current speed change in **(Figure 8.66)**. The difference in mean settled density is

shown in **(Figure 8.67)** and a cluster analysis for settled density is included in **(Figure 8.68)** and current speed change is repeated in **(Figure 8.69)**.

Changes in total surfclam larval settlement and settled density 9) show most notable shifts in surfclam larval settlement in the New Jersey region within the areas east of WEA7 and south of WEA6. Areas of estimated larvae settlement decrease (shown in blue in these plots) are seen mainly concentrated in WEAs 5 and 6 and adjacent New Jersey destination areas (NJ5 and NJ7), along the outer-coast portion of NJ2 toward Delmarva (DMV5). Areas of larvae settlement increase (shown in red) are also seen in the New Jersey region within WEA7 and to the south of WEAs 5 and 6. The change larval settlement is less when compared to the 15 MW Full Build-out but is still along the same order of magnitude (i.e., the mean difference in total larval settlement for both scenarios is up to 10^6 larvae).

The cluster analyses **(Figure 8.65 and Figure 8.68)** show hotspots of change in surfclam settlement, reflecting the key areas discussed above, with clusters of decreased settlement around WEAs 5 and 6, and in the New Jersey region (NJ7, NJ5, and NJ2). Less intense clusters of decrease are seen near WEAs 10 and 11. Clusters of increased settlement are predominantly to the southeast of WEA7 in the New Jersey region.

The change in mean surfclam larvae settlement per destination area **(Figure 8.70)** show the same regional patterns shown in difference plots and the cluster analyses. Namely, overall increase in mean settled larvae occur in New Jersey (NJ2 and NJ5) and Delmarva (DMV2). Overall decrease occurs in New Jersey (NJ7 and WEA6). The swarm plot in **(Figure 8.71)** shows that the greatest magnitude of settlement is in New Jersey (NJ5, NJ2), Delaware (DMV2 and DMV5), and to a lesser extent South Virginia (SVA2, SVA5) and Long Island (LI2). Destination areas with greatest change are those where there is clear stratification of increase and decrease in settlement, as seen in NJ5, NJ2, and WEA6 and an increase is seen in DMV. Areas with little net change are where there is a mix between orange and blue points within destination areas, for example LI2.

As seen in **(Figure 8.66 and Figure 8.69)** current speeds are noticeably reduced within and to the south of the 12 MW WEAs at levels that do not exceed 0.025 ms^{-1} . There are also areas of marginally elevated current speeds, i.e., $\leq 0.008 \text{ ms}^{-1}$, in the vicinity of the WEAs, noticeably along Long Island, west of WEAs 5 and 6, and along the New Jersey coast; as well as along nearshore areas near Delaware Bay and North Carolina. While there appears to be no clear direct spatial correlation with changes in larval settlement, closer analyses suggests that reductions in current speeds, especially in and around WEAs, marginally slow larvae transport in key connectivity corridors leading to reduced settlement in some areas and corresponding increases in others. An analysis of the connectivity results in **(Figure 8.72)** suggests how current speed changes could affect the distribution and ultimately the settlement destination of larvae. Most settled surfclam larvae in the model domain originate from the New Jersey and Delmarva areas. Patterns of increased and decreased settlement in the New Jersey area are complicated and there is no clear disruption to north south or south north transport of surfclam larvae, although the intensity of change occurring in the region with the densest aggregation of WEAs suggests that there is some hydrodynamic affect occurring from the introduction of the OSW farms.

From the connectivity analysis the hotspot of increased settlement in NJ5 south of WEA6 appears to be coming from the New Jersey spawning area. This suggests that slowed currents in the MAB are contributing to higher settlement of larvae spawned in new jersey in the same new jersey region. North to south transport may be slowed, which could be indicated by the reduction in larvae from new jersey settling in NJ2 - the next destination area to the south. This hotspot of increase spills into NJ2, which appears to be an increase in settlement mainly from the Delmarva region- indicating south to north transport is also affected, however there is no clear area where there is a reduction in larvae settling from Delmarva. There is a hotspot of decrease in settlement in WEAs 5 and 6 and NJ7, which appears to mainly

be resulting from a reduction in larvae from the northern spawning regions, which could explain the increase in settlement in the Long Island areas.

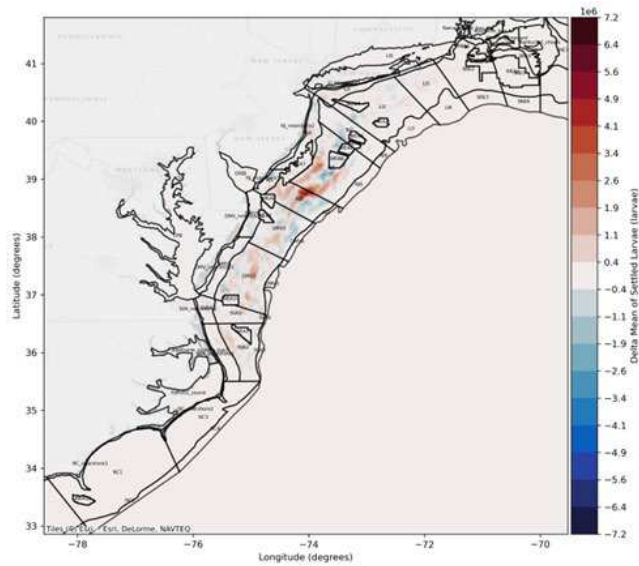


Figure 8.64. Difference in Total Settled Larvae 12 MW Full Build-Out vs. Baseline 2017

Difference in total surfclam settled larvae for model year 2017. Showing the difference in the mean of all ensemble baseline results and mean of all ensembles 12 MW full build-out results. Settled larvae averaged for each model grid element. Red shows an increase in settlement in the 12 MW scenario compared to the baseline, blue shows a decrease in settlement compared to the baseline.

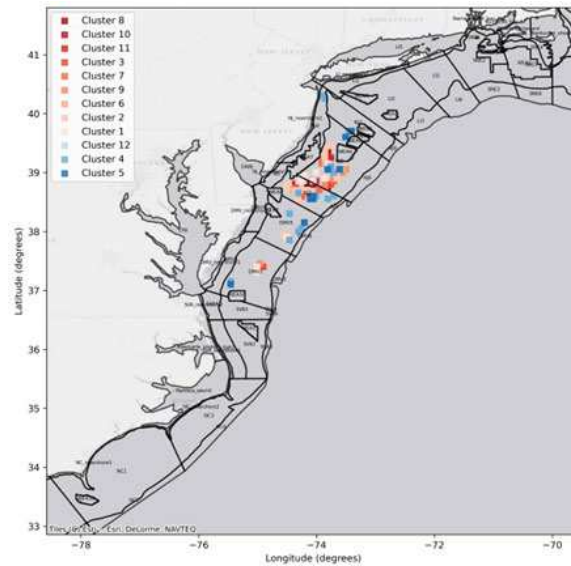


Figure 8.65. DBSCAN (Density-Based Spatial Clustering of Applications with Noise) Difference in Total Settled Larvae 12 MW Full Build-Out vs. Baseline 2017

Spatial clusters identified using DBSCAN to filter out noise from the difference plot and identify areas of greatest change. Clusters of settlement increase are identified in red and clusters with settlement decrease are shown in blue.

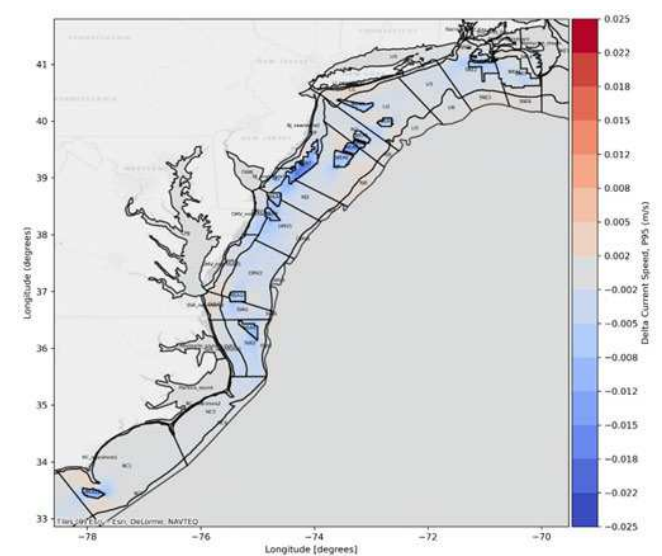


Figure 8.66. Change in Current Speed 12 MW Full Build-Out vs. Baseline 2017

Difference in the depth averaged current speed for model year 2017. Showing the difference in the 95th percentile non-exceedance probability baseline results and 95th percentile non-exceedance probability 12 MW full build-out results

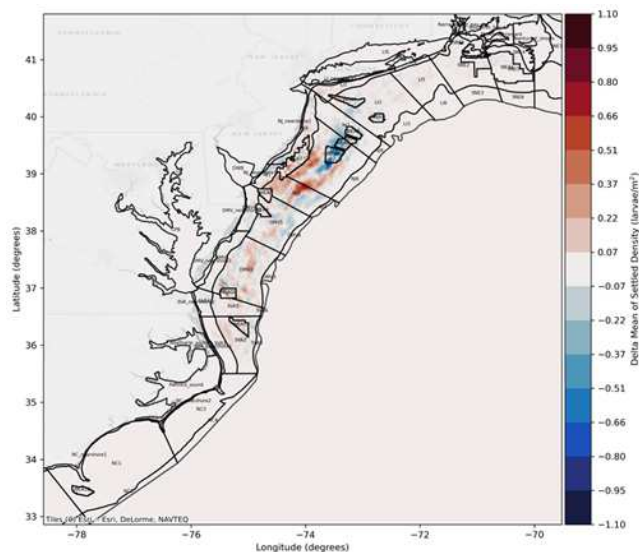


Figure 8.67. Difference in Settled Larvae Density 12 MW Full Build-Out vs. Baseline 2017

Difference in surfclam larvae density settled larvae for model year 2017. Showing the difference in the mean of all ensemble baseline results and mean of all ensembles 12 MW full build-out results. Settled larvae averaged for each model grid element. Red shows an increase in settlement in the 12 MW scenario compared to the baseline, blue shows a decrease in settlement compared to the baseline.

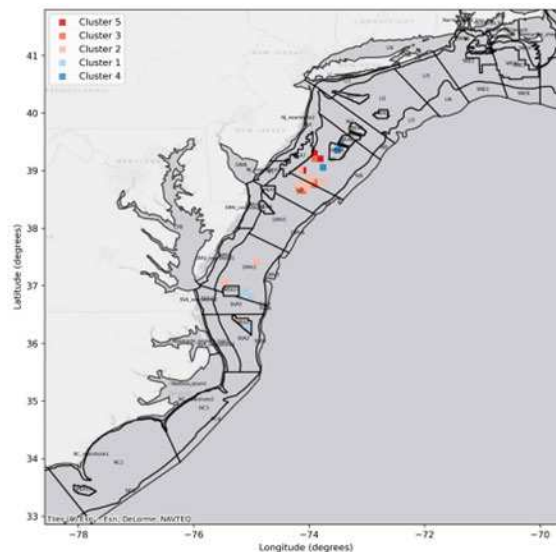


Figure 8.68. DBSCAN (Density-Based Spatial Clustering of Applications with Noise) Difference in Surfclam Settled Larvae density 12 MW Full Build-Out vs. Baseline 2017

Spatial clusters identified using DBSCAN to filter out noise from the difference plot and identify areas of greatest change. Clusters of settlement increase are identified in red and clusters with settlement decrease are shown in blue.

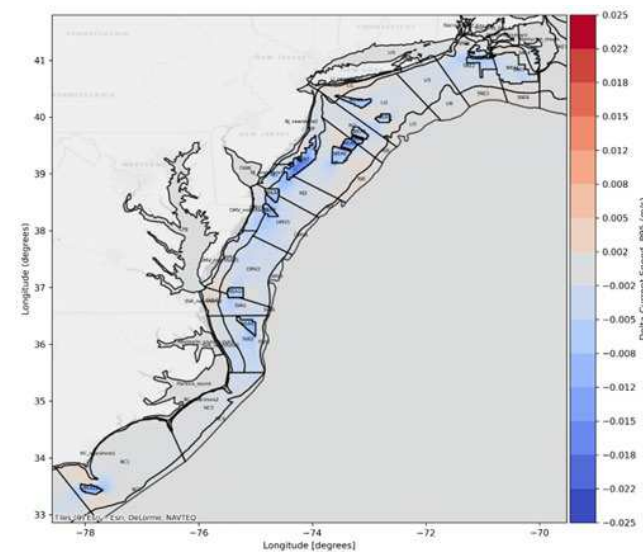


Figure 8.69. Change in Current Speed 12 MW Full Build-Out vs. Baseline 2017

Difference in the depth averaged current speed for model year 2017. Showing the difference in the mean of 95th percentile non-exceedance probability ensemble baseline results and mean of 95th percentile non-exceedance probability ensemble 12 MW full build-out results.

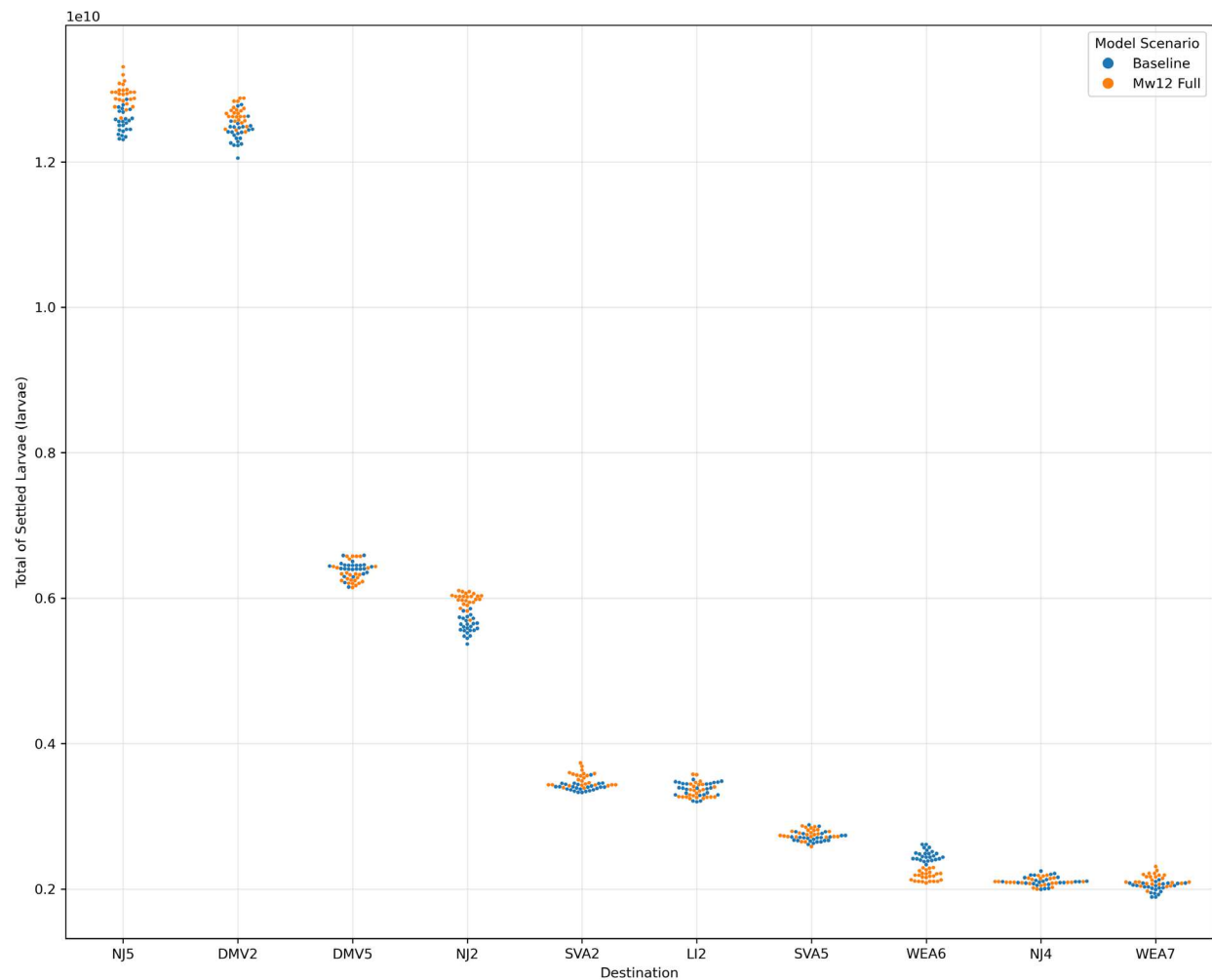


Figure 8.71. Swarm Plot Showing Surfclam Settlement in Top 10 Destinations for 2017

Swarm plot shows the settlement for each model run of the ensemble (i.e., each point represents a model result) for 2017. Blue points show the baseline results and orange show the 12 MW full build-out number of settled larvae in the top 10 destinations where there is greatest larval settlement.

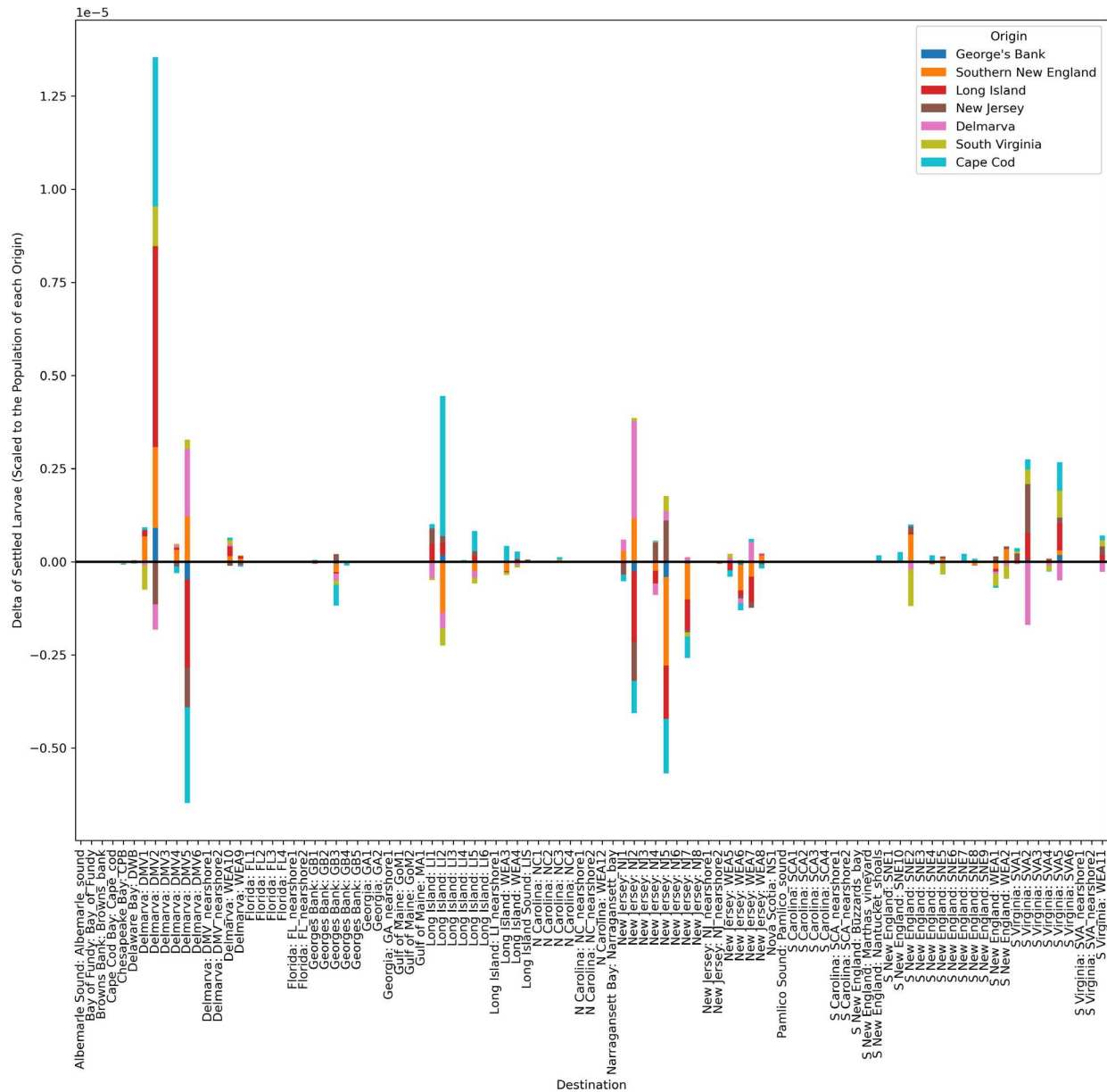


Figure 8.72. Surfclam Connectivity Difference 2017

Bar chart shows the difference in surfclam larvae settlement in each destination area, by origin for model year 2017. Bars are colored by origin area and results show the difference in export probabilities, i.e., the difference in the likelihood of settlement scaled to the number of larvae released from a particular origin region between the baseline and 12MW full build-out results. Bars below the x axis, show a decrease in settlement in a particular destination area, results above the x axis show an increase in a settlement in a destination area.

8.4.3 Summer Flounder

While the difference plots for sea scallop and surfclam reveal regional patterns of change in settlement concentrated in the New Jersey region, changes in summer flounder settlement are concentrated along the coast and are less apparent in the total settled larvae difference plot in **Figure 8.73** and cluster analysis plot **Figure 8.74**; and have little to no overlap with areas of current speed change (**Figure 8.75**).

These changes in total summer flounder settlement are more discernable along the coast in higher resolution plots in **Figure 8.76**, **Figure 8.77** and **Figure 8.78**. Few areas of change in settled larvae density are apparent throughout the model domain (**Figure 8.79**, **Figure 8.80**). Areas of settled density change also have little overlap with areas of current speed change (**Figure 8.81**).

The cluster analysis of settled larvae and the cluster analysis of settled density show different cluster areas, suggesting that some noise may still be present after being processed by DBSCAN (**Figure 8.74**, **Figure 8.77** and **Figure 8.80**). However, there appears to be some increase in settlement in the southern regions in these plots, with clusters of increased settlement present along the coast of North Carolina and Delmarva. The Long Island area appears to have a mix of increased and decreased total settlement (**Figure 8.74**, **Figure 8.77**), however these areas are not intense (lighter red/blue indicating weaker statistical strength), and are not present in the settled density cluster analysis (**Figure 8.80**). Both cluster analyses do identify areas of decreased settlement in the Nantucket Shoals area, north of WEA1 and 2. The area of change identified with the 15 MW build-out scenario west of WEA7 is not found in the 12 MW scenario. The limited number of clusters identified by DBSCAN indicates that there are few areas of settlement change estimated for summer flounder that can be distinguished from noise in the modeled results.

The change in average summer flounder larvae settlement per destination area, (**Figure 8.82**) and the swarm plot of the most common settlement destination areas (**Figure 8.83**) both provide a broader destination area perspective of the average changes in settlement of summer flounder larvae. These plots show increased settlement New Jersey (NJ Nearshore1, Nearshore2), and Delmarva (DMV Nearshore1 and 2), and decreases in South Virginia (SVA Nearshore1 and 2), Long Island (LI4) and North Carolina (NC Nearshore2). It should be noted when considering the relevance of these changes in settlement, that the largest change in settlement per destination area shown in the bar plot (**Figure 8.82**) is three orders of magnitude lower than the total settlement in each destination area, shown in the swarm plot. In addition, although there are areas of settlement change identified in the cluster analysis and average settlement bar chart, the swarm plot highlights that there is high variability among ensembles and, due to the mixed nature of the blue and orange points, there is little to no clear difference between baseline and scenario results at the destination area level. However, the bar plot shows the change in settlement averaged over destination areas, which potentially obscures the finer scale changes in settlement seen in the difference and cluster plots. The diffuse shoreward transport of summer founder larvae from east coast broad outer shelf spawning areas could be influenced by marginally reduced current speeds in and around OSW areas.

The lack of a) identified clusters of change, b) that the mixed and noisy changes in total settlement are on a spatial scale smaller than destination areas, and c) inconsistencies between scenario results, make the interpretation of the connectivity plot (**Figure 8.84**) challenging and less meaningful than for the other species. However, some broader picture insights can be surmised. There is some overlap in the areas of greatest settlement increase and decrease and changes in connectivity. For example, in LI4 there is an average decrease in settlement in the bar plot (**Figure 8.82**) and a decrease in this destination area in the connectivity plot in larvae originating from all regions. The average increase in settlement seen in NJ nearshore1 and 2 in **Figure 8.82**, is also shown to originate from all regions in the connectivity plot. These areas of decreased and increased larval settlement are also apparent in the 15 MW connectivity results, although there isn't much consistency between them within the other destination regions.

These results suggest that a finer scale local assessment of settlement change for summer flounder, concentrated around coastal areas near WEAs may allow for greater understanding of changes in larval settlement that may occur with the introduction of OSW developments.

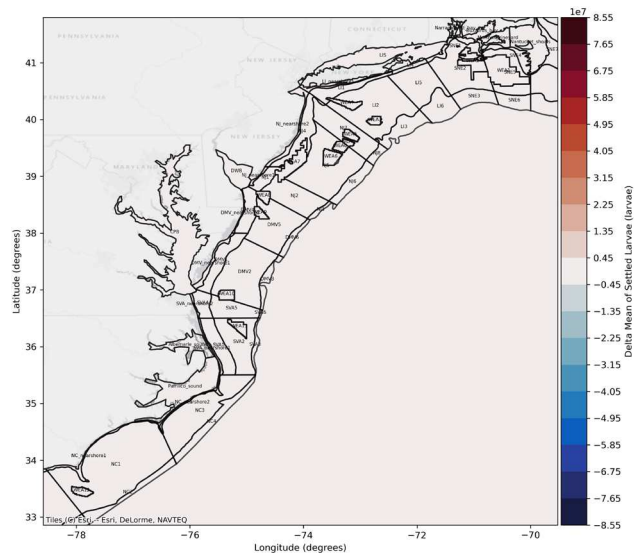


Figure 8.73. Difference in Settled Larvae 12 MW Full Build-Out vs. Baseline 2017

Difference in total summer flounder larvae settled larvae for model year 2017. Showing the difference in the mean of all ensemble baseline results and mean of all ensembles 12 MW full build-out results. Settled larvae averaged for each model grid element. Red shows an increase in settlement in the 12 MW scenario compared to the baseline, blue shows a decrease in settlement compared to the baseline.

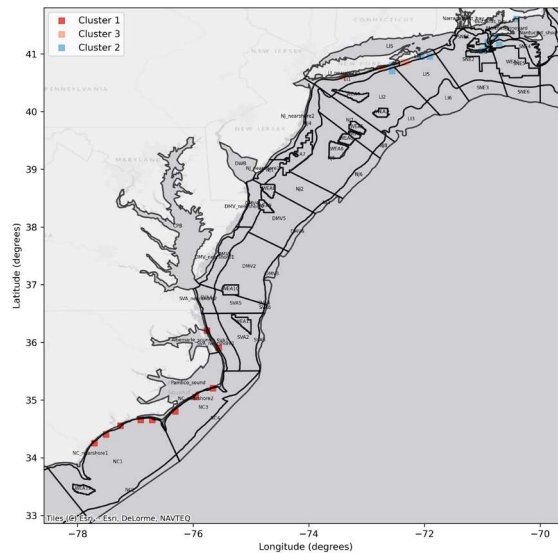


Figure 8.74. DBSCAN (Density-Based Spatial Clustering of Applications with Noise) Difference in Settled Larvae 12 MW Full Build-Out vs. Baseline 2017

Spatial clusters identified using DBSCAN to filter out noise from the difference plot and identify areas of greatest change. Clusters of settlement increase are identified in red and clusters with settlement decrease are shown in blue.

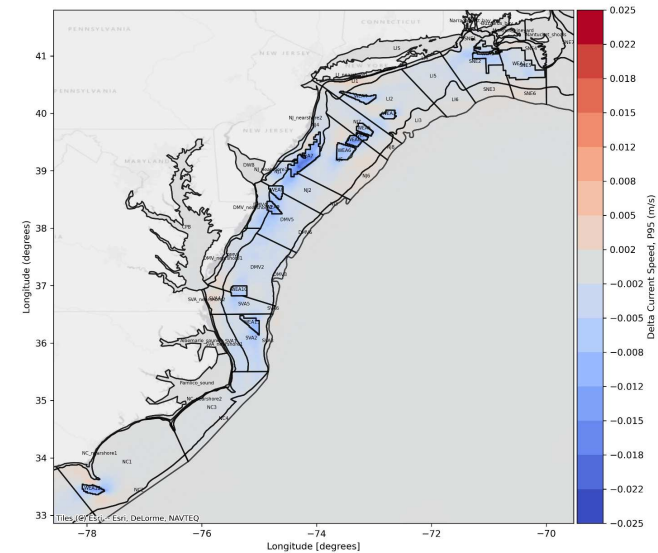


Figure 8.75. Change in Current Speed 12 MW Full Build-Out vs. Baseline 2017

Difference in the depth averaged current speed for model year 2017. Showing the difference in the 95th percentile non-exceedance probability baseline results and 95th percentile non-exceedance probability 12 MW full build-out results

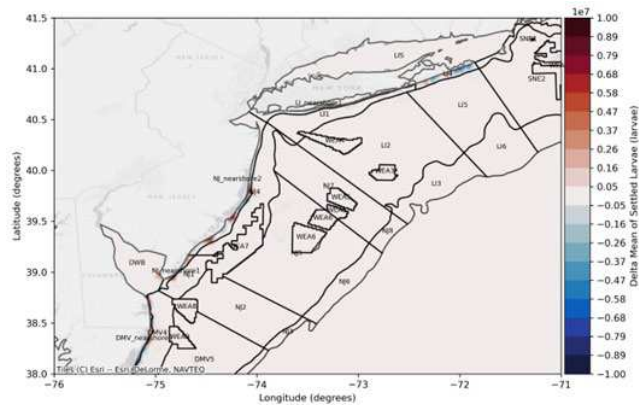


Figure 8.76. Higher Resolution Difference in Total Settled Larvae 12 MW Full Build-Out vs. Baseline 2017

Difference in total summer flounder settled larvae for model year 2017. Showing the difference in the mean of all ensemble baseline results and mean of all ensembles 12 MW full build-out results. Settled larvae averaged for each model grid element. Red shows an increase in settlement in the 12 MW scenario compared to the baseline, blue shows a decrease in settlement compared to the baseline.

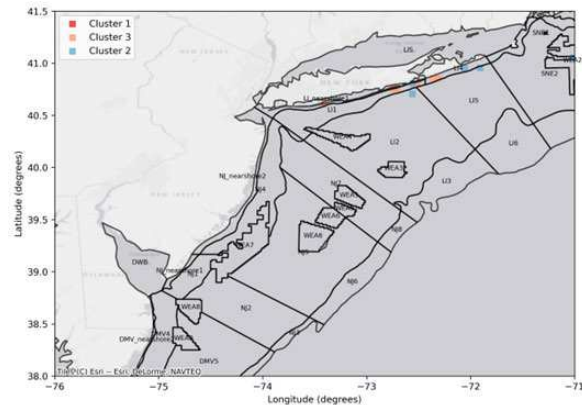


Figure 8.77. Higher Resolution DBSCAN (Density-Based Spatial Clustering of Applications with Noise) Difference in Settled Larvae 12 MW Full Build-Out vs. Baseline 2017
Spatial clusters identified using DBSCAN to filter out noise from the difference plot and identify areas of greatest change. Clusters of settlement increase are identified in red and clusters with settlement decrease are shown in blue.

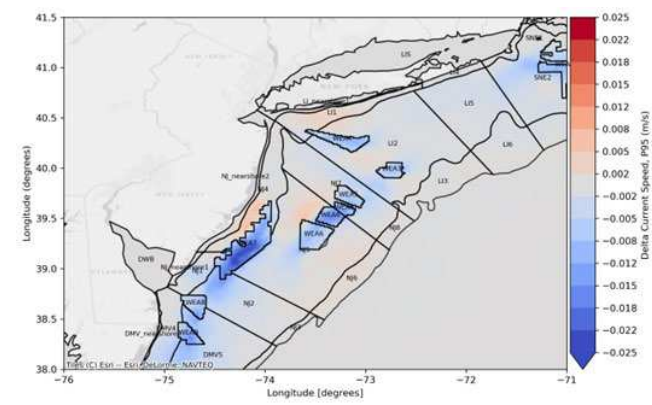


Figure 8.78. Higher Resolution Change in Current Speed 12 MW Full Build-Out vs. Baseline 2017
Difference in the depth averaged current speed for model year 2017. Showing the difference in the mean of 95th percentile non-exceedance probability ensemble baseline results and mean of 95th percentile non-exceedance probability ensemble 12 MW full build-out results.

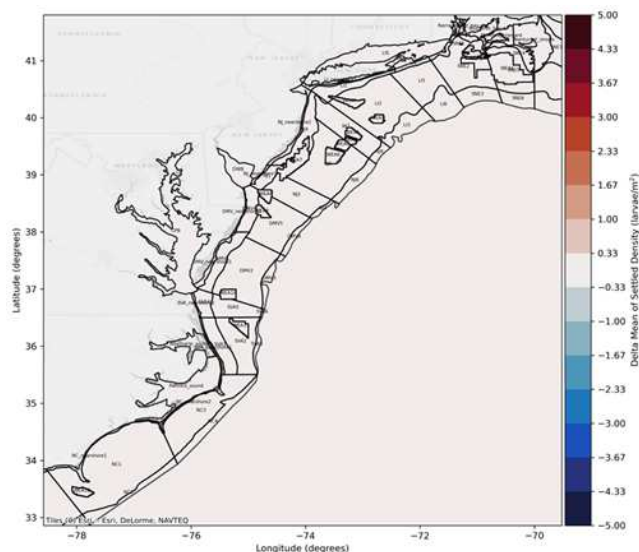


Figure 8.79. Difference in Settled Larvae Density 12 MW Full Build-Out vs. Baseline 2017

Difference in summer flounder larvae settled density for model year 2017. Showing the difference in the mean of all ensemble baseline results and mean of all ensembles 12 MW full build-out results. Settled larvae averaged for each model grid element. Red shows an increase in settlement in the 12 MW scenario compared to the baseline, blue shows a decrease in settlement compared to the baseline.

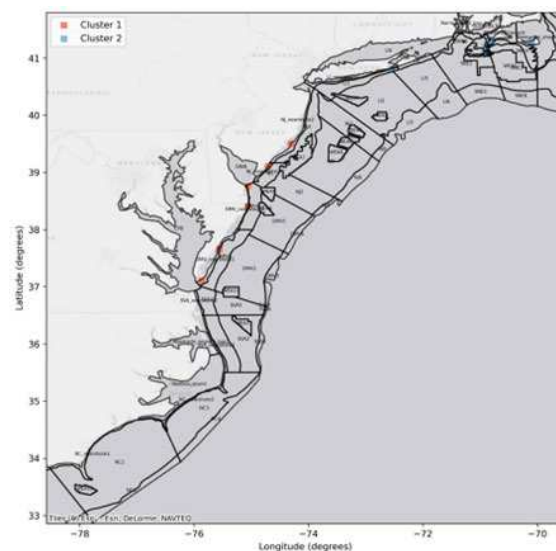


Figure 8.80. DBSCAN (Density-Based Spatial Clustering of Applications with Noise) Difference in Settled Larvae Density 12 MW Full Build-Out vs. Baseline 2017

Spatial clusters identified using DBSCAN to filter out noise from the difference plot and identify areas of greatest change. Clusters of settlement increase are identified in red and clusters with settlement decrease are shown in blue.

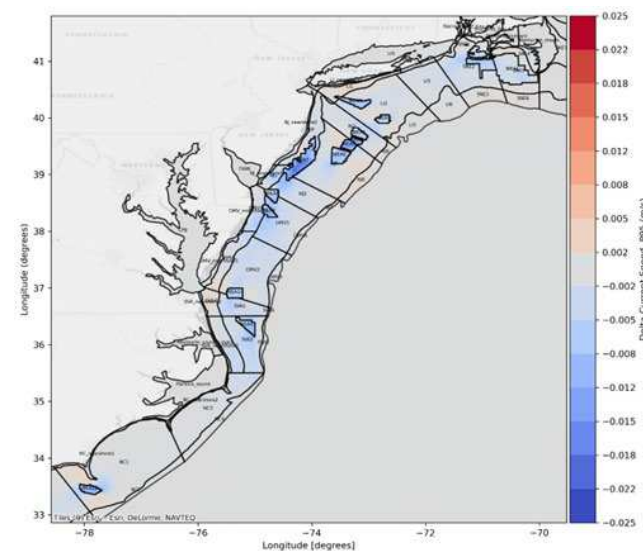
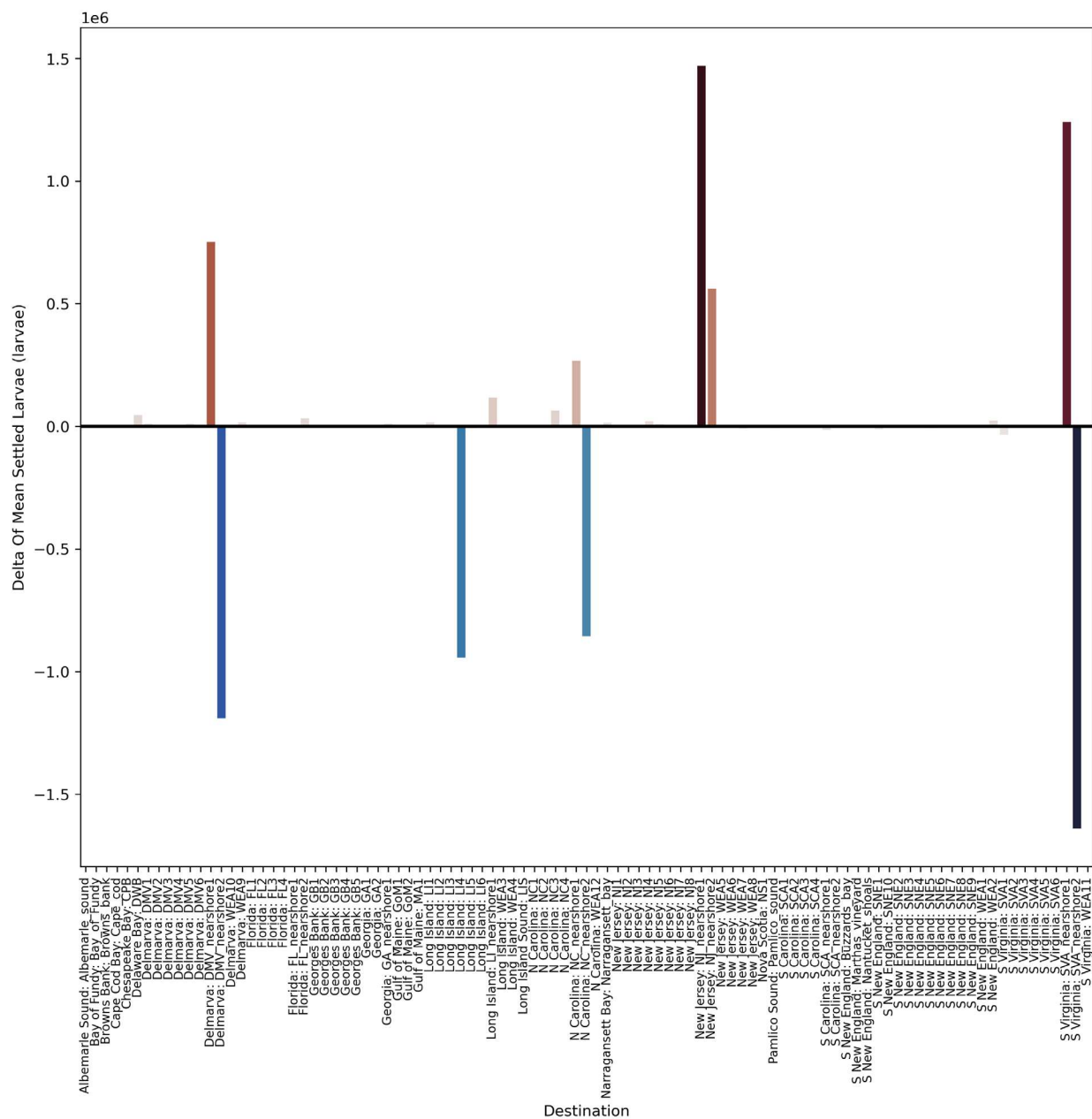


Figure 8.81. Change in Current Speed 12 MW Full Build-Out vs. Baseline 2017

Difference in the depth averaged current speed for model year 2017. Showing the difference in the mean of 95th percentile non-exceedance probability ensemble baseline results and mean of 95th percentile non-exceedance probability ensemble 12 MW full build-out results.



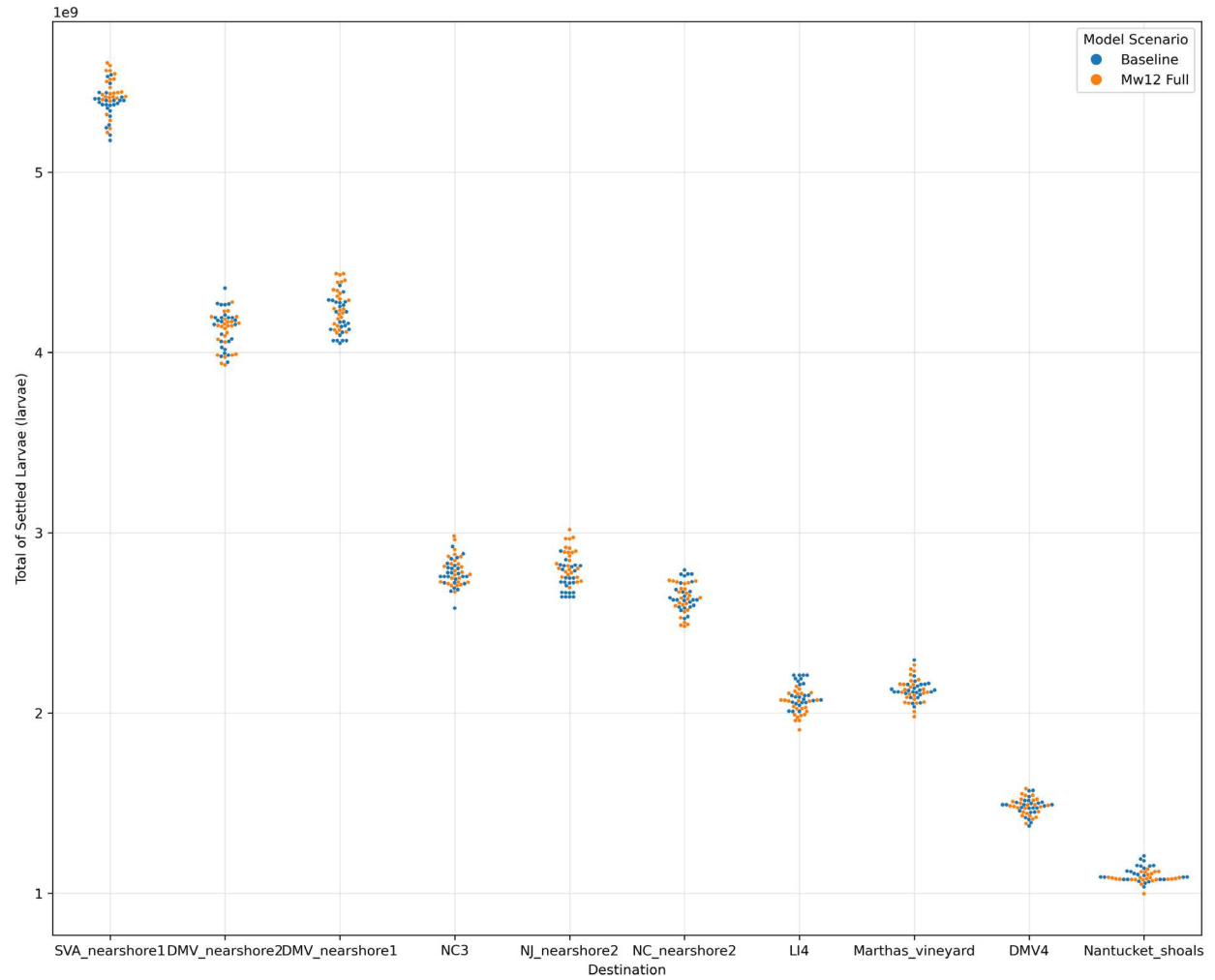


Figure 8.83. Swarm Plot Showing Summer Flounder Settlement in Top 10 Destinations for 2017
 Swarm plot shows the settlement for each model run of the ensemble (i.e., each point represents a model result) for 2017. Blue points show the baseline results and orange show the Scenario 4: 12 MW full build-out number of settled larvae in the top 10 destinations where there is greatest larval settlement.

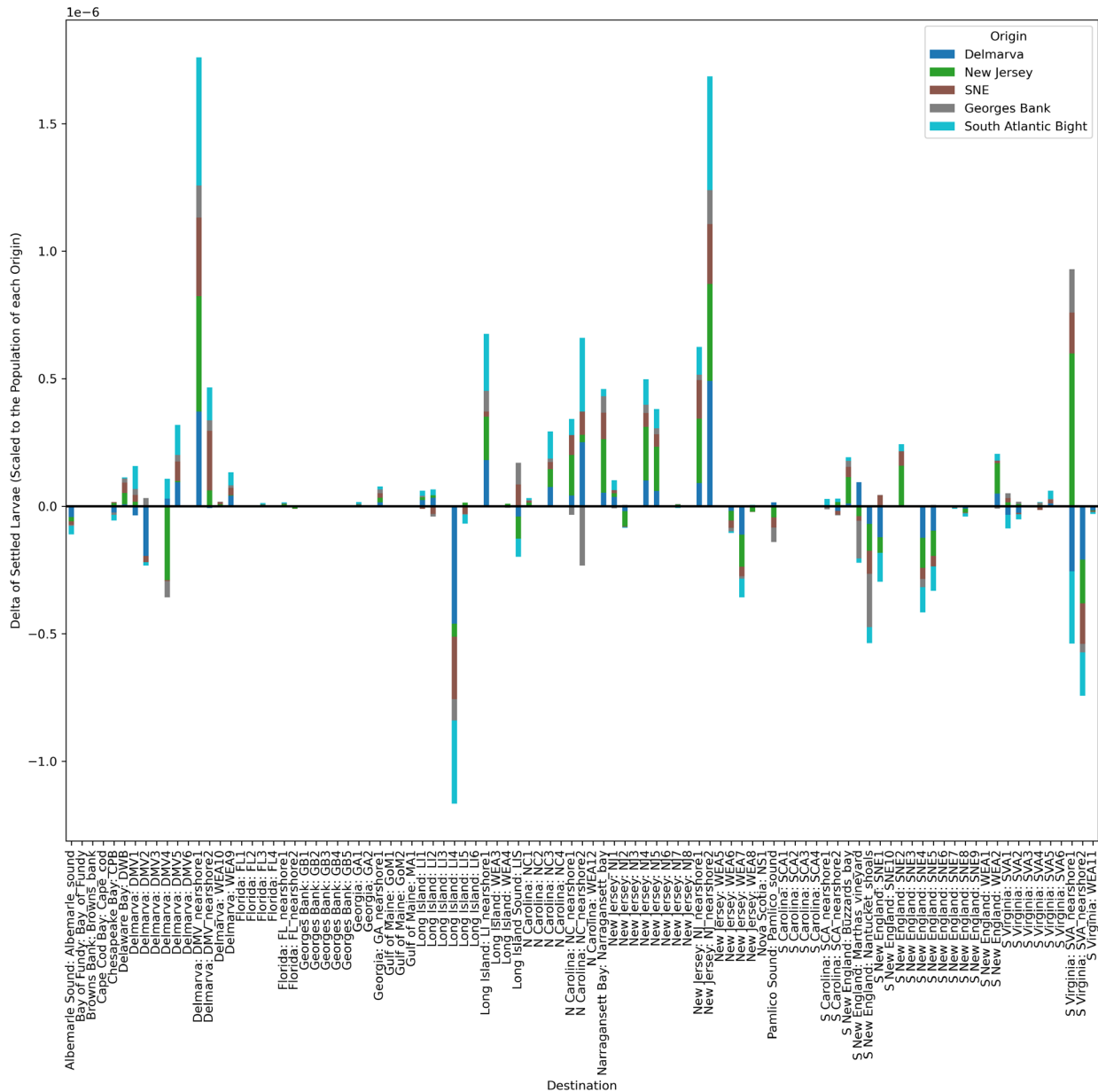


Figure 8.84. Summer Flounder Connectivity Difference 2017

Bar chart shows the difference in summer flounder larvae settlement in each destination area, by origin for model year 2017. Bars are colored by origin area and results show the difference in export probabilities, i.e., the difference in the likelihood of settlement scaled to the number of larvae released from a particular origin region between the baseline and 12 MW full build-out results. Bars below the x axis, show a decrease in settlement in a particular destination area, results above the x axis show an increase in a settlement in a destination area.

8.5 Sensitivity Analysis – Double the Wind-wake Effect for 15 MW Full Build-out

The sensitivity analysis was carried out for sea scallop for the year 2017. This involved doubling the wind-wake effect on the current speeds estimated for the 15 MW full build-out scenario and investigating the effect on larval dispersal and settlement. This section describes the differences between the 15 MW

scenario results for 2017 and the sensitivity analysis results, rather than the specific changes in settlement and connectivity that are induced by the doubling of the wind-wake effect.

Changes in total sea scallop settlement induced by doubling the wind-wake effect for the 15 MW Full Build-out against the 2017 baseline are shown in **Figure 8.85** and the corresponding cluster analysis plot **Figure 8.86**. The change in current speed resulting from the doubled wind-wake effect is shown in **Figure 8.87** (and **Figure 8.90**), showing up to roughly doubled current speed change compared to the 15 MW Full Build-out scenario. Changes in settled sea scallop density are shown in figures **Figure 8.88** and **Figure 8.89**. Patterns of estimated decreased and increased settlement of sea scallop larvae in the difference plots and in those shown in the cluster analyses for the sensitivity analysis are similar to the 15 MW and 12 MW build-out scenarios for 2017. However, the magnitude of decreased or increased settlement appears to be roughly doubled. This magnitude of change is also apparent in the average change per destination area bar plot (**Figure 8.91**), where the same destination areas show increased or decreased settlement, but the sensitivity test results show changes ~1.5 to 2 times greater than changes estimated in the 15 MW Full Build-out scenario. The swarm plot in (**Figure 8.92**) also shows greater distance between baseline and scenario ensemble results. Most destination areas with mixed clusters in the swarm plot (showing minimal change from the baseline) remain the same, however, WEA6 shows some separation with the sensitivity analysis, with a decrease in settlement not seen in the 15 MW results.

The change in connectivity resulting from the doubled wind wake effect is shown in **Figure 8.93**. Again, patterns of change remain similar to those found for the 15 MW scenario, with similar increase and decrease in settlement in the same destination regions, of larvae from the same spawning regions. However, the change resulting from the sensitivity analysis is an order of magnitude greater than that of the 15 MW scenario.

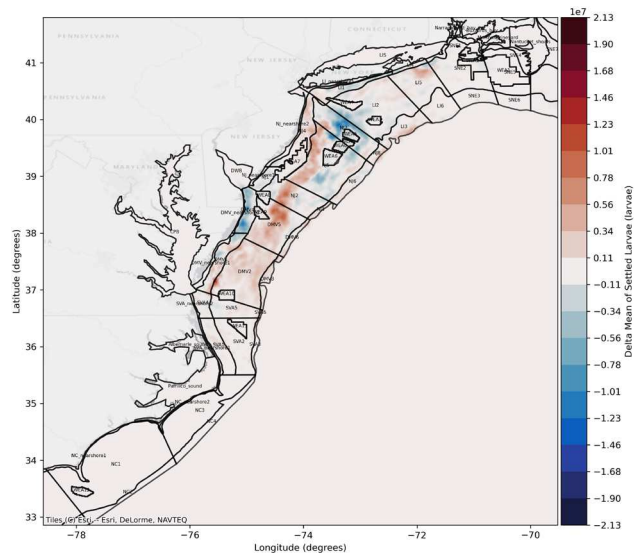


Figure 8.85. Difference in Total Settled Larvae Sensitivity Test vs. Baseline 2017

Difference in total sea scallop settled larvae for model year 2017. Showing the difference in the mean of all ensemble baseline results and mean of all ensemble sensitivity test results. Settled larvae averaged for each model grid element. Red shows an increase in settlement in the sensitivity test compared to the baseline, blue shows a decrease in settlement compared to the baseline.

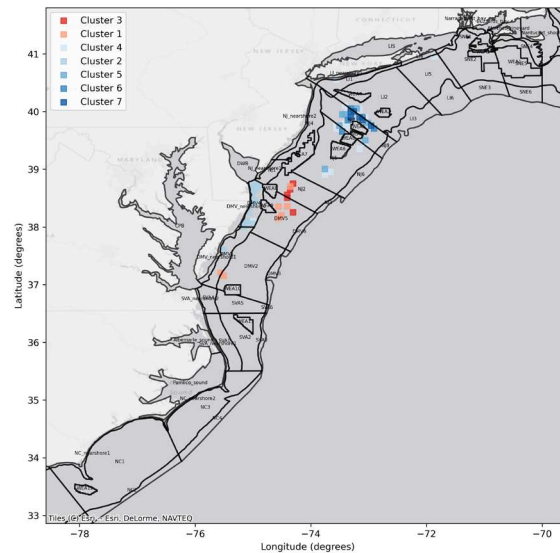


Figure 8.86. DBSCAN (Density-Based Spatial Clustering of Applications with Noise) Difference in Total Settled Larvae Sensitivity Test vs. Baseline 2017

Spatial clusters identified using DBSCAN to filter out noise from the difference plot and identify areas of greatest change. Clusters of settlement increase are identified in red and clusters with settlement decrease are shown in blue.

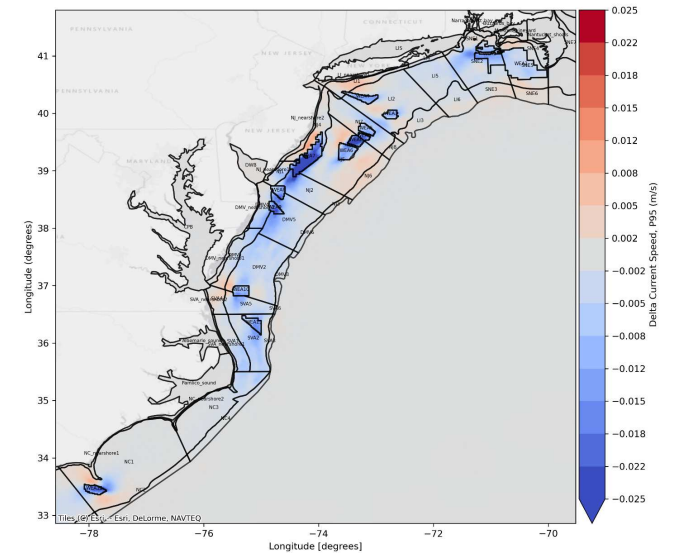


Figure 8.87. Change in Current Speed Sensitivity Test vs. Baseline 2017

Difference in the depth averaged current speed for model year 2017. Showing the difference in the 95th percentile non-exceedance probability baseline results and 95th percentile non-exceedance probability double Scenario 5: 15 MW Full Build-out results.

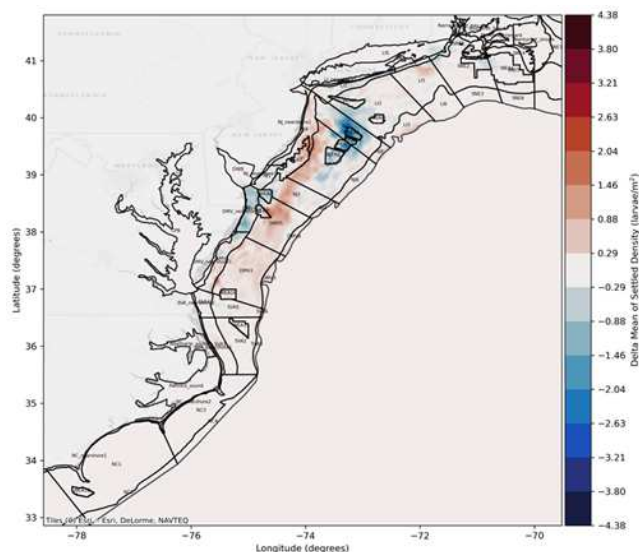


Figure 8.88. Difference in Settled Larvae Density Sensitivity Test vs. Baseline 2017

Difference in sea scallop settled larvae density for model year 2017. Showing the difference in the mean of all ensemble baseline results and mean of all ensemble sensitivity test results. Settled larvae averaged for each model grid element. Red shows an increase in settlement in the sensitivity test compared to the baseline, blue shows a decrease in settlement compared to the baseline.

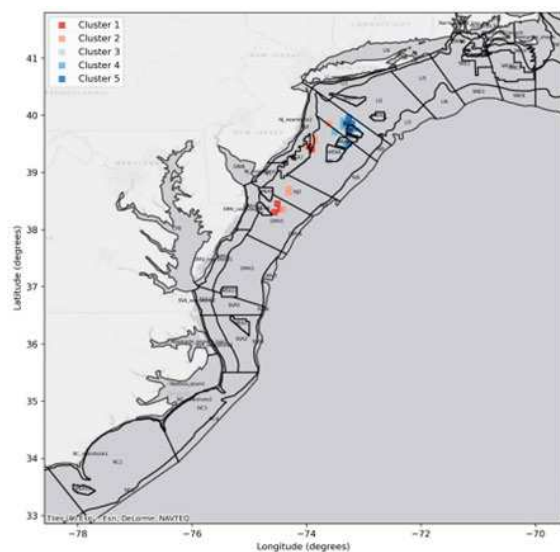


Figure 8.89. DBSCAN (Density-Based Spatial Clustering of Applications with Noise) Difference in Settled Larvae Density Sensitivity Test vs. Baseline 2017

Spatial clusters identified using DBSCAN to filter out noise from the difference plot and identify areas of greatest change. Clusters of settlement increase are identified in red and clusters with settlement decrease are shown in blue.

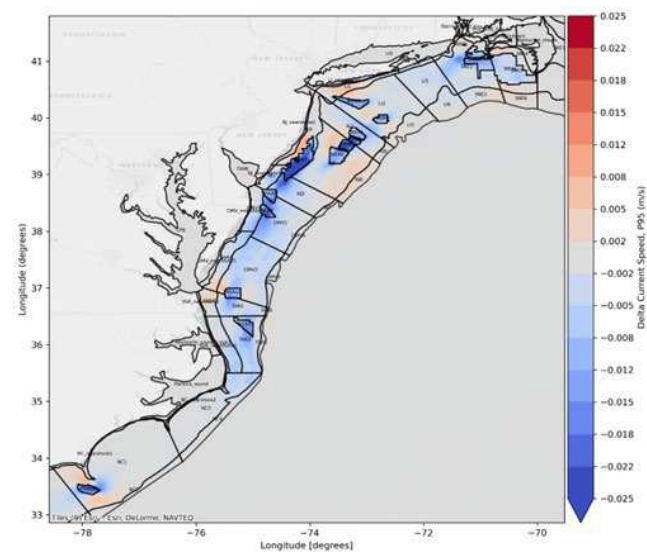


Figure 8.90. Change in Current Speed Sensitivity Test vs. Baseline 2017

Difference in the depth averaged current speed for model year 2017. Showing the difference in the mean of 95th percentile non-exceedance probability ensemble baseline results and mean of 95th percentile non-exceedance probability ensemble sensitivity test results.

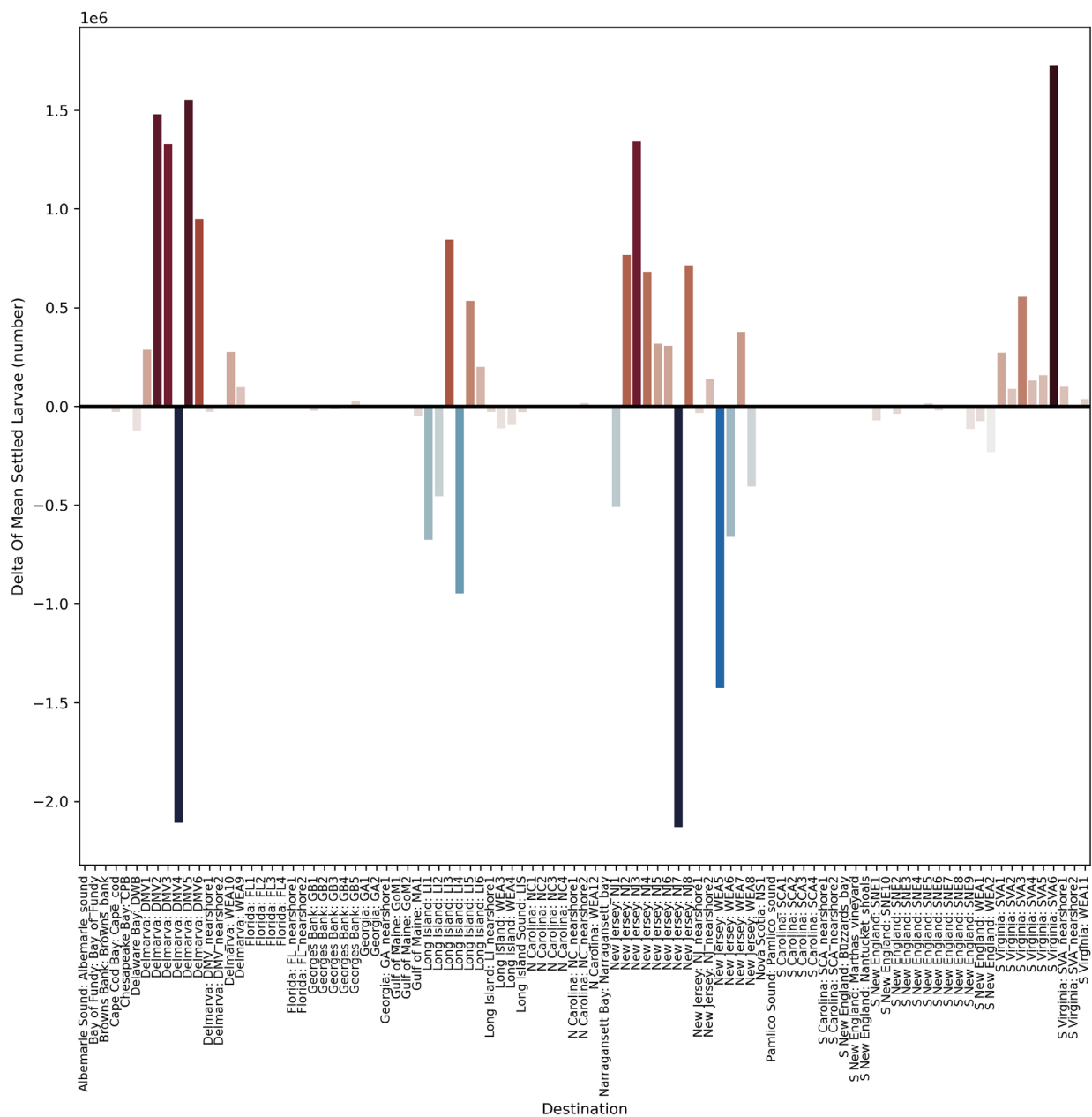


Figure 8.91. Average Change in Sea Scallop Settlement in Each Destination Area Sensitivity Test vs. Baseline 2017

Bar chart shows the average change in settlement in each destination area for model year 2017. Showing the difference in the mean of all ensemble baseline results and mean of all ensemble sensitivity test results.

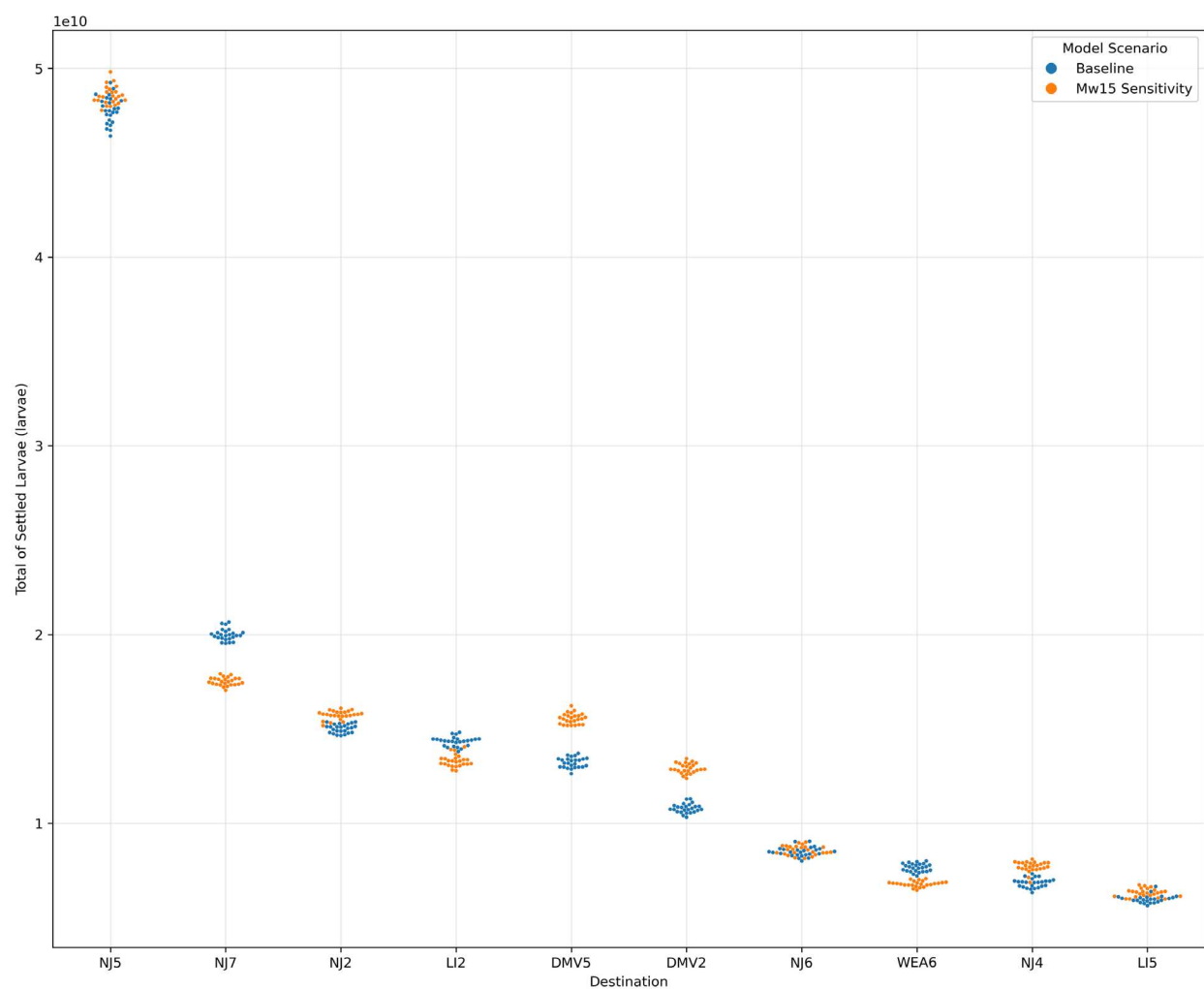


Figure 8.92. Swarm Plot Showing Sea Scallop Settlement in Top 10 Destinations for 2017

Swarm plot shows the settlement for each model run of the ensemble (i.e., each point represents a model result) for 2017. Blue points show the baseline results and orange show the sensitivity test number of settled larvae in the top 10 destinations where there is greatest larval settlement.

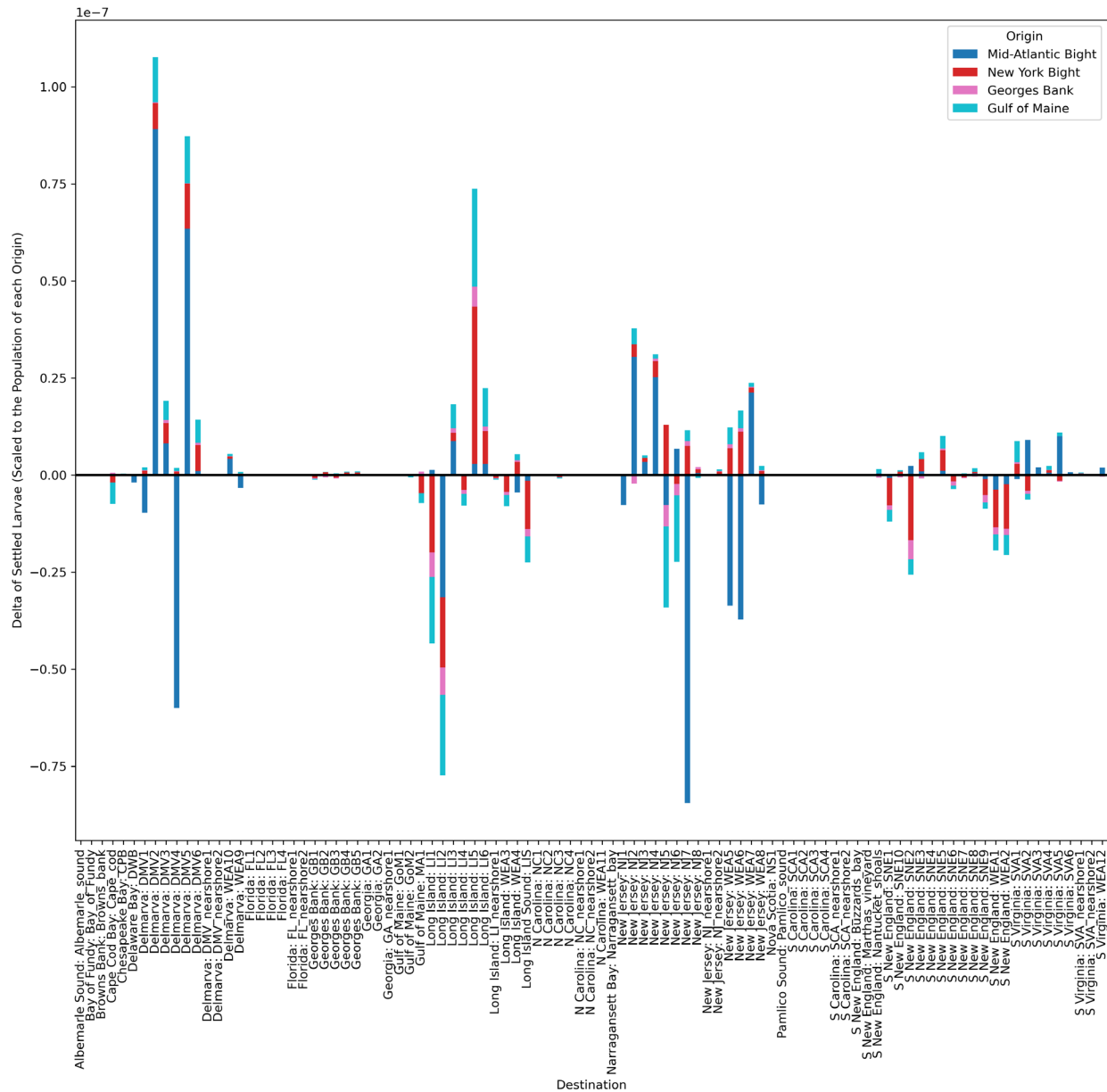


Figure 8.93. Sea Scallop Connectivity Difference 2017

Bar chart shows the difference in sea scallop larvae settlement in each destination area, by origin for model year 2017. Bars are colored by origin area and results show the difference in export probabilities, i.e., the difference in the likelihood of settlement scaled to the number of larvae released from a particular origin region between the baseline and sensitivity test results. Bars below the x axis, show a decrease in settlement in a particular destination area, results above the x axis show an increase in a settlement in a destination area.

9 Larval Dispersal Modeling Conclusions

This section summarizes the overall findings of the ABM modeling carried out and provides suggestions of the relevance these changes may have from a fisheries perspective. The following subsections provide detailed conclusions, overall, the study finds:

- Changes in sea scallop and surfclam settlement were estimated by the ABM, primarily in the New Jersey region around the confluence of OSW developments in the region, and to a less extent through Delmarva.
- Localized patches of increased settlement were found in the center and along the coast of New Jersey, while decreased settlement was estimated to the north of the New Jersey area for both sea scallop and surfclam and to the south of the New Jersey region for surfclam.
- The estimated changes in settlement are likely a result of slowed transport of larvae in both north-to-south and south-to-north directions within the New Jersey area.
- The estimated changes in sea scallop and surfclam settlement are four to five orders of magnitude lower than total settlement, and it is unlikely that there will be relevant ecological, or fisheries impacts on a regional level.
- However, given the persistence of the changes, and the intense hotspots of change identified, there could be impacts on the localized sub-population level.
- Changes in summer flounder settlement were also estimated along the coast, but no clear patterns or consistencies between scenarios emerged. There could be localized impacts in the New Jersey region resulting from the introduction of the OSW developments for summer flounder, as the 15 MW scenario identified change close to the OSW areas.
- However, it is difficult to conclude whether there will be relevant impacts for summer flounder, given their ability to move to appropriate habitat.
- More localized studies are likely required to provide further insight into the relevance of the local level changes identified, as well as consideration of survival and recruitment in the areas of settlement change identified in the model results.

9.1 Baseline Larval Dispersal Evaluation

Sea scallop and surfclam larval settlement distribution was assessed against observed biomass data and essential fish habitat. The results show a considerable overlap between the modeled and the observed distribution of the settled larvae. This indicates that the baseline ABM provides an accurate prediction of larval settlement for these species. Agreement between the modeled and observational distribution was demonstrated in the biomass comparison figures indicating that the baseline ABM provides a reasonable estimate of larval settlement for these species. Further pattern-oriented modeling was carried out and showed quantitatively that there is a good match between modeled and observed larvae settlement distribution. The timing of life stages within the model also matched timings found in the scientific literature. Effort was made to replicate the vertical distribution in the water column of sea scallop and surfclam larvae, by determining vertical movement in response to temperature.

Summer flounder larval distribution could not be directly compared to observational data, as data were only available for juvenile and adult life stages. However, movement of summer flounder larvae to the shore was included in the model, and the expected settlement of summer flounder larvae along the coast was seen in modeled results. Similar life stage and vertical movement was also included in the summer flounder ABM.

Overall, baseline results show expected patterns in settled larvae distribution that agree well with observational data where available.

9.2 OSW Induced Changes in Settlement Dispersal

When analyzing the OSW Scenario ABM results for all scenarios and years of analysis, it is apparent that the introduction of OSW farms does affect the settlement of surfclam and sea scallop larvae through the reduction of current speed and shifts in connectivity pathways. The results for sea scallops and surfclam illustrate change in settlement concentrated in the MAB offshore New Jersey, and, as one might expect, the intensity of the change in settlement generally declines with wind turbine power rating, from the worst-case sensitivity test and full build-out 15MW scenarios to the partial 12MW scenario for all target species. These observations are further explained in the subsections below along with closing comments on which OSW altered oceanic conditions are theorized to be behind the observed shifts in pattern of settlement.

9.2.1 Sea Scallop and Surfclam

When examining the difference in mean settled larvae, mean settled larvae density plots, and related DBSCAN cluster analysis plots for sea scallop and surfclam, the apparent trend is that changes in settlement typically occur offshore of New Jersey, often extending southwards towards Delmarva with variations in areas of larvae settlement decreases and increases. Examples of this are clearly described in **section 8.37.1** and **section Error! Reference source not found.** as well as in the presented results for partial 15 MW and 12 MW build-out scenarios presented in **Appendix C**.

The pattern of larvae settlement change seen for sea scallop and surfclam for all years, and each build-out scenario, is concentrated in the MAB offshore New Jersey within the confluence of WEAs. For sea scallop, increased settlement is estimated along the coast of New Jersey and in WEA7, and south through Delmarva. Decreased settlement is seen in and to the north and south of WEA5 and 6 offshore of New Jersey and southwards along the coast of Delaware. Surfclam results differ slightly to sea scallop with an increase in settlement estimated south of WEA6 and to the east of WEA7 offshore New Jersey. Decreased settlement is estimated in WEA5 and 6 offshore New Jersey, and to the south in Delmarva adjacent to WEAs 8 and 9. These patterns of change are more apparent in the 15 MW partial build-out scenario for both species, but also discernable for the 12 MW scenarios - albeit observable with a more diffuse spread and, generally, a lower level of change in settlement and settlement density.

No clear direct spatial correlation between changes in larvae settlement and current changes (i.e., noticeably – yet marginally reduced current speeds within and in the vicinity of WEAs) were identified. However, the connectivity analysis results, aided in the development of a hypothesis regarding the key oceanic influences causing the estimated changes in larval settlement.

It is likely that slowed transport of sea scallop and surfclam larvae in key connectivity corridors could lead to reduced settlement in some areas and corresponding increases in others. In this regard, further analyses (with the connectivity analysis output) suggested that the spawning release area (i.e., whether to the north or south of the model domain) and pertinent predominant north-south or south-north currents were influential in causing changes in settlement. Currents along the shelf tend to flow north to south, however there is some reversal of this direction from time to time. However, the most prominent pattern for sea scallop larvae was that spawning in the MAB/New Jersey region is slightly slowed in a northerly direction causing an initial area of increased settlement in the south and areas of decreases further north of the New Jersey region. Surfclam larvae spawned in the New Jersey region appear to be slowed in both directions, resulting in an increase in settlement in the middle of the region, and areas of decreased settlement to the north and south. It is clear that there is an influence on settlement from the introduction of the OSW areas, and that given the number of OSW areas within the same New Jersey region, impacts are observed on the transport of larvae in most directions within the New Jersey region.

It should be noted that the estimated change in larvae settlement does not indicate the exact change in the number or proportion of individuals expected to settle successfully in a destination area or region. The ABM is set-up with computational limits and a best estimate of fecundity, and spawning dynamics has been incorporated into the model setup. At the destination area level, changes in settlement observed for sea scallop and surfclam were four and five orders of magnitude lower than the total number of larvae settling in a destination area, indicating that the proportional change in settled larvae, to total settled larvae is small.

The potential relevance of these changes in sea scallop and surfclam settlement is discussed in more detail in **Section 9.4**.

9.2.2 Summer Flounder

An analysis of summer flounder difference in mean settled larvae, mean settled larvae density, and DBSCAN cluster analysis plots, do not produce similar consistent patterns of change across the full and partial 15 MW and 12 MW scenarios. This can be seen in the swarm plot below (**Figure 9.1**) where the results from each build-out scenario are shown together. The points representing total settled larvae in each destination area for each scenario (different colors) are strongly mixed, showing now discernable change from baseline compared to scenario results, as well as a great degree of spread in the results of individual scenario runs. In fact, the only scenario that produced somewhat discernable results was the 15 MW 2017 scenario, where regional cluster plots and higher resolution difference plots showed that changes in larvae settlement, both increases and decreases, were apparent in nearshore destination areas of New Jersey with some increases evident near Delaware Bay and along Delmarva shorelines. However, as destination area results can mask the finer scale changes in larvae settlement (i.e., due to averaging in larger destination areas) these results do not translate to the bar plots and swarm plots; as apparent in destination areas with the largest decreases not aligning with difference and cluster results. Nonetheless, when examining regional and higher resolution difference plots, a conclusion can be drawn that the diffuse shoreward summer flounder larvae migration from outer shelf spawning areas could be influenced by marginally reduced current speeds in and around OSW areas closest to shore (e.g., WEA7). Thus, a larva's shoreward swimming (active drift) would be influenced and slightly repositioned before shoreward transport capabilities engage and before settlement along inshore areas.

This hypothesis, however, seems to lose merit when examining the 12 MW and partial build out scenarios (**Appendix C**), as the same increase and decreases changes are either not fully repeated or are very different. For example, the summer flounder 12 MW scenario regional settlement difference plots do show, albeit at lower intensities, results in nearshore destination areas of New Jersey Delaware Bay and along Delmarva shorelines. However, the other difference plots (incl. the cluster plot), and all difference plot for partial 15 MW and 12 MW build out scenarios present, varied settled and settled density differences along shorelines of Long Island and North Carolina, as well as into areas of around Martha's Vineyard.

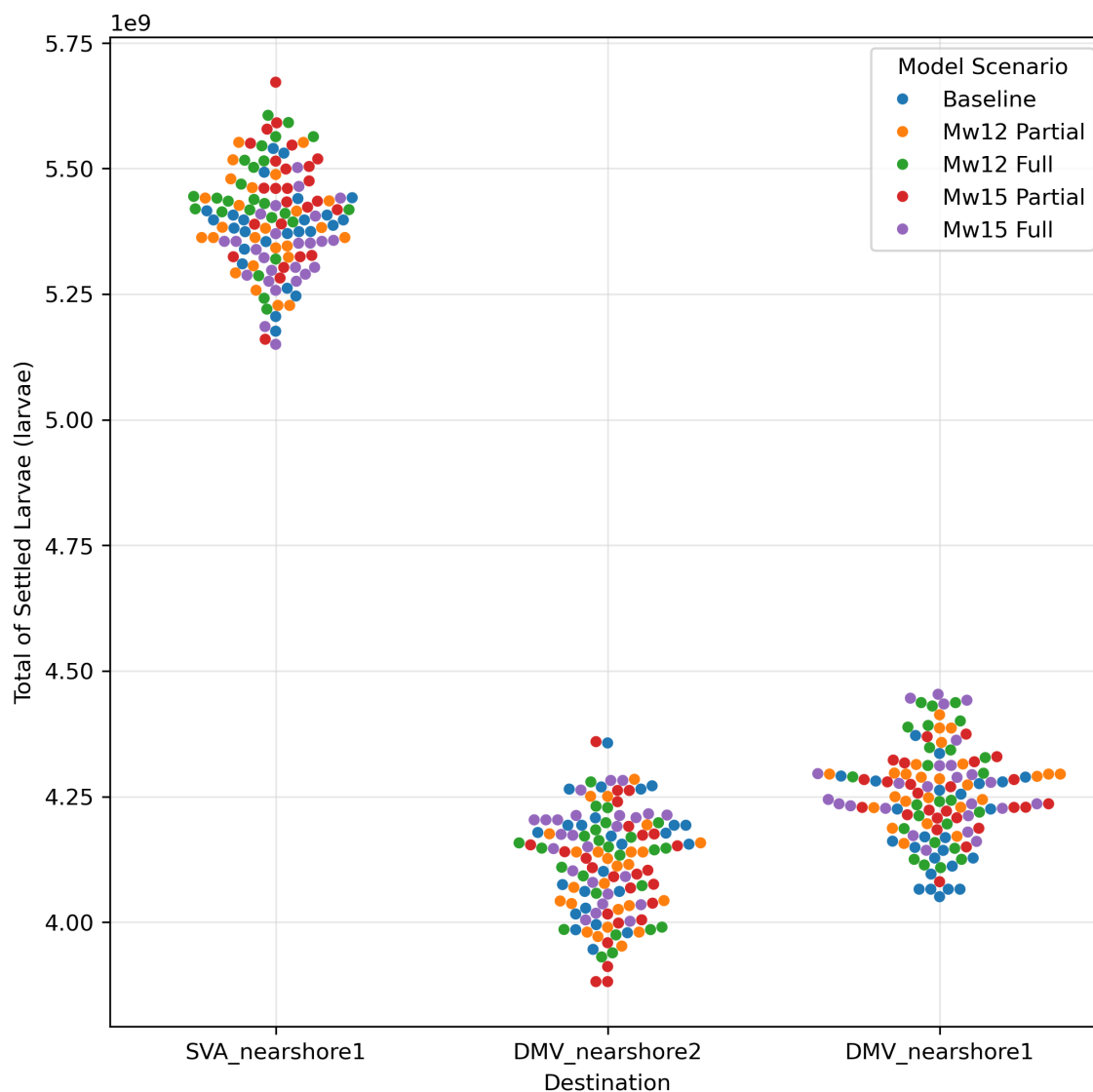


Figure 9.1. Swarm Plot Showing Summer Flounder Settlement in Top 3 Destinations for Each Scenario

Swarm plot shows the settlement for each model run of the ensemble (i.e., each point represents a model result) for 2017. The number of settled larvae in the top 3 destinations where there is greatest larval settlement are shown. Blue points show the baseline results, orange are Scenario 2: 12 MW partial, green Scenario 4: 12MW full build-out, red Scenario 3: 15 MW partial, purple Scenario 5: 15 MW full build-out scenarios and brown is the sensitivity test.

Thus, the change in summer flounder settlement is noisy, and no clear patterns of change emerge from the overall results. There are areas of both increase and decrease along the coast, which are on a scale smaller than the destination areas used in this study. Summer flounder larvae are not noticeably reduced along shore, and the strong mix of baseline and scenario results shown in the swarm plot suggest that there are small scale shifts in larval settlement for this species. In addition, larvae that reach the coast will metamorphose into juveniles, which have the ability to seek appropriate habitat, potentially reducing the impact of any shift in settlement seen in the model results.

A local, more refined scale assessment concentrated along the coast of the MAB, Long Island, and around Nantucket Shoals could be beneficial for identifying whether the noisy changes in summer flounder

settlement found in these results could have an impact on the recruitment of larvae and successful metamorphosis into juveniles.

9.3 OSW Induced Changes to Connectivity

The connectivity analysis results were so far used as a tool to provide information on the possible mechanisms resulting in patterns of larval settlement change – i.e., from which direction the transport of larvae is slowed. From an ecological perspective, changes in connectivity resulting from the marginal slowing of current speeds apparent in the OSW build-out scenarios could have implications for recruitment and population dynamics, resulting in longer term impacts beyond the larval life stage included in this study. The shifts in connectivity seen in the model results include a reduction in surfclam and sea scallop larvae that have spawned both from the north and the south of New Jersey. Slowed transport to the north appears to be increasing settlement of larvae spawned in southern regions south of WEAs 5 and 6; while slowed transport from north to south also appears to be reducing settlement in northern areas, especially for surfclam.

Changes in connectivity are evident on the destination area scale, however when looking at the changes more broadly, shifts in connectivity are not apparent regionally. That is to say, most shifts in destination area settlement occur within their broader regions, such as in New Jersey – changes that occur in larval settlement occur on a finer scale within this region. For example, there may be reduced settlement of sea scallop larvae from Delmarva around WEAs 5 and 6, but settlement of these larvae still occurs within the New Jersey region. Clear regional changes in connectivity are therefore not observed for either of the three species, under all scenarios and modeled years.

The changes in connectivity that are displayed in the bar plots show changes in connectivity that are proportional to the amount of larvae released from each spawning area. As a result, smaller spawning areas can appear to contribute greatly to reduced or increased settlement in certain destination areas, where the absolute change in the number of settled individuals may be relatively small compared to other larger spawning areas. This is important to consider when evaluating impact and when comparing scenarios to the baseline. For example, a 50% reduction in settlement from a particular spawning area with low biomass may have no measurable impact on population recruitment, while in another case with large spawning biomass, the same 50% reduction could result in population and fisheries relevant changes in recruitment.

On a finer scale, reduced settlement in certain areas within New Jersey may have locally important fisheries related effects, which are discussed in **section 9.4**. The New Jersey area appears to mostly self-recruit – with large proportions of both surfclam and sea scallop larvae that settle in this area also spawning here. Settlement within New Jersey from other areas is proportionally much lower, and the shifts in settlement from the north and south spawning regions may therefore have marginal impacts on recruitment of sea scallop and surfclam in the New Jersey region. It is noted however, that settlement does not necessarily equal recruitment, as areas identified as having high settlement from ABM in other studies of shellfish connectivity have coincided with relatively low biomass and abundance (Dankers, 1993, Andresen et al., 2014; Hansen et al., 2023), and drawing conclusions without local studies and biomass data is difficult.

9.4 Relevance of Changes in Larval Transport and Settlement

The target species, sea scallop, surfclam, and summer flounder all support valuable regional fisheries (e.g., Gaichas et al., 2018). Changes in settlement of sea scallop and surfclam are seen primarily in the New Jersey region, where there are active fishing efforts for these species. **Figure 9.2**. Delineation of Fisheries Areas in the Study Area shows that there are areas of both bottom dredge (red) and hydraulic

dredge (green) scallop and clam fishing in the areas identified by the modeling results as having the localized areas of settlement increase and decrease. To understand the relevance of the modeling results to these fisheries we must consider the basic life history characteristics of the focal species.

The three species generally have two-phase life cycles, the first being a pelagic phase consisting of planktonic eggs and larvae shed into the water column to be carried by currents until a suitable site for settlement to the seafloor is detected. The second phase is the post-settlement benthic phase where settled individuals grow and survive to maturity or harvestable size. The process of settling to the seafloor and growing to maturity or harvestable size in fishery species is termed recruitment (Richards and Lindeman, 1987). The vagaries of larval dispersal and mortality as well as post-settlement survival contribute to uncertainty in estimating recruitment in most marine fisheries. Modeling results discussed in sections above depict effects of WEA placement on planktonic transport of larvae to settlement (the pelagic phase). Thus, we can only speculate on the relevance of these findings to recruitment of market-sized individuals into the fishery as this will depend on growth and survival beyond settlement.

The 15 MW full-buildout scenarios were found to slow the prevailing currents enough to alter larval settlement in sea scallops and surfclams adjacent to the WEAs. These results were revealed by plotting differences between baseline scenarios and 15 MW scenarios for each of three years (2017, 2018, and 2020). Persistent reduction in modeled settlement was most pronounced south of WEAs 5 and 6 and generally offshore of New Jersey. The modeled areas represent hotspots of reduced settlement that may ultimately result in densities too low to support commercial harvest.

Over the entire geographic area represented by the modeling domain these differences are small but persistent (over the life of the projects, about 30 years). It is not clear if there is a threshold of larval abundance below which impacts to adult age classes may be expected but fishery scientists consider <1.5 billion individuals as low to medium larval recruitment/settlement of sea scallops for the MAB (Hart and Chang, 2022). It is not likely that the modeled changes in settlement will lead to measurable declines in the landings of sea scallops over the MAB region; however, spatial persistence of the change may be relevant to local scale patches (subpopulations) or beds of sea scallops and any local fisheries they may support.

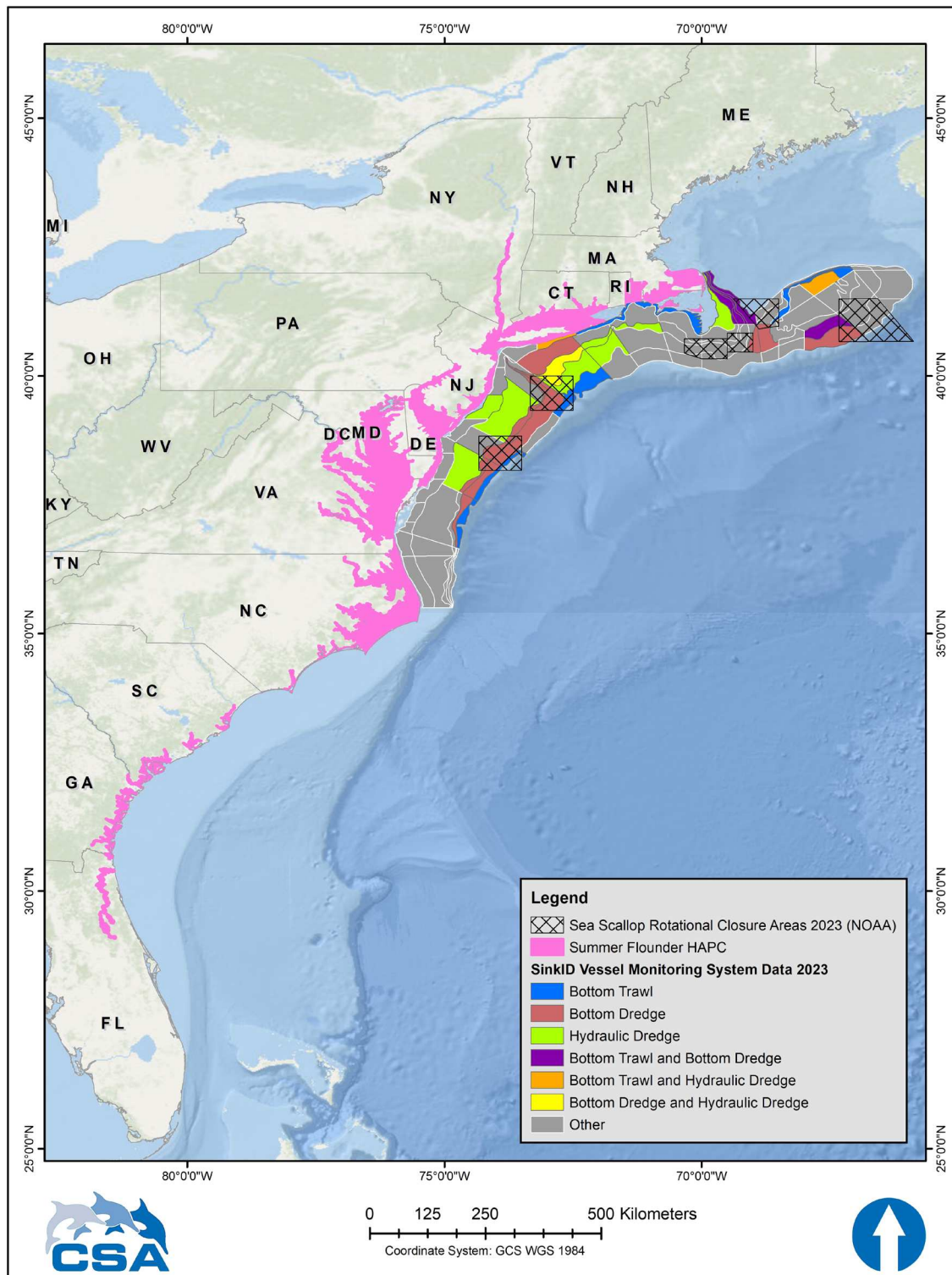


Figure 9.2. Delineation of Fisheries Areas in the Study Area

This map shows areas of fishing activity and the main methods of harvest, generated from VIMS data, details of the different areas are given in Appendix D.

The same scenarios described above for sea scallop generated similar changes in surfclam settlement. The presence of larger 15 MW structures alter larval settlement and create areas with persistent change relative to baseline estimates of settlement south and inshore of WEAs 5 and 6. Again, the New Jersey shelf was affected but indication of the slowing currents was observed adjacent to all but the southernmost WEAs. Because surfclam produce large numbers of offspring which are dispersed over a wide area, no regional effects on populations or fishery landings are expected from the modeled changes in settlement. To illustrate the excessive abundance and distribution of surfclam recruits versus mature adults, Timbs et al (2018) examined areal extent of two age classes over the seafloor across the MAB and subregions (Delmarva, New Jersey, Long Island, and Southern New England). They estimated that in the MAB, the seafloor area occupied by recruits (settled individuals) was on average 55% greater than the area occupied by adult or market-sized surfclam. Off New Jersey they found an average reduction of 21.5% in the area from recruits to larger surfclam. Their findings illustrate the abundance of early life stage individuals over the entire region are capable of replenishing existing age classes from depleted areas.

The two bivalve species exhibited similar patterns in transport and settlement over the modeling domain, but summer flounder differed. No appreciable changes from baseline were observed in modeled scenarios for summer flounder with the exception of shifts in larval transport to the north or south near the WEAs. Pre-settlement summer flounder are also competent swimmers which may facilitate shoreward movement towards shallow water and entrances to rivers, bays, or estuaries. Nearshore settlement is a well-established aspect of summer flounder life history, and although not specifically studied, settlement and grow-out may also occur nearshore coastal waters (Hoey et al., 2020). Any local scale shifts in settlement therefore may be mitigated by the ability of juvenile summer flounder to swim to appropriate habitats.

The persistent effects on current flow, larval transport, and settlement of the two bivalve species may be relevant to fisheries at a local scale where small patches or beds of sea scallops or surfclams depend on larval input from outside sources south or north of the WEAs. These potential effects should be evaluated at the scale of individual project (COPs) with input from local fishers engaged sea scallop or surfclam harvest.

10 Summary and Follow-up Research

10.1 Analysis Explanations

10.1.1 Hydrodynamics

Regional hydrodynamic models were developed for this study, that describe the currents, temperature, and salinity variations as well as wave conditions of the U.S. East Coast. The models were validated with available observational data and were used to hindcast the hydrodynamic conditions for years 2017, 2018, and 2020. The validation shows that the model provides a realistic representation of the conditions in the model domain, both qualitatively and quantitatively. The models were applied to simulate baseline hydrodynamic conditions, with no WTGs, and five OSW scenarios and one sensitivity analysis. There were four scenarios for 2017, comprising: 1) 12 MW partial build-out, 2) 15 MW partial build-out, 3) 12 MW full build-out and 4) 15 MW full build-out. The fifth scenario included a 15 MW full build-out for years 2017, 2018, and 2020. The sensitivity analysis doubled the wind wake effect for the 15 MW full build-out scenario for 2017.

The results of the modeling study clearly reveal that the introduction of the OSW structures into the Massachusetts-Rhode Island, New York Bight, Maryland-Delaware, Virginia-North Carolina and North Carolina-South Carolina offshore areas modify oceanic responses of current magnitude, sea temperature, wave heights and bed shear stresses by:

- Reducing the current magnitude through added flow resistance as described in **Section 5.2**,
- Reducing current magnitude and wave height by extracting of energy from the wind by the OSW turbines as described in **Section 5.2.1** (current), **Section 5.2.2** (wind), **Section 5.4** (waves) with requisite description of changes in **Section 5.5** (bed shear stress),
- Influencing the temperature stratification by introducing additional mixing as described in **Section 5.6**.

Maximum changes to 95th percentile non-exceedance probability depth averaged current speeds in all WEAs for Scenario 5 (15 MW Full Build-out), the scenario with the most pertinent change, ranged from approximately -5.0% and +1.7%. The biggest reduction in 95th percentile non-exceedance probability significant wave heights (H_{m0}) were observed in the New York Bight (NY Bight) / Maryland-Delaware (MD-DE) region. Here, wave height reduction was on the order of 10 cm for waves that were in the order of 2.5 m H_{m0} or ~4% lower. Modeled changes in bed shear stress were also small, leading to the conclusion that WTGs should have no increased effect on deposition and marginal reductions in the potential of seabed sediment mobilization in the WEAs. Effects on thermal stratification were also minimal, and while the degree to which the thermocline was shifted depended on the season, the greatest shift to the thermocline was 3 m in winter.

The aim of this study was to determine regional scale impacts on oceanic responses from OSW developments. At the time of writing, there were no known comprehensive observational studies published that investigate baseline conditions and resulting changes from regional OSW farm development. This is also pointed out by National Academies of Sciences, Engineering, and Medicine (2023) (or NASEM (2023)). As support for developing the study conducted by NASEM (2023) was provided by BOEM we note that the work conducted and reported on by the NASEM committee was closely aligned with this study's objectives.

10.1.2 Larval Dispersal

Agent-based models were developed for sea scallop, summer flounder, and surfclam and used to estimate baseline and OSW build-out larval dispersal patterns. Through the use of ensemble modeling, connectivity analysis, and statistical methods, settlement and settlement density differences resulting from the OSW build-out scenarios were evaluated. Each target species ABM model template was calibrated and evaluated against available observation datasets and referenced parameter benchmarks. Evaluation analyses show that the modeled baseline results align with expected patterns in settled larvae distribution and therefore provide a solid basis for the analysis of the influence of OSW induced oceanic change on the dispersal of target species larvae. ABMs were executed for full and partial 12 MW and 15 MW build-out scenarios, for either 2017 (surf clam and summer flounder) or one 2017, 2018, and 2020 (sea scallop) hindcast years.

The results of the ABM study reveal that the introduction of the OSW structures into the Massachusetts-Rhode Island, New York Bight, Maryland-Delaware, Virginia-North Carolina and North Carolina-South Carolina offshore areas may result in changes in larval dispersal and settlement, namely:

- Increase and decrease in sea scallop and surfclam settlement mainly around New Jersey OSW developments and to a lesser extent in Delmarva as described in **Section 8.3**. The estimated changes in sea scallop and surfclam settlement are four to five orders of magnitude lower than total settlement, and it is unlikely that there will be relevant ecological, or fisheries impacts on a regional level. However, given the persistence of the changes, and the locally substantial changes identified, there could be impacts on the localized sub-population level for these species.
- Changes in sea scallop and surfclam settlement appear to be due to both slowed north-to-south and south-to-north larval transport in the New Jersey area as described in **Section 8.3**
- Local scale areas of increase and decrease in summer flounder settlement were estimated along the coast with no distinct patterns but appear to be concentrated close to WEAs as described in **Section 8.3.3**. It is challenging to conclude whether there will be relevant impacts for summer flounder, given their ability to move to appropriate habitat. More localized studies are likely required to provide further insight into the relevance of the local level changes identified, as well as consideration of survival and recruitment in the areas of settlement change identified in the model results.
- The 15 MW scenario results in greater changes in settlement than the 12 MW and partial scenarios, but the changes remain on the same order of magnitude.

The modeling undertaken for this Project was carried out at a regional level and identified regional patterns of increases and decreases in target species larvae settlement. It is acknowledged however, that there are likely localized details of OSW build-out influences to oceanic conditions that could lend additional insight to explanations of the mechanisms behind the changes in settlement estimated for the OSW build-out scenarios. This could be especially pertinent to understanding impact mechanisms, and potential mitigation approaches, in the vicinity of New Jersey and Delmarva where the most prominent and consistent settlement changes were estimated. Here, more localized, spatially and temporally refined post-processing of model results could provide additional explanatory evidence of how altered oceanic conditions in and around WEAs influence the dispersal of larvae.

The problem of discerning the difference between unstructured or inconsistent results (i.e., model noise), with explainable patterned results was apparent in the results for summer flounder. The 15 MW build-out scenario, which showed some explainable result, were inconsistent with the 12MW scenario results, and between full and partial build out scenarios. The cause of this noise could be attributed to several factors such as the combination of very small levels of change and inherent stochasticity in the ABM modeling, or the influence of regional level of result post-processing (e.g., analysis of results for smaller destination areas may be more revealing). This noise, however, does not necessarily negate observable patterns of

change. It is apparent that changes in settlement are likely where there is a confluence of WEAs and more localized and focused post-processing of results could aid in revealing patterns of settlement and connectivity change while also isolating the related processes.

As mentioned in **section 9.3**, settlement does not necessarily equal recruitment into the fishery, as areas identified as having high settlement from ABM in other studies of shellfish connectivity have coincided with relatively low biomass and abundance (e.g., Hansen et al., 2023). Drawing conclusions in terms of target species population level impacts without dedicated localized monitoring and recruitment success studies is not possible. Such studies are therefore necessary to fully understand the relevance of the change in target species larvae settlement dispersal and connectivity carried out for this project.

10.2 Follow-up Research

From the above discussion, it is evident that there are a number of ways in which the oceanic modeling (HDM) and ABM, and related connectivity analyses, can be further developed to provide more insight. Related recommendations in this regard are classified in terms of their application in further localized analyses, Construction and Operations Plans (COPs) and Environmental Impact Statement (EIS) analyses, and post-development monitoring.

10.2.1 Localized Analyses - ABM

The main recommendations for potential improvement for the ABM with respect to larval settlement and connectivity include the following collection of either dedicated separate research or relatively small modeling or analysis steps:

- Improve effectiveness and/or local specificity of ABM analyses through:
 - developing area and species-specific impact threshold limits for acceptability of changes in larvae settlement
 - collection and application of dedicated local observational data / knowledge, especially in hotspot areas of estimated settlement change and in the New Jersey region where most changes were found.
 - execution of spatially and temporally refined ABM result post-processing for all species.
- Extend the ABM modeling analyses to include:
 - development of target species to juvenile stages, to better understand the impacts of OSW related oceanic changes to recruitment
 - Inclusion of the artificial reef effect (Mineur et al., 2012; Degraer et al., 2020; Glarou et al., 2020) in ABM analyses, with specific focus on the ‘Spillover Effect’ (van Berkel et al., 2020). This would allow for a better understanding of the potential for OSW monopiles to provide habitat for certain species.

10.2.2 Observations and Modeling to Support Improvement to the Hydrodynamic Model OSW Farm Monopile and WTG Parameterization

The main recommendations for potential improvement for the HDM involve improved parameterization of the monopile wake and the WTG wind wakes. The HDM employed a sub-grid model approach to ensure energy is converted accurately. Each turbine is implemented as sub-grid feature using extra source terms for the drag force from the tower as a mean momentum sink, a source term for turbulent kinetic energy from the extra production in the wake, and an increase the eddy viscosity adding mixing of momentum, temperature and salinity. This approach follows normal practice in ocean models (Rennau, 2012; Jakobsen, 2010) or wind resource modeling (Fitch, 2012). There is a potential for future improvement of the HDM due to uncertainties in the hydrodynamic response due to the ocean wakes from the monopiles. This uncertainty may be reduced by further study (observations and modeling) of the wake

mixing around large monopiles that may inform the parameterization within the sub-grid modeling approach. Additionally, there may be uncertainties in the hydrodynamic response due to the wind wakes from the WTGs on the air-sea interactions that may be reduced by further study of the wake deficits, turbulence and heat exchange (observations and modeling) around individual WTG and large-scale OSW farms. This work on the WTG wind wakes may inform the parameterization employed in this study.

11 References

11.1 References: Hydrodynamics

- Andersen OB, Knudsen P. 2009. DNSC08 mean sea surface and mean dynamic topography models, *J. Geophys. Res.*, 114, C11001, doi:10.1029/2008JC005179.
- Andres, M. 2016. On the recent destabilization of the Gulf Stream path downstream of Cape Hatteras, *Geophys. Res. Lett.*, 43, 9836–9842, doi:10.1002/2016GL069966.
- Chen C, Beardsley RC, Qi J, Lin H. 2016. Use of Finite-Volume Modeling and the Northeast Coastal Ocean Forecast System in Offshore Wind Energy Resource Planning. Final Report to the U.S. Department of the Interior, Bureau of Ocean Energy Management, Office of Renewable Energy Programs. BOEM 2016-050. 131pp
- Chen K, He R, Powell BS, Gawarkiewicz GG, Moore AM, Arango HG 2014. Data assimilative modeling investigation of Gulf Stream warm core ring interaction with continental shelf and slope circulation. *Journal of Geophysical Research: Oceans*, 119, 5968–5991. <https://doi.org/10.1002/2014JC009898>
- Chen Z, Kwon Y-O, Chen K, Fratantoni P, Gawarkiewicz G, Joyce TM. 2020. Long-term SST variability on the northwest Atlantic continental shelf and slope. *Geophysical Research Letters*, 47, e2019GL085455. <https://doi.org/10.1029/2019GL085455>
- Chen C, Zhao L, Lin H, He P, Li S, Wu Z, Qi J, Xu Q, Stokesbury K, Wang L. 2024. Potential impacts of offshore wind energy development on physical processes and scallop larval dispersal over the US Northeast shelf. *Progress in Oceanography*. 224:103263.
- Christiansen N, Daewel U, Djath B, Schrum C. 2022. Emergence of Large-Scale Hydrodynamic Structures Due to Atmospheric Offshore Wind Farm Wakes. *Frontiers in Marine Science*, 9, doi:10.3389/fmars.2022.818501
- [DHI] DHI Water & Environment. 2017. (unpublished industry report) MetOcean Hindcast Study - Vineyard Offshore Wind Farm MA, USA, DHI, Copenhagen.
- [DHI] DHI A/S. 2024. (web-published) MIKE 3 Flow Model FM Hydrodynamic and Transport Module Scientific Documentation DHI, Copenhagen. [MIKE 3 Flow Model FM - Hydrodynamic and Transport Module \(mikepoweredbydhi.help\)](#)
- Donlon, C.J., Martin, M., Stark, J., Roberts-Jones, J., Fiedler, E., and Wimmer, W. 2012, The Operational Sea Surface Temperature and Sea Ice Analysis (OSTIA) system. *Remote Sensing of the Environment*. doi: 10.1016/j.rse.2010.10.017 2011.
- [FEHY] FEhmarnbelt HYdrography. 2010a. (unpublished industry report) “Initial study of mixing and parameterisation refined flow (CFD). Analyses of the mixing of density stratified currents”. Report 11802650-14-E1TR0035.
- FEHY. 2010b. (unpublished industry report) “Initial study of mixing and parameterisation - physical model experiments”, Vol. I – III. Report 11802650-14-E1TR0015.
- FEHY (Petersen OS, Burchard H.) 2011. (unpublished industry report) Parameterisation of bridge piers and ferry mixing. Report 11802650-14-E1TR0041

- Fernando HJ. 1991. Turbulent Mixing in Stratified Fluids. *Annu. Rev. Fluid Mech.* 23:455–493.
- Floeter J, van Beusekom JEE, Auch D, Callies U, Carpenter J, Dudeck T, Eberle S, Eckhardt A, Gloe D, Hänselmann K, et al. 2017. Pelagic effects of offshore wind farm foundations in the stratified North Sea. *Prog. Oceanogr.* 156:154–173.
- Frandsen S. 1992. On the wind speed reduction in the center of large clusters of wind turbines. *J. Wind. Eng. Ind. Aerodyn.* 39:251–265.
- Fratantoni, PS, Pickart, RS. 2007. The western North Atlantic shelfbreak current system in summer. *Journal of Physical Oceanography*, 37(10):2509–2533.
- Fredsoe J. 1984. Turbulent boundary layers in combined wave current motion. *J. Hydraul. Eng. ASCE*, Vol. 110, No. HY8, pp. 1103-1120
- Friedland KD, Miles T, Goode AG, Powell, E. N., & Brady, D. C. 2022. The Middle Atlantic Bight Cold Pool is warming and shrinking: Indices from in situ autumn seafloor temperatures. *Fisheries Oceanography*, 31(2), 217–223. <https://doi.org/10.1111/fog.12573>
- Gangopadhyay A, Gawarkiewicz G, Silva ENS, Silver AM, Monim M, Clark J. 2020. A census of the warm-core rings of the Gulf Stream: 1980–2017. *Journal of Geophysical Research: Oceans*, 125, e2019JC016033. <https://doi.org/10.1029/2019JC016033>
- Gawarkiewicz G, Todd RE, Zhang w, Partida J, Gangopadhyay A, Monim M-U-H, Fratantoni P, Malek Mercer A, Dent M. 2018. The changing nature of shelf-break exchange revealed by the OOI Pioneer Array. *Oceanography* 31(1):60–70, <https://doi.org/10.5670/oceanog.2018.110>.
- Großelindemann H, Ryan S, Ummerhofer CC, Martin T, Biastoch A. 2022. Marine Heatwaves and Their Depth Structures on the Northeast U.S. Continental Shelf. *Front. Clim.* 4:857937. doi: 10.3389/fclim.2022.857937
- Grubert JP. 1989. Interfacial Mixing in Stratified Channel Flows. *J. Hydraul. Eng.* 115:887–905.
- Good S, Fiedler E, Mao C, Martin MJ, Maycock A, Reid R, Roberts-Jones J, Searle T, Waters J, While, J, Worsfold M. 2020. The Current Configuration of the OSTIA System for Operational Production of Foundation Sea Surface Temperature and Ice Concentration Analyses. *Remote Sens.* 2020, 12, 720. doi: 10.3390/rs12040720
- Helber RW, Townsend TL, Barron CN, Dastugue JM, Carnes MR. 2013. Validation Test Report for the Improved Synthetic Ocean Profile (ISOP) System, Part I: Synthetic Profile Methods and Algorithm. *NRL Memo. Report*, NRL/MR/7320—13-9364.
- Holmboe J. 1962. On the behavior of symmetric waves in stratified shear layers. *Deep-Sea Res. Oceanogr. Abstr.* 9:395–396.
- Ivey GN, Imberger J. 1991. On the Nature of Turbulence in a Stratified Fluid. Part I: The Energetics of Mixing. *J. Phys. Oceanogr.* 21:650–658.
- Iqbal M. 1983. *An Introduction to Solar Radiation*, Academic Press, Toronto

- Jakobsen F, Hansen IS, Ottesen Hansen N-E, Østrup-Rasmussen F. 2010. Flow resistance in the Great Belt, the biggest strait between the North Sea and the Baltic Sea. *Estuar. Coast. Shelf Sci.* 87:325–332.
- Jensen B, Carstensen S, Christensen ED. 2018. Mixing of Stratified Flow around Bridge Piers in Steady Current. *J. Hydraul. Eng.* 144(8):04018041. doi:10.1061/(asce)hy.1943-7900.0001481
- Johnson TL, van Berkel JJ, Mortensen LO, Bell MA, Tiong I, Hernandez, B, Snyder, DB, Thomsen, F, Svenstrup Petersen, O: 2021. Hydrodynamic modeling, particle tracking and agent-based modeling of larvae in the U.S. mid-Atlantic bight. Lakewood (CO): US Department of the Interior, Bureau of Ocean Energy Management. OCS Study BOEM 2021-049. 232 p.
- Jones O, Zyserman JA, Wu Y. 2014. Influence of apparent roughness on pipeline design conditions under combined waves and current. *Proceedings of the ASME 2014 33rd International Conference on Ocean, Offshore and Arctic Engineering.*
- Joyce T, Backus R, Baker K, Blackwelder P, Brown O, Cowles T, et al. 1984. Rapid evolution of a Gulf Stream warm-core ring. *Nature*, 308(5962):837–840. <https://doi.org/10.1038/308837a0>.
- Lentz SJ. 2017. Seasonal warming of the Middle Atlantic Bight Cold Pool. *J. Geophys. Res. Oceans.* 122:941–954.
- Li Y, Fratantoni PS, Chen C, Hare JA, Sun Y, Beardsley RC, Ji R., 2015. Spatio-temporal patterns of stratification on the Northwest Atlantic shelf. *Prog. Oceanogr.* 134:123-137 (2015). <http://dx.doi.org/10.1016/j.pocean.2015.01.003>
- Lind G, Falkenmark M. 1972. Hydrology en inledning till vattenressurslaran, Studenlitteratur (in Swedish)
- Loder J, Petrie B, Gawarkiewicz G. 1998. The coastal ocean off northeastern North America: A large-scale view. *The Sea*. 11:105–138.
- National Academies of Sciences, Engineering, and Medicine. 2023. Potential Hydrodynamic Impacts of Offshore Wind Energy on Nantucket Shoals Regional Ecology: An Evaluation from Wind to Whales. Washington, DC: The National Academies Press. <https://doi.org/10.17226/27154>.
- [NOAA] National Oceanic and Atmospheric Administration. 2003. NOS standards for evaluating operational nowcast and forecast hydrodynamic model systems. NOAA, Silver Springs, Maryland. NOAA Technical report NOA CS 17.
- O'Reilly J, Zetlin C. 1998. Seasonal horizontal and vertical distribution of phytoplankton chlorophyll northeast us continental shelf ecosystem. NOAA Technical report NMFS 139. Fish. Bull.
- Ørsted. 2020. Metadata for current measurements at the U.S. East Coast. Report Rev. no.: 06354878_A, 13 July 2020
- Peltier WR, Caulfield CP. 2003. Mixing efficiency in stratified shear flow. *Annu. Rev. Fluid Mech.* 35:135–167.
- Peña A, Rathmann O. 2013. Atmospheric stability-dependent infinite wind-farm models and the wake-decay coefficient. *Wind. Energy.* 17:1269–1285.

- Rennau H, Schimmels S, Burchard H. 2012. On the effect of structure-induced resistance and mixing on inflows into the Baltic Sea: A numerical model study, *Coastal Engineering*, Volume 60, 2012, Pages 53-68, ISSN 0378-3839, <https://doi.org/10.1016/j.coastaleng.2011.08.002>
- Roarty H, Glenn S, Brodie J, Nazzaro L, Smith M, Handel E, Kohut J, Updyke T, Atkinson L, Boicourt W, et al. 2020. Annual and Seasonal Surface Circulation Over the Mid-Atlantic Bight Continental Shelf Derived From a Decade of High Frequency Radar Observations. *J. Geophys. Res. Oceans*. 125(11). doi:10.1029/2020jc016368
- Rouse H, Dodu J. 1955. Turbulent diffusion across a density discontinuity. *La Houille Blanche*:522–532.
- Sahlberg J. 1984. A hydrodynamic model for heat contents calculations on lakes at the ice formation date. Document D4: 1984, Swedish council for Building Research
- Schimmels, S. 2008. Numerical Simulation of the Influence of Circular Cylinders on Mixing and Entrainment in Natural Density Currents. Bericht Nr. 75, Institut für Strömungsmechanik, Leibniz Universität Hannover, Deutschland. ISSN: 0177 – 9028
- Schultze LKP, Merkelbach LM, Horstmann J, Raasch S, Carpenter JR. 2020. Increased Mixing and Turbulence in the Wake of Offshore Wind Farm Foundations. *JGR Oceans*, 125, 8. doi.org/10.1029/2019JC015858
- Smyth WD, Winters KB. 2003. Turbulence and Mixing in Holmboe Waves. *J. Phys. Oceanogr.* 33:694–711.
- Soulsby R, Clarke S. 2005. Bed Shear-stresses Under Combined Waves and Currents on Smooth and Rough Beds. HR Wallingford Ltd.
- Strang EJ, Fernando HJ. 2001. Entrainment and mixing in stratified shear flows. *J. Fluid Mech.* 428:349–386.
- Stark, JD, Donlon CJ, Martin MJ, McCulloch ME. 2007. OSTIA: An operational, high resolution, real time, global sea surface temperature analysis system., *Oceans 07 IEEE Aberdeen*, conference proceedings. Marine challenges: coastline to deep sea. Aberdeen, Scotland. IEEE.
- Stevenson D, Chiarella L, Stephan D, Reid R, Wilhelm K, McCarthy J, Pentony M. 2004. Characterization of the fishing practices and marine benthic ecosystems of the northeast US shelf, and an evaluation of the potential effects of fishing on essential habitat. NOAA Tech Memo NMFS NE 181; 179 p.
- Turner JS. 1973. Buoyancy effects in fluids Cambridge [Eng.]: University Press. pp. 367
- Rodi W. 1980. Turbulence Models and Their Application in Hydraulics – A State of the Art Review, Special IAHR Publication.
- Williams J.J., Esteves L.S, 2017. Guidance on Setup, Calibration, and Validation of Hydrodynamic, Wave, and Sediment Models for Shelf Seas and Estuaries. *Advances in Civil Engineering Volume 2017*, Article ID 5251902, 25 pages, <https://doi.org/10.1155/2017/5251902>

Zhang, W. G., & Gawarkiewicz, G. G. 2015. Dynamics of the direct intrusion of Gulf Stream ring water onto the Mid-Atlantic Bight shelf. *Geophysical Research Letters*, 42, 7687–7695.
<https://doi.org/10.1002/2015GL065530>

11.2 References: Wind Turbine Wake Loss Model

Akhtar N, Geyer B, Schrum C. 2022. Impacts of accelerating deployment of offshore windfarms on near-surface climate. *Scientific Reports*, 12(1). <https://doi.org/10.1038/s41598-022-22868-9>

Al Halabi M. 2023. Comparing wind farm production data to engineering wake model simulations [University of South-Eastern Norway]. <https://hdl.handle.net/11250/3073039>

Archer CL, Colle BA, Veron DL, Veron F, Sienkiewicz MJ. 2016. On the predominance of unstable atmospheric conditions in the marine boundary layer offshore of the U.S. northeastern coast. *Journal of Geophysical Research*, 121(15), 8869–8885. <https://doi.org/10.1002/2016JD024896>

Archer CL, Wu S, Vassel-Be-Hagh A, Brodie, JF, Delgado R, St. Pé A, Oncley S, Semmer S. 2019. The VERTEX field campaign: observations of near-ground effects of wind turbine wakes. *Journal of Turbulence*, 20(1), 64–92. <https://doi.org/10.1080/14685248.2019.1572161>

Bak C, Zahle F, Bitsche R, Kim T, Yde A, Henriksen L C, Hansen M H, Blasques J P A A, Gaunaa M and Natarajan A .2013. The DTU 10-MW reference wind turbine *Danish Wind Power Research 2013*

Breedt HJ, Craig KJ, Jothiprakasham VD. 2018. Monin-Obukhov similarity theory and its application to wind flow modeling over complex terrain.

Canadillas B, Beckenbauer M, Trujillo JJ, Dörenkämper M, Foreman R, Neumann T, Lampert A. 2022. Offshore wind farm cluster wakes as observed by long-range-scanning wind lidar measurements and mesoscale modeling, *Wind Energy Science*, 7, 3, pp. 1241-1262, doi:10.5194/wes-7-1241-2022

Cheng Y, Zhang M, Zhang Z, Xu J. 2019. A new analytical model for wind turbine wakes based on Monin-Obukhov similarity theory. *Applied Energy*, 239, 96–106.
<https://doi.org/10.1016/j.apenergy.2019.01.225>

Christiansen MB, Hasager, CB. 2005. Wake effects of large offshore wind farms identified from satellite SAR. *Remote Sensing of Environment*, 98, 251-268. <https://doi.org/10.1016/j.rse.2005.07.009>

Djath B, Schulz-Stellenfleth J. 2019. Wind speed deficits downstream offshore wind parks – A new automatised estimation technique based on satellite synthetic aperture radar data, *Meteorologische Zeitschrift* Vol. 28 No. 6 (2019), p. 499 – 515, DOI: 10.1127/metz/2019/0992.

Dorrell RM, Lloyd CJ, Lincoln BJ, Rippeth TP, Taylor JR, Caulfield C, Cille P, Sharples J, Polton JA, Scannell BD, Greaves DM, Hall RA, Simpson JH. 2022. Anthropogenic Mixing in Seasonally Stratified Shelf Seas by Offshore Wind Farm Infrastructure. In *Frontiers in Marine Science* (Vol. 9). Frontiers Media S.A. <https://doi.org/10.3389/fmars.2022.830927>

Fischereit J, Brown R, Larsén XG, Badger J, Hawkes G. 2022. Review of Mesoscale Wind-Farm Parametrizations and Their Applications, *Bound.-Lay. Meteorol.*, 182, 175–224,
<https://doi.org/10.1007/s10546-021-00652-y>.

- Fitch A C, Olson J B and Lundquist J K. 2013. Parameterization of wind farms in climate models J. Clim. 26 6439–58
- Fitch A C, Olson J B, Lundquist J K, Dudhia J, Gupta A K, Michalakes J and Barstad I. 2012. Local and mesoscale impacts of wind farms as parameterized in a mesoscale NWP model Mon. Weather Rev. 140 3017–38, <https://doi.org/10.1175/MWR-D-11-00352.1>
- Frandsen ST. 2007. Turbulence and turbulence-generated structural loading in wind turbine clusters. Denmark. Forskningscenter Risoe. Risoe-R No. 1188 (EN) .
<https://orbit.dtu.dk/en/publications/turbulence-and-turbulence-generated-structural-loading-in-wind-tu>
- Golbazi M, Archer CL, Alessandrini S. 2022. Surface impacts of large offshore wind farms, Environ. Res. Lett. 17 064021. DOI 10.1088/1748-9326/ac6e49
- Han X, Liu D, Xu C, Shen W, Li L, Xue F. 2019. Monin-Obukhov similarity theory for modeling of wind turbine wakes under atmospheric stable conditions: Breakdown and modifications. Applied Sciences (Switzerland), 9(20). <https://doi.org/10.3390/app9204256>
- International Electrotechnical Commission. 2017. IEC 61400:2017 International Standard: Wind energy generation systems. <https://webstore.iec.ch/publication/29062>
- Monin AS, Obukhov AM. 1954. Basic laws of turbulent mixing in the surface layer of the atmosphere. Tr. Akad. Nauk. SSSR Geophiz. Inst. 24 (151): 163–187.
- Paskyabi MB. 2015. Offshore wind farm wake effect on stratification and coastal upwelling. Energy Procedia, 80, 131–140. <https://doi.org/10.1016/j.egypro.2015.11.415>
- Paskyabi MB, Fer I. 2012. Upper ocean response to large wind farm effect in the presence of surface gravity waves. Energy Procedia, 24, 245–254. <https://doi.org/10.1016/j.egypro.2012.06.106>
- Pedersen MM, Forsting AM, van der Laan P, Riva R, Romàn LAA, Risco JC, Friis-Møller M, Quick J, Christiansen JPS, Rodrigues RV, Olsen BT, Réthoré PE. 2023. PyWake 2.5.0: An open-source wind farm simulation tool. DTU Wind, Technical University Denmark.
<https://topfarm.pages.windenergy.dtu.dk/PyWake/>
- Raghukumar K, Chartrand C, Chang G, Cheung L, Roberts J. 2022. Effect of Floating Offshore Wind Turbines on Atmospheric Circulation in California. Frontiers in Energy Research, <https://doi.org/10.3389/fenrg.2022.863995>
- Skamarock C, Klemp B, Dudhia J, Gill O, Liu Z, Berner J, Wang W, Powers G, Duda G, Barker D, Huang X-Y. 2021. A Description of the Advanced Research WRF Model Version 4.3, Tech. Rep. NCAR/TN-556+STR), NCAR/UCAR [code], <https://doi.org/10.5065/1dfh-6p97>.
- Shapiro CR, Gayme DF, Meneveau C. 2018. Modeling yawed wind turbine wakes: a lifting line approach, J. Fluid Mech., 841, R1, doi:10.1017/jfm.2018.75.
- van der Laan MP, Kelly MC, Sørensen NN. 2017. A new k-epsilon model consistent with Monin–Obukhov similarity theory. Wind Energy, 20(3), 479–489. <https://doi.org/10.1002/we.2017>

- Wu S, Archer CL, Mirocha JD. 2023. New insights on wind turbine wakes from large-eddy simulation: Wake contraction, dual nature, and temperature effects. *Wind Energy*. <https://doi.org/10.1002/we.2827>
- Wu YT, Porté-Agel F. 2011. Large-Eddy Simulation of Wind-Turbine Wakes: Evaluation of Turbine Parametrisations. *Boundary-Layer Meteorology*, 138(3), 345–366. <https://doi.org/10.1007/s10546-010-9569-x>
- Zhou L, Tian Y, Roy SB, Thorncroft C, Bosart LF, Hu Y. 2012. Impacts of wind farms on land surface temperature *Nat. Clim. Change* 2, 539.
- Zong H, Porté-Agel F. 2020. A momentum-conserving wake super-position method for wind farm power prediction, *J. Fluid Mech.*, 889, 1–5, <https://doi.org/10.1017/jfm.2020.77>.

11.3 References: Agent-Based Models and Methods

- Allain G, Petigas P, Lazure P, Grellier P. 2007. Biophysical modeling of larval drift, growth and survival for the prediction of anchovy (*Engraulis encrasicolus*) recruitment in the Bay of Biscay (NE Atlantic). *Fish. Oceanogr.* 16:489–505.
- An, L., Grimm, V., Sullivan, A., Turner B.L., Malleson, N., Heppenstall, A., Vincenot, C., Robinson, D., Ye, X., Liu, J., Lindkvist, E., and Tang, W. 2021. Challenges, tasks, and opportunities in modeling agent-based complex systems, *Ecological Modeling*, 457, 109685, <https://doi.org/10.1016/j.ecolmodel.2021.109685>
- Andresen H, Strasser M, van der Meer J. 2014. Estimation of density-dependent mortality of juvenile bivalves in the Wadden Sea. *PLOS ONE* 9: e102491
- Benson T, de Bie J, Gaskell J, Vezza P, Kerr JR, Lumbroso D, Owen MR, Kemp PS. 2021. Agent-based modeling of juvenile eel migration via selective tidal stream transport. *Ecol. Model.* 443:109448.
- Dankers N. 1993. Integrated estuarine management obtaining a sustainable yield of bivalve resource while maintaining environmental quality. In: Dame R (ed) *Bivalve filter feeders in estuarine and coastal ecosystem processes*. NATO ASI Series, Vol G33. Springer, Berlin, p 479–511
- Darnaude AM, Arnaud-Haond S, Hunter E, Gaggiotti O et al. 2022. Unifying approaches to Functional Marine Connectivity for improved marine resource management: the European SEA-UNICORN COST Action. *Res Ideas Outcomes* 8: e80223
- Davies KTA, Gentleman WC, DiBacco C, Johnson CL. 2014. Semi-annual spawning in marine scallops strengthens larval recruitment and connectivity on Georges Bank: a model study. *Mar. Ecol. Prog. Ser.* 516:209-227.
- De Roos AM, Persson L. 2005. Unstructured Population Models: Do Population-Level Assumptions Yield General Theory? *Ecological Paradigms* Lost:31–62.
- Degraer S, Carey D, Coolen J, Hutchison Z, Kerckhof F, Rumes B, Vanaverbeke J. 2020. Offshore Wind Farm Artificial Reefs Affect Ecosystem Structure and Functioning: A Synthesis. *Oceanogr.* 33(4):48–57. doi:10.5670/oceanog.2020.405

- Ester, Martin, Hans-Peter Kriegel, Jörg Sander and Xiaowei Xu. 1996. A Density-Based Algorithm for Discovering Clusters in Large Spatial Databases with Noise. Knowledge Discovery and Data Mining. <https://www.dbs.ifi.lmu.de/Publikationen/Papers/KDD-96.final.frame.pdf>
- Faillietaz R, Paris CB, Irisson J-O. 2018. Larval Fish Swimming Behavior Alters Dispersal Patterns From Marine Protected Areas in the North-Western Mediterranean Sea. *Front. Mar. Sci.* 5.
- Fogarty M. 2019 Mar. Dataset: Sea Scallop Biomass. NEFSC Project. Northeast Ocean Data Portal. Available from: <https://www.northeastoceandata.org/data-download/>.
- FEHY. 2013. Fehmarnbelt Gixed Link EIA. Marine Water. Hydrography of the Fehmarnbel Area- Impact Assessment. Vol. II. Hørsholm, Denmark. FEHY consortium / co DHI. 107 p. Report No. E1RT0058. <https://vvmdocumentation.femern.com/en/4.%20E1TR0058%20Vol%20IIfa23.pdf?filename=files/B/R/4.%20E1TR0058%20Vol%20II.pdf>
- Gallagher, C.A., Chudzinska, M., Larsen-Gray, A., Pollock, C.J., Sells, S.N., White, P.J.C., and Berger, U. 2021. From theory to practice in pattern-oriented modeling: identifying and using empirical patterns in predictive models. *Biol. Rev.* 96 1868-1888. doi: 10.1111/brv.12729.
- [GEBCO] GEBCO Bathymetric Compilation Group 2020. 2020. The GEBCO_2020 Grid - a continuous terrain model of the global oceans and land. British Oceanographic Data Centre, National Oceanography Centre, NERC, UK. [accessed 2020 May 10]. doi:10.5285/a29c5465-b138-234d-e053-6c86abc040b9.
- Geweke, J. 1991. Evaluating the Accuracy of Sampling-Based Approaches to the Calculation of Posterior Moments. Fourth Valencia International Meeting on Bayesian Statistics, Peñíscola, Spain, April 15-20, 1991. <https://pdfs.semanticscholar.org/2e86/50b01dd557ffb15113c795536ea7c6ab1088.pdf>
- Glarou M, Zrust M, Svendsen JC. 2020. Using Artificial-Reef Knowledge to Enhance the Ecological Function of Offshore Wind Turbine Foundations: Implications for Fish Abundance and Diversity. *J. Mar. Sci. Eng.* 8(5):332. doi:10.3390/jmse8050332
- Goodman, L. A., & Kruskal, W. H. 1979. Measures of association for cross classifications. Measures of association for cross classifications, 2-34.
- Grimm V, Frank K, Jeltsch F, Brandl R, Uchmański J, Wissel C. 1996. Pattern-oriented modeling in population ecology. *Sci. Total Environ.* 183(1-2):151–166. doi:10.1016/0048-9697(95)04966-5
- Grimm V, Railsback SF. 2005. Individual-based Modeling and Ecology, Princeton University Press.
- Grimm V. 2005. Pattern-Oriented Modeling of Agent-Based Complex Systems: Lessons from Ecology. *Science.* 310(5750):987–991. doi:10.1126/science.1116681
- Grimm V, Railsback SF, Vincenot CE, Berger U, Gallagher C, DeAngelis DL, Edmonds B, Ge J, Giske J, Groeneveld J, et al. 2020. The ODD Protocol for Describing Agent-Based and Other Simulation Models: A Second Update to Improve Clarity, Replication, and Structural Realism. *J. Artif. Soc. Soc. Simul.* 23.
- Hansen, F.T., Pastor, A., Christensen, A. and Stuer-Lauridsen, F. 2024. Using biophysical modeling and marine connectivity to assess the risk of natural dispersal of non-indigenous species to comply with

the Ballast Water Management Convention. *Biol Invasions*. <https://doi.org/10.1007/s10530-024-03327-0>

- Hansen, F., Erichsen, A., Saurel, C., & Freitas, P. 2024. Assessing the demographic connectivity of common cockles in a shallow estuary as a basis for fisheries management and stock protection efforts. *Marine Ecology Progress Series*, 731, 293–313. <https://doi.org/10.3354/meps14297>
- Hare J. 2015. Abundance and proportion of ichthyoplankton of the Northeast U.S. Shelf from surveys conducted during the MARMAP (1977-1987) and EcoMon (1999-2008) programs. Biological and Chemical Oceanography Data Management Office (BCO-DMO). (Version 1) Version Date 2015-06-16. doi:10.1575/1912/bco-dmo.560448.1
- Heinänen S, Chudzinska ME, Brandi Mortensen J, Teo TZ, Rong Utne K, Doksæter Sivle L, Thomsen F. 2018. Integrated modeling of Atlantic mackerel distribution patterns and movements: A template for dynamic impact assessments. *Ecol. Model.* 387:118–133.
- Houde ED. 2002. Chapter 3. Mortality. In: Fuiman, L. A. and R. G. Werner (eds.), *Fishery science: The unique contribution of early life stages*. Blackwell Scientific Publishing, Oxford.
- Jenkins GP, Welsford DC, Keough MJ, Hamer PA. 1998. Diurnal and tidal vertical migration of pre-settlement King George whiting *Sillaginodes punctata* in relation to feeding and vertical distribution of prey in a temperate bay. *Mar. Ecol. Prog. Ser.* 170:239–248.
- Johnson, TL, J. van Berkel, L. O. Mortensen, M. A. Bell, I. Tiong, B. Hernandez, D. B. Snyder, F. Thomsen, and O. S. Petersen. 2021. *Hydrodynamic Modeling, Particle Tracking and Agent Based Modeling of Larvae in the U.S. Mid-Atlantic Bight*. Sterling, VA: U.S. Department of the Interior, Bureau of Ocean Energy Management.
- Kritzer JP, Sale PF. 2006. *Marine Metapopulations*. Academic Press. Amsterdam. 544 pp.
- Methratta ET. 2020. Monitoring fisheries resources at offshore wind farms: BACI vs. BAG designs. *ICES J. Mar. Sci.* 77(3):890–900. doi:10.1093/icesjms/fsaa026
- Mineur F, Cook E, Minchin D, Bohn K, Macleod A, Maggs C. 2012. Changing coasts: marine aliens and artificial structures. *Oceanogr. Mar. Biol.* 50:189-234, <https://doi.org/10.1201/b12157-5>.
- Mortensen LO, Chudzinska ME, Slabbekoorn H, Thomsen F. 2021. Agent-based models to investigate sound impact on marine animals: Bridging the gap between effects on individual behaviour and population level consequences. *Oikos*. 130(7) 1074-1086. doi.org/10.1111/oik.08078.
- Murphy, J.M., Sexton, D.M.H., Barnett, D.N., Jones, G.S., Webb, M.J., Collins, M., Stainforth, D.A., 2004. Quantification of modeling uncertainties in a large ensemble of climate change simulations. *Nature* 430, 768–772.
- Parry HR, Bithell M. 2012. Large Scale Agent-Based Modeling: A Review and Guidelines for Model Scaling. In: Heppenstall A, Crooks A, See L, Batty M. (eds) *Agent-Based Models of Geographical Systems*. Springer, Dordrecht. https://doi.org/10.1007/978-90-481-8927-4_14
- Parry HR, Evans AJ. 2008. A comparative analysis of parallel processing and super-individual methods for improving the computational performance of a large individual-based model. *Ecol. Model.* 214:141-152.

- Parker, W.S. 2013. Ensemble modeling, uncertainty and robust predictions. *WIREs Clim Change* 2013, 4:213–223. doi: 10.1002/wcc.220
- Scheffer M, Baveco JM, DeAngelis DL, Rose KA, van Nes EH. 1995. Super-individuals a simple solution for modeling large populations on an individual basis. *Ecol. Model.* 80:161–170.
- Pata, P. R., & Yñiguez, A. T. 2019. Larval connectivity patterns of the North Indo-West Pacific coral reefs. *PLoS ONE*, 14(7). <https://doi.org/10.1371/journal.pone.0219913>
- [NEFSC] Northeast Fisheries Science Center. 2021: Sea Scallop Survey. NOAA National Centers for Environmental Information. [updated 2020 May 14; accessed 2020 Jun 18]. <https://www.fisheries.noaa.gov/inport/item/22564>.
- [NOAA] National Oceanic and Atmospheric Administration. 2018. Essential Fish Habitat – Data Inventory. [accessed 2020 Sep 07]. <https://www.habitat.noaa.gov/application/efhinventory/index.html>.
- NOAA. 2007. Magnuson-Stevens Fishery Conservation and Management Act. Second Printing - As Amended Through January 12, 2007.
- NOAA. 2004. NCEI Multibeam Bathymetry Database (MBBDB). [accessed 2020 May 10]. <https://doi.org/doi:10.7289/V56T0JNC>.
- Northeast Fisheries Science Center Bottom Trawl survey data - Ocean Biodiversity Information System. 2021. Dataset: Northeast Fisheries Science Center Bottom Trawl Survey. Available from: <https://obis.org/dataset/23f104bf-b4c9-4144-955d-121c583f20d2>.
- [NROC] Northeast Regional Ocean Council. 2009. Northeast Ocean Data Portal. [accessed 2020 Mar 02]. www.northeastoceandata.org.
- Rea M.L. and Parker R.A. 1992. “Designing and Conducting Survey Research A Comprehensive Guide,” Jossey-Bass Publishers, San Francisco.
- Richards WJ, Lindeman KC. 1987. Recruitment dynamics of reef fishes: Planktonic processes, settlement and demersal ecologies, and fishery analysis. *Bulletin of Marine Science* 41(2):392–410.
- Schober, P., Boer, C., and Schwarte, L.A. 2018. Correlation Coefficients: Appropriate Use and Interpretation. *Anesthesia & Analgesia* 126(5):p 1763-1768. DOI: 10.1213/ANE.0000000000002864
- Scikit-learn. 2024. sklearn.cluster. DBSCAN. <https://scikit-learn.org/stable/modules/generated/sklearn.cluster.DBSCAN.html>
- Shmookler R. 2016. Dataset: Scallop biomass (meat weight in kilograms) northeast United States. Northeast Ocean Data. Available from: <https://www.northeastoceandata.org/files/metadata/Themes/Fish/ScallopBiomass.pdf> Northeast Fisheries Science Center for the Northeast Regional Ocean Council, prepared by the Marine-life Data and Analysis Team (MDAT).
- Sinclair M. 1988. Marine populations: an essay on population regulation and speciation. University of Washington Press, Seattle.

- [SMASST] School of Marine Science and Technology, University of Massachusetts Dartmouth. 2016. Average (2003-2012) Presence/Abundance from SMASST Survey Northeast United States. [accessed 2020 Sep 07].
- Steves BP, Cowen RK, Malchoff MA. 1999. Settlement and nursery habitats for demersal fishes on the continental shelf of the New York Bight. *Fish. Bull.* 98:167-188.
- Stillman, R.A., Railsback, S.F., Giske, J., Berger, U., Grimm, V., 2015. Making predictions in a changing world: the benefits of individual- based ecology. *Bioscience* 65, 140–145
- Stokesbury KE. 2016. Dataset: Sea Scallops 2003-2012 Abundance (SMASST Average Presence/Abundance Dataset) (TNC). NE Ocean Data, Northeast Ocean Data, Northeast Ocean Data. Available from: <https://easterndivision.s3.amazonaws.com/Marine/MooreGrant/AveragePresenceAbundanceSMASST.pdf>.
- Stokesbury KE. 2020. Dataset: Sea Scallops Potential Reproductive Output. Available from: <https://www.northeastoceandata.org/data-download/>.
- Stokesbury, KE and Bethoney ND. 2020. How many sea scallops are there and why does it matter? *Frontiers in Ecology and the Environment*. 18(9):513-519.
- Swearer, S. E., Treml, E. A., & Shima, J. S. 2019. A review of biophysical models of marine larval dispersal. In *Oceanography and Marine Biology* (Vol. 57, pp. 325–356). CRC Press. <https://doi.org/10.1201/9780429026379-7>
- Tian T, Fiksen Ø, Folkvord A. 2007. Estimating larval fish growth under size-dependent mortality: a numerical analysis of bias. *Can. J. Fish. Aquat.* 64:554–562.
- Thomsen F, Mortensen LO, van Berkel JJ. 2019. Agent-Based Modeling: Dynamic Mapping of the Movements of Marine Life. *Environment Coastal and Offshore (ECO)*, Special Issue Ocean Sound, 31-33.
- [USGS] United States Geological Survey. 2000. CONMAP Sediment Maps. <https://pubs.usgs.gov/of/2000/of00-358/mapping/conmap/conmapsg.htm>
- USGS. 2005. CONMAPSG: Continental Margin Mapping (CONMAP) sediments grain size distribution for the United States East Coast Continental Margin. Open File Report 2005-1001, US Geological Survey, Coastal and Marine Geology Program, Woods Hole Science Center, Woods Hole, MA. [accessed 2020 Jun 15].
- van Berkel JJ, Burchard H, Christensen A, Mortensen LO, Svenstrup Petersen O, Thomsen F. 2020. The effects of offshore wind farms on hydrodynamics and implications for fishes. *Oceanogr.* 33(4):108–117, <https://doi.org/10.5670/oceanog.2020.410>.
- Virtanen P, Gommers R, Oliphant,TE, Haberland,M, Reddy T, Cournapeau D, Burovski E, Peterson P, Weckesser W, Bright J, van der Walt SJ, Brett M, Wilson J, Millman KJ, Mayorov N, Nelson ARJ, Jones E, Kern R, Larson E, ... Vázquez-Baeza Y. 2020. SciPy 1.0: fundamental algorithms for scientific computing in Python. *Nature Methods*, 17(3), 261–272. <https://doi.org/10.1038/s41592-019-0686-2>

11.4 References: Sea Scallop

- Bethoney ND, Asci S, Stokesbury KDE. 2016. Implications of extremely high recruitment events into the U.S. sea scallop fishery. *Mar. Ecol. Prog. Ser.* 547: 137-147.
- Carey JD, Stokesbury KDE. 2011. An assessment of juvenile and adult sea scallop, *Placopecten magellanicus*, distribution in the northwest Atlantic using high-resolution still imagery. *J. Shellfish Res.* 30 (3): 569–582.
- Culliney JL. 1974. Larval development of the giant scallop *Placopecten magellanicus* (Gmelin). *Biol. Bull.* 147:321–332.
- Gaichas SK, DePiper GS, Seagraves RJ, Muffley BW, Sabo MG, Colburn LL, Loftus AJ. 2018. Implementing ecosystem approaches to fishery management: Risk assessment in the U.S. Mid-Atlantic. *Frontiers in Marine Science* 5:442. doi: 10.3389/fmars.2018.00442.
- Gallager, S.M., J.L. Manuel, D.A. Manning, and R. O’Dor. 1996. Ontogenetic changes in the vertical distribution of giant scallop larvae, *Placopecten magellanicus*, in 9-m deep mesocosms as a function of light, food, and temperature stratification. *Mar. Biol.* 124: 679-692.
- Hare JA, Walsh HJ, Wuenschel MJ. 2006. Sinking rates of late-stage fish larvae: Implications for larval ingress into estuarine nursery habitats. *J. Exp. Mar. Biol. Ecol.* 330(2), 493-504.
- Hart DR, Chute AS. 2004. Essential fish habitat source document: sea scallop, *Placopecten magellanicus*, life history and habitat characteristics. NOAA Tech Memo NMFS NE-189, Woods Hole, MA. 21p.
- Hart, D. R., Munroe, D. M., Caracappa, J. C., Haidvogel, D., Shank, B. V., Rudders, D. B., Klinck, J. M., Hofmann, E. E., and Powell, E. N. 2020. Spillover of sea scallops from rotational closures in the Mid-Atlantic Bight (United States). – *ICES Journal of Marine Science*, 77: 1992– 2002.
- Hart DR, Chang J. 2022. Estimating natural mortality for Atlantic sea scallops (*Placopecten magellanicus*) using a size-based stock assessment model. *Fisheries Research* 254. <https://doi.org/10.1016/j.fishres.2022.106423>.
- Langton RW, Robinson WE, Schick D. 1987. Fecundity and reproductive effort of sea scallops *Placopecten magellanicus* from the Gulf of Maine. *Mar. Ecol. Prog. Ser.* 37: 19-25.
- MacKenzie, C.L., Jr., A.S. Merrill, and F.M. Serchuk. 1978. Sea scallop resources off the northeastern U.S. coast, 1975. *Mar. Fish. Rev.* 40(2): 19-23.
- McGarvey R, Serchuk FM, McLaren IA. 1992. Statistics of Reproduction and Early Life History Survival of the Georges Bank Sea Scallop (*Placopecten magellanicus*) Population. *J. Northwest Atl. Fish. Sci.* 13:83–99.
- Munroe DM, Haidvogel D, Caracappa JC, Klinck JM, Powell EN, Hofmann EE, Shank BV, Hart DR. 2018. Modeling larval dispersal and connectivity for Atlantic sea scallop (*Placopecten magellanicus*) in the Middle Atlantic Bight. *Fish. Res.* 208:7–15.
- [NEFMC] New England Fishery Management Council. 2014. Framework 25 to the Scallop Including a Final Environmental Assessment (EA), an Initial Regulatory Flexibility Analysis and Stock Assessment and Fishery Evaluation (SAFE Report), Newburyport, MA.

- Packer, D.B., L.M. Cargnelli, S.J. Griesbach, and S.E. Shumway. 1999. Essential fish habitat source document: Sea Scallop, *Placopecten magellanicus*, life history and habitat characteristics. NOAA Tech. Mem. NMFS-NE-134. 21 p.
- Pearce CM, Manuel JL, Gallager SM, Manning DA, O'Dor RK, Bourget E. 2004. Depth and timing of settlement of veligers from different populations of giant scallop, *Placopecten magellanicus* (Gmelin), in thermally stratified mesocosms. J. Exp. Mar. Biol. Ecol. 312:187–214.
- Scheffer, M., Baveco, J.M., DeAngelis, D.L., Rose, K.A. and van Nes, E. 1995. Super-individuals a simple solution for modeling large populations on an individual basis. Ecological modeling, 80(2-3), pp.161-170.
- Stewart PL, Arnold SH. 1994. Environmental requirements of the sea scallop (*Placopecten magellanicus*) in eastern Canada and its response to human impacts. Can. Tech. Rep. Fish. Aquat. Sci. 2005: 1-36
- Stokesbury KDE. 2012. Stock Definition and Recruitment: Implications for the U.S. Sea Scallop (*Placopecten magellanicus*) Fishery from 2003 to 2011. Rev. Fish. Sci. Aquac., 20:3, 154-164.
- Stokesbury KDE, Harris BP, Marino MC, Nogueira JJ. 2007. Sea scallop mass mortality in a Marine Protected Area. Mar. Ecol. Prog. Ser. 349:151–158.
- Stokesbury KDE, O'Keefe, CE, Harris, BP. 2016. Fisheries Sea Scallop, *Placopecten magellanicus*. Pp.719-736, in: Shumway, S.E. and Parsons, G.J. (eds), *Scallops: Biology, Ecology, Aquaculture, and Fisheries*. Elsevier.
- Thouzeau G, Robert G, Smith SJ. 1991. Spatial variability in distribution and growth of juvenile and adult sea scallops *Placopecten magellanicus* (Gmelin) on eastern Georges Bank (Northwest Atlantic). Mar. Ecol. Prog. Ser. 74:205–218.
- Tian RC, Chen C, Stokesbury KDE, Rothschild B, Cowles GW, Xu Q, Hu S, Harris BP, Marino MC II. 2009. Modeling the connectivity between sea scallop populations in the Middle Atlantic Bight and over Georges Bank. Mar. Ecol. Prog. Ser. 380:147–160.
- Torre MP, Tanaka KR, Chen Y. 2018. A spatiotemporal Evaluation of Atlantic Sea Scallop *Placopecten magellanicus* Habitat in the Gulf of Maine Using a Bioclimate Envelope Model. Mar. Coast. Fish. 10:224–235.
- Tremblay JM, Loder J, Werner F, Naimie C, Page F, Sinclair M. 1994. Drift of sea scallop larvae *Placopecten magellanicus* on Georges Bank: a model study of the roles of mean advection, larval behavior and larval origin. Deep Sea Res. Part II Top. Stud. Oceanogr. 41:7–49.
- Tremblay MJ, Sinclair M. 1990. Sea scallop larvae *Placopecten magellanicus* on Georges Bank: vertical distribution in relation to water column stratification and food. Mar Ecol Prog Ser 61:1–15
- Tremblay AM, Sinclair MM. 1988. The Vertical and Horizontal Distribution of Sea Scallop (*Placopecten magellanicus*) Larvae in the Bay of Fundy in 1984 and 1985. J. Northwest Atl. Fish. Sci. 8:43–53.

11.5 References: Surfclam

- Cargnelli LM, Griesbach SJ, Packer DB, Weissberger E. 1999. Essential Fish Habitat Source Document: Atlantic Surfclam *Spisula solidissima*, Life History and Habitat Characteristics. NOAA Tech Mem NMFS-NE 142:1–13.
- Castagna M, Chanley P. 1973. Salinity tolerance of some marine bivalves from inshore and estuarine environments in Virginia waters on the western Mid-Atlantic coast. *Malacologia* 12:47-96.
- Fay CW, Neves RJ, Pardue GB. 1983. Species profiles: life histories and environmental requirements of coastal fishes and invertebrates (Mid-Atlantic): surfclam. U.S. Fish Wildl Serv, Div Biol Serv, FWS/OBS-82/11.13. 23 p.
- Gaichas SK, DePiper GS, Seagraves RJ, Muffley BW, Sabo MG, Colburn LL, Loftus AJ. 2018. Implementing ecosystem approaches to fishery management: Risk assessment in the U.S. Mid-Atlantic. *Frontiers in Marine Science* 5:442. doi: 10.3389/fmars.2018.00442.
- Jacobson L, Hennen D. 2019. Northeast Fisheries Science Center Improving the NEFSC Clam Survey for Atlantic Surfclams and Ocean Quahogs. Available from: <http://www.nefsc.noaa.gov/publications/>.
- NOAA. 2022. NOAA Fisheries Office of Science and Technology, Commercial Landings Query. Available from: www.fisheries.noaa.gov/foss, Accessed 12-28-2023.
- Ma H, Grassle JP, Rosario JM. 2006. Initial recruitment and growth of surfclams (*Spisula solidissima* Dillwyn) on the inner continental shelf of New Jersey. *J Shellfish Res* 25:481–489.
- Loosanoff VL, Davis HC. 1963. Rearing of bivalve mollusks. *Adv. Mar. Biol.* 1:1-136.
- Mann R, Campos BC, Luckenback MW. 1991. Swimming rate and responses of larvae of three mactrid bivalves to salinity discontinuities. *Mar Ecol Prog Ser* 68:257-269.
- Munroe DM, Powell EN, Klinck JM, Scheld AM, Borsetti S, Beckensteiner J, Hofmann EE. 2022. The Atlantic surfclam fishery and offshore wind energy development: 1. Model development and verification. *ICES J Mar Sci* 79(6):1787–1800. DOI: 10.1093/icesjms/fsac108.
- Palmer CT. 1991. Life and death of a small-scale fishery surfclam dredging in southern Maine. *MAST Marit Anthropol Stud* 4:56–72.
- Ropes JW. 1968. Reproductive Cycle of the surfclam, *Spisula solidissima*, in Offshore New Jersey. *Bull* 135(2).
- Ropes JW. 1979. Shell length at sexual maturity of surfclams, *Spisula solidissima*, from an inshore habitat. *Proc Nat Shellfish Assoc* 69:85-91.
- Ropes JR. 1980. Biological and Fisheries Data on the Atlantic surfclam *Spisula solidissima*. Woods Hole Laboratory, Northeast Fisheries Center, National Oceanic and Atmospheric Administration, Tech. Ser. Rep. No. 24.

- Shanks AL, Brink L. 2005. Upwelling, downwelling, and cross-shelf transport of bivalve larvae: test of a hypothesis. *Mar Ecol Prog Ser* 302:1–12.
- Snelgrove PVR, Grassle JP, Butman CA. 1998. Sediment choice by settling larvae of the bivalve, *Spisula solidissima* (Dillwyn), in flow and still water. *J Exp Mar Biol Ecol* 231.
- Walker RL, Hurley DH, Jansen ML. 1996. Fecundity of the Southern Atlantic Surfclam *Spisula solidissima* similis. *Prog Fish-Culturist* 58(4):253–257. DOI: 10.1577/1548-8640(1996)058<0253:FOTSAS>2.3.CO;2.
- Walker RL, O’Beirn FX. 1996. Embryonic and Larval Development of *Spisula solidissima* similis (Say, 1822) (Bivalvia: Mactridae). *Veliger* 39(1).
- Weinberg JR, Dahlgren TG, Halanych KM. 2002. Influence of Rising Sea Temperature on Commercial Bivalve Species of the U.S. Atlantic Coast. *Am Fish Soc Symp* 32:131-140.
- Weinberg JR. 2005. Bathymetric shift in the distribution of Atlantic surfclams: Response to warmer ocean temperature. *ICES J Mar Sci* 62(7):1444–1453. DOI: 10.1016/j.icesjms.2005.04.020.
- Weissberger EJ, Grassle JP. 2003. Settlement, first-year growth, and mortality of surfclams, *Spisula solidissima*. *Estuar Coast Shelf Sci* 56(3-4):
- Wright DA, Kennedy VS, Roosenberg WH, Castagna M, Mihursky JA. 1983. Temperature tolerance of embryos and larvae of five bivalve species under simulated power plant entrainment conditions: a synthesis. *Mar Biol* 77:271-278.
- Zhang X, Haidvogel D, Munroe D, Powell EN, Klinck J, Mann R, Castruccio FS. 2015. Modeling larval connectivity of the Atlantic surfclams within the Middle Atlantic Bight: Model development, larval dispersal and metapopulation connectivity. *Estuar Coast Shelf Sci* 153:38–53. DOI: 10.1016/j.ecss.2014.11.033.
- Zhang X, Munroe D, Haidvogel D, Powell EN. 2016. Atlantic surfclam connectivity within the Middle Atlantic Bight: Mechanisms underlying variation in larval transport and settlement. *Estuar Coast Shelf Sci* 173:65–78. DOI: 10.1016/j.ecss.2016.02.019.

11.6 References: Summer Flounder

- Able KW, Kaiser SC. 1994. Synthesis of summer flounder habitat parameters. 68 p. NOAA Coastal Ocean Program Decision Analysis Series No. 1.
- Able KW, Sullivan MC, Hare JA, Bath-Martin G, Taylor JC, Hagan R. 2010. Larval abundance of summer flounder (*Paralichthys dentatus*) as a measure of recruitment and stock status. *Fish. Bull.* 109: 68-78.
- Barbut L, Groot CC, Delerue-Ricard S, Vandamme S, Volckaert FA, Lacroix G. 2019. How larval traits of six flatfish species impact connectivity. *Limnol. Oceanogr.* 64:1150–1171.
- Benson T, de Bie J, Gaskell J, Vezza P, Kerr JR, Lumbroso D, Owen MR, Kemp PS. 2021. Agent-based modeling of juvenile eel migration via selective tidal stream transport. *Ecol. Model.* 443:109448.
- Bisbal GA, Bengtson DA. 1995. Effects of delayed feeding on survival and growth of summer flounder *Paralichthys dentatus* larvae. *Mar. Ecol. Prog. Ser.* 121:301–306.

- Burke JS, Miller JS, Hoss DE. 1991. Immigration and settlement pattern of *Paralichthys dentatus* and *P. lethostigma* in an estuarine nursery ground, North Carolina, USA. *Neth. J. Sea Res.* 27: 393–405.
- Drake PT, Edwards CA, Morgan SG, Satterthwaite EV. 2018. Shoreward swimming boosts modeled nearshore larval supply and pelagic connectivity in a coastal upwelling region, *Journal of Marine Systems*, Volume 187, Pages 96–110, ISSN 0924-7963, <https://doi.org/10.1016/j.jmarsys.2018.07.004>.
- Faillietaz R, Paris CB, Irisson J-O. 2018. Larval Fish Swimming Behavior Alters Dispersal Patterns From Marine Protected Areas in the North-Western Mediterranean Sea. *Front. Mar. Sci.* 5.
- Forward RB, Reinsel KA, Peters DS, Tankersley RA, Churchill JH, Crowder LB, Hettler WF, Warlen SM, Green MD. 1999. Transport of fish larvae through a tidal inlet. *Fish. Oceanogr.* 8:153–172.
- Gaichas SK, DePiper GS, Seagraves RJ, Muffley BW, Sabo MG, Colburn LL, Loftus AJ. 2018. Implementing ecosystem approaches to fishery management: Risk assessment in the U.S. Mid-Atlantic. *Frontiers in Marine Science* 5:442. doi: 10.3389/fmars.2018.00442.
- Gilbert CR. 1986. Species profiles: life histories and environmental requirements of coastal fishes and invertebrates (south Florida): southern, gulf, and summer flounders. U.S. Fish Wildl. Serv. Biol. Rep. 82 (11.54): 24.
- Hare, JA, Walsh, HJ, Wuenschel, MJ. 2006. Sinking rates of late-stage fish larvae: Implications for larval ingress into estuarine nursery habitats. *J. Exp. Mar. Biol. Ecol.* 330(2), 493–504.
- Henderson MJ, Fabrizio MC. 2014. Small-Scale Vertical Movements of Summer Flounder Relative to Diurnal, Tidal, and Temperature Changes. *Mar. Coast. Fish.* 6(1):108–118. doi:10.1080/19425120.2014.893468
- Hoey JA, Pinsky ML. 2018 Genomic signatures of environmental selection despite near-panmixia in summer flounder. *Evol. Appl.* 11:1732–1747.
- Hoey JA, Fodrie FJ, Walker QA, Hilton EJ, Kellison GT, Targett TE, Taylor JC, Able KW, Pinsky ML. 2020. Using multiple natural tags provides evidence for extensive larval dispersal across space and through time in summer flounder. *Mol. Ecol.* 29:1421–1435.
- Houde ED. 1989. Comparative Growth, Mortality, and Energetics of Marine Fish Larvae: Temperature and Implied Latitudinal Effects. *Fish. Bull. U.S.* 87:471–495.
- Howson UA, Targett TE. 2019. Comparison of thermohaline optima for juveniles of two sympatric paralichthyid flounders: ecophysiological evaluation of estuarine nursery quality. *Estuaries Coast.* 43: 135–150.
- Johns DM, Howell WH. 1980. Yolk Utilization in Summer Flounder (*Paralichthys dentatus*) Embryos and Larvae Reared at Two Temperatures. *Mar. Ecol. Prog. Ser.* 2:1–8.
- Keefe M, Able KW. 1993. Patterns of metamorphosis in summer flounder, *Paralichthys dentatus*. *J. Fish Biol.* 42:713–728.
- Kraus RT, Musick JA. 2001. A brief interpretation of summer flounder, *Paralichthys dentatus*, movements and stock structure with new tagging data on juveniles. *Mar. Fish. Rev.* 63(3): 1–6.
- Martinez GM, Bolker JA. 2003. Embryonic and Larval Staging of Summer Flounder (*Paralichthys dentatus*). *J. Morphol.* 255:162–176.

- Miller JM, Burke JS, Fitzhugh GR. 1991. Early life history patterns of Atlantic North American flatfish: Likely (and unlikely) factors controlling recruitment. *Neth. J. Sea Res.* 27:261–275.
- Morse WW. 1981. Reproduction of the summer flounder, *Paralichthys dentatus* (L.). *J. Fish Biol.* 19:189–203.
- Packer DB, Griesbach SJ, Berrien PL, Zetlin CA, Johnson DL, Morse WW. 1999. Essential fish habitat source document: Summer flounder, *Paralichthys dentatus*, life history and habitat characteristics. NOAA Tech Memo NMFS NE 151: 88.
- Perretti CT, Thorson JT. 2019. Spatio-temporal dynamics of summer flounder (*Paralichthys dentatus*) on the Northeast U.S. shelf. *Fish. Res.* 215: 62-68.
- Smith WG. 1973. The distribution of summer flounder, *Paralichthys dentatus*, eggs and larvae on the continental shelf between Cape Cod and Cape Lookout, 1965-66 *Fish. Bull.* 71 (2):527- 548.
- Taylor, D.L., McNamee, J., Lake, J., Gervasi, C.L. and Palance, D.G., 2016. Juvenile winter flounder (*Pseudopleuronectes americanus*) and summer flounder (*Paralichthys dentatus*) utilization of southern New England nurseries: comparisons among estuarine, tidal river, and coastal lagoon shallow-water habitats. *Estuaries and Coasts*, 39, pp.1505-1525.
- Terciero M. 2018. The summer flounder chronicles III: struggling with success, 2011–2016. *Rev. Fish Biol. Fish.* 28:381–404.
- van Maaren CC, Daniels HV. 2000. Temperature Tolerance and Oxygen Consumption Rates for Juvenile Southern Flounder Acclimated to Five Different Temperatures. In *Spawning and Maturation of Aquaculture Species*. Tamaru, C.C., Tamaru, C.S., McVey, J.P., and Ikuta, K. (eds) *Proceedings of the United States-Japan Natural Resources meeting*. UJNR Technical Report No. 28: 135-140.



Department of the Interior (DOI)

The Department of the Interior protects and manages the Nation's natural resources and cultural heritage; provides scientific and other information about those resources; and honors the Nation's trust responsibilities or special commitments to American Indians, Alaska Natives, and affiliated island communities.



Bureau of Ocean Energy Management (BOEM)

The mission of the Bureau of Ocean Energy Management is to manage development of U.S. Outer Continental Shelf energy and mineral resources in an environmentally and economically responsible way.

BOEM Environmental Studies Program

The mission of the Environmental Studies Program is to provide the information needed to predict, assess, and manage impacts from offshore energy and marine mineral exploration, development, and production activities on human, marine, and coastal environments. The proposal, selection, research, review, collaboration, production, and dissemination of each of BOEM's Environmental Studies follows the DOI Code of Scientific and Scholarly Conduct, in support of a culture of scientific and professional integrity, as set out in the DOI Departmental Manual (305 DM 3).

Appendix A: Supplementary Hydrodynamic Modeling Results

A.1 Model Quality Indices

To obtain an objective and quantitative measure of how well the model data compared to the observed data, several statistical parameters so-called quality indices (QI's) are calculated.

Prior to the comparisons, the model data are synchronized to the time stamps of the observations so that both time series had equal length and overlapping time stamps. For each valid observation, measured at time t , the corresponding model value is found using linear interpolation between the model time steps before and after t . Only observed values that had model values within \pm the representative sampling or averaging period of the observations are included (e.g. for 10-min observed wind speeds measured every 10 min compared to modeled values every hour, only the observed value every hour is included in the comparison).

The comparisons of the synchronized observed and modeled data are illustrated in (some of) the following figures:

- Time series plot including general statistics
- Scatter plot including quantiles, QQ-fit and QI's (dots colored according to the density)
- Histogram of occurrence vs. magnitude or direction
- Dual rose plot (overlapping roses)

The quality indices are described below. Their definitions are listed in **Table A.1**. Most of the quality indices are based on the entire data set, and hence the quality indices should be considered averaged measures and may not be representative of the accuracy during rare conditions.

The MEAN represents the mean of modeled data, while the BIAS is the mean difference between the modeled and observed data. AME is the mean of the absolute difference, and RMSE is the root mean square of the difference. The MEAN, BIAS, AME and RMSE are given as absolute values and relative to the average of the observed data in percent in the scatter plot.

The scatter index (SI) is a non-dimensional measure of the difference calculated as the unbiased root-mean-square difference relative to the mean absolute value of the observations. In open water, an SI below 0.2 is usually considered a small difference (excellent agreement) for significant wave heights. In confined areas or during calm conditions, where mean significant wave heights are generally lower, a slightly higher SI may be acceptable (the definition of SI implies that it is negatively biased (lower) for time series with high mean values compared to time series with lower mean values (and same scatter/spreading), although it is normalized).

EV is the explained variation and measures the proportion [0 - 1] to which the model accounts for the variation (dispersion) of the observations.

The correlation coefficient (CC) is a non-dimensional measure reflecting the degree to which the variation of the first variable is reflected linearly in the variation of the second variable. A value close to 0 indicates very limited or no (linear) correlation between the two data sets, while a value close to 1 indicates a very high or perfect correlation. Typically, a CC above 0.9 is considered a high correlation (good agreement) for wave heights. It is noted that CC is 1 (or -1) for any two fully linearly correlated variables, even if they are not 1:1. However, the slope and intercept of the linear relation may be different from 1 and 0, respectively, despite CC of 1 (or -1).

The Q-Q line slope and intercept are found from a linear fit to the data quantiles in a least-square sense. The lower and uppermost quantiles are not included on the fit. A regression line slope different from 1 may indicate a trend in the difference.

The peak ratio (PR) is the average of the N_{peak} highest model values divided by the average of the N_{peak} highest observations. The peaks are found individually for each data set through the Peak-Over-Threshold (POT) method applying an average annual number of exceedances of 4 and an inter-event time of 36 hours. A general underestimation of the modeled peak events results in PR below 1, while an overestimation results in a PR above 1.

An example of a peak plot is shown in **Figure A.1**. 'X' represents the observed peaks (x-axis), while 'Y' represents the modeled peaks (y-axis), both represented by circles ('o') in the plot. The joint (coinciding) peaks, defined as any X and Y peaks within ± 36 hours of each other (i.e. less than or equal to the number of individual peaks), are represented by crosses ('x'). Hence, the joint peaks ('x') overlap with the individual peaks ('o') only if they occur at the same time exactly. Otherwise, the joint peaks ('x') represent an additional point in the plot, which may be associated with the observed and modeled individual peaks ('o') by searching in the respective X and Y-axis directions, see example with red lines in **Figure A.1**. It is seen that the 'X' peaks are often underneath the 1:1 line, while the 'Y' peaks are often above the 1:1 line.

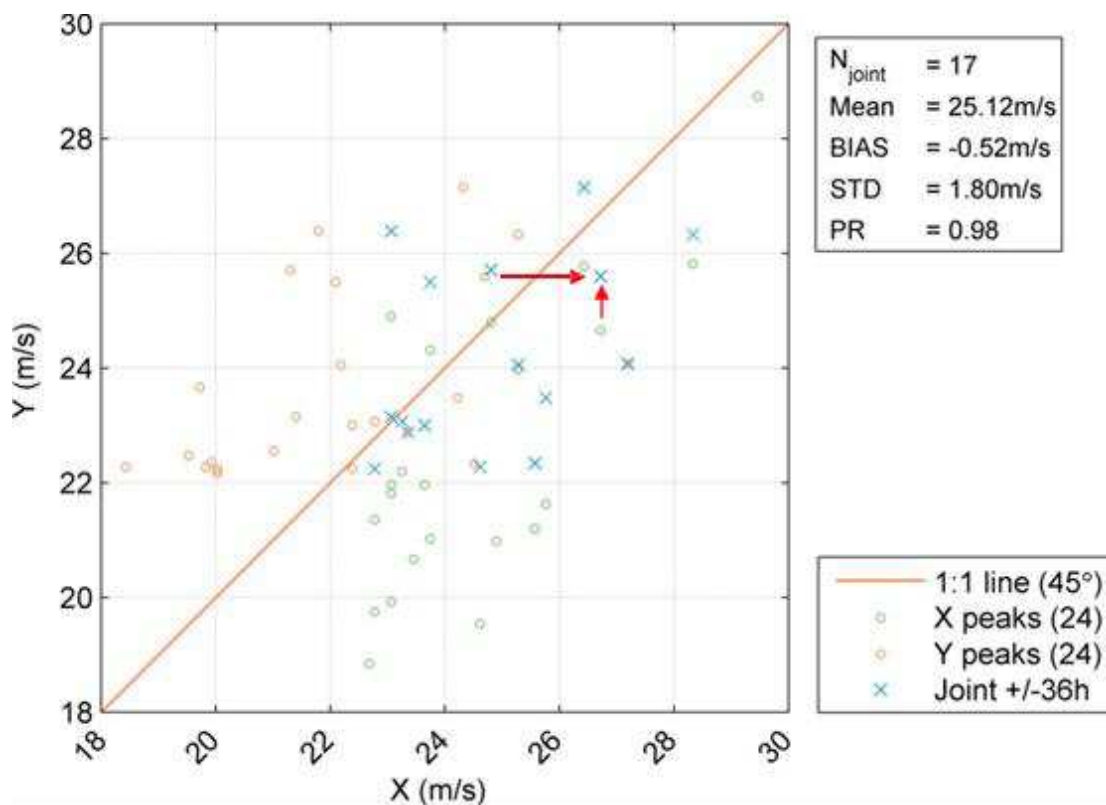


Figure A.1. Example of Peak Event Plot (Wind Speed)

Table A.1. Definition of Model Quality Indices (X = Observation, Y = Model)

Abbreviation	Description	Definition
N	Number of data (synchronized)	—
MEAN	Mean of Y data, Mean of X data	$\bar{Y} = \frac{\sum_{i=1}^N Y_i}{N}, \quad \bar{X} = \frac{\sum_{i=1}^N X_i}{N}$
STD	Standard deviation of Y data, Standard deviation of X data	$\sqrt{\frac{\sum_{i=1}^N (Y_i - \bar{Y})^2}{N - 1}}, \quad \sqrt{\frac{\sum_{i=1}^N (X_i - \bar{X})^2}{N - 1}}$
BIAS	Mean difference	$\bar{Y} - \bar{X} = \sum_{i=1}^N (Y - X)_i$
AME	Absolute mean difference	$\sum_{i=1}^N (Y - X)_i$
RMSE	Root mean square difference	$\sqrt{\sum_{i=1}^N (Y - X_i)^2}$
SI	Scatter index (unbiased)	$\frac{\sqrt{\sum_{i=1}^N (Y - X - BIAS)_i^2}}{\sum_{i=1}^N X_i }$
EV	Explained variance	$\frac{\sum_{i=1}^N (X_i - \bar{X})^2 - \sum_{i=1}^N [(X_i - \bar{X}) - (Y_i - \bar{Y})]^2}{\sum_{i=1}^N (X_i - X)^2}$
CC	Correlation coefficient	$\frac{\sum_{i=1}^N (X_i - \bar{X})(Y_i - \bar{Y})}{\sqrt{\sum_{i=1}^N (X_i - \bar{X})^2 (Y_i - \bar{Y})^2}}$
QQ	Quantile-Quantile (line slope and intercept)	Linear least square fit to quantiles
PR	Peak ratio (of N_{peak} highest events)	$PR = \frac{\sum_{i=1}^{N_{peak}} Y_i}{\sum_{i=1}^{N_{peak}} X_i}$

Table A.2. Locations and Deployment Details of Observational Stations

Name of Observational Station	Latitude	Longitude	Layer Extracted	Water Depth (m)	Time Period of Measurement
Pioneer Inshore	40.36N	70.88W	Near surface	3.62	Nov 2017 – Dec 2020
			Midwater	47.3	
			Near Bottom	63.2	
Pioneer Upstream Inshore	40.36N	70.78W	Near surface	4.23	Jan 2017 – Dec 2020
			Midwater	47.2	
			Near Bottom	62.8	
Pioneer Central Surface	40.13N	70.78W	Near surface	6.3	Jun 2017 – Dec 2020
			Midwater	66.4	
			Near Bottom	123	
MVCO	41.20N	70.80W	Near surface	25	Mar 2017 – Dec 2017
			Midwater	5	Mar 2017 – Sep 2018
			Near Bottom	1	Mar 2017 – Sep 2018
NOAA ADCP S44024	42.33N	65.91W	Near surface	2	Jan 2017 – Dec 2020
			Midwater	98	
NOAA ADCP S44034	44.10N	68.11W	Near surface	2	Jan 2017 – Dec 2020
			Midwater	46	
			Near Bottom	90	
NOAA ADCP S44033	44.05N	69.00W	Near surface	2	Jan 2017 – Dec 2020
			Midwater	50	
NOAA ADCP S44032	43.72N	69.36W	Near surface	2	Jan 2017 – Dec 2020
NOAA ADCP S44030	43.18N	70.43W	Near surface	2	Jan 2017 – Dec 2020
NOAA Station 44088	36.61N	74.84W	Near surface	1	Jul 2020– Dec 2020
NOAA Station 44064	37.00N	76.09W	Near surface	3	May 2018 – Jun 2020
NOAA Station 44072	37.20N	76.27W	Near surface	3	Feb 2018 – Dec 2020
NOAA Station 41108	33.72N	78.02W	Near surface	1	Feb 2020 – Dec 2020
NOAA Station 41112	30.71N	81.29W	Near surface	1	Aug 2020 – Dec 2020
Atlantic Shores	39.37N	73.89W	Near surface	5	Jan 2020 – May 2020
			Midwater	15	
			Near Bottom	28	
NYSERDA N05	39.97N	72.72W	Near surface	5	Jan 2020 – Dec 2020
			Midwater	25	
			Near Bottom	50	
NYSERDA N06	39.55N	73.43W	Near surface	5	Jan 2020 – Dec 2020
			Midwater	15	
			Near Bottom	32	
Ørsted 180	40.92N	70.93W	Near surface	55.55	Sep 2017 – Dec 2018
Ørsted 190	41.12N	70.58W	Near surface	42.2	Aug 2017 – Dec 2018
Ørsted 220	39.13N	74.17W	Near surface	28.6	Aug 2017 – Dec 2018
Ørsted 230	39.07N	74.44W	Near surface	18.6	Aug 2018 – Jun 2020
Ørsted 240	41.08N	71.22W	Near surface	35.38	Jan 2020 – Aug 2020
Ørsted 250	38.68N	74.76W	Near surface	15	Nov 2018 – May 2020
RODEO	36.90N	75.49W	Near Surface	25	Aug 2020 – Dec 2020

Specific to the Coastal Pioneer Array maintained by Ocean Observation Initiative, this array consists of several profiler moorings including a velocity profiler ADCP. This array is located approximately 120 km south of Martha's Vineyard (39.6 N, 70.6 W) at the shelf edge (**Figure A.3**). The stations used for model comparisons include the central surface, inshore, and upstream inshore stations, details of which are given in **Table A.3**. Observational data for each station including time series, current rose, scatter, and frequency of exceedance plots, are compared to model output in the Figures below.

Table A.3. Ocean Observation Initiative Pioneer Array Stations used for Model Comparisons

Profiler	Bottom (m)	Intermediate (m)	Surface (m)	Total Depth (m)
Central Surface	-122.0	-66.0	-10.1	135
Inshore	-63.0	-47.0	-10.5	92
Upstream Inshore	-63.0	-47.0	-10.6	95

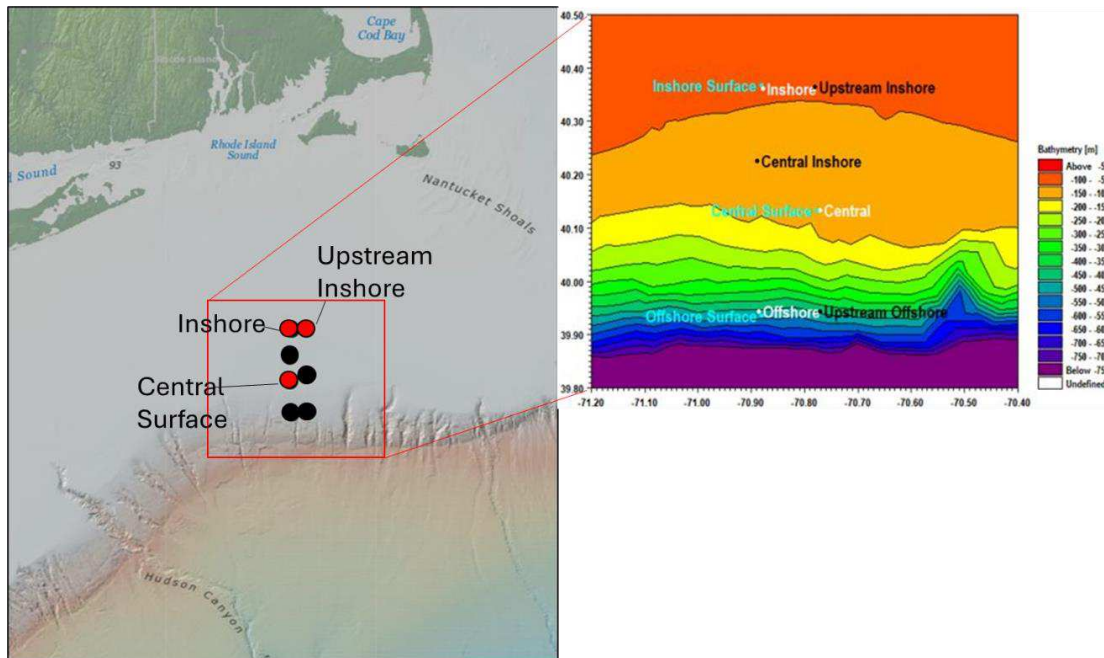


Figure A.3. Ocean Observation Initiative Pioneer Array location. Red Stations are Stations used for Model Comparisons

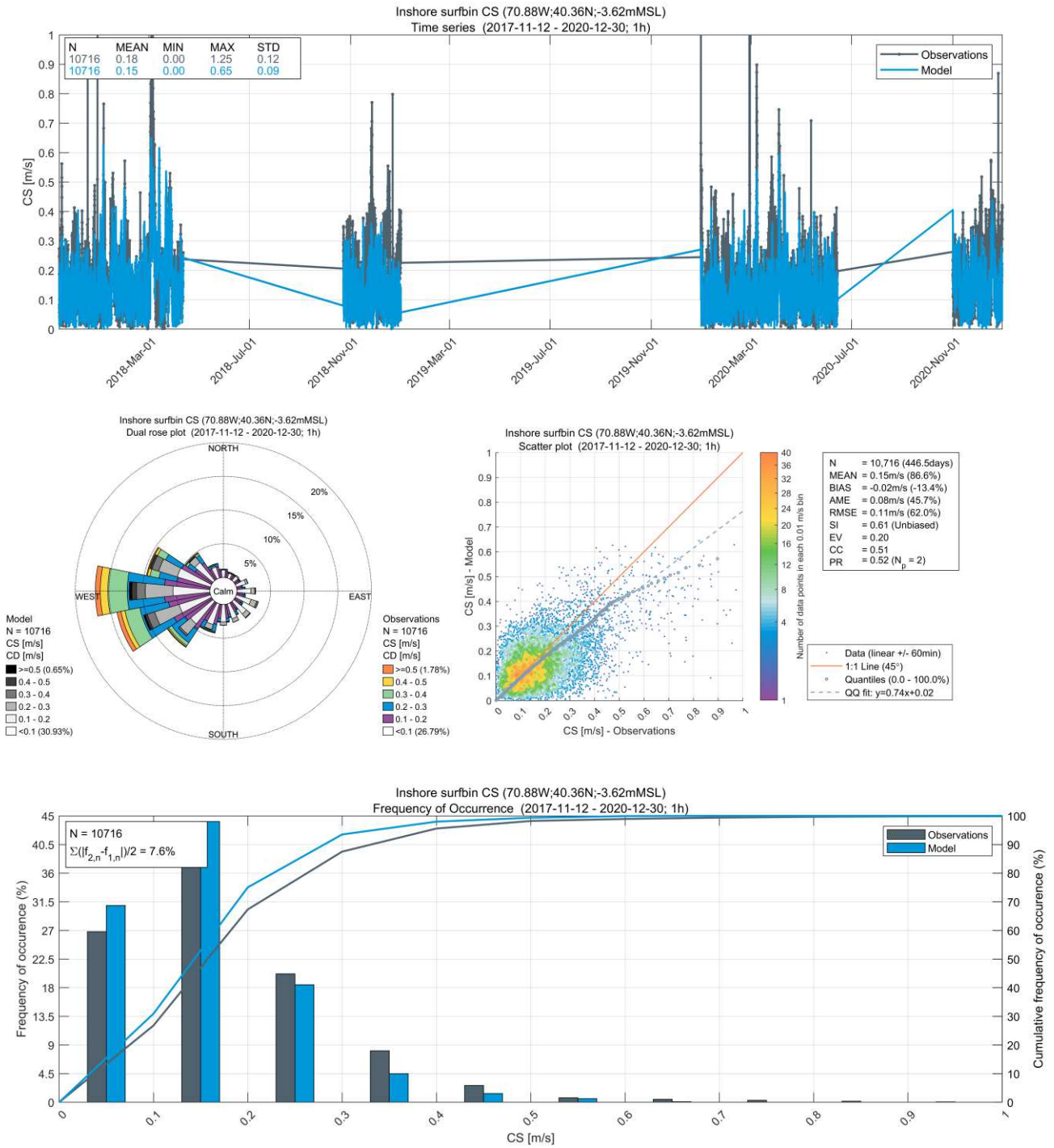


Figure A.4. Pioneer Inshore – Near Surface Layer 2017 (~3 years) Current Speeds (CS) and Current Direction (CD) Observational Data vs Model Results

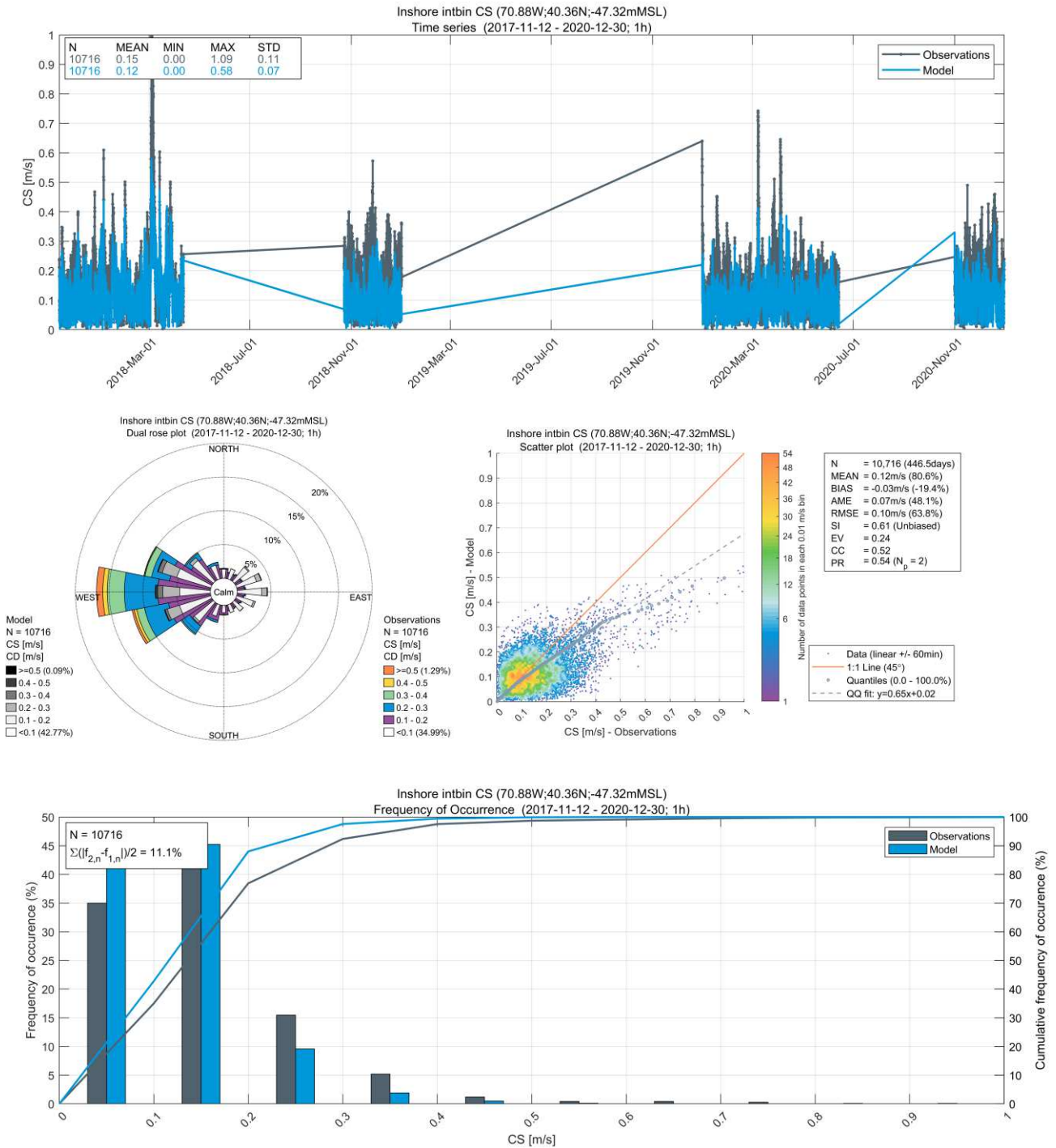


Figure A.5. Pioneer Inshore –Midwater 2017 (~3 years) Current Speeds (CS) and Current Direction (CD) Observational Data vs. Model Results

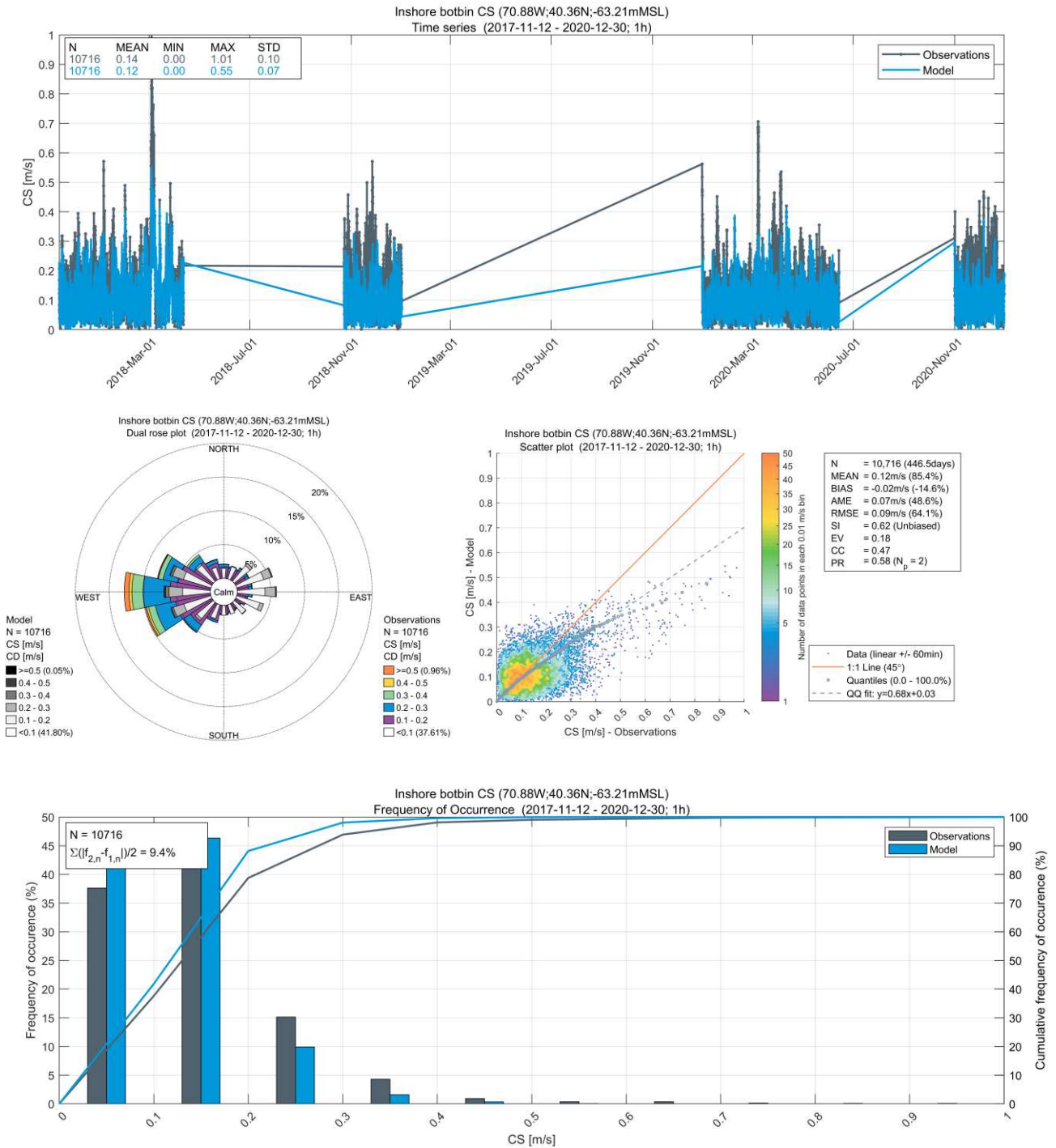


Figure A.6. Pioneer Inshore –Near Bottom 2017 (~3 years) Current Speeds (CS) and Current Direction (CD) Observational Data vs. Model Results

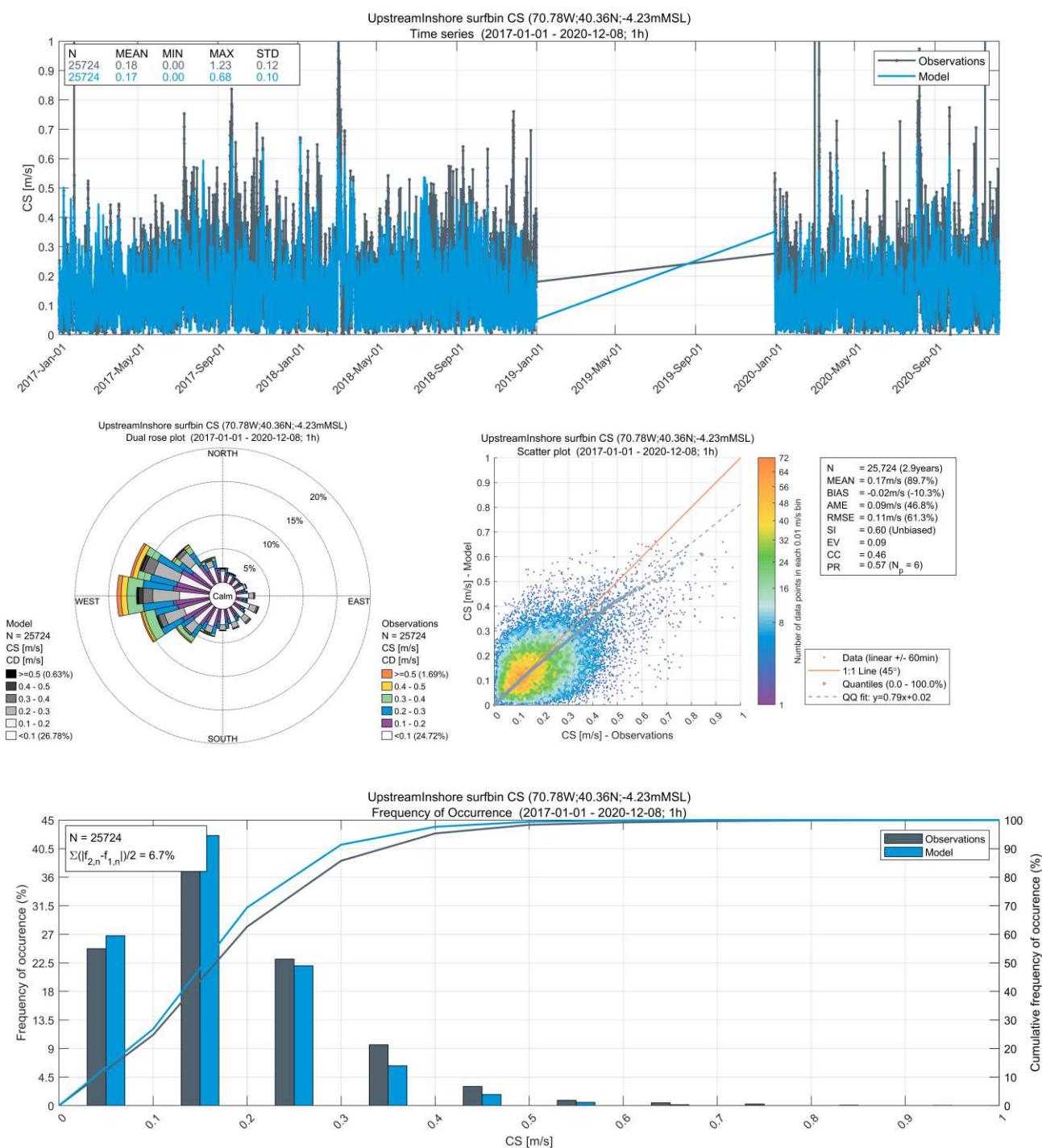


Figure A.7. Pioneer Upstream Inshore– Near Surface Layer 2017 (~4 years) Current Speeds (CS) and Current Direction (CD) Observational Data vs. Model Results

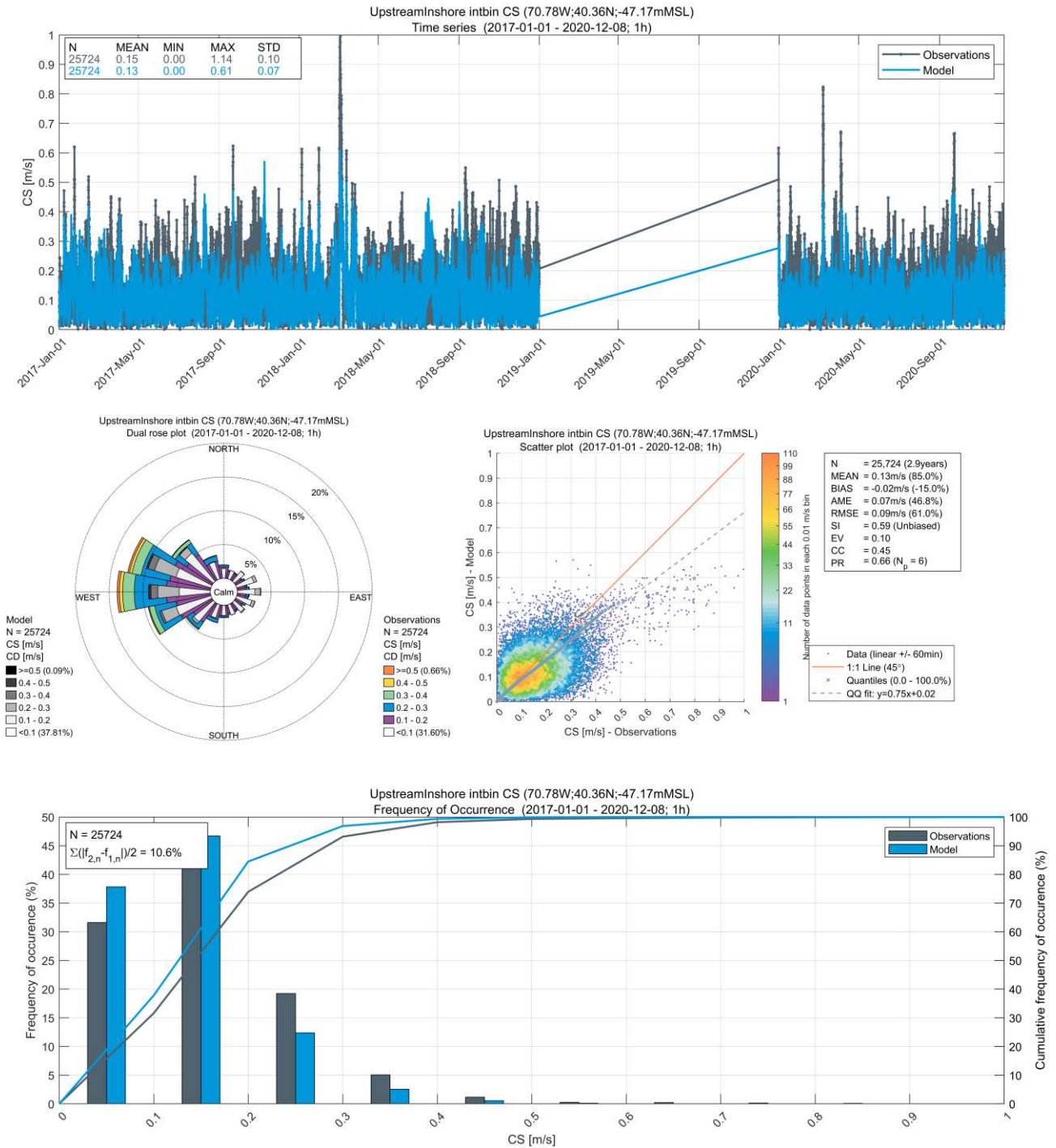


Figure A.8. Pioneer Upstream Inshore – Midwater 2017 (~4 years) Current Speeds (CS) and Current Direction (CD) Observational Data vs. Model Results

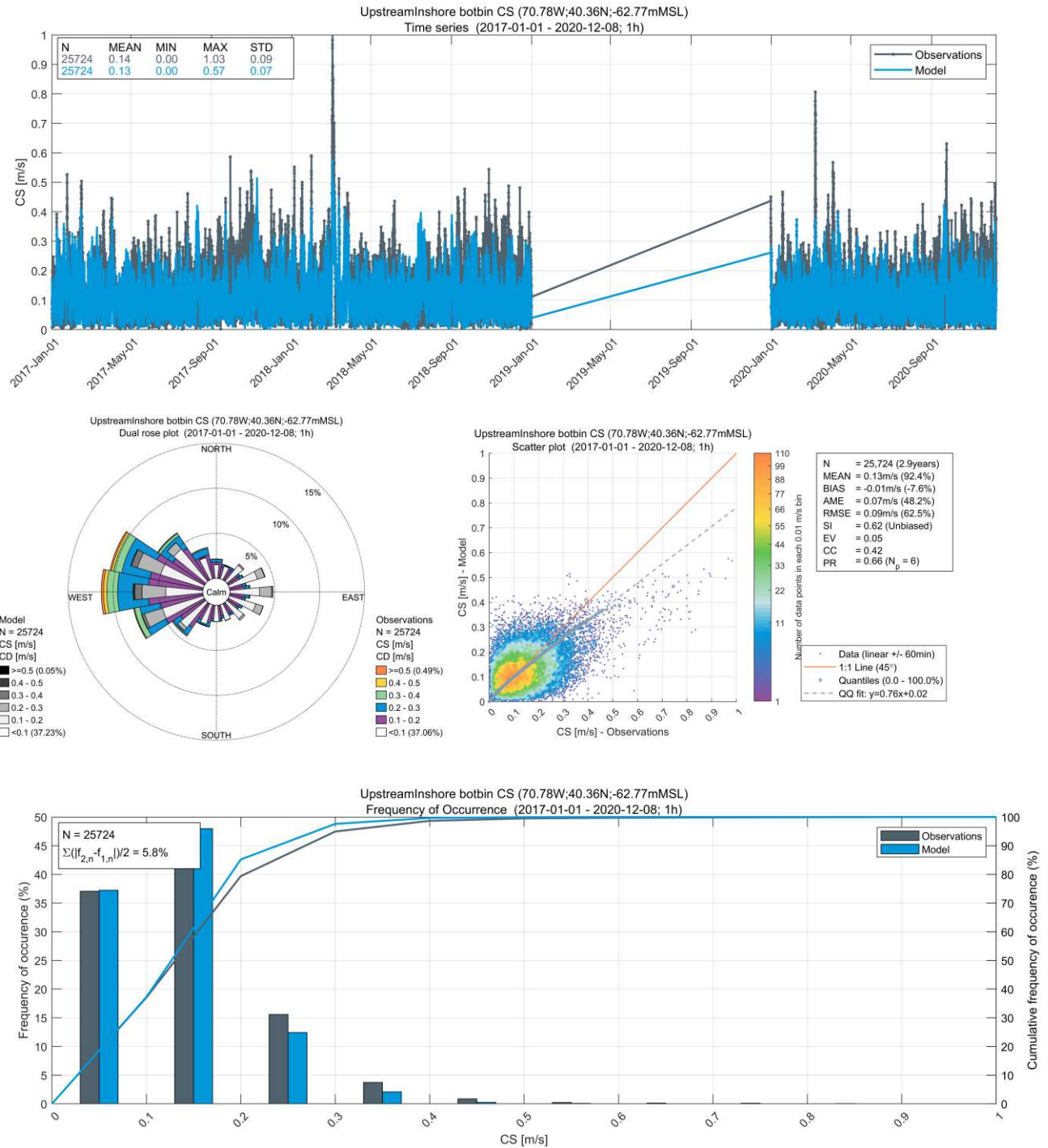


Figure A.9. Pioneer Upstream Inshore – Near Bottom 2017 (~4 years) Current Speeds (CS) and Current Direction (CD) Observational Data vs. Model Results

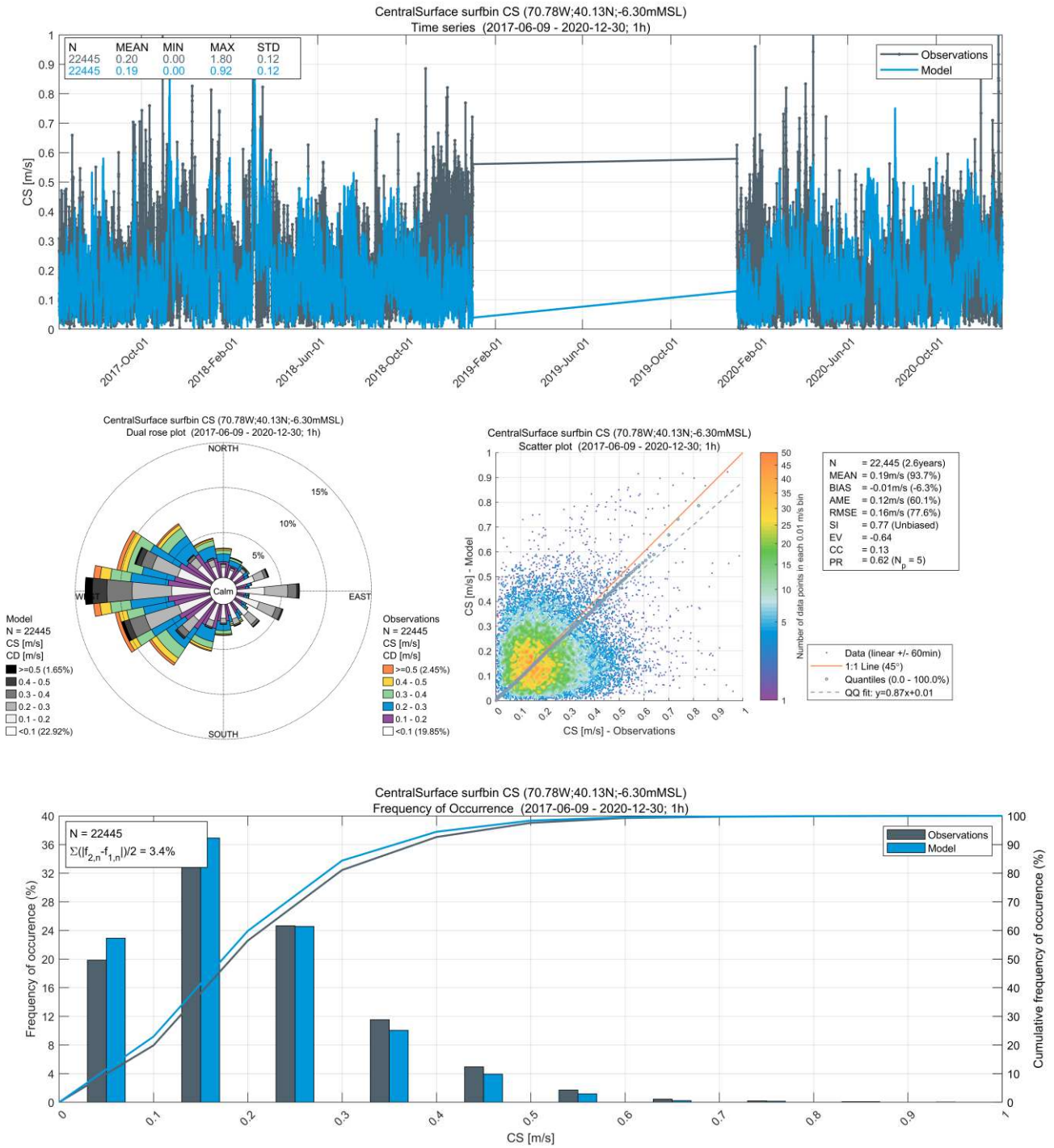


Figure A.10. Pioneer Central Surface – Near Surface Layer 2017 (~3.5 years) Current Speeds (CS) and Current Direction (CD) Observational Data vs. Model Results

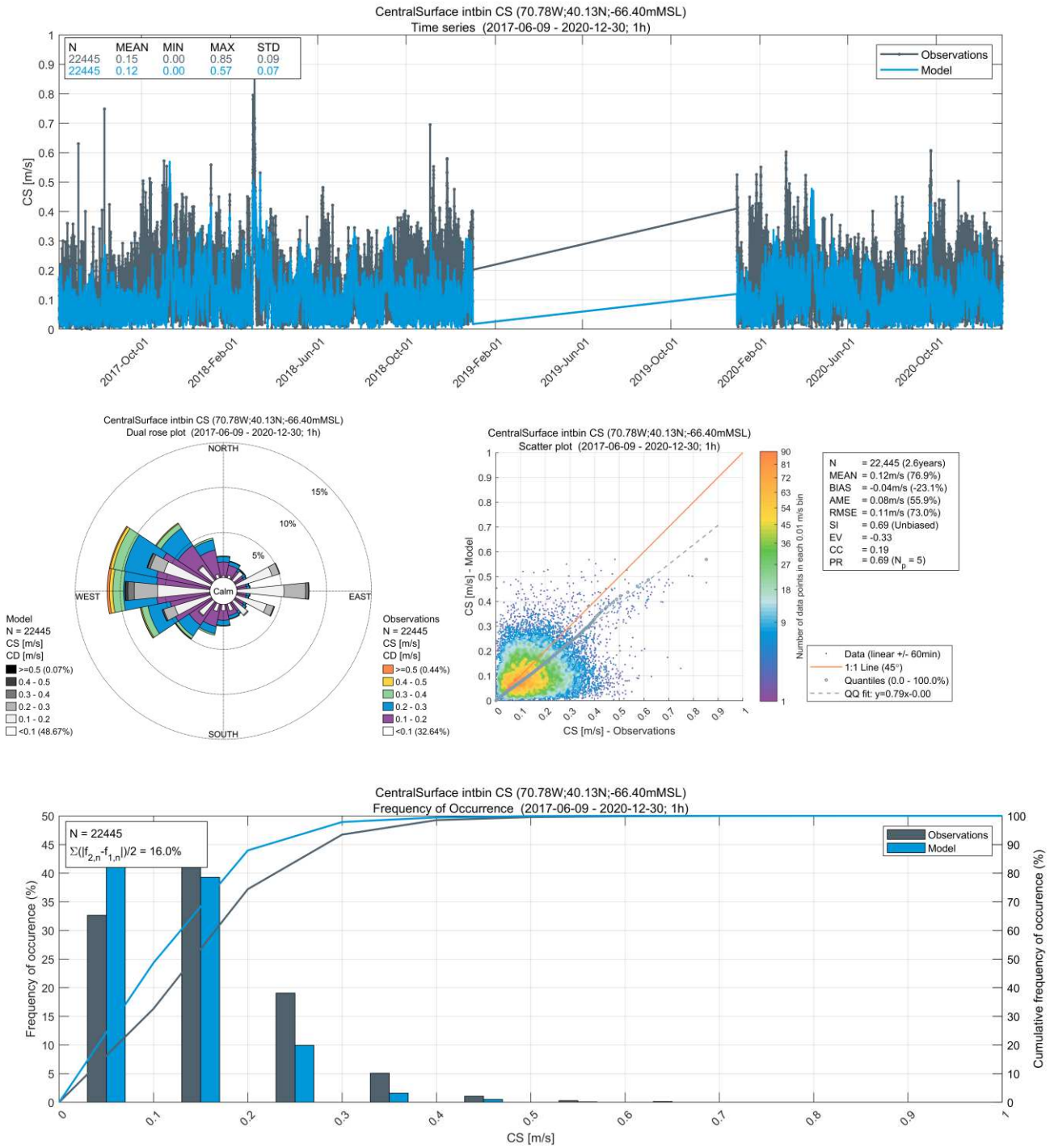


Figure A.11. Pioneer Central Surface – Midwater 2017 (~3.5 years) Current Speeds (CS) and Current Direction (CD) Observational Data vs. Model Results

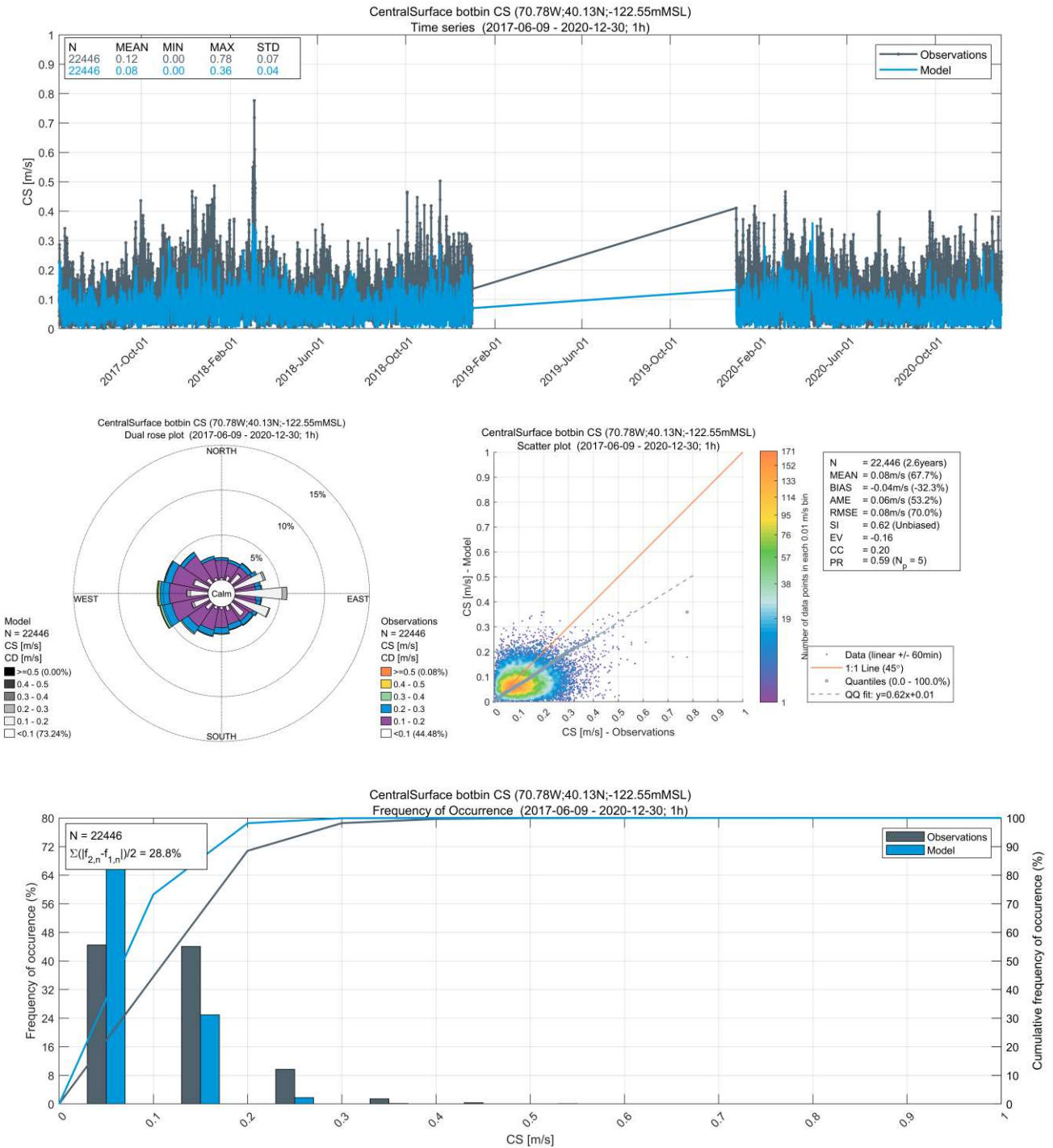


Figure A.12. Pioneer Central Surface – Near Bottom 2017 (~3.5 years) Current Speeds (CS) and Current Direction (CD) Observational Data vs. Model Results

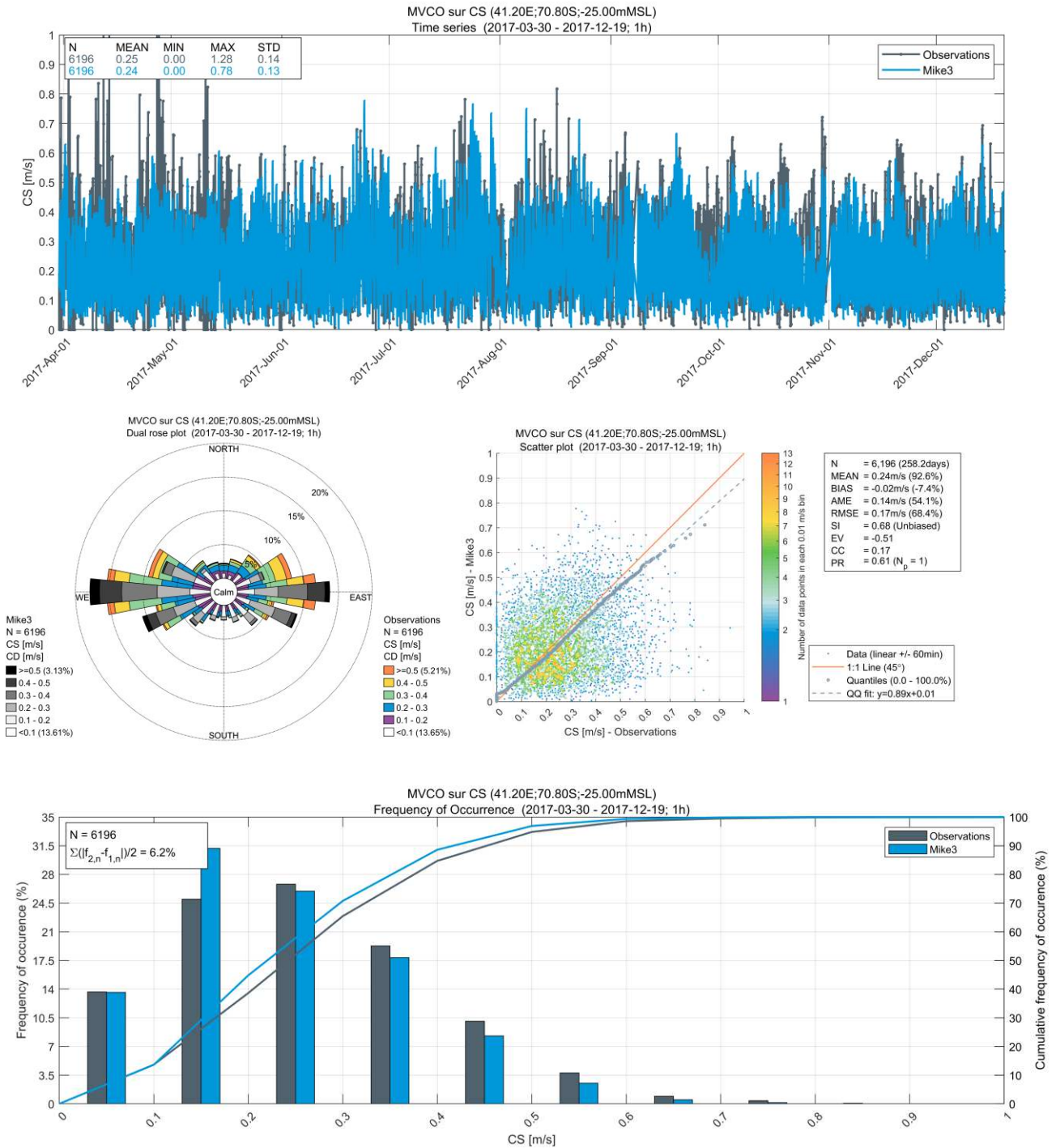


Figure A.13. MVCO – Near Surface Layer 2017 (~8 months) Current Speeds (CS) and Current Direction (CD) Observational Data vs Model Results

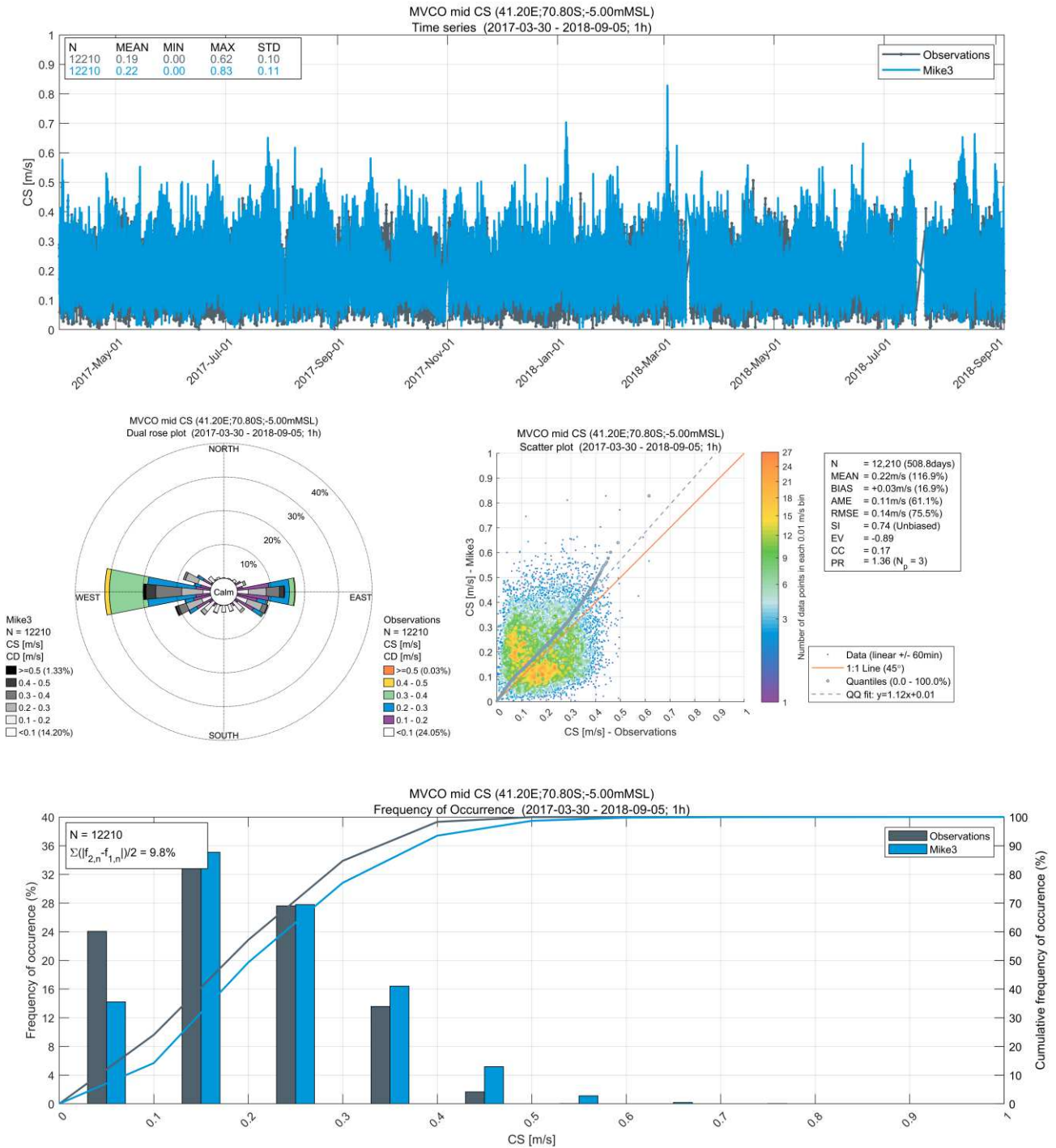


Figure A.14. MVCO – Midwater 2017 (~1.5 years) Current Speeds (CS) and Current Direction (CD) Observational Data vs Model Results

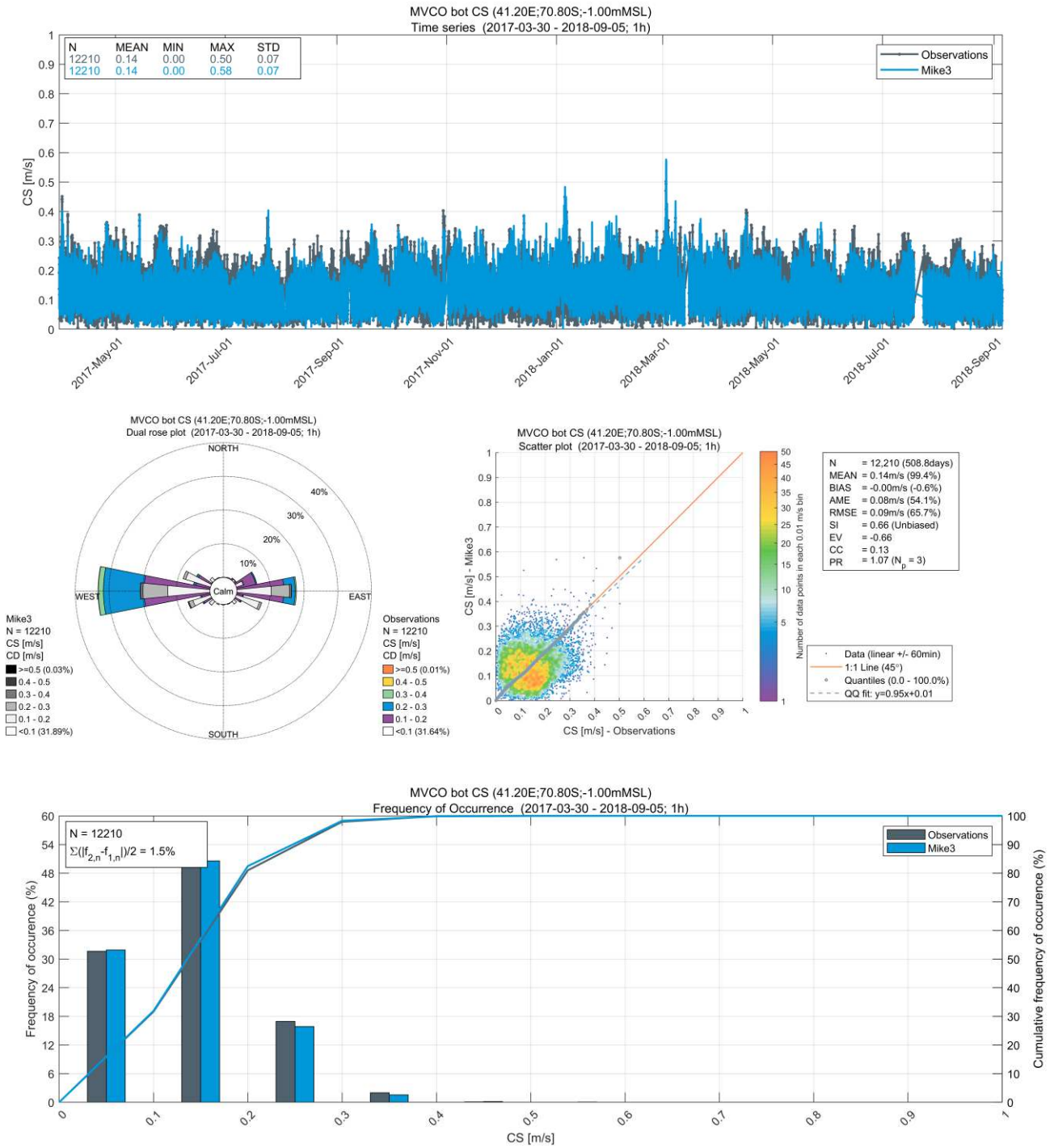


Figure A.15. MVCO – Near Bottom 2017 (~1.5 years) Current Speeds (CS) and Current Direction (CD) Observational Data vs Model Results

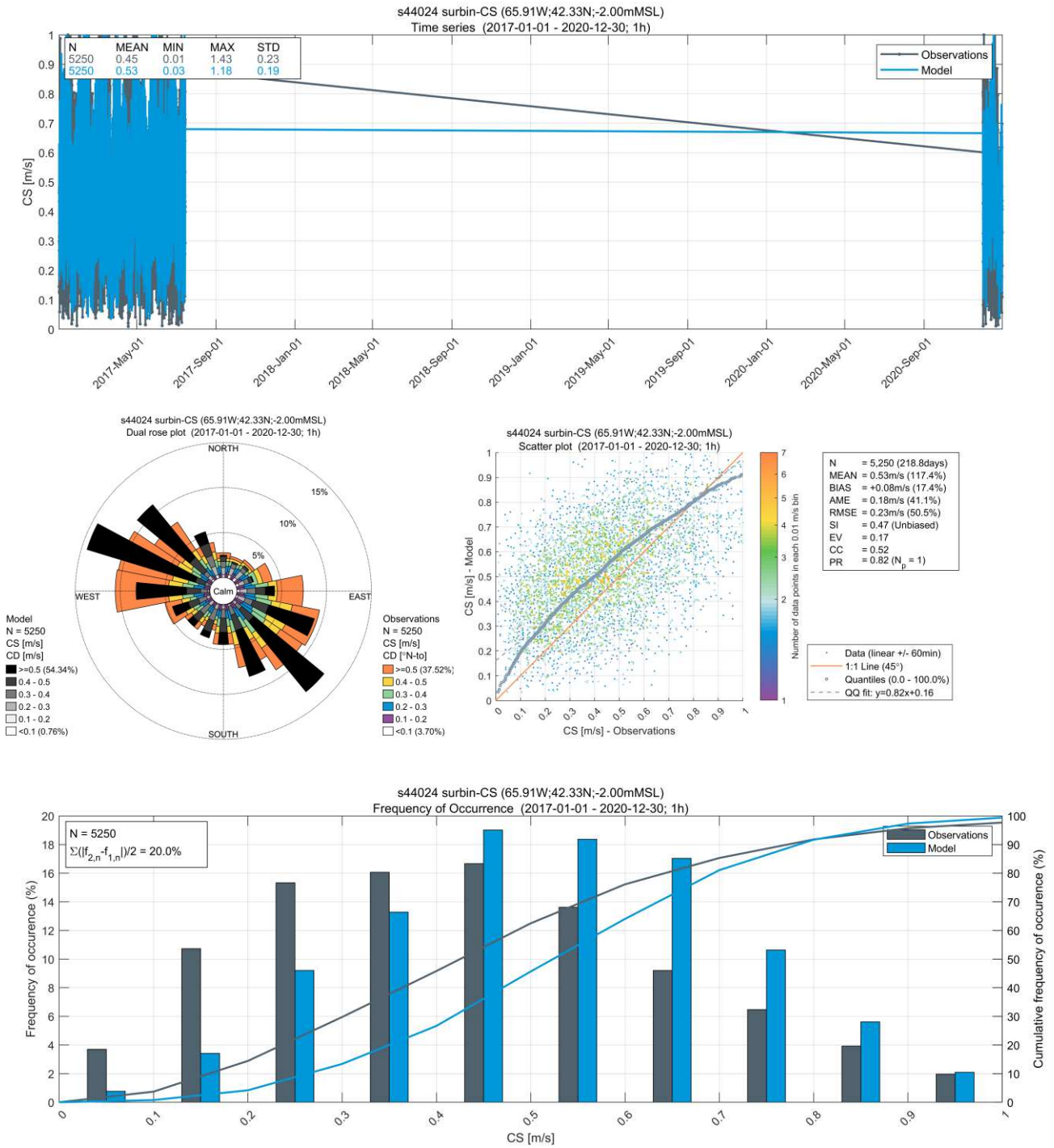


Figure A.16. NOAA ADCP S44024 – Near Surface Layer 2017 (~4 years) Current Speeds (CS) and Current Direction (CD) Observational Data vs Model Results

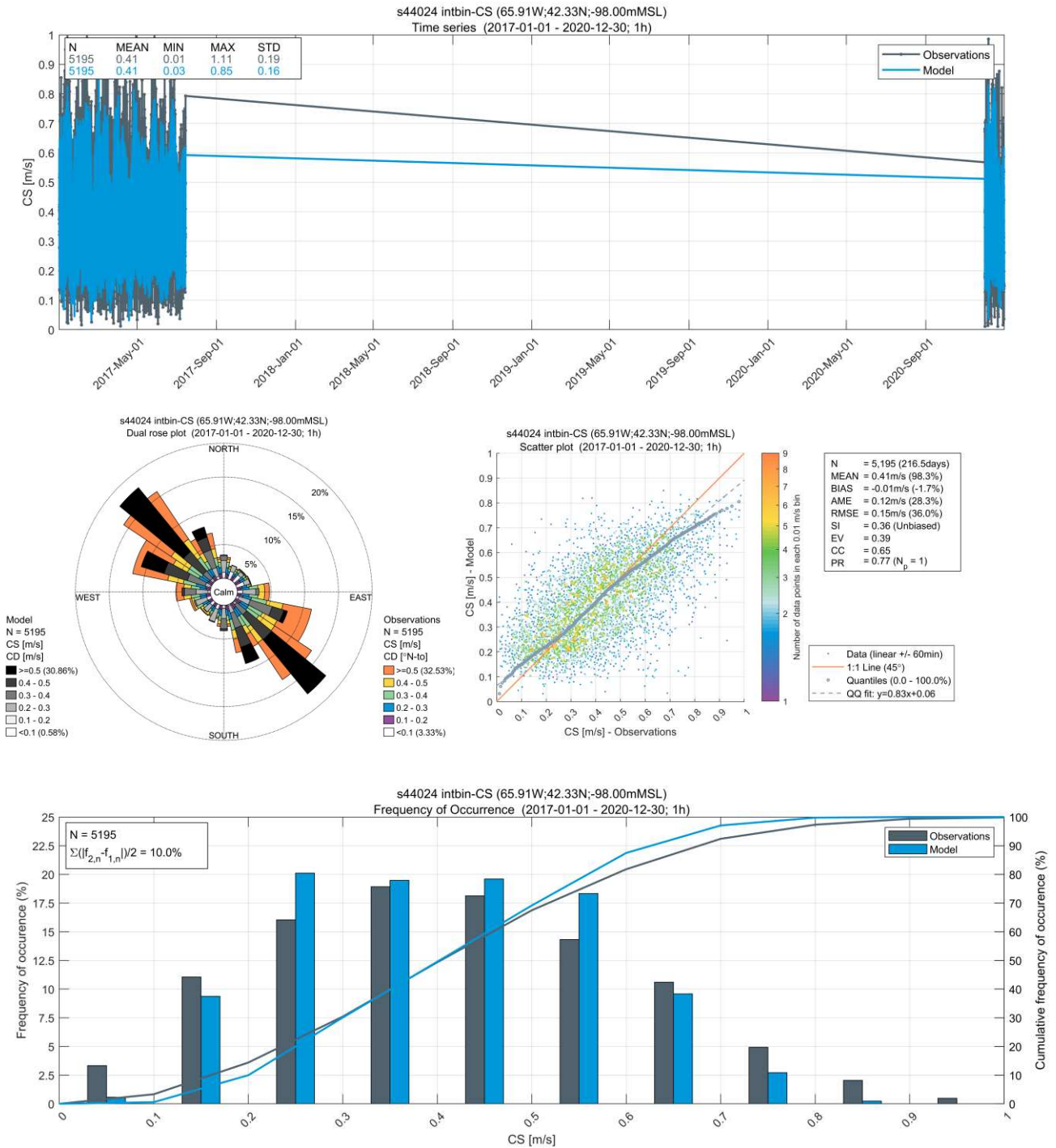


Figure A.17. NOAA ADCP S44024 – Midwater 2017 (~4 years) Current Speeds (CS) and Current Direction (CD) Observational Data vs Model Results

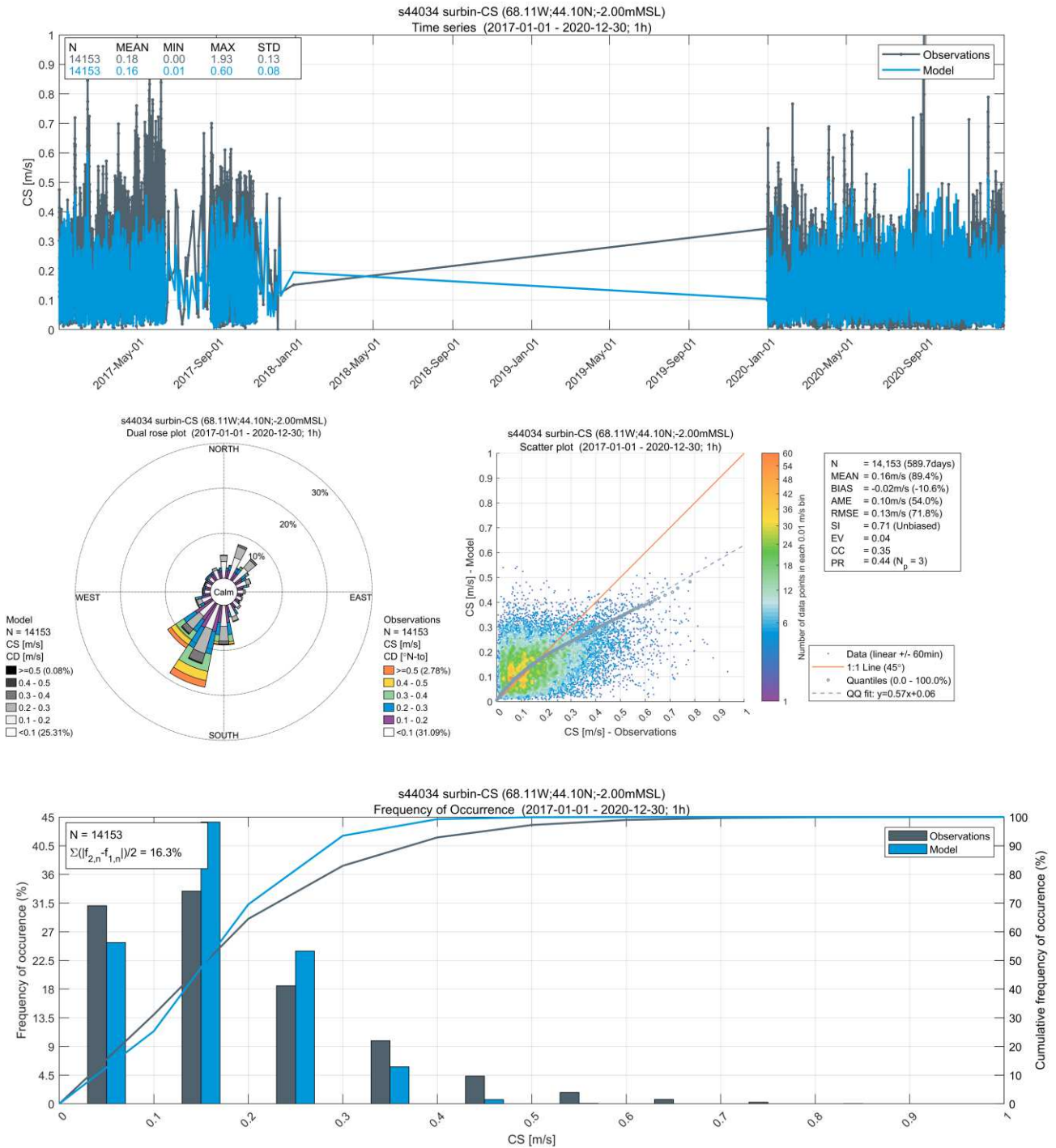


Figure A.18. NOAA ADCP S44034 – Near Surface Layer 2017 (~4 years) Current Speeds (CS) and Current Direction (CD) Observational Data vs Model Results

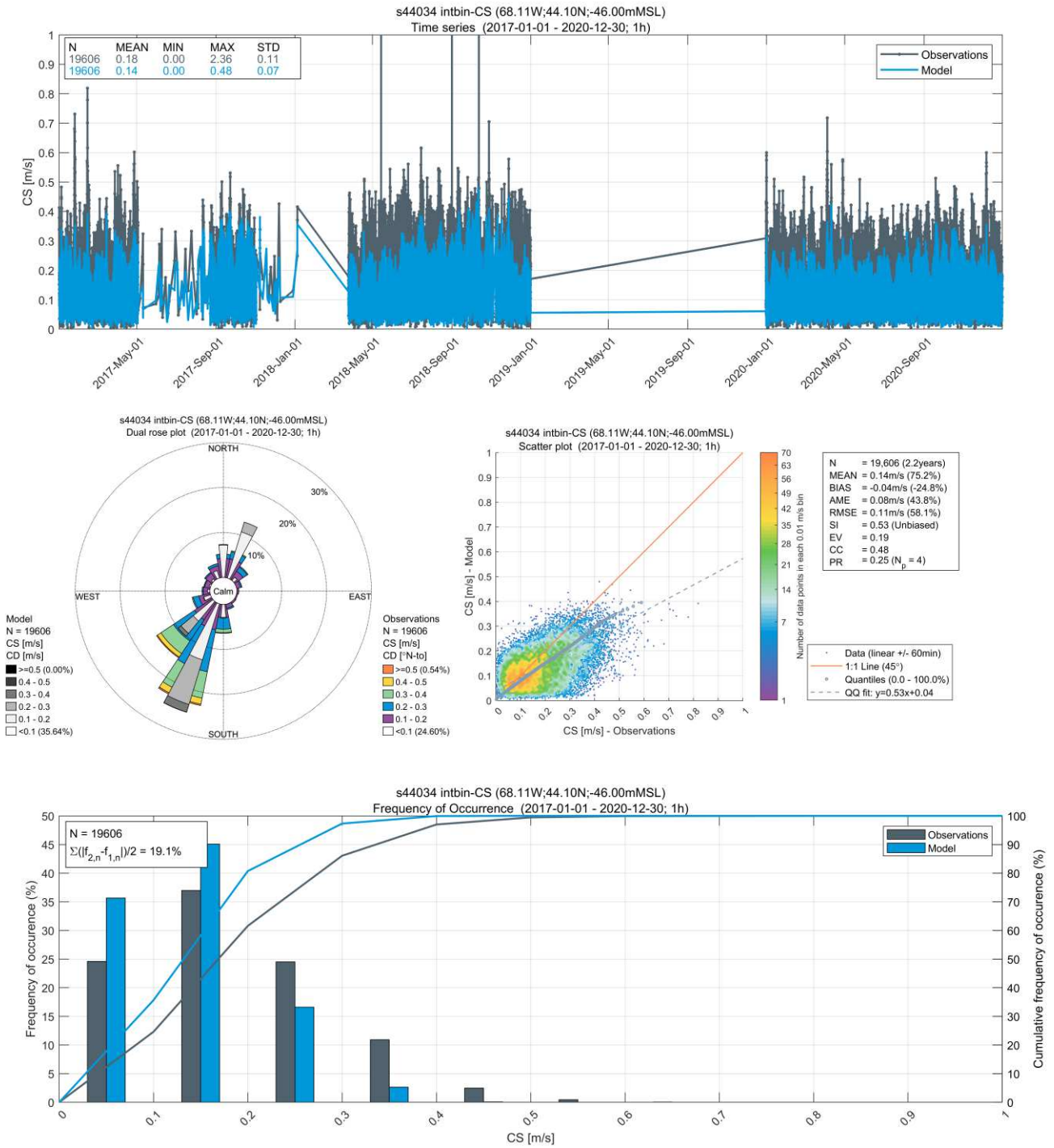


Figure A.19. NOAA ADCP S44034 – Midwater Layer 2017 (~4 years) Current Speed (CS) and Current Direction (CD) Observational Data vs Model Results

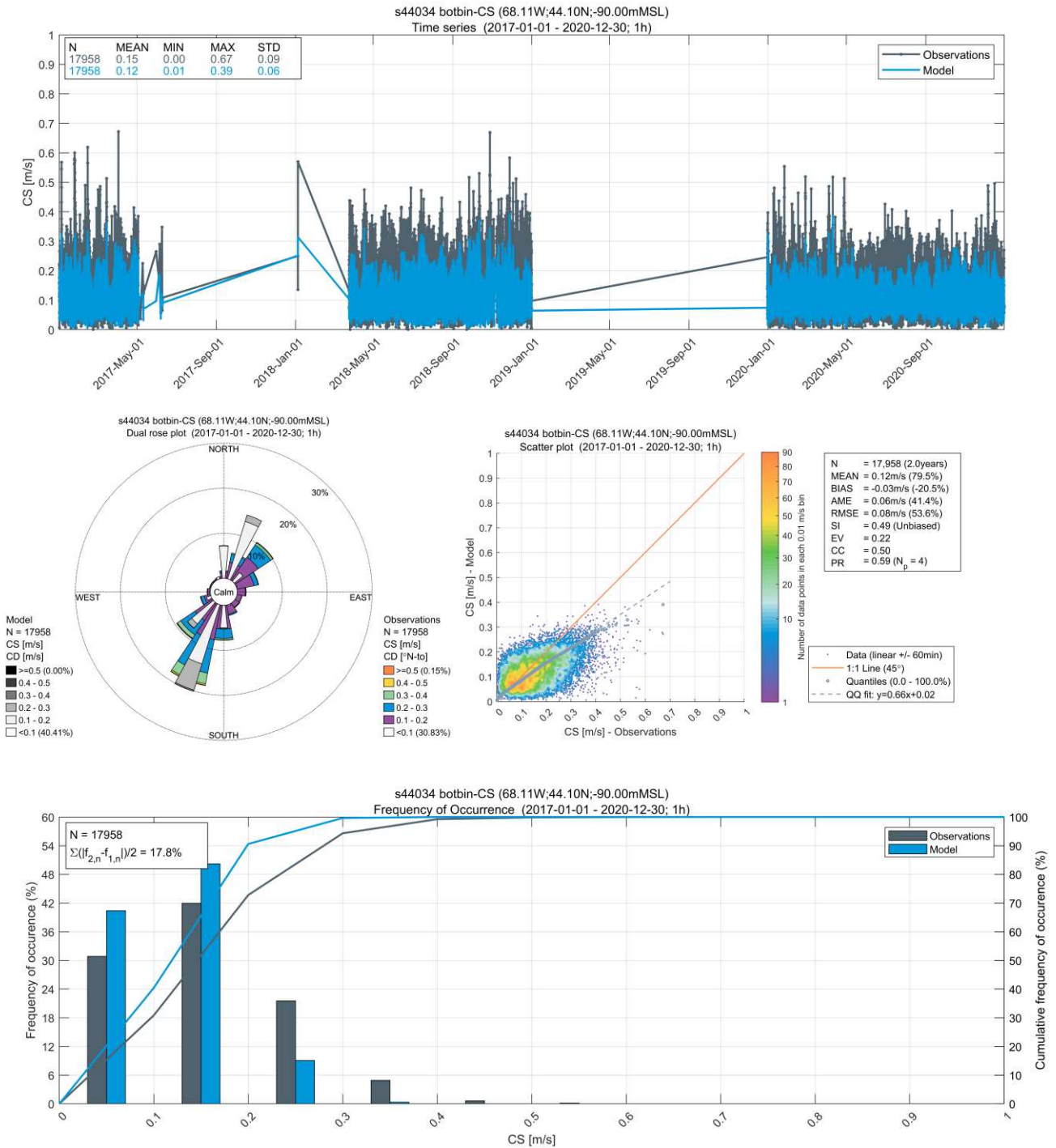


Figure A.20. NOAA ADCP S44034 – Near Bottom Layer 2017 (~4 years) Current Speed (CS) and Current Direction (CD) Observational Data vs Model Results

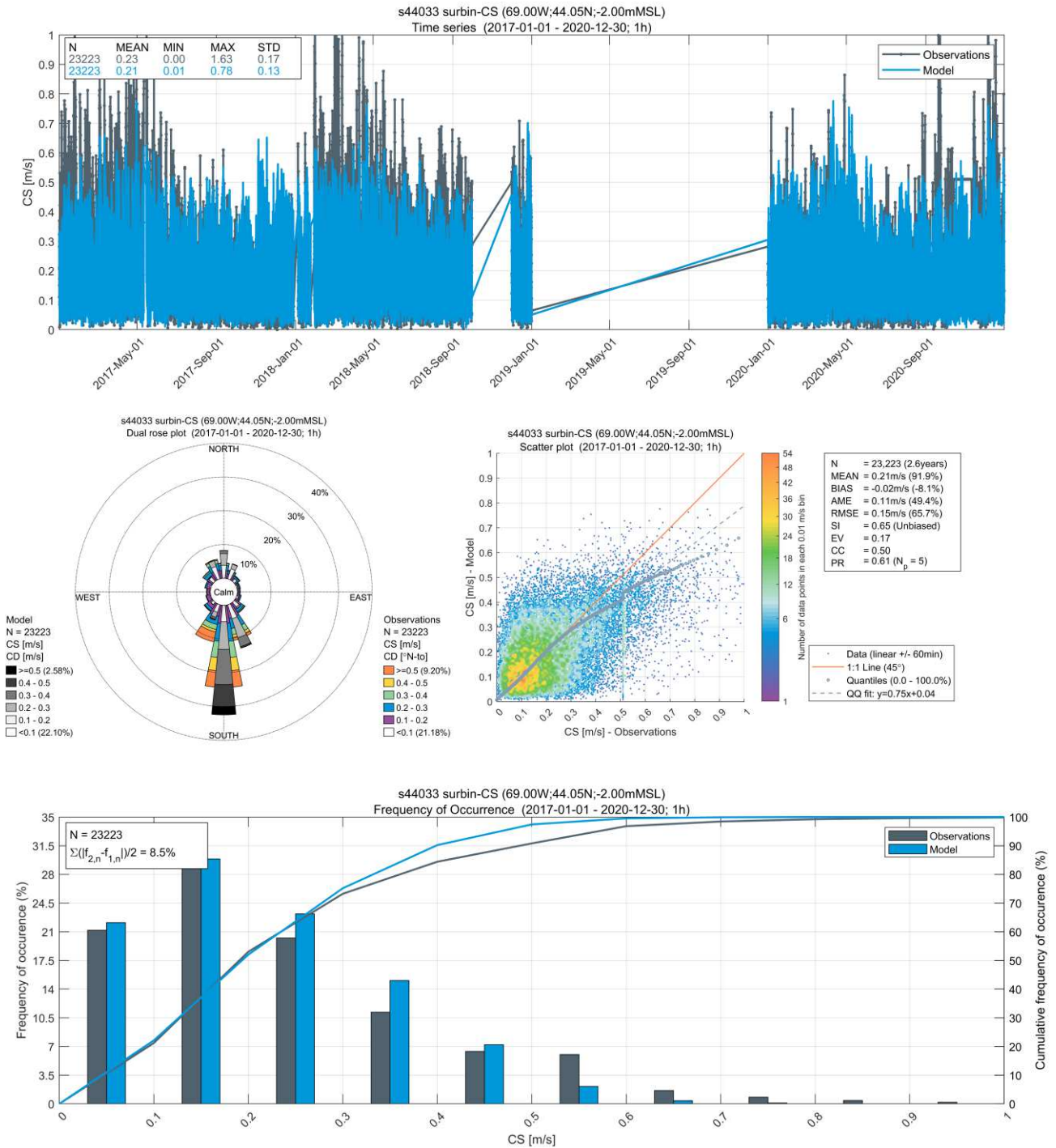


Figure A.21. NOAA ADCP S44033 – Near Surface Layer 2017 (~4 years) Current Speed (CS) and Current Direction (CD) Observational Data vs Model Results

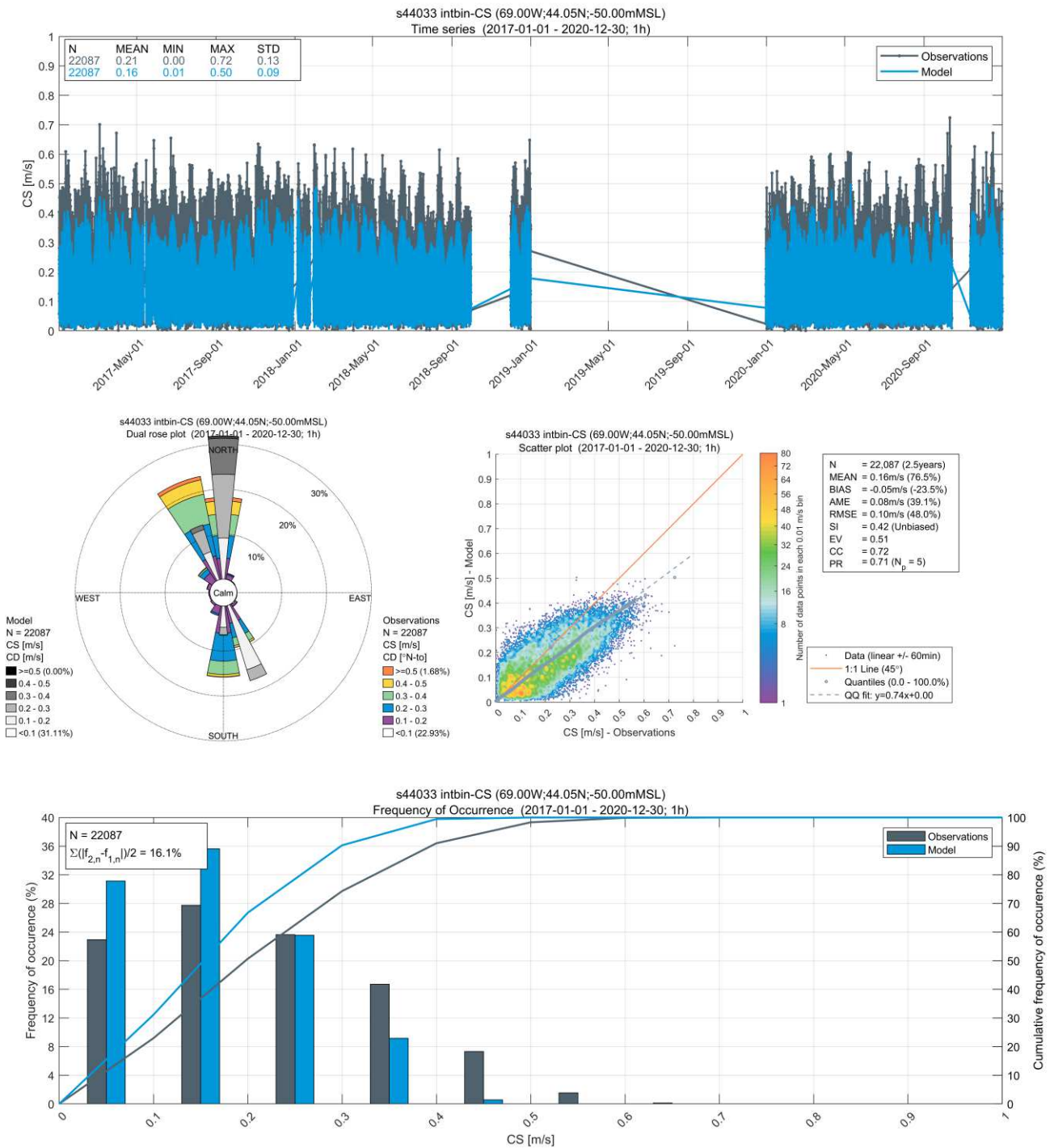


Figure A.22. NOAA ADCP S44033 – Midwater Layer 2017 (~4 years) Current Speed (CS) and Current Direction (CD) Observational Data vs Model Results

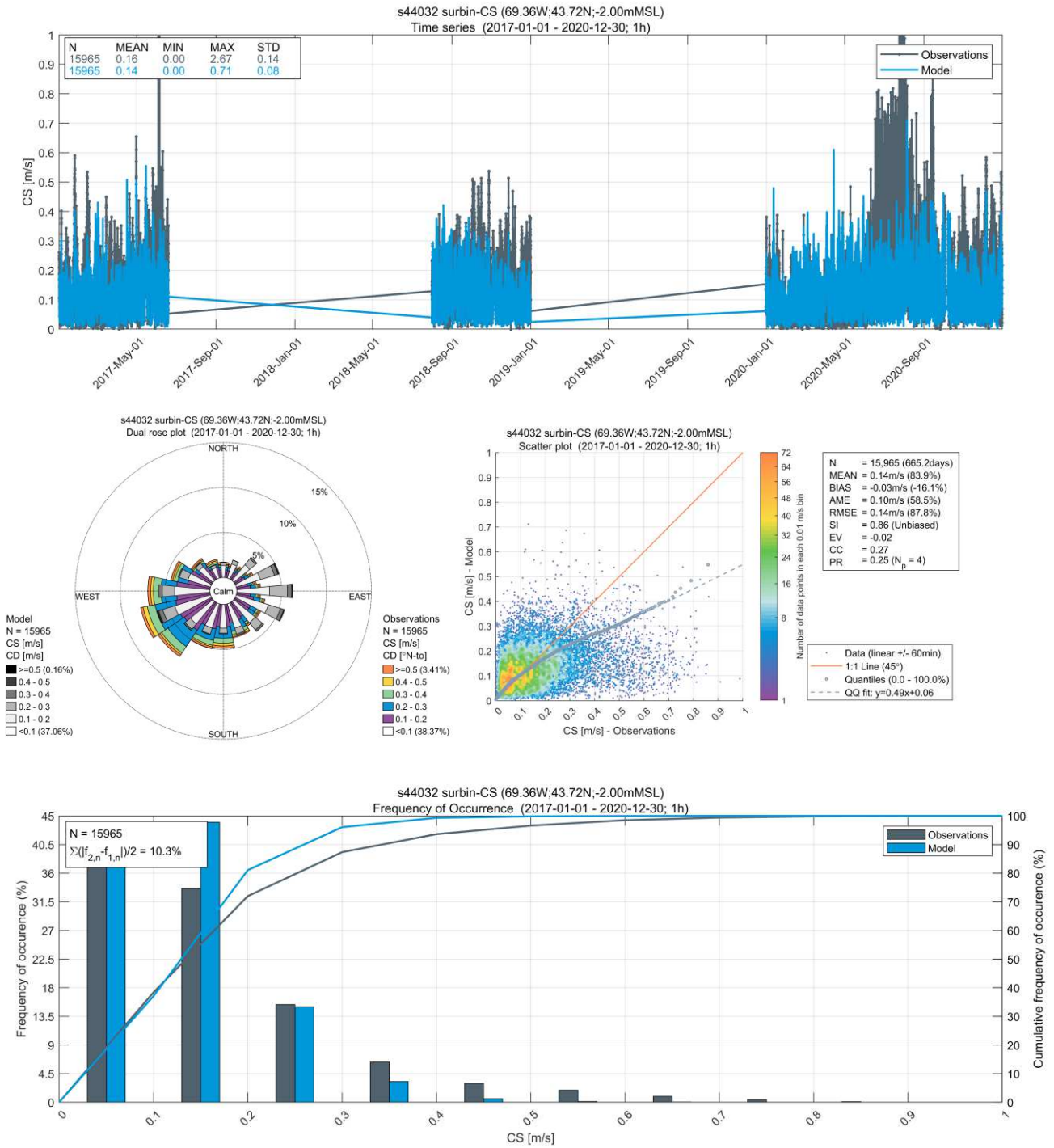


Figure A.23. NOAA ADCP S44032 – Near Surface Layer 2017 (~4 years) Current Speed (CS) and Current Direction (CD) Observational Data vs Model Results

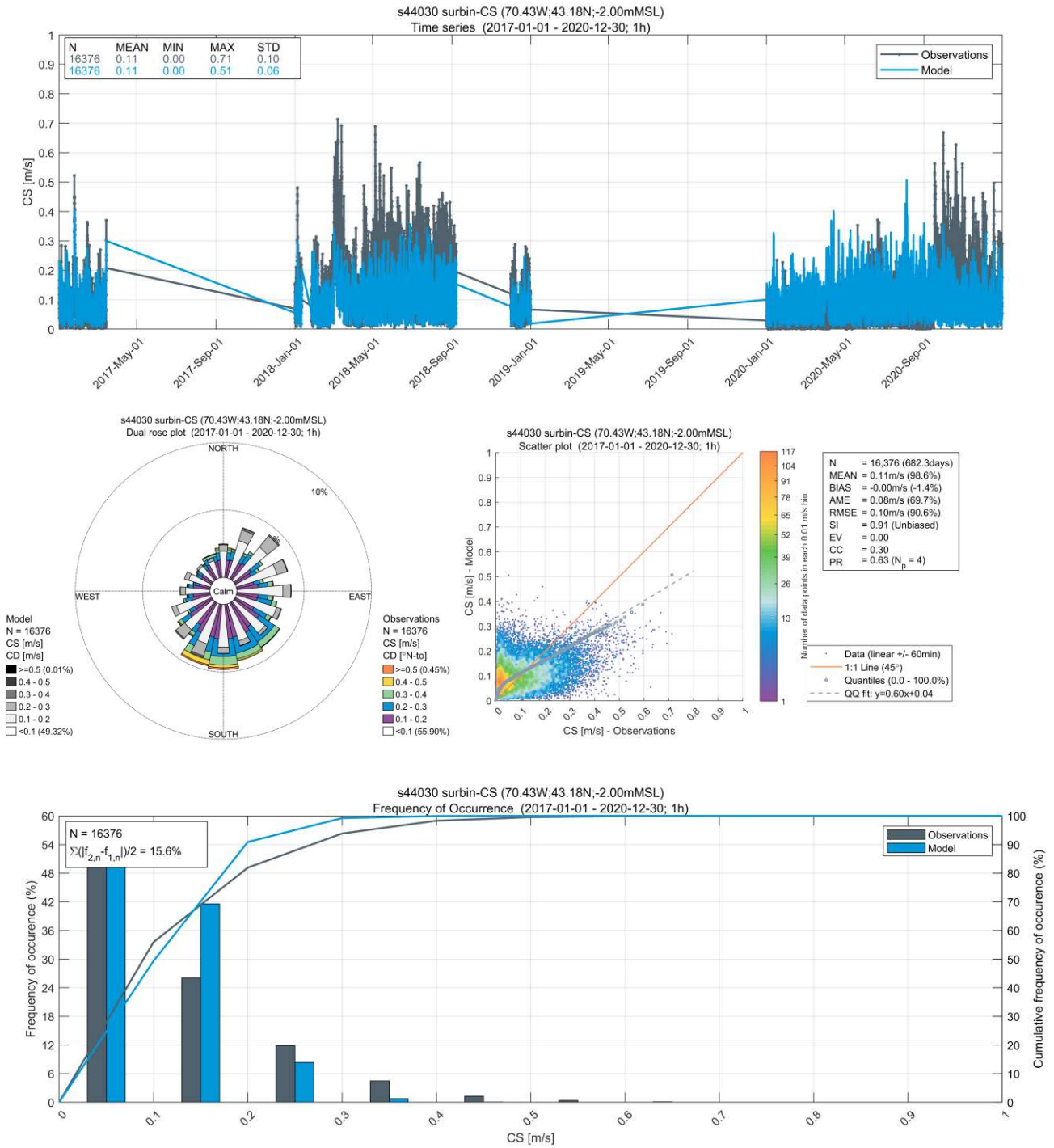


Figure A.24. NOAA ADCP S44030 – Near Surface Layer 2017 (~4 years) Current Speed (CS) and Current Direction (CD) Observational Data vs Model Results

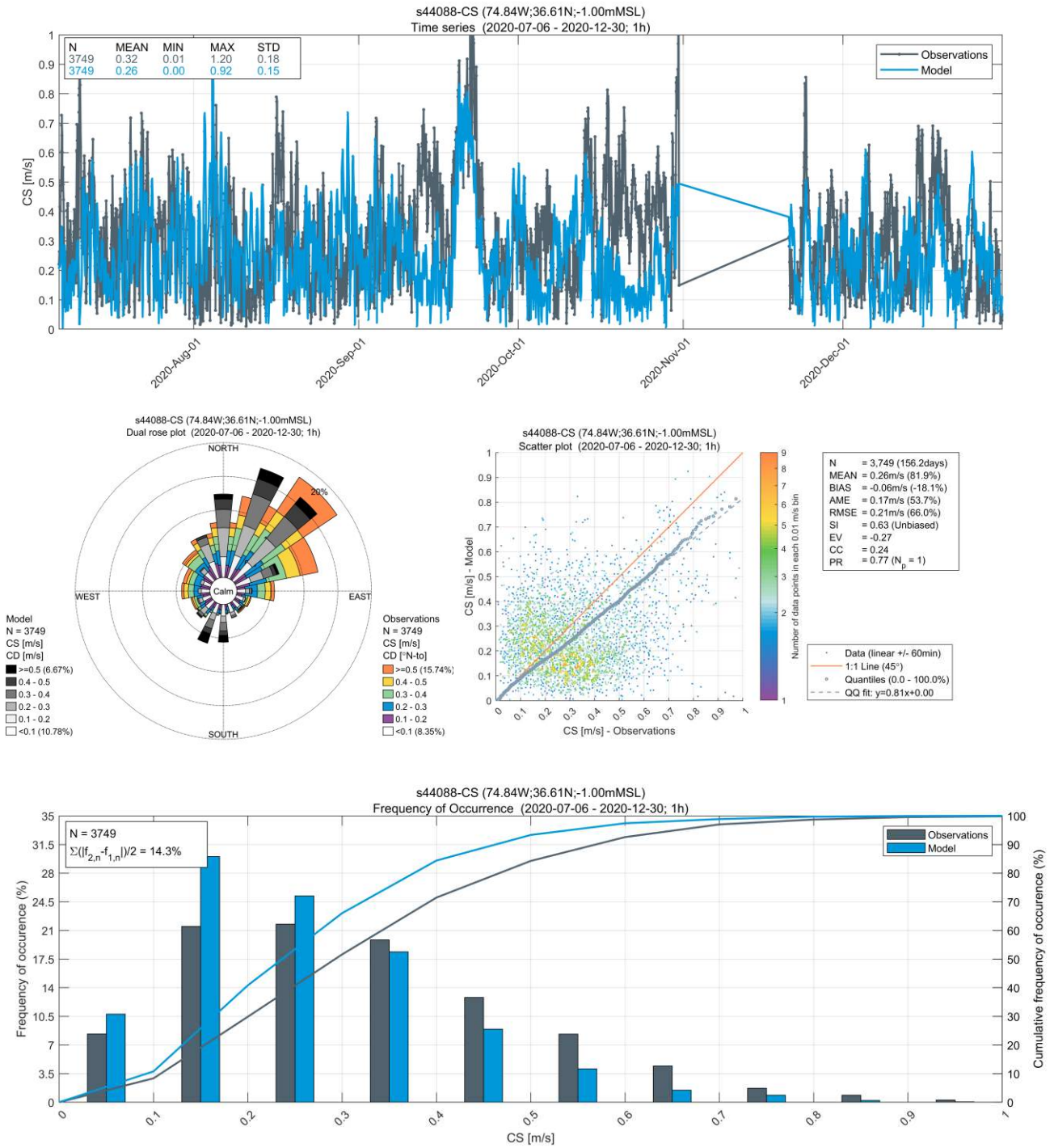


Figure A.25. NOAA Station 44088 – Near Surface Layer 2020 (~5.5 months) Current Speed (CS) and Current Direction (CD) Observational Data vs Model Results

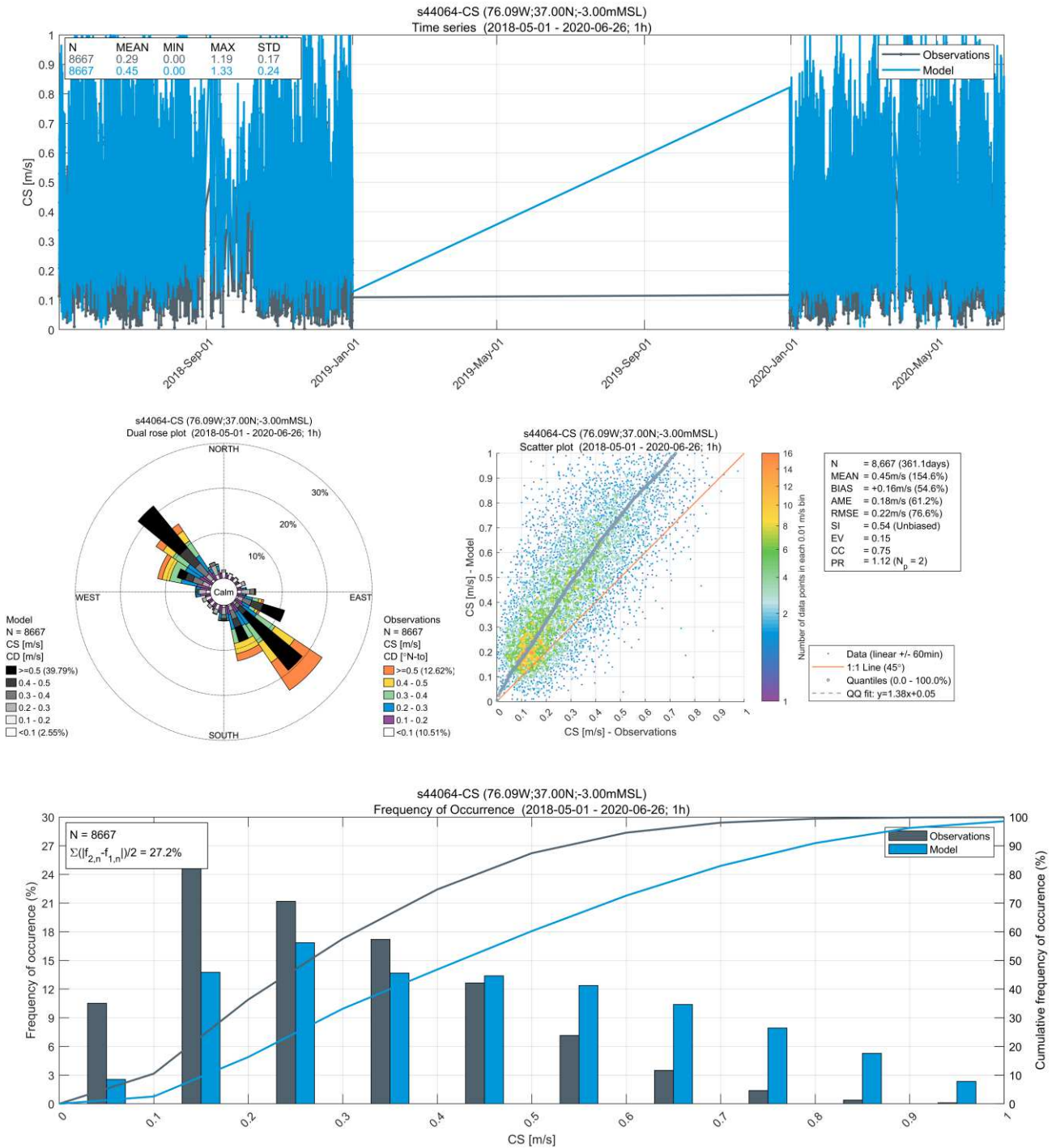


Figure A.26. NOAA Station 44064 – Near Surface Layer 2018 (~2 years) Current Speed (CS) and Current Direction (CD) Observational Data vs Model Results

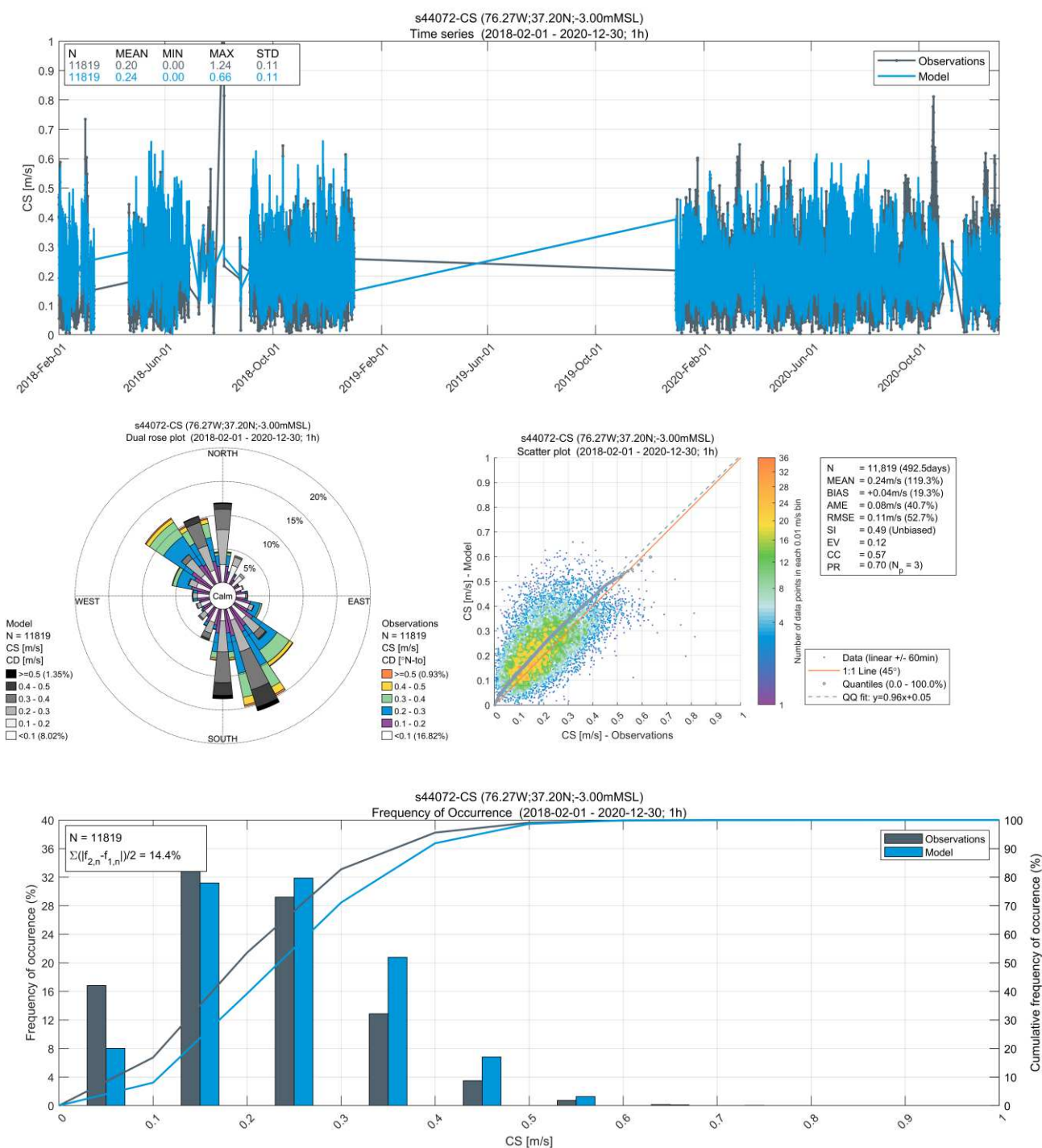


Figure A.27. NOAA Station 44072 – Near Surface Layer 2018 (~2 years 11 months) Current Speed (CS) and Current Direction (CD) Observational Data vs Model Results

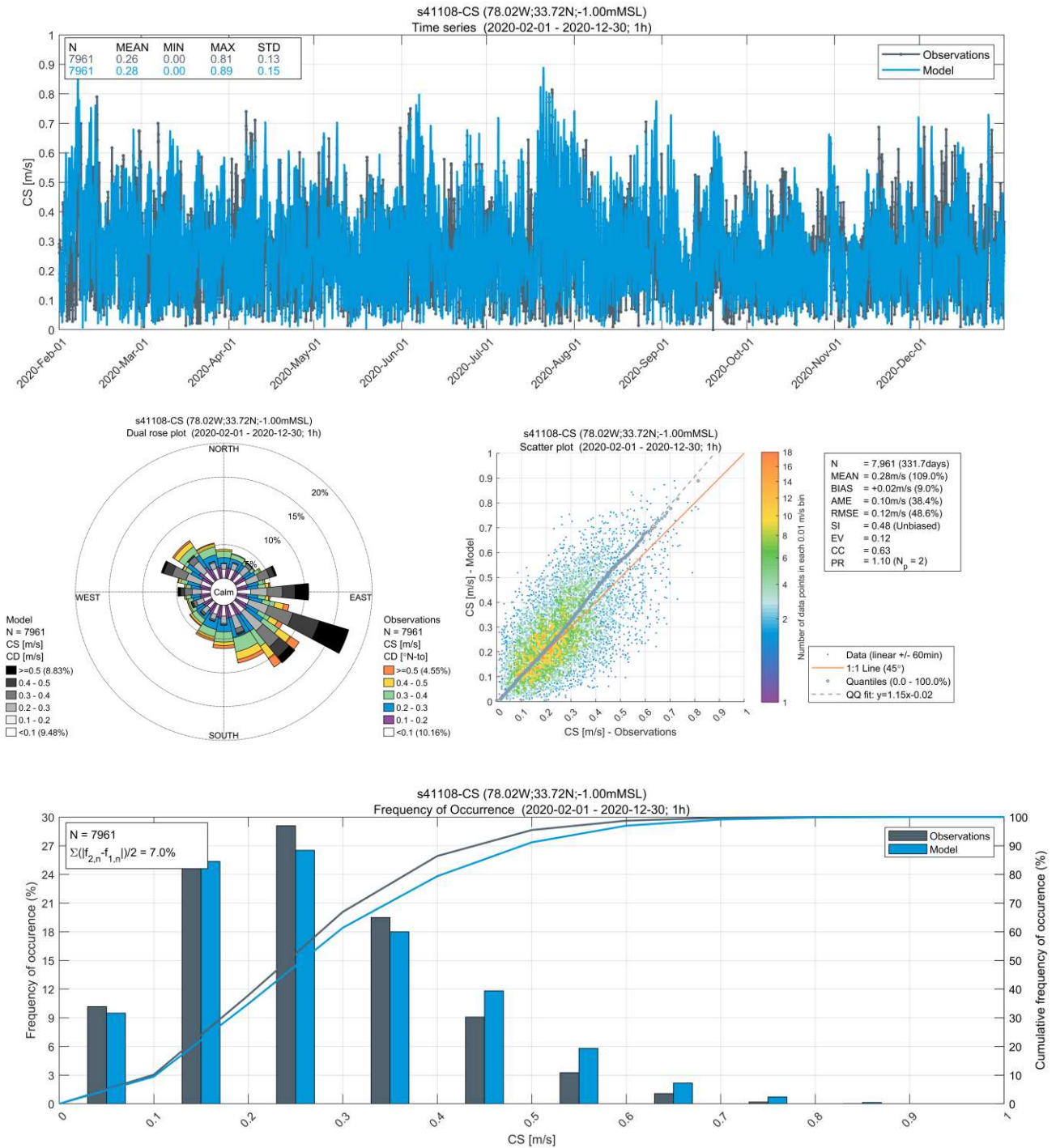


Figure A.28. NOAA Station 41108 – Near Surface Layer 2020 (~11 months) Current Speed (CS) and Current Direction (CD) Observational Data vs Model Results

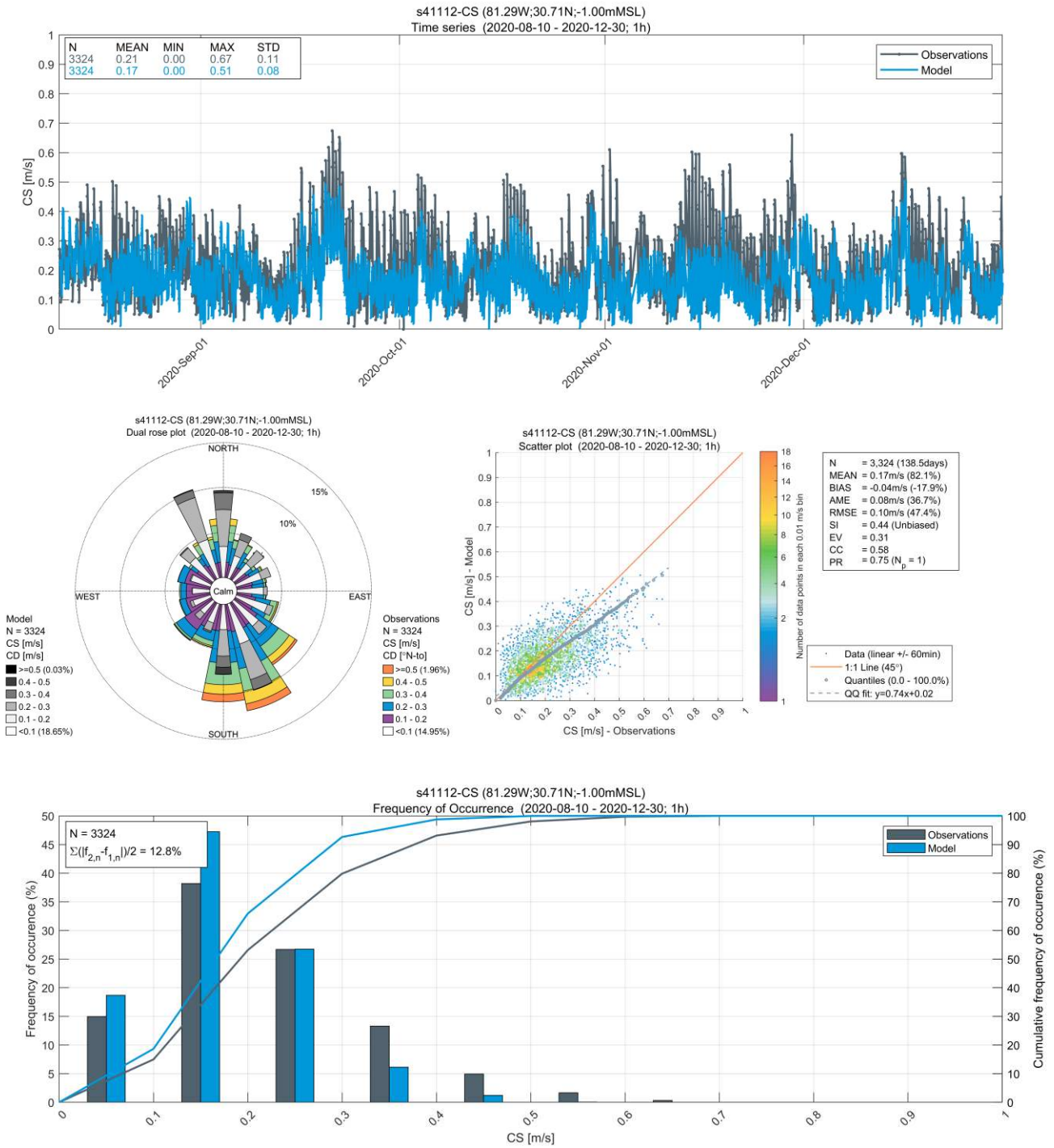


Figure A.29. NOAA Station 41112 – Near Surface Layer 2020 (~5 months) Current Speed (CS) and Current Direction (CD) Observational Data vs Model Results

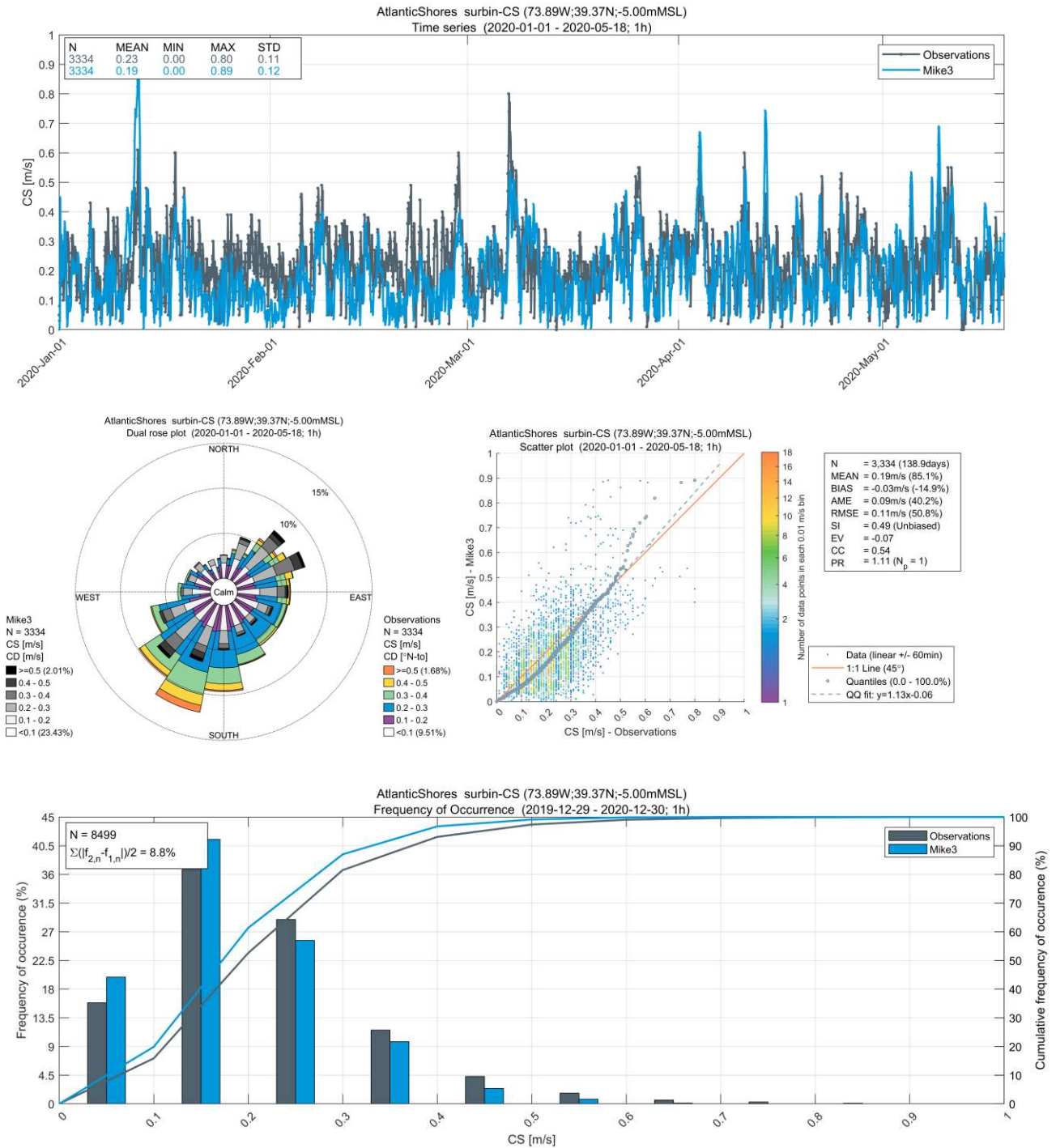


Figure A.30. Atlantic Shores – Near Surface Layer 2020 (~5 months) Current Speed (CS) and Current Direction (CD) Observational Data vs Model Results

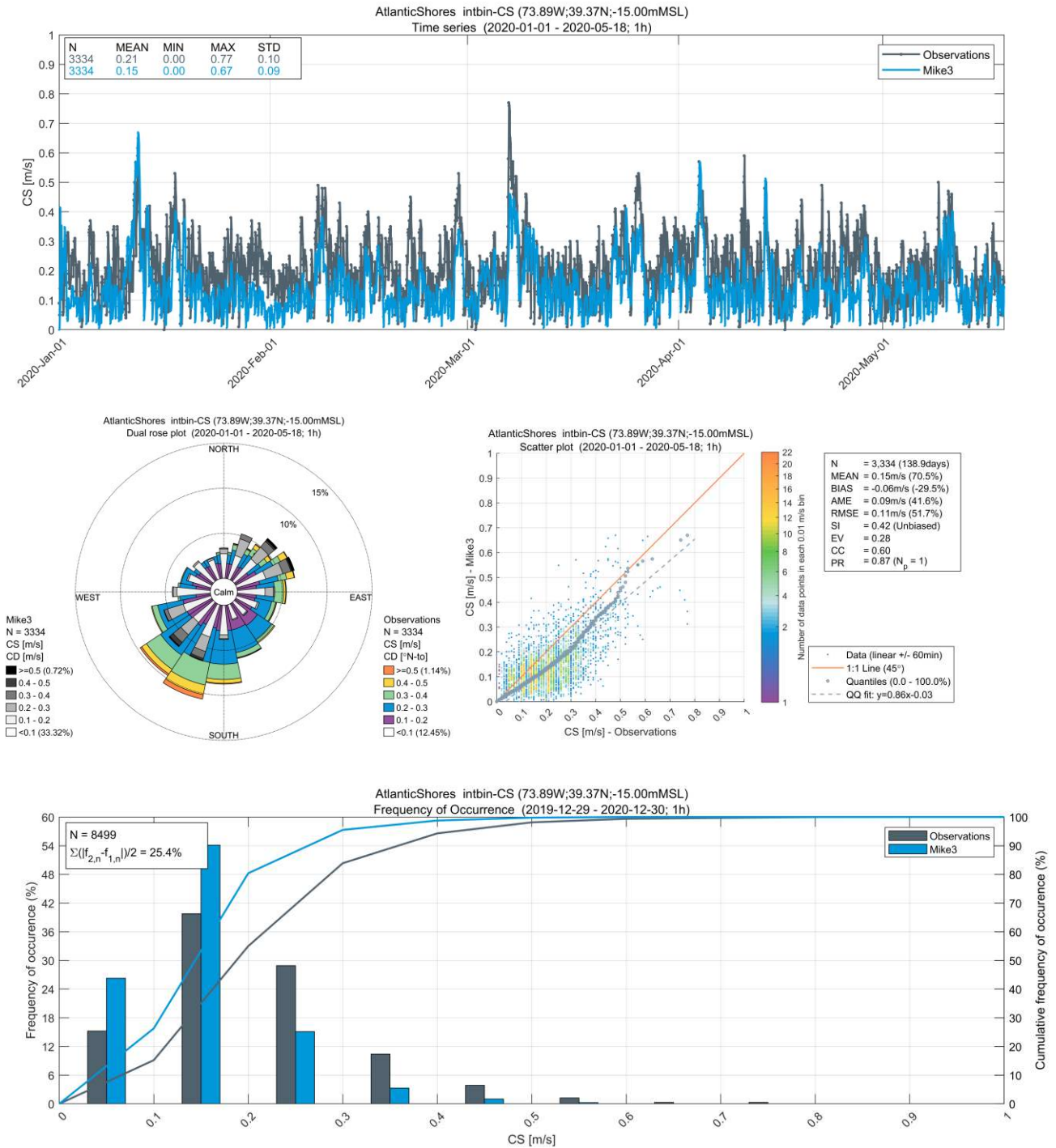


Figure A.31. Atlantic Shores – Midwater Layer 2020 (~5 months) Current Speed (CS) and Current Direction (CD) Observational Data vs Model Results

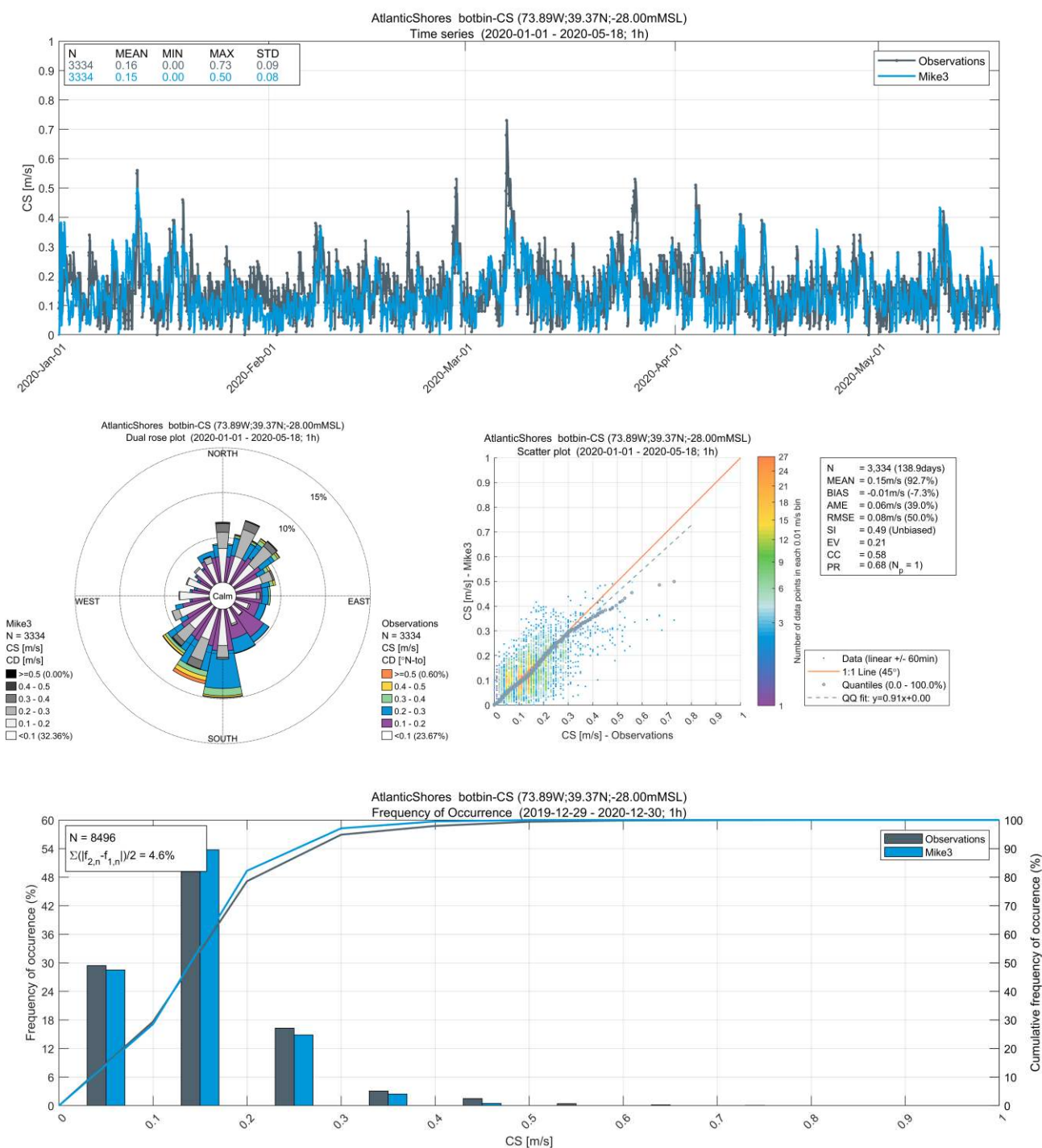


Figure A.32. Atlantic Shores – Near Bottom Layer 2020 (~5 months) Current Speed (CS) and Current Direction (CD) Observational Data vs Model Results

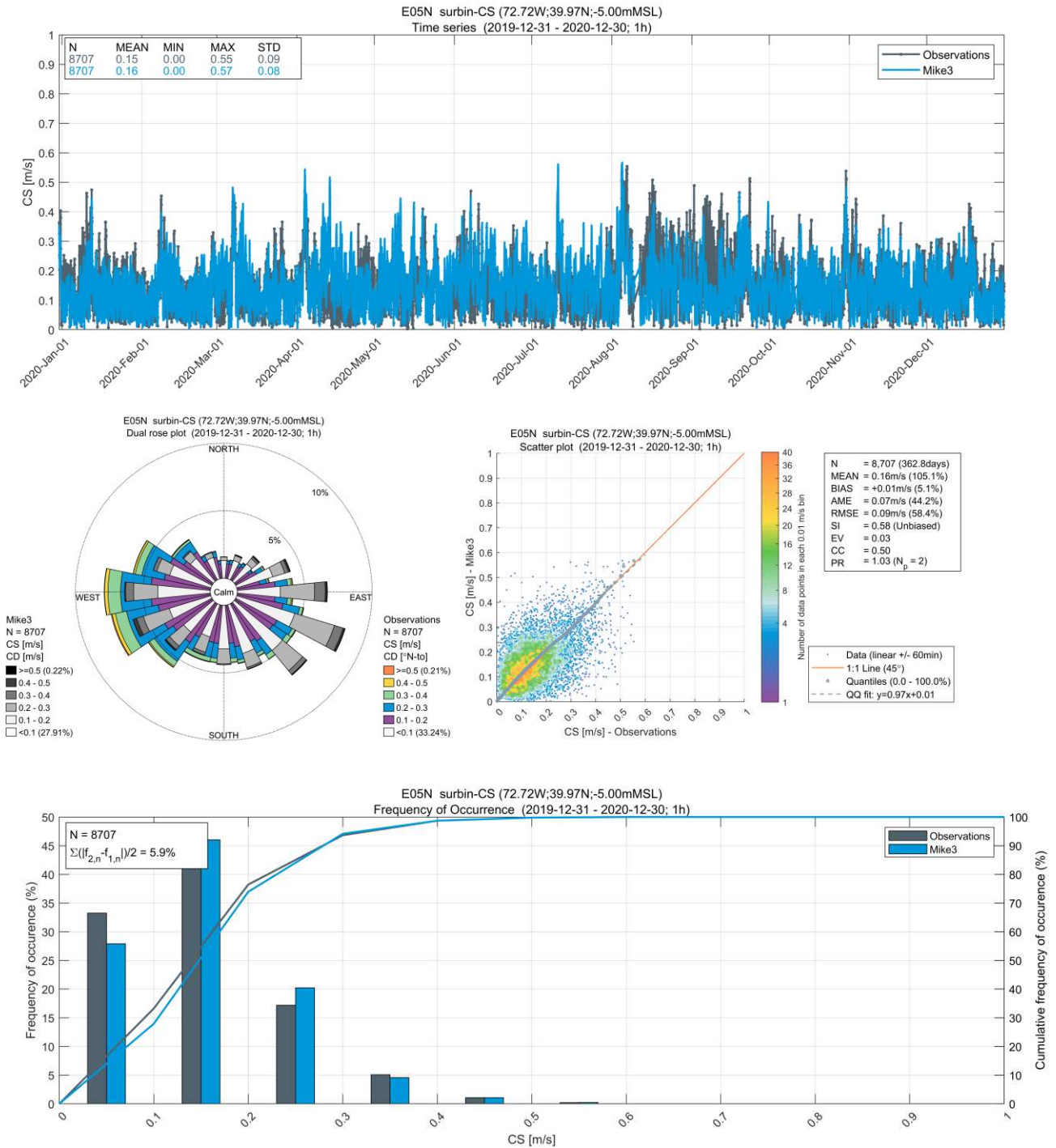


Figure A.33. NYSERDA N05 – Near Surface Layer 2020 (~1 year) Current Speed (CS) and Current Direction (CD) Observational Data vs Model Results

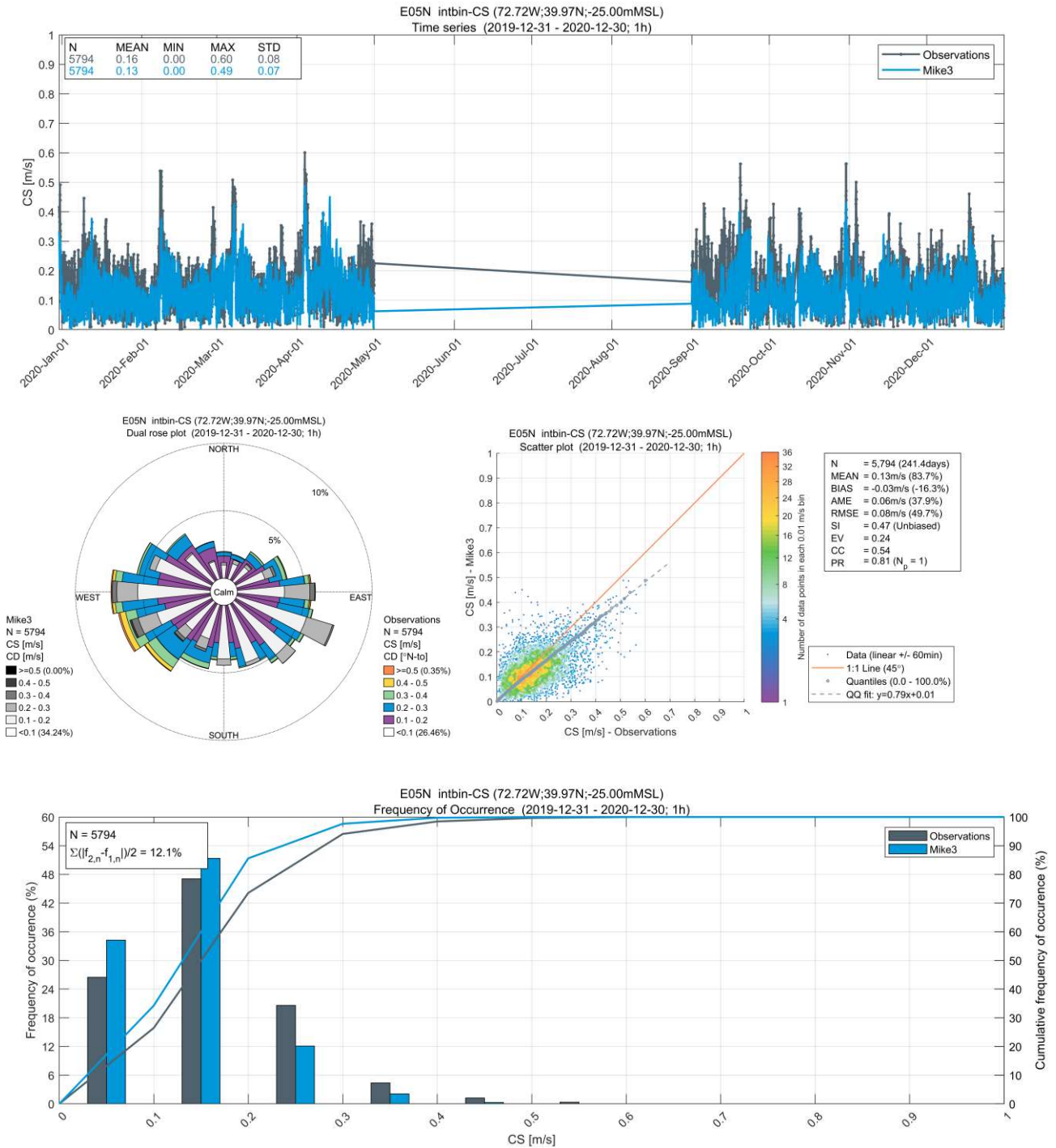


Figure A.34. NYSEDA N05 – Midwater Layer 2020 (~1 year) Current Speed (CS) and Current Direction (CD) Observational Data vs Model Results

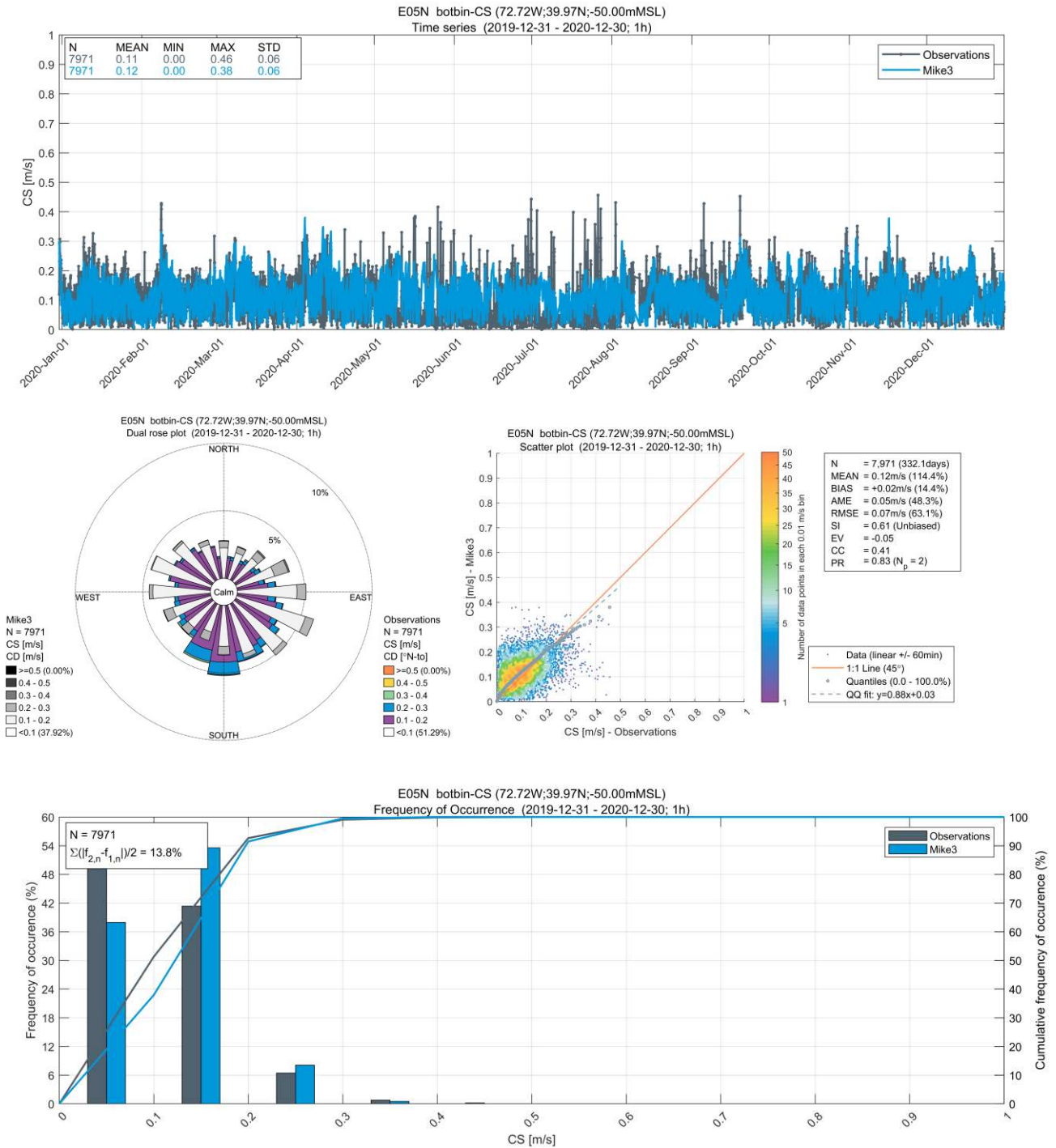


Figure A.35. NYSERDA N05 – Near Bottom Layer 2020 (~1 year) Current Speed (CS) and Current Direction (CD) Observational Data vs Model Results

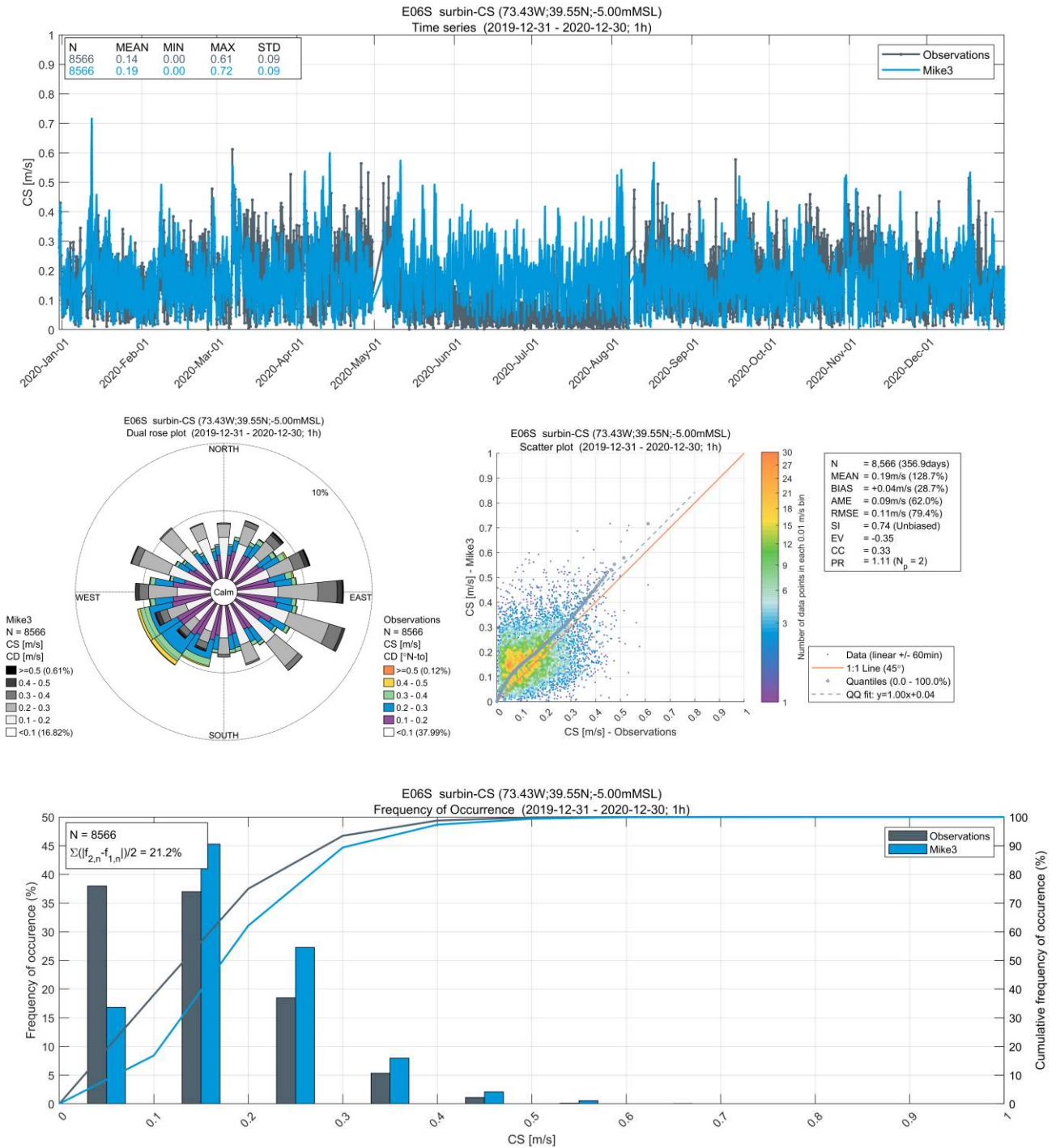


Figure A.36. NYSEDA N06 – Near Surface Layer 2020 (~1 year) Current Speed (CS) and Current Direction (CD) Observational Data vs Model Results

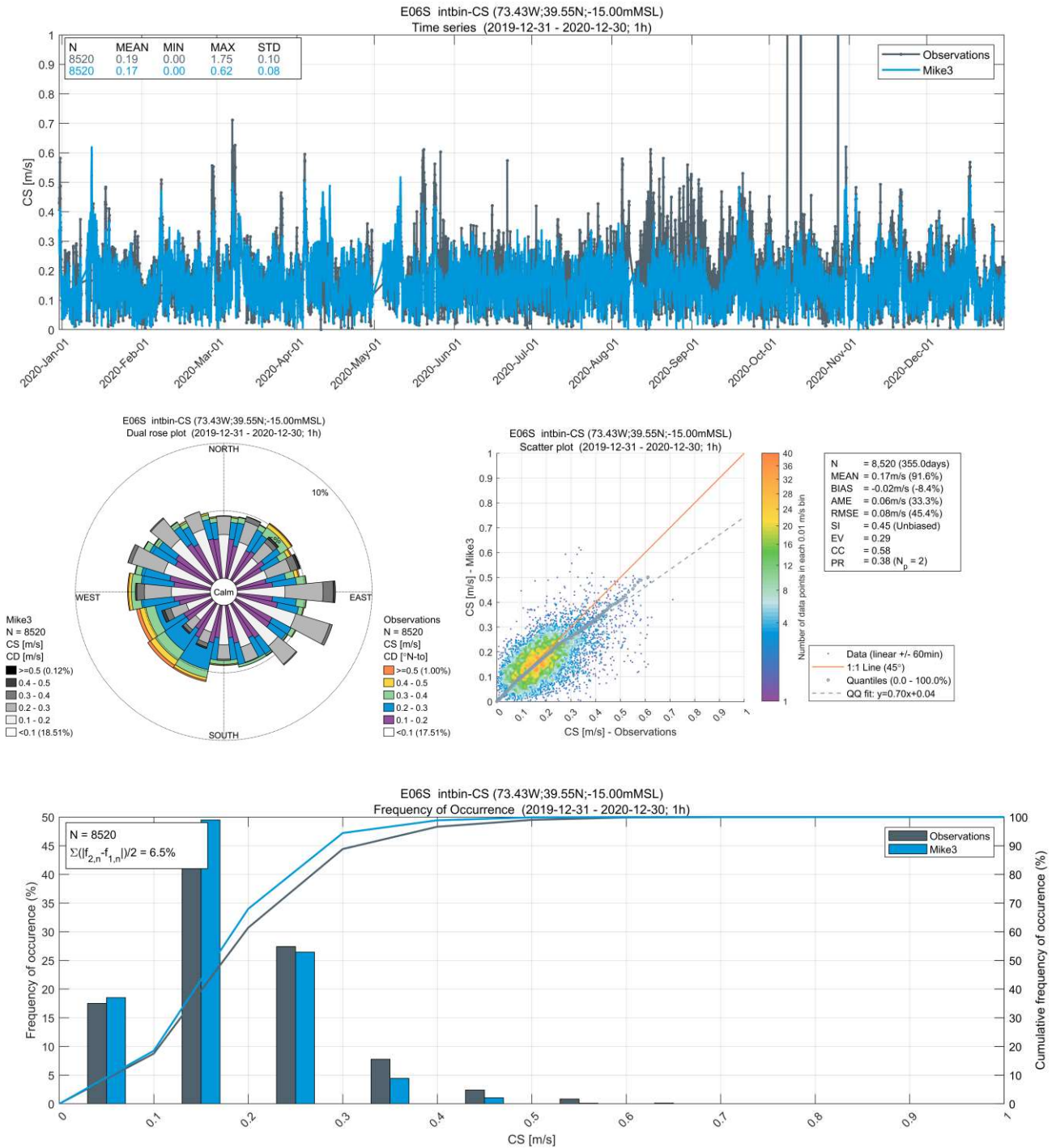


Figure A.37. NYSERDA N06 – Midwater Layer 2020 (~1 year) Current Speed (CS) and Current Direction (CD) Observational Data vs Model Results

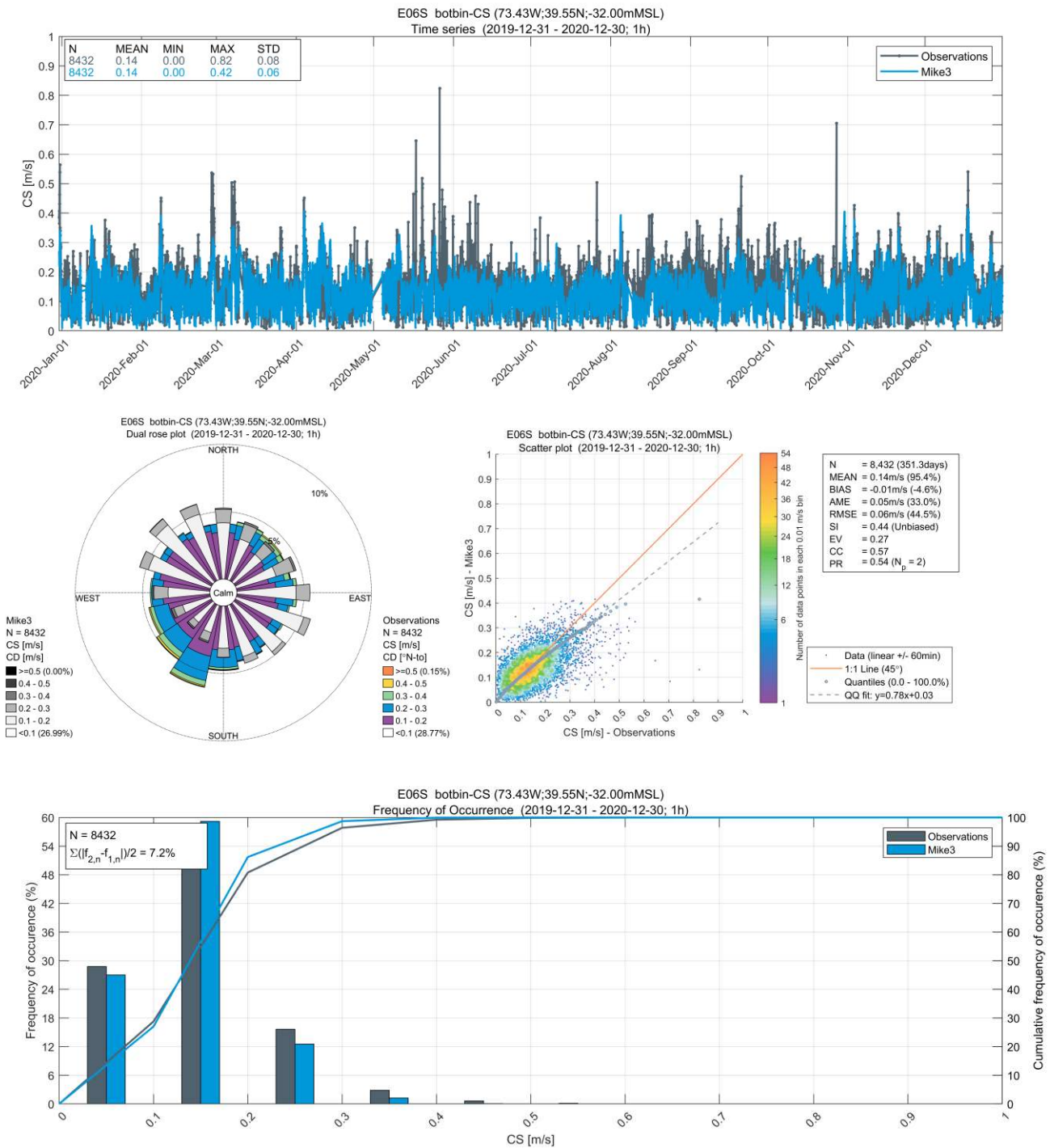


Figure A.38. NYSERDA N06 – Near Bottom Layer 2020 (~1 year) Current Speed (CS) and Current Direction (CD) Observational Data vs Model Results

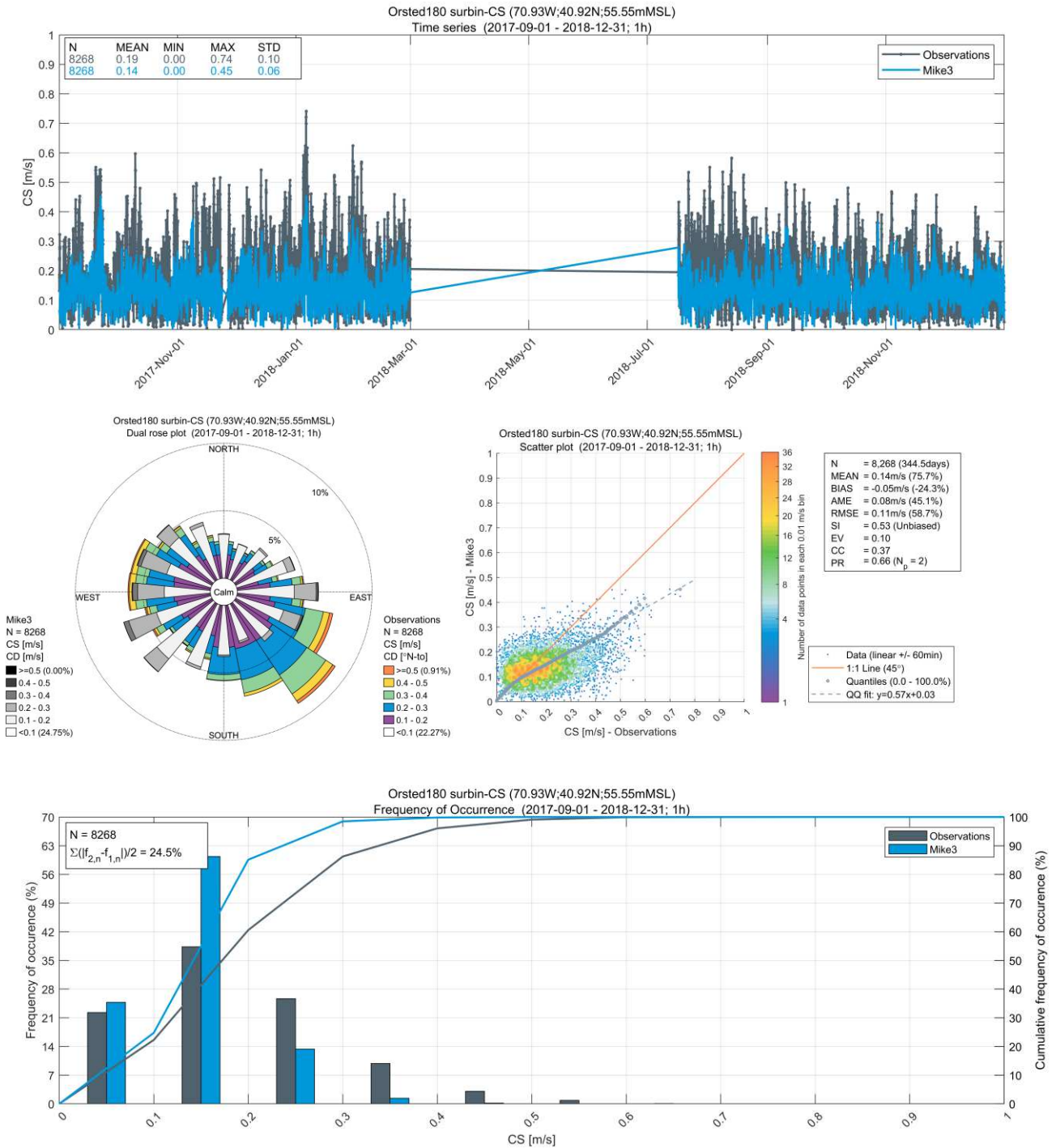


Figure A.39. Ørsted 180 – Near Surface Layer 2017 (~1 year 10 months) Current Speed (CS) and Current Direction (CD) Observational Data vs Model Results

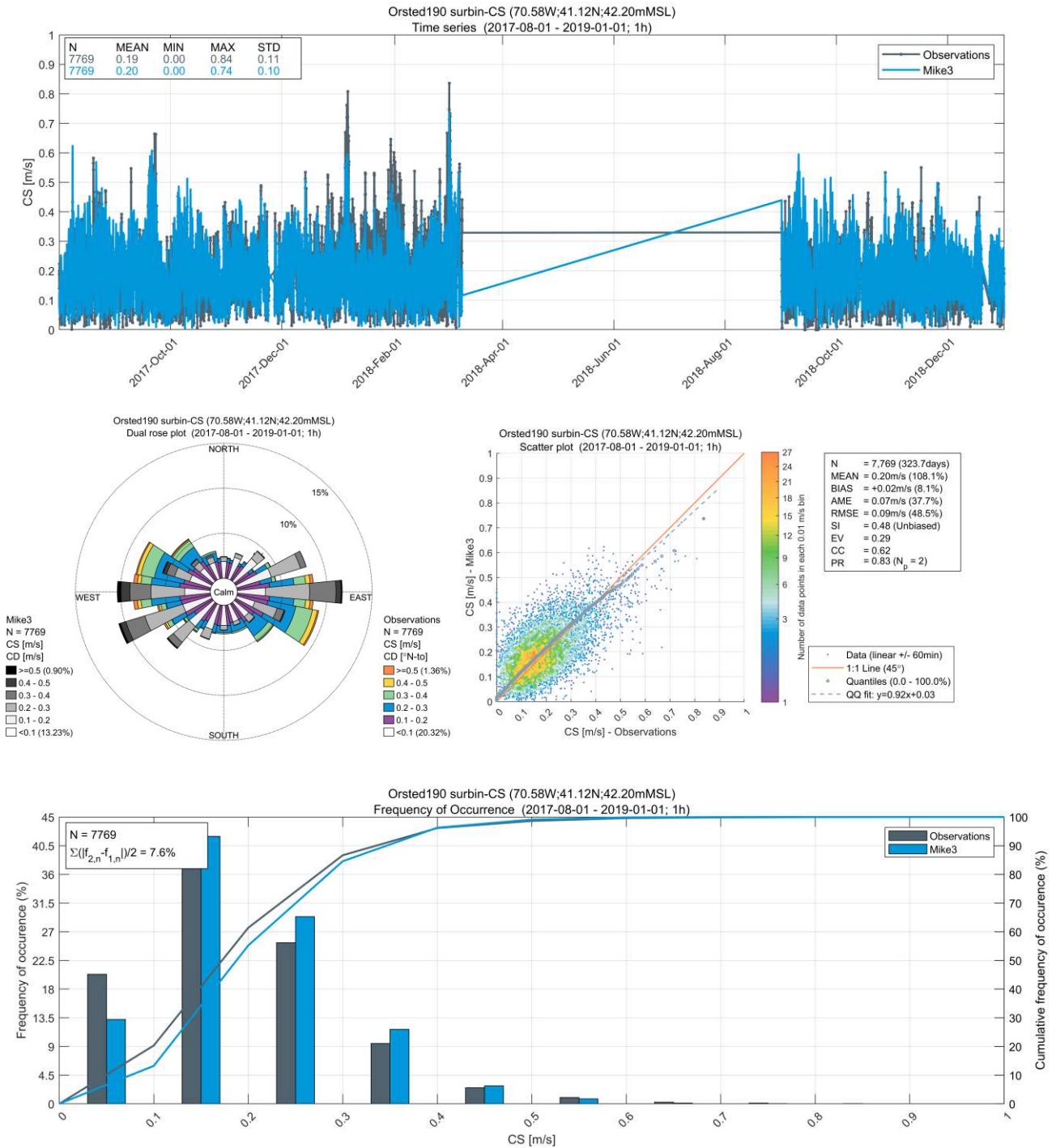


Figure A.40. Ørsted 190 – Near Surface Layer 2017 (~1 year 8 months) Current Speed (CS) and Current Direction (CD) Observational Data vs Model Results

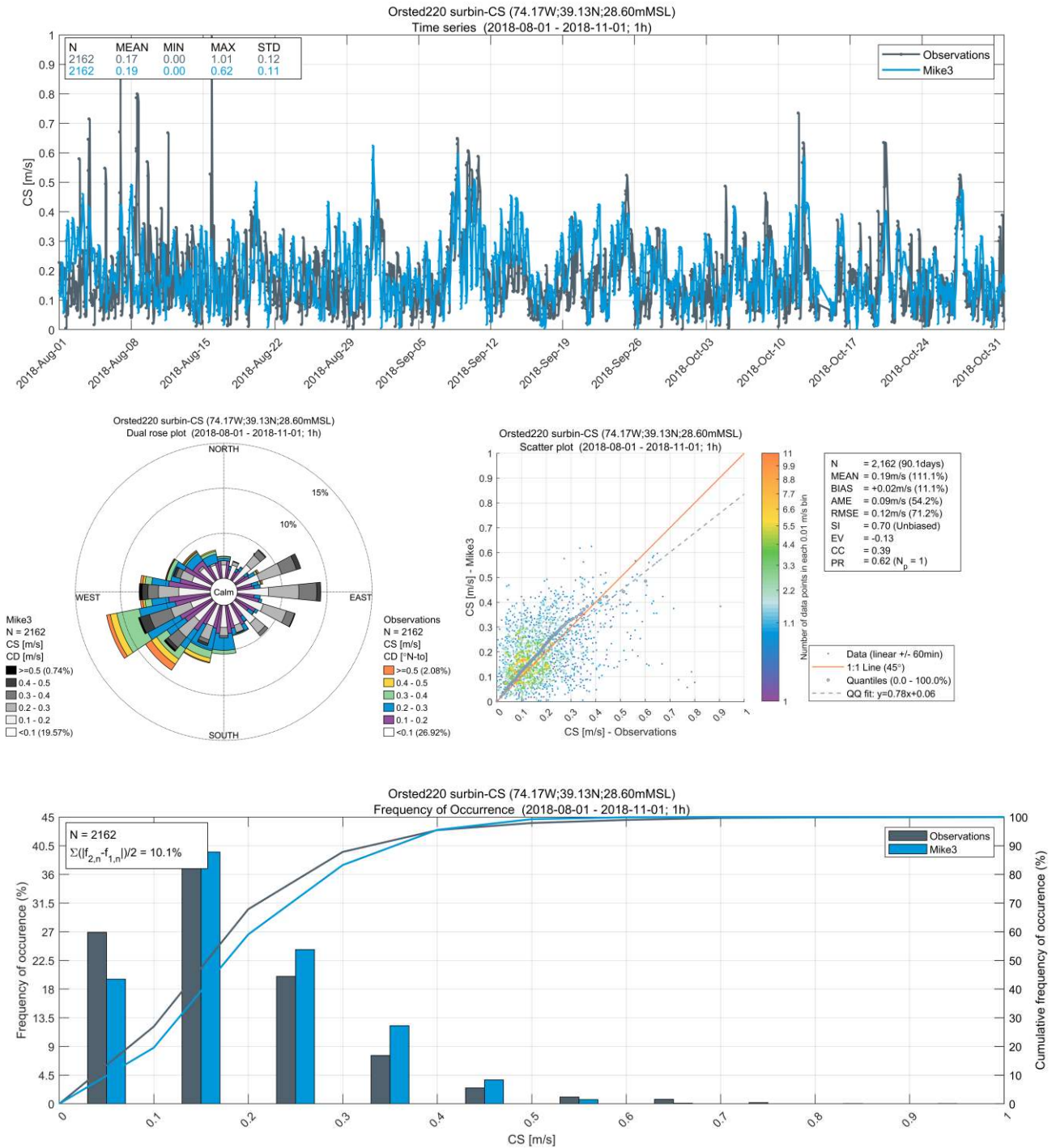


Figure A.41. Ørsted 220 – Near Surface Layer 2018 (~3 months) Current Speed (CS) and Current Direction (CD) Observational Data vs Model Results

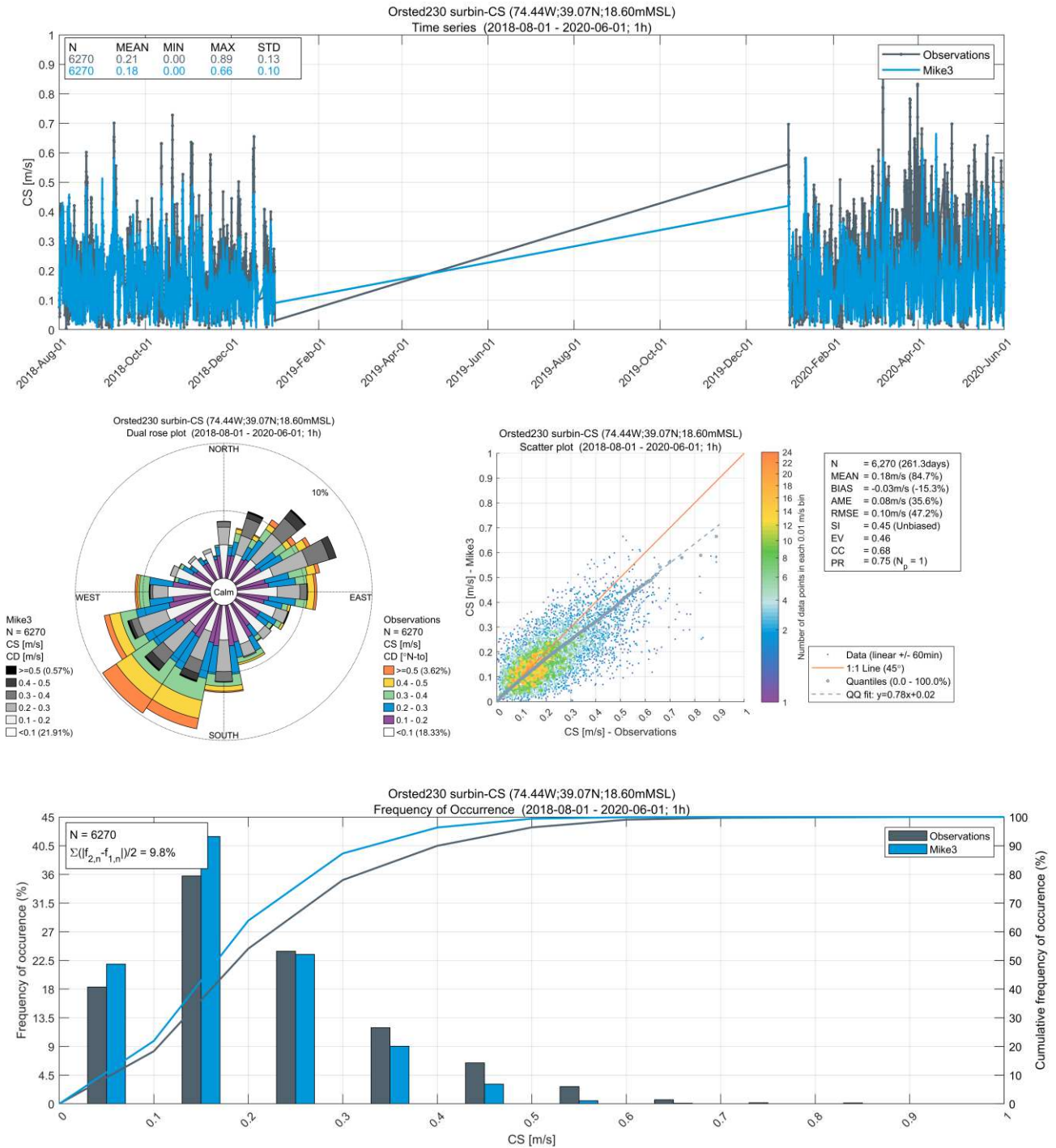


Figure A.42. Ørsted 230 – Near Surface Layer 2018 (~1 year 10 months) Current Speed (CS) and Current Direction (CD) Observational Data vs Model Results

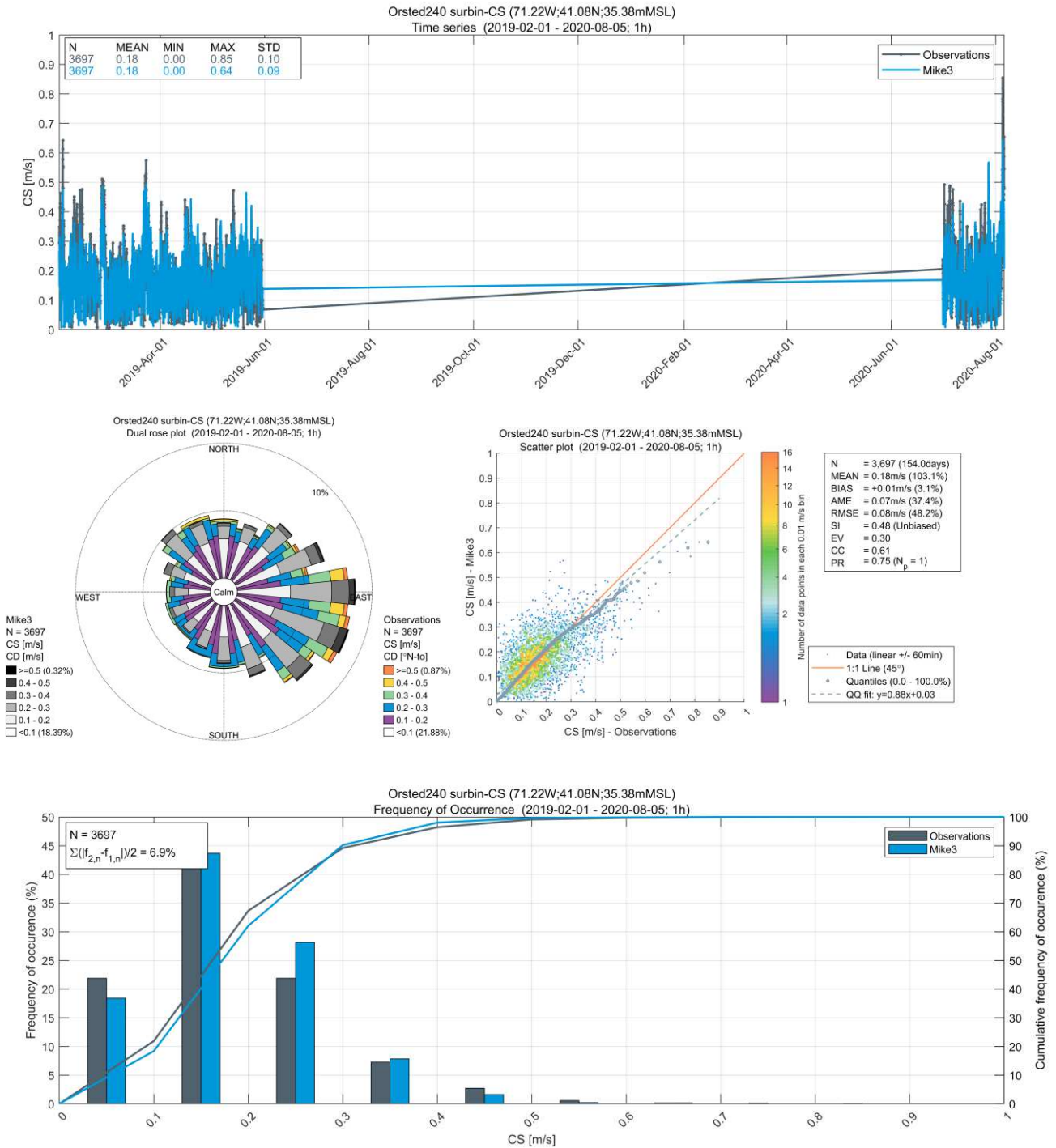


Figure A.43. Ørsted 240 – Near Surface Layer 2019 (~1 year 6 months) Current Speed (CS) and Current Direction (CD) Observational Data vs Model Results

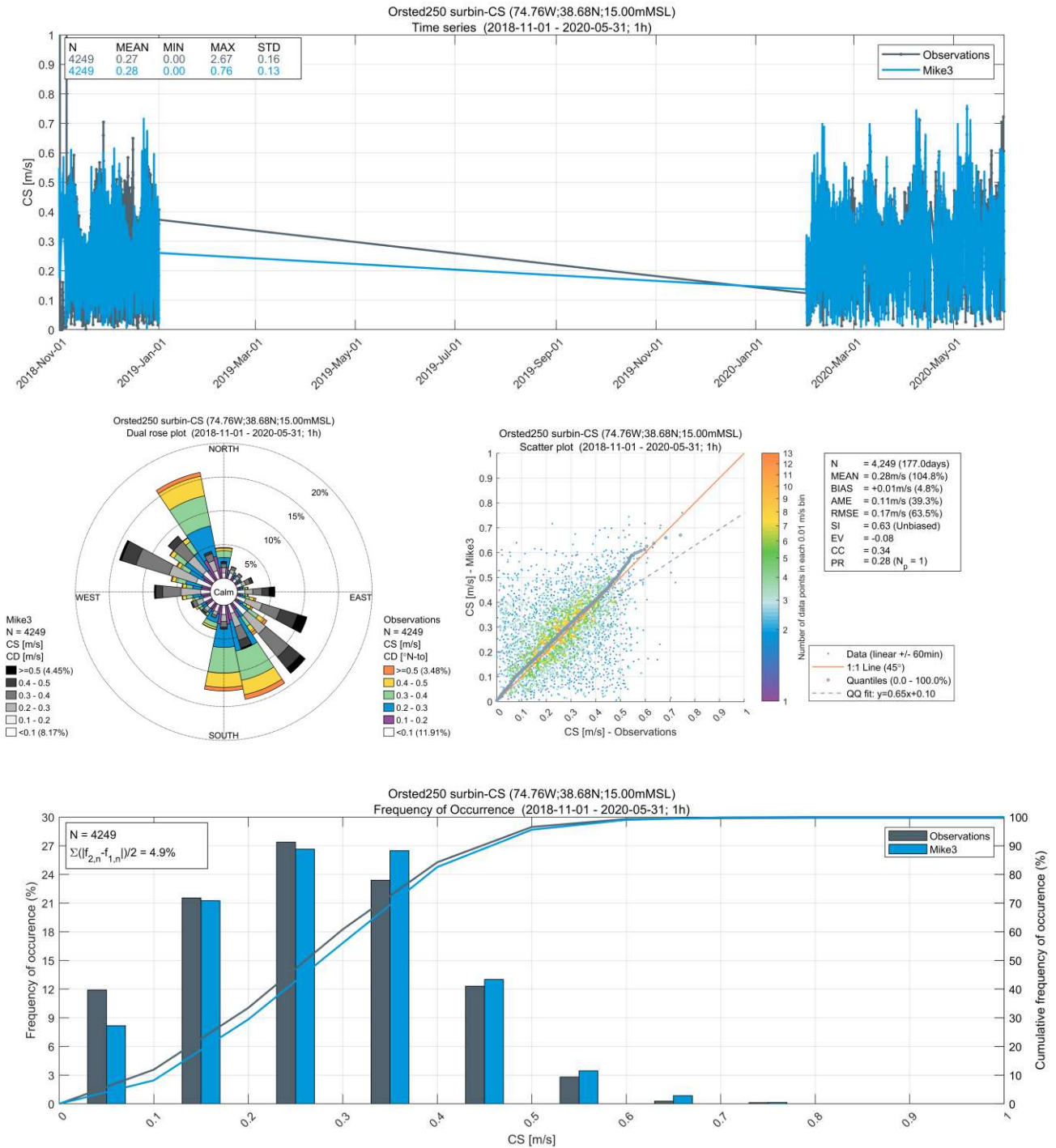


Figure A.44. Ørsted 250 – Near Surface Layer 2018 (~1 year 7 months) Current Speed (CS) and Current Direction (CD) Observational Data vs Model Results

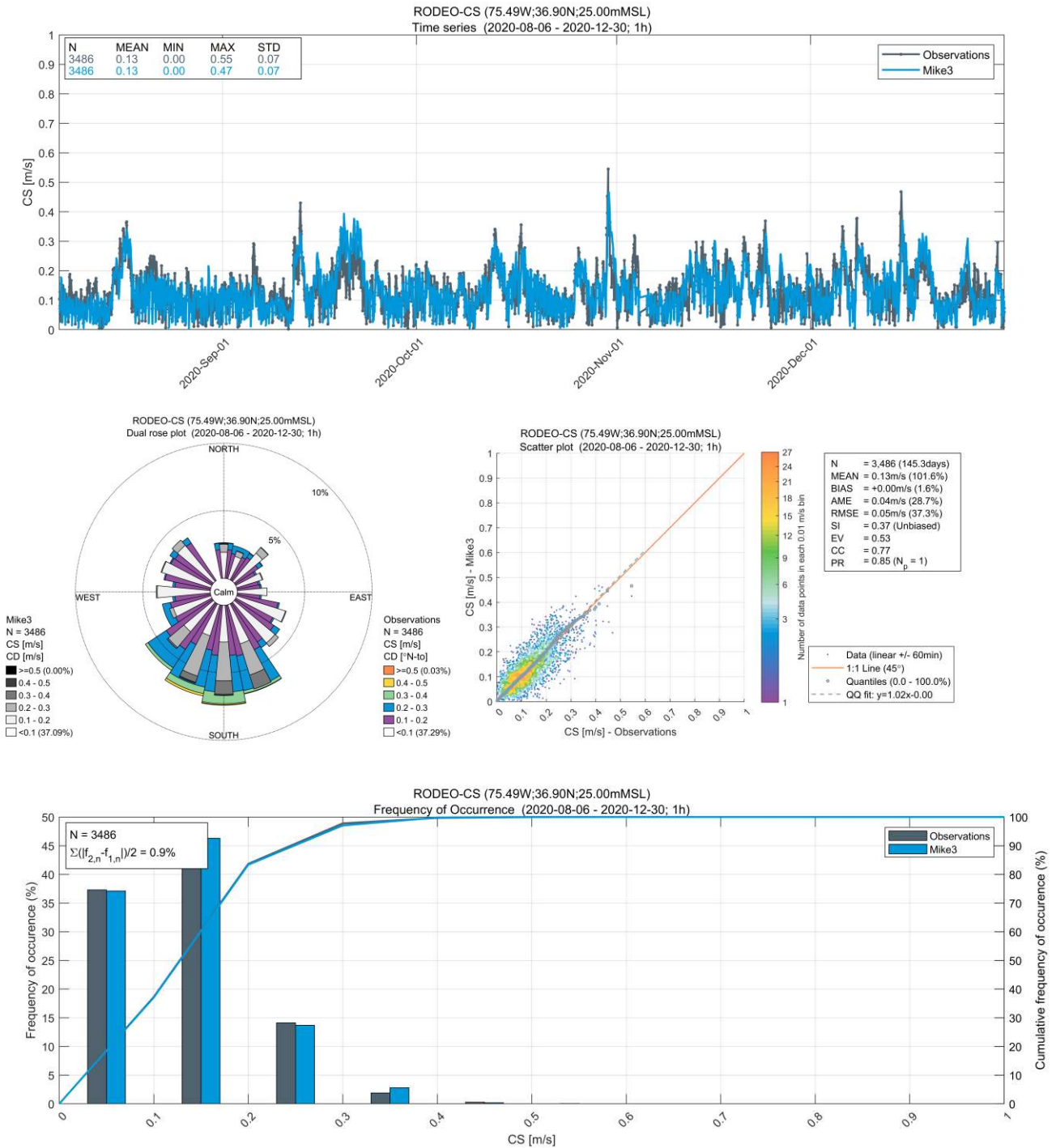


Figure A.45. RODEO – Depth Average Current Speed 2020 (~5 months) Current Speed (CS) and Current Direction (CD) Observational Data vs Model Results

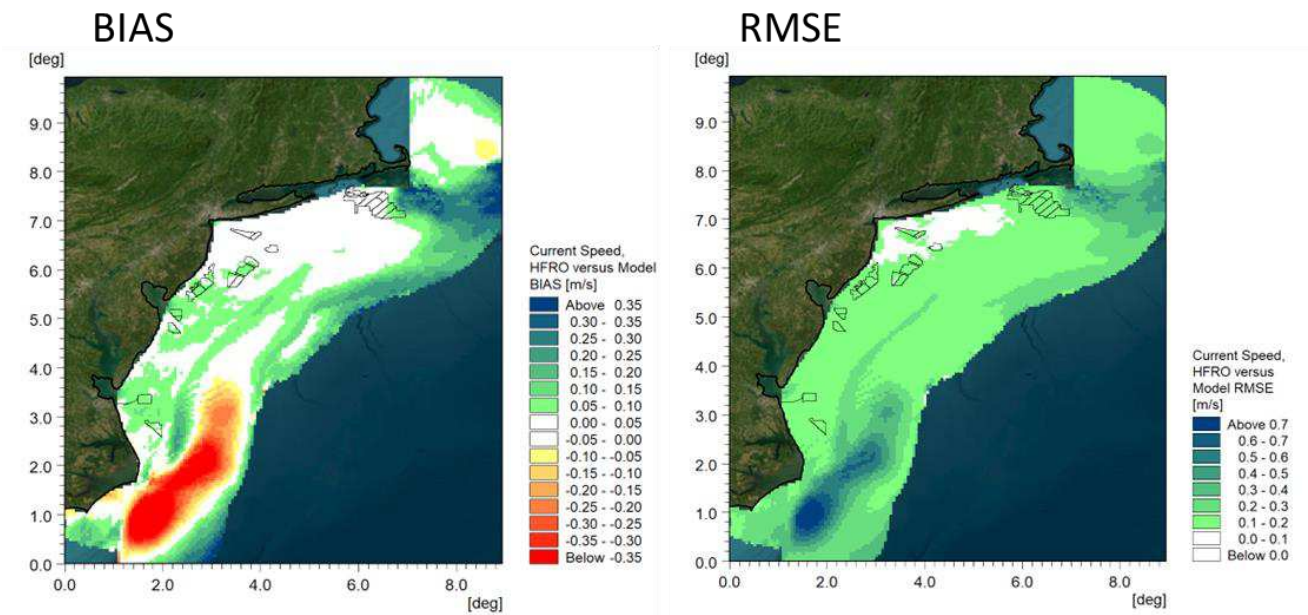


Figure A.46. High Frequency Radar Observations versus Model Metric Maps (2017)

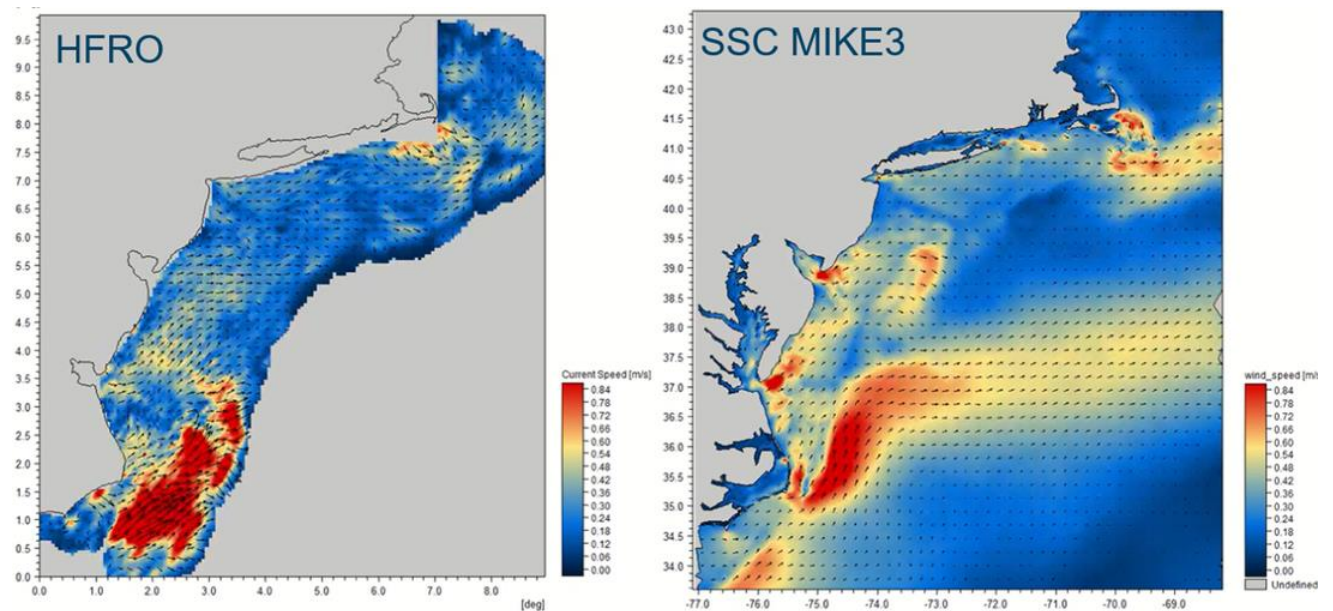


Figure A.47. High Frequency Radar Observations versus Model – Snapshot 01-Jan-2017

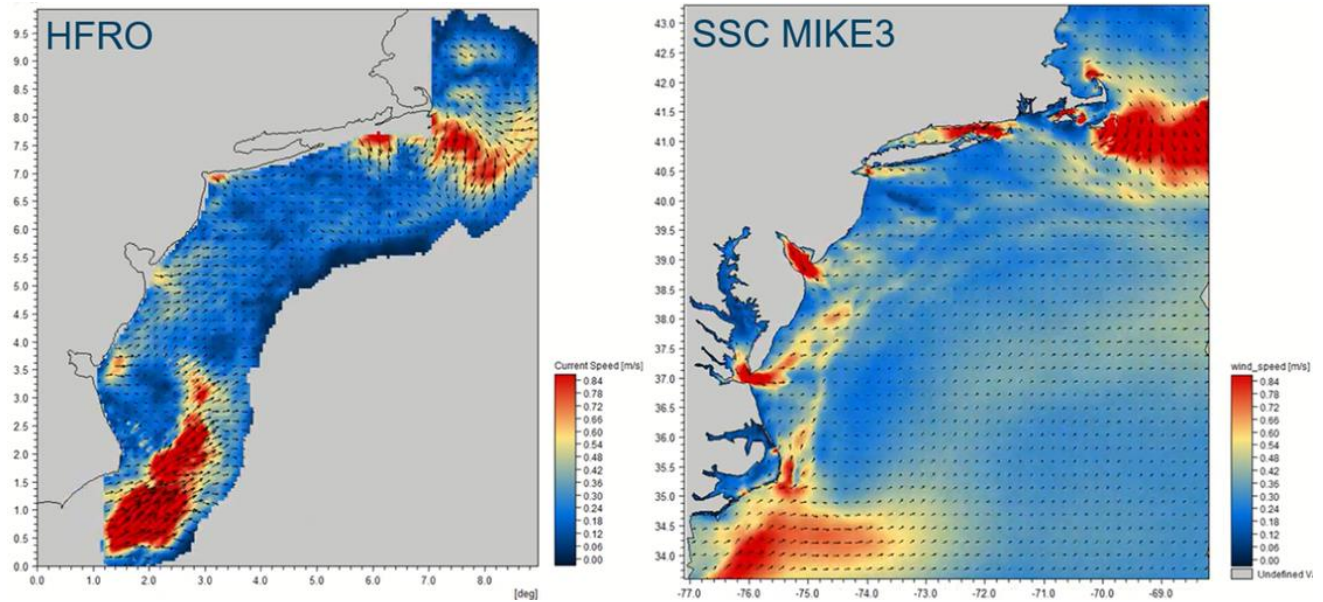


Figure A.48. High Frequency Radar Observations versus Model – Snapshot 01-Mar-2017

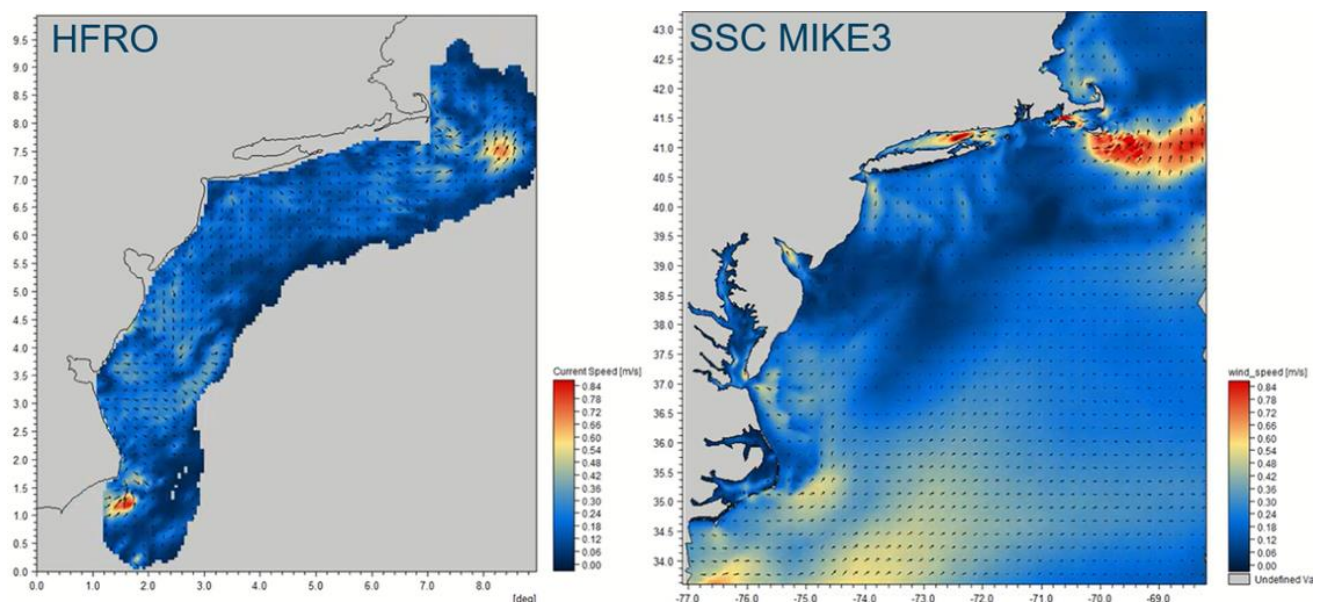


Figure A.49. High Frequency Radar Observations versus Model – Snapshot 01-Jun-2017

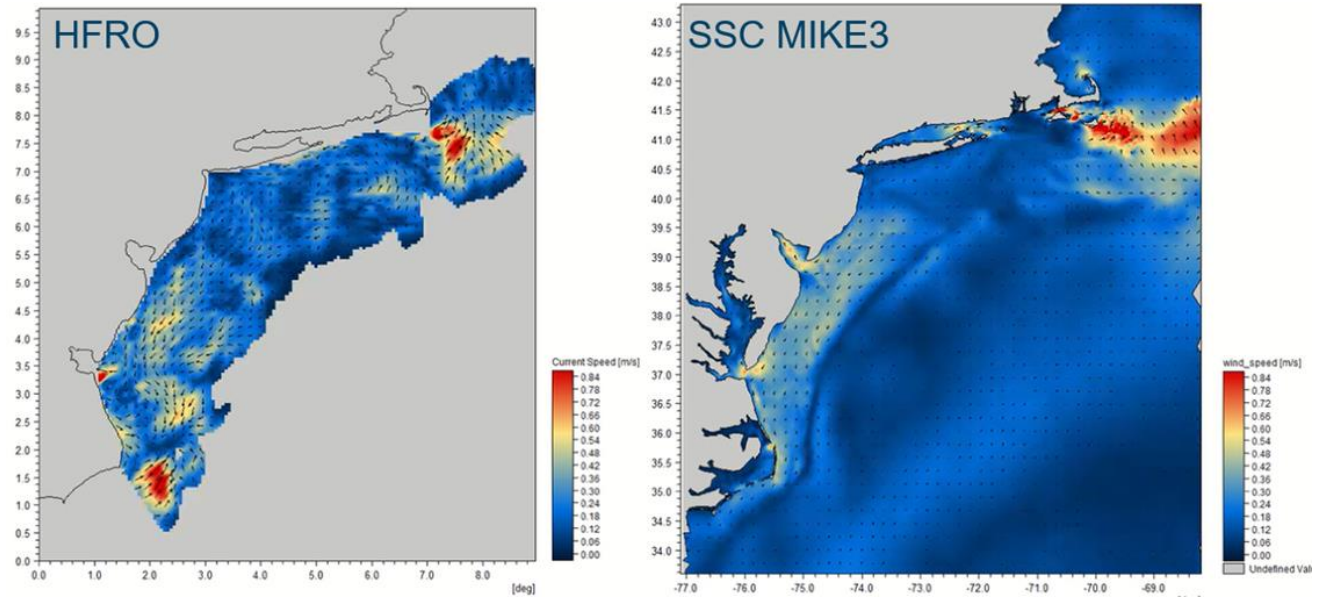


Figure A.50. High Frequency Radar Observations versus Model – Snapshot 01-Oct-2017

A.2.2 Hydrodynamic Model Baseline Wave Validation Plots

Observational data from NDBC stations including wave H_{m0} time series, wave H_{m0} frequency of occurrence, wave H_{m0} wave rose and wave H_{m0} Q-Q scatter, wave mean period time series and wave mean period frequency of occurrence are compared to model output in the following plots. Please note that Station 44025 results are contained in the main body of the report and are not repeated here in this Appendix.

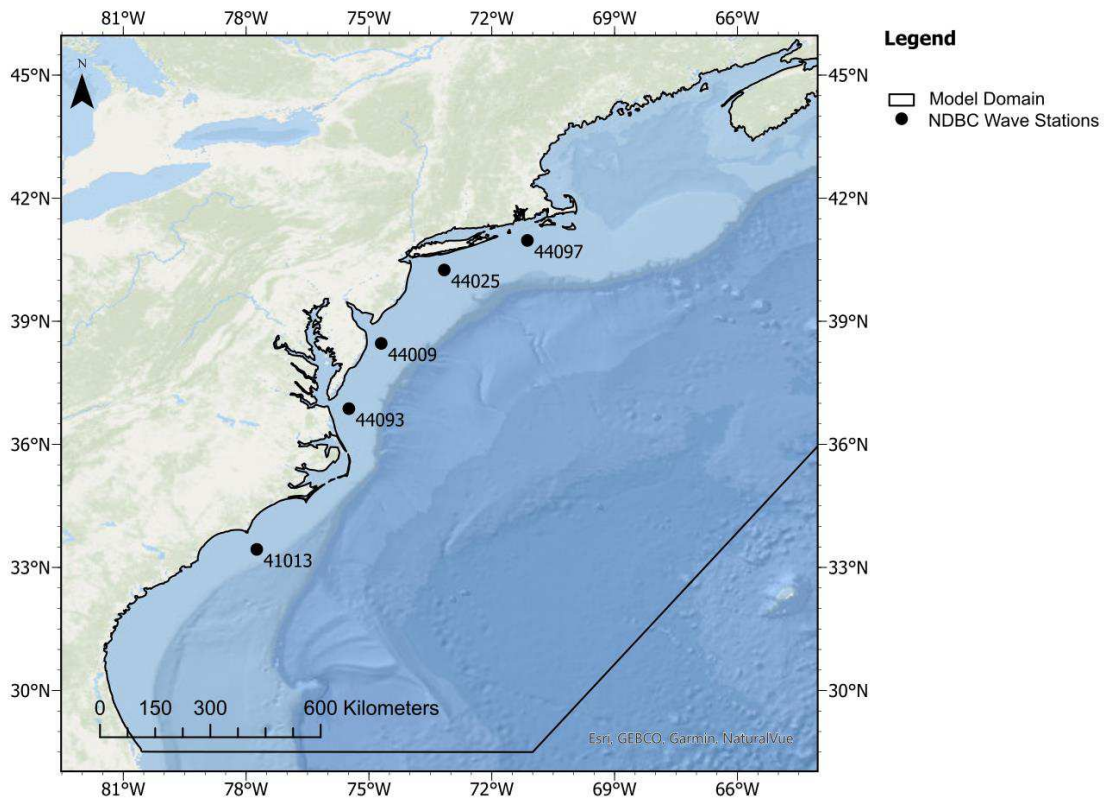
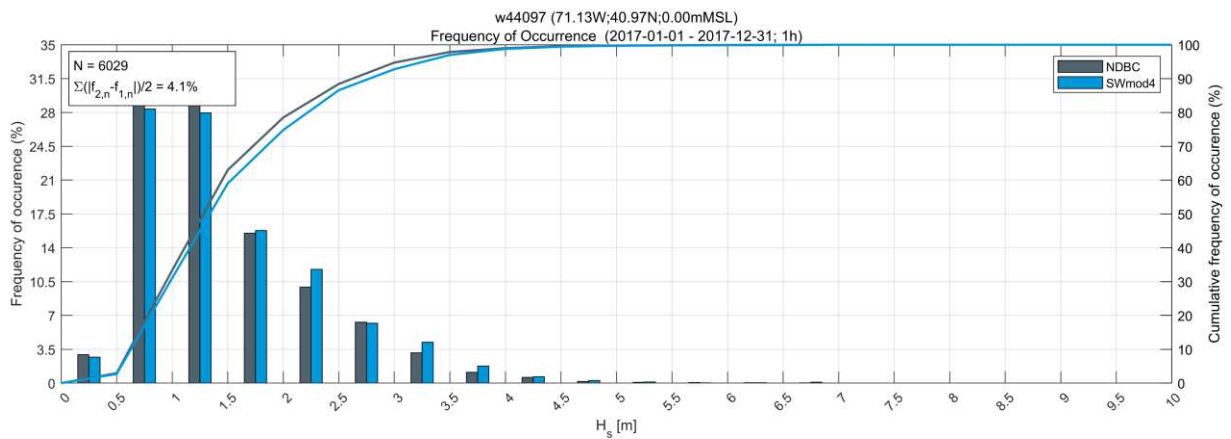
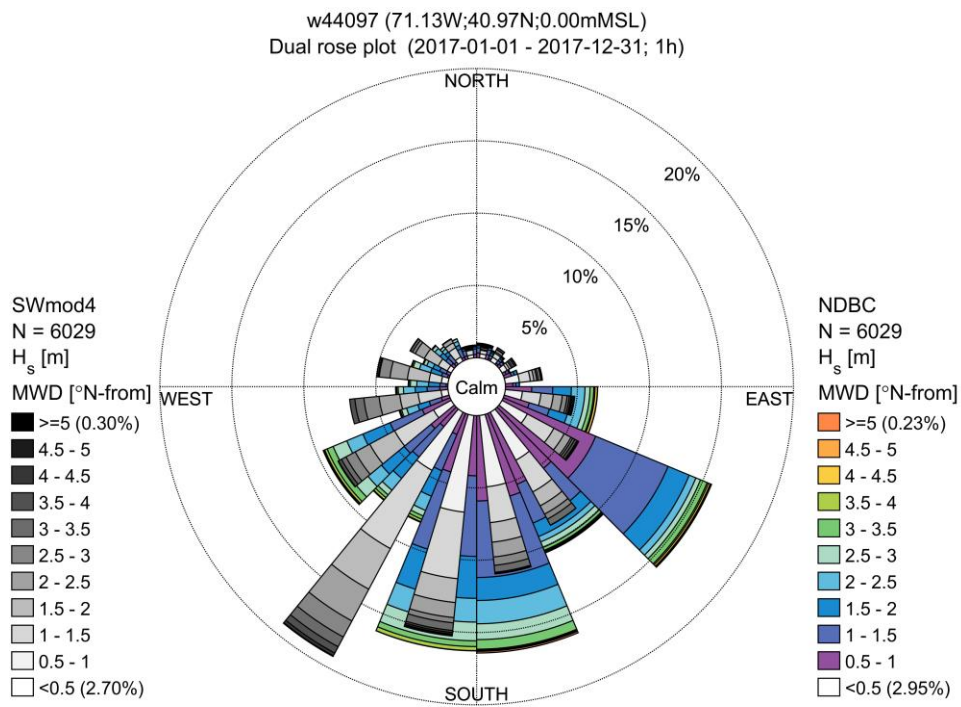
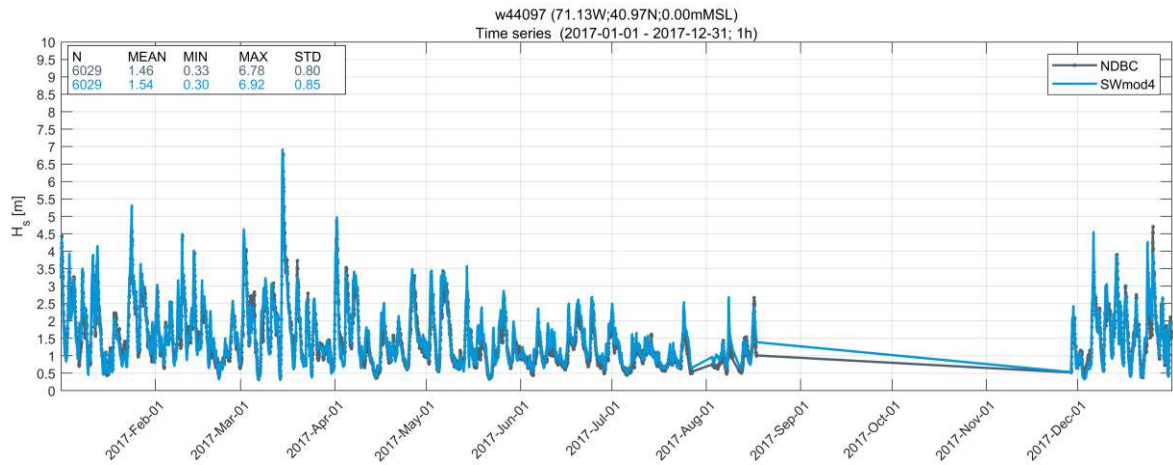


Figure A.51. NDBC Wave Stations, Used to Validate Model Wave Results

Table A.4. Wave Station Details

Name of Observation Station	Station ID	Latitude	Longitude	Water Depth (m)
Block Island, RI	44097	40°58'2" N	71°7'25" W	49
Long Island, NY	44025	40°15'30" N	73°10'29" W	40.2
Barnegat, NJ	44091	39°46'5" N	73°46'13" W	25.6
Delaware Bay, DE	44009	38°27'35" N	74°41'31" W	24
OSW Energy Area, VA	44093	36°52'21" N	75°29'30" W	26.82
Frying Pan Shoals, NC	41013	33°26'28" N	77°45'50" W	33



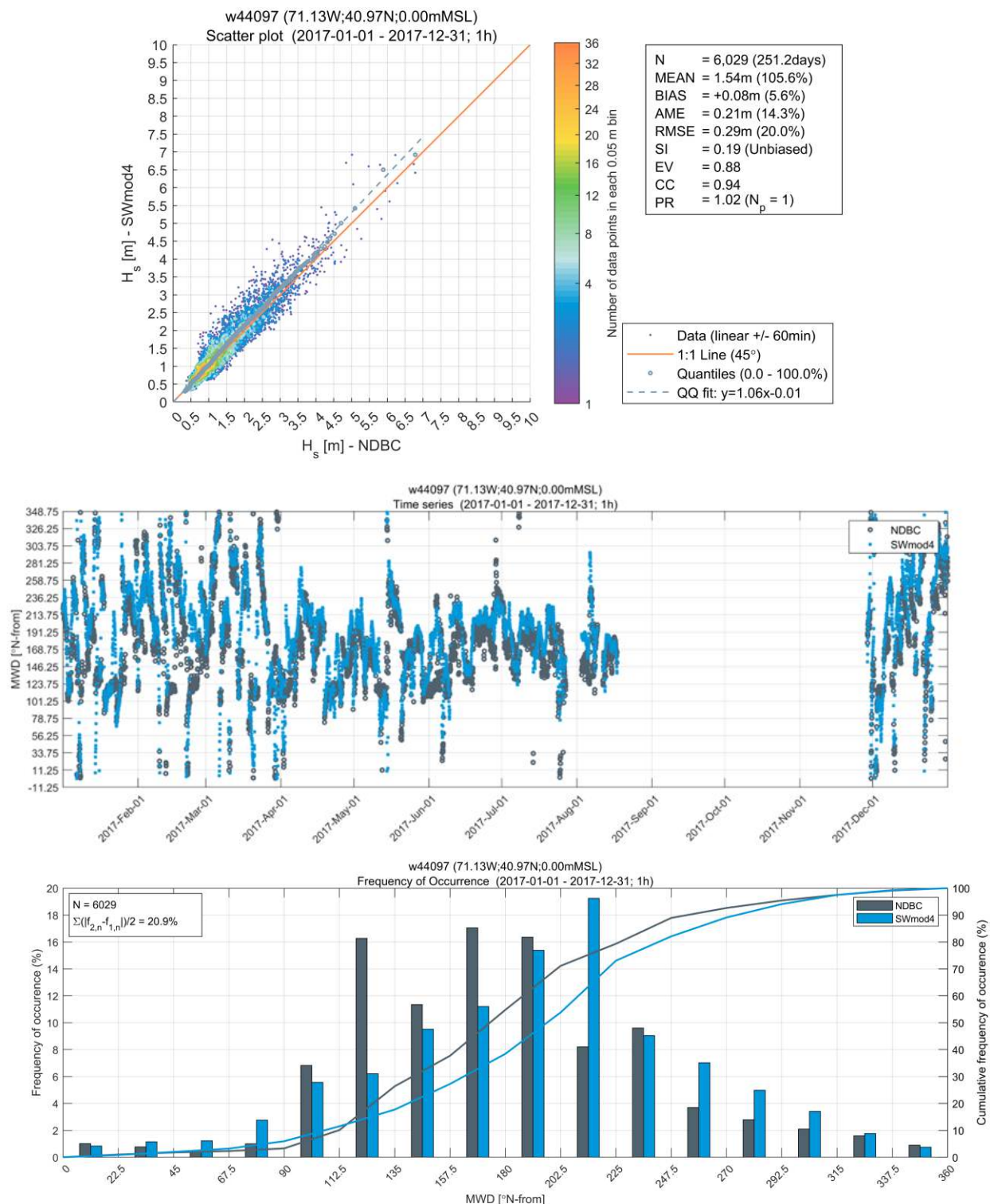
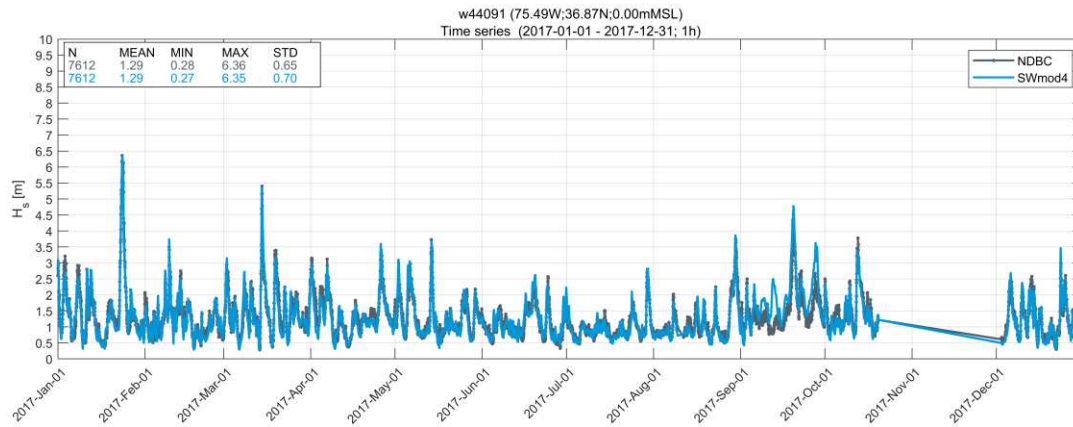
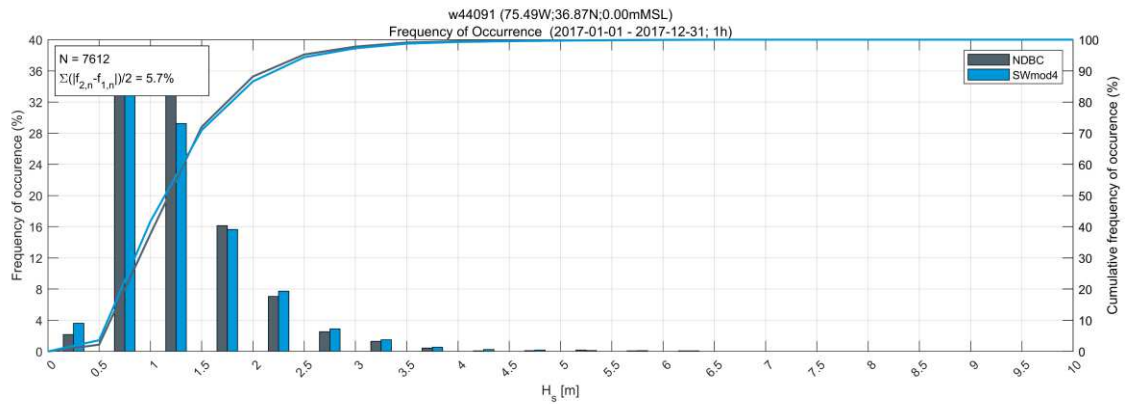
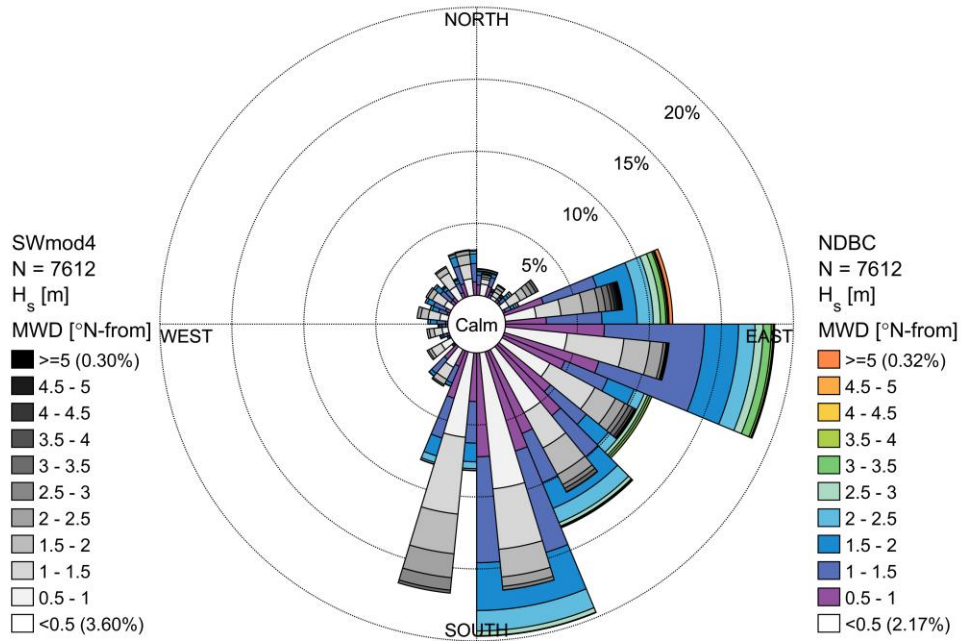


Figure A.52. Station 44097 - Block Island, RI: Wave Measurement vs. Model Results

H_{m0} time series, wave H_{m0} frequency of occurrence, wave H_{m0} wave rose and wave H_{m0} Q-Q scatter, wave mean direction time series and wave mean direction frequency of occurrence.



w44091 (75.49W;36.87N;0.00mMSL)
Dual rose plot (2017-01-01 - 2017-12-31; 1h)



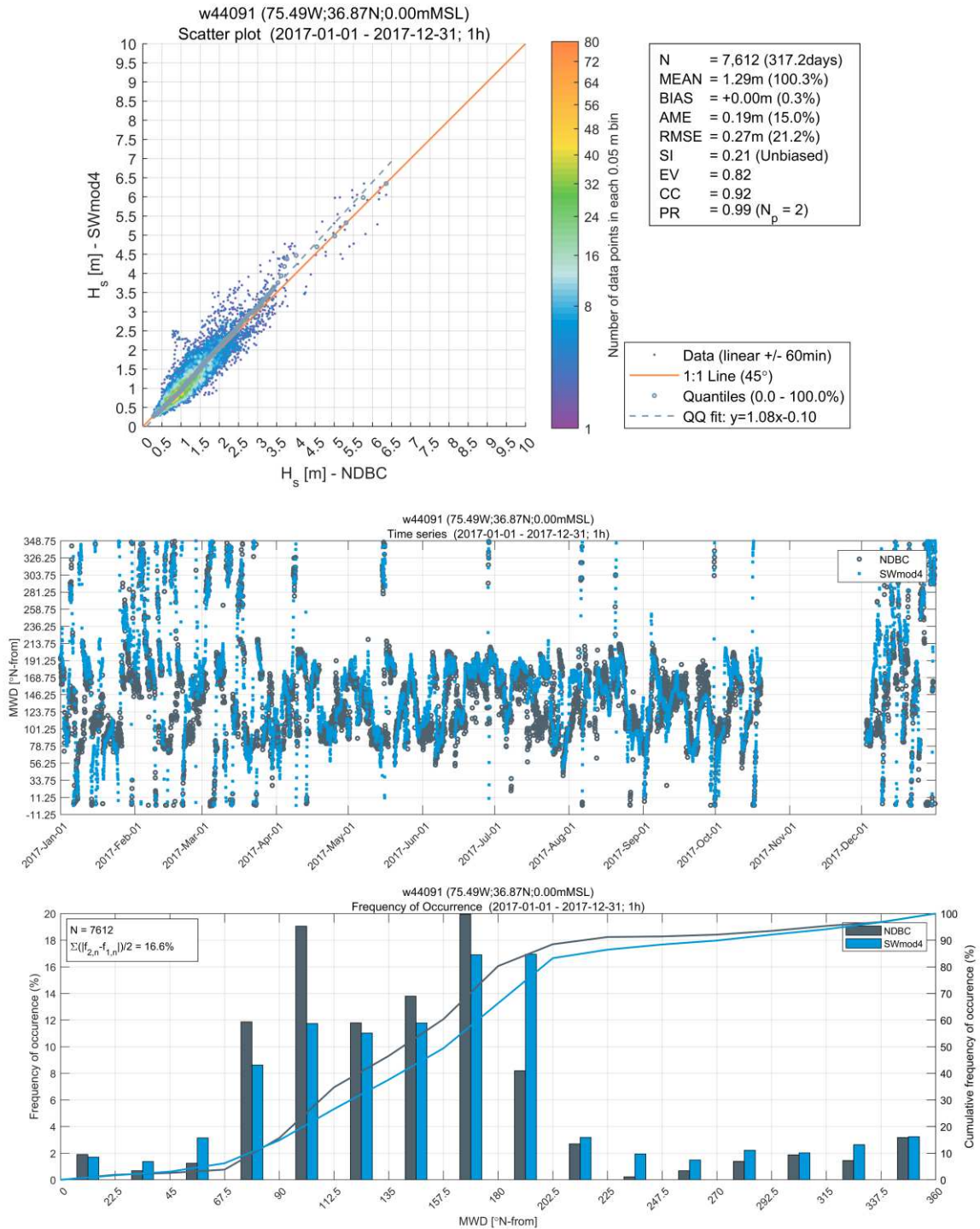
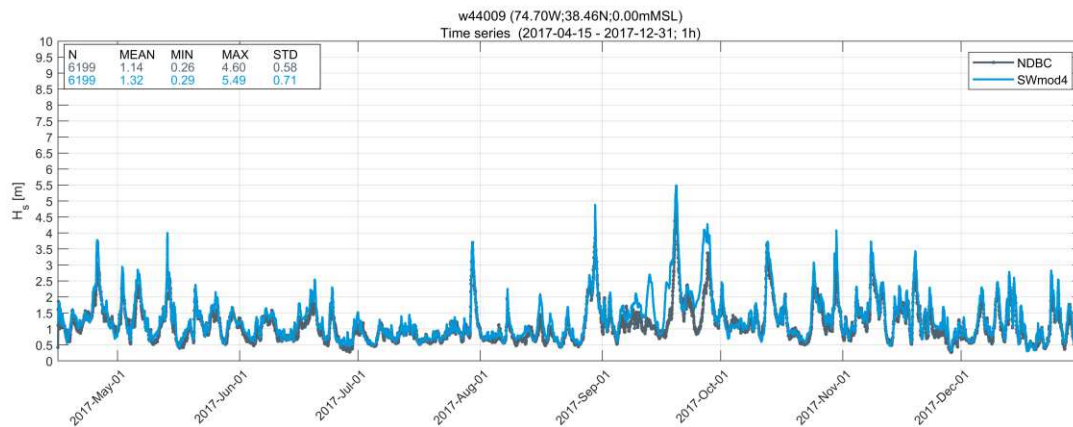
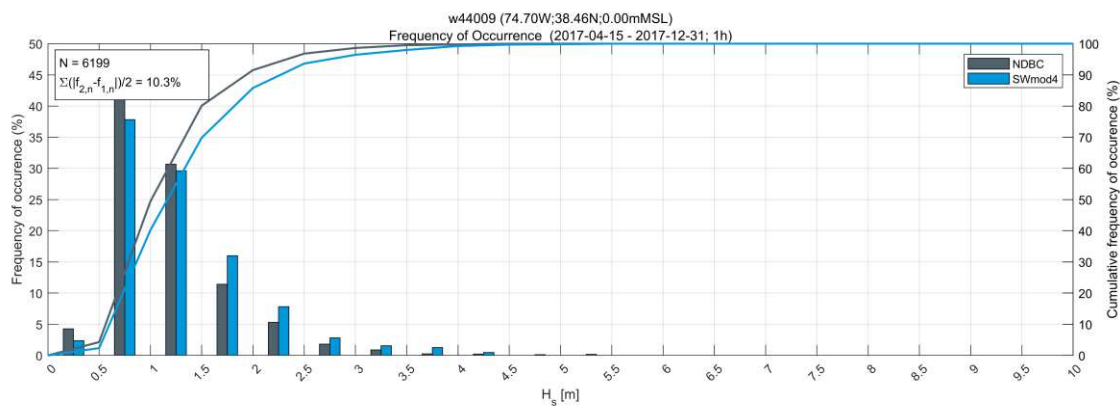
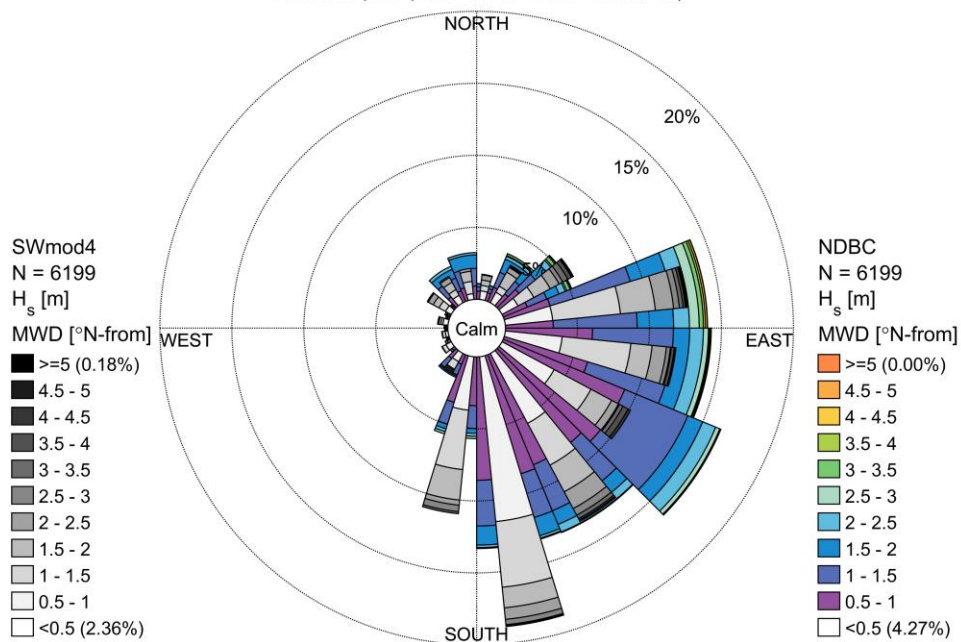


Figure A.53. Station 44091 - Barnegat, NJ: Wave Measurement vs. Model Results

H_{m0} time series, wave H_{m0} frequency of occurrence, wave H_{m0} wave rose and wave H_{m0} Q-Q scatter, wave mean direction time series and wave mean direction frequency of occurrence.



w44009 (74.70W;38.46N;0.00mMSL)
Dual rose plot (2017-04-15 - 2017-12-31; 1h)



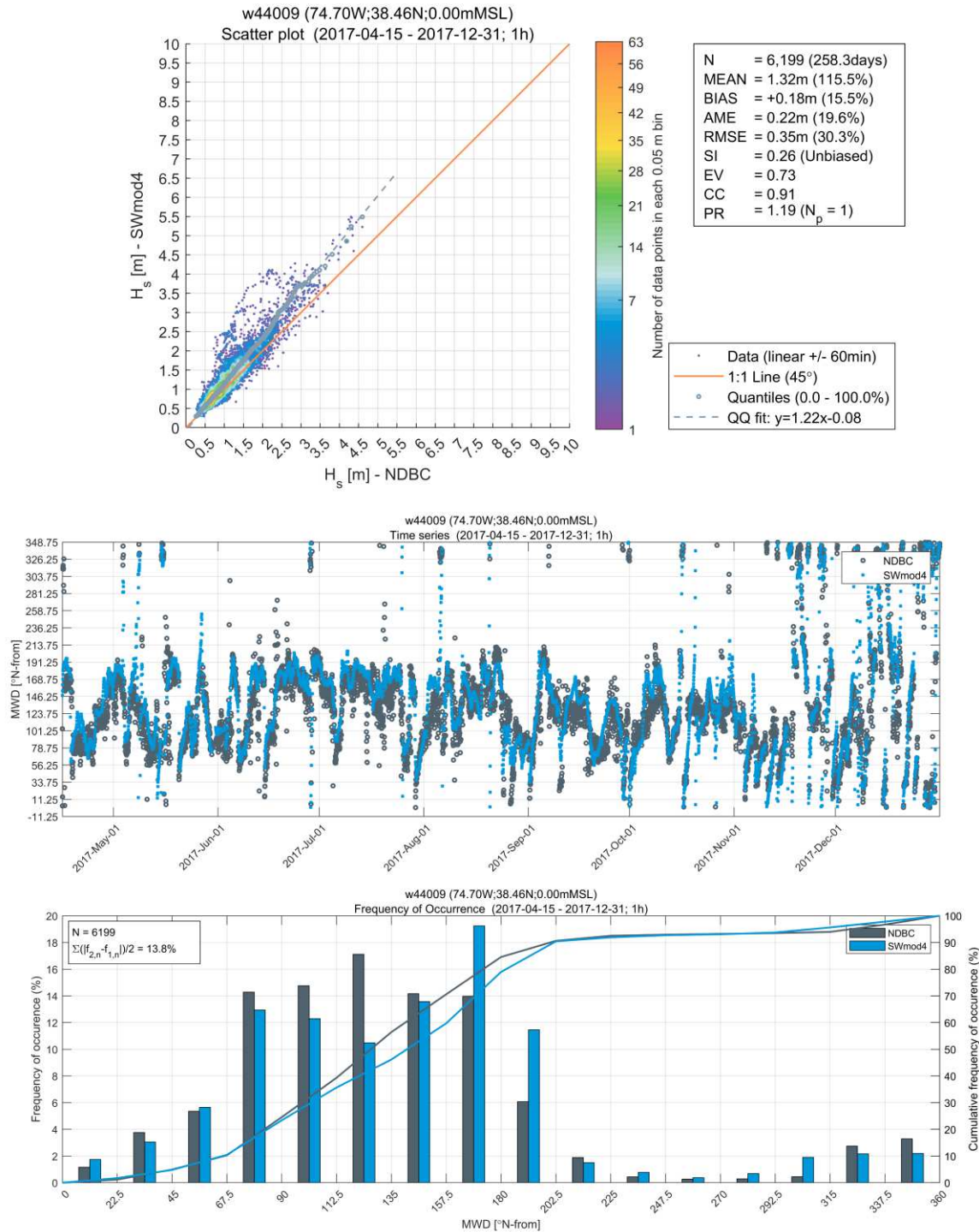
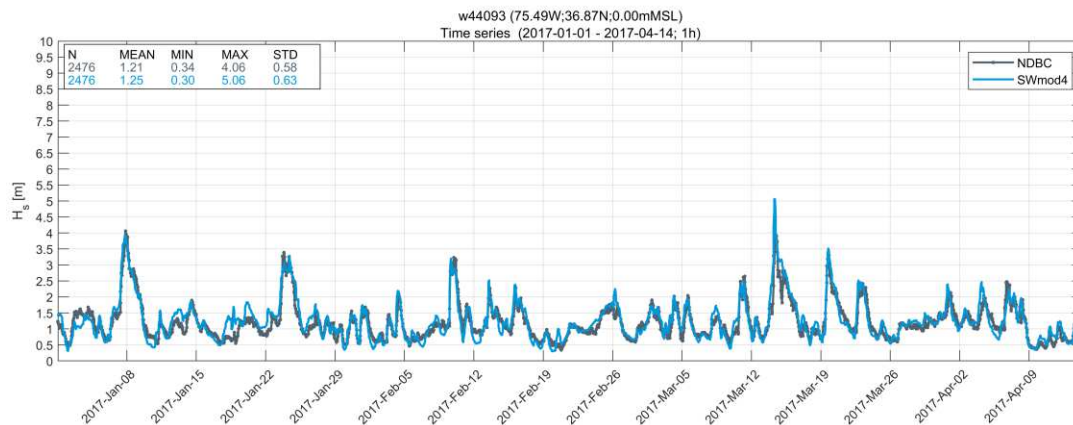
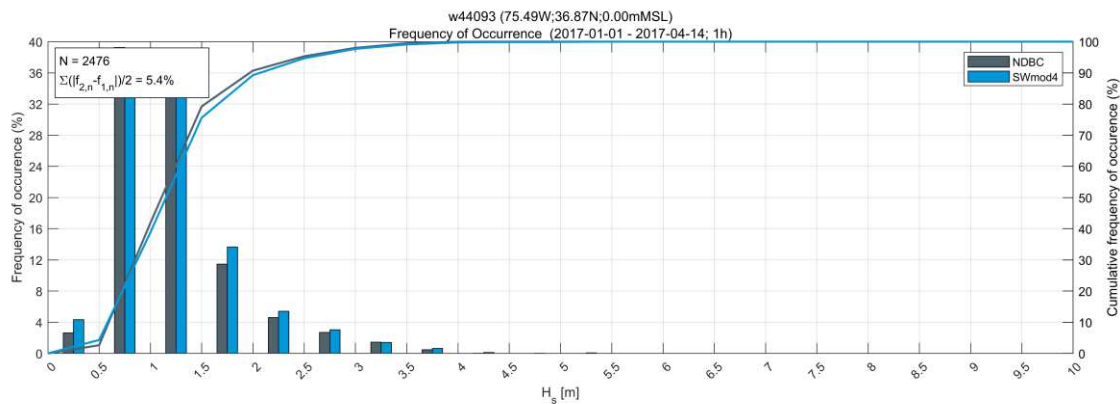
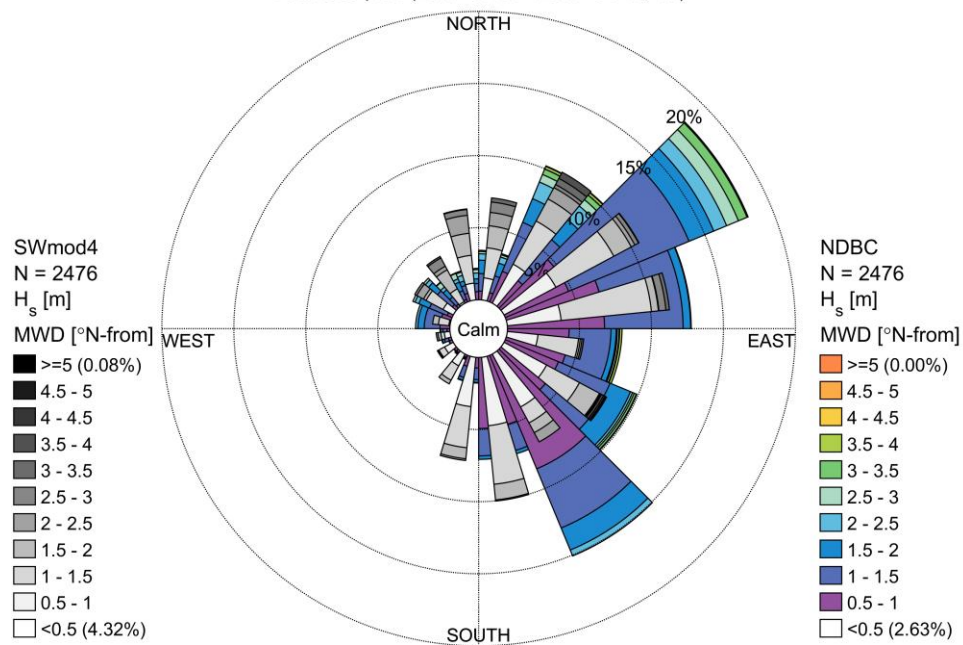


Figure A.54. Station 44009 - Delaware Bay, DE: Wave Measurement vs. Model Results

H_{m0} time series, wave H_{m0} frequency of occurrence, wave H_{m0} wave rose and wave H_{m0} Q-Q scatter, wave mean direction time series and wave mean direction frequency of occurrence.



w44093 (75.49W;36.87N;0.00mMSL)
Dual rose plot (2017-01-01 - 2017-04-14; 1h)



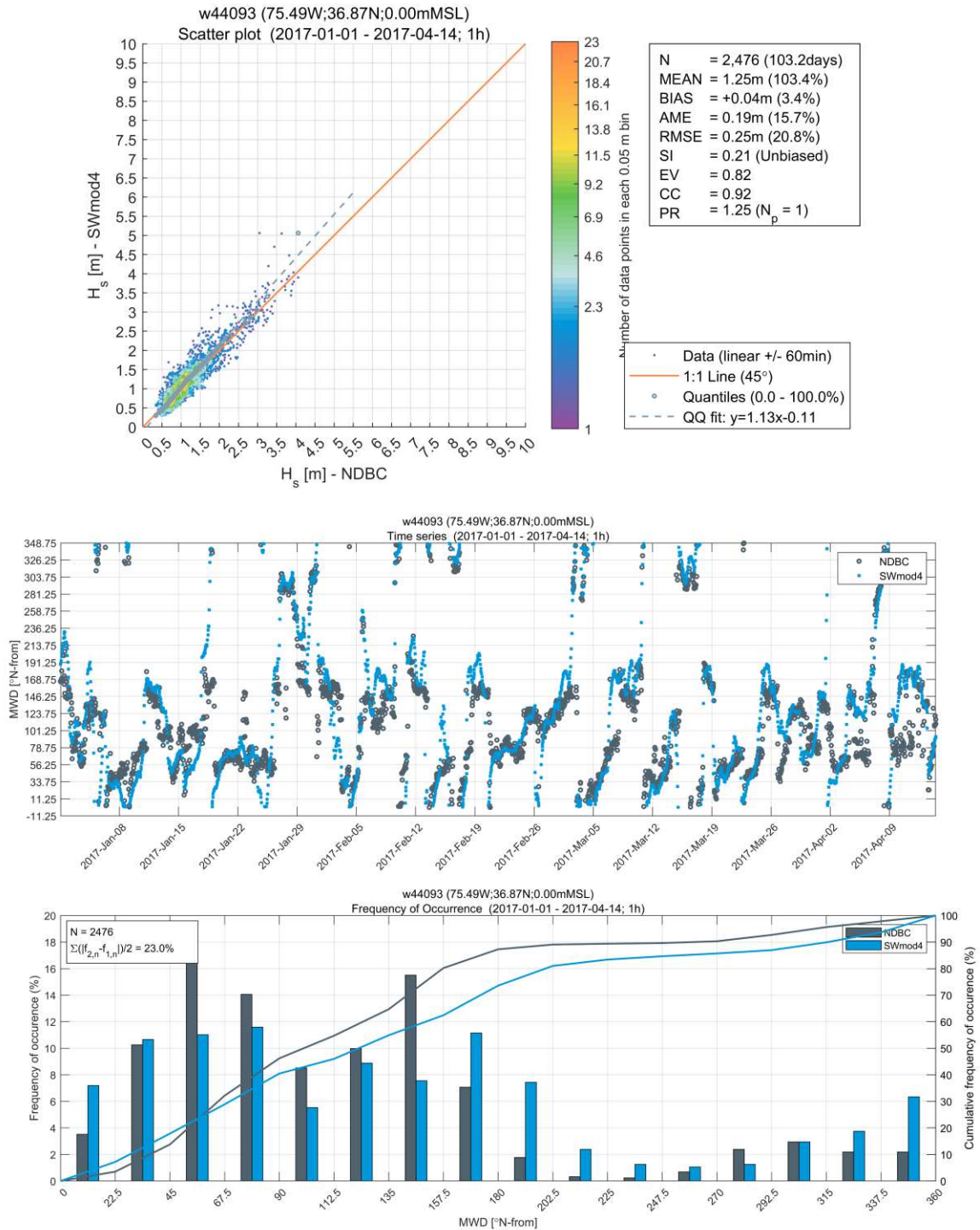
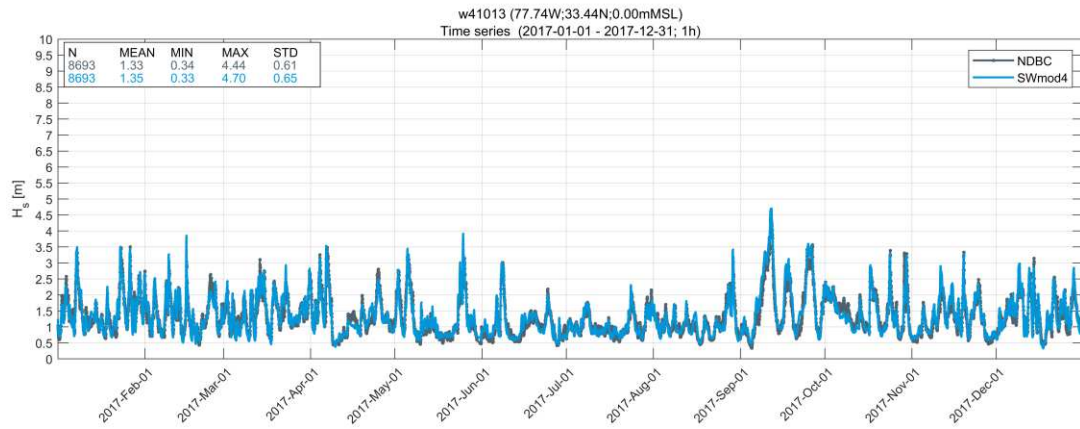
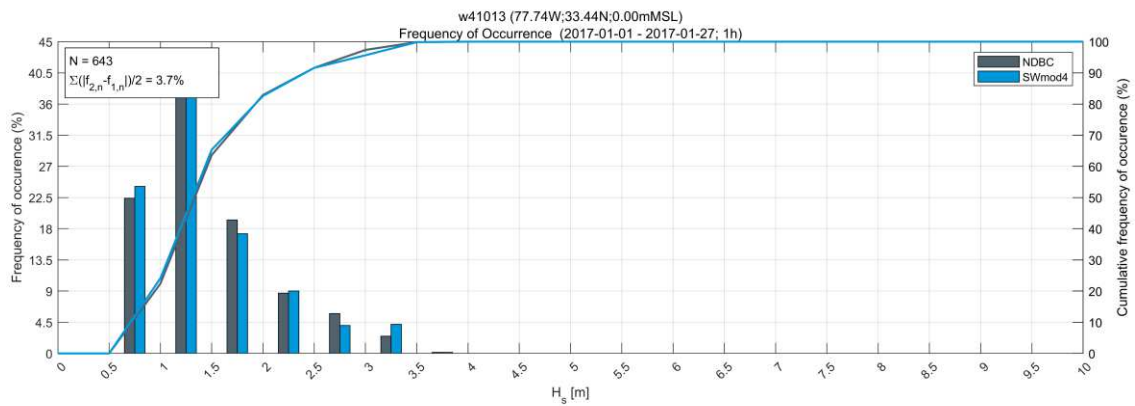
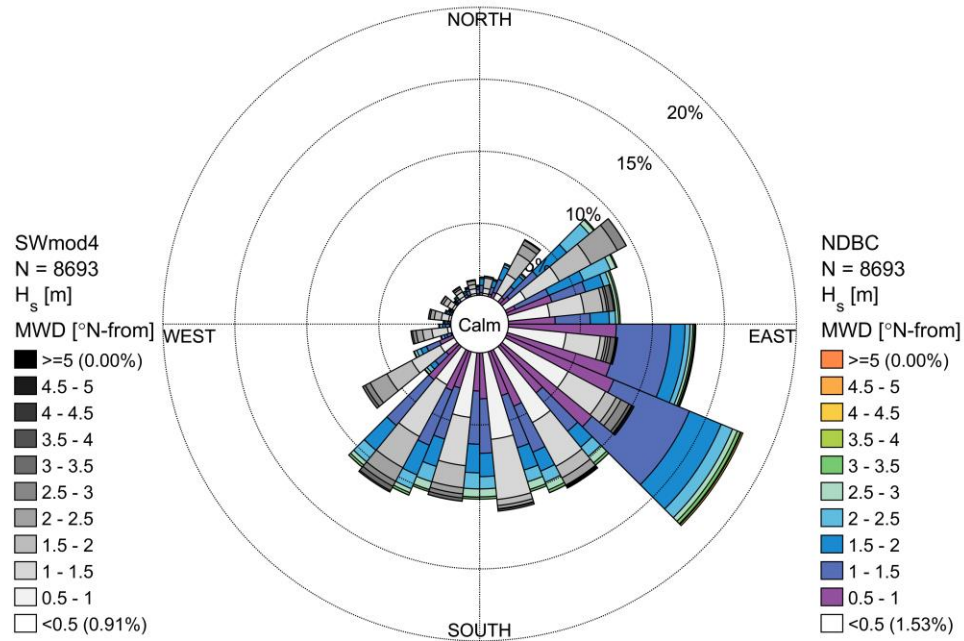


Figure A.55. Station 44093 - OSW Energy Area, VA: Wave Measurement vs. Model Results

H_{m0} time series, wave H_{m0} frequency of occurrence, wave H_{m0} wave rose and wave H_{m0} Q-Q scatter, wave mean direction time series and wave mean direction frequency of occurrence.



w41013 (77.74W;33.44N;0.00mMSL)
Dual rose plot (2017-01-01 - 2017-12-31; 1h)



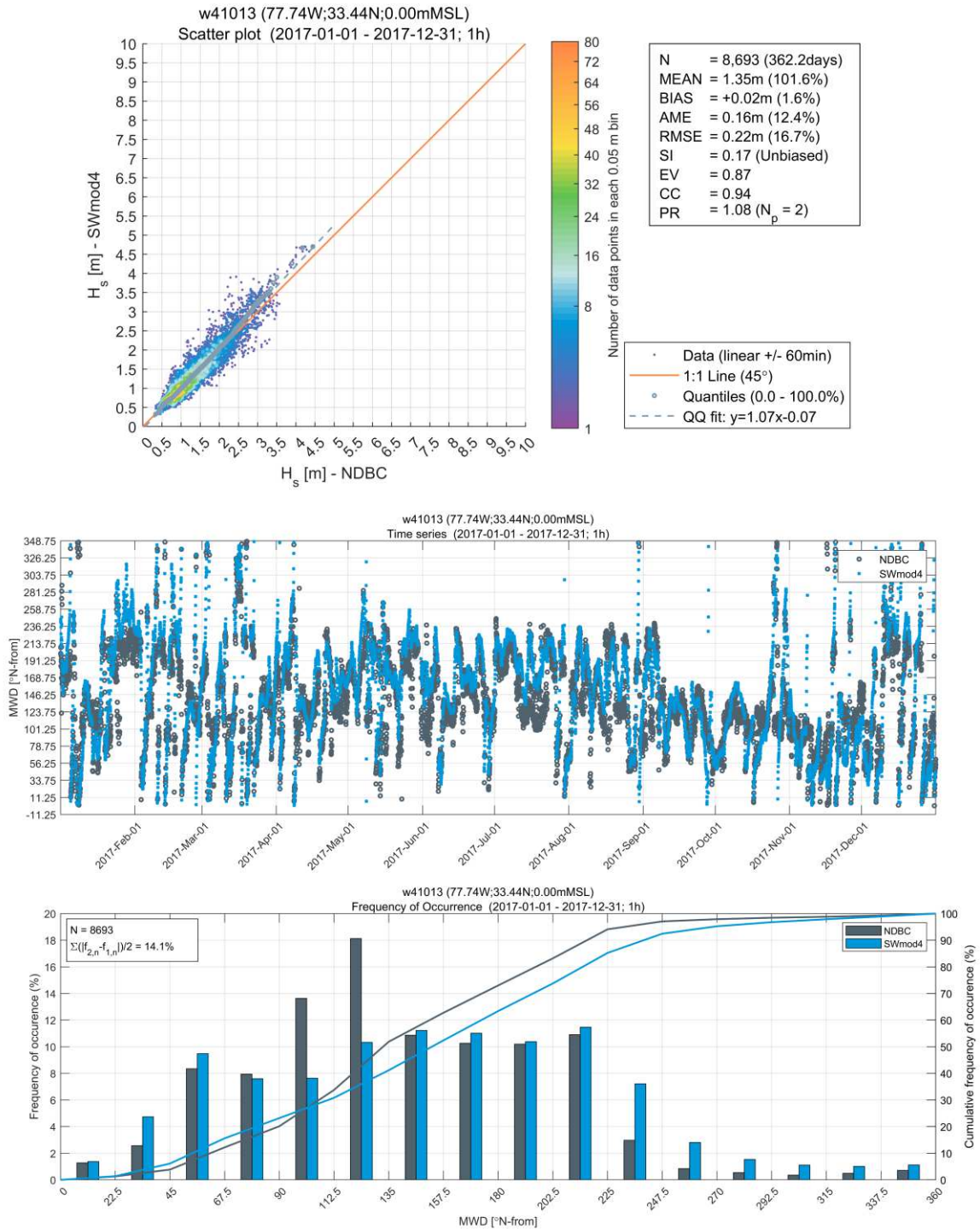


Figure A.56. Station 41013 - Frying Pan Shoals, NC: Wave Measurement vs. Model Results
 H_{m0} time series, wave H_{m0} frequency of occurrence, wave H_{m0} wave rose and wave H_{m0} Q-Q scatter, wave mean direction time series and wave mean direction frequency of occurrence.

A.2.3 Hydrodynamic Model Baseline Water Level Validation Plots

Observational water level data from NOAA tide and current stations (**Figure A.57**) are compared to model results in the following plots.

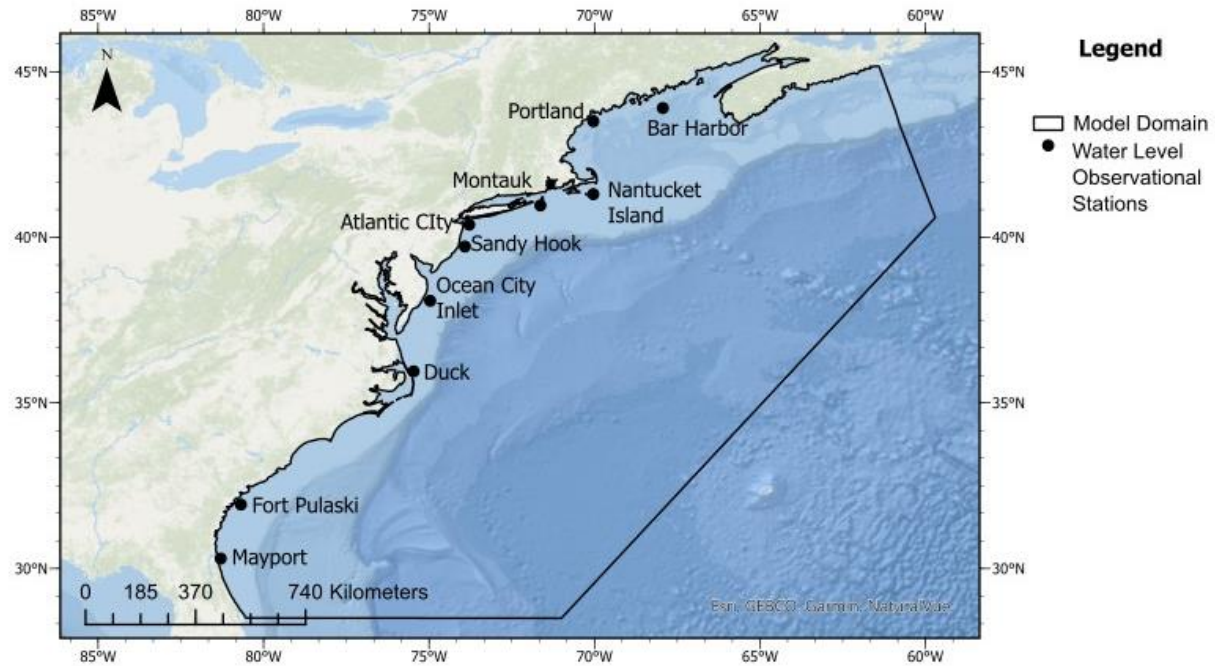


Figure A.57. Water Level Measurement Locations

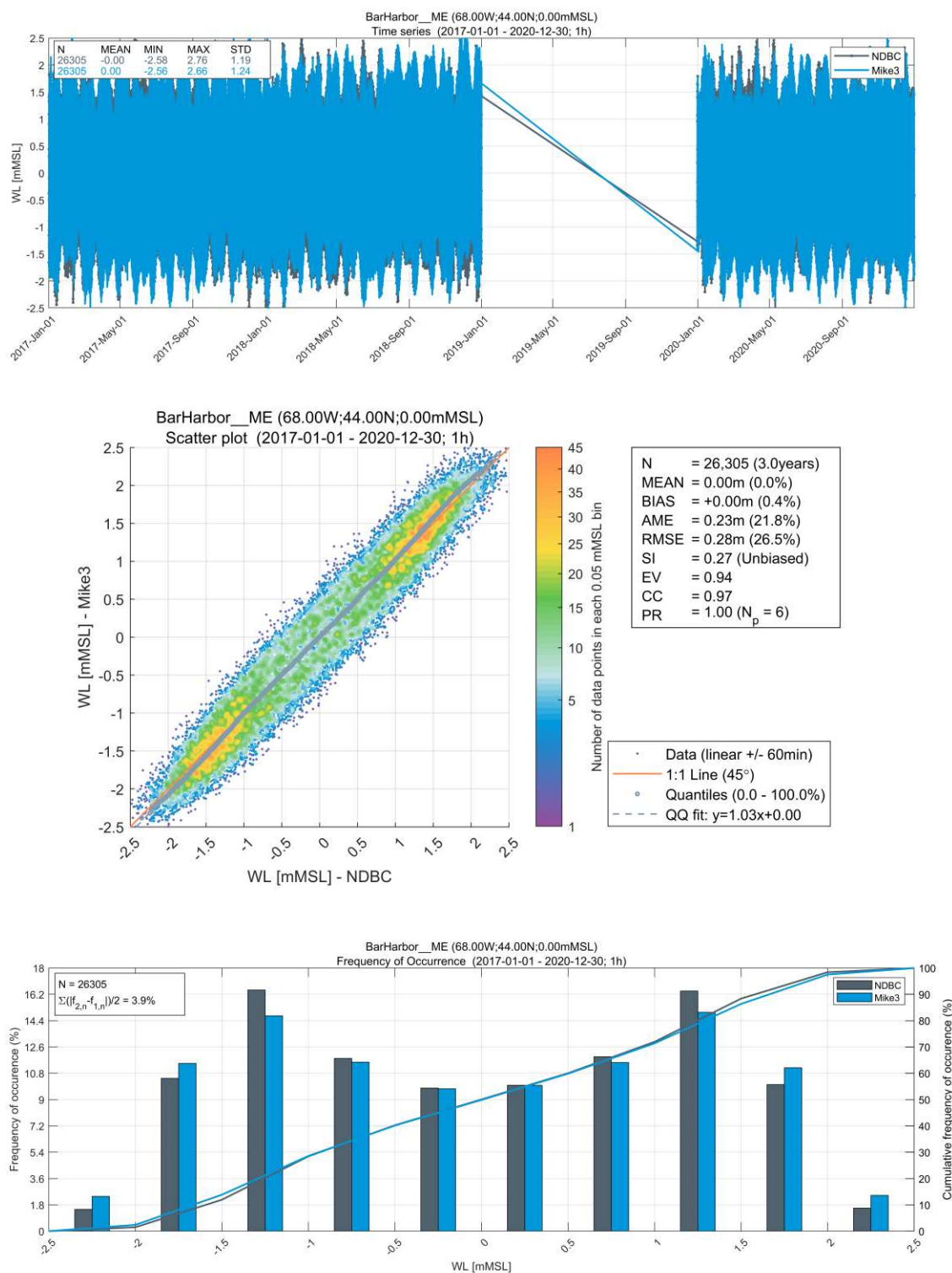


Figure A.58. Bar Harbor Station Water Level Measurements vs. Model Results

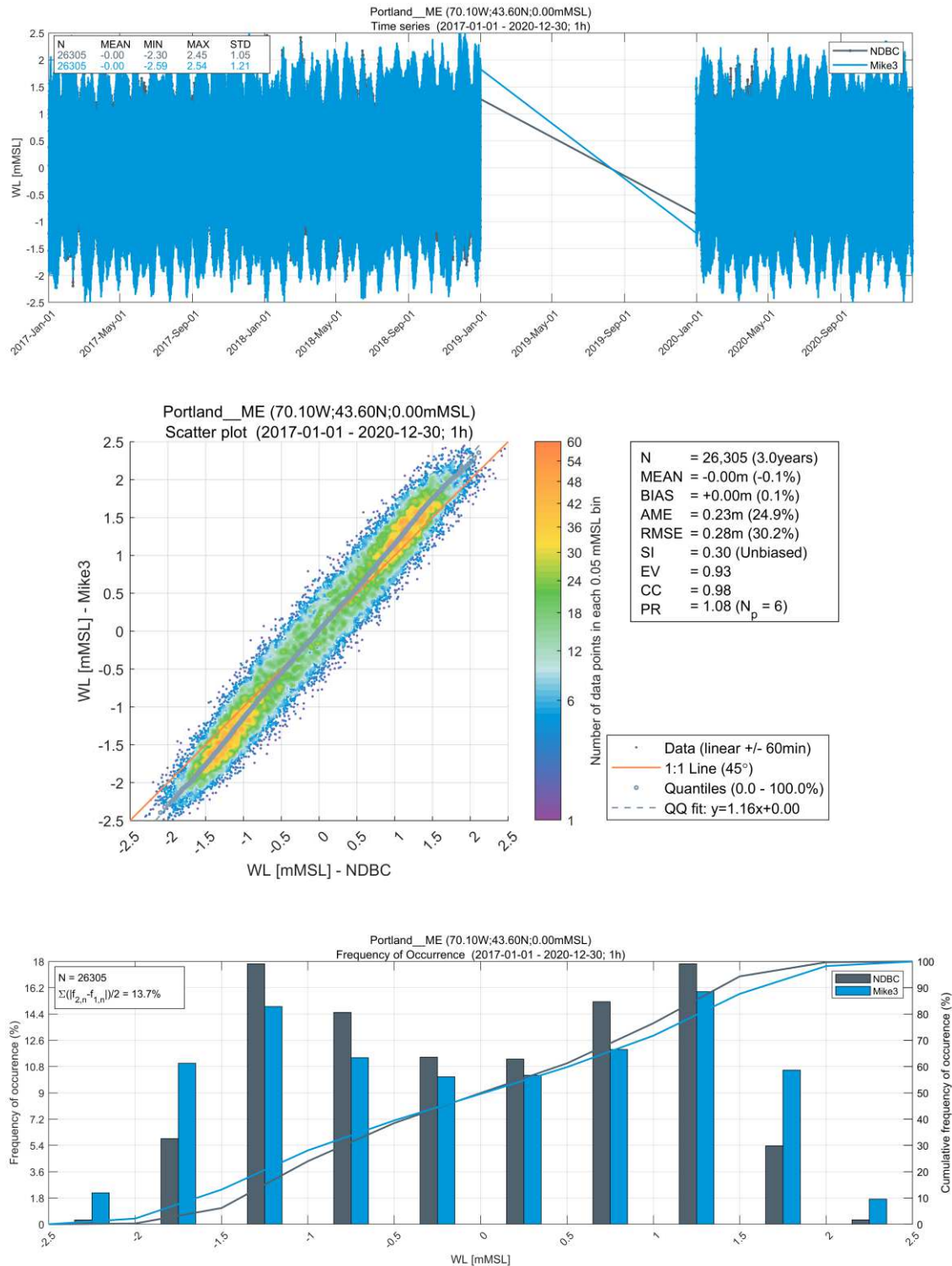


Figure A.59. Portland Water Level Measurements vs. Model Results

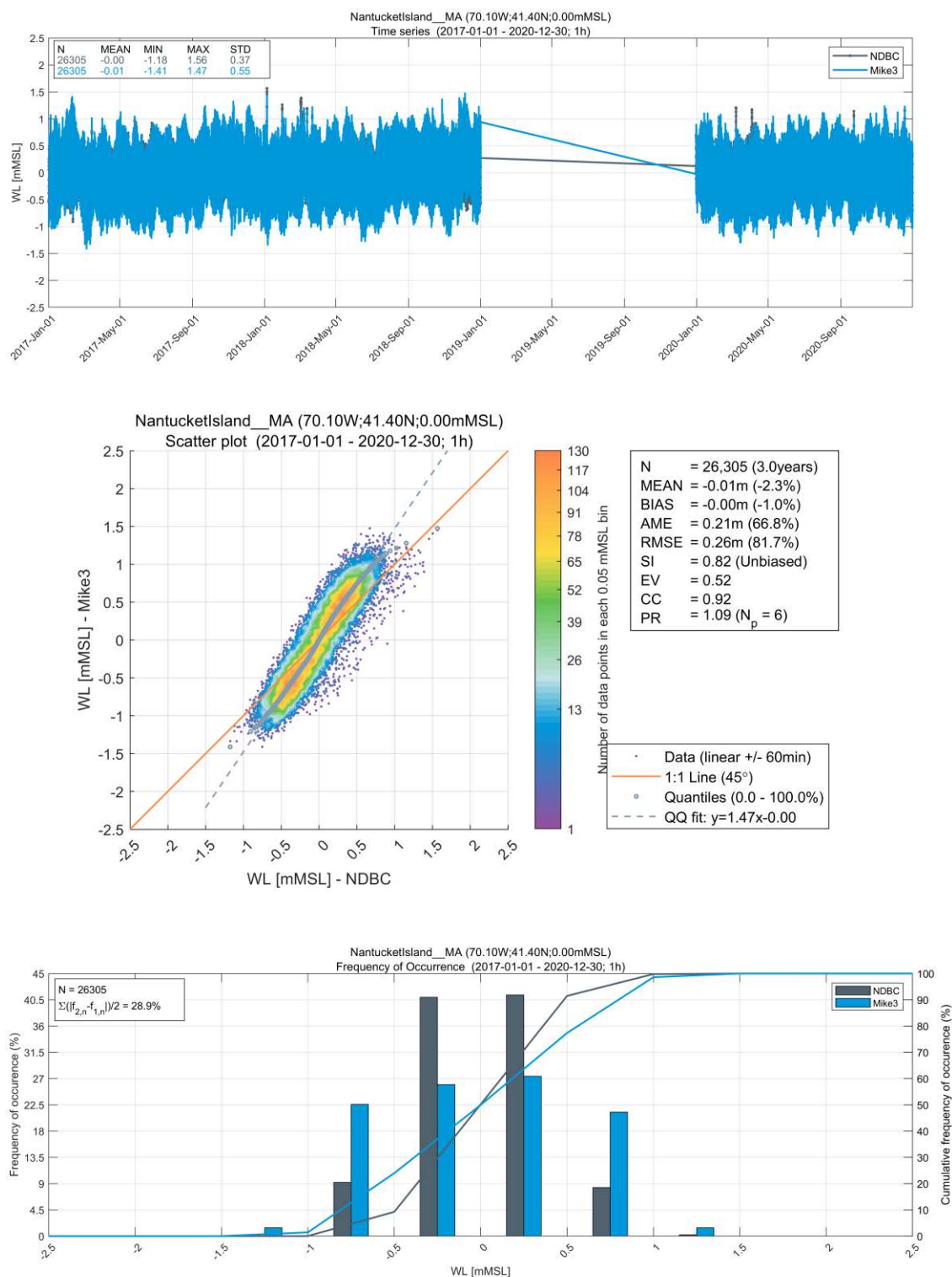


Figure A.60. Nantucket Island Station Water Level Measurements vs. Model Results

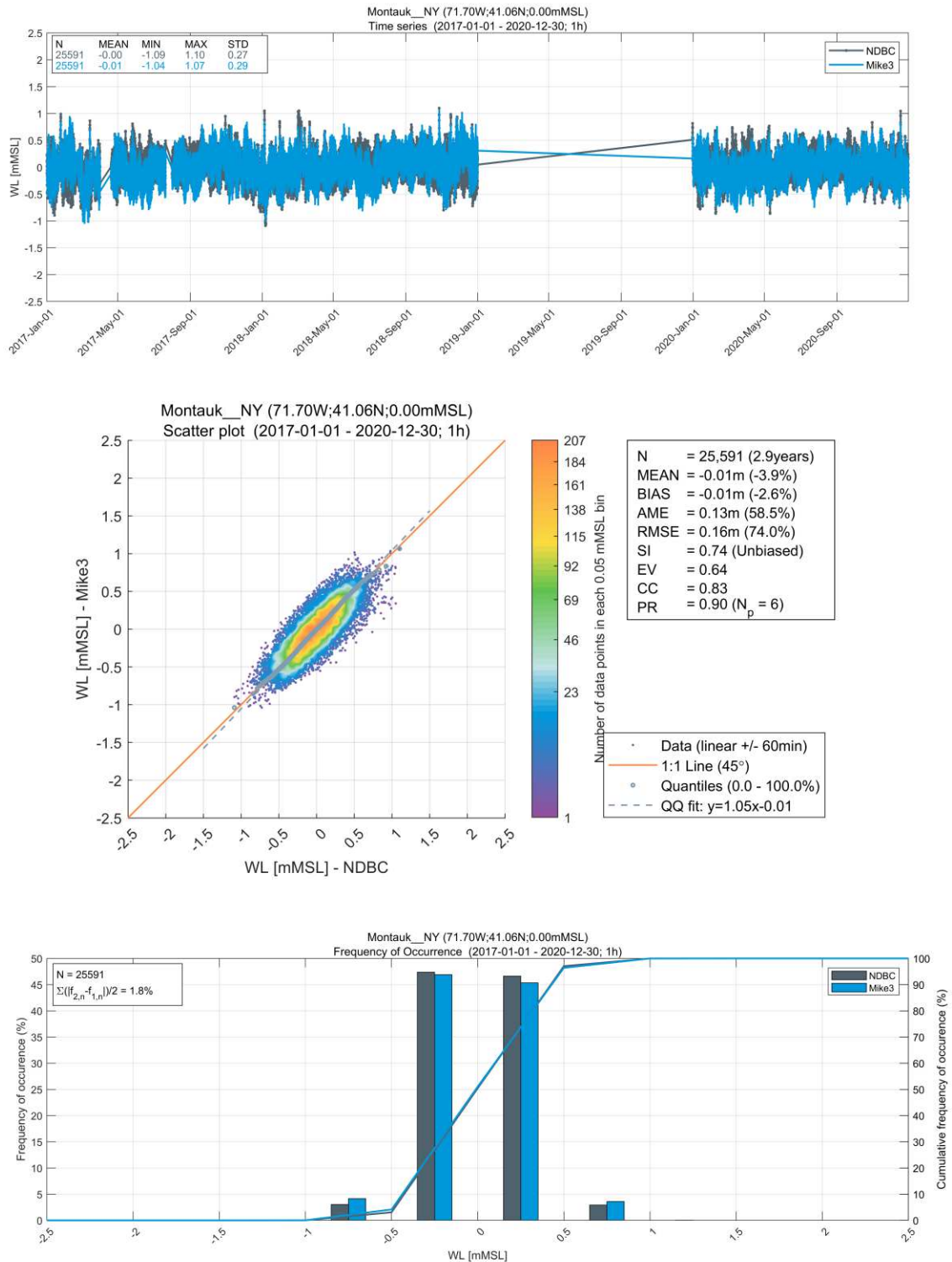


Figure A.61. Montauk Station Water Level Measurements vs. Model Results

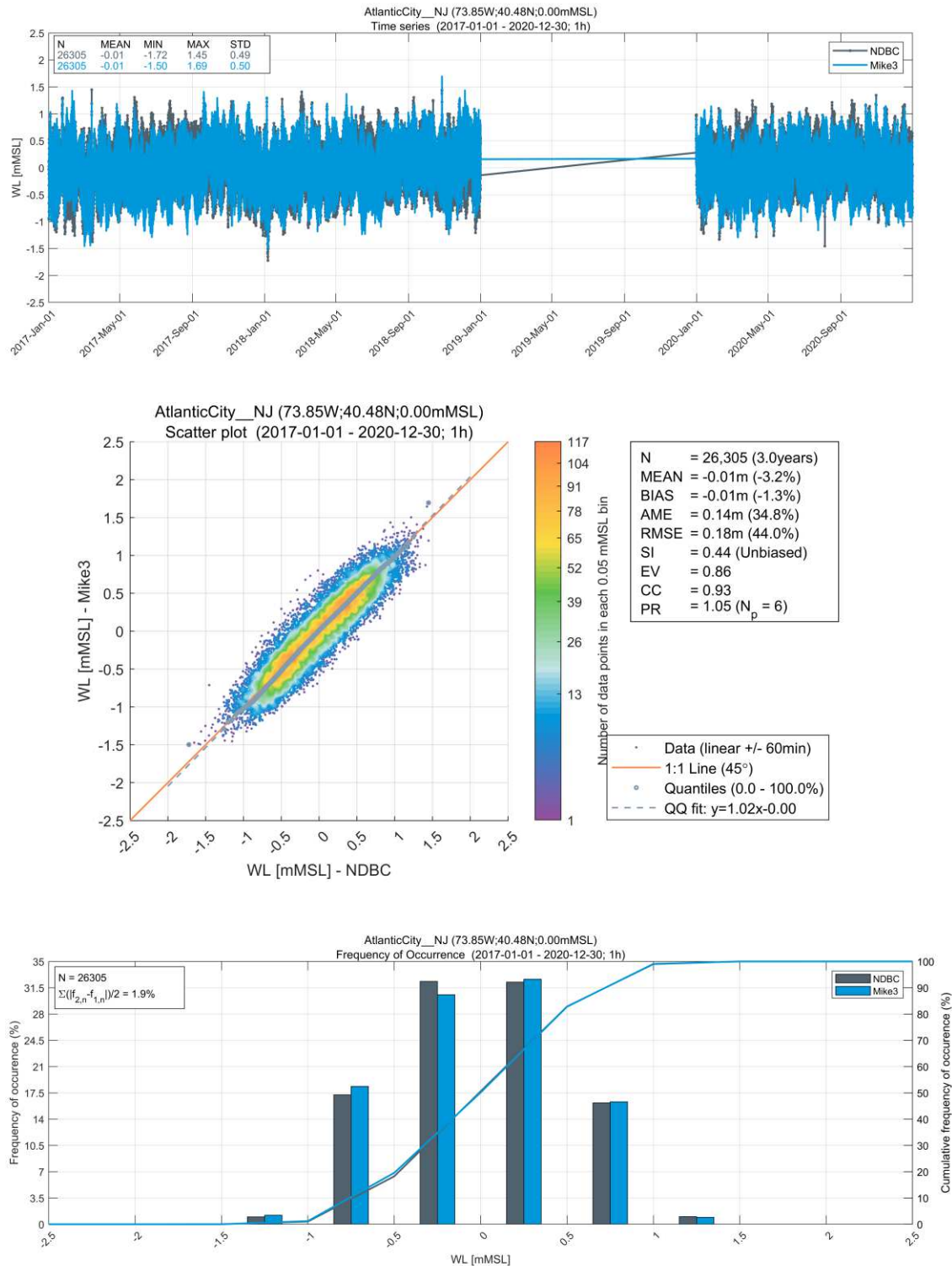


Figure A.62. Atlantic City Station Water Level Measurements vs. Model Results

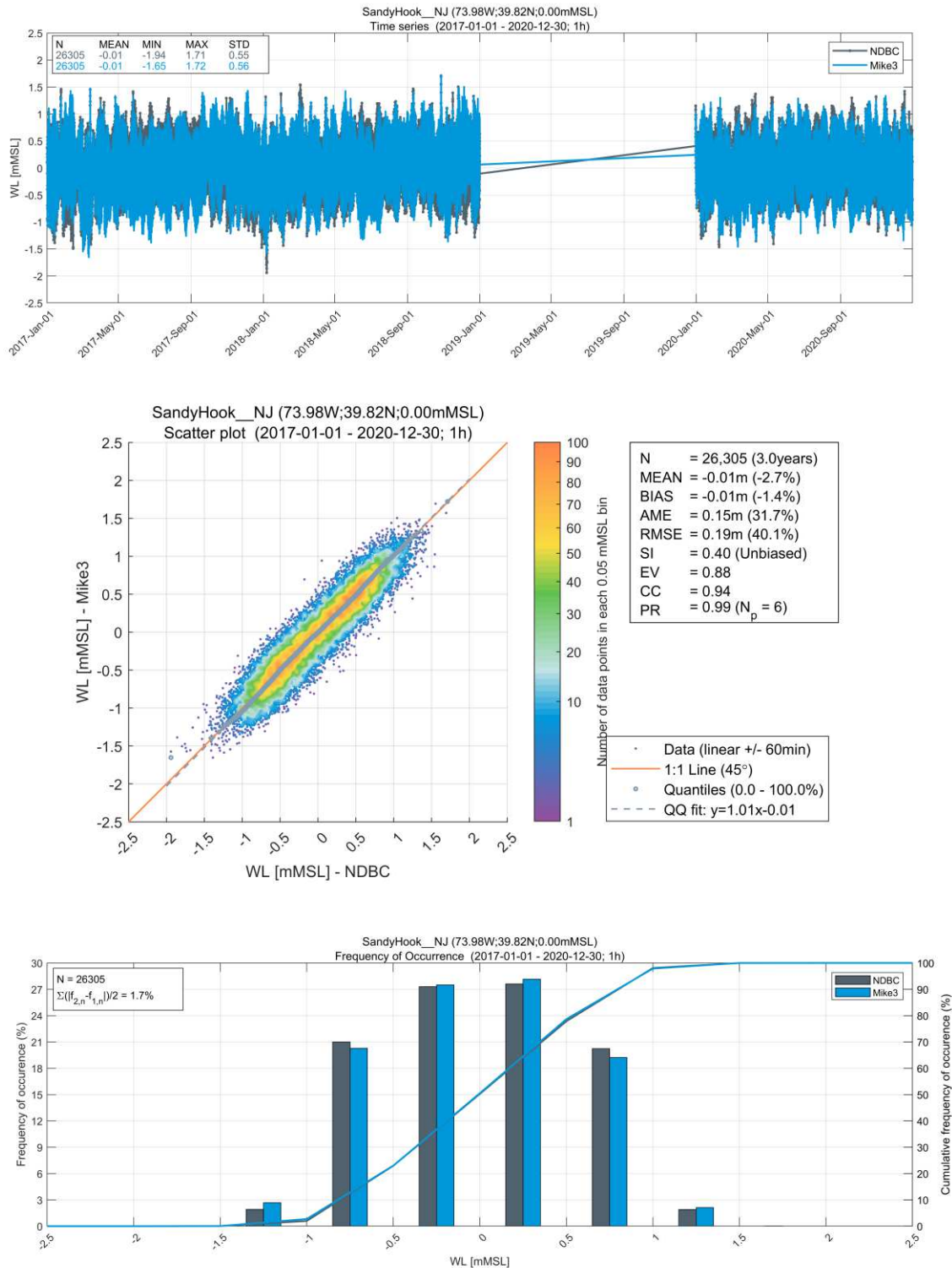


Figure A.63. Sandy Hook Station Water Level Measurements vs. Model Results

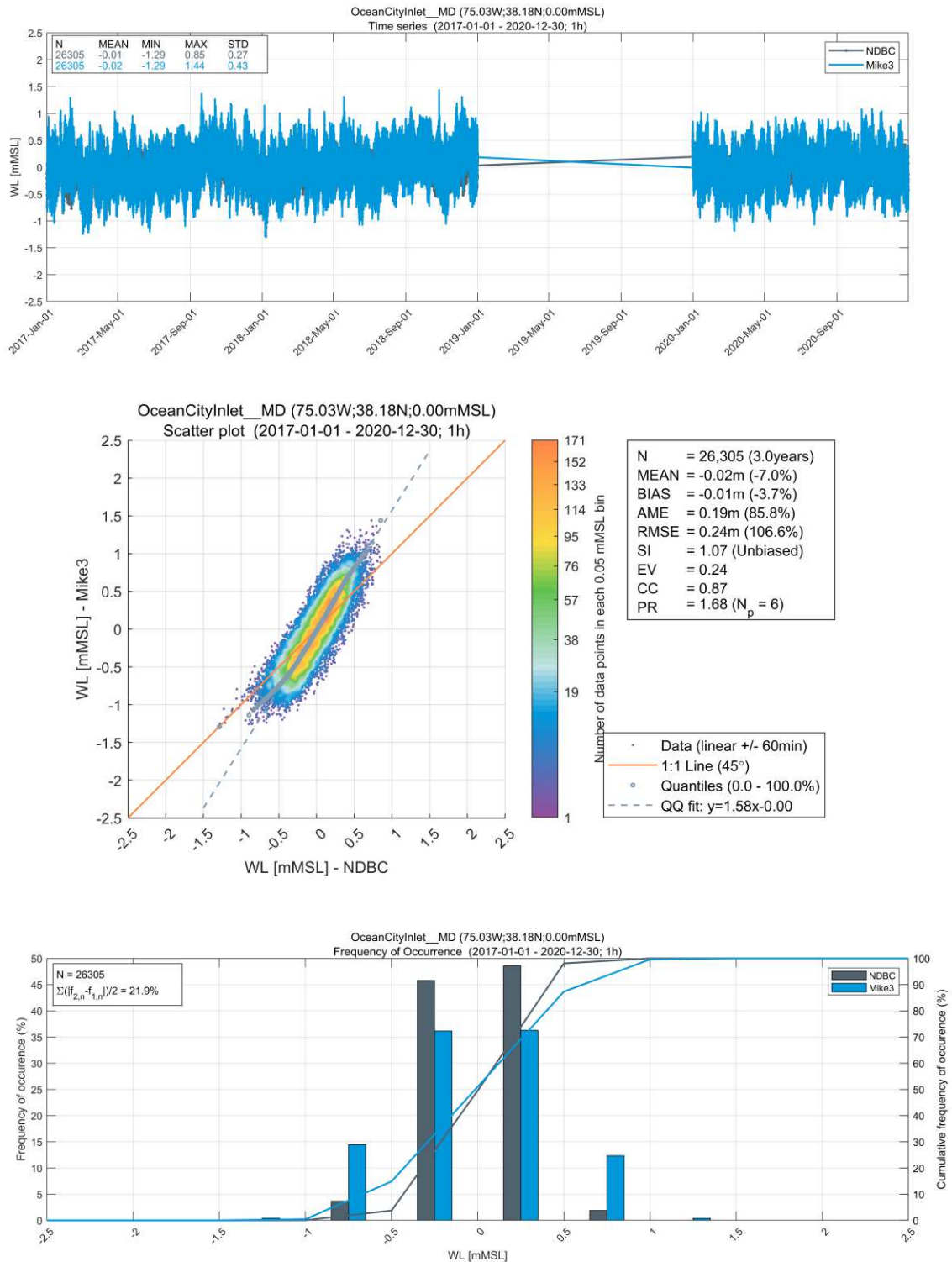


Figure A.64. Ocean City Inlet Station Water Level Measurements vs. Model Results

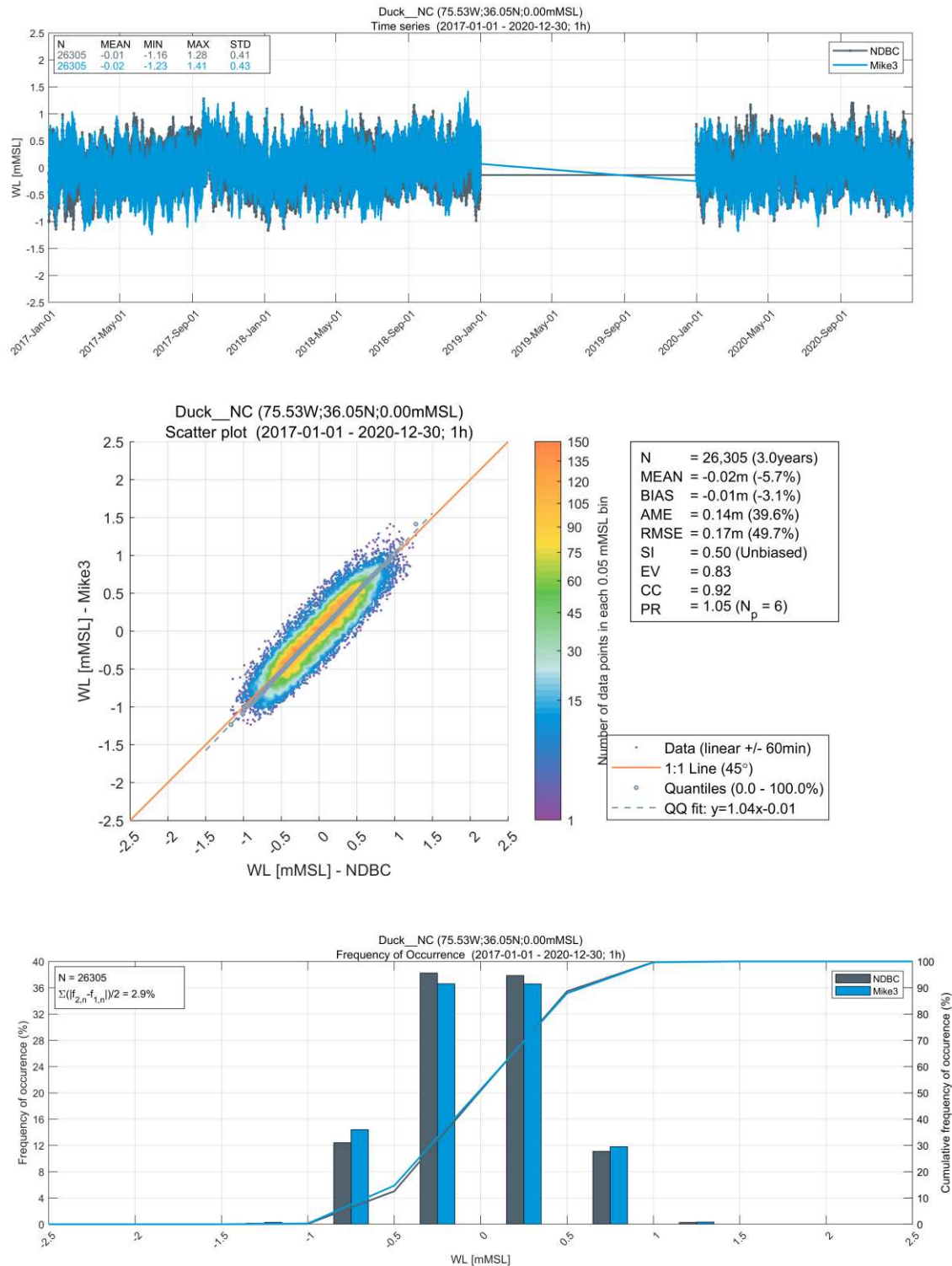


Figure A.65. Duck Station Water Level Measurements vs. Model Results

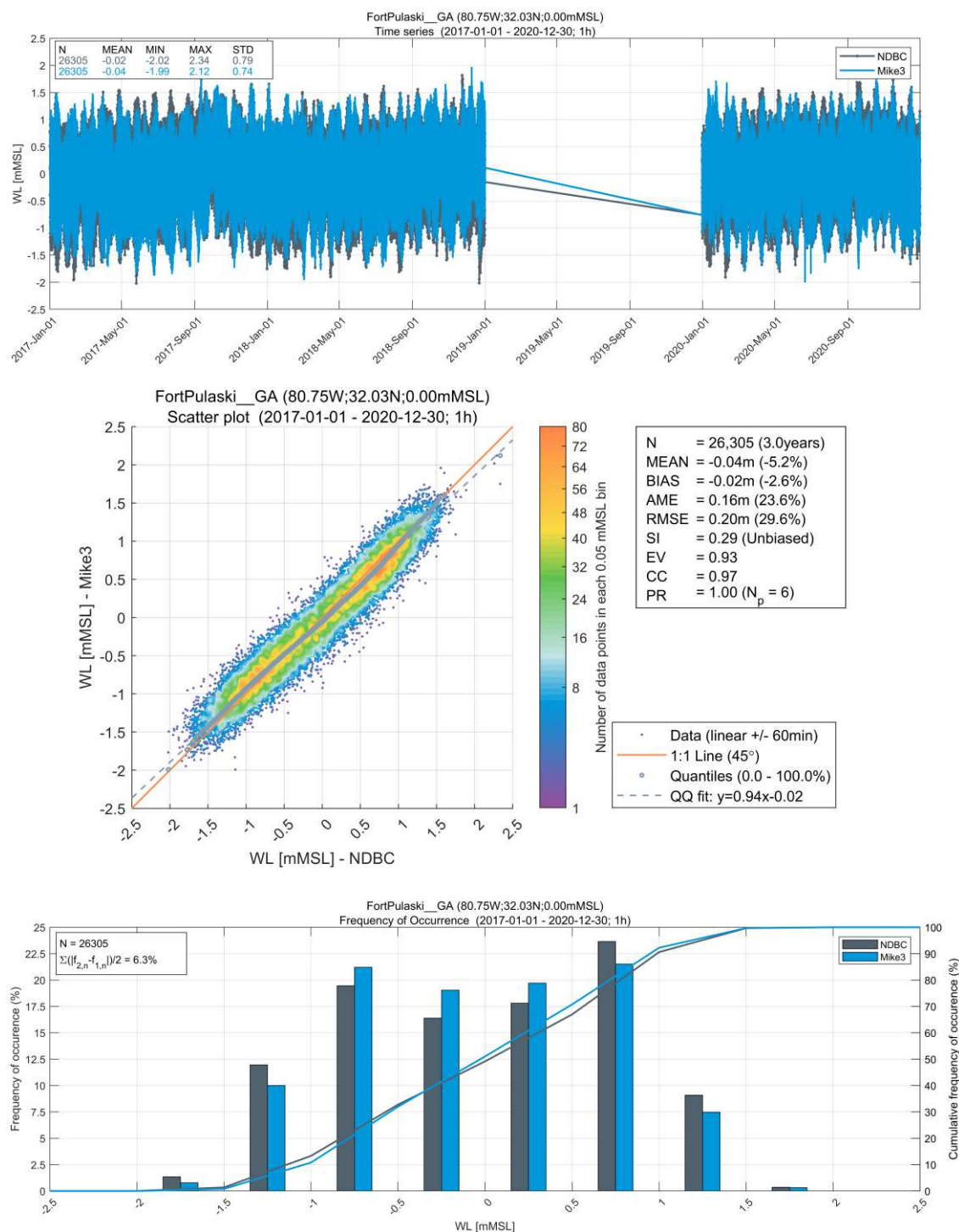


Figure A.66. Fort Pulaski Station Water Level Measurements vs. Model Results

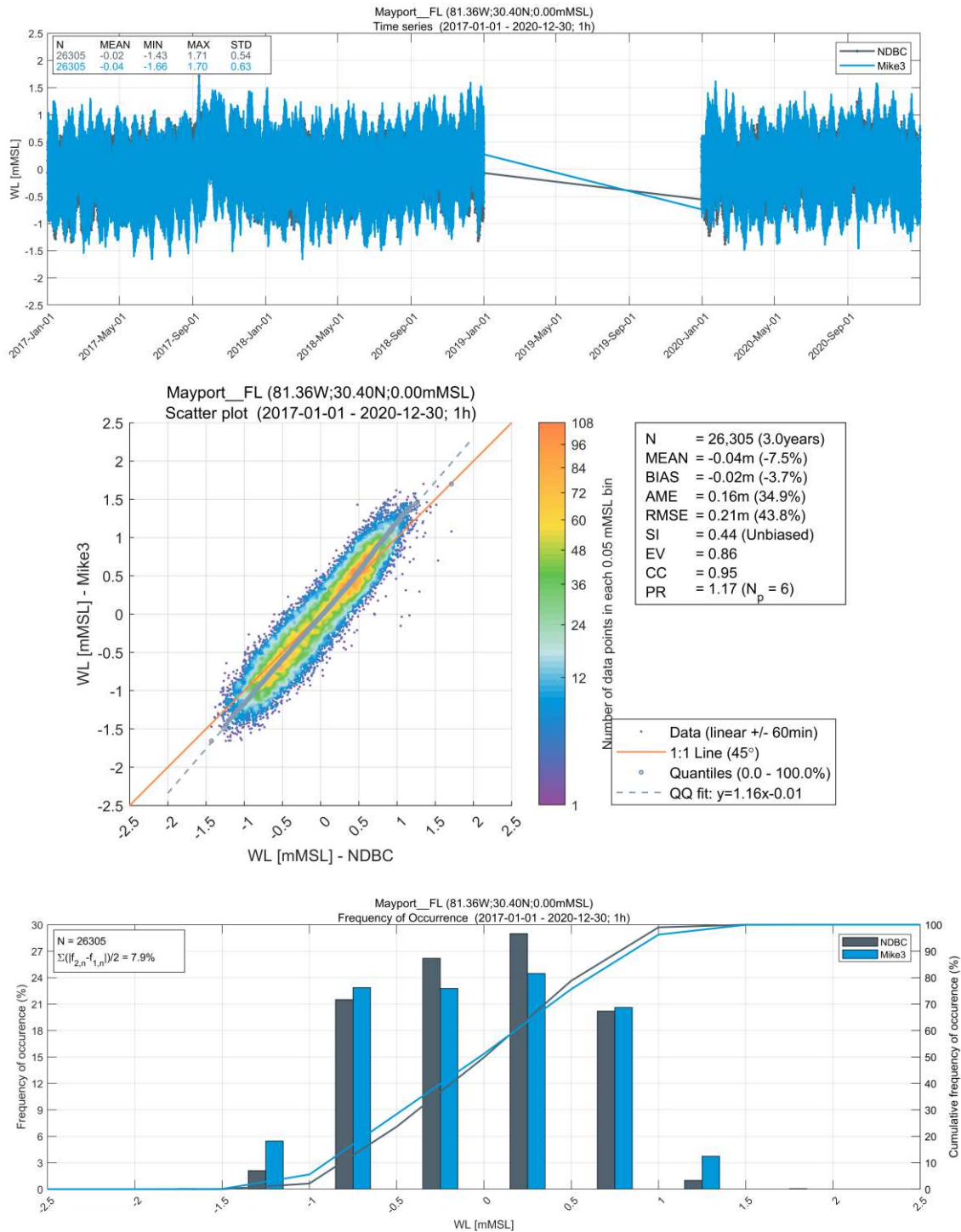


Figure A.67. Mayport Station Water Level Measurements vs. Model Results

A.2.4 Hydrodynamic Model Baseline Sea Temperature Validation Plots from NDBC Buoys

Observational sea surface temperature (1.5 m below water line) data from NDBC buoys are compared to model results in the following plots.

Table A.5. Locations of NDBC Buoys

Name of Observational Station	Latitude	Longitude
44008 – Nantucket, MA	40.504 N	69.248 W
44097 - Block Island, RI	40.967 N	71.126 W
44017 - Montauk Point, NY	40.693 N	72.049 W
44025 - Long Island, NY	40.251 N	73.164 W
44065 - New York Harbor Entrance	40.369 N	73.703 W
44027 – Jonesport, ME	44.28 N	67.30 W
44005 – Gulf of Maine, ME	43.20 N	69.13 W
44098 – Jeffreys Ledge, ME	42.80 N	70.17 W
44011 – Georges Bank	41.09 N	66.56 W
44091 – Barnegat, NJ	39.77 N	73.77 W
44066 – Texas Tower	39.62 N	72.64 W
44009 – Delaware Bay, DE	38.46 N	74.69 W
44058 – Stingray Point, VA	37.57 N	76.26 W
44099 – Cape Henry, VA	36.91 N	75.72 W
44014 – Virginia Beach, VA	36.60N	74.84 W
44095 – Oregon Inlet, NC	35.75 N	75.33 W
41025 – Diamond Shoals, NC	35.01 N	75.45 W
41108 – Wilmington Harbor, NC	33.72 N	78.02 W
41013 – Fryingpan Shoals, NC	33.44 N	33.44 W
41004 – Edisto, SC	32.50 N	79.10 W
41008 – Grays Reef, GA	31.40 N	80.87 W

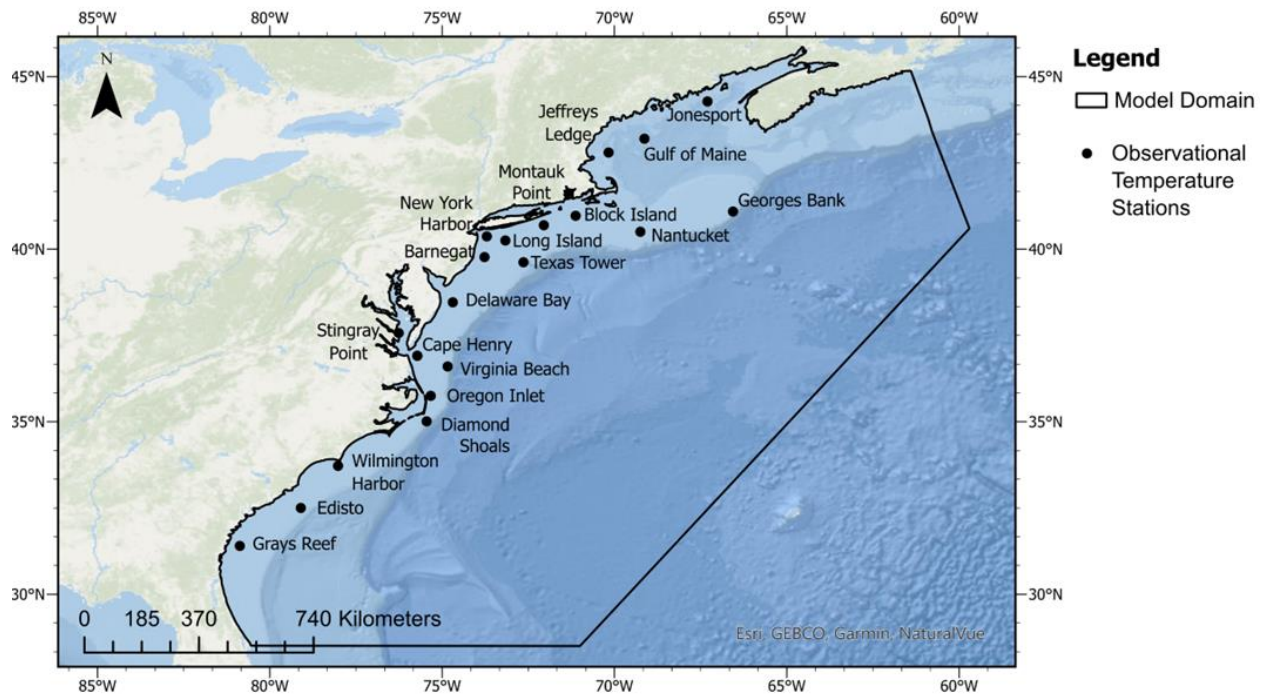


Figure A.68. Sea Temperature Measurement Locations

The time series, scatter plots frequency of occurrence plots follow for the NDBC buoy stations.

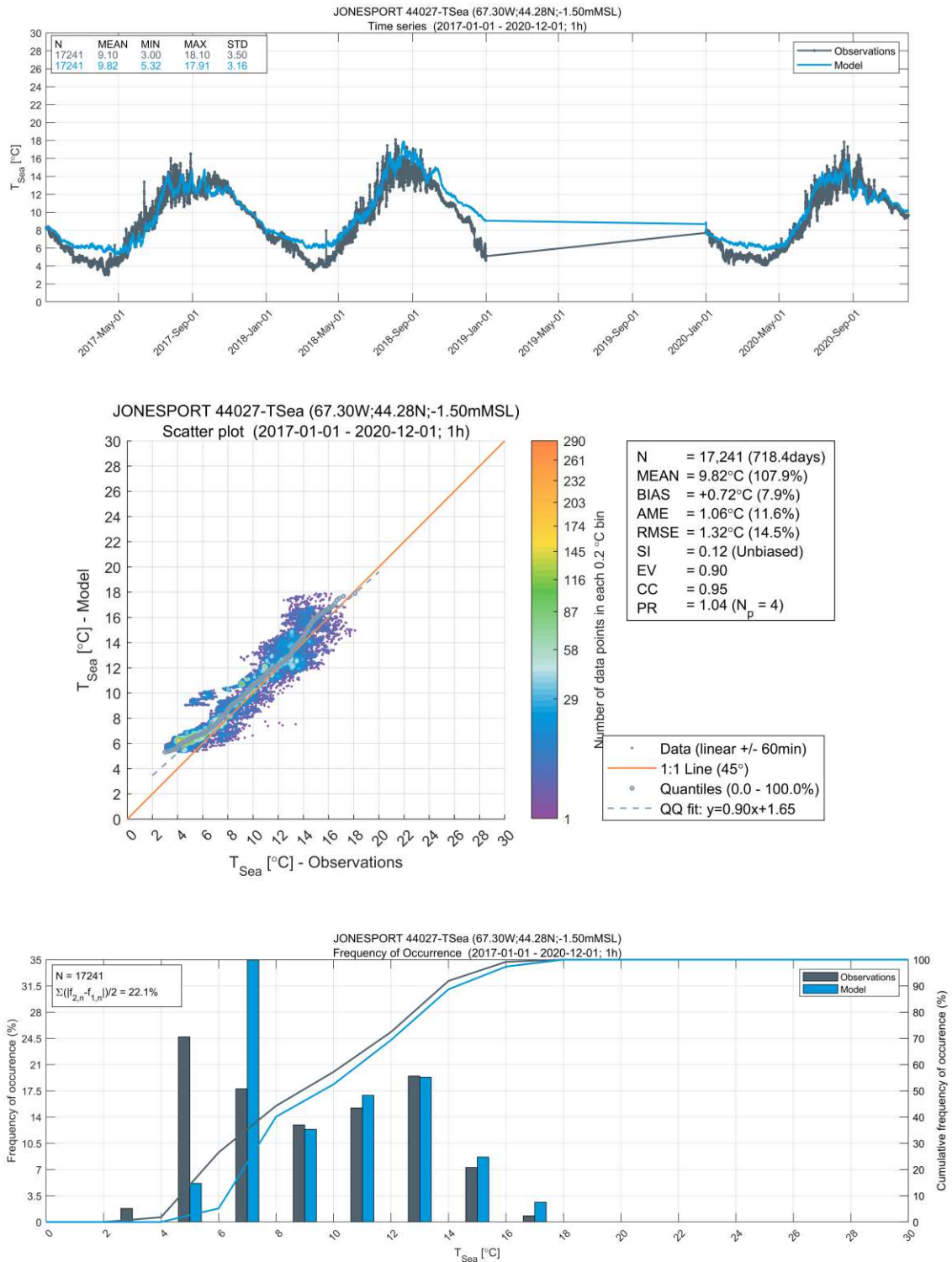


Figure A.69. Jonesport Sea Temperature Measurements at 1.5 m Depth vs. Model Results

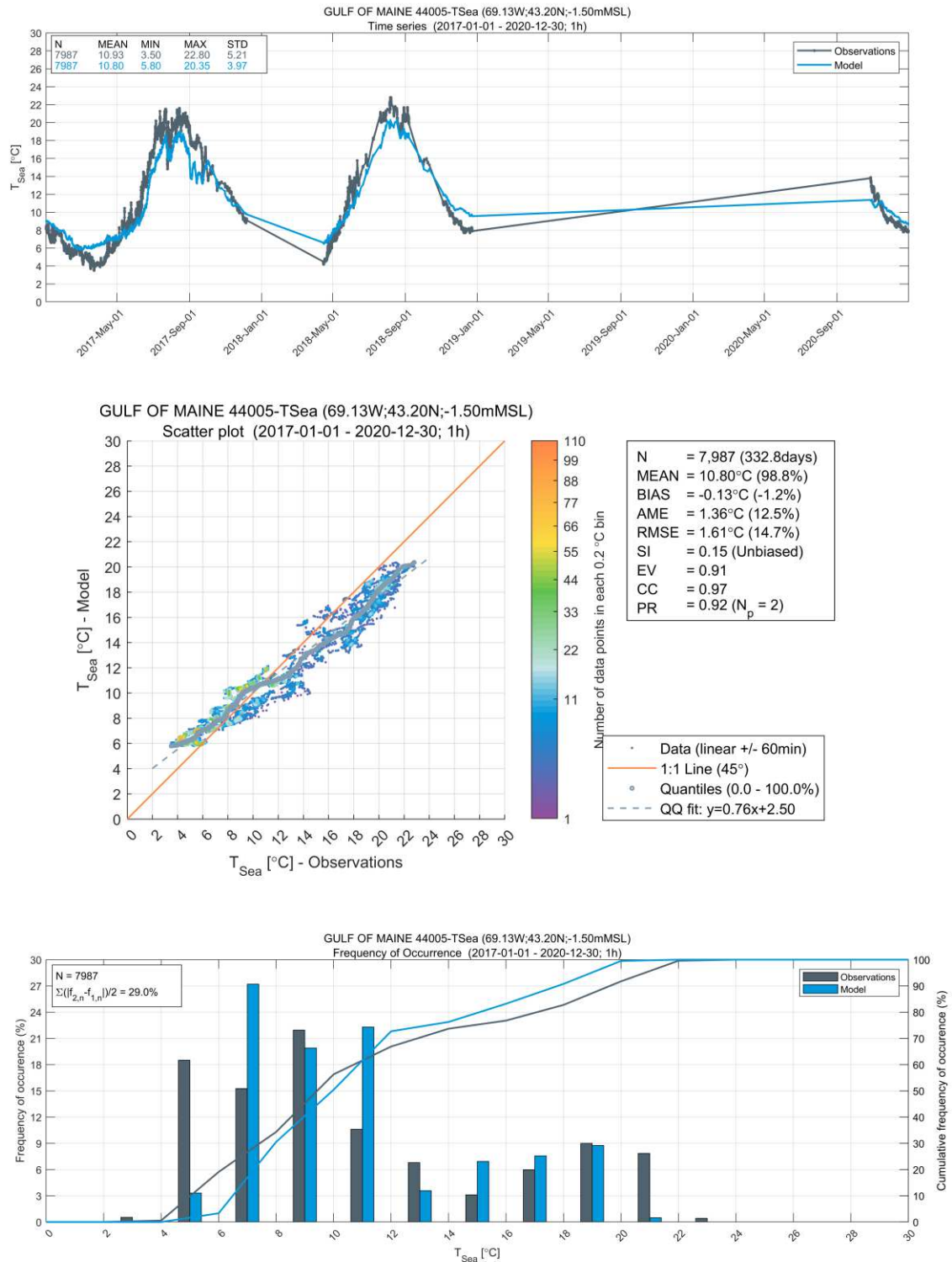


Figure A.70. Gulf of Maine Sea Temperature Measurements at 1.5 m Depth vs. Model Results

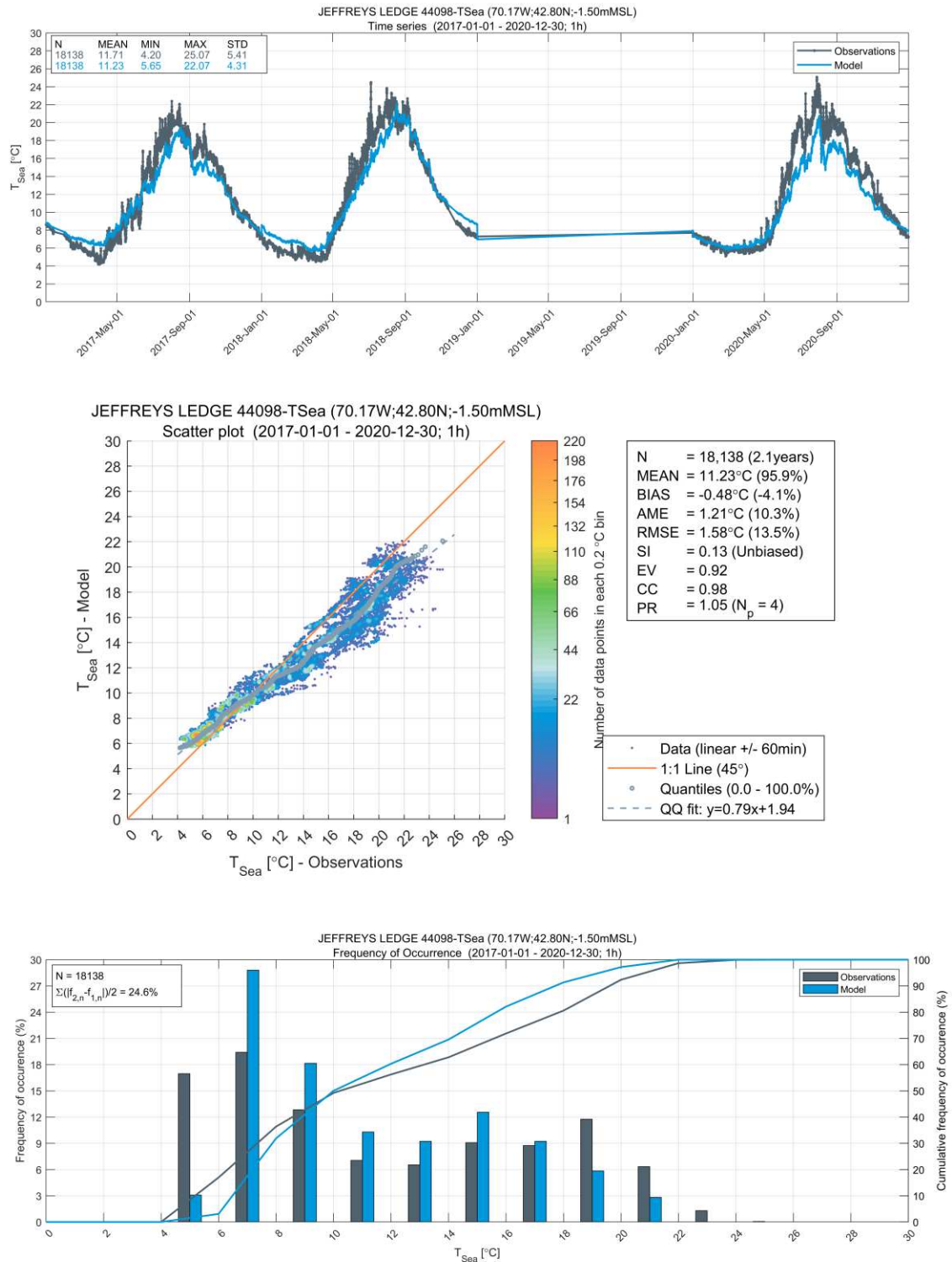


Figure A.71. Jeffreys Ledge Sea Temperature Measurements at 1.5 m Depth vs. Model Results

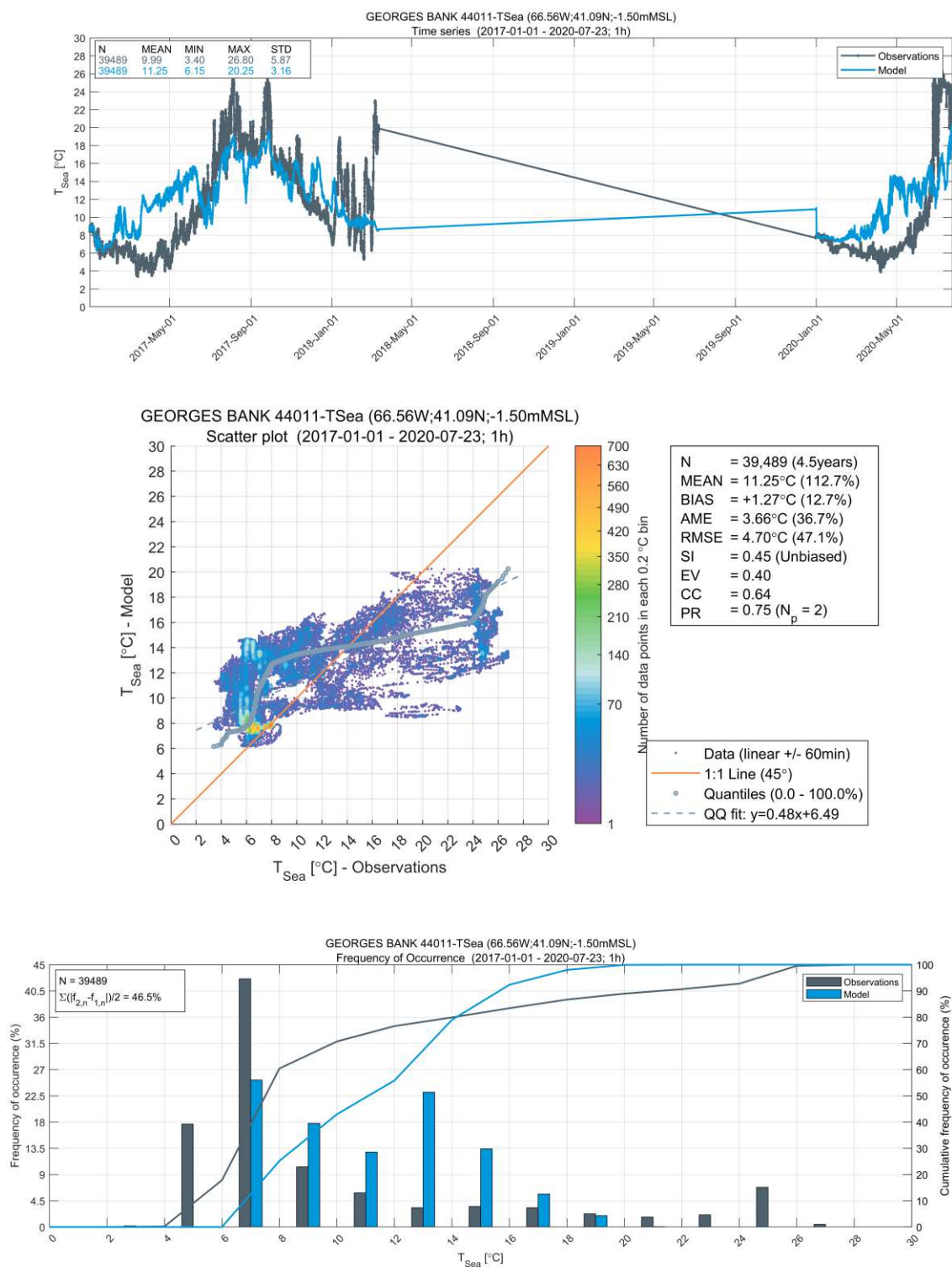


Figure A.72. Georges Bank Sea Temperature Measurements at 1.5 m Depth vs. Model Results

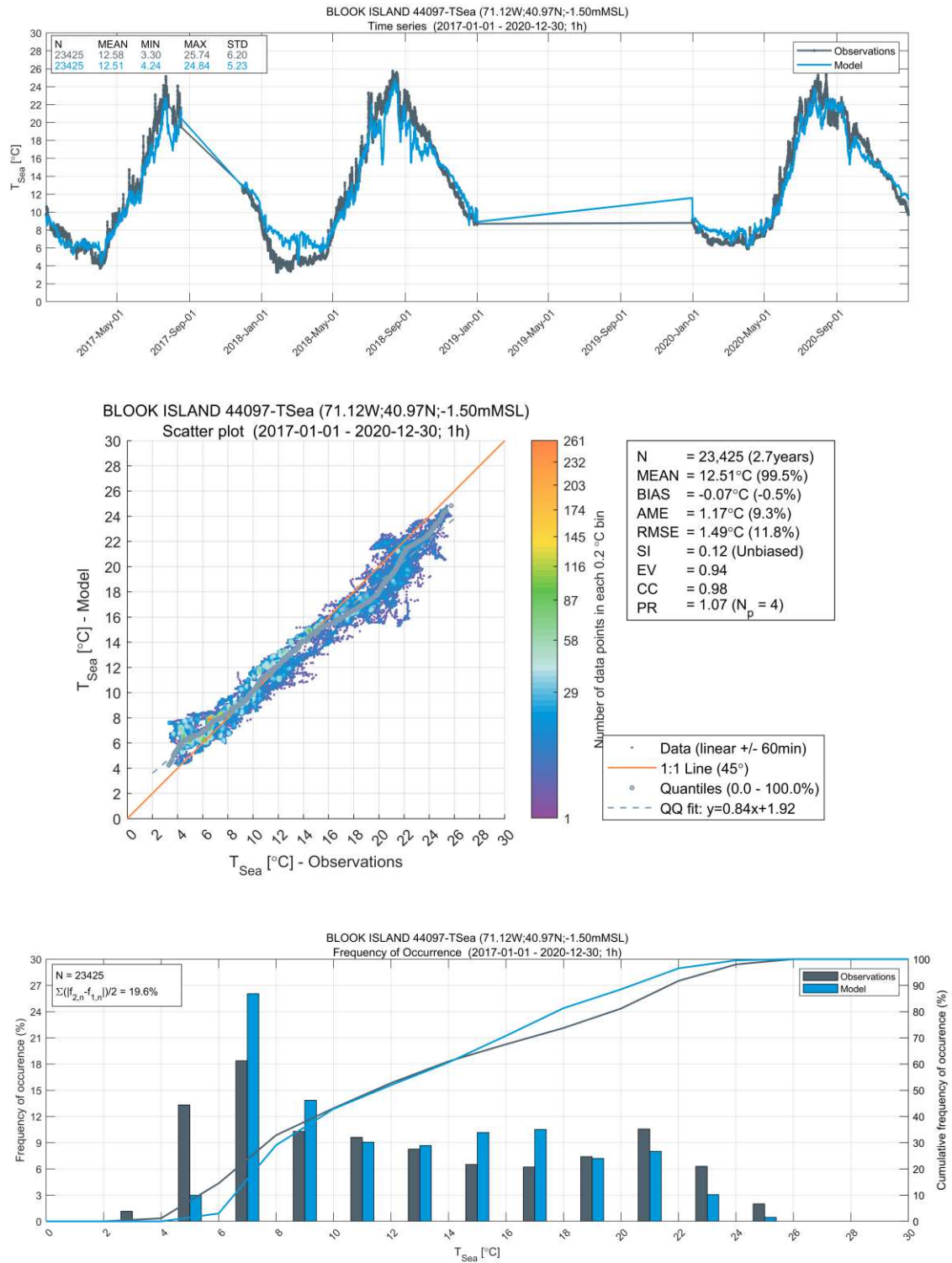


Figure A.73. Blook Island Sea Temperature Measurements at 1.5 m Depth vs. Model Results

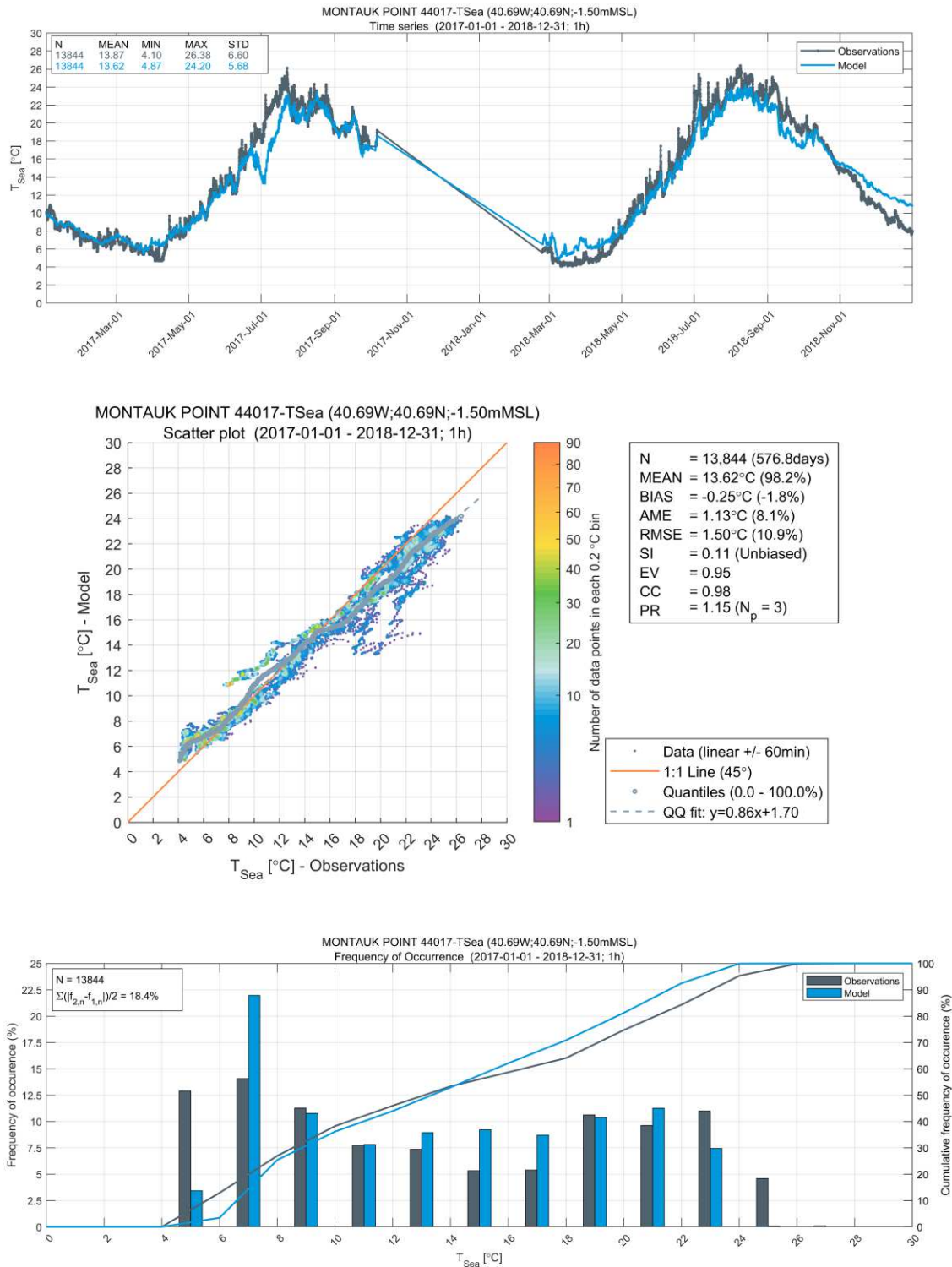


Figure A.74. Montauk Point Sea Temperature Measurements at 1.5 m Depth vs. Model Results

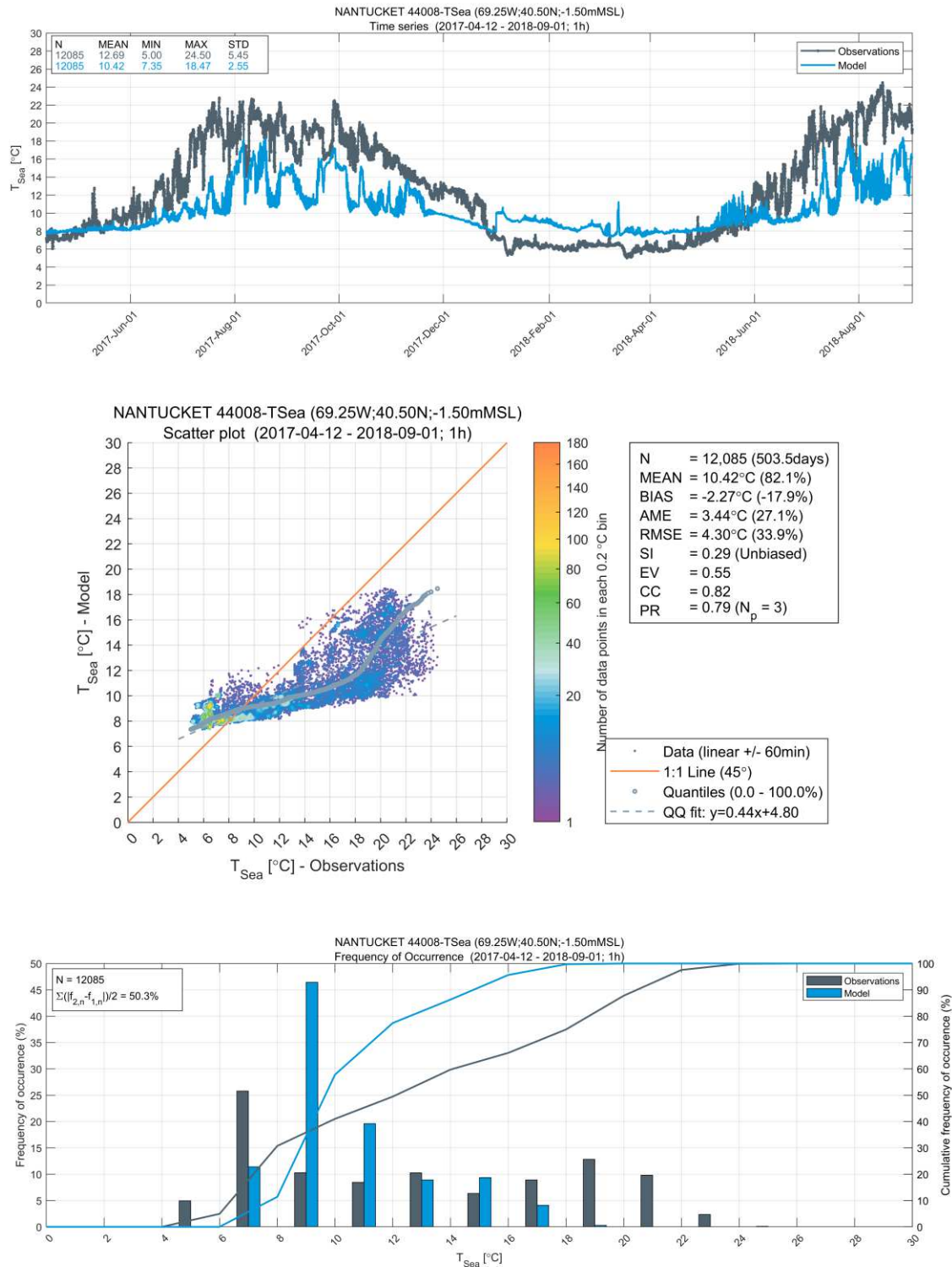


Figure A.75. Nantucket Sea Temperature Measurements at 1.5 m Depth vs. Model Results

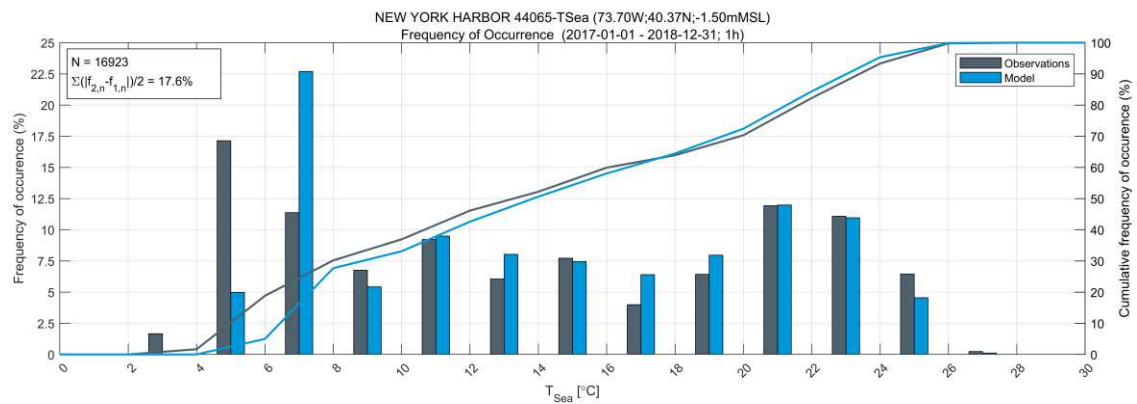
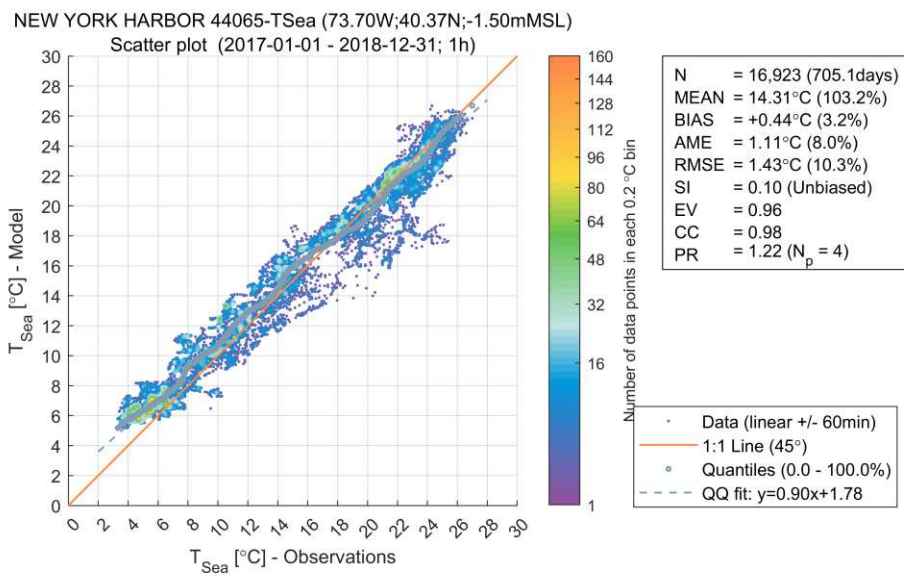
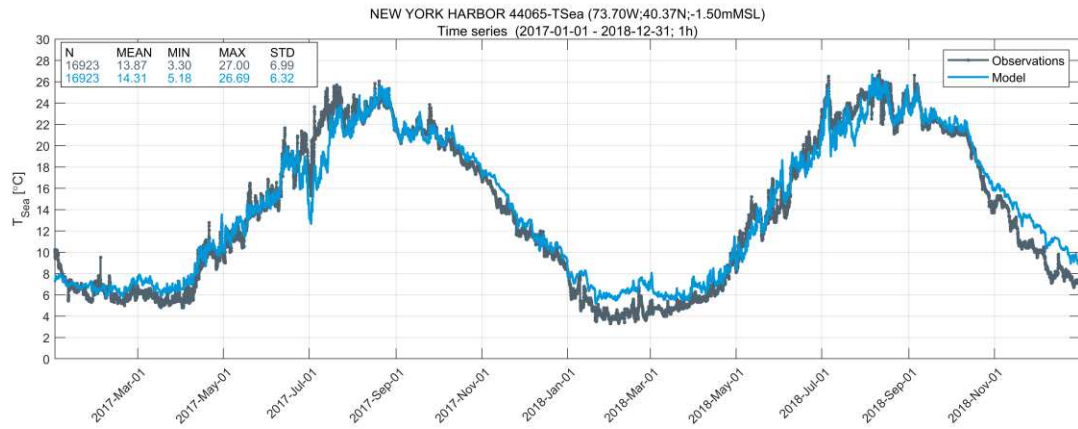


Figure A.76. New York Harbor Sea Temperature Measurements at 1.5 m Depth vs. Model Results

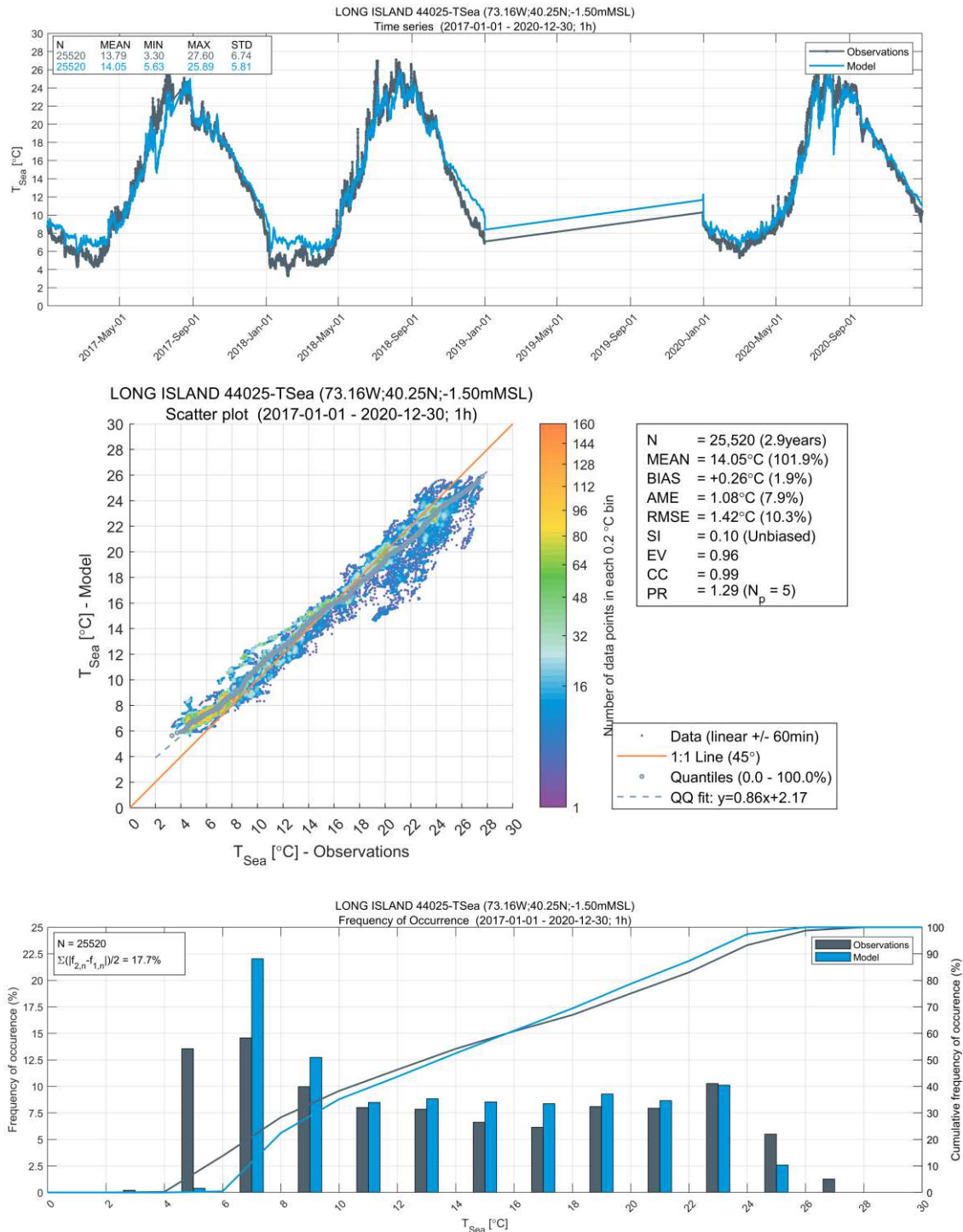


Figure A.77. Long Island Sea Temperature Measurements at 1.5 m Depth vs. Model Results

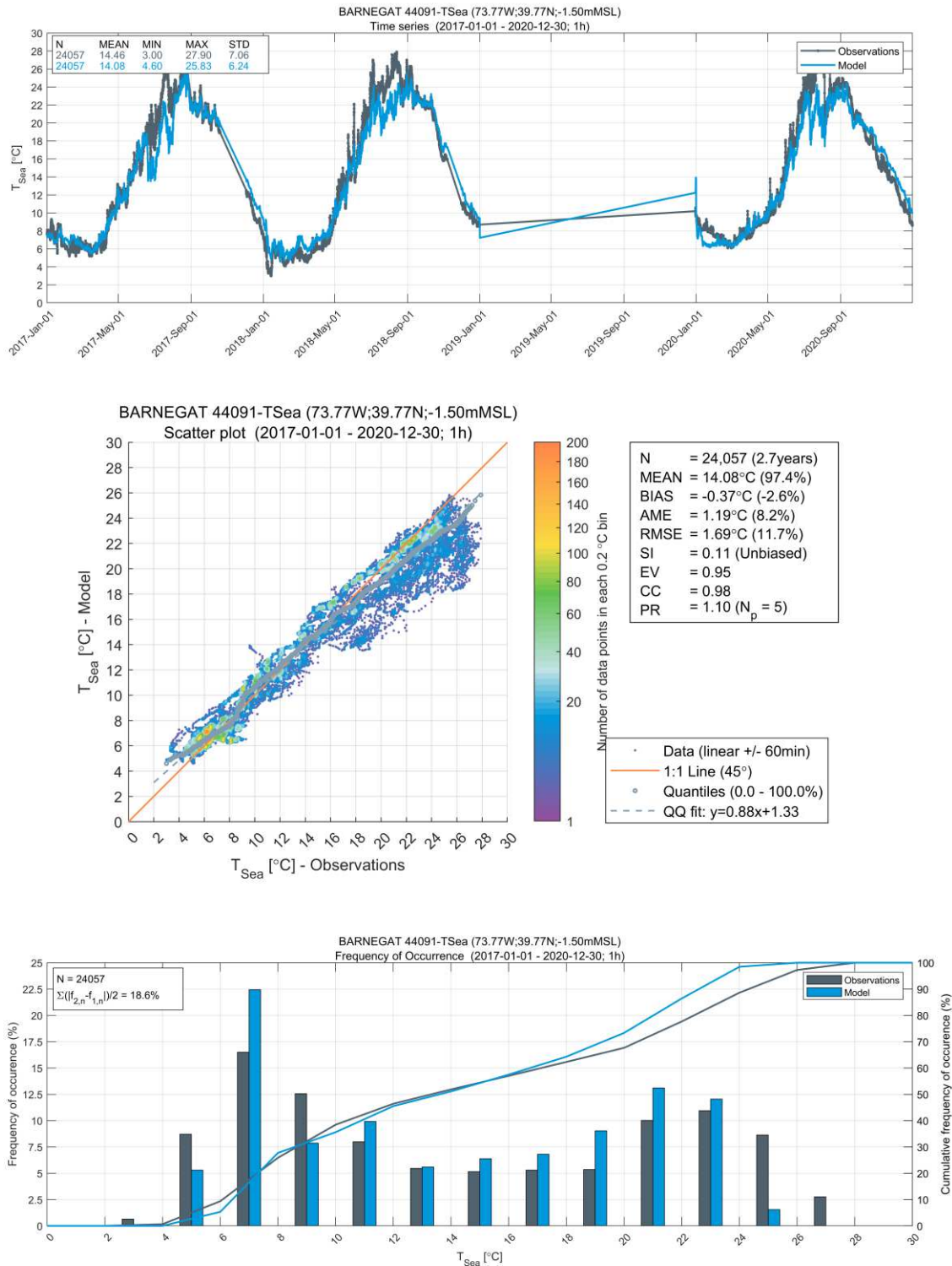


Figure A.78. Barnegat Sea Temperature Measurements at 1.5 m Depth vs. Model Results

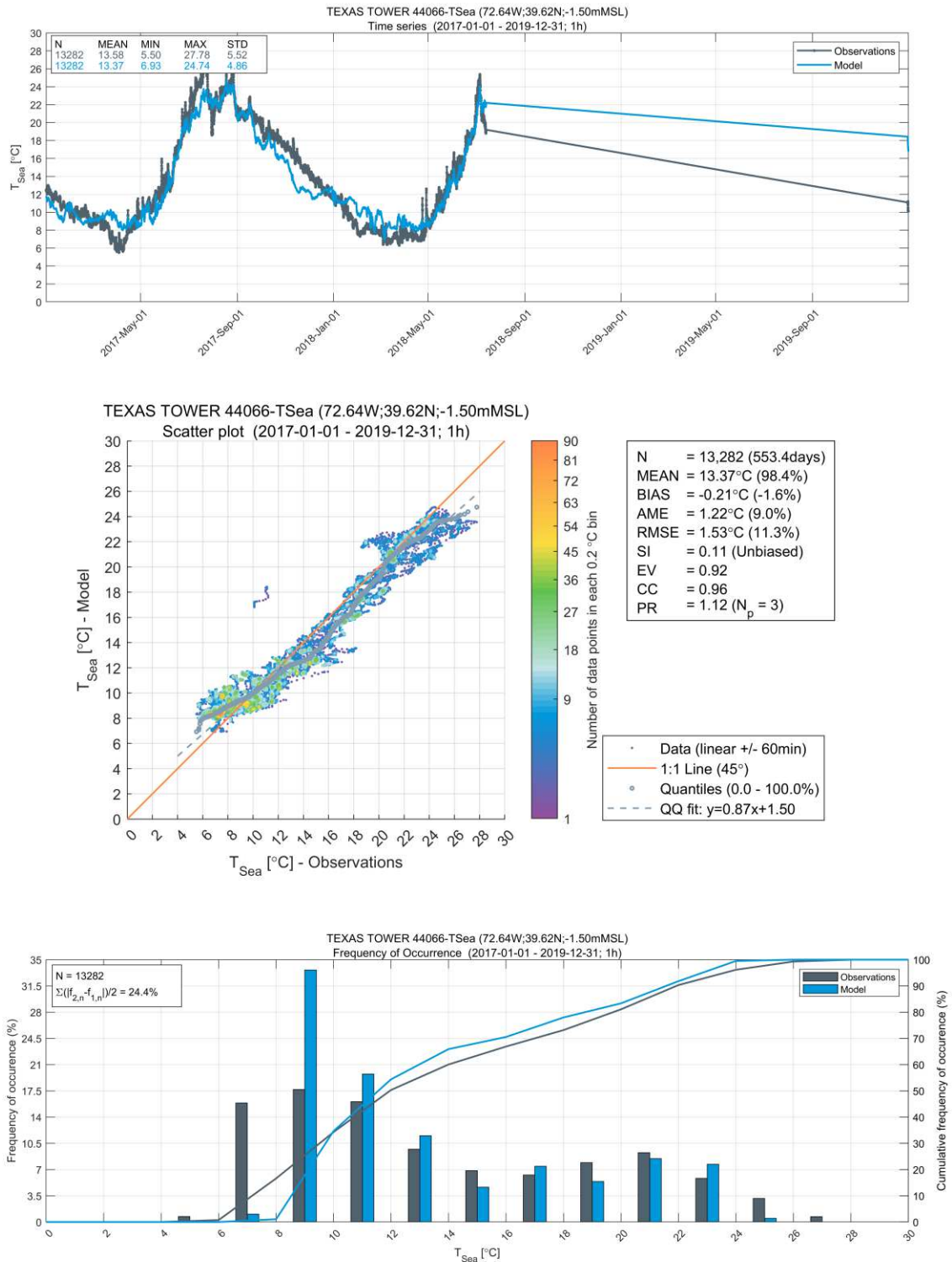


Figure A.79. Texas Tower Sea Temperature Measurements at 1.5 m Depth vs. Model Results

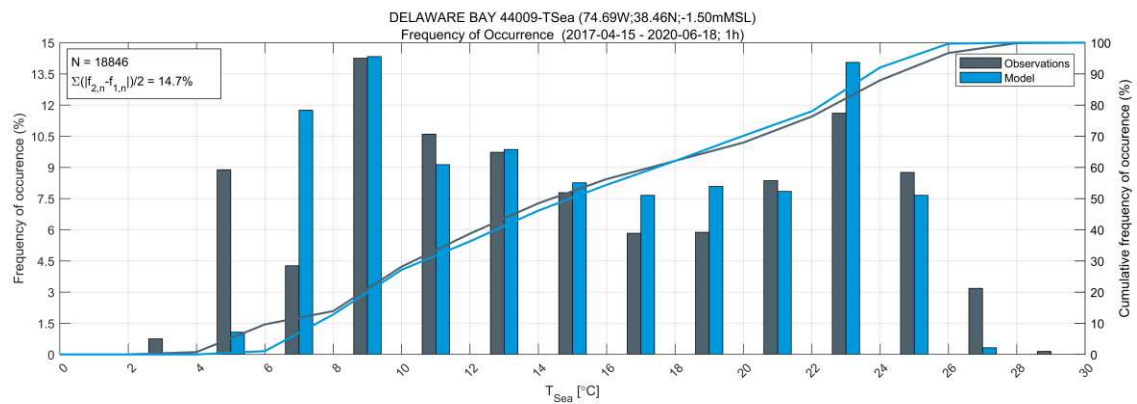
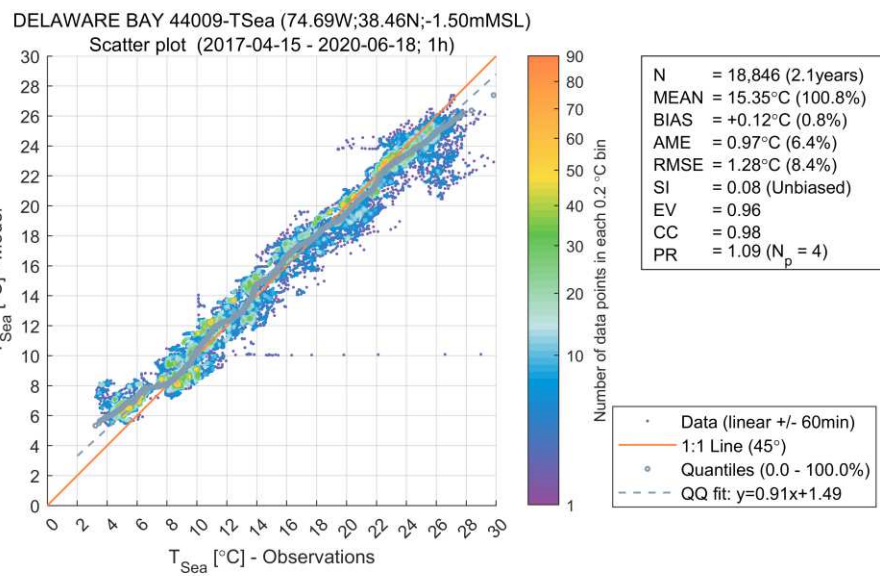
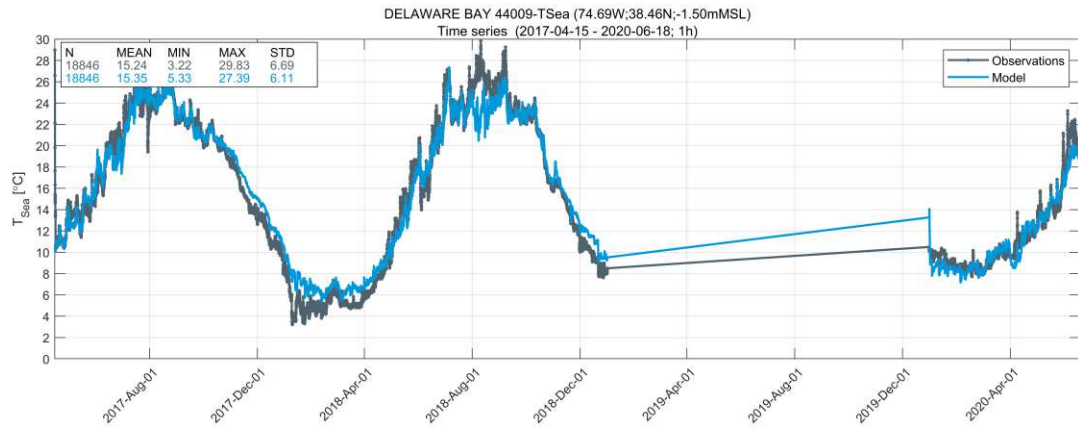


Figure A.80. Delaware Bay Sea Temperature Measurements at 1.5 m Depth vs. Model Results

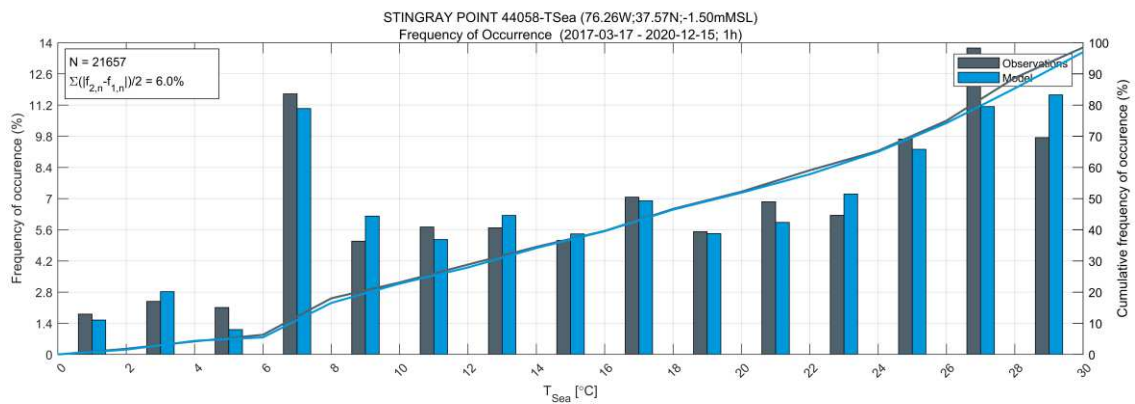
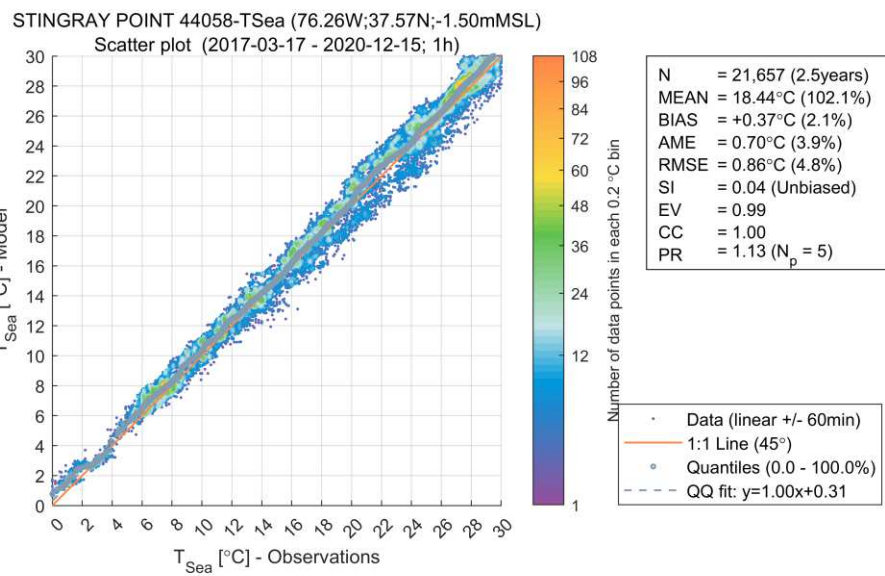
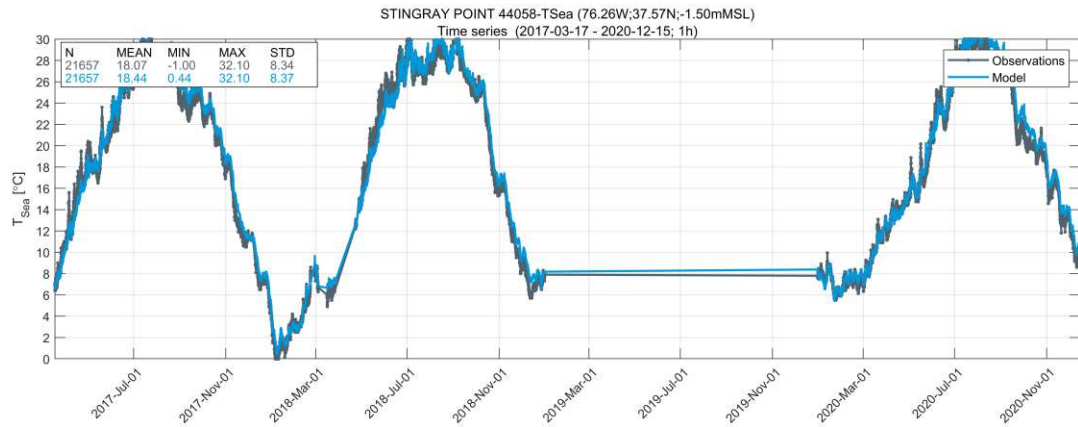


Figure A.81. Stingray Point Sea Temperature Measurements at 1.5 m Depth vs. Model Results

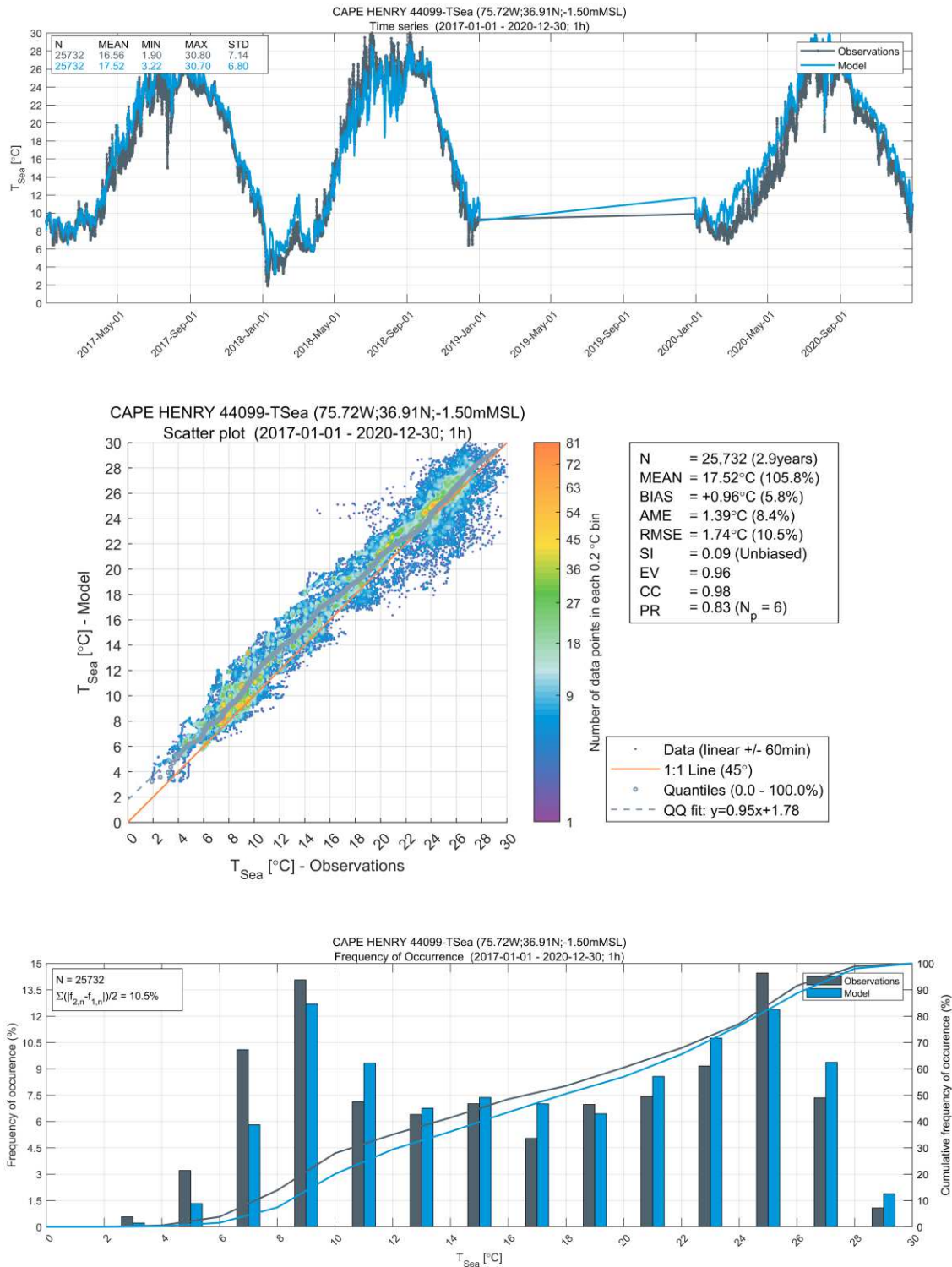


Figure A.82. Cape Henry Sea Temperature Measurements at 1.5 m Depth vs. Model Results

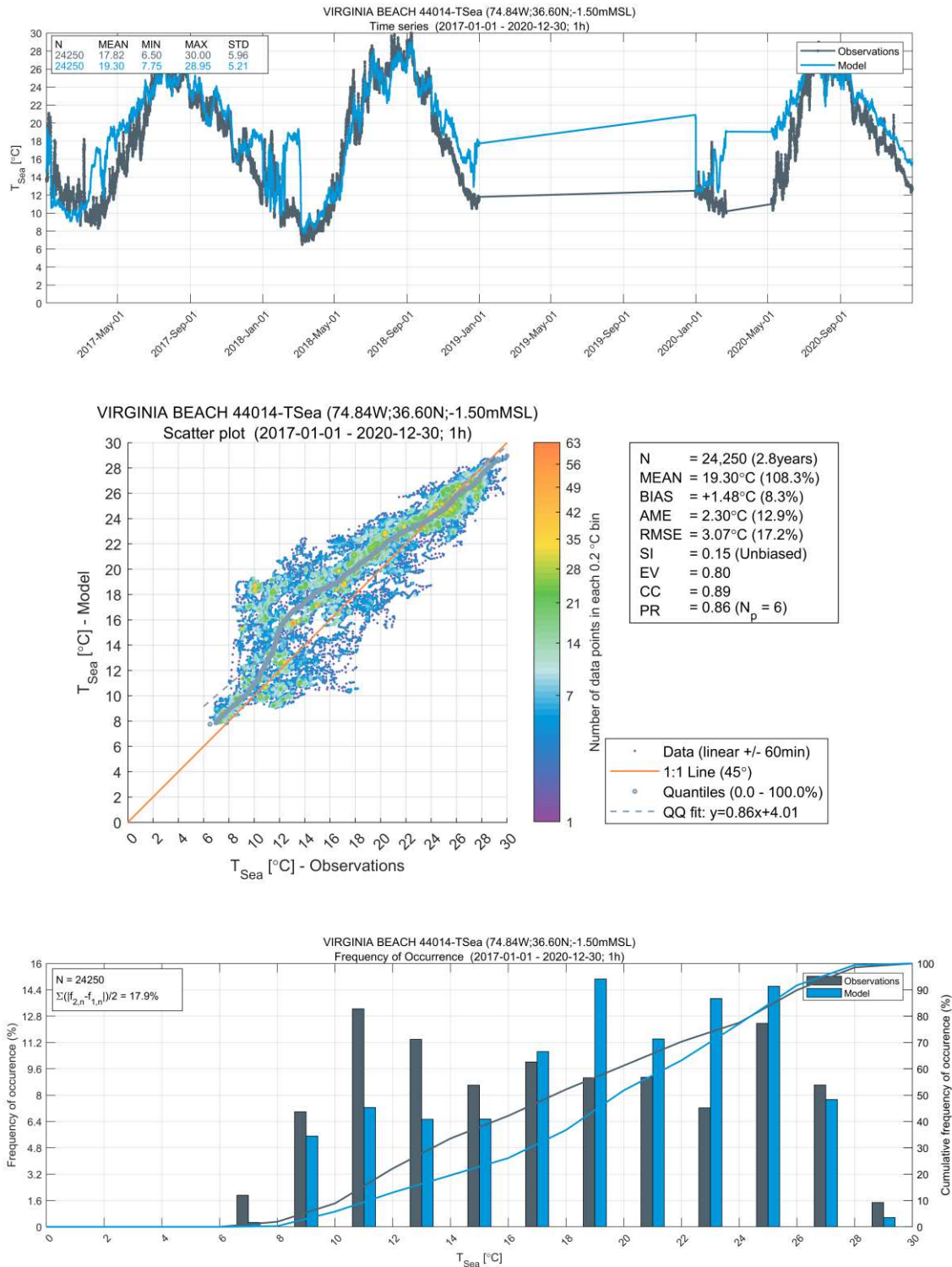


Figure A.83. Virginia Beach Sea Temperature Measurements at 1.5 m Depth vs. Model Results

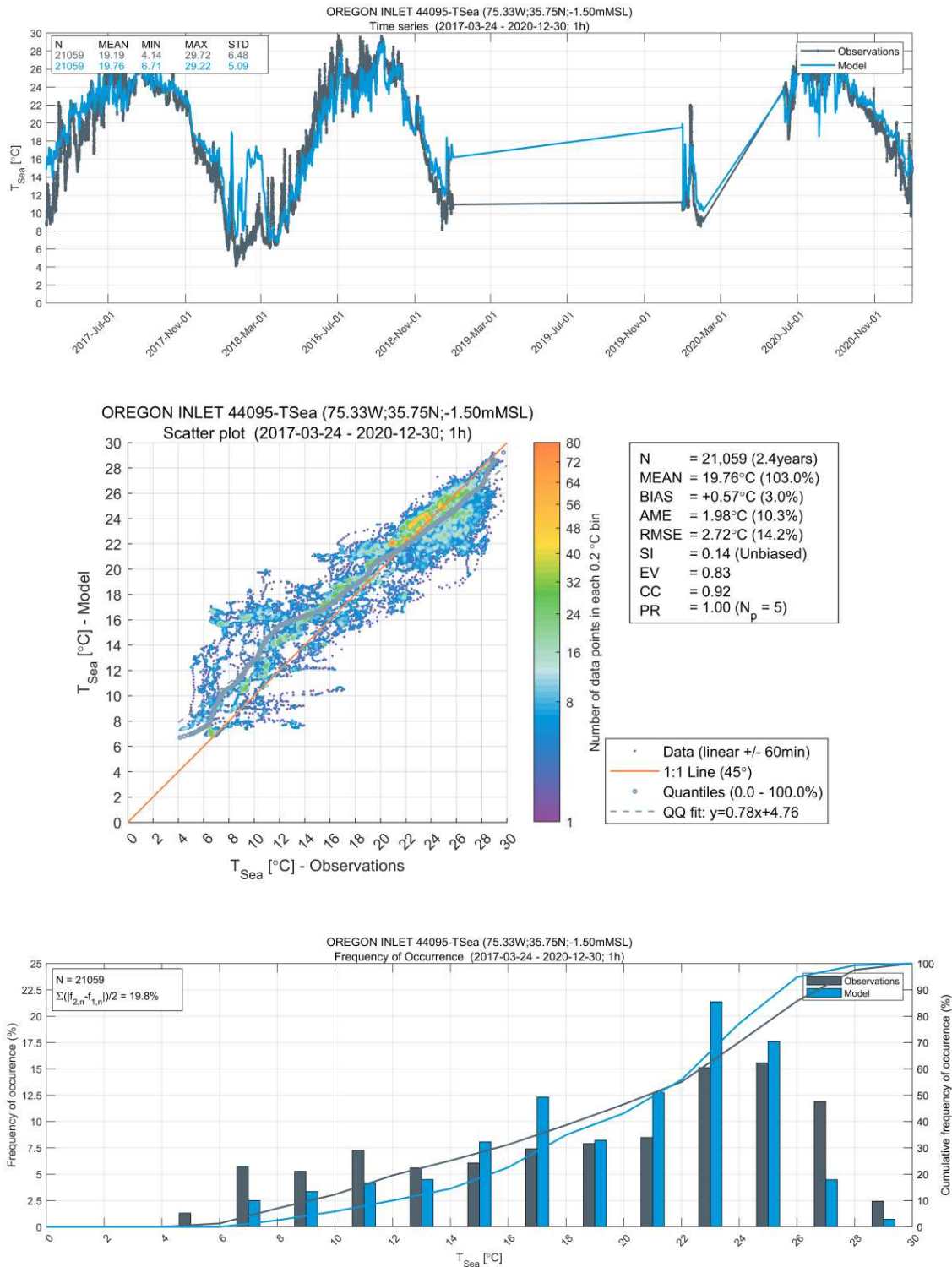


Figure A.84. Oregon Inlet Sea Temperature Measurements at 1.5 m Depth vs. Model Results

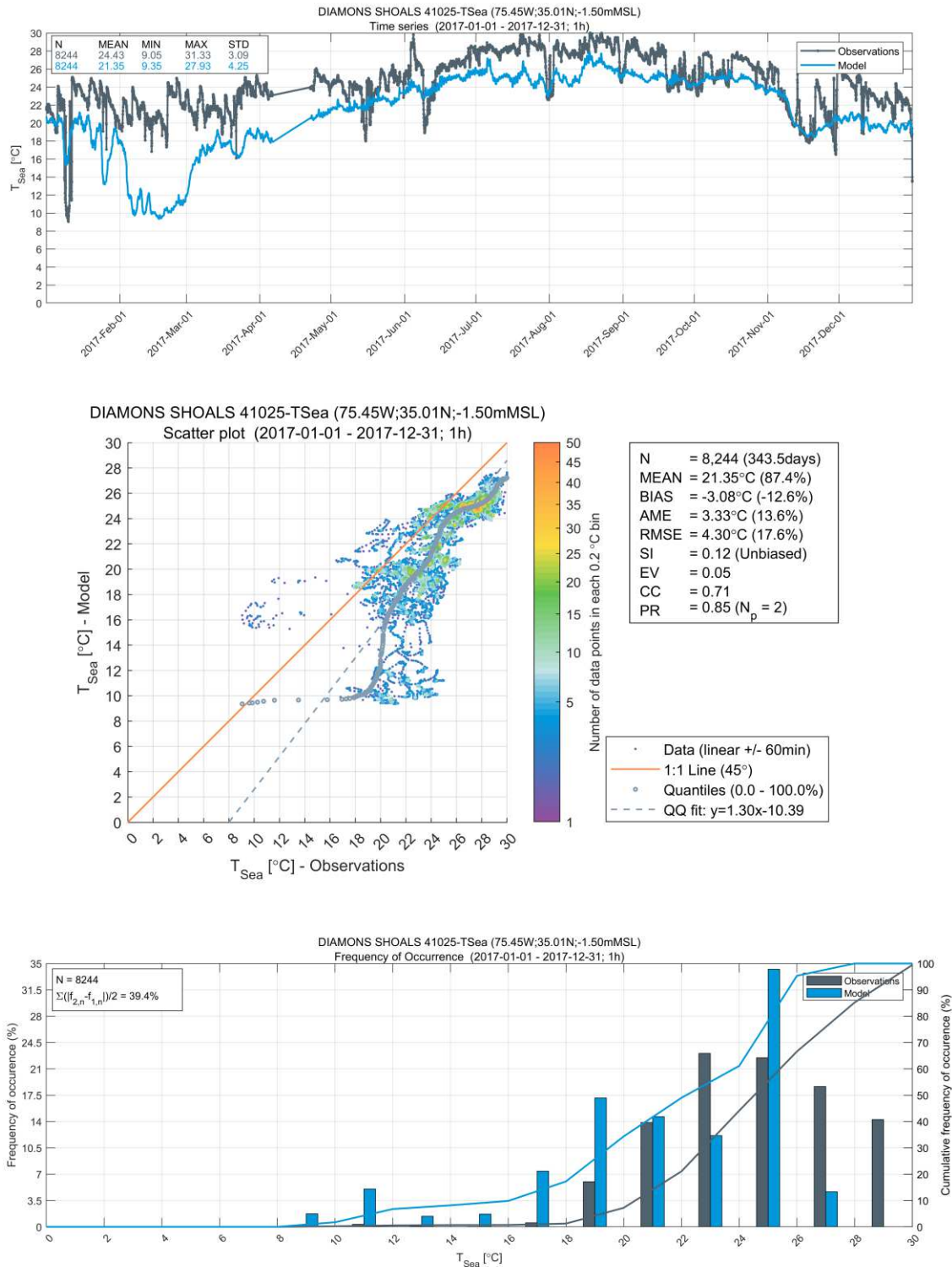


Figure A.85. Diamons Shoals Sea Temperature Measurements at 1.5 m Depth vs. Model Results

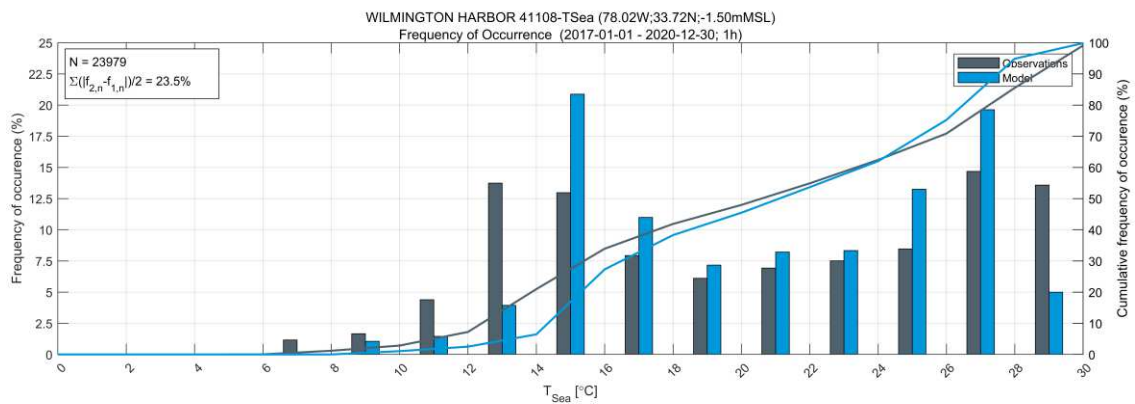
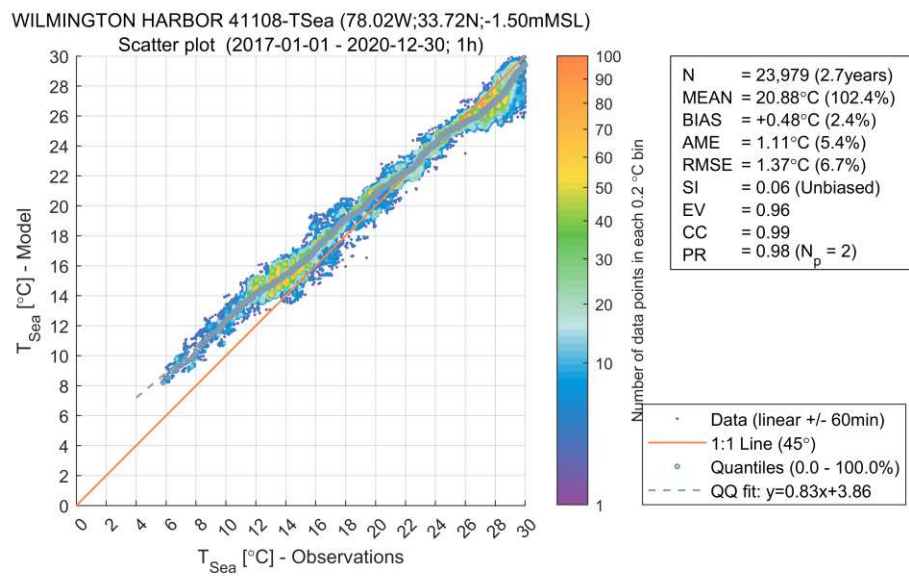
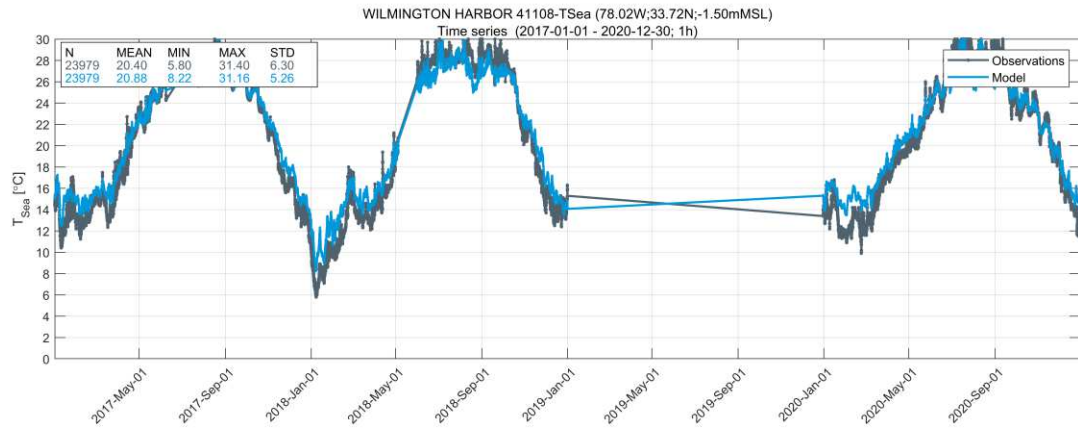


Figure A.86. Wilmington Harbor Sea Temperature Measurements at 1.5 m Depth vs. Model Results

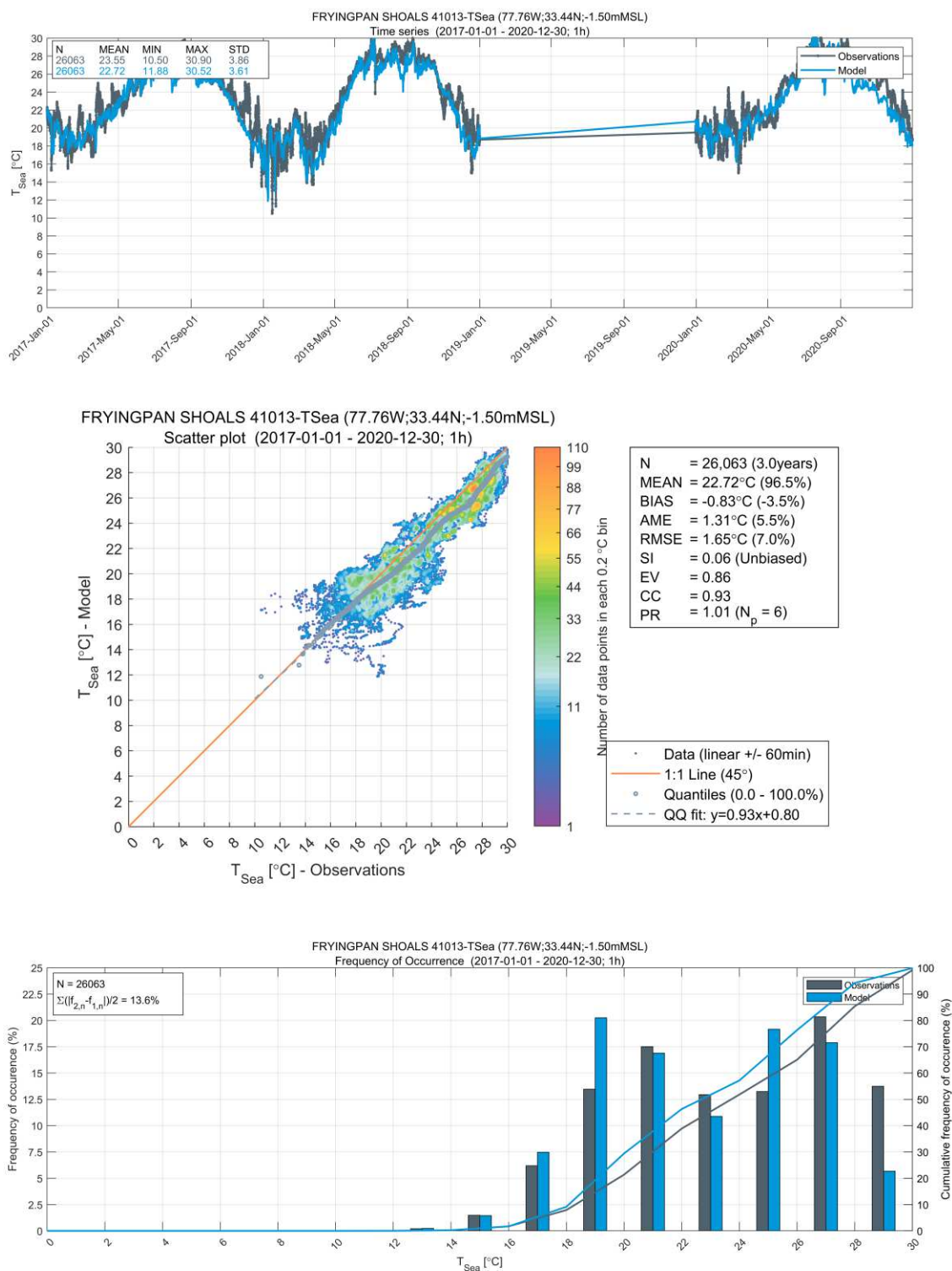


Figure A.87. Fryingpan Shoals Sea Temperature Measurements at 1.5 m Depth vs. Model Results

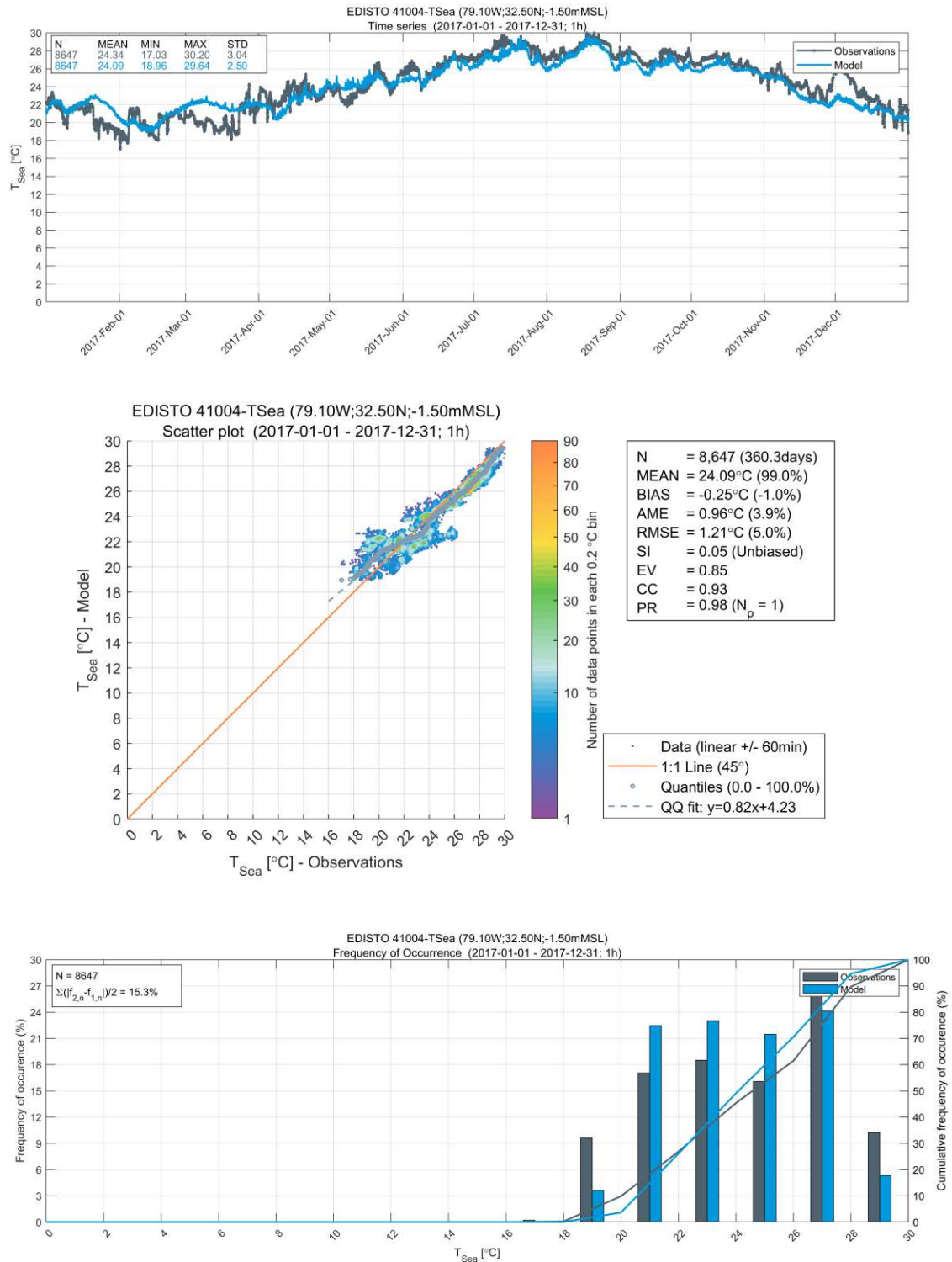


Figure A.88. Edisto Sea Temperature Measurements at 1.5 m Depth vs. Model Results

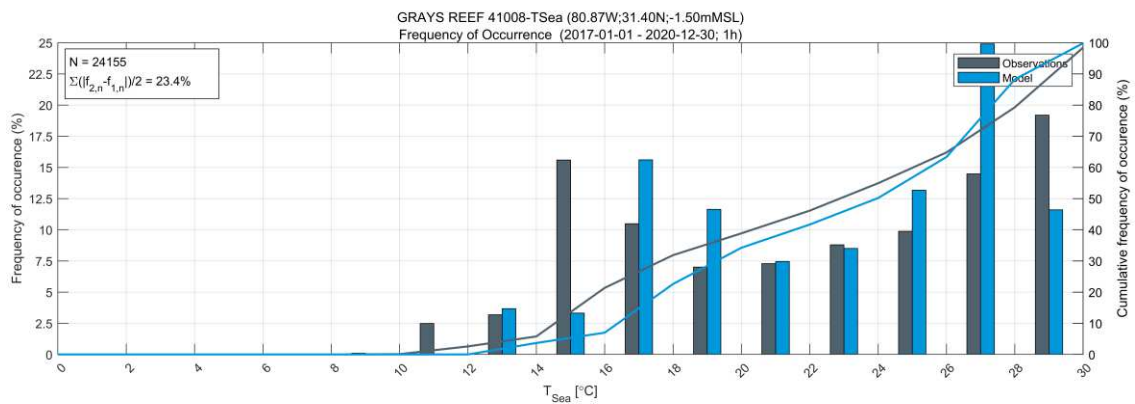
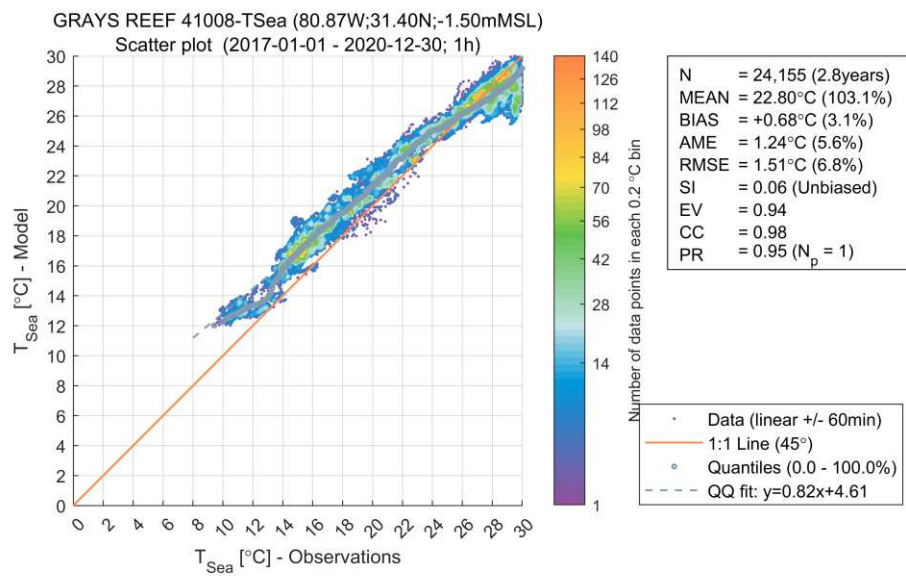
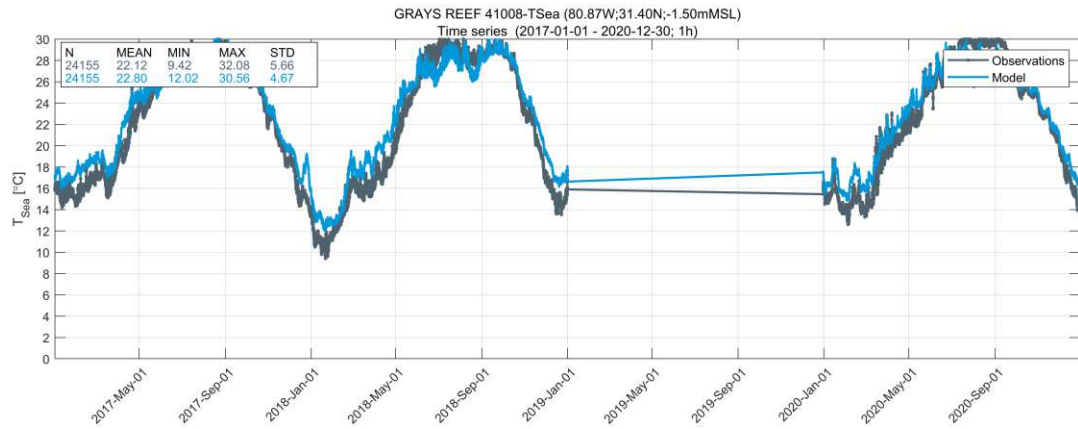


Figure A.89. Grays Reef Sea Temperature Measurements at 1.5 m Depth vs. Model Results

For the year 2017, regional sea surface temperature OSTIA satellite measurements side-by-side model results are presented below. The difference between the observations and the model results are also included. Each set of three represents the averages for the four seasons (winter, January-February-March, spring, April-May-June, summer, July-August-September and fall, October-November-December). RMSE plots for the years 2107, 2018 and 2020 follow the 2017 side-by-side plots

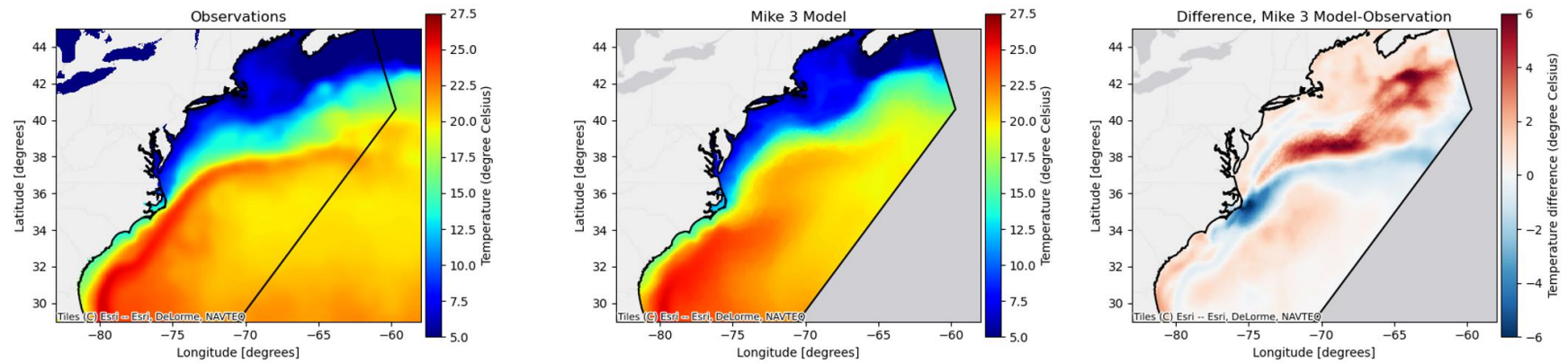


Figure A.90. Average Satellite Surface Temperature January-February-March (JFM) 2017 Period
OSTIA Observation (right), Model (center), Difference (right)

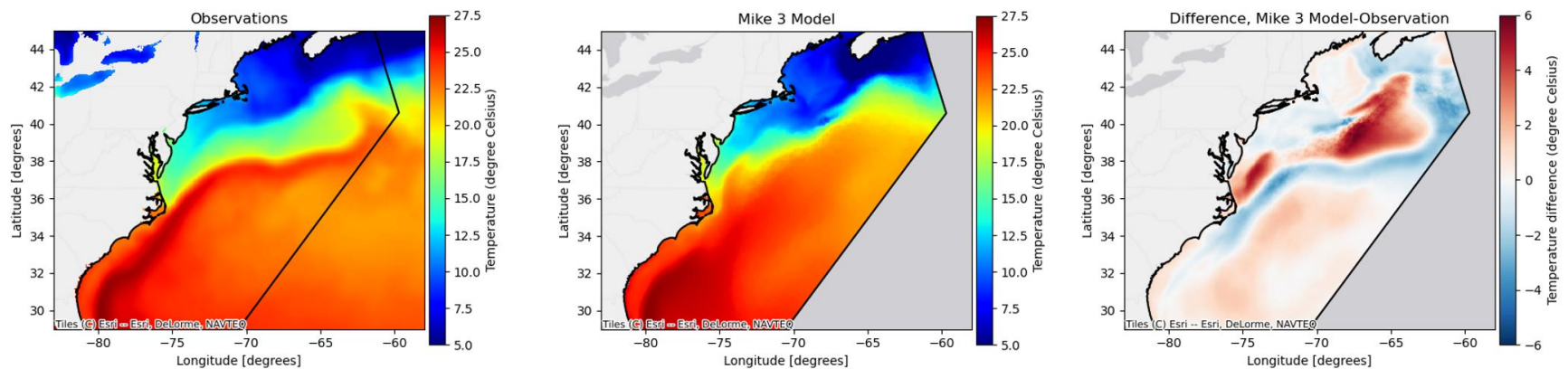


Figure A.91. Average Satellite Surface Temperature April-May-June (AMJ) 2017 Period
OSTIA Observation (right), Model (center), Difference (right)

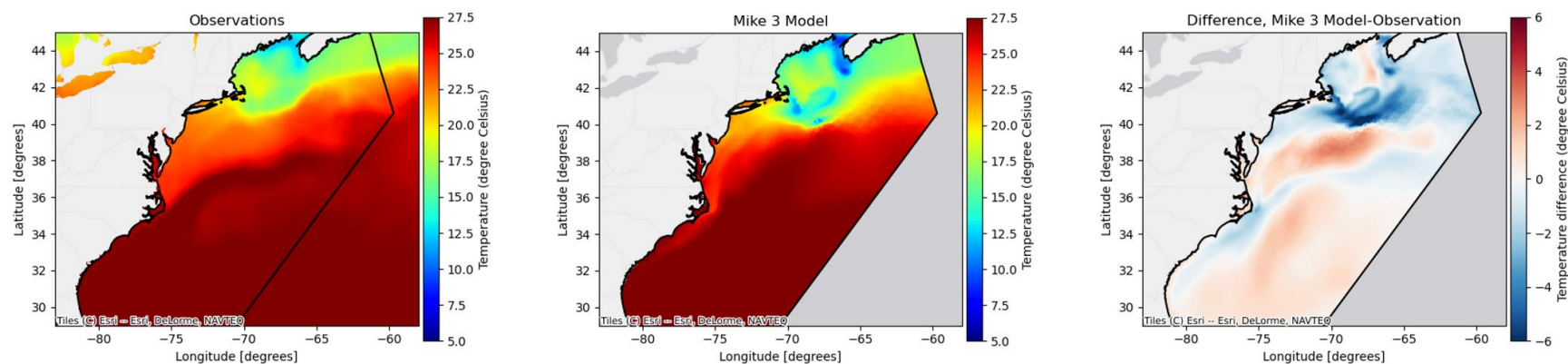


Figure A.92. Average Satellite Surface Temperature July-August-September (JAS) 2017 Period
OSTIA Observation (right), Model (center), Difference (right)

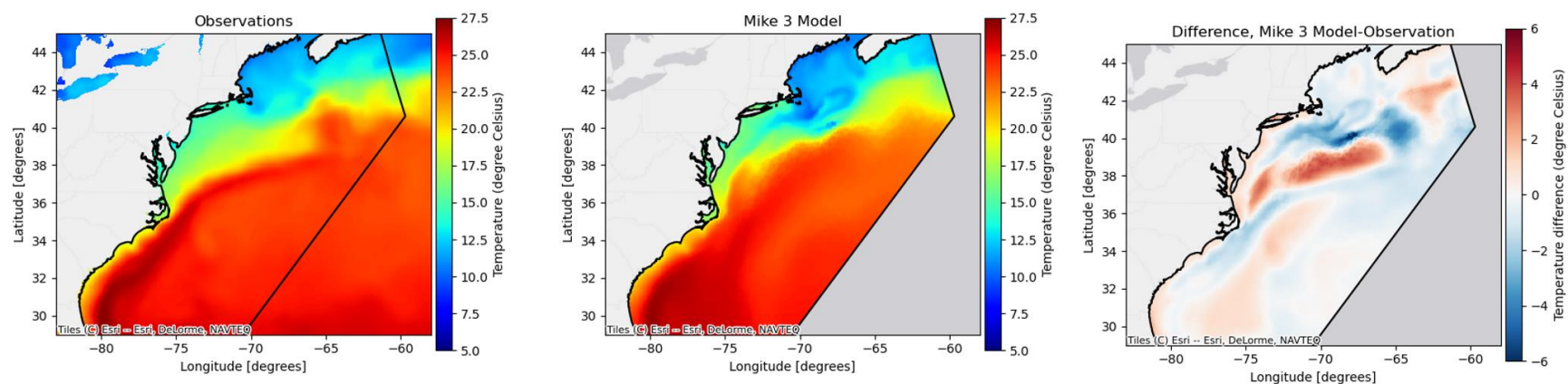


Figure A.93. Average Satellite Surface Temperature October-November-December (OND) 2017 Period
OSTIA Observation (right), Model (center), Difference (right)

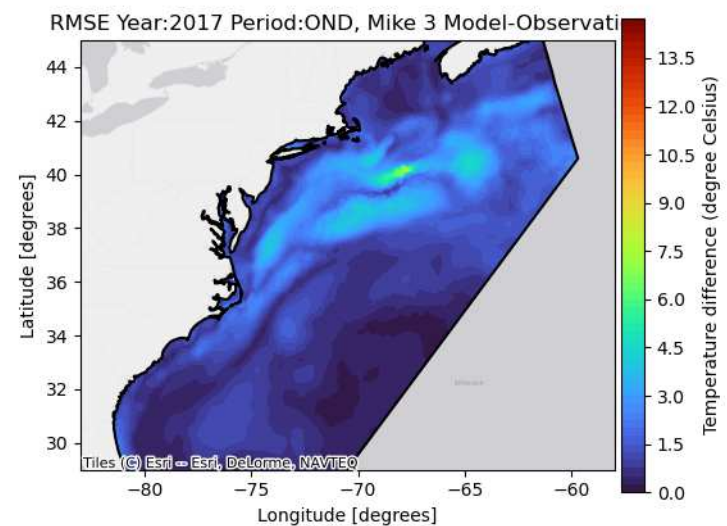
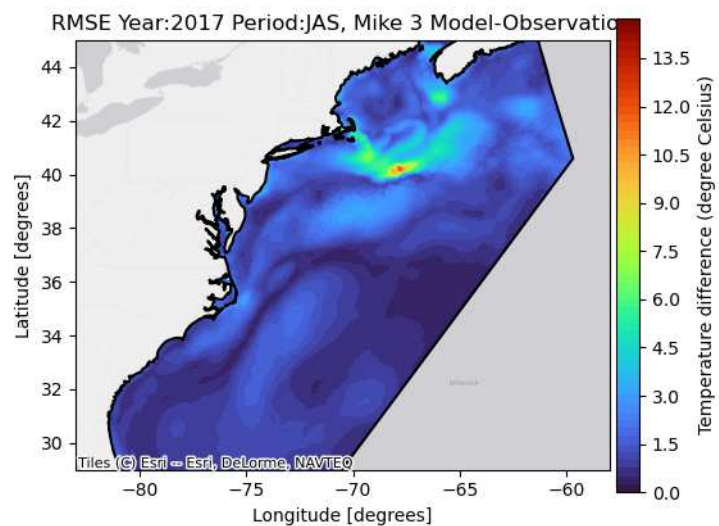
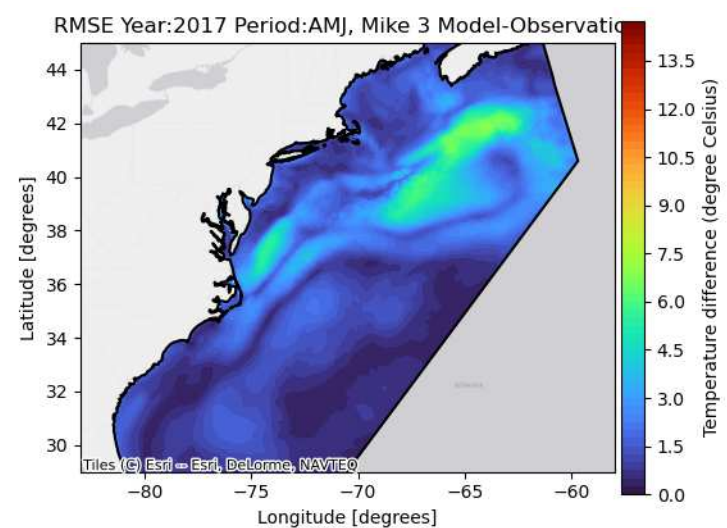
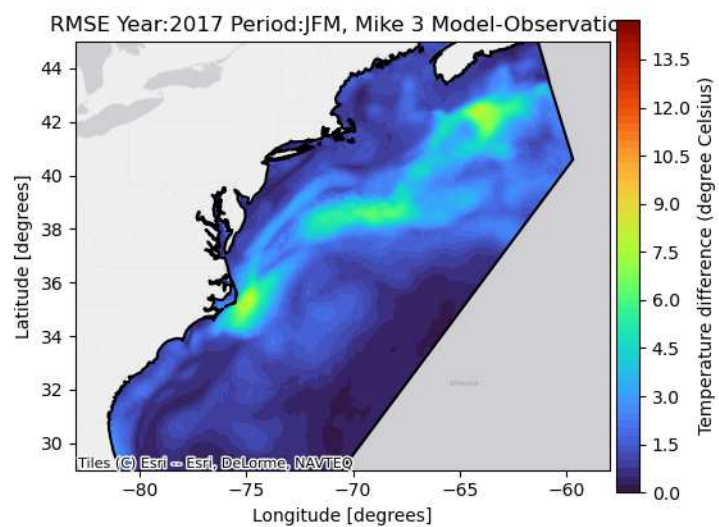


Figure A.94. Satellite Surface Temperature (OSTIA) vs. MIKE3 Model RMSE metric four 4 seasonal groupings in 2017
 January-February-March 2017 (Upper left), April-May-June (Upper right), July-August-September (Lower left), October-November-December (Lower right)

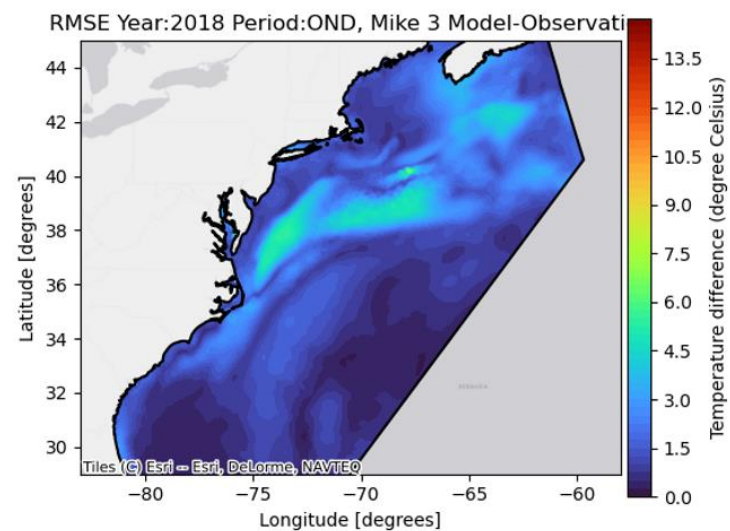
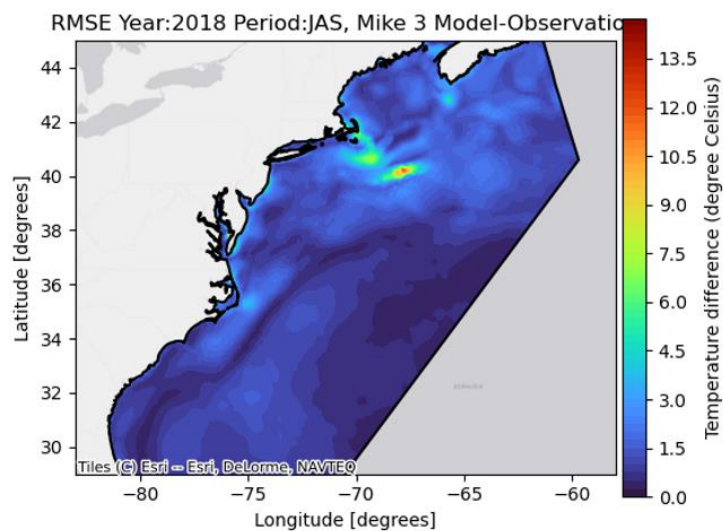
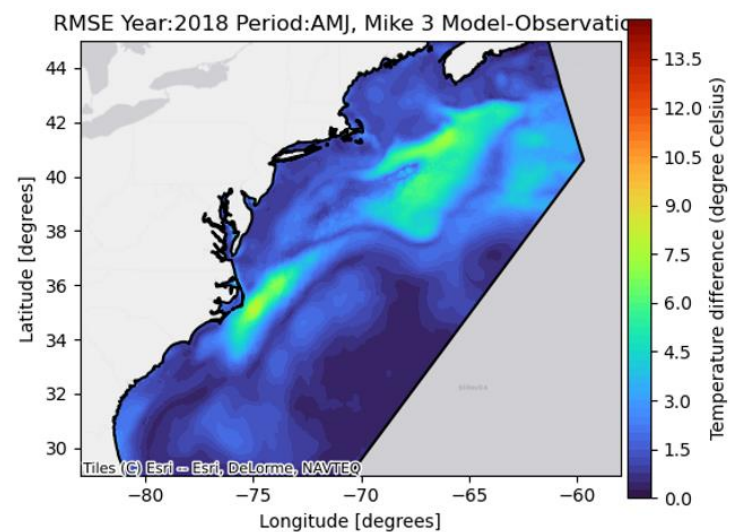
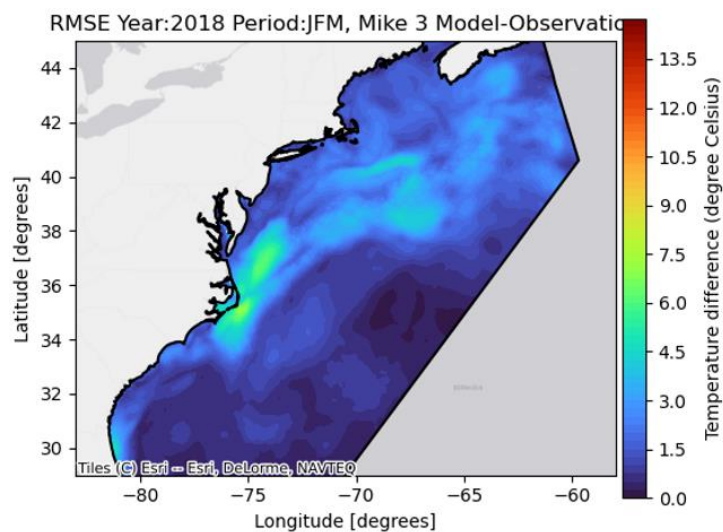


Figure A.95. Satellite Surface Temperature (OSTIA) vs. MIKE3 Model RMSE metric four 4 seasonal groupings in 2018
 January-February-March 2017 (Upper left), April-May-June (Upper right), July-August-September (Lower left), October-November-December (Lower right)

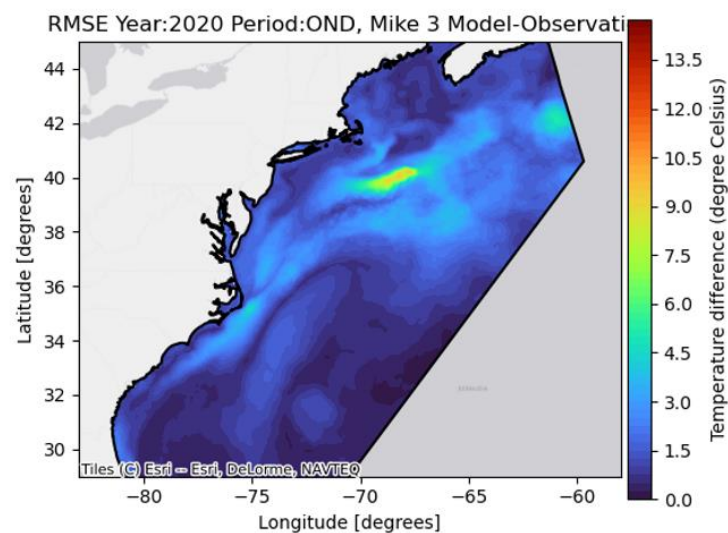
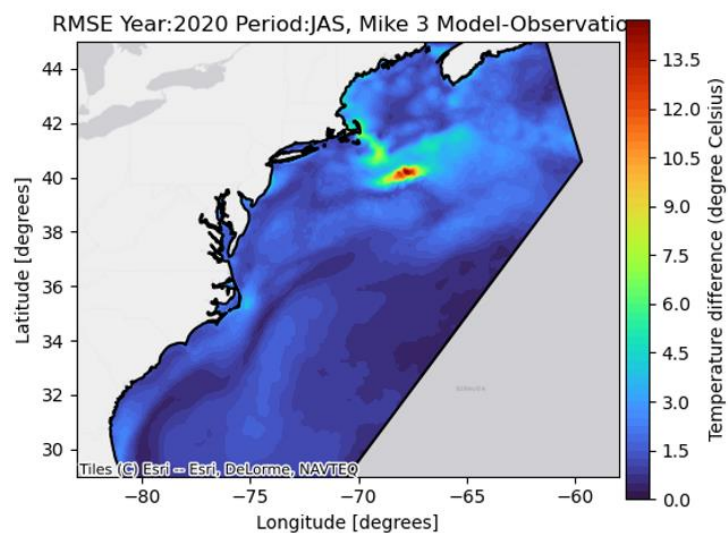
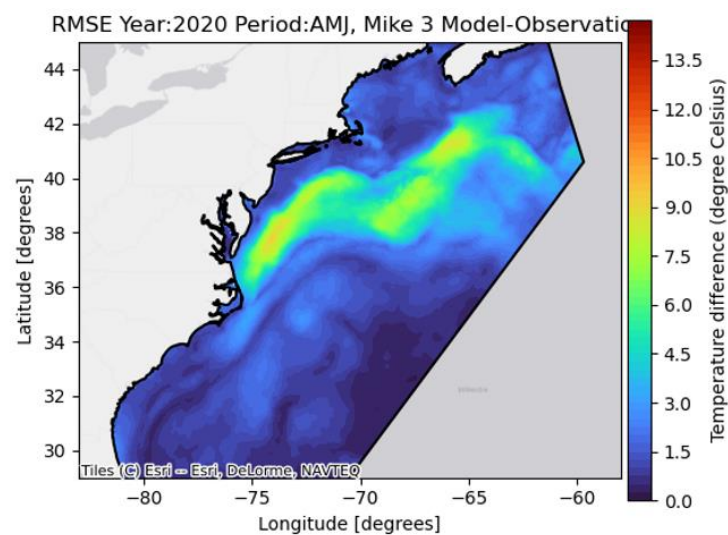
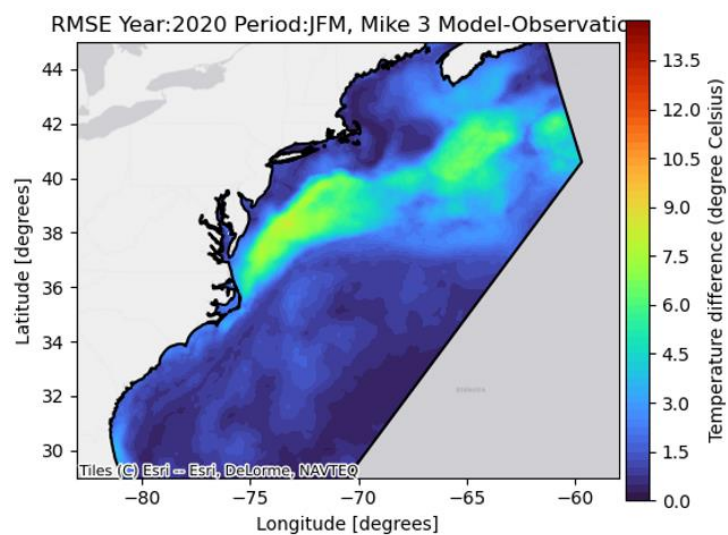


Figure A.96. Satellite Surface Temperature (OSTIA) vs. MIKE3 Model RMSE metric four 4 seasonal groupings in 2020
 January-February-March 2020 (Upper left), April-May-June (Upper right), July-August-September (Lower left), October-November-December (Lower right)

A.2.5 Hydrodynamic Model Baseline Sea Temperature Profile Validation Plots from Pioneer Array stations

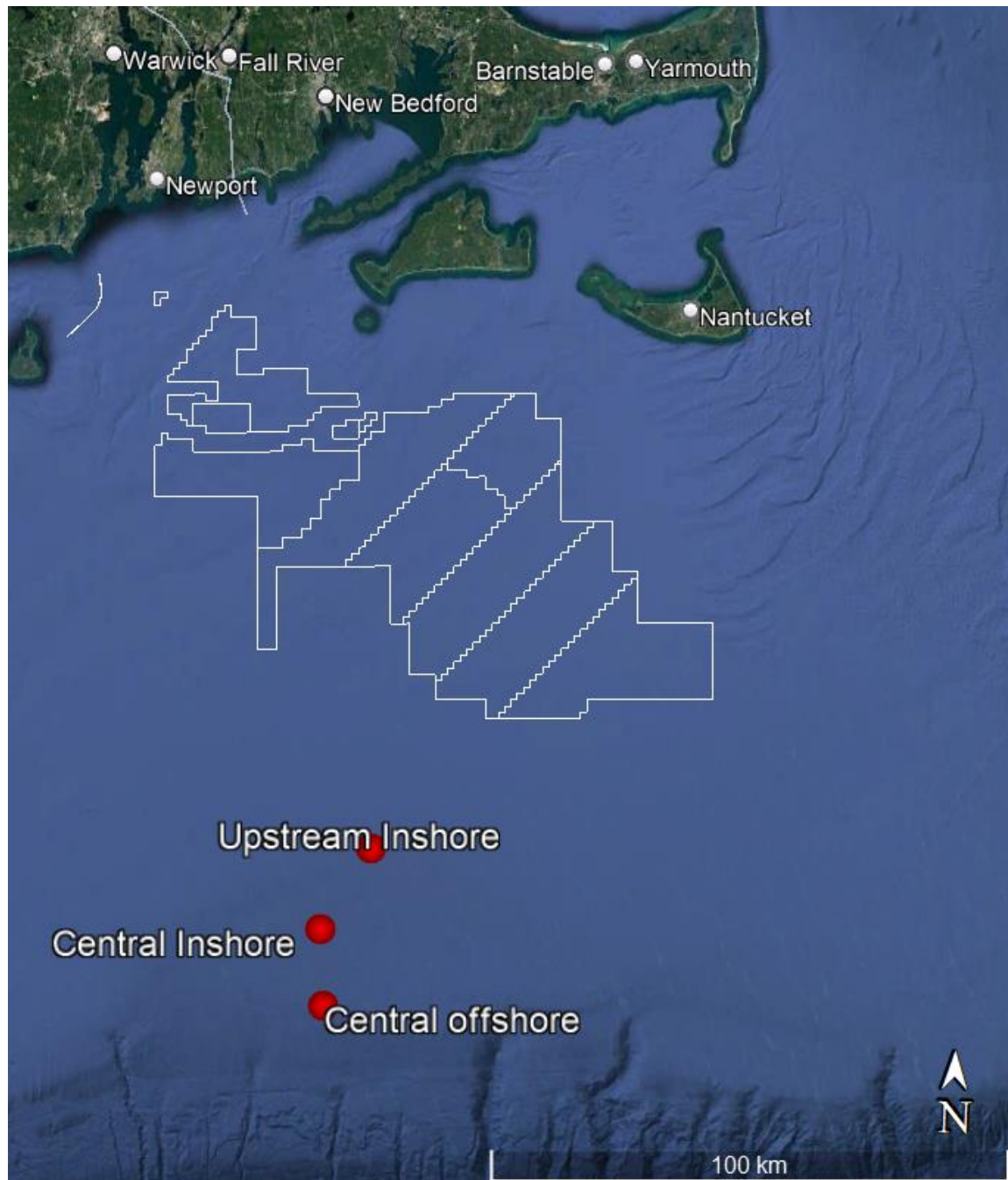


Figure A.97. Pioneer Array station locations – Upstream Inshore, Central Inshore and Central Offshore

Stations shown relative to MA-RI WEAs to the north and the shelf break to the south

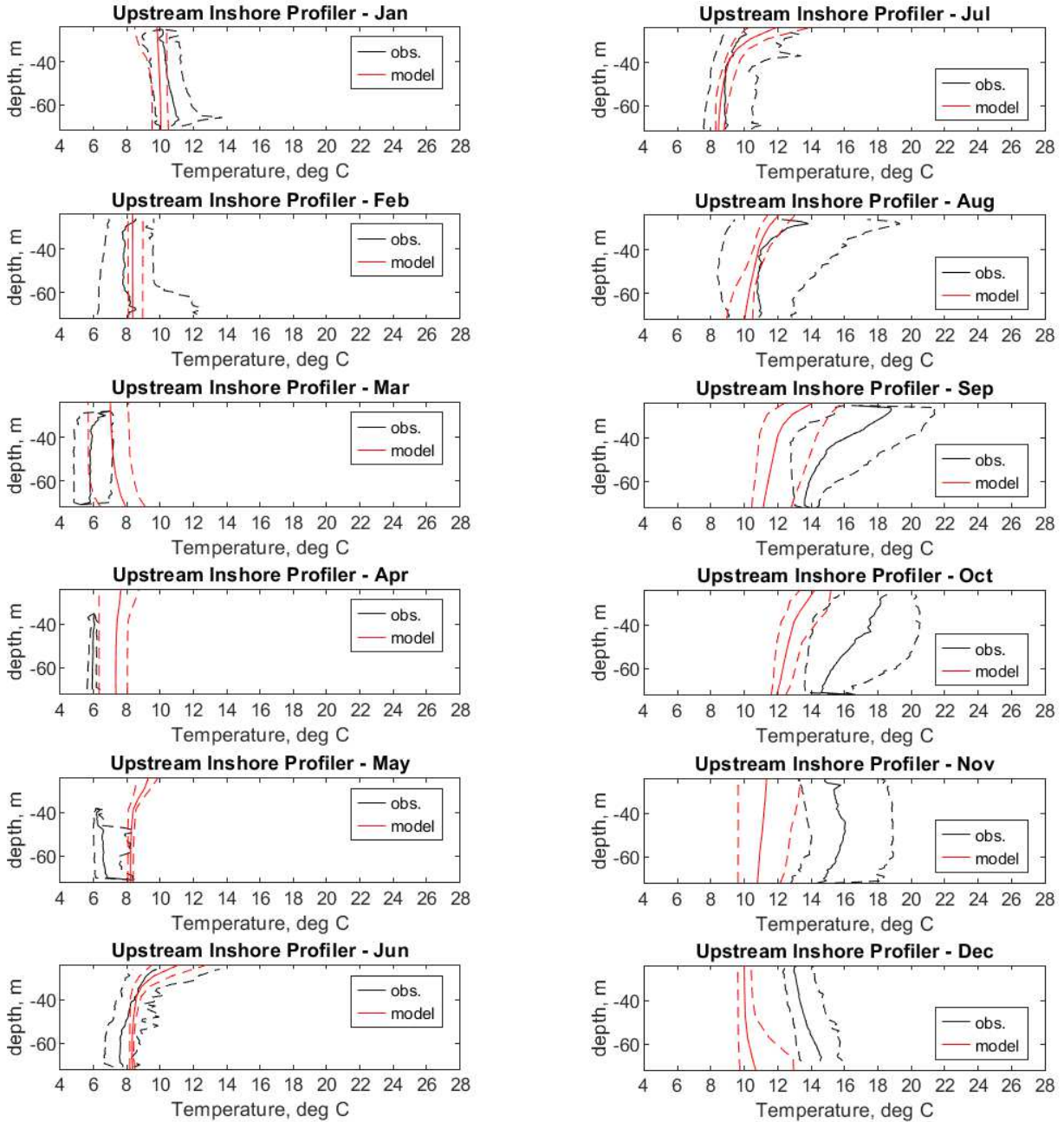


Figure A.98. Upstream Inshore station vertical temperature profile overlays of monthly observations and model results for 2017: January to June (left) and July to December (right)
Solid black: Mean of observations. Dashed black 5th and 95th percentile of observations. Solid red: Mean of model results. Dashed red 5th and 95th percentile of model results

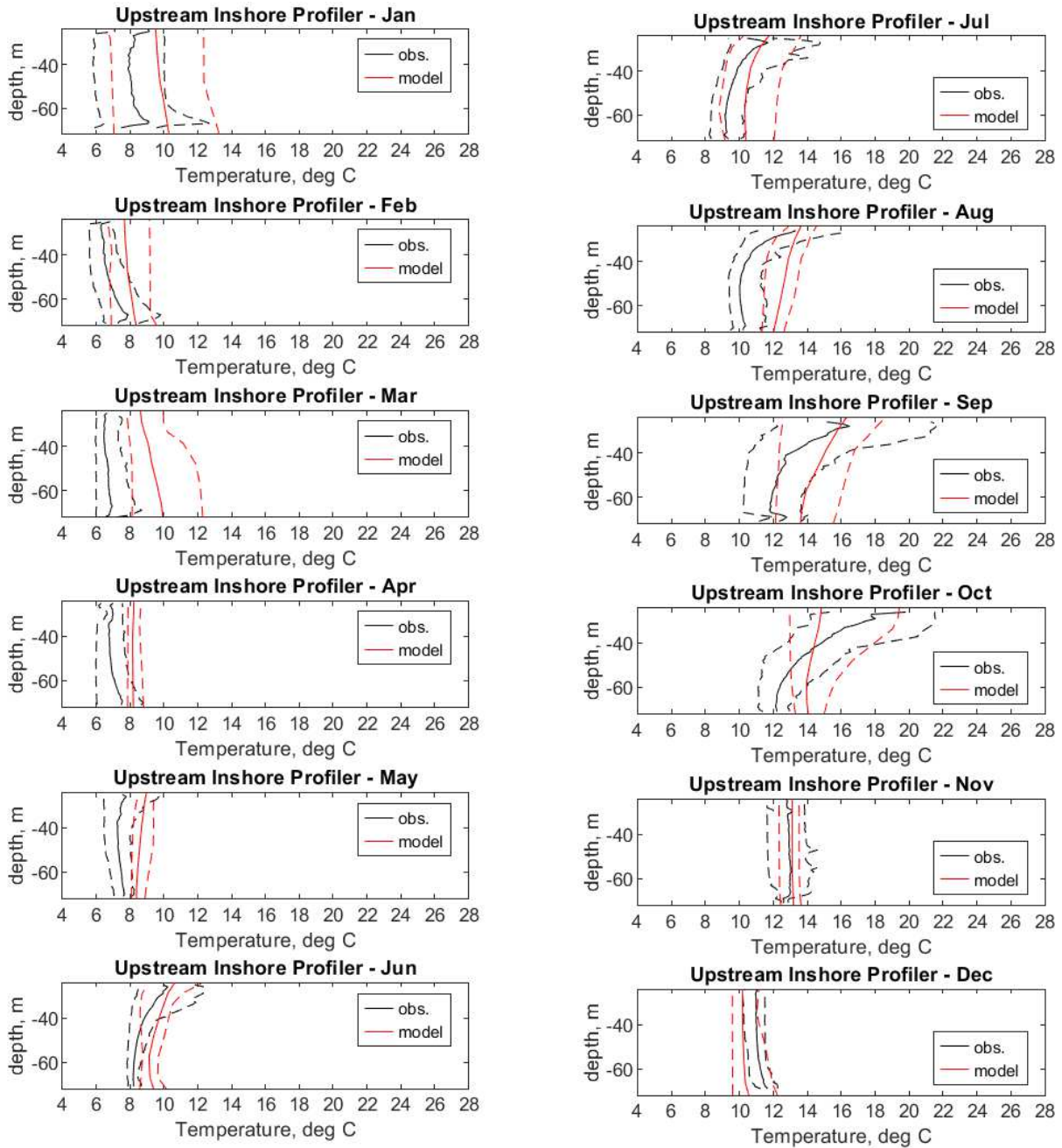


Figure A.99. Upstream Inshore station vertical temperature profile overlays of monthly observations and model results for 2018: January to June (left) and July to December (right)
Solid black: Mean of observations. Dashed black 5th and 95th percentile of observations. Solid red: Mean of model results. Dashed red 5th and 95th percentile of model results

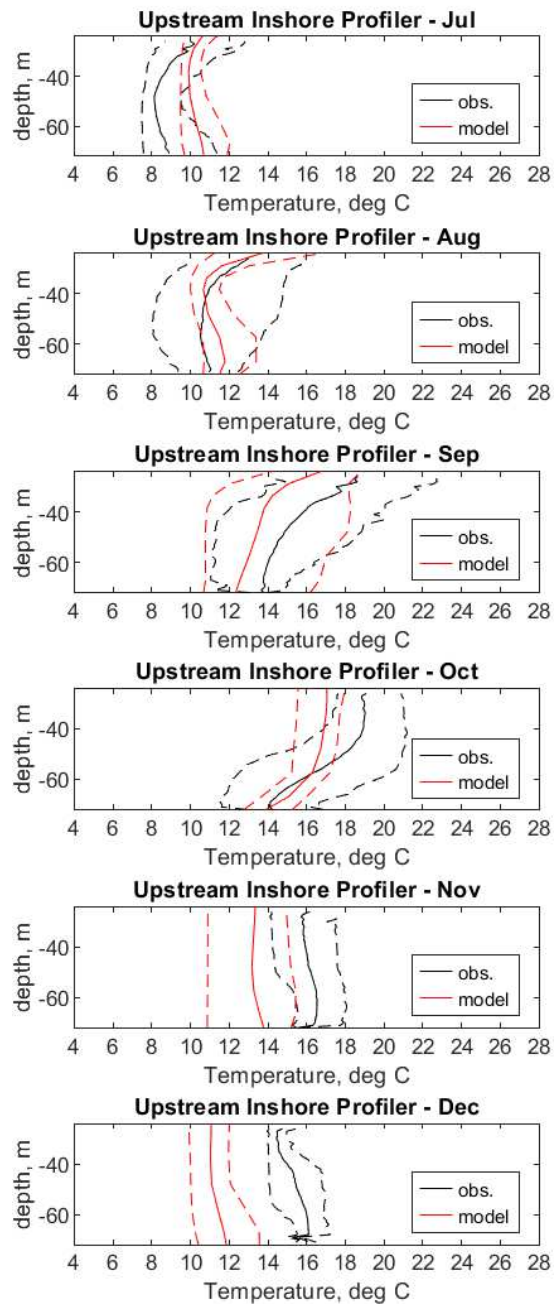


Figure A.100. Upstream Inshore station vertical temperature profile overlays of monthly observations and model results for 2020: July to December

Solid black: Mean of observations. Dashed black 5th and 95th percentile of observations. Solid red: Mean of model results. Dashed red 5th and 95th percentile of model results

(Note: there were no observational data for January to May and only partial information for June, therefore these plots were omitted)

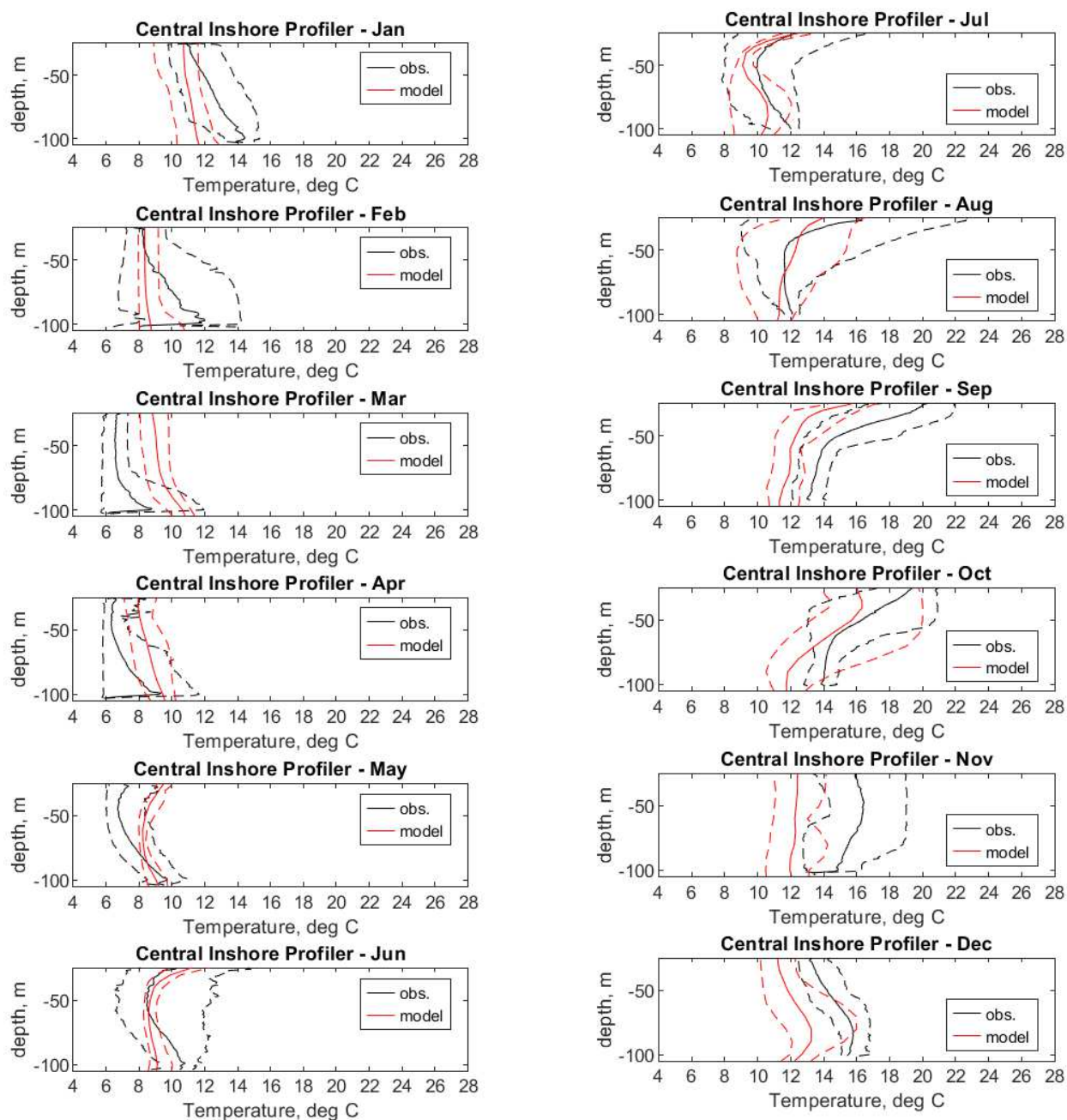


Figure A.101. Central Inshore station vertical temperature profile overlays of monthly observations and model results for 2017: January to June (left) and July to December (right)
Solid black: Mean of observations. Dashed black 5th and 95th percentile of observations. Solid red: Mean of model results. Dashed red 5th and 95th percentile of model results

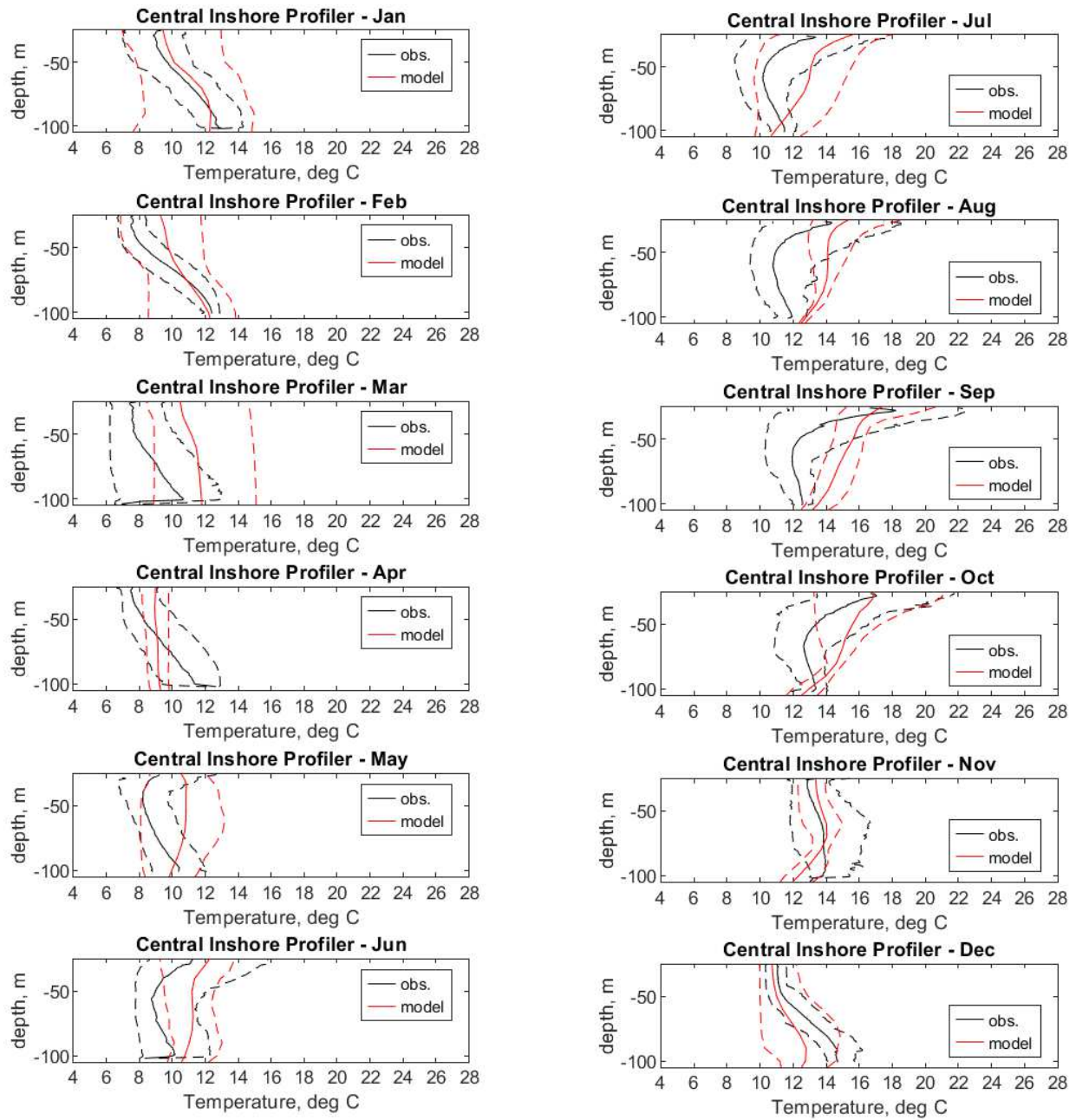


Figure A.102. Central Inshore station vertical temperature profile overlays of monthly observations and model results for 2018: January to June (left) and July to December (right)
Solid black: Mean of observations. Dashed black 5th and 95th percentile of observations. Solid red: Mean of model results. Dashed red 5th and 95th percentile of model results

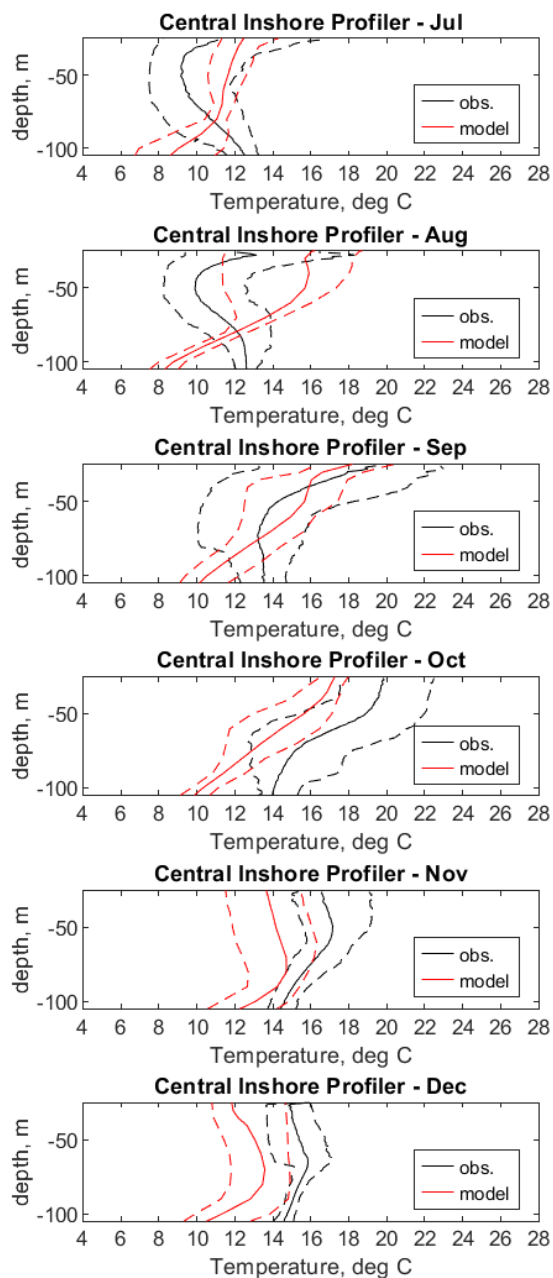


Figure A.103. Central Inshore station vertical temperature profile overlays of monthly observations and model results for 2020: July to December

Solid black: Mean of observations. Dashed black 5th and 95th percentile of observations. Solid red: Mean of model results. Dashed red 5th and 95th percentile of model results

(Note: there were no observational data for January to May and only partial information for June, therefore these plots were omitted)

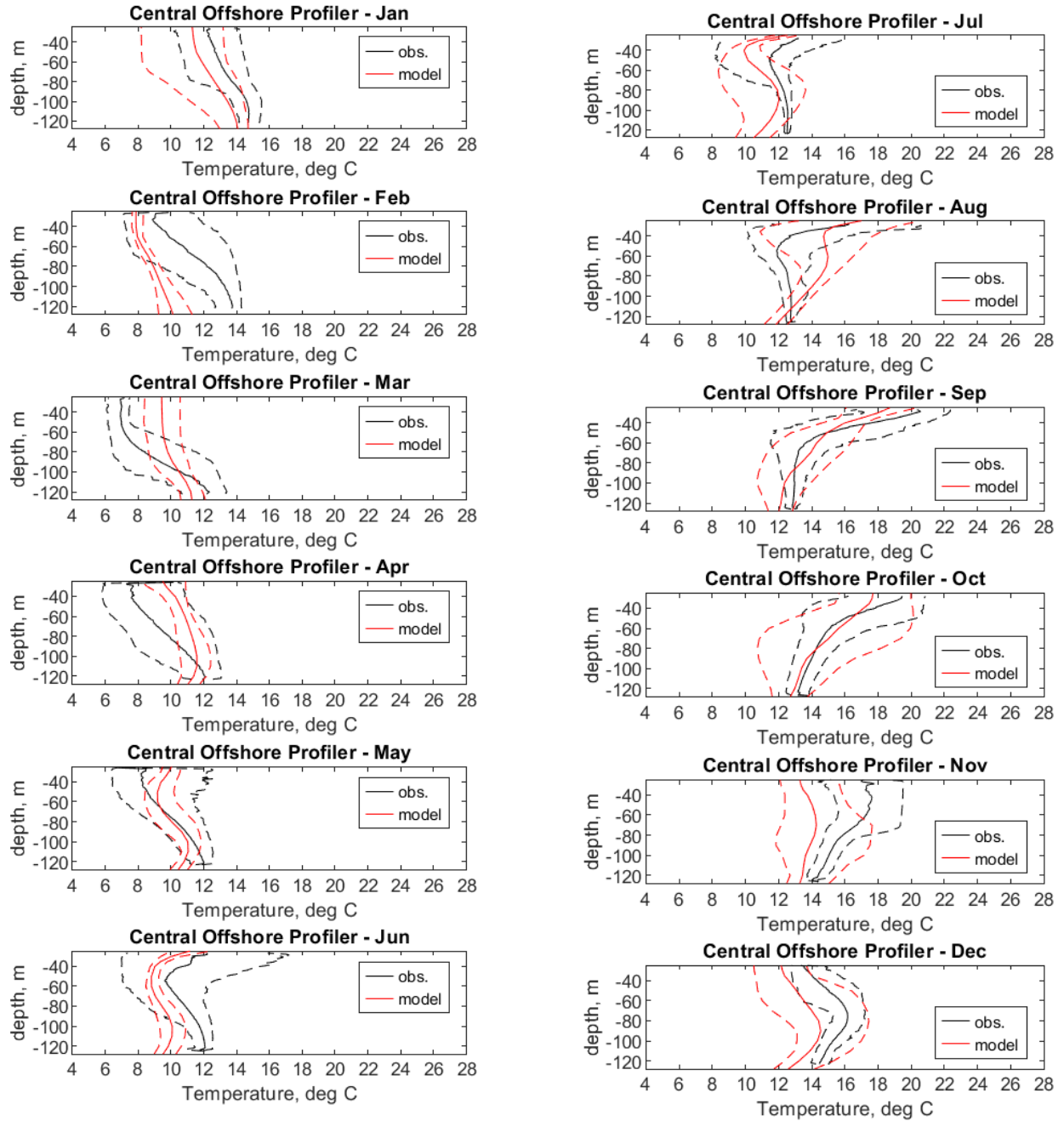


Figure A.104. Central Offshore station vertical temperature profile overlays of monthly observations and model results for 2017: January to June (left) and July to December (right)
Solid black: Mean of observations. Dashed black 5th and 95th percentile of observations. Solid red: Mean of model results. Dashed red 5th and 95th percentile of model results

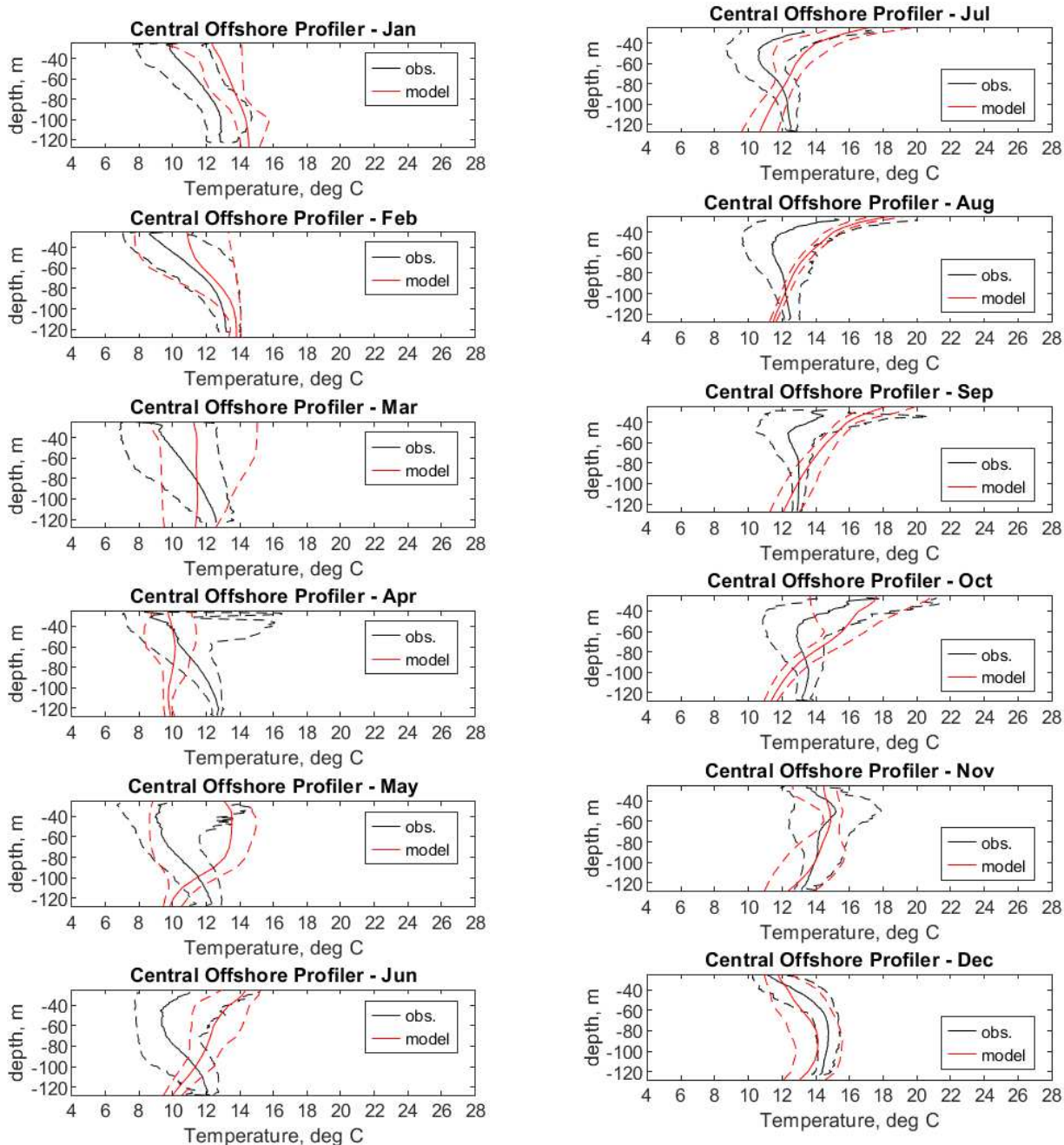


Figure A.105. Central Offshore station vertical temperature profile overlays of monthly observations and model results for 2018: January to June (left) and July to December (right)
Solid black: Mean of observations. Dashed black 5th and 95th percentile of observations. Solid red: Mean of model results. Dashed red 5th and 95th percentile of model results

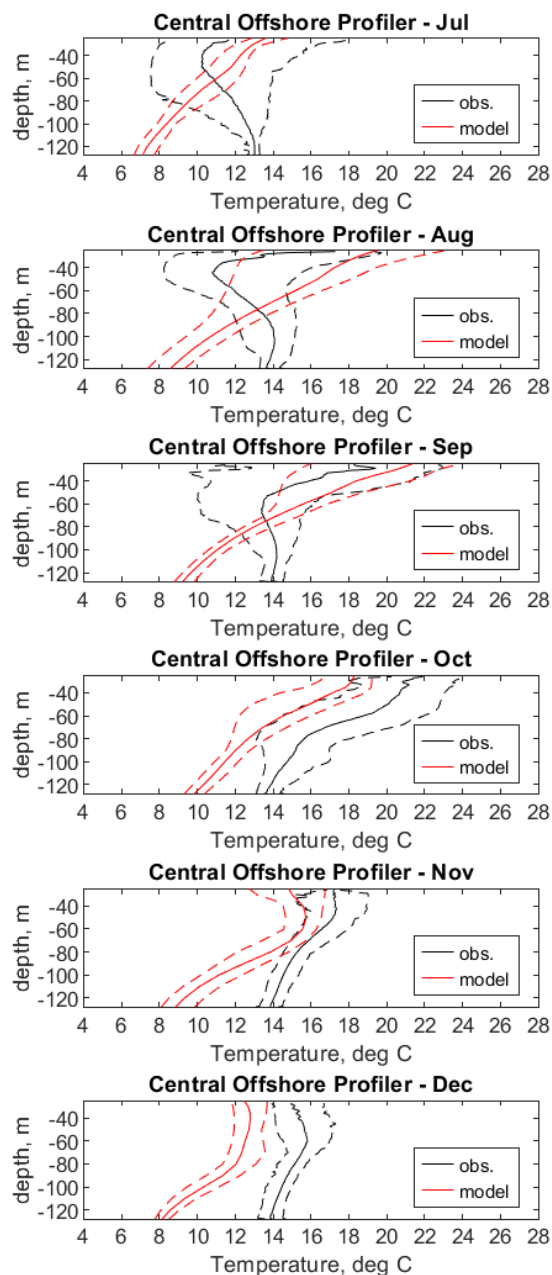


Figure A.106. Central Offshore station vertical temperature profile overlays of monthly observations and model results for 2020: July to December

Solid black: Mean of observations. Dashed black 5th and 95th percentile of observations. Solid red: Mean of model results. Dashed red 5th and 95th percentile of model results

(Note: there were no observational data for January to May and only partial information for June, therefore these plots were omitted)

A.2.6 Hydrodynamic Model Locations of WTGs

See the following pages for the Latitude and Longitude of the WTGs for the:

- “COP” + “Generic” or Full Build-out Scenarios
- “COP only” or Partial Build-out Scenarios

Table A.6. Locations of Wind Turbine Generators for Full Build-out

Latitude	Longitude
39.44145	-73.3522
39.4545	-73.3646
39.45471	-73.3781
39.46777	-73.4046
39.46798	-73.4172
39.45085	-74.1333
39.45085	-74.1208
39.45085	-74.1082
39.45085	-74.0957
39.45085	-74.0832
39.45085	-74.0706
39.45085	-74.0581
39.45085	-74.0456
39.45085	-74.033
39.45085	-74.0205
39.45085	-74.008
39.45085	-73.9954
39.45085	-73.9829
39.45085	-73.9704
39.46338	-74.0456
39.46338	-74.033
39.46338	-74.0205
39.46338	-74.008
39.46338	-73.9954
39.46338	-73.9829
39.46338	-73.9704
39.47591	-74.0456
39.47591	-74.033
39.47591	-74.0205
39.47591	-74.008
39.47591	-73.9954
39.47591	-73.9829
39.47591	-73.9704
39.47591	-73.9578
39.47591	-73.9453
39.48844	-74.0456
39.48844	-74.033

Latitude	Longitude
39.48844	-74.0205
39.48844	-74.008
39.48844	-73.9954
39.48844	-73.9829
39.48844	-73.9704
39.48844	-73.9578
39.48844	-73.9453
39.50097	-74.0456
39.50097	-74.033
39.50097	-74.0205
39.50097	-74.008
39.50097	-73.9954
39.50097	-73.9829
39.50097	-73.9704
39.50097	-73.9578
39.50097	-73.9453
39.5135	-73.9829
39.5135	-73.9704
39.5135	-73.9578
39.5135	-73.9453
39.52603	-73.9829
39.52603	-73.9704
39.52603	-73.9578
39.52603	-73.9453
39.53856	-73.9829
39.53856	-73.9704
39.53856	-73.9578
39.53856	-73.9453
39.55109	-74.0456
39.55109	-74.033
39.55109	-74.0205
39.55109	-74.008
39.55109	-73.9954
39.55109	-73.9829
39.55109	-73.9704
39.55109	-73.9578
39.55109	-73.9453
39.56362	-74.0456
39.56362	-74.033
39.56362	-74.0205

Latitude	Longitude
39.56362	-74.008
39.56362	-73.9954
39.56362	-73.9829
39.56362	-73.9704
39.56362	-73.9578
39.56362	-73.9453
39.57615	-74.0456
39.57615	-74.033
39.57615	-74.0205
39.57615	-74.008
39.57615	-73.9954
39.57615	-73.9829
39.57615	-73.9704
39.57615	-73.9578
39.57615	-73.9453
39.43832	-74.0957
39.43832	-74.0832
39.43832	-74.0706
39.43832	-74.0581
39.43832	-74.0456
39.43832	-74.033
39.43832	-74.0205
39.43832	-74.008
39.43832	-73.9954
39.43832	-73.9829
39.43832	-73.9704
39.42579	-74.0957
39.42579	-74.0832
39.42579	-74.0706
39.42579	-74.0581
39.42579	-74.0456
39.42579	-74.033
39.42579	-74.0205
39.42579	-74.008
39.42579	-73.9954
39.42579	-73.9829
39.42579	-73.9704
39.41326	-74.0957
39.41326	-74.0832
39.41326	-74.0706

Latitude	Longitude
39.41326	-74.0581
39.41326	-74.0456
39.41326	-74.033
39.41326	-74.0205
39.41326	-74.008
39.41326	-73.9954
39.41326	-73.9829
39.41326	-73.9704
39.41326	-73.9578
39.41326	-73.9453
39.40073	-74.0957
39.40073	-74.0832
39.40073	-74.0706
39.40073	-74.0581
39.40073	-74.0456
39.40073	-74.033
39.40073	-74.0205
39.40073	-74.008
39.40073	-73.9954
39.40073	-73.9829
39.40073	-73.9704
39.40073	-73.9578
39.40073	-73.9453
39.3882	-74.0957
39.3882	-74.0832
39.3882	-74.0706
39.3882	-74.0581
39.3882	-74.0456
39.3882	-74.033
39.3882	-74.0205
39.3882	-74.008
39.3882	-73.9954
39.3882	-73.9829
39.3882	-73.9704
39.3882	-73.9578
39.3882	-73.9453
39.37567	-74.033
39.37567	-74.0205
39.37567	-74.008
39.37567	-73.9954

Latitude	Longitude
39.37567	-73.9829
39.37567	-73.9704
39.37567	-73.9578
39.37567	-73.9453
39.36314	-74.0205
39.36314	-74.008
39.36314	-73.9954
39.36314	-73.9829
39.36314	-73.9704
39.36314	-73.9578
39.36314	-73.9453
39.35061	-74.008
39.35061	-73.9954
39.35061	-73.9829
39.35061	-73.9704
39.35061	-73.9578
39.35061	-73.9453
39.33808	-73.9954
39.33808	-73.9829
39.33808	-73.9704
39.33808	-73.9578
39.33808	-73.9453
39.32555	-73.9829
39.32555	-73.9704
39.58868	-74.0205
39.58868	-74.008
39.58868	-73.9954
39.58868	-73.9829
39.58868	-73.9704
39.58868	-73.9578
39.58868	-73.9453
39.60121	-74.0205
39.60121	-74.008
39.60121	-73.9954
39.60121	-73.9829
39.60121	-73.9704
39.60121	-73.9578
39.60121	-73.9453
39.61374	-74.0205
39.61374	-74.008

Latitude	Longitude
39.61374	-73.9954
39.61374	-73.9829
39.61374	-73.9704
39.61374	-73.9578
39.61374	-73.9453
39.62627	-73.9954
39.62627	-73.9829
39.62627	-73.9704
39.62627	-73.9578
39.62627	-73.9453
39.6388	-73.9578
39.6388	-73.9453
39.65133	-73.9578
39.65133	-73.9453
39.66386	-73.9578
39.66386	-73.9453
40.88758	-70.4359
40.75263	-70.6085
39.1204	-74.3032
39.1863	-74.1977
39.1646	-74.2349
39.2146	-74.2255
39.2006	-74.241
39.1893	-74.2583
39.1753	-74.2761
38.2864	-74.6818
38.3208	-74.7246
38.3702	-74.7651
38.3883	-74.7786
38.3883	-74.8443
33.3729	-77.7911
33.3729	-77.8041
33.3729	-77.8172
33.3729	-77.8303
33.3729	-77.8433
33.3729	-77.8564
33.3729	-77.8694
33.3729	-77.8825
33.3729	-77.8955
33.3859	-77.765

Latitude	Longitude
33.3859	-77.778
33.3859	-77.7911
33.3859	-77.8041
33.3859	-77.8172
33.3859	-77.8303
33.3859	-77.8433
33.3859	-77.8564
33.3859	-77.8694
33.3859	-77.8825
33.3859	-77.8955
33.3859	-77.9086
33.3859	-77.9216
33.3859	-77.9347
33.3989	-77.7519
33.3989	-77.765
33.3989	-77.778
33.3989	-77.7911
33.3989	-77.8041
33.3989	-77.8172
33.3989	-77.8303
33.3989	-77.8433
33.3989	-77.8564
33.3989	-77.8694
33.3989	-77.8825
33.3989	-77.8955
33.3989	-77.9086
33.3989	-77.9216
33.3989	-77.9347
33.3989	-77.9477
33.3989	-77.9608
33.3989	-77.9739
33.3989	-77.9869
33.4119	-77.7258
33.4119	-77.7389
33.4119	-77.7519
33.4119	-77.765
33.4119	-77.778
33.4119	-77.7911
33.4119	-77.8041
33.4119	-77.8172

Latitude	Longitude
33.4119	-77.8303
33.4119	-77.8433
33.4119	-77.8564
33.4119	-77.8694
33.4119	-77.8825
33.4119	-77.8955
33.4119	-77.9086
33.4119	-77.9216
33.4119	-77.9347
33.4119	-77.9477
33.4119	-77.9608
33.4119	-77.9739
33.4119	-77.9869
33.4119	-78
33.4119	-78.013
33.4119	-78.0261
33.5289	-77.8955
33.5289	-78
33.5289	-78.013
33.5289	-78.0261
33.5289	-78.0391
33.5289	-78.0522
33.5289	-78.0652
33.5289	-78.0783
33.5159	-77.8694
33.5159	-77.8825
33.5159	-77.8955
33.5159	-77.9086
33.5159	-77.9216
33.5159	-77.9347
33.5159	-77.9477
33.5159	-77.9608
33.5159	-77.9739
33.5159	-77.9869
33.5159	-78
33.5159	-78.013
33.5159	-78.0261
33.5159	-78.0391
33.5159	-78.0522
33.5159	-78.0652

Latitude	Longitude
33.5159	-78.0783
33.5029	-77.8433
33.5029	-77.8564
33.5029	-77.8694
33.5029	-77.8825
33.5029	-77.8955
33.5029	-77.9086
33.5029	-77.9216
33.5029	-77.9347
33.5029	-77.9477
33.5029	-77.9608
33.5029	-77.9739
33.5029	-77.9869
33.5029	-78
33.5029	-78.013
33.5029	-78.0261
33.5029	-78.0391
33.5029	-78.0522
33.5029	-78.0652
33.5029	-78.0783
33.4899	-77.7911
33.4899	-77.8041
33.4899	-77.8172
33.4899	-77.8303
33.4899	-77.8433
33.4899	-77.8564
33.4899	-77.8694
33.4899	-77.8825
33.4899	-77.8955
33.4899	-77.9086
33.4899	-77.9216
33.4899	-77.9347
33.4899	-77.9477
33.4899	-77.9608
33.4899	-77.9739
33.4899	-77.9869
33.4899	-78
33.4899	-78.013
33.4899	-78.0261
33.4899	-78.0391

Latitude	Longitude
33.4899	-78.0522
33.4899	-78.0652
33.4899	-78.0783
33.4769	-77.778
33.4769	-77.7911
33.4769	-77.8041
33.4769	-77.8172
33.4769	-77.8303
33.4769	-77.8433
33.4769	-77.8564
33.4769	-77.8694
33.4769	-77.8825
33.4769	-77.8955
33.4769	-77.9086
33.4769	-77.9216
33.4769	-77.9347
33.4769	-77.9477
33.4769	-77.9608
33.4769	-77.9739
33.4769	-77.9869
33.4769	-78
33.4769	-78.013
33.4769	-78.0261
33.4769	-78.0391
33.4769	-78.0522
33.4769	-78.0652
33.4769	-78.0783
33.4639	-77.7519
33.4639	-77.765
33.4639	-77.778
33.4639	-77.7911
33.4639	-77.8041
33.4639	-77.8172
33.4639	-77.8303
33.4639	-77.8433
33.4639	-77.8564
33.4639	-77.8694
33.4639	-77.8825
33.4639	-77.8955
33.4639	-77.9086

Latitude	Longitude
33.4639	-77.9216
33.4639	-77.9347
33.4639	-77.9477
33.4639	-77.9608
33.4639	-77.9739
33.4639	-77.9869
33.4639	-78
33.4639	-78.013
33.4639	-78.0261
33.4639	-78.0391
33.4639	-78.0522
33.4639	-78.0652
33.4639	-78.0783
33.4509	-77.7389
33.4509	-77.7519
33.4509	-77.765
33.4509	-77.778
33.4509	-77.7911
33.4509	-77.8041
33.4509	-77.8172
33.4509	-77.8303
33.4509	-77.8433
33.4509	-77.8564
33.4509	-77.8694
33.4509	-77.8825
33.4509	-77.8955
33.4509	-77.9086
33.4509	-77.9216
33.4509	-77.9347
33.4509	-77.9477
33.4509	-77.9608
33.4509	-77.9739
33.4509	-77.9869
33.4509	-78
33.4509	-78.013
33.4509	-78.0261
33.4509	-78.0391
33.4509	-78.0522
33.4379	-77.7128
33.4379	-77.7258

Latitude	Longitude
33.4379	-77.7389
33.4379	-77.7519
33.4379	-77.765
33.4379	-77.778
33.4379	-77.7911
33.4379	-77.8041
33.4379	-77.8172
33.4379	-77.8303
33.4379	-77.8433
33.4379	-77.8564
33.4379	-77.8694
33.4379	-77.8825
33.4379	-77.8955
33.4379	-77.9086
33.4379	-77.9216
33.4379	-77.9347
33.4379	-77.9477
33.4379	-77.9608
33.4379	-77.9739
33.4379	-77.9869
33.4379	-78
33.4379	-78.013
33.4379	-78.0261
33.4379	-78.0391
33.4379	-78.0522
33.4249	-77.7128
33.4249	-77.7258
33.4249	-77.7389
33.4249	-77.7519
33.4249	-77.765
33.4249	-77.778
33.4249	-77.7911
33.4249	-77.8041
33.4249	-77.8172
33.4249	-77.8303
33.4249	-77.8433
33.4249	-77.8564
33.4249	-77.8694
33.4249	-77.8825
33.4249	-77.8955

Latitude	Longitude
33.4249	-77.9086
33.4249	-77.9216
33.4249	-77.9347
33.4249	-77.9477
33.4249	-77.9608
33.4249	-77.9739
33.4249	-77.9869
33.4249	-78
33.4249	-78.013
33.4249	-78.0261
33.4249	-78.0391
33.4249	-78.0522
33.4249	-77.6997
36.14609	-75.0034
36.19296	-75.009
36.1991	-75.0208
36.20523	-75.0326
36.21136	-75.0444
36.2175	-75.0562
36.22363	-75.068
36.22977	-75.0798
36.2359	-75.0916
36.24203	-75.1034
36.24817	-75.1152
36.2543	-75.127
36.2045	-75.003
36.21063	-75.0148
36.21677	-75.0266
36.2229	-75.0384
36.22903	-75.0502
36.23517	-75.062
36.2413	-75.0738
36.24743	-75.0856
36.25357	-75.0974
36.2597	-75.1092
36.26584	-75.121
36.27197	-75.1328
36.42191	-75.0548
36.42805	-75.0666
36.2337	-75.0028

Latitude	Longitude
36.23983	-75.0146
36.24597	-75.0264
36.2521	-75.0382
36.25823	-75.05
36.26437	-75.0618
36.2705	-75.0736
36.27664	-75.0854
36.28277	-75.0972
36.2889	-75.109
36.29504	-75.1208
36.30117	-75.1326
36.25137	-75.0086
36.2575	-75.0204
36.26364	-75.0322
36.26977	-75.044
36.2759	-75.0558
36.28204	-75.0676
36.28817	-75.0794
36.2943	-75.0912
36.30044	-75.103
36.30657	-75.1148
36.31271	-75.1266
36.31884	-75.1384
36.2629	-75.0026
36.26904	-75.0144
36.27517	-75.0262
36.2813	-75.038
36.28744	-75.0498
36.29357	-75.0616
36.2997	-75.0734
36.30584	-75.0852
36.31197	-75.097
36.31811	-75.1088
36.32424	-75.1206
36.33037	-75.1324
36.37971	-75.0018
36.38584	-75.0136
36.41038	-75.0608
36.41651	-75.0726
36.42265	-75.0844

Latitude	Longitude
36.42878	-75.0962
36.36818	-75.0078
36.37431	-75.0196
36.38044	-75.0314
36.38658	-75.0432
36.39271	-75.055
36.39885	-75.0668
36.40498	-75.0786
36.41111	-75.0904
36.41725	-75.1022
36.42338	-75.114
36.16376	-75.0092
36.16989	-75.021
36.17603	-75.0328
36.1753	-75.0032
36.18143	-75.015
36.18756	-75.0268
36.1937	-75.0386
36.19983	-75.0504
36.20596	-75.0622
36.2121	-75.074
36.21823	-75.0858
36.35051	-75.002
36.35664	-75.0138
36.36278	-75.0256
36.36891	-75.0374
36.37504	-75.0492
36.38118	-75.061
36.38731	-75.0728
36.39345	-75.0846
36.39958	-75.0964
36.40571	-75.1082
36.41185	-75.12
36.41798	-75.1318
36.33897	-75.008
36.34511	-75.0198
36.35124	-75.0316
36.35738	-75.0434
36.36351	-75.0552
36.36964	-75.067

Latitude	Longitude
36.37578	-75.0788
36.38191	-75.0906
36.38804	-75.1024
36.39418	-75.1142
36.40031	-75.126
36.40645	-75.1378
36.22217	-75.0088
36.2283	-75.0206
36.23443	-75.0324
36.24057	-75.0442
36.2467	-75.056
36.25283	-75.0678
36.25897	-75.0796
36.2651	-75.0914
36.27124	-75.1032
36.27737	-75.115
36.2835	-75.1268
36.28964	-75.1386
36.32131	-75.0022
36.32744	-75.014
36.33357	-75.0258
36.33971	-75.0376
36.34584	-75.0494
36.35198	-75.0612
36.35811	-75.073
36.36424	-75.0848
36.37038	-75.0966
36.37651	-75.1084
36.38264	-75.1202
36.38878	-75.132
36.30977	-75.0082
36.31591	-75.02
36.32204	-75.0318
36.32817	-75.0436
36.33431	-75.0554
36.34044	-75.0672
36.34658	-75.079
36.35271	-75.0908
36.35884	-75.1026
36.36498	-75.1144

Latitude	Longitude
36.37111	-75.1262
36.2921	-75.0024
36.29824	-75.0142
36.30437	-75.026
36.31051	-75.0378
36.31664	-75.0496
36.32277	-75.0614
36.32891	-75.0732
36.33504	-75.085
36.34117	-75.0968
36.34731	-75.1086
36.35344	-75.1204
36.35958	-75.1322
36.28057	-75.0084
36.2867	-75.0202
36.29284	-75.032
36.29897	-75.0438
36.30511	-75.0556
36.31124	-75.0674
36.31737	-75.0792
36.32351	-75.091
36.32964	-75.1028
36.33577	-75.1146
36.34191	-75.1264
36.34804	-75.1382
38.5094	-74.638
38.5094	-74.651
38.5224	-74.6251
38.5224	-74.638
38.5224	-74.651
38.5224	-74.6639
38.5224	-74.6768
38.5354	-74.6251
38.5354	-74.638
38.5354	-74.651
38.5354	-74.6639
38.5354	-74.6768
38.5354	-74.6897
38.5484	-74.6251
38.5484	-74.638

Latitude	Longitude
38.5484	-74.651
38.5484	-74.6639
38.5484	-74.6768
38.5484	-74.6897
38.5484	-74.7026
38.5614	-74.6122
38.5614	-74.6251
38.5614	-74.638
38.5614	-74.651
38.5614	-74.6639
38.5614	-74.6768
38.5614	-74.6897
38.5614	-74.7026
38.5744	-74.6122
38.5744	-74.6251
38.5744	-74.638
38.5744	-74.651
38.5744	-74.6639
38.5744	-74.6768
38.5744	-74.6897
38.5744	-74.7026
38.5744	-74.7155
38.5874	-74.6122
38.5874	-74.6251
38.5874	-74.638
38.5874	-74.651
38.5874	-74.6639
38.5874	-74.6768
38.5874	-74.6897
38.5874	-74.7026
38.5874	-74.7155
38.5874	-74.7284
38.5874	-74.7413
38.6004	-74.6122
38.6004	-74.6251
38.6004	-74.638
38.6004	-74.651
38.6004	-74.6639
38.6004	-74.6768
38.6004	-74.6897

Latitude	Longitude
38.6004	-74.7026
38.6004	-74.7155
38.6004	-74.7284
38.6004	-74.7413
38.6004	-74.7542
38.6134	-74.5993
38.6134	-74.6122
38.6134	-74.6251
38.6134	-74.638
38.6134	-74.651
38.6134	-74.6639
38.6134	-74.6768
38.6134	-74.6897
38.6134	-74.7026
38.6134	-74.7155
38.6134	-74.7284
38.6134	-74.7413
38.6134	-74.7542
38.6134	-74.7671
38.6264	-74.5993
38.6264	-74.6122
38.6264	-74.6251
38.6264	-74.638
38.6264	-74.651
38.6264	-74.6639
38.6264	-74.6768
38.6264	-74.6897
38.6264	-74.7026
38.6264	-74.7155
38.6264	-74.7284
38.6264	-74.7413
38.6264	-74.7542
38.6264	-74.7671
38.6264	-74.7801
38.6264	-74.793
38.6394	-74.5993
38.6394	-74.6122
38.6394	-74.6251
38.6394	-74.638
38.6394	-74.651

Latitude	Longitude
38.6394	-74.6639
38.6394	-74.6768
38.6394	-74.6897
38.6394	-74.7026
38.6394	-74.7155
38.6394	-74.7284
38.6394	-74.7413
38.6394	-74.7542
38.6394	-74.7671
38.6394	-74.7801
38.6394	-74.793
38.6524	-74.5993
38.6524	-74.6122
38.6524	-74.6251
38.6524	-74.638
38.6524	-74.651
38.6524	-74.6639
38.6524	-74.6768
38.6524	-74.6897
38.6524	-74.7026
38.6524	-74.7155
38.6524	-74.7284
38.6524	-74.7413
38.6524	-74.7542
38.6524	-74.7671
38.6524	-74.7801
38.6524	-74.793
39.27487	-74.2823
39.27487	-74.2952
39.27487	-74.308
39.26187	-74.2695
39.26187	-74.2823
39.26187	-74.2952
39.26187	-74.308
39.26187	-74.3208
39.24887	-74.2567
39.24887	-74.2695
39.24887	-74.2823
39.24887	-74.2952
39.24887	-74.308

Latitude	Longitude
39.24887	-74.3208
39.23587	-74.2567
39.23587	-74.2695
39.23587	-74.308
39.23587	-74.3208
39.22287	-74.2438
39.22287	-74.2567
39.22287	-74.2695
39.22287	-74.308
39.22287	-74.3208
39.20987	-74.2695
39.20987	-74.308
39.20987	-74.3208
39.19687	-74.2823
39.19687	-74.2952
39.19687	-74.308
39.19687	-74.3208
39.19687	-74.3337
39.19687	-74.3465
39.19687	-74.3593
39.19687	-74.3721
39.19687	-74.385
39.18387	-74.2952
39.18387	-74.308
39.18387	-74.3208
39.18387	-74.3337
39.18387	-74.3465
39.18387	-74.3593
39.18387	-74.3721
39.18387	-74.385
39.18387	-74.3978
39.17087	-74.308
39.17087	-74.3208
39.17087	-74.3978
39.17087	-74.4106
39.15787	-74.3208
39.15787	-74.3978
39.15787	-74.4106
39.15787	-74.4235
39.13187	-74.3593

Latitude	Longitude
39.13187	-74.3721
39.13187	-74.385
39.11887	-74.385
39.10587	-74.385
39.10587	-74.4491
39.10587	-74.462
39.10587	-74.4748
38.6654	-74.5993
38.6654	-74.6122
38.6654	-74.6251
38.6654	-74.638
38.6654	-74.651
38.6654	-74.6639
38.6654	-74.6768
38.6654	-74.6897
38.6654	-74.7026
38.6654	-74.7155
38.6654	-74.7284
38.6654	-74.7413
38.6654	-74.7542
38.6654	-74.7671
38.6654	-74.7801
38.6654	-74.793
38.6784	-74.5993
38.6784	-74.6122
38.6784	-74.6251
38.6784	-74.638
38.6784	-74.651
38.6784	-74.6639
38.6784	-74.6768
38.6784	-74.6897
38.6784	-74.7026
38.6784	-74.7155
38.6784	-74.7284
38.6784	-74.7413
38.6784	-74.7542
38.6784	-74.7671
38.6784	-74.7801
38.6784	-74.793
38.6914	-74.5993

Latitude	Longitude
38.6914	-74.6122
38.6914	-74.6251
38.6914	-74.638
38.6914	-74.651
38.6914	-74.6639
38.6914	-74.6768
38.6914	-74.6897
38.6914	-74.7026
38.6914	-74.7155
38.6914	-74.7284
38.6914	-74.7413
38.6914	-74.7542
38.6914	-74.7671
38.6914	-74.7801
38.6914	-74.793
38.6914	-74.8059
38.6914	-74.8188
38.6914	-74.8317
38.7044	-74.5993
38.7044	-74.6122
38.7044	-74.6251
38.7044	-74.638
38.7044	-74.651
38.7044	-74.6639
38.7044	-74.6768
38.7044	-74.6897
38.7044	-74.7026
38.7044	-74.7155
38.7044	-74.7284
38.7044	-74.7413
38.7044	-74.7542
38.7044	-74.7671
38.7044	-74.7801
38.7044	-74.793
38.7044	-74.8059
38.7044	-74.8188
38.7044	-74.8317
38.7174	-74.5993
38.7174	-74.6122
38.7174	-74.6251

Latitude	Longitude
38.7174	-74.638
38.7174	-74.651
38.7174	-74.6639
38.7174	-74.6768
38.7174	-74.6897
38.7174	-74.7026
38.7174	-74.7155
38.7174	-74.7284
38.7174	-74.7413
38.7174	-74.7542
38.7174	-74.7671
38.7174	-74.7801
38.7174	-74.793
38.7174	-74.8059
38.7174	-74.8188
38.7174	-74.8317
38.7304	-74.6122
38.7304	-74.6251
38.7304	-74.638
38.7304	-74.651
38.7304	-74.6639
38.7304	-74.6768
38.7304	-74.6897
38.7304	-74.7026
38.7304	-74.7155
38.7304	-74.7284
38.7304	-74.7413
38.7304	-74.7542
38.7304	-74.7671
38.7304	-74.7801
38.7304	-74.793
38.7304	-74.8059
38.7304	-74.8188
38.7304	-74.8317
38.91087	-74.3978
38.91087	-74.4106
38.91087	-74.4235
38.91087	-74.4363
38.92387	-74.3978
38.92387	-74.4106

Latitude	Longitude
38.92387	-74.4235
38.92387	-74.4363
38.93687	-74.3978
38.93687	-74.4106
38.93687	-74.4235
38.93687	-74.4363
38.94987	-74.3465
38.94987	-74.3593
38.94987	-74.3721
38.94987	-74.385
38.94987	-74.3978
38.94987	-74.4106
38.94987	-74.4235
38.94987	-74.4363
38.96287	-74.3465
38.96287	-74.3593
38.96287	-74.3721
38.96287	-74.385
38.96287	-74.3978
38.96287	-74.4106
38.96287	-74.4235
38.96287	-74.4363
38.97587	-74.3465
38.97587	-74.3593
38.97587	-74.3721
38.97587	-74.385
38.97587	-74.3978
38.97587	-74.4106
38.97587	-74.4235
38.97587	-74.4363
38.98887	-74.2952
38.98887	-74.308
38.98887	-74.3208
38.98887	-74.3337
38.98887	-74.3465
38.98887	-74.3593
38.98887	-74.3721
38.98887	-74.385
38.98887	-74.3978
38.98887	-74.4106

Latitude	Longitude
38.98887	-74.4235
38.98887	-74.4363
39.00187	-74.2823
39.00187	-74.2952
39.00187	-74.308
39.00187	-74.3208
39.00187	-74.3337
39.00187	-74.3465
39.00187	-74.3593
39.00187	-74.3721
39.00187	-74.385
39.00187	-74.3978
39.00187	-74.4106
39.00187	-74.4235
39.00187	-74.4363
39.01487	-74.2695
39.01487	-74.2823
39.01487	-74.2952
39.01487	-74.308
39.01487	-74.3208
39.01487	-74.3337
39.01487	-74.3465
39.01487	-74.3593
39.01487	-74.3721
39.01487	-74.385
39.01487	-74.3978
39.01487	-74.4106
39.01487	-74.4235
39.01487	-74.4363
39.02787	-74.308
39.02787	-74.3208
39.02787	-74.3337
39.02787	-74.3465
39.02787	-74.3593
39.02787	-74.3721
39.02787	-74.385
39.02787	-74.3978
39.02787	-74.4106
39.02787	-74.4235
39.02787	-74.4363

Latitude	Longitude
39.04087	-74.3208
39.04087	-74.3337
39.04087	-74.3465
39.04087	-74.3593
39.04087	-74.3721
39.04087	-74.385
39.04087	-74.3978
39.04087	-74.4106
39.04087	-74.4235
39.04087	-74.4363
39.04087	-74.4491
39.04087	-74.462
39.04087	-74.4748
39.04087	-74.4876
39.04087	-74.5005
39.05387	-74.3337
39.05387	-74.3465
39.05387	-74.3593
39.05387	-74.3721
39.05387	-74.385
39.05387	-74.3978
39.05387	-74.4106
39.05387	-74.4235
39.05387	-74.4363
39.05387	-74.4491
39.05387	-74.462
39.05387	-74.4748
39.05387	-74.4876
39.05387	-74.5005
39.06687	-74.3465
39.06687	-74.3593
39.06687	-74.3721
39.06687	-74.385
39.06687	-74.3978
39.06687	-74.4106
39.06687	-74.4235
39.06687	-74.4363
39.06687	-74.4491
39.06687	-74.462
39.06687	-74.4748

Latitude	Longitude
39.06687	-74.4876
39.06687	-74.5005
39.07987	-74.3593
39.07987	-74.3721
39.07987	-74.385
39.07987	-74.3978
39.07987	-74.4106
39.07987	-74.4235
39.07987	-74.4363
39.07987	-74.4491
39.07987	-74.462
39.07987	-74.4748
39.07987	-74.4876
39.07987	-74.5005
39.09287	-74.3721
39.09287	-74.385
39.09287	-74.4491
39.09287	-74.462
39.09287	-74.4748
39.09287	-74.4876
39.09287	-74.5005
39.1942	-73.4693
39.1942	-73.4822
39.1942	-73.4952
39.1942	-73.5082
39.1942	-73.5212
39.1942	-73.5341
39.1942	-73.5471
39.1942	-73.5601
39.1942	-73.5731
39.1942	-73.5861
39.1942	-73.599
39.1942	-73.612
39.1942	-73.625
39.1942	-73.638
39.1942	-73.6509
39.2072	-73.4693
39.2072	-73.4822
39.2072	-73.4952
39.2072	-73.5082

Latitude	Longitude
39.2072	-73.5212
39.2072	-73.5341
39.2072	-73.5471
39.2072	-73.5601
39.2072	-73.5731
39.2072	-73.5861
39.2072	-73.599
39.2072	-73.612
39.2072	-73.625
39.2072	-73.638
39.2072	-73.6509
39.2202	-73.4433
39.2202	-73.4563
39.2202	-73.4693
39.2202	-73.4822
39.2202	-73.4952
39.2202	-73.5082
39.2202	-73.5212
39.2202	-73.5341
39.2202	-73.5471
39.2202	-73.5601
39.2202	-73.5731
39.2202	-73.5861
39.2202	-73.599
39.2202	-73.612
39.2202	-73.625
39.2202	-73.638
39.2202	-73.6509
39.2332	-73.4433
39.2332	-73.4563
39.2332	-73.4693
39.2332	-73.4822
39.2332	-73.4952
39.2332	-73.5082
39.2332	-73.5212
39.2332	-73.5341
39.2332	-73.5471
39.2332	-73.5601
39.2332	-73.5731
39.2332	-73.5861

Latitude	Longitude
39.2332	-73.599
39.2332	-73.612
39.2332	-73.625
39.2332	-73.638
39.2332	-73.6509
39.2462	-73.4174
39.2462	-73.4303
39.2462	-73.4433
39.2462	-73.4563
39.2462	-73.4693
39.2462	-73.4822
39.2462	-73.4952
39.2462	-73.5082
39.2462	-73.5212
39.2462	-73.5341
39.2462	-73.5471
39.2462	-73.5601
39.2462	-73.5731
39.2462	-73.5861
39.2462	-73.599
39.2462	-73.612
39.2462	-73.625
39.2462	-73.638
39.2462	-73.6509
39.2592	-73.4174
39.2592	-73.4303
39.2592	-73.4433
39.2592	-73.4563
39.2592	-73.4693
39.2592	-73.4822
39.2592	-73.4952
39.2592	-73.5082
39.2592	-73.5212
39.2592	-73.5341
39.2592	-73.5471
39.2592	-73.5601
39.2592	-73.5731
39.2592	-73.5861
39.2592	-73.599
39.2592	-73.612

Latitude	Longitude
39.2592	-73.625
39.2592	-73.638
39.2592	-73.6509
39.2722	-73.4044
39.2722	-73.4174
39.2722	-73.4303
39.2722	-73.4433
39.2722	-73.4563
39.2722	-73.4693
39.2722	-73.4822
39.2722	-73.4952
39.2722	-73.5082
39.2722	-73.5212
39.2722	-73.5341
39.2722	-73.5471
39.2722	-73.5601
39.2722	-73.5731
39.2722	-73.5861
39.2722	-73.599
39.2722	-73.612
39.2722	-73.625
39.2722	-73.638
39.2852	-73.4044
39.2852	-73.4174
39.2852	-73.4303
39.2852	-73.4433
39.2852	-73.4563
39.2852	-73.4693
39.2852	-73.4822
39.2852	-73.4952
39.2852	-73.5082
39.2852	-73.5212
39.2852	-73.5341
39.2852	-73.5471
39.2852	-73.5601
39.2852	-73.5731
39.2852	-73.5861
39.2852	-73.599
39.2852	-73.612
39.2852	-73.625

Latitude	Longitude
39.2852	-73.638
39.2982	-73.3914
39.2982	-73.4044
39.2982	-73.4174
39.2982	-73.4303
39.2982	-73.4433
39.2982	-73.4563
39.2982	-73.4693
39.2982	-73.4822
39.2982	-73.4952
39.2982	-73.5082
39.2982	-73.5212
39.2982	-73.5341
39.2982	-73.5471
39.2982	-73.5601
39.2982	-73.5731
39.2982	-73.5861
39.2982	-73.599
39.2982	-73.612
39.2982	-73.625
39.2982	-73.638
39.3112	-73.3784
39.3112	-73.3914
39.3112	-73.4044
39.3112	-73.4174
39.3112	-73.4303
39.3112	-73.4433
39.3112	-73.4563
39.3112	-73.4693
39.3112	-73.4822
39.3112	-73.4952
39.3112	-73.5082
39.3112	-73.5212
39.3112	-73.5341
39.3112	-73.5471
39.3112	-73.5601
39.3112	-73.5731
39.3112	-73.5861
39.3112	-73.599
39.3112	-73.612

Latitude	Longitude
39.3112	-73.625
39.3112	-73.638
39.3242	-73.3654
39.3242	-73.3784
39.3242	-73.3914
39.3242	-73.4044
39.3242	-73.4174
39.3242	-73.4303
39.3242	-73.4433
39.3242	-73.4563
39.3242	-73.4693
39.3242	-73.4822
39.3242	-73.4952
39.3242	-73.5082
39.3242	-73.5212
39.3242	-73.5341
39.3242	-73.5471
39.3242	-73.5601
39.3242	-73.5731
39.3242	-73.5861
39.3242	-73.599
39.3242	-73.612
39.3242	-73.625
39.3242	-73.638
39.3372	-73.3654
39.3372	-73.3784
39.3372	-73.3914
39.3372	-73.4044
39.3372	-73.4174
39.3372	-73.4303
39.3372	-73.4433
39.3372	-73.4563
39.3372	-73.4693
39.3372	-73.4822
39.3372	-73.4952
39.3372	-73.5082
39.3372	-73.5212
39.3372	-73.5341
39.3372	-73.5471
39.3372	-73.5601

Latitude	Longitude
39.3372	-73.5731
39.3372	-73.5861
39.3372	-73.599
39.3372	-73.612
39.3372	-73.625
39.3372	-73.638
39.3502	-73.3525
39.3502	-73.3654
39.3502	-73.3784
39.3502	-73.3914
39.3502	-73.4044
39.3502	-73.4174
39.3502	-73.4303
39.3502	-73.4433
39.3502	-73.4563
39.3502	-73.4693
39.3502	-73.4822
39.3502	-73.4952
39.3502	-73.5082
39.3502	-73.5212
39.3502	-73.5341
39.3502	-73.5471
39.3502	-73.5601
39.3502	-73.5731
39.3502	-73.5861
39.3502	-73.599
39.3502	-73.612
39.3502	-73.625
39.3502	-73.638
39.3632	-73.3395
39.3632	-73.3525
39.3632	-73.3654
39.3632	-73.3784
39.3632	-73.3914
39.3632	-73.4044
39.3632	-73.4174
39.3632	-73.4303
39.3632	-73.4433
39.3632	-73.4563
39.3632	-73.4693

Latitude	Longitude
39.3632	-73.4822
39.3632	-73.4952
39.3632	-73.5082
39.3632	-73.5212
39.3632	-73.5341
39.3632	-73.5471
39.3632	-73.5601
39.3632	-73.5731
39.3632	-73.5861
39.3632	-73.599
39.3632	-73.612
39.3632	-73.625
39.3632	-73.638
39.3762	-73.3265
39.3762	-73.3395
39.3762	-73.3525
39.3762	-73.3654
39.3762	-73.3784
39.3762	-73.3914
39.3762	-73.4044
39.3762	-73.4174
39.3762	-73.4303
39.3762	-73.4433
39.3762	-73.4563
39.3762	-73.4693
39.3762	-73.4822
39.3762	-73.4952
39.3762	-73.5082
39.3762	-73.5212
39.3762	-73.5341
39.3762	-73.5471
39.3762	-73.5601
39.3762	-73.5731
39.3762	-73.5861
39.3762	-73.599
39.3762	-73.612
39.3762	-73.625
39.3762	-73.638
39.3892	-73.3265
39.3892	-73.3395

Latitude	Longitude
39.3892	-73.3525
39.3892	-73.3654
39.3892	-73.3784
39.3892	-73.3914
39.3892	-73.4044
39.3892	-73.4174
39.3892	-73.4303
39.3892	-73.4433
39.3892	-73.4563
39.3892	-73.4693
39.3892	-73.4822
39.3892	-73.4952
39.3892	-73.5082
39.3892	-73.5212
39.3892	-73.5341
39.3892	-73.5471
39.3892	-73.5601
39.3892	-73.5731
39.3892	-73.5861
39.3892	-73.599
39.3892	-73.612
39.3892	-73.625
39.3892	-73.638
39.4022	-73.3525
39.4022	-73.3654
39.4022	-73.3784
39.4022	-73.3914
39.4022	-73.4044
39.4022	-73.4174
39.4022	-73.4303
39.4022	-73.4433
39.4022	-73.4563
39.4022	-73.4693
39.4022	-73.4822
39.4022	-73.4952
39.4022	-73.5082
39.4022	-73.5212
39.4022	-73.5341
39.4022	-73.5471
39.4022	-73.5601

Latitude	Longitude
39.4022	-73.5731
39.4022	-73.5861
39.4022	-73.599
39.4022	-73.612
39.4022	-73.625
39.4022	-73.638
39.4152	-73.3784
39.4152	-73.3914
39.4152	-73.4044
39.4152	-73.4174
39.4152	-73.4303
39.4152	-73.4433
39.4152	-73.4563
39.4152	-73.4693
39.4152	-73.4822
39.4152	-73.4952
39.4152	-73.5082
39.4152	-73.5212
39.4152	-73.5341
39.4152	-73.5471
39.4152	-73.5601
39.4152	-73.5731
39.4152	-73.5861
39.4152	-73.599
39.4152	-73.612
39.4152	-73.625
39.4152	-73.638
39.4282	-73.2876
39.4282	-73.3006
39.4282	-73.4174
39.4282	-73.4303
39.4282	-73.4433
39.4282	-73.4563
39.4282	-73.4693
39.4282	-73.4822
39.4282	-73.4952
39.4282	-73.5082
39.4282	-73.5212
39.4282	-73.5341
39.4282	-73.5471

Latitude	Longitude
39.4282	-73.5601
39.4282	-73.5731
39.4282	-73.5861
39.4282	-73.599
39.4282	-73.612
39.4282	-73.625
39.4282	-73.638
39.4412	-73.2876
39.4412	-73.3006
39.4412	-73.3135
39.4412	-73.3265
39.4412	-73.3395
39.4412	-73.4952
39.4412	-73.5082
39.4412	-73.5212
39.4412	-73.5341
39.4412	-73.5471
39.4412	-73.5601
39.4412	-73.5731
39.4412	-73.5861
39.4412	-73.599
39.4412	-73.612
39.4412	-73.625
39.4412	-73.638
39.4542	-73.2746
39.4542	-73.2876
39.4542	-73.3006
39.4542	-73.3135
39.4542	-73.3265
39.4542	-73.3395
39.4542	-73.3525
39.4542	-73.5471
39.4542	-73.5601
39.4542	-73.5731
39.4542	-73.5861
39.4542	-73.599
39.4542	-73.612
39.4542	-73.625
39.4672	-73.2616
39.4672	-73.2746

Latitude	Longitude
39.4672	-73.2876
39.4672	-73.3006
39.4672	-73.3135
39.4672	-73.3265
39.4672	-73.3395
39.4672	-73.3525
39.4672	-73.3654
39.4672	-73.3784
39.4672	-73.3914
39.4672	-73.5731
39.4672	-73.5861
39.4672	-73.599
39.4672	-73.612
39.4672	-73.625
39.4802	-73.2486
39.4802	-73.2616
39.4802	-73.2746
39.4802	-73.2876
39.4802	-73.3006
39.4802	-73.3135
39.4802	-73.3265
39.4802	-73.3395
39.4802	-73.3525
39.4802	-73.3654
39.4802	-73.3784
39.4802	-73.3914
39.4802	-73.4044
39.4802	-73.4174
39.4802	-73.4303
39.4802	-73.4433
39.4802	-73.4563
39.4802	-73.4693
39.4802	-73.4822
39.4802	-73.612
39.4802	-73.625
39.4932	-73.2357
39.4932	-73.2486
39.4932	-73.2616
39.4932	-73.2746
39.4932	-73.2876

Latitude	Longitude
39.4932	-73.3006
39.4932	-73.3135
39.4932	-73.3265
39.4932	-73.3395
39.4932	-73.3525
39.4932	-73.3654
39.4932	-73.3784
39.4932	-73.3914
39.4932	-73.4044
39.4932	-73.4174
39.4932	-73.4303
39.4932	-73.4433
39.4932	-73.4563
39.4932	-73.4693
39.5062	-73.2357
39.5062	-73.2486
39.5062	-73.2616
39.5062	-73.2746
39.5062	-73.2876
39.5062	-73.3006
39.5062	-73.3135
39.5062	-73.3265
39.5062	-73.3395
39.5062	-73.3525
39.5062	-73.3654
39.5062	-73.3784
39.5062	-73.3914
39.5062	-73.4044
39.5062	-73.4174
39.5062	-73.4303
39.5062	-73.4433
39.5062	-73.4563
39.5062	-73.4693
39.5192	-73.2227
39.5192	-73.2357
39.5192	-73.2486
39.5192	-73.2616
39.5192	-73.2746
39.5192	-73.2876
39.5192	-73.3006

Latitude	Longitude
39.5192	-73.3135
39.5192	-73.3265
39.5192	-73.3395
39.5192	-73.3525
39.5192	-73.3654
39.5192	-73.3784
39.5192	-73.3914
39.5192	-73.4044
39.5192	-73.4174
39.5192	-73.4303
39.5192	-73.4433
39.5192	-73.4563
39.5322	-73.1967
39.5322	-73.2097
39.5322	-73.2227
39.5322	-73.2357
39.5322	-73.2486
39.5322	-73.2616
39.5322	-73.2746
39.5322	-73.2876
39.5322	-73.3006
39.5322	-73.3135
39.5322	-73.3265
39.5322	-73.3395
39.5322	-73.3525
39.5322	-73.3654
39.5322	-73.3784
39.5322	-73.3914
39.5322	-73.4044
39.5322	-73.4174
39.5322	-73.4303
39.5322	-73.4433
39.5322	-73.4563
39.5452	-73.1448
39.5452	-73.1578
39.5452	-73.1708
39.5452	-73.1838
39.5452	-73.1967
39.5452	-73.2097
39.5452	-73.2227

Latitude	Longitude
39.5452	-73.2357
39.5452	-73.2486
39.5452	-73.2616
39.5452	-73.2746
39.5452	-73.2876
39.5452	-73.3006
39.5452	-73.3135
39.5452	-73.3265
39.5452	-73.3395
39.5452	-73.3525
39.5452	-73.3654
39.5452	-73.3784
39.5452	-73.3914
39.5452	-73.4044
39.5452	-73.4174
39.5452	-73.4303
39.5582	-73.1319
39.5582	-73.1448
39.5582	-73.1578
39.5582	-73.1708
39.5582	-73.1838
39.5582	-73.1967
39.5582	-73.2097
39.5582	-73.2227
39.5582	-73.2357
39.5582	-73.2486
39.5582	-73.2616
39.5582	-73.2746
39.5582	-73.2876
39.5582	-73.3006
39.5582	-73.3135
39.5582	-73.3265
39.5582	-73.3395
39.5582	-73.3525
39.5582	-73.3654
39.5582	-73.3784
39.5582	-73.3914
39.5582	-73.4044
39.5582	-73.4174
39.5582	-73.4303

Latitude	Longitude
39.5712	-73.1319
39.5712	-73.1448
39.5712	-73.1578
39.5712	-73.1708
39.5712	-73.1838
39.5712	-73.1967
39.5712	-73.2097
39.5712	-73.2227
39.5712	-73.2357
39.5712	-73.2486
39.5712	-73.2616
39.5712	-73.2746
39.5712	-73.2876
39.5712	-73.3006
39.5712	-73.3135
39.5712	-73.3265
39.5712	-73.3395
39.5712	-73.3525
39.5712	-73.3654
39.5712	-73.3784
39.5712	-73.3914
39.5712	-73.4044
39.5712	-73.4174
39.5712	-73.4303
39.5842	-73.1059
39.5842	-73.1189
39.5842	-73.1319
39.5842	-73.1448
39.5842	-73.1578
39.5842	-73.1708
39.5842	-73.1838
39.5842	-73.1967
39.5842	-73.2097
39.5842	-73.2227
39.5842	-73.2357
39.5842	-73.2486
39.5842	-73.2616
39.5842	-73.2746
39.5842	-73.2876
39.5842	-73.3006

Latitude	Longitude
39.5842	-73.3135
39.5842	-73.3265
39.5842	-73.3395
39.5842	-73.3525
39.5842	-73.3654
39.5842	-73.3784
39.5842	-73.3914
39.5842	-73.4044
39.5842	-73.4174
39.5842	-73.4303
39.5972	-73.1319
39.5972	-73.1448
39.5972	-73.1578
39.5972	-73.1708
39.5972	-73.1838
39.5972	-73.1967
39.5972	-73.2097
39.5972	-73.2227
39.5972	-73.2357
39.5972	-73.2486
39.5972	-73.2616
39.5972	-73.2746
39.5972	-73.2876
39.5972	-73.3006
39.5972	-73.3135
39.5972	-73.3265
39.5972	-73.3395
39.5972	-73.3525
39.5972	-73.3654
39.5972	-73.3784
39.5972	-73.3914
39.5972	-73.4044
39.5972	-73.4174
39.6102	-73.054
39.6102	-73.067
39.6102	-73.1708
39.6102	-73.1838
39.6102	-73.1967
39.6102	-73.2097
39.6102	-73.2227

Latitude	Longitude
39.6102	-73.2357
39.6102	-73.2486
39.6102	-73.2616
39.6102	-73.2746
39.6102	-73.2876
39.6102	-73.3006
39.6232	-73.054
39.6232	-73.067
39.6232	-73.0799
39.6232	-73.0929
39.6232	-73.1967
39.6232	-73.2097
39.6232	-73.2227
39.6232	-73.2357
39.6232	-73.2486
39.6232	-73.2616
39.6232	-73.2746
39.6232	-73.2876
39.6232	-73.3006
39.6362	-73.054
39.6362	-73.067
39.6362	-73.0799
39.6362	-73.0929
39.6362	-73.1059
39.6362	-73.1189
39.6362	-73.1319
39.6362	-73.2227
39.6362	-73.2357
39.6362	-73.2486
39.6362	-73.2616
39.6362	-73.2746
39.6362	-73.2876
39.6362	-73.3006
39.6492	-73.028
39.6492	-73.041
39.6492	-73.054
39.6492	-73.067
39.6492	-73.0799
39.6492	-73.0929
39.6492	-73.1059

Latitude	Longitude
39.6492	-73.1189
39.6492	-73.1319
39.6492	-73.1448
39.6492	-73.1578
39.6492	-73.2616
39.6492	-73.2746
39.6492	-73.2876
39.6492	-73.3006
39.6622	-73.0151
39.6622	-73.028
39.6622	-73.041
39.6622	-73.054
39.6622	-73.067
39.6622	-73.0799
39.6622	-73.0929
39.6622	-73.1059
39.6622	-73.1189
39.6622	-73.1319
39.6622	-73.1448
39.6622	-73.1578
39.6622	-73.1708
39.6622	-73.1838
39.6622	-73.2876
39.6622	-73.3006
39.6752	-73.0151
39.6752	-73.028
39.6752	-73.041
39.6752	-73.054
39.6752	-73.067
39.6752	-73.0799
39.6752	-73.0929
39.6752	-73.1059
39.6752	-73.1189
39.6752	-73.1319
39.6752	-73.1448
39.6752	-73.1578
39.6752	-73.1708
39.6752	-73.1838
39.6752	-73.1967
39.6752	-73.2097

Latitude	Longitude
39.6752	-73.2227
39.6752	-73.2357
39.7142	-73.067
39.7142	-73.0799
39.7142	-73.0929
39.7142	-73.1059
39.7142	-73.1189
39.7142	-73.1319
39.7142	-73.1448
39.7142	-73.1578
39.7142	-73.1708
39.7142	-73.1838
39.7142	-73.1967
39.7142	-73.2097
39.7142	-73.2227
39.7142	-73.2357
39.7142	-73.2486
39.7142	-73.2616
39.7142	-73.2746
39.7142	-73.2876
39.7142	-73.3006
39.8182	-73.1967
39.8182	-73.2097
39.8182	-73.2227
39.8182	-73.2357
39.8182	-73.2486
39.8182	-73.2616
39.8182	-73.2746
39.8052	-73.1838
39.8052	-73.1967
39.8052	-73.2097
39.8052	-73.2227
39.8052	-73.2357
39.8052	-73.2486
39.8052	-73.2616
39.8052	-73.2746
39.7922	-73.1578
39.7922	-73.1708
39.7922	-73.1838
39.7922	-73.1967

Latitude	Longitude
39.7922	-73.2097
39.7922	-73.2227
39.7922	-73.2357
39.7922	-73.2486
39.7922	-73.2616
39.7922	-73.2746
39.7792	-73.1448
39.7792	-73.1578
39.7792	-73.1708
39.7792	-73.1838
39.7792	-73.1967
39.7792	-73.2097
39.7792	-73.2227
39.7792	-73.2357
39.7792	-73.2486
39.7792	-73.2616
39.7792	-73.2746
39.7662	-73.1319
39.7662	-73.1448
39.7662	-73.1578
39.7662	-73.1708
39.7662	-73.1838
39.7662	-73.1967
39.7662	-73.2097
39.7662	-73.2227
39.7662	-73.2357
39.7662	-73.2486
39.7662	-73.2616
39.7662	-73.2746
39.7662	-73.2876
39.7662	-73.3006
39.7532	-73.1189
39.7532	-73.1319
39.7532	-73.1448
39.7532	-73.1578
39.7532	-73.1708
39.7532	-73.1838
39.7532	-73.1967
39.7532	-73.2097
39.7532	-73.2227

Latitude	Longitude
39.7532	-73.2357
39.7532	-73.2486
39.7532	-73.2616
39.7532	-73.2746
39.7532	-73.2876
39.7532	-73.3006
39.7402	-73.1059
39.7402	-73.1189
39.7402	-73.1319
39.7402	-73.1448
39.7402	-73.1578
39.7402	-73.1708
39.7402	-73.1838
39.7402	-73.1967
39.7402	-73.2097
39.7402	-73.2227
39.7402	-73.2357
39.7402	-73.2486
39.7402	-73.2616
39.7402	-73.2746
39.7402	-73.2876
39.7402	-73.3006
39.7272	-73.0799
39.7272	-73.0929
39.7272	-73.1059
39.7272	-73.1189
39.7272	-73.1319
39.7272	-73.1448
39.7272	-73.1578
39.7272	-73.1708
39.7272	-73.1838
39.7272	-73.1967
39.7272	-73.2097
39.7272	-73.2227
39.7272	-73.2357
39.7272	-73.2486
39.7272	-73.2616
39.7272	-73.2746
39.7272	-73.2876
39.7272	-73.3006

Latitude	Longitude
39.6882	-73.028
39.6882	-73.041
39.6882	-73.054
39.6882	-73.067
39.6882	-73.0799
39.6882	-73.0929
39.6882	-73.1059
39.6882	-73.1189
39.6882	-73.1319
39.6882	-73.1448
39.6882	-73.1578
39.6882	-73.1708
39.6882	-73.1838
39.6882	-73.1967
39.6882	-73.2097
39.6882	-73.2227
39.6882	-73.2357
39.6882	-73.2486
39.6882	-73.2616
39.6882	-73.2746
39.7012	-73.041
39.7012	-73.054
39.7012	-73.067
39.7012	-73.0799
39.7012	-73.0929
39.7012	-73.1059
39.7012	-73.1189
39.7012	-73.1319
39.7012	-73.1448
39.7012	-73.1578
39.7012	-73.1708
39.7012	-73.1838
39.7012	-73.1967
39.7012	-73.2097
39.7012	-73.2227
39.7012	-73.2357
39.7012	-73.2486
39.7012	-73.2616
39.7012	-73.2746
39.7012	-73.2876

Latitude	Longitude
39.7012	-73.3006
40.0461	-72.6396
40.0461	-72.6528
40.0461	-72.6659
40.0461	-72.6791
40.0461	-72.6922
40.0461	-72.7054
40.0461	-72.7186
40.0461	-72.7317
40.0461	-72.7449
40.0461	-72.758
40.0461	-72.7712
40.0461	-72.7843
40.0331	-72.6396
40.0331	-72.6528
40.0331	-72.6659
40.0331	-72.6791
40.0331	-72.6922
40.0331	-72.7054
40.0331	-72.7186
40.0331	-72.7317
40.0331	-72.7449
40.0331	-72.758
40.0331	-72.7712
40.0331	-72.7843
40.0201	-72.6396
40.0201	-72.6528
40.0201	-72.6659
40.0201	-72.6791
40.0201	-72.6922
40.0201	-72.7054
40.0201	-72.7186
40.0201	-72.7317
40.0201	-72.7449
40.0201	-72.758
40.0201	-72.7712
40.0201	-72.7843
40.0071	-72.6265
40.0071	-72.6396
40.0071	-72.6528

Latitude	Longitude
40.0071	-72.6659
40.0071	-72.6791
40.0071	-72.6922
40.0071	-72.7054
40.0071	-72.7186
40.0071	-72.7317
40.0071	-72.7449
40.0071	-72.758
40.0071	-72.7712
40.0071	-72.7843
39.9941	-72.6396
39.9941	-72.6528
39.9941	-72.6659
39.9941	-72.6791
39.9941	-72.6922
39.9941	-72.7054
39.9941	-72.7186
39.9941	-72.7317
39.9941	-72.7449
39.9941	-72.758
39.9941	-72.7712
39.9941	-72.7843
39.9941	-72.7975
39.9941	-72.8107
39.9941	-72.8238
39.9941	-72.837
39.9941	-72.8501
39.9811	-72.6396
39.9811	-72.6528
39.9811	-72.6659
39.9811	-72.6791
39.9811	-72.6922
39.9811	-72.7054
39.9811	-72.7186
39.9811	-72.7317
39.9811	-72.7449
39.9811	-72.758
39.9811	-72.7712
39.9811	-72.7843
39.9811	-72.7975

Latitude	Longitude
39.9811	-72.8107
39.9811	-72.8238
39.9811	-72.837
39.9811	-72.8501
39.9811	-72.8633
39.9811	-72.8764
39.9811	-72.8896
39.9031	-72.6659
39.9031	-72.6791
39.9161	-72.6528
39.9161	-72.6659
39.9161	-72.6791
39.9161	-72.6922
39.9161	-72.7054
39.9161	-72.7186
39.9161	-72.7317
39.9161	-72.7449
39.9161	-72.758
39.9161	-72.7712
39.9161	-72.7843
39.9161	-72.7975
39.9161	-72.8107
39.9161	-72.8238
39.9291	-72.6528
39.9291	-72.6659
39.9291	-72.6791
39.9291	-72.6922
39.9291	-72.7054
39.9291	-72.7186
39.9291	-72.7317
39.9291	-72.7449
39.9291	-72.758
39.9291	-72.7712
39.9291	-72.7843
39.9291	-72.7975
39.9291	-72.8107
39.9291	-72.8238
39.9291	-72.837
39.9291	-72.8501
39.9421	-72.6265

Latitude	Longitude
39.9421	-72.6396
39.9421	-72.6528
39.9421	-72.6659
39.9421	-72.6791
39.9421	-72.6922
39.9421	-72.7054
39.9421	-72.7186
39.9421	-72.7317
39.9421	-72.7449
39.9421	-72.758
39.9421	-72.7712
39.9421	-72.7843
39.9421	-72.7975
39.9421	-72.8107
39.9421	-72.8238
39.9421	-72.837
39.9421	-72.8501
39.9421	-72.8633
39.9551	-72.6265
39.9551	-72.6396
39.9551	-72.6528
39.9551	-72.6659
39.9551	-72.6791
39.9551	-72.6922
39.9551	-72.7054
39.9551	-72.7186
39.9551	-72.7317
39.9551	-72.7449
39.9551	-72.758
39.9551	-72.7712
39.9551	-72.7843
39.9551	-72.7975
39.9551	-72.8107
39.9551	-72.8238
39.9551	-72.837
39.9551	-72.8501
39.9551	-72.8633
39.9551	-72.8764
39.9551	-72.6133
39.9681	-72.6396

Latitude	Longitude
39.9681	-72.6528
39.9681	-72.6659
39.9681	-72.6791
39.9681	-72.6922
39.9681	-72.7054
39.9681	-72.7186
39.9681	-72.7317
39.9681	-72.7449
39.9681	-72.758
39.9681	-72.7712
39.9681	-72.7843
39.9681	-72.7975
39.9681	-72.8107
39.9681	-72.8238
39.9681	-72.837
39.9681	-72.8501
39.9681	-72.8633
39.9681	-72.8764
39.9681	-72.8896
40.17	-73.1395
40.17	-73.1528
40.183	-73.0864
40.183	-73.0996
40.183	-73.1129
40.183	-73.1262
40.183	-73.1395
40.183	-73.1528
40.183	-73.1661
40.183	-73.1793
40.313	-72.9801
40.313	-72.9934
40.313	-73.0067
40.313	-72.9668
40.3	-72.9801
40.3	-72.9934
40.3	-73.0067
40.3	-73.0199
40.3	-73.0332
40.3	-73.0465
40.3	-72.9668

Latitude	Longitude
40.287	-72.9801
40.287	-72.9934
40.287	-73.0067
40.287	-73.0199
40.287	-73.0332
40.287	-73.0465
40.287	-73.0598
40.287	-73.0731
40.287	-72.9668
40.274	-72.9801
40.274	-72.9934
40.274	-73.0067
40.274	-73.0199
40.274	-73.0332
40.274	-73.0465
40.274	-73.0598
40.274	-73.0731
40.274	-73.0864
40.274	-72.9668
40.261	-72.9934
40.261	-73.0067
40.261	-73.0199
40.261	-73.0332
40.261	-73.0465
40.261	-73.0598
40.261	-73.0731
40.261	-73.0864
40.261	-73.0996
40.261	-73.1129
40.248	-73.0067
40.248	-73.0199
40.248	-73.0332
40.248	-73.0465
40.248	-73.0598
40.248	-73.0731
40.248	-73.0864
40.248	-73.0996
40.248	-73.1129
40.248	-73.1262
40.235	-73.0199

Latitude	Longitude
40.235	-73.0332
40.235	-73.0465
40.235	-73.0598
40.235	-73.0731
40.235	-73.0864
40.235	-73.0996
40.235	-73.1129
40.235	-73.1262
40.235	-73.1395
40.235	-73.1528
40.222	-73.0465
40.222	-73.0598
40.222	-73.0731
40.222	-73.0864
40.222	-73.0996
40.222	-73.1129
40.222	-73.1262
40.222	-73.1395
40.222	-73.1528
40.222	-73.1661
40.2261	-73.1773
40.209	-73.0598
40.209	-73.0731
40.209	-73.0864
40.209	-73.0996
40.209	-73.1129
40.209	-73.1262
40.209	-73.1395
40.209	-73.1528
40.209	-73.1661
40.209	-73.1793
40.196	-73.0731
40.196	-73.0864
40.196	-73.0996
40.196	-73.1129
40.196	-73.1262
40.196	-73.1395
40.196	-73.1528
40.196	-73.1661
40.196	-73.1793

Latitude	Longitude
40.196	-73.1926
40.196	-73.2059
40.958	-71.208
40.991	-71.231
40.993	-71.121
41.008	-71.232
41.015	-70.858
41.015	-70.836
41.031	-70.858
41.032	-70.836
41.041	-71.255
41.041	-71.233
41.042	-71.211
41.064	-70.881
41.065	-70.859
41.065	-70.837
41.082	-70.837
41.075	-71.19
41.076	-71.168
41.076	-71.146
41.077	-71.124
41.077	-71.102
41.077	-71.08
41.092	-71.191
41.093	-71.169
41.093	-71.146
41.093	-71.124
41.094	-71.102
41.094	-71.08
41.109	-71.191
41.109	-71.169
41.11	-71.147
41.11	-71.125
41.11	-71.103
41.111	-71.081
41.29	-71.286
41.228	-71.063
41.21	-71.128
41.211	-71.084
41.211	-71.062

Latitude	Longitude
41.128	-71.059
40.711	-71.025
40.728	-71.025
40.745	-71.026
40.761	-71.026
40.778	-71.027
40.795	-71.027
40.812	-71.028
40.828	-71.028
40.845	-71.029
40.845	-71.007
40.846	-70.985
40.846	-70.963
40.846	-70.941
40.847	-70.919
40.847	-70.897
40.847	-70.875
40.848	-70.853
40.862	-71.029
40.862	-71.007
40.862	-70.985
40.863	-70.963
40.863	-70.941
40.863	-70.919
40.864	-70.897
40.864	-70.875
40.864	-70.853
40.865	-70.831
40.878	-71.03
40.879	-71.008
40.879	-70.986
40.879	-70.964
40.88	-70.942
40.88	-70.92
40.88	-70.898
40.881	-70.876
40.881	-70.854
40.882	-70.832
40.882	-70.81
40.895	-71.03

Latitude	Longitude
40.895	-71.008
40.896	-70.986
40.896	-70.964
40.896	-70.942
40.897	-70.92
40.897	-70.898
40.897	-70.876
40.898	-70.854
40.898	-70.832
40.899	-70.81
40.899	-70.788
40.913	-70.965
40.913	-70.943
40.913	-70.921
40.914	-70.899
40.914	-70.877
40.915	-70.855
40.915	-70.833
40.915	-70.811
40.916	-70.789
40.93	-70.921
40.93	-70.899
40.931	-70.877
40.931	-70.855
40.932	-70.833
40.932	-70.811
40.932	-70.789
40.933	-70.767
40.933	-70.745
40.947	-70.922
40.947	-70.9
40.948	-70.878
40.948	-70.856
40.948	-70.834
40.949	-70.812
40.949	-70.79
40.949	-70.768
40.95	-70.746
40.964	-70.9
40.964	-70.878

Latitude	Longitude
40.965	-70.856
40.965	-70.834
40.965	-70.812
40.966	-70.79
40.966	-70.768
40.966	-70.746
40.967	-70.724
40.967	-70.702
40.981	-70.879
40.981	-70.857
40.982	-70.835
40.982	-70.813
40.982	-70.791
40.983	-70.769
40.983	-70.747
40.983	-70.725
40.984	-70.703
40.998	-70.857
40.998	-70.835
40.999	-70.813
40.999	-70.791
40.999	-70.769
41	-70.747
41	-70.725
41	-70.703
41.001	-70.681
41.001	-70.659
41.015	-70.814
41.016	-70.792
41.016	-70.77
41.016	-70.748
41.017	-70.726
41.017	-70.704
41.017	-70.681
41.018	-70.659
41.018	-70.637
41.032	-70.814
41.032	-70.792
41.033	-70.77
41.033	-70.748

Latitude	Longitude
41.033	-70.726
41.034	-70.704
41.034	-70.682
41.034	-70.66
41.035	-70.638
41.035	-70.616
41.049	-70.792
41.049	-70.77
41.05	-70.748
41.05	-70.726
41.05	-70.704
41.051	-70.682
41.051	-70.66
41.051	-70.638
41.052	-70.616
41.052	-70.594
41.066	-70.793
41.066	-70.771
41.066	-70.749
41.067	-70.727
41.067	-70.705
41.067	-70.683
41.068	-70.661
41.068	-70.639
41.068	-70.617
41.069	-70.595
41.069	-70.573
41.082	-70.815
41.083	-70.771
41.083	-70.749
41.083	-70.727
41.084	-70.705
41.084	-70.683
41.084	-70.661
41.085	-70.639
41.085	-70.617
41.085	-70.595
41.086	-70.573
41.086	-70.551
41.099	-70.794

Latitude	Longitude
41.099	-70.772
41.1	-70.75
41.1	-70.728
41.1	-70.706
41.101	-70.684
41.101	-70.662
41.101	-70.64
41.102	-70.617
41.102	-70.595
41.102	-70.573
41.103	-70.551
41.103	-70.529
41.118	-70.64
41.118	-70.618
41.119	-70.596
41.119	-70.574
41.119	-70.552
41.119	-70.53
41.12	-70.508
41.135	-70.596
41.136	-70.574
41.136	-70.552
41.136	-70.53
41.136	-70.508
41.12	-70.486
41.137	-70.486
41.137	-70.464
40.603	-70.474
40.603	-70.452
40.605	-70.321
40.605	-70.343
40.604	-70.365
40.604	-70.387
40.604	-70.408
40.604	-70.43
40.62	-70.474
40.62	-70.453
40.622	-70.321
40.621	-70.343
40.621	-70.365

Latitude	Longitude
40.621	-70.387
40.621	-70.409
40.62	-70.431
40.641	-70.037
40.641	-70.059
40.641	-70.081
40.641	-70.103
40.64	-70.124
40.64	-70.146
40.64	-70.168
40.64	-70.19
40.639	-70.212
40.639	-70.234
40.639	-70.256
40.639	-70.278
40.638	-70.3
40.638	-70.322
40.638	-70.343
40.638	-70.365
40.637	-70.387
40.637	-70.409
40.637	-70.431
40.658	-70.037
40.658	-70.059
40.657	-70.081
40.657	-70.103
40.657	-70.125
40.657	-70.147
40.657	-70.169
40.656	-70.19
40.656	-70.212
40.656	-70.234
40.656	-70.256
40.655	-70.278
40.655	-70.3
40.655	-70.322
40.655	-70.344
40.654	-70.366
40.654	-70.388
40.654	-70.409

Latitude	Longitude
40.675	-70.037
40.674	-70.059
40.674	-70.081
40.674	-70.103
40.674	-70.125
40.673	-70.147
40.673	-70.169
40.673	-70.191
40.673	-70.213
40.673	-70.235
40.672	-70.256
40.672	-70.278
40.672	-70.3
40.672	-70.322
40.671	-70.344
40.671	-70.366
40.671	-70.388
40.691	-70.038
40.691	-70.06
40.691	-70.081
40.691	-70.103
40.69	-70.125
40.69	-70.147
40.69	-70.169
40.69	-70.191
40.689	-70.213
40.689	-70.235
40.689	-70.257
40.689	-70.279
40.689	-70.301
40.688	-70.323
40.688	-70.344
40.688	-70.366
40.708	-70.038
40.708	-70.06
40.707	-70.082
40.707	-70.104
40.707	-70.126
40.707	-70.148
40.707	-70.169

Latitude	Longitude
40.706	-70.191
40.706	-70.213
40.706	-70.235
40.706	-70.257
40.705	-70.279
40.705	-70.301
40.705	-70.323
40.705	-70.345
40.725	-70.038
40.724	-70.06
40.724	-70.082
40.724	-70.104
40.724	-70.126
40.724	-70.148
40.723	-70.17
40.723	-70.192
40.723	-70.214
40.723	-70.235
40.722	-70.257
40.722	-70.279
40.722	-70.301
40.722	-70.323
40.741	-70.038
40.741	-70.06
40.741	-70.082
40.741	-70.104
40.74	-70.126
40.74	-70.148
40.74	-70.17
40.74	-70.192
40.74	-70.214
40.739	-70.236
40.739	-70.258
40.739	-70.28
40.739	-70.302
40.756	-70.214
40.756	-70.236
40.756	-70.258
40.756	-70.28
40.773	-70.214

Latitude	Longitude
40.773	-70.236
40.772	-70.258
40.79	-70.215
40.789	-70.237
40.806	-70.215
40.806	-70.237
40.636	-70.519
40.653	-70.519
39.02716	-74.2845
39.03708	-74.2952
39.0473	-74.3062
39.05752	-74.3172
39.06775	-74.3282
39.07796	-74.3392
39.08818	-74.3503
39.0984	-74.3613
39.10862	-74.3723
39.03759	-74.2678
39.04781	-74.2788
39.05804	-74.2898
39.06826	-74.3008
39.07848	-74.3118
39.0887	-74.3229
39.09892	-74.3339
39.10914	-74.3449
39.11936	-74.3559
39.1301	-74.3395
39.11988	-74.3285
39.10966	-74.3175
39.09944	-74.3065
39.08922	-74.2954
39.07899	-74.2844
39.06877	-74.2734
39.05854	-74.2624
39.04832	-74.2514
39.05904	-74.235
39.06927	-74.246
39.0795	-74.257
39.08972	-74.268
39.09995	-74.279

Latitude	Longitude
39.11017	-74.2901
39.13062	-74.3121
39.14084	-74.3231
39.15157	-74.3067
39.14135	-74.2957
39.13113	-74.2847
39.1209	-74.2737
39.11068	-74.2626
39.10045	-74.2516
39.09022	-74.2406
39.07999	-74.2296
39.06977	-74.2186
39.08049	-74.2022
39.09072	-74.2132
39.10095	-74.2242
39.11118	-74.2352
39.1214	-74.2462
39.13163	-74.2572
39.14186	-74.2683
39.15208	-74.2793
39.16231	-74.2903
39.16281	-74.2629
39.15258	-74.2519
39.14236	-74.2408
39.13213	-74.2298
39.1219	-74.2188
39.11167	-74.2078
39.10144	-74.1968
39.09121	-74.1858
39.11361	-74.1781
39.12383	-74.1892
39.13405	-74.2002
39.14426	-74.2112
39.15448	-74.2223
39.17491	-74.2443
39.02736	-74.2568
39.03809	-74.2404
39.04881	-74.224
39.05953	-74.2076
39.07025	-74.1912

Latitude	Longitude
39.08097	-74.1748
39.09316	-74.1561
39.10339	-74.1671
39.11485	-74.1495
39.12508	-74.1606
39.13531	-74.1716
39.14553	-74.1826
39.15576	-74.1936
39.16599	-74.2046
39.17621	-74.2157
39.18643	-74.2267
39.19722	-74.2102
39.17696	-74.1878
39.16682	-74.1767
39.15669	-74.1655
39.14655	-74.1543
39.13642	-74.1432
39.12628	-74.132
39.13699	-74.1156
39.14713	-74.1267
39.15726	-74.1379
39.1674	-74.1491
39.17754	-74.1602
39.18767	-74.1714
39.19781	-74.1826
39.20794	-74.1937
40.66675	-70.6946
40.66707	-70.6727
40.66739	-70.6508
40.6677	-70.6289
40.68343	-70.695
40.68375	-70.6731
40.68406	-70.6512
40.68438	-70.6293
40.68468	-70.6074
40.70011	-70.6954
40.70043	-70.6735
40.70074	-70.6516
40.70105	-70.6297
40.70136	-70.6078

Latitude	Longitude
40.70166	-70.5858
40.71678	-70.6958
40.7171	-70.6739
40.71742	-70.652
40.71773	-70.6301
40.71804	-70.6082
40.71834	-70.5862
40.71864	-70.5643
40.73346	-70.6963
40.73378	-70.6743
40.7341	-70.6524
40.73441	-70.6305
40.73472	-70.6086
40.73502	-70.5866
40.73532	-70.5647
40.73561	-70.5428
40.74981	-70.7186
40.75014	-70.6967
40.75046	-70.6748
40.75077	-70.6528
40.75108	-70.6309
40.7517	-70.587
40.752	-70.5651
40.75229	-70.5432
40.75258	-70.5212
40.76681	-70.6971
40.76713	-70.6752
40.76745	-70.6532
40.76776	-70.6313
40.76807	-70.6094
40.76837	-70.5874
40.76867	-70.5655
40.76897	-70.5436
40.76926	-70.5216
40.76955	-70.4997
40.78381	-70.6756
40.78413	-70.6536
40.78444	-70.6317
40.78475	-70.6098
40.78505	-70.5878

Latitude	Longitude
40.78535	-70.5659
40.78565	-70.5439
40.78594	-70.522
40.78623	-70.5001
40.8008	-70.6541
40.80112	-70.6321
40.80142	-70.6102
40.80173	-70.5882
40.80203	-70.5663
40.80232	-70.5443
40.80262	-70.5224
40.81779	-70.6325
40.8181	-70.6106
40.81841	-70.5886
40.81871	-70.5667
40.819	-70.5447
40.83508	-70.589
40.83538	-70.5671
40.85176	-70.5894
40.78651	-70.4781
40.8029	-70.5004
40.80319	-70.4785
40.80347	-70.4565
40.81929	-70.5228
40.81958	-70.5008
40.81987	-70.4789
40.82015	-70.4569
40.82042	-70.4349
40.83568	-70.5451
40.83597	-70.5231
40.83626	-70.5012
40.83654	-70.4792
40.83682	-70.4573
40.83737	-70.4133
40.8371	-70.4353
40.85206	-70.5675
40.85236	-70.5455
40.85265	-70.5235
40.85294	-70.5016
40.85322	-70.4796

Latitude	Longitude
40.8535	-70.4576
40.85432	-70.3917
40.85405	-70.4137
40.85378	-70.4357
40.86904	-70.5459
40.86933	-70.5239
40.86962	-70.5019
40.8699	-70.48
40.87018	-70.458
40.87126	-70.3701
40.87099	-70.3921
40.87073	-70.4141
40.87046	-70.436
40.88571	-70.5463
40.88601	-70.5243
40.88629	-70.5023
40.88658	-70.4803
40.88686	-70.4584
40.8882	-70.3485
40.88794	-70.3705
40.88767	-70.3924
40.88741	-70.4144
40.90297	-70.5027
40.90326	-70.4807
40.90354	-70.4587
40.90513	-70.3268
40.90487	-70.3488
40.90462	-70.3708
40.90435	-70.3928
40.90408	-70.4148
40.90381	-70.4367
40.91965	-70.5031
40.91993	-70.4811
40.92021	-70.4591
40.92206	-70.3052
40.92181	-70.3272
40.92155	-70.3492
40.92129	-70.3711
40.92103	-70.3931
40.92076	-70.4151

Latitude	Longitude
40.92049	-70.4371
40.93661	-70.4815
40.93689	-70.4595
40.93797	-70.3715
40.93771	-70.3935
40.93744	-70.4155
40.93717	-70.4375
40.95357	-70.4598
40.95465	-70.3718
40.95439	-70.3938
40.95412	-70.4158
40.95385	-70.4378
40.97133	-70.3722
40.97107	-70.3942
40.9708	-70.4162
40.97053	-70.4382
40.98801	-70.3725
40.98774	-70.3945
40.98748	-70.4165
41.00469	-70.3729
41.00442	-70.3949
36.3712	-75.1422
36.2658	-75.1428
36.30932	-75.1452
36.35284	-75.1475
36.29096	-75.1505
36.33448	-75.1529
36.2726	-75.1558
36.31612	-75.1582
36.35964	-75.1605
36.29776	-75.1635
36.34128	-75.1659
36.32292	-75.1712
36.30456	-75.1765
36.41472	-75.1446
36.39636	-75.1499
36.378	-75.1552
36.42152	-75.1576
36.40316	-75.1629
36.3848	-75.1682

Latitude	Longitude
36.42832	-75.1706
36.36644	-75.1736
36.40996	-75.1759
36.34808	-75.1789
36.3916	-75.1813
36.32972	-75.1842
36.37324	-75.1866
36.41676	-75.189
36.35488	-75.1919
36.3984	-75.1943
36.33652	-75.1972
36.38004	-75.1996
36.42356	-75.202
36.36168	-75.2049
36.4052	-75.2073
36.34332	-75.2102
36.38684	-75.2126
36.43035	-75.215
36.36847	-75.2179
36.41199	-75.2203
36.35011	-75.2232
36.39363	-75.2256
36.37527	-75.2309
36.41879	-75.2334
36.35691	-75.2363
36.40042	-75.2387
36.38206	-75.244
36.42558	-75.2464
36.3637	-75.2493
36.40722	-75.2517
36.38885	-75.257
36.43237	-75.2594
36.37049	-75.2623
36.41401	-75.2647
36.39564	-75.27
36.43916	-75.2725
36.42079	-75.2778
36.46431	-75.2802
36.40243	-75.2831
36.44595	-75.2855

Latitude	Longitude
36.42758	-75.2908
36.4711	-75.2932
36.40922	-75.2961
36.45273	-75.2985
36.43437	-75.3038
36.416	-75.3091
36.45952	-75.3116
36.44115	-75.3169
36.42279	-75.3222
36.4663	-75.3246
36.44793	-75.3299
36.97739	-75.4557
36.97735	-75.4235
36.99325	-75.2541
36.99322	-75.2697
36.99318	-75.2853
36.99314	-75.3009
36.9931	-75.3164
36.99306	-75.332
36.99302	-75.3476
36.99276	-75.4255
36.99271	-75.4411
36.9779	-75.221
36.97787	-75.2366
36.97783	-75.2522
36.9778	-75.2678
36.97776	-75.2833
36.97768	-75.3145
36.97764	-75.33
36.9776	-75.3456
36.97729	-75.4391
36.96247	-75.2191
36.96244	-75.2347
36.9624	-75.2502
36.96237	-75.2658
36.96233	-75.2814
36.96226	-75.3125
36.96222	-75.3281
36.96217	-75.3437
36.96212	-75.3592

Latitude	Longitude
36.96208	-75.3748
36.96203	-75.3904
36.96197	-75.4059
36.96192	-75.4215
36.96186	-75.4371
36.96181	-75.4526
36.96175	-75.4682
36.94698	-75.2483
36.94694	-75.2638
36.94691	-75.2794
36.94687	-75.295
36.94683	-75.3105
36.94679	-75.3261
36.9467	-75.3572
36.94665	-75.3728
36.9466	-75.3884
36.94655	-75.4039
36.94649	-75.4195
36.94644	-75.4351
36.94638	-75.4506
36.94632	-75.4662
36.94626	-75.4818
36.93158	-75.2308
36.93155	-75.2463
36.93151	-75.2619
36.93148	-75.2775
36.93144	-75.293
36.9314	-75.3086
36.93136	-75.3241
36.93132	-75.3397
36.93127	-75.3553
36.93122	-75.3708
36.93117	-75.3864
36.93112	-75.402
36.93107	-75.4175
36.93101	-75.4331
36.93096	-75.4486
36.9309	-75.4642
36.93083	-75.4798
36.91616	-75.2288

Latitude	Longitude
36.91613	-75.2444
36.91609	-75.2599
36.91606	-75.2755
36.91598	-75.3066
36.91594	-75.3222
36.9159	-75.3377
36.91585	-75.3533
36.91581	-75.3689
36.91576	-75.3844
36.91571	-75.4
36.9156	-75.4311
36.91554	-75.4466
36.91548	-75.4622
36.91542	-75.4778
36.90073	-75.2269
36.90067	-75.258
36.90063	-75.2735
36.90056	-75.3047
36.90051	-75.3202
36.90047	-75.3358
36.90033	-75.3824
36.90028	-75.398
36.90023	-75.4135
36.90017	-75.4291
36.90011	-75.4447
36.90005	-75.4602
36.89999	-75.4758
36.8853	-75.2249
36.88527	-75.2405
36.88524	-75.256
36.8852	-75.2716
36.88517	-75.2871
36.88509	-75.3182
36.88504	-75.3338
36.8849	-75.3805
36.8848	-75.4116
36.88475	-75.4271
36.88469	-75.4427
36.88463	-75.4582
36.88457	-75.4738

Latitude	Longitude
36.86987	-75.223
36.86984	-75.2385
36.86981	-75.2541
36.86977	-75.2696
36.86974	-75.2852
36.8697	-75.3007
36.86966	-75.3163
36.86962	-75.3318
36.86957	-75.3474
36.86953	-75.3629
36.86948	-75.3785
36.86943	-75.394
36.86937	-75.4096
36.86932	-75.4251
36.86926	-75.4407
36.8692	-75.4562
36.86914	-75.4718
36.85445	-75.221
36.85442	-75.2366
36.85439	-75.2521
36.85435	-75.2677
36.85432	-75.2832
36.85428	-75.2988
36.85424	-75.3143
36.8542	-75.3299
36.85411	-75.3609
36.85406	-75.3765
36.85401	-75.392
36.85396	-75.4076
36.8539	-75.4231
36.85385	-75.4387
36.85379	-75.4542
36.85373	-75.4698
36.83902	-75.2191
36.83899	-75.2346
36.83896	-75.2502
36.83893	-75.2657
36.83889	-75.2813
36.83885	-75.2968
36.83881	-75.3123

Latitude	Longitude
36.83877	-75.3279
36.83873	-75.3434
36.83868	-75.359
36.83863	-75.3745
36.83858	-75.3901
36.83853	-75.4056
36.83848	-75.4212
36.83842	-75.4367
36.83836	-75.4522
36.8383	-75.4678
36.82359	-75.2171
36.82356	-75.2327
36.82353	-75.2482
36.8235	-75.2638
36.82346	-75.2793
36.82342	-75.2948
36.82338	-75.3104
36.82334	-75.3259
36.8233	-75.3415
36.82325	-75.357
36.82321	-75.3725
36.82316	-75.3881
36.8231	-75.4036
36.82305	-75.4192
36.82299	-75.4347
36.82294	-75.4502
36.82288	-75.4658
36.99282	-75.4099
36.99287	-75.3943
36.99292	-75.3788
36.99297	-75.3632
36.97755	-75.3612
36.9775	-75.3768
36.97745	-75.3923
36.9774	-75.4079
36.99332	-75.223
36.99329	-75.2386
36.99265	-75.4566
36.97772	-75.2989
36.97717	-75.4702

Latitude	Longitude
36.9623	-75.2969
36.96168	-75.4838
36.94704	-75.2171
36.94701	-75.2327
36.94674	-75.3417
36.91602	-75.2911
36.91565	-75.4155
36.9007	-75.2424
36.90059	-75.2891
36.90043	-75.3513
36.90038	-75.3669
36.88513	-75.3027
36.885	-75.3493
36.88495	-75.3649
36.88485	-75.396
36.85415	-75.3454
36.88683	-75.4916
36.89629	-75.4916
38.30264	-74.6618
38.4379	-74.7868
38.30298	-74.8247
38.31985	-74.822
38.33672	-74.8193
38.35358	-74.8166
38.37045	-74.8139
38.38732	-74.8112
38.40419	-74.8086
38.42106	-74.8058
38.43792	-74.8031
38.45479	-74.8004
38.31987	-74.8383
38.33674	-74.8356
38.35361	-74.833
38.37048	-74.8303
38.38734	-74.8276
38.40421	-74.8249
38.42108	-74.8222
38.43795	-74.8195
38.45482	-74.8168
38.31989	-74.8546

Latitude	Longitude
38.33676	-74.8519
38.35363	-74.8493
38.3705	-74.8466
38.40423	-74.8412
38.4211	-74.8385
38.43797	-74.8358
38.45484	-74.8331
38.38738	-74.8602
38.40425	-74.8575
38.42112	-74.8548
38.43799	-74.8521
38.45486	-74.8494
38.286	-74.7623
38.30287	-74.7595
38.31974	-74.7568
38.3366	-74.7541
38.35347	-74.7514
38.37034	-74.7487
38.3872	-74.746
38.40407	-74.7433
38.42094	-74.7406
38.28603	-74.7785
38.3029	-74.7758
38.31977	-74.7731
38.33664	-74.7704
38.3535	-74.7677
38.38724	-74.7623
38.4041	-74.7596
38.42097	-74.7569
38.30293	-74.7921
38.3198	-74.7894
38.33666	-74.7867
38.35353	-74.784
38.3704	-74.7813
38.40413	-74.7759
38.421	-74.7732
38.43787	-74.7705
38.30296	-74.8084
38.31982	-74.8057
38.33669	-74.803

Latitude	Longitude
38.35356	-74.8003
38.37043	-74.7976
38.38729	-74.7949
38.40416	-74.7922
38.42103	-74.7895
38.28586	-74.6971
38.30273	-74.6944
38.31959	-74.6916
38.33646	-74.6889
38.35332	-74.6862
38.25217	-74.7188
38.26903	-74.7161
38.2859	-74.7134
38.30276	-74.7107
38.31963	-74.7079
38.3365	-74.7052
38.35336	-74.7025
38.37023	-74.6998
38.2522	-74.7351
38.26907	-74.7324
38.28594	-74.7297
38.3028	-74.727
38.33653	-74.7215
38.3534	-74.7188
38.37027	-74.7161
38.38713	-74.7134
38.25224	-74.7514
38.2691	-74.7487
38.28597	-74.746
38.30284	-74.7433
38.3197	-74.7405
38.33657	-74.7378
38.35344	-74.7351
38.3703	-74.7324
38.38717	-74.7297
38.40403	-74.727
38.25227	-74.7677
38.26914	-74.765
38.25185	-74.6048
38.2519	-74.6211

Latitude	Longitude
38.26877	-74.6184
38.25195	-74.6374
38.26882	-74.6347
38.28568	-74.6319
38.252	-74.6537
38.26886	-74.651
38.28573	-74.6482
38.30259	-74.6455
38.25204	-74.67
38.26891	-74.6672
38.28577	-74.6645
38.3195	-74.6591
38.25209	-74.6863
38.26895	-74.6835
38.30268	-74.6781
38.31955	-74.6753
38.33641	-74.6726
38.25213	-74.7025
38.26899	-74.6998
39.31653	-73.9432
39.31491	-73.9559
39.31328	-73.9687
39.29812	-73.955
39.29649	-73.9677
39.28133	-73.9541
39.2797	-73.9668
39.26454	-73.9531
39.26291	-73.9658
39.37103	-74.177
39.36938	-74.1898
39.37066	-74.0488
39.36902	-74.0615
39.36739	-74.0743
39.36575	-74.087
39.36411	-74.0997
39.36247	-74.1124
39.36083	-74.1252
39.35918	-74.1379
39.35754	-74.1506
39.35589	-74.1633

Latitude	Longitude
39.35424	-74.176
39.35259	-74.1888
39.3555	-74.0351
39.35387	-74.0478
39.35224	-74.0606
39.3506	-74.0733
39.34896	-74.086
39.34732	-74.0987
39.34568	-74.1115
39.34404	-74.1242
39.34239	-74.1369
39.34075	-74.1496
39.3391	-74.1623
39.33745	-74.175
39.34035	-74.0214
39.33871	-74.0342
39.33708	-74.0469
39.33545	-74.0596
39.33381	-74.0723
39.33217	-74.085
39.33053	-74.0978
39.32889	-74.1105
39.32725	-74.1232
39.3256	-74.1359
39.32396	-74.1486
39.32231	-74.1613
39.32067	-74.1741
39.31902	-74.1868
39.32519	-74.0078
39.32356	-74.0205
39.32192	-74.0332
39.32029	-74.0459
39.31866	-74.0586
39.31702	-74.0713
39.31538	-74.0841
39.31374	-74.0968
39.3121	-74.1095
39.31046	-74.1222
39.30882	-74.1349
39.30717	-74.1476

Latitude	Longitude
39.30552	-74.1603
39.30388	-74.1731
39.30223	-74.1858
39.30058	-74.1985
39.29893	-74.2112
39.29727	-74.2239
39.29562	-74.2366
39.31166	-73.9814
39.31003	-73.9941
39.3084	-74.0068
39.30677	-74.0195
39.30513	-74.0322
39.3035	-74.045
39.30187	-74.0577
39.30023	-74.0704
39.29859	-74.0831
39.29695	-74.0958
39.29531	-74.1085
39.29367	-74.1212
39.29203	-74.1339
39.29038	-74.1466
39.28874	-74.1594
39.28709	-74.1721
39.28544	-74.1848
39.28379	-74.1975
39.28214	-74.2102
39.28048	-74.2229
39.27883	-74.2356
39.27717	-74.2483
39.29487	-73.9804
39.29324	-73.9931
39.29161	-74.0059
39.28998	-74.0186
39.28834	-74.0313
39.28671	-74.044
39.28508	-74.0567
39.28344	-74.0694
39.2818	-74.0821
39.28016	-74.0948
39.27852	-74.1075

Latitude	Longitude
39.27688	-74.1202
39.27524	-74.133
39.27359	-74.1457
39.27195	-74.1584
39.2703	-74.1711
39.26865	-74.1838
39.267	-74.1965
39.26535	-74.2092
39.27808	-73.9795
39.27645	-73.9922
39.27482	-74.0049
39.27319	-74.0176
39.27155	-74.0303
39.26992	-74.043
39.26829	-74.0557
39.26665	-74.0684
39.26501	-74.0811
39.26337	-74.0939
39.26173	-74.1066
39.26009	-74.1193
39.25845	-74.132
39.2568	-74.1447
39.25516	-74.1574
39.25351	-74.1701
39.25186	-74.1828
39.26128	-73.9785
39.25966	-73.9912
39.25803	-74.0039
39.2564	-74.0167
39.25476	-74.0294
39.25313	-74.0421
39.2515	-74.0548
39.24986	-74.0675
39.24822	-74.0802
39.24658	-74.0929
39.24494	-74.1056
39.2433	-74.1183
39.24166	-74.131
39.24001	-74.1437
39.23837	-74.1564

Latitude	Longitude
39.23672	-74.1691
39.23507	-74.1818
39.24449	-73.9776
39.24287	-73.9903
39.24124	-74.003
39.23961	-74.0157
39.23797	-74.0284
39.23634	-74.0411
39.23471	-74.0538
39.23307	-74.0665
39.23143	-74.0792
39.22979	-74.0919
39.22815	-74.1046
39.22651	-74.1173
39.22487	-74.13
39.22322	-74.1427
39.22158	-74.1554
39.21993	-74.1681
39.21828	-74.1808
39.21663	-74.1935
39.22445	-74.002
39.22282	-74.0147
39.22118	-74.0274
39.21955	-74.0401
39.21792	-74.0528
39.21628	-74.0655
39.21464	-74.0782
39.213	-74.0909
39.21136	-74.1036
39.20972	-74.1163
39.20808	-74.129
39.20643	-74.1417
39.20479	-74.1544
39.20314	-74.1671
39.20603	-74.0138
39.20439	-74.0265
39.20276	-74.0392
39.20113	-74.0519
39.19949	-74.0646
39.19785	-74.0773

Latitude	Longitude
39.19621	-74.09
39.19457	-74.1027
39.19293	-74.1153
39.19129	-74.128
39.18964	-74.1407
39.18434	-74.0509
39.1827	-74.0636
39.18106	-74.0763
39.17942	-74.089
39.17778	-74.1017
39.17614	-74.1144
39.1745	-74.1271
39.16591	-74.0626
39.16427	-74.0753
39.16263	-74.088
39.16099	-74.1007
39.15935	-74.1134
39.14584	-74.087
40.31535	-73.2611
40.30686	-73.2757
40.29837	-73.2902
40.28987	-73.3048
40.28138	-73.3194
40.27288	-73.334
40.26608	-73.3485
40.29286	-73.0893
40.27893	-73.1041
40.29569	-73.1036
40.26836	-73.1187
40.28722	-73.1182
40.29851	-73.1179
40.25788	-73.1334
40.27874	-73.1328
40.29004	-73.1325
40.30133	-73.1322
40.24769	-73.148
40.25898	-73.1477
40.27027	-73.1474
40.28156	-73.1471
40.29286	-73.1468

Latitude	Longitude
40.30372	-73.1465
40.2505	-73.1623
40.2618	-73.162
40.27264	-73.1617
40.28438	-73.1614
40.29567	-73.161
40.24202	-73.1768
40.25332	-73.1765
40.26461	-73.1762
40.27545	-73.176
40.2872	-73.1756
40.29849	-73.1753
40.21547	-73.1919
40.23354	-73.1914
40.24484	-73.1911
40.25613	-73.1908
40.26743	-73.1905
40.27872	-73.1902
40.29001	-73.1899
40.3013	-73.1896
40.2048	-73.2065
40.22506	-73.206
40.23636	-73.2057
40.24765	-73.2054
40.25894	-73.2051
40.27024	-73.2048
40.28153	-73.2045
40.29282	-73.2042
40.30412	-73.2039
40.20255	-73.2209
40.21658	-73.2206
40.22787	-73.2203
40.23917	-73.22
40.25046	-73.2197
40.26175	-73.2194
40.27305	-73.2191
40.28434	-73.2188
40.29563	-73.2185
40.30693	-73.2182
40.21263	-73.235

Latitude	Longitude
40.23068	-73.2345
40.24197	-73.2343
40.25327	-73.234
40.26456	-73.2337
40.27586	-73.2334
40.29844	-73.2328
40.30974	-73.2325
40.22209	-73.2491
40.23349	-73.2488
40.24478	-73.2485
40.25562	-73.2483
40.26737	-73.2479
40.27866	-73.2477
40.28996	-73.2474
40.30125	-73.2471
40.31254	-73.2468
40.22838	-73.2633
40.24759	-73.2628
40.25888	-73.2625
40.27017	-73.2622
40.28147	-73.2619
40.29276	-73.2617
40.30405	-73.2614
40.23467	-73.2775
40.25039	-73.2771
40.26123	-73.2768
40.27298	-73.2765
40.28427	-73.2762
40.29556	-73.2759
40.24095	-73.2917
40.25319	-73.2914
40.26448	-73.2911
40.27578	-73.2908
40.28707	-73.2905
40.24723	-73.3059
40.26728	-73.3054
40.27858	-73.3051
40.25352	-73.3201
40.27008	-73.3197
40.2598	-73.3343

Latitude	Longitude
40.31815	-73.2754
40.30966	-73.29
40.32095	-73.2897
40.30117	-73.3045
40.31246	-73.3042
40.32375	-73.304
40.29267	-73.3191
40.30396	-73.3188
40.31526	-73.3185
40.32655	-73.3183
40.28417	-73.3337
40.29547	-73.3334
40.30676	-73.3331
40.31805	-73.3328
40.32935	-73.3326
40.27567	-73.3482
40.29826	-73.3477
40.30956	-73.3474
40.32085	-73.3471
40.33214	-73.3469
40.27213	-73.3627
40.28976	-73.3623
40.30105	-73.362
40.31235	-73.3617
40.32364	-73.3614
40.33494	-73.3612
40.2784	-73.3769
40.29255	-73.3766
40.30385	-73.3763
40.31514	-73.376
40.32643	-73.3757
40.33773	-73.3755
40.28468	-73.3911
40.29566	-73.3908
40.30663	-73.3906
40.31793	-73.3903
40.32922	-73.39
40.34052	-73.3898
40.29095	-73.4053
40.30942	-73.4049

Latitude	Longitude
40.32072	-73.4046
40.33201	-73.4043
40.34331	-73.4041
40.29722	-73.4195
40.31221	-73.4192
40.3235	-73.4189
40.3348	-73.4187
40.34609	-73.4184
40.30349	-73.4337
40.31499	-73.4335
40.32629	-73.4332
40.33758	-73.433
40.34888	-73.4327
40.30976	-73.448
40.35166	-73.447
40.31602	-73.4622
40.35444	-73.4613
40.32228	-73.4764
40.35722	-73.4756
40.32855	-73.4906
40.36	-73.4899
40.33481	-73.5049
40.36277	-73.5043
40.34106	-73.5191
40.36554	-73.5186
40.34732	-73.5333
40.36832	-73.5329
40.35358	-73.5476
40.37109	-73.5472
40.35983	-73.5618
40.37386	-73.5615
40.60276	-70.4959
40.60248	-70.5178
40.61944	-70.4963
40.61916	-70.5182
40.63668	-70.4529
40.6364	-70.4748
40.63612	-70.4967
40.63554	-70.5405
40.63525	-70.5624

Latitude	Longitude
40.63495	-70.5843
40.63465	-70.6062
40.63434	-70.628
40.65363	-70.4314
40.65336	-70.4533
40.65308	-70.4752
40.6528	-70.4971
40.65222	-70.5409
40.65193	-70.5628
40.65163	-70.5847
40.65133	-70.6066
40.65102	-70.6285
40.67058	-70.4098
40.67031	-70.4317
40.67004	-70.4536
40.66976	-70.4755
40.66948	-70.4974
40.66919	-70.5193
40.6689	-70.5412
40.66861	-70.5631
40.66831	-70.5851
40.66801	-70.607
40.68753	-70.3883
40.68726	-70.4102
40.68699	-70.4321
40.68672	-70.454
40.68644	-70.4759
40.68616	-70.4978
40.68587	-70.5197
40.68558	-70.5416
40.68528	-70.5635
40.68499	-70.5854
40.70447	-70.3667
40.70421	-70.3886
40.70394	-70.4105
40.70367	-70.4324
40.7034	-70.4544
40.70312	-70.4763
40.70283	-70.4982
40.70255	-70.5201

Latitude	Longitude
40.70226	-70.542
40.70196	-70.5639
40.7214	-70.3451
40.72115	-70.367
40.72088	-70.389
40.72062	-70.4109
40.72035	-70.4328
40.72007	-70.4547
40.7198	-70.4766
40.71951	-70.4986
40.71923	-70.5205
40.71894	-70.5424
40.73834	-70.3235
40.73808	-70.3454
40.73783	-70.3674
40.73756	-70.3893
40.7373	-70.4112
40.73703	-70.4332
40.73675	-70.4551
40.73647	-70.477
40.73619	-70.4989
40.7359	-70.5209
40.75527	-70.3019
40.75502	-70.3238
40.75476	-70.3458
40.7545	-70.3677
40.75424	-70.3896
40.75398	-70.4116
40.75371	-70.4335
40.75343	-70.4554
40.75315	-70.4774
40.75287	-70.4993
40.77219	-70.2803
40.77195	-70.3022
40.7717	-70.3242
40.77144	-70.3461
40.77118	-70.3681
40.77092	-70.39
40.77066	-70.4119
40.77038	-70.4339

Latitude	Longitude
40.77011	-70.4558
40.76983	-70.4777
40.78911	-70.2587
40.78887	-70.2806
40.78862	-70.3026
40.78838	-70.3245
40.78812	-70.3465
40.78786	-70.3684
40.7876	-70.3903
40.78733	-70.4123
40.78706	-70.4342
40.78679	-70.4562
40.80579	-70.259
40.80555	-70.2809
40.8053	-70.3029
40.80505	-70.3248
40.8048	-70.3468
40.80454	-70.3687
40.80428	-70.3907
40.80401	-70.4126
40.80374	-70.4346
40.82294	-70.2154
40.82271	-70.2373
40.82247	-70.2593
40.82223	-70.2813
40.82198	-70.3032
40.82173	-70.3252
40.82148	-70.3471
40.82122	-70.3691
40.82096	-70.391
40.82069	-70.413
40.83915	-70.2596
40.83891	-70.2816
40.83866	-70.3035
40.83841	-70.3255
40.83816	-70.3475
40.8379	-70.3694
40.83764	-70.3914
40.85583	-70.2599
40.85559	-70.2819

Latitude	Longitude
40.85534	-70.3039
40.85509	-70.3258
40.85484	-70.3478
40.85458	-70.3698
40.87251	-70.2602
40.87227	-70.2822
40.87202	-70.3042
40.87177	-70.3262
40.87152	-70.3481
40.88919	-70.2606
40.88895	-70.2825
40.8887	-70.3045
40.88845	-70.3265
40.90587	-70.2609
40.90563	-70.2829
40.90538	-70.3049
40.92255	-70.2612
40.92231	-70.2832
40.90268	-70.5249
40.74948	-70.7405
40.76616	-70.741
40.76649	-70.719
40.78284	-70.7414
40.78316	-70.7195
40.78349	-70.6975
40.79951	-70.7418
40.79984	-70.7199
40.80017	-70.698
40.80049	-70.676
40.81619	-70.7423
40.81652	-70.7203
40.81684	-70.6984
40.81716	-70.6764
40.81748	-70.6545
40.83286	-70.7427
40.83319	-70.7208
40.83352	-70.6988
40.83384	-70.6768
40.83416	-70.6549
40.83447	-70.6329

Latitude	Longitude
40.83478	-70.611
40.84818	-70.831
40.84853	-70.809
40.84887	-70.7871
40.84921	-70.7651
40.84954	-70.7432
40.84987	-70.7212
40.8502	-70.6992
40.85052	-70.6773
40.85083	-70.6553
40.85115	-70.6333
40.85146	-70.6114
40.8652	-70.8095
40.86554	-70.7875
40.86588	-70.7656
40.86622	-70.7436
40.86655	-70.7216
40.86687	-70.6997
40.86719	-70.6777
40.86751	-70.6557
40.86782	-70.6338
40.86813	-70.6118
40.86844	-70.5898
40.86874	-70.5678
40.88222	-70.788
40.88256	-70.766
40.88289	-70.744
40.88322	-70.7221
40.88355	-70.7001
40.88387	-70.6781
40.88419	-70.6561
40.8845	-70.6342
40.88481	-70.6122
40.88512	-70.5902
40.88542	-70.5682
40.89923	-70.7664
40.89957	-70.7445
40.8999	-70.7225
40.90022	-70.7005
40.90055	-70.6785

Latitude	Longitude
40.90086	-70.6566
40.90118	-70.6346
40.90149	-70.6126
40.90179	-70.5906
40.90209	-70.5686
40.90239	-70.5467
40.91591	-70.7669
40.91624	-70.7449
40.91657	-70.7229
40.9169	-70.7009
40.91722	-70.679
40.91754	-70.657
40.91785	-70.635
40.91816	-70.613
40.91847	-70.591
40.91877	-70.569
40.91907	-70.547
40.91936	-70.5251
40.93325	-70.7234
40.93358	-70.7014
40.9339	-70.6794
40.93422	-70.6574
40.93453	-70.6354
40.93484	-70.6134
40.93515	-70.5914
40.93545	-70.5694
40.93575	-70.5474
40.93604	-70.5254
40.93633	-70.5034
40.94993	-70.7238
40.95025	-70.7018
40.95057	-70.6798
40.95089	-70.6578
40.95121	-70.6358
40.95152	-70.6138
40.95182	-70.5918
40.95213	-70.5698
40.95242	-70.5478
40.95272	-70.5258
40.953	-70.5038

Latitude	Longitude
40.95329	-70.4818
40.96725	-70.6802
40.96757	-70.6582
40.96788	-70.6362
40.96819	-70.6142
40.9685	-70.5922
40.9688	-70.5702
40.9691	-70.5482
40.96939	-70.5262
40.96968	-70.5042
40.96997	-70.4822
40.98393	-70.6806
40.98425	-70.6586
40.98456	-70.6366
40.98487	-70.6146
40.98518	-70.5926
40.98548	-70.5706
40.98578	-70.5486
40.98607	-70.5266
40.98636	-70.5046
41.00124	-70.637
41.00155	-70.615
41.00185	-70.593
41.00216	-70.571
41.00245	-70.549
41.00275	-70.527
41.01822	-70.6154
41.01853	-70.5934
40.97025	-70.4602
40.98665	-70.4826
40.98693	-70.4606
40.9872	-70.4386
41.00304	-70.505
41.00332	-70.4829
41.0036	-70.4609
41.00415	-70.4169
41.00388	-70.4389
41.01883	-70.5714
41.01913	-70.5494
41.01943	-70.5274

Latitude	Longitude
41.01972	-70.5053
41.02	-70.4833
41.02028	-70.4613
41.0211	-70.3952
41.02083	-70.4173
41.02056	-70.4393
41.03521	-70.5938
41.03551	-70.5718
41.03581	-70.5498
41.0361	-70.5277
41.03639	-70.5057
41.03668	-70.4837
41.03696	-70.4617
41.03804	-70.3736
41.03778	-70.3956
41.03751	-70.4176
41.03724	-70.4396
41.05219	-70.5722
41.05249	-70.5502
41.05278	-70.5281
41.05307	-70.5061
41.05336	-70.4841
41.05364	-70.462
41.05472	-70.3739
41.05446	-70.3959
41.05419	-70.418
41.05391	-70.44
41.06916	-70.5506
41.06946	-70.5285
41.06975	-70.5065
41.07003	-70.4844
41.07032	-70.4624
41.0714	-70.3743
41.07114	-70.3963
41.07087	-70.4183
41.07059	-70.4404
41.08613	-70.5289
41.08642	-70.5069
41.08671	-70.4848
41.08699	-70.4628

Latitude	Longitude
41.08781	-70.3967
41.08754	-70.4187
41.08727	-70.4407
41.1031	-70.5072
41.10339	-70.4852
41.10367	-70.4632
41.10395	-70.4411
41.12035	-70.4635
41.12063	-70.4415
40.95931	-71.1201
40.96195	-71.0113
40.99476	-71.0544
40.9956	-70.9667
40.99799	-70.8792
41.01079	-71.1001
41.03023	-70.9463
41.03001	-70.9026
40.96082	-71.0322
41.01001	-71.1218
40.95706	-71.2741
40.95749	-71.2521
40.95792	-71.2301
40.95877	-71.1861
40.95918	-71.1641
40.95959	-71.1421
40.9604	-71.0982
40.9608	-71.0762
40.96119	-71.0542
40.97373	-71.2747
40.97417	-71.2527
40.97459	-71.2307
40.97502	-71.2087
40.97544	-71.1867
40.97585	-71.1647
40.97626	-71.1427
40.97667	-71.1207
40.97707	-71.0987
40.97747	-71.0767
40.97787	-71.0547
40.9904	-71.2752

Latitude	Longitude
40.99084	-71.2532
40.99169	-71.2092
40.99211	-71.1872
40.99252	-71.1652
40.99293	-71.1432
40.99374	-71.0992
40.99414	-71.0772
41.00707	-71.2758
41.00751	-71.2538
41.00836	-71.2098
41.00878	-71.1878
41.00919	-71.1658
41.00961	-71.1438
41.01082	-71.0777
41.04647	-70.9467
40.91156	-71.0307
40.91195	-71.0087
40.91233	-70.9867
40.92824	-71.0312
40.92862	-71.0092
40.929	-70.9872
40.92938	-70.9652
40.92975	-70.9432
40.94491	-71.0317
40.9453	-71.0097
40.94568	-70.9877
40.94605	-70.9657
40.94643	-70.9437
40.96235	-70.9882
40.96273	-70.9662
40.9631	-70.9442
40.96347	-70.9222
40.97826	-71.0327
40.97864	-71.0107
40.97902	-70.9887
40.9794	-70.9667
40.97977	-70.9447
40.98014	-70.9227
40.98051	-70.9007
40.99493	-71.0332

Latitude	Longitude
40.99531	-71.0112
40.9957	-70.9892
40.99645	-70.9452
40.99682	-70.9232
40.99718	-70.9012
41.0116	-71.0337
41.01199	-71.0117
41.01237	-70.9897
41.01275	-70.9677
41.01312	-70.9457
41.01349	-70.9237
41.01386	-70.9016
41.01422	-70.8796
41.02827	-71.0342
41.02866	-71.0122
41.02904	-70.9902
41.02942	-70.9682
41.03016	-70.9241
41.03089	-70.8801
41.01018	-71.0557
41.0279	-71.0554
41.02374	-71.2764
41.02418	-71.2544
41.0246	-71.2324
41.02503	-71.2104
41.02455	-71.1883
41.02497	-71.1663
41.02628	-71.1443
41.02669	-71.1223
41.0261	-71.1003
41.02749	-71.0783
41.07504	-71.212
41.0779	-71.0578
41.07829	-71.0358
41.07868	-71.0137
41.07906	-70.9917
41.07944	-70.9697
41.07982	-70.9476
41.09171	-71.2126
41.09457	-71.0583

Latitude	Longitude
41.09496	-71.0363
41.09535	-71.0143
41.09573	-70.9922
41.09611	-70.9702
41.09649	-70.9481
41.10753	-71.2572
41.10796	-71.2352
41.10838	-71.2131
41.11124	-71.0588
41.11164	-71.0368
41.11202	-71.0148
41.11241	-70.9927
41.11279	-70.9707
41.11316	-70.9486
41.11353	-70.9266
41.1139	-70.9045
41.11426	-70.8825
41.11462	-70.8604
41.11497	-70.8384
41.27675	-71.1304
41.26008	-71.1298
41.243	-71.1514
41.24341	-71.1293
41.24382	-71.1072
41.24422	-71.0851
41.24462	-71.063
41.22592	-71.1729
41.22633	-71.1508
41.22674	-71.1288
41.22715	-71.1067
41.22755	-71.0846
41.20883	-71.1944
41.20925	-71.1724
41.20966	-71.1503
41.21048	-71.1061
41.19173	-71.216
41.19216	-71.1939
41.19258	-71.1718
41.19299	-71.1497
41.1934	-71.1277

Latitude	Longitude
41.19381	-71.1056
41.17506	-71.2154
41.17549	-71.1933
41.1759	-71.1713
41.17632	-71.1492
41.17673	-71.1271
41.17713	-71.1051
41.15754	-71.2589
41.15797	-71.2369
41.15839	-71.2148
41.15882	-71.1928
41.15923	-71.1707
41.15965	-71.1487
41.16006	-71.1266
41.16046	-71.1045
41.16086	-71.0825
41.16126	-71.0604
41.16165	-71.0384
41.16204	-71.0163
41.16243	-70.9942
41.16281	-70.9722
41.16318	-70.9501
41.14339	-71.1261
41.14379	-71.104
41.14419	-71.0819
41.14459	-71.0599
41.14498	-71.0378
41.14537	-71.0158
41.14575	-70.9937
41.14613	-70.9717
41.14651	-70.9496
41.1242	-71.2578
41.12463	-71.2358
41.12505	-71.2137
41.12547	-71.1917
41.12671	-71.1255
41.12712	-71.1035
41.12752	-71.0814
41.12831	-71.0373
41.1287	-71.0153

Latitude	Longitude
41.12908	-70.9932
41.12946	-70.9712
41.12984	-70.9491
41.13021	-70.9271
41.13057	-70.905
41.13094	-70.883
41.13129	-70.8609
41.13165	-70.8389

Table A.7. Locations of Wind Turbine Generators for Partial Buildout comprising WTGs with COP

Latitude	Longitude
39.1204	-74.3032
39.1863	-74.1977
39.1646	-74.2349
39.2146	-74.2255
39.2006	-74.241
39.1893	-74.2583
39.1753	-74.2761
38.2864	-74.6818
38.3208	-74.7246
38.3702	-74.7651
38.3883	-74.7786
38.3883	-74.8443
36.14609	-75.0034
36.19296	-75.009
36.1991	-75.0208
36.20523	-75.0326
36.21136	-75.0444
36.2175	-75.0562
36.22363	-75.068
36.22977	-75.0798
36.2359	-75.0916
36.24203	-75.1034

Latitude	Longitude
36.24817	-75.1152
36.2543	-75.127
36.2045	-75.003
36.21063	-75.0148
36.21677	-75.0266
36.2229	-75.0384
36.22903	-75.0502
36.23517	-75.062
36.2413	-75.0738
36.24743	-75.0856
36.25357	-75.0974
36.2597	-75.1092
36.26584	-75.121
36.27197	-75.1328
36.42191	-75.0548
36.42805	-75.0666
36.2337	-75.0028
36.23983	-75.0146
36.24597	-75.0264
36.2521	-75.0382
36.25823	-75.05
36.26437	-75.0618
36.2705	-75.0736
36.27664	-75.0854
36.28277	-75.0972
36.2889	-75.109
36.29504	-75.1208
36.30117	-75.1326
36.25137	-75.0086
36.2575	-75.0204
36.26364	-75.0322
36.26977	-75.044
36.2759	-75.0558
36.28204	-75.0676
36.28817	-75.0794
36.2943	-75.0912
36.30044	-75.103
36.30657	-75.1148
36.31271	-75.1266
36.31884	-75.1384

Latitude	Longitude
36.2629	-75.0026
36.26904	-75.0144
36.27517	-75.0262
36.2813	-75.038
36.28744	-75.0498
36.29357	-75.0616
36.2997	-75.0734
36.30584	-75.0852
36.31197	-75.097
36.31811	-75.1088
36.32424	-75.1206
36.33037	-75.1324
36.37971	-75.0018
36.38584	-75.0136
36.41038	-75.0608
36.41651	-75.0726
36.42265	-75.0844
36.42878	-75.0962
36.36818	-75.0078
36.37431	-75.0196
36.38044	-75.0314
36.38658	-75.0432
36.39271	-75.055
36.39885	-75.0668
36.40498	-75.0786
36.41111	-75.0904
36.41725	-75.1022
36.42338	-75.114
36.16376	-75.0092
36.16989	-75.021
36.17603	-75.0328
36.1753	-75.0032
36.18143	-75.015
36.18756	-75.0268
36.1937	-75.0386
36.19983	-75.0504
36.20596	-75.0622
36.2121	-75.074
36.21823	-75.0858
36.35051	-75.002

Latitude	Longitude
36.35664	-75.0138
36.36278	-75.0256
36.36891	-75.0374
36.37504	-75.0492
36.38118	-75.061
36.38731	-75.0728
36.39345	-75.0846
36.39958	-75.0964
36.40571	-75.1082
36.41185	-75.12
36.41798	-75.1318
36.33897	-75.008
36.34511	-75.0198
36.35124	-75.0316
36.35738	-75.0434
36.36351	-75.0552
36.36964	-75.067
36.37578	-75.0788
36.38191	-75.0906
36.38804	-75.1024
36.39418	-75.1142
36.40031	-75.126
36.40645	-75.1378
36.22217	-75.0088
36.2283	-75.0206
36.23443	-75.0324
36.24057	-75.0442
36.2467	-75.056
36.25283	-75.0678
36.25897	-75.0796
36.2651	-75.0914
36.27124	-75.1032
36.27737	-75.115
36.2835	-75.1268
36.28964	-75.1386
36.32131	-75.0022
36.32744	-75.014
36.33357	-75.0258
36.33971	-75.0376
36.34584	-75.0494

Latitude	Longitude
36.35198	-75.0612
36.35811	-75.073
36.36424	-75.0848
36.37038	-75.0966
36.37651	-75.1084
36.38264	-75.1202
36.38878	-75.132
36.30977	-75.0082
36.31591	-75.02
36.32204	-75.0318
36.32817	-75.0436
36.33431	-75.0554
36.34044	-75.0672
36.34658	-75.079
36.35271	-75.0908
36.35884	-75.1026
36.36498	-75.1144
36.37111	-75.1262
36.2921	-75.0024
36.29824	-75.0142
36.30437	-75.026
36.31051	-75.0378
36.31664	-75.0496
36.32277	-75.0614
36.32891	-75.0732
36.33504	-75.085
36.34117	-75.0968
36.34731	-75.1086
36.35344	-75.1204
36.35958	-75.1322
36.28057	-75.0084
36.2867	-75.0202
36.29284	-75.032
36.29897	-75.0438
36.30511	-75.0556
36.31124	-75.0674
36.31737	-75.0792
36.32351	-75.091
36.32964	-75.1028
36.33577	-75.1146

Latitude	Longitude
36.34191	-75.1264
36.34804	-75.1382
40.2261	-73.1773
40.958	-71.208
40.991	-71.231
40.993	-71.121
41.008	-71.232
41.01	-71.122
41.015	-70.858
41.015	-70.836
41.027	-71.122
41.031	-70.858
41.032	-70.836
41.041	-71.255
41.041	-71.233
41.042	-71.211
41.064	-70.881
41.065	-70.859
41.065	-70.837
41.082	-70.837
41.075	-71.19
41.076	-71.168
41.076	-71.146
41.077	-71.124
41.077	-71.102
41.077	-71.08
41.092	-71.191
41.093	-71.169
41.093	-71.146
41.093	-71.124
41.094	-71.102
41.094	-71.08
41.109	-71.191
41.109	-71.169
41.11	-71.147
41.11	-71.125
41.11	-71.103
41.111	-71.081
41.29	-71.286
41.228	-71.063

Latitude	Longitude
41.21	-71.128
41.128	-71.059
40.878	-71.03
40.879	-71.008
40.895	-71.03
40.895	-71.008
40.896	-70.986
40.896	-70.964
40.913	-70.965
40.913	-70.943
40.93	-70.921
40.947	-70.922
40.964	-70.9
40.981	-70.879
40.998	-70.857
40.998	-70.835
41.082	-70.815
41.099	-70.794
41.12	-70.486
40.62	-70.474
40.806	-70.237
40.636	-70.54
40.653	-70.519
40.72	-70.455
39.02716	-74.2845
39.03708	-74.2952
39.0473	-74.3062
39.05752	-74.3172
39.06775	-74.3282
39.07796	-74.3392
39.08818	-74.3503
39.0984	-74.3613
39.10862	-74.3723
39.03759	-74.2678
39.04781	-74.2788
39.05804	-74.2898
39.06826	-74.3008
39.07848	-74.3118
39.0887	-74.3229
39.09892	-74.3339

Latitude	Longitude
39.10914	-74.3449
39.11936	-74.3559
39.1301	-74.3395
39.11988	-74.3285
39.10966	-74.3175
39.09944	-74.3065
39.08922	-74.2954
39.07899	-74.2844
39.06877	-74.2734
39.05854	-74.2624
39.04832	-74.2514
39.05904	-74.235
39.06927	-74.246
39.0795	-74.257
39.08972	-74.268
39.09995	-74.279
39.11017	-74.2901
39.13062	-74.3121
39.14084	-74.3231
39.15157	-74.3067
39.14135	-74.2957
39.13113	-74.2847
39.1209	-74.2737
39.11068	-74.2626
39.10045	-74.2516
39.09022	-74.2406
39.07999	-74.2296
39.06977	-74.2186
39.08049	-74.2022
39.09072	-74.2132
39.10095	-74.2242
39.11118	-74.2352
39.1214	-74.2462
39.13163	-74.2572
39.14186	-74.2683
39.15208	-74.2793
39.16231	-74.2903
39.16281	-74.2629
39.15258	-74.2519
39.14236	-74.2408

Latitude	Longitude
39.13213	-74.2298
39.1219	-74.2188
39.11167	-74.2078
39.10144	-74.1968
39.09121	-74.1858
39.11361	-74.1781
39.12383	-74.1892
39.13405	-74.2002
39.14426	-74.2112
39.15448	-74.2223
39.17491	-74.2443
39.02736	-74.2568
39.03809	-74.2404
39.04881	-74.224
39.05953	-74.2076
39.07025	-74.1912
39.08097	-74.1748
39.09316	-74.1561
39.10339	-74.1671
39.11485	-74.1495
39.12508	-74.1606
39.13531	-74.1716
39.14553	-74.1826
39.15576	-74.1936
39.16599	-74.2046
39.17621	-74.2157
39.18643	-74.2267
39.19722	-74.2102
39.17696	-74.1878
39.16682	-74.1767
39.15669	-74.1655
39.14655	-74.1543
39.13642	-74.1432
39.12628	-74.132
39.13699	-74.1156
39.14713	-74.1267
39.15726	-74.1379
39.1674	-74.1491
39.17754	-74.1602
39.18767	-74.1714

Latitude	Longitude
39.19781	-74.1826
39.20794	-74.1937
36.3712	-75.1422
36.2658	-75.1428
36.30932	-75.1452
36.35284	-75.1475
36.29096	-75.1505
36.33448	-75.1529
36.2726	-75.1558
36.31612	-75.1582
36.35964	-75.1605
36.29776	-75.1635
36.34128	-75.1659
36.32292	-75.1712
36.30456	-75.1765
36.41472	-75.1446
36.39636	-75.1499
36.378	-75.1552
36.42152	-75.1576
36.40316	-75.1629
36.3848	-75.1682
36.42832	-75.1706
36.36644	-75.1736
36.40996	-75.1759
36.34808	-75.1789
36.3916	-75.1813
36.32972	-75.1842
36.37324	-75.1866
36.41676	-75.189
36.35488	-75.1919
36.3984	-75.1943
36.33652	-75.1972
36.38004	-75.1996
36.42356	-75.202
36.36168	-75.2049
36.4052	-75.2073
36.34332	-75.2102
36.38684	-75.2126
36.43035	-75.215
36.36847	-75.2179

Latitude	Longitude
36.41199	-75.2203
36.35011	-75.2232
36.39363	-75.2256
36.37527	-75.2309
36.41879	-75.2334
36.35691	-75.2363
36.40042	-75.2387
36.38206	-75.244
36.42558	-75.2464
36.3637	-75.2493
36.40722	-75.2517
36.38885	-75.257
36.43237	-75.2594
36.37049	-75.2623
36.41401	-75.2647
36.39564	-75.27
36.43916	-75.2725
36.42079	-75.2778
36.46431	-75.2802
36.40243	-75.2831
36.44595	-75.2855
36.42758	-75.2908
36.4711	-75.2932
36.40922	-75.2961
36.45273	-75.2985
36.43437	-75.3038
36.416	-75.3091
36.45952	-75.3116
36.44115	-75.3169
36.42279	-75.3222
36.4663	-75.3246
36.44793	-75.3299
36.97739	-75.4557
36.97735	-75.4235
36.99325	-75.2541
36.99322	-75.2697
36.99318	-75.2853
36.99314	-75.3009
36.9931	-75.3164
36.99306	-75.332

Latitude	Longitude
36.99302	-75.3476
36.99276	-75.4255
36.99271	-75.4411
36.9779	-75.221
36.97787	-75.2366
36.97783	-75.2522
36.9778	-75.2678
36.97776	-75.2833
36.97768	-75.3145
36.97764	-75.33
36.9776	-75.3456
36.97729	-75.4391
36.96247	-75.2191
36.96244	-75.2347
36.9624	-75.2502
36.96237	-75.2658
36.96233	-75.2814
36.96226	-75.3125
36.96222	-75.3281
36.96217	-75.3437
36.96212	-75.3592
36.96208	-75.3748
36.96203	-75.3904
36.96197	-75.4059
36.96192	-75.4215
36.96186	-75.4371
36.96181	-75.4526
36.96175	-75.4682
36.94698	-75.2483
36.94694	-75.2638
36.94691	-75.2794
36.94687	-75.295
36.94683	-75.3105
36.94679	-75.3261
36.9467	-75.3572
36.94665	-75.3728
36.9466	-75.3884
36.94655	-75.4039
36.94649	-75.4195
36.94644	-75.4351

Latitude	Longitude
36.94638	-75.4506
36.94632	-75.4662
36.94626	-75.4818
36.93158	-75.2308
36.93155	-75.2463
36.93151	-75.2619
36.93148	-75.2775
36.93144	-75.293
36.9314	-75.3086
36.93136	-75.3241
36.93132	-75.3397
36.93127	-75.3553
36.93122	-75.3708
36.93117	-75.3864
36.93112	-75.402
36.93107	-75.4175
36.93101	-75.4331
36.93096	-75.4486
36.9309	-75.4642
36.93083	-75.4798
36.91616	-75.2288
36.91613	-75.2444
36.91609	-75.2599
36.91606	-75.2755
36.91598	-75.3066
36.91594	-75.3222
36.9159	-75.3377
36.91585	-75.3533
36.91581	-75.3689
36.91576	-75.3844
36.91571	-75.4
36.9156	-75.4311
36.91554	-75.4466
36.91548	-75.4622
36.91542	-75.4778
36.90073	-75.2269
36.90067	-75.258
36.90063	-75.2735
36.90056	-75.3047
36.90051	-75.3202

Latitude	Longitude
36.90047	-75.3358
36.90033	-75.3824
36.90028	-75.398
36.90023	-75.4135
36.90017	-75.4291
36.90011	-75.4447
36.90005	-75.4602
36.89999	-75.4758
36.8853	-75.2249
36.88527	-75.2405
36.88524	-75.256
36.8852	-75.2716
36.88517	-75.2871
36.88509	-75.3182
36.88504	-75.3338
36.8849	-75.3805
36.8848	-75.4116
36.88475	-75.4271
36.88469	-75.4427
36.88463	-75.4582
36.88457	-75.4738
36.86987	-75.223
36.86984	-75.2385
36.86981	-75.2541
36.86977	-75.2696
36.86974	-75.2852
36.8697	-75.3007
36.86966	-75.3163
36.86962	-75.3318
36.86957	-75.3474
36.86953	-75.3629
36.86948	-75.3785
36.86943	-75.394
36.86937	-75.4096
36.86932	-75.4251
36.86926	-75.4407
36.8692	-75.4562
36.86914	-75.4718
36.85445	-75.221
36.85442	-75.2366

Latitude	Longitude
36.85439	-75.2521
36.85435	-75.2677
36.85432	-75.2832
36.85428	-75.2988
36.85424	-75.3143
36.8542	-75.3299
36.85411	-75.3609
36.85406	-75.3765
36.85401	-75.392
36.85396	-75.4076
36.8539	-75.4231
36.85385	-75.4387
36.85379	-75.4542
36.85373	-75.4698
36.83902	-75.2191
36.83899	-75.2346
36.83896	-75.2502
36.83893	-75.2657
36.83889	-75.2813
36.83885	-75.2968
36.83881	-75.3123
36.83877	-75.3279
36.83873	-75.3434
36.83868	-75.359
36.83863	-75.3745
36.83858	-75.3901
36.83853	-75.4056
36.83848	-75.4212
36.83842	-75.4367
36.83836	-75.4522
36.8383	-75.4678
36.82359	-75.2171
36.82356	-75.2327
36.82353	-75.2482
36.8235	-75.2638
36.82346	-75.2793
36.82342	-75.2948
36.82338	-75.3104
36.82334	-75.3259
36.8233	-75.3415

Latitude	Longitude
36.82325	-75.357
36.82321	-75.3725
36.82316	-75.3881
36.8231	-75.4036
36.82305	-75.4192
36.82299	-75.4347
36.82294	-75.4502
36.82288	-75.4658
36.99282	-75.4099
36.99287	-75.3943
36.99292	-75.3788
36.99297	-75.3632
36.97755	-75.3612
36.9775	-75.3768
36.97745	-75.3923
36.9774	-75.4079
36.99332	-75.223
36.99329	-75.2386
36.99265	-75.4566
36.97772	-75.2989
36.97717	-75.4702
36.9623	-75.2969
36.96168	-75.4838
36.94704	-75.2171
36.94701	-75.2327
36.94674	-75.3417
36.91602	-75.2911
36.91565	-75.4155
36.9007	-75.2424
36.90059	-75.2891
36.90043	-75.3513
36.90038	-75.3669
36.88513	-75.3027
36.885	-75.3493
36.88495	-75.3649
36.88485	-75.396
36.85415	-75.3454
36.88683	-75.4916
36.89629	-75.4916
38.30264	-74.6618

Latitude	Longitude
38.4379	-74.7868
38.30298	-74.8247
38.31985	-74.822
38.33672	-74.8193
38.35358	-74.8166
38.37045	-74.8139
38.38732	-74.8112
38.40419	-74.8086
38.42106	-74.8058
38.43792	-74.8031
38.45479	-74.8004
38.31987	-74.8383
38.33674	-74.8356
38.35361	-74.833
38.37048	-74.8303
38.38734	-74.8276
38.40421	-74.8249
38.42108	-74.8222
38.43795	-74.8195
38.45482	-74.8168
38.31989	-74.8546
38.33676	-74.8519
38.35363	-74.8493
38.3705	-74.8466
38.40423	-74.8412
38.4211	-74.8385
38.43797	-74.8358
38.45484	-74.8331
38.38738	-74.8602
38.40425	-74.8575
38.42112	-74.8548
38.43799	-74.8521
38.45486	-74.8494
38.286	-74.7623
38.30287	-74.7595
38.31974	-74.7568
38.3366	-74.7541
38.35347	-74.7514
38.37034	-74.7487
38.3872	-74.746

Latitude	Longitude
38.40407	-74.7433
38.42094	-74.7406
38.28603	-74.7785
38.3029	-74.7758
38.31977	-74.7731
38.33664	-74.7704
38.3535	-74.7677
38.38724	-74.7623
38.4041	-74.7596
38.42097	-74.7569
38.30293	-74.7921
38.3198	-74.7894
38.33666	-74.7867
38.35353	-74.784
38.3704	-74.7813
38.40413	-74.7759
38.421	-74.7732
38.43787	-74.7705
38.30296	-74.8084
38.31982	-74.8057
38.33669	-74.803
38.35356	-74.8003
38.37043	-74.7976
38.38729	-74.7949
38.40416	-74.7922
38.42103	-74.7895
38.28586	-74.6971
38.30273	-74.6944
38.31959	-74.6916
38.33646	-74.6889
38.35332	-74.6862
38.25217	-74.7188
38.26903	-74.7161
38.2859	-74.7134
38.30276	-74.7107
38.31963	-74.7079
38.3365	-74.7052
38.35336	-74.7025
38.37023	-74.6998
38.2522	-74.7351

Latitude	Longitude
38.26907	-74.7324
38.28594	-74.7297
38.3028	-74.727
38.33653	-74.7215
38.3534	-74.7188
38.37027	-74.7161
38.38713	-74.7134
38.25224	-74.7514
38.2691	-74.7487
38.28597	-74.746
38.30284	-74.7433
38.3197	-74.7405
38.33657	-74.7378
38.35344	-74.7351
38.3703	-74.7324
38.38717	-74.7297
38.40403	-74.727
38.25227	-74.7677
38.26914	-74.765
38.25185	-74.6048
38.2519	-74.6211
38.26877	-74.6184
38.25195	-74.6374
38.26882	-74.6347
38.28568	-74.6319
38.252	-74.6537
38.26886	-74.651
38.28573	-74.6482
38.30259	-74.6455
38.25204	-74.67
38.26891	-74.6672
38.28577	-74.6645
38.3195	-74.6591
38.25209	-74.6863
38.26895	-74.6835
38.30268	-74.6781
38.31955	-74.6753
38.33641	-74.6726
38.25213	-74.7025
38.26899	-74.6998

Latitude	Longitude
39.31653	-73.9432
39.31491	-73.9559
39.31328	-73.9687
39.29812	-73.955
39.29649	-73.9677
39.28133	-73.9541
39.2797	-73.9668
39.26454	-73.9531
39.26291	-73.9658
39.37103	-74.177
39.36938	-74.1898
39.37066	-74.0488
39.36902	-74.0615
39.36739	-74.0743
39.36575	-74.087
39.36411	-74.0997
39.36247	-74.1124
39.36083	-74.1252
39.35918	-74.1379
39.35754	-74.1506
39.35589	-74.1633
39.35424	-74.176
39.35259	-74.1888
39.3555	-74.0351
39.35387	-74.0478
39.35224	-74.0606
39.3506	-74.0733
39.34896	-74.086
39.34732	-74.0987
39.34568	-74.1115
39.34404	-74.1242
39.34239	-74.1369
39.34075	-74.1496
39.3391	-74.1623
39.33745	-74.175
39.34035	-74.0214
39.33871	-74.0342
39.33708	-74.0469
39.33545	-74.0596
39.33381	-74.0723

Latitude	Longitude
39.33217	-74.085
39.33053	-74.0978
39.32889	-74.1105
39.32725	-74.1232
39.3256	-74.1359
39.32396	-74.1486
39.32231	-74.1613
39.32067	-74.1741
39.31902	-74.1868
39.32519	-74.0078
39.32356	-74.0205
39.32192	-74.0332
39.32029	-74.0459
39.31866	-74.0586
39.31702	-74.0713
39.31538	-74.0841
39.31374	-74.0968
39.3121	-74.1095
39.31046	-74.1222
39.30882	-74.1349
39.30717	-74.1476
39.30552	-74.1603
39.30388	-74.1731
39.30223	-74.1858
39.30058	-74.1985
39.29893	-74.2112
39.29727	-74.2239
39.29562	-74.2366
39.31166	-73.9814
39.31003	-73.9941
39.3084	-74.0068
39.30677	-74.0195
39.30513	-74.0322
39.3035	-74.045
39.30187	-74.0577
39.30023	-74.0704
39.29859	-74.0831
39.29695	-74.0958
39.29531	-74.1085
39.29367	-74.1212

Latitude	Longitude
39.29203	-74.1339
39.29038	-74.1466
39.28874	-74.1594
39.28709	-74.1721
39.28544	-74.1848
39.28379	-74.1975
39.28214	-74.2102
39.28048	-74.2229
39.27883	-74.2356
39.27717	-74.2483
39.29487	-73.9804
39.29324	-73.9931
39.29161	-74.0059
39.28998	-74.0186
39.28834	-74.0313
39.28671	-74.044
39.28508	-74.0567
39.28344	-74.0694
39.2818	-74.0821
39.28016	-74.0948
39.27852	-74.1075
39.27688	-74.1202
39.27524	-74.133
39.27359	-74.1457
39.27195	-74.1584
39.2703	-74.1711
39.26865	-74.1838
39.267	-74.1965
39.26535	-74.2092
39.27808	-73.9795
39.27645	-73.9922
39.27482	-74.0049
39.27319	-74.0176
39.27155	-74.0303
39.26992	-74.043
39.26829	-74.0557
39.26665	-74.0684
39.26501	-74.0811
39.26337	-74.0939
39.26173	-74.1066

Latitude	Longitude
39.26009	-74.1193
39.25845	-74.132
39.2568	-74.1447
39.25516	-74.1574
39.25351	-74.1701
39.25186	-74.1828
39.26128	-73.9785
39.25966	-73.9912
39.25803	-74.0039
39.2564	-74.0167
39.25476	-74.0294
39.25313	-74.0421
39.2515	-74.0548
39.24986	-74.0675
39.24822	-74.0802
39.24658	-74.0929
39.24494	-74.1056
39.2433	-74.1183
39.24166	-74.131
39.24001	-74.1437
39.23837	-74.1564
39.23672	-74.1691
39.23507	-74.1818
39.24449	-73.9776
39.24287	-73.9903
39.24124	-74.003
39.23961	-74.0157
39.23797	-74.0284
39.23634	-74.0411
39.23471	-74.0538
39.23307	-74.0665
39.23143	-74.0792
39.22979	-74.0919
39.22815	-74.1046
39.22651	-74.1173
39.22487	-74.13
39.22322	-74.1427
39.22158	-74.1554
39.21993	-74.1681
39.21828	-74.1808

Latitude	Longitude
39.21663	-74.1935
39.22445	-74.002
39.22282	-74.0147
39.22118	-74.0274
39.21955	-74.0401
39.21792	-74.0528
39.21628	-74.0655
39.21464	-74.0782
39.213	-74.0909
39.21136	-74.1036
39.20972	-74.1163
39.20808	-74.129
39.20643	-74.1417
39.20479	-74.1544
39.20314	-74.1671
39.20603	-74.0138
39.20439	-74.0265
39.20276	-74.0392
39.20113	-74.0519
39.19949	-74.0646
39.19785	-74.0773
39.19621	-74.09
39.19457	-74.1027
39.19293	-74.1153
39.19129	-74.128
39.18964	-74.1407
39.18434	-74.0509
39.1827	-74.0636
39.18106	-74.0763
39.17942	-74.089
39.17778	-74.1017
39.17614	-74.1144
39.1745	-74.1271
39.16591	-74.0626
39.16427	-74.0753
39.16263	-74.088
39.16099	-74.1007
39.15935	-74.1134
39.14584	-74.087
40.31535	-73.2611

Latitude	Longitude
40.30686	-73.2757
40.29837	-73.2902
40.28987	-73.3048
40.28138	-73.3194
40.27288	-73.334
40.26608	-73.3485
40.29286	-73.0893
40.27893	-73.1041
40.29569	-73.1036
40.26836	-73.1187
40.28722	-73.1182
40.29851	-73.1179
40.25788	-73.1334
40.27874	-73.1328
40.29004	-73.1325
40.30133	-73.1322
40.24769	-73.148
40.25898	-73.1477
40.27027	-73.1474
40.28156	-73.1471
40.29286	-73.1468
40.30372	-73.1465
40.2505	-73.1623
40.2618	-73.162
40.27264	-73.1617
40.28438	-73.1614
40.29567	-73.161
40.24202	-73.1768
40.25332	-73.1765
40.26461	-73.1762
40.27545	-73.176
40.2872	-73.1756
40.29849	-73.1753
40.21547	-73.1919
40.23354	-73.1914
40.24484	-73.1911
40.25613	-73.1908
40.26743	-73.1905
40.27872	-73.1902
40.29001	-73.1899

Latitude	Longitude
40.3013	-73.1896
40.2048	-73.2065
40.22506	-73.206
40.23636	-73.2057
40.24765	-73.2054
40.25894	-73.2051
40.27024	-73.2048
40.28153	-73.2045
40.29282	-73.2042
40.30412	-73.2039
40.20255	-73.2209
40.21658	-73.2206
40.22787	-73.2203
40.23917	-73.22
40.25046	-73.2197
40.26175	-73.2194
40.27305	-73.2191
40.28434	-73.2188
40.29563	-73.2185
40.30693	-73.2182
40.21263	-73.235
40.23068	-73.2345
40.24197	-73.2343
40.25327	-73.234
40.26456	-73.2337
40.27586	-73.2334
40.29844	-73.2328
40.30974	-73.2325
40.22209	-73.2491
40.23349	-73.2488
40.24478	-73.2485
40.25562	-73.2483
40.26737	-73.2479
40.27866	-73.2477
40.28996	-73.2474
40.30125	-73.2471
40.31254	-73.2468
40.22838	-73.2633
40.24759	-73.2628
40.25888	-73.2625

Latitude	Longitude
40.27017	-73.2622
40.28147	-73.2619
40.29276	-73.2617
40.30405	-73.2614
40.23467	-73.2775
40.25039	-73.2771
40.26123	-73.2768
40.27298	-73.2765
40.28427	-73.2762
40.29556	-73.2759
40.24095	-73.2917
40.25319	-73.2914
40.26448	-73.2911
40.27578	-73.2908
40.28707	-73.2905
40.24723	-73.3059
40.26728	-73.3054
40.27858	-73.3051
40.25352	-73.3201
40.27008	-73.3197
40.2598	-73.3343
40.31815	-73.2754
40.30966	-73.29
40.32095	-73.2897
40.30117	-73.3045
40.31246	-73.3042
40.32375	-73.304
40.29267	-73.3191
40.30396	-73.3188
40.31526	-73.3185
40.32655	-73.3183
40.28417	-73.3337
40.29547	-73.3334
40.30676	-73.3331
40.31805	-73.3328
40.32935	-73.3326
40.27567	-73.3482
40.29826	-73.3477
40.30956	-73.3474
40.32085	-73.3471

Latitude	Longitude
40.33214	-73.3469
40.27213	-73.3627
40.28976	-73.3623
40.30105	-73.362
40.31235	-73.3617
40.32364	-73.3614
40.33494	-73.3612
40.2784	-73.3769
40.29255	-73.3766
40.30385	-73.3763
40.31514	-73.376
40.32643	-73.3757
40.33773	-73.3755
40.28468	-73.3911
40.29566	-73.3908
40.30663	-73.3906
40.31793	-73.3903
40.32922	-73.39
40.34052	-73.3898
40.29095	-73.4053
40.30942	-73.4049
40.32072	-73.4046
40.33201	-73.4043
40.34331	-73.4041
40.29722	-73.4195
40.31221	-73.4192
40.3235	-73.4189
40.3348	-73.4187
40.34609	-73.4184
40.30349	-73.4337
40.31499	-73.4335
40.32629	-73.4332
40.33758	-73.433
40.34888	-73.4327
40.30976	-73.448
40.35166	-73.447
40.31602	-73.4622
40.35444	-73.4613
40.32228	-73.4764
40.35722	-73.4756

Latitude	Longitude
40.32855	-73.4906
40.36	-73.4899
40.33481	-73.5049
40.36277	-73.5043
40.34106	-73.5191
40.36554	-73.5186
40.34732	-73.5333
40.36832	-73.5329
40.35358	-73.5476
40.37109	-73.5472
40.35983	-73.5618
40.37386	-73.5615
40.60276	-70.4959
40.60248	-70.5178
40.61944	-70.4963
40.61916	-70.5182
40.63668	-70.4529
40.6364	-70.4748
40.63612	-70.4967
40.63583	-70.5186
40.63525	-70.5624
40.63495	-70.5843
40.63465	-70.6062
40.63434	-70.628
40.65363	-70.4314
40.65336	-70.4533
40.65308	-70.4752
40.6528	-70.4971
40.65222	-70.5409
40.65193	-70.5628
40.65163	-70.5847
40.65133	-70.6066
40.65102	-70.6285
40.67058	-70.4098
40.67031	-70.4317
40.67004	-70.4536
40.66976	-70.4755
40.66948	-70.4974
40.66919	-70.5193
40.6689	-70.5412

Latitude	Longitude
40.66861	-70.5631
40.66831	-70.5851
40.66801	-70.607
40.68753	-70.3883
40.68726	-70.4102
40.68699	-70.4321
40.68672	-70.454
40.68644	-70.4759
40.68616	-70.4978
40.68587	-70.5197
40.68558	-70.5416
40.68528	-70.5635
40.68499	-70.5854
40.70447	-70.3667
40.70421	-70.3886
40.70394	-70.4105
40.70367	-70.4324
40.7034	-70.4544
40.70312	-70.4763
40.70283	-70.4982
40.70255	-70.5201
40.70226	-70.542
40.70196	-70.5639
40.7214	-70.3451
40.72115	-70.367
40.72088	-70.389
40.72062	-70.4109
40.72035	-70.4328
40.7198	-70.4766
40.71951	-70.4986
40.71923	-70.5205
40.71894	-70.5424
40.73834	-70.3235
40.73808	-70.3454
40.73783	-70.3674
40.73756	-70.3893
40.7373	-70.4112
40.73703	-70.4332
40.73675	-70.4551
40.73647	-70.477

Latitude	Longitude
40.73619	-70.4989
40.7359	-70.5209
40.75527	-70.3019
40.75502	-70.3238
40.75476	-70.3458
40.7545	-70.3677
40.75424	-70.3896
40.75398	-70.4116
40.75371	-70.4335
40.75343	-70.4554
40.75315	-70.4774
40.75287	-70.4993
40.77219	-70.2803
40.77195	-70.3022
40.7717	-70.3242
40.77144	-70.3461
40.77118	-70.3681
40.77092	-70.39
40.77066	-70.4119
40.77038	-70.4339
40.77011	-70.4558
40.76983	-70.4777
40.78911	-70.2587
40.78887	-70.2806
40.78862	-70.3026
40.78838	-70.3245
40.78812	-70.3465
40.78786	-70.3684
40.7876	-70.3903
40.78733	-70.4123
40.78706	-70.4342
40.78679	-70.4562
40.80579	-70.259
40.80555	-70.2809
40.8053	-70.3029
40.80505	-70.3248
40.8048	-70.3468
40.80454	-70.3687
40.80428	-70.3907
40.80401	-70.4126

Latitude	Longitude
40.80374	-70.4346
40.82294	-70.2154
40.82271	-70.2373
40.82247	-70.2593
40.82223	-70.2813
40.82198	-70.3032
40.82173	-70.3252
40.82148	-70.3471
40.82122	-70.3691
40.82096	-70.391
40.82069	-70.413
40.83915	-70.2596
40.83891	-70.2816
40.83866	-70.3035
40.83841	-70.3255
40.83816	-70.3475
40.8379	-70.3694
40.83764	-70.3914
40.85583	-70.2599
40.85559	-70.2819
40.85534	-70.3039
40.85509	-70.3258
40.85484	-70.3478
40.85458	-70.3698
40.87251	-70.2602
40.87227	-70.2822
40.87202	-70.3042
40.87177	-70.3262
40.87152	-70.3481
40.88919	-70.2606
40.88895	-70.2825
40.8887	-70.3045
40.88845	-70.3265
40.90587	-70.2609
40.90563	-70.2829
40.90538	-70.3049
40.92255	-70.2612
40.92231	-70.2832
40.74948	-70.7405
40.76616	-70.741

Latitude	Longitude
40.76649	-70.719
40.78284	-70.7414
40.78316	-70.7195
40.78349	-70.6975
40.79951	-70.7418
40.79984	-70.7199
40.80017	-70.698
40.80049	-70.676
40.81619	-70.7423
40.81652	-70.7203
40.81684	-70.6984
40.81716	-70.6764
40.81748	-70.6545
40.83286	-70.7427
40.83319	-70.7208
40.83352	-70.6988
40.83384	-70.6768
40.83416	-70.6549
40.83447	-70.6329
40.84818	-70.831
40.84853	-70.809
40.84887	-70.7871
40.84921	-70.7651
40.84954	-70.7432
40.84987	-70.7212
40.8502	-70.6992
40.85052	-70.6773
40.85083	-70.6553
40.85115	-70.6333
40.85146	-70.6114
40.8652	-70.8095
40.86554	-70.7875
40.86588	-70.7656
40.86622	-70.7436
40.86655	-70.7216
40.86687	-70.6997
40.86719	-70.6777
40.86751	-70.6557
40.86782	-70.6338
40.86813	-70.6118

Latitude	Longitude
40.86844	-70.5898
40.88222	-70.788
40.88256	-70.766
40.88289	-70.744
40.88322	-70.7221
40.88355	-70.7001
40.88387	-70.6781
40.88419	-70.6561
40.8845	-70.6342
40.88481	-70.6122
40.88512	-70.5902
40.88542	-70.5682
40.89923	-70.7664
40.89957	-70.7445
40.8999	-70.7225
40.90022	-70.7005
40.90055	-70.6785
40.90086	-70.6566
40.90118	-70.6346
40.90149	-70.6126
40.90179	-70.5906
40.90209	-70.5686
40.90239	-70.5467
40.91624	-70.7449
40.91657	-70.7229
40.9169	-70.7009
40.91722	-70.679
40.91754	-70.657
40.91785	-70.635
40.91816	-70.613
40.91847	-70.591
40.91877	-70.569
40.91907	-70.547
40.91936	-70.5251
40.93325	-70.7234
40.93358	-70.7014
40.9339	-70.6794
40.93422	-70.6574
40.93453	-70.6354
40.93484	-70.6134

Latitude	Longitude
40.93515	-70.5914
40.93545	-70.5694
40.93575	-70.5474
40.93604	-70.5254
40.93633	-70.5034
40.95025	-70.7018
40.95057	-70.6798
40.95089	-70.6578
40.95121	-70.6358
40.95152	-70.6138
40.95182	-70.5918
40.95213	-70.5698
40.95242	-70.5478
40.95272	-70.5258
40.953	-70.5038
40.95329	-70.4818
40.96725	-70.6802
40.96757	-70.6582
40.96788	-70.6362
40.96819	-70.6142
40.9685	-70.5922
40.9688	-70.5702
40.9691	-70.5482
40.96939	-70.5262
40.96968	-70.5042
40.96997	-70.4822
40.98425	-70.6586
40.98456	-70.6366
40.98487	-70.6146
40.98518	-70.5926
40.98548	-70.5706
40.98578	-70.5486
40.98607	-70.5266
40.98636	-70.5046
41.00124	-70.637
41.00155	-70.615
41.00185	-70.593
41.00216	-70.571
41.00245	-70.549
41.00275	-70.527

Latitude	Longitude
41.01822	-70.6154
41.01853	-70.5934
40.97025	-70.4602
40.98665	-70.4826
40.98693	-70.4606
40.9872	-70.4386
41.00304	-70.505
41.00332	-70.4829
41.0036	-70.4609
41.00415	-70.4169
41.00388	-70.4389
41.01883	-70.5714
41.01913	-70.5494
41.01943	-70.5274
41.01972	-70.5053
41.02	-70.4833
41.02028	-70.4613
41.0211	-70.3952
41.02083	-70.4173
41.02056	-70.4393
41.03521	-70.5938
41.03551	-70.5718
41.03581	-70.5498
41.0361	-70.5277
41.03639	-70.5057
41.03668	-70.4837
41.03696	-70.4617
41.03804	-70.3736
41.03778	-70.3956
41.03751	-70.4176
41.03724	-70.4396
41.05219	-70.5722
41.05249	-70.5502
41.05278	-70.5281
41.05307	-70.5061
41.05336	-70.4841
41.05364	-70.462
41.05472	-70.3739
41.05446	-70.3959
41.05419	-70.418

Latitude	Longitude
41.05391	-70.44
41.06916	-70.5506
41.06946	-70.5285
41.06975	-70.5065
41.07003	-70.4844
41.07032	-70.4624
41.0714	-70.3743
41.07114	-70.3963
41.07087	-70.4183
41.07059	-70.4404
41.08613	-70.5289
41.08642	-70.5069
41.08671	-70.4848
41.08699	-70.4628
41.08781	-70.3967
41.08754	-70.4187
41.08727	-70.4407
41.1031	-70.5072
41.10339	-70.4852
41.10367	-70.4632
41.10395	-70.4411
41.12035	-70.4635
41.12063	-70.4415
41.13703	-70.4639
40.95931	-71.1201
40.96195	-71.0113
40.99476	-71.0544
40.9956	-70.9667
40.99799	-70.8792
41.01079	-71.1001
41.03023	-70.9463
41.03001	-70.9026
40.96082	-71.0322
40.95706	-71.2741
40.95749	-71.2521
40.95792	-71.2301
40.95877	-71.1861
40.95918	-71.1641
40.95959	-71.1421
40.9604	-71.0982

Latitude	Longitude
40.9608	-71.0762
40.96119	-71.0542
40.97373	-71.2747
40.97417	-71.2527
40.97459	-71.2307
40.97502	-71.2087
40.97544	-71.1867
40.97585	-71.1647
40.97626	-71.1427
40.97667	-71.1207
40.97707	-71.0987
40.97747	-71.0767
40.97787	-71.0547
40.9904	-71.2752
40.99084	-71.2532
40.99169	-71.2092
40.99211	-71.1872
40.99252	-71.1652
40.99293	-71.1432
40.99374	-71.0992
40.99414	-71.0772
41.00707	-71.2758
41.00751	-71.2538
41.00836	-71.2098
41.00878	-71.1878
41.00919	-71.1658
41.00961	-71.1438
41.01082	-71.0777
41.04647	-70.9467
40.91156	-71.0307
40.91195	-71.0087
40.91233	-70.9867
40.92824	-71.0312
40.92862	-71.0092
40.929	-70.9872
40.92938	-70.9652
40.92975	-70.9432
40.94491	-71.0317
40.9453	-71.0097
40.94568	-70.9877

Latitude	Longitude
40.94605	-70.9657
40.94643	-70.9437
40.96235	-70.9882
40.96273	-70.9662
40.9631	-70.9442
40.96347	-70.9222
40.97826	-71.0327
40.97864	-71.0107
40.97902	-70.9887
40.9794	-70.9667
40.97977	-70.9447
40.98014	-70.9227
40.98051	-70.9007
40.99493	-71.0332
40.99531	-71.0112
40.9957	-70.9892
40.99645	-70.9452
40.99682	-70.9232
40.99718	-70.9012
41.0116	-71.0337
41.01199	-71.0117
41.01237	-70.9897
41.01275	-70.9677
41.01312	-70.9457
41.01349	-70.9237
41.01386	-70.9016
41.01422	-70.8796
41.02827	-71.0342
41.02866	-71.0122
41.02904	-70.9902
41.02942	-70.9682
41.03016	-70.9241
41.03089	-70.8801
41.01018	-71.0557
41.0279	-71.0554
41.02374	-71.2764
41.02418	-71.2544
41.0246	-71.2324
41.02503	-71.2104
41.02455	-71.1883

Latitude	Longitude
41.02497	-71.1663
41.02628	-71.1443
41.0261	-71.1003
41.02749	-71.0783
41.07504	-71.212
41.0779	-71.0578
41.07829	-71.0358
41.07868	-71.0137
41.07906	-70.9917
41.07944	-70.9697
41.07982	-70.9476
41.09171	-71.2126
41.09457	-71.0583
41.09496	-71.0363
41.09535	-71.0143
41.09573	-70.9922
41.09611	-70.9702
41.09649	-70.9481
41.10753	-71.2572
41.10796	-71.2352
41.10838	-71.2131
41.11124	-71.0588
41.11164	-71.0368
41.11202	-71.0148
41.11241	-70.9927
41.11279	-70.9707
41.11316	-70.9486
41.11353	-70.9266
41.1139	-70.9045
41.11426	-70.8825
41.11462	-70.8604
41.11497	-70.8384
41.27675	-71.1304
41.26008	-71.1298
41.243	-71.1514

Latitude	Longitude
41.24341	-71.1293
41.24382	-71.1072
41.24422	-71.0851
41.24462	-71.063
41.22592	-71.1729
41.22633	-71.1508
41.22674	-71.1288
41.22715	-71.1067
41.22755	-71.0846
41.20883	-71.1944
41.20925	-71.1724
41.20966	-71.1503
41.21048	-71.1061
41.21088	-71.0841
41.21128	-71.062
41.19173	-71.216
41.19216	-71.1939
41.19258	-71.1718
41.19299	-71.1497
41.1934	-71.1277
41.19381	-71.1056
41.17506	-71.2154
41.17549	-71.1933
41.1759	-71.1713
41.17632	-71.1492
41.17673	-71.1271
41.17713	-71.1051
41.15754	-71.2589
41.15797	-71.2369
41.15839	-71.2148
41.15882	-71.1928
41.15923	-71.1707
41.15965	-71.1487
41.16006	-71.1266
41.16046	-71.1045

Latitude	Longitude
41.16086	-71.0825
41.16126	-71.0604
41.16165	-71.0384
41.16204	-71.0163
41.16243	-70.9942
41.16281	-70.9722
41.16318	-70.9501
41.14339	-71.1261
41.14379	-71.104
41.14419	-71.0819
41.14459	-71.0599
41.14498	-71.0378
41.14537	-71.0158
41.14575	-70.9937
41.14613	-70.9717
41.14651	-70.9496
41.1242	-71.2578
41.12463	-71.2358
41.12505	-71.2137
41.12547	-71.1917
41.12671	-71.1255
41.12712	-71.1035
41.12752	-71.0814
41.12831	-71.0373
41.1287	-71.0153
41.12908	-70.9932
41.12946	-70.9712
41.12984	-70.9491
41.13021	-70.9271
41.13057	-70.905
41.13094	-70.883
41.13129	-70.8609
41.13165	-70.8389

A.3 Additional Hydrodynamic Model Scenario 5: 15 MW Full Build-out Plots

A.3.1 Additional Hydrodynamic Model Scenario 5: 15 MW Full Build-out Thermal Stratification Plots

The effect of the WTGs on the sea surface wind stress can be seen in the vertical thermal stratification due to the slowing of the currents inside the OSW farms. The most effect is from the 15 MW full build-out scenario. The following figures show the results for the OSW developments not included in the main report.

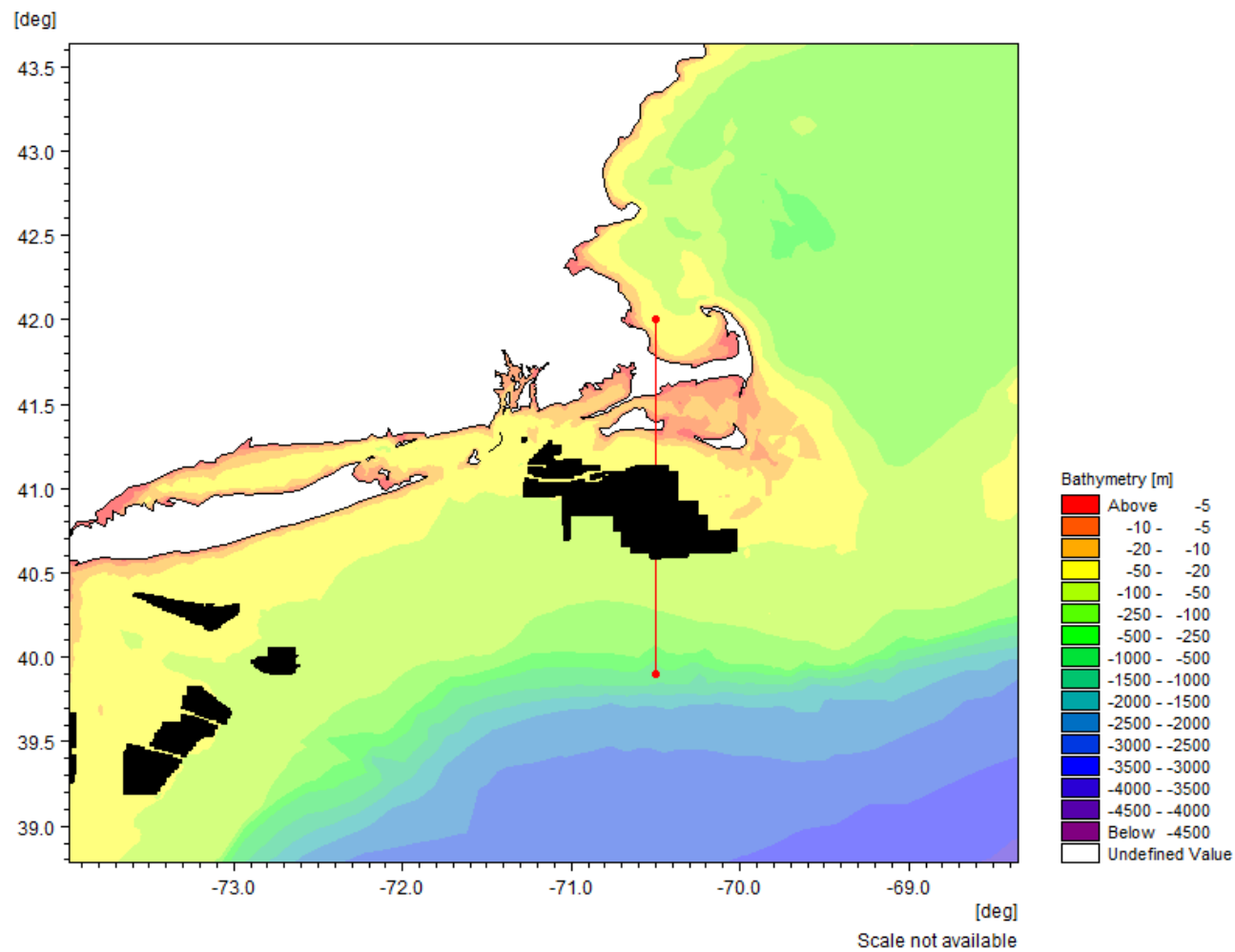


Figure A.107. Thermal Transect Location MA-RI

The figure shows the transect through one set of the MA-RI OSW farms with a line orientation from the South and headed North.

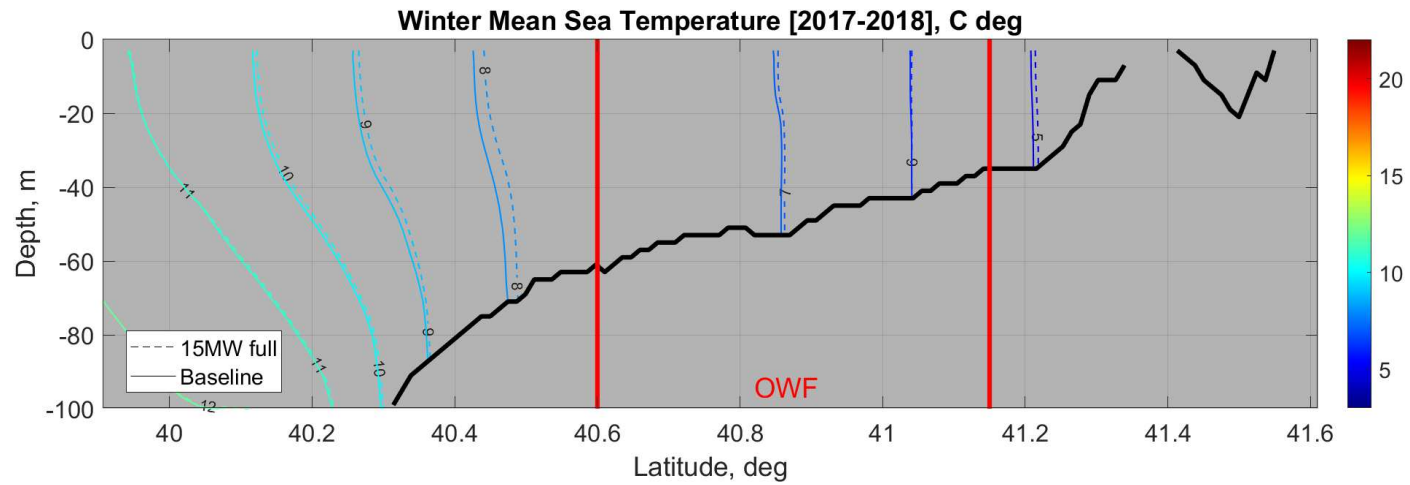


Figure A.108. Average Winter Vertical Temperature Structure of a South-North Transect at MA-RI

The figure shows the 2017-2018 Winter average temperature contours from a transect for Scenario 5: 15 MW full build-out OSW and the same transect for Scenario 1: Baseline.

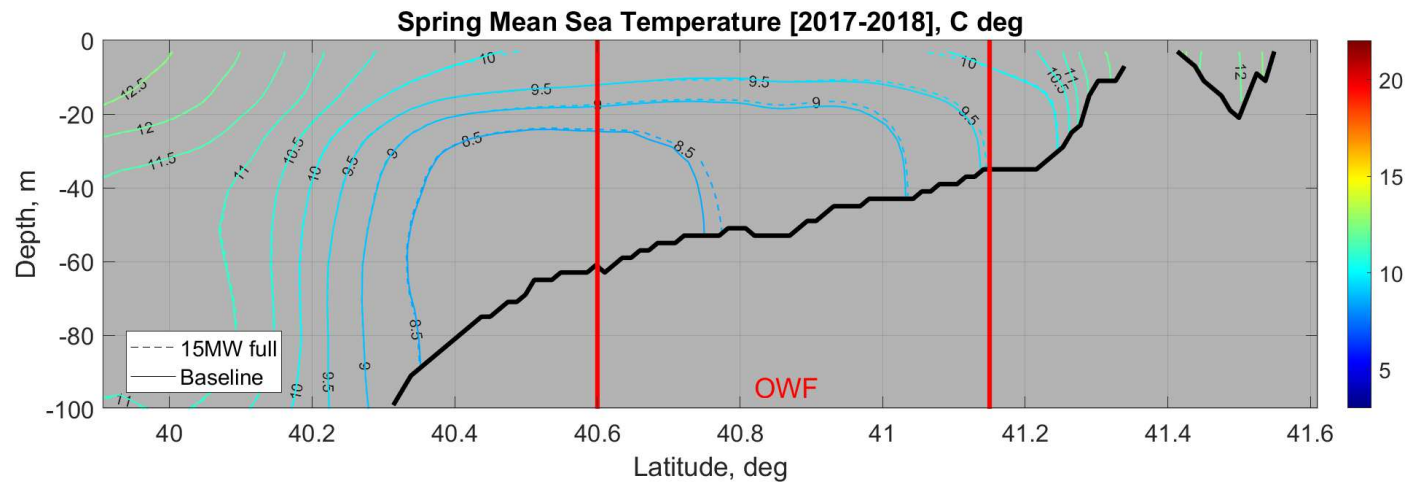


Figure A.109. Average Spring Vertical Temperature Structure of a South-North Transect at MA-RI

The figure shows the 2017-2018 Spring average temperature contours from a transect for Scenario 5: 15 MW full build-out OSW and the same transect for Scenario 1: Baseline.

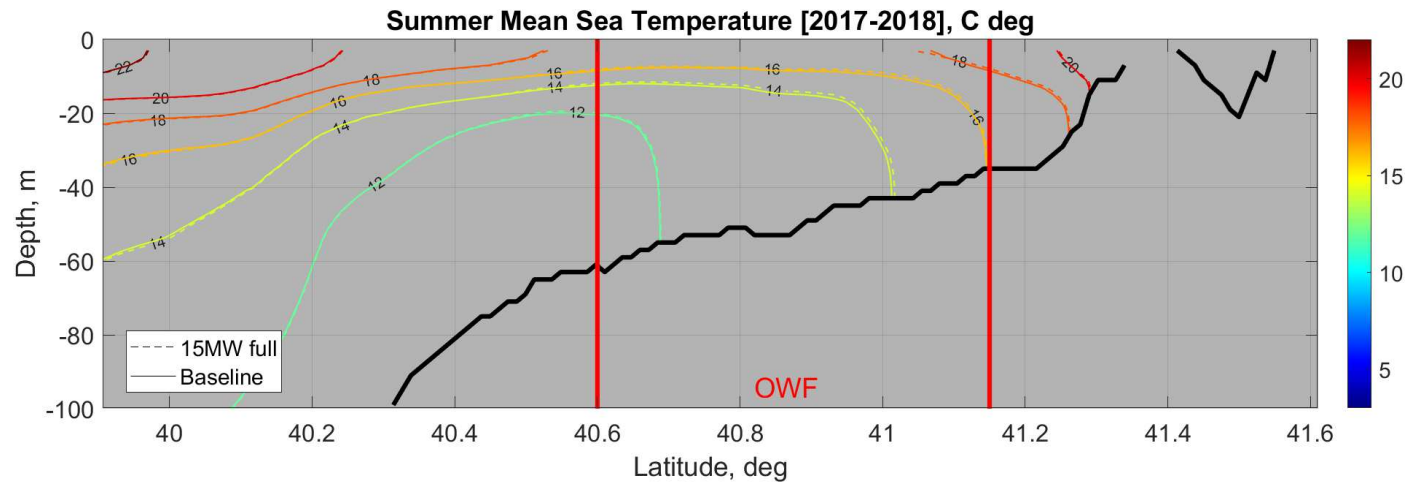


Figure A.110. Average Summer Vertical Temperature Structure of a South-North Transect at MA-RI

The figure shows the 2017-2018 Summer average temperature contours from a transect for Scenario 5: 15 MW full build-out OSW and the same transect for Scenario 1: Baseline.

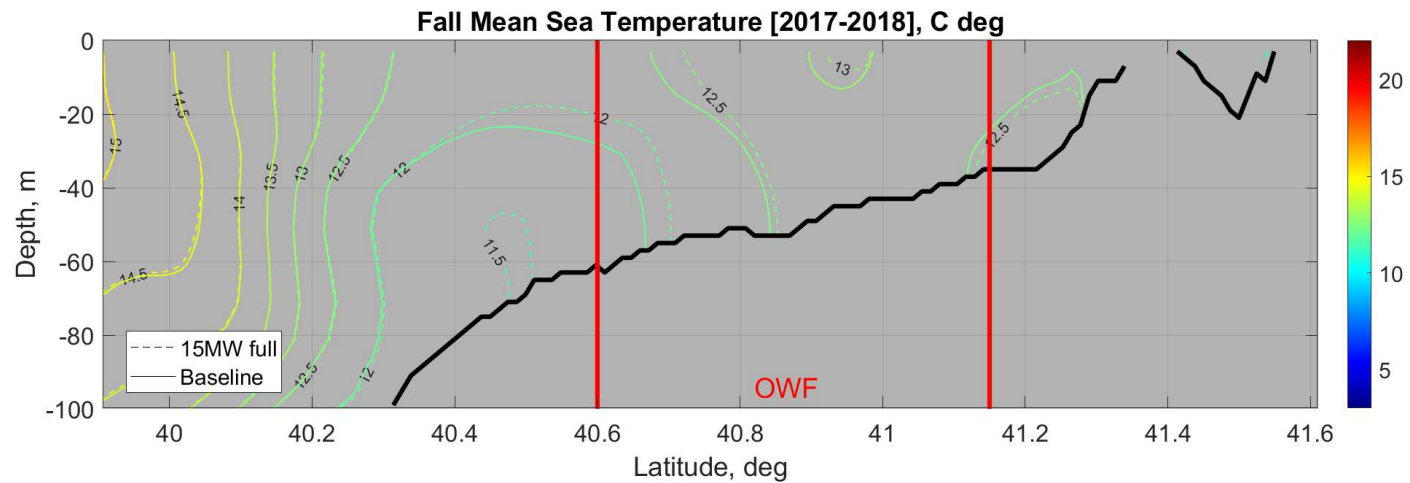


Figure A.111. Average Fall Vertical Temperature Structure of a South-North Transect at MA-RI

The figure shows the 2017-2018 Fall average temperature contours from a transect for Scenario 5: 15 MW full build-out OSW and the same transect for Scenario 1: Baseline.

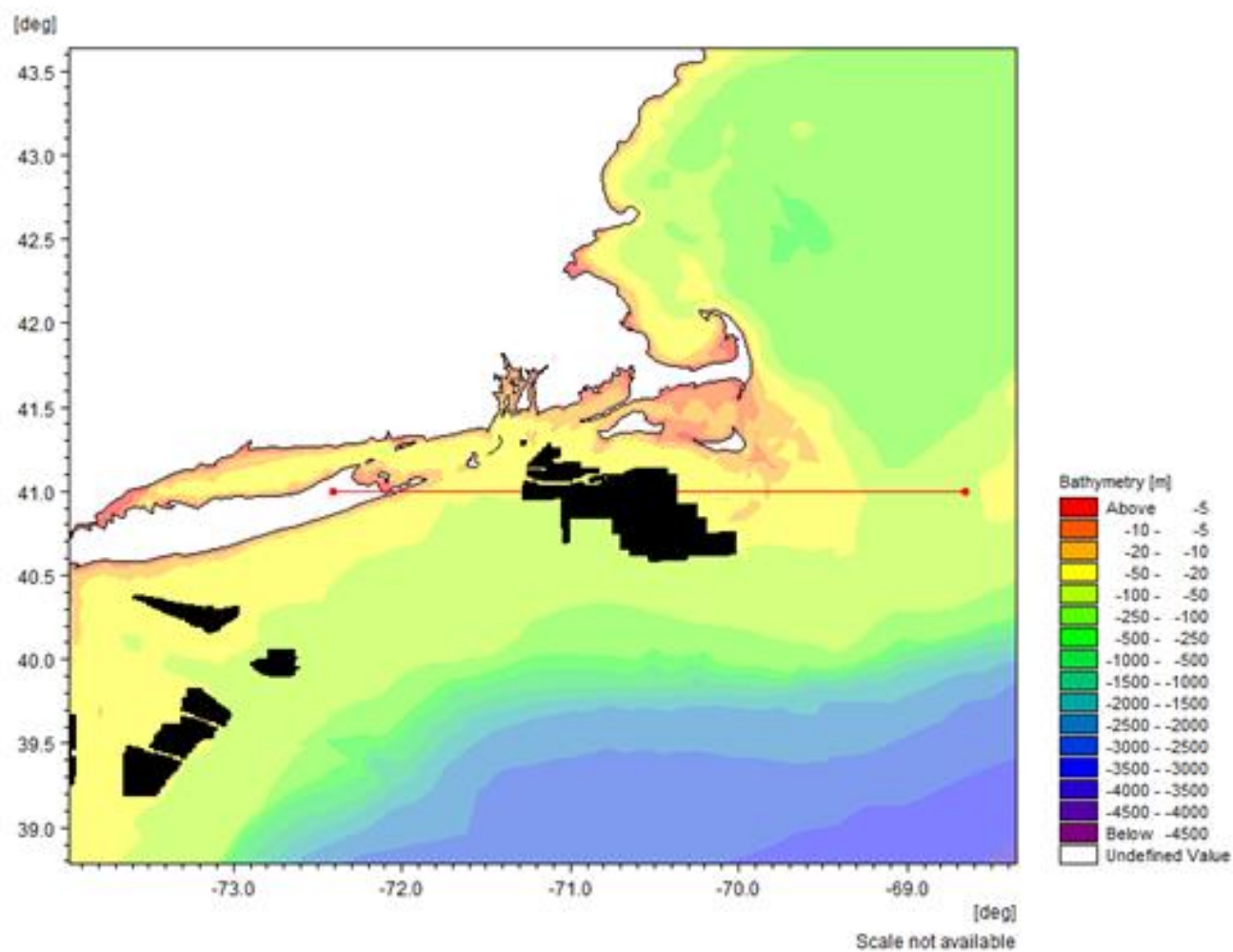


Figure A.112. Thermal Transect Location MA-RI

The figure shows the transect through one set of the MA-RI OSW farms with a line orientation from the West and headed East.

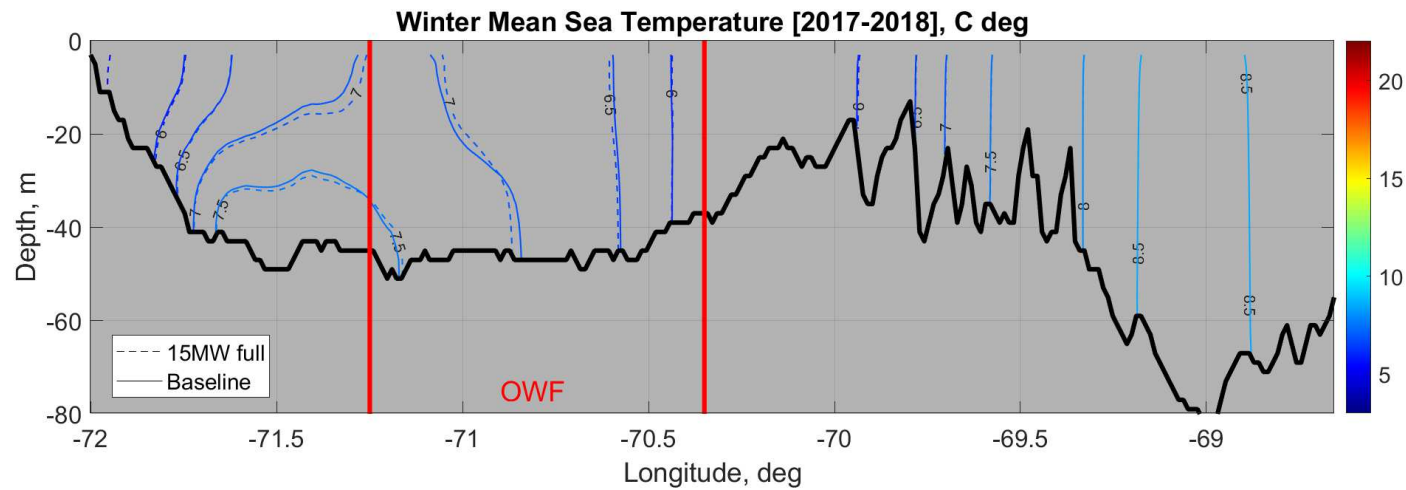


Figure A.113. Average Winter Vertical Temperature Structure of a West-East Transect at MA-RI

The figure shows the 2017-2018 Winter average temperature contours from a transect for Scenario 5: 15 MW full build-out OSW and the same transect for Scenario 1: Baseline.

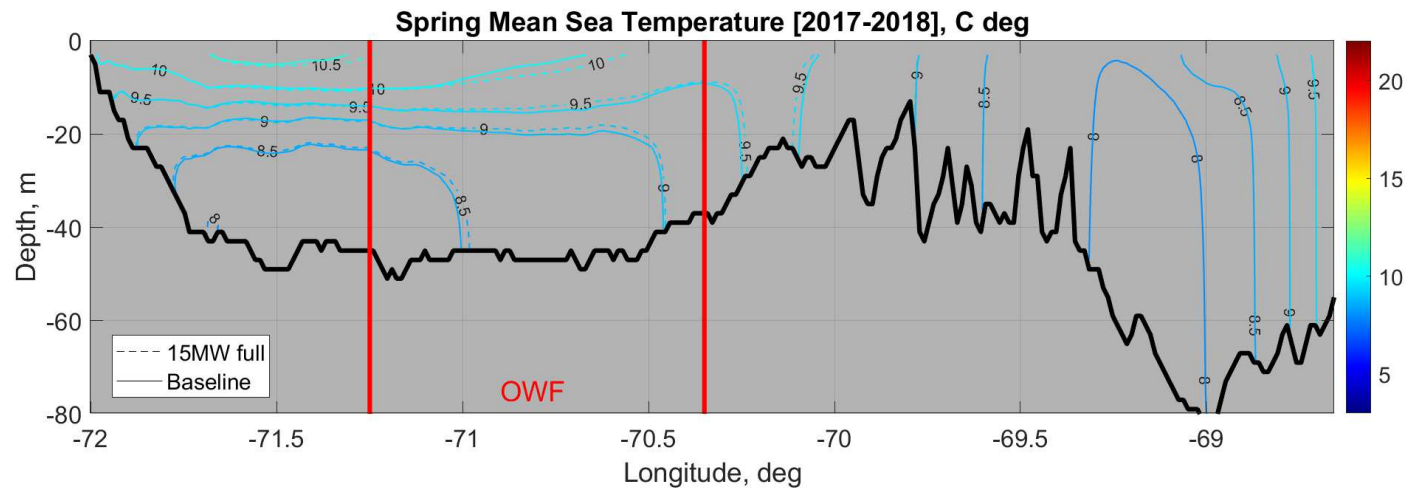


Figure A.114. Average Spring Vertical Temperature Structure of a West-East Transect at MA-RI

The figure shows the 2017-2018 Spring average temperature contours from a transect for Scenario 5: 15 MW full build-out OSW and the same transect for Scenario 1: Baseline.

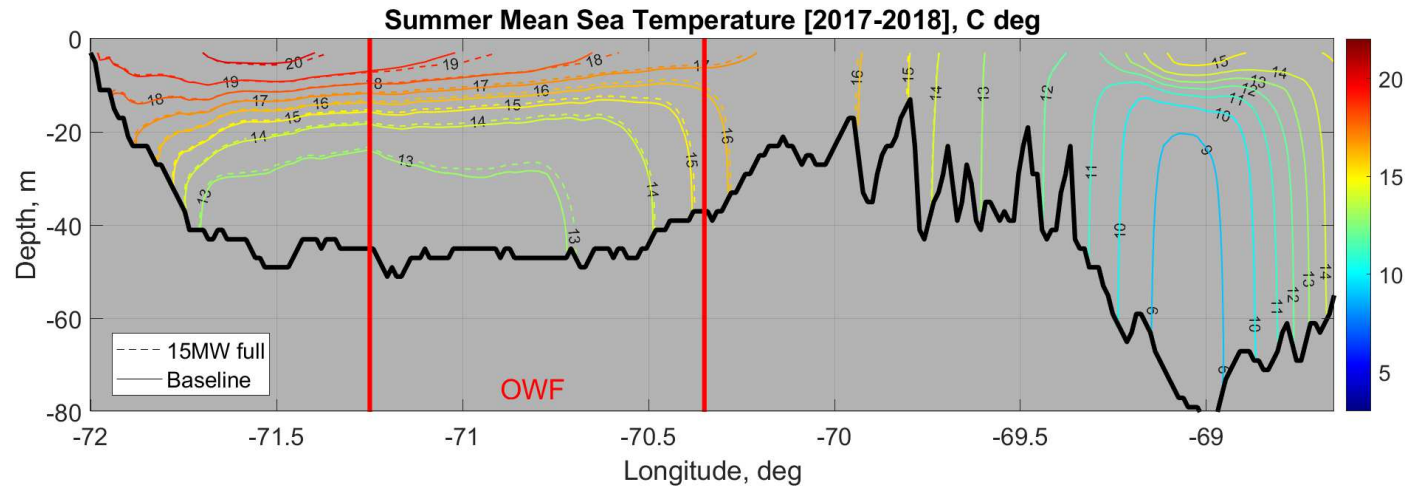


Figure A.115. Average Summer Vertical Temperature Structure of a West-East Transect at MA-RI

The figure shows the 2017-2018 Summer average temperature contours from a transect for Scenario 5: 15 MW full build-out OSW and the same transect for Scenario 1: Baseline.

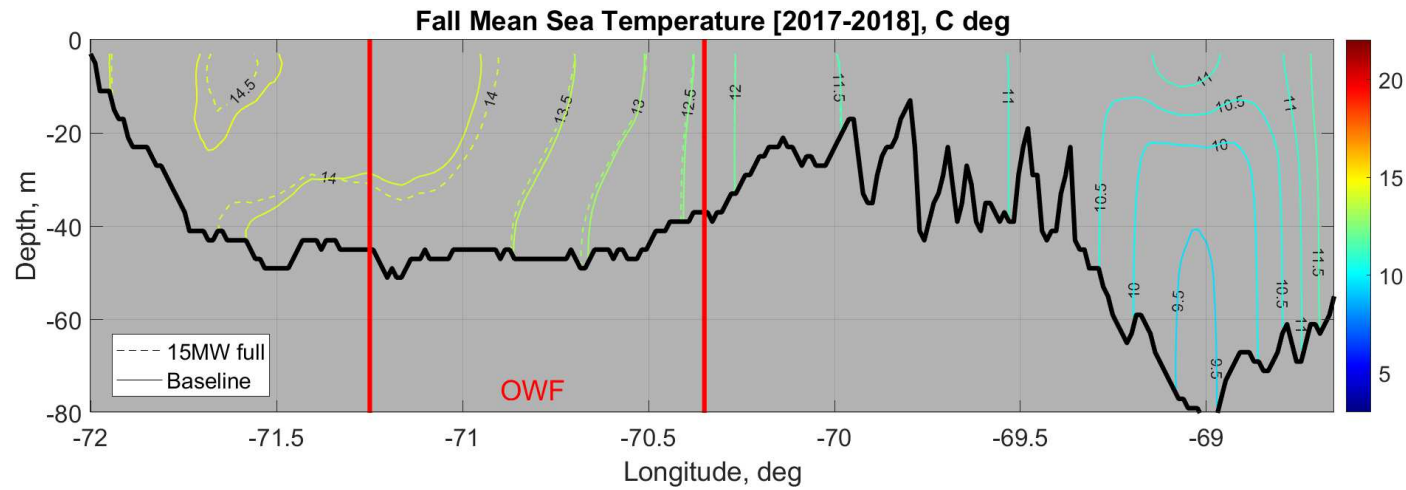


Figure A.116. Average Fall Vertical Temperature Structure of a West-East Transect at MA-RI

The figure shows the 2017-2018 Fall average temperature contours from a transect for Scenario 5: 15 MW full build-out OSW and the same transect for Scenario 1: Baseline.

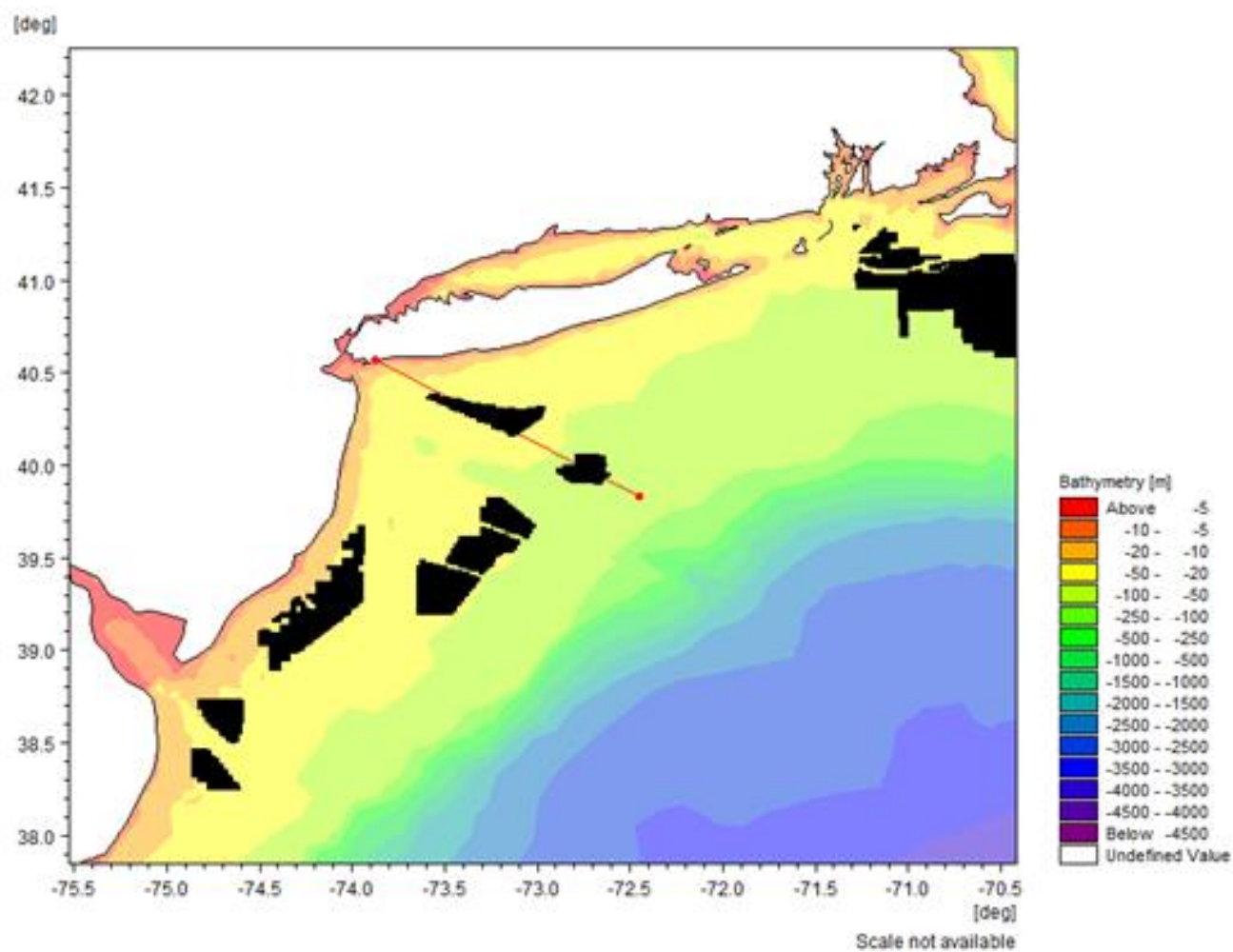


Figure A.117. Thermal Transect Location NY Bight – Cross-Shore Profile A

The figure shows the transect through one set of the NY Bight OSW farms with a line orientation from the Southeast and headed Northwest.

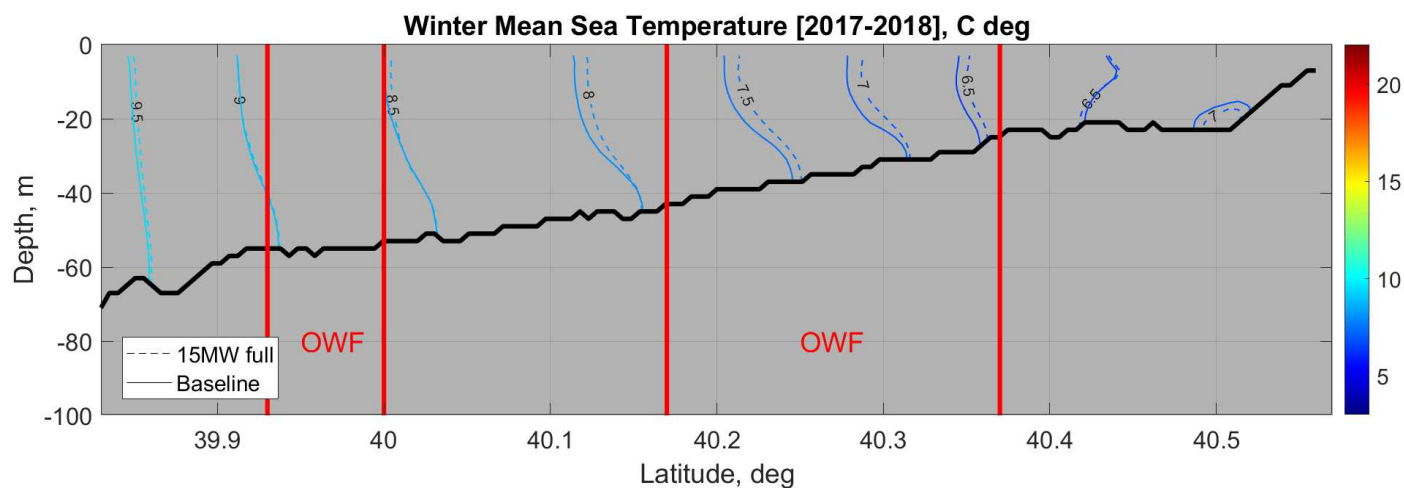


Figure A.118. Average Winter Vertical Temperature Structure of a Southeast-Northwest Transect at NY Bight – Cross-Shore Profile A
The figure shows the 2017-2018 Winter average temperature contours from a transect for Scenario 5: 15 MW full build-out OSW and the same transect for Scenario 1: Baseline.

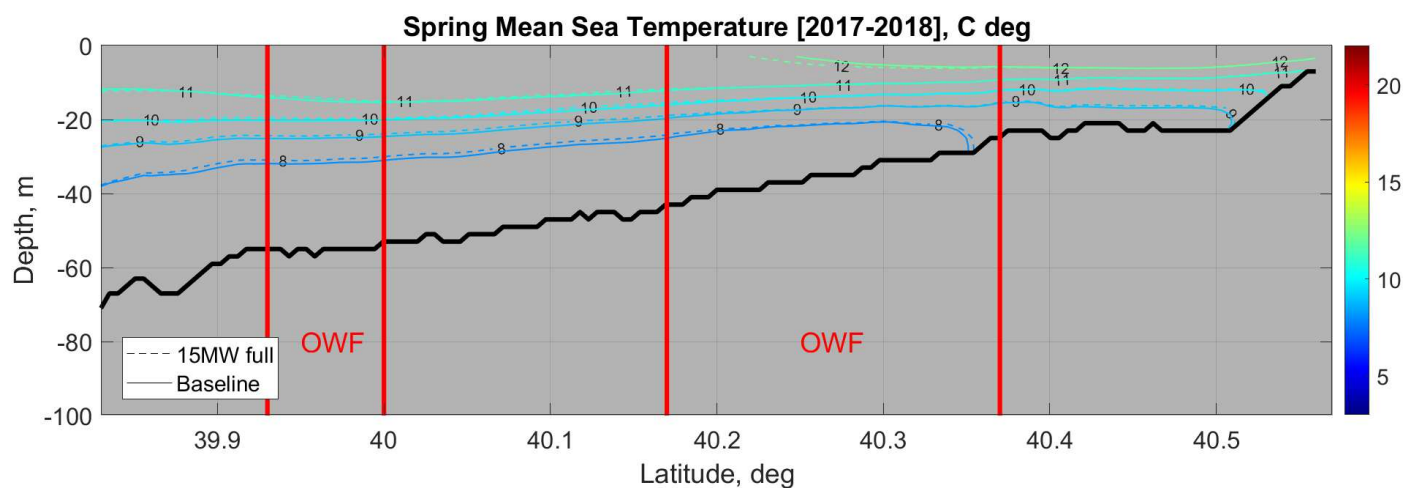


Figure A.119. Average Spring Vertical Temperature Structure of a Southeast-Northwest Transect at NY Bight – Cross-Shore Profile A
The figure shows the 2017-2018 Spring average temperature contours from a transect for Scenario 5: 15 MW full build-out OSW and the same transect for Scenario 1: Baseline.

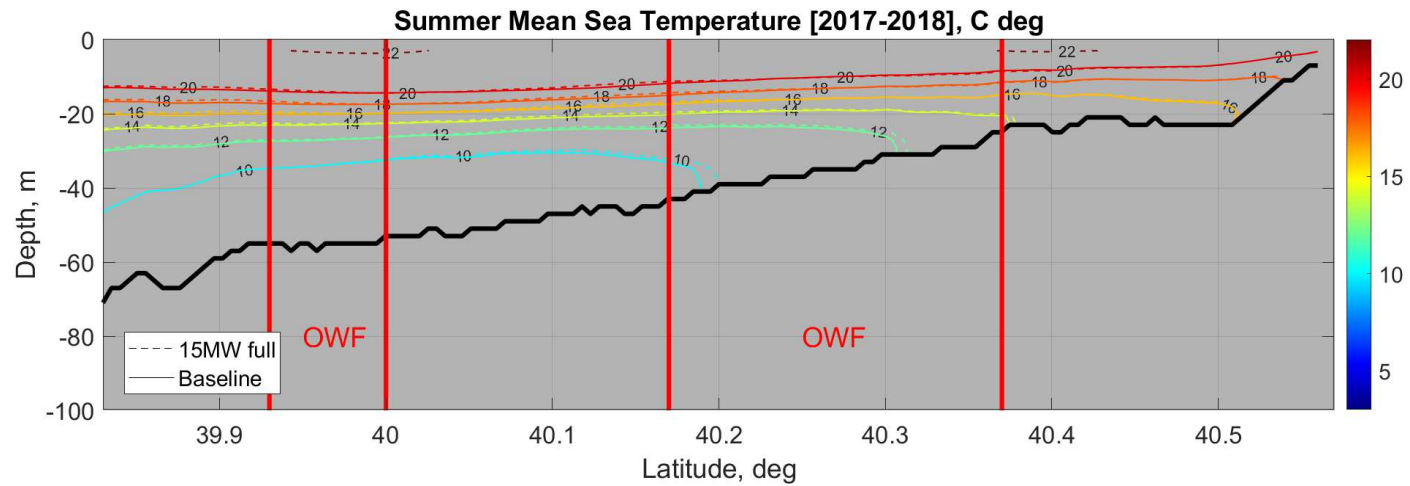


Figure A.120. Average Summer Vertical Temperature Structure of a Southeast-Northwest Transect at NY Bight – Cross-Shore Profile A
The figure shows the 2017-2018 Summer average temperature contours from a transect for Scenario 5: 15 MW full build-out OSW and the same transect for Scenario 1: Baseline.

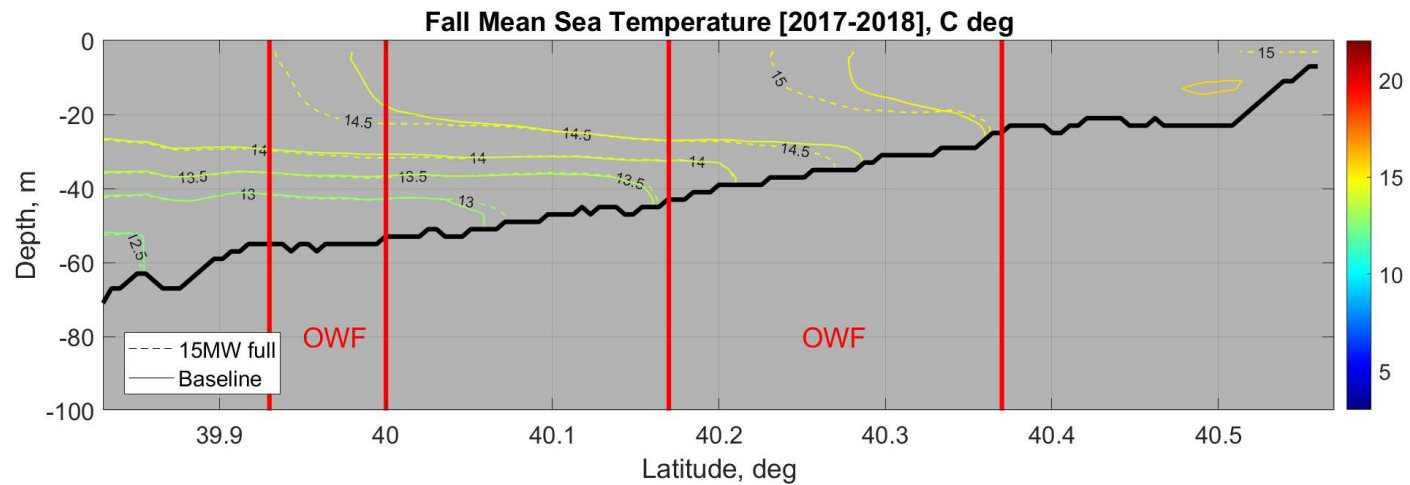


Figure A.121. Average Fall Vertical Temperature Structure of a Southeast-Northwest Transect at NY Bight – Cross-Shore Profile A
The figure shows the 2017-2018 Fall average temperature contours from a transect for Scenario 5: 15 MW full build-out OSW and the same transect for Scenario 1: Baseline.

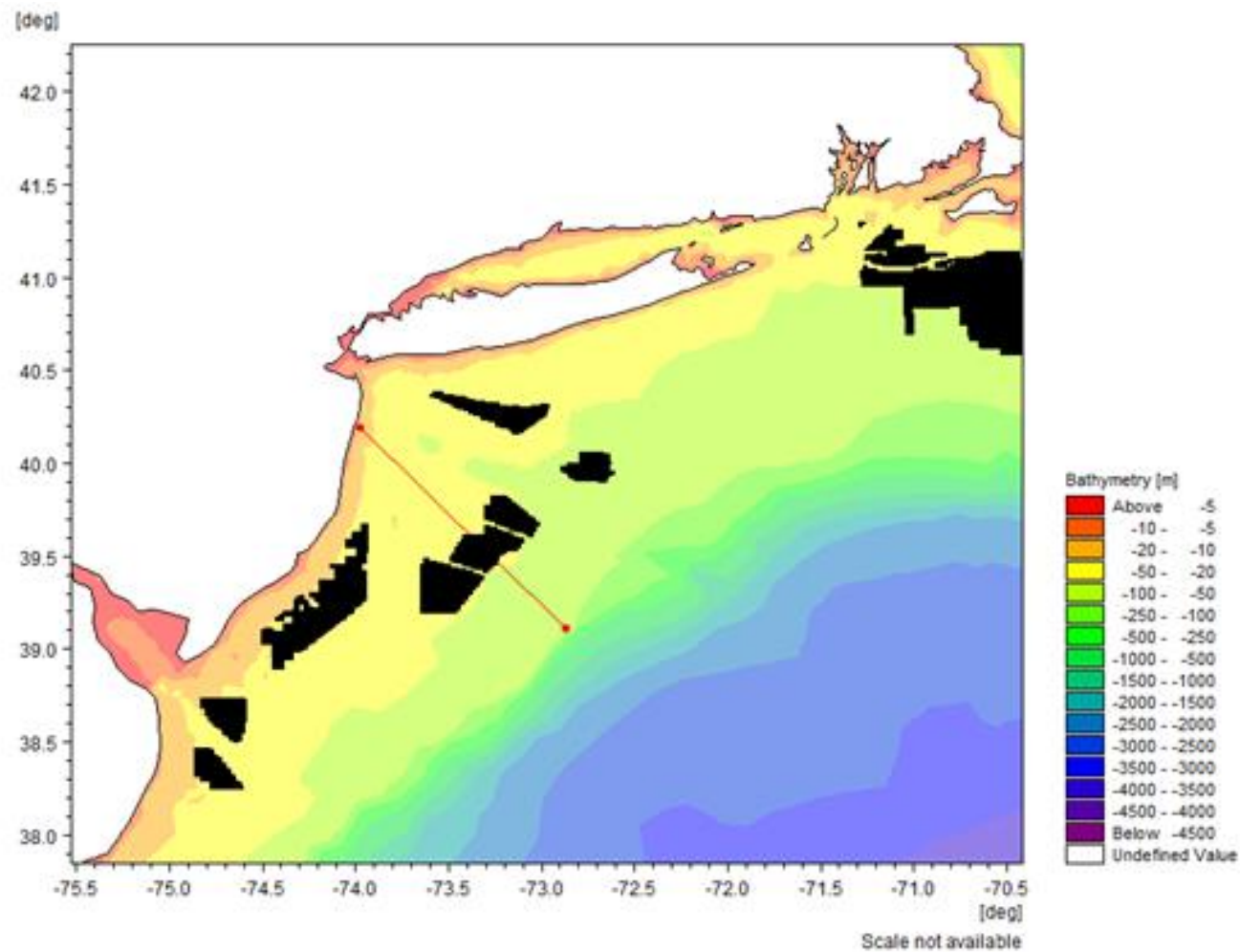


Figure A.122. Thermal Transect Location NY Bight – Cross-Shore Profile B

The figure shows the transect through one set of the NY Bight OSW farms with a line orientation from the Southeast and headed Northwest.

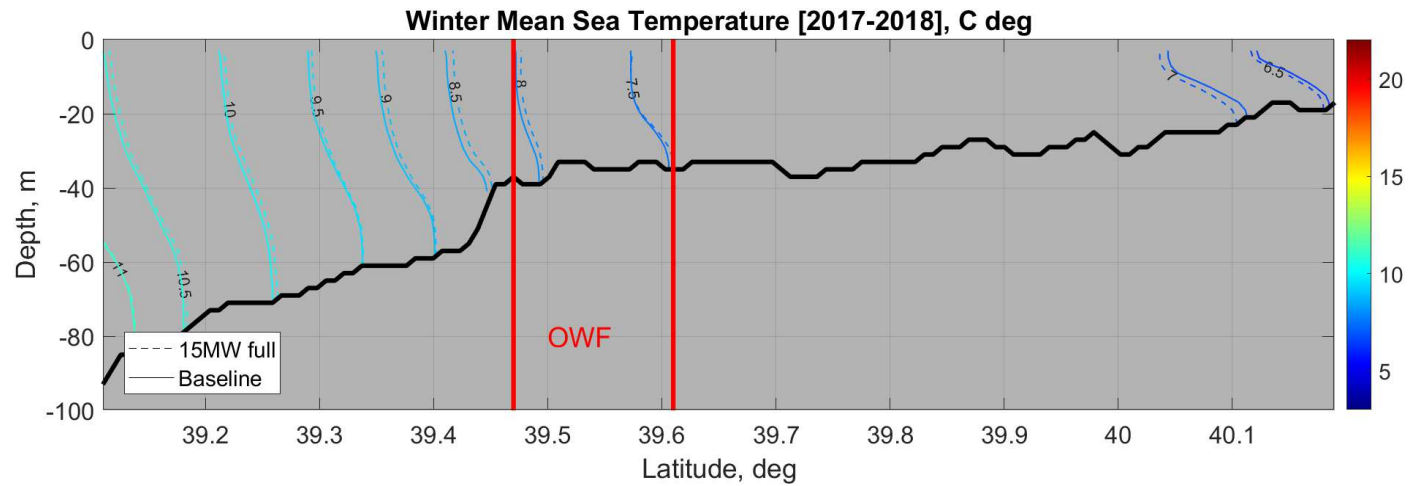


Figure A.123. Average Winter Vertical Temperature Structure of a Southeast-Northwest Transect at NY Bight – Cross-Shore Profile B

The figure shows the 2017-2018 Winter average temperature contours from a transect for Scenario 5: 15 MW full build-out OSW and the same transect for Scenario 1: Baseline.

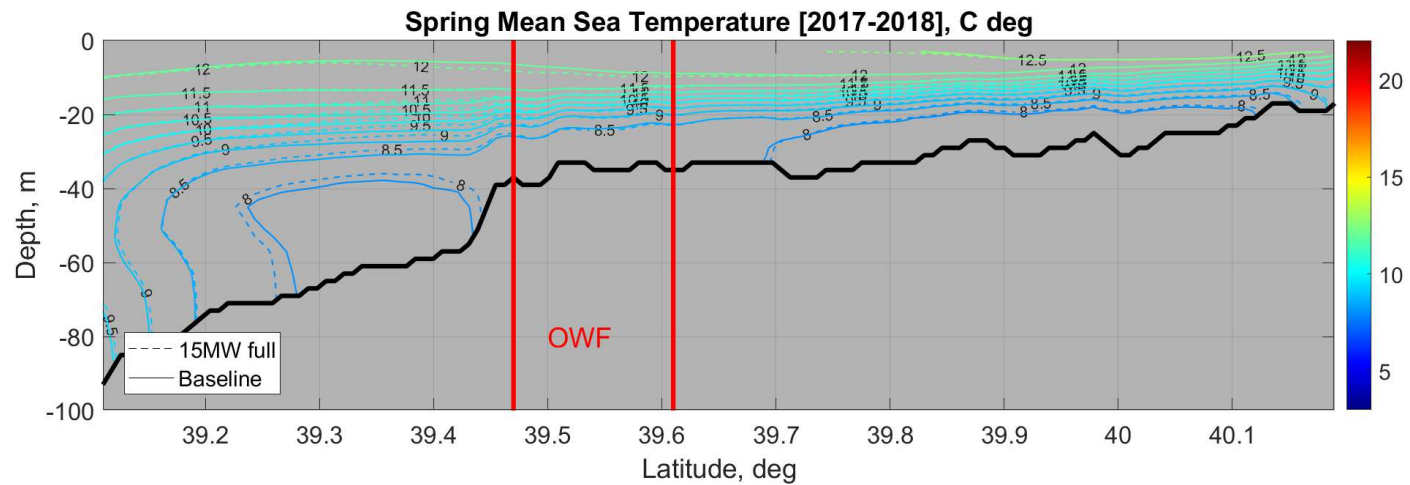


Figure A.124. Average Spring Vertical Temperature Structure of a Southeast-Northwest Transect at NY Bight – Cross-Shore Profile B

The figure shows the 2017-2018 Spring average temperature contours from a transect for Scenario 5: 15 MW full build-out OSW and the same transect for Scenario 1: Baseline.

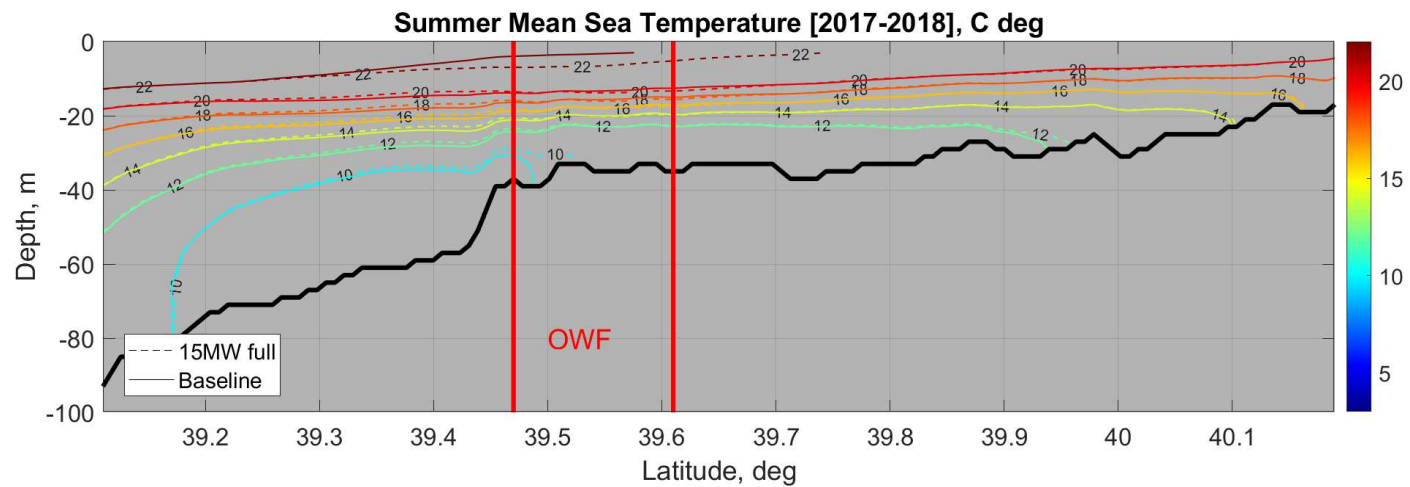


Figure A.125. Average Summer Vertical Temperature Structure of a Southeast-Northwest Transect at NY Bight – Cross-Shore Profile B
The figure shows the 2017-2018 Summer average temperature contours from a transect for Scenario 5: 15 MW full build-out OSW and the same transect for Scenario 1: Baseline.

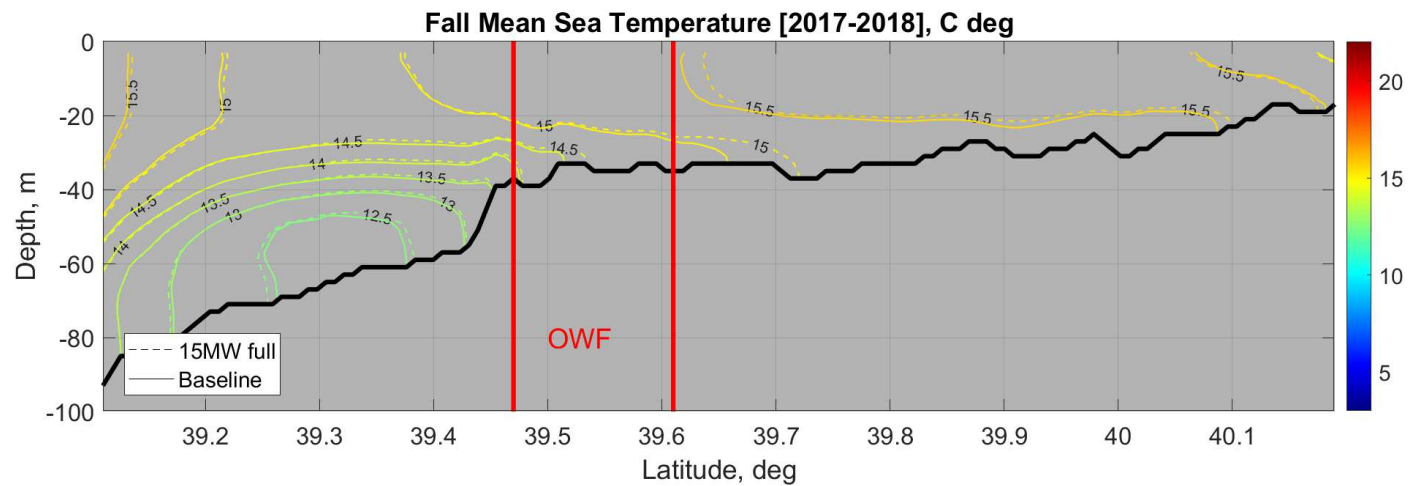


Figure A.126. Average Fall Vertical Temperature Structure of a Southeast-Northwest Transect at NY Bight – Cross-Shore Profile B
The figure shows the 2017-2018 Fall average temperature contours from a transect for Scenario 5: 15 MW full build-out OSW and the same transect for Scenario 1: Baseline.

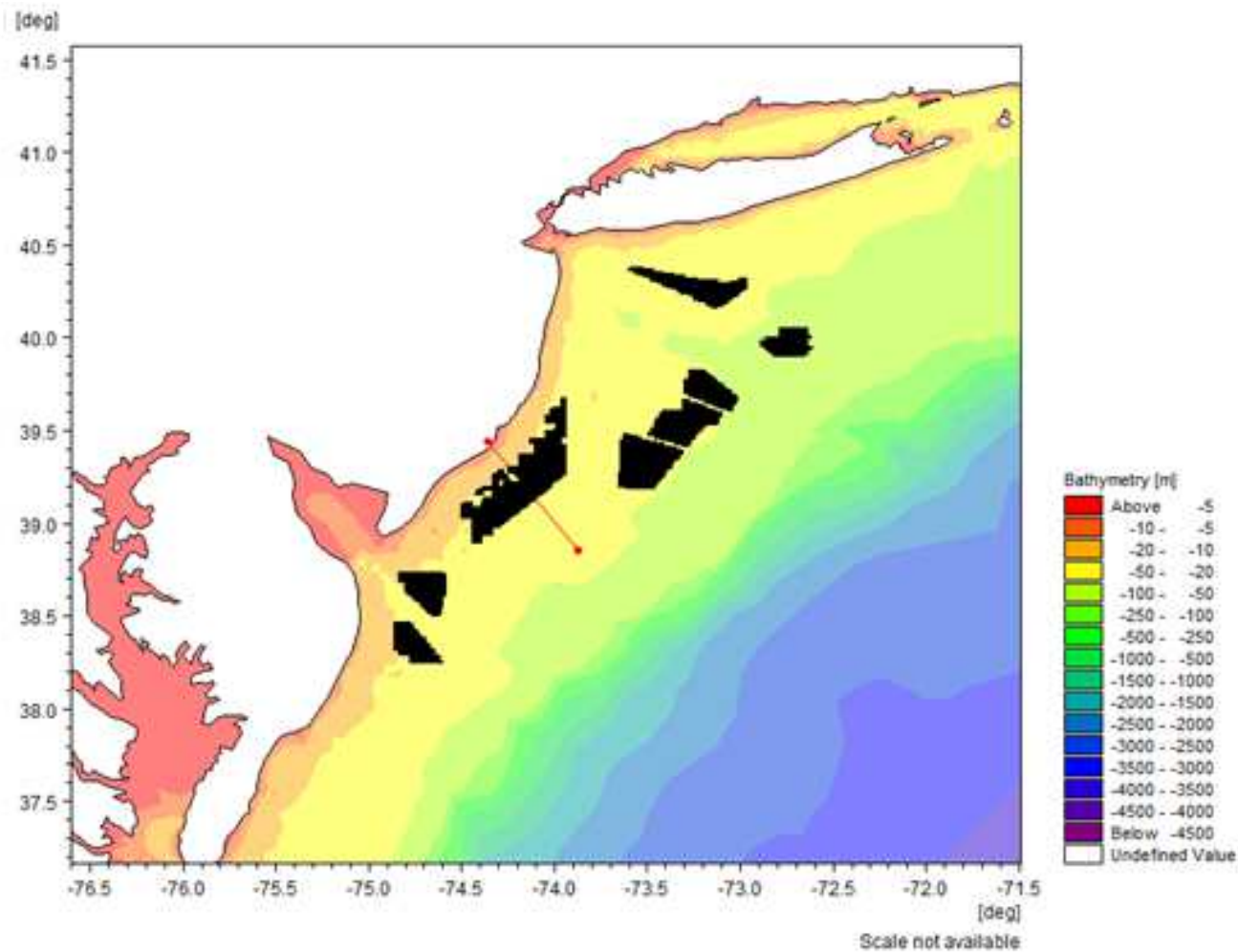


Figure A.127. Thermal Transect Location NY Bight – Cross-Shore Profile C

The figure shows the transect through one set of the NY Bight OSW farms with a line orientation from the Southeast and headed Northwest.

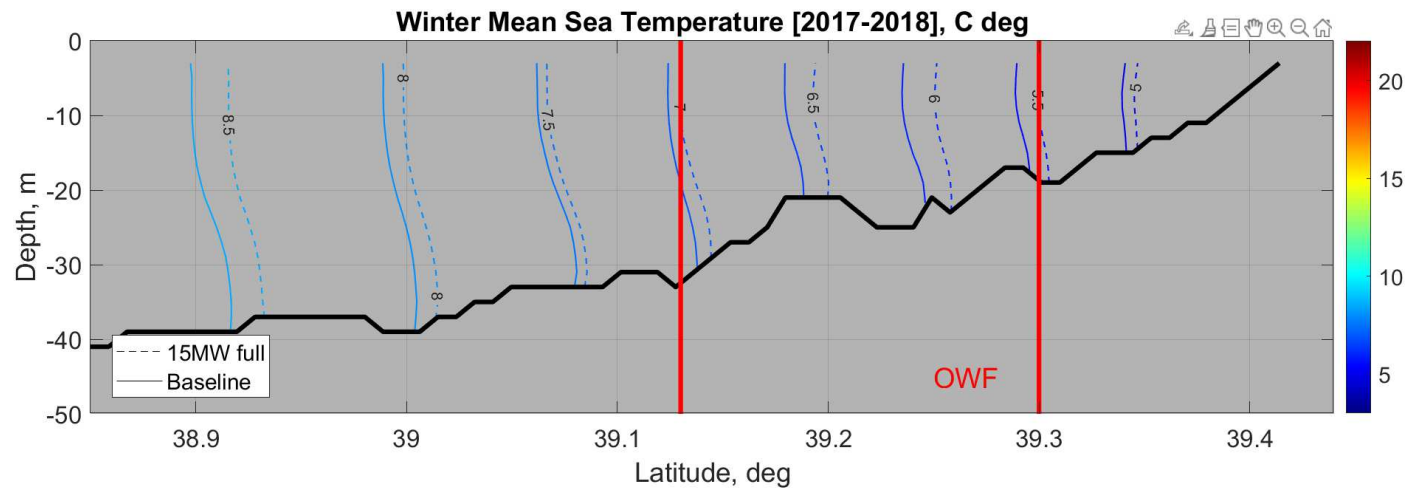


Figure A.128. Average Winter Vertical Temperature Structure of a Southeast-Northwest Transect at NY Bight – Cross-Shore Profile C
The figure shows the 2017-2018 Winter average temperature contours from a transect for Scenario 5: 15 MW full build-out OSW and the same transect for Scenario 1: Baseline.

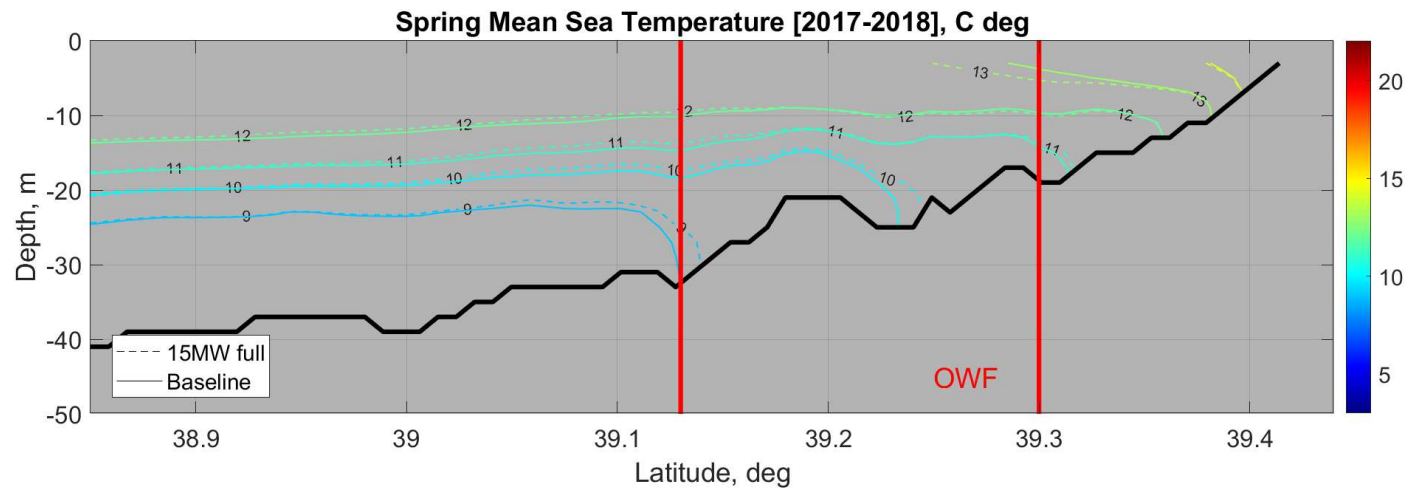


Figure A.129. Average Spring Vertical Temperature Structure of a Southeast-Northwest Transect at NY Bight – Cross-Shore Profile C
The figure shows the 2017-2018 Spring average temperature contours from a transect for Scenario 5: 15 MW full build-out OSW and the same transect for Scenario 1: Baseline.

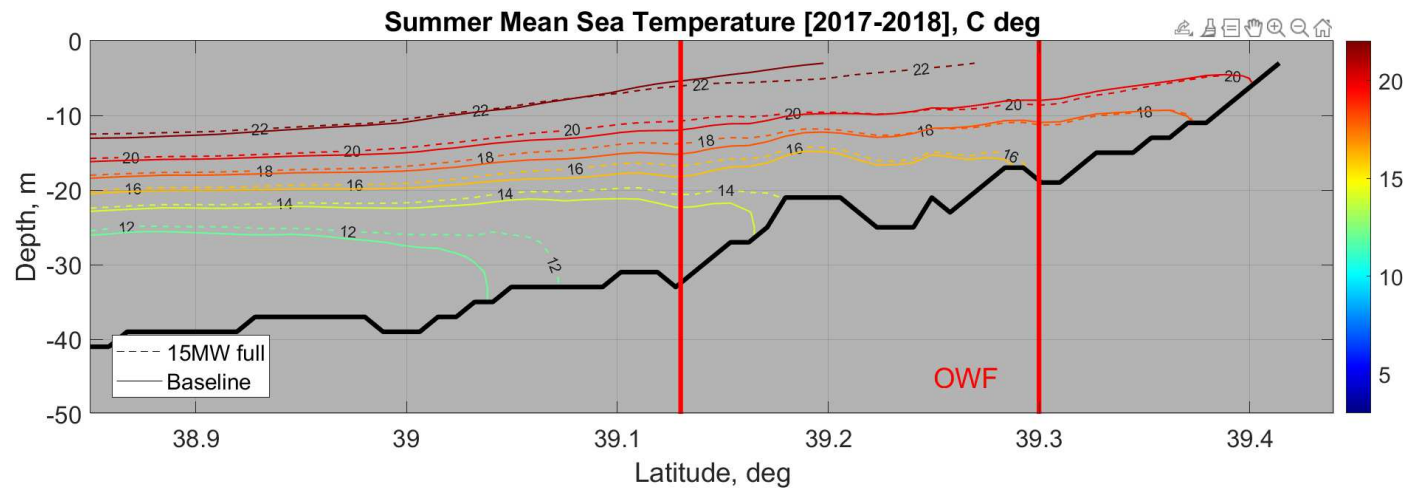


Figure A.130. Average Summer Vertical Temperature Structure of a Southeast-Northwest Transect at NY Bight – Cross-Shore Profile C
The figure shows the 2017-2018 Summer average temperature contours from a transect for Scenario 5: 15 MW full build-out OSW and the same transect for Scenario 1: Baseline.

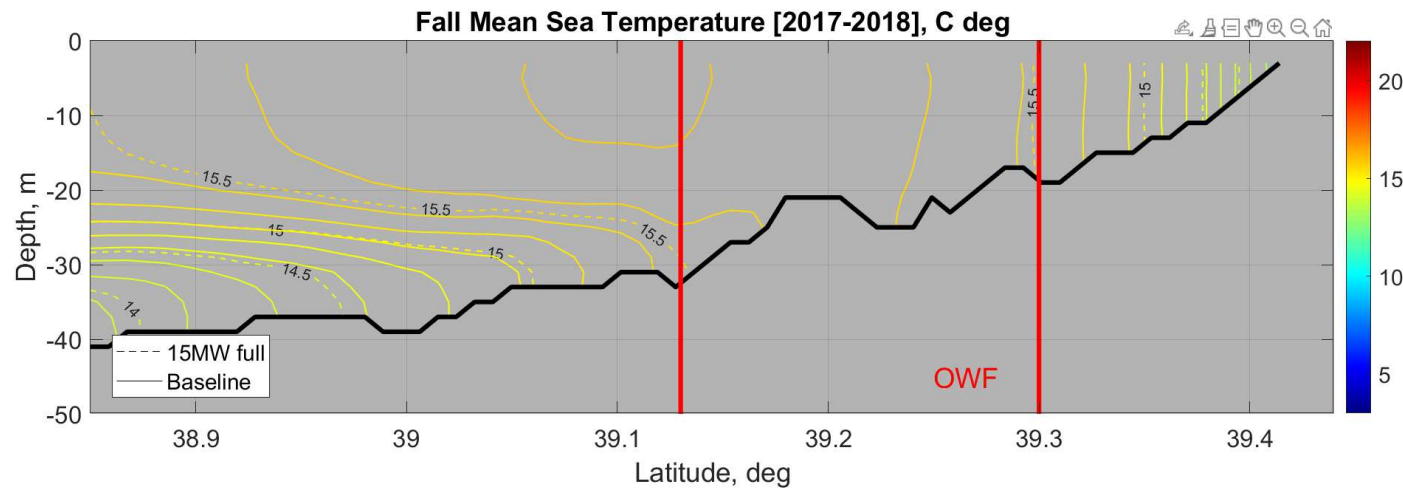


Figure A.131. Average Fall Vertical Temperature Structure of a Southeast-Northwest Transect at NY Bight – Cross-Shore Profile C
The figure shows the 2017-2018 Fall average temperature contours from a transect for Scenario 5: 15 MW full build-out OSW and the same transect for Scenario 1: Baseline.

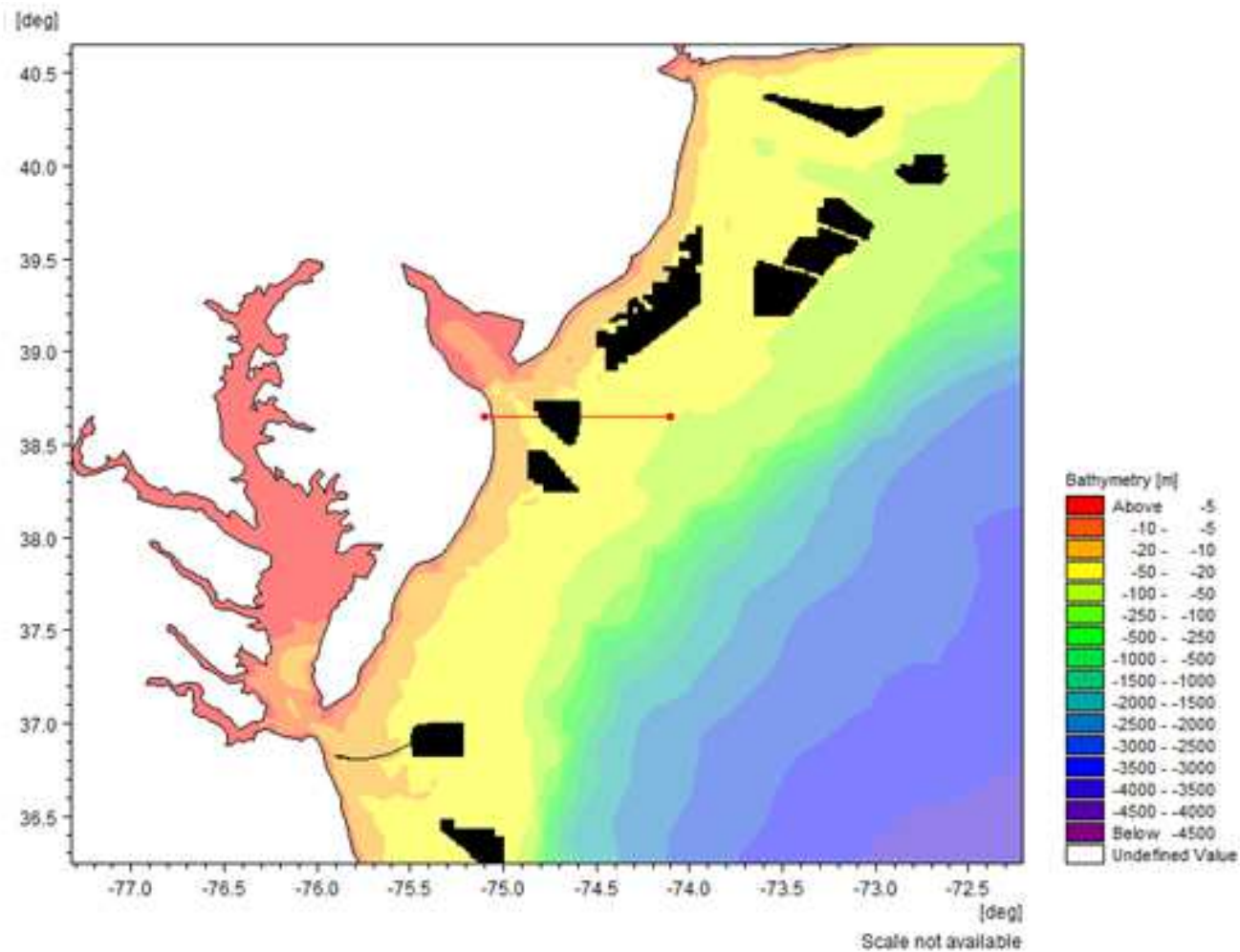


Figure A.132. Thermal Transect Location NY Bight – Cross-Shore Profile D

The figure shows the transect through one set of the NY Bight OSW farms with a line orientation from the West and headed East.

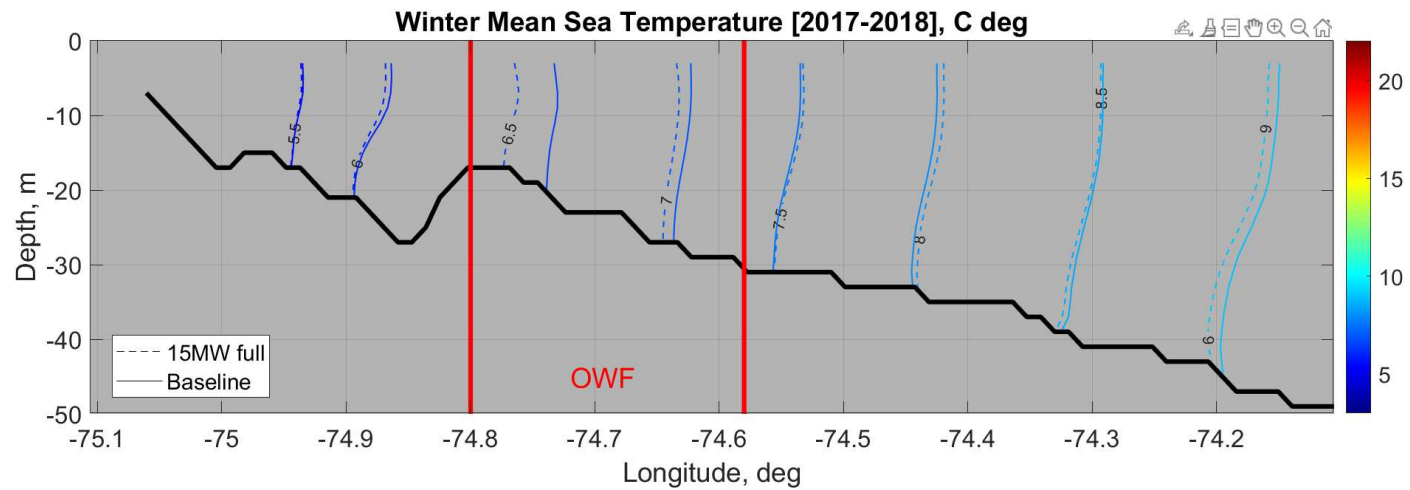


Figure A.133. Average Winter Vertical Temperature Structure of a West-East Transect at NY Bight – Cross-Shore Profile D

The figure shows the 2017-2018 Winter average temperature contours from a transect for Scenario 5: 15 MW full build-out OSW and the same transect for Scenario 1: Baseline.

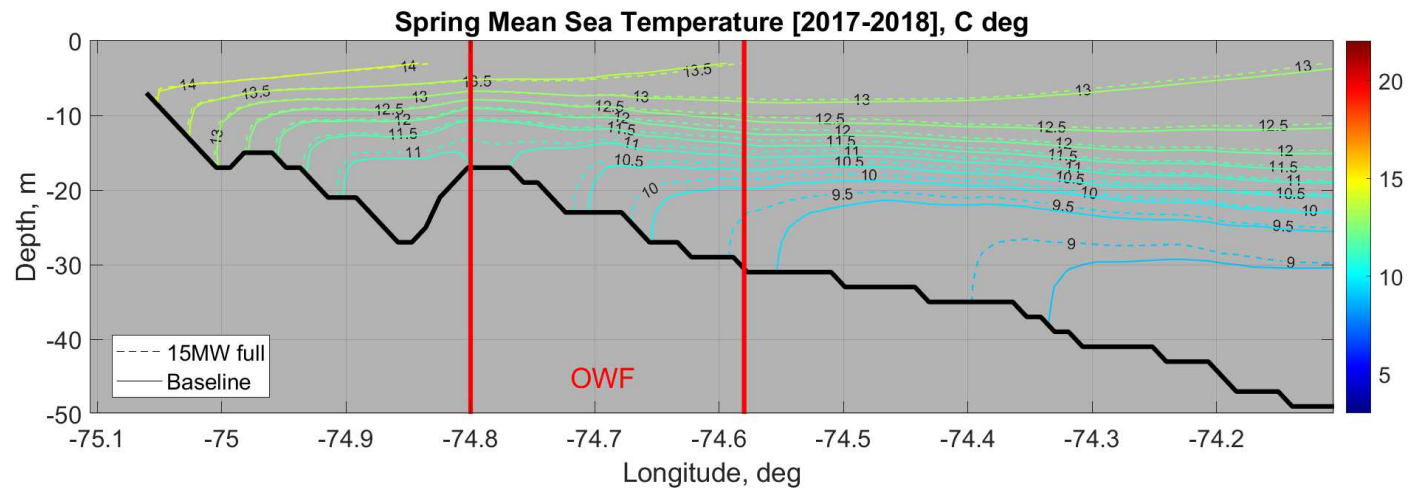


Figure A.134. Average Spring Vertical Temperature Structure of a West-East Transect at NY Bight – Cross-Shore Profile D

The figure shows the 2017-2018 Spring average temperature contours from a transect for Scenario 5: 15 MW full build-out OSW and the same transect for Scenario 1: Baseline.

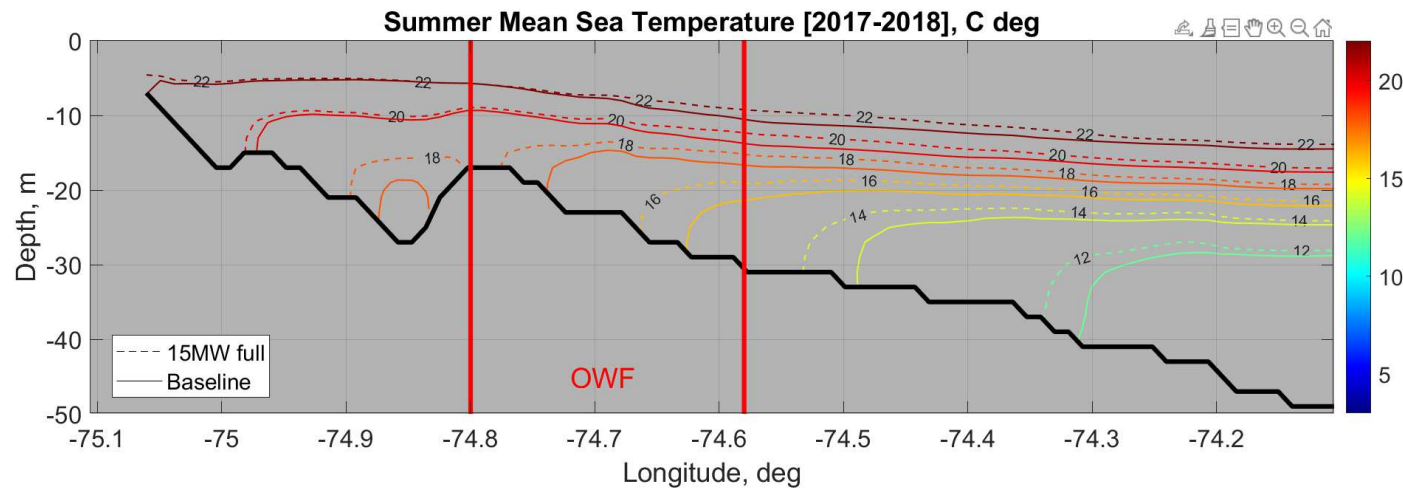


Figure A.135. Average Summer Vertical Temperature Structure of a West-East Transect at NY Bight – Cross-Shore Profile D

The figure shows the 2017-2018 Summer average temperature contours from a transect for Scenario 5: 15 MW full build-out OSW and the same transect for Scenario 1: Baseline.

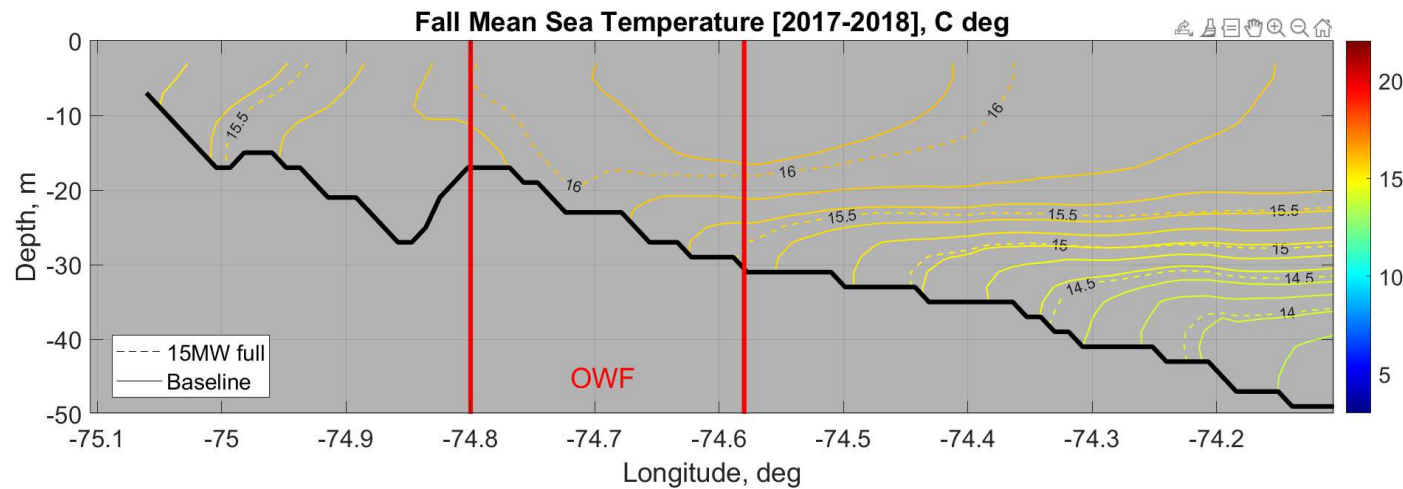


Figure A.136. Average Fall Vertical Temperature Structure of a West-East Transect at NY Bight – Cross-Shore Profile D

The figure shows the 2017-2018 Fall average temperature contours from a transect for Scenario 5: 15 MW full build-out OSW and the same transect for Scenario 1: Baseline.

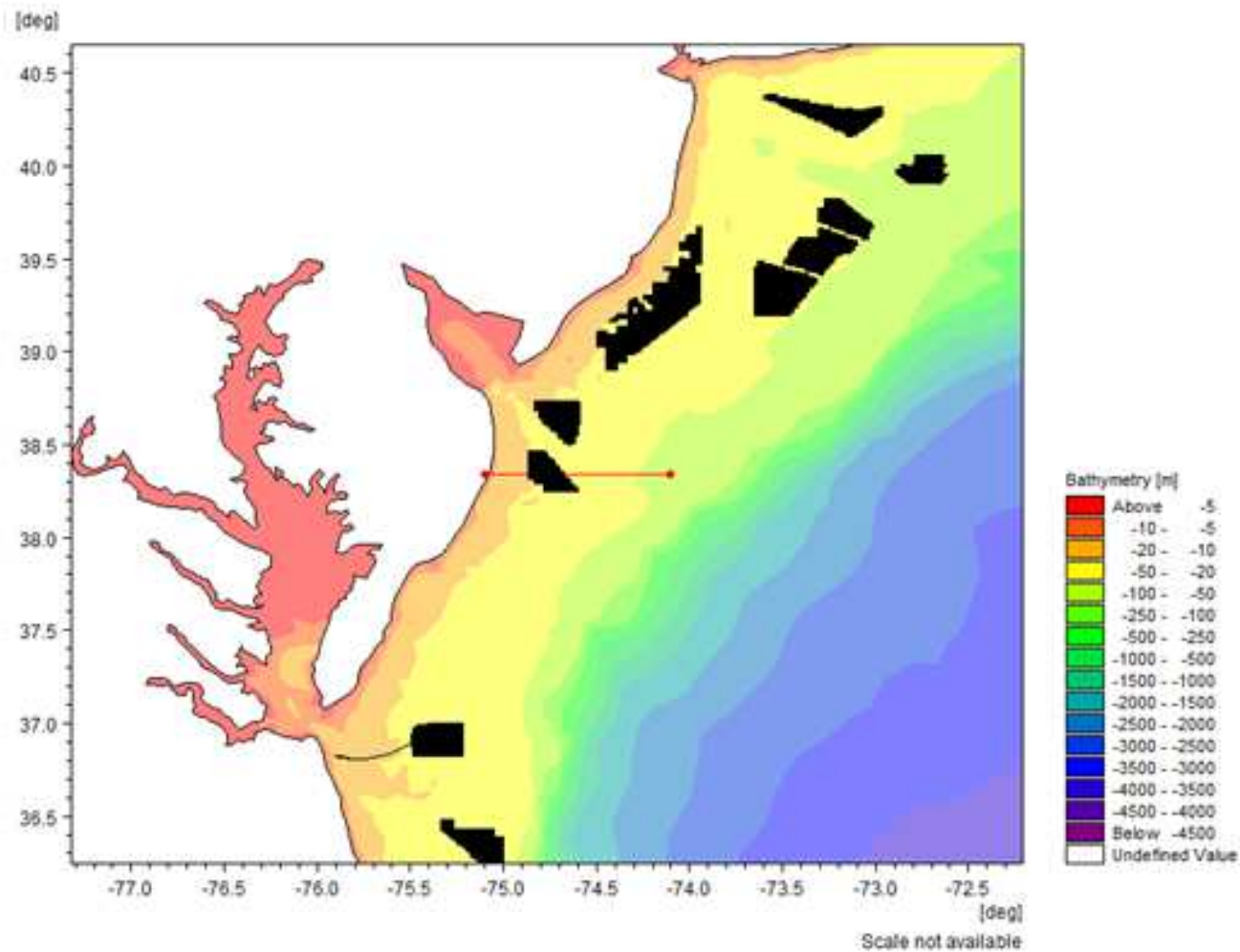


Figure A.137. Thermal Transect Location NY Bight – Cross-Shore Profile E

The figure shows the transect through one set of the NY Bight OSW farms with a line orientation from the West and headed East.

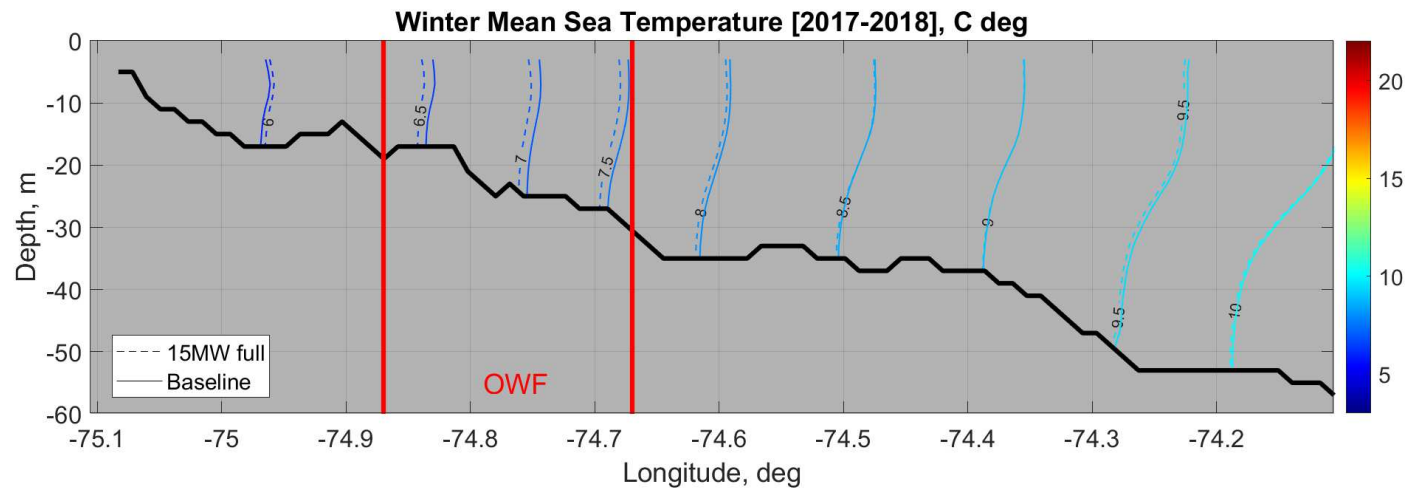


Figure A.138. Average Winter Vertical Temperature Structure of a West-East Transect at NY Bight – Cross-Shore Profile E
The figure shows the 2017-2018 Winter average temperature contours from a transect for Scenario 5: 15 MW full build-out OSW and the same transect for Scenario 1: Baseline.

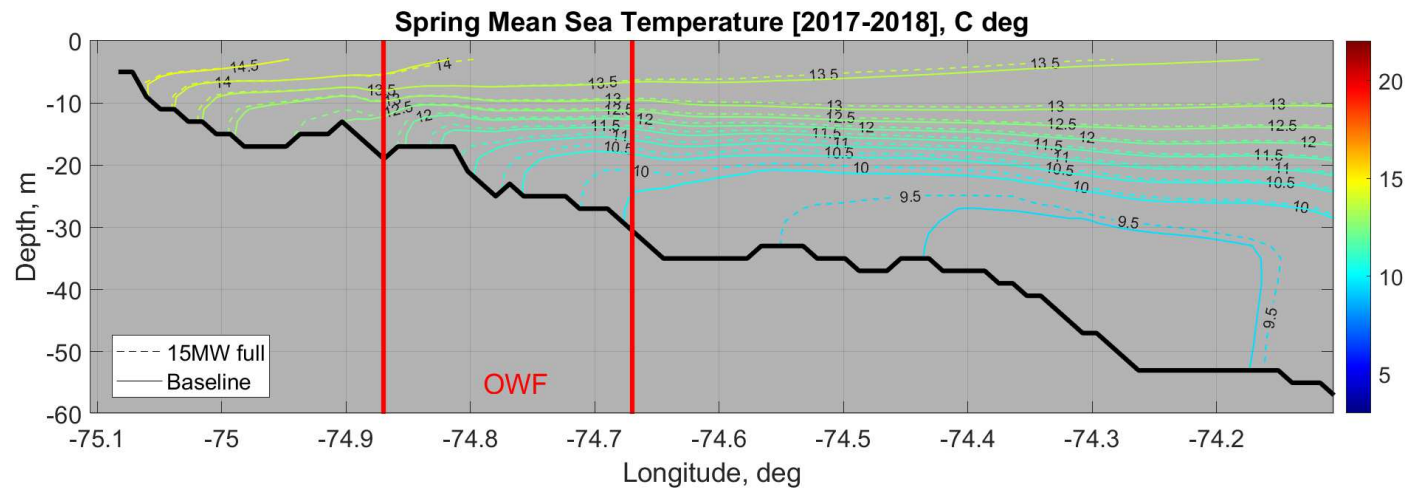


Figure A.139. Average Spring Vertical Temperature Structure of a West-East Transect at NY Bight – Cross-Shore Profile E
The figure shows the 2017-2018 Spring average temperature contours from a transect for Scenario 5: 15 MW full build-out OSW and the same transect for Scenario 1: Baseline.

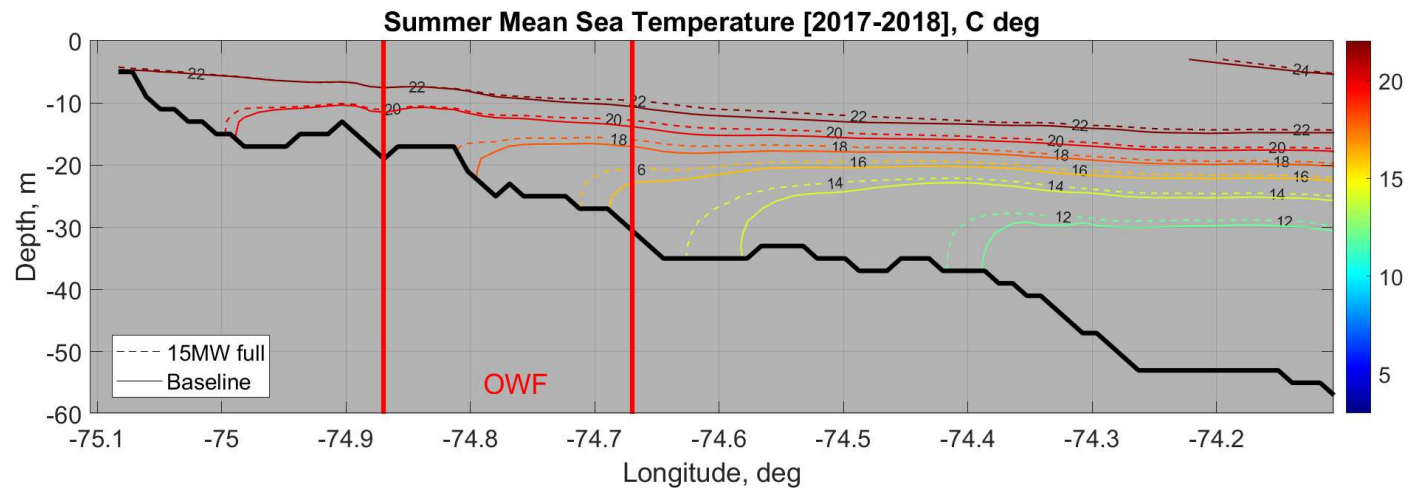


Figure A.140. Average Summer Vertical Temperature Structure of a West-East Transect at NY Bight – Cross-Shore Profile E

The figure shows the 2017-2018 Summer average temperature contours from a transect for Scenario 5: 15 MW full build-out OSW and the same transect for Scenario 1: Baseline.

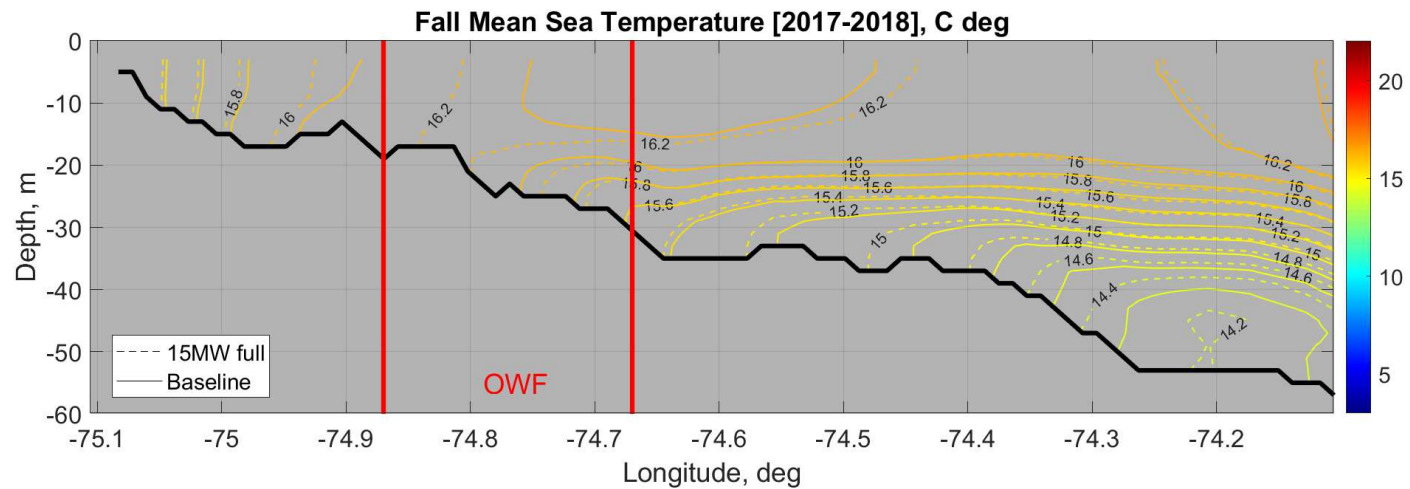


Figure A.141. Average Fall Vertical Temperature Structure of a West-East Transect at NY Bight – Cross-Shore Profile E

The figure shows the 2017-2018 Fall average temperature contours from a transect for Scenario 5: 15 MW full build-out OSW and the same transect for Scenario 1: Baseline.

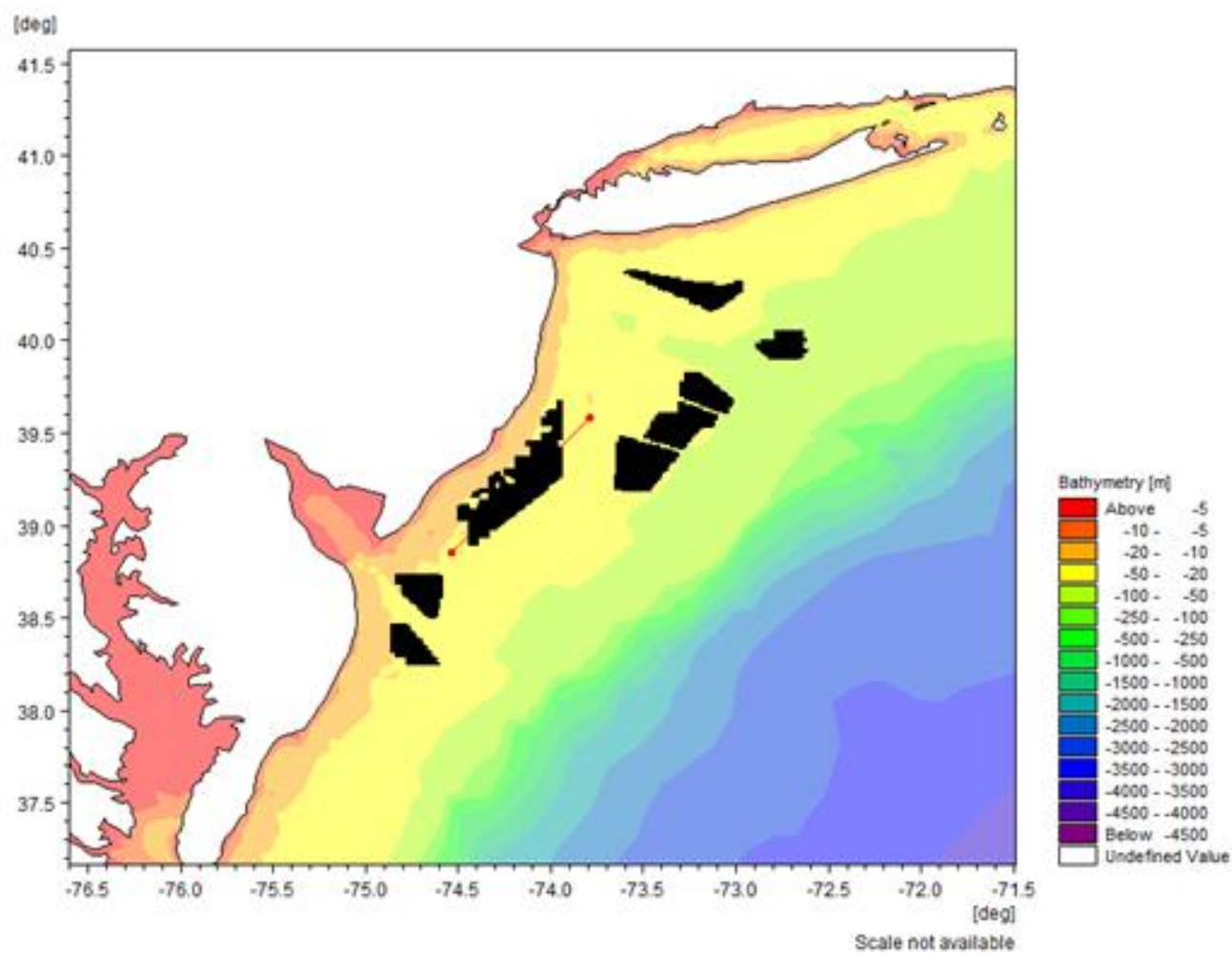


Figure A.142. Thermal Transect Location NY Bight – Long-Shore Profile B

The figure shows the transect through one set of the NY Bight OSW farms with a line orientation from the Southwest and headed Northeast.

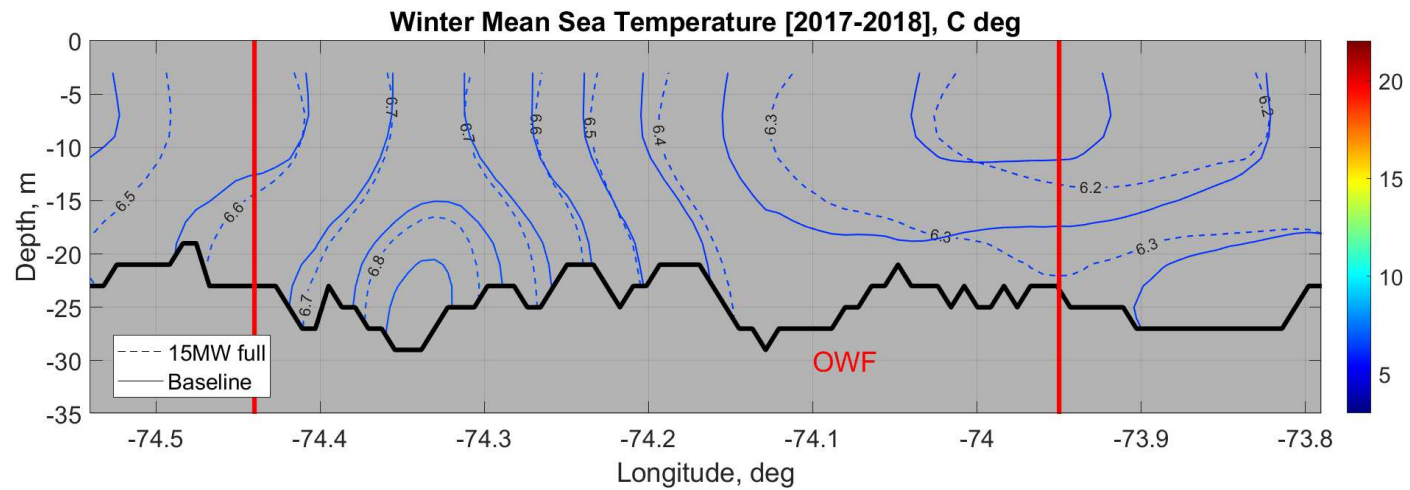


Figure A.143. Average Winter Vertical Temperature Structure of a Southwest-Northeast Transect at NY Bight – Long-Shore Profile B
The figure shows the 2017-2018 Winter average temperature contours from a transect for Scenario 5: 15 MW full build-out OSW and the same transect for Scenario 1: Baseline.

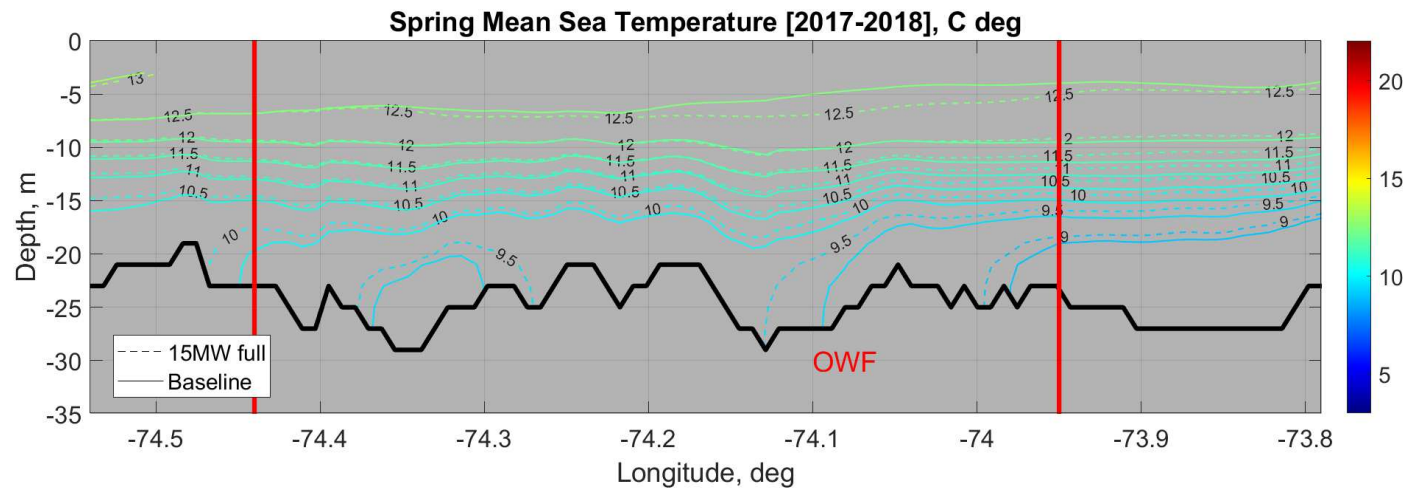


Figure A.144. Average Spring Vertical Temperature Structure of a Southwest-Northeast Transect at NY Bight – Long-Shore Profile B
The figure shows the 2017-2018 Spring average temperature contours from a transect for Scenario 5: 15 MW full build-out OSW and the same transect for Scenario 1: Baseline.

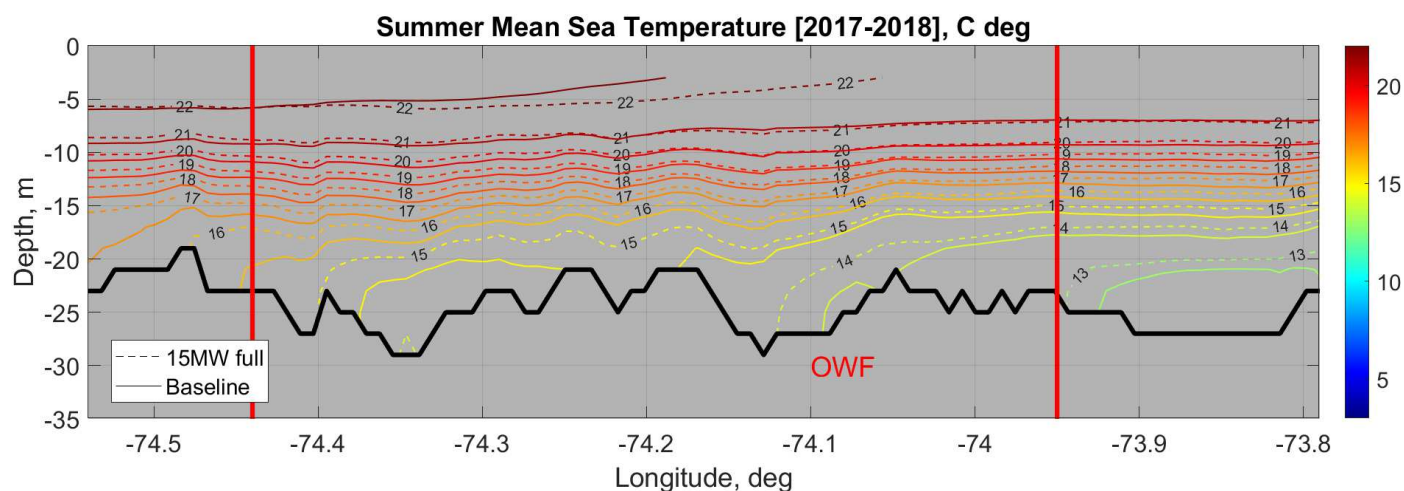


Figure A.145. Average Summer Vertical Temperature Structure of a Southwest-Northeast Transect at NY Bight – Long-Shore Profile B
The figure shows the 2017-2018 Summer average temperature contours from a transect for Scenario 5: 15 MW full build-out OSW and the same transect for Scenario 1: Baseline.

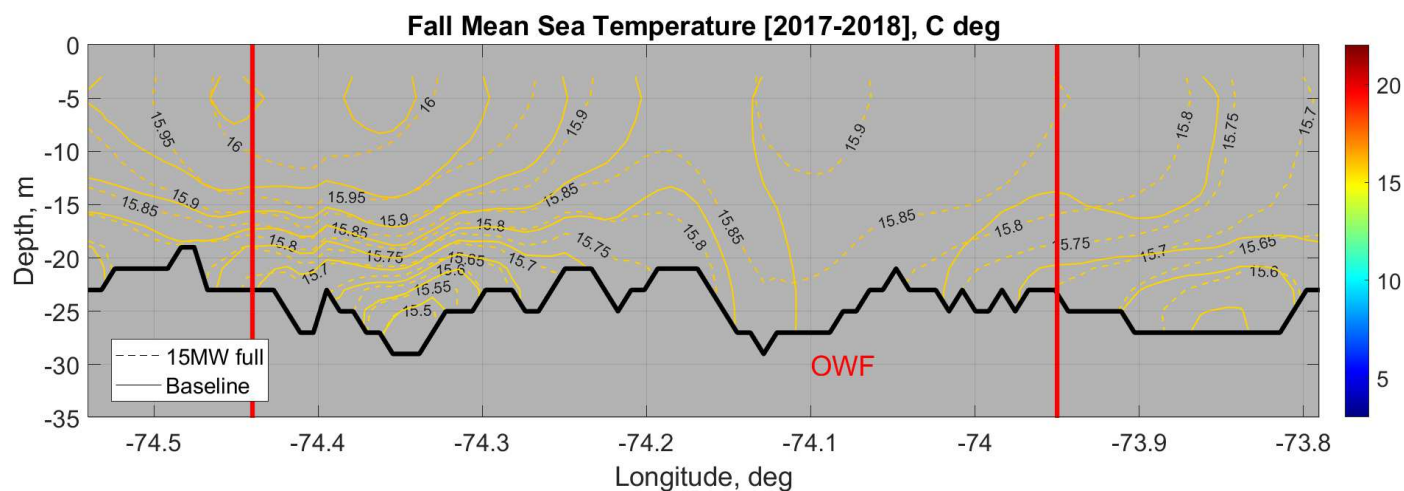


Figure A.146. Average Fall Vertical Temperature Structure of a Southwest-Northeast Transect at NY Bight – Long-Shore Profile B
The figure shows the 2017-2018 Fall average temperature contours from a transect for Scenario 5: 15 MW full build-out OSW and the same transect for Scenario 1: Baseline.

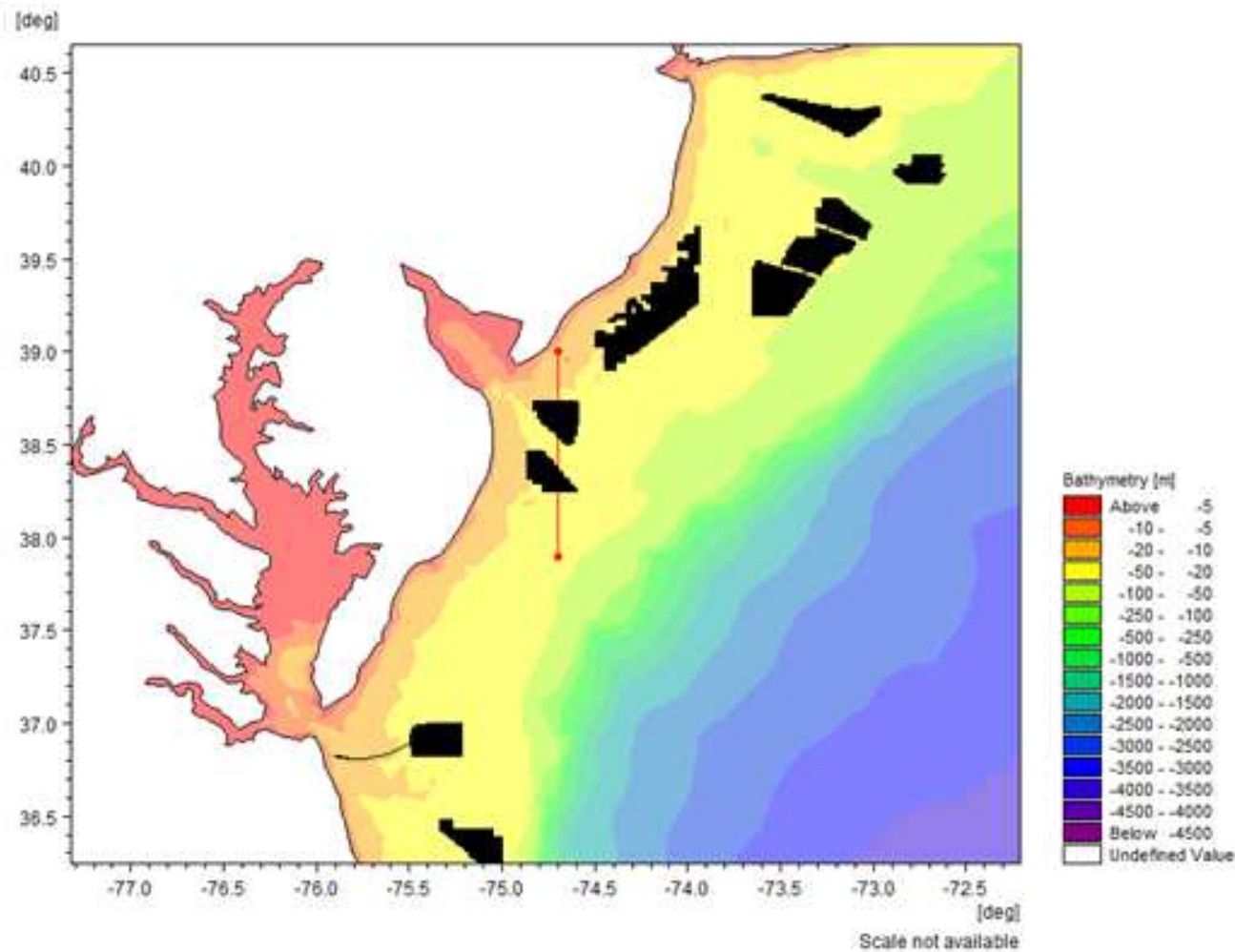


Figure A.147. Thermal Transect Location NY Bight – Long-Shore Profile C

The figure shows the transect through one set of the NY Bight OSW farms with a line orientation from the South and headed North.

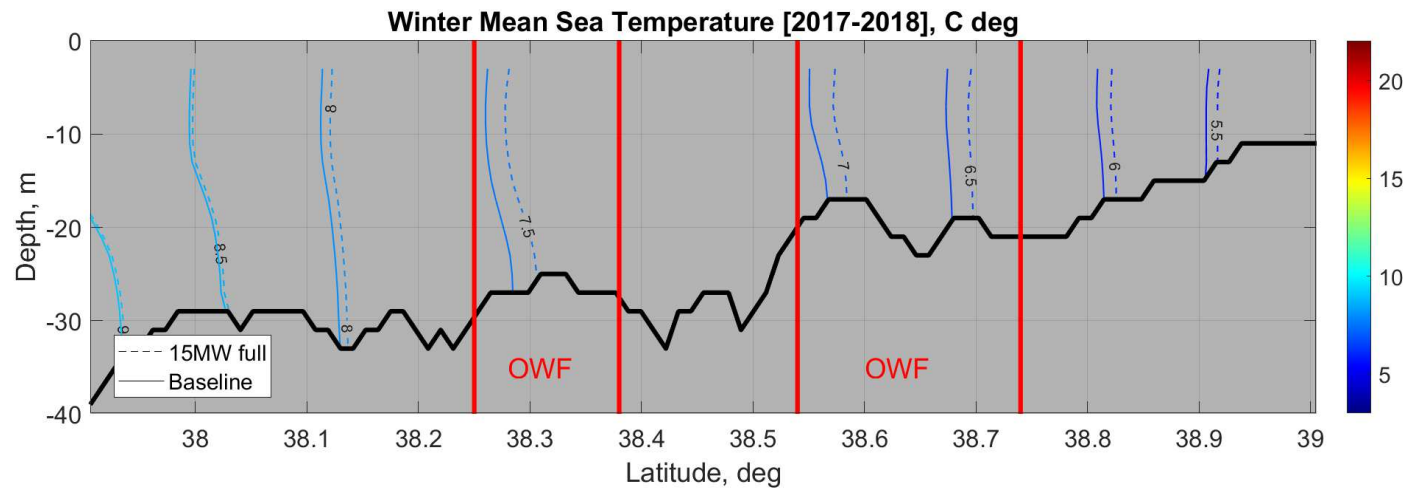


Figure A.148. Average Winter Vertical Temperature Structure of a South-North Transect at NY Bight – Long-Shore Profile C
The figure shows the 2017-2018 Winter average temperature contours from a transect for Scenario 5: 15 MW full build-out OSW and the same transect for Scenario 1: Baseline

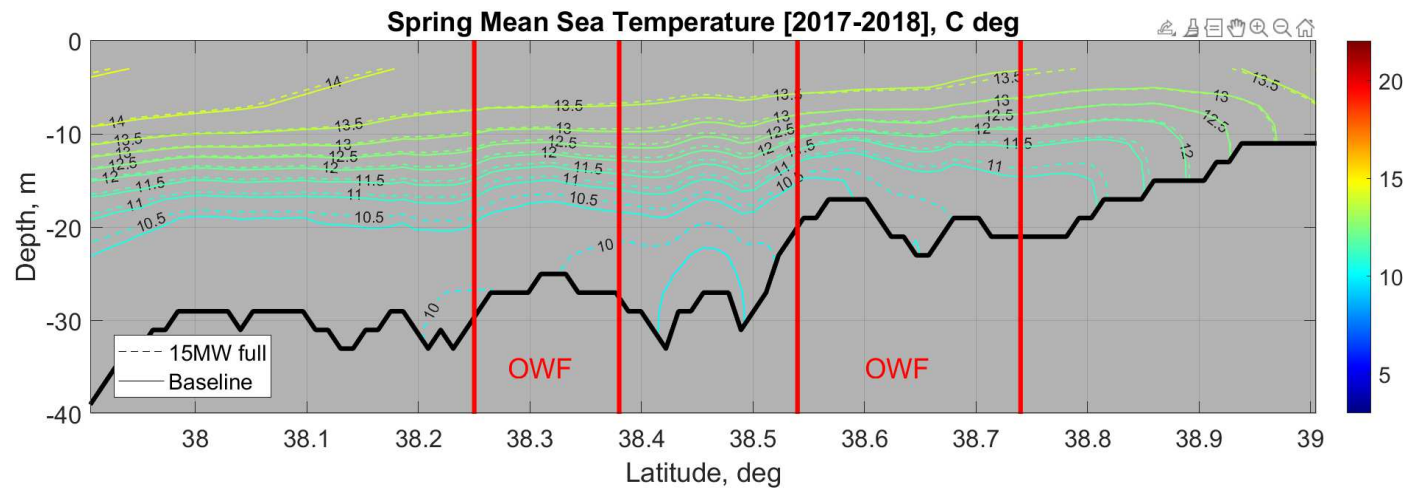


Figure A.149. Average Spring Vertical Temperature Structure of a South-North Transect at NY Bight – Long-Shore Profile C
The figure shows the 2017-2018 Spring average temperature contours from a transect for Scenario 5: 15 MW full build-out OSW and the same transect for Scenario 1: Baseline.

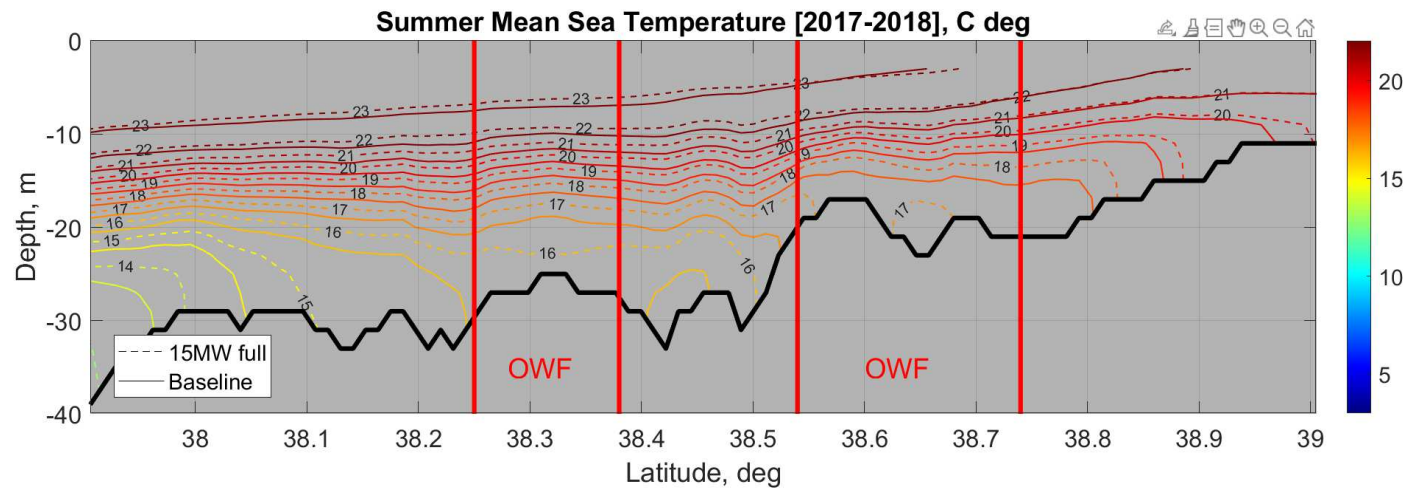


Figure A.150. Average Summer Vertical Temperature Structure of a South-North Transect at NY Bight – Long-Shore Profile C
The figure shows the 2017-2018 Summer average temperature contours from a transect for Scenario 5: 15 MW full build-out OSW and the same transect for Scenario 1: Baseline.

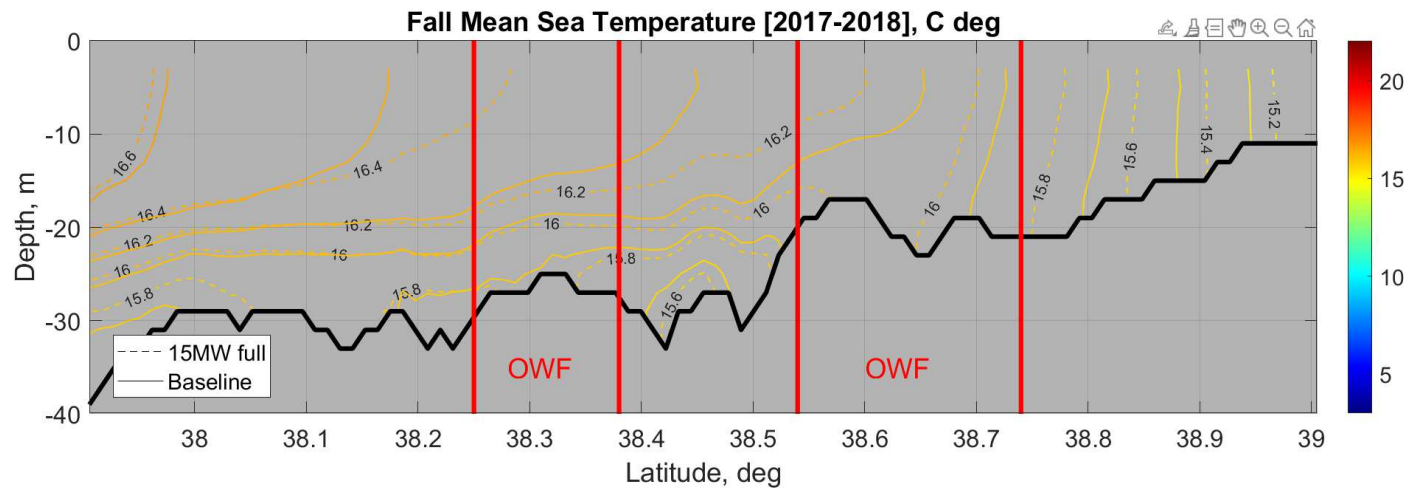


Figure A.151. Average Fall Vertical Temperature Structure of a South-North Transect at NY Bight – Long-Shore Profile C
The figure shows the 2017-2018 Fall average temperature contours from a transect for Scenario 5: 15 MW full build-out OSW and the same transect for Scenario 1: Baseline.

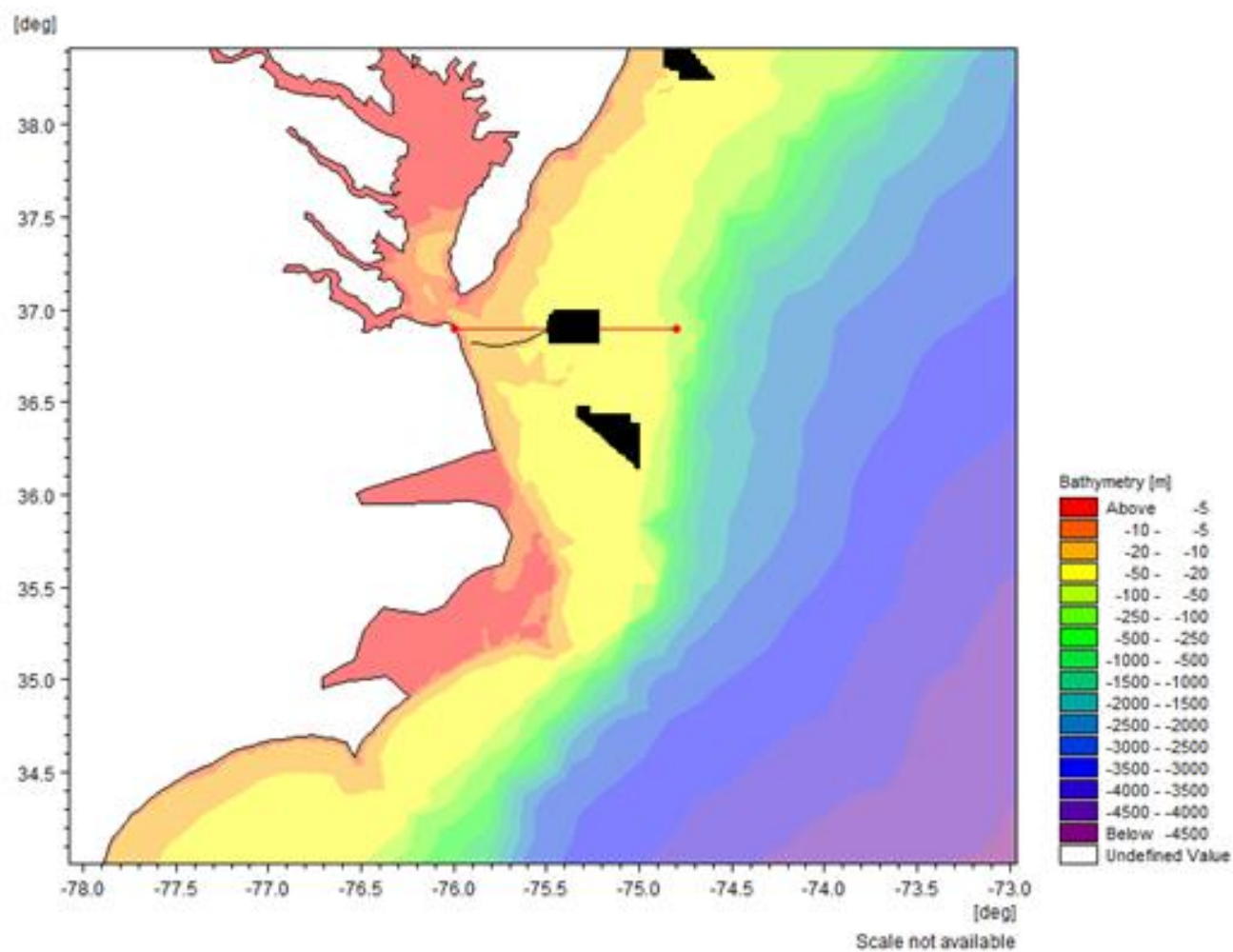


Figure A.152. Thermal Transect Location VA-NC – Cross-Shore Profile A

The figure shows the transect through one set of the VA-NC OSW farms with a line orientation from the East and headed West.

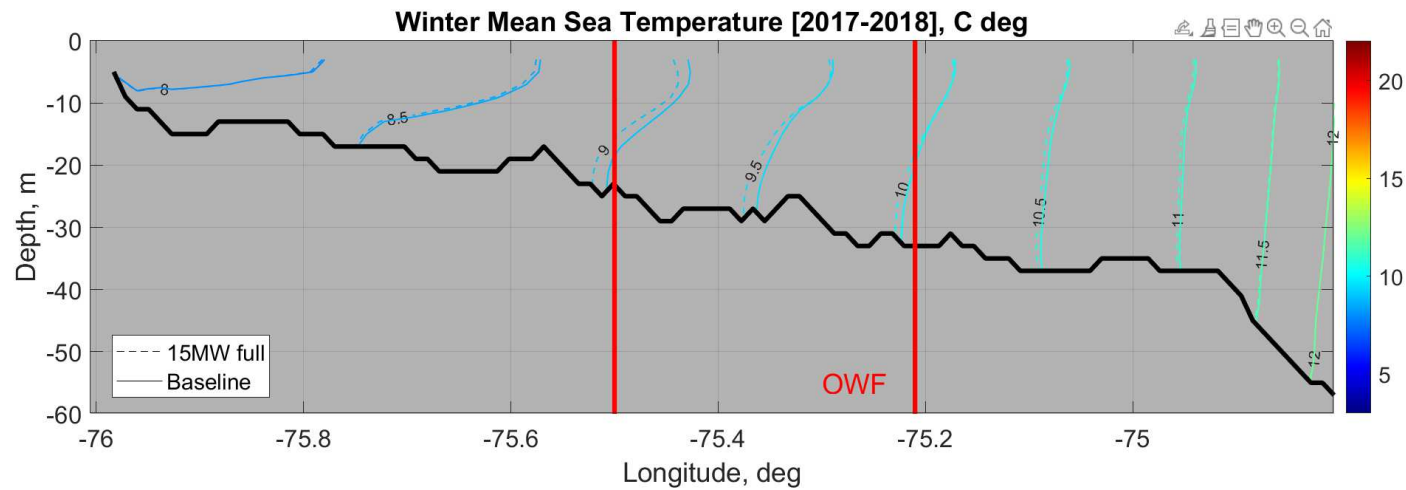


Figure A.153. Average Winter Vertical Temperature Structure of an East-West Transect at VA-NC – Cross-Shore Profile A
The figure shows the 2017-2018 Winter average temperature contours from a transect for Scenario 5: 15 MW full build-out OSW and the same transect for Scenario 1: Baseline.

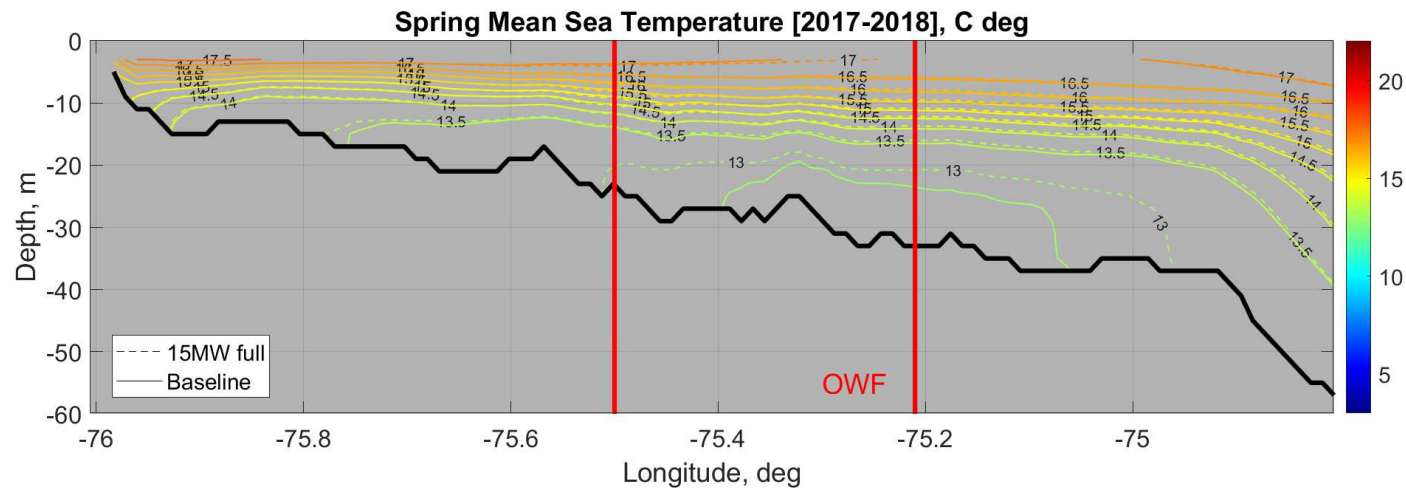


Figure A.154. Average Spring Vertical Temperature Structure of an East-West Transect at VA-NC – Cross-Shore Profile A
The figure shows the 2017-2018 Spring average temperature contours from a transect for Scenario 5: 15 MW full build-out OSW and the same transect for Scenario 1: Baseline.

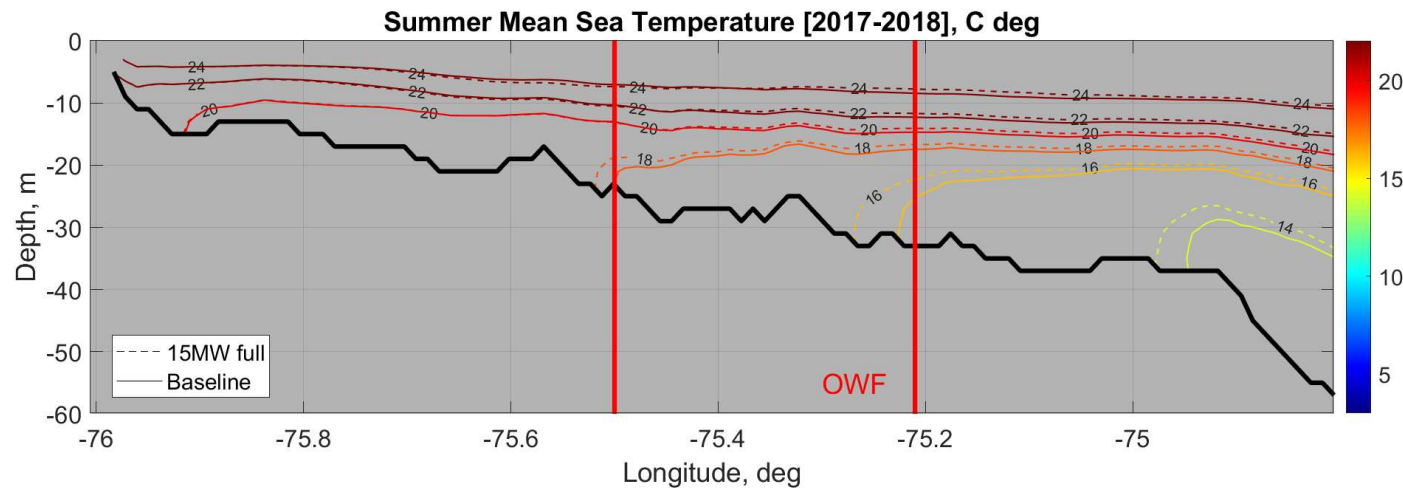


Figure A.155. Average Summer Vertical Temperature Structure of an East-West Transect at VA-NC – Cross-Shore Profile A
The figure shows the 2017-2018 Summer average temperature contours from a transect for Scenario 5: 15 MW full build-out OSW and the same transect for Scenario 1: Baseline.

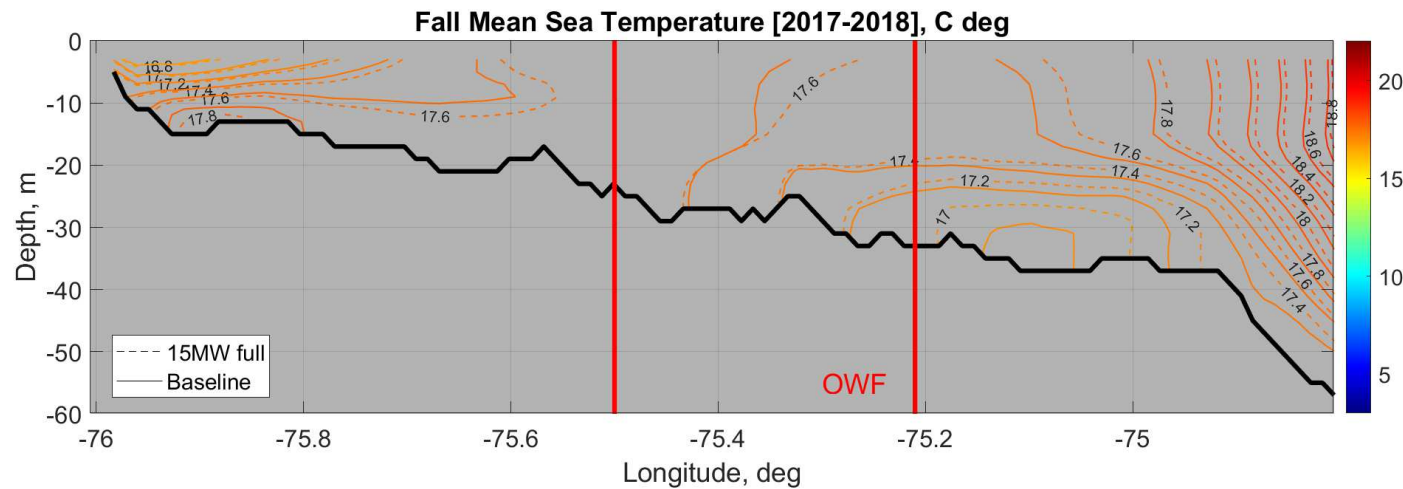


Figure A.156. Average Fall Vertical Temperature Structure of an East-West Transect at VA-NC – Cross-Shore Profile A
The figure shows the 2017-2018 Fall average temperature contours from a transect for Scenario 5: 15 MW full build-out OSW and the same transect for Scenario 1: Baseline.

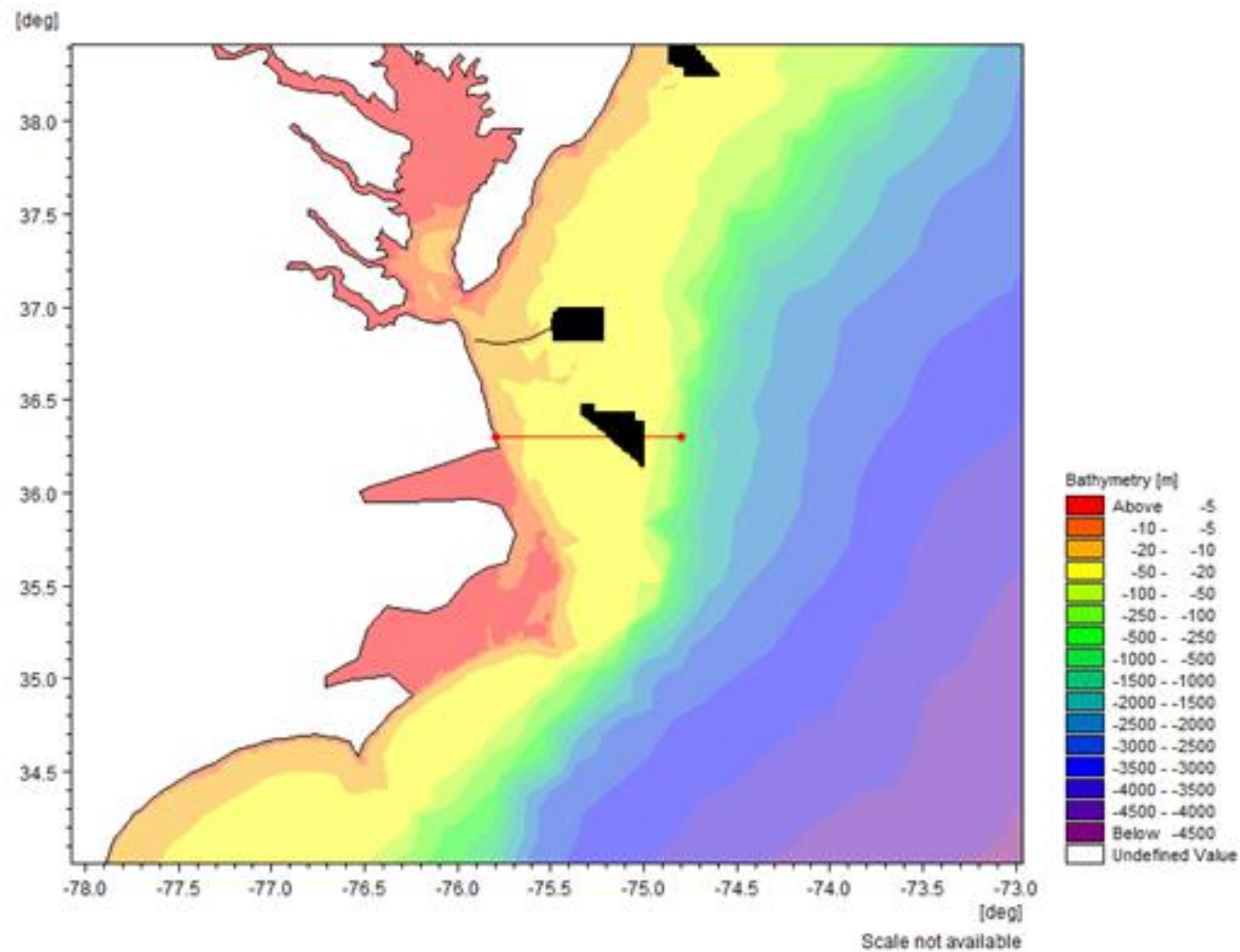


Figure A.157. Thermal Transect Location VA-NC – Cross-Shore Profile B

The figure shows the transect through one set of the VA-NC OSW farms with a line orientation from the East and headed West.

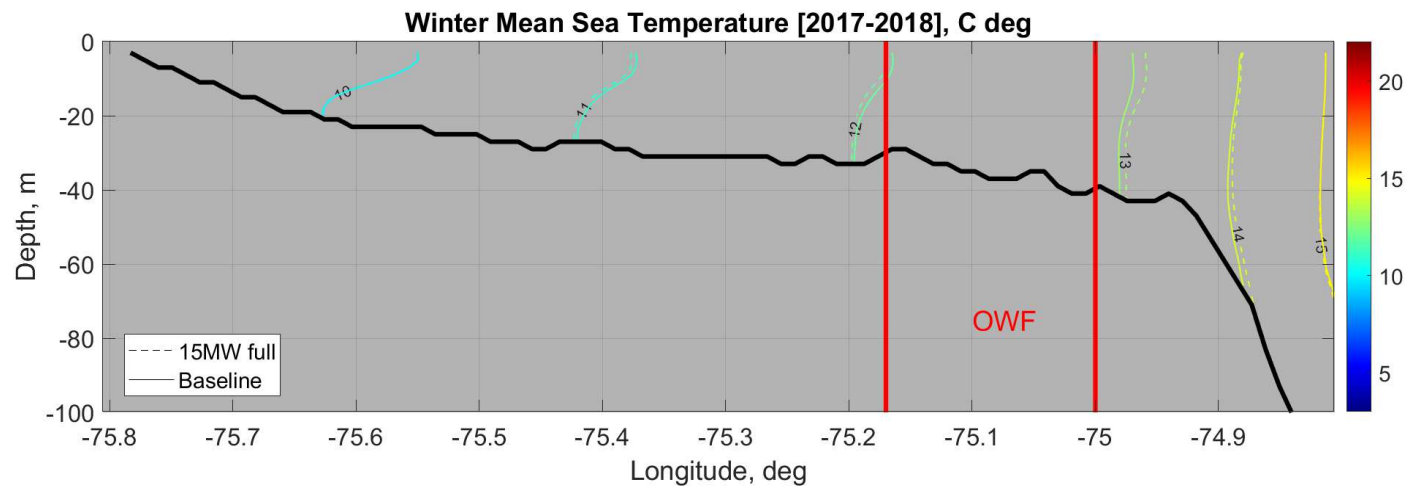


Figure A.158. Average Winter Vertical Temperature Structure of an East-West Transect at VA-NC – Cross-Shore Profile B
The figure shows the 2017-2018 Winter average temperature contours from a transect for Scenario 5: 15 MW full build-out OSW and the same transect for Scenario 1: Baseline.

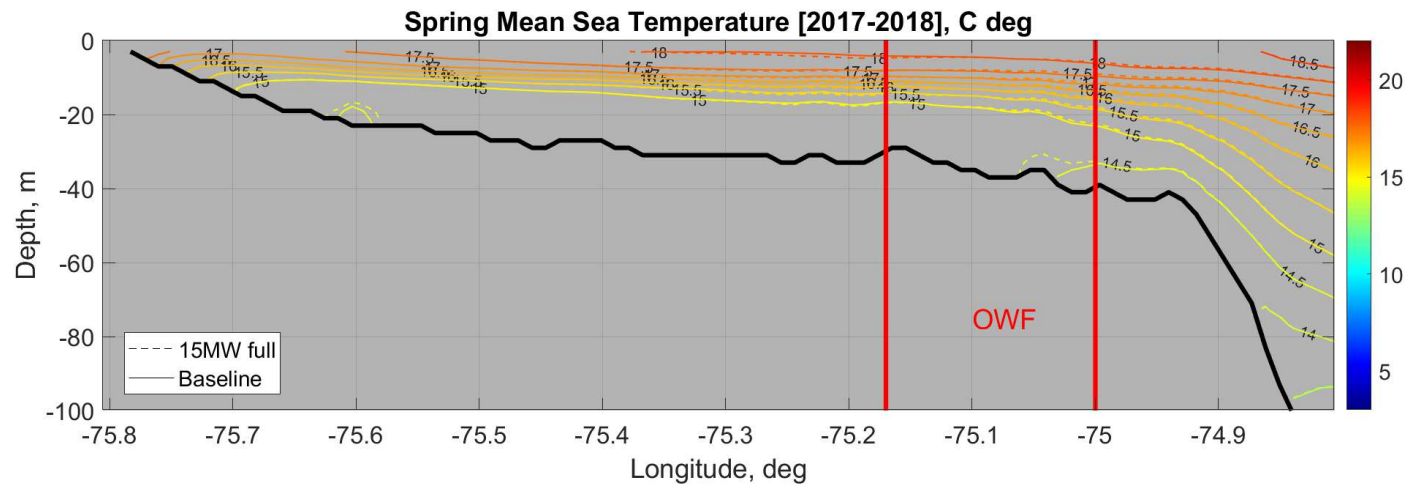


Figure A.159. Average Spring Vertical Temperature Structure of an East-West Transect at VA-NC – Cross-Shore Profile B
The figure shows the 2017-2018 Spring average temperature contours from a transect for Scenario 5: 15 MW full build-out OSW and the same transect for Scenario 1: Baseline.

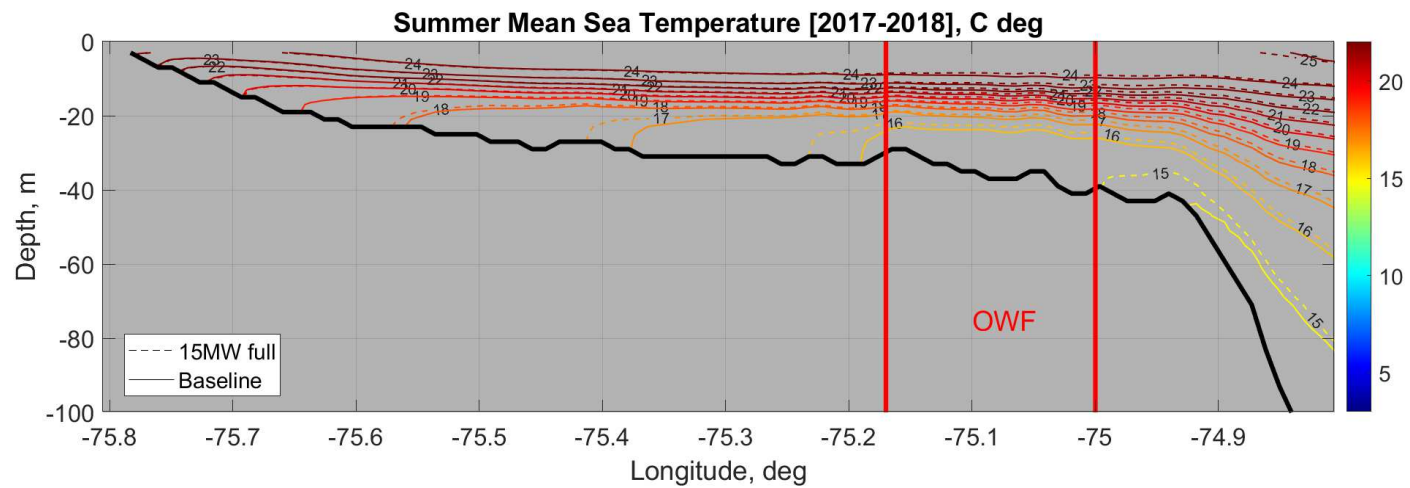


Figure A.160. Average Summer Vertical Temperature Structure of an East-West Transect at VA-NC – Cross-Shore Profile B
The figure shows the 2017-2018 Summer average temperature contours from a transect for Scenario 5: 15 MW full build-out OSW and the same transect for Scenario 1: Baseline.

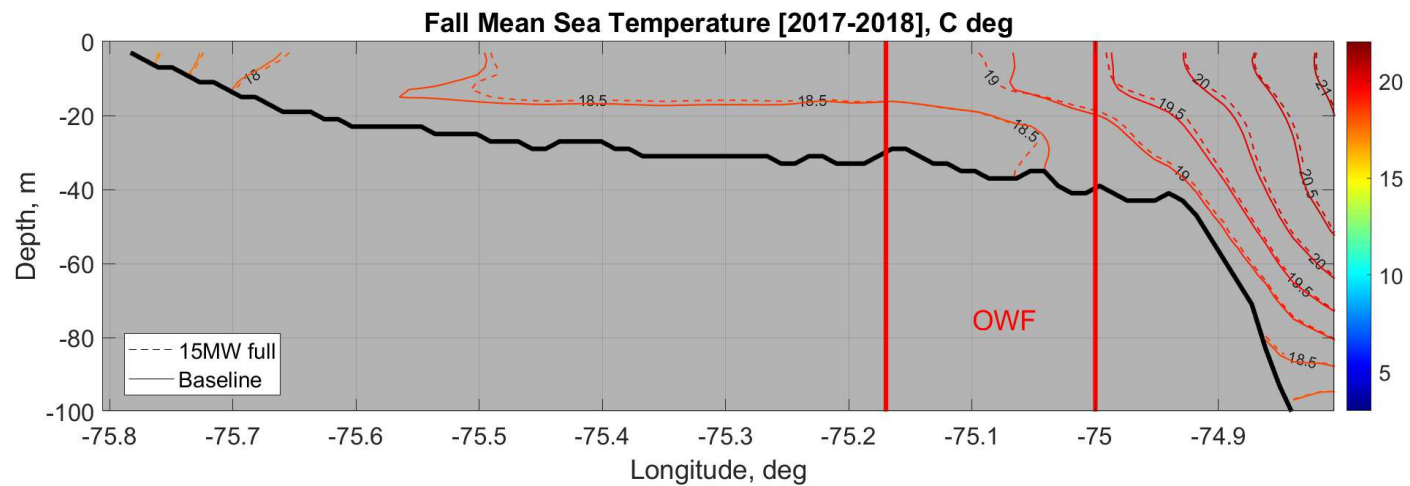


Figure A.161. Average Fall Vertical Temperature Structure of an East-West Transect at VA-NC – Cross-Shore Profile B
The figure shows the 2017-2018 Fall average temperature contours from a transect for Scenario 5: 15 MW full build-out OSW and the same transect for Scenario 1: Baseline.

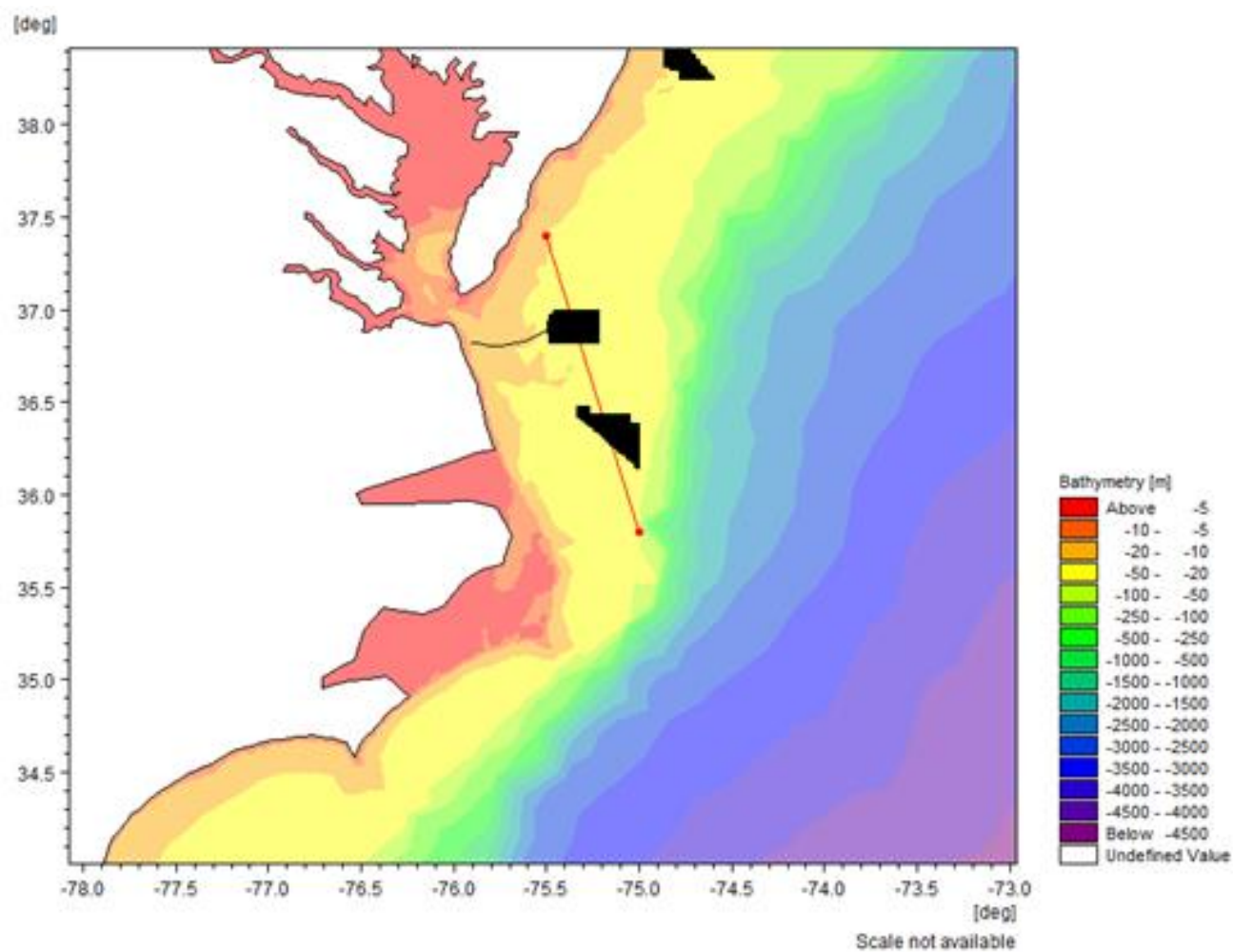


Figure A.162. Thermal Transect Location VA-NC – Long-Shore Profile A

The figure shows the transect through one set of the VA-NC OSW farms with a line orientation from the South and headed Northwest.

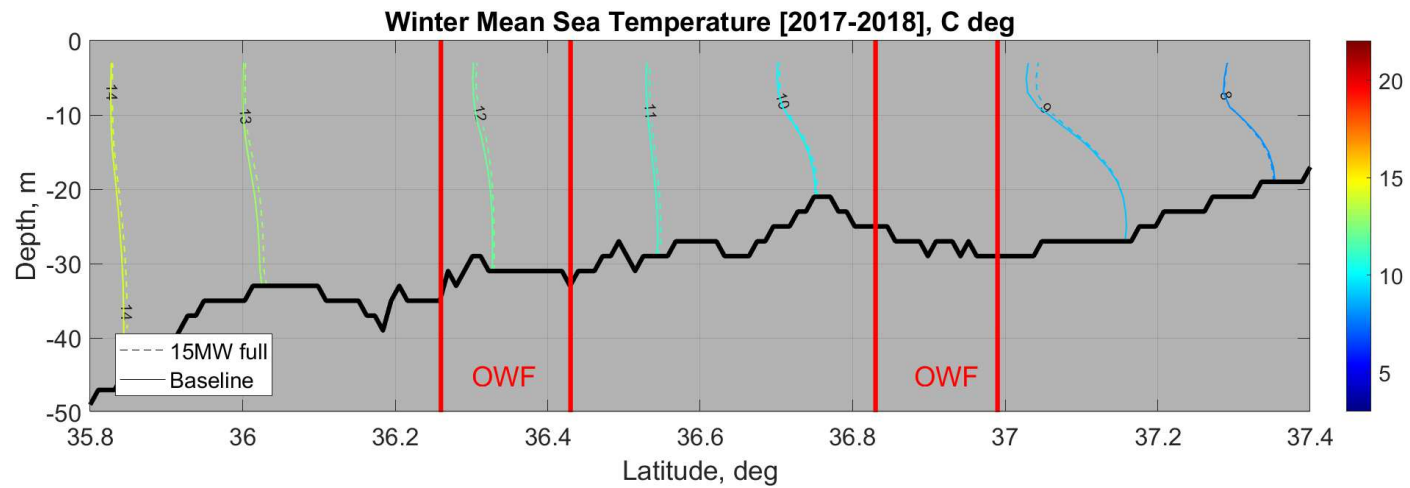


Figure A.163. Average Winter Vertical Temperature Structure of a South-Northwest Transect at VA-NC – Long-Shore Profile A
The figure shows the 2017-2018 Winter average temperature contours from a transect for Scenario 5: 15 MW full build-out OSW and the same transect for Scenario 1: Baseline.

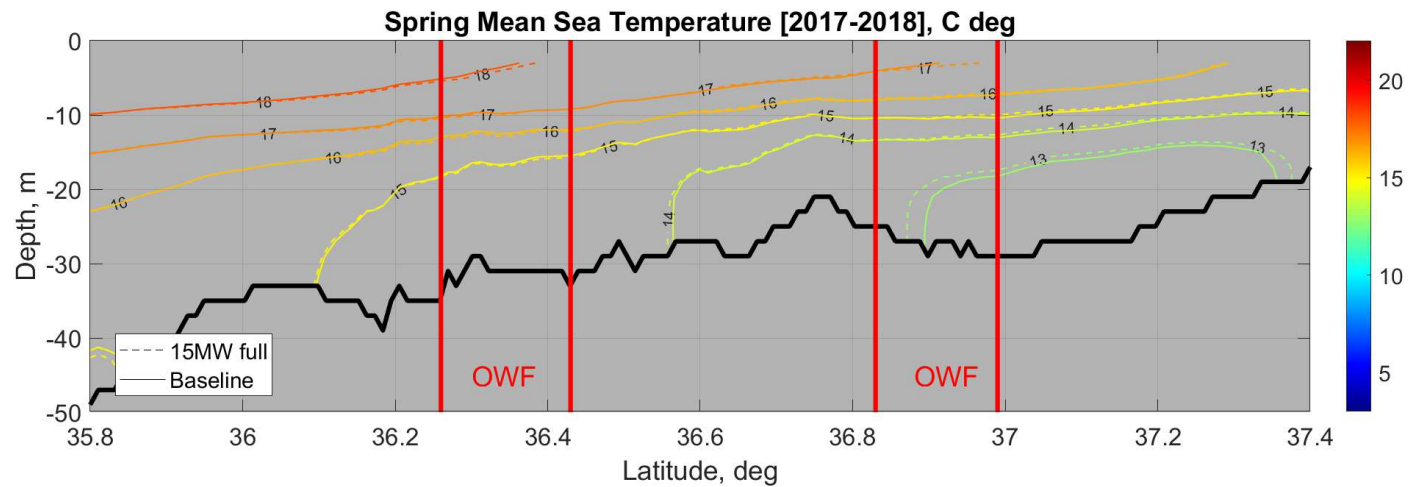


Figure A.164. Average Spring Vertical Temperature Structure of a South-Northwest Transect at VA-NC – Long-Shore Profile A
The figure shows the 2017-2018 Spring average temperature contours from a transect for Scenario 5: 15 MW full build-out OSW and the same transect for Scenario 1: Baseline.

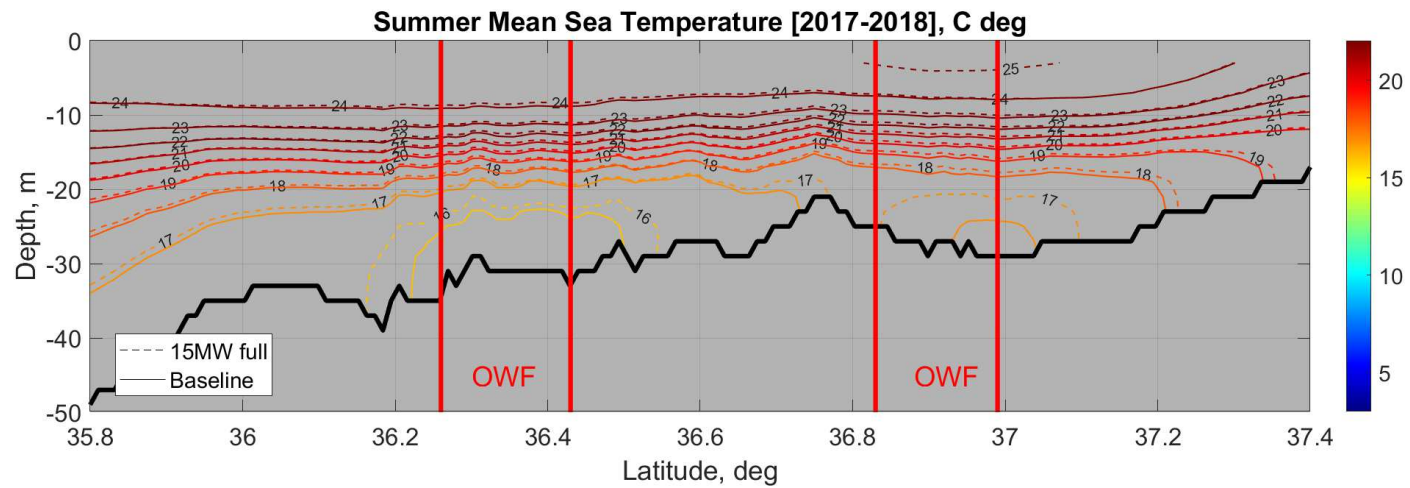


Figure A.165. Average Summer Vertical Temperature Structure of a South-Northwest Transect at VA-NC – Long-Shore Profile A
The figure shows the 2017-2018 Summer average temperature contours from a transect for Scenario 5: 15 MW full build-out OSW and the same transect for Scenario 1: Baseline.

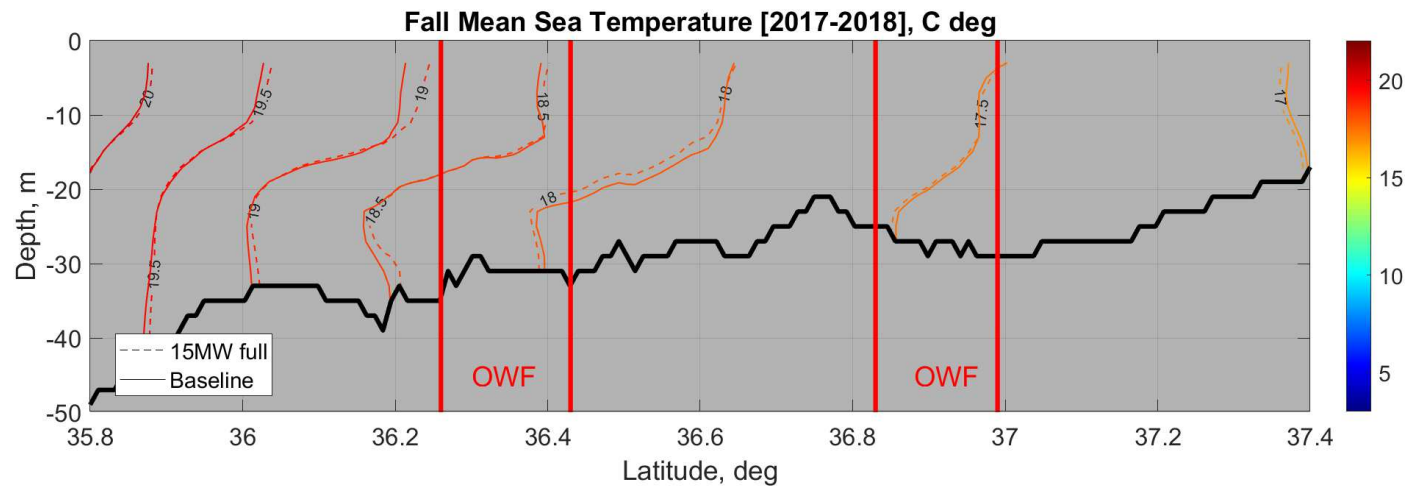


Figure A.166. Average Fall Vertical Temperature Structure of a South-Northwest Transect at VA-NC – Long-Shore Profile A
The figure shows the 2017-2018 Fall average temperature contours from a transect for Scenario 5: 15 MW full build-out OSW and the same transect for Scenario 1: Baseline.

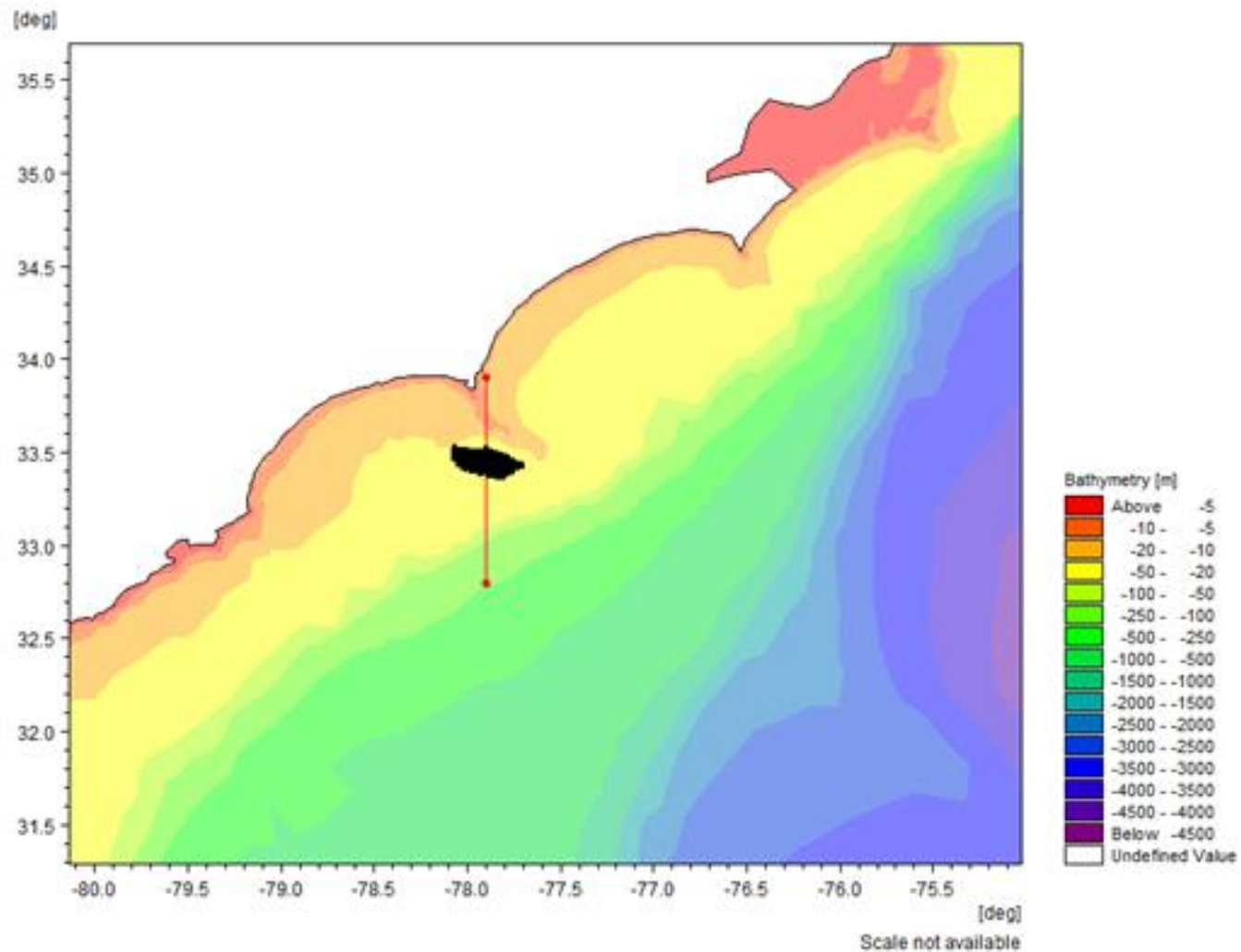


Figure A.167. Thermal Transect Location South Carolina – North-South Profile

The figure shows the transect through one set of the NC-SC OSW farms with a line orientation from the South and headed North.

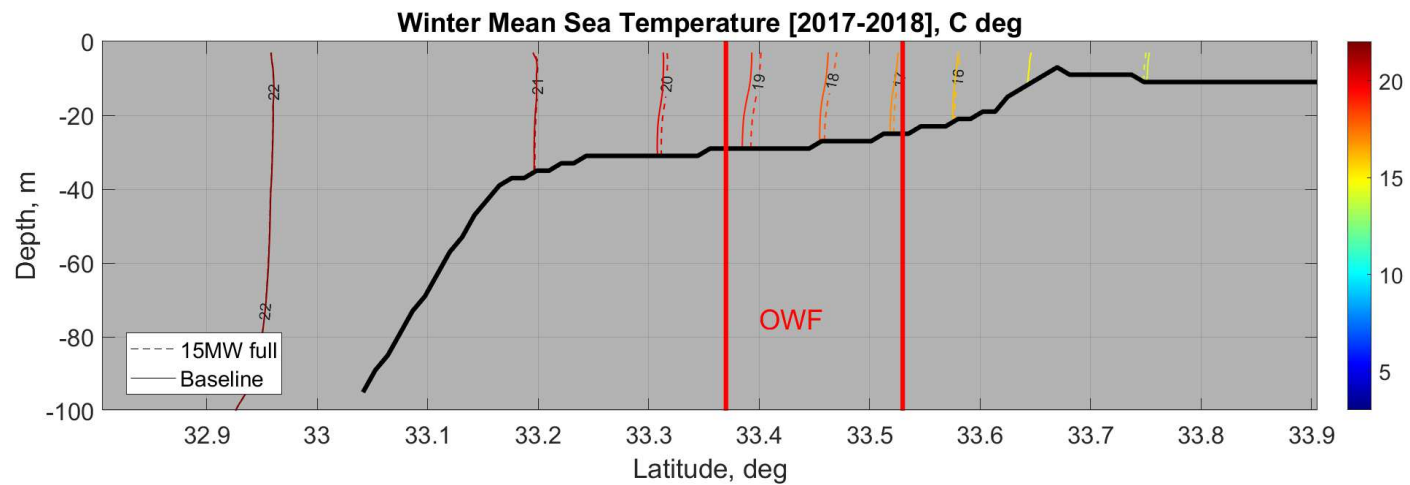


Figure A.168. Average Winter Vertical Temperature Structure of a South-North Transect at South Carolina – North-South Profile
The figure shows the 2017-2018 Winter average temperature contours from a transect for Scenario 5: 15 MW full build-out OSW and the same transect for Scenario 1: Baseline.

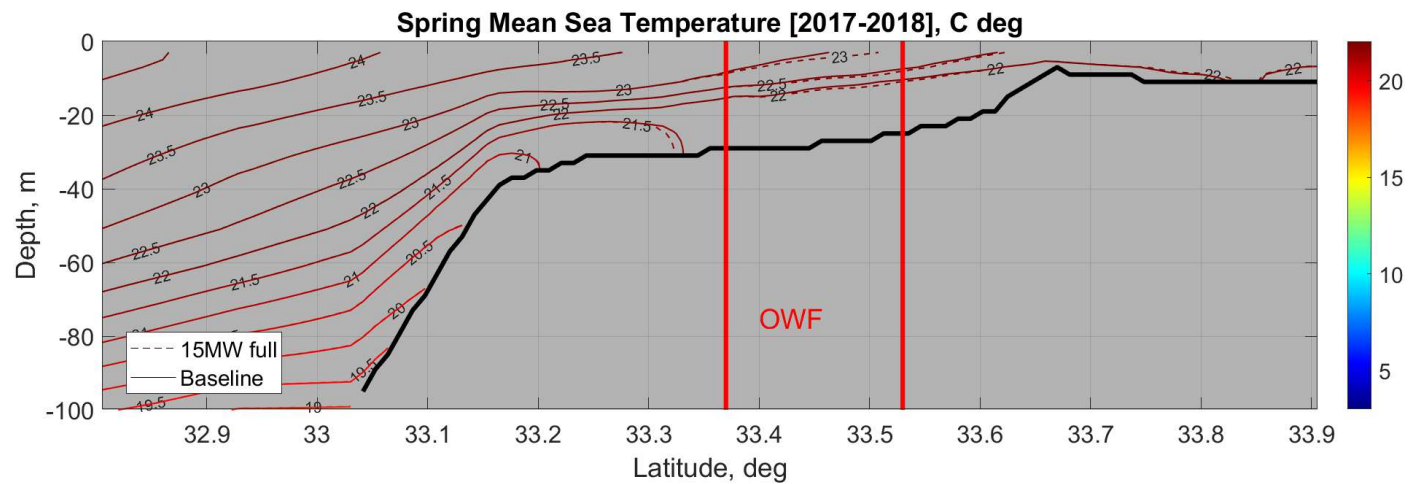


Figure A.169. Average Spring Vertical Temperature Structure of a South-North Transect at South Carolina – North-South Profile
The figure shows the 2017-2018 Spring average temperature contours from a transect for Scenario 5: 15 MW full build-out OSW and the same transect for Scenario 1: Baseline.

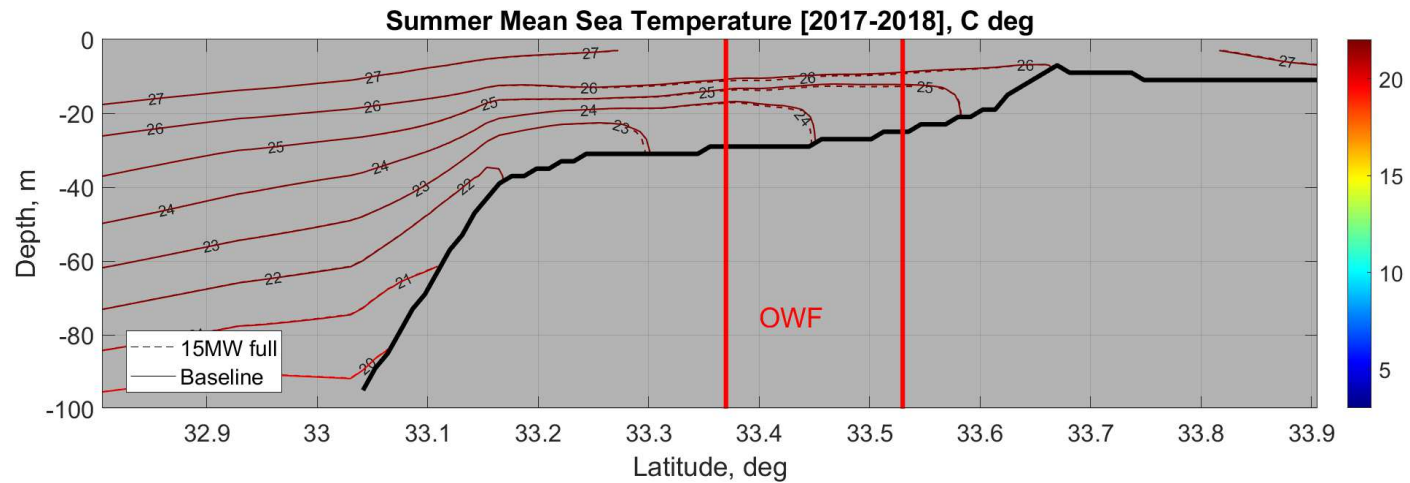


Figure A.170. Average Summer Vertical Temperature Structure of a South-North Transect at South Carolina – North-South Profile
The figure shows the 2017-2018 Summer average temperature contours from a transect for Scenario 5: 15 MW full build-out OSW and the same transect for Scenario 1: Baseline.

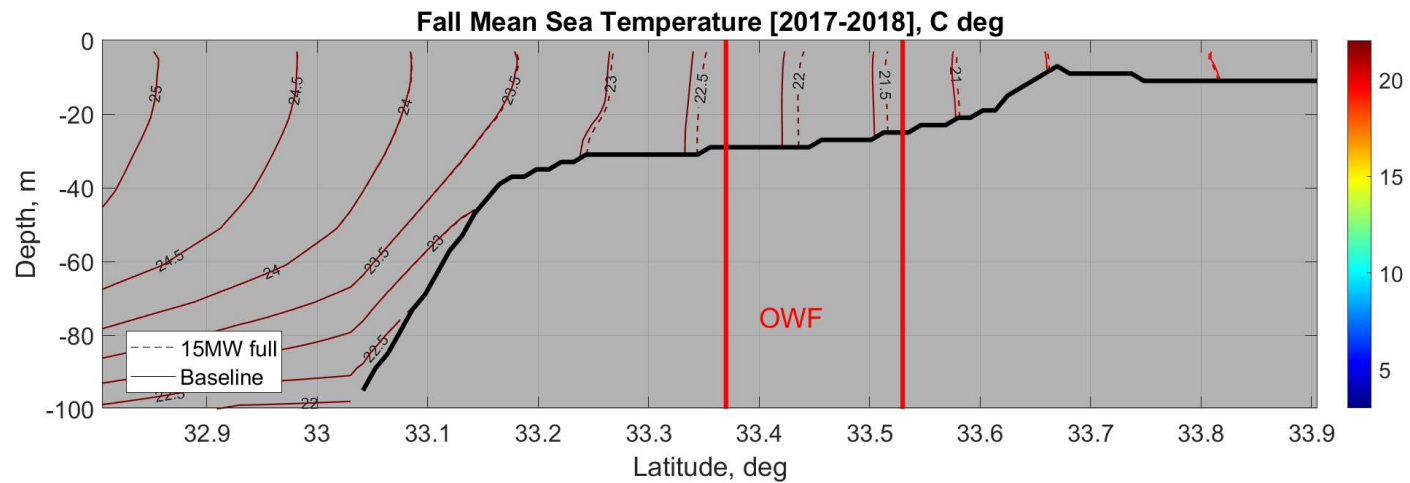


Figure A.171. Average Fall Vertical Temperature Structure of a South-North Transect at South Carolina – North-South Profile
The figure shows the 2017-2018 Fall average temperature contours from a transect for Scenario 5: 15 MW full build-out OSW and the same transect for Scenario 1: Baseline.

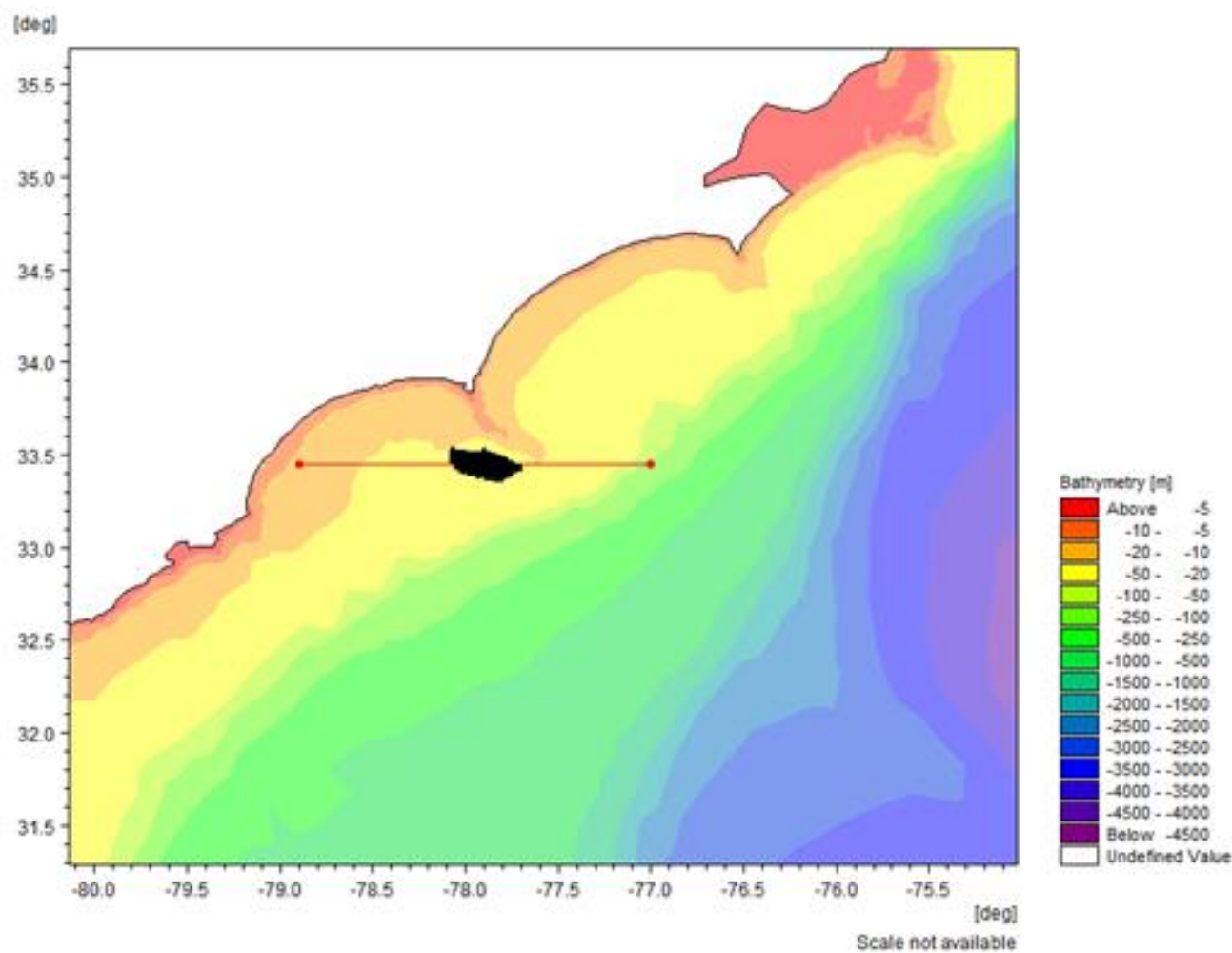


Figure A.172. Thermal Transect Location South Carolina – East-West Profile

The figure shows the transect through one set of the NC-SC OSW farms with a line orientation from the West and headed East.

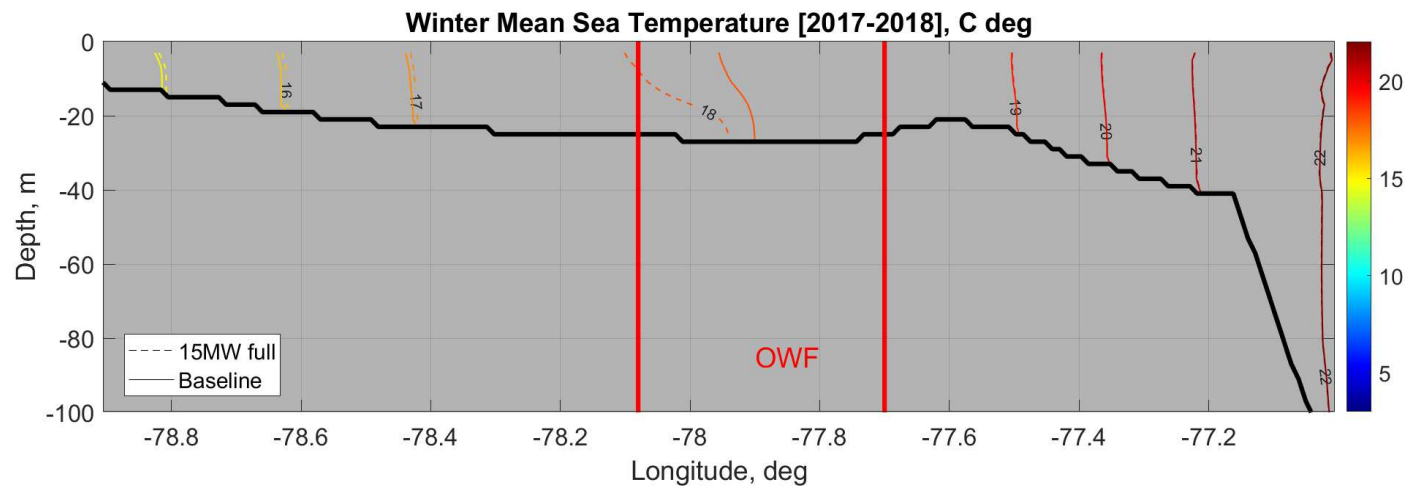


Figure A.173. Average Winter Vertical Temperature Structure of a West-East Transect at South Carolina – East-West Profile
The figure shows the 2017-2018 Winter average temperature contours from a transect for Scenario 5: 15 MW full build-out OSW and the same transect for Scenario 1: Baseline.

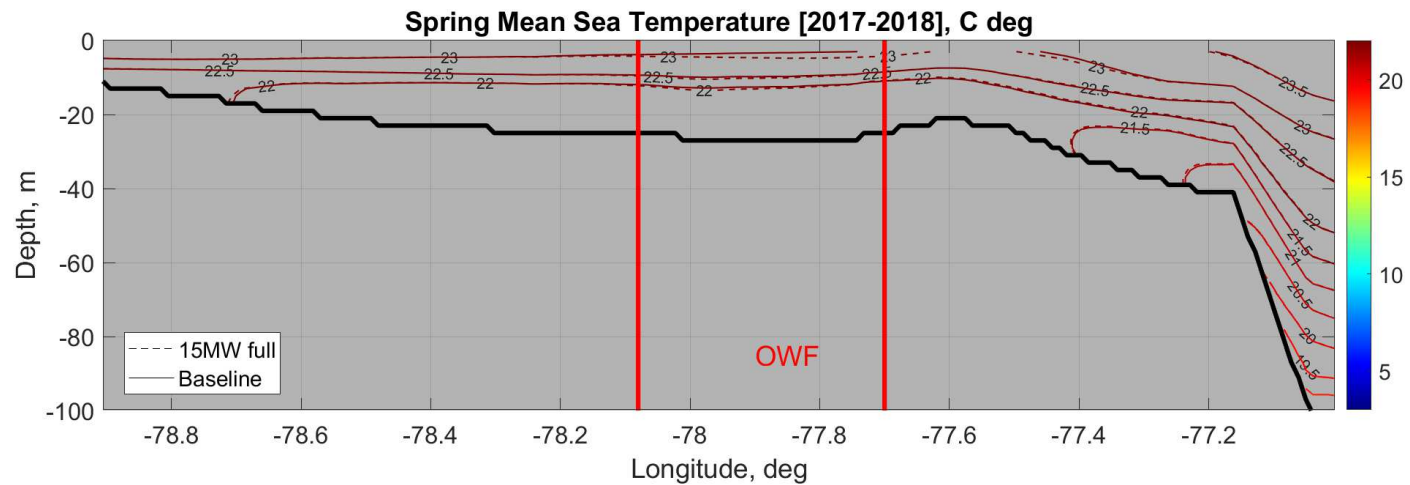


Figure A.174. Average Spring Vertical Temperature Structure of a West-East Transect at South Carolina – East-West Profile
The figure shows the 2017-2018 Spring average temperature contours from a transect for Scenario 5: 15 MW full build-out OSW and the same transect for Scenario 1: Baseline.

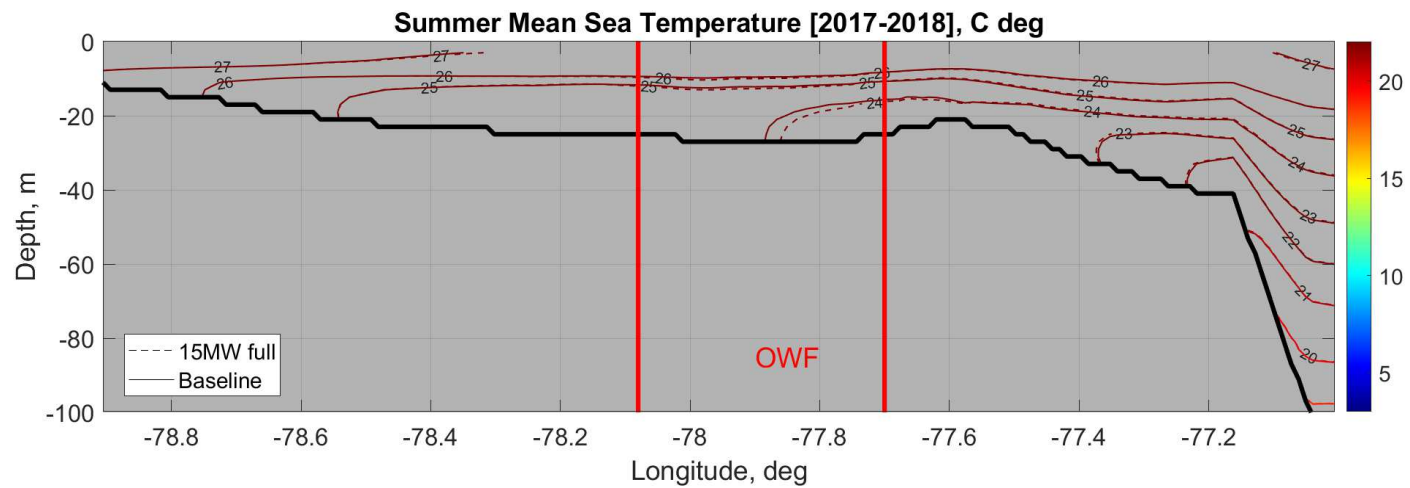


Figure A.175. Average Summer Vertical Temperature Structure of a West-East Transect at South Carolina – East-West Profile

The figure shows the 2017-2018 Summer average temperature contours from a transect for Scenario 5: 15 MW full build-out OSW and the same transect for Scenario 1: Baseline.

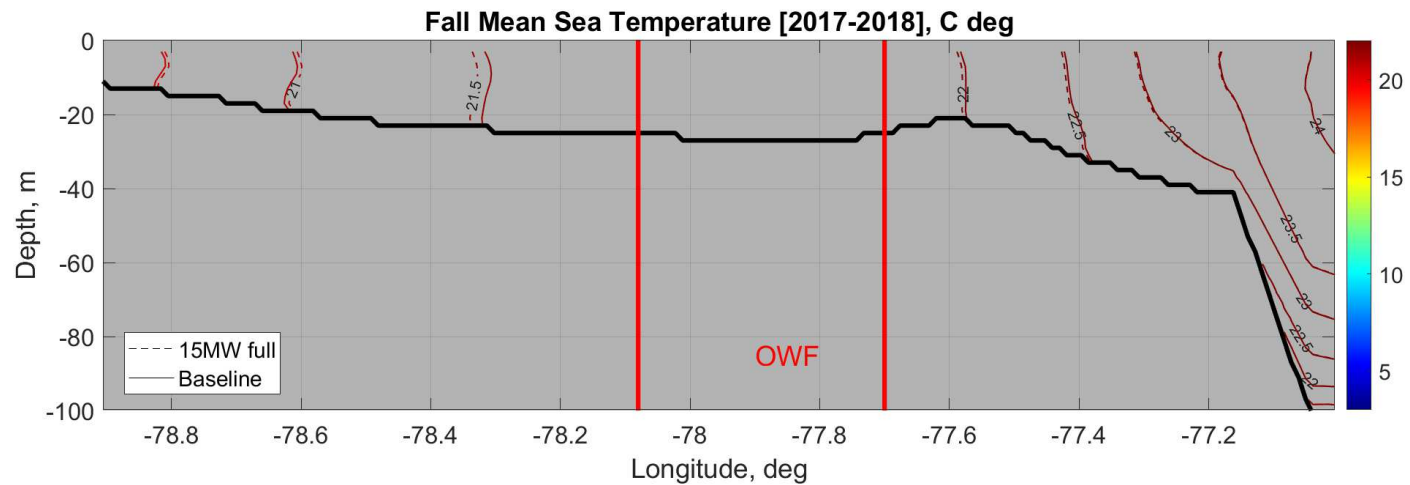


Figure A.176. Average Fall Vertical Temperature Structure of a West-East Transect at South Carolina – East-West Profile

The figure shows the 2017-2018 Fall average temperature contours from a transect for Scenario 5: 15 MW full build-out OSW and the same transect for Scenario 1: Baseline

B Agent-Based Model Overview, Design Concepts and Details (ODD) Protocol

The descriptions of the surf clam, sea scallop and summer flounder ABMs follow the updated “Overview, Design concepts, Details” protocol, which is a standard format for describing and disseminating individual based models (Grimm et al. 2020). Some sections in this ODD have been previously described in the main body of the report (Section 6.2) and are repeated in the following sections for completeness of the ODD.

B.1 Purpose

The purpose of the models is to simulate the larval transport of selected key species, namely the *sea scallop* (*Placopecten magellanicus*), *surf clam* (*Spisula solidissima*), and *summer flounder* (*Paralichthys dentatus*), and changes in transport patterns, if any, arising from the alteration of oceanographic transport patterns in the indicated study area because of offshore wind farm projects. The results of this study will be used to assess impact on larval transport and settlement resulting from wind turbine placement along the east coast of the US; and will be used to evaluate the need for, and the formation of, mitigation measures if deemed necessary.

The models are evaluated by their ability to reproduce larval dispersal and settlement patterns. The following evaluations may only be performed after satisfactory calibration and validation of the hydrodynamic forcings that are inputs to the ABM. The evaluation of the baseline results is described in Sections 6.7 and 7.4 of the main report. The methods of evaluation used were:

1. **Larvae dispersal pattern.** This pattern reflects the horizontal and vertical migration of larvae across the simulated life stages. As the larvae develop from an initial state of passive drifter, whereby their movements are predominantly dependent on hydrodynamic forcings, to later stages of development when the larvae develop limited capability for horizontal and/or vertical swimming, thereby exerting control over their migration patterns to a certain extent. These dispersal patterns, if sufficiently replicated, provide indication that parameterized movement processes of agents within the model are representative of real-life larval movement processes.
2. **Settlement location of larvae.** This pattern reflects how pre-transformation larvae select locations suitable for settlement, depending on environmental factors including temperature, salinity, water depth and riverbed/seabed substrate type. Settlement of larvae occurs when a super-agent carries within it competent larvae (i.e., larvae that are ready to settle). The number of competent larvae in an agent is determined by growth processes built into the model. Depending on the species being modeled, settlement characteristics of competent larvae may vary substantially (e.g., summer flounder larvae migrate to settle along the shoreline, while sea scallop and surf clam larvae settle along the shelf). These settlement patterns, if sufficiently replicated, provide an indication that the parameterized zygote/larval growth, mortality, and settlement processes within the model are adequately descriptive of real-life larval growth, mortality, and settlement processes.

B.2 Entities, State Variables, and Scales

B.2.1 Entities

The following entities are included in the models: super-agents, grid cells, and the global environment. Super agents represent a group of simulated species at post-fertilization, pre-transformation life stages (i.e., zygotes and larvae of the three species). Grid cells, (i.e., virtual geographical location) represent the oceanic and estuarine conditions such as salinity, temperature, horizontal and vertical current speeds, and direction. The global environment primarily provides temporal information.

B.2.2 State Variables

The model comprises **global** variables that only change across time. In the models, the global variables are related to the time of the instance being simulated. The global variables are presented in **Table B.1** below.

Table B.1. Global State Variables

Variable Name	Variable Type and Units	Meaning
Timestamp	Datetime, yyyy-mm-dd hh:mm:ss	Datetime of simulated instance
Is_daytime	Binary	Indicates if the current timestep is during daytime (TRUE) or nighttime (FALSE).

Grid cells are the smallest computational two-dimensional area in the model; each grid cell represents a polygon in the transverse plane, which in turn represents the entire water column within the spatial footprint of the cell. The model comprises grid cell state variables that change over the time of the model simulation, computed for each cell in the model mesh. The grid cell state variables are related to numbers and densities of settled larvae, as well as the cumulative numbers and densities of transported agents within the model domain. The grid cell state variables are presented in **Table B.2** below.

Table B.2. Grid Cell State Variables

Variable Name	Variable Type and Units	Meaning
Settled_Larvae_Density	Real number, larvae/m ²	Number of settled larvae per square meter
Settled_Larvae_Absolute	Real number, larvae	Number of settled larvae (in the grid) in absolute numbers
Cumulative_All	Real number, agents/m ²	Cumulative density of live agents passing through the area, indicating transport rate in the area
Cumulative_Competent	Real number, agents/m ²	Cumulative density of live competent (i.e. ready to settle) agents passing through the area, indicating transport rate in the area

Super-agents are objects containing a group of individual agents (i.e. zygotes and larvae) of each modeled species. The zygotes and larvae are mobile and dynamic organisms that grow or decay (die) over the simulation period. During their growth, the individual agents undergo three main development stages – first, they are initialized as zygotes, which are then incubated and hatch as larvae. After a stipulated larval development time period, the larvae grow to be competent and can settle. During the growth process, a proportion of individuals contained in the super-agents die due to natural mortality. The super-agents are predominantly driven, spatially, by hydrodynamic forcings and by the larvae’s swimming ability which is developed at later stages of growth.

The super-agent state variables are presented in **Table B.3** below and comprise dynamic and static variables. Dynamic variables change over time, such as the number of zygotes and larvae contained within the super-agent, and the cumulative distance traveled by the super-agent. Static variables stay constant through the super-agent’s lifetime, such as growth parameters, which are randomly sampled for each super-agent (e.g. minimum incubation time required for competency acquisition), as well as the coordinates at which the particular super-agent was spawned or released at.

Table B.3. Super-Agent State Variables

Variable Name	Variable Type and Units	Meaning
sv_Live_agents	Real number; number of agents	Number of zygotes/larvae alive in super-agent
sv_n_zygotes	Real number; number of zygotes	Number of live zygotes in the agent
sv_n_larvae	Real number; number of larvae	Number of live pre-competent (i.e., not ready to settle) larvae in the agent
sv_n_competent_larvae	Real number; number of larvae	Number of live settle-ready larvae in the agent
sv_n_settled	Real number; number of settled larvae	Number of settled larvae from the agent that have settled
sv_dead_individuals	Real total; number of dead individuals	Total number of dead individuals
sv_larvae_development_minimum	Real number; days	Minimum time to pass before larvae can start settling, from time of hatching, sampled from a normal distribution
sv_larvae_development_maximum	Real number; days	Maximum time to pass before larvae can start settling, from time of hatching, sampled from a normal distribution, after this time competency is lost and individual dies
sv_Competency_Gain	Binary; unitless	Indicates if an individual has gained competency (1) or not (0)
sv_Competency_Loss	Binary; unitless	Indicates if an individual has lost competency (1)

Variable Name	Variable Type and Units	Meaning
av_spawn_ID	String; unitless	Source spawning ground ID of zygote
sv_sink_ID	String; unitless	SinkID area of settled larvae
sv_Home_X	Real number; dec degrees	X-coordinate of zygote release point
sv_Home_Y	Real number; dec degrees	Y-coordinate of zygote release point
sv_Home_Z	Real number; m	Z-coordinate of zygote release point
sv_cumulative_dist	Real number; km	Cumulative distance travelled by larvae before settlement
sv_displacement_dist	Real number; km	Euclidean distance from spawn location to settlement location
sv_displacement_dir	Real number; dec degrees	Direction from spawn location to settlement location
sv_zygote_incubation_min	Real number; hours	Minimum incubation time required for zygote to hatch sampled from a normal distribution
sv_zygote_incubation_max	Real number; hours	Incubation time required for zygote to fail to hatch and die, sampled from a normal distribution
sv_SAL_affected	Real number; number of individuals	Number of individuals in an agent negatively affected by salinity
sv_TEMP_affected	Real number; number of individuals	Number of individuals in an agent negatively affected by temperature
AGE	Real number, seconds	Age of super agent
XPOS	Real number	X-coordinate of super-agent at current timestep
YPOS	Real number	Y-coordinate of super-agent at current timestep
ZPOS	Real number	Z-coordinate of super-agent at current timestep
sv_feeding_age	Real number; days	First-feeding age of larvae, sampled from normal distribution. Only active in Summer Flounder (<i>Paralichthys dentatus</i>) ABM.

B.2.3 Scales

The model's spatial extent for the ABM is identical to the spatial extent of the regional hydrodynamic model, as described in **Section 2.1** and **Section 6.4** of the main report. For ease of reference, an excerpt of the description is replicated in this section. The geographic extent of the regional hydrodynamic model was approximately from offshore Nova Scotia to offshore Florida. The model was established in hindcast

mode, using MIKE 3 FM HD. Data is included for the years 2017, 2018, 2019 and 2020 for the sea scallop ABM and 2017 for the summer flounder and surf clam ABMs, with targeted localized resolution in the project areas (i.e., the Wind Energy Areas). The model's space is represented as bounded and not toroidal, therefore super-agents leaving the boundary of an edge of the domain will not reappear in grid cells along the opposite edge.

The model was bounded on the south near Cape Canaveral at 80.6°W 28.5°N, and extends eastwards out past the shelf to 71.0°W 28.5°N. From here the eastern-most boundary extends to the north off the Nova Scotian shelf at 59.7°W 40.6°N. The northern boundary continues inshore to 61.4°W 45.2°N, the remaining boundary continues along the coastline to the point near Cape Canaveral.

The flexible mesh of the model allows for efficient focusing of computer resources around the areas of interest, while avoiding unnecessary resolution and computational demands in areas where high resolution is not essential to the problem at hand. Therefore, the grid cells are smaller in area within the study area (i.e., higher resolution), and resolution is coarser at areas further from the study area. The water body within the model extent is stratified into layers, of 17 sigma levels in the top 100 m of the water column and 25 z-levels of 10 m to 500 m resolution below the sigma levels. Super-agents are capable of traversing along the horizontal plane (across grid cells) and vertical plane (across the sigma and z-levels).

The model runs at 300-second (or 5-minutes) time steps from the start date to the end date of the simulation. Therefore, computations are performed, and state variables and super-agent positions are updated for up to 288 times per day of the simulation.

B.3 Process Overview and Scheduling

B.3.1 Processes

The model is developed to cover the early life stages of the three identified species, from zygote stage to pre-transformation larval stage. It is structured in five processes: one related to movement (vertical and horizontal) of the agents, one related to natural survival and mortality, two concerning development of the agent, namely the hatching of eggs and the development of larvae, and the final one related to settling of the agent.

The super-agents and grid cells update their state variables at every time step over the entire model simulation period. Super-agents perform each of their processes at every time step of the simulation, until there are no live agents left in the super-agent (i.e., all agents have either died or settled). It is also worthy to note that if a super-agent's age exceeds the stochastically determined maximum incubation time period or maximum larval development time period, all remaining zygotes die, and all remaining non-competent larvae die in these respective scenarios.

B.3.2 Schedule

All model calculations of state variables and updates of environmental forcings occur at a discrete time step size of five (5) minutes over the simulation period. At the beginning of each model time step, the following sequential order is applied:

- Release new super-agents into the model domain relative to time-varying normalized agent-release rates.
- Update of Eulerian meteorological and hydrodynamic forcings, e.g., currents and water levels.
- Calculation and evaluation of Lagrangian arithmetic expressions and sub-modules based on updated values obtained from above step and the previous status of the super-agent.
- Update of new super-agent position (x, y, z) and Lagrangian state-variables based on calculations.

B.4 Agent-Based Model: Design Concepts

B.4.1 Basic Principles

The general concept of the model is to account for growth and mortality features, movement patterns and settlement characteristics of larvae, and couple it with high-resolution, high-accuracy 3D current and flow fields in order to attempt to simulate a more realistic dispersal and settlement pattern than what can be achieved with standard passive drift particle-tracking algorithms and/or with 2nd order advection-dispersion transport models. The main mechanisms important for dispersal of larvae which the model attempts to replicate have been identified in the existing literature and are:

- Changes in larvae settlement rate and population abundance as a function of mortality and growth parameters (Allain et al. 2007)
- Changes in settlement probability as a function of life stage, substrate material, and environmental variables including temperature, water depth, and salinity
- Changes in fish larval dispersal patterns, and hence recruitment rates at different sink areas, as a result of larval fish swimming speeds (Faillettaz et al. 2018)
- Changes in vertical migration patterns of larvae as a function of daylight and tidal conditions (Jenkins et al. 1998, Benson et al. 2021)

B.4.2 Emergence

The transport patterns that arise between spawn and sink locations can be described as a long intricate series of sequential interactions between predicted oceanographic forcings with the included zygotes/larval properties. While the level of interaction is complex, it is still largely predictable and thus cannot be labelled as a true emergent property of the system components.

B.4.3 Objectives

The objective measures used by the models is the change in settlement density of larvae at sink locations, and changes in larval transport between the sites. The level of impacts brought about by the offshore wind farms in each of the proposed configurations are assessed based on these dynamics.

B.4.4 Stochasticity

Stochasticity is applied in the model at different levels to varying degrees. The following processes are either semi- or fully dependent on stochastic processes:

- Upon the release of each super-agent, a random number is sampled from a normal distribution to determine the number of zygotes to be contained within the super-agent, in order to account for the varying levels of fecundity of each individual mature reproducing adult.
- Upon the release of each super-agent, random numbers are sampled from a normal distribution to determine the following growth parameters: minimum and maximum zygote incubation time and minimum and maximum larval development time, to account for varying pelagic larval duration for each individual super-agent.
- Mortality rates from time-step to time-step are controlled by an age-dependent survivorship Type III curve (Houde 2002), with curve parameters input by the user.
- Zygote incubation and larval development rates from time-step to time-step are controlled by an age-dependent sigmoidal gain/loss curve (Tian et al. 2007), with curve parameters input by the user.

- Horizontal and vertical dispersion of super-agents in order to account for the effects of unresolved turbulence in the hydrodynamic model. The magnitude of dispersion is scaled to the magnitude of the predicted currents.
- Release points of super-agents are randomly determined by the model (within the user-determined release areas) to account for indeterministic nature of mature adult migration.

B.4.5 Observation

In order to identify overall settlement success and periods where high settlement occurs, the model outputs analyzed in post-processing are the dispersal patterns and settlement density of larvae across the model domain at the end of simulation, as well as over time.

B.4.6 Other Concepts

The other standard concepts proposed by the ODD protocol, including *adaptation*, *learning*, *prediction*, *sensing*, *interaction*, and collectives are not implemented in the present modeling study.

B.5 Initialization

For each model source setup, a set number of super-agents to be released was randomly scattered within user-determined spawning areas located in the model domain. The spawning areas are selected based on spawning characteristics and preferences of adults for the studied species and verified against observational data (see **Section 6.4** for datasets used for each species). The volumes of released super-agents over the simulation period were scaled to the abundance observation data collected in the area of study to represent the spawning activity and seasonality in these areas (**Section 6.4**). A total of 34,272 super-agents were released for sea scallop, 30,000 for surf clam, and 27,528 for summer flounder over each model's simulation period. Graphical representations of the release time series can be found in **Section 6.4** of the main report.

Upon the first time-step, fecundity level (number of zygotes) and growth properties (zygote incubation and larval development time) are sampled from normal distributions defined by means and given standard deviations, which are parameterized with values available from literature of similar studies on the species under study. Super-agents for all three species are released at 5 m above the seabed. Initially, released super-agents are assumed to be passive drifters along the transverse plane, but as the eggs of all three species are known to be buoyant, the super-agents migrate vertically through the water column towards the water surface during the initial stage of their lifetime.

B.6 Input Data

The larvae ABMs are directly coupled to the HDM. Thus, built-in forcings of horizontal current speed (ms^{-1}) and direction (degrees), vertical current speed (ms^{-1}), water level (m), temperature ($^{\circ}\text{C}$) and salinity are directly read by the ABM following the same spatiotemporal definitions of the hydrodynamic model. Substrate suitability maps generated based on benthic substrate maps suitable for settlement and are required as input to determine settling probabilities of competent larvae (Section 6). Timeseries data of super-agent release rates were generated based on abundance data and values reported by literature for the modeled species.

B.6.1 Constants

B.6.1.1 Mortality and Growth

The specific life-stage durations and fecundities applicable to each species have been parameterized in the ABM (please see Section 6 for details). Mortality rates follow age-dependent survivorship Type III curve, where undeveloped zygotes die after the maximum incubation time and non-competent larvae die after maximum larvae development time is reached. Zygote incubation and larvae development rates follow age-dependent sigmoidal gain/loss curve, “Age” refers to the time elapsed since the agent was released. Constants for shaping curves and other parameters can be seen in Tables B4, B5 and B6 for each species.

Table B.4. Model Constants for Mortality and Growth Processes for Sea Scallops Zygotes and Larvae

Constant Name	Description	Unit	Value	Reference
General Settings				
c_particle_removal	Set to 1 for removing dead individuals from simulation	-	1	User defined
c_avg_eggs_per_ind	Average number of eggs per individual	eggs	50,000,000	McGarvey et al., 1992; Langton et al., 1987
c_sd_eggs_per_ind	Variation in number of eggs per individual	eggs	200,000	McGarvey et al., 1992; Langton et al., 1987
Mortality – Age-Dependent Type III Survivorship Curve				
c_min_mortality	Minimum daily instantaneous mortality rate	daily	0.01	User defined
c_max_mortality	Maximum daily instantaneous mortality rate	daily	0.3	Hart and Chute 2004
c_lambda_mortality	Scale parameter of mortality curve	-	0.1	User defined
c_alpha_mortality	Shape parameter of mortality curve	-	0.76	User defined
Growth / Competency Loss – Age-Dependent Sigmoidal Curve				
Zygotes				
c_avg_min_incubation_time	Mean minimum incubation time before zygote can develop into larvae	hours	30	Culliney et al. 1974; Hart and Chute 2004
c_var_min_incubation_time	Variance of minimum incubation time before zygote can develop into larvae	hours	2	User defined

Constant Name	Description	Unit	Value	Reference
c_avg_max_incubation_time	Mean maximum incubation time before zygote can develop into larvae	hours	40	Hart and Chute 2004; Culliney et al. 1974
c_var_max_incubation_time	Variance of maximum incubation time before zygote can develop into larvae	hours	2	User defined
Growth / Competency Loss – Age-Dependent Sigmoidal Curve				
<i>Zygotes</i>				
c_var_incubation_prob	Variance in daily incubation probability	/day	0.001	User defined
c_incubation_prob_max	Maximum probability of incubation	/day	0.7	User defined
c_incubation_prob_alpha	Shape parameter of development from zygote to larvae	-	0.5	User defined
c_incubation_prob_period	Period of time at which maximum probability of incubation occurs	days	3	Hart and Chute 2004; Culliney et al. 1974
<i>Larvae</i>				
c_min_larvae_development_time	Minimum time before larvae become competent	days	28	Pearce et al. 2004
c_var_min_larvae_development_time	Variance in minimum time before larvae become competent	days	1	User defined
c_competency_gain_prob_con	Constant daily probability of becoming competent after development period is completed	/day	0.18	User defined
c_competency_gain_prob_max	Maximum daily probability of competency gain	/day	1	User defined
c_competency_gain_prob_alpha	Shape parameter for sigmoidal competency gain curve	-	0.2	User defined
c_competency_gain_prob_period	Days before a larvae experiences maximum probability of competency gain	days	40	Tremblay et al. 1994; Pearce et al. 2004; McGarvey et al., 1992
c_competency_gain_prob_var	Variance in probability of competence gain	/day	0.001	User defined
c_competency_loss_prob_con	Constant daily probability of competency loss, meaning the larvae wont be able to settle and die	/day	0.05	User defined
c_competency_loss_prob_max	Maximum daily probability of competency loss	-	1	User defined
c_competency_loss_alpha	Shape parameter for the sigmoidal competency loss curve	-	0.1	User defined

Constant Name	Description	Unit	Value	Reference
c_competency_loss_period	Days before a larvae experiences maximum probability of competency loss	days	80	Tremblay et al. 1994; Pearce et al. 2004; McGarvey et al., 1992
c_competency_loss_prob_var	Variance in probability of competence loss	days	0.001	User defined
c_settle_coefficient	coefficient modifier to translate habitat quality into settlement probability. The coefficient should, when multiplied with the habitat index, result in a daily settlement probability.	-	1	1

Table B.5. Model Constants for Mortality and Growth Processes for Surf Clam Zygotes and Larvae

Constant Name	Description	Unit	Value	Reference
General Settings				
C_particle_removal	Set to 1 for removing dead individuals from simulation	-	1	User defined
C_avg_eggs_per_ind	Average number of eggs per individual	eggs	3,300,000	Walker et al. 1996
C_sd_eggs_per_ind	Variation in number of eggs per individual	eggs	1,640,000	Walker et al. 1996
Mortality – Age-Dependent Type III Survivorship Curve				
C_min_mortality	Minimum daily instantaneous mortality rate	daily	0.05	User defined
C_max_mortality	Maximum daily instantaneous mortality rate	daily	0.3	User defined
C_lambda_mortality	Scale parameter of mortality curve	-	0.1	User defined
C_alpha_mortality	Shape parameter of mortality curve	-	0.76	User defined
Growth / Competency Loss – Age-Dependent Sigmoidal Curve				
Zygotes				
C_avg_min_incubation_time	Mean minimum incubation time before zygote can develop into larvae	hours	9	Loosanoff and Davis 1963; Ropes 1980; Walker and O'Beirn 1996
C_var_min_incubation_time	Variance of minimum incubation time before zygote can develop into larvae	hours	0.5	User defined

Constant Name	Description	Unit	Value	Reference
C_avg_max_incubation_time	Mean maximum incubation time before zygote can develop into larvae	hours	40	Loosanoff and Davis 1963; Ropes 1980; Walker and O'Beirn 1996
C_var_max_incubation_time	Variance of maximum incubation time before zygote can develop into larvae	hours	0.5	User defined
C_var_incubation_prob	Variance in daily incubation probability	/day	0.001	User defined
C_incubation_prob_max	Maximum probability of incubation	/day	0.7	User defined
C_incubation_prob_alpha	Shape parameter of development from zygote to larvae	-	0.5	User defined
C_incubation_prob_period	Period of time at which maximum probability of incubation occurs	days	1	Loosanoff and Davis 1963; Ropes 1980; Walker and O'Beirn 1996
<i>Larvae</i>				
c_min_larvae_development_time	Minimum time before larvae become competent	days	18	Fay et al. 1983
c_var_min_larvae_development_time	Variance in minimum time before larvae become competent	days	0.5	User defined
c_competency_gain_prob_con	Constant daily probability of becoming competent after development period is completed	/day	0.18	User defined
c_competency_gain_prob_max	Maximum daily probability of competency gain	/day	1	User defined
c_competency_gain_prob_alpha	Shape parameter for sigmoidal competency gain curve	-	0.6	User defined
c_competency_gain_prob_period	Days before a larvae experiences maximum probability of competency gain	days	19	Fay et al. 1983
c_competency_gain_prob_var	Variance in probability of competence gain	/day	0	User defined
c_competency_loss_prob_con	Constant daily probability of competency loss, meaning the larvae wont be able to settle and die	/day	0.05	User defined
c_competency_loss_prob_max	Maximum daily probability of competency loss	-	1	User defined
c_competency_loss_alpha	Shape parameter for the sigmoidal competency loss curve	-	0.3	User defined

Constant Name	Description	Unit	Value	Reference
c_competency_loss_period	Days before a larvae experiences maximum probability of competency loss	days	34	Fay et al. 1983
c_competency_loss_prob_var	Variance in probability of competence loss	days	0.001	User defined
c_settle_coefficient	coefficient modifier to translate habitat quality into settlement probability. The coefficient should, when multiplied with the habitat index, result in a daily settlement probability.	-	1	User defined

Table B.6. Model Constants for Mortality and Growth Processes for Summer Flounder Zygotes and Larvae

Constant Name	Description	Unit	Value	Reference
General Settings				
C_particle_removal	Set to 1 for removing dead individuals from simulation	-	1	User defined
C_avg_eggs_per_ind	Average number of eggs per individual	eggs	1,700,000	Hare 2015
C_sd_eggs_per_ind	Variation in number of eggs per individual	eggs	200,000	Hare 2015
Mortality – Age-Dependent Type III Survivorship Curve				
C_min_mortality	Minimum daily instantaneous mortality rate	daily	0.01	User defined
C_max_mortality	Maximum daily instantaneous mortality rate	daily	0.3	User defined
C_lambda_mortality	Scale parameter of mortality curve	-	0.1	User defined
C_alpha_mortality	Shape parameter of mortality curve	-	0.76	User defined
Growth / Competency Loss – Age-Dependent Sigmoidal Curve				
Zygotes				
C_avg_min_incubation_time	Mean minimum incubation time before zygote can develop into larvae	days	2	Bisbal and Bengtson 1995, Johns and Howell 1980, Packer et al. 1999
C_var_min_incubation_time	Variance of minimum incubation time before zygote can develop into larvae	days	0.1	User defined
C_avg_max_incubation_time	Mean maximum incubation time before zygote can develop into larvae	days	4	Bisbal and Bengtson 1995, Johns and Howell 1980, Packer et al. 1999

Constant Name	Description	Unit	Value	Reference
C_var_max_incubation_time	Variance of maximum incubation time before zygote can develop into larvae	days	0.5	User defined
C_var_incubation_prob	Variance in daily incubation probability	/day	0.0001	User defined
C_incubation_prob_max	Maximum probability of incubation	/day	0.7	User defined
C_incubation_prob_alpha	Shape parameter of development from zygote to larvae	-	0.5	User defined
C_incubation_prob_period	Period of time at which maximum probability of incubation occurs	days	2.5	Bisbal and Bengtson 1995, Johns and Howell 1980, Packer et al. 1999
<i>Larvae</i>				
c_avg_feeding_age	Average age when larvae start to feed	days	7	Martinez and Bolker, 2003
c_var_feeding_age	variance of age at which larvae starts to feed	days	2	User defined
c_min_larvae_development_time	Minimum time before larvae become competent	days	25	Keefe and Able 1993
c_var_min_larvae_development_time	Variance in minimum time before larvae become competent	days	3	User defined
c_competency_gain_prob_con	Constant daily probability of becoming competent after development period is completed	/day	0.18	User defined
c_competency_gain_prob_max	Maximum daily probability of competency gain	/day	0.4	User defined
c_competency_gain_prob_alpha	Shape parameter for sigmoidal competency gain curve	-	0.2	User defined
c_competency_gain_prob_period	Days before a larvae experiences maximum probability of competency gain	days	30	Houde 1989, Burke et al. 1991, Keefe and Able 1993, van Maaren and Daniels 2000
c_competency_gain_prob_var	Variance in probability of competence gain	/day	0.0001	User defined
c_competency_loss_prob_con	Constant daily probability of competency loss, meaning the larvae wont be able to settle and die	/day	0.05	User defined
c_competency_loss_prob_max	Maximum daily probability of competency loss	-	0.1	User defined

Constant Name	Description	Unit	Value	Reference
c_competency_loss_alpha	Shape parameter for the sigmoidal competency loss curve	-	0.2	User defined
c_competency_loss_period	Days before a larvae experiences maximum probability of competency loss	days	54	van Maaren and Daniels 2000
c_competency_loss_prob_var	Variance in probability of competence loss	days	0.0001	User defined
c_settle_coefficient	coefficient modifier to translate habitat quality into settlement probability. The coefficient should, when multiplied with the habitat index, result in a daily settlement probability.	-	1	User defined

B.7 Sub-Models

Following sections describes the sub-models guiding the behaviors of the overall ABM.

B.7.1 Global Processes

The model is governed by a set of arithmetic expressions. Global expressions that apply across the entire ABM are provided in **Table B.7**.

Table B.7. Overview of Global Processes

Arithmetic Expression Name	Algorithm	Description
ae_dt1	$IF([AGE]==ce_wqdt, 1, 0)$	Determines that something is only true in the first-time step of the model
ae_ndt	$86400/ce_wqdt$	Number of time steps per day
ae_water_temperature	f_temp	Water temperature in occupied cell read from the HD input
ae_water_depth	f_depth	Water depth in occupied cell read from the HD input

B.7.2 Movement

The parameterization of movement and settlement characteristics, rationale and source references are documented in detail in **Section 6** of the main report. Arithmetic expressions relating to movement used in the ABM are provided in **Tables B8 and B9**.

Table B.8. Overview of Processes Related to Movement

Arithmetic Expression Name	Algorithm	Description
Horizontal Movement		
ae_rhdir	f_cdir	Current direction in occupied cell, read from HD input
ae_rhspd	f_cspd	Current speed in occupied cell, read from HD input
Vertical Movement		
ae_zygot_vspd	$IF[AGE] < 3600,$ $c_start_bouyancy_zygot * U_RAND()$, $f_vspd -$ $(c_maximum_bouyancy_zygot * U_RAND())$	Vertical speed of zygote dominated super agents
ae_larvae_vspd	$IF(f_temp > c_threshold_thermocline_tmax, -$ $f_vspd + (ABS(N_RAND2(c_avg_sett_spd, POW(c_sd_sett_spd, 2))))),$ $IF(f_temp < c_threshold_thermocline_tmin, -f_vspd -$ $(ABS(N_RAND2(c_avg_sett_spd, POW(c_sd_sett_spd, 2))))),$ $-f_vspd)$	Vertical speed of larvae dominated super agents. Temperature dependent direction – larvae will swim away from maximum or minimum temperature thresholds ($c_threshold_thermocline_tmax$ or $c_threshold_thermocline_tmin$) set by the user to the relevant ranges for each species. (See Section 6 in main report).
ae_settle_spd	$N_RAND2(c_avg_sett_spd,$ $c_sett_spd_sd) + f_vspd$	Vertical speed of settlement ready larvae
ae_rvspd	$IF(sv_n_zygots > sv_n_larvae,$ $ae_zygot_vspd, IF(sv_n_larvae >$ $sv_n_competent_larvae,$ $ae_larvae_vspd, ae_settle_vspd))$	Selection of which vertical speed to use.

Table B.9. Overview of Processes Related to Settling

Arithmetic Expression Name	Algorithm	Description
Settling		
ae_depth_check	$IF(ABS(ae_water_depth) < ABS(c_threshold_min_depth), 0, IF(ABS(ae_water_depth) > ABS(c_threshold_max_depth), 0, 1))$	Checking if agent depth is within depth requirements for settlement
ae_settle_prob	$IF(ae_depth_check < 1, 0, (c_settle_coefficient * ce_habitat))$	Estimating settlement probability given habitat quality
ae_settle_success	$(1 - POW(1 - MIN(ae_settle_prob, 1)), (1/ae_ndt))) * sv_n_competent_larvae$	Number of competent larvae from a super-agent that have successfully settled
ae_displacement_calculation	$DISTANCE_TO(sv_Home_X, sv_Home_Y, sv_Home_Z)$	Distance from Origin
ae_direction_calculation	$GETANGLE(sv_Home_X, sv_Home_Y, [XPOS], [YPOS])$	Direction from Origin
ae_distance_travelled	$GETDISTANCE([PREV_XPOS], [PREV_YPOS], [PREV_ZPOS], [XPOS], [YPOS], [ZPOS])$	Distance travelled
ae_n_settle_individuals	$IF(ae_settle_success > 0, Settled_Larvae_Absolute::+(ae_settle_success), 0)$	Edit grid cell state variable with number of settled individuals
ae_setteling_density	$Settled_Larvae_Density::+(ae_settle_success/f_bed_area)$	Edit grid cell state variable with density of settled individuals
ae_setteling_pos_X	[XPOS]	x coordinate of current position (decimal degrees)
ae_setteling_pos_Y	[YPOS]	y coordinate of current position (decimal degrees)

B.7.3 Mortality and Growth

The parameterization of growth and mortality characteristics, rationale and source references are documented in detail in Section 6 of the main report. Arithmetic expressions relating to growth and mortality used in the ABM are provided in Table B.10.

Table B.10. Overview of Processes Related to Settling

Arithmetic Expression Name	Algorithm	Description
Mortality		
ae_Death	$IF(sv_Live_agents < 10, 1, 0)$	Determines whether a super-agent has died, based on the number of live agents contained within it.

Arithmetic Expression Name	Algorithm	Description
ae_removal_check	<i>IF(ae_Death==0,0, IF(c_particle_removal==1,REMOVE{ (CLC, -1)},0))</i>	Expression to remove super-agent when dead
ae_mort_weibull	<i>IF([AGE]>0,c_lamda_mort*c_alpha_mort* POW((c_lamda_mort*[AGE]/86400),(c_alpha_mort-1)),c_max_mort)</i>	Weibull mortality curve
ae_corr_weibull	<i>IF(ae_mort_weibull>c_max_mort,c_max_mort, IF(ae_mort_weibull<c_min_mort,c_min_mort,ae_mort_weibull))</i>	Correction of Weibull curve
ae_zygot_mortality_rate	<i>IF(MORTALITY_SETTINGS==0, 0, IF(MORTALITY_SETTINGS==1, c_zygot_con_mort, IF(MORTALITY_SETTINGS==2, ae_corr_weibull,0)))</i>	Selection of constant mortality or Weibull mortality for zygotes
ae_larval_mortality_rate	<i>IF(MORTALITY_SETTINGS==0, 0, IF(MORTALITY_SETTINGS==1, c_larval_con_mort, IF(MORTALITY_SETTINGS==2, ae_corr_weibull,0)))</i>	Selection of constant mortality or Weibull mortality for larvae
Zygote Growth		
ae_settling_n_egg	<i>IF(ae_dt1 == 1, N RAND2(c_avg_eggs_pr_ind, c_sd_eggs_pr_ind),0)</i>	Estimator for starting number of zygotes
ae_sample_min_incubation_time	<i>IF(ae_dt1==1,ABS(N RAND2(c_avg_min_incubation_time,c_var_min_incubation_time)*ae_ndt),0)</i>	Sampler for minimum incubation time
ae_sample_max_incubation_time	<i>IF(ae_dt1==1,ABS(N RAND2(c_avg_max_incubation_time,c_var_max_incubation_time)*ae_ndt),0)*IF(ZYGOT_INCUBATION_SETTINGS==2,1,0)</i>	Sampler for maximum incubation time
ae_incubation_check	<i>IF((([AGE]/3600)<=sv_incubation_min,0,1)</i>	Check if minimum incubation time has passed
ae_incubation_failure	<i>IF((([AGE]/3600)>sv_incubation_max,1,0)</i>	Check if maximum incubation time has passed
ae_incubation_sigmoidal	<i>c_incubation_prob_max/(1+EXP(-(c_incubation_prob_alpha*([AGE]/86400)-(c_incubation_prob_period/2))))</i>	Age-dependent type III probability of incubation sigmoid curve
ae_incubation_prob	<i>IF(LARVAE_DEVELOPMENT_SETTINGS==0, 1, IF(LARVAE_DEVELOPMENT_SETTINGS==1, c_competent_gain_prob_con, IF(LARVAE_DEVELOPMENT_SETTINGS==2, ae_incubation_sigmoidal,0)))</i>	Selection of type of incubation probability.

Arithmetic Expression Name	Algorithm	Description
ae_n_zygot_incubated	$IF(ae_incubation_check < 1, 0,$ $IF(ae_incubation_failure == 1, 0,$ $IF(sv_n_zygots < 1, 0, (1-POW((1-$ $MIN(N_RAND2(ae_incubation_prob,$ $c_var_incubation_prob),$ $1)),(1/ae_ndt))) * sv_n_zygots)))$	Number of zygotes incubated per time step, depending on age and time
ae_n_zygot_death	$IF(sv_n_zygots < 1, 0,$ $IF(ae_incubation_failure == 1,$ $sv_n_zygots,$ $(1-POW((1-$ $MIN(ae_zygot_mortality_rate,$ $1)),(1/ae_ndt))) * sv_n_zygots))$	Number of zygote death depending on age and time
Larve Growth		
ae_sample_min_develop	$IF(ae_dt1==1, ABS(N_RAND2(c_min_l$ $arvae_development_time, c_var_min_l$ $arvae_development_time)), 0)$	Sampler for minimum development time
ae_competent_check	$IF((([AGE]/86400) <= sv_development_$ $minimum, 0, 1)$	Check if minimum development time has passed
ae_competent_gain_prob_sigm	$c_competent_gain_prob_max / (1 + EXP$ $(-$ $c_competent_gain_prob_alpha * (([AGE]$ $]/86400) -$ $(c_competent_gain_prob_period/2))))$	age-dependent probability of gaining competence
ae_competent_gain_prob	$IF(LARVAE_DEVELOPMENT_SETTI$ $NGS == 0, 0,$ $IF(LARVAE_DEVELOPMENT_SETTI$ $NGS == 1,$ $c_competent_gain_prob_con,$ $IF(LARVAE_DEVELOPMENT_SETTI$ $NGS == 2,$ $ae_competent_gain_prob_sigm, 0)))$	Probability of larvae gaining competence depending on probability type selected
ae_settle_ready_larvae	$IF(ae_competent_check < 1, 0,$ $IF(sv_n_larvae < 1, 0,$ $(1-POW((1-$ $MIN(N_RAND2(ae_competent_gain_pr$ $ob, c_competent_gain_prob_var),$ $1)),(1/ae_ndt))) * sv_n_larvae))$	Number of settlement ready larvae per time step
ae_competent_loss_prob_sigm	$c_competent_loss_prob_max / (1 + EXP($ $-$ $c_competent_loss_alpha * (([AGE]/864$ $00) - (c_competent_loss_period/2))))$	Age-dependent probability of gaining competence

Arithmetic Expression Name	Algorithm	Description
ae_competent_loss_prob	$IF(LARVAE_DEVELOPMENT_SETT \\ NGS==0, 0, \\ IF(LARVAE_DEVELOPMENT_SETT \\ NGS==1, \\ c_competency_loss_prob_con, \\ IF(LARVAE_DEVELOPMENT_SETT \\ NGS==2, \\ ae_competent_loss_prob_sigm,0)))$	Probability of losing competence dependent on probability setting.
ae_larvae_competent_loss	$IF(sv_n_competent_larvae < 1, 0, \\ (1-POW((1- \\ MIN(N_RAND2(ae_competent_loss_p \\ rob, c_competent_loss_prob_var), \\ 1)), (1/ae_ndt))))*sv_n_competent_larva \\ e)$	Number of larvae losing competence per time step
ae_larvae_death	$IF(sv_n_larvae < 1, 0, \\ IF(ae_water_temperature > \\ c_threshold_tmax, sv_n_larvae, \\ (1-POW((1- \\ MIN(ae_larval_mortality_rate, \\ 1)), (1/ae_ndt))))*sv_n_larvae))$	Number of larvae dying per time step.

B.8 References

- Allain G, Petigas P, Lazure P, Grellier P. 2007. Biophysical modeling of larval drift, growth and survival for the prediction of anchovy (*Engraulis encrasicolus*) recruitment in the Bay of Biscay (NE Atlantic). *Fish. Oceanogr.* 16:489–505.
- Benson T, de Bie J, Gaskell J, Vezza P, Kerr JR, Lumbroso D, Owen MR, Kemp PS. 2021. Agent-based modeling of juvenile eel migration via selective tidal stream transport. *Ecol. Model.* 443:109448.
- Bisbal GA, Bengtson DA. 1995. Effects of delayed feeding on survival and growth of summer flounder *Paralichthys dentatus* larvae. *Mar. Ecol. Prog. Ser.* 121:301–306.
- Culliney JL. 1974. Larval development of the giant scallop *Placopecten magellanicus* (Gmelin). *Biol. Bull.* 147:321–332.
- Faillietaz R, Paris CB, Irisson J-O. 2018. Larval Fish Swimming Behavior Alters Dispersal Patterns From Marine Protected Areas in the North-Western Mediterranean Sea. *Front. Mar. Sci.* 5.
- Fay CW, Neves RJ, Pardue GB. 1983. Species profiles: life histories and environmental requirements of coastal fishes and invertebrates (Mid-Atlantic): surf clam. US Fish Wildl Serv, Div Biol Serv, FWS/OBS-82/11.13. 23 p.
- Grimm V, Railsback SF, Vincenot CE, Berger U, Gallagher C, DeAngelis DL, Edmonds B, Ge J, Giske J, Groeneveld J, et al. 2020. The ODD Protocol for Describing Agent-Based and Other Simulation Models: A Second Update to Improve Clarity, Replication, and Structural Realism. *J. Artif. Soc. Soc. Simul.* 23.

- Hare JA, Walsh HJ, Wuenschel MJ. 2006. Sinking rates of late-stage fish larvae: Implications for larval ingress into estuarine nursery habitats. *J. Exp. Mar. Biol. Ecol.* 330(2), 493-504.
- Hart DR, Chute AS. 2004. Essential fish habitat source document: sea scallop, *Placopecten magellanicus*, life history and habitat characteristics. NOAA Tech Memo NMFS NE-189, Woods Hole, MA. 21p.
- Houde ED. 1989. Comparative Growth, Mortality, and Energetics of Marine Fish Larvae: Temperature and Implied Latitudinal Effects. *Fish. Bull. U.S.* 87:471-495.
- Jenkins GP, Welsford DC, Keough MJ, Hamer PA. 1998. Diurnal and tidal vertical migration of pre-settlement King George whiting *Sillaginodes punctata* in relation to feeding and vertical distribution of prey in a temperate bay. *Mar. Ecol. Prog. Ser.* 170:239-248.
- Johns DM, Howell WH. 1980. Yolk Utilization in Summer Flounder (*Paralichthys dentatus*) Embryos and Larvae Reared at Two Temperatures. *Mar. Ecol. Prog. Ser.* 2:1-8.
- Keefe M, Able KW. 1993. Patterns of metamorphosis in summer flounder, *Paralichthys dentatus*. *J. Fish Biol.* 42:713-728.
- Langton RW, Robinson WE, Schick D. 1987. Fecundity and reproductive effort of sea scallops *Placopecten magellanicus* from the Gulf of Maine. *Mar. Ecol. Prog. Ser.* 37:19-25.
- Loosanoff VL, Davis HC. 1963. Rearing of bivalve mollusks. *Adv. Mar. Biol.* 1:1-136.
- Martinez GM, Bolker JA. 2003. Embryonic and Larval Staging of Summer Flounder (*Paralichthys dentatus*). *J. Morphol.* 255:162-176.
- McGarvey R, Serchuk FM, McLaren IA. 1992. Statistics of Reproduction and Early Life History Survival of the Georges Bank Sea Scallop (*Placopecten magellanicus*) Population. *J. Northwest Atl. Fish. Sci.* 13:83-99.
- Packer DB, Griesbach SJ, Berrien PL, Zetlin CA, Johnson DL, Morse WW. 1999. Essential fish habitat source document: Summer flounder, *Paralichthys dentatus*, life history and habitat characteristics. NOAA Tech Memo NMFS NE 151:88.
- Pearce CM, Manuel JL, Gallager SM, Manning DA, O'Dor RK, Bourget E. 2004. Depth and timing of settlement of veligers from different populations of giant scallop, *Placopecten magellanicus* (Gmelin), in thermally stratified mesocosms. *J. Exp. Mar. Biol. Ecol.* 312:187-214.
- Remblay JM, Loder J, Werner F, Naimie C, Page F, Sinclair M. 1994. Drift of sea scallop larvae *Placopecten magellanicus* on Georges Bank: a model study of the roles of mean advection, larval behavior and larval origin. *Deep Sea Res. Part II Top. Stud. Oceanogr.* 41:7-49.
- Ropes JR. 1980. Biological and Fisheries Data on the Atlantic Surf Clam *Spisula solidissima*. Woods Hole Laboratory, Northeast Fisheries Center, National Oceanic and Atmospheric Administration, Tech. Ser. Rep. No. 24.
- Tian T, Fiksen Ø, Folkvord A. 2007. Estimating larval fish growth under size-dependent mortality: a numerical analysis of bias. *Can. J. Fish. Aquat.* 64:554-562.

- Van Maaren CC, Daniels HV. 2000. Temperature Tolerance and Oxygen Consumption Rates for Juvenile Southern Flounder Acclimated to Five Different Temperatures. In Spawning and Maturation of Aquaculture Species. Tamaru, C.C., Tamaru, C.S., McVey, J.P., and Ikuta, K. (eds) Proceedings of the United States-Japan Natural Resources meeting. UJNR Technical Report No. 28:135-140.
- Walker RL, O'beirn FX. 1996. Embryonic and Larval Development of *Spisula solidissima similis* (Say, 1822) (Bivalvia: Mactridae). *Veliger* 39(1).

Appendix C: Supplementary ABM Modeling Results

C.1 12 MW Full Build-out

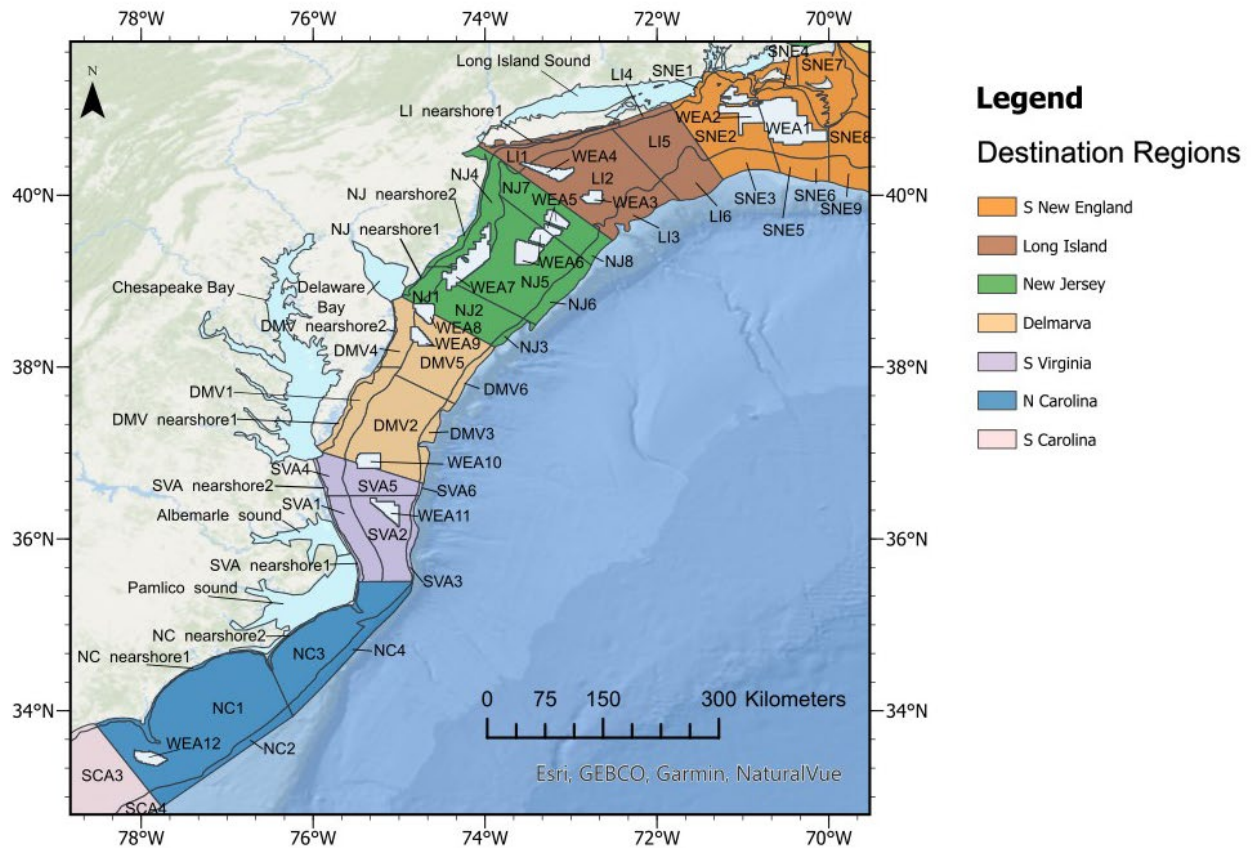


Figure C.1. Destination Reference Map Showing Each Destination Area and Names, Colors Represent Broad Regions

C.1.1 Sea Scallop 2017

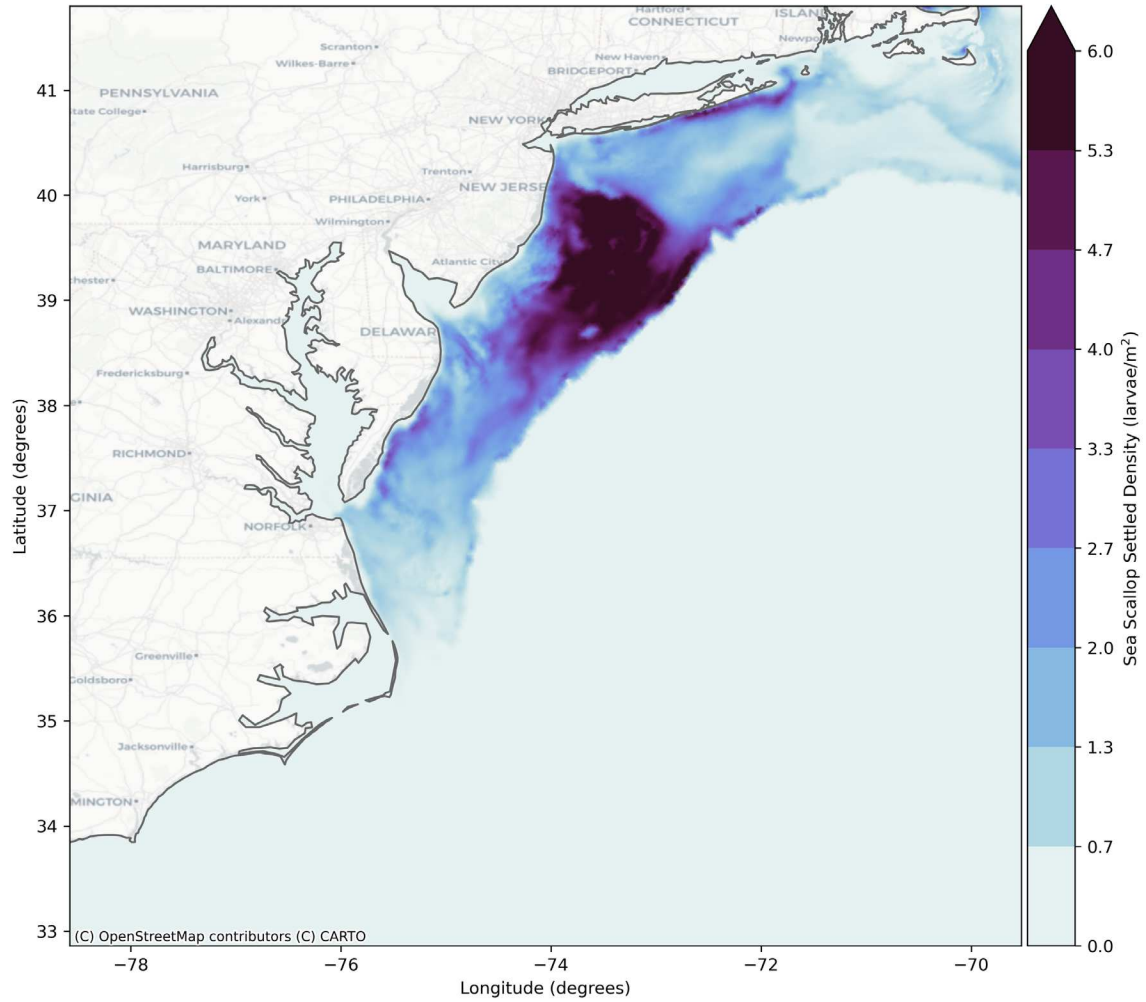


Figure C.2. Sea Scallop Baseline Settled Density for 12MW Full Build-Out

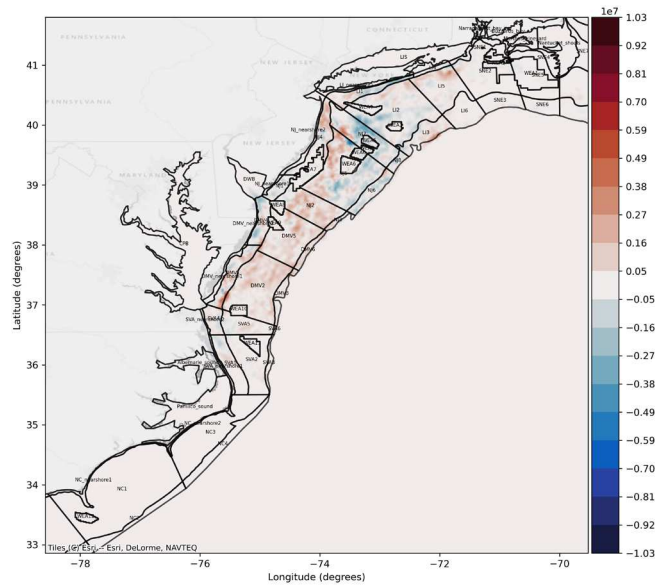


Figure C.3. Difference in Settled Larvae 12MW Full Build-Out vs Baseline 2017

Difference in total sea scallop settled larvae for model year 2017. Showing the difference in the mean of all ensemble baseline results and mean of all ensemble 12 MW full build-out results. Settled larvae averaged for each model grid element. Red shows an increase in settlement in the 12 MW scenario compared to the baseline, blue shows a decrease in settlement compared to the baseline.

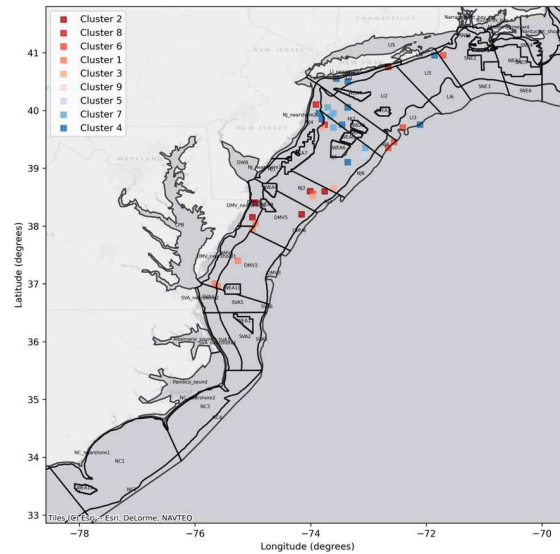


Figure C.4. DBSCAN (Density-Based Spatial Clustering of Applications with Noise) Difference in Settled Larvae 12MW Full Build-Out vs Baseline 2017

Spatial clusters identified using DBSCAN to filter out noise from the difference plot and identify areas of greatest change. Clusters of settlement increase are identified in red and clusters with settlement decrease are shown in blue.

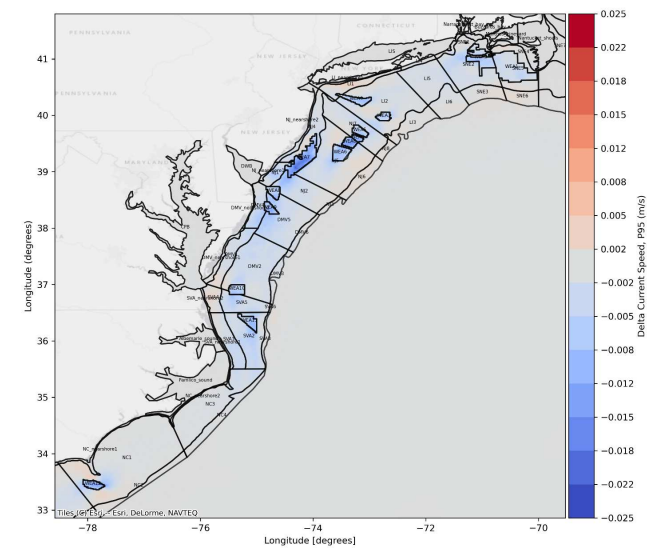


Figure C.5 Change in Current Speed 12MW Full Build-Out vs Baseline 2017

Difference in the depth averaged current speed for model year 2017. Showing the difference in the 95th percentile non-exceedance probability baseline results and 95th percentile non-exceedance probability 12 MW full build-out results

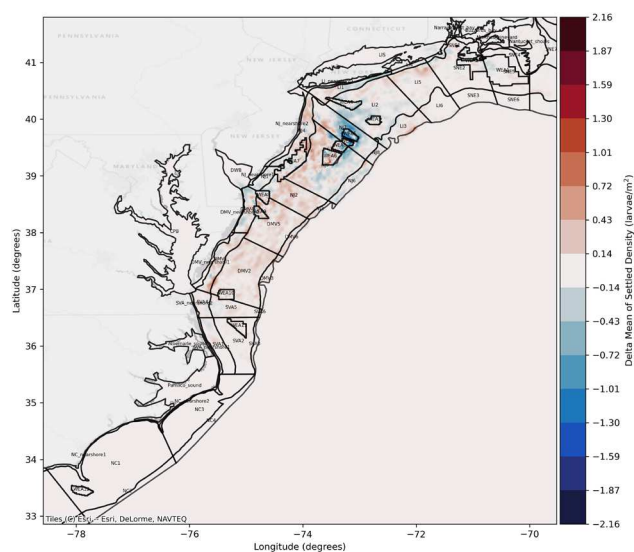


Figure C.6. Difference in Settled Density 12MW Full Build-Out vs Baseline 2017

Difference in total sea scallop larvae settled larvae for model year 2017. Showing the difference in the mean of all ensemble baseline results and mean of all ensemble 12 MW partial build-out results. Settled larvae averaged for each model grid element. Red shows an increase in settlement in the 12 MW scenario compared to the baseline, blue shows a decrease in settlement compared to the baseline.

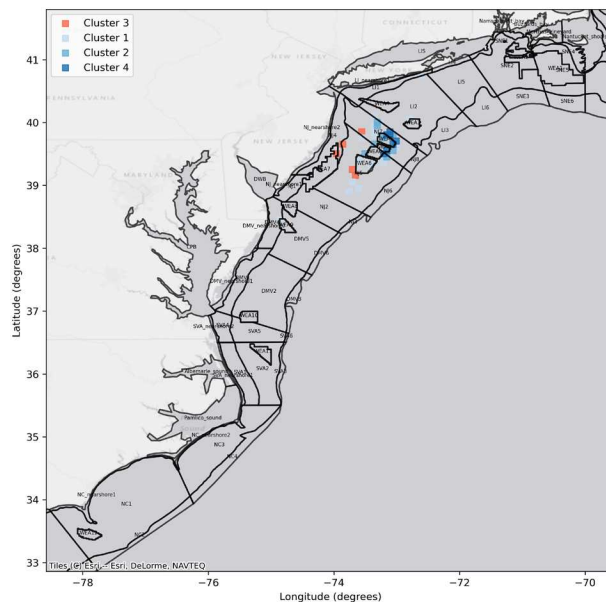


Figure C.7. DBSCAN (Density-Based Spatial Clustering of Applications with Noise) Difference in Settled Density 12MW Full Build-Out vs Baseline 2017

Spatial clusters identified using DBSCAN to filter out noise from the difference plot and identify areas of greatest change. Clusters of settlement increase are identified in red and clusters with settlement decrease are shown in blue.

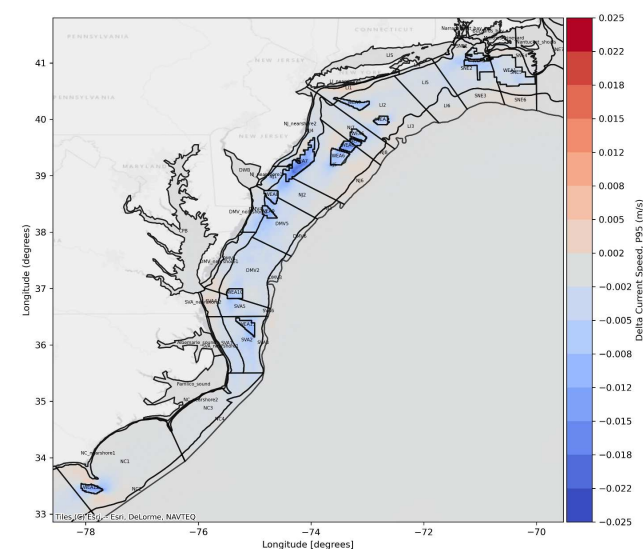


Figure C.8 Change in Current Speed 12MW Full Build-Out vs Baseline 2017

Difference in the depth averaged current speed for model year 2017. Showing the difference in the 95th percentile non-exceedance probability baseline results and 95th percentile non-exceedance probability 12 MW full build-out results

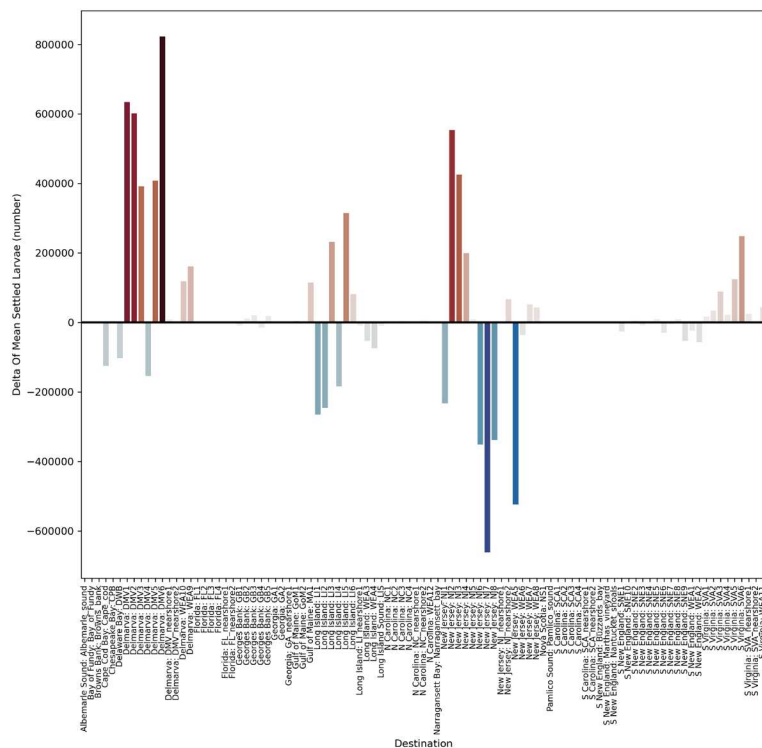


Figure C.9. Average Change in Sea Scallop Settlement in Each Destination Area 12MW Full Build-Out vs Baseline 2017

Bar chart shows the average change in settlement in each destination area for model year 2017. Showing the difference in the mean of all ensemble baseline results and mean of all ensemble 12 MW full build-out results.

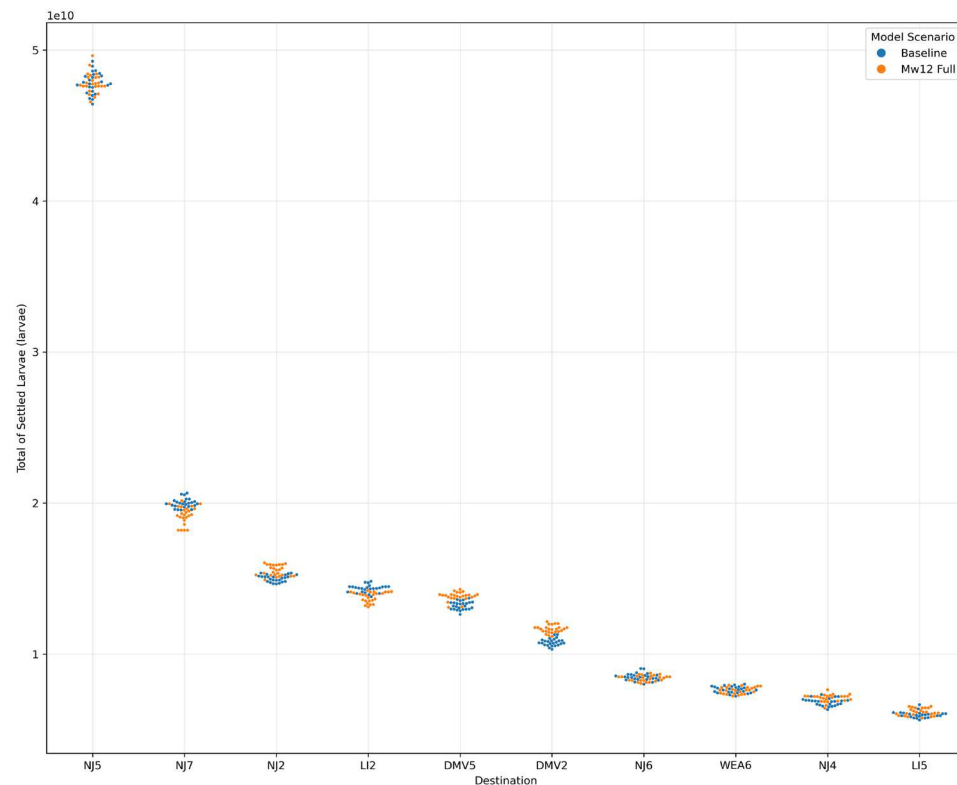


Figure C.10. Swarm Plot Showing Sea Scallop Settlement in Top 10 Destinations for 2017

Swarm plot shows the settlement for each model run of the ensemble (i.e., each point represents a model result) for 2017. Blue points show the baseline results and orange show the 12 MW full build-out number of settled larvae in the top 10 destinations where there is greatest larval settlement.

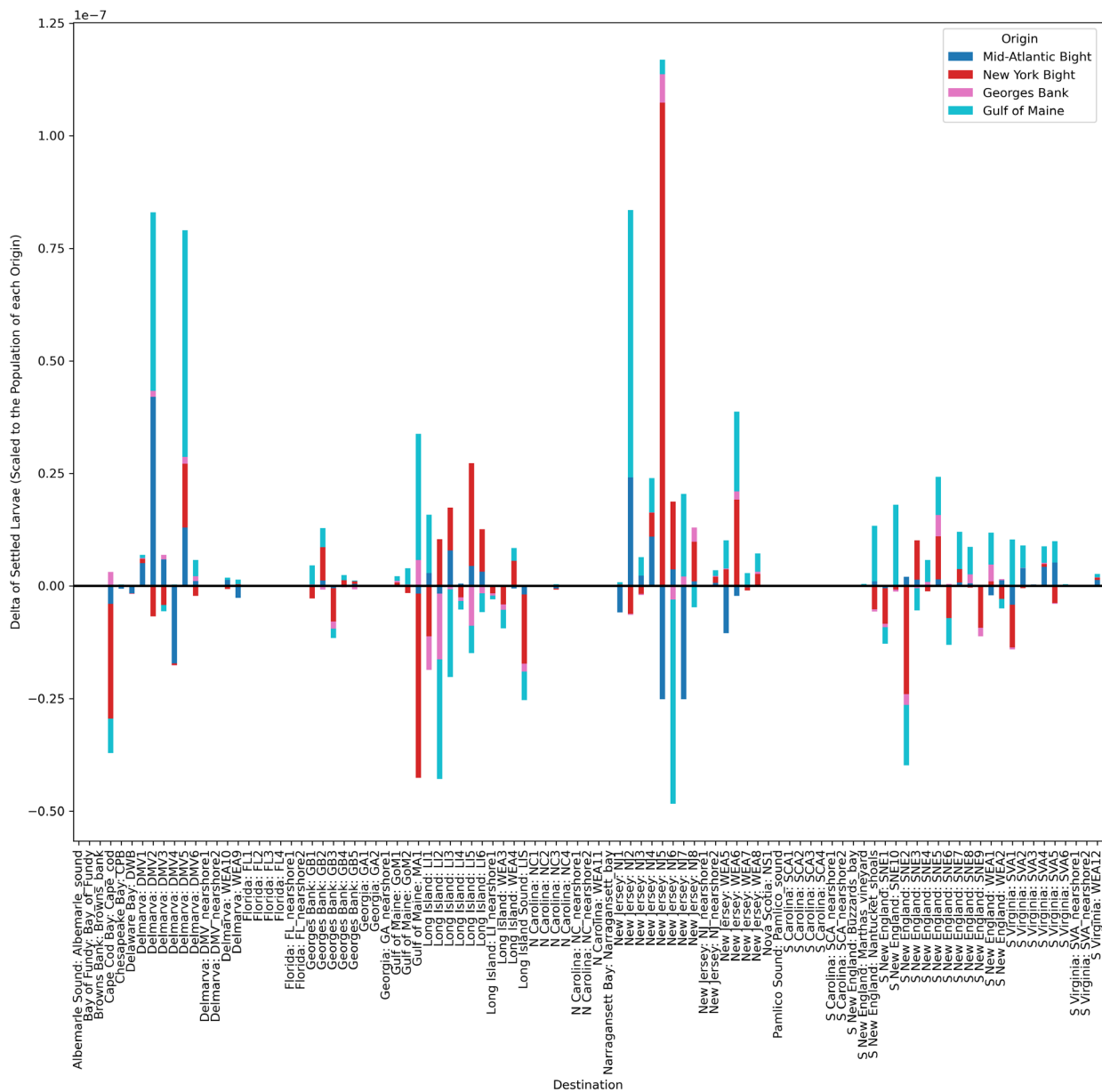


Figure C.11. Sea Scallop Connectivity Difference 2017

Bar chart shows the difference in sea scallop larvae settlement in each destination area, by origin for model year 2017. Bars are colored by origin area and results show the difference in export probabilities, i.e., the difference in the likelihood of settlement scaled to the number of larvae released from a particular origin region between the baseline and 12MW full build-out results. Bars below the x axis, show a decrease in settlement in a particular destination area, results above the x axis show an increase in a settlement in a destination area.

C.1.2 Surf Clam 2017

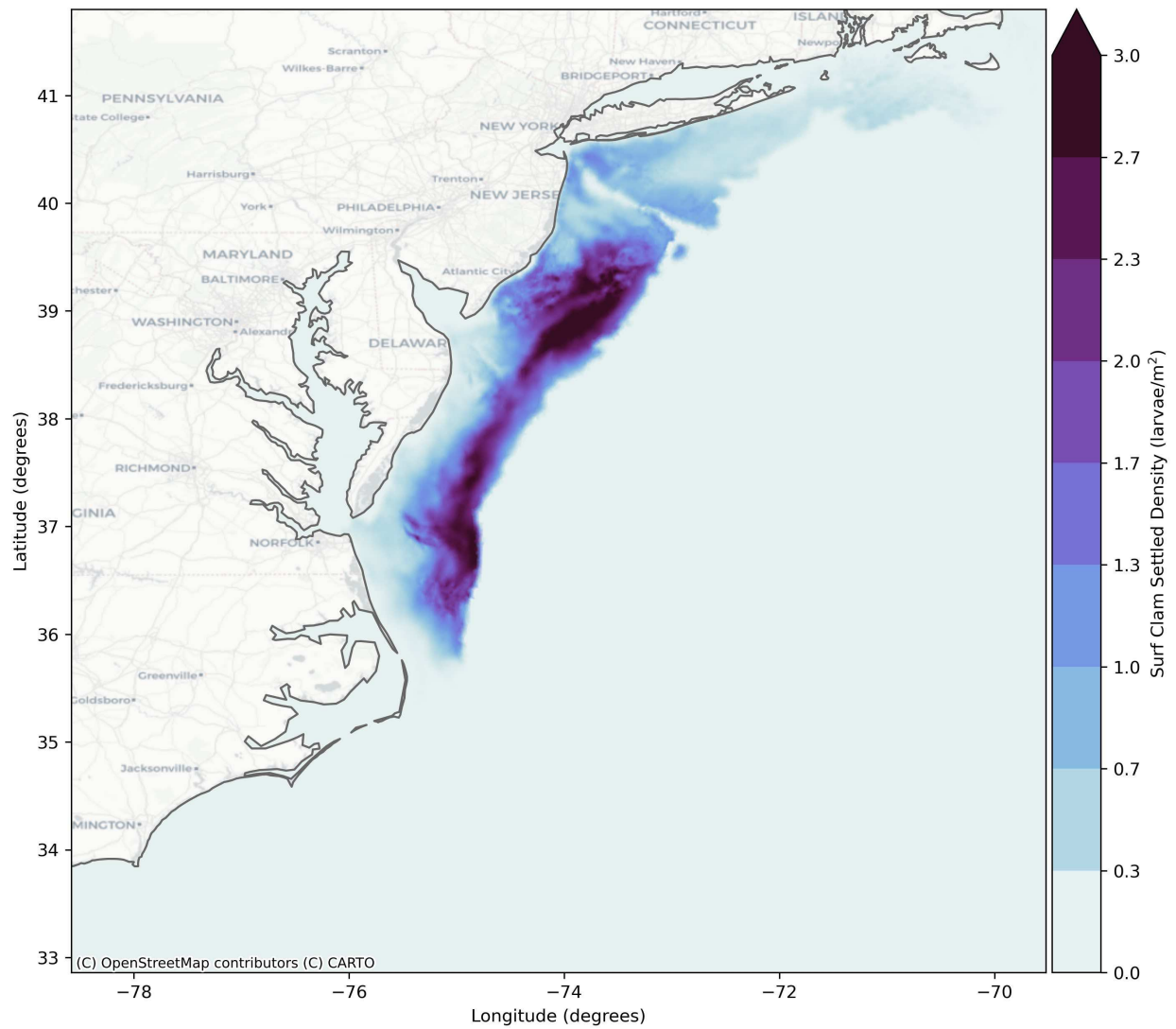


Figure C.12. Surf Clam Baseline Settled Density for 12MW Full Build-Out

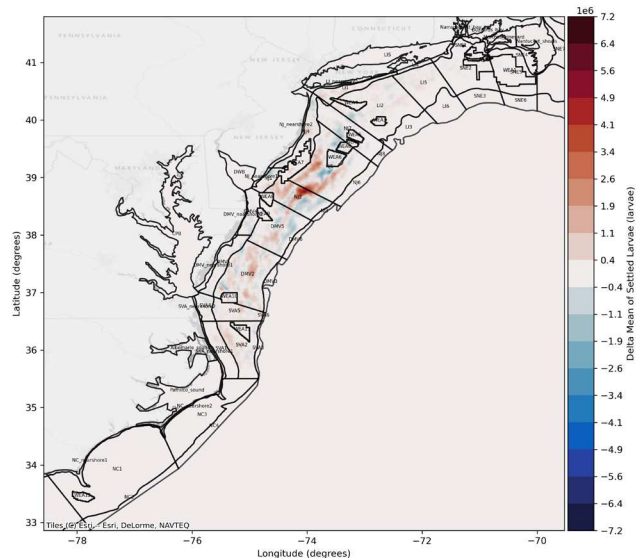


Figure C.13. Difference in Settled Larvae 12MW Full Build-Out vs Baseline 2017

Difference in total surf clam larvae settled larvae for model year 2017. Showing the difference in the mean of all ensemble baseline results and mean of all ensemble 12 MW full build-out results. Settled larvae averaged for each model grid element. Red shows an increase in settlement in the 12 MW scenario compared to the baseline, blue shows a decrease in settlement compared to the baseline.

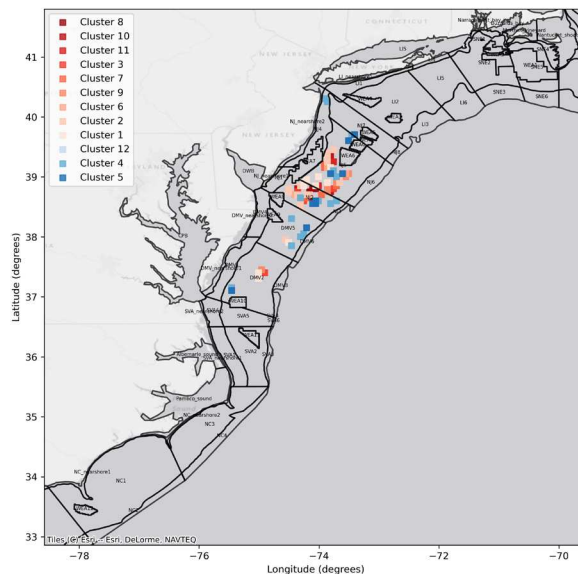


Figure C.14. DBSCAN (Density-Based Spatial Clustering of Applications with Noise) Difference in Settled Larvae 12MW Full Build-Out vs Baseline 2017

Spatial clusters identified using DBSCAN to filter out noise from the difference plot and identify areas of greatest change. Clusters of settlement increase are identified in red and clusters with settlement decrease are shown in blue.

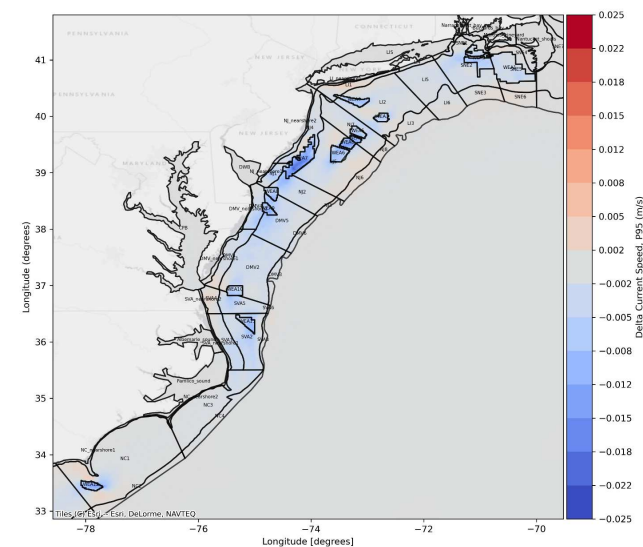


Figure C.15 Change in Current Speed 12MW Full Build-Out vs Baseline 2017

Difference in the depth averaged current speed for model year 2017. Showing the difference in the 95th percentile non-exceedance probability baseline results and 95th percentile non-exceedance probability 12 MW full build-out results

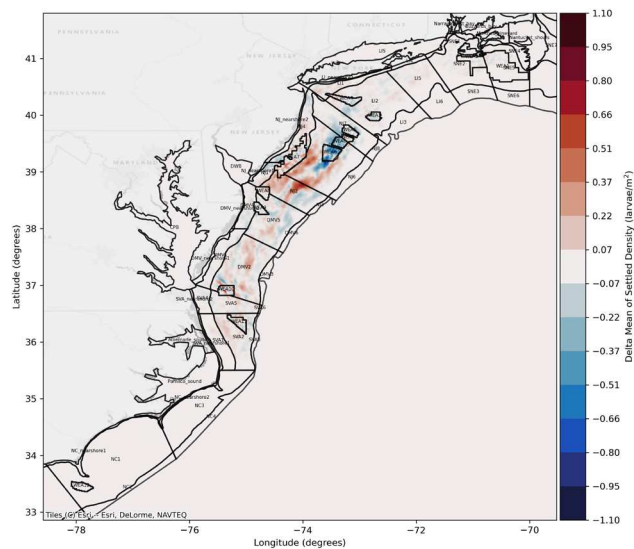


Figure C.16. Difference in Settled Density 12MW Full Build-Out vs Baseline 2017

Difference in total surf clam larvae settled larvae for model year 2017. Showing the difference in the mean of all ensemble baseline results and mean of all ensemble 12 MW partial build-out results. Settled larvae averaged for each model grid element. Red shows an increase in settlement in the 12 MW scenario compared to the baseline, blue shows a decrease in settlement compared to the baseline.

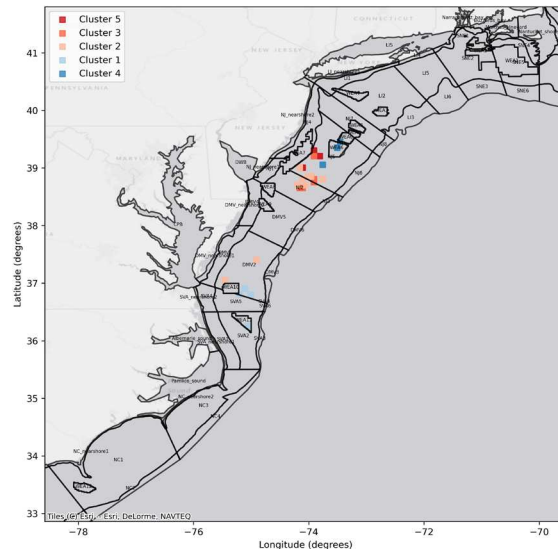


Figure C.17. DBSCAN (Density-Based Spatial Clustering of Applications with Noise) Difference in Settled Density 12MW Full Build-Out vs Baseline 2017

Spatial clusters identified using DBSCAN to filter out noise from the difference plot and identify areas of greatest change. Clusters of settlement increase are identified in red and clusters with settlement decrease are shown in blue.

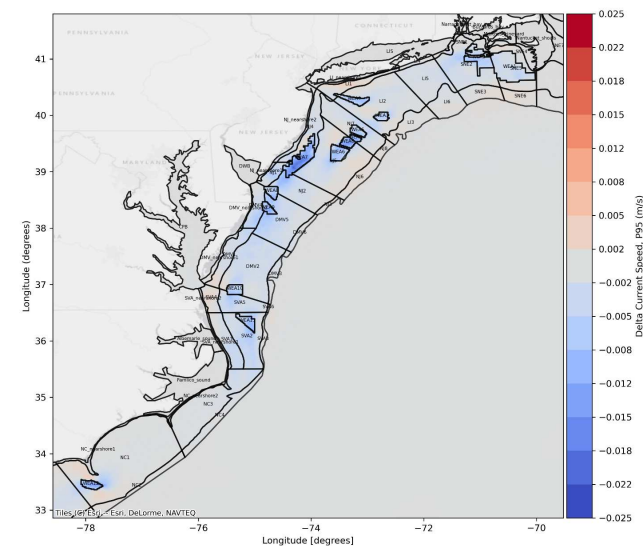


Figure C.18 Change in Current Speed 12MW Full Build-Out vs Baseline 2017

Difference in the depth averaged current speed for model year 2017. Showing the difference in the 95th percentile non-exceedance probability baseline results and 95th percentile non-exceedance probability 12 MW full build-out results

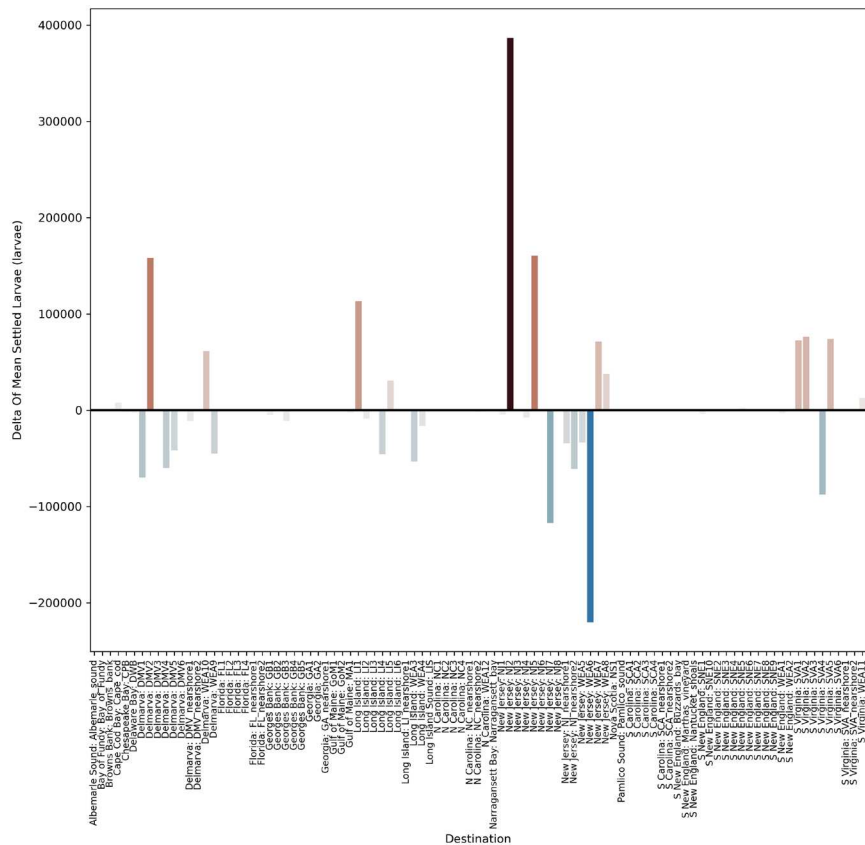


Figure C.19. Average Change in Surf Clam Settlement in Each Destination Area 12MW Partial Build-Out vs Baseline 2017

Bar chart shows the average change in settlement in each destination area for model year 2017. Showing the difference in the mean of all ensemble baseline results and mean of all ensemble 12 MW partial build-out results.

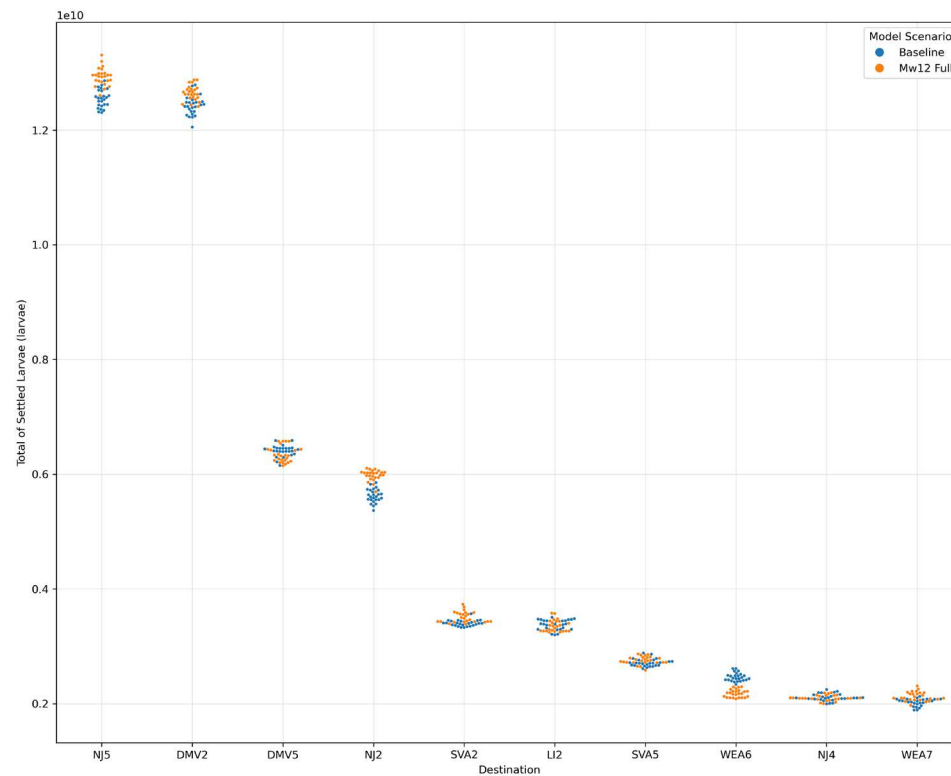


Figure C.20. Swarm Plot Showing Surf Clam Settlement in Top 10 Destinations for 2017

Swarm plot shows the settlement for each model run of the ensemble (i.e., each point represents a model result) for 2017. Blue points show the baseline results and orange show the 12 MW partial build-out number of settled larvae in the top 10 destinations where there is greatest larval settlement

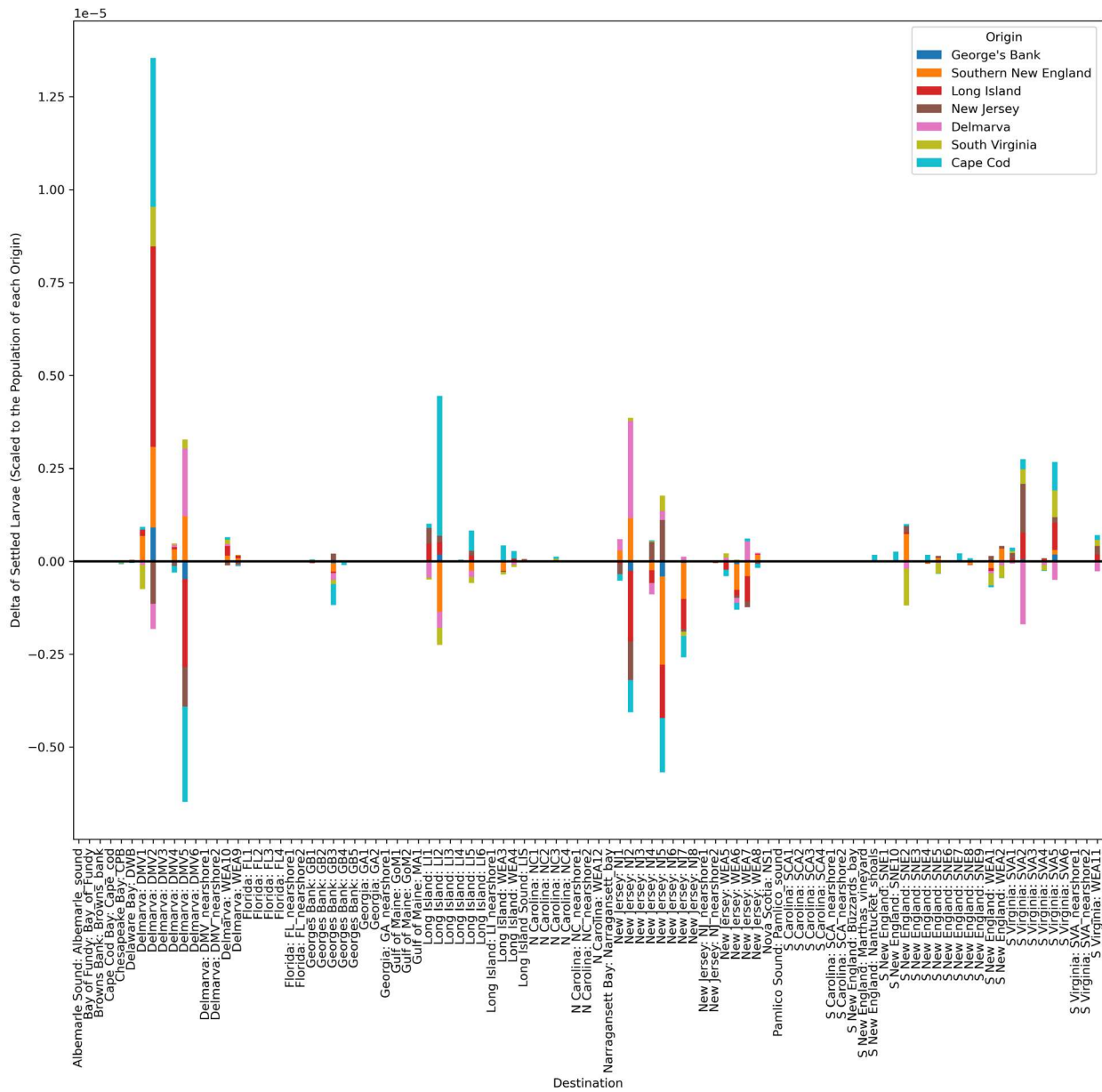


Figure C.21. Surf Clam Connectivity Difference 2017

Bar chart shows the difference in surf clam larvae settlement in each destination area, by origin for model year 2017. Bars are colored by origin area and results show the difference in export probabilities, i.e., the difference in the likelihood of settlement scaled to the number of larvae released from a particular origin region between the baseline and 12MW full build-out results. Bars below the x axis, show a decrease in settlement in a particular destination area, results above the x axis show an increase in a settlement in a destination area.

C.1.3 Summer Flounder 2017

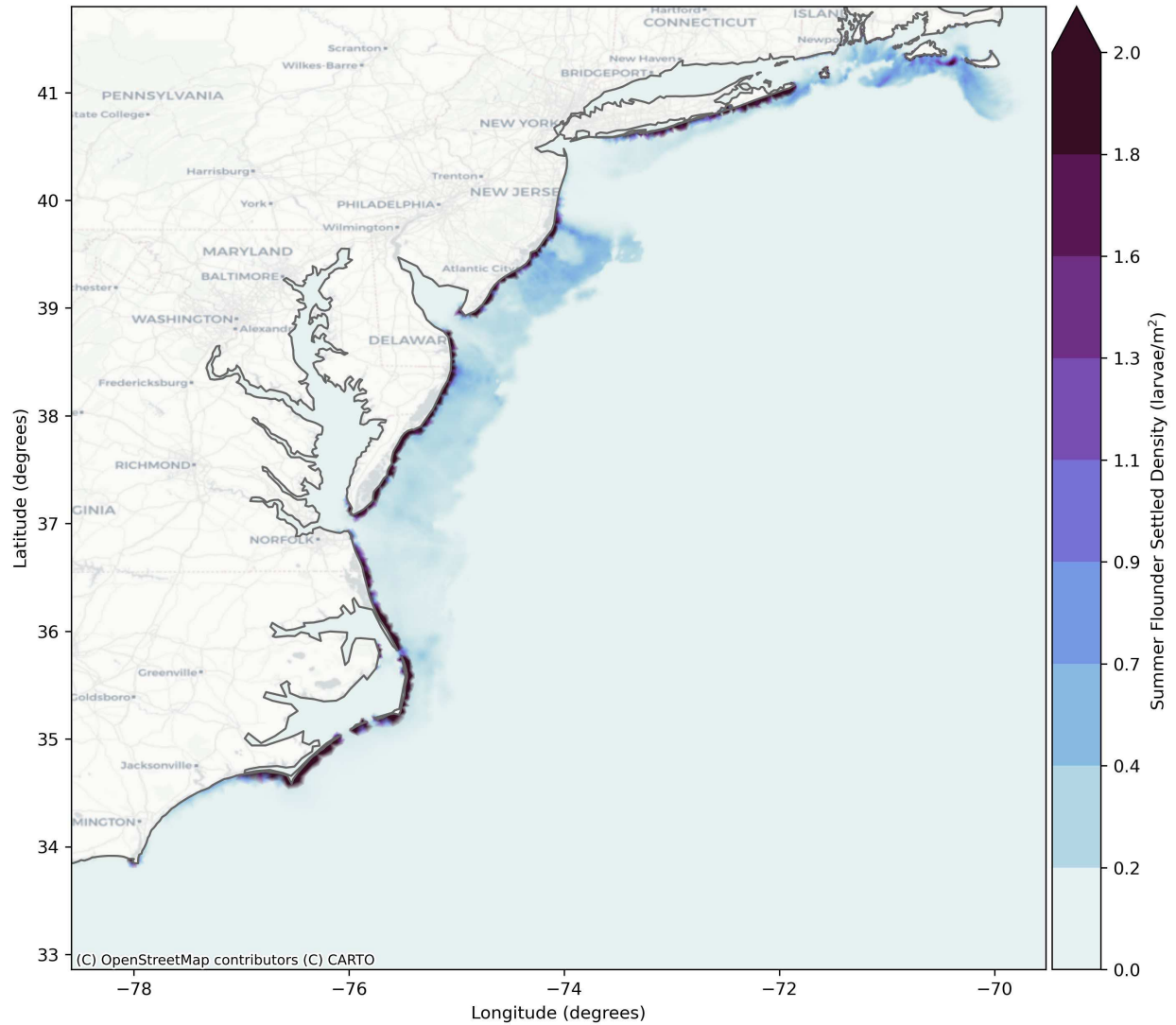


Figure C.22. Summer Flounder Baseline Settled Density for 12MW Full Build-Out

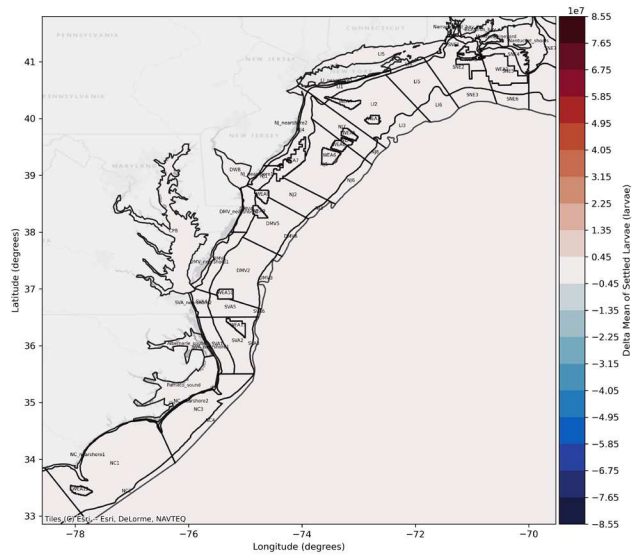


Figure C.23. Difference in Settled Larvae 12MW Full Build-Out vs Baseline 2017

Difference in total summer flounder larvae settled larvae for model year 2017. Showing the difference in the mean of all ensemble baseline results and mean of all ensemble 12 MW full build-out results. Settled larvae averaged for each model grid element. Red shows an increase in settlement in the 12 MW scenario compared to the baseline, blue shows a decrease in settlement compared to the baseline.

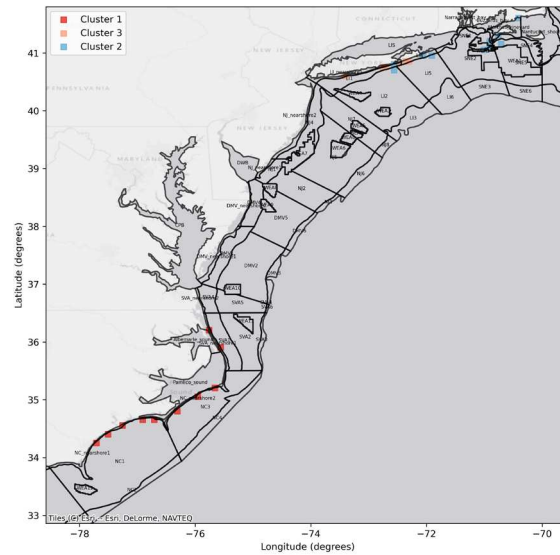


Figure C.24. DBSCAN (Density-Based Spatial Clustering of Applications with Noise) Difference in Settled Larvae 12MW Full Build-Out vs Baseline 2017

Spatial clusters identified using DBSCAN to filter out noise from the difference plot and identify areas of greatest change. Clusters of settlement increase are identified in red and clusters with settlement decrease are shown in blue.

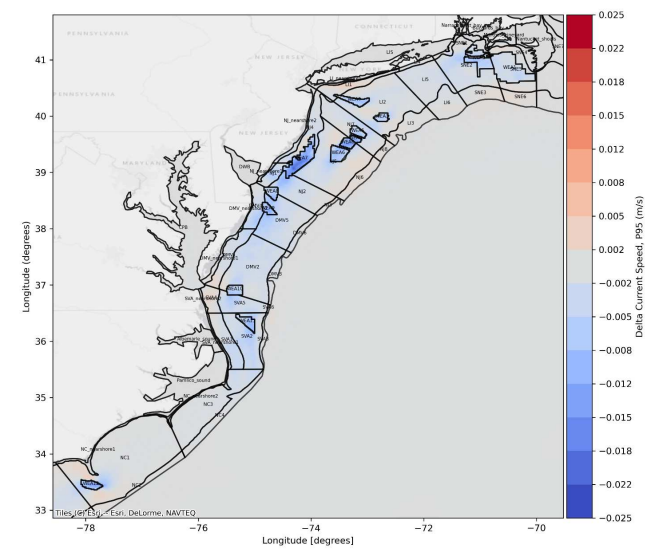


Figure C.25 Change in Current Speed 12MW Full Build-Out vs Baseline 2017

Difference in the depth averaged current speed for model year 2017. Showing the difference in the 95th percentile non-exceedance probability baseline results and 95th percentile non-exceedance probability 12 MW full build-out results

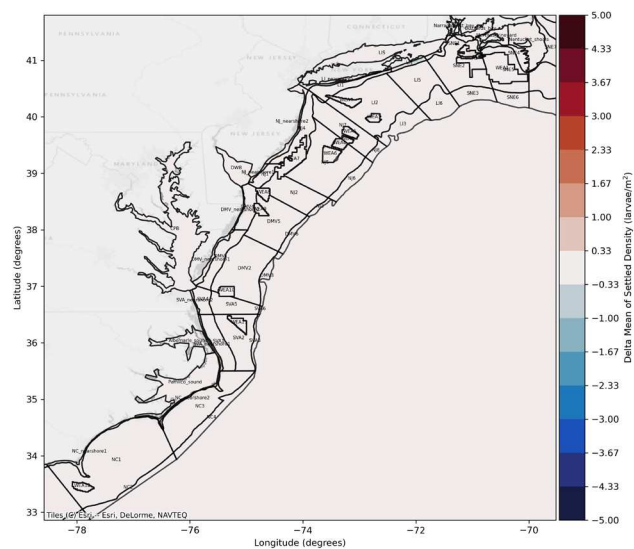


Figure C.26. Difference in Settled Density 12MW Full Build-Out vs Baseline 2017

Difference in total summer flounder larvae settled larvae for model year 2017. Showing the difference in the mean of all ensemble baseline results and mean of all ensemble 12 MW full build-out results. Settled larvae averaged for each model grid element. Red shows an increase in settlement in the 12 MW scenario compared to the baseline, blue shows a decrease in settlement compared to the baseline.

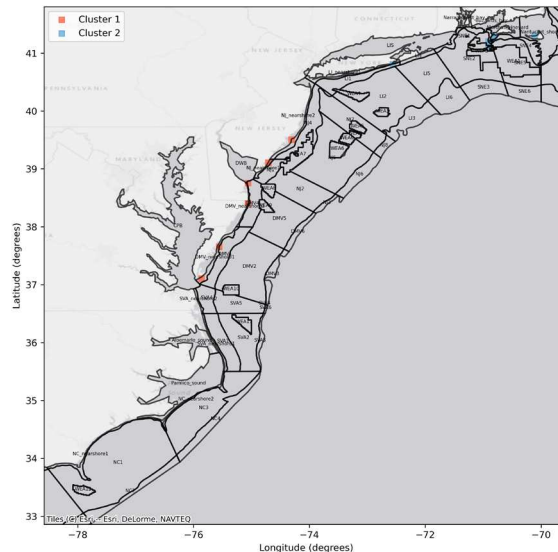


Figure C.27. DBSCAN (Density-Based Spatial Clustering of Applications with Noise) Difference in Settled Density 12MW Full Build-Out vs Baseline 2017

Spatial clusters identified using DBSCAN to filter out noise from the difference plot and identify areas of greatest change. Clusters of settlement increase are identified in red and clusters with settlement decrease are shown in blue.

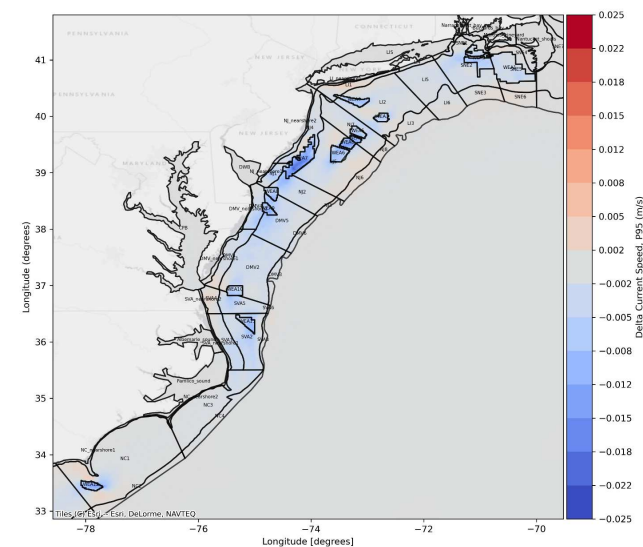
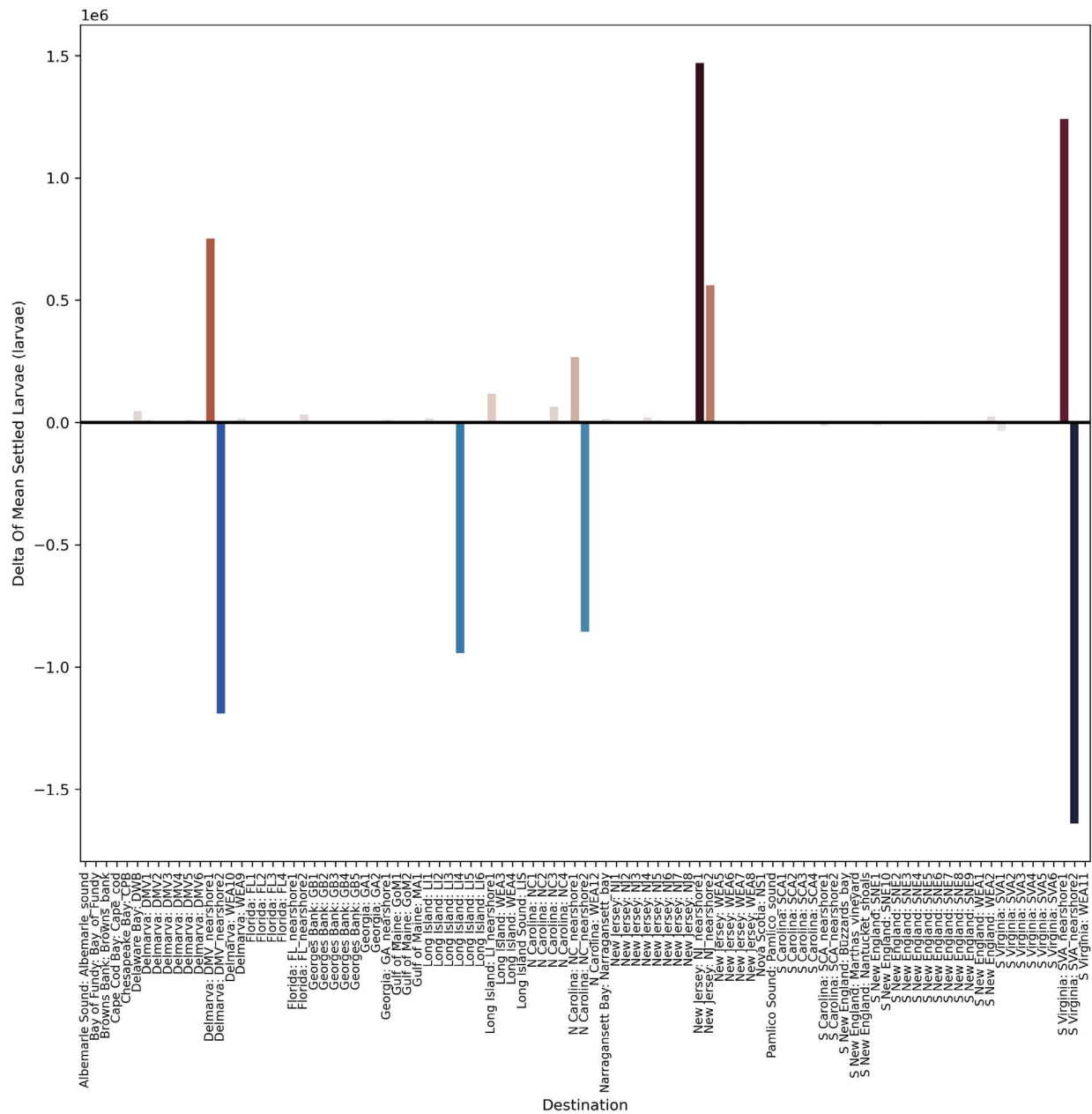


Figure C.28 Change in Current Speed 12MW Full Build-Out vs Baseline 2017

Difference in the depth averaged current speed for model year 2017. Showing the difference in the 95th percentile non-exceedance probability baseline results and 95th percentile non-exceedance probability 12 MW full build-out results



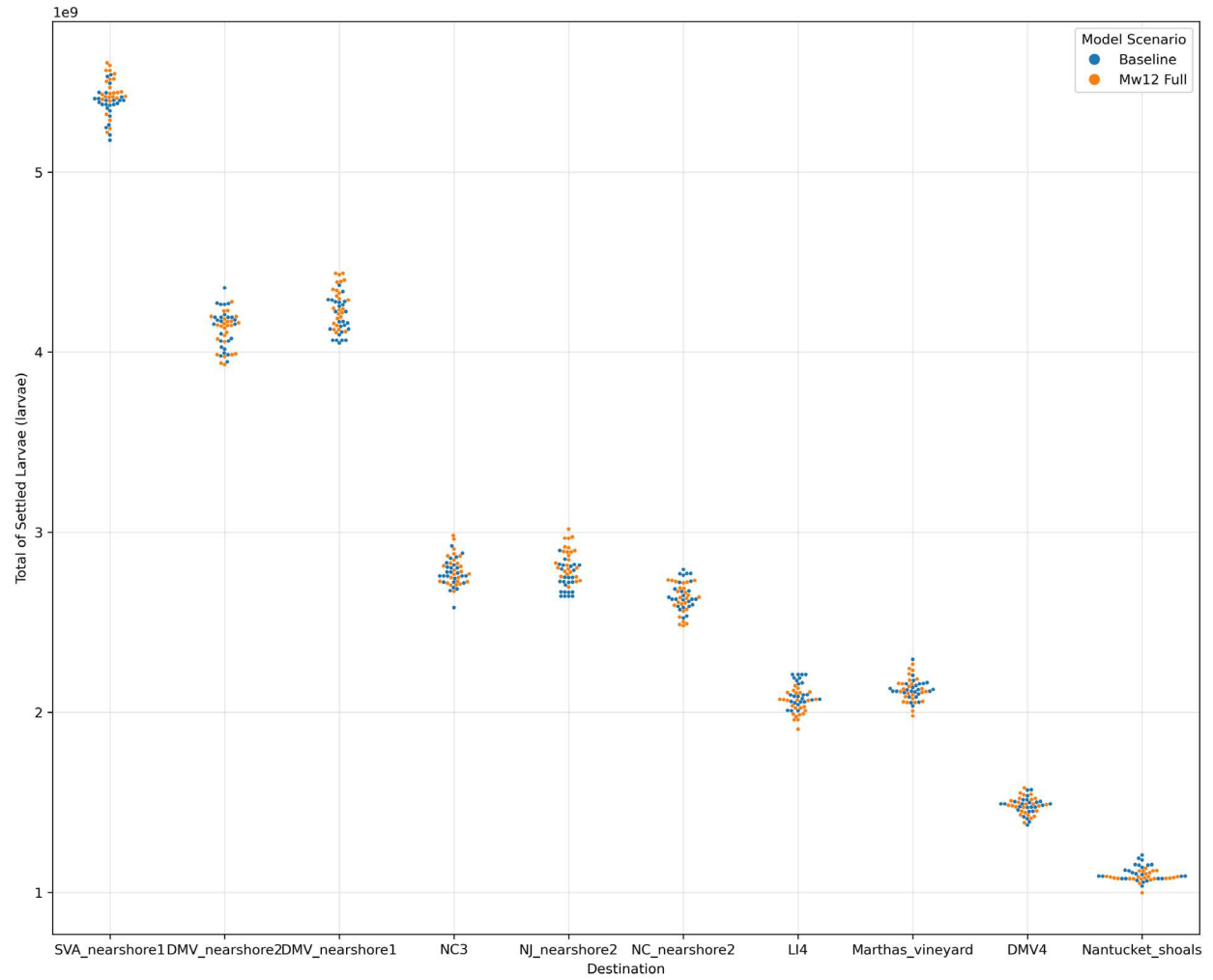


Figure C.30. Swarm Plot Showing Summer Flounder Settlement in Top 10 Destinations for 2017
 Swarm plot shows the settlement for each model run of the ensemble (i.e., each point represents a model result) for 2017. Blue points show the baseline results and orange show the 12 MW full build-out number of settled larvae in the top 10 destinations where there is greatest larval settlement.

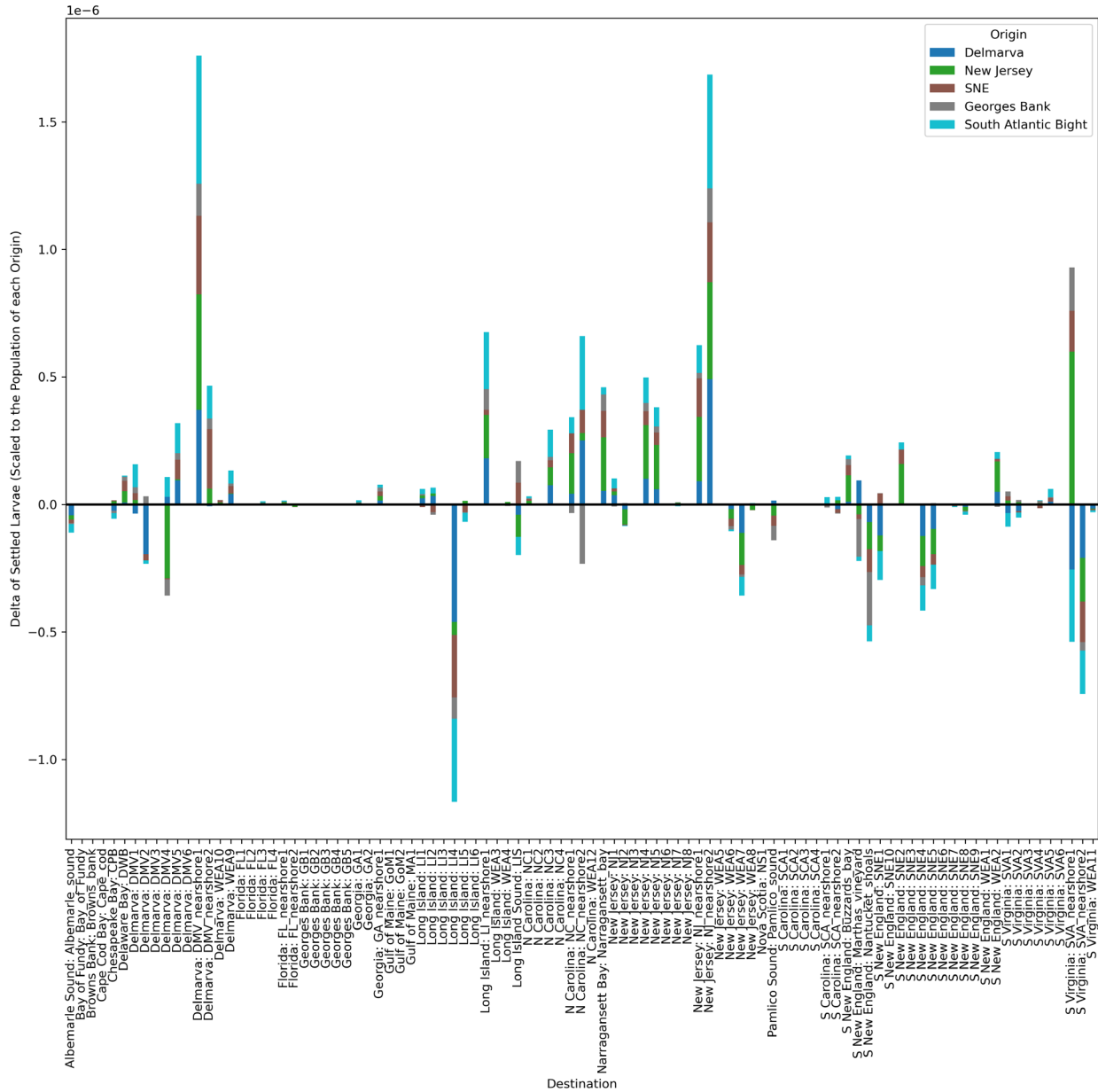


Figure C.31. Summer Flounder Connectivity Difference 2017

Bar chart shows the difference in summer flounder larvae settlement in each destination area, by origin for model year 2017. Bars are colored by origin area and results show the difference in export probabilities, i.e., the difference in the likelihood of settlement scaled to the number of larvae released from a particular origin region between the baseline and 12MW full build-out results. Bars below the x axis, show a decrease in settlement in a particular destination area, results above the x axis show an increase in a settlement in a destination area.

C.2 12 MW Partial Build-out

C.2.1 Sea Scallop 2017

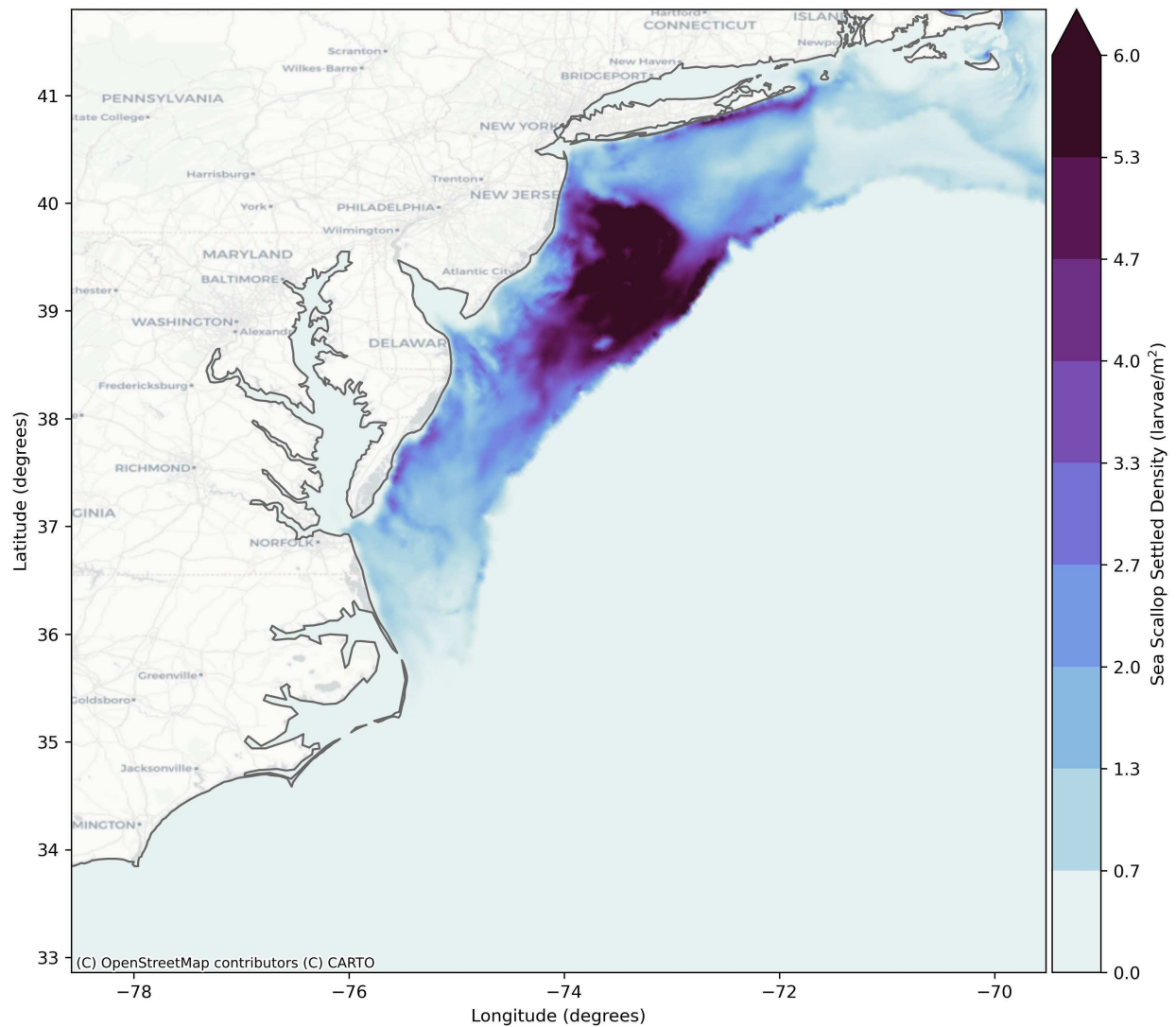


Figure C.32. Sea Scallop Baseline Settled Density for 12MW Partial Build-Out

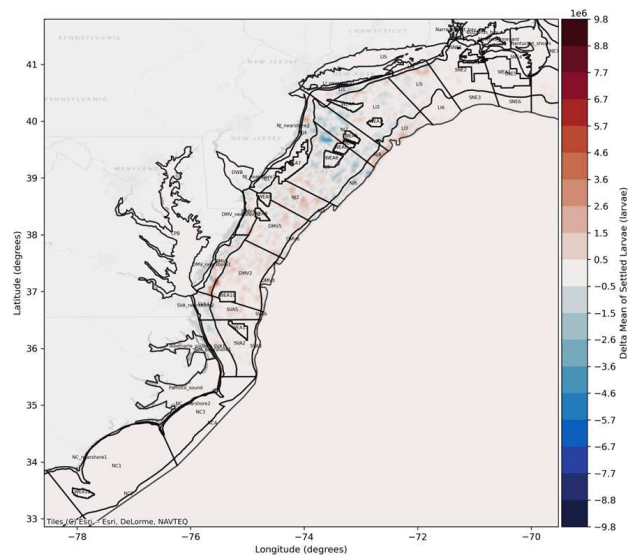


Figure C.33. Difference in Settled Larvae 12MW Partial Build-Out vs Baseline 2017

Difference in total sea scallop larvae settled larvae for model year 2017. Showing the difference in the mean of all ensemble baseline results and mean of all ensemble 12 MW partial build-out results. Settled larvae averaged for each model grid element. Red shows an increase in settlement in the 12 MW scenario compared to the baseline, blue shows a decrease in settlement compared to the baseline.

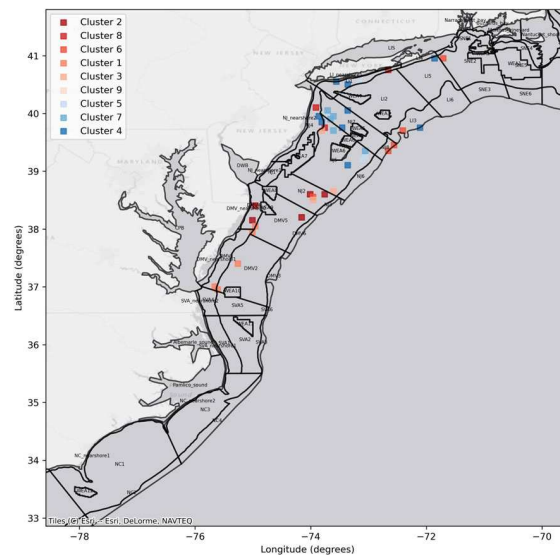


Figure C.34. DBSCAN (Density-Based Spatial Clustering of Applications with Noise) Difference in Settled Larvae 12MW Partial Build-Out vs Baseline 2017

Spatial clusters identified using DBSCAN to filter out noise from the difference plot and identify areas of greatest change. Clusters of settlement increase are identified in red and clusters with settlement decrease are shown in blue.

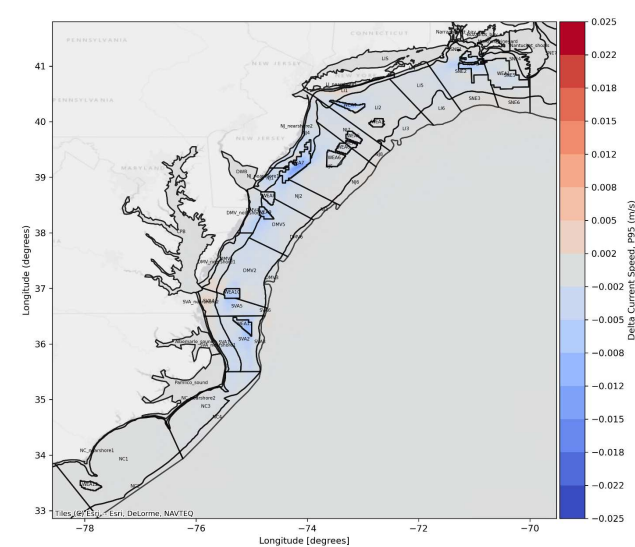
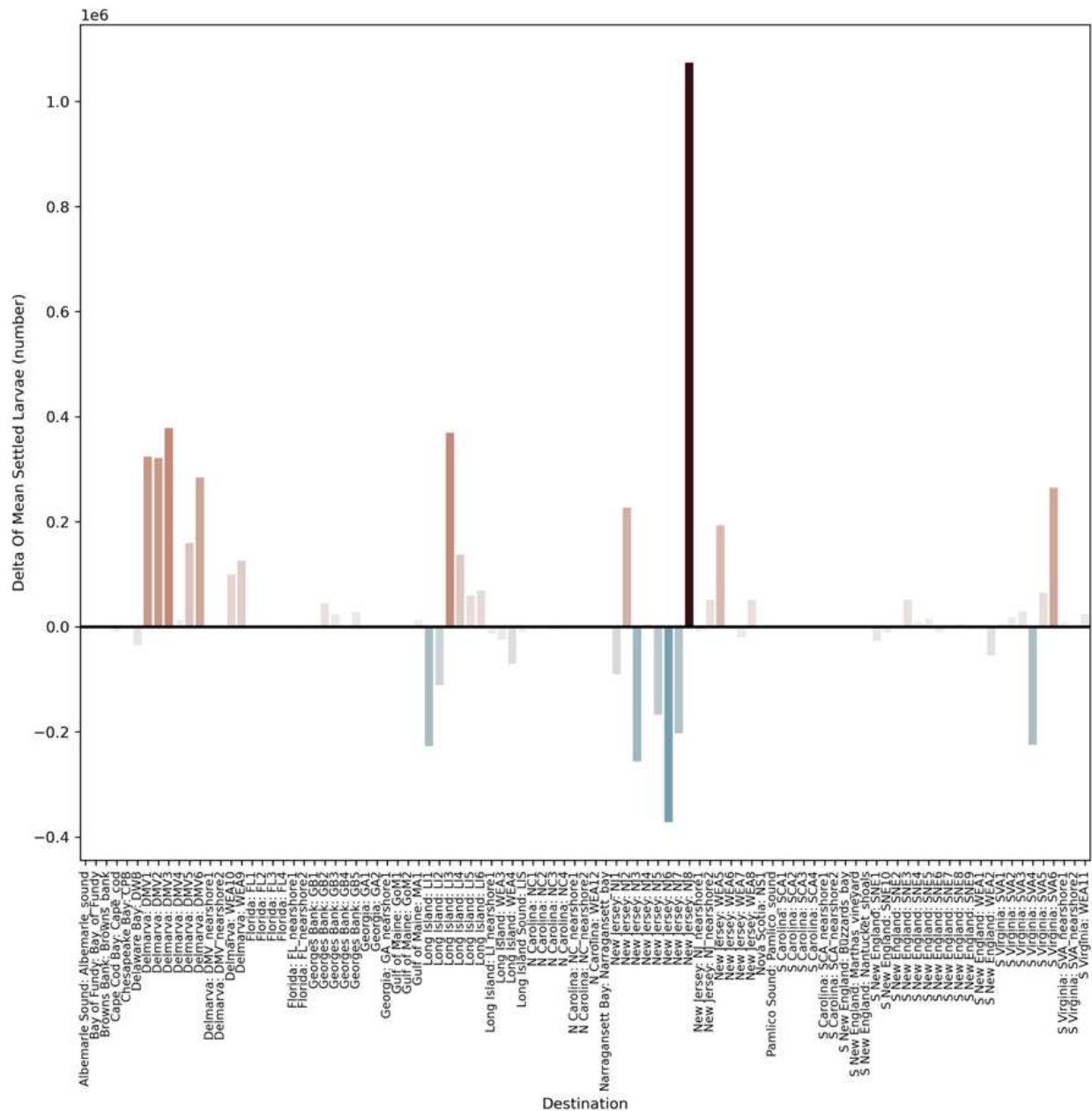


Figure C.35 Change in Current Speed 12MW Partial Build-Out vs Baseline 2017

Difference in the depth averaged current speed for model year 2017. Showing the difference in the 95th percentile non-exceedance probability baseline results and 95th percentile non-exceedance probability 12 MW partial build-out results



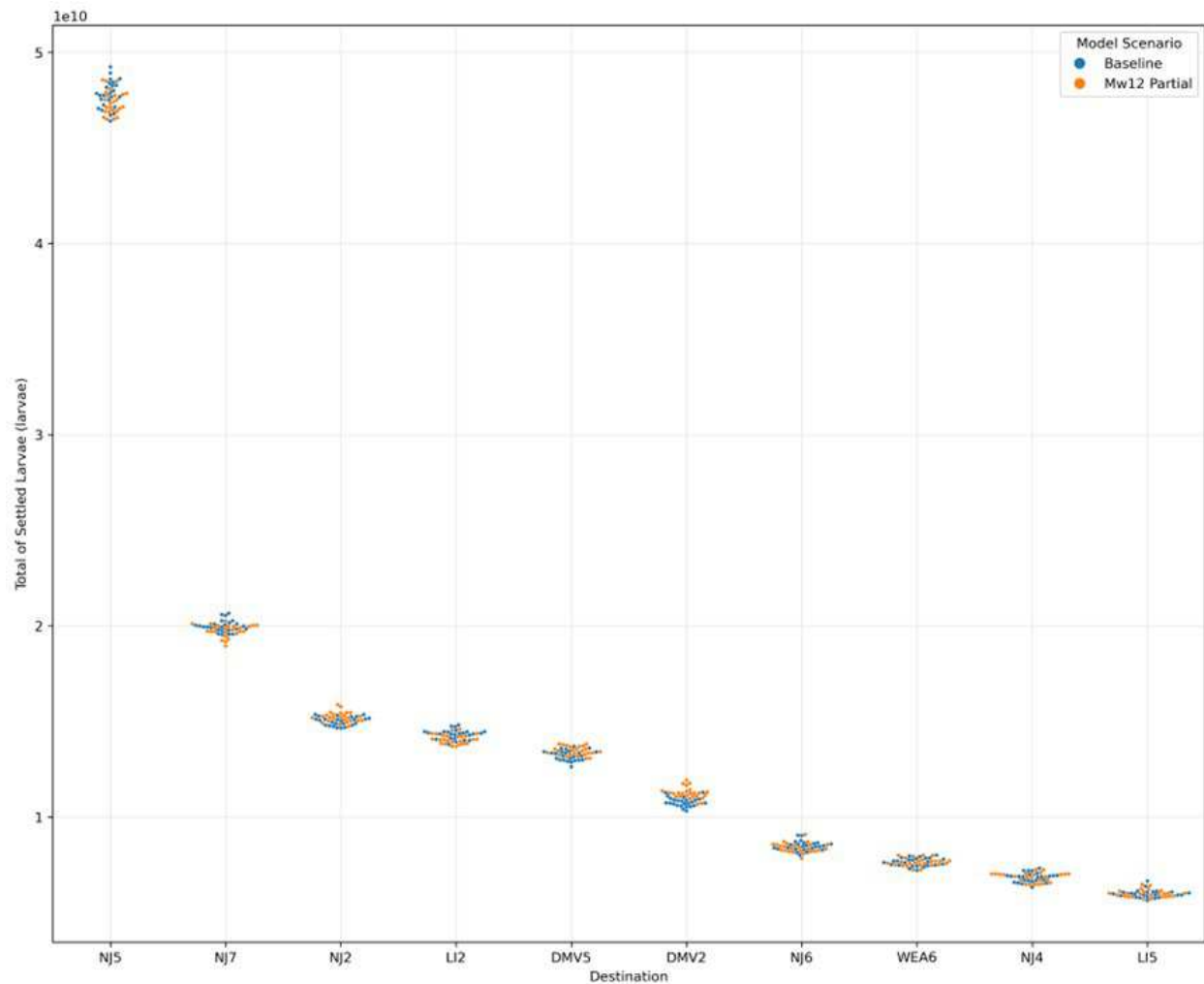


Figure C.37. Swarm Plot Showing Sea Scallop Settlement in Top 10 Destinations for 2017

Swarm plot shows the settlement for each model run of the ensemble (i.e., each point represents a model result) for 2017. Blue points show the baseline results and orange show the 12 MW partial build-out number of settled larvae in the top 10 destinations where there is greatest larval settlement.

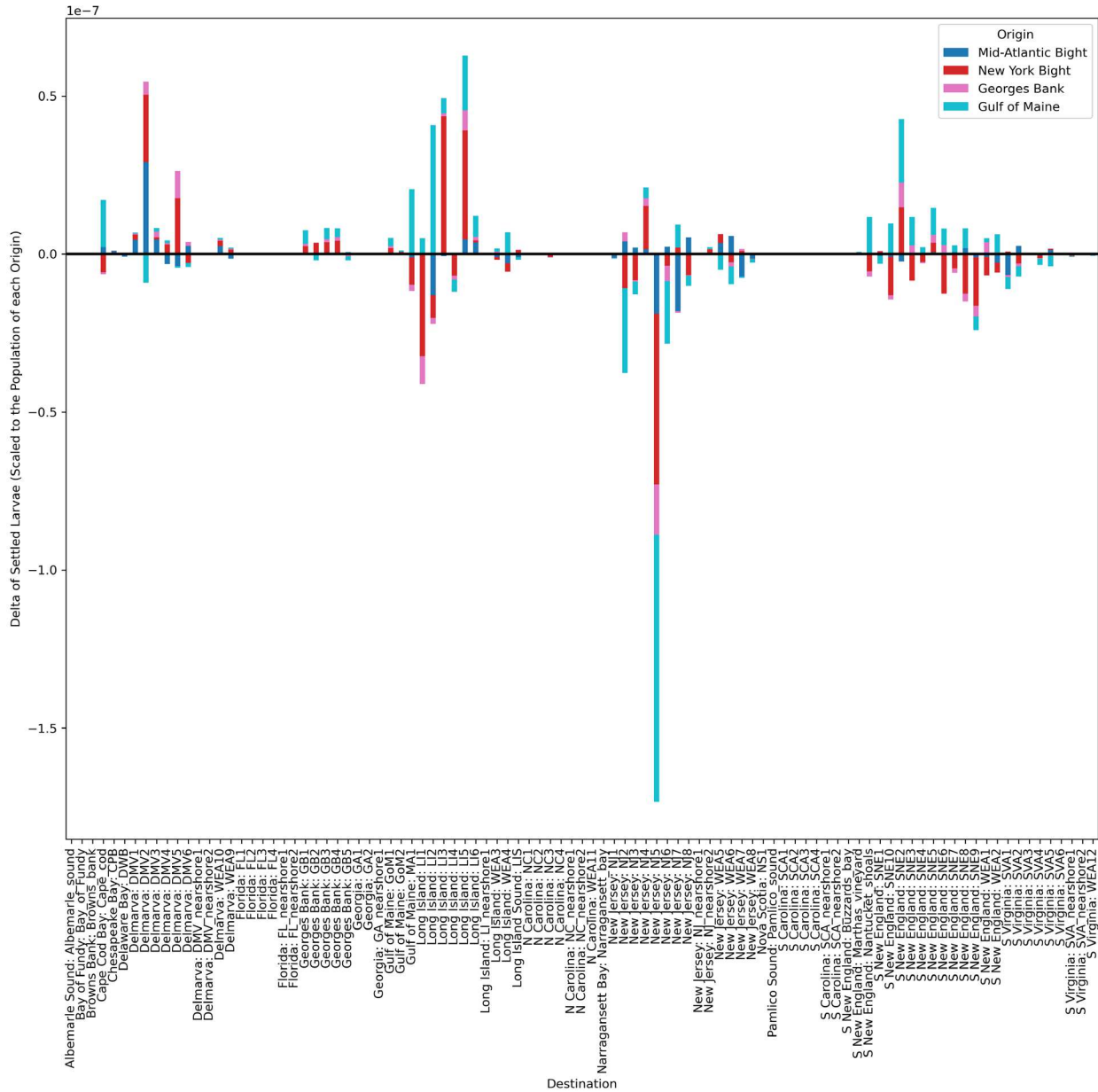


Figure C.38. Sea Scallop Connectivity Difference 2017

Bar chart shows the difference in sea scallop larvae settlement in each destination area, by origin for model year 2017. Bars are colored by origin area and results show the difference in export probabilities, i.e., the difference in the likelihood of settlement scaled to the number of larvae released from a particular origin region between the baseline and 12MW partial build-out results. Bars below the x axis, show a decrease in settlement in a particular destination area, results above the x axis show an increase in a settlement in a destination area.

C.2.2 Surf Clam 2017

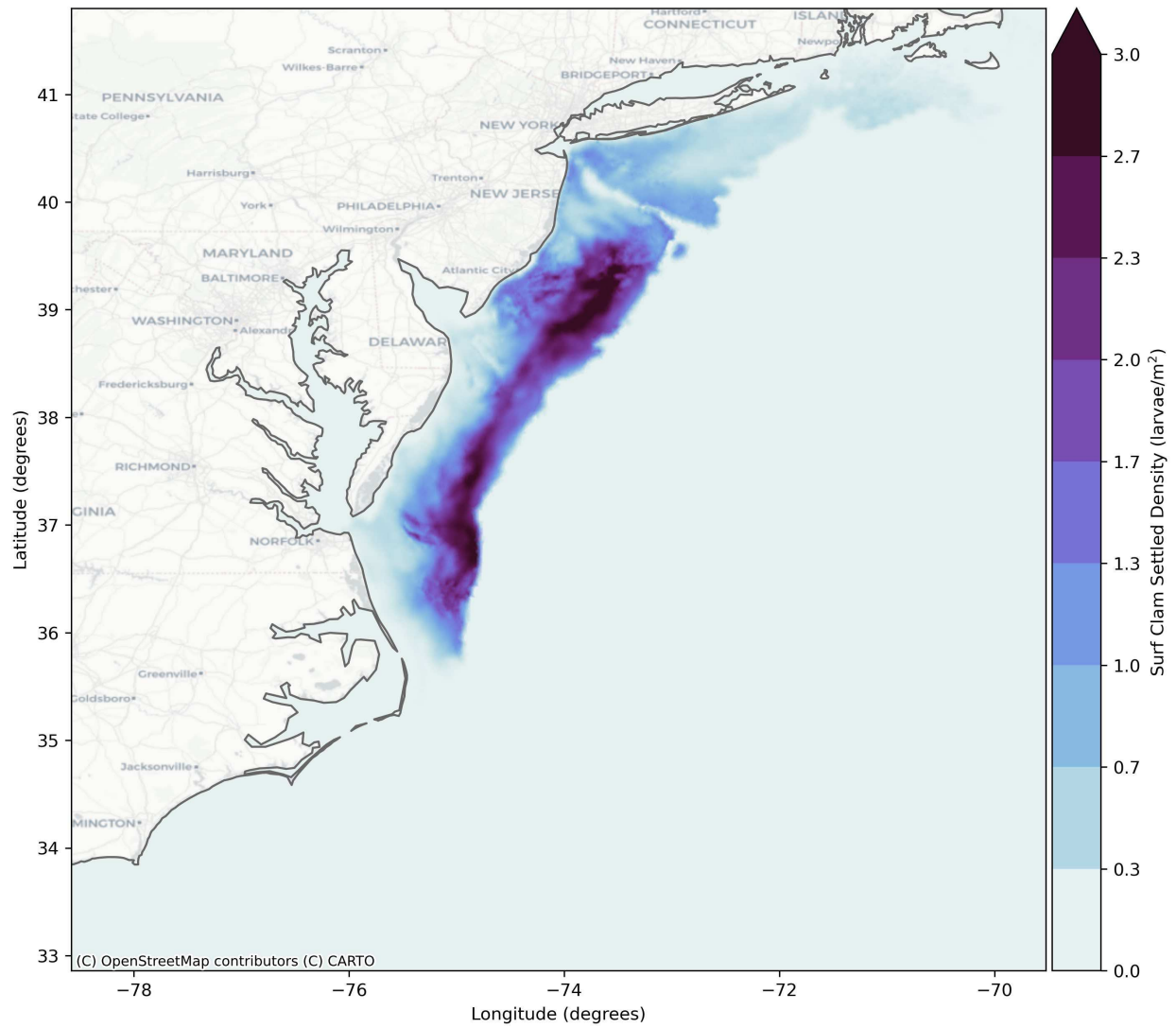


Figure C.39. Surf Clam Baseline Settled Density for 12MW Partial Build-Out

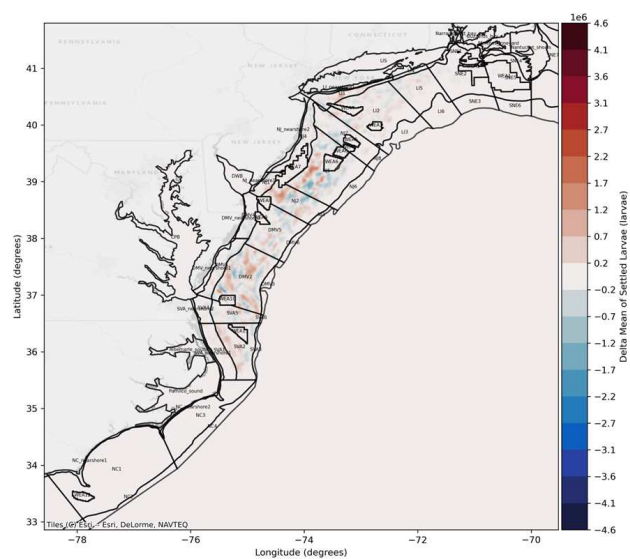


Figure C.40. Difference in Settled Larvae 12MW Partial Build-Out vs Baseline 2017

Difference in total surf clam larvae settled larvae for model year 2017. Showing the difference in the mean of all ensemble baseline results and mean of all ensemble 12 MW partial build-out results. Settled larvae averaged for each model grid element. Red shows an increase in settlement in the 12 MW scenario compared to the baseline, blue shows a decrease in settlement compared to the baseline.

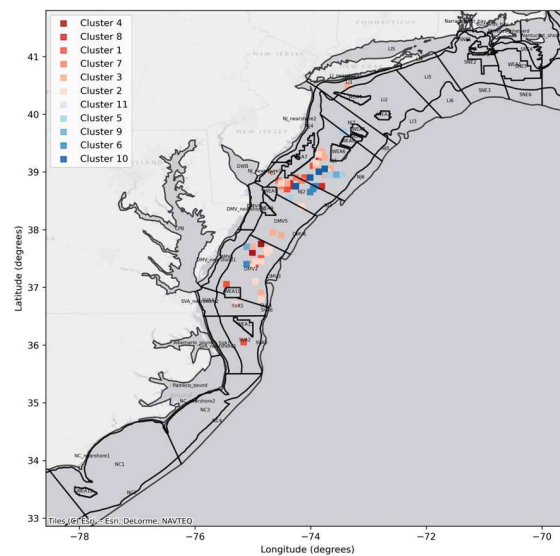


Figure C.41. DBSCAN (Density-Based Spatial Clustering of Applications with Noise) Difference in Settled Larvae 12MW Partial Build-Out vs Baseline 2017

Spatial clusters identified using DBSCAN to filter out noise from the difference plot and identify areas of greatest change. Clusters of settlement increase are identified in red and clusters with settlement decrease are shown in blue.

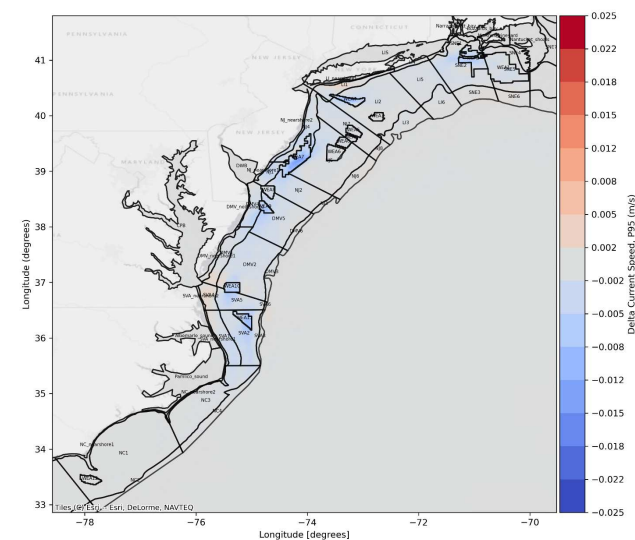


Figure C.42 Change in Current Speed 12MW Partial Build-Out vs Baseline 2017

Difference in the depth averaged current speed for model year 2017. Showing the difference in the 95th percentile non-exceedance probability baseline results and 95th percentile non-exceedance probability 12 MW partial build-out results

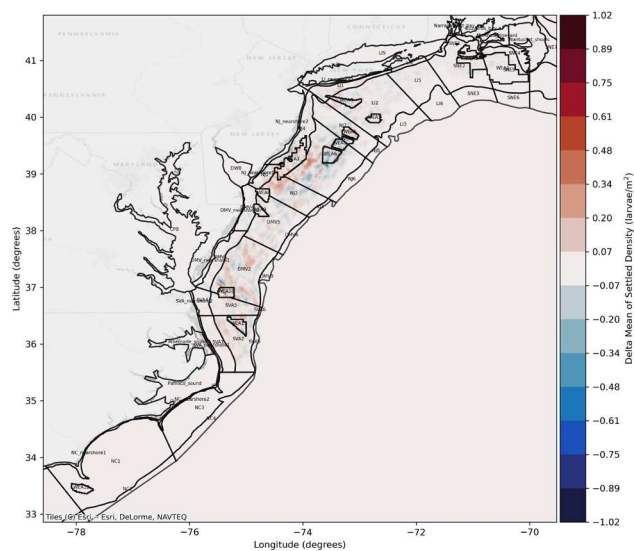


Figure C.43. Difference in Settled Density 12MW Partial Build-Out vs Baseline 2017

Difference in total surf clam larvae settled larvae for model year 2017. Showing the difference in the mean of all ensemble baseline results and mean of all ensemble 12 MW partial build-out results. Settled larvae averaged for each model grid element. Red shows an increase in settlement in the 12 MW scenario compared to the baseline, blue shows a decrease in settlement compared to the baseline.

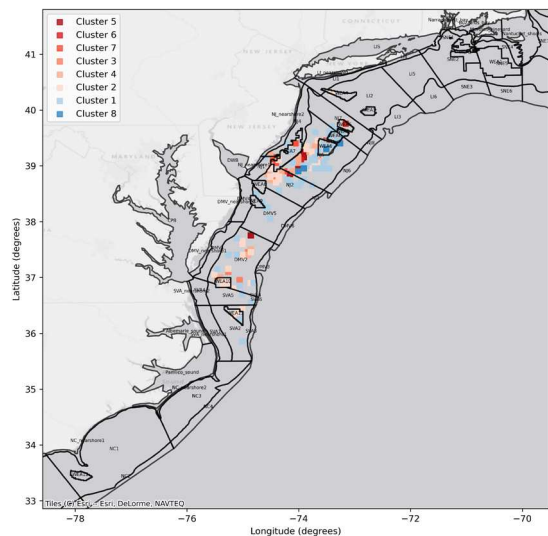


Figure C.44. DBSCAN (Density-Based Spatial Clustering of Applications with Noise) Difference in Settled Density 12MW Partial Build-Out vs Baseline 2017

Spatial clusters identified using DBSCAN to filter out noise from the difference plot and identify areas of greatest change. Clusters of settlement increase are identified in red and clusters with settlement decrease are shown in blue.

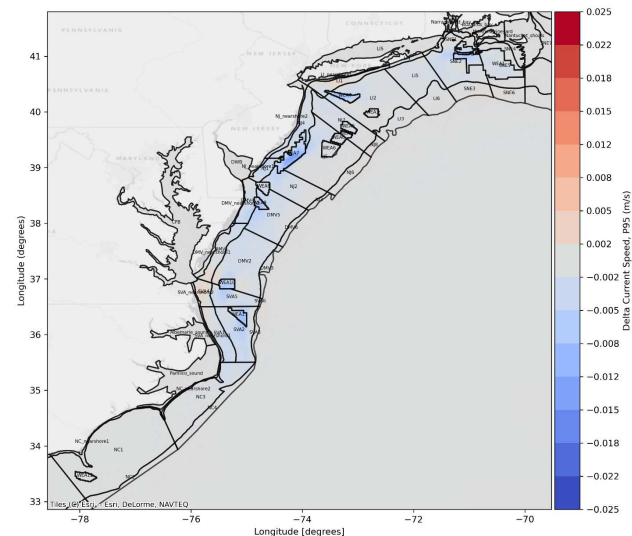


Figure C.45 Change in Current Speed 12MW Partial Build-Out vs Baseline 2017

Difference in the depth averaged current speed for model year 2017. Showing the difference in the 95th percentile non-exceedance probability baseline results and 95th percentile non-exceedance probability 12 MW partial build-out results

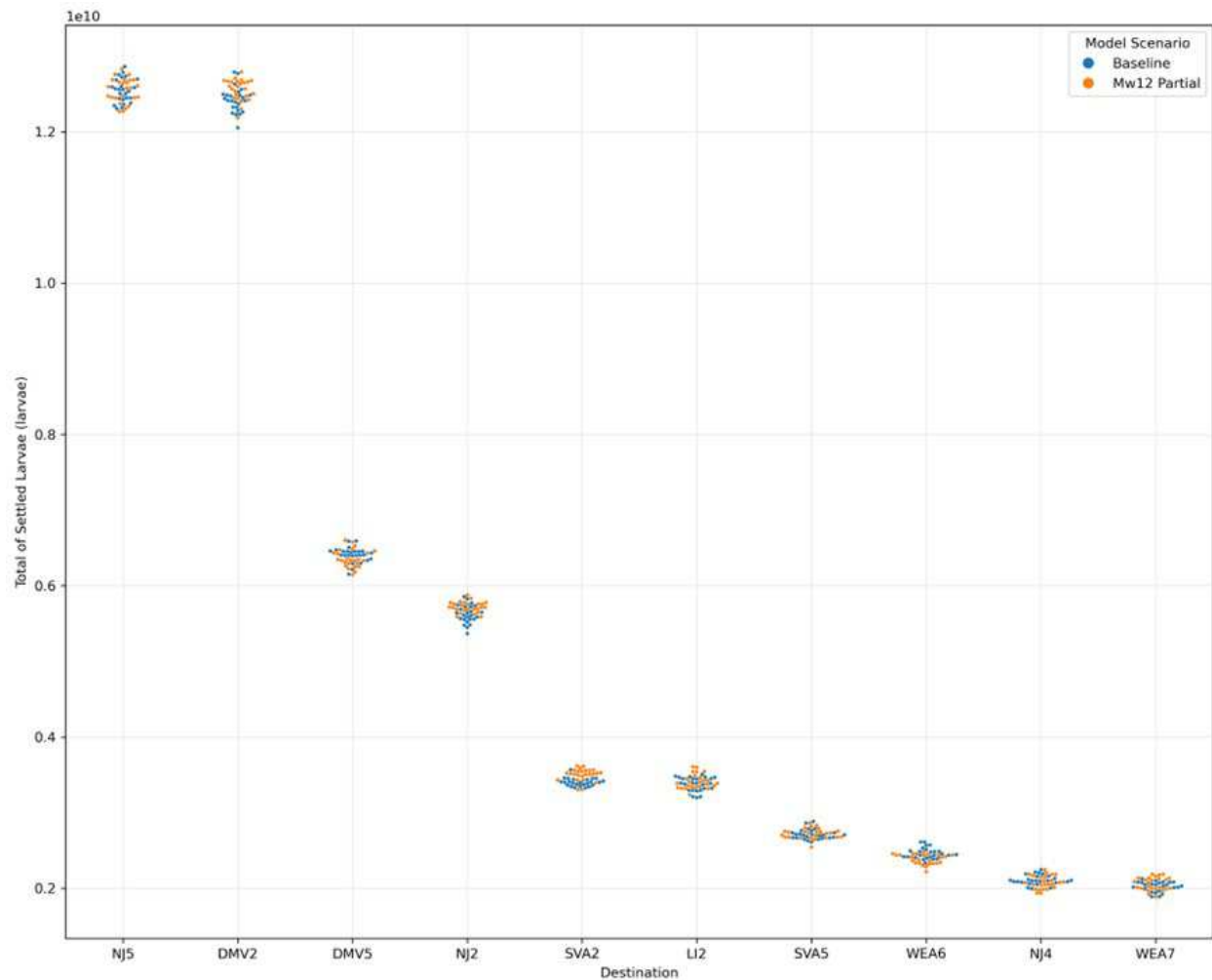


Figure C.47. Swarm Plot Showing Surf Clam Settlement in Top 10 Destinations for 2017

Swarm plot shows the settlement for each model run of the ensemble (i.e., each point represents a model result) for 2017. Blue points show the baseline results and orange show the 12 MW partial build-out number of settled larvae in the top 10 destinations where there is greatest larval settlement.

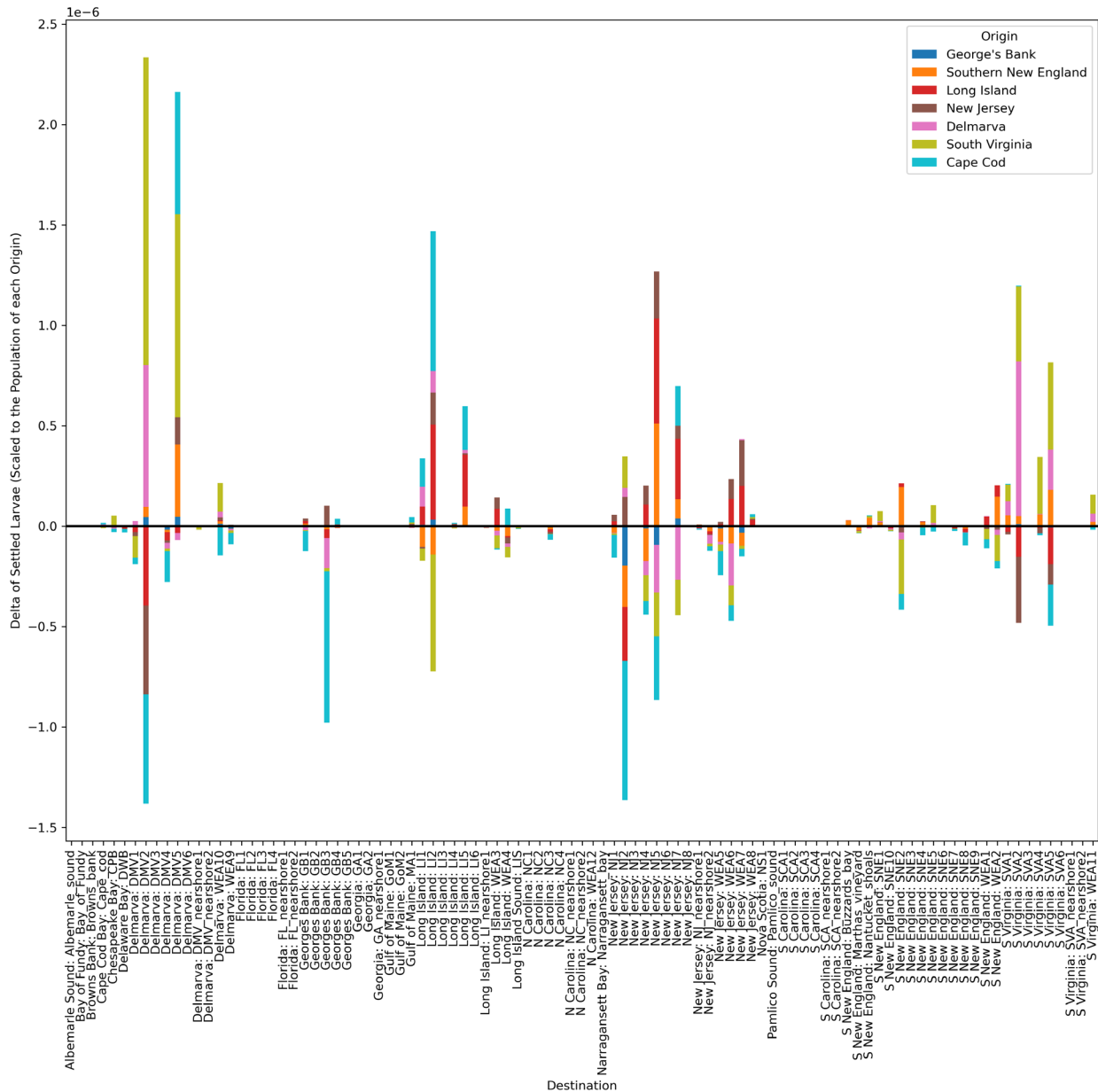


Figure C.48. Surf Clam Connectivity Difference 2017

Bar chart shows the difference in surf clam larvae settlement in each destination area, by origin for model year 2017. Bars are colored by origin area and results show the difference in export probabilities, i.e., the difference in the likelihood of settlement scaled to the number of larvae released from a particular origin region between the baseline and 12MW partial build-out results. Bars below the x axis, show a decrease in settlement in a particular destination area, results above the x axis show an increase in a settlement in a destination area.

C.2.3 Summer Flounder 2017

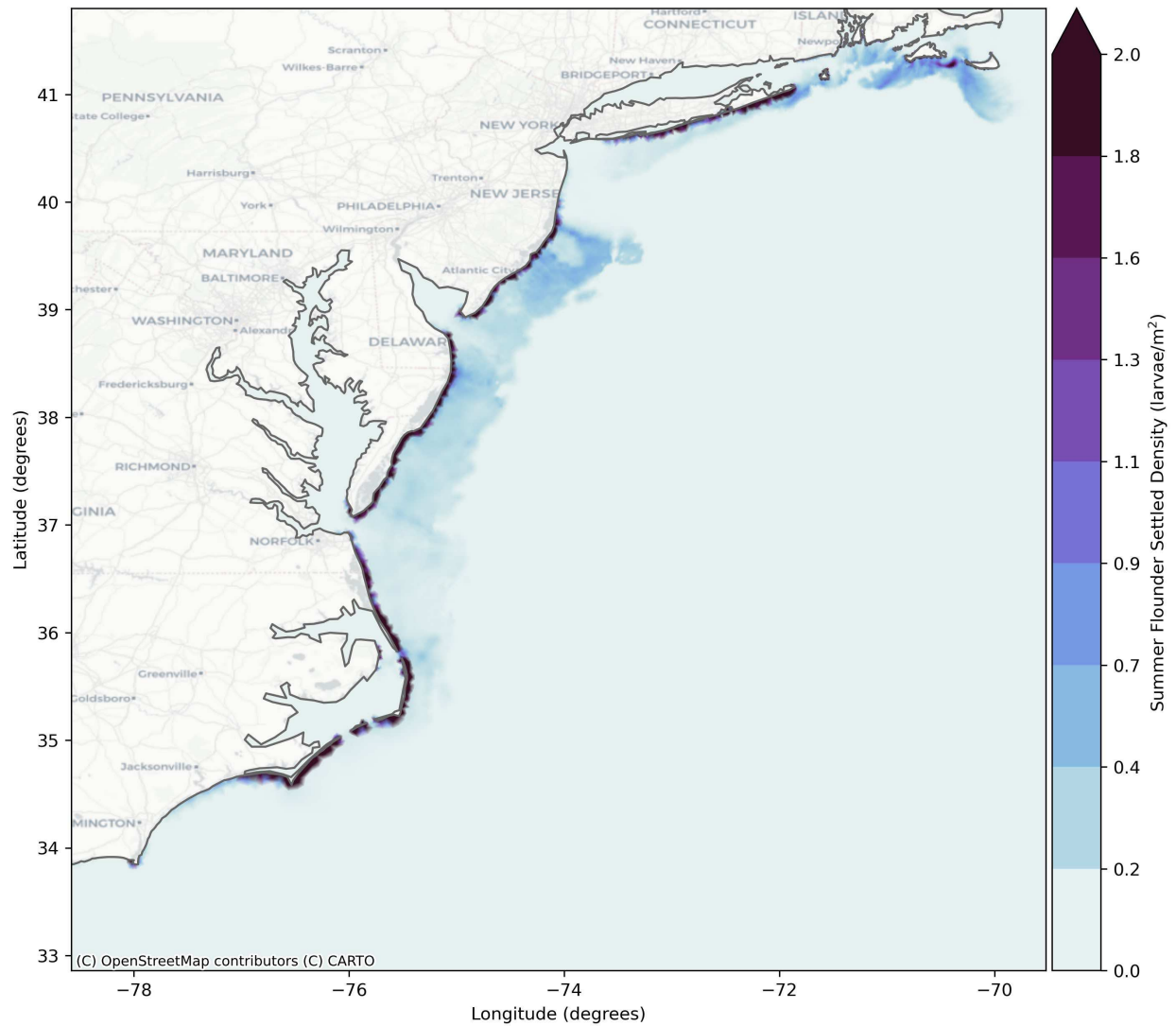


Figure C.49. Summer Flounder Baseline Settled Density for 12MW Partial Build-Out

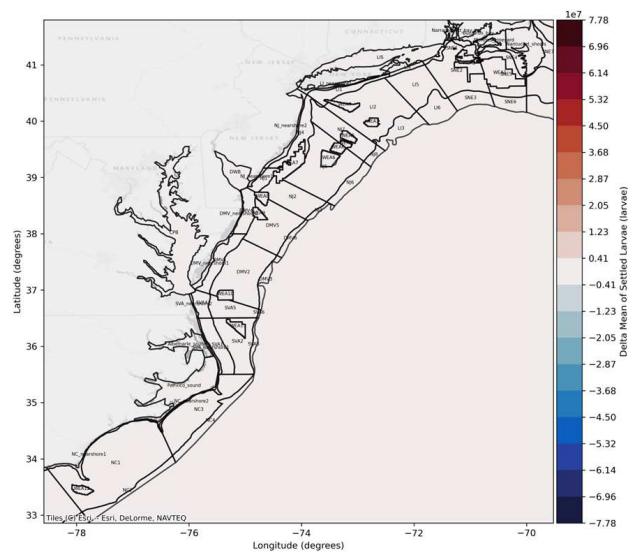


Figure C.50. Difference in Settled Larvae 12MW Partial Build-Out vs Baseline 2017

Difference in total surf clam larvae settled larvae for model year 2017. Showing the difference in the mean of all ensemble baseline results and mean of all ensemble 12 MW partial build-out results. Settled larvae averaged for each model grid element. Red shows an increase in settlement in the 12 MW scenario compared to the baseline, blue shows a decrease in settlement compared to the baseline.

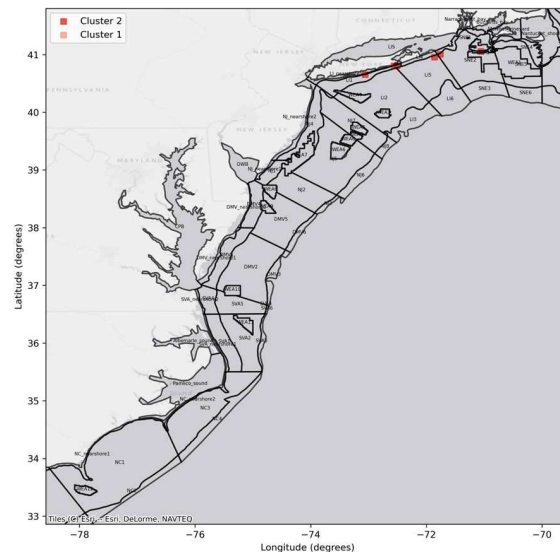


Figure C.51. DBSCAN (Density-Based Spatial Clustering of Applications with Noise) Difference in Settled Larvae 12MW Partial Build-Out vs Baseline 2017

Spatial clusters identified using DBSCAN to filter out noise from the difference plot and identify areas of greatest change. Clusters of settlement increase are identified in red and clusters with settlement decrease are shown in blue.

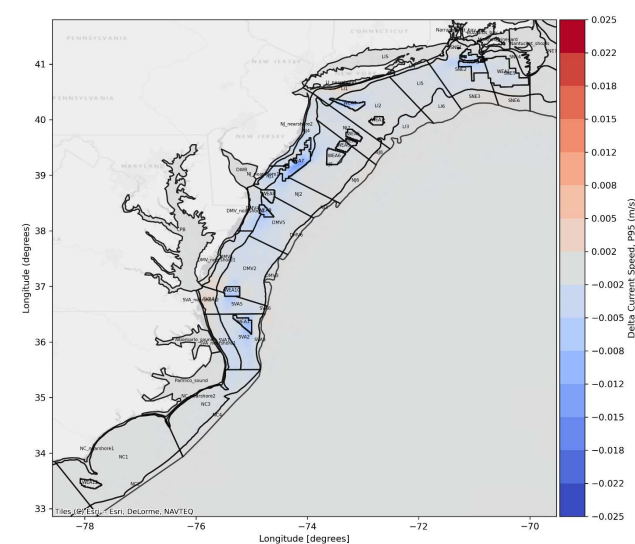


Figure C.52 Change in Current Speed 12MW Partial Build-Out vs Baseline 2017

Difference in the depth averaged current speed for model year 2017. Showing the difference in the 95th percentile non-exceedance probability baseline results and 95th percentile non-exceedance probability 12 MW partial build-out results

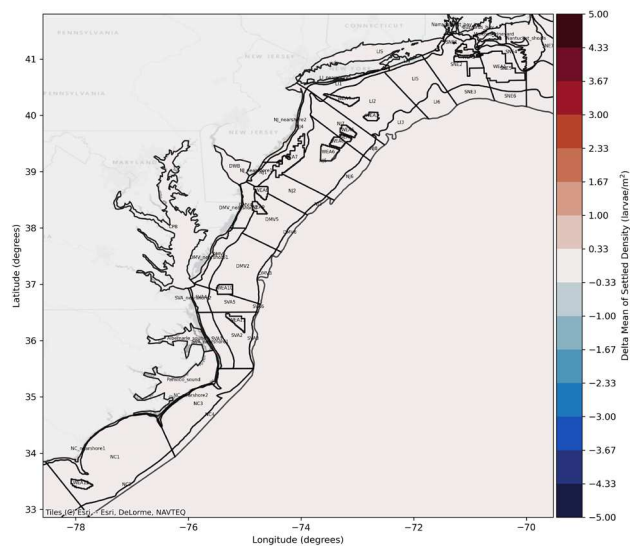


Figure C.53. Difference in Settled Density 12MW Partial Build-Out vs Baseline 2017

Difference in total surf clam larvae settled larvae for model year 2017. Showing the difference in the mean of all ensemble baseline results and mean of all ensemble 12 MW partial build-out results. Settled larvae averaged for each model grid element. Red shows an increase in settlement in the 12 MW scenario compared to the baseline, blue shows a decrease in settlement compared to the baseline.

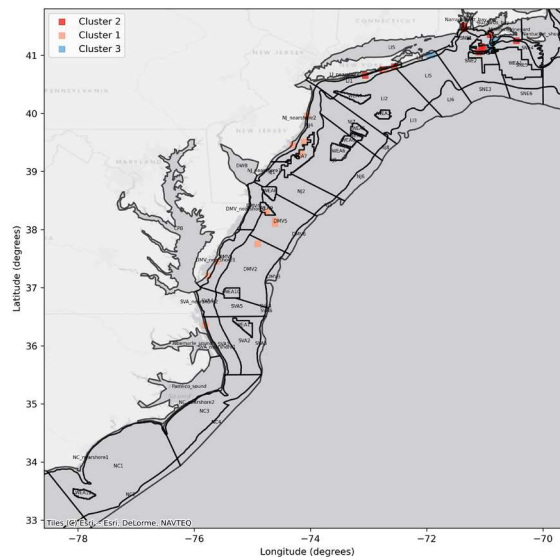


Figure C.54. DBSCAN (Density-Based Spatial Clustering of Applications with Noise) Difference in Settled Density 12MW Partial Build-Out vs Baseline 2017

Spatial clusters identified using DBSCAN to filter out noise from the difference plot and identify areas of greatest change. Clusters of settlement increase are identified in red and clusters with settlement decrease are shown in blue.

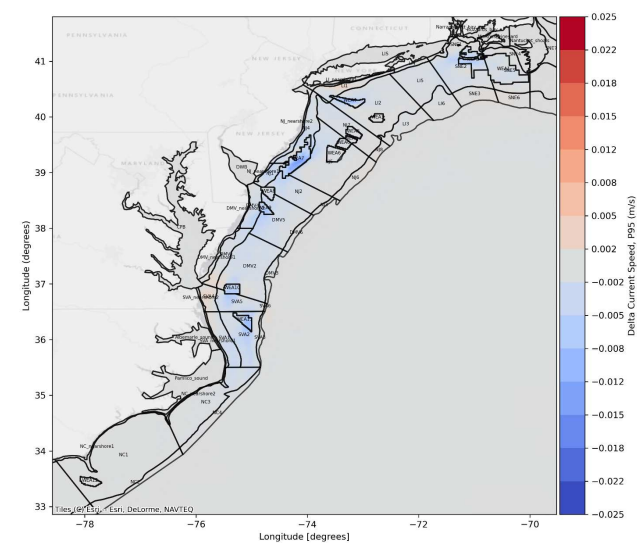


Figure C.55 Change in Current Speed 12MW Partial Build-Out vs Baseline 2017

Difference in the depth averaged current speed for model year 2017. Showing the difference in the 95th percentile non-exceedance probability baseline results and 95th percentile non-exceedance probability 12 MW partial build-out results

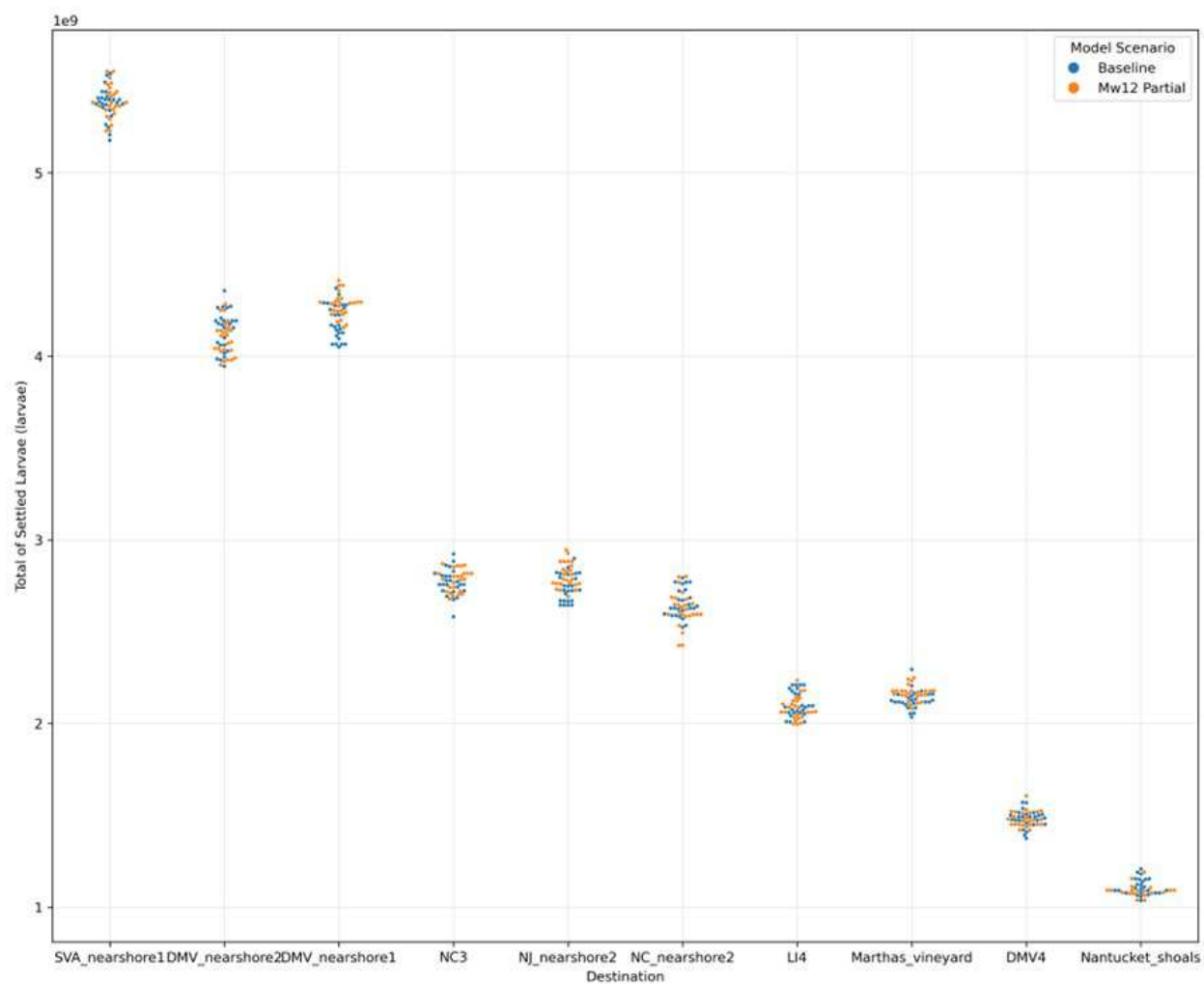


Figure C.57. Swarm Plot Showing Summer Flounder Settlement in Top 10 Destinations for 2017
 Swarm plot shows the settlement for each model run of the ensemble (i.e., each point represents a model result) for 2017. Blue points show the baseline results and orange show the 12 MW partial build-out number of settled larvae in the top 10 destinations where there is greatest larval settlement.

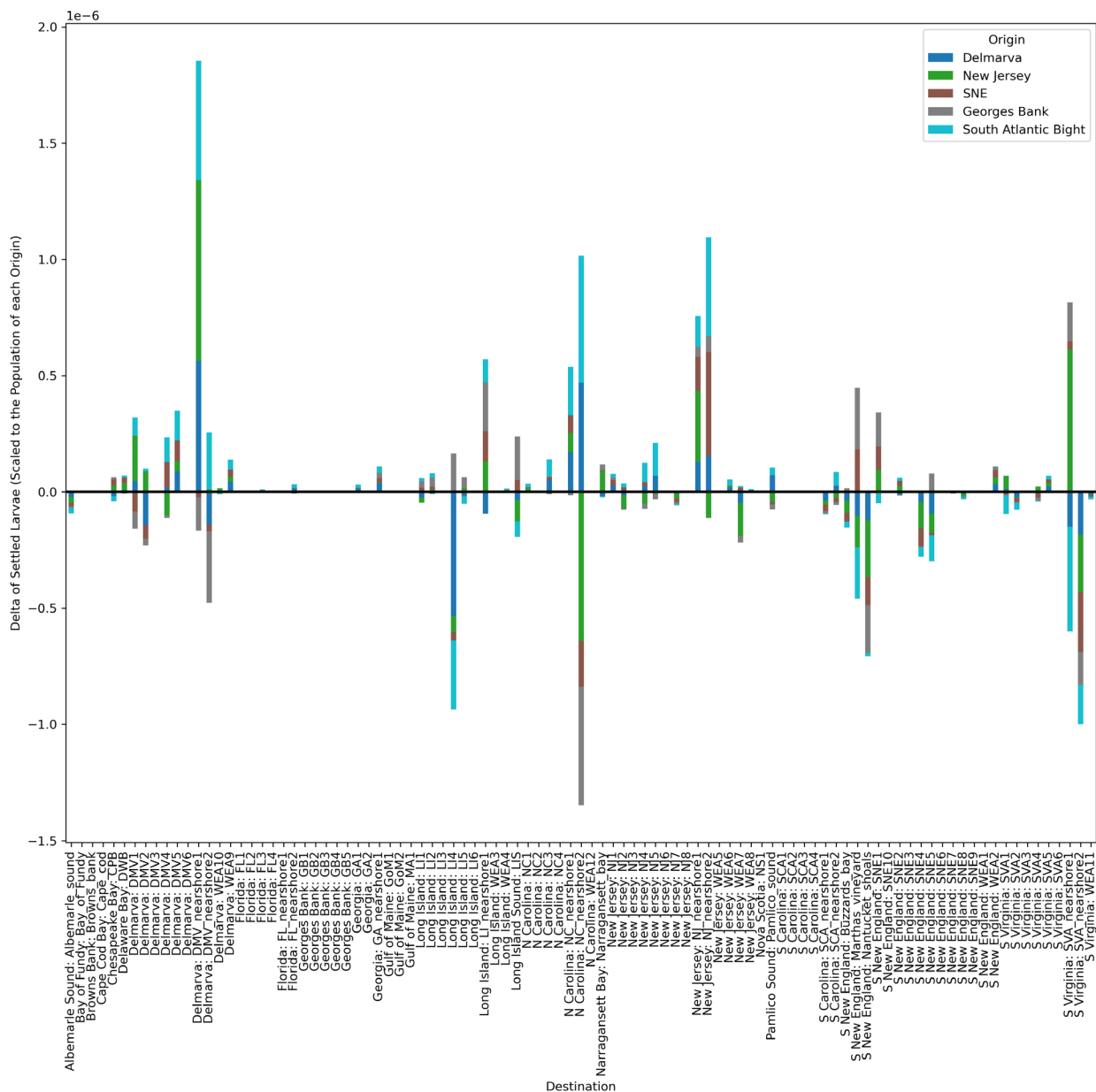


Figure C.58. Summer Flounder Connectivity Difference 2017

Bar chart shows the difference in summer flounder larvae settlement in each destination area, by origin for model year 2017. Bars are colored by origin area and results show the difference in export probabilities, i.e., the difference in the likelihood of settlement scaled to the number of larvae released from a particular origin region between the baseline and 12MW partial build-out results. Bars below the x axis, show a decrease in settlement in a particular destination area, results above the x axis show an increase in a settlement in a destination area.

C.3 15 MW Full Build-out

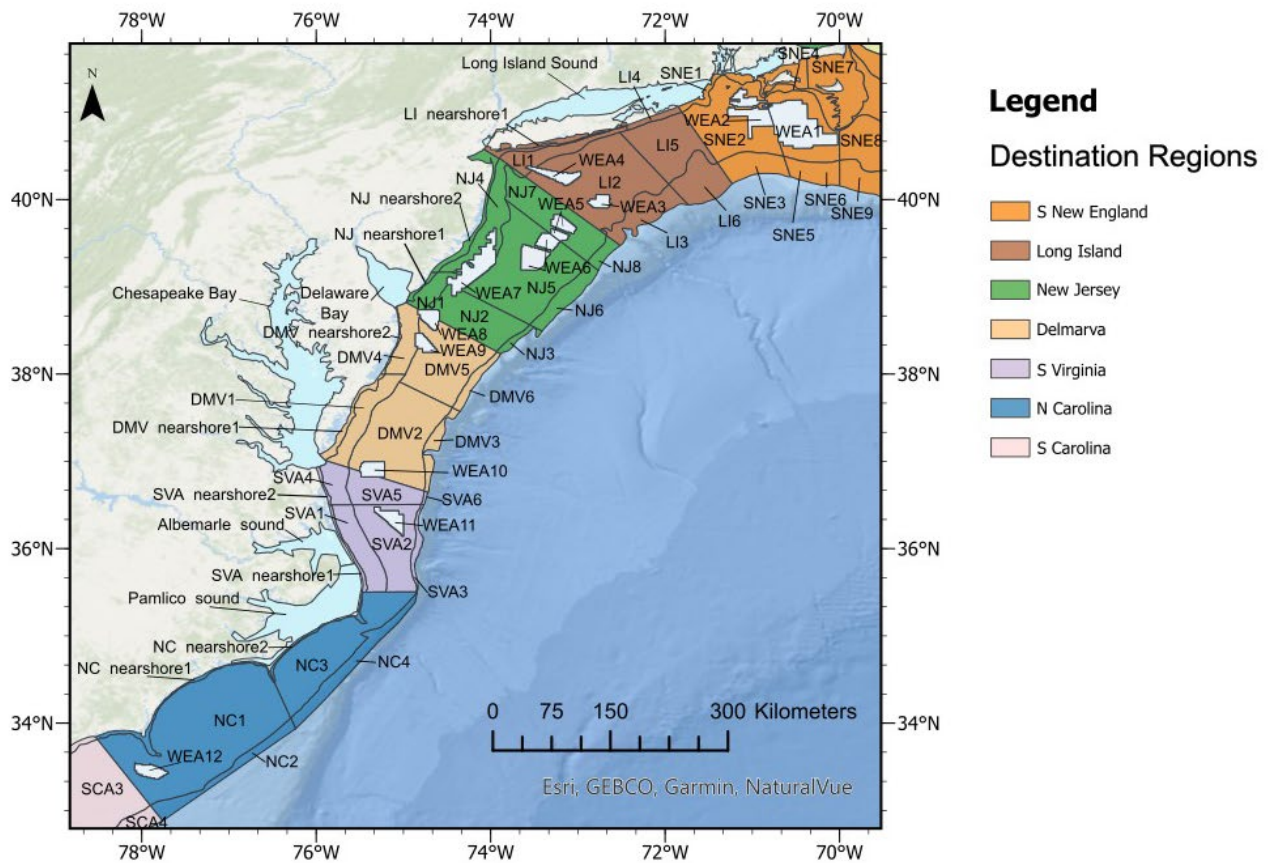


Figure C.59. Destination Reference Map Showing Each Destination Area and Names, Colors Represent Broad Regions

C.3.1 Sea Scallop 2017

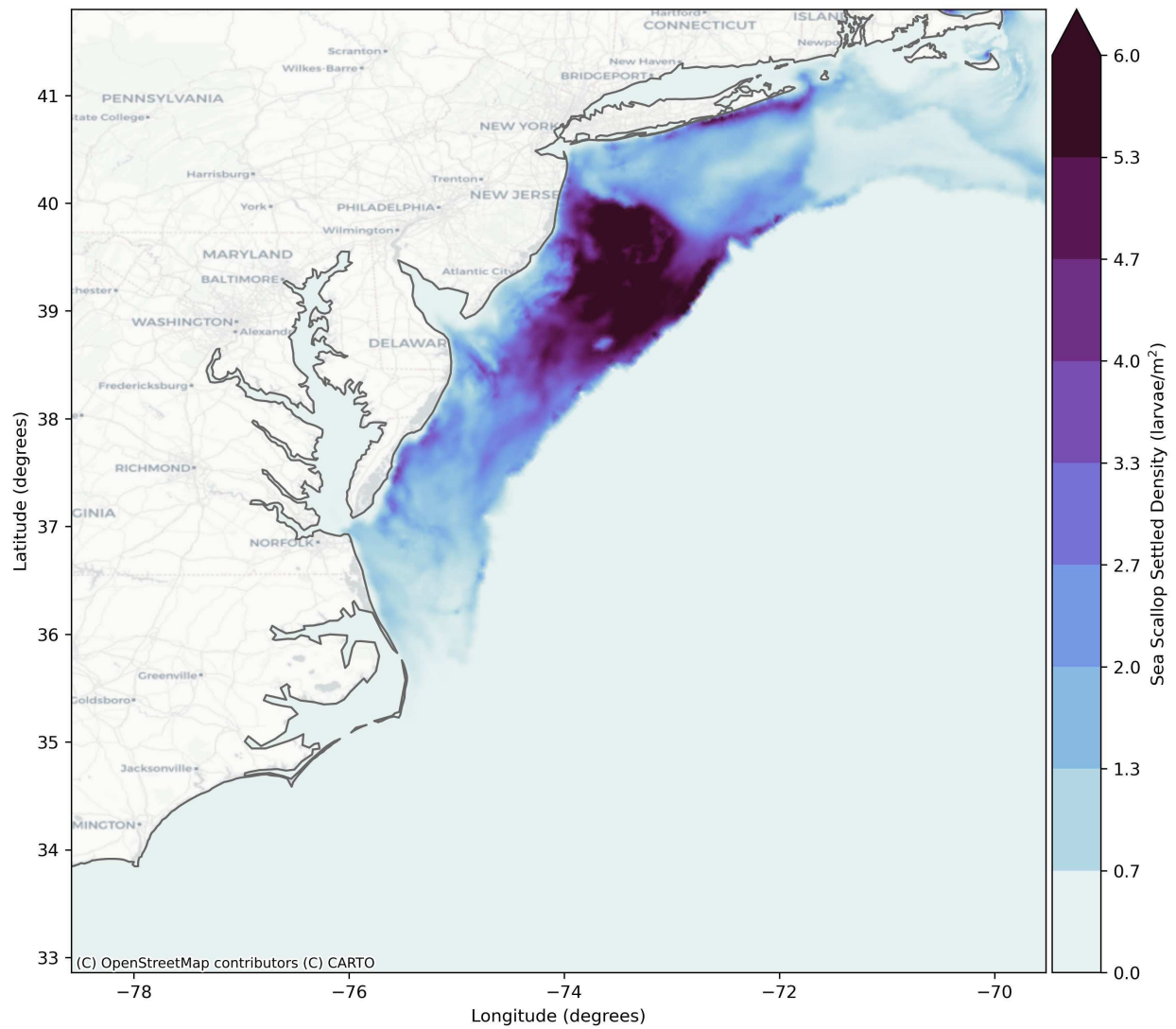


Figure C.60. Sea Scallop Baseline Settled Density for 15MW Full Build-Out

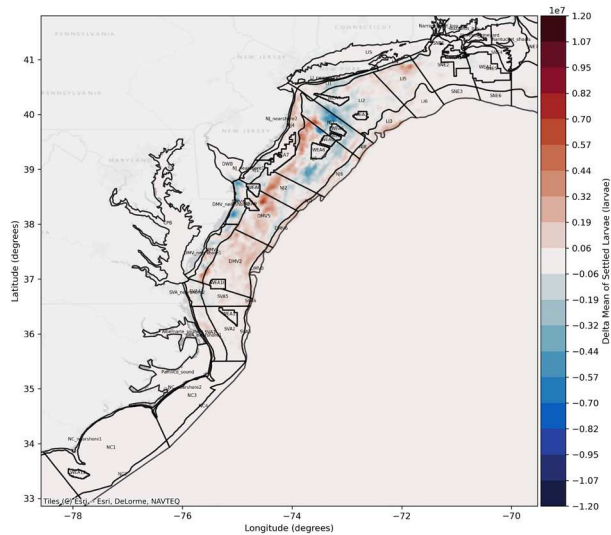


Figure C.61. Difference in Settled Larvae 15MW Full Build-Out vs Baseline 2017

Difference in total sea scallop larvae settled larvae for model year 2017. Showing the difference in the mean of all ensemble baseline results and mean of all ensemble 15 MW full build-out results. Settled larvae averaged for each model grid element. Red shows an increase in settlement in the 15 MW scenario compared to the baseline, blue shows a decrease in settlement compared to the baseline.

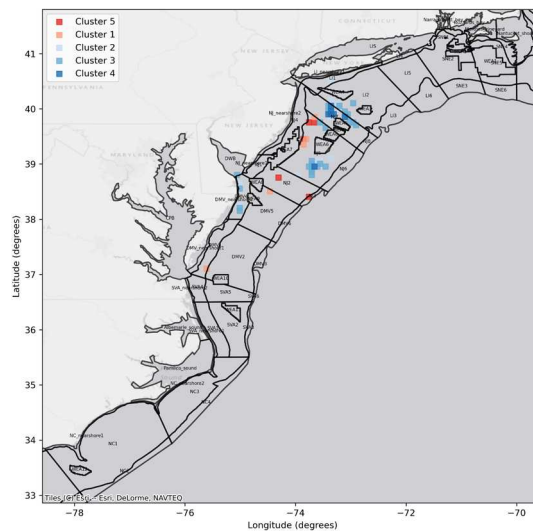


Figure C.62. DBSCAN (Density-Based Spatial Clustering of Applications with Noise) Difference in Settled Larvae 15MW Full Build-Out vs Baseline 2017

Spatial clusters identified using DBSCAN to filter out noise from the difference plot and identify areas of greatest change. Clusters of settlement increase are identified in red and clusters with settlement decrease are shown in blue.

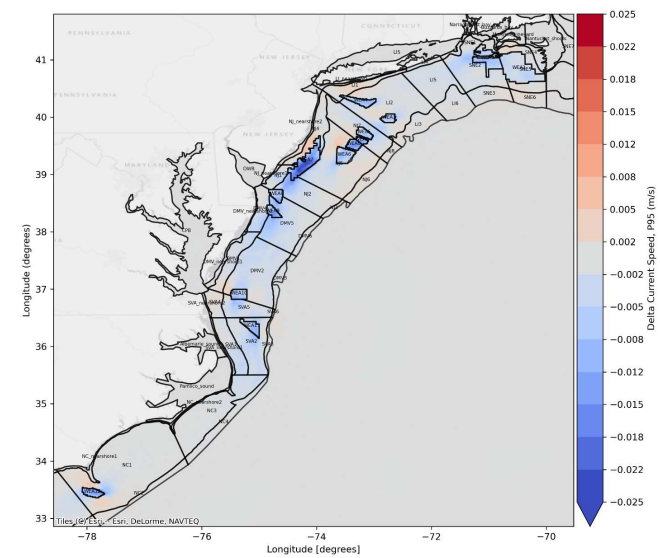


Figure C.63 Change in Current Speed 15MW Full Build-Out vs Baseline 2017

Difference in the depth averaged current speed for model year 2017. Showing the difference in the 95th percentile non-exceedance probability baseline results and 95th percentile non-exceedance probability 15 MW full build-out results

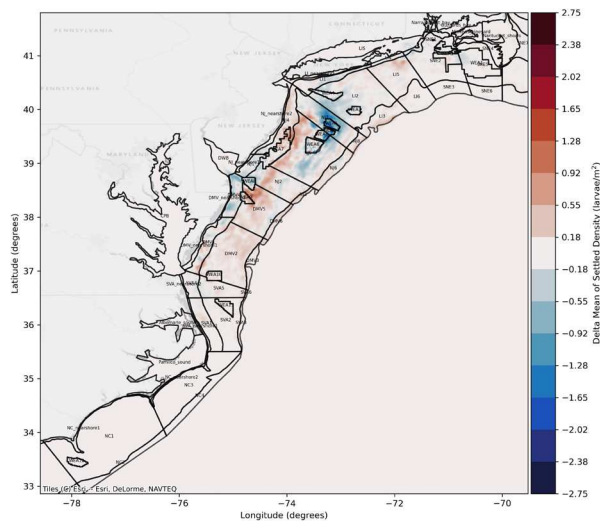


Figure C.64. Difference in Settled Density 15MW Full Build-Out vs Baseline 2017

Difference in total sea scallop larvae settled larvae for model year 2017. Showing the difference in the mean of all ensemble baseline results and mean of all ensemble 15 MW partial build-out results. Settled larvae averaged for each model grid element. Red shows an increase in settlement in the 15 MW scenario compared to the baseline, blue shows a decrease in settlement compared to the baseline.

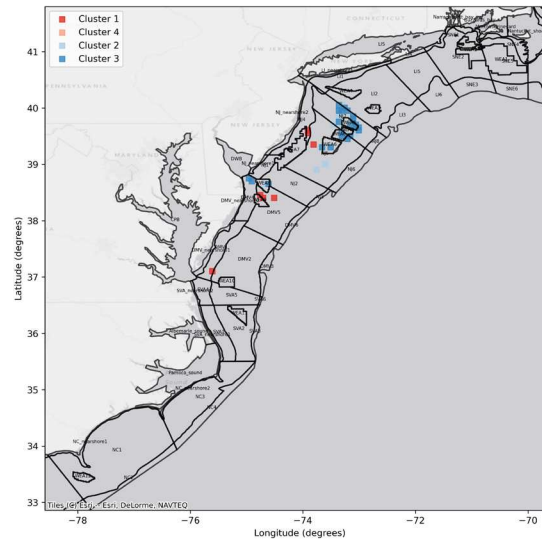


Figure C.65. DBSCAN (Density-Based Spatial Clustering of Applications with Noise) Difference in Settled Density 15MW Full Build-Out vs Baseline 2017

Spatial clusters identified using DBSCAN to filter out noise from the difference plot and identify areas of greatest change. Clusters of settlement increase are identified in red and clusters with settlement decrease are shown in blue.

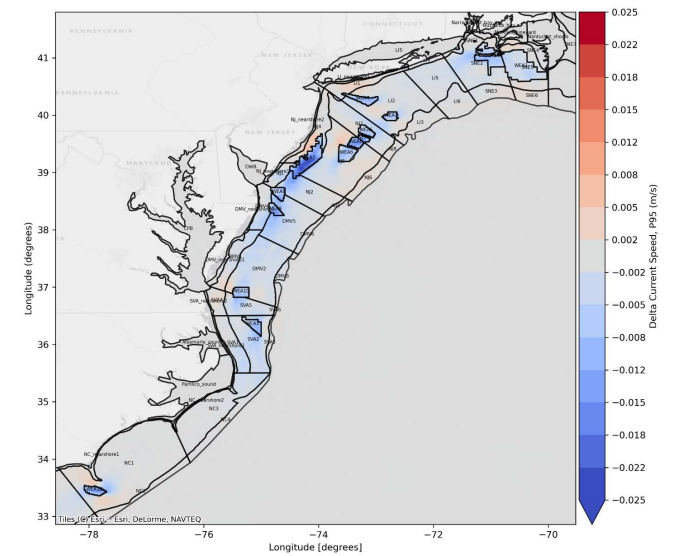


Figure C.66 Change in Current Speed 15MW Full Build-Out vs Baseline 2017

Difference in the depth averaged current speed for model year 2017. Showing the difference in the 95th percentile non-exceedance probability baseline results and 95th percentile non-exceedance probability 15 MW full build-out results

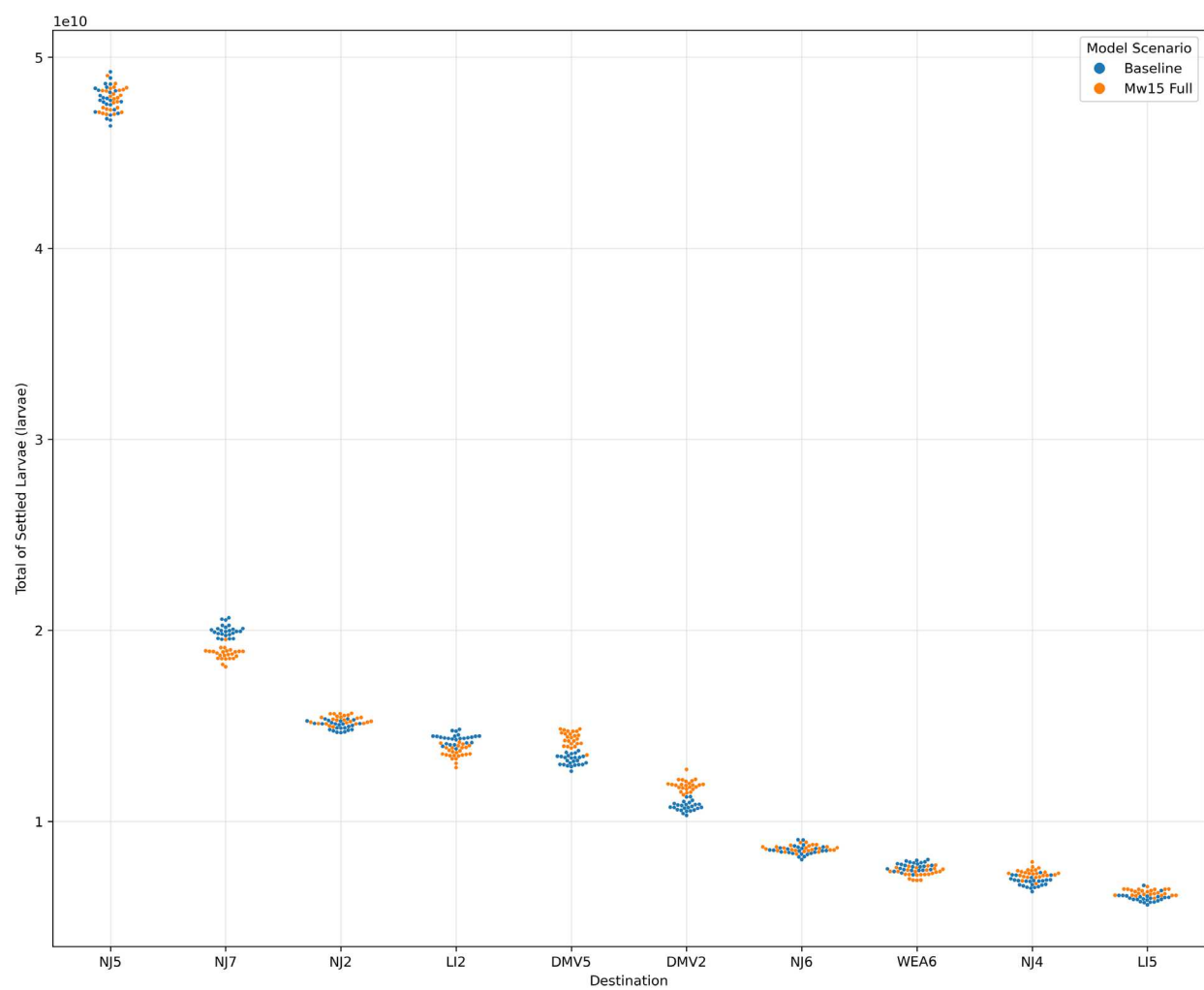


Figure C.68. Swarm Plot Showing Sea Scallop Settlement in Top 10 Destinations for 2017

Swarm plot shows the settlement for each model run of the ensemble (i.e., each point represents a model result) for 2017. Blue points show the baseline results and orange show the 15 MW full build-out number of settled larvae in the top 10 destinations where there is greatest larval settlement.

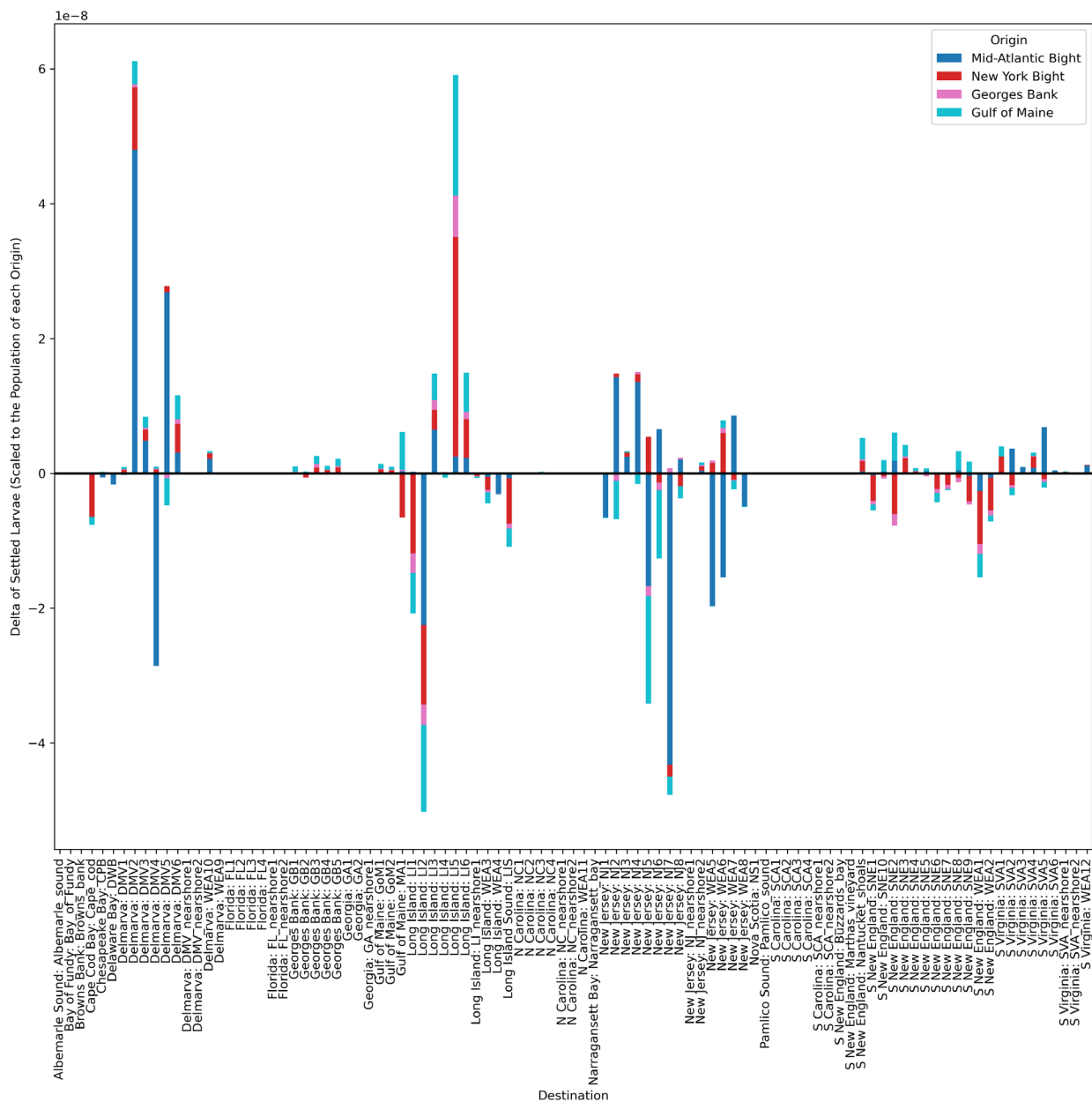


Figure C.69. Sea Scallop Connectivity Difference 2017

Bar chart shows the difference in sea scallop larvae settlement in each destination area, by origin for model year 2017. Bars are colored by origin area and results show the difference in export probabilities, i.e., the difference in the likelihood of settlement scaled to the number of larvae released from a particular origin region between the baseline and 15MW full build-out results. Bars below the x axis, show a decrease in settlement in a particular destination area, results above the x axis show an increase in a settlement in a destination area.

C.3.2 Sea Scallop 2018

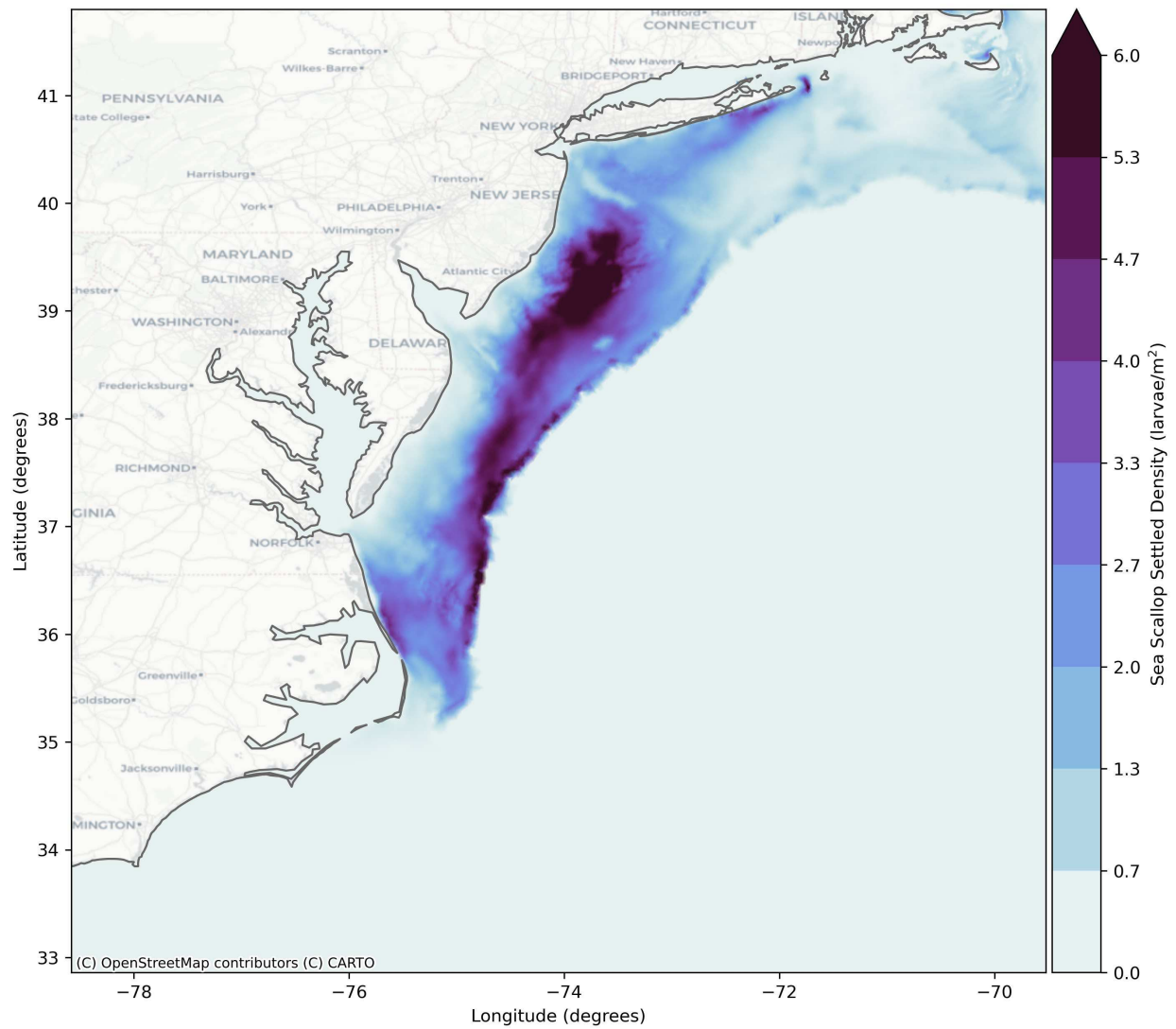


Figure C.70. Sea Scallop Baseline Settled Density for 15MW Full Build-Out

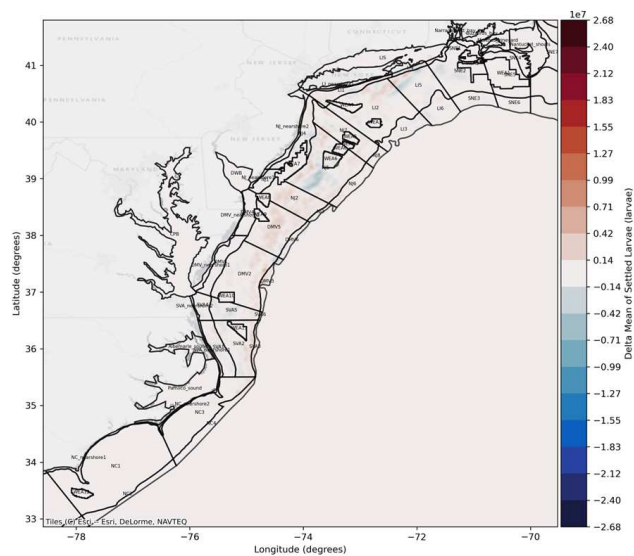


Figure C.71. Difference in Total Settled Larvae 15MW Full Build-Out vs Baseline 2018

Difference in total sea scallop larvae settled larvae for model year 2018. Showing the difference in the mean of all ensemble baseline results and mean of all ensemble 15 MW full build-out results. Settled larvae averaged for each model grid element. Red shows an increase in settlement in the 15 MW scenario compared to the baseline, blue shows a decrease in settlement compared to the baseline.

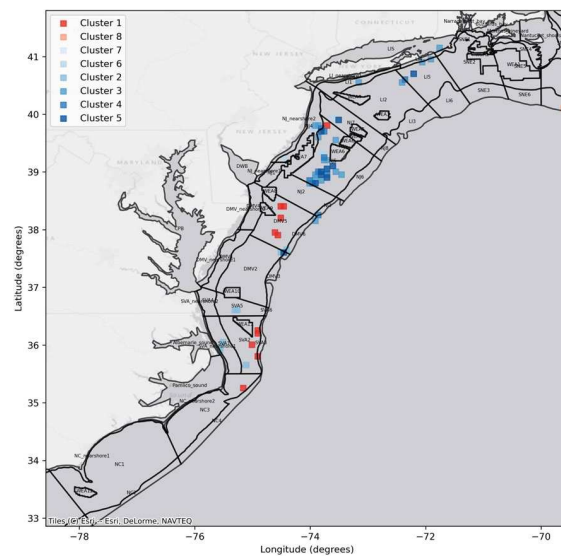


Figure C.72. DBSCAN (Density-Based Spatial Clustering of Applications with Noise) Difference in Total Settled Larvae 15MW Full Build-Out vs Baseline 2018

Spatial clusters identified using DBSCAN to filter out noise from the difference plot and identify areas of greatest change. Clusters of settlement increase are identified in red and clusters with settlement decrease are shown in blue.

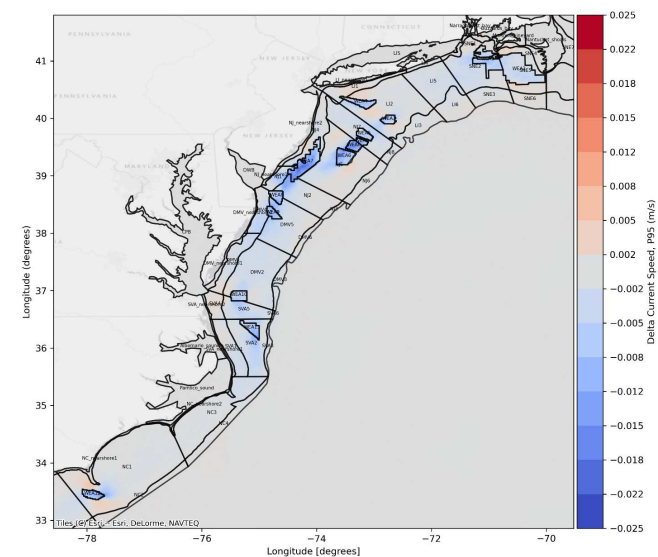


Figure C.73. Change in Current Speed 15MW Full Build-Out vs Baseline 2018

Difference in the depth averaged current speed for model year 2018. Showing the difference in the 95th percentile non-exceedance probability baseline results and 95th percentile non-exceedance probability 15 MW full build-out results

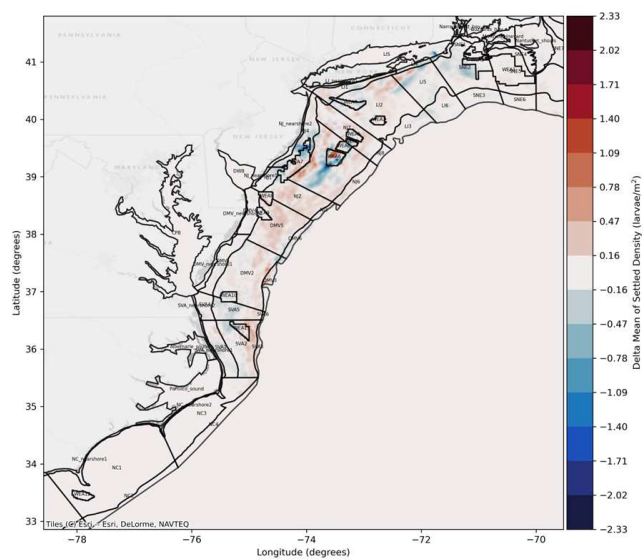


Figure C.74. Difference in Settled Larvae Density 15MW Full Build-Out vs Baseline 2018

Difference in sea scallop settled larvae density for model year 2018. Showing the difference in the mean of all ensemble baseline results and mean of all ensemble 15 MW full build-out results. Settled larvae averaged for each model grid element. Red shows an increase in settlement in the 15 MW scenario compared to the baseline, blue shows a decrease in settlement compared to the baseline.

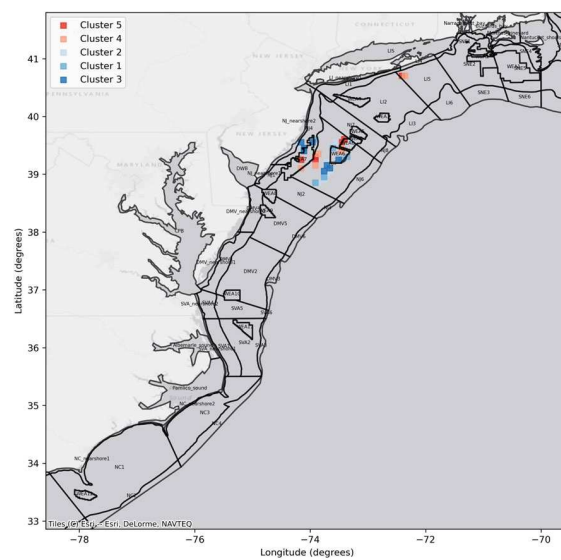


Figure C.75. DBSCAN (Density-Based Spatial Clustering of Applications with Noise) Difference in Settled Larvae Density 15MW Full Build-Out vs Baseline 2018

Spatial clusters identified using DBSCAN to filter out noise from the difference plot and identify areas of greatest change. Clusters of settlement increase are identified in red and clusters with settlement decrease are shown in blue.

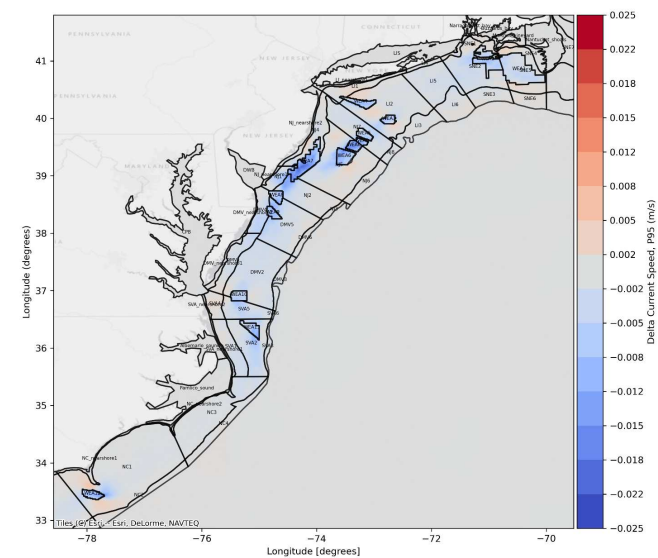


Figure C.76. Change in Current Speed 15MW Full Build-Out vs Baseline 2018

Difference in the depth averaged current speed for model year 2018. Showing the difference in the 95th percentile non-exceedance probability baseline results and 95th percentile non-exceedance probability 15 MW full build-out results

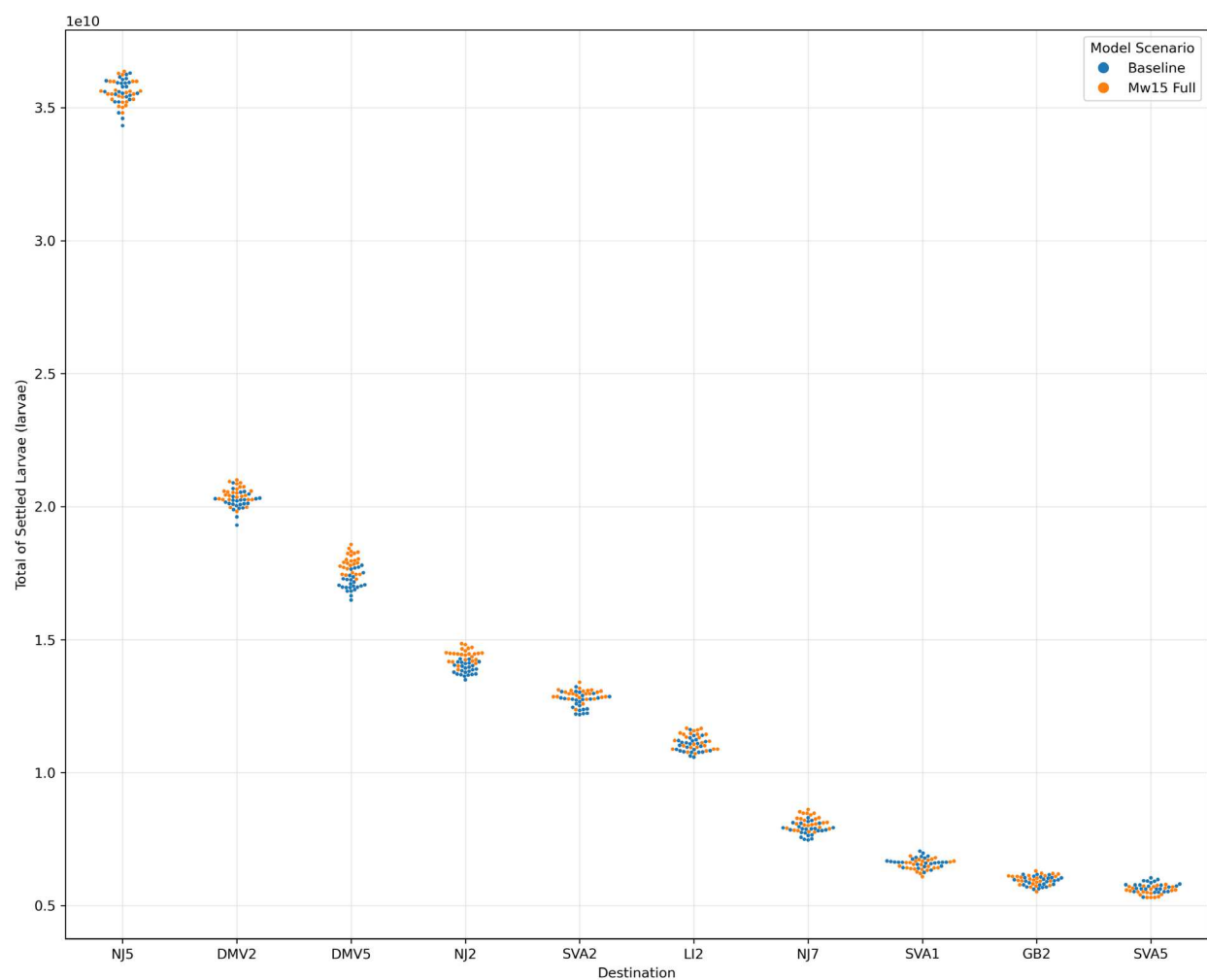


Figure C.78. Swarm Plot Showing Sea Scallop Settlement in Top 10 Destinations for 2018

Swarm plot shows the settlement for each model run of the ensemble (i.e., each point represents a model result) for 2018. Blue points show the baseline results and orange show the 15 MW full build-out number of settled larvae in the top 10 destinations where there is greatest larval settlement.

C.3.3 Sea Scallop 2020

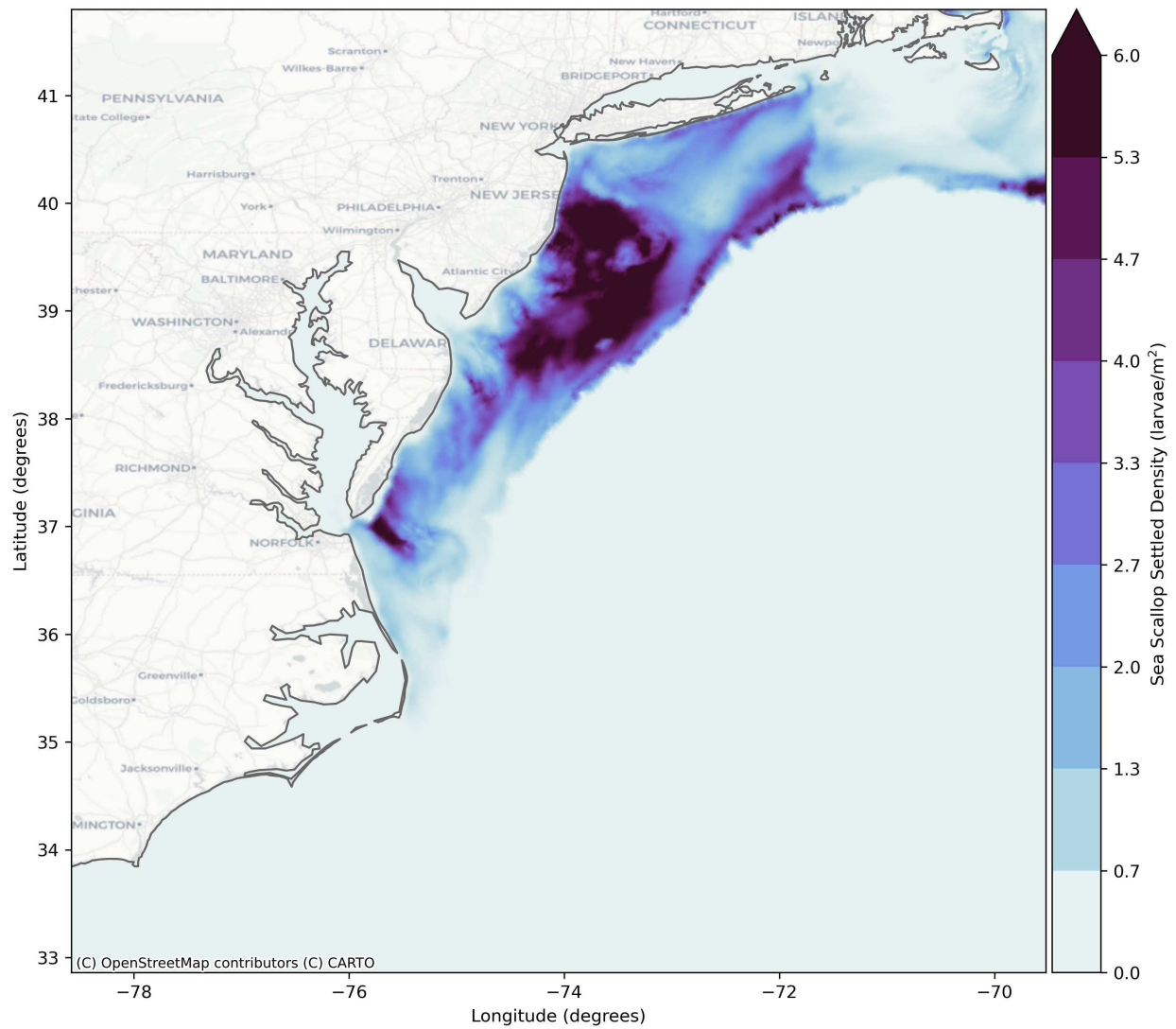


Figure C.80. Sea Scallop Baseline Settled Density for 15MW Full Build-Out

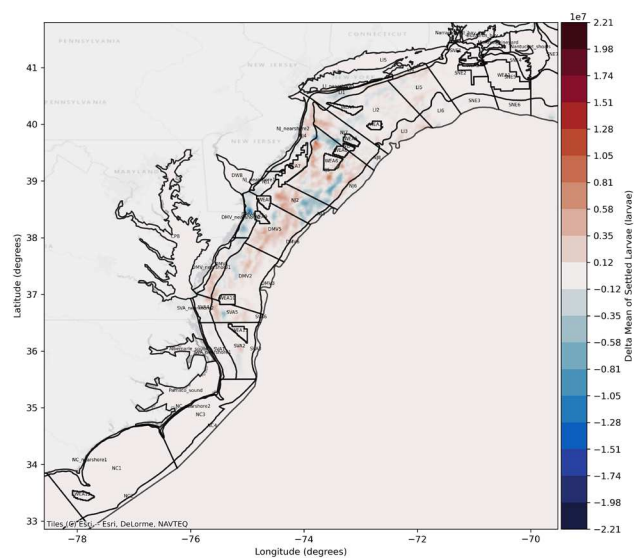


Figure C.81. Difference in Total Settled Larvae 15MW Full Build-Out vs Baseline 2020

Difference in total sea scallop settled larvae for model year 2020. Showing the difference in the mean of all ensemble baseline results and mean of all ensemble 15 MW full build-out results. Settled larvae averaged for each model grid element. Red shows an increase in settlement in the 15 MW scenario compared to the baseline, blue shows a decrease in settlement compared to the baseline.

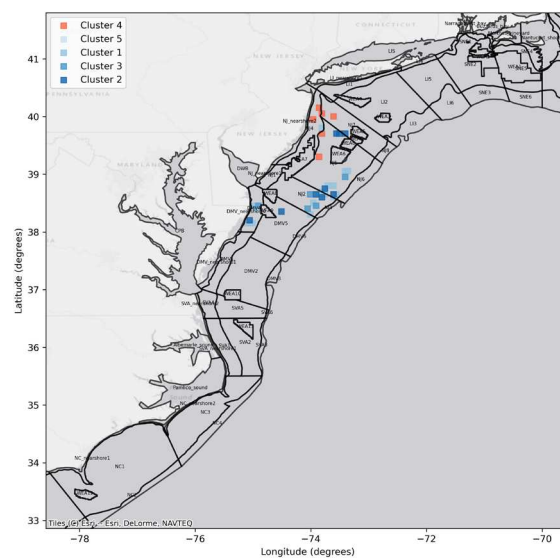


Figure C.82. DBSCAN (Density-Based Spatial Clustering of Applications with Noise) Difference in Total Settled Larvae 15MW Full Build-Out vs Baseline 2020

Spatial clusters identified using DBSCAN to filter out noise from the difference plot and identify areas of greatest change. Clusters of settlement increase are identified in red and clusters with settlement decrease are shown in blue.

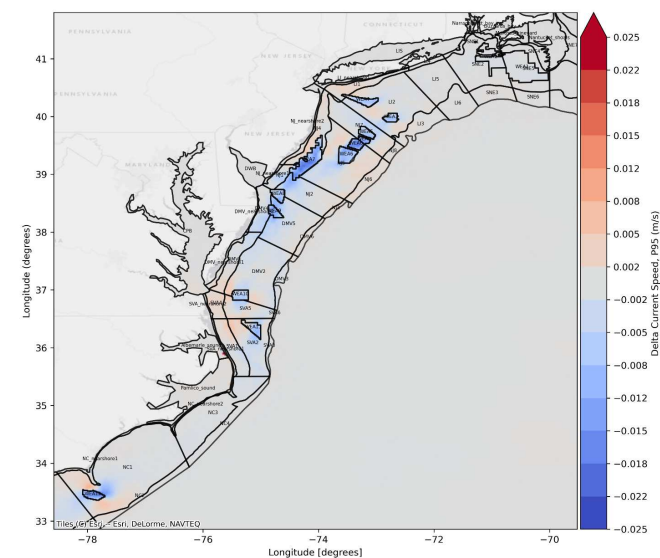


Figure C.83. Change in Current Speed 15MW Full Build-Out vs Baseline 2020

Difference in the depth averaged current speed for model year 2020. Showing the difference in the 95th percentile non-exceedance probability baseline results and 95th percentile non-exceedance probability 15 MW full build-out results

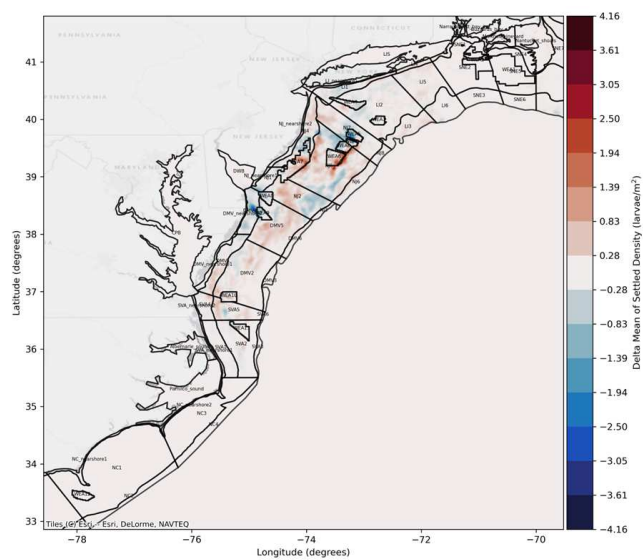


Figure C.84. Difference in Settled Larvae Density 15MW Full Build-Out vs Baseline 2020

Difference in sea scallop settled larvae density for model year 2020. Showing the difference in the mean of all ensemble baseline results and mean of all ensemble 15 MW full build-out results. Settled larvae averaged for each model grid element. Red shows an increase in settlement in the 15 MW scenario compared to the baseline, blue shows a decrease in settlement compared to the baseline.

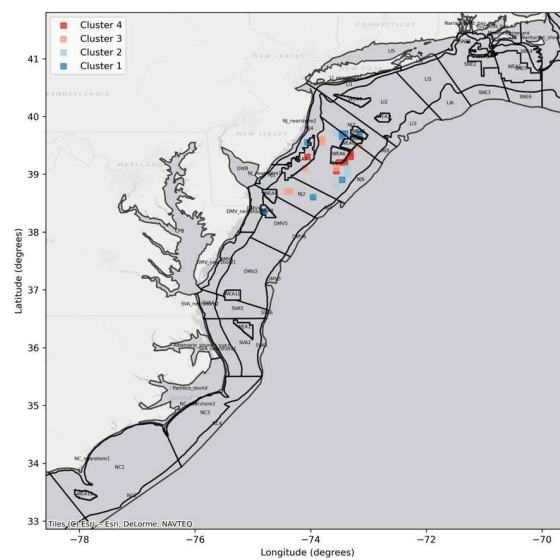


Figure C.85. DBSCAN (Density-Based Spatial Clustering of Applications with Noise) Difference in Settled Larvae Density 15MW Full Build-Out vs Baseline 2020

Spatial clusters identified using DBSCAN to filter out noise from the difference plot and identify areas of greatest change. Clusters of settlement increase are identified in red and clusters with settlement decrease are shown in blue.

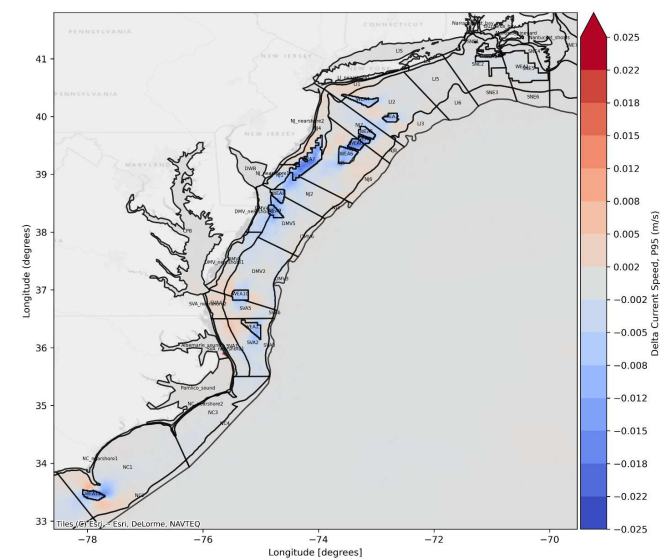


Figure C.86. Change in Current Speed 15MW Full Build-Out vs Baseline 2020

Difference in the depth averaged current speed for model year 2020. Showing the difference in the 95th percentile non-exceedance probability baseline results and 95th percentile non-exceedance probability 15 MW full build-out results.

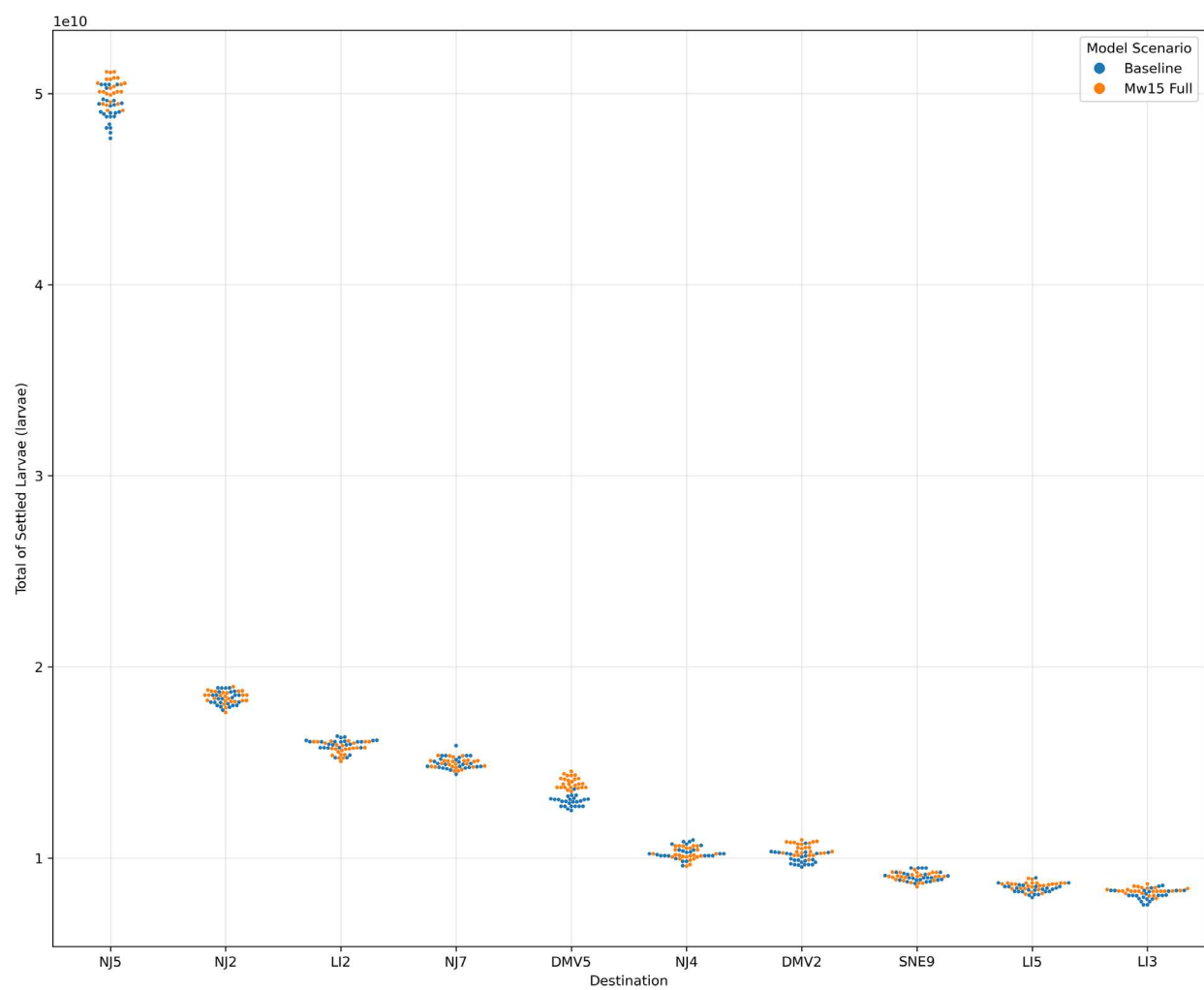


Figure C.88. Swarm Plot showing Sea Scallop Settlement in Top 10 Destinations for 2020

Swarm plot shows the settlement for each model run of the ensemble (i.e., each point represents a model result) for 2020. Blue points show the baseline results and orange show the 15 MW full build-out number of settled larvae in the top 10 destinations where there is greatest larval settlement.

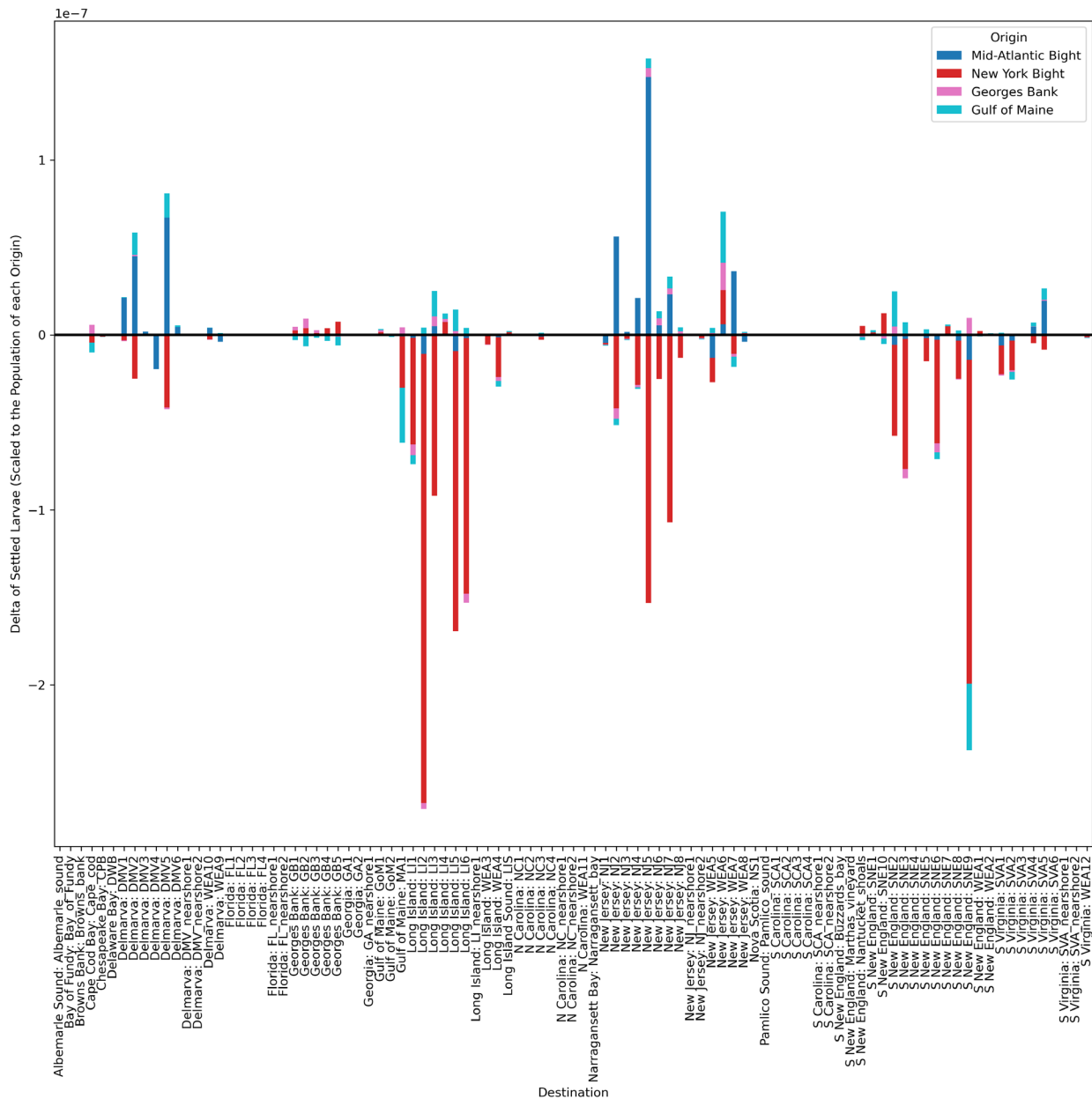


Figure C.89. Sea Scallop Connectivity Difference 2020
 Bar chart shows the difference in sea scallop larvae settlement in each destination area, by origin for model year 2020. Bars are colored by origin area and results show the difference in export probabilities, i.e., the difference in the likelihood of settlement scaled to the number of larvae released from a particular origin region between the baseline and 15MW full build-out results. Bars below the x axis, show a decrease in settlement in a particular destination area, results above the x axis show an increase in a settlement in a destination area.

C.3.4 Surf Clam 2017

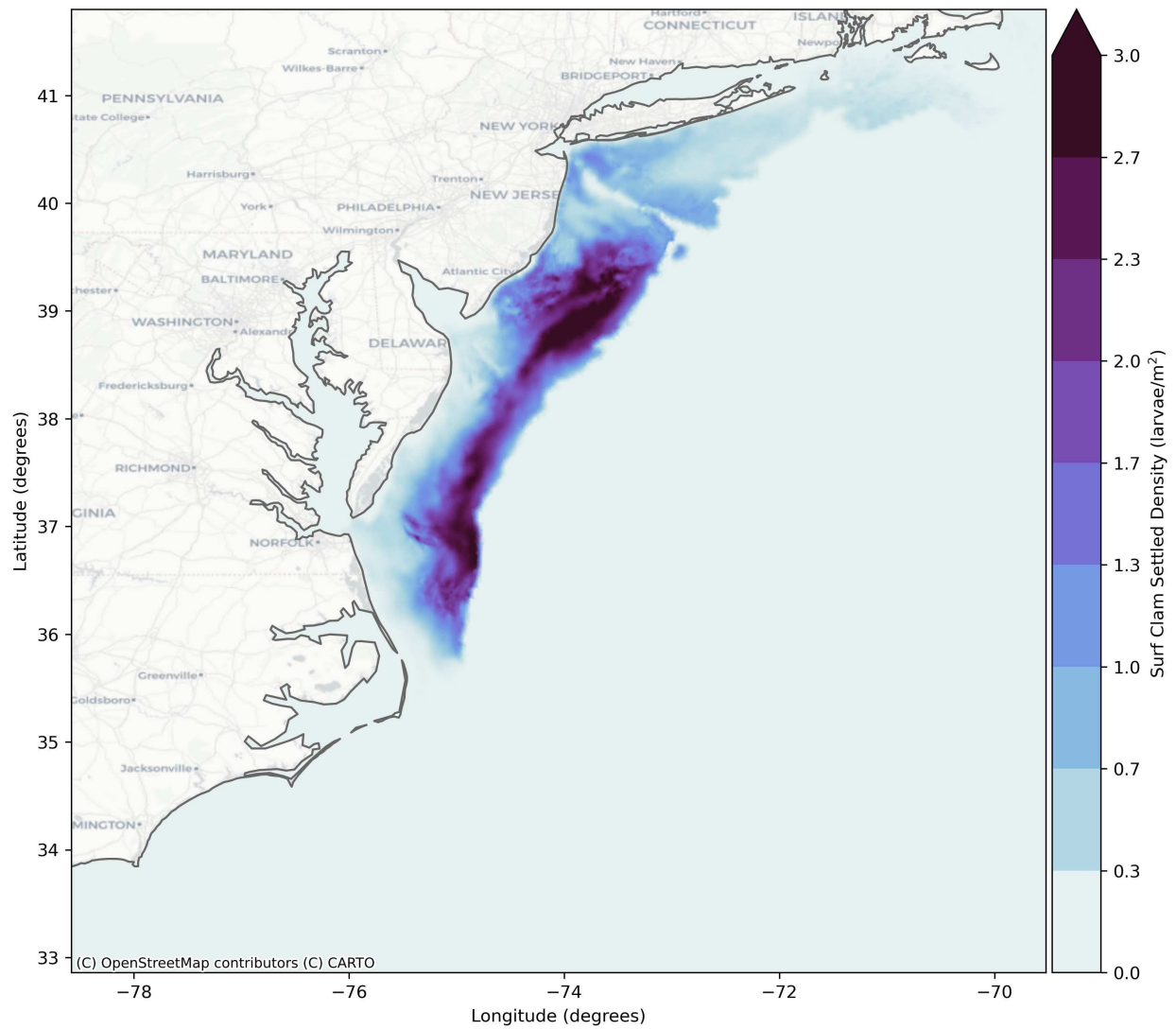


Figure C.90. Surf Clam Baseline Settled Density for 15MW Full Build-Out

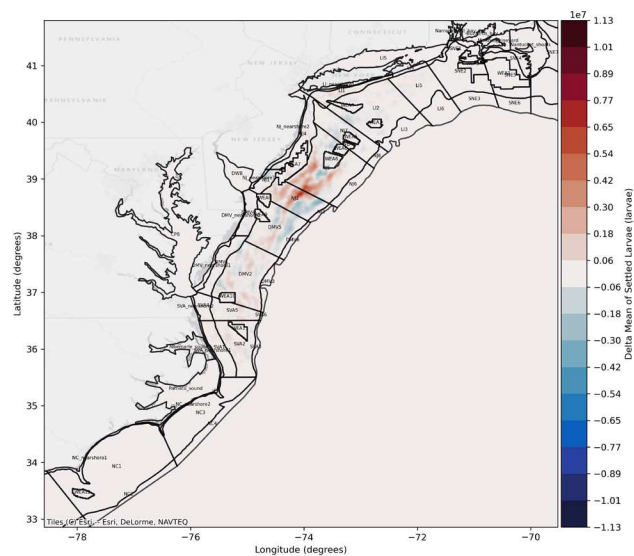


Figure C.91. Difference in Total Settled Larvae 15MW Full Build-Out vs Baseline 2017

Difference in total surf clam settled larvae for model year 2017. Showing the difference in the mean of all ensemble baseline results and mean of all ensemble 15 MW full build-out results. Settled larvae averaged for each model grid element. Red shows an increase in settlement in the 15 MW scenario compared to the baseline, blue shows a decrease in settlement compared to the baseline.

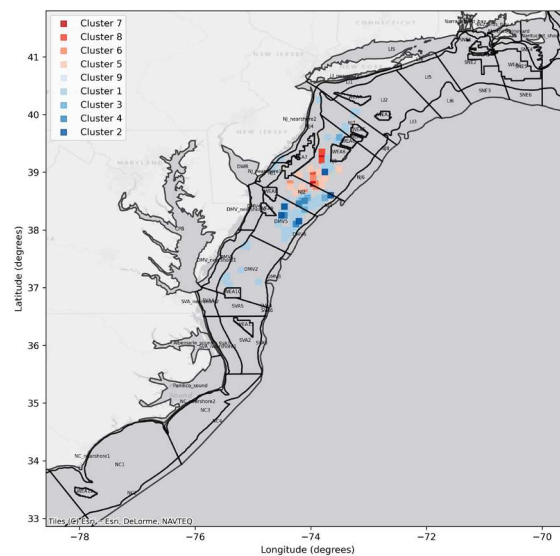


Figure C.92. DBSCAN (Density-Based Spatial Clustering of Applications with Noise) Difference in Total Settled Larvae 15MW Full Build-Out vs Baseline 2017

Spatial clusters identified using DBSCAN to filter out noise from the difference plot and identify areas of greatest change. Clusters of settlement increase are identified in red and clusters with settlement decrease are shown in blue.

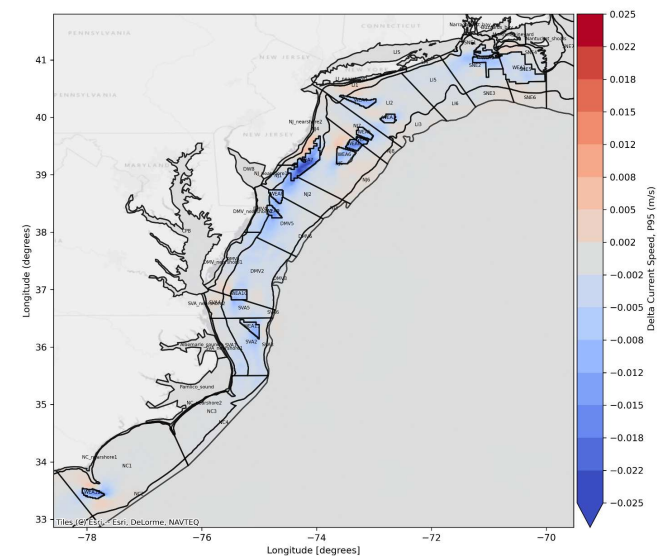


Figure C.93. Change in Current Speed 15MW Full Build-Out vs Baseline 2017

Difference in the depth averaged current speed for model year 2017. Showing the difference in the 95th percentile non-exceedance probability baseline results and 95th percentile non-exceedance probability 15 MW full build-out results

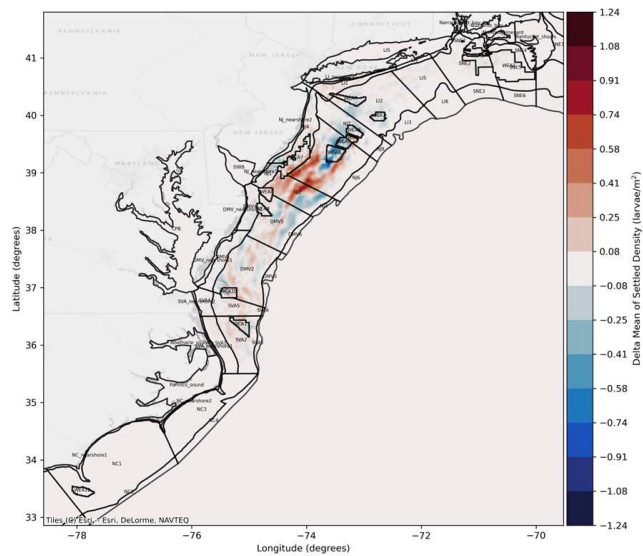


Figure C.94. Difference in Settled Larvae Density 15MW Full Build-Out vs Baseline 2017

Difference in surf clam settled larvae density for model year 2017. Showing the difference in the mean of all ensemble baseline results and mean of all ensemble 15 MW full build-out results. Settled larvae averaged for each model grid element. Red shows an increase in settlement in the 15 MW scenario compared to the baseline, blue shows a decrease in settlement compared to the baseline.

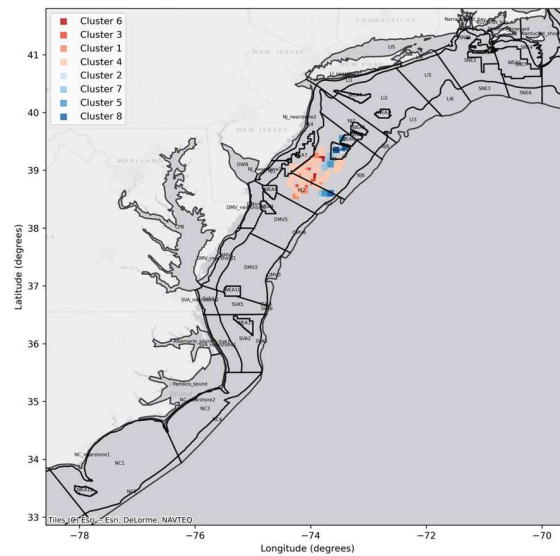


Figure C.95. DBSCAN (Density-Based Spatial Clustering of Applications with Noise) Difference in Settled Larvae Density 15MW Full Build-Out vs Baseline 2017

Spatial clusters identified using DBSCAN to filter out noise from the difference plot and identify areas of greatest change. Clusters of settlement increase are identified in red and clusters with settlement decrease are shown in blue.

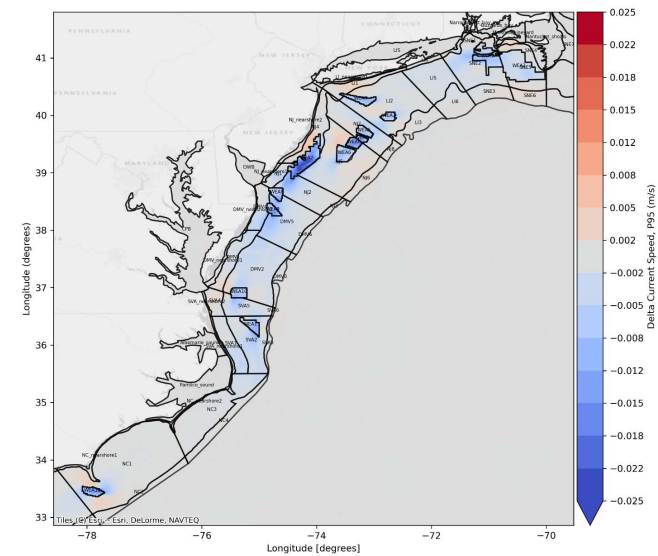


Figure C.96. Change in Current Speed 15MW Full Build-Out vs Baseline 2017

Difference in the depth averaged current speed for model year 2017. Showing the difference in the 95th percentile non-exceedance probability baseline results and 95th percentile non-exceedance probability 15 MW full build-out results

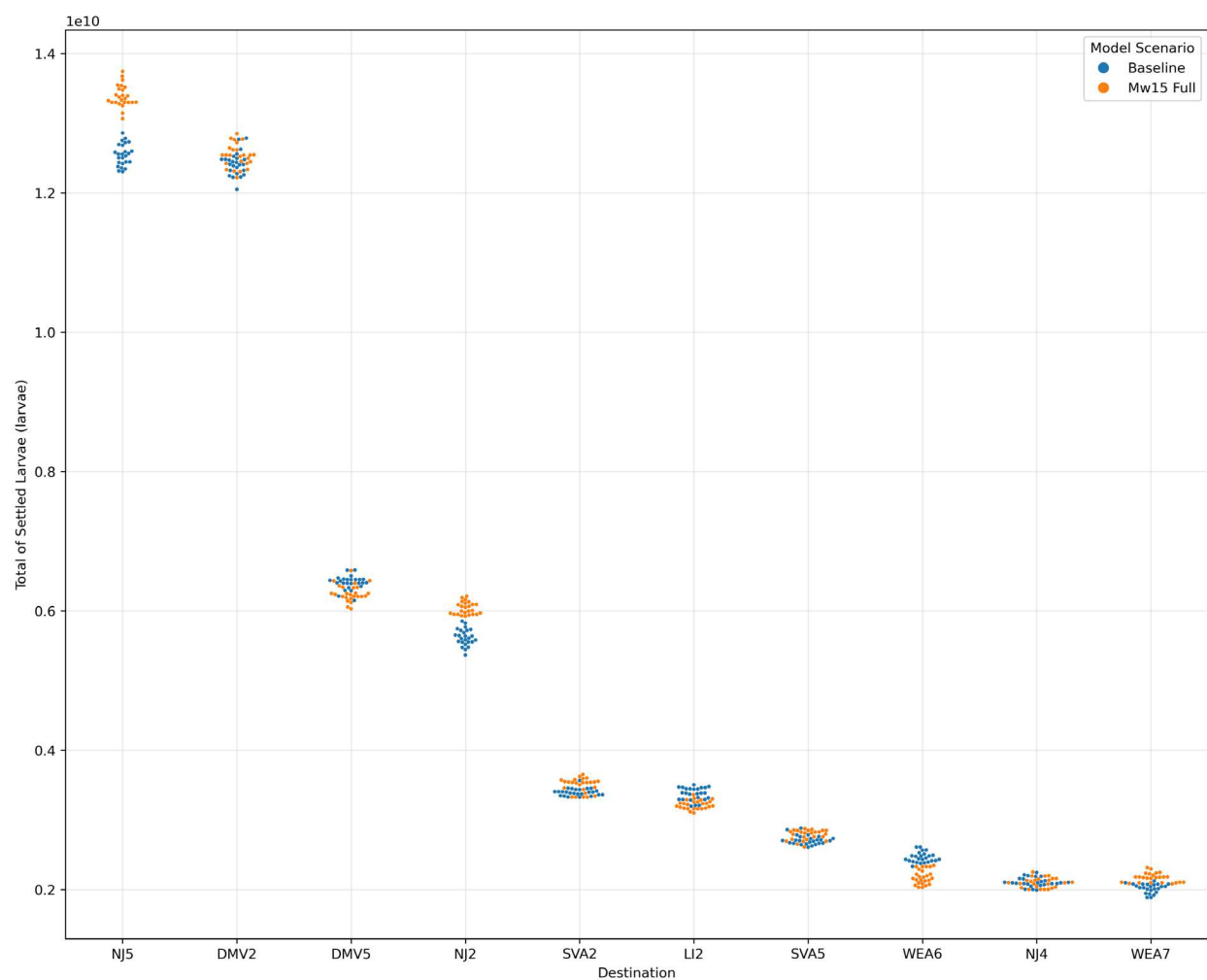


Figure C.98. Swarm Plot Showing Surf Clam Settlement in Top 10 Destinations for 2017

Swarm plot shows the settlement for each model run of the ensemble (i.e., each point represents a model result) for 2017. Blue points show the baseline results and orange show the 15 MW full build-out number of settled larvae in the top 10 destinations where there is greatest larval settlement.

Bar chart shows the average change in settlement in each destination area for model year 2017. Showing the difference in the mean of all ensemble baseline results and mean of all ensemble 15 MW full build-out results.

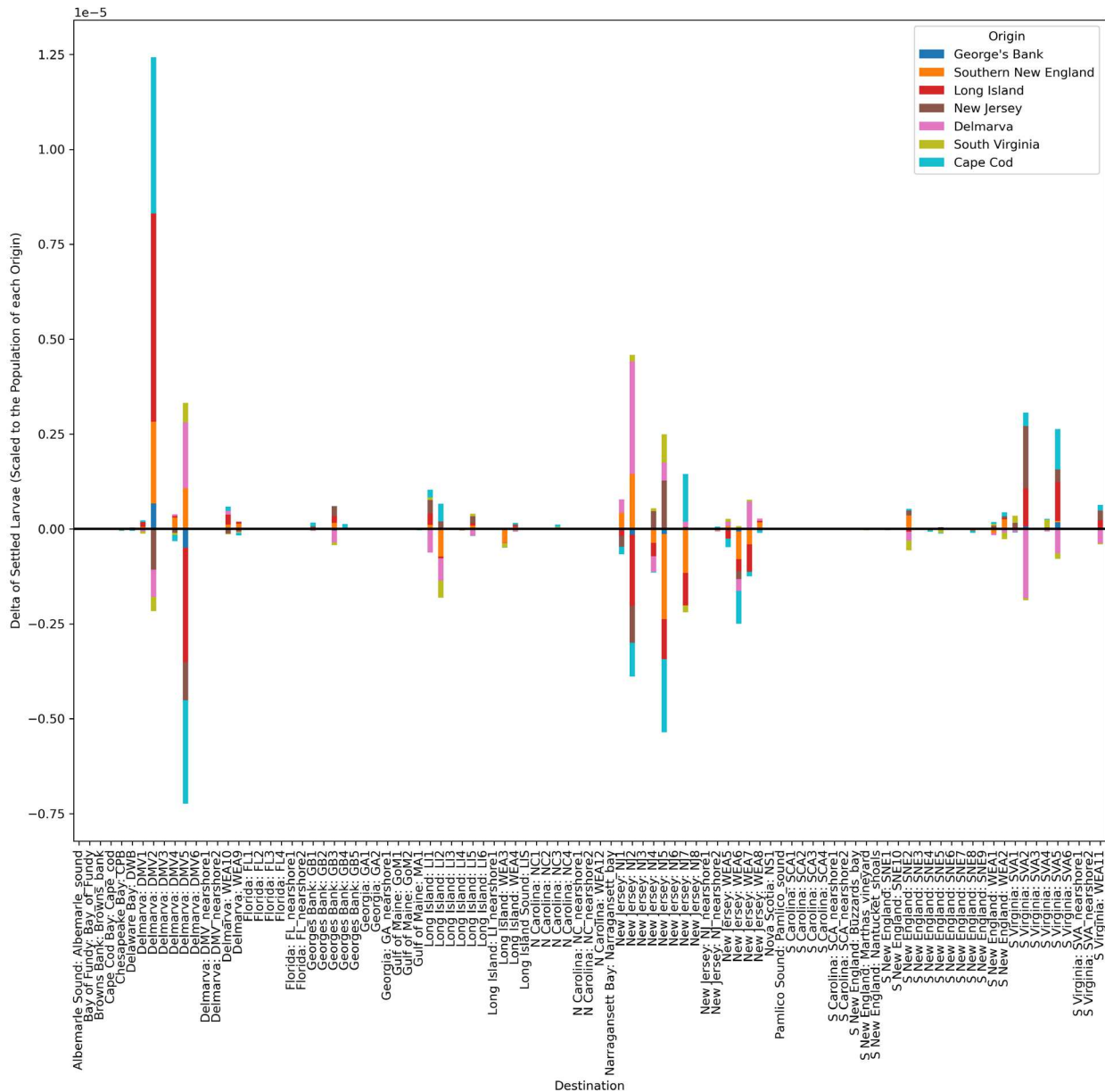


Figure C.99. Surf Clam Connectivity Difference 2017

Bar chart shows the difference in surf clam larvae settlement in each destination area, by origin for model year 2017. Bars are colored by origin area and results show the difference in export probabilities, i.e., the difference in the likelihood of settlement scaled to the number of larvae released from a particular origin region between the baseline and 15MW full build-out results. Bars below the x axis, show a decrease in settlement in a particular destination area, results above the x axis show an increase in a settlement in a destination area.

C.3.5 Summer Flounder 2017

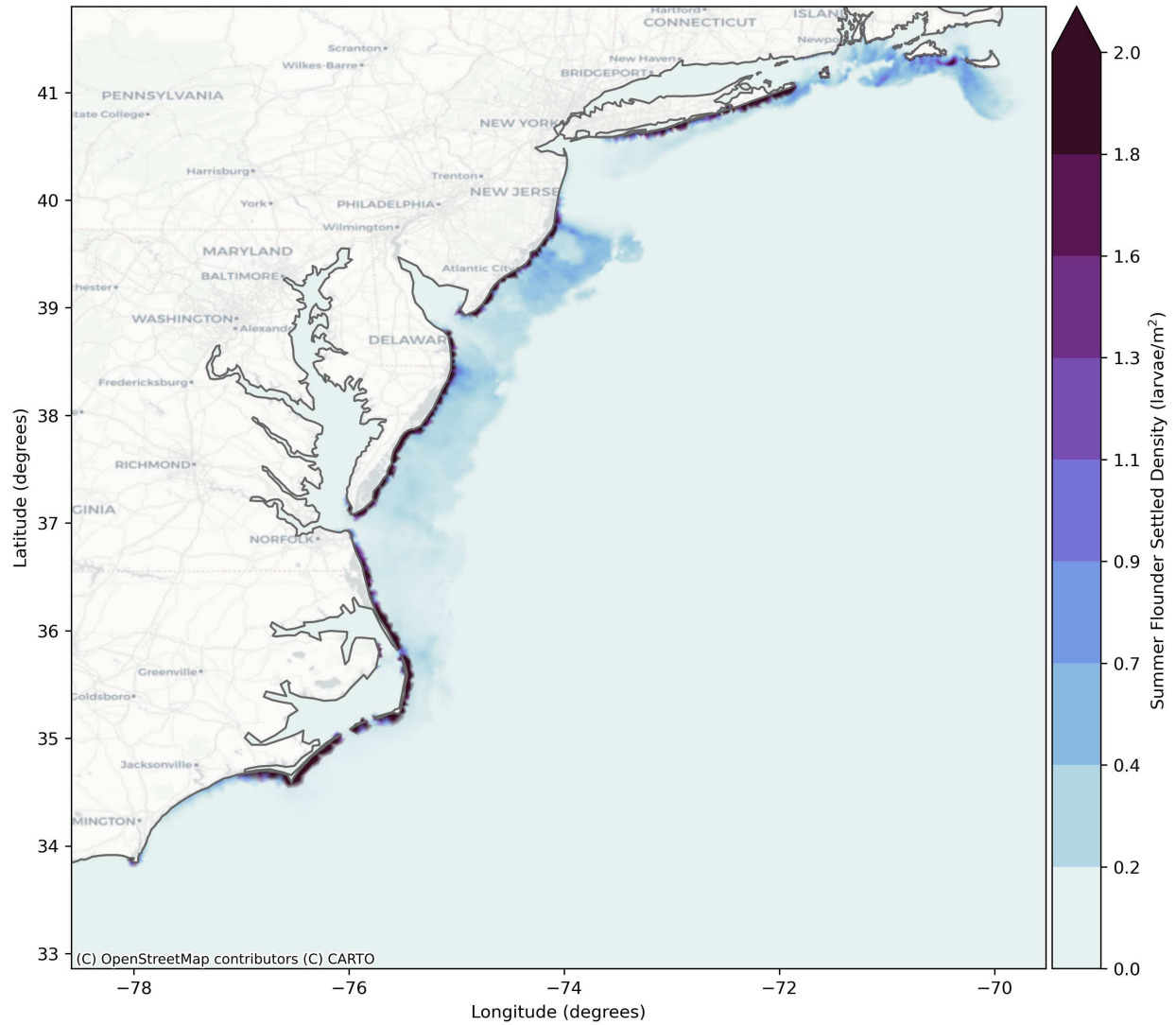


Figure C.100. Summer Flounder Baseline Settled Density for 15MW Full Build-Out

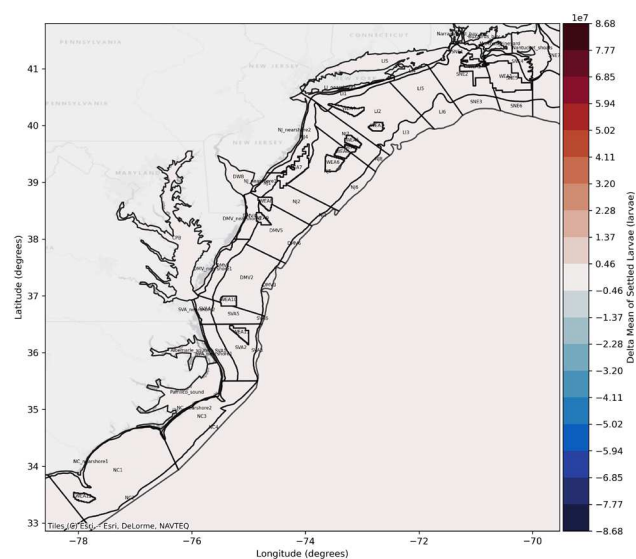


Figure C.101. Difference in Settled Larvae 15MW Full Build-Out vs Baseline 2017

Difference in total summer flounder larvae settled larvae for model year 2017. Showing the difference in the mean of all ensemble baseline results and mean of all ensemble 15 MW full build-out results. Settled larvae averaged for each model grid element. Red shows an increase in settlement in the 15 MW scenario compared to the baseline, blue shows a decrease in settlement compared to the baseline.

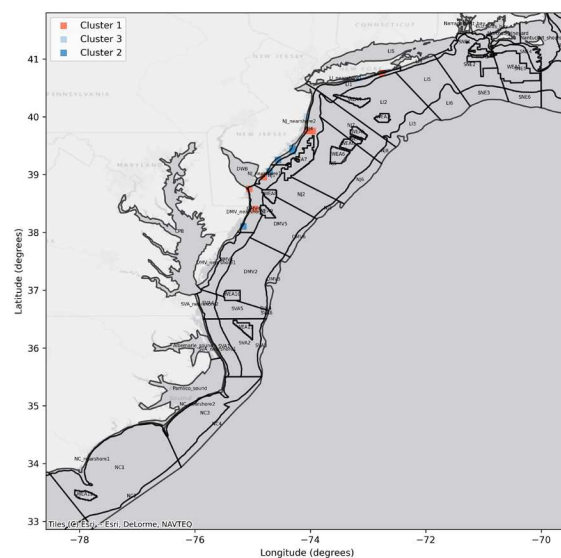


Figure C.102. DBSCAN (Density-Based Spatial Clustering of Applications with Noise) Difference in Settled Larvae 15MW Full Build-Out vs Baseline 2017

Spatial clusters identified using DBSCAN to filter out noise from the difference plot and identify areas of greatest change. Clusters of settlement increase are identified in red and clusters with settlement decrease are shown in blue.

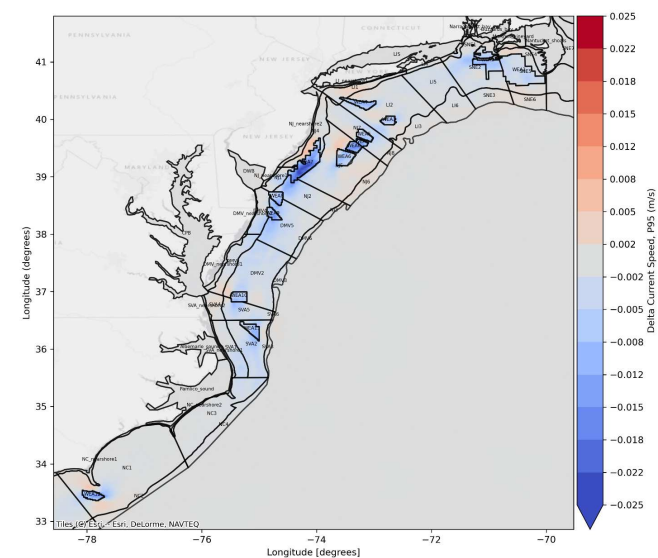


Figure C.103. Change in Current Speed 15MW Full Build-Out vs Baseline 2017

Difference in the depth averaged current speed for model year 2017. Showing the difference in the 95th percentile non-exceedance probability baseline results and 95th percentile non-exceedance probability 15 MW full build-out results

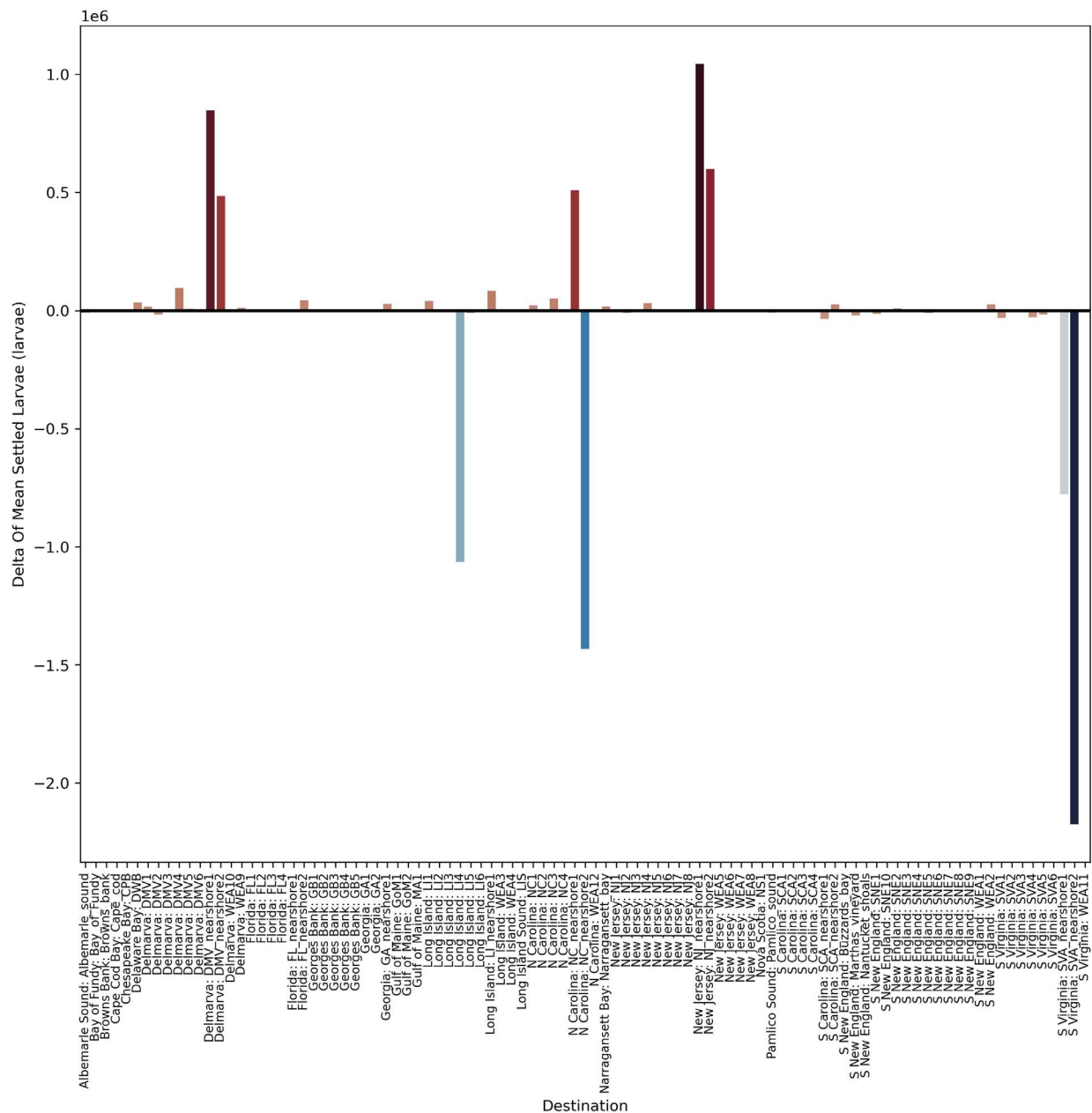


Figure C.104. Change in Average Summer Flounder Settlement in Each Destination Area 15MW Full Build-Out vs Baseline 2017

Bar chart shows the change in average settlement in each destination area for model year 2017. Showing the difference in the mean of all ensemble baseline results and mean of all ensemble 15 MW full build-out results.

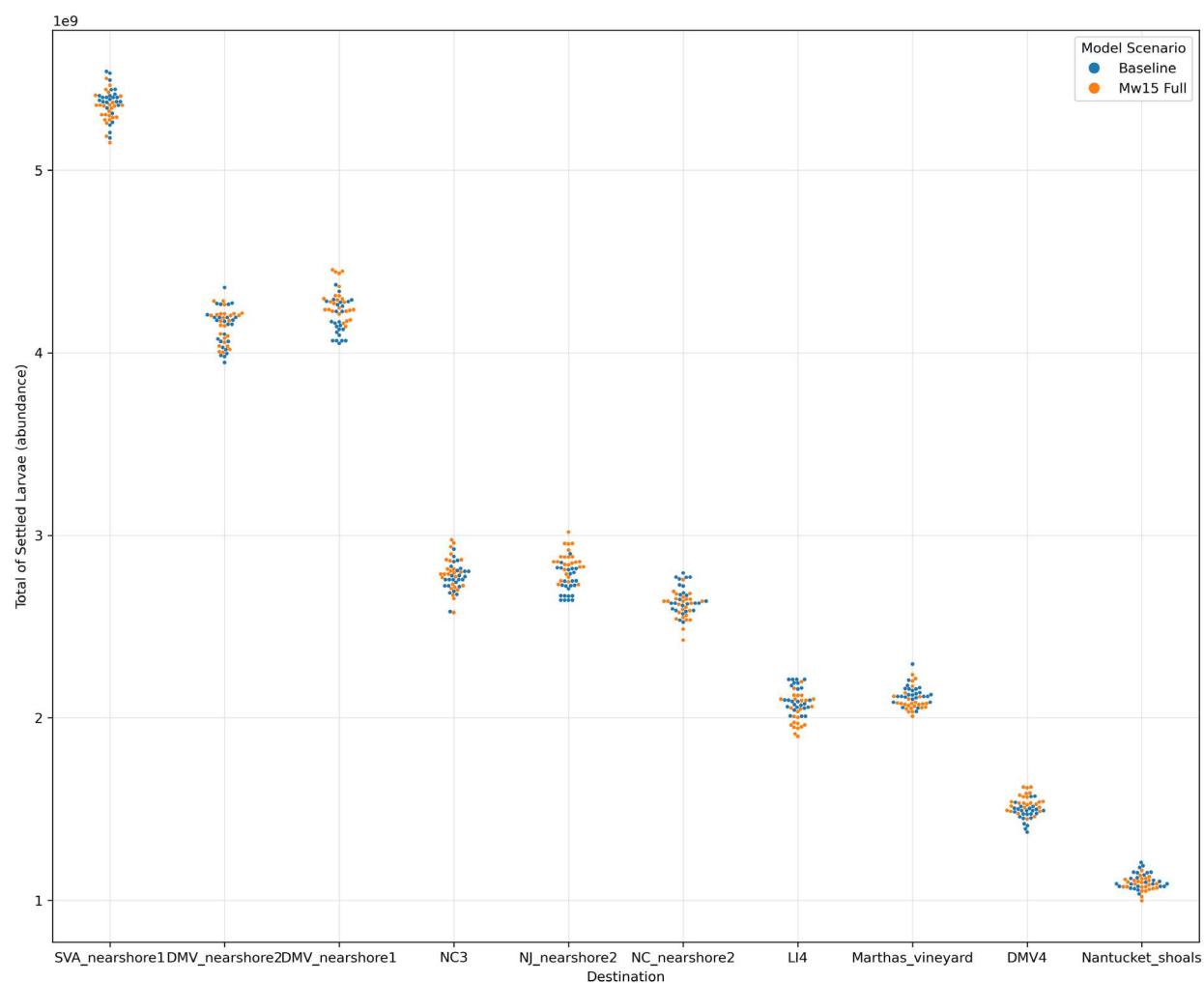


Figure C.105. Swarm Plot Showing Summer Flounder Settlement in most common Destinations for 2017

Swarm plot shows the settlement for each model run of the ensemble (i.e., each point represents a model result) for 2017. Blue points show the baseline results and orange show the 15 MW full build-out number of settled larvae in the most common destinations, where there is greatest larval settlement.

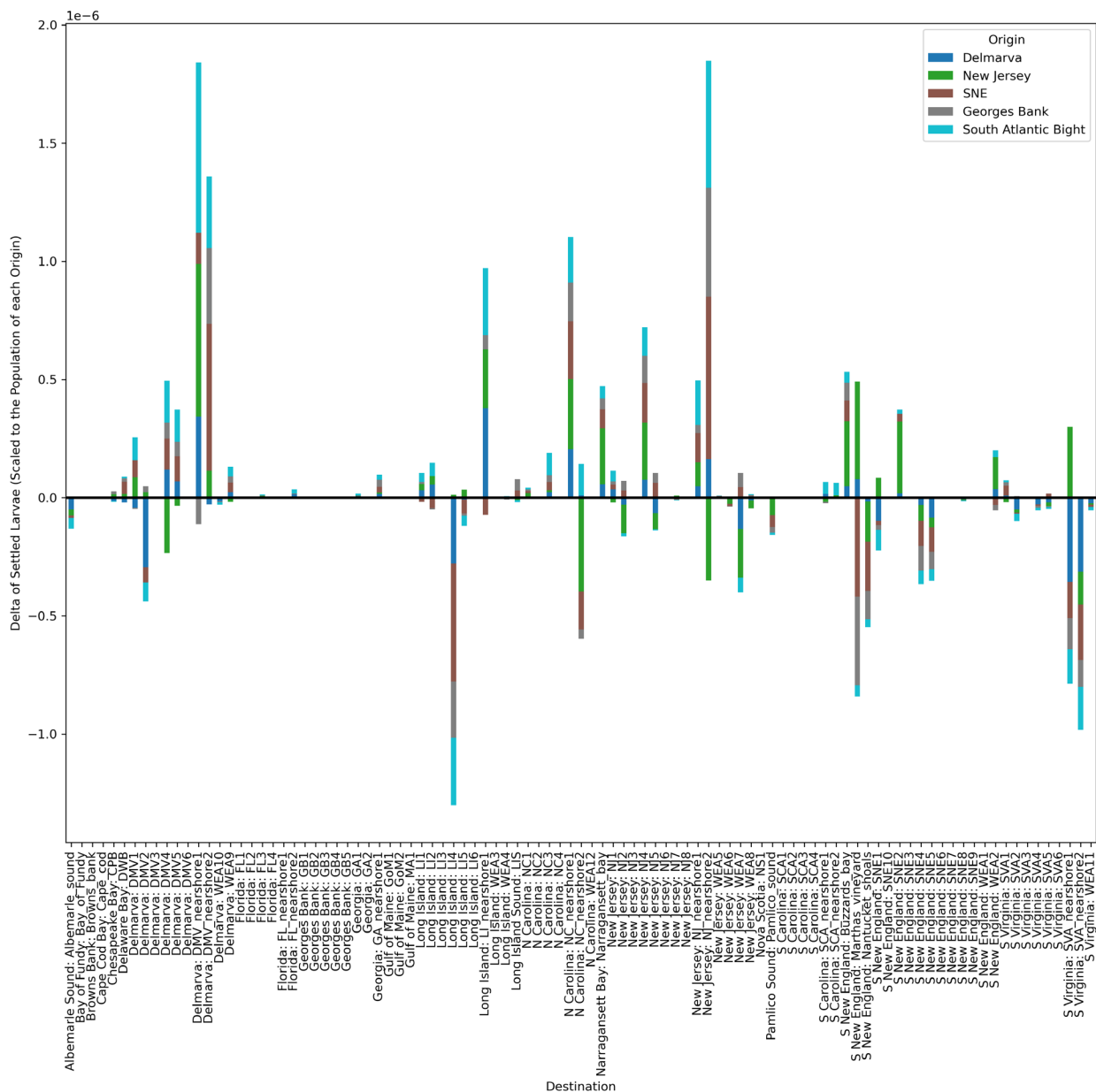


Figure C.106. Summer Flounder Connectivity Difference 2017

Bar chart shows the difference in summer flounder larvae settlement in each destination area, by origin for model year 2017. Bars are colored by origin area and results show the difference in export probabilities, i.e., the difference in the likelihood of settlement scaled to the number of larvae released from a particular origin region between the baseline and 15MW full build-out results. Bars below the x axis, show a decrease in settlement in a particular destination area, results above the x axis show an increase in a settlement in a destination area.

C.4 15 MW Partial Build-out

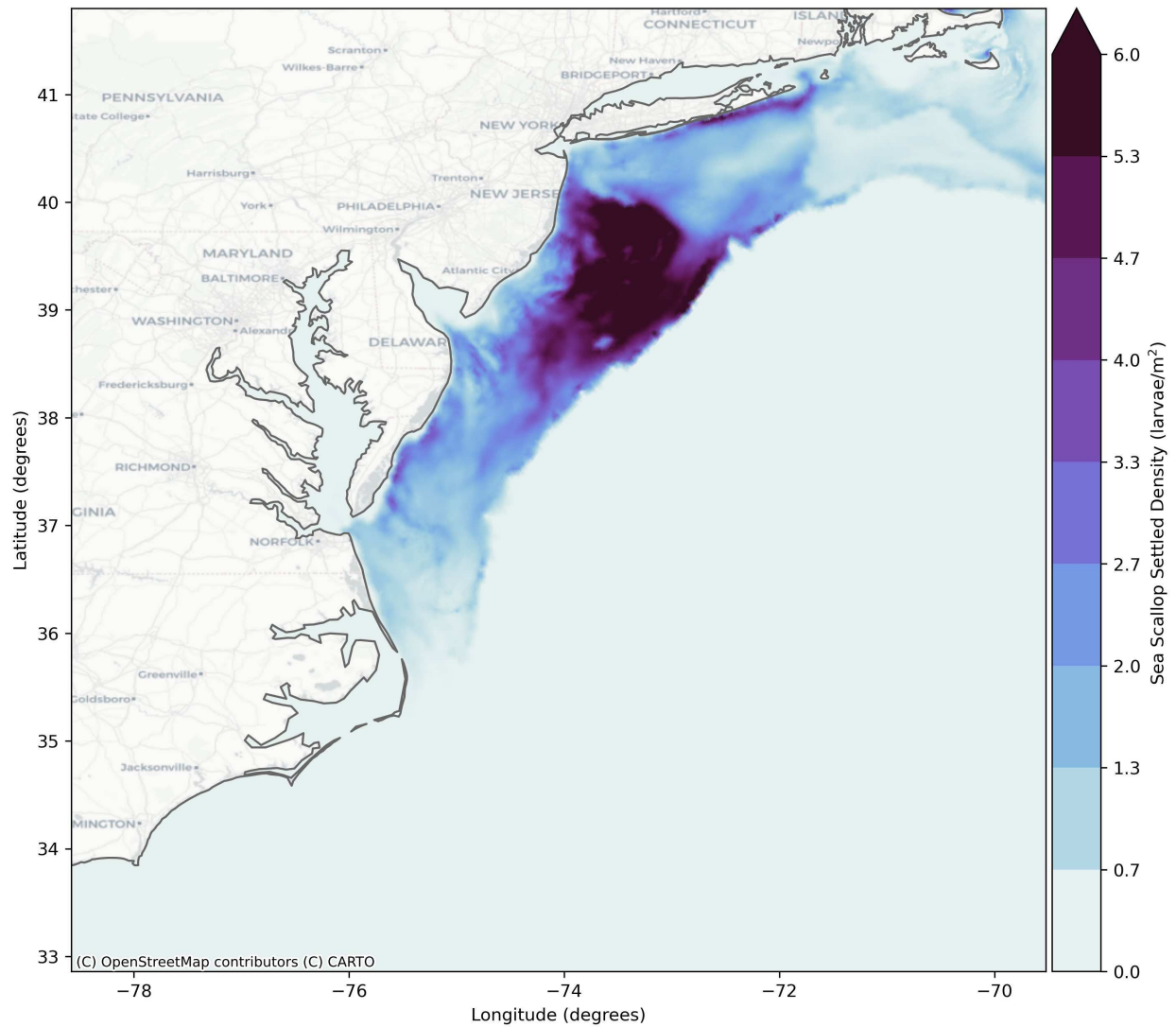


Figure C.107. Summer Flounder Baseline Settled Density for 15MW Partial Build-Out

C.4.1 Sea Scallop 2017

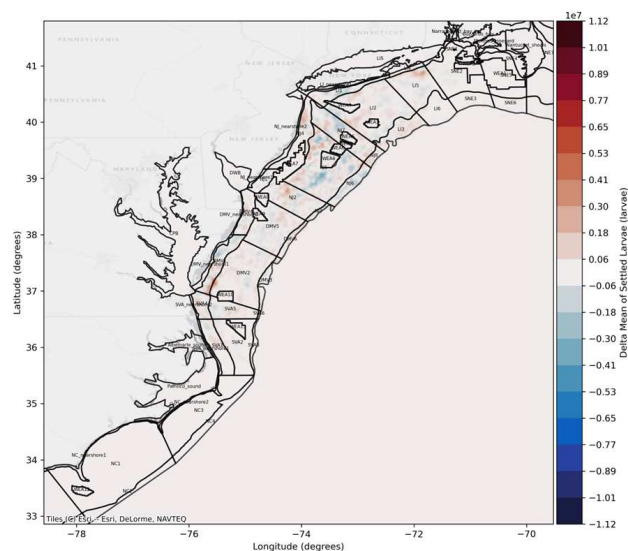


Figure C.108. Difference in Settled Larvae 15MW Partial Build-Out vs Baseline 2017

Difference in total sea scallop larvae settled larvae for model year 2017. Showing the difference in the mean of all ensemble baseline results and mean of all ensemble 15 MW partial build-out results. Settled larvae averaged for each model grid element. Red shows an increase in settlement in the 12 MW scenario compared to the baseline, blue shows a decrease in settlement compared to the baseline.

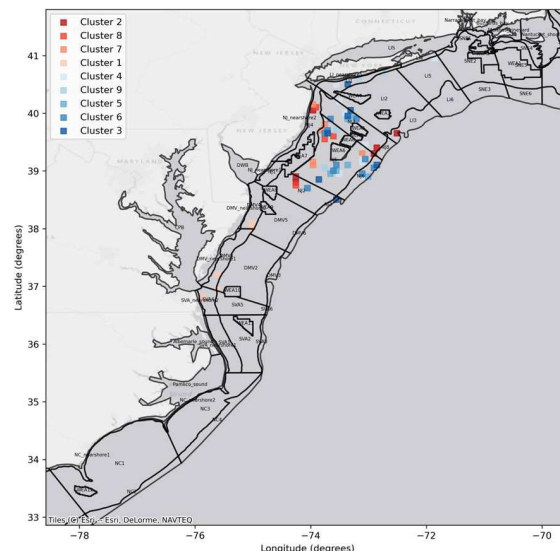


Figure C.109. DBSCAN (Density-Based Spatial Clustering of Applications with Noise) Difference in Settled Larvae 15MW Partial Build-Out vs Baseline 2017

Spatial clusters identified using DBSCAN to filter out noise from the difference plot and identify areas of greatest change. Clusters of settlement increase are identified in red and clusters with settlement decrease are shown in blue.

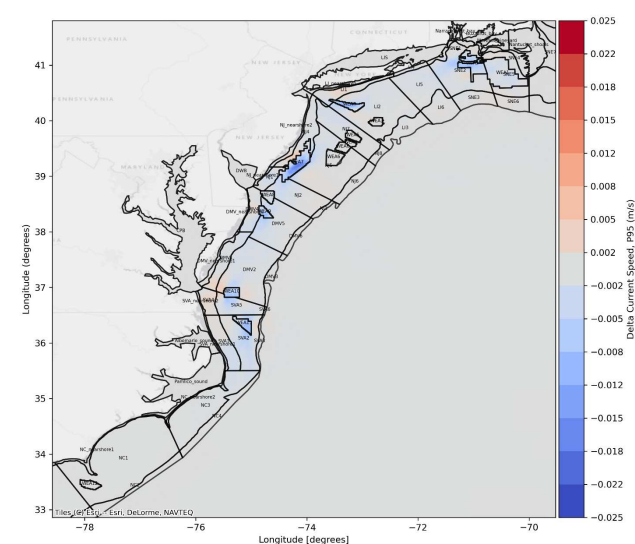


Figure C.110. Change in Current Speed 15MW Partial Build-Out vs Baseline 2017

Difference in the depth averaged current speed for model year 2017. Showing the difference in the 95th percentile non-exceedance probability baseline results and 95th percentile non-exceedance probability 15 MW partial build-out results.

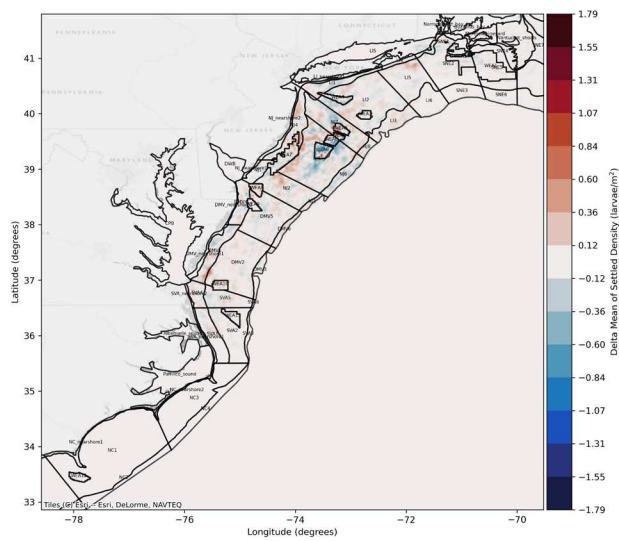


Figure C.111. Difference in Settled Density 15MW Partial Build-Out vs Baseline 2017

Difference in total sea scallop larvae settled larvae for model year 2017. Showing the difference in the mean of all ensemble baseline results and mean of all ensemble 15 MW partial build-out results. Settled larvae averaged for each model grid element. Red shows an increase in settlement in the 12 MW scenario compared to the baseline, blue shows a decrease in settlement compared to the baseline.

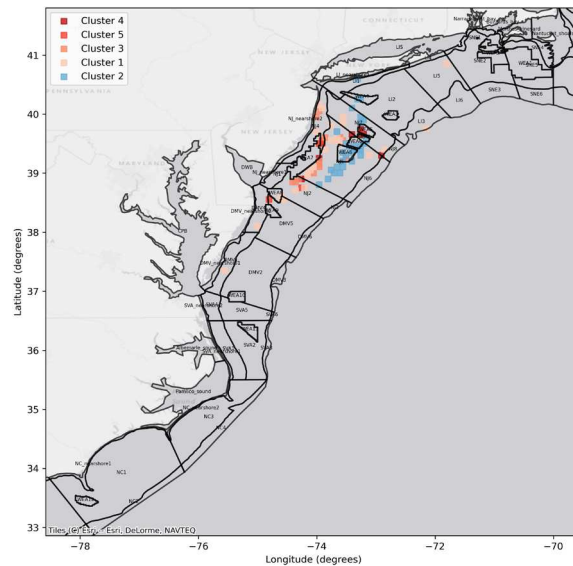


Figure C.112. DBSCAN (Density-Based Spatial Clustering of Applications with Noise) Difference in Settled Density 15MW Partial Build-Out vs Baseline 2017

Spatial clusters identified using DBSCAN to filter out noise from the difference plot and identify areas of greatest change. Clusters of settlement increase are identified in red and clusters with settlement decrease are shown in blue.

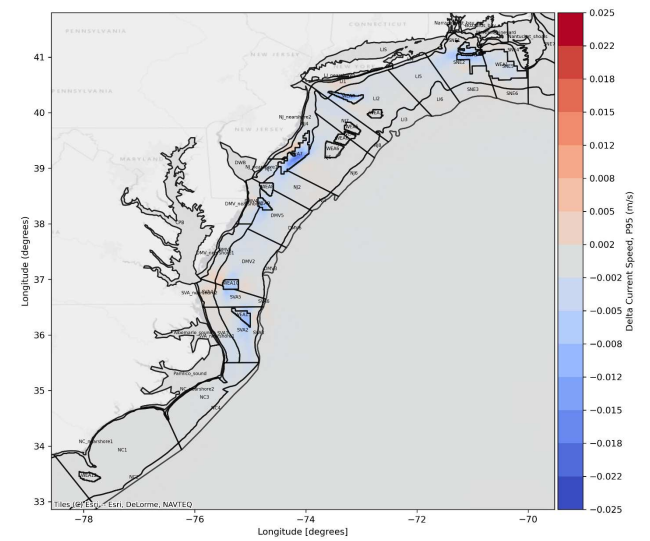


Figure C.113. Change in Current Speed 15MW Partial Build-Out vs Baseline 2017

Difference in the depth averaged current speed for model year 2017. Showing the difference in the 95th percentile non-exceedance probability baseline results and 95th percentile non-exceedance probability 15 MW partial build-out results.

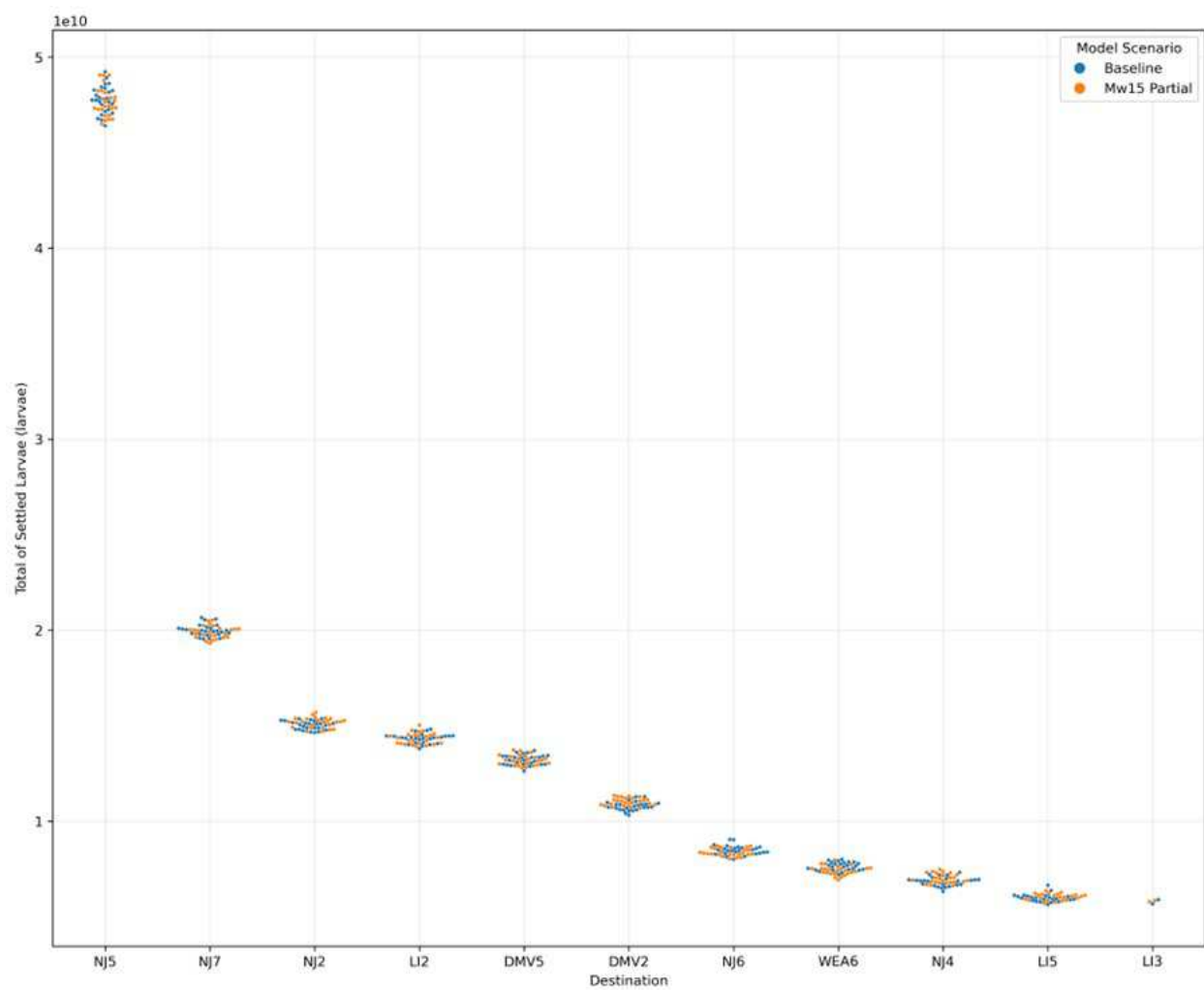


Figure C.115. Swarm Plot Showing Sea Scallop Settlement in Top 10 Destinations for 2017

Swarm plot shows the settlement for each model run of the ensemble (i.e., each point represents a model result) for 2017. Blue points show the baseline results and orange show the 15 MW partial build-out number of settled larvae in the top 10 destinations where there is greatest larval settlement.

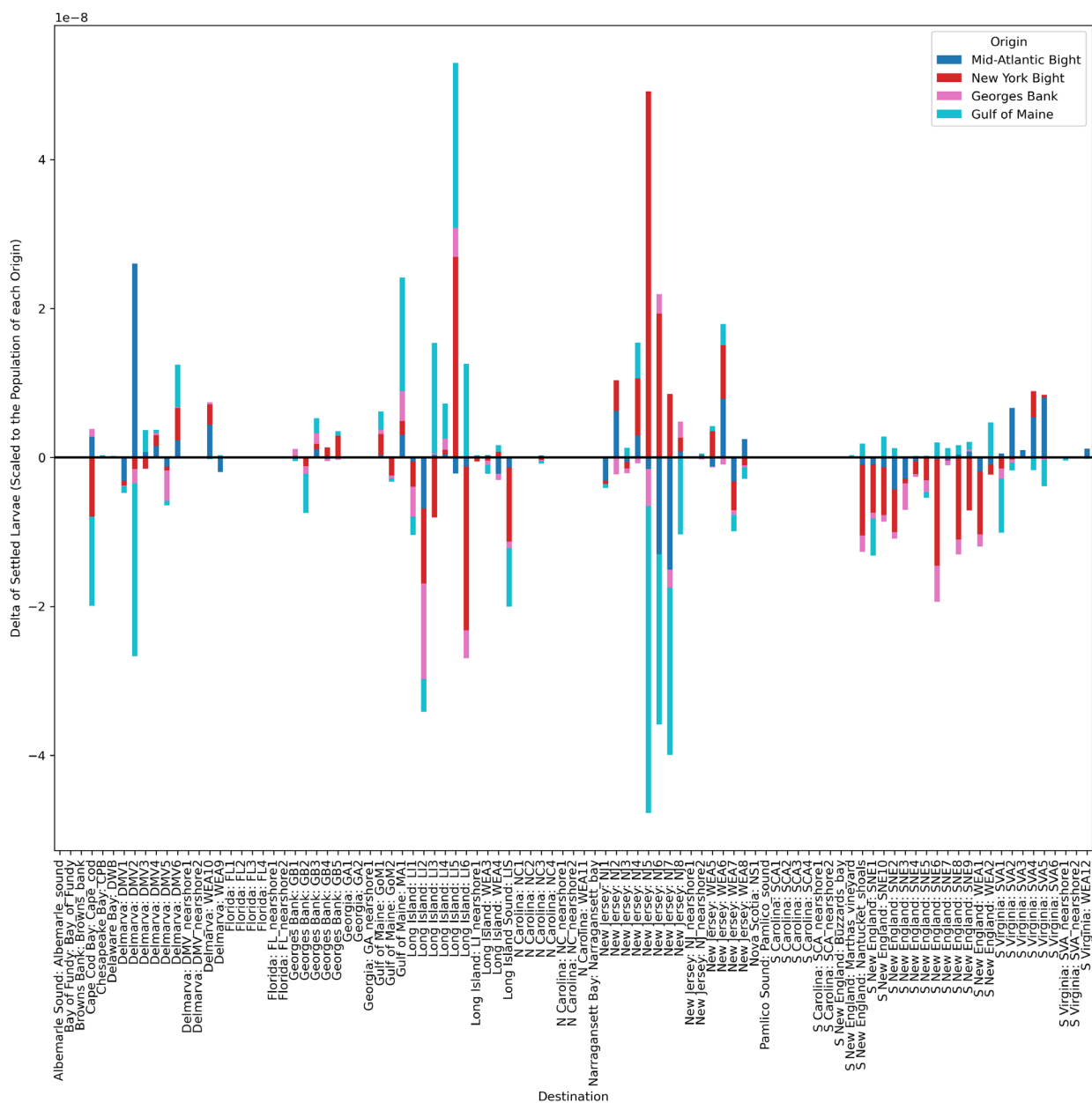


Figure C.116. Sea Scallop Connectivity Difference 2017

Bar chart shows the difference in sea scallop larvae settlement in each destination area, by origin for model year 2017. Bars are colored by origin area and results show the difference in export probabilities, i.e., the difference in the likelihood of settlement scaled to the number of larvae released from a particular origin region between the baseline and 15MW partial build-out results. Bars below the x axis, show a decrease in settlement in a particular destination area, results above the x axis show an increase in a settlement in a destination area.

C.4.2 Surf Clam 2017

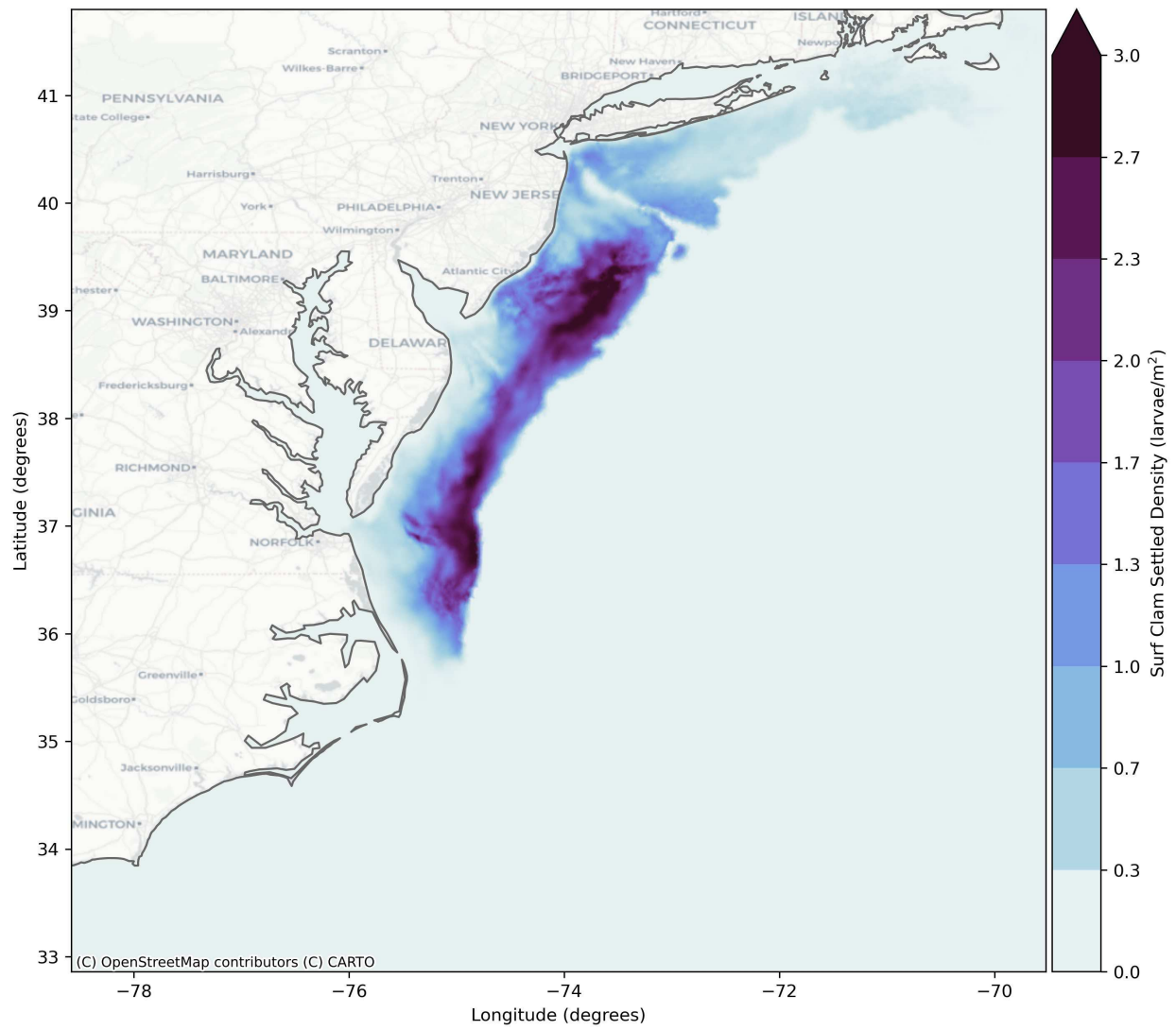


Figure C.117. Surf Clam Baseline Settled Density for 15MW Partial Build-Out

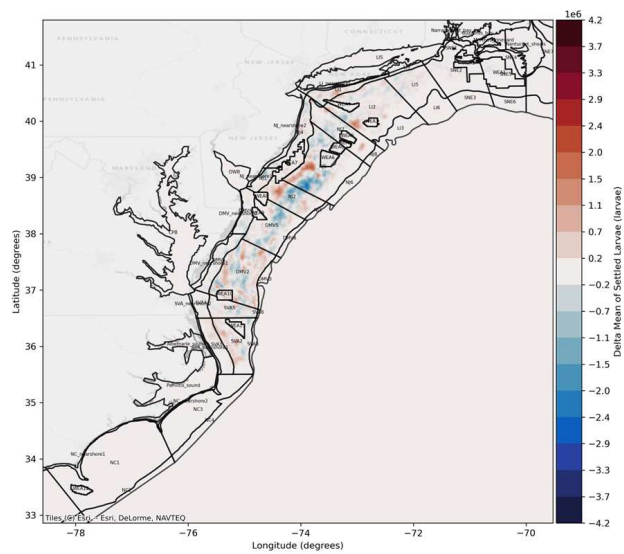


Figure C.118. Difference in Settled Larvae 15MW Partial Build-Out vs Baseline 2017

Difference in total surf clam larvae settled larvae for model year 2017. Showing the difference in the mean of all ensemble baseline results and mean of all ensemble 15 MW partial build-out results. Settled larvae averaged for each model grid element. Red shows an increase in settlement in the 12 MW scenario compared to the baseline, blue shows a decrease in settlement compared to the baseline.

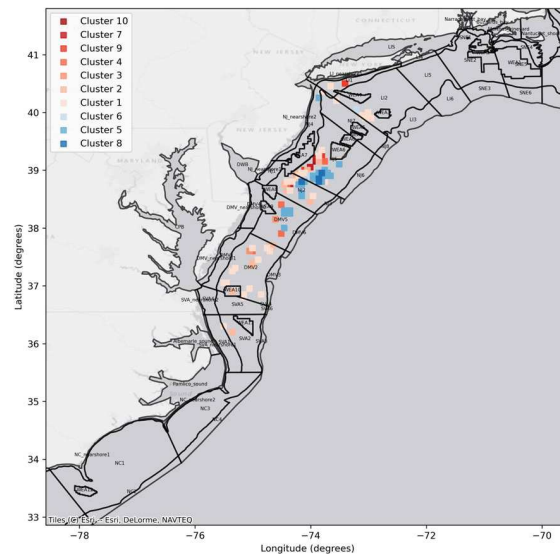


Figure C.119. DBSCAN (Density-Based Spatial Clustering of Applications with Noise) Difference in Settled Larvae 15MW Partial Build-Out vs Baseline 2017

Spatial clusters identified using DBSCAN to filter out noise from the difference plot and identify areas of greatest change. Clusters of settlement increase are identified in red and clusters with settlement decrease are shown in blue.

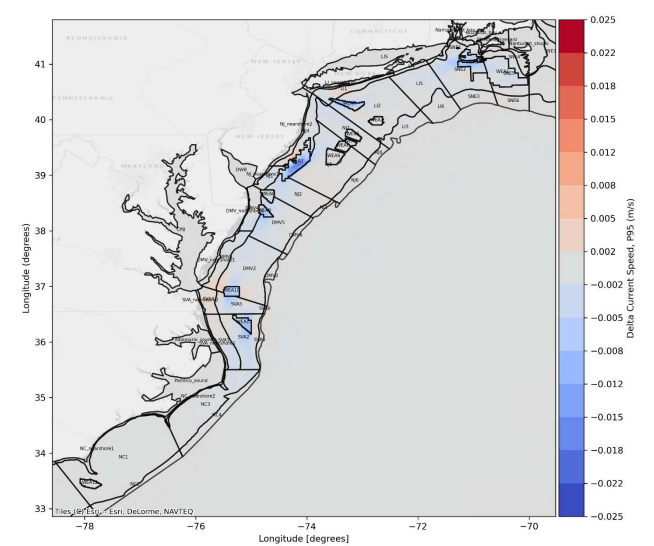


Figure C.120 Change in Current Speed 15MW Partial Build-Out vs Baseline 2017

Difference in the depth averaged current speed for model year 2017. Showing the difference in the 95th percentile non-exceedance probability baseline results and 95th percentile non-exceedance probability 15 MW partial build-out results.

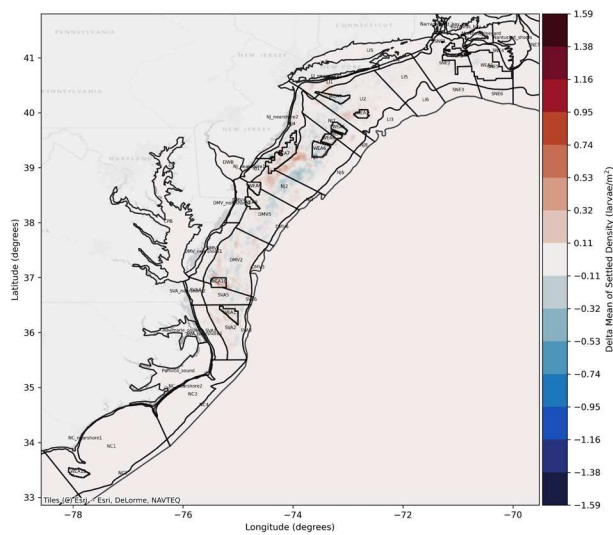


Figure C.121. Difference in Settled Density 15MW Partial Build-Out vs Baseline 2017

Difference in total surf clam larvae settled larvae for model year 2017. Showing the difference in the mean of all ensemble baseline results and mean of all ensemble 15 MW partial build-out results. Settled larvae averaged for each model grid element. Red shows an increase in settlement in the 12 MW scenario compared to the baseline, blue shows a decrease in settlement compared to the baseline.

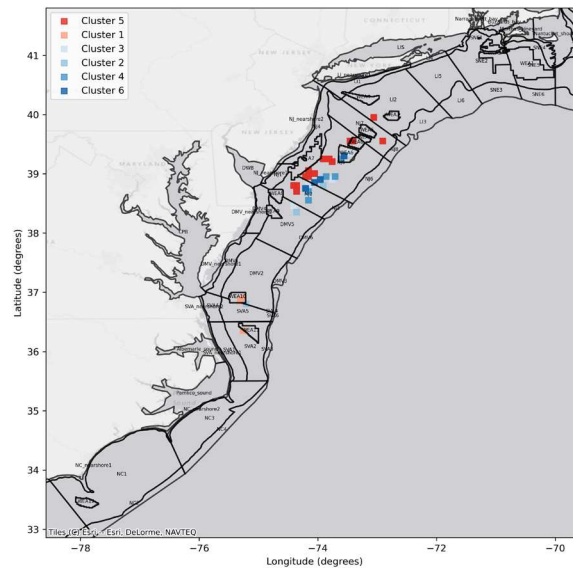


Figure C.122. DBSCAN (Density-Based Spatial Clustering of Applications with Noise) Difference in Settled Density 15MW Partial Build-Out vs Baseline 2017

Spatial clusters identified using DBSCAN to filter out noise from the difference plot and identify areas of greatest change. Clusters of settlement increase are identified in red and clusters with settlement decrease are shown in blue.

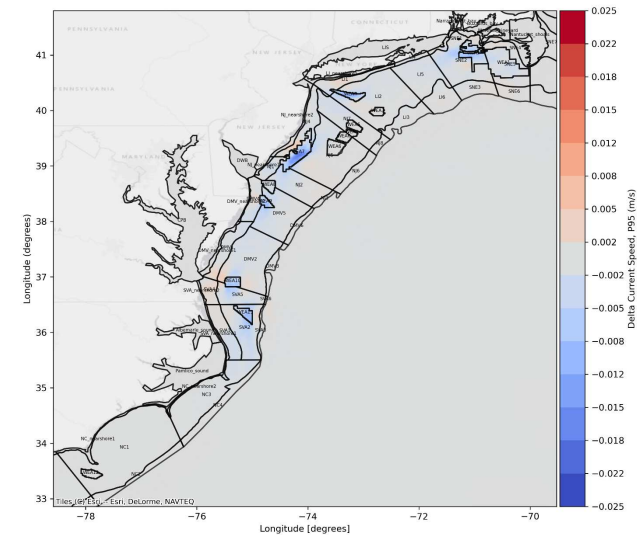


Figure C.123 Change in Current Speed 15MW Partial Build-Out vs Baseline 2017

Difference in the depth averaged current speed for model year 2017. Showing the difference in the 95th percentile non-exceedance probability baseline results and 95th percentile non-exceedance probability 15 MW partial build-out results.

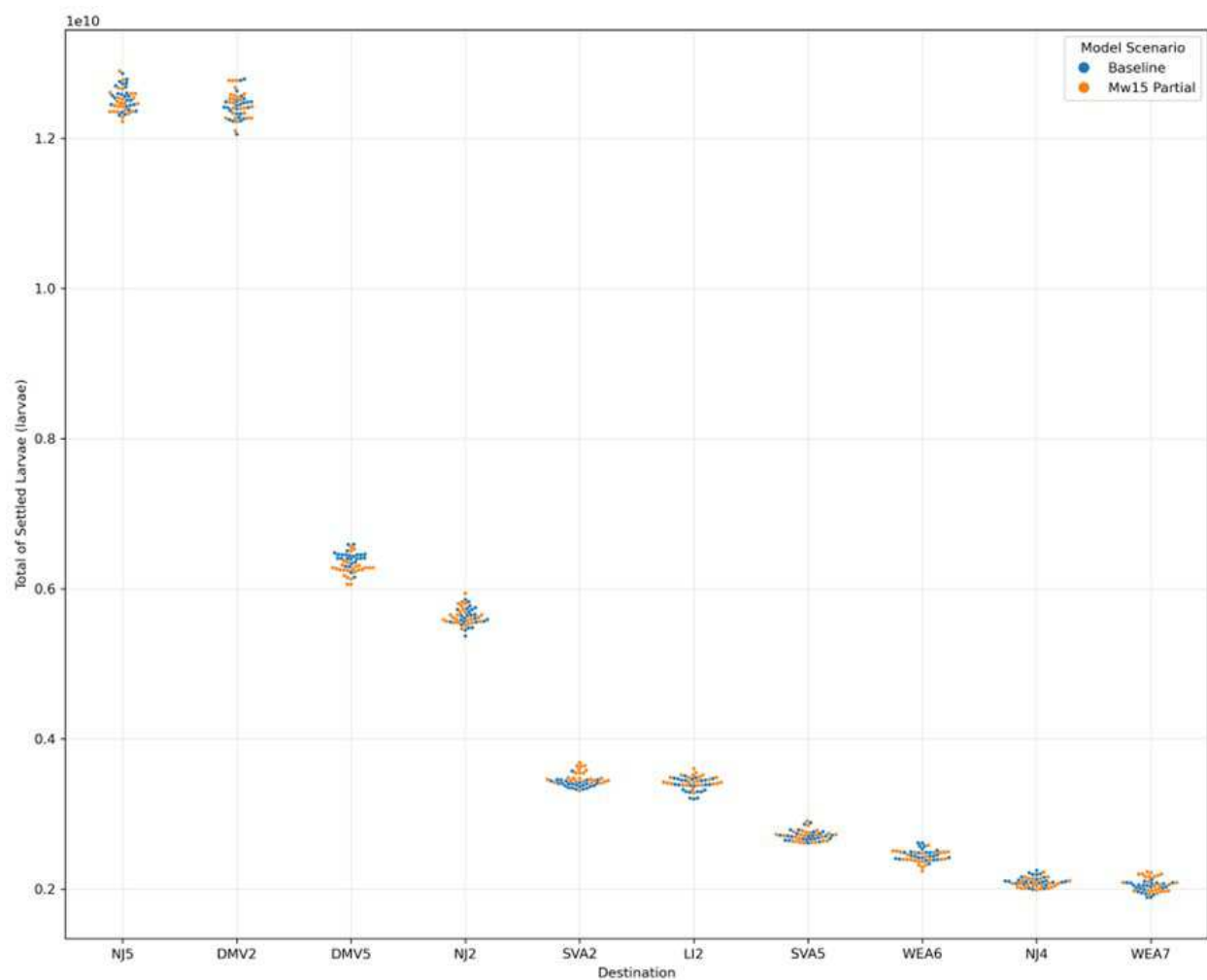


Figure C.125. Swarm Plot Showing Surf Clam Settlement in Top 10 Destinations for 2017
 Swarm plot shows the settlement for each model run of the ensemble (i.e., each point represents a model result) for 2017. Blue points show the baseline results and orange show the 15 MW partial build-out number of settled larvae in the top 10 destinations where there is greatest larval settlement.

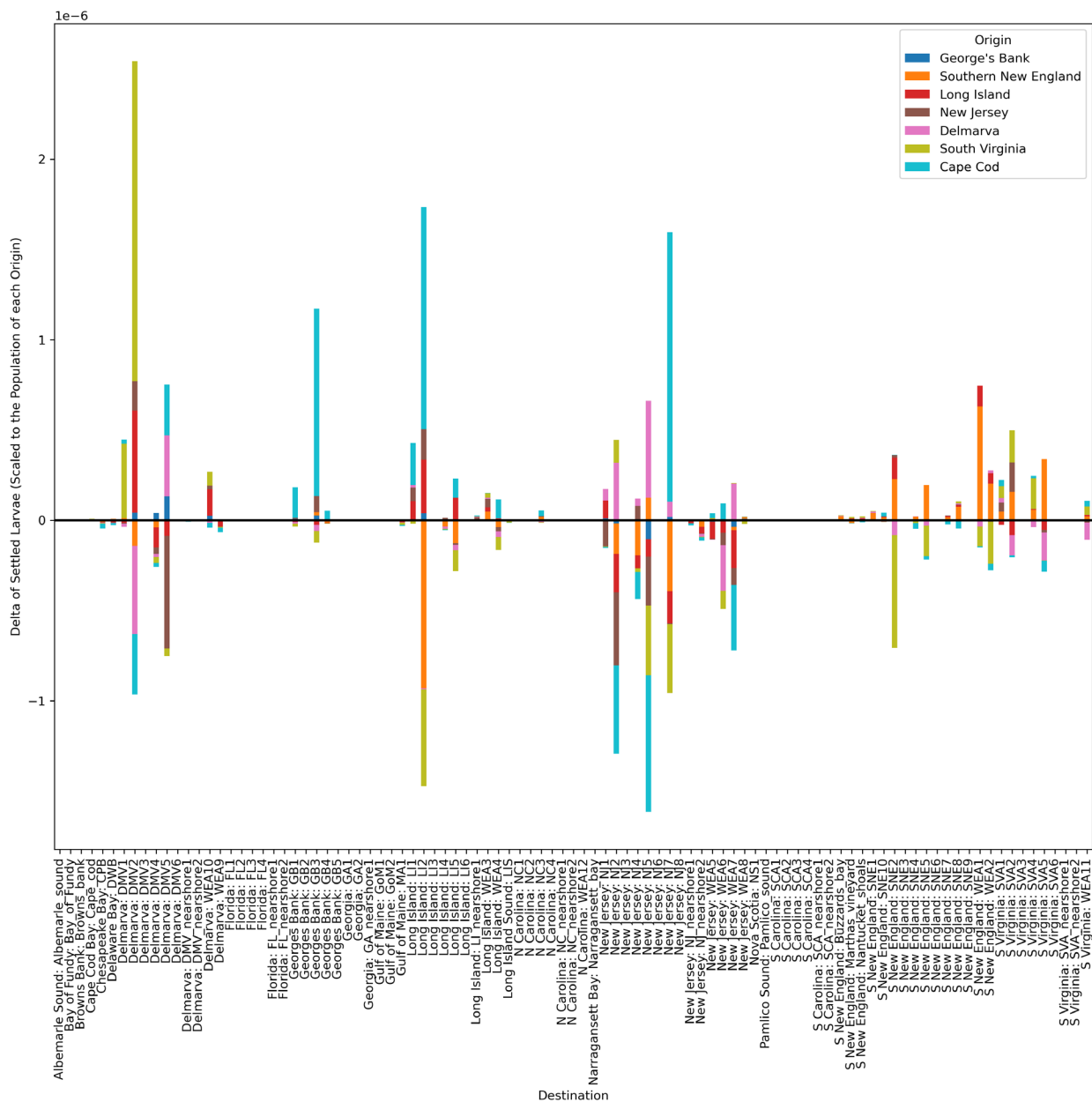


Figure C.126. Surf Clam Connectivity Difference 2017

Bar chart shows the difference in sea scallop larvae settlement in each destination area, by origin for model year 2017. Bars are colored by origin area and results show the difference in export probabilities, i.e., the difference in the likelihood of settlement scaled to the number of larvae released from a particular origin region between the baseline and 15MW partial build-out results. Bars below the x axis, show a decrease in settlement in a particular destination area, results above the x axis show an increase in a settlement in a destination area.

C.4.3 Summer Flounder 2017

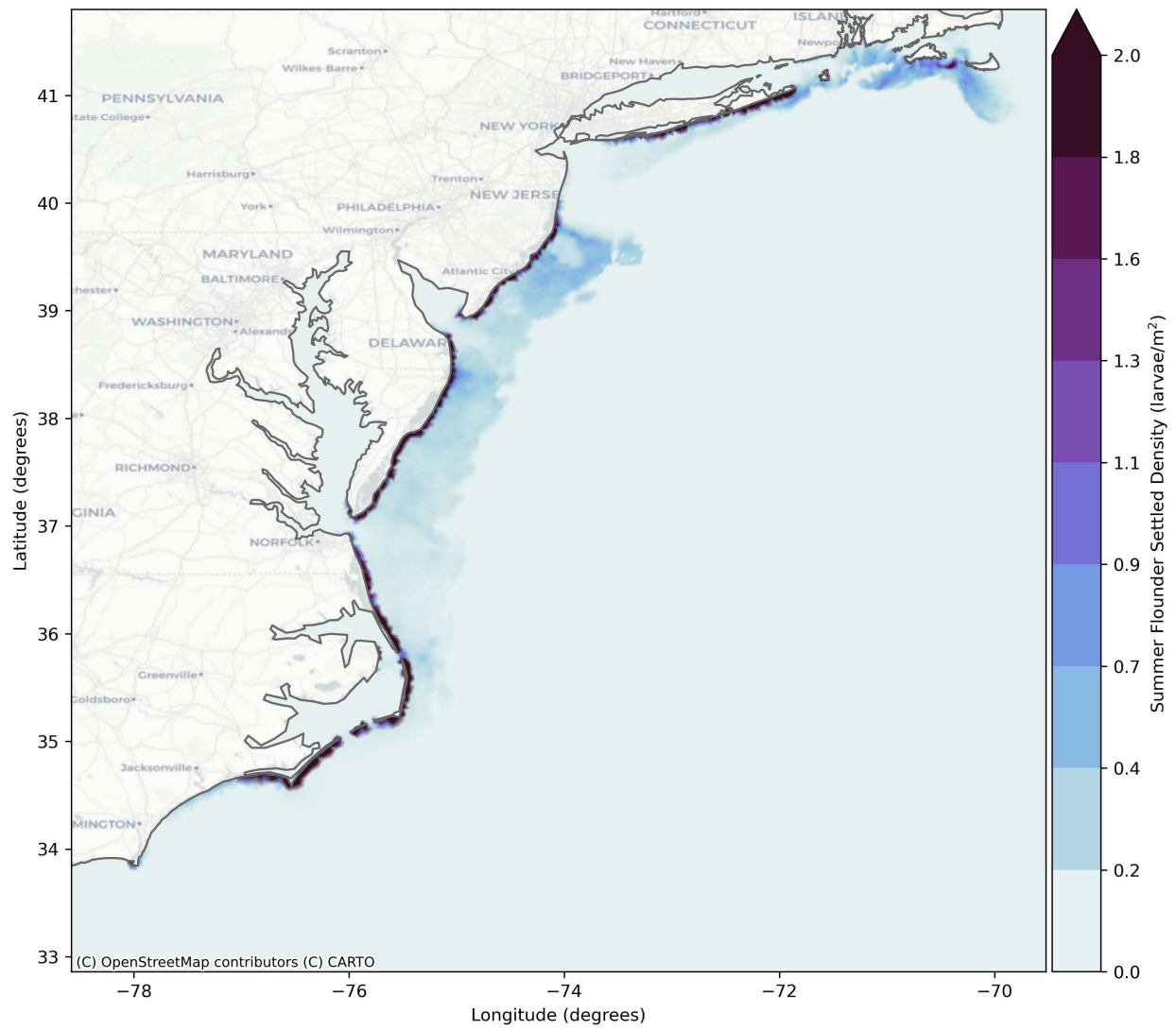


Figure C.127. Summer Flounder Baseline Settled Density for 15MW Partial Build-Out

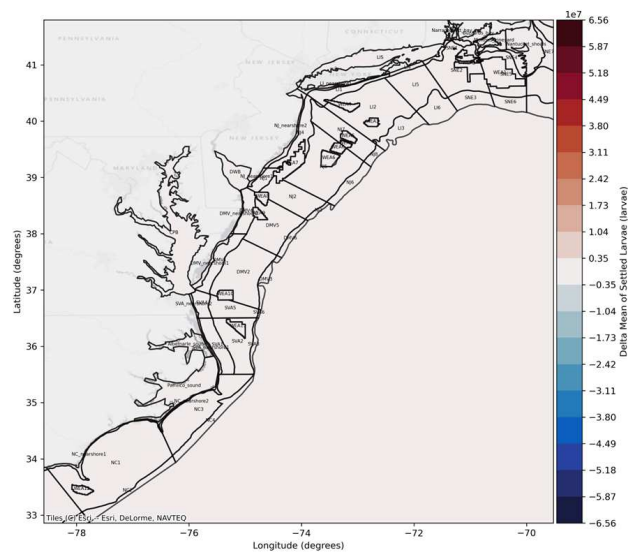


Figure C.128. Difference in Settled Larvae 15MW Partial Build-Out vs Baseline 2017

Difference in total summer flounder larvae settled larvae for model year 2017. Showing the difference in the mean of all ensemble baseline results and mean of all ensemble 15 MW partial build-out results. Settled larvae averaged for each model grid element. Red shows an increase in settlement in the 12 MW scenario compared to the baseline, blue shows a decrease in settlement compared to the baseline.

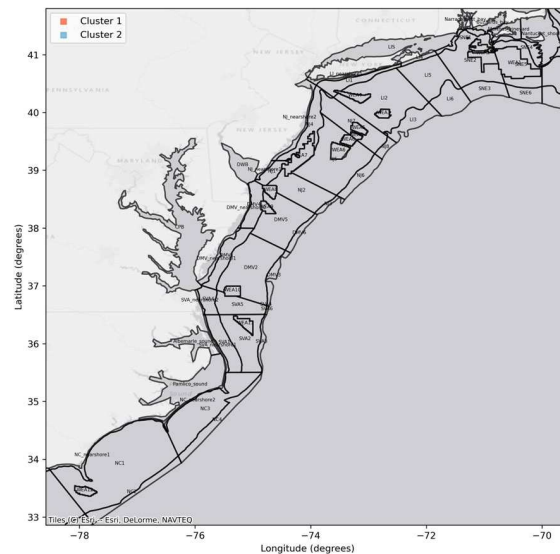


Figure C.129. DBSCAN (Density-Based Spatial Clustering of Applications with Noise) Difference in Settled Larvae 15MW Partial Build-Out vs Baseline 2017

Spatial clusters identified using DBSCAN to filter out noise from the difference plot and identify areas of greatest change. Clusters of settlement increase are identified in red and clusters with settlement decrease are shown in blue.

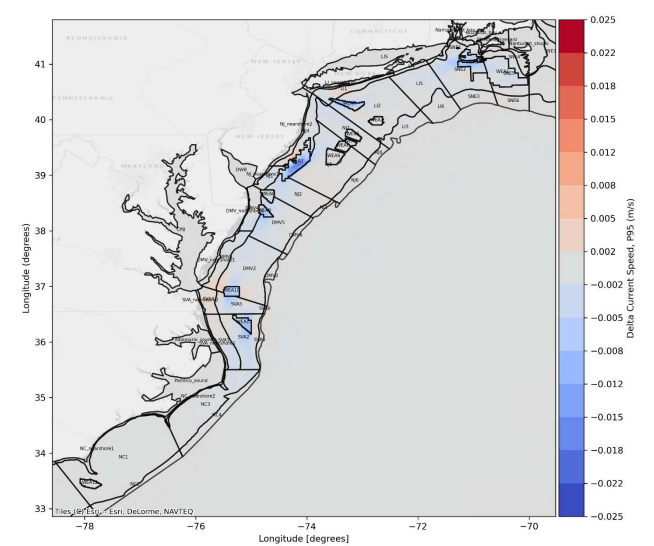


Figure C.130. Change in Current Speed 15MW Partial Build-Out vs Baseline 2017

Difference in the depth averaged current speed for model year 2017. Showing the difference in the 95th percentile non-exceedance probability baseline results and 95th percentile non-exceedance probability 15 MW partial build-out results..

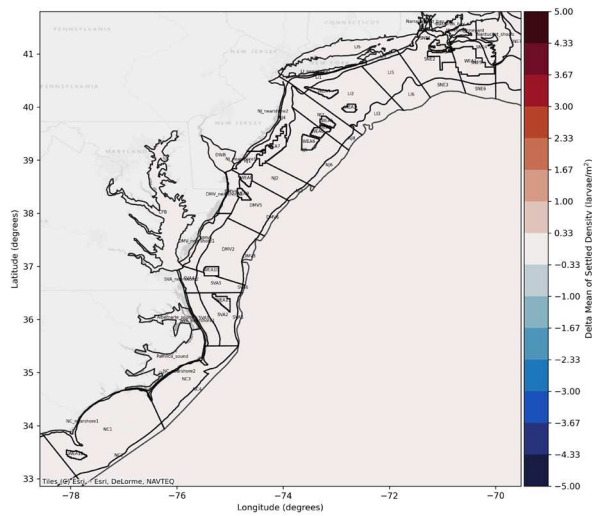


Figure C.131. Difference in Settled Density 15MW Partial Build-Out vs Baseline 2017

Difference in total summer flounder larvae settled larvae for model year 2017. Showing the difference in the mean of all ensemble baseline results and mean of all ensemble 15 MW partial build-out results. Settled larvae averaged for each model grid element. Red shows an increase in settlement in the 12 MW scenario compared to the baseline, blue shows a decrease in settlement compared to the baseline.

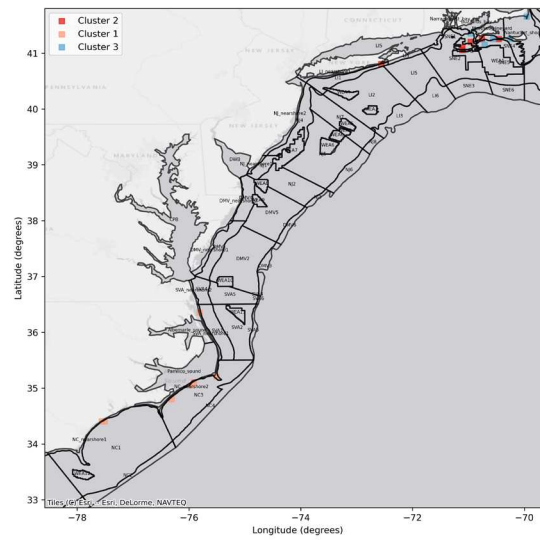


Figure C.132. DBSCAN (Density-Based Spatial Clustering of Applications with Noise) Difference in Settled Density 15MW Partial Build-Out vs Baseline 2017

Spatial clusters identified using DBSCAN to filter out noise from the difference plot and identify areas of greatest change. Clusters of settlement increase are identified in red and clusters with settlement decrease are shown in blue.

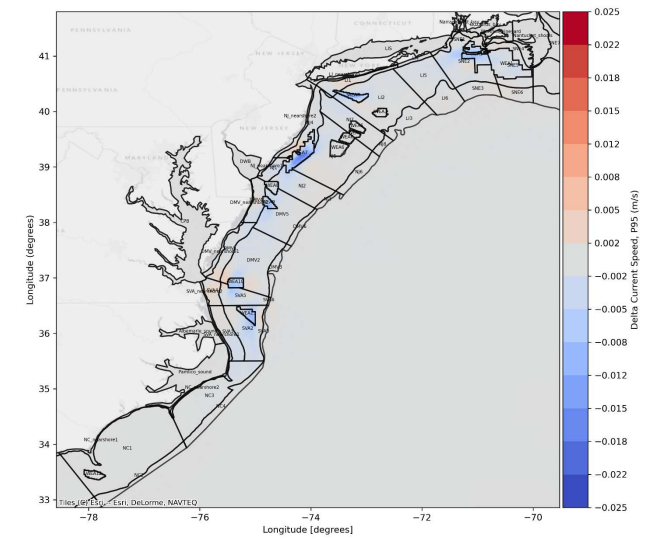


Figure C.133. Change in Current Speed 15MW Partial Build-Out vs Baseline 2017

Difference in the depth averaged current speed for model year 2017. Showing the difference in the 95th percentile non-exceedance probability baseline results and 95th percentile non-exceedance probability 15 MW partial build-out results.

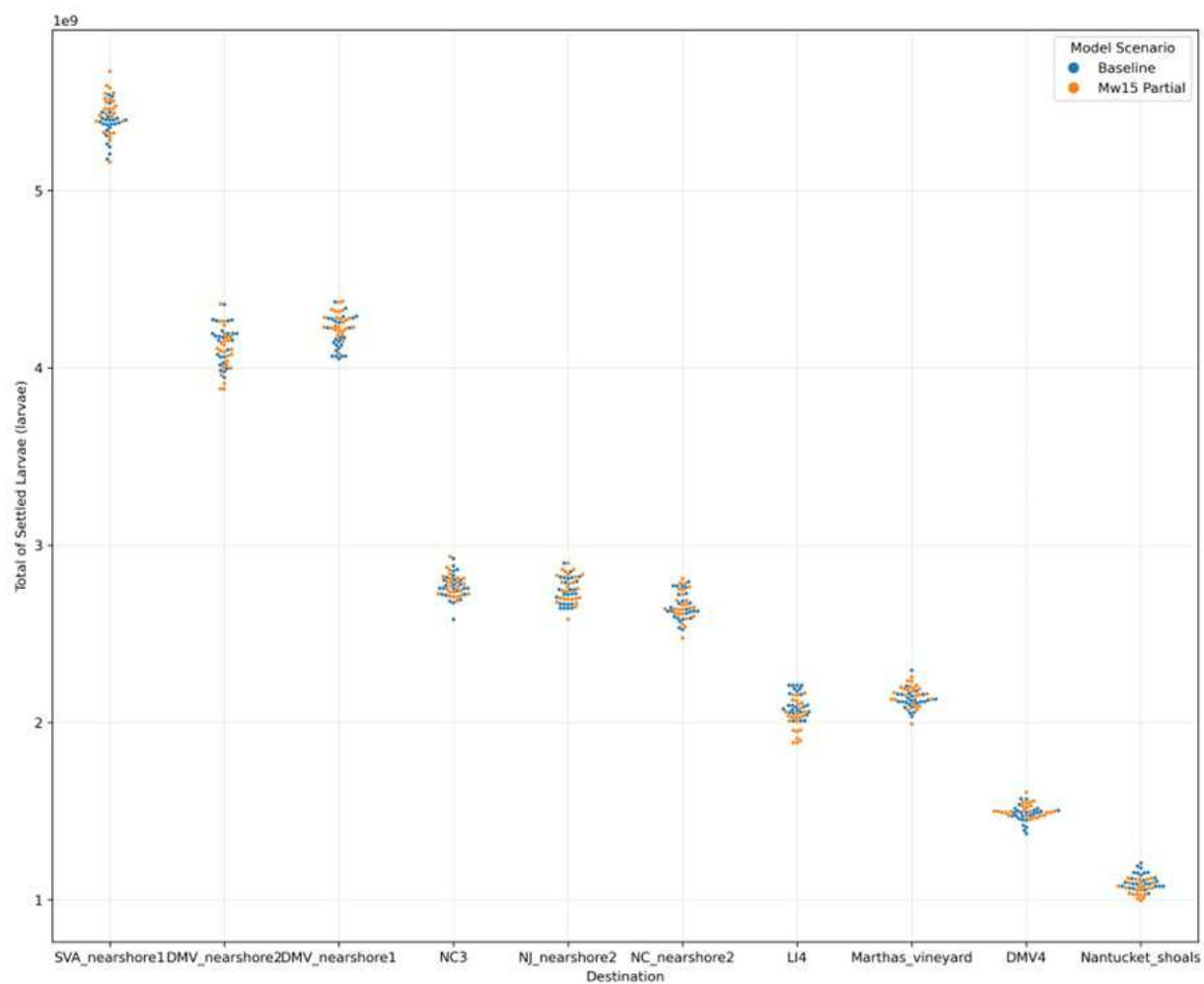


Figure C.135. Swarm Plot Showing Summer Flounder Settlement in Top 10 Destinations for 2017
 Swarm plot shows the settlement for each model run of the ensemble (i.e., each point represents a model result) for 2017. Blue points show the baseline results and orange show the 15 MW partial build-out number of settled larvae in the top 10 destinations where there is greatest larval settlement.

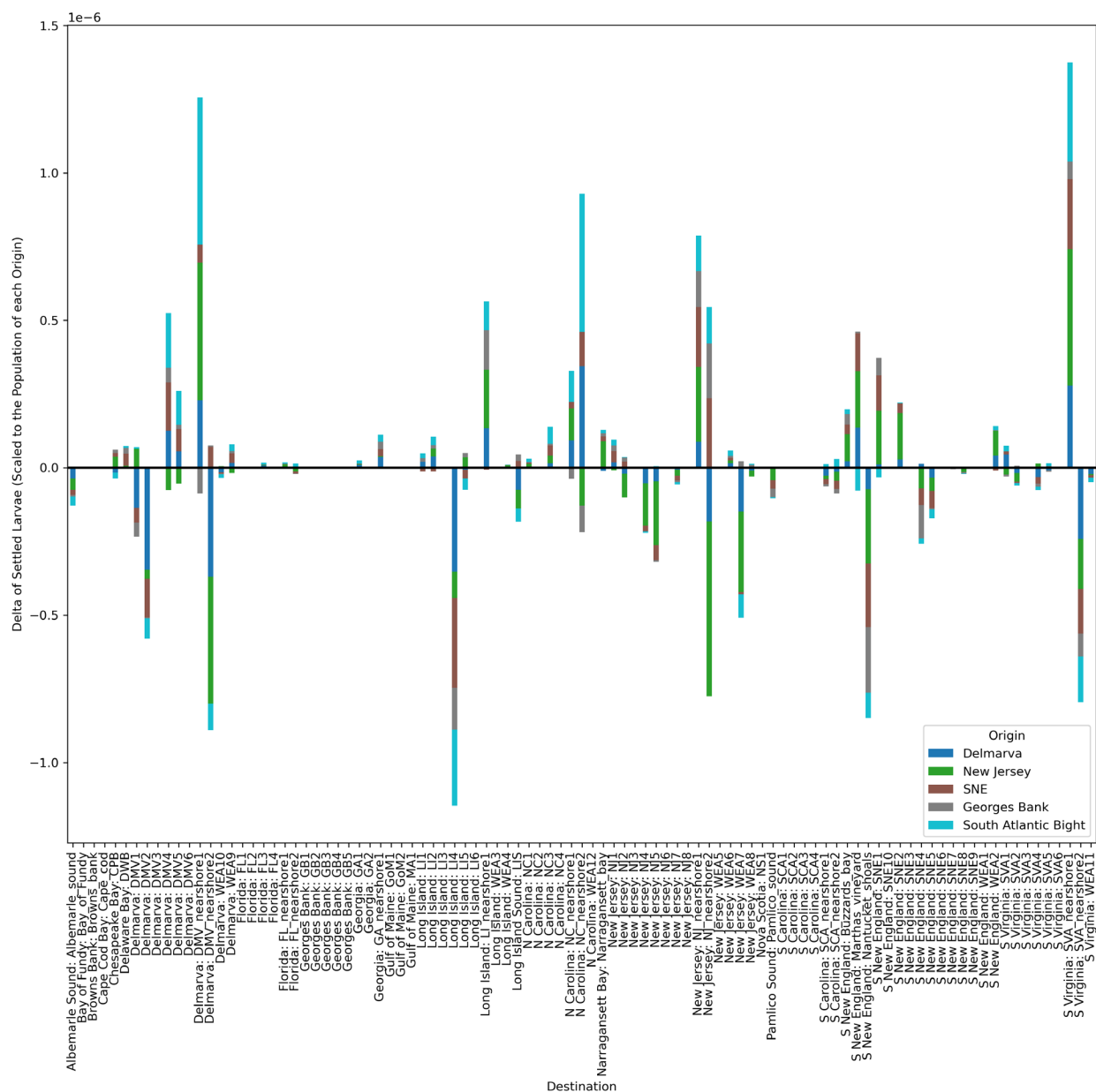


Figure C.136. Summer Flounder Connectivity Difference 2017

Bar chart shows the difference in summer flounder larvae settlement in each destination area, by origin for model year 2017. Bars are colored by origin area and results show the difference in export probabilities, i.e., the difference in the likelihood of settlement scaled to the number of larvae released from a particular origin region between the baseline and 15MW partial build-out results. Bars below the x axis, show a decrease in settlement in a particular destination area, results above the x axis show an increase in a settlement in a destination area.

Appendix D: Connectivity Mapping Overview, Design Concepts and Details (ODD) Protocol

D.1 Destination Area Mapping

This section provides an overview of how the destination maps were developed and the rationale for choosing certain delineations.

D.1.1 Shellfish Specific Destinations

The Northeast Fisheries Science Center (NEFSC) conducts periodic surveys of abundance, biomass, length, and weight of various fisheries pertinent shellfish along the continental shelf region of the East Coast. NEFSC shellfish survey data is divided by regions historically used for assessment of survey, fishery, and stock distribution patterns. These areas are Georges Bank (GB), Southern New England (SNE), Long Island (LI), New Jersey (NJ), Delmarva (DMV), and South Virginia (SVA). These regions are further divided into subareas, or “strata”, which are defined by depth in Jacobson and Hennen, 2019. Of these depth-defined strata, there are inshore strata which begin from the state water boundary along the 9 m isobath, and near-shelf strata which cover depths between 73 – 110 m (Jacobson and Hennen, 2019).

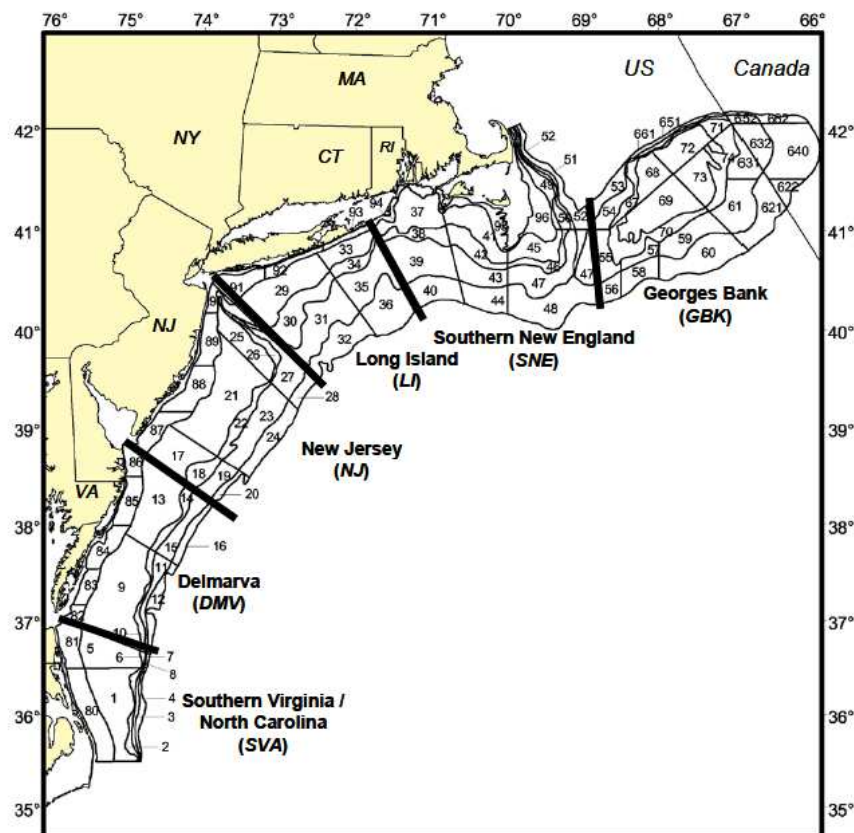


Figure D.1. NEFSC Shellfish Regions, for Atlantic Surf Clam, Ocean Quahog, and Atlantic Sea Scallop Surveys

(From Jacobson and Hennen, 2019)

Where there is spatial overlap, destination units on the NEFSC shellfish strata were grouped into the six larger regions historically used for stock assessments (GB, SNE, LI, NJ, DMV and SVA). The six regions were considered too broad, while the original NEFSC strata were too detailed for the purpose of assessing OSW related impacts on larval distribution and settlement. The destination map was therefore tailored to be specifically useful for this assessment of OSW impacts. The destination map requires greatest resolution within and near to the WEAs to allow for the potential localized impacts of the OSW development to be assessed. The destination map is therefore based on modified NEFSC strata, with the addition of WEAs as individual destination units.

NEFSC strata were combined along bathymetry isolines while maintaining regional delineations, and each region was required to have at least two destinations per bathymetric category. Strata were merged between 10 m and 20 m, 20 m and 70 m and 70 m and 110 m, and additional destinations were created (i.e., not based on strata) between 10 m and the shoreline, to create four bathymetric categories. These depth categories were chosen to provide greater resolution in the nearshore and offshore areas. The nearshore is of particular interest for summer flounder, while near-shelf destinations were included to capture any increased transport of shellfish larvae towards the shelf. The 20 m – 70 m zone was created to capture the high densities of surf clam and sea scallop larval settlement within these areas, while the division of regions along the strata delineations perpendicular to the shoreline provide adequate resolution for the analysis.

Full WEAs were included as individual destination units, with no further delineation by leasing state or individual lease. Where WEAs intercept strata, WEAs were either divided, or left intact and the underlying strata dissolved, depending on the resulting size of the WEA after division. Where a division of a WEA along a strata boundary would result in a destination unit with an area less than 200 km², the WEA was kept intact. In the case of the New York-New Jersey WEA that includes five separate areas across three strata and two regions, these were divided by strata, resulting in WEA3, 5, and 6.

Where there is no spatial overlap between the NEFSC shellfish strata and potential shellfish larval settling areas, state-based regions were created. Cape Cod was included as a separate destination. The Massachusetts region is one destination which extends along the shelf to the 110 m isobath, to be consistent with the rest of the destination map; and because this is where the shelf area ends, and settlement is no longer expected. Destination units to the North of this area within the Gulf of Maine and into Canadian waters have been coarsely defined as these are well beyond the WEA study areas.

D.1.2 Summer Flounder Specific Destinations

To the south of SVA, the destination map becomes specific to Summer Flounder. Destinations are continued to be divided by bathymetry (along the shoreline to 10 m and between 70 m and 110 m) for consistency. Destination units are assigned to regions grouped by state. Summer flounder larvae move inshore to settle, making the nearshore (shoreline to 10 m) destinations most important for this species. Summer Flounder also settle in estuaries, and each estuary resolved within the model domain has been defined as a unique destination unit.

D.1.3 Additional Areas for Qualitative Analysis

The following additional areas were not included as specific destination units but were compared to settlement difference maps to allow for further analysis and the discussion of implications of any impacts identified. These areas are shown and their relevance discussed in Section 9.1.4. in the main report.

D.1.3.1 Areas of Intense Fishing Activity

To identify areas of intense fishing activity, data from Vessel Monitoring System (VMS) programs for bottom trawl, sea scallop and surf clam fishing activities were mapped. VMS data were available from National Marine Fisheries Service (NMFS) for Surf clam, Sea Scallop, multispecies trawl, monkfish, and general trawl (> 65 ft and < 65 ft). Areas classified as ‘very high use’ and ‘high use’ were associated with cells taken from the Northeast Fishery Science Center shellfish survey grid. Sea Scallop Rotational Closure Areas

To curb overfishing of sea scallops, NMFS uses a rotational spatial closure program. This management practice essentially closes broad areas of the shelf to scallop dredging to protect adult spawning stocks (Hart et al, 2020). Spawning adults will broadcast eggs and larvae from these closed areas with some portion being transported beyond closure boundaries and replenishing the adjacent, fished areas (Hart et al, 2020). Closed areas would also represent favorable settlement habitats as they would not be subjected to effects of mobile fishing gear described above. Areas closed to Sea scallop fishing may also benefit larval survival and spawning of surf clams and summer flounder and would be considered sources rather than sinks.

D.1.3.2 Summer Flounder Habitat Areas of Particular Concern

Some areas are protected by Magnuson-Stevens Act Essential Fish Habitat (EFH). Habitat Areas of Particular Concern (HAPCs) are a subset of EFH that deserve special attention because they provide extremely important ecological functions and/or are extremely vulnerable to degradation. Relevant to this project is the HAPC developed to protect habitat used by juvenile summer flounder (NMFS). The formal definition of the summer flounder HAPC is as follows:

“All native species subaquatic vegetation (SAV), including macroalgae, seagrasses, and freshwater and tidal macrophytes in any size bed, as well as loose aggregations, within adult and juvenile summer flounder EFH is HAPC. If native species of SAV are eliminated then exotic species should be protected because of functional value; however, all efforts should be made to restore native species.”

These areas would permit settling larvae of summer flounder afford some protection of habitat associated with seagrass meadows in inland waters. Summer flounder HAPC affords protection of inshore nursery habitat along the entire modeling domain from Long Island Sound, New York to the St. Johns River, Florida.

D.2 References

Jacobson L, Hennen D. 2019. Northeast Fisheries Science Center Improving the NEFSC Clam Survey for Atlantic Surfclams and Ocean Quahogs. Available from: <http://www.nefsc.noaa.gov/publications/>.